# Asymmetric Y-branch Plastic Optical Fiber Coupler

**A. A. Ehsan[1], S. S. Shaari[1], and M. K. Abd Rahman[2]**

[1]Institute of Microengineering & Nanoelectronics
Universiti Kebangsaan Malaysia, Bangi, Selangor, Malaysia
[2]Faculty of Applied Science, Universiti Teknologi MARA
Shah Alam, Selangor, Malaysia

**Abstract**— Asymmetric Y-branch plastic optical fiber (POF) coupler based on metal- and acrylic-based substrates have been developed. The POF coupler devices utilized two optical designs: a Y-branch structure and an attenuation technique based on lateral displacement of two fibers. The Y-branch designs are based on two waveguide taper structures namely the hollow waveguide taper and the high index contrast waveguide taper. The non-symmetrical coupling ratios are obtained by attenuation due to the lateral displacement of two adjoining fibers at the output port. Fabrication of the device is done by producing the device structures on a metal and acrylic blocks using high speed CNC machining tool. The coupling ratio of the fabricated metal-based coupler ranges from 14.23% to 85.77% with excess loss varies from 6.3 dB to 8.33 dB. Similarly, the fabricated acrylic-based device has coupling ratio ranges from 8.01% to 91.99% with excess loss varying from 5.42 dB to 7.64 dB.

## 1. INTRODUCTION

Large core optical fiber such as Plastic Optical Fiber (POF) is a well known medium for optical data communication due to its highly large-core size, multimode properties, low cost and robust characteristics. The Y-branch couplers are the simplest and cheapest type optical splitting device constructed by polishing two fibers and gluing them together. Nevertheless, the coupling ratio is fixed at 50 : 50 ratio and non-symmetrical coupling ratio and variable type couplers would be difficult to manufacture.

Planar-based waveguide symmetrical coupling ratio Y-branch couplers have been reported by H. Mizuno et al. [1], T. Klotzbuecher et al. [2] and Y. Takezawa et al. [3] with large core sizes (1000 μm). These devices utilized mold inserts which have been fabricated using hot embossing, laser-LIGA and injection molding techniques. However, all of these devices required expensive production equipment and in-factory precision assembly tools. In addition to the symmetrical coupling ratio couplers, there have been several reported designs on the non-symmetrical coupling ratio couplers. S. Suzuki et al. [4] and H. B. Lin et al. [5] reported singlemode asymmetric Y-branch coupler whereas H.Kurokawa et al. [6] and J. D. Love et al. [7] reported multimode version of the asymmetric coupler. The device reported by S. Suzuki is a Y-branch coupler with the center axis of the branching output waveguide and that of the taper waveguide shifted from each other. The asymmetric coupler proposed by H. B. Lin et al. used microprisms where the power-splitting ratio is controlled by varying the lengths of prisms. The multimode device by H. Kurokawa uses mirror-finished reflection at the reflecting surface of the waveguide to divide the optical power, independent of the branch corner. J. D. Love's asymmetric multimode Y-junction splitter is a wavelength independent device where the power splitting ratio is controlled by the geometry size of the output branch.

The work demonstrated in this paper showed how metal- and acrylic-based asymmetric Y-branch POF couplers can be implemented using a single structured Y-branch. The new proposed device will reduce the cost of having separate and bulky external variable attenuators attached to a standalone symmetrical Y-branch coupler. The POF devices are constructed using both metal and acrylic substrate materials. Two optical designs are used for device construction: a waveguide taper and simple attenuation technique based on lateral displacement of two fibers for the non-symmetrical coupling ratios. The waveguide taper are based on two unique designs namely the a hollow waveguide taper [8] and the high index contrast waveguide taper [9]. Devices have been modelled using non-sequential ray tracing technique and then fabricated using CNC machine.

## 2. DEVICE DESIGN

The design of the asymmetric coupler is based on a simple Y-branch structure. The non-symmetrical coupling ratio is obtained using this structure by using a simple concept o attenuation caused by

Figure 1: Generic Y-branch coupler with movable output fibers.



(a)             (b)             (c)
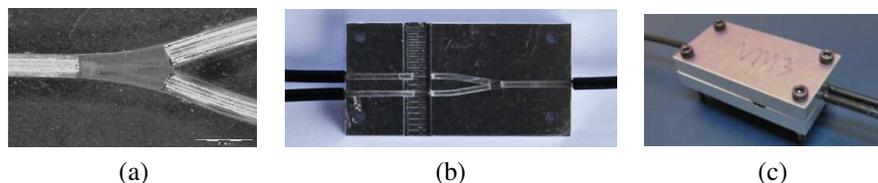
Figure 2: Fabricated components for metal-based coupler (a) hollow waveguide taper structure, (b) assembled device block, (c) enclosed device.

the lateral displacement of two fibers. A simple concept of attenuation caused by the lateral displacement of two fibers is utilized for generating the non-symmetrical coupling ratios. The loss associated to this is given by the following relationship [10].

$$\alpha = -10 \log \left[ 1 - \frac{2SA_N}{3\,n\,d} \right] \tag{1}$$

where $S$ is the separation between the two fibers, $A_N$ is the numerical aperture of the fibers, $n$ is the refractive index of the fibers and $d$ is the diameter of the fibers.

Figure 1 shows a generic design structure for the proposed variable Y-branch POF coupler. The device consisted of a rectangular block with Y-branch structure engraved on it. POF fibers are slotted into this structure and arranged accordingly as shown in the figure. The input fiber is a non-movable fiber. The output fibers however are divided into two sections: non-movable and movable fibers. The fibers after the middle splitting junction are short non-movable fibers whereas the two outermost output fibers are defined as movable fibers.

Based on Figure 1, a relationship between the coupling ratios and the output fibers lateral displacement ($S_1$ and $S_2$) can be obtained. Hence, the coupling ratio equation in terms of the output fibers lateral displacement ($S_1$ and $S_2$) is given by following relationship [11],

$$CR = \frac{1 - RS_1}{2 - RS_1 - RS_2} \tag{2}$$

where $R$ is the value of $R = \frac{2A_N}{3nd}$ where the parameters $A_N$, $n$ and $d$ are defined earlier.

In the asymmetric mode, only one of the output fiber is moved where it will be shifted at a pre-determined step. The displacement varies from 0.1 mm to 4.4 mm, with a 0.1 mm step whereas the other output fiber remains stationary. We can simplify Equation (2) into terms involving the coupling ratio and fiber displacement $S_1$ only ($S_2 = 0$), shown as follows.

$$CR = \frac{1 - RS_1}{2 - RS_1} \tag{3}$$

Using the standard value of a step index (SI) POF fiber, where $A_N = 0.5$, $n = 1.49$ and $d = 1\,\text{mm}$, gives $R = 223.71$. The use of a symmetrical Y-branch coupler will ensure that the output power is divided equally by the waveguide taper in the middle. The coupling ratios for the design asymmetric coupler vary from 0.8% to 99.2%.

## 3. DEVICE FABRICATION

The fabrication of this Y-branch POF coupler is done using a simple and low cost technique. The designed structures are engraved onto aluminium and acrylic blocks using Roland's EGX-400

(a)                                         (b)
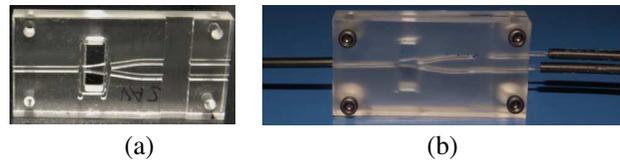
Figure 3: Fabricated components for acrylic-based coupler (a) device block, (b) assembled and enclosed device.
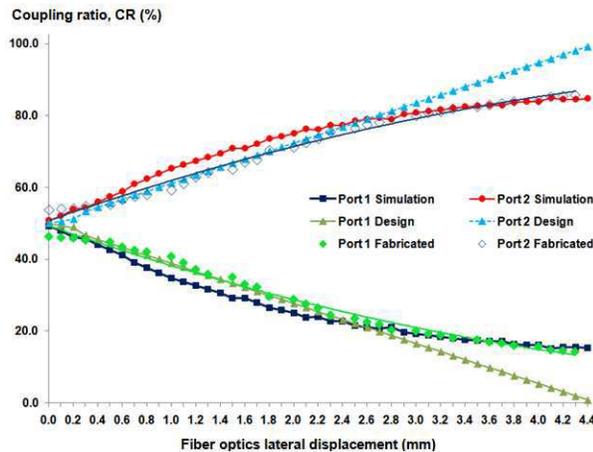


Figure 4: Metal-based asymmetric POF coupler: coupling ratios for fabricated devices.
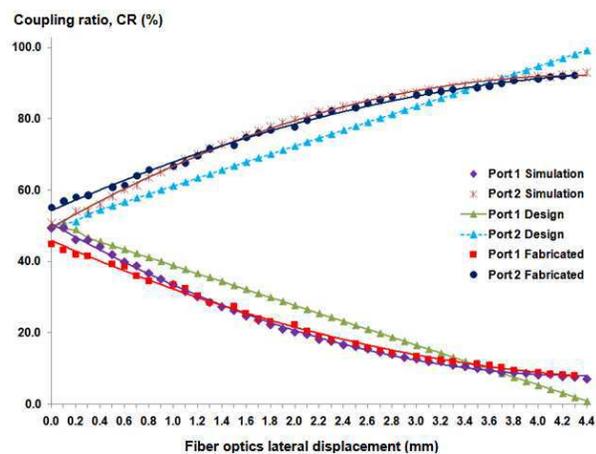
Figure 5: Acrylic-based asymmetric POF coupler: coupling ratios for fabricated devices.

desktop CNC machine at a spindle speed between 15,000 to 30,000 rpm. After the device structure has been engraved, short SI POF fibers comprising the components for the input, middle non movable and output movable fibers are inserted into the engraved slots. A top enclosing block is then used to enclosed the device structure. Both the metal- and acrylic-based POF devices are engraved and assembled using similar processes. Figure 2(a) provides a close view of the metal-based hollow waveguide taper structure. Figure 2(b) shows how the POF fibers are inserted and positioned into the U-groove slots of the metal device block. Figure 2(c) is the assembled device with the top block enclosing the whole device structure. Figure 3(a) shows the acrylic-based device block whereas Figure 3(b) is the assembled acrylic-based coupler.

The insertion loss of this device has been tested at a wavelength of 650 nm using Advanced Fiber Solution's FF-OS417 LED source and OM210 optical power meter. The effective input power is 0 dBm. In the metal-based coupler, the insertion loss of the device at the 3 dB mode is 9.65 dB and 9.0 dB respectively with an excess loss of 6.3 dB while the coupling ratios are 46.27% and 53.73%. Similarly, in the acrylic-based coupler, the insertion loss of the device at the 3 dB mode is 8.3 dB and 9.5 dB respectively with an excess loss of 5.85 dB while the coupling ratios are at 56.86% and 43.14%. In the non-symmetrical coupling ratio mode, the output fibers are moved laterally using a single-axis miniature translation stage with a 250 μm displacement per revolution.

Figure 4 is the plot of the coupling ratios against the output fiber lateral displacement for the fabricated metal-based asymmetric Y-branch POF coupler. As a comparison, both the coupling ratios for the designed and simulated devices are included. The fabricated asymmetric coupler shows coupling ratios variation from 46.27% down to 14.23% for port 1 and from 53.73% to 85.77% for port 2. The excess loss of this device varies from 6.3 dB to 8.33 dB. Similarly, Figure 5 is the plot of the coupling ratios against the output fiber lateral displacement for the fabricated acrylic-based asymmetric Y-branch POF coupler. As a comparison, both the coupling ratios for designed and simulated devices are included. The fabricated asymmetric coupler shows coupling ratios variation from 44.84% down to 8.01% for port 1 and 55.16% to 91.99% for port 2. The excess loss of this device varies from 5.42 dB to 7.64 dB.

## 4. CONCLUSION

A metal- and acrylic-based asymmetric Y-branch POF coupler prototypes have been designed, fabricated and assembled. The proposed simple attenuation technique caused by the lateral dis-

placement of two fibers has been proven to provide the required non-symmetrical coupling ratios. It avoids the used of bulky external attenuators attached to a symmetrical Y-branch coupler. The device manufactured using CNC machine has given a range of coupling ratios from 14.23% to 85.77% for the metal-based coupler and from 8.01% to 91.99% for the acrylic-based coupler. The results showed that both Y-branch couplers can perform as a 3 dB and an asymmetric coupler. It showed that the integration of the designed waveguide taper and the simple fiber attenuation technique can produce a low cost dual-function and compact optical device as shown.

**REFERENCES**

1. Mizuno, H., O. Sugihara, T. Kaino, N. Okamoto, and M. Ohama, "Compact Y-branch-type polymeric optical waveguide devices with large-core connectable to plastic optical fibers," *Jap. J. Appl. Phys.*, Vol. 44, No. 2, 8504–8506, 2005.
2. Klotzbuecher, T., T. Braune, D. Dadic, M. Sprzagala, and A. Koch, "Fabrication of optical $1 \times 2$ POF couplers using the laser-LIGA technique," *Proc. SPIE*, 121–132, Brugge, Belgium, 2003.
3. Takezawa, Y., S. Akasaka, S. Ohara, T. Ishibashi, H. Asano, and N. Taketani, "Low excess losses in a Y-branching plastic optical waveguide formed through injection molding," *Appl. Opt.*, Vol. 33, No. 12, 2307–2312, 1994.
4. Suzuki, S., T. Kitoh, Y. Inoue, Y. Yamada, Y. Hibino, K. Moriwaki, and M. Yanagisawa, "Integrated optic Y-branching waveguides with an asymmetric branching ratio," *Electron. Lett.*, Vol. 32, No. 8, 735–736, 1996.
5. Lin, H. B., J. Y. Su, R. S. Cheng, and W. S. Wang, "Novel optical single-mode asymmetric-branches for variable power splitting," *IEEE J. Quant. Electron.*, Vol. 35, No. 7, 1092–1096, 1999.
6. Kurokawa, H., H. Kawashima, H. Kasai, M. Kuroda, T. Yoshimura, and K. Asam, "An asymmetric optical splitter and its application to optical monitoring devices," *LEOS 14th Ann. Meet.*, Vol. 1, 232–233, San Diego, USA, 2001.
7. Love, J. D. and W. M. Henry, "Asymmetric multimode Y-junction splitters," *J. Opt. Quant. Electron.*, Vol. 29, 379–392, 1997.
8. Ehsan, A. A., S. Shaari, and M. K. Abd-Rahman, "Metal-based asymmetric hollow optical waveguide couplers," *J. Microengineering and Nanoelectronics*, Vol. 1, No. 1, 87–93, 2010.
9. Ehsan, A. A., S. Shaari, and M. K. Abd-Rahman, "Plastic optical fiber coupler with high index contrast waveguide taper," *Progress In Electromagnetics Research C*, Vol. 20, 125–138, 2011.
10. Weinert, A., *Plastic Optical Fibers: Principles, Components and Installation*, MCD Verlag, Munich, 1999.
11. Ehsan, A. A., S. Shaari, and M. K. Abd-Rahman, "Variable coupling ratio Y-branch plastic optical fiber (POF) coupler with suspended waveguide taper," *Progress In Electromagnetics Research C*, Vol. 23, 249–263, 2011.

# On the Improved Characterization of the Faraday Effect

**J. Tioh**, **R. J. Weber**, and **M. Mina**

Department of Electrical and Computer Engineering, Iowa State University, Ames, IA 50011, USA

**Abstract**— The Faraday effect has found a great many scientific and practical applications, including optical networking where it is a potential enabler of better scaling, transparent networks that are bit-rate, protocol and format insensitive. In order to analyze an optical network device or system consisting of fibers, films, birefringent, and magnetic materials, it is helpful to have an analysis structure. Often Jones Calculus is employed to perform such an analysis, with the effect of reflections being neglected for the sake of simplicity in standard analyses. This discourse expounds on the improved characterization of Faraday rotation using the formalism of matrix notation that alleviates the shortcomings of standard Jones Calculus. This formalism is essential for the proper analysis of magneto-optic devices.

## 1. INTRODUCTION

Michael Faraday experimentally observed a rotation of the plane of polarization when light was transmitted through glass in a direction parallel to that of an applied magnetic field in 1845 [1]. This constituted the first demonstration magneto-optics, followed by the observation of a broadening of the spectral lines emitted by a sodium flame when it was placed between the poles of an electromagnet by Pieter Zeeman in 1896 [2]. Since these pioneering discoveries, magneto-optics has become a captivating field of research, finding a great many scientific and practical applications [3–8]. In optical networking, magneto-optic (MO) devices are a potential enabler of better scaling, transparent networks that are bit-rate, protocol and format insensitive, which is the authors' topic of inquiry [9–12].

Analyzing MO devices or systems, possibly consisting of fibers, films, birefringent, and magnetic materials in the case of optical networks, is made easier by having an analysis structure. Jones calculus [13] is often employed to perform such an analysis, with the effect of reflections being neglected for the sake of simplicity. This discourse expounds on an improved formulation for characterizing Faraday rotation using the formalism of matrix notation that alleviates the shortcomings of standard Jones calculus. The two representations applied to characterizing structures at optical frequencies are the scattering ($S$) and transmission ($T$) matrices [14, 15], which are more commonly and conventionally used in millimeter wave analyses.

## 2. NON-RECIPROCAL TRANSMISSION LINE

Consider a hypothetical transmission line that has different propagation constants (PCs) and characteristic impedances (CIs) for each direction of propagation. Assuming $a$ and $b$ variables as shown in Figure 1 and normalization to an external CI $Z_0^E$, one can derive the $S$ and $T$ parameters as :

$$T_{11} = -\left[\left(Z_0^+ - Z_0^E\right)\left(Z_0^- - Z_0^E\right)e^{j\beta^+ z} + \left(Z_0^+ + Z_0^E\right)\left(Z_0^- + Z_0^E\right)e^{-j\beta^- z}\right] / \left[2\left(Z_0^+ + Z_0^-\right)Z_0^E\right] \quad (1)$$

$$T_{12} = \left[\left(Z_0^+ - Z_0^E\right)\left(Z_0^- + Z_0^E\right)e^{j\beta^+ z} - \left(Z_0^+ - Z_0^E\right)\left(Z_0^- + Z_0^E\right)e^{-j\beta^- z}\right] / \left[2\left(Z_0^+ + Z_0^-\right)Z_0^E\right] \quad (2)$$

$$T_{21} = -\left[\left(Z_0^+ + Z_0^E\right)\left(Z_0^- - Z_0^E\right)e^{j\beta^+ z} + \left(Z_0^+ + Z_0^E\right)\left(Z_0^- - Z_0^E\right)e^{-j\beta^- z}\right] / \left[2\left(Z_0^+ + Z_0^-\right)\right] \quad (3)$$
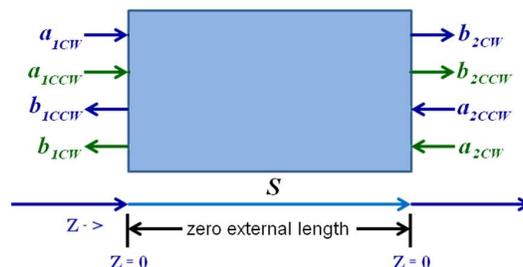


Figure 1: Transmission line block labeled in its own $a$ and $b$ variables.

$$T_{22} = \left[ \left(Z_0^+ + Z_0^E\right) \left(Z_0^- + Z_0^E\right) e^{j\beta^+ z} - \left(Z_0^+ - Z_0^E\right) \left(Z_0^- - Z_0^E\right) e^{-j\beta^- z} \right] / \left[ 2 \left(Z_0^+ + Z_0^-\right) \right] \tag{4}$$

$$S_{11} = \frac{\left(Z_0^+ - Z_0^E\right) \left(Z_0^- + Z_0^E\right) - \left(Z_0^+ - Z_0^E\right) \left(Z_0^- + Z_0^E\right) e^{-j(\beta^+ + \beta^-)z}}{\left(Z_0^+ + Z_0^E\right) \left(Z_0^- + Z_0^E\right) - \left(Z_0^+ - Z_0^E\right) \left(Z_0^- - Z_0^E\right) e^{-j(\beta^+ + \beta^-)z}} \tag{5}$$

$$S_{12} = \left[ 2 Z_0^E \left(Z_0^+ + Z_0^-\right) e^{-j\beta^- z} \right] / \left[ \left(Z_0^+ + Z_0^E\right) \left(Z_0^- + Z_0^E\right) - \left(Z_0^+ - Z_0^E\right) \left(Z_0^- - Z_0^E\right) e^{-j(\beta^+ + \beta^-)z} \right] \tag{6}$$

$$S_{21} = \left[ 2 Z_0^E \left(Z_0^+ + Z_0^-\right) e^{-j\beta^+ z} \right] / \left[ \left(Z_0^+ + Z_0^E\right) \left(Z_0^- + Z_0^E\right) - \left(Z_0^+ - Z_0^E\right) \left(Z_0^- - Z_0^E\right) e^{-j(\beta^+ + \beta^-)z} \right] \tag{7}$$

$$S_{22} = \frac{\left(Z_0^- - Z_0^E\right) \left(Z_0^+ + Z_0^E\right) - \left(Z_0^- - Z_0^E\right) \left(Z_0^+ + Z_0^E\right) e^{-j(\beta^+ + \beta^-)z}}{\left(Z_0^+ + Z_0^E\right) \left(Z_0^- + Z_0^E\right) - \left(Z_0^+ - Z_0^E\right) \left(Z_0^- - Z_0^E\right) e^{-j(\beta^+ + \beta^-)z}} \tag{8}$$

where $Z_0^+$ and $Z_0^-$ are the CIs and $\beta^+$ and $\beta^-$ are the PCs for waves in the positive and negative directions respectively. Normalization to either CI does not simplify the equations. Moreover, doing so would prevent the $S$ matrix from being converted to a $T$ matrix to be used for cascading since the adjacent port impedances would be dissimilar. The differences between the CIs (and hence PCs) might be small but it is the accumulated phase shift difference that is important. Changing the direction of bias magnetism results in $S_{12}$ becoming $S_{21}$ and $S_{22}$ becoming $S_{11}$.

## 3. WAVE FORMULATION FOR NON-RECIPROCAL MEDIUM

One might attempt to directly extend the equations above for use with plane wave fields. However, in plane wave characterizations, there are two orthogonal axes for the electric field. For a particular Device Under Test (DUT), there might also be coupling between the two orthogonal electric fields at the ports.

Several assumptions are made in the following analysis; waves in the fiber and magnetic material are plane waves (justifiable since the guiding behavior of fibers keeps the Gaussian wave profiles from changing), the longitudinal distance through the material is short and modes generated in the interface between the fiber and material are insignificant. A superposition of circularly polarized (CP) waves (a clockwise (CW) and a counter-clockwise (CCW) CP wave) will be used to describe wave propagation in the ferrite material and in the interconnecting fibers since linearly polarized (LP) waves do not exist in anisotropic magnetic media.

Assuming plane wave travel in the $z$ direction, there are four different CP (eight LP) waves traversing the magnetic region. In magnetic material, the two forward waves travel with different phase velocities as well as different CIs and likewise for the two reverse travelling waves. The CI and phase velocity of a CW wave travelling in the forward direction is the same as that of a CCW wave travelling in the reverse direction. An analysis via Maxwell's equations shows that plane waves entering from an isotropic magnetic material into a magnetic material generate CP waves in the magnetic material with the coupling taking place at the boundary.

For port-to-port phase delay calculations, the input and output boundaries are considered to be at $z = 0$. This describes a DUT inserted into a fiber as in Figure 2.

For port-to-port phase delay calculations, the input and output boundaries are considered to be at $z = 0$. This describes a DUT that is inserted into a fiber at $z = 0$ as shown in Figure 2. The wave coupling at the input will be described in terms of the continuity of tangential electric and
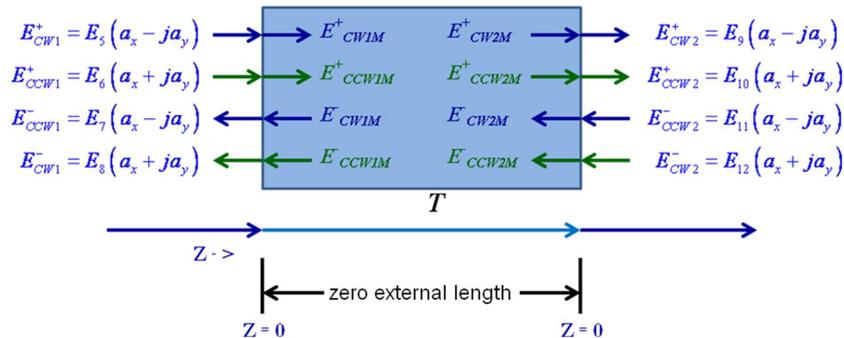
Figure 2: Notation for port-to-port phase delay calculations.

magnetic fields. The CI and PC of the material has a subscript 1 for forward CW as well as reverse CCW waves and a subscript 2 for forward CCW and reverse CW waves.

Waves in the material will have subscripts 1–4. A four port $T$ matrix will be formed. The physical input port will consist of two electromagnetic ports (one for each of the two orthogonal CP waves) and likewise for the physical output ports. The fiber material impedance will be chosen as the $T$ matrix normalization impedance. It is necessary to use the same normalization impedance on both ports to allow cascading of the matrices for analysis. Throughout this analysis, characteristic impedance will be used to mean material impedivity. The tangential electric and magnetic field values at the input (9)–(12) and output (13)–(16) boundaries are:

$$E^+_{CW1M} = E_1 \left(a_x - ja_y\right) \qquad H^+_{CW1M} = \frac{E_1}{\eta_1} \left(ja_x + a_y\right)$$

$$E^+_{CCW1M} = E_2 \left(a_x + ja_y\right) \qquad H^+_{CCW1M} = \frac{E_2}{\eta_2} \left(-ja_x + a_y\right) \tag{9}$$

$$E^-_{CCW1M} = E_3 \left(a_x - ja_y\right) \qquad H^-_{CCW1M} = \frac{E_3}{\eta_1} \left(-ja_x - a_y\right)$$

$$E^-_{CW1M} = E_4 \left(a_x + ja_y\right) \qquad H^-_{CW1M} = \frac{E_4}{\eta_2} \left(ja_x - a_y\right) \tag{10}$$

$$E^+_{CW1} = E_5 \left(a_x - ja_y\right) \qquad H^+_{CW1} = \frac{E_5}{\eta_f} \left(ja_x + a_y\right)$$

$$E^+_{CCW1} = E_6 \left(a_x + ja_y\right) \qquad H^+_{CCW1} = \frac{E_6}{\eta_f} \left(-ja_x + a_y\right) \tag{11}$$

$$E^-_{CCW1} = E_7 \left(a_x - ja_y\right) \qquad H^-_{CCW1} = \frac{E_7}{\eta_f} \left(-ja_x - a_y\right)$$

$$E^-_{CW1} = E_8 \left(a_x + ja_y\right) \qquad H^-_{CW1} = \frac{E_8}{\eta_f} \left(ja_x - a_y\right) \tag{12}$$

$$E^+_{CW2M} = E_1 \left(a_x - ja_y\right) e^{-j\beta_1 L} \qquad H^+_{CW2M} = \frac{E_1}{\eta_1} \left(ja_x + a_y\right) e^{-j\beta_1 L}$$

$$E^+_{CCW2M} = E_2 \left(a_x + ja_y\right) e^{-j\beta_2 L} \qquad H^+_{CCW2M} = \frac{E_2}{\eta_2} \left(-ja_x + a_y\right) e^{-j\beta_2 L} \tag{13}$$

$$E^-_{CCW2M} = E_3 \left(a_x - ja_y\right) e^{j\beta_1 L} \qquad H^-_{CCW2M} = \frac{E_3}{\eta_1} \left(-ja_x - a_y\right) e^{j\beta_1 L}$$

$$E^-_{CW2M} = E_4 \left(a_x + ja_y\right) e^{j\beta_2 L} \qquad H^-_{CW2M} = \frac{E_4}{\eta_2} \left(ja_x - a_y\right) e^{j\beta_2 L} \tag{14}$$

$$E^+_{CW2} = E_9 \left(a_x - ja_y\right) \qquad H^+_{CW2} = \frac{E_9}{\eta_f} \left(ja_x + a_y\right)$$

$$E^+_{CCW2} = E_{10} \left(a_x + ja_y\right) \qquad H^+_{CCW2} = \frac{E_{10}}{\eta_f} \left(-ja_x + a_y\right) \tag{15}$$

$$E^-_{CCW2} = E_{11} \left(a_x - ja_y\right) \qquad H^-_{CCW2} = \frac{E_{11}}{\eta_f} \left(-ja_x - a_y\right)$$

$$E^-_{CW2} = E_{12} \left(a_x + ja_y\right) \qquad H^-_{CW2} = \frac{E_{12}}{\eta_f} \left(ja_x - a_y\right) \tag{16}$$

where unit vectors $\vec{a}$ are in the $x$ or $y$ direction, $\eta_f$ is the fiber material CI, $\eta_1$ is the magnetic material CI in the forward-CW direction, $\eta_2$ is the magnetic material CI in the forward-CCW direction and $L$ is the length of the magnetic material.

Applying the boundary conditions at the input (17) and output (18) yields:

$$
\begin{pmatrix} E_1 \\ E_2 \\ E_3 \\ E_4 \end{pmatrix} = \frac{1}{2\eta_f} \begin{pmatrix} \eta_1+\eta_f & 0 & -(\eta_1-\eta_f) & 0 \\ 0 & \eta_2+\eta_f & 0 & -(\eta_2-\eta_f) \\ -(\eta_1-\eta_f) & 0 & \eta_1+\eta_f & 0 \\ 0 & -(\eta_2-\eta_f) & 0 & \eta_2+\eta_f \end{pmatrix} \begin{pmatrix} E_5 \\ E_6 \\ E_7 \\ E_8 \end{pmatrix}
\tag{17}
$$

$$
\begin{pmatrix} E_1 \\ E_2 \\ E_3 \\ E_4 \end{pmatrix} = \frac{1}{2\eta_f} \begin{pmatrix} (\eta_1+\eta_f)\,e^{+j\beta_1 L} & 0 & -(\eta_1-\eta_f)\,e^{+j\beta_1 L} & 0 \\ 0 & (\eta_2+\eta_f)\,e^{+j\beta_2 L} & 0 & -(\eta_2-\eta_f)\,e^{+j\beta_2 L} \\ -(\eta_1-\eta_f)\,e^{-j\beta_1 L} & 0 & (\eta_1+\eta_f)\,e^{-j\beta_1 L} & 0 \\ 0 & -(\eta_2-\eta_f)\,e^{-j\beta_2 L} & 0 & (\eta_2+\eta_f)\,e^{-j\beta_2 L} \end{pmatrix}
$$
$$
\begin{pmatrix} E_9 \\ E_{10} \\ E_{11} \\ E_{12} \end{pmatrix}
\tag{18}
$$

The input and output waves are related using forward $T$ parameters as:

$$
\left( \begin{Bmatrix} E_5 \\ E_6 \\ E_7 \\ E_8 \end{Bmatrix} \right) = \begin{pmatrix} (T_{UL}) & (T_{UR}) \\ (T_{LL}) & (T_{LR}) \end{pmatrix} \left( \begin{Bmatrix} E_9 \\ E_{10} \\ E_{11} \\ E_{12} \end{Bmatrix} \right)
\tag{19}
$$

$$
(T_{UL}) = \begin{pmatrix} \dfrac{(\eta_1+\eta_f)^2 e^{j\beta_1 L}-(\eta_1-\eta_f)^2 e^{-j\beta_1 L}}{4\eta_f \eta_1} & 0 \\ 0 & \dfrac{(\eta_2+\eta_f)^2 e^{j\beta_2 L}-(\eta_2-\eta_f)^2 e^{-j\beta_2 L}}{4\eta_f \eta_2} \end{pmatrix}
$$

$$
(T_{UR}) = \begin{pmatrix} \dfrac{-(\eta_1^2-\eta_f^2)(e^{j\beta_1 L}-e^{-j\beta_1 L})}{4\eta_f \eta_1} & 0 \\ 0 & \dfrac{-(\eta_2^2-\eta_f^2)(e^{j\beta_2 L}-e^{-j\beta_2 L})}{4\eta_f \eta_2} \end{pmatrix}
$$

$$
(T_{LL}) = \begin{pmatrix} \dfrac{(\eta_1^2-\eta_f^2)(e^{j\beta_1 L}-e^{-j\beta_1 L})}{4\eta_f \eta_1} & 0 \\ 0 & \dfrac{(\eta_2^2-\eta_f^2)(e^{j\beta_2 L}-e^{-j\beta_2 L})}{4\eta_f \eta_2} \end{pmatrix}
\tag{20}
$$

$$
(T_{LR}) = \begin{pmatrix} \dfrac{-(\eta_1-\eta_f)^2 e^{j\beta_1 L}+(\eta_1+\eta_f)^2 e^{-j\beta_1 L}}{4\eta_f \eta_1} & 0 \\ 0 & \dfrac{-(\eta_2-\eta_f)^2 e^{j\beta_2 L}+(\eta_2+\eta_f)^2 e^{-j\beta_2 L}}{4\eta_f \eta_2} \end{pmatrix}
$$

With the source on the input port and terminations on the output port, we obtain the relationships in (21). Conversely with the source on the output and terminations on the input ports, we obtain the relationships in (22).

$$
\begin{pmatrix} E_9 \\ E_{10} \end{pmatrix} = (T_{UL})^{-1} \begin{pmatrix} E_5 \\ E_6 \end{pmatrix} \qquad \begin{pmatrix} E_7 \\ E_8 \end{pmatrix} = (T_{LL})(T_{UL})^{-1} \begin{pmatrix} E_5 \\ E_6 \end{pmatrix}
\tag{21}
$$

$$
\begin{pmatrix} E_9 \\ E_{10} \end{pmatrix} = -(T_{UL})^{-1}(T_{UR}) \begin{pmatrix} E_{11} \\ E_{12} \end{pmatrix} \qquad \begin{pmatrix} E_7 \\ E_8 \end{pmatrix} = \left( -(T_{LL})(T_{UL})^{-1}(T_{UR})+(T_{LR}) \right) \begin{pmatrix} E_{11} \\ E_{12} \end{pmatrix}
\tag{22}
$$

The input and output waves are related using reverse $T$ parameters as:

$$
\left( \begin{Bmatrix} E_9 \\ E_{10} \\ E_{11} \\ E_{12} \end{Bmatrix} \right) = \begin{pmatrix} (T_{R-UL}) & (T_{R-UR}) \\ (T_{R-LL}) & (T_{R-LR}) \end{pmatrix} \left( \begin{Bmatrix} E_5 \\ E_6 \\ E_7 \\ E_8 \end{Bmatrix} \right)
\tag{23}
$$

$$(T_{R-UL}) = \begin{pmatrix} \dfrac{(\eta_1+\eta_f)^2 e^{-j\beta_1 L} - (\eta_1-\eta_f)^2 e^{j\beta_1 L}}{4\eta_f \eta_1} & 0 \\ 0 & \dfrac{(\eta_2+\eta_f)^2 e^{-j\beta_2 L} - (\eta_2-\eta_f)^2 e^{j\beta_2 L}}{4\eta_f \eta_2} \end{pmatrix}$$

$$(T_{R-UR}) = \begin{pmatrix} \dfrac{-(\eta_1^2-\eta_f^2)(e^{-j\beta_1 L} - e^{j\beta_1 L})}{4\eta_f \eta_1} & 0 \\ 0 & \dfrac{-(\eta_2^2-\eta_f^2)(e^{-j\beta_2 L} - e^{j\beta_2 L})}{4\eta_f \eta_2} \end{pmatrix}$$

$$(T_{R-LL}) = \begin{pmatrix} \dfrac{(\eta_1^2-\eta_f^2)(e^{-j\beta_1 L} - e^{j\beta_1 L})}{4\eta_f \eta_1} & 0 \\ 0 & \dfrac{(\eta_2^2-\eta_f^2)(e^{-j\beta_2 L} - e^{j\beta_2 L})}{4\eta_f \eta_2} \end{pmatrix} \tag{24}$$

$$(T_{R-LR}) = \begin{pmatrix} \dfrac{-(\eta_1-\eta_f)^2 e^{-j\beta_1 L} + (\eta_1+\eta_f)^2 e^{j\beta_1 L}}{4\eta_f \eta_1} & 0 \\ 0 & \dfrac{-(\eta_2-\eta_f)^2 e^{-j\beta_2 L} + (\eta_2+\eta_f)^2 e^{j\beta_2 L}}{4\eta_f \eta_2} \end{pmatrix}$$

With the source on the input port and terminations on the output port, we obtain the relationships in (25). Conversely with the source on the output and terminations on the input ports, we obtain the relationships in (26).

$$\begin{pmatrix} E_7 \\ E_8 \end{pmatrix} = -(T_{R-LR})^{-1}(T_{R-LL}) \begin{pmatrix} E_5 \\ E_6 \end{pmatrix}$$

$$\begin{pmatrix} E_9 \\ E_{10} \end{pmatrix} = \left( (T_{R-UL}) - (T_{R-UR})(T_{R-LR})^{-1}(T_{R-LL}) \right) \begin{pmatrix} E_5 \\ E_6 \end{pmatrix} \tag{25}$$

$$\begin{pmatrix} E_7 \\ E_8 \end{pmatrix} = (T_{R-LR})^{-1} \begin{pmatrix} E_{11} \\ E_{12} \end{pmatrix} \qquad \begin{pmatrix} E_9 \\ E_{10} \end{pmatrix} = (T_{R-UR})(T_{R-LR})^{-1} \begin{pmatrix} E_{11} \\ E_{12} \end{pmatrix} \tag{26}$$

The $S$ matrix for an $x$-axis polarized wave can be determined from adding the appropriate wave pairs. Likewise the $S$ matrix for a $y$-axis polarized wave can be determined from subtracting the appropriate wave pairs. However, since a single axis oriented input can give a dual axis output, the concept of the $S$ matrix would need to be extended based on its use similar to the concept of common and differential mode $S$ matrices. Likewise, a single axis oriented input can give reflections back from the input on both the $x$-axis and $y$-axis.

Using $a$ and $b$ variables from $S$ parameter notation, the $T$ matrix can be used to relate these variables. However, an additional comment is necessary. In the S parameter notation, $a$ variables represent quantities incident on a port while $b$ variables represent quantities reflected from a port. Since the preceding analysis has been developed using modes and direction, it is necessary to point out that the top part of sub-matrices represent one mode pair and the bottom part of sub-matrices represent the other mode pair. Therefore some $a$ and / or $b$ variables will have opposite subscripts (CW & CCW) because some of them are in the positive $z$ direction and some in the negative $z$ direction.

The $S$ matrix of a non-reciprocal transmission line with two different CP waves is given below. Notice that transmission is between the same senses of polarization but reflection is between opposite senses of polarization.

$$\left( \begin{Bmatrix} b_{1CCW} \\ b_{1CW} \\ b_{2CW} \\ b_{2CCW} \end{Bmatrix} \right) = \begin{pmatrix} (S_{11}) & (S_{12}) \\ (S_{21}) & (S_{22}) \end{pmatrix} \left( \begin{Bmatrix} a_{1CW} \\ a_{1CCW} \\ a_{2CCW} \\ a_{2CW} \end{Bmatrix} \right) \tag{27}$$

$$(S_{11}) = \begin{pmatrix} \dfrac{(\eta_1^2-\eta_f^2)(e^{j\beta_1 L} - e^{-j\beta_1 L})}{(\eta_1+\eta_f)^2 e^{j\beta_1 L} - (\eta_1-\eta_f)^2 e^{-j\beta_1 L}} & 0 \\ 0 & \dfrac{(\eta_2^2-\eta_f^2)(e^{j\beta_2 L} - e^{-j\beta_2 L})}{(\eta_2+\eta_f)^2 e^{j\beta_2 L} - (\eta_2-\eta_f)^2 e^{-j\beta_2 L}} \end{pmatrix}$$

$$(S_{12}) = \begin{pmatrix} \dfrac{4\eta_f \eta_1}{(\eta_1+\eta_f)^2 e^{j\beta_1 L} - (\eta_1-\eta_f)^2 e^{-j\beta_1 L}} & 0 \\ 0 & \dfrac{4\eta_f \eta_2}{(\eta_2+\eta_f)^2 e^{j\beta_2 L} - (\eta_2-\eta_f)^2 e^{-j\beta_2 L}} \end{pmatrix}$$

$$
(S_{21}) = \begin{pmatrix} \dfrac{4\eta_f\eta_1}{(\eta_1+\eta_f)^2 e^{j\beta_1 L}-(\eta_1-\eta_f)^2 e^{-j\beta_1 L}} & 0 \\ 0 & \dfrac{4\eta_f\eta_2}{(\eta_2+\eta_f)^2 e^{j\beta_2 L}-(\eta_2-\eta_f)^2 e^{-j\beta_2 L}} \end{pmatrix}
$$

$$
(S_{22}) = \begin{pmatrix} \dfrac{(\eta_1^2-\eta_f^2)(e^{j\beta_1 L}-e^{-j\beta_1 L})}{(\eta_1+\eta_f)^2 e^{j\beta_1 L}-(\eta_1-\eta_f)^2 e^{-j\beta_1 L}} & 0 \\ 0 & \dfrac{(\eta_2^2-\eta_f^2)(e^{j\beta_2 L}-e^{-j\beta_2 L})}{(\eta_2+\eta_f)^2 e^{j\beta_2 L}-(\eta_2-\eta_f)^2 e^{-j\beta_2 L}} \end{pmatrix}
$$

(28)

The effect of an air gap or other inserted material having a different CI from that of the fiber can be accommodated using the four-port $T$ matrix for two CP travelling waves shown below. This matrix can be generated from the magnetic material matrix assuming the material constants are the same in both directions.

$$
(T_{UL}) = \frac{1}{2\eta_f\eta_m} \begin{pmatrix} 2\eta_f\eta_m\cos(\beta_m L)+j\left(\eta_m^2+\eta_f^2\right)\sin(\beta_m L) & \\ 0 & \\ & 0 \\ & 2\eta_f\eta_m\cos(\beta_m L)+j\left(\eta_m^2+\eta_f^2\right)\sin(\beta_m L) \end{pmatrix}
$$

(29)

$$
(T_{UR}) = \frac{1}{2\eta_f\eta_m} \begin{pmatrix} -j\left(\eta_m^2-\eta_f^2\right)\sin(\beta_m L) & 0 \\ 0 & -j\left(\eta_m^2-\eta_f^2\right)\sin(\beta_m L) \end{pmatrix}
$$

$$
(T_{LL}) = \frac{1}{2\eta_f\eta_m} \begin{pmatrix} +j\left(\eta_m^2-\eta_f^2\right)\sin(\beta_m L) & 0 \\ 0 & +j\left(\eta_m^2-\eta_f^2\right)\sin(\beta_m L) \end{pmatrix}
$$

(30)

$$
(T_{LR}) = \frac{1}{2\eta_f\eta_m} \begin{pmatrix} 2\eta_f\eta_m\cos(\beta_m L)-j\left(\eta_m^2+\eta_f^2\right)\sin(\beta_m L) & \\ 0 & \\ & 0 \\ & 2\eta_f\eta_m\cos(\beta_m L)-j\left(\eta_m^2+\eta_f^2\right)\sin(\beta_m L) \end{pmatrix}
$$

(31)

$$
(T_{R\text{-}UL}) = \frac{1}{2\eta_f\eta_m} \begin{pmatrix} 2\eta_f\eta_m\cos(\beta_m L)-j\left(\eta_m^2+\eta_f^2\right)\sin(\beta_m L) & \\ 0 & \\ & 0 \\ & 2\eta_f\eta_m\cos(\beta_m L)-j\left(\eta_m^2+\eta_f^2\right)\sin(\beta_m L) \end{pmatrix}
$$

(32)

$$
(T_{R\text{-}UR}) = \frac{1}{2\eta_f\eta_m} \begin{pmatrix} j\left(\eta_m^2-\eta_f^2\right)\sin(\beta_m L) & 0 \\ 0 & j\left(\eta_m^2-\eta_f^2\right)\sin(\beta_m L) \end{pmatrix}
$$

$$
(T_{R\text{-}LL}) = \frac{1}{2\eta_f\eta_m} \begin{pmatrix} -j\left(\eta_m^2-\eta_f^2\right)\sin(\beta_m L) & 0 \\ 0 & -j\left(\eta_m^2-\eta_f^2\right)\sin(\beta_m L) \end{pmatrix}
$$

(33)

$$
(T_{R-LR}) = \frac{1}{2\eta_f\eta_m} \begin{pmatrix} 2\eta_f\eta_m\cos(\beta_m L)+j\left(\eta_m^2+\eta_f^2\right)\sin(\beta_m L) & \\ 0 & \\ & 0 \\ & 2\eta_f\eta_m\cos(\beta_m L)+j\left(\eta_m^2+\eta_f^2\right)\sin(\beta_m L) \end{pmatrix}
$$

(34)

where the subscript $m$ refers to material parameters of the inserted section and the subscript $f$ refers to reference material parameters of the fiber. For an air gap, the subscript $m$ would refer to free space while for a matching section such as index matching material, the subscript $m$ would refer to the parameters of that material.

When using a linear excitation, e.g., an $x$-axis excitation, $E_5$ and $E_6$ ($a_{1CW} = a_{1CCW}$) would be set equal to each other. For a $y$-axis excitation, $E_5$ and $E_6$ would be set to the negative of each other ($a_{1CW} = -a_{1CCW}$). Similarly, when determining the axis of rotation for the polarization, the tangent ratio of the appropriate values of the port excitations would be used.

## 4. CONCLUSIONS

A tractable formulation for analyzing complex structures consisting of fibers, films, birefringent and magnetic materials is reported. This addresses the shortcomings of standard Jones Calculus and is integral for the proper analysis of magneto-optic devices.

**REFERENCES**

1. Faraday, M., *Experimental Researches in Electricity*, Vol. 3, London, 1855.
2. Zeeman, P., "On the influence of magnetism on the nature of the light emitted by a substance," *Phil. Mag.*, Vol. 43, 226–236, 1897.
3. Panmand, R. P., et al., "Functionality of bismuth sulfide quantum dots/wires-glass nanocomposite as an optical current sensor with enhanced Verdet constant," *J. Appl. Phys.*, Vol. 109, No. 3, 033101–033101-7, February 2011.
4. White, A. D., G. B. McHale, and D. A. Goerz, "Advances in optical fiber-based Faraday rotation diagnostics," *IEEE PPC*, 1358–1363, January 2010.
5. Gao, Q., L. Li, and G. Niu, "Research on aircraft skin cracks recognition based on the crack-isolated method," *ICBECS*, 1–4, April 2010.
6. Ghosh, S., et al., "Electrical control of spin coherence in ZnO," *Appl. Phys. Lett.*, Vol. 92, No. 16, 162109–162109-3, April 2008.
7. Kikkawa, J. M. and D. D. Awschalom, "Resonant spin amplification in n-type GaAs," *Phys. Rev. Lett.*, Vol. 80, No. 19, 4313–4316, May 2008.
8. Moses, A. J., P. I. Williams, and O. A. Hoshtanar, "A novel instrument for real-time dynamic domain observation in bulk and micromagnetic materials," *IEEE. Trans. Mag.*, Vol. 41, No. 10, 3736–3738, October 2005.
9. Tioh, J., R. J. Weber, and M. Mina, "Improved formulation for Faraday rotation characterization," *J. Appl. Phys.*, Vol. 109, No. 7, 07E334–07E334-3, April 2011.
10. Tioh, J., M. Mina, and R. J. Weber, "All-optical integrated switch utilizing Faraday rotation," *IEEE Trans. Mag.*, Vol. 46, No. 6, 2474–2477, June 2010.
11. Bahuguna, R., J. Tioh, M. Mina, and R. J. Weber, "magneto-optic-based fiber switch for optical communications," *IEEE Trans. Mag.*, Vol. 42, No. 10, 3099–3101, October 2006.
12. Kemmet, S., M. Mina, and R. J. Weber, "Magnetic pulse generation for high-speed magneto-optic switching," *J. Appl. Phys.*, Vol. 109, No. 7, 07E333–07E333-3, April 2011.
13. Jones, R. C., "A new calculus for the treatment of optical systems," *J. Optical Society of America*, Vol. 31, No. 7, 488–493, July 1941.
14. Kurokawa, K., "Power waves and the scattering matrix," *IEEE Trans. MTT*, Vol. 13, No. 2, 194–202, 1965.
15. Matthews, E. W., "The use of scattering matrices in microwave circuits," *IRE Trans. MTT*, Vol. 3, No. 3, 21–26, April 1955.

# The Intensity Modulation of THz-quantum Cascade Lasers by NIR Optical Pulse Injection

**S. Saito**[1], **Y. Sakasegawa**[1], **N. Sekine**[1], **M. Ashida**[2], **and I. Hosako**[1]

[1]National Institute for Information and Communications Technology, Japan
[2]Graduate School of Engineering Science, Osaka University, Japan

**Abstract**— THz-Quantum Cascade Lasers (THz-QCLs) are coherent and strong light sources for spectroscopy and imaging and expected as light sources for the high-speed communication because their potential of high-speed modulation is predicted by theory. The response of THz-QCLs to optical pulse injection is expected to obtain the information of carrier dynamics. We have built the modulation measurement system for THz-QCLs with NIR optical pulse. When the 770 nm optical pulse injected into THz-QCL before the current pulse injection, it was observed that output intensity from the THz-QCL was reduced. It is considered the photo-excited plasma at the facet worked as a mirror for THz wave. As a result, output from THz-QCL was decreased.

## 1. INTRODUCTION

For long time, THz wave, which lies in the frequency between the inrared and millimeter wave (from 100 GHz to 10 THz) has long been treated by the limited reseachers in the field such as astronomy, physics, chemics and so on, because strong absorption lines exit in THz wave region band and the light source and detector were not easy to operate. However, technologinal development in photonics and material technology in these decade is enabling THz research to be applied in various fields [1–3]. Especially, THz spectroscopy and imaging of artific material is the evidence of new method [4]. The electromagnetic wave of GHz frequency is used as a carrier of the personal communication, mobile phone or wireless LAN in the daily use and the demand for high-speed communications is increasing. THz wave is desired as a carrier for high-speed communication. After the lasing of THz wave from quantum cascade structure [5], extensive research of THz quantum cascade lasers (THz-QCLs) has been investigated. THz-QCLs are small size, high intensity and coherent light sources and are used for the spectoroscopy field. Furthermore, THz-QCLs are expected as light sources for short-range ultra high-speed wireless communications, because it is predicted that the THz-QCLs are able to have the modulation bandwidth more than 100 GHz in theory [6]. By electrical method, it was reported that the modulation bandwidth of THz QCLs was approximately several ten GHz [7, 8]. The bandwidth in the research is limited by parasitic circuit components, therefore the intrinsic properties of THz QCLs have not been clarified. The intensity modulation measurement with external optical cw light injection has been reported [9], and the reduction of output power of THz-QCL was observed.

The optical injection method has many advantege of the carrier excitation. We can select the excitation of the electon state by tuning the photon energy and polarization of the light. In addition, when we use the short pulse laser, the number of carriers are changed in short time. In order to observe the response to rapid-change of the carrier number in the THz-QCLs we have built the modulation measurement system for THz-QCLs with NIR optical pulse injection. And the wavelength of optical pulse injection were tuned avobe and beow the bandgap energy of GaAs, that the well of THz-QCLs consist of. As a result, it was observed that output intensity from the THz-QCL was reduced. This is explained that carrier excitaion of THz-QCLs and cavity condition and decreasing the carrier number contribiute to lasing.

## 2. SAMPLE AND EXPERIMENTAL SETUP

Figure 1 shows schematic diagram of the experimental setup for optical pulse injection measurements. The temperature of the baseplate that THz-QCL attatched was kept at 15 K. The THz-QCL used in this study was a GaAs/AlGaAs multi quantum well with a resonant phonon-depopularion-type active region. The number of units was 480. Waveguide to confine the THz wave was a semi-insulating surface plasmon type. Lasing frequency of THz-QCL was $\sim 3.1$ THz [10]. The source of the optical injection pulse was the combination of optical parametric amplifier laser and Ti : S regeneretive amplifier laser pumped by pulse green laser. The wavelengths of optical pulse injection were 770 nm and 1350 nm. The former is corresponding to the higher energy than bandgap
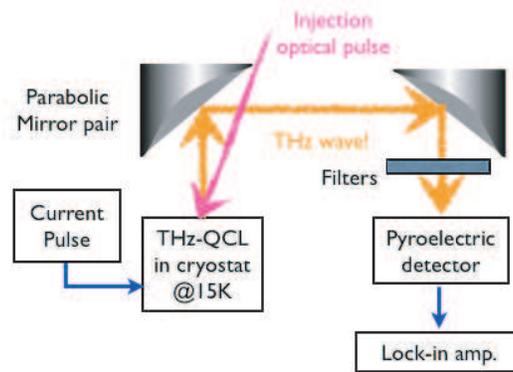
Figure 1: Schematic diagram of the experimental setup for optical pulse injection measurements. The baseplate temperature was kept at 15 K and the output power was measured by a pyroelectric detector using the lock-in technique. The optical pulse was injected by the Otical parametric amplifier system pumped by regenerative amplifier sytem.

energy of GaAs and it can exicte the electron from valence band to conduction band. The later is lower than the bandgap energy of GaAs but it can excite the electron in the conduction band. The optical pulse duration was about 150 fs. The output power of THz-QCL was measured by a pyroelectric detector using the lock-in technique. The reference signal of lock-in detection was provided by the power supply of the regenetive amplifier laser, 1kHz repitation rate. Pulse current was injected syncronize to the reference signal and 300 ns duration. The interval between the optical pulse and the current pulse was controled by delay generator.

## 3. RESULTS AND DISCUSSION

Black line in Figure 2 shows the light-current (L-I) caracteristics without the optical pulse injection. The light output increased at $\sim 5$ A current, and threshold of THz-QCL in this experiment is this current. The threshold is corresponing to $\sim 0.7\,\mathrm{kA/cm^2}$, the current density. The dips around 5.42 A and 5.8 A current were caused by absorption of air. This is confirmed by He gas purge between the THz-QCL cryostat and the detector. The red, green, and blue curves in Figure 2 show the L-I characteristics with 770 nm optical pulse injection. Time interevals were $-400$, 0, and 300 ns, respctively. Photon energy of 770 nm wavelength is higher than bandgap of GaAs. And the photon can excite the transition between the valence and conduction band of GaAs. Injection optical power was about 0.6 mW. Zero time delay was difined as optical pulse and current pulse inject at the same time Negative time delay means that current pulse injected before the optical pulse. There is no difference between the absence (black curve) and absence (red curve) of optical pulse injection. On the contrary, at zero time delay (green blue curve) and positive delay (blue curve), the light output was decreased.

Because of the absorption intensity of GaAs for 770 nm wavelength light is about 1 μm, injected photon were absrobed by the facet of the THz-QCL and the photoexcited carriers exist in the high density. From this condition, plasma frequency is calculated and it is higher than 4 THz. We can consider the plasma at the facet will work as a mirror for THz wave. As a result, output from THz-QCL was decreased. Plasma changed the mirror at the end of cavity, as a result, laser intensity was decreased.

Figure 3 shows L-I characteristics without and with 1350 nm optical pulse injection. Photon energy of the pulse is lower than Eg of GaAs. And the optical pulse cannot cause the transition between the valence and conduction band of GaAs. But it excite free carriers in the conduction band. Reduction of output is observed when the optical pulse is injected. Absorption coeffecent for 1350 nm is small, as a result, it is considered that the injected optical pulse excited uniformly the carriers in the conduction band of THz-QCL. Conduction electrons confined in the quntum well are excited by injected pulse and become free carrier in the continuum state. This cause the decrease of the electron that contribute to the lasing of THz-QCL and light output was decreased. This is suported by the phenomena that current just after the optical pulse injection is increased. The carriers take a shortcut way by excitation into the continuum state by optical pulse injection. This reduction by injection of optical pulse agrees with the precedent study in quality [9].
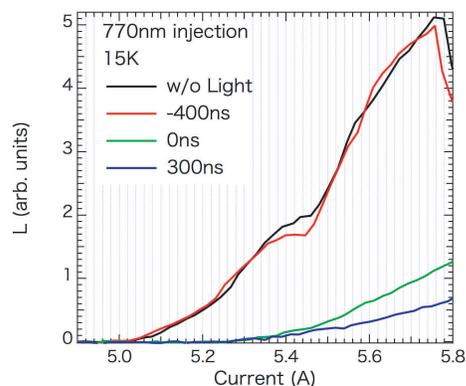
Figure 2: The light-current (L-I) characteristics of the THz QCL without the optical pulse injection and with various intervals between the 770 nm optical and current pulse injection.
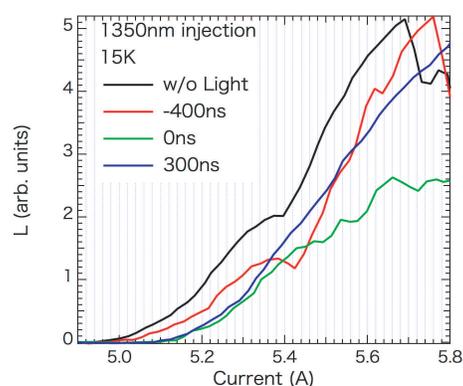
Figure 3: The L-I characteristics of the THz QCL without and with various intervals between the 1350 nm optical and current pulse injection.

## 4. CONCLUSIONS

In order to the observe the response of THz-QCLs to the optical pulse injection, we have built the external optical pulse injection measurement system. In the system, the current pulses and the optical pulses injected to THz QCLs were synchronized. The reduction of output from THz-QCLs was observed when the optical pulses and the current pulses were injected simultaneously. The reduction is explained that the plasmon at the facet excited by the optical pulse above the bandgap energy confined into the THz wave inside of the THz-QCL and carrier number that should contribute to lasing was decreased by the optical pulse below the bandgap.

## ACKNOWLEDGMENT

## REFERENCES

1. Ferguson, B. and X.-C. Zhang, "Materials for terahertz science and technology," *Nature Materials*, Vol. 1, No. 1, 26–33, Sep. 2002.
2. Sakai, K., Ed., *Terahertz Optoelectronics*, Springer, Heidelberg, Berlin, Aug. 2005.
3. Tonouchi, M., "Cutting-edge terahertz technology," *Nature Photonics*, Vol. 1, No. 2, 97–105, Feb. 2007.
4. Fukunaga, K. and Y. Ogawa, H. Shin'ichiro, and I. Hosako, "Terahertz spectroscopy for art conservation," *IEICE Electronics Express*, Vol. 4, No. 8, 258–263, Apr. 2007.
5. Kohler, R., A. Tredicucci, F. Beltram, H. E. Beere, E. H. Linfield, et al., "Terahertz semiconductor-heterostructure laser," *Nature*, Vol. 417, No. 6885, 156–159, May 2002.
6. Mustfa, N., et al., "Terahertz bandwidth prediction for amplitude modulation response of unipolar intersubband semiconductor lasers," *IEEE Photon. Tech. Letter*, Vol. 11, No. 5, 527–529, May 1999.
7. Barbieri, S., W. Maineult, S. S. Dhillon, C. Sirtori, et al., "13 GHz direct modulation of terahertz quantum cascade lasers," *App. Phys. Let.*, Vol. 91, No. 14, 143510-1–3, Oct. 2007.
8. Maineult, W., L. Ding, P. Gellie, P. Filloux, C. Sirtori, et al., "Microwave modulation of terahertz quantum cascade lasers: A transmission-line approach," *App. Phys. Let.*, Vol. 96, No. 2, 021108-1–3, Jan. 2010.
9. Sekine, N. and I. Hosako, "Intensity modulation of terahertz quantum cascade lasers under external light injection," *App. Phys. Let.*, Vol. 95, No. 20, 201106-1–3, Nov. 2009.
10. Hosako, I., N. Sekine, M. Patrashin, S. Saito, K. Fukunaga, et al., "At the dawn of a new era in terahertz technology," *Proceedings of the IEEE*, Vol. 95, No. 8, 1611–1623, Aug. 2007.

# Phononic Band Gaps in One Dimensional Mass Spring System

**Arafa H. Aly**, **Ahmed Mehaney**, and **Hassan S. Hanafey**

Physics Department, Faculty of Sciences, Beni-Sef University, Egypt

**Abstract**— In this work, we have studied theoretically the band gap effect in 1D mass spring system, as well as the mechanical vibrations (longitudinal waves) in infinite periodic lattice subjected to periodic force loading. We have investigated how the number of unit cells affected on the band structure, and on the number of frequency band gaps. We have investigate also how the arranging of the mass that subjected to force loading (i.e., vibrations) affected on creation of band gaps, therefore we have treated the homogenous lattice as a special case approximation. In 1D mass spring system the band structure response and band gaps number were shown to be insensitive to damping force and small imperfections. One dimensional mass spring system can be used as a filter for longitudinal waves and other applications like sound transducer and micromechanical resonators.

## 1. INTRODUCTION

Atoms in crystal cannot move independent of each other. If one atom moved or displaced around its equilibrium position, it exerts by a force on neighboring atoms, which causes them to move and vibrate also. As a consequence, these resultant vibrations and displacements of the crystal called **phonon**, which is considered as wave of lattice vibration that propagate through crystal lattice and solid material. Additionally atoms in a solid are never static but they are in random motion, these vibration can not be controlled naturally but the appearance of new artificial structure known as (**phononic crystals**) make such control possible over phonon [1]. These crystals can be created with periodic placement of two or more materials of different density and/or elastic constant. This periodic structure result in interference and scattering of acoustic wave at interface between the two materials that result in existence of the so called (**phononic band gap**) [2]. This phenomenon similar to band gap in semiconductors where electrons can occupy certain energy band and not allowed in other bands (electronic band gap), also this phenomenon exist for electromagnetic waves in (photonic crystal), i.e., periodic structure of two or more materials of different refractive index, where light can travel in certain frequency ranges and not allowed in other ranges (photonic band gap) [3]. But we must distinguish between light wave and sound wave, where light waves are electromagnetic waves that can travel through vacuum and have two independent polarization (transverse waves). While sound are mechanical waves cannot travel through vacuum as light, it is considered as acoustic waves (waves passing through a gas or a liquid) or elastic waves (those passing through solid), it have three polarization two of these are transverse (shear waves) and one is longitudinal waves (compression wave). It depends mainly on the medium where it propagates, where in liquid it is considered as longitudinal waves while in solid as both longitudinal and transverse waves [4]. More details about wave propagation in periodic structure and frequency band gaps can be found in Ref. [5]. In this work we are interested in studying the band gap effect of finite periodicity and discrete mass spring system, where crystal lattice structure can be modeled by mass and spring network in a micro-electo-mechanical system (**MEMS**) [6]. These systems describe the dynamical behavior of periodic structure where the mechanical vibration of masses connected with springs can be considered as longitudinal wave, and through these vibrations of the Whole system, phononic band gaps for certain frequencies of longitudinal waves can be created, where waves are not allowed to propagate through these bands. First we introduce an example deals with 1D structure (**Section 2**) consist of infinite number of masses and springs unit cells [7]. The unit cell describe the repetitive units in the periodic structure, this model can be used as an application, i.e., as a filter for acoustic waves when we analyze the vibrational response of this periodic structure that subjected to periodic force loading in the band gap frequency range. Secondly we deal with a special case approximation (**Section 3**), number of different masses and springs, and investigate the frequency band gaps ranges, after that we will show how the number of masses and springs affect on the response in the band gap frequency range and on the number of the band gaps. We also will prove that damping vibrations dose not has great effect on the band structure and band gaps in 1D mass spring system. We will explain two cases deals with the position of the first mass that subjected to periodic force loading and the result of changing this position on the band structure, especially in homogenous unit cells.

## 2. THEORETICAL ANALYSIS

### 2.1. 1D Infinite Lattice

We have considered the infinite 1D mass spring system consist of unit cells. The unit cell have $N$ masses $m_j$ coupled with spring $k_j$ and anchored to ground with spring $k_j'$ [7] as in Fig. 1. This unit cell is repeated periodically to describe the infinite lattice (or micro structure). We have two different cases for this structure, if the unit cell made up of masses and springs of the same kind is said to be homogenous unit cell and the corresponding structure is also homogenous. While if it made up of different masses and/or springs is said to be inhomogeneous unit cell and the corresponding structure is periodic. Firstly we will analyze theoretically wave propagating in periodic structure as in Fig. 1.

Results are the dispersion relations that relate the frequency of wave propagating through lattice structure to wave number; moreover it gives us all information about propagation and show the band structure of Material (or lattice).

The force balance equation of this system (simple harmonic motion equation) [8] can be written as

$$m\,\ddot{u} + k\,u = 0 \tag{1}$$

where $m$, $k$ and $u$ denotes the vectors of masses, spring (stiffness) constant and displacement constants, respectively. Also $\omega^2 = k/m$, where $\omega$ is the angular frequency of longitudinal waves that propagate through system. The small amplitude displacement of the $(p+j)$ mass is derived from Eq. (1) and analyzed as in Fig. 2 as follow,

$$m_j\,\ddot{u}_{p+j} = -k_j\,(u_{p+j} - u_{p+j+1}) - k_{j-1}\,(u_{p+j} - u_{p+j-1}) - k_j'\,u_{p+j} \tag{2}$$

where $p$ is an arbitrary integer. This equation can be written also as

$$m_j\,\ddot{u}_{p+j} = k_j\,(u_{p+j+1} - u_{p+j}) - k_{j-1}\,(u_{p+j} - u_{p+j-1}) - k_j'\,u_{p+j} \tag{3}$$

because of it was considered as a one type of harmonic motion equations, the solution of Eq. (3) is sinusoidal wave of the form

$$u_{p+j}(t) = A_j\,e^{i((p+j)\gamma - \omega t)} \tag{4}$$

where $A_j$ is the wave amplitude, $\gamma$ is the wave number, i.e., $\gamma = |\omega/c| = |k|$ Since $c$ is the wave velocity and $k$ is the wave vector.

By sub Eq. (4) into Eq. (3) result in

$$-m_j\,A_j\,\omega^2 = k_j\,e^{i\gamma}\,A_{j+1} - k_j\,A_j - k_{j-1}\,A_j + k_{j-1}\,e^{-i\gamma}\,A_{j-1} - k_j'\,A_j \tag{5}$$

This produces $N$ linear complex equations of the form

$$\left(\omega_j^2 + \frac{k_j'}{m_j} - \omega^2\right) A_j = c_j^2 e^{i\gamma} A_{j+1} + \left(\omega_j^2 - c_j^2\right) e^{-i\gamma} A_{j-1} \qquad j = 1, \ldots, N \tag{6}$$

where we are assumed the two parameters
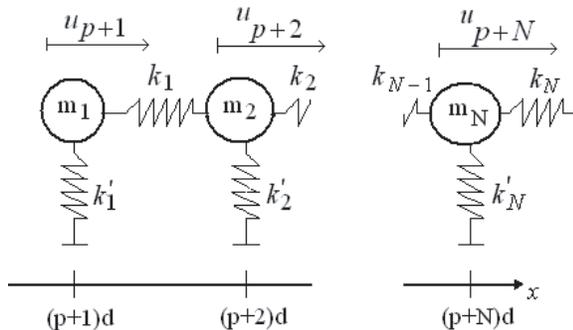


Figure 1: The 1-D unit cell with $N$ masses $(mj)$ and $2 \times N$ springs $(kj, k'j)$ [6].
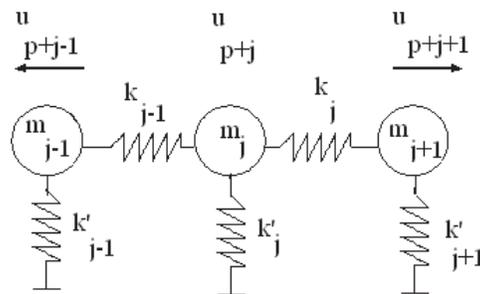
Figure 2: An example of displacement on mass $m_j$ and its effect on neighboring masses.
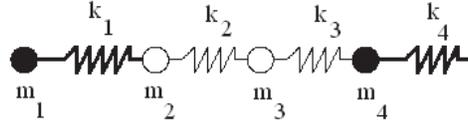
Figure 3: unit cell with $N = 4$ masses and springs.

$$\omega_j^2 = \frac{k_j + k_{j-1}}{m_j}, \qquad c_j^2 = \frac{k_j}{m_j} \tag{7}$$

By using Eq. (6) that represents the dispersion relation between the frequency ($\omega$) and the wave number ($\gamma$), we can deal with any number of masses and springs, and draw the band structure of any system. But an infinite number of unit cells are considered, so we apply the following boundary conditions

$$A_{j-1} = A_N, \ \ j = 1 \text{ and } A_{j+1} = A_1, \quad j = N \tag{8}$$

## 3. RESULTS AND DISCUSSION

### 3.1. Wave Propagation through Unit Cells

Wave propagation through unit cells depend mainly on the type of the unit cells. It well known gaps exist only for inhomogeneous infinite lattice, due to the difference in mechanical properties of the materials constructing the crystal structure. While no gaps exist for the homogenous unit cells and all frequencies are allowed to propagate through structure. But in this system it depend on where the force loading began, since the position of the mass that subjected to the force of vibration affected on the band structure especially in the case of homogenous unit cell. Here we will introduce an example for illustrating the band structure of the system in the two cases, i.e., homogenous and inhomogeneous unit cells.

Firstly we consider an inhomogeneous unit cell consist of four masses system ($N = 4$) Corresponding to 0.15 m rod with middle 50% Lead[1] and the two ends of Nickel[2] as illustrated in Fig. 3. Where the middle representing material with lower stiffness constant ($k$) and mass ratio ($m$) comparable to the two ends material.

The values of masses and springs are listed in Equation (9).

$$m_1 = m_4 = 4 \, \text{kg} \ \text{ and } \ m_2 = m_3 = 1.5 \, \text{kg}$$
$$k_1 = k_4 = 213.76 \times 10^9 \, \text{kg/m} \cdot \text{s}^2 \text{ and } k_2 = k_3 = 15.444 \times 10^9 \, \text{kg/m} \cdot \text{s}^2 \tag{9}$$

Now, we consider the mass ($m_1$) is subjected to force loading, and we obtained the resultant frequency on the last mass ($m_4$). According to Eqs. (6)–(8), the frequency response of the system can be represented by the equations

$$\left(\omega_1^2 + \frac{k_1'}{m_1} - \omega^2\right) A_1 = c_1^2 e^{i\gamma} A_2 + (\omega_1^2 - c_1^2) e^{-i\gamma} A_4 \tag{10}$$

$$\left(\omega_2^2 + \frac{k_2'}{m_2} - \omega^2\right) A_2 = c_2^2 e^{i\gamma} A_3 + (\omega_2^2 - c_2^2) e^{-i\gamma} A_1 \tag{11}$$

$$\left(\omega_3^2 + \frac{k_3'}{m_3} - \omega^2\right) A_3 = c_3^2 e^{i\gamma} A_4 + (\omega_3^2 - c_3^2) e^{-i\gamma} A_2 \tag{12}$$

$$\left(\omega_4^2 + \frac{k_4'}{m4} - \omega^2\right) A_4 = c_4^2 e^{i\gamma} A_1 + (\omega_4^2 - c_4^2) e^{-i\gamma} A_3 \tag{13}$$

From these equations the dispersion relation is plotted for the wave number ($\gamma$) versus the frequency ($\omega$) as in Fig. 4. As it well known the values of any amplitude are constant number in any case, so we assume firstly that all amplitudes values ($A_1, A_2, \ldots$) are equals as in Fig. 4, after that to confirm the results we consider any values for $A_1, A2, \ldots$. We have taken for example $A_1 = 1 \, \text{cm}$, $A_2 = 2 \, \text{cm}$, $A_3 = 3 \, \text{cm}$, $A_4 = 4 \, \text{cm}$.

---

[1] $E_{LEAD} = 15.444 \times 10^9 \, \text{N/m}^2$, $\rho_{LEAD} = 11.34 \times 10^3 \, \text{kg/m}^3$.
[2] $E_{NIC} = 213.76 \times 10^9 \, \text{N/m}^2$, $\rho_{NIC} = 8.8 \times 10^3 \, \text{kg/m}^3$.

Because of this structure considered as a periodic structure, all propagating modes (waves) will be the same in the irreducible brillouin zone. So we don't need to plot all values of ($\gamma$) because each two neighboring masses are move in phase or anti phase corresponding to $\gamma N = 0$ and $\pi$ respectively so the minimum and maximum points of B. Z is 0 and $\pi$ [7]. But from 0 to $\pi$ we can take many values as in Figs. 4(b), 4(c) and 4(d), in order to illustrate the zone that appear the band gap sharply inside the structure as in Fig. 4(d) $(3 : \pi)$. We can consider this range (zone) the accurate rang of the band gap values inside the structure. Due to periodicity the curve would simply be repeated if a larger range by the same value of $\gamma(3 : \pi)$ were graphed.

In Fig. 4, we assumed that all amplitudes have the same value, and there is a damping force (vibrations) represented by the ground springs, where we considered $k'_1 = k_1, k'_2 = k_2, \ldots$ We notice that as in Fig. 4(a) at small values of the wave number the relation is linear. If the wave number taken to be zero, the frequency equal to zero as in red line in the figure. This make the masses to have the same amplitude and move in phase. As the wave number began to increase, the frequency also increased as in all Figs. 4(a), 4(b), 4(c) and 4(d), this causes the masses to move at the same amplitude but out of phase. We can note also there is no gap exist in Fig. 4(a), but as the range of ($\gamma$) shifted from $(0 : \pi)$ to $(2 : \pi)$ and $(3 : \pi)$, the gaps begin to appear sharply Figs. 4(c) and 4(d). Where in Fig. 4(c) there are two band gaps approximately at $\omega = (3.2\text{--}3.7)$, $(4.1\text{--}5) \times 10^5$ Hz, and in Fig. 4(d) there are three large band gaps approximately at $\omega = (3.1\text{--}4)$, $(4\text{--}4.1)$ and $(4.1\text{--}5.65) \times 10^5$ Hz. Therefore no waves can propagate in these frequency ranges, As a consequence we can take these regions as the zone that shows the band gaps inside structure especially in the last Fig. 4(d).

Now we will investigate what the result is if there isn't any damping in the system, i.e.,

$$k'_1 = k'_2 = k'_3 = k'_4 = 0.$$

We had taken the range $\gamma N = 3 : \pi$ as in Fig. 5. More details can be found in Ref. [9].

We can note in Fig. 5 that the effect of damping was not very sensitive in the band structure and in the formation of band gaps, but there is a slightly change in frequency band gaps values where the three band gaps range became are at $\omega = (2.8\text{--} 3.3)$, $(3.3\text{--}3.4)$ and $(3.4\text{---}5.6) \times 10^5$ Hz, so we comment the absence of damping in changing band gaps rang only. Now we will consider that,
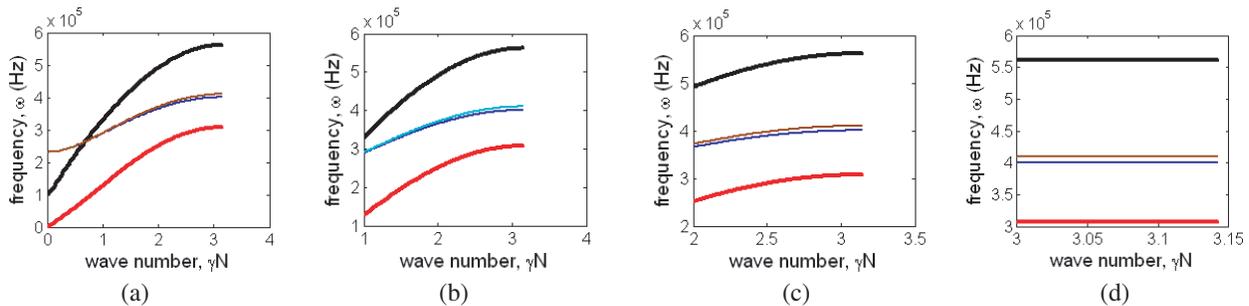


Figure 4: Band structure of wave propagation in infinite periodic lattice, which show the dispersion curve of one dimensional mass spring system for wave number, (a) $\gamma N = 0 : \pi$. (b) $\gamma N = 1 : \pi$, (c) $\gamma N = 2 : \pi$ and (d) $\gamma N = 3 : \pi$.
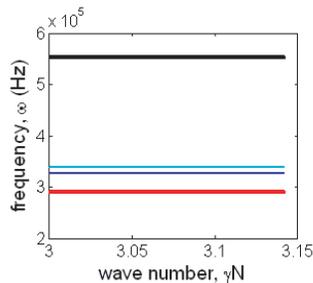


Figure 5: Band structure of wave propagation in infinite periodic lattice without damping.
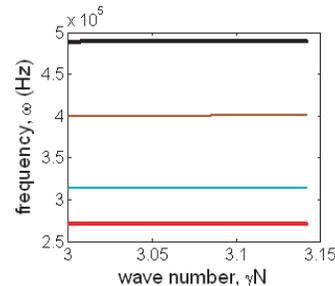
Figure 6: Band structure of wave propagation in infinite periodic lattice with damping and different amplitudes.

there is a damping force and different amplitude values, we will take the assumption $A_1 = 1\,\text{cm}$, $A_2 = 2\,\text{cm}$, $A_3 = 3\,\text{cm}$, $A_4 = 4\,\text{cm}$. We can note in Fig. 6 when the amplitudes have different values, there is not significant difference in the band structure and number of band gaps, but there is a slightly difference in band gaps ranges where the three band gaps range became approximately at $\omega = (2.7\text{–}3.15)$, $(3.15\text{–}4)$ and $(4\text{–}4.9) \times 10^5\,\text{Hz}$.

## 4. CONCLUSION

In this work, we had studied phononic band gaps in one dimensional mass spring system. These structures can be used as an acoustic wave filter, furthermore can be utilized in micro-structure (unit cells) for producing micromechanical resonator that can be used in many other applications. It was shown how the 1D mass spring system can be used in the creation of frequency band gaps in infinite periodic lattice, and how the number of unit cells affected on the band structure of the system and on number of band gaps. The response in the band gaps was not very sensitive to moderate amount of damping forces, and also when all amplitudes have the same value. We have seen how the arranging of the mass that subjected to the force loading effected on the structure, especially in the case of homogenous unit cell. There are a frequency band gaps in the homogenous structure only if the force loading began at the first mass,and there is not any gaps if it began at any mass else inside the system.

Finally more results and applications will be obtained, if we study this phenomenon in 1D and 2D mass spring systems. An extension of this work is the application of topology optimization in the design of systems and structures with phononic band gaps materials, more details can be found in Ref. [10].

### REFERENCES

1. Gorishyy, T., M. Maldovan, C. Ullal, and E. Thomas, "Sound ideas," *Physics World*, 24–29, 2005.
2. Rayleigh, L., "On the maintenance of vibrations by forces of double frequency, and on the propagation of waves through a medium endowed with a periodic structure," *Philosophical Magazine*, 24–37, 1887.
3. Yablonovitch, E., "Photonic crystals: Semiconductors of light," *Scientific American*, 285–291, 2001.
4. Armenise, M. N., C. E. Campanella, C. Ciminelli, F. Dell'Olio, and V. M. N. Passro, "Photonic and phononic band gap structures: Modelling and application," *Physics Procedia*, Vol. 3, 357–364, 2010.
5. Brillouin, L., *Wave Propagation in Periodic Structure*, Dover Publication Inc, New York, 1953.
6. Cao, Z. J., "One and two-dimensional mass and spring computational models for phononic band gaps analysis," A Thesis Presented to the University of Walterloo in Fulfillment of the Thesis Requirement for the Degree of Master of Applied Science in Electrical and Computer Engineering, 1–104, 2009.
7. Jensen, J. S., "Phononic band gaps and vibrations in one and two dimensional mass spring structures," *Journal of Sound and Vibration*, Vol. 266, No. 5, 1053–1078, 2003.
8. Barger, V. and M. Olsson, *Classical Mechanics*, Ch. 1, McGraw-Hill Book Co., New York, 1973.
9. Gürgöze, M. and S. Zeren, "Consideration of the masses of helical springs in forced vibrations of damped combined systems," Vol. 38, 4, 2011.
10. Sigmund, O. and J. S. Jensen, "Topology optimization of phononic band gap materials and structures," *Fifth Word Congress on Computational Mechanics*, Vienna, 2002.

# The Influence of the Electromagnetic Wave on the Nonlinear Acoustoelectric Effect in a Superlattice

**N. V. Hieu, N. Q. Bau**, and **N. V. Nhan**

Faculty of Physics, Hanoi University of Science
Vietnam National University, Hanoi, Vietnam

**Abstract**— The influence of the electromagnetic wave on the nonlinear acoustoelectric effect (AE) in a superlattice (SL) is investigated for an acoustic wave whose wavelength $\lambda = 2\pi/q$ is smaller than the mean free path $l$ of the electrons and hypersound in the region $ql \gg 1$ (where $q$ is the acoustic wave number). The dependence of the AE current $j^{ac}$ on the acoustic intensity $\Phi$, the acoustic wave number $q$, the intensity $E$ and frequency $\Omega$ of the electromagnetic wave are obtained by using the Boltzmann kinetic equation in the case of relaxation time of momentum $\tau$ constant approximation, and the degenerate electron gas. Numerical calculation is done, and the result is discussed for a typical GaAs/AlAs SL. At $\omega_q = 10^{11}\,\mathrm{s}^{-1}$, $\Omega\tau = 10^{-1}$, $\Delta = 1.6 \cdot 10^{-20} J$ (here $\omega_{\vec{q}}$ is frequency of sound wave, $2\Delta$ is the width of the lowest energy miniband), the acoustoelectric current behaviour in the same manner as the constant electric field. At this frequency $\omega_{\vec{q}} = 10^{11}\,\mathrm{s}^{-1}$ the graph is symmetrical about the origin. As $\omega_{\vec{q}}$ increases the symmetry breaks down and at $\omega_{\vec{q}} = 10^{13}\,\mathrm{s}^{-1}$ we obtaine the ratio $|j_z^{ac}/j_0^{ac}|_{\min}/|j_z^{ac}/j_0^{ac}|_{\max}$ is larger than in the case absence of the electromagnetic wave.

## 1. INTRODUCTION

When an acoustic wave is absorbed by a conductor, the transfer of the momentum from the acoustic wave to the conduction electron may give rise to a current usually called the AE current, $j^{ac}$, in the case of an open circuit, a constant electric field, $E^{ac}$. The study of this effect is crucial, because of the complementary role it may play in the understanding of the properties of the superlattice (SL), which, we believe, should find an important place in the acoustoelectronic devices. The study of the AE effect in bulk materials have received a lot of attention [1–5].

It is well known that in a low dimensional systems (QW, superlattices, quantum wires...), the motion of electrons is restricted in one dimension or two dimensions, so they can flow freely in two dimensions or one dimension. The confinement of electrons in a low dimensional systems changes the electron mobility remarkably. This results in a number of new phenomena, which concern a reduction of the sample dimensions. The effect, for example, electron-phonon interaction and scattering rates [6,7], dc electrical conductivity [8,9] and optical properties also been investigated [10–15], differ from those in a bulk semiconductors, and we think the electron confinement in the SL is also influential the AE effect. Recently, the AE effect was studied by theory in a one-dimensional channel [16], in a finite-length ballistic quantum channel [17–19], in a SL [20–25] for the case absence of the electromagnetic wave. In addition, in the case absence of the electromagnetic wave, the AE was also measured by experiment in a two dimensional system (Quantum well, SL) [26,27], in a quantum wire [28], and in a carbon nanotube [29]. However, in the SL, the nonlinear AE effect and the influence of electromagnetic wave on it in the case of the degenerate electron gas were still open for studying.

In this paper, we studied the nonlinear AE effect and the influence of electromagnetic wave on the AE effect. We examined this effect in the SL for the case of electron relaxation time is not dependent on the energy and the degenerate electron gas. We will show that the periodicity of the energy spectrum of the electron along the SL axis cause a nonlinear dependence of the $j^{ac}$ on the wavenumber $q$, and the frequency of the electromagnetic wave modulates the AE current. In addition, we noted that the AE current is negative or positive depending on the direction of the constant electric field.

This paper is organized as followed. In Section 2, we outline the theory and conditions necessary to solve the problem, in Section 3 we discuss the results, and in Section 4 we come to a conclusion.

## 2. ACOUSTOELECTRIC CURRENT

By using the classical Boltzmann kenetic equation method, we calculated the acoustoelectric current in the SL. The acoustic wave is considered a hypersound in the region $ql \gg 1$ ( $l$ is the electron mean free path, $q$ is the acoustic wave number). Under such circumstances the acoustic wave can

be interpreted as monochromatic phonons having the 3D phonon distribution function $N(\vec{k})$, and can be presented in the form [28]

$$N(\vec{k}) = \frac{(2\pi)^3}{\hbar \omega_{\vec{q}} v_s} \Phi \delta(\vec{k} - \vec{q}), \tag{1}$$

where $\hbar = 1$, $\vec{k}$ is the current phonon wave vector, $\Phi$ is the sound flux density, $\omega_{\vec{q}}$ and $v_s$ are the frequency, and the group velocity of sound wave with the wave vector $\vec{q}$, respectively.

It is assumed that the sound wave and the applied electric field $\vec{E}$ propagates along the $z$ axis of the SL. The problem was solved in the quasi-classical case, i.e., $2\Delta \gg \tau^{-1}$, $2\Delta \gg eEd$ ($\tau$ is the relaxation time, $d$ is the period of the SL, $2\Delta$ is the width of the lowest energy miniband and $e$ is the electron charge). The density of the acoustoelectric current can be written in the form

$$j^{ac} = \frac{2e}{(2\pi)^3} \int U_{n,n'}^{ac} \psi_i(\vec{p}) d^3\vec{p}. \tag{2}$$

Here, $\psi_i(\vec{p})$ is the solution of the Boltzmann kinetic equation in the absence of the magnetic field, $\vec{p}$ is the electron momentum vector and

$$U_{n,n'}^{ac} = \frac{2\pi\Phi}{\omega_{\vec{q}} v_s} \sum_{n,n'} \left\{ |G_{\vec{p}-\vec{q},\vec{p}}|^2 [f(\epsilon_{n,\vec{p}-\vec{q}}) - f(\epsilon_{n',\vec{p}})] \delta(\epsilon_{n,\vec{p}-\vec{q}} - \epsilon_{n',\vec{p}} + \omega_{\vec{q}}) \right.$$

$$\left. + |G_{\vec{p}+\vec{q},\vec{p}}|^2 [f(\epsilon_{n',\vec{p}+\vec{q}}) - f(\epsilon_{n,\vec{p}})] \delta(\epsilon_{n',\vec{p}+\vec{q}} - \epsilon_{n,\vec{p}} - \omega_{\vec{q}}) \right\}, \tag{3}$$

where $f(\epsilon_{n,\vec{p}})$ is the distribution function, $\epsilon_{n,\vec{p}}$ is the energy spectrum of the electron, $n$ and $n'$ denote quantization of the energy spectrum, and $G_{\vec{p}\pm\vec{q},\vec{p}}$ is the matrix element of the electron-phonon interaction. Introducing a new term $\vec{p}' = \vec{p} - \vec{q}$ in the first term of the integrals in Equation (3) and taking into account of the fact that

$$|G_{\vec{p},\vec{p}'}|^2 = |G_{\vec{p}',\vec{p}}|^2, \tag{4}$$

the matrix element of the electron-phonon interaction for $qd \ll 1$ is given

$$|G\vec{p}, \vec{q}|^2 = \frac{\wedge^2 \vec{q}^2}{2\sigma\omega_{\vec{q}}}, \tag{5}$$

where $\wedge$ is the deformation potential constant and $\sigma$ is the density of the SL.

We can express Equation (2) in the form

$$j_i^{ac} = -\frac{e\Phi}{2\pi^2 v_s \omega_{\vec{q}}} \sum_{n,n'} \int |G_{\vec{p}+\vec{q},\vec{p}}|^2 [f(\epsilon_{n',\vec{p}+\vec{q}}) - f(\epsilon_{n,\vec{p}})][\psi_i(\vec{p}+\vec{q}) - \psi_i(\vec{p})] \times \delta(\epsilon_{n',\vec{p}+\vec{q}} - \epsilon_{n,\vec{p}} - \omega_{\vec{q}}) d^3\vec{p}, \tag{6}$$

where the vector $\psi_i(\vec{p})$, as indicated [29], is the mean free path $l_i(\vec{p})$.

In solving Equation (6) we considered a situation whereby the sound was propagating along the SL axis $(oz)$, thus the acoustoelectric current in Equation (6) in the direction of the SL axis becomes

$$j_z^{ac} = -\frac{e\Phi\vec{q}^2\tau\wedge^2}{4\pi^2 v_s \omega_{\vec{q}}^2 \sigma} \sum_{n,n'} \int [f(\epsilon_{n',\vec{p}+\vec{q}}) - f(\epsilon_{n,\vec{p}})][l_z(\vec{p}+\vec{q}) - l_z(\vec{p})] \delta(\epsilon_{n',\vec{p}+\vec{q}} - \epsilon_{n,\vec{p}} - \omega_{\vec{q}}) d^3\vec{p}, \tag{7}$$

the distribution function in the presence of the applied field $\vec{E}$ is obtained by solving the Boltzmann equation in the $\tau$ approximation. This function is given

$$f(\vec{p}) = \int_0^\infty \frac{dt}{\tau} \exp(-t/\tau) f_0(\vec{p} - e\vec{E}t), \tag{8}$$

here

$$f_0(\vec{p}) = \Theta(\epsilon_F - \epsilon_{n,\vec{p}}) = \begin{cases} 0 & \epsilon_{n,\vec{p}} > \epsilon_F \\ 1 & \epsilon_{n,\vec{p}} < \epsilon_F, \end{cases} \tag{9}$$

where $\epsilon_F$ is Fermi energy. The energy spectrum $\epsilon_{n,\vec{p}}$ of the electron in the SL is given using the usual notation by $\epsilon_{n,\vec{p}} = \frac{\vec{p}_\perp^2}{2m} + \Delta_n(1 - \cos(p_z d))$, $\vec{p}_\perp$ and $p_z$ are the transverse and longitudinal (relative to the SL axis) components of the quasi-momentum, respectively; $\Delta_n$ is the half width of the $n$th allowed miniband, $m$ is the effective mass of electron.

We assumed that electrons are confined to the lowest conduction miniband ($n = n' = 1$) and omitted the miniband indicated. That is say that the field does not induce transitions between the filled and empty minibands, thus the $\Delta_n$ can be written as $\Delta$.

Substituting Equation (8) and the energy spectrum into Equation (7), we obtained the acoustoelectric current

$$j_z^{ac} = j_0^{ac} \int_0^\infty \frac{dt}{\tau} \exp\left(\frac{-t}{\tau}\right) \sin\left(eEt - \frac{q}{2}\right) d \times \left[A \sin\frac{qd}{2} + (1 - A^2)^{1/2} \cos\frac{qd}{2}\right], \quad (10)$$

here

$$j_0^{ac} = \frac{em\Phi\vec{q}^2\tau \wedge^2 \Delta}{\pi v_s \omega_{\vec{q}}^2 \sigma}\left[1 - \left(\frac{\omega_{\vec{q}}}{2\Delta \sin(qd/2)}\right)^2\right]^{1/2}, \quad A = \frac{\omega_{\vec{q}}}{2\Delta} + \cos\frac{qd}{2}\left[1 - \left(\frac{\omega_{\vec{q}}}{2\Delta \sin(qd/2)}\right)^2\right]^{1/2}.$$

Equation (10) is acoustoelectric current in the case of the presence of electromagnetic field $\vec{E}$ applide along the $z$ axis and the degenerate electron gas.

## 3. NUMERICAL RESULTS AND DISCUSSIONS

We considered an electromagnetic field of the form $E_0 + E_1 \sin\Omega t$. Under such conditions we replaced the electric field $E$ in Equation (10) with $E_0 + E_1 \sin\Omega t$ and averaged the results overtime. From the Figure 1. It is noted that for $\omega_q = 10^{11}\,\mathrm{s}^{-1}$, $\Omega\tau = 10^{-1}$, $\Delta = 1.6 \cdot 10^{-20}J$, the acoustoelectric current behaviour in the same manner as the constant electric field. The $E_1$ in this case is behaving as a modulator. At this frequency $\omega_q = 10^{11}\,\mathrm{s}^{-1}$ the graph is symmetrical about the origin. As $\omega_q$ increases, it can see in Figure 2 the symmetry breaks down at $\omega_q = 10^{13}\,\mathrm{s}^{-1}$. We obtained that the absolute value of the maximum peak $|j_z^{ac}/j_0^{ac}|_{\max}$ is smaller than the absolute minimum value $|j_z^{ac}/j_0^{ac}|_{\min}$, and the ratio $|j_z^{ac}/j_0^{ac}|_{\min}/|j_z^{ac}/j_0^{ac}|_{\max}$ is about 4, which is quiet big. We examined herein, the behaviour of the acoustoelectric current $j_z^{ac}$ when the dc field $E_0$ is kept constant and the amplitude of the ac field $E_1$ is varied, we observed that for $\omega_q = 10^{11}\,\mathrm{s}^{-1}$ and $E_0 = 0$, the acoustoelectric current is very small and tends to zero at $E_1 = 1.6.10^4\,\mathrm{Vm}^{-1}$. This can be explained from the fact that at $\omega_q = \Omega$, the phonon energy is not high enough to impact much momentum to the conduction electrons, therefore very low current is observed. With increase in the phonon frequency $\omega_q = 10^{13}\,\mathrm{s}^{-1}$, $j_z^{ac}$ increased rapidly even in the absence of $E_0$. This is expected because
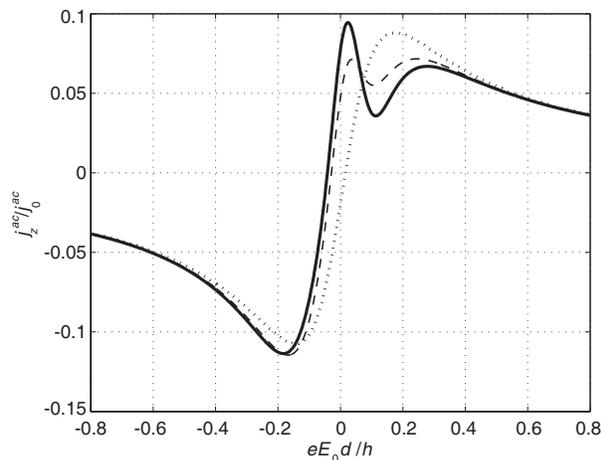


Figure 1: The dependence of $j_z^{ac}/j_0^{ac}$ on the $eE_0 d\tau/h$: $eE_1 d\tau/h = 0$ (dotted line); $eE_1 d\tau/h = 0.25$ (dashed line); $eE_1 d\tau/h = 0.35$ (solid line); $\omega_{\vec{q}} = 10^{11}\,\mathrm{s}^{-1}$; $\Omega = 10^{11}\,\mathrm{s}^{-1}$.
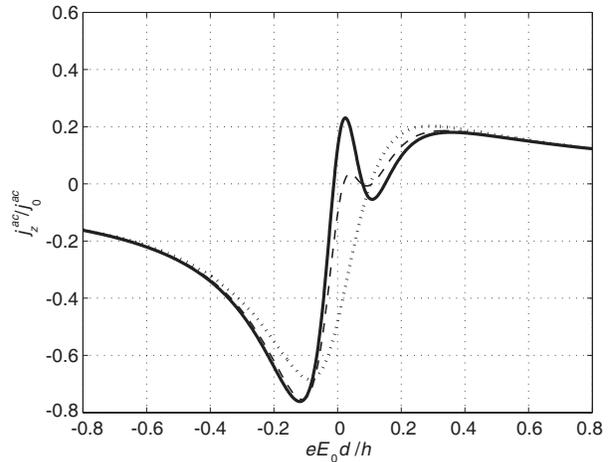
Figure 2: The dependence of $j_z^{ac}/j_0^{ac}$ on the $eE_0 d\tau/h$: $eE_1 d\tau/h = 0$ (dotted line); $eE_1 d\tau/h = 0.25$ (dashed line); $eE_1 d\tau/h = 0.35$ (solid line); $\omega_{\vec{q}} = 10^{13}\,\mathrm{s}^{-1}$; $\Omega = 10^{11}\,\mathrm{s}^{-1}$.
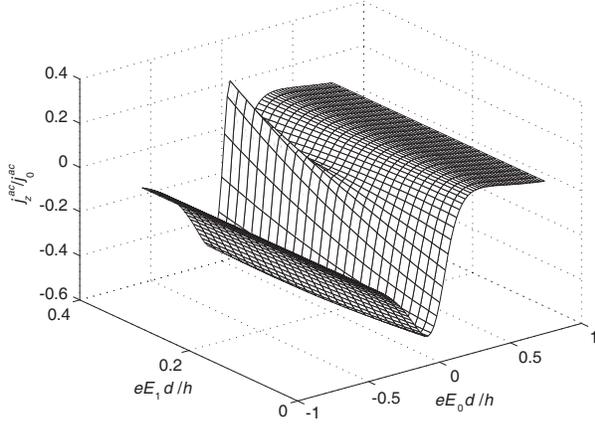
Figure 3: The dependence of $j_z^{ac}/j_0^{ac}$ on the $eE_0d\tau/h$ and $eE_1d\tau/h$ for $\omega_{\vec{q}} = 10^{13}\,\text{s}^{-1}$; $\Omega = 10^{11}\,\text{s}^{-1}$.
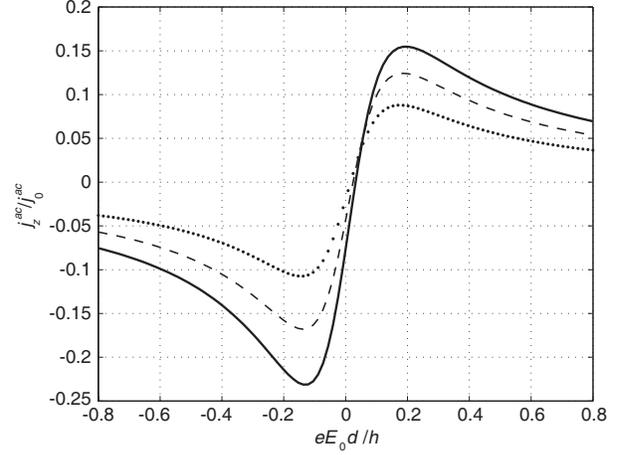
Figure 4: The dependence of $j_z^{ac}/j_0^{ac}$ on the $eEd\tau/h$: $\omega_{\vec{q}} = 2 \times 10^{11}\,\text{s}^{-1}$ (solid line); $\omega_{\vec{q}} = 1.5 \times 10^{11}\,\text{s}^{-1}$ (dashed line); $\omega_{\vec{q}} = 10^{11}\,\text{s}^{-1}$ (dotted line).

the phonon acquires enough energy to impact momentum to the conduction electrons. It is worth noting that about $E_0 = 2.10^5\,\text{Vm}^{-1}$ and above, $E_1$ ceased to modulate the acoustoelectric current. In the Figure 3 we present the three-dimensional graphs of $j_z^{ac}/j_0^{ac}$ against $E_0$ and $E_1$. It see when $\omega_q = 10^{13}\,\text{s}^{-1}$, the symmetry breaks down.

In this situation the field is a constant, Equation (10) was solved analytically and the result was given as

$$
\begin{aligned}
j_z^{ac} = & -j_0^{ac}\frac{1}{(eEd\tau)^2 + 1}\left[1 - eEd\tau\tan^{-1}(qd/2)\right] \\
& \times \left[A\sin^2(qd/2) + (1 - A^2)^{1/2}\sin(qd/2)\cos(qd/2)\right],
\end{aligned}
\tag{11}
$$

Equation (11) is the analytical expression of acoustoelectric current in the case of the presence of external electric field. From Equation (11) it is observed that

$$
E > E_0 = \frac{1}{ed\tau}\tan(qd/2).
$$

This is condition of external electric field applied to acoustoelectric current changes direction. The acoustoelectric current changes sign and the value $E_0$ can be interpreted as a threshold field. $E_0$ is a function of the SL parameters $d$, frequency $\omega_{\vec{q}}$ and the wavenumber $q$. For instances, at $d = 10^{-8}\,\text{m}$, $\tau = 10^{-12}\,\text{s}$, and $\omega_{\vec{q}} = 10^{11}\,\text{s}^{-1}$, the threshold field $E_0 = 31.94\,\text{Vcm}^{-1}$, which is small but can still be observed. This result approximates the result in [21], therefore we want to emphasize which satisfaction of our result with the result in [21], gives credence to Equation (10). The dependence of the acoustoelectric current $j_z^{ac}$ on constant electric field $E$ has been studied in Figure 4. The dependence of $j_z^{ac}/j_0^{ac}$ on $E$ for given $\omega_{\vec{q}}$ is not linear. The electric field is positive and the current increases, reaching a maximum and then decreasing. It is noteworthy to show that a similar nonlinear relation was obtained for a TAV experiment on Si/SiO$_2$ and this result agree with result [32].

## 4. CONCLUSION

We have studied the acoustoelectric current in SL in the presence of a constant and the electromagnetic wave and noted a strong nonlinear dependence of $j_z^{ac}$ on both $E_0$ and $E_1$ which strongly depends on $\omega_{\vec{q}}$ of the acoustic wave, the SL parameters $\Delta$ and $d$ is the miniband width and the period of the SL, respectively. The dominant mechanism for such nonlinear behaviour is the periodicity of the energy spectrum of the electron along the SL axis. We observed that in the absence of dc field $E_0$, when $\omega_{\vec{q}} = 10^{11}\,\text{s}^{-1}$, $j_z^{ac}$ is very small and tends to zero at $E_1 = 1.6.10^4\,\text{Vm}^{-1}$. Futhermore increase in $\omega_{\vec{q}}$ to $10^{13}\,\text{s}^{-1}$ shot up the acoustoelectric current $j_z^{ac}$ dramatically, and the symmetry breaks down, the ratio $|j_z^{ac}/j_0^{ac}|_{\text{min}}/|j_z^{ac}/j_0^{ac}|_{\text{max}}$ is about 4. When $E_0$ is introduced, $j_z^{ac}$ increased with the increase of $E_0$.

The results above indicate that there exists some peaks which disappear in the bulk semiconductor [31], the cause of the difference is because of the low-dimensional systems' characteristics, meaning in the SL the energy spectrum of the electron is quantized because of the electron confinement in the SL.

The numerical result obtained for a GaAs/AlAs SL shows that there exists a threshold field $E_0$ for which the acoustoelectric current changes direction and this value increases with an increase in $\omega_{\vec{q}}$, when $d = 10^{-8}$ m, $\tau = 10^{-12}$ s, and $\omega_{\vec{q}} = 10^{11}$ s$^{-1}$, the threshold field $E_0 = 31.94$ Vcm$^{-1}$, when $\omega_{\vec{q}} = 2 \times 10^{11}$ s$^{-1}$, the threshold field $E_0 = 33.5$ Vcm$^{-1}$. Our result indicates that the acoustoelectric current exists even if the relaxation time $\tau$ of the carrier does not depend on the carrier energy. This differs from the bulk semiconductor, because in the bulk semiconductor [30] indicated that the dominant mechanism for the appearance of the acoustoelectric effect depends on an acoustic wave propagating direction and the relaxation time $\tau$ of the carrier depends on the carrier energy.

## ACKNOWLEDGMENT

**REFERENCES**

1. Parmenter, R. H., "The acousto-electric effect," *Phys. Rev.*, Vol. 89, 990, 1953.
2. Johri, G. and H. N. Spector, "Nonlinear AE effect in semiconductor," *Phys. Rev.*, Vol. 15, 4955, 1959.
3. Kogami, M. and S. Tanaka, "AME and AE effect in N-InSb at low temperature," *J. Phys. Soc. Japan*, Vol. 30, 775, 1970.
4. Eckstein, S. G., "AE effect in Cds semiconductor," *J. Appl. Phys.*, Vol. 35, 2702, 1964.
5. Epshtein, E. M. and Y. V. Gulyaev, "AE effect in Cds pole semiconductor," *Sov. Phys. Solid State.*, Vol. 9, 288, 1967.
6. Mori, N. and T. Ando, "Electronoptical-phonon interaction in single and double heterostructures," *Phys. Rev.*, Vol. 40, 6175, 1989.
7. Pozela, J. and V. Juciene, "Electron mobility and electron scattering by polar optical phonons in heterostructure quantum wells," *Sov. Phys. Tech. Semicond.*, Vol. 29, 459, 1995.
8. Vasilopoulos, P., M. Charbonneau, and C. N. van Vlier, "Linear and nonlinear electrical conduction in quasi-two-dimensional quantum-wells," *Phys. Rev.*, Vol. 35, 1334, 1987.
9. Suzuki, A., "Theory of hot-electron magnetophonon resonance in quasitwo-dimensional quantum well structure," *Phys. Rev.*, Vol. 45, 6731, 1992.
10. Shmelev, G. M., L. A. Chaikovskii, and N. Q. Bau, "HF conduction in semiconductors superlattices," *Soc. Phys. Tech. Semicond.*, Vol. 12, 1932, 1978.
11. Bau, N. Q. and T. C. Phong, "Calculations of the absorption coefficient of a weak electromagnetic wave by free carriers in quantum wells by the Kubo-Mori method," *J. Phys. Soc. Japan*, Vol. 3875, 1998.
12. Bau, N. Q., N. V. Nhan, and T. C. Phong, "Calculations of the absorption coefficient of a weak Electromagnetic wave by free carriers in doped superlattices by using the Kubo-Mori method," *J. Korean Phys. Soc.*, Vol. 41, 149, 2002.
13. Bau, N. Q., L. Dinh, and T. C. Phong, "Absorption coefficient of a weak electromagnetic wave by confined electron in quantum wire," *J. Korean Phys. Soc.*, Vol. 51, 1325, 2007.
14. Bau, N. Q., C. Navy, and G. M. Shmelev, "Influence of laser radiation on the absorption of weak EMW by free electron in SL," *Proceeding: Korea-SPIE*, Vol. 2778, 814, 1996.
15. Bau, N. Q., D. M. Hung, and N. B. Ngoc, "The nonlinear absorption coeffcient of a strong electromagnetic wave caused by conffined electrons in quantum wells," *J. Korean Phys. Soc.*, Vol. 54, 765, 2009.
16. Shilton, J. M., D. R. Mace, and V. I. Talyanskii, "On the acoustoelectric current in a one-dimensional channel," *J. Phys.: Condens. Matter.*, Vol. 8, 337, 1996.
17. Wohlman, O. E., Y. Levinson, and Y. M. Galperin, "Acoustoelectric effect in a finite-length ballistic quantum channel," *Phys. Rev.*, Vol. 62, 7283, 2000.
18. Zimbovskaya, N. A. and G. Gumbs, "Single electron transport of a quantum dot formed by surface acoustic waves through a narrow channel in a perpendicular," *J. Phys.: Condens. Matter.*, Vol. 13, 409, 2001.

19. Galperin, Y. M., O. E. Wohlman, and Y. Levinson, "Quantized acoustoelectric current in a finite-length ballistic quantum channel: The noise spectrum," *Phys. Rev.*, Vol. B63, 153309, 2001.
20. Mensah, S. Y. and F. K. A. Allotey, "AE effect in semiconductor SL," *J. Phys: Condens. Matter.*, Vol. 6, 6783, 1994.
21. Mensah, S. Y. and F. K. A. Allotey, "Nonlinear AE effect in semiconductor SL," *J. Phys.: Condens. Matter.*, Vol. 12, 5225, 2000.
22. Mensah, S. Y. and N. G. Mensah, "The influence of electric field on AE effect in semiconductor SL," *J. Phys: Superlattices and Micros.*, Vol. 37, 87, 2005.
23. Vyun, V. A., Y. O. Kanter, S. M. Kikkarin, V. V. Pnev, A. A. Fedorov, and I. B. Yakovkin, "AE interaction of surface acoustic wave in GaAs-InGaAs SL," *Solid State Communications*, Vol. 78, 823, 1991.
24. Bau, N. Q., N. V. Hieu, and T. C. Phong, "The nonlinear AE effect in a SL," *Coms. Phys.*, Vol. 3, 249, 2010.
25. Bau, N. Q. and N. V. Hieu, "Theory of the acoustomagnetoelectric effect in a superlattice," *PIERS Proceeding*, 342–346, Xian, China, March 22–26, 2010.
26. Tabib-Azar, M. and P. Das, "Experimental study of the acoustoelectric effects in SL," *Appl. Phys. Lett.*, Vol. 51, 436, 1987.
27. Shilton, J. M., D. R. Mace, and V. I. Talyanskii, "Experimental study of the acoustoelectric effects in GaAs-AlGaAs QW," *J. Phys.: Condens. Matter.*, Vol. 7, 7675, 1995.
28. Cunningham, J., M. Pepper, and V. I. Talyanskii, "Acoustoelectric current in submicron-separated quantum wires," *Appl. Phys. Lett.*, Vol. 86, 152105, 2005.
29. Astley, M. R., M. Kataoka, and C. J. B. Ford, "Acoustoelectric effect in carbon nanotubes," *J. Appl. Phys.*, Vol. 103, 096102, 2008.
30. Weinreich, G., T. M. Sanders, and H. G. White, "AE effect in N-type Germanium," *Phys. Rev.*, Vol. 114, 33, 1959.
31. Johri, J. and H. N. Spector, "The AE effect in semiconductor," *Phys. Rev.*, Vol. 15, 4955, 1977.
32. Palma, F., "TAV experiment on Si/Si$_{02}$," *J. Apply. Phys. Rev.*, Vol. 66, 292, 1989.

# Ability to Increase a Weak Electromagnetic Wave by Confined Electrons in Quantum Wells in the Presence of Laser Radiation

**N. V. Nhan[1], N. T. T. Nhan[2], N. V. Nghia[2], S. T. L. Anh[2], and N. Q. Bau[2]**

[1]Department of Physics, Academy of Defence Force — Air Force, Hanoi, Vietnam
[2]Department of Physics, College of Natural Sciences, Hanoi National University, Hanoi, Vietnam

**Abstract**— The analytic expressions for the absorption coefficient (ACF) of a weak electromagnetic wave (EMW) caused by confined electrons in the presence of laser radiation in quantum wells are obtained by using the quantum kinetic equation for electrons in the case of electron-optical phonon scattering. The dependence of the ACF of a weak EMW on the intensity $E_{01}$ and frequency $\Omega_1$ of the external laser radiation; the intensity $E_{02}$ and frequency $\Omega_2$ of the weak EMW; the temperature $T$ of the system and the width $L$ of quantum well are analyzed. The results are numerically calculated, plotted, and discussed for AlAs/GaAs/AlAs quantum well. The numerical results show that ACF of a weak EMW in a quantum well can get negative values. So, by the presence of laser radiation, in some conditions, the weak EMW is increased. This is different from the case of the absence of laser radiation.

## 1. INTRODUCTION

In recent times, there has been more and more interest in studying and discovering the behavior of low-dimensional system, in particular, quantum wells. The confinement of electrons in these systems considerably enhances the electron mobility and leads to their unusual behaviors under external stimuli. As a result, the properties of low-dimensional systems, especially the optical properties, are very different in comparison with those of normal bulk semiconductors [1–5]. The linear absorption of a weak EMW by confined electrons in low-dimensional systems has been investigated by using the Kubo-Mori method [6–9], the nonlinear absorption of a strong EMW by confined electrons in low-dimensional systems has been studied by using the quantum kinetic equation method [10–15]. The influence of laser radiation on the absorption of a weak EMW by free electrons in normal bulk semiconductors has been investigated by using the quantum kinetic equation method [17], and the presence of laser radiation, in some conditions, the weak EMW is increased. However, the influence of laser radiation on the absorption of a weak EMW in quantum wells is still open for study. Researching the influence of laser radiation on the absorption of a weak EMW play an important role in experiment. Because, it is difficult to directly measure the ACF of the strong EMW (laser radiation) by experiment. Therefore, in this paper, we study ability to increase weak EMW by confined electrons in quantum wells in the presence of laser radiation. The electron-optical phonon scattering mechanism is considered. The ACF of a weak EMW in the presence of laser radiation field are obtained by using the quantum kinetic equation for electrons in a quantum well. Then, we estimate numerical values for the specific AlAs/GaAs/AlAs quantum well to clarify our results.

## 2. THE ABSORPTION COEFFICIENT OF A WEAK EMW IN THE PRESENCE OF LASER RADIATION FIELD IN A QUANTUM WELL

It is well known that the motion of an electron in a quantum well is confined and that its energy spectrum is quantized into discrete levels. We assume that the quantization direction is the $z$ direction. The Hamiltonian of the electron-optical phonon system in a quantum well in the second quantization representation can be written as:

$$H = \sum_{n,\vec{p}_\perp} \varepsilon_{n,\vec{p}_\perp}\left(\vec{p}_\perp - \frac{e}{\hbar c}\vec{A}(t)\right) a^+_{n,\vec{p}_\perp} a_{n,\vec{p}_\perp} + \sum_{\vec{q}} \hbar\omega_{\vec{q}} b^+_{\vec{q}} b_{\vec{q}} + \sum_{n,n',\vec{p}_\perp,\vec{q}} C_{\vec{q}} I_{n,n'}(q_z) a^+_{n',\vec{p}_\perp+\vec{q}_\perp} a_{n,\vec{p}_\perp} (b_{\vec{q}} + b^+_{-\vec{q}})$$

(1)

where $n$ denotes the quantization of the energy spectrum in the $z$ direction ($n = 1, 2, \ldots$), $(n, \vec{p}_\perp)$ and $(n', \vec{p}_\perp + \vec{q}_\perp)$ are electron states before and after scattering, respectively. $\vec{p}_\perp (\vec{q}_\perp)$ is the in plane $(x, y)$ wave vector of the electron (phonon), $a^+_{n,\vec{p}_\perp}$ and $a_{n,\vec{p}_\perp}$ ($b^+_{\vec{q}}$ and $b_{\vec{q}}$) are the creation and the annihilation operators of electron (phonon), respectively. $\vec{q} = (\vec{q}_\perp, q_z)$, $\vec{A}(t) = \frac{c}{\Omega_1}\vec{E}_{01}\cos(\Omega_1 t + \varphi_1) +$

$\frac{c}{\Omega_2}\vec{E}_{02}\cos(\Omega_2 t)$ is the vector potential of EMW, $\omega_{\vec{q}} \approx \omega_0$ is the frequency of an optical phonon. $C_{\vec{q}}$ is the electron-optical phonon interaction constant [16]

$$|C_{\vec{q}}|^2 = \frac{2\pi e^2 \hbar \omega_0}{V \varepsilon_0 q^2}\left(\frac{1}{\chi_\infty} - \frac{1}{\chi_0}\right) \tag{2}$$

Here $V$, $e$, $\varepsilon_0$ are the normalization volume, the electron charge and the electronic constant (often $V = 1$), $\chi_0$ and $\chi_\infty$ are the static and the high-frequency dielectric constants, respectively. The electron form factor $I_{n,n'}(q_z)$ is written as:

$$I_{n,n'}(q_z) = \frac{2}{L}\int\limits_0^L \sin\left(\frac{n\pi}{L}z\right)\sin\left(\frac{n'\pi}{L}z\right)e^{iq_z z}dz \tag{3}$$

In quantum well, the electron energy takes the simple form:

$$\varepsilon_{n,\vec{p}_\perp} = \frac{\hbar^2 \vec{p}_\perp^2}{2m^*} + \frac{\hbar^2\pi^2 n^2}{2m^* L^2} \tag{4}$$

Here, $m^*$ is the effective mass of electron, $L$ is the width of a quantum well.

In order to establish the quantum kinetic equations for electrons in a quantum well, we use the general quantum equation for statistical average value of the electron particle number operator (or electron distribution function) $n_{n,\vec{p}_\perp}(t) = \left\langle a_{n,\vec{p}_\perp}^+ a_{n,\vec{p}_\perp}\right\rangle_t$ [16]:

$$i\hbar\frac{\partial n_{n,\vec{p}_\perp}(t)}{\partial t} = \left\langle \left[a_{n,\vec{p}_\perp}^+ a_{n,\vec{p}_\perp}, H\right]\right\rangle_t \tag{5}$$

where $\langle\psi\rangle_t$ denotes a statistical average value at the moment $t$, and $\langle\psi\rangle_t = Tr(\hat{W}\hat{\psi})$ ($\hat{W}$ being the density matrix operator). Starting from the Hamiltonian in Eq. (1) and using the commutative relations of the creation and the annihilation operators, we obtain the quantum kinetic equation for electrons in a quantum well:

$$\frac{\partial n_{n,\vec{p}_\perp}(t)}{\partial t} = -\frac{1}{\hbar^2}\sum_{n',\vec{q}}|C_{\vec{q}}|^2\,|I_{n,n'}(q_z)|^2\sum_{l,s,m,f=-\infty}^{+\infty}J_l(\vec{a}_1\vec{q}_\perp)J_s(\vec{a}_1\vec{q}_\perp)J_m(\vec{a}_2\vec{q}_\perp)J_f(\vec{a}_2\vec{q}_\perp)$$

$$e^{i\{[(s-l)\Omega_1+(m-f)\Omega_2-i\delta]t+(s-l)\varphi_1\}}$$

$$\times \int\limits_{-\infty}^t dt_2 \left\{\left[n_{n,\vec{p}_\perp}(t_2)N_{\vec{q}} - n_{n',\vec{p}_\perp+\vec{q}_\perp}(t_2)(N_{\vec{q}}+1)\right]e^{\frac{i}{\hbar}[\varepsilon_{n'}(\vec{p}_\perp+\vec{q}_\perp)-\varepsilon_n(\vec{p}_\perp)-\hbar\omega_{\vec{q}}-s\hbar\Omega_1-m\hbar\Omega_2+i\hbar\delta](t-t_2)}\right.$$

$$+ \left[n_{n,\vec{p}_\perp}(t_2)(N_{\vec{q}}+1) - n_{n',\vec{p}_\perp+\vec{q}_\perp}(t_2)N_{\vec{q}}\right]e^{\frac{i}{\hbar}[\varepsilon_{n'}(\vec{p}_\perp+\vec{q}_\perp)-\varepsilon_n(\vec{p}_\perp)+\hbar\omega_{\vec{q}}-s\hbar\Omega_1-m\hbar\Omega_2+i\hbar\delta](t-t_2)}$$

$$- \left[n_{n',\vec{p}_\perp-\vec{q}_\perp}(t_2)N_{\vec{q}} - n_{n,\vec{p}_\perp}(t_2)(N_{\vec{q}}+1)\right]e^{\frac{i}{\hbar}[\varepsilon_n(\vec{p}_\perp)-\varepsilon_{n'}(\vec{p}_\perp-\vec{q}_\perp)-\hbar\omega_{\vec{q}}-s\hbar\Omega_1-m\hbar\Omega_2+i\hbar\delta](t-t_2)}$$

$$\left. - \left[n_{n',\vec{p}_\perp-\vec{q}_\perp}(t_2)(N_{\vec{q}}+1) - n_{n,\vec{p}_\perp}(t_2)N_{\vec{q}}\right]e^{\frac{i}{\hbar}[\varepsilon_n(\vec{p}_\perp)-\varepsilon_{n'}(\vec{p}_\perp-\vec{q}_\perp)+\hbar\omega_{\vec{q}}-s\hbar\Omega_1-m\hbar\Omega_2+i\hbar\delta](t-t_2)}\right\} \tag{6}$$

If we consider similar problem but in the normal bulk semiconductors, that authors V. L. Malevich, E. M. Epstein published, we will see that Eq. (6) has similarity to the quantum kinetic equation for electrons in the bulk semiconductor [17].

It is well known that to obtain the explicit solutions from Eq. (6) is very difficult. In this paper, we use the first-order tautology approximation method to solve this equation [16–18]. In detail, in Eq. (6), we choose the initial approximation of $n_{n,\vec{p}_\perp}(t)$ as:

$$n_{n,\vec{p}_\perp}^0(t_2) = \bar{n}_{n,\vec{p}_\perp}, \quad n_{n,\vec{p}_\perp+\vec{q}_\perp}^0(t_2) = \bar{n}_{n,\vec{p}_\perp+\vec{q}_\perp}, \quad n_{n,\vec{p}_\perp-\vec{q}_\perp}^0(t_2) = \bar{n}_{n,\vec{p}_\perp-\vec{q}_\perp}$$

where $\bar{n}_{n,\vec{p}_\perp}$ is the balanced distribution function of electrons. We perform the integral with respect to $t_2$; next, we perform the integral with respect to $t$ of Eq. (6). The expression for the unbalanced

electron distribution function can be written as:

$$n_{n,\vec{p}_\perp}(t) = \bar{n}_{n,\vec{p}_\perp} - \frac{1}{\hbar} \sum_{n',\vec{q}} |C_{\vec{q}}|^2 |I_{n,n'}(q_z)|^2 \sum_{k,s,r,m=-\infty}^{+\infty} J_s(\vec{a}_1\vec{q}_\perp) J_{k+s}(\vec{a}_1\vec{q}_\perp) J_m(\vec{a}_2\vec{q}_\perp) J_{r+m}(\vec{a}_2\vec{q}_\perp)$$

$$\frac{e^{-i\{[k\Omega_1+r\Omega_2+i\delta]t+k\varphi_1\}}}{k\Omega_1 + r\Omega_2 + i\delta} \left\{ \frac{\bar{n}_{n',\vec{p}_\perp-\vec{q}_\perp} N_{\vec{q}} - \bar{n}_{n,\vec{p}_\perp}(N_{\vec{q}}+1)}{\varepsilon_n(\vec{p}_\perp) - \varepsilon_{n'}(\vec{p}_\perp - \vec{q}_\perp) - \hbar\omega_{\vec{q}} - s\hbar\Omega_1 - m\hbar\Omega_2 + i\hbar\delta} \right.$$

$$+ \frac{\bar{n}_{n',\vec{p}_\perp-\vec{q}_\perp}(N_{\vec{q}}+1) - \bar{n}_{n,\vec{p}_\perp} N_{\vec{q}}}{\varepsilon_n(\vec{p}_\perp) - \varepsilon_{n'}(\vec{p}_\perp - \vec{q}_\perp) + \hbar\omega_{\vec{q}} - s\hbar\Omega_1 - m\hbar\Omega_2 + i\hbar\delta}$$

$$- \frac{\bar{n}_{n,\vec{p}_\perp} N_{\vec{q}} - \bar{n}_{n',\vec{p}_\perp+\vec{q}_\perp}(N_{\vec{q}}+1)}{\varepsilon_{n'}(\vec{p}_\perp + \vec{q}_\perp) - \varepsilon_n(\vec{p}_\perp) - \hbar\omega_{\vec{q}} - s\hbar\Omega_1 - m\hbar\Omega_2 + i\hbar\delta}$$

$$\left. - \frac{\bar{n}_{n,\vec{p}_\perp}(N_{\vec{q}}+1) - \bar{n}_{n',\vec{p}_\perp+\vec{q}_\perp} N_{\vec{q}}}{\varepsilon_{n'}(\vec{p}_\perp + \vec{q}_\perp) - \varepsilon_n(\vec{p}_\perp) + \hbar\omega_{\vec{q}} - s\hbar\Omega_1 - m\hbar\Omega_2 + i\hbar\delta} \right\} \tag{7}$$

where $\vec{a}_1 = \frac{e\vec{E}_{01}}{m^*\Omega_1^2}$, $\vec{a}_2 = \frac{e\vec{E}_{02}}{m^*\Omega_2^2}$, $N_{\vec{q}}$ is the balanced distribution function of phonons, $\vec{E}_{01}$ and $\Omega_1$ are the intensity and frequency of a strong EMW (laser radiation), $\vec{E}_{02}$ and $\Omega_2$ are the intensity and frequency of a weak EMW; $\varphi_1$ is the phase difference between two electromagnetic waves, $J_k(x)$ is the Bessel function.

The carrier current density formula in a quantum well takes the form:

$$\vec{j}_\perp(t) = \frac{e\hbar}{m^*} \sum_{n,\vec{p}_\perp} \left( \vec{p}_\perp - \frac{e}{\hbar c}\vec{A}(t) \right) n_{n,\vec{p}_\perp}(t) \tag{8}$$

Because the motion of electrons is confined along the $z$ direction in a quantum well, we only consider the in plane $(x, y)$ current density vector of electrons $\vec{j}_\perp(t)$.

The ACF of a weak EMW by confined electrons in the quantum well takes the simple form [16]:

$$\alpha = \frac{8\pi}{c\sqrt{\chi_\infty}E_{02}^2} \left\langle \vec{j}_\perp(t)\vec{E}_{02}\sin\Omega_2 t \right\rangle_t \tag{9}$$

From the Eqs. (7)–(9) we established the ACF of a weak EMW in quantum well:

$$\alpha = \frac{e^4\omega_0 n_0}{\varepsilon_0 c\sqrt{2\pi k_B T m^*\chi_\infty}m^*\Omega_2^3 Z} \left( \frac{1}{\chi_\infty} - \frac{1}{\chi_0} \right) \sum_{n,n'=1}^{+\infty} II_{n,n'} \left\{ (D_{0,1} - D_{0,-1}) - \frac{1}{2}(H_{0,1} - H_{0,-1}) \right.$$

$$+ \frac{3}{32}(G_{0,1} - G_{0,-1}) + \frac{1}{4}(H_{-1,1} - H_{-1,-1} + H_{1,1} - H_{1,-1})$$

$$\left. - \frac{1}{16}(G_{-1,1} - G_{-1,-1} + G_{1,1} - G_{1,-1}) + \frac{1}{64}(G_{-2,1} - G_{-2,-1} + G_{2,1} - G_{2,-1}) \right\} \tag{10}$$

where:

$$D_{s,m} = \pi e^{-\frac{\xi_{s,m}}{2k_B T}} \left( \frac{4m^{*2}\xi_{s,m}^2}{\hbar^4} \right)^{1/4} K_{1/2}\left( \frac{|\xi_{s,m}|}{2k_B T} \right) \left[ e^{-\frac{\varepsilon_n}{k_B T}}(N_{\omega_0}+1) - e^{-\frac{\varepsilon_{n'}-\xi_{s,m}}{k_B T}} N_{\omega_0} \right]$$

$$H_{s,m} = a_1^2\left( \frac{\pi}{2} + \frac{\pi}{4}\cos 2\gamma \right) e^{-\frac{\xi_{s,m}}{2k_B T}} \left( \frac{4m^{*2}\xi_{s,m}^2}{\hbar^4} \right)^{3/4} K_{3/2}\left( \frac{|\xi_{s,m}|}{2k_B T} \right) \left[ e^{-\frac{\varepsilon_n}{k_B T}}(N_{\omega_0}+1) - e^{-\frac{\varepsilon_{n'}-\xi_{s,m}}{k_B T}} N_{\omega_0} \right]$$

$$G_{s,m} = a_1^4\left( \frac{3\pi}{8} + \frac{\pi}{4}\cos 2\gamma \right) e^{-\frac{\xi_{s,m}}{2k_B T}} \left( \frac{4m^{*2}\xi_{s,m}^2}{\hbar^4} \right)^{5/4} K_{5/2}\left( \frac{|\xi_{s,m}|}{2k_B T} \right) \left[ e^{-\frac{\varepsilon_n}{k_B T}}(N_{\omega_0}+1) - e^{-\frac{\varepsilon_{n'}-\xi_{s,m}}{k_B T}} N_{\omega_0} \right]$$

$$\varepsilon_n = \frac{\hbar^2\pi^2 n^2}{2m^* L^2}; \quad \varepsilon_{n'} = \frac{\hbar^2\pi^2 n'^2}{2m^* L^2}; \quad N_{\omega_0} = \frac{1}{e^{\frac{\hbar\omega_0}{k_B T}}-1}; \quad Z = \sum_{n=1}^{+\infty} e^{-\frac{\hbar^2\pi^2 n^2}{2m^* k_B T L^2}}; \quad II_{n,n'} = \frac{\pi}{L}(2 + \delta_{n,n'})$$

$$\xi_{s,m} = \frac{\hbar^2\pi^2}{2m^* L^2}(n'^2 - n^2) + \hbar\omega_0 - s\hbar\Omega_1 - m\hbar\Omega_2, \quad \text{with } s = -2, -1, 0, 1, 2; \quad m = -1, 1.$$

$\gamma$ is the angle between two vectors $\vec{E}_{01}$ and $\vec{E}_{02}$.

Equation (10) is the expression of ACF of a weak EMW in the presence of external laser radiation in a quantum well.

From the expression of ACF of a weak EMW, we see that ACF of a weak EMW is independent on $E_{02}$; only dependent on $E_{01}$, $\Omega_1$, $\Omega_2$, $T$, and $L$.

## 3. NUMERICAL RESULTS AND DISCUSSION

In order to clarify the mechanism for the absorption of a weak EMW in a quantum well in the presence of laser radiation, in this section, we will evaluate, plot, and discuss the expression of the ACF for the case of a specific quantum well: AlAs/GaAs/AlAs. The parameters used in the calculations are as follows [9, 16]: $\chi_\infty = 10.9$, $\chi_0 = 12.9$, $m = 0.067m_0$, $m_0$ being the mass of free electron, $n_0 = 10^{23}\,\mathrm{m}^{-3}$, $\hbar\omega_0 = 36.25\,\mathrm{meV}$, $\gamma = \frac{\pi}{3}$.

Figure 1 describes the dependence of $\alpha$ on the temperature $T$, with $L = 10 \times 10^{-8}\,\mathrm{m}$, $\Omega_1 = 3 \times 10^{13}\,\mathrm{Hz}$, $\Omega_2 = 10^{13}\,\mathrm{Hz}$, and three different values of $E_{01}$. Figure 1 shows that when the temperature $T$ of the system rises up from 30 K to 400 K, the curve has a maximum and a minimum.

Figure 2 describes the dependence of $\alpha$ on $\Omega_1$, with $L = 5 \times 10^{-8}\,\mathrm{m}$, $\Omega_2 = 5 \times 10^{13}\,\mathrm{Hz}$, $T = 70\,\mathrm{K}$ and three different values of $E_{01}$. This Figure shows that the dependence of $\alpha$ on $\Omega_1$ is nonlinear, when the frequency $\Omega_1$ rises up, ACF speeds up too, then gradually reduce to a certain value, and curve has a maximum value.

Figure 3 describes the dependence of $\alpha$ on $\Omega_2$, with $L = 2 \times 10^{-8}\,\mathrm{m}$, $E_{01} = 4 \times 10^6\,\mathrm{V/m}$, $T = 70\,\mathrm{K}$ and three different values of $\Omega_1$. This figure shows that the curve has a maximum where $\Omega_2 = \omega_0$.

Figure 4 shows ACF as a function of the intensity $E_{01}$ of laser radiation, with $L = 5 \times 10^{-8}\,\mathrm{m}$, $\Omega_1 = 8 \times 10^{13}\,\mathrm{Hz}$, $\Omega_2 = 5 \times 10^{13}\,\mathrm{Hz}$, and three different values of $T$. From the figure we see that the curve can have a maximum or no maximum in the investigative interval.
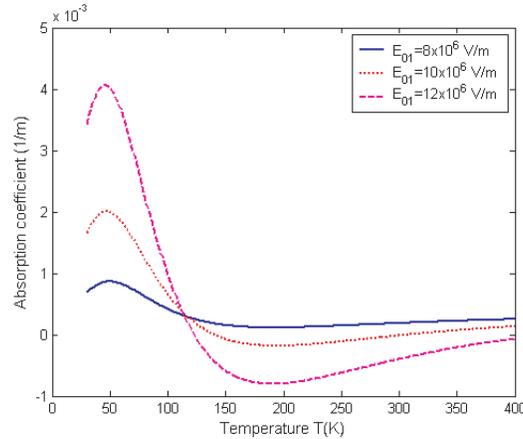


Figure 1: The dependence of $\alpha$ on $T$.
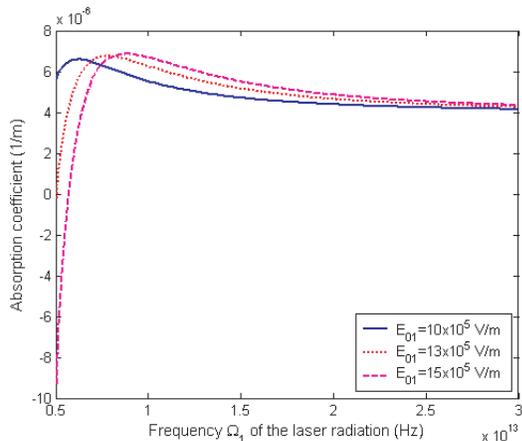


Figure 2: The dependence of $\alpha$ on $\Omega_1$.
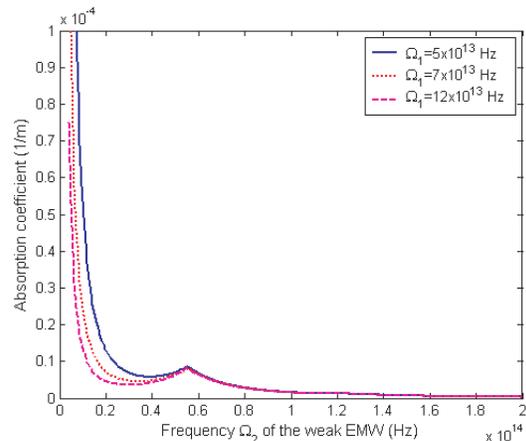


Figure 3: The dependence of $\alpha$ on $\Omega_2$.
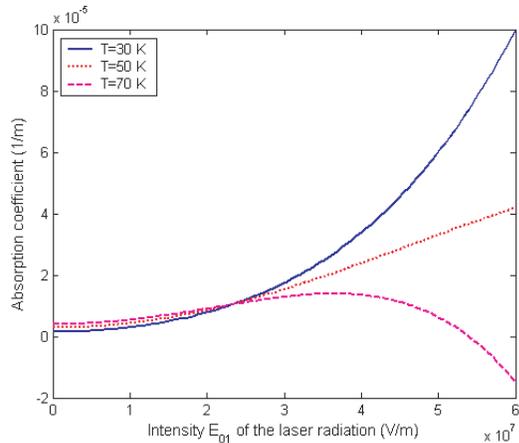
Figure 4: The dependence of $\alpha$ on $E_{01}$.
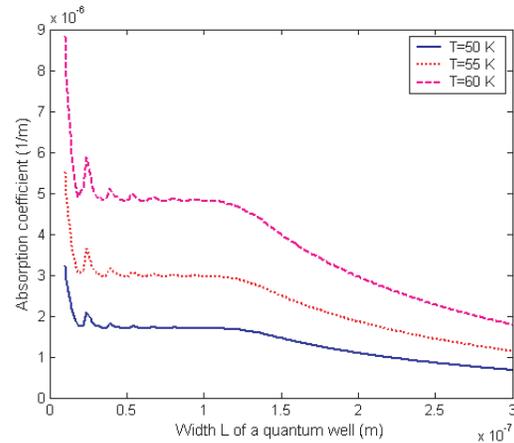


Figure 5: The dependence of $\alpha$ on $L$.

Figure 5 shows ACF as a function of the width $L$ of a quantum well, with $\Omega_1 = 8 \times 10^{13}$ Hz, $\Omega_2 = 10^{13}$ Hz, $E_{01} = 7 \times 10^5$ V/m, and three different values of $T$. From the figure we see that the curve has many maxima and minima in the investigative interval, these maxima gradually reduce.

These figures show that under influence of laser radiation, ACF of a weak EMW in a quantum well can get negative values, it means that ACF becomes increased coefficient. So, by the presence of strong electromagnetic waves, in some conditions, the weak electromagnetic wave is increased. This is different from the case of the absence of laser radiation.

## 4. CONCLUSION

In this paper, we investigated ability to increase weak EMW by confined electrons in quantum wells in the presence of laser radiation. We obtained an analytical expression of the ACF of a weak EMW in quantum well. We numerically calculated and graphed the ACF for AlAs/GaAs/AlAs quantum well to clarify. These results showed that by the presence of strong electromagnetic waves, in some conditions, the weak electromagnetic wave is increased.

## ACKNOWLEDGMENT

## REFERENCES

1. Tsu, R. and L. Esaki, "Tunneling in a finite superlattice," *Appl. Phys. Lett.*, Vol. 22, No. 11, 562–564, 1973.
2. Harris, Jr., J. S, "From bloch functions to quantum wells," *J. Mod. Phys. B*, Vol. 4, 1149–1179, 1990.
3. Zhao, P., "Phonon amplification by absorption of an intense laser field in a quantum well of polar material," *Phys. Rev. B*, Vol. 49, No. 19, 13589–13599, 1994.
4. Nishiguchi, N., "Resonant acoustic-phonon modes in a quantum wire," *Phys. Rev. B*, Vol. 52, No. 7, 5279–5288, 1995.
5. Dingle, R., "Confined carries quantum states in ultra-thin semiconductor heterostructures," *Festkorperprobleme XV*, H. J. Queisser, Pergamon Vieweg, New York, 1975.
6. Bau, N. Q., N. T. Toan, Chhoumn Navy, and T. C. Phong, "The theory of absorption of a weak electromagnetic wave by free electrons in semiconductors superlattices," *J. Comm. Phys.*, Vol. 6, No. 1, 30–40, 1996.
7. Bau, N. Q., N. V. Nhan, and T. C. Phong, "Parametric resonance of acoustic and optical phonons in a quantum well," *J. Kor. Phys. Soc.*, Vol. 42, No. 5, 647–651, 2003.
8. Bau, N. Q. and T. C. Phong, "Calculations of the absorption coefficient of a weak electromagnetic wave by free carriers in quantum wells by the Kubo-Mori method," *J. Phys. Soc. Jpn.*, Vol. 67, 3875, 1998.
9. Bau, N. Q., N. V. Nhan, and T. C. Phong, "Calculations of the absorption coefficient of a weak Electromagnetic wave by free carriers in doped superlattices by using the Kubo-Mori Method," *J. Korean. Phys. Soc.*, Vol. 41, 149–154, 2002.

10. Bau, N. Q. and H. D. Trien, "The nonlinear absorption of a strong electromagnetic wave in low-dimensional systems," *Wave Propagation*, Ch. 22, 461–482, Intech, 2011.
11. Bau, N. Q., L. T. Hung, and N. D. Nam, "The nonlinear absorption coefficient of a strong electromagnetic wave by confined electrons in quantum wells under the influences of confined phonons," *Journal of Electromagnetic Waves and Applications*, Vol. 24, No. 13, 1751–1761, 2010.
12. Bau, N. Q., D. M. Hung, and L. T. Hung, "The influences of confined phonons on the nonlinear absorption coefficient of a strong electromagnetic wave by confined electrons in doping superlattices," *PIER Letters*, Vol. 15, 175–185, 2010.
13. Bau, N. Q., D. M. Hung, and N. B. Ngoc, "The nonlinear absorption coeffcient of a strong electromagnetic wave caused by confined electrons in quantum wells," *J. Korean. Phys. Soc.*, Vol. 42, No. 2, 765–773, 2009.
14. Bau, N. Q., L. T. Hung, and H. D. Trien, "Effect of magnetic field on nonlinear absorption of a strong electromagnetic wave in low-dimensional systems," *Behaviour of Electromagnetic Waves in Different Media and Structures*, Ch. 14 , 275–300, Intech, 2011.
15. Vasilopoulos, P., M. Charbonneau, and C. M. Van Vliet, "Linear and nonlinear electrical conduction in quasi-two-dimensional quantum wells," *Phys. Rev. B.*, Vol. 35, 1334, 1987.
16. Pavlovich, V. V. and E. M. Epstein, "Quantum theory of absorption of electromagnetic wave by free carries in semiconductors," *Sov. Phys. Solid State*, Vol. 19, 1760, 1977.
17. Malevich, V. L. and E. M. Epstein, "Nonlinear optical properties of conduction electrons in semiconductors," *Sov. Quantum Electronic*, Vol. 1, 1468–1470, 1974.
18. Epstein, E. M., "Interaction of a strong electromagnetic wave on electron properties of semiconductors," *Communication of HEE of USSR, Radio-Physics*, Vol. 18, 785–811, 1975.

# NMR Measurement of the Relaxations and Conductivity of Gel Electrolytes

**R. Korinek**[1, 2]**, K. Bartusek**[1, 2]**, K. Ostanina**[2]**, and M. Musil**[3]

[1]Institute of Scientific Instruments of the ASCR, v.v.i.
Kralovopolska 147, 612 64 Brno, Czech Republic
[2]Department of Theoretical and Experimental Electrical Engineering
Brno University of Technology, Kolejni 2906/4, 612 00 Brno, Czech Republic
[3]Department of Electrotechnology
Brno University of Technology, Technicka 10, 602 00 Brno, Czech Republic

**Abstract**— The article deals with the relaxation times and conductivity measurements of polymer gel electrolytes based on the sodium perchlorate ($NaClO_4$). For measurement of $T_1$ and $T_2$ relaxation times based on NMRS method was used. To approximation, two-exponential function (equation for inversion recovery and hahn echo techniques) was used. The calculation was performed using genetic algorithm (GA). Gel polymer electrolytes are based on inorganic salt $NaClO_4$. The aim is to find a suitable solid electrolyte for use in electrochemical industry and especially to improve their safety. In the paper a methodology of NMR relaxation times measurement is presented. The results are compared with measurements of conductivity gel during polymerization. The experiment was performed on the 4.7 T NMR system at the Institute of Scientific Instruments of the ASCR in Brno.

## 1. INTRODUCTION

There are other methods for evaluating properties of conducting gels (Li, Na), but NMR spectroscopy offers a deeper insight into the behaviour of polymer gel electrolyte during the UV or thermal polymerization process. Mainly, we are able to determine the time (relatively exactly) when the polymerization process is completed. After this, there should not be other processes when the electrolyte is exposed to heat or UV radiation.

In liquid is used as a solvent, commonly flammable or toxic organic compounds (acetonitrile, N, N-dimethylformamide, dimethoxyethane, etc.) are frequently used [1]. Liquid electrolytes are now very widespread and we want to replace them by safer solid electrolytes. Advantage of gel electrolytes over liquid gel electrolytes is their higher safety.

The aim of our interest is primarily to examine the properties of ions in these gels. In our case the Na$^+$ ions. Mobility of cations in polymer electrolytes has previously been investigated by measuring the linewidth of solid state nuclear magnetic resonance spectroscopy (NMRS) in [2, 3]. An electrolyte behaviour during UV polymerization, we have already discussed in [4] and also in [5].

There is a direct proportionality between MR relaxation and conductivity of the electrolyte. Along with the relaxation times $T_1$ and $T_2$ we also interested in the course of conductivity changes during the UV polymerization process. Relaxation and conductivity were measured in polymer gels before polymerization and after complete UV polymerization.

There are three factors that have affect on the precession of the magnetization vector. It is the inhomogeneity of the magnetic field, longitudinal $T_1$ relaxation and transverse relaxation $T_2$. After subsides electromagnetic pulse excitation, relaxation takes place. Relaxation is the process by which the density matrix elements approach their thermodynamic equilibrium values. We have two types of relaxation times. Relaxation time $T_1$ determines the rate at which the population adjust to thermodynamic equilibrium. $T_2$ type relaxation time determines the rate at which the transverse magnetization relaxes to zero [6].

### 1.1. Liquids [6]

Molecules in liquids are in rapid motion with respect to the inverse Larmor frequency. The $T_1$ relaxation of an isolated spin pair is

$$\frac{1}{T_1} = \left(\frac{\mu_0}{4\pi}\right)^2 \gamma^4 h^2 I \left(I + 1\right) \frac{3}{2} \left[J^{(1)}\left(\omega_L\right) + J^{(2)}\left(2\omega_L\right)\right], \tag{1}$$

where $h$ is Plancks constant dividend by $2\pi$, $I$ is spin quantum number, $\gamma$ is gyromagnetic ratio, $J(\omega_L)$ is spectral density of motion at frequency $\omega_L$. $J(\omega_L)$ is characterized by the frequency

$\omega_c = 1/\tau_c$ ($\tau_c$ is correlation time), where $J(\omega_L)$ approaches zero as $\omega \gg \omega_c$. Clearly the fastest motion possible is the free reorientation of a molecule, so that, depending on the type of motion, the cut-off frequency $\omega_c$ is anywhere between zero and $10^{13}$ Hz. The $T_2$ relaxation also depends on the spectral density at frequency zero and is

$$\frac{1}{T_2} = \left(\frac{\mu_0}{4\pi}\right)^2 \gamma^4 h^2 I(I+1) \frac{3}{2}\left[J^{(0)}(0) + \frac{5J^{(1)}(\omega_L)}{2} + \frac{J^{(2)}(2\omega_L)}{4}\right]. \tag{2}$$

The key assumption in the derivation of $T_2$ is that the strength $\delta_D$ of the dipole-dipole field is small compared to the cut-off frequency $\omega_c$. This is the fast motion limit, where the anisotropy of the lineshape is motionally narrowed. Than, the spectral densities are given by [6, 7]

$$J^{(0)}(\omega) = \frac{24}{15 r_{ij}^6} \frac{\tau_c}{1 + \omega^2 \tau_c^2}, \tag{3}$$

$$J^{(1)}(\omega) = \frac{4}{15 r_{ij}^6} \frac{\tau_c}{1 + \omega^2 \tau_c^2}, \tag{4}$$

$$J^{(2)}(2\omega) = \frac{16}{15 r_{ij}^6} \frac{\tau_c}{1 + \omega^2 \tau_c^2}, \tag{5}$$

where $r_{ij}^6$ is internuclear distance.

Regimes of slow and fast motion are discriminated by the $T_1$ minimum, where the correlation time is of the order of the Larmor period. For small molecules at room temperature $T_1$ and $T_2$ are the same. On the other side of the $T_1$ minimum, molecular motion is slow compared to the Larmor period. $T_1$ and $T_2$ diverge. This situation is typical for viscous liquid or restricted motion in polymers well above the glass transition temperature. Because $T_2$ is short, yet $T_1$ is long [6].

So there is a temperature or narrow temperature range, below which is an amorphous glassy polymer, it has the rubbery properties. This temperature is called the glass transition temperature $T_g$ and is one of the most important characteristics of the polymer [8].

### 1.2. Solids and Slow Motion [6]

For $^1$H the homonuclear dipole-dipole coupling lings together. In this case, the expression for $T_1$ still remains valid, but the expression for $T_2$ changes. It will be

$$\frac{1}{T_2} = \left(\frac{\mu_0}{4\pi}\right)^2 \gamma^4 h^2 I(I+1) \frac{3}{2} \frac{J^{(0)}(\omega_L)}{4} = M_2 \tau_c, \tag{6}$$

where $M_2$ is the second moment of the lineshape function. The rate $T_1^{-1}$ of transverse relaxation is proportional to the correlation time $\tau_c$ of molecular motion.

According to Williamson [9], for fully dissociated ions, the Nernst-Einstein equation can be used to give a calculated value of the ionic conductivity, $\sigma_{calc}$, from the diffusion coefficients of the cation and anion in polymer gel. In our case:

$$\sigma_{calc} = \frac{n q^2}{4\pi}\left[D\left(Na^+\right)\right], \tag{7}$$

where $n$ is the number of anions and/or cations per unit volume of solution and $q$ is the charge on ion. The relationship between $T_1$ relaxation and diffusion is given by the relationship [10]

$$\frac{1}{T_1} = \left(\frac{1}{T_1}\right)_{inter} + \left(\frac{1}{T_1}\right)_{intra} = \frac{\gamma^4 h^2 I(I+1)}{D} \cdot \frac{8\pi N \rho r^6 + 10\sigma^3}{15\sigma r^6}, \tag{8}$$

where $N$ is number of spins per molecule, $D$ — diffusion coefficient.

It follows a linear dependence of $T_1$ a $D$.

## 2. EXPERIMENTAL SETUP

The measurement was performed using the 4.7 T MRI system at Institute of Scientific Instruments Academy of Science of the Czech Republic in Brno (Figure 1(c)). To measure the gels, two probes

were used simultaneously. Probe for measurement of hydrogen nuclei $^1$H (Figure 1(b)) is a shielded surface saddle coil (diameter 76 mm) and probe for measurement of sodium nuclei $^{23}$Na (Figure 1(a)) is a simple two-threaded saddle coil (diameter 26 mm). All samples and their UV polymerization were mixed at Department of Elektrotechnology in Brno. Oxygen was removed in a stream of nitrogen. All components were bought from Sigma-Aldrich company. In Table 1 we can see the composition of individual samples.

The electrolyte is compound of $NaClO_4$, propylene carbonate (PC) mixed with methyl methacrylate (MMA), initiator of polymerization benzoin-n-butyl ether (BBE) and (EDMA — $C_{12}H_{17}NO_2$). Sample No. 1 has a volume relationship between liquid electrolyte and macromolecular matrix component 1 : 1.75, which is tested and functional. Addition of both the PC will cause the samples will be softer, more liquid. Second, they exhibit greater ionic conductivity.

## 3. RESULTS

Into the gels were gradually adding the appropriate concentration of PC. This leads to increasing the conductivity of the solution.



(a)

(b)

(c)
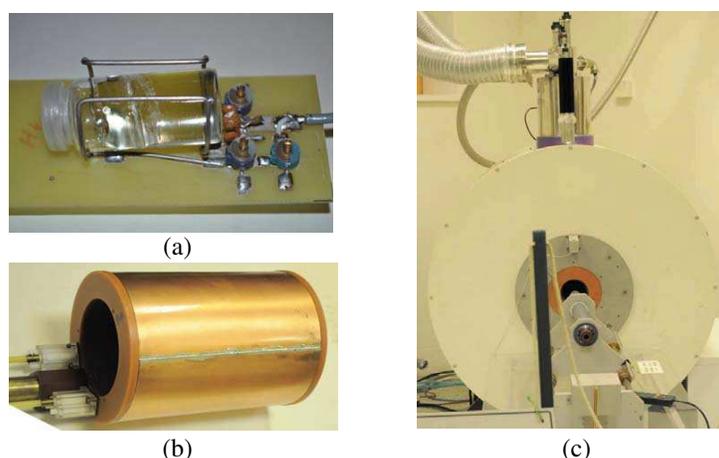
Figure 1: (a) Probe of sodium nuclei ($^{23}$Na), the resonance frequency is 51 MHz. (b) Probe for measurement of hydrogen nuclei ($^1$H), the resonance frequency is 200 MHz. (c) 4.7 T MRI system at the Institute of Scientific Instruments in Brno.

Table 1: Composition of the measured samples.

| Sample No. | | 1 | 2 | 3 | 4 | 5 | 6 |
|---|---|---|---|---|---|---|---|
| V | [ml] | 12.1 | 12.7 | 13.3 | 13.9 | 14.5 | 15.1 |
| PC | [ml] | 4.184 | 4.784 | 5.384 | 5.984 | 6.584 | 7.184 |
| $NaClO_4$ | [g] | 0.538 | 0.538 | 0.538 | 0.538 | 0.538 | 0.538 |
| MMA | [ml] | 7.657 | 7.657 | 7.657 | 7.657 | 7.657 | 7.657 |
| EDMA | [µl] | 43 | 43 | 43 | 43 | 43 | 43 |
| BEE | [g] | 0.17 | 0.17 | 0.17 | 0.17 | 0.17 | 0.17 |

Table 2: Conductivity of the measured samples after polymerization.

| Sample No. | $R$ [Ω] | Conductivity [S·cm$^{-1}$] | Thickness (cm) | Relative representation of the PC (based on sample 1) |
|---|---|---|---|---|
| 1 | 3009 | 1.32232E-05 | 0.080 | 1.000 |
| 2 | 1472 | 3.04092E-05 | 0.090 | 1.143 |
| 3 | 597 | 5.41513E-05 | 0.065 | 1.287 |
| 4 | 430 | 1.04098E-04 | 0.090 | 1.430 |
| 5 | 322 | 1.15844E-04 | 0.075 | 1.574 |
| 6 | 173 | 2.44367E-04 | 0.085 | 1.717 |

| Sample No. | $T_2$ [ms] ($^{23}$Na) | $T_1$ [ms] ($^{23}$Na) |
|:---:|:---:|:---:|
| 1 | 4.3 | 3.9 |
| 2 | 4.3 | 4 |
| 3 | 4.3 | 3.9 |
| 4 | 4.4 | 4 |
| 5 | 4.3 | 3.9 |
| 6 | 4.6 | 3.9 |



Table 3: Relaxation $T_1$ and $T_2$ of sodium before polymerization.
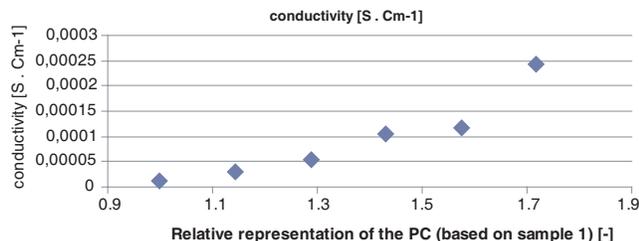
Figure 2: Changes in conductivity dependence on the amount of added PC.

In Table 2, we can see the change in conductivity with increasing number of PC in the overall solution. Furthermore we can seen that the relaxation times according to our expectations does not really change. Relaxation time $T_1$ is equal or at least greater than $T_2$. We can see that in our case is $T_1$ smaller than $T_2$. This is caused by error measurement. In fact, $T_1$ and $T_2$ are equal and around 4 ms.

## 4. CONCLUSIONS

The conductivity measurements of the polymerized samples, we can see that the conductivity depends on the ratio solvent and Na ions. The amount of solvent is bigger therefore mobility of ions in the structure of the gel is greater. Relaxation of sodium in our case is very short. The measurement results will contribute to the study of changes in the structure of gel electrolytes.

**REFERENCES**

1. Reiter, J., J. Vondrak, J. Velicka, and Z. Micka, "Nové elektrolyty nejen pro chemické zdroje elektrické energie," *Chem. Listy*, Vol. 100, 133–139, 2006.
2. Forsyth, M., M. E. Smith, P. Meakin, and D. R. MacFarlane, *J. Polym. Sci. Polym. Phys.*, Vol. 32, 2077, 1994.
3. Chung, S. H., P. Heitjans, R. Winter, W. Bzaucha, Z. Florjanczyk, and Y. Onoda, *Solid State Ionics*, Vol. 112, 153, 1998.
4. Korinek, R., J. Vondrak, and K. Bartusek, *ECS Trans.*, Vol. 32, 11–16, 2010.
5. Korinek, R., K. Bartusek, and J. Vondrak, *ECS Trans.*, Vol. 40, 2011 (in press).
6. Blumich, B., *NMR Imaging of Materials*, Clarendon Press, Oxford, 2000.
7. Farrar, T. C., *Introduction to Pulse NMR Spectroscopy*, Farragut, Madison, 1987.
8. Prokopova, I., *Makromolekulární Chemie*, 2nd Edition, VSCHT, Praha, 2007.
9. Williamson, M. J., et al., "NMR measurements of self diffusion in polymer gel electrolytes," *Polymer*, Vol. 40, 7177–7185, 1999.
10. Lo, S.-W., "Correlations on NMR relaxation time with viscosity/temperature, diffusion coefficient and Gas/Oil ratio of methane-hydrocarbon mixtures," 2000.

# Phase and Amplitude Control of Optical Bistability in the Closed-loop Three-coupled Quantum Wells

**M. Mahmoudi and N. Heidari**

Department of Physics, University of Zanjan, P. O. Box 45195-313, Zanjan, Iran

**Abstract**— We investigate the optical properties of a weak probe field in a closed-loop ladder-type configuration in an asymmetric semiconductor three-coupled quantum well system. It is shown that, the dispersion, absorption and optical bistability behavior of the system can be controlled by both of the amplitude and relative phase of applied fields. Moreover, it is demonstrated that in the gain region of the absorption spectrum, the considerable output is obtained for zero input.

## 1. INTRODUCTION

One of the interesting nanostructure semiconductor devices is three-coupled quantum wells (TCQW) system. Moreover the phase-dependent gain and absorption properties of mid- to far-infrared light have been investigated [1]. Phase-controlled gain-assisted slow light propagation is another interesting application of TCQW system [2].

On the other hand, control of light by light is important in all-optical switching and optical computing. all-optical switching devices based on optical bistability (OB). Optical bistability in a three-level atomic system inside the optical ring cavity has been studied [3].

The relative phase of applied laser fields is an important parameter for controlling the atomic coherence. It is shown that the phase dependent behavior, in a closed-loop system, is only valid in the multi-photon resonance condition, so the phase-dependent process contributing to the probe field susceptibility only occurs at a specific frequency [4].

In this paper, we analyze the controllability of OB in the ladder-type closed-loop TCQW structure via the intensity and the relative phase of the applied fields.

## 2. MODELS AND EQUATIONS

Let us consider an asymmetric ladder-type TCQW system consisting of a wide well and two narrow wells as shown in Fig. 1(a). A tunable infrared probe field of frequency $\omega_p$ with Rabi-frequency $\Omega_p = E_p \wp_{21}/\hbar$ applies to the transition $|1\rangle \rightarrow |2\rangle$. Two infrared pumping laser fields of frequencies $\omega_c$ and $\omega_d$ with Rabi frequencies $\Omega_c$ and $\Omega_d$ are applied to transitions $|2\rangle - |3\rangle$ and $|3\rangle - |4\rangle$, respectively. We apply a signal infrared laser field of frequency $\omega_s$ and Rabi frequencies $\Omega_s$ to
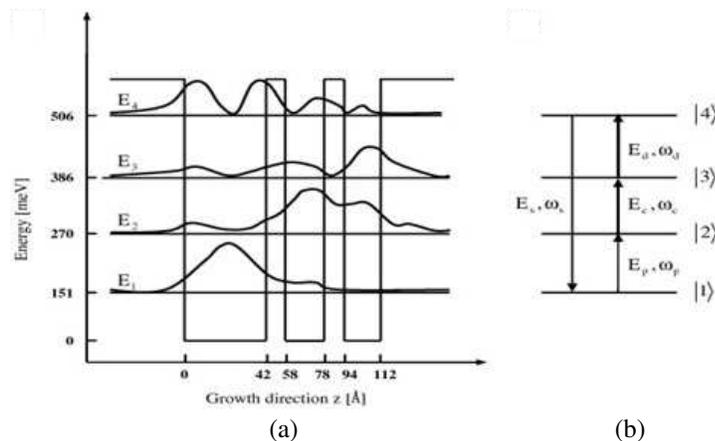


Figure 1: (a) Schematic energy-band diagram for a single period of the asymmetric AlInAs/GaInAs TCQW structure. (b) Four energy levels in cascade configuration.
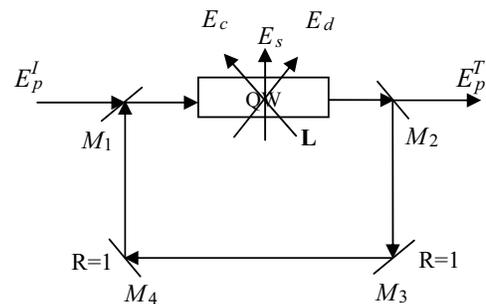
Figure 2: A unidirectional ring cavity containing TCQW sample of length $L$ and four mirrors.

transition $|1\rangle - |4\rangle$. The Hamiltonian in the interaction picture is given by

$$
\begin{aligned}
H_{int}^I &= \Delta_p |2\rangle\langle 2| + (\Delta_p + \Delta_c)|3\rangle\langle 3| + (\Delta_p + \Delta_c + \Delta_d)|4\rangle\langle 4| \\
&\quad - \left(\Omega_p e^{i\varphi_p}|2\rangle\langle 1| + \Omega_c e^{i\varphi_c}|3\rangle\langle 2| + \Omega_d e^{i\varphi_d}|4\rangle\langle 3| + \Omega_s e^{i\varphi_s}|4\rangle\langle 1| + h.c.\right).
\end{aligned}
\tag{1}
$$

where $\Delta_p = \omega_{21} - \omega_p$, $\Delta_c = \omega_{32} - \omega_c$, $\Delta_d = \omega_{43} - \omega_d$ and $\Delta_s = \omega_{41} - \omega_s$ are the detuning of applied laser fields. Note that the multi-photon resonance condition, i.e., $\Delta_s = \Delta_p + \Delta_c + \Delta_d$ is fulfilled. The time-dependent quantum state of the system is defined as

$$
|\Psi(t)\rangle = A_1(t)|1\rangle + A_2(t)e^{i\varphi_p}|2\rangle + A_3(t)e^{i(\varphi_p + i\varphi_c)}|3\rangle + A_4(t)e^{i\varphi_s}|4\rangle
\tag{2}
$$

where $A_j\,(j = 1 - 4)$ is the probability amplitude of level $|j\rangle$. By using the Schrodinger equation, the equation of motion for the probability amplitudes can be obtained as

$$
\begin{aligned}
\frac{\partial A_1}{\partial t} &= i\Omega_p A_2 + i\Omega_s A_4 \\
\frac{\partial A_2}{\partial t} &= i(-\Delta_p + i\gamma_2)A_2 + i\Omega_p A_1 + i\Omega_c A_3 \\
\frac{\partial A_3}{\partial t} &= i(-(\Delta_p + \Delta_c) + i\gamma_3)A_3 + i\Omega_c A_2 + i\Omega_d A_4 e^{-i\varphi} \\
\frac{\partial A_4}{\partial t} &= i(-(\Delta_p + \Delta_c + \Delta_d) + i\gamma_4)A_4 + i\Omega_s A_1 + i\Omega_d A_3 e^{i\varphi} \\
|A_1|^2 &+ |A_2|^2 + |A_3|^2 + |A_4|^2 = 1
\end{aligned}
\tag{3}
$$

where $\gamma_i = (i = 2, 3, 4)$ is the spontaneous emission rate of the level $|i\rangle$ and $\varphi = \varphi_p + \varphi_c + \varphi_d - \varphi_s$ shows the relative phase of applied fields. The response of the system to the applied fields is determined by the susceptibility $\chi_p = N\wp_{21}A_2 A_1^*/(\varepsilon_0 E_p)$. The real and imaginary parts of $\chi_p$ correspond to the dispersion and the absorption of the weak probe field, respectively. If $\text{Im}(\chi_p)\langle 0$ the system exhibits gain, while for $\text{Im}(\chi_p)\rangle 0$ the probe field will be attenuated.

Now, we put the TCQW sample in a unidirectional ring cavity as shown in Fig. 2. Where the probe field circulating in the ring cavity while the signal and two pumping fields does not circulate in the cavity. Under slowly varying envelop approximation, the dynamics response of the probe field is governed by Maxwell's equation. For a perfectly tuned cavity, the boundary conditions in the steady-state limit between the incident field $E_P^I$ and transmitted field $E_P^T$ are

$$
E_P(0) = \sqrt{T}E_P^I + RE_p(L),
\tag{4a}
$$
$$
E_P(L) = E_P^T/\sqrt{T},
\tag{4b}
$$

Note that $R$ is the feedback mechanism due to the reflection from mirror $M_2$. According to the mean-field limit and using the boundary condition, we obtain the input-output relationship,

$$
y = x - 2iC\gamma_2 A_2 A_1^*
\tag{5}
$$

where $y = \wp_{21}E_P^I/(\hbar\sqrt{T})$, $x = \wp_{21}E_P^T/(\hbar\sqrt{T})$ and $C = N\omega_P L\wp_{21}^2/(2\hbar\varepsilon_0 cT\gamma_2)$.

## 3. RESULTS AND DISCUSSIONS

Now, we present the numerical results for obtaining the OB behavior under various parametric conditions. We solve the Equation (3) numerically in the steady state condition and use the Equation (5) to get the result for the optical bistability. In Fig. 3, we display the OB behavior of probe field for different values of pumping field. Using system parameters are $\wp_{21} = e \times 1.3\,\text{nm}$, $N = 10^{24}\,\text{m}^{-3}$, $E_1 = 151\,\text{mev}$, $E_2 = 270\,\text{mev}$, $E_3 = 386\,\text{mev}$, $E_4 = 506\,\text{mev}$, $\gamma_3 = 8\,\text{mev}$, $\gamma_2 = 10\,\text{mev}$. Other parameters are $\Delta_c = \Delta_p = \Delta_d = \Delta_s = 0$, $\Omega_s = \Omega_p(a)$, $\Omega_s = 0(b)$, $\Omega_d = 30\,\text{mev}$, $\Omega_c = 20\,\text{mev}$ (star) $30\,\text{mev}$ (dashed), $32.4\,\text{mev}$ (dotted), $35\,\text{mev}$ (dash-dotted), $40\,\text{mev}$ (solid). An investigation on Fig. 3(a) shows that by increasing the intensity of pumping field ($\Omega_c$), the OB threshold decreases. To explain the physics of phenomena, we show the absorption spectrum of the system in Fig. 4(a). For $\Omega_c = 20\,\text{mev}$ (star) the absorption peak is established around zero detuning of probe field. Then the OB curve (star line) in Fig. 3(a) is due to the absorption.

(a)              (b)
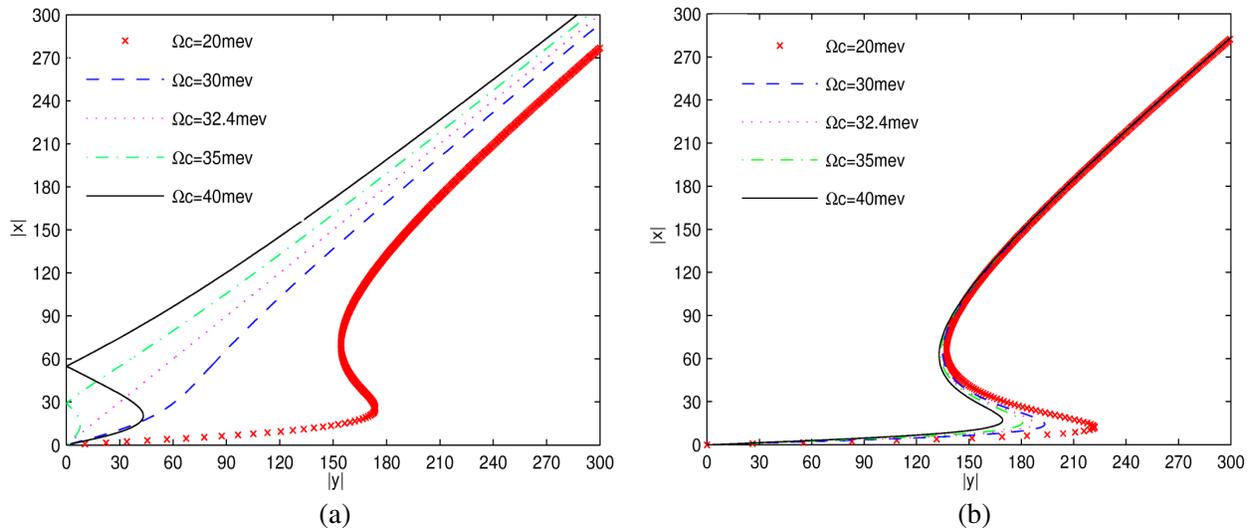
Figure 3: The optical bistability behavior of probe field for different values of pumping field $\Omega_c$ for $\Omega_s = \Omega_p(a)$ and $\Omega_s = 0(b)$. Using system parameters are $\Delta_c = \Delta_p = \Delta_d = \Delta_s = 0$, $C = 50$.



(a)              (b)
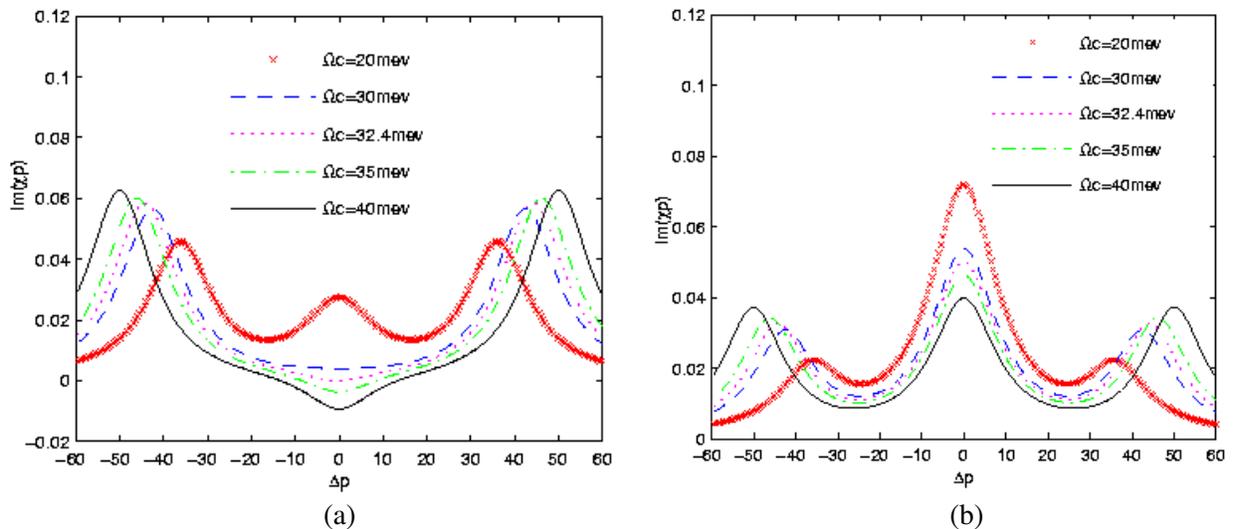
Figure 4: The absorption spectrum of probe field versus the detuning $\Delta_p$ for different values of pumping field $\Omega_c$ for $\Omega_s = \Omega_p(a)$ and $\Omega_s = 0(b)$. Using parameters are $\Delta_c = \Delta_d = \Delta_s = 0$, $\Omega_p = 0.5$ mev.

For $\Omega_c = 32.4$ mev (dotted), the electromagnetically induced transparency (EIT) window appears around zero detuning as shown in Fig. 4(a), then the OB behavior disappeared in dotted curve of Fig. 3(a). For higher values of pumping intensity, the system shows the gain around zero detuning. Then dash-dotted and solid curves in Fig. 3(a) are corresponding to the gain in system. The interesting result is the obtaining the zero value for upper return point of OB, when the spectrum of the system switches from absorption to the gain. It is worth to understand that for $\Omega_s = 0.0$, such result cannot be obtained, as shown in Fig. 3(b). The point can be explained via absorption spectrum, mentioned in Fig. 4(b). In this case the system does not show the gain behavior around zero detuning. Then the gain property of the system has a major role in establishing of zero value for upper return point in OB behavior of the system.

In Fig. 5, we show the OB behavior of the system for different relative phase of applied fields, i.e., $\varphi = 0.0$ (solid), $\varphi = \pi/6$ (dashed), $\varphi = \pi/4$ (dash-dotted), $\varphi = \pi/2$ (dotted). Physical origin of the phase-dependent behavior is the scattering of two pumping and signal fields into the probe mode in the probe frequency.
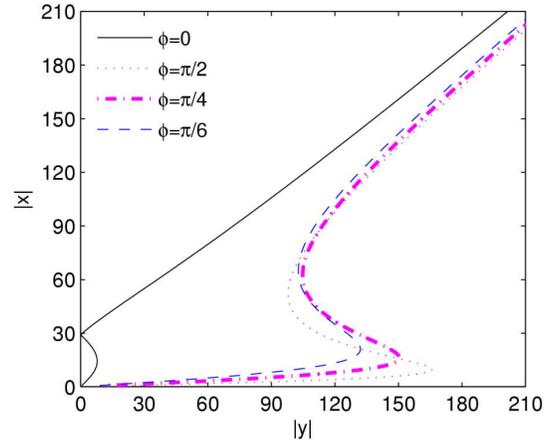
Figure 5: The optical bistability behavior of the probe field for different relative phase. Using parameters are $\Omega_c = 35\,\mathrm{mev}$, $\Omega_d = 30\,\mathrm{mev}$.

## 4. CONCLUSION

In conclusion, we have investigated the OB behavior in a ladder-type closed-loop asymmetric semiconductor TCQW system. It was shown that the optical properties of such a system can be controlled either intensity or relative phase of applied fields. Moreover, it is demonstrated that in the gain region of spectrum, the zero return point is obtained for OB curve.

**REFERENCES**

1. Hao, X., J. Li, C. L. Ding, P. Song, and X. Yang, *Opt. Commun.*, Vol. 282, 2009.
2. Han, D., Y. Zeng, Y. Bai, S. Dong, C. Huang, and H. Lu, *Phys. Lett. A*, Vol. 375, 2011.
3. Mousavi, S. M., L. Safari, M. Mahmoudi, and M. Sahrai, *J. Phys. B: At. Mol. Opt. Phys.*, Vol. 43, 2010.
4. Mahmoudi, M., *J. Evers, Phys. Rev. A*, Vol. 74, 2006.

# Amorphous Silicon-based Thin Film Solar Cells

**Shokri Alforgani**[1], **M. Sbeta**[2], **and A. Abugalia**[2]

[1]Plasma Research Laboratory, Libya
[2]Center for Solar Energy Studies oe, Libya

**Abstract**— The electric and the photo characteristics of solar cells were studied at TU-Delft (Holland). The deposition technique that was used is an rf PECVD AMOR deposition system "radiofrequency Plasma Enhanced Chemical Vapor Deposition" on an amorphous thin films that has been deposited on a supporting substrate made from glass. High quality thin films were deposited at temperature of 180°C and an rf power of 4 watts, while CVD "Chemical Vapor Deposition" techniques require higher temperature range to produce similar quality films. Another system is used (Leybold deposition system CVD) for depositing metallic contacts from either silver (Ag) or aluminum (Al). AMOR and Leybold systems were used to deposit devices and layers with different specifications. Two substrates were used for layer; glass-based and c-Si wafer-based while TCO-coated glass substrate was used for devices. Three types of glass-based layers; $p$, $n$ and $i$ were deposited with 300 nm thickness each. Three 300 nm intrinsic layers of c-Si based-wafer were deposited at three different rf powers; 3 W, 4 W and 5 W. On the other hand three devices with three different thicknesses; 150 nm, 300 nm and 450 nm were deposited on TCO-coated substrate. The measured performances of solar cells.

## 1. INTRODUCTION

Due to the interest in its basic physics and many possible applications, hydrogenated amorphous silicon (a-Si:H) has been intensively studied in the last twenty years [1, 2], though the distribution of the defect states in the energy gap is still the subject of considerable controversy [3]. Because of the critical effect of the defect states on the transport properties and recombination kinetics in this material, many of the studies were focused on determining the energy distribution of these states. Correspondingly, quite a few experimental methods, which have been previously used for crystalline semiconductors, were extended to suit studies of a-Si:H.

In thin-film solar cells the active semiconductor is a polycrystalline or amorphous thin film that has been deposited on a supporting substrate made from glass, ceramic, metal, plastic, or another semiconductor. Because of the important role of Hydrogen in the newly made amorphous silicon doped films, the electronic grade amorphous silicon is therefore called hydrogenated amorphous silicon (a-Si:H). Due to high absorption coefficient of a-Si:H in the visible range of the solar spectrum, 1 mm thick, a-Si:H layer is sufficient to absorb 90% of usable solar radiation energy. Low processing temperature.

## 2. EXPERIMENTAL PROCEDURES

Three solar cells were manufactured (deposited) by **RF PECVD** "radio frequency Plasma Enhanced Chemical Vapor Deposition". The deposition has been carried out for the three devices at the same condition (temperature, pressure and power) but the only difference in this was the thickness (150 nm, 300 nm and 450 nm). The conditions of deposition process were as follows:

- Temperature of substrate ($\sim 180$°C).
- Pressure [initial & operable] ($< 1 \times 10^{-7}$ Torr & 0.7 mbar).
- Mass flow of gases.
- rf power ($\sim 4$ W).

### 2.1. Performance Measurements of Devices

*2.1.1. Light I-V Curve Measurement (Sun Simulator) Has Been Carried out and the Following Was Found*

- -V characteristics curve.
- Short I circuit current, $I_{sc}$.
- Open circuit voltage, $V_{oc}$.
- Fill factor.
- Efficiency.
- Series resistance, $R_s$.
- Parallel resistance, $R_p$.

*2.1.2. Light-induced Degradation Test*
- Light exposure.
- Comparing the device performance before (initial) and after (degraded) light exposure.
- Degradation ratio.

*2.1.3. Spectral Response Measurement*

- External quantum efficiency, QE (*l*).

## 3. RESULTS AND DISCUSSIONS

### 3.1. Light I-V Curve Before Degradation
The initial I-V characteristics curves of three devices.
This curve shows the relationship between current and voltage for three devices which have different thicknesses before degradation.
The device 150 nm was stable in 12 mA and drop in $\sim 0.775$ V.
The device 300 nm was stable in 14 mA and drop in $\sim 0.785$ V.
The device 450 nm was stable in 15 mA and drop in $\sim 0.795$ V.

### 3.2. Light I-V Curve after Degradation. Figure 2
This curve shows the relationship between current and voltage for three devices which have different thicknesses before degradation.
The device 150 nm was stable in 11.8 mA and drop in $\sim 0.775$ V.
The device 300 nm was stable in 13.9 mA and drop in $\sim 0.785$ V.
The device 450 nm was stable in 14.8 mA and drop in $\sim 081$ V.

### 3.3. Figure 3
This curve shows the relationship between current and voltage for the device which is 150 nm thickness after the cell has exposed to (IR) For 15 min, from the figure below the stability was at 12 mA where as the voltage was variable but when the curve reach to $\sim 0.785$ V there was a drop down.

### 3.4. Figure 4
This curve shows the relationship between current and voltage for the device which is 150 nm thickness after the cell has exposed to (IR) For 15 min, from the figure below the stability was at 12 mA where as the voltage was variable but when the curve reach to $\sim 0.785$ V there was a drop down.

### 3.5. Figure 5
This curve shows the relationship between the voltage and crrrent for the 450 nm thickness device before and after degradation and were initial curve was stable in 15 mA and drop in $\sim 0.78$ V but the Degraded curve was stable in 14.8 mA and drop in $\sim 0.83$ V.
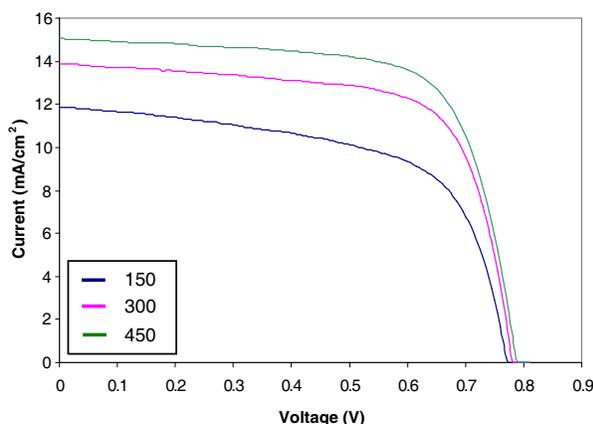


Figure 1.
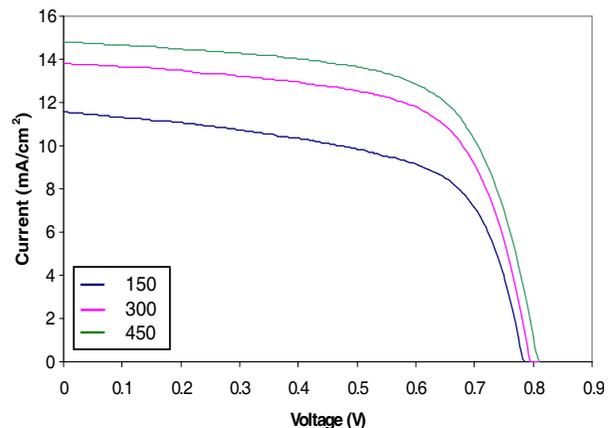


Figure 2. The degraded I-V characteristics curves of three devices.
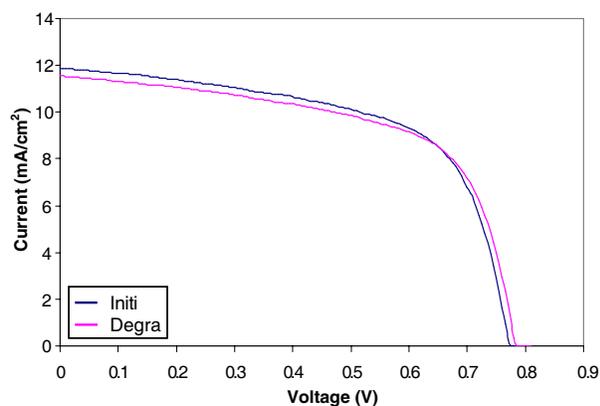
Figure 3. Initial and degraded of I-V curve of 150 nm device.
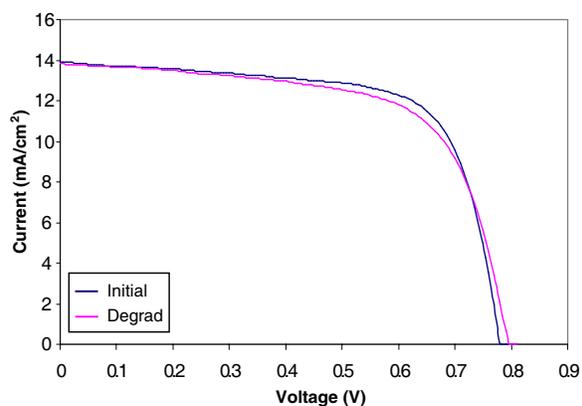


Figure 4. Initial and degraded I-V characteristics curve of 300 nm device.
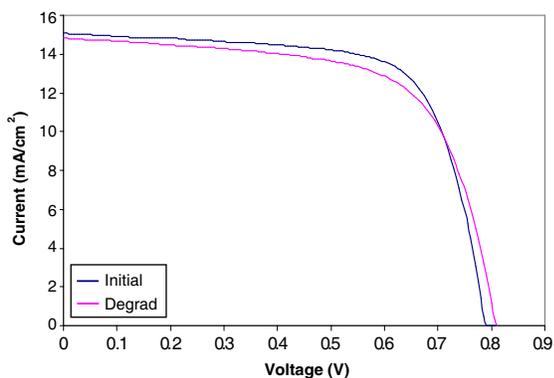


Figure 5. Initial and degraded I-V characteristics curves of 450 nm device.
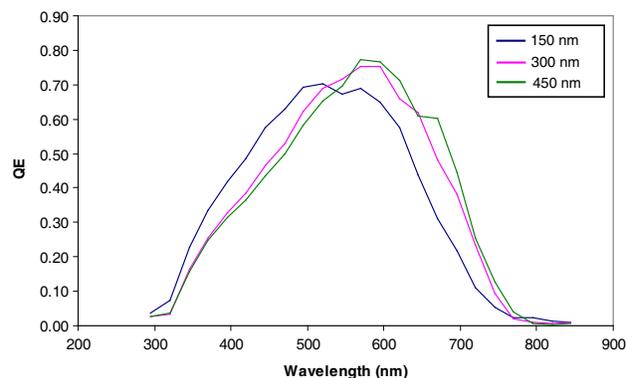


Figure 6. Initial quantum efficiency of different devices.
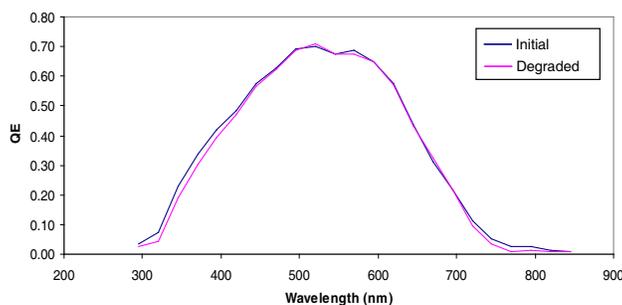


Figure 7.

### 3.6. Figure 6

This figure shows the relationship between wavelength and Quantum efficiency for the three devices.

- At 150 nm thickness the highest QE was 0.71 at the wavelength of 520 nm.
- At 300 nm thickness the highest QE was 0.753 at the wavelength of 595 nm.
- At 450 nm thickness the highest QE was 0.774 at the wavelength of 570 nm.

### 3.7. Figure 7

This curve shows the relationship between current and voltage for the device which is 150 nm thickness after the cell has exposed to (IR) For 15 min, from the figure below the stability was at 12 mA where as the voltage was variable but when the curve reach to $\sim 0.785$ V there was a drop down.

### 4. CONCLUSION

The three layers of $I$, $n$ and $p$ types were deposited on a substrates of glass. These layers were made under these conditions: Conditions of deposition process

Table 1. Summary of results of performance measurements of devices.

| Thickness (nm) | 150 | | 300 | | 450 | |
|---|---|---|---|---|---|---|
| Cell area (cm$^2$) | 0.16 | 0.16 | 0.16 | 0.16 | 0.16 | 0.16 |
| Light exposure (15 min) (3 sun laser light 670 nm) | Before | After | Before | After | Before | After |
| light power (mW/cm$^2$) | 100 | 100 | 100 | 100 | 100 | 100 |
| $V_{oc}$ (V) | 0.78 | 0.79 | 0.79 | 0.80 | 0.79 | 0.81 |
| $J_{sc}$ (mA/cm$^2$) | 11.87 | 11.56 | 13.90 | 13.85 | 15.06 | 14.81 |
| $P_m$ (mW/cm$^2$) | 5.61 | 5.56 | 7.50 | 7.13 | 8.29 | 7.82 |
| $FF$ | 0.61 | 0.61 | 0.69 | 0.65 | 0.70 | 0.65 |
| $E\!f\!f$ (%) | 5.61 | 5.56 | 7.50 | 7.13 | 8.29 | 7.82 |
| $R_s$ (ohm*cm$^2$) | 6.45 | 7.53 | 5.22 | 6.28 | 5.37 | 6.47 |
| $R_p$ (ohm*cm$^2$) | 457 | 457 | 576 | 533 | 833 | 792 |
| $E\!f\!f$. degradation (%) | 1.03 | | 4.93 | | 5.67 | |
| Max. QE (%) | 70.1 at 520 nm | | 75.4 at 570 nm | | 77.4 at 470 nm | |

- Temperature of substrate ($\sim 180°$C).
- Pressure [initial & operable] ($<1 \times 10^{-7}$ Torr & 0.7 mbar).
- Mass flow of gases.
- rf power ($\sim 4$ W).

The photoconductivity, dark conductivity and absorption coefficient were measured and found that under the above conditions the measured parameters were improved.

Three solar cells differ in thickness were made under the above conditions. As the thickness of the solar cells increased the efficiency was improved. When these cells exposed to sun laser light for 15 minutes, the efficiency degradation was better in the cell that has higher thickness.

The difference of efficiency and efficiency degradation (before and after the solar cells were exposed to light) was more in the higher thickness. Therefore the solar cells were deposited in conditions that improved their efficiencies.

**ACKNOWLEDGMENT**

**REFERENCES**

1. Zeman, M., *Advanced Amorphous Silicon Solar Cell Technologies*, 2006.
2. Mollar, H. J., *Semiconductor for Solar Cell*, 1993.
3. Trijssenaar, M., *Hydrgenated Amorphous Silicon and p/I-hetrojunctions*, 1995.
4. www.plasmaequip.com.
5. www.enwikipedia.org.

# Determination of Moisture Content of Maize Kernel (*Zea mays L.*) by Reflectance Measurement at Wavelengths 300 nm to 800 nm Using Optical Technique

**A. M. Norimi**, **Z. Abbas**, **A. Jusoh**, and **M. A. Ismail**

Faculty of Science, Department of Physic, Universiti Putra Malaysia
43400 UPM Serdang, Selangor Darul Ehsan, Malaysia

**Abstract**— This paper presents a method to determine moisture content of single maize kernel based on optical reflectance measurement at wavelengths from 300 nm to 800 nm. The method provides a simple, fast, non-destructive and accurate technique to establish the relationship between reflectance and moisture content. The actual amount of moisture content was determined by standard oven drying method. The optical measurement setup consists of a UV-VIS-NIR light source, an integrated set of seven 440 μm diameter fibers with six illumination fibers encircling one detection fiber, a spectrometer, and a sample holder ensuring that the direction of the incident beam was normal to the sample surface. The results suggest that the percentage of reflectance decreases with moisture content. Calibration equations were established at wavelengths 380 nm, 450 nm and 590 nm corresponding to UV-VIS boundary, carotenoid pigment absorption and yellow colour wavelengths. The lowest mean relative error of the optical fiber technique to determine moisture content based on reflectance measurements was 0.037 at 590 nm.

## 1. INTRODUCTION

The quality of vegetables and fruits are usually inspected visually based on colour. Moisture content is the main parameter influencing the colour of fruits and vegetables. Controlling the amount of moisture content is a major critical issue in monitoring the quality of foods and other products in industries [1–4]. Many techniques have been used including the more recent fiber optic method [5–8].

For agricultural application, methods to determine moisture content of grains are grouped into primary and secondary methods. Primary methods also known as direct methods involve measurement of the mass of fresh and total dried samples. In the secondary methods, moisture content is determined indirectly from the empirical relationship between some physical or chemical characteristics and actual moisture content obtained using standard oven drying method [9].

## 2. MATERIALS AND METHOD

### 2.1. Sample Preparation

Single maize kernels were selected from the Universiti Putra Malaysia farm with initial moisture contents about 80% wet basis. The samples were weighed and dried, then weighed again according to standardized procedures. The samples moisture content was expressed as a percentage. The percentage of moisture content determined by conventional oven method was calculated using the following equation [10]:

$$Moisture\ Content\,(\%) = \frac{M_{wet} - M_{dry}}{M_{wet}} \times 100 \tag{1}$$

where, $M_{wet}$ is the weight of sample before drying and $M_{dry}$ is the weight of the dried sample.

### 2.2. Reflectance Measurement

Nondestructive, UV-VIS-NIR optical spectroscopic measurements were performed between 300 nm to 800 nm. The measurement setup consists of (i) a UV-VIS-NIR light source (Ocean optics, DH2000-BAL), (ii) a bifurcated fiber (Ocean optics, R400-7-UV-VIS), (iii) a spectrometer (Ocean optics, USB4000-UV-VIS), and a reflection probe holder ensures that the distance between the probe and sample is fixed and the same for all measurements.

## 3. RESULTS AND DISCUSSIONS

The variation in the reflectance with wavelength at different moisture content for single maize kernel is shown in Figure 1. The reflectance values were almost constant for wavelength from 300 nm to

380 nm. Rapid increased in the values of reflectance was observed between 380 nm and 550 nm for all the maize of different moisture percentages. These suggest the presence of the carotenoids pigment in maize [11]. The two peaks between 450 nm and 550 nm were due to the zeaxanthin and lutein carotenoids.

Based on pigment analysis, only 380 nm, 450 nm, and 590 nm wavelengths are chosen to develop the calibration equations between reflectance and moisture contents. Figure 2 shows the relationship between reflectance and moisture content for the selected wavelengths. Strong correlations were observed based on the high regression coefficient ($R^2$).

The calibration equations are listed in Table 1. The accuracy of the equations in the determination of moisture content was tested by measuring the reflectance on a set of new samples of single maize kernel. The predicted moisture content values were then compared with the actual moisture
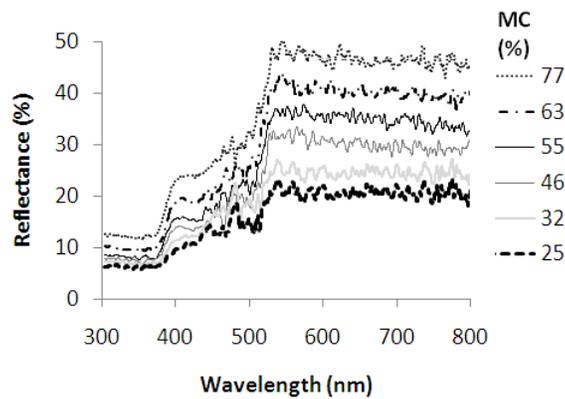


Figure 1: Variation in the spectral reflectance characteristic of single maize kernel according to moisture content at 300 nm to 800 nm.
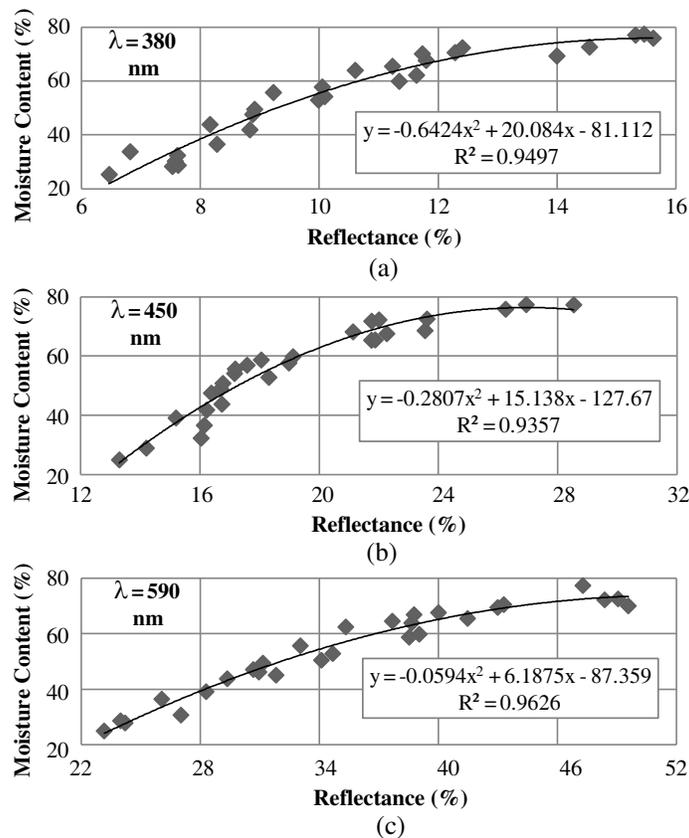


Figure 2: Relationship between moisture content and reflectance at (a) 380 nm, (b) 450 nm, and (c) 590 nm for single maize kernels.

Table 1: Mean relative error between true and predicted moisture content for single maize kernel.

| Wavelength (nm) | Calibration Equation ($x$ = reflectance, $R$) | $R^2$ | Mean Relative Error |
|---|---|---|---|
| 380 | MC $= -0.6424x^2 + 20.084x - 81.112$ | 0.9819 | 0.038 |
| 450 | MC $= -0.2807x^2 + 15.138x - 127.67$ | 0.9681 | 0.047 |
| 590 | MC $= -0.0594x^2 + 6.1875x - 87.359$ | 0.9823 | 0.037 |

content obtained using oven drying method. These models were compared to true moisture content that was obtained from conventional oven method. The mean relative error between the predicted and actual moisture content was as low as 3.7% at 590 nm whilst the highest error was only 4.7% at 450 nm.

## 4. CONCLUSION

An optical technique for non-destructive and accurate measurement of moisture content has been successfully used to determine moisture content in single maize kernel based on reflectance measurement. The accuracy of sensor was determined by comparing the predicted moisture content with the actual moisture content using oven drying. The moisture content predicted by optical technique has been proved accurate with mean relative error below 5%.

**REFERENCES**

1. Ruan, R. R. and P. L. Chen, *Water in Food and Biological Materials*, 75–77, Technomic Publishing Company, 1998.
2. Papadopoulos, M. C., A. R. El Boushy, A. E. Roodbeen, and E. H. Ketelaars, "Effects of processing time and moisture content on amino acid composition and nitrogen characteristics of feather meal," *Animal Feed Science and Technology*, Vol. 14, 279–290, 1986.
3. Amin, M. N., M. A. Hossain, and K. C. Roy, "Effects of moisture content on some physical properties of lentil seeds," *Journal of Food Engineering*, Vol. 65, 83–87, 2004.
4. Wang, N. and J. G. Brennan, "Thermal conductivity of potato as a function of moisture content," *Journal of Food Engineering*, Vol. 17, 153–160, 1992.
5. Andersson, S., M. Prager, and E. I. A. Johansson, "Carotenoid content and reflectance of yellow and red nuptial plumages in widowbirds (Euplectes spp.)," *Functional Ecology*, Vol. 21, 272–281, 2007.
6. Mateo, M. J., D. J. O'Callaghan, C. D. Everard, M. Castillo, F. A. Payne, and C. P. O'Donnell, "Evaluation of on-line optical sensing techniques for monitoring curd moisture content and solids in whey during syneresis," *Food Research International*, Vol. 43, No. 1, 177–182, 2010.
7. Romano, G., D. Argyropoulos, M. Nagle, M. T. Khan, and J. Muller, "Combination of digital images and laser light to predict moisture content and color of bell pepper simultaneously during drying," *Journal of Food Engineering*, Vol. 109, No. 3, 438–448, 2012.
8. Mantanus, J., E. Ziemons, P. Lebrun, E. Rozet, R. Klinkenberg, B. Streel, B. Evrard, and P. Hubert, "Moisture content determination of pharmaceutical pellets by near infrared spectroscopy: Method development and validation," *Analytica Chimica Acta*, Vol. 642, 186–192, 2009.
9. Chen, C., "Evaluation of air oven moisture content determination methods for rough rice," *Biosystems Engineering*, Vol. 86, No. 4, 447–457, 2003.
10. Chin, H. C., "Method of measuring the dry rubber content of field latex," *RRIM Training Manual on Analytical Chemistry, Latex and Rubber Analysis*, Vol. 63, Rubber Research Institute Malaysia, Kuala Lumpur, 1979.
11. Gross, J., *Pigments in Vegetables: Chlorophylls and Carotenoids*, Van Nostran Reinhold, USA, 1991.

# Simulation of High Power GaInNAs-GaNAs Double Quantum-well Laser Diodes for Raman Amplifier Pumping

**M. Faiez Ali**[1], **M. Kamil Abd-Rahman**[1], **M. Salleh Mohd Deni**[1], **and M. S. Alias**[2]

[1]Faculty of Applied Science, Universiti Teknologi MARA, Shah Alam 40450, Malaysia
[2]Advance Physical Technologies Laboratory, Telekom Malaysia Research & Development (TMR&D)
Lingkaran Teknorat Timur, Cyberjaya Selangor 63000, Malaysia

**Abstract**— We present theoretical analysis via simulations on high power GaInNAs-GaNAs quantum-well (QW) broad area laser diode operated in the 1.204–1.242 μm wavelength regime. The structure is based on previous other group experimental work. Simulation design is based on 2D cross section which is treated as perpendicular to the optical axis and lasing direction. We strongly believed that the increased number of quantum wells has leading effects on the increment of the optical confinement factor (OCF) as compared to increment of nitrogen doping. A maximum total power output of more than 4.5 W and lasing spectrum around 1242 nm is obtained for the proposed structure. The device shows potential application to be used as pumping source for Raman amplifiers.

## 1. INTRODUCTION

Since it was first proposed by Kondow et al. [1], GaInNAs systems has shown capabilities in extending the emission spectra of laser diodes around 1.3 μm up to 1.5 μm. The key behind this possibility is well explained by using band anti crossing (BAC) model which was explained by Shan et al. [2] where the theory behind the reduction and splitting of conduction band is demonstrated. Resulting from this knowledge, previous developments of this quaternary alloys has demonstrated excellent optical, electrical and thermal properties which include long wavelength emission spectrum up to 1.5 μm [3], very low threshold current density [4], and high power output [5–7]. While most researchers focused on extending the emission spectrum (1.3–1.5 μm) and lowering the threshold current density, there was only little progress reported on progress in increasing the output power of these GaInNAs laser diodes. Recent progress shows a very high output power up to 8.9 W [5–7] continuous wave under room temperature. These achievements are applicable in developing high pumping source for Raman amplifiers which require lasers emission around 1.3 μm.

In this paper, we proposed design structures that show possibility in extending the emission wavelength and increasing the output power for GaInNAs laser diodes. 2D simulation software [8] is implemented to investigate electrical and optical properties for each design. The physical models that describe the device structures will be discussed and results of the electrical and optical output characteristics will be demonstrated.

## 2. PHYSICAL MODELS

### 2.1. Optical Modes

For optical modes calculation, a solution of scalar Helmholtz equation is used

$$\left\{ \frac{\partial^2}{\partial x^2} + \frac{\partial^2}{\partial y^2} + k_0^2 \left( \varepsilon(x,y) - n_{eff,m}^2 \right) \right\} E_m(x,y,z) = 0 \tag{1}$$

where $k_0$ is wavenumber, $\varepsilon$ is optical dielectric constant, $n_{eff,m}$ is effective index and $E_m(x,y,z)$ is the electric field. In the laplacian term above, $z$ axis is neglected since we only simulates 2D $(x,y)$ planes. Numbers of longitudinal and transverse modes are predetermined before running all optical modes calculations.

### 2.2. Recombination Process

Three recombination processes were considered in this work, Auger recombination, SRH recombination, bulk spontaneous recombination and stimulated recombination which applied on above threshold condition. Auger recombination process is governed by

$$R^{\text{Auger}} = \left( C_e^{\text{Auger}} n_e + C_h^{\text{Auger}} n_h \right) \left( n_e n_h - n_i^2 \right) \tag{2}$$

where $C_e$ and $C_h$ are Auger coefficients for electrons and hole, and $n_i$ is intrinsic carrier density in which dependent on the temperature. SRH recombination is governed by

$$R^{\mathrm{SRH}} = \frac{n_e n_h - n_i^2}{\tau_h^{\mathrm{SRH}}(n_e + n_e^{\mathrm{trap}}) + \tau_e^{\mathrm{SRH}}(n_h + n_h^{\mathrm{trap}})} \tag{3}$$

where $\tau_e^{\mathrm{SRH}}$ and $\tau_h^{\mathrm{SRH}}$ are electrons and holes lifetime. For the bulk spontaneous recombination which is applied outside the region of the quantum well, the equation is governed by

$$R^{\mathrm{spon,bulk}} = B(n_e n_h - n_i^2) \tag{4}$$

where $B$ is the Einstein coefficient material parameter. Above the threshold, stimulated recombination is governed by

$$R^{\mathrm{stim}} = \Sigma_{m,\omega} S_{m,\omega} |E_m|^2 \frac{c}{n_{eff,m}} g(\omega) \tag{5}$$

where $g(\omega)$ is account for gain spectrum.

## 3. CALIBRATION OF MATERIAL PARAMETERS

Calibrations of material parameters are conducted based on other group reported experimental data [5]. Good agreement is obtained on the threshold spectrum and optical power output. This indicates possible modification can be utilized on the conventional structure for further improvement.

The peak of photoluminescence (PL) spectra is calibrated and matched by adjusting the bowing parameters of $Ga_{1-x}In_xN_yAs_{1-y}$ alloys. In pertaining good agreement with the experimental and simulations data, several other material parameters are calibrated. Some of the calibrated parameters are listed in Table 1 and referred in [8].

## 4. DEVICE STRUCTURES AND SIMULATION

Figure 1 shows the schematic view of broad area (BA) laser as in [5]. For our proposed structure, we introduced extra active region with 7 nm $GaN_{0.01}As_{0.99}$ barrier and different cavity length of 800 μm.

A 2D laser simulation package [8] is utilized for analyzing characteristics of the proposed structure. Table 1 listed some of the material parameters applied for the structures while the physical models involved are explained in Section 2. The rest of the physical models are given in detailed in other literatures [9, 10].

## 5. RESULTS AND DISCUSSION

### 5.1. Material and Optical Properties

Figure 2(a) shows the mode profile coupled with the real refractive index values. It can be seen that the mode is mostly confined within the active region. Optical confinement factor (OCF) of 0.88% indicates that more electrons are confined due to the depth of the QW. This reflects by using $Ga_{1-x}In_xN_yAs_{1-y}$ QW, one can possibly achieve a deeper QW and indirectly allowed the structure to be able to maintain the electron confinement and to prevent unwanted flows of electrons under excessive heat condition.
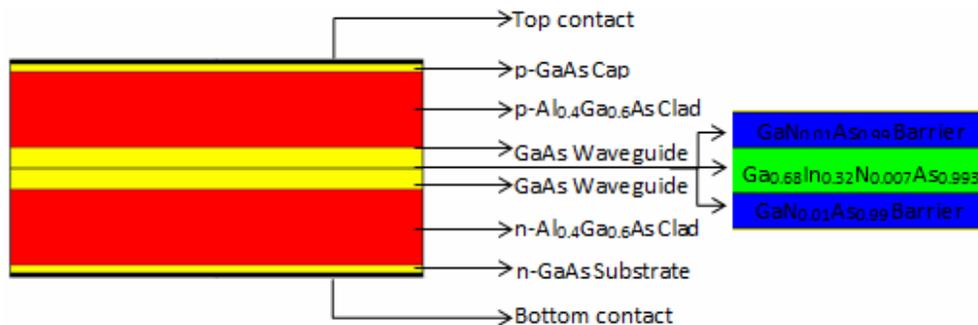


Figure 1: Schematic view of the simulated $Ga_{0.68}In_{0.32}N_{0.007}As_{0.993}$ BA laser.

Table 1: Material parameters used in this study at 293.15°K.

| Parameter | Symbol | Unit | GaAs | $Al_{0.4}Ga_{0.6}As$ | $GaN_{0.01}As_{0.99}$ | $Ga_{0.68}In_{0.32}N_{0.007}As_{0.993}$ |
|---|---|---|---|---|---|---|
| Refractive Index | $n_r$ | - | 3.2989 | 3.1291 | 3.2905 | 3.3578 |
| Auger Coefficient | $C_e$ | $m^6/s$ | $1.9 \times 10^{-43}$ | $1.14 \times 10^{-43}$ | $1.99 \times 10^{-48}$ | $1.76 \times 10^{-43}$ |
| Electron mobility | $\mu_n$ | $m^2/(Vs)$ | 0.85 | 0.518 | 0.843 | 1.419 |
| Hole mobility | $\mu_p$ | $m^2/(Vs)$ | 0.04 | 0.04 | 0.04 | 0.04 |
| Thermal Conductivity | $k$ | W/Kcm | 0.44 | 0.11 | 0.45 | 0.39 |
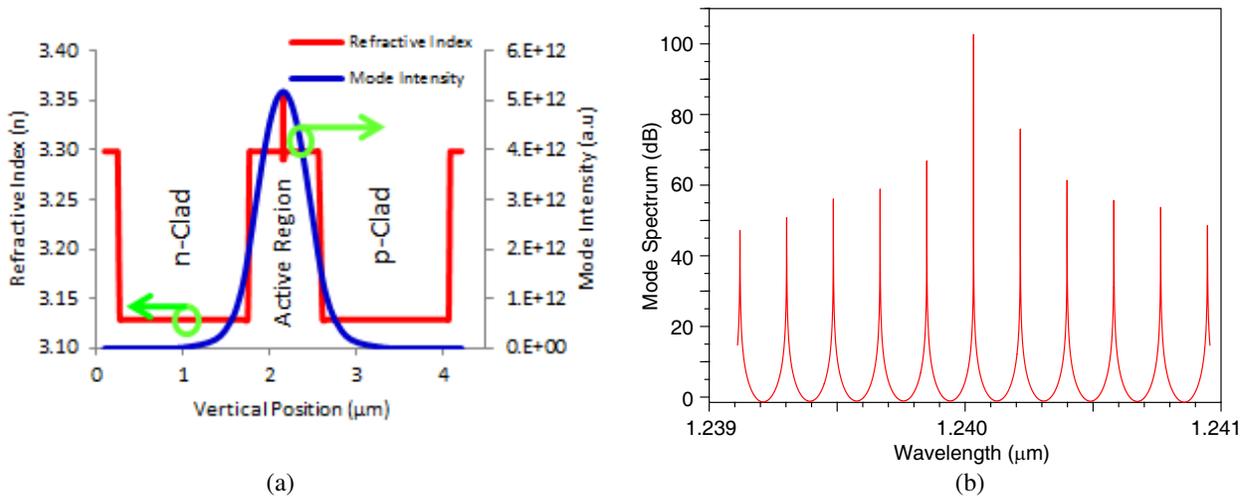


Figure 2: Calibrated profiles for SQW $Ga_{0.68}In_{0.32}N_{0.007}As_{0.993}$ BA laser. (a) Refractive index profile coupled with mode intensity and (b) output optical spectrum above threshold.

Under PL spectra, the highest peak obtained is around $1.204\,\mu m$ which indicates the points where the device shows the spontaneous emission around $1.204\,\mu m$. Supposedly we predict that the BA laser will start lasing above $1.204\,\mu m$. After careful calibration being made, optical spectrum of $1.240\,\mu m$ above threshold is obtained as shown in Figure 2(b). The result is in good agreement with [5].

For our simulation model we introduced double quantum well (DQW) with cavity length of $800\,\mu m$ on the conventional structure. Here, we noticed there are increment in the number of OCF about 1.74% as shown in Figure 3(a) and also the optical spectrum of $1.242\,\mu m$ above threshold as shown in Figure 3(b). We strongly believed that the increased number of quantum wells has leading effects on the increment of the optical confinement factor (OCF) as compared to increment of nitrogen, while increment of nitrogen will results in extension of emission of lasing wavelength of the device up to several nm. Increment of about $\sim 2\,nm$ per QW, proves that addition of nitrogen did extend the wavelength as our result is in agreement as what have been reported in [11]. However, we assumed that this result is possible provided the same growth technique including annealing prior to fabrication process is considered for this proposed structure.

### 5.2. Electrical Properties

For our proposed structure, the L-I-V characteristics are shown in Figure 4(a). Slightly lower threshold current density of $126.3\,A/cm^2$ per QW is obtained for this proposed structure. It shows that the majority of recombination process here is governed by stimulated recombination which applied above the threshold condition. It is crucial to minimize the spontaneous recombination process before threshold as this will determine the threshold point for the laser diode. We also believed that the reduction on the threshold current density compared in [5] is due to the efficiency of current spreading on the device structure. This reflects that the proposed structure has minimum

(a)



(b)
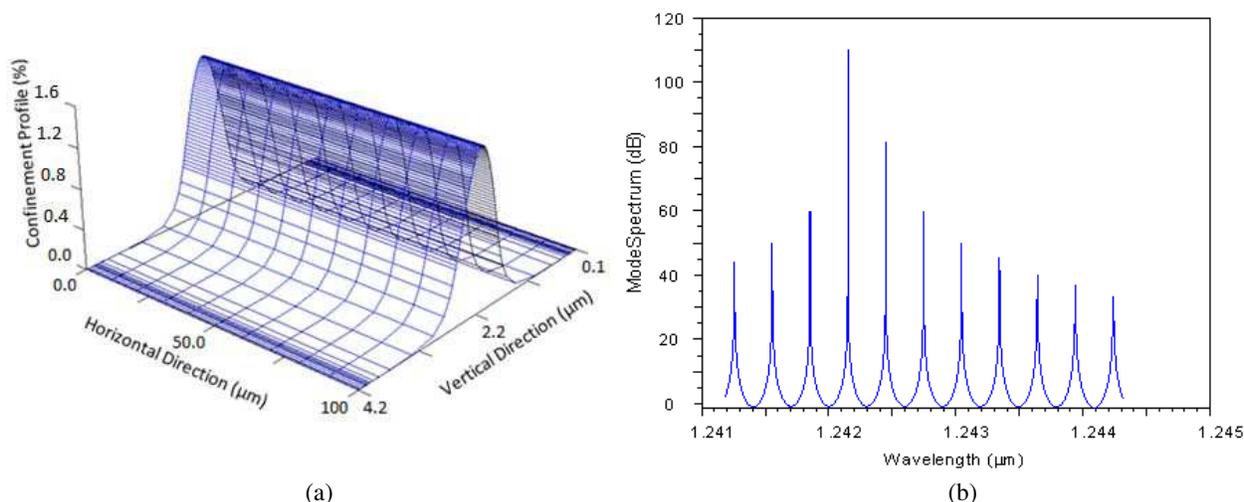
Figure 3: Simulated profiles for DQW $Ga_{0.68}In_{0.32}N_{0.007}As_{0.993}$ BA laser. (a) Mode confinement profile. (b) Output optical spectrum above threshold.



(a)



(b)
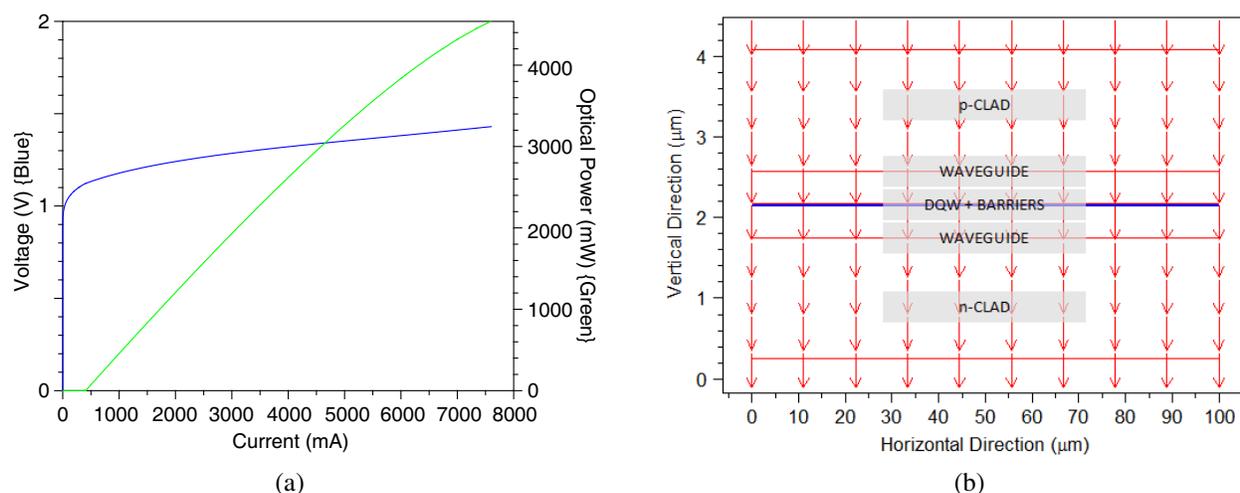
Figure 4: Simulated profiles for DQW $Ga_{0.68}In_{0.32}N_{0.007}As_{0.993}$ BA laser. (a) L-I-V characteristics. (b) 2D view of current distribution of the proposed structure.

defects on crystalline quality as it is lattice matched to GaAs. Figure 4(b) shows the current flows in 2D planes. As the cavity length is shortened and total area is reduced, injection current can be efficiently spread due to small surface area.

The slope efficiency of $0.37\,W/A$ per facet (difference is about $0.01\,W$ per facet) and total maximum output power $(P_o)$ around $4.5\,W$ at $293.15\,K$ is obtained for this proposed structure. However, $P_o$ is still limited by thermal roll-over due to the self-heating effect of the structure. Since our proposed device is relatively small compared to the original design in [5], we assumed that our proposed device exhibits high quality characteristics and can be propose as pumping source for Raman amplifier.

## 6. CONCLUSION

We have investigated theoretical analysis of SQW and DQW $Ga_{0.68}In_{0.32}N_{0.007}As_{0.993}$ BA laser. Our analysis shows good agreement with the previous group experimental work [5]. We have introduced DQW on the conventional structure and observed increment on the lasing spectrum roughly around $3\,nm$ per QW. The emission lasing wavelength above threshold for our proposed DQW $Ga_{0.68}In_{0.32}N_{0.007}As_{0.993}$ BA laser is estimated around $1.242\,\mu m$ while maintained total output power around $4.5\,W$. The device is assumed to exhibit good crystalline quality as we obtained low threshold current density of about $126.3\,A/cm^2$ per QW.

**ACKNOWLEDGMENT**

**REFERENCES**

1. Kondow, M., K. Uomi, A. Niwa, T. Kitatani, S. Watahiki, and Y. Yazawa, "GaInNAs: A novel material for long-wavelength-range laser diodes with excellent high-temperature performance," *Jpn. J. Appl. Phys.*, Vol. 35, 1273–1275, 1996.
2. Shan, W., W. Walukiewicz, J. W. Ager III, E. E. Haller, J. F. Geisz, D. J. Friedman, J. M. Olson, and S. R. Kurtz, "Band anticrossing in GaInNAs alloys," *Phys. Rev. Lett.*, Vol. 82, No. 6, 1221–1224, 1999.
3. Fischer, M., D. Gollub, M. Reinhardt, M. Kamp, and A. Forchel, "GaInNAs for GaAs based lasers for the 1.3 to 1.5 μm range," *J. Cryst. Growth*, Vol. 251, No. 1–4, 353–359, 2003.
4. Wang, S. M., Y. Q. Wei, X. D. Wang, Q. X. Zhao, M. Sadeghi, and A. Larsson, "Very low threshold current density 1.3 μm GaInNAs single-quantum well lasers grown by molecular beam epitaxy," *J. Cryst. Growth*, Vol. 278, No. 1–4, 734–738, 2005.
5. Bisping, D., S. Schneider, S. Höfling, S. Habermann, M. Fischer, J. Koeth, and A. Forchel, "1240 nm high-power GaInNAs laser diodes," *Opt. Express*, Vol. 15, No. 23, 15187–15192, 2007.
6. Bisping, D., D. Pucicki, S. Hofling, S. Habermann, D. Ewert, M. Fischer, J. Koeth, and A. Forchel, "High-temperature high-power operation of GaInNAs laser diodes in the 1220–1240-nm wavelength range," *IEEE Photonics Technology Letters*, Vol. 20, No. 21, 1766–1768, 2008.
7. Bisping, D., D. Pucicki, M. Fischer, J. Koeth, C. Zimmermann, P. Weinmann, S. Hofling, M. Kamp, and A. Forchel, "GaInNAs-based high-power and tapered laser diodes for pumping applications," *IEEE Journal of Selected Topics in Quantum Electronics*, Vol. 15, No. 3, 968–972, 2009.
8. RSoft Design Group, Inc., LaserMOD 1999–2006.
9. Madelung, O., *Semiconductors — Basic Data*, 2nd Edition, Springer-Verlag, Berlin, 1996.
10. Vurgaftmana, I., J. R. Meyer, and L. R. Ram-Mohan, "Band parameters for III–V compound semiconductors and their alloys," *Journal of Applied Physics*, Vol. 89, No. 11, 5815–5875, 2001.
11. Rao, E. V. K., A. Ougazzaden, Y. Le Bellego, and M. Juhel, "Optical properties of low band gap GaAs$_{(1-x)}$Nx layers: Influence of post-growth treatments," *Applied Physics Letters*, Vol. 72, No. 12, 1409–1411, 1998.

# Three Layers Configuration Microstrip Patch Antenna for Unmanned Aerial Vehicle Synthetic Aperture Radar

**P. N. Tan**[1], **V. Gobi**[2], **Y. K. Chan**[1], **T. S. Lim**[1], **and V. C. Koo**[1]

[1]Faculty of Engineering and Technology, Multimedia Media University
Jalan Ayer Keroh Lama, Bukit Beruang, Melaka 75450, Malaysia
[2]Faculty of Engineering, Multimedia University
Jalan Multimedia, Cyberjaya, Selangor 63100, Malaysia

**Abstract**— A side looking microstrip patch antenna for Unmanned Aerial Vehicle Synthetic Aperture Radar (UAVSAR) has been designed and developed. The antenna operates at 5.3 GHz with a minimum requirement bandwidth of 80 MHz. 3 Layers configuration with probe fed method has been adopted to eliminate spurious radiation from feed network. The performance of the antenna has been measured in anechoic chamber and flight measurements for UAVSAR with the antenna have been conducted several times to produce SAR image of the test site.

## 1. INTRODUCTION

The first Synthetic Aperture Radar (SAR) prototype operates with Yagi-Uda antenna at 930 MHz was developed in Arizona nearly 40 years ago. With the abilities of operating at all weather condition and operating at day and night, SAR has become an important tool for wide range of applications such as: geological mapping, mining [1], oil pollution monitoring [2], military surveillance, oceanography [3] and etc.. With proper selected frequency band, the microwave signal can even penetrate through cloud and forest canopy and hence allow the SAR sensor to obtain SAR data of the test site [4].

With the advancement of microwave technology, the operating frequency of SAR has been shifted to much higher frequency. L- , C- and X-band become popular frequencies for SAR applications and horn and slotted waveguide antenna have been used as SAR antennas until microstrip patch antenna has become the dominant choice nowadays.

In years 2009, a 3 layers configuration microstrip patch antenna has been developed for a C-band Unmanned Aerial Vehicle Synthetic Aperture Radar (UAVSAR). As the UAVSAR sensor adopted stripmap scan method, the UAVSAR antenna has a look angle of 30° with low sidelobe level and it is single polarize. Table 1 shows some selected specification of the UAVSAR.

## 2. ANTENNA DEVELOPMENT

Probe fed method and three layers configuration have been adopted for the ease of feeding network design. The top layer consists of radiating elements; the feeding network is fabricated on the bottom layer while the ground plane is located at the middle layer. Probe fed method is adopted by using a probe to connect the feeding network to the radiating elements. By utilizing 3 layers configuration and probe fed method, spurious radiation from the feeding network will be eliminated.

To achieve beamwidth of 24° and look angle of 30° with the maximum sidelobe level of −15 dB, an array with 6 elevation elements has been designed. The feeding network is designed with two feeding ports instead of 1 feeding port to avoid power lose due to excessive length of microstrip transmission line. The excitation coefficient of each of the radiating elements in the array was calculated based on Wooward-Lawson synthesis. The length of microstrip transmission line acts as phase shifter while T-junction power divider is utilized to distribute the signals' magnitude

Table 1: Design specification of UAVSAR.

| Mode of Operation | Stripmap |
|---|---|
| Altitude | 1 km |
| Incident Angle | 30° |
| Swath Width | 525 m |
| Azimuth Beamwidth | 3° |
| Elevation Beamwidth | 24° |

accordingly. Meanwhile, an uniform azimuth array with 24 radiating elements since no beam shaping applied in azimuth plane. However the antenna has been divided to 3 subpanels with each panel consists of 6 elevation radiating elements and 8 azimuth radiating elements. These panels are jointed and connected through equal length coaxial cable to a 3 way power dividers. This configuration allows the antenna to operate at either single antenna or dual antenna mode. The feeding network of antenna subpanel is shown in Figure 1 and front view of developed UAVSAR antenna is shown in Figure 2.

## 3. ANTENNA MEASUREMENT

The radiation pattern of the antenna is measured in anechoic chamber to ensure the accuracy of the result and the comparison of simulated and measured radiation pattern is shown in Figure 3. The elevation radiation pattern of the antenna shows the main lobe is located at $30°$ away from center with beamwidth of $24°$ to provide wider swath width. From the radiation pattern, the highest power level of sidelobe appears at $-45°$ to $-55°$ with the maximum sidelobe power level of $-15\,\mathrm{dB}$ which helps to overcome left-right ambiguity issue which is a common challenge in airborne SAR
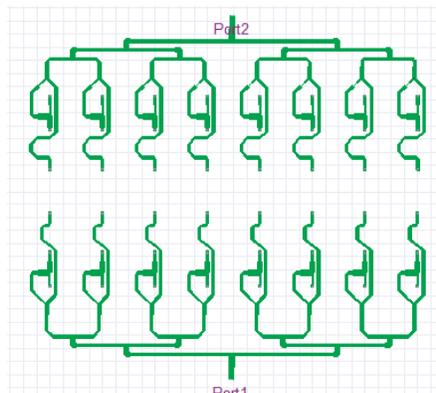


Figure 1: Feeding network of antenna subpanel.
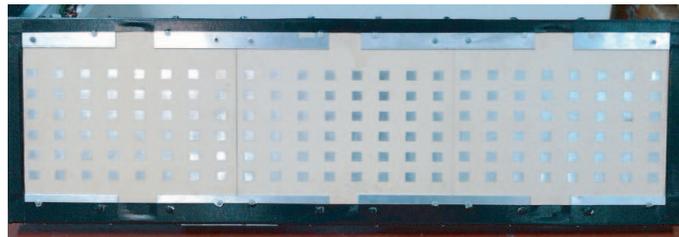


Figure 2: Front view of UAVSAR antenna with supporting structure.



(a)          (b)
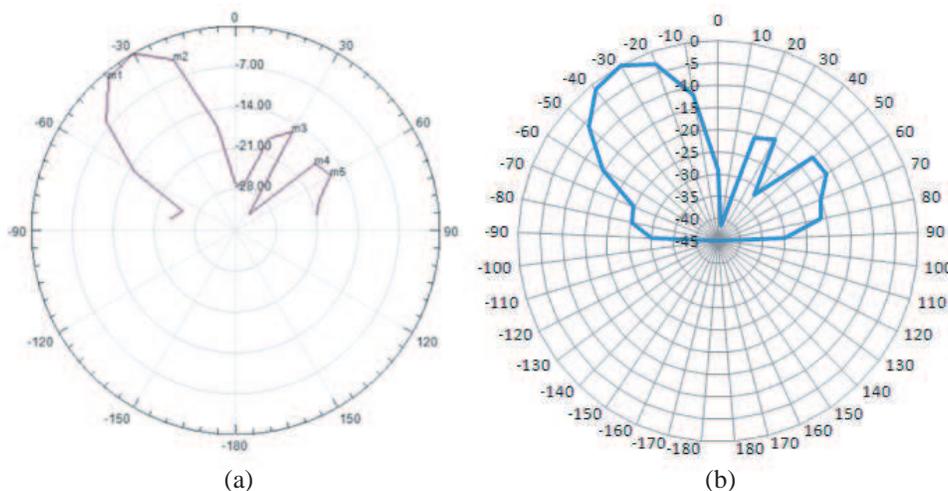
Figure 3: (a) Simulated radiation pattern. (b) Measured radiation pattern in anechoic chamber.

Figure 4: SAR image with river, roads and forested area observed.

system. The measured result shows the return loss value at 5.3 GHz achieve $-32.381$ dB with gain of 18.5 dBi.

Upon satisfactory of the indoor measurement results, the antenna is then integrated to the UAVSAR sensor for flight measurement purpose and installed underneath the UAV. Several flight measurements have been conducted at end of 2010 in Mersing, Malaysia to obtain SAR image of the test site. The produced SAR image proves the capability of the UAVSAR system. An example of SAR image is shown in Figure 4 where clear signature such as river, roads and forested area are observed.

## 4. CONCLUSIONS

A 3 layers configuration UAVSAR antenna has been design and developed. A series of indoor measurements have been conducted to verify the performance of the UAVSAR antenna. Low sidelobe level of the antenna ensures the UAVSAR system is able to capture returned signal from the scanned area without capturing undesired signal due to left right ambiguity. The flight measurement result proved that the developed microstrip patch antenna with UAVSAR system is able to produce SAR image of the imaging area.

## ACKNOWLEDGMENT

## REFERENCES

1. Lynne, G. L. and G. R. Taylor, "Geological assessment of SIR-B imagery of the amadeus basin," *IEEE Trans. on Geosc. and Remote Sensing*, Vol. 24, No. 4, 575–581, 1986.
2. Hovland, H. A., J. A. Johannessen, and G. Digranes, "Slick detection in SAR images," *Proceeding of the 1994 International Geoscience and Remote Sensing Symposium*, 2038–2040, 1994.
3. Walker, B., G. Sander, M. Thompson, B. Burns, R. Fellerhoff, and D.Dubbert, "A high-resolution, four-band SASR Testbed with real-time image formation," *Proceeding of the 1986 International Geoscience and Remote Sensing Symposium*, 1881–1885, 1996.
4. Chan, Y. K., B. K. Chung, and H. T. Chuah, "Transmitter and receiver design of an experimental airborne synthetic aperture radar sensor," *Progress In Electromagnetics Research*, Vol. 49, 203–218, 2004.

# Design and Development of a Miniature C-band RF Transceiver for Synthetic Aperture Radar

**Kuo Shen Yee**, **Yee Kit Chan**, **Wai Lee Fabian Kung**,
**Voon Chet Koo**, **and Ming Yam Chua**

Faculty of Engineering & Technology, Multimedia University
Jalan Air Keroh Lama, Melaka 75450, Malaysia

**Abstract**— Synthetic Aperture Radar is an effective tool for earth's resource monitoring. Typical SAR systems are operated on satellites, spacecrafts or airplanes. Recently, unmanned aerial vehicle (UAV) has become an alternative flying platform for SAR. The main reason of choosing UAV is due to its capability to fly and operate remotely without the crew or pilot on the flying platform. Moreover, a small UAV can operate at lower power and fuel consumption, hence reducing the overall operating cost. However, due to its space and weight constraints, it is a challenging task to design a UAV-based SAR sensor. Most of the commercially available RF components are in standard sizes and some are too bulky to be fitted into the flying platform. Thus, the design of a miniature RF transceiver is of great interest. Main components of the RF transceiver include an up-convert mixer, a power amplifier, a high power amplifier, a low noise amplifier, a down-convert mixer, a band-pass filter and a low-pass filter. The RF transceiver will operate in C-band, with more than 30 dB gain in total. This paper highlights the design of a miniature RF transceiver module for UAV-based SAR.

## 1. INTRODUCTION

Synthetic Aperture Radar SAR is a radar imaging technology that capable of high resolution images of stationary surface target and terrain [1]. SAR principle was established in year 1951 by Carl Wiley where a one-to-one correspondence exists between the along-track coordinate of reflecting object (being linearly traversed by a radar beam) and the instantaneous Doppler shift of the signal reflected to the radar by that object [2].

Consequently, Doppler frequency analysis is implemented in order to improve the radar image resolution. The application to airborne radar was developed where the radar system is mounted on a flying platform and the forward motion of actual antenna would be used to synthesize a very long antenna [3]. This allowed the use of a smaller size antenna with also longer wavelengths where each position a pulse is transmitted, the return echo passes through the receiver. These returned signals are recorded in an "echoes store" since the Doppler frequency variation of each point on the ground would have a unique signature [3]. Furthermore, due to its all whether capability, SAR becomes a very attractive tool for environmental monitoring in regions which are affected by clouds or darkness and for military reconnaissance [4].

Unmanned Aerial Vehicle (UAV) is dedicated as an alternative flying platform for SAR systems due to its reliability and cost concern for research and development. Moreover, the capability to fly and operate remotely without a crew or pilot on the flying platform eliminates human casualties which makes it highly desirable. However, the ready-made SAR systems and SAR components are too bulky to be fitted into the flying platform due to the limitation and constrain of space of carrier system. Focusing this in mind, a miniature RF transceiver is a very effective solution to miniaturize the SAR system in a whole.

Therefore, the design of a miniature RF transceiver is of great interest. This paper describes the conceptual design, the RF transceiver and current status of the development process.

## 2. DESIGN SPECIFICATIONS

Table 1 summarizes the design parameters of the RF transceiver, as follows.

## 3. SYSTEM DESCRIPTION

The RF transceiver is formed by a transmitting channel, an antenna and a receiving channel. Figure 1 illustrates the block diagram of the RF transceiver.

Table 1: Design specifications.

| Operating Frequency | 5.3 GHz |
|---|---|
| Transmitting Power | 47 dBm |
| Waveform Type | Linear FM |
| Bandwidth | 80 MHz |
| Transmitting Channel Gain | 70 dB |
| Receiving Channel Gain | 30 dB |
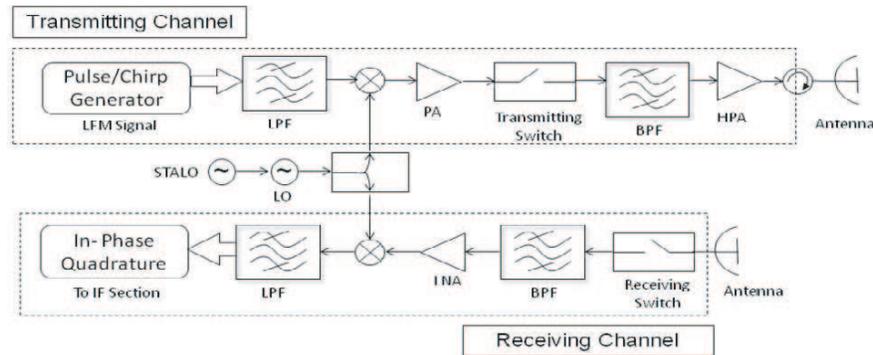


Figure 1: Block Diagram of RF transceiver.

### 3.1. Transmitting Channel

The transmitting channel consists of a chirp generator, an up-convert mixer, a power amplifier (PA), a high power amplifier (HPA), a transmitting switch, a low-pass filter and a band-pass filter. The transmitting signal is forwarded to the antenna for transmitting purposes. The chirp generator generates the desired linear frequency modulated (LFM) chirp with a bandwidth of 80 MHz which is then up-converted by the up-convert mixer with a carrier frequency to a higher band of frequency for transmission. The PA will then pre-amplify the signal while the HPA will amplify the signal to the desired output power which will then be radiated by the antenna [5]. The transmitting switch which is controlled by the timing window supplied by the timing module decides the transmission period while the isolator prevents internal reflections.

### 3.2. Receiving Channel

The receiving channel on the other hand consists of a receiving switch, a low noise amplifier (LNA), a down-convert mixer, a low-pass filter and a band-pass filter. The LNA amplifies the received echo from the receiving antenna to a very low noise Figure to improve the sensitivity of the RF transceiver. The amplified signal is then down-converted by the down-convert mixer with the carrier frequency again to produce a full phase intermediate frequency signal (In-phase and Quadrature) [5]. The timing window again controls the reception period for the receiving switch.

The Stable Local Oscillator (STALO) operates to generate a 10 MHz frequency for the RF transceiver. It functions to keep the entire RF transceiver coherent to its frequency. Thus, the entire system will be synchronized to the STALO. Meanwhile the Local Oscillator (LO) functions to generate a 5.3 GHz carrier frequency for the up-convert mixer and the down-convert mixer. Then, the carrier frequency will feed to both the up-convert and down-convert mixer.

### 4. RESULTS AND DISCUSSIONS

The prototypes of the LNA and down-convert mixer are successfully constructed. IC based RF components have been selected for the prototyping. The performance characteristics of both the modules have been verified and measured. The prototype of the LNA is shown in Figure 2(b).

Figure 2(a) and the gain measurement result of the LNA by using a VNA is evident in Figure 2(b) below. The best amplification for the current state is 2.5 dB at 5.3 GHz.

The prototype of the down-convert mixer is shown in Figure 3(a). A 5.34 GHz RF signal is input to the RF In port of the mixer and a 5.3 GHz carrier frequency is input to the LO port of the mixer. The baseband of the IQ channel is measured by the spectrum analyzer. A 40 MHz signal is

(a)

(b)
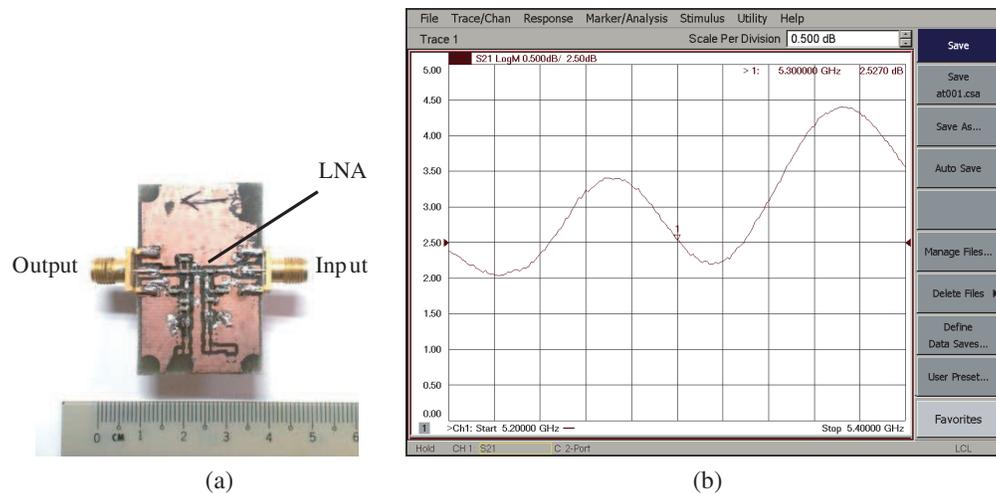
Figure 2: (a) Prototype of LNA module. (b) Measured result of LNA module.



(a)

(b)
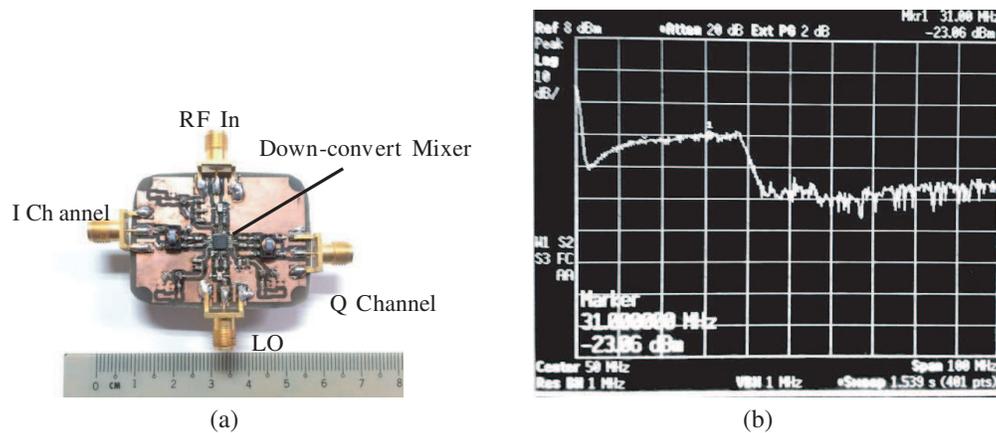
Figure 3: (a) Prototype of down-convert mixer module. (b) Measured result of down-convert mixer module.
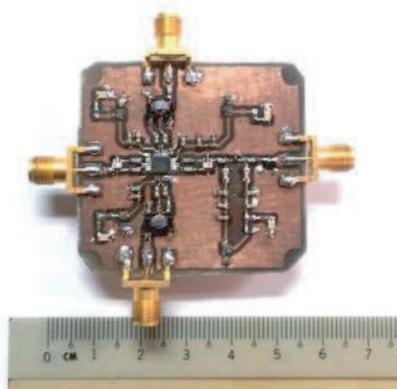


Figure 4: Integration of LNA and down-convert mixer.

presented at the base-band. The measured base-band result is shown in Figure 3(b). The results prove that the down convert mixer functions as intended.

The prototype integration of both the LNA and down-convert mixer has been assembled as in Figure 4.

## 5. CONCLUSION

A RF SAR transceiver is developed. The prototype of the LNA and down-convert mixer has been designed and tested. The integration of both the LNA and down-convert mixer is successful and

it's applicable for the receiving channel of the RF transceiver. For further enhancements, the gain of the receiving channel shall be improved and the transmitting channel shall be constructed and tested. It is then followed by the full setup of the RF transceiver.

**REFERENCES**

1. Patel, V. M., G. R. Easley, D. M. Healy, Jr. and R. Chellappa, "Compressed synthetic aperture radar," *IEEE Journal of Selected Topics in Signal Processing*, Vol. 4, No. 2, April 2010.
2. (Walt) McCandless, S. W., Jr. and C. R. Jasckon, *Principle of Synthetic Aperture Radar.*
3. Chan, Y. K. and V. C. Koo, "An introduction to Synthetic Aperture Radar (SAR)," *Progress In Electromagnetic Research B*, Vol. 2, 27–60, 2008.
4. Kingsley, S. and S. Quegan, *Understanding Radar System*, SciTech, 1999.
5. Kit, C. Y., A. M. Khuzi, G. Ventharatnam, C. B. Kuan, and C. H. Teik, "The design and development for airborne SAR," *IEEE International Geoscience and Remote Sensing Symposium Proceedings, IGARSS*, 2000.

# FPGA-based Pre-processing Unit for Real-time Synthetic Aperture Radar (SAR) Imaging

**Y. C. Lee**, **V. C. Koo**, and **Y. K. Chan**

Multimedia University, Melaka, Malaysia

**Abstract**— Synthetic Aperture Radar (SAR) is a powerful microwave remote sensing technique which is capable in producing high resolution images from the measurements of the earth surface independent of weather conditions. Range-Doppler algorithm (RDA) is commonly used for the processing of SAR data by massively utilizing Fast Fourier Transform (FFT) and Inverse Fast Fourier Transform (IFFT) operations. The implementation of radix-2 FFT in Field Programmable Gate Array (FPGA) is presented in this paper. This paper highlights the design and development of a FPGA-based pre-processing unit for real-time SAR imaging. Particularly, an efficient FFT processing module has been developed. The proposed architecture significantly reduced the hardware resources while achieving the reasonably high processing speed and throughput rate.

## 1. INTRODUCTION

Radar was originally developed for the purposes of military during World War II. The initial purpose of radar was to track ships and aircrafts through darkness and heavy weather. It has experienced a steady growth, with advances in radio frequency (RF) technology, antennas, and more recently, digital technology [1]. According to Carl Wiley [2], Synthetic Aperture Radar (SAR) was first proposed in 1951 which described the use of Doppler frequency analysis in order to improve the radar image resolution. With the radar system mounted on a flying platform (e.g., UAV), the forward motion of the actual antenna is used to synthesize a long antenna. This allows the use of longer wavelengths and still capable to achieve good resolution with reasonable antenna structures and size.

Range-Doppler algorithm (RDA) is one of the image formation techniques which commonly used in processing the collected SAR data into an image. Figure 1 shows the functional block diagram of the RDA. The main purpose of SAR imaging system is to achieve elevation and azimuth pulse compression. These compressions are done by the range-Doppler algorithm which is designed to achieve block processing efficiency, using frequency domain operations in both range and azimuth, while maintaining the simplicity of one-dimensional operations [3]. The algorithm starts with the range compression in which a range FFT is performed followed by a range matched filtering multiplication. Figure 2 shows the range compression in frequency domain by making use of FFT and IFFT.

After the multiplication of matched filtering, a range IFFT is performed in order to complete the range compression. Once the range compression is done, an azimuth FFT is carried out in order
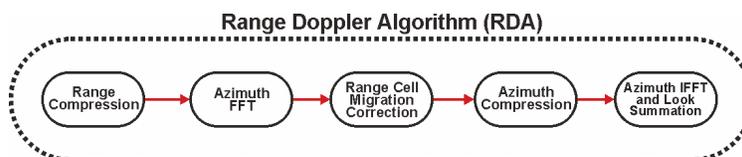


Figure 1: Functional block diagram of the RDA.
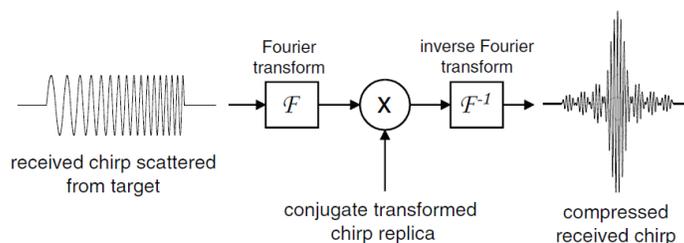


Figure 2: Range compression in frequency domain.

to transforms the data into the range Doppler domain; range time and azimuth frequency domain. Doppler centroid estimation and most of the subsequent operations such as Range Cell Migration Correction (RCMC) are performed. Once all operations are done, an azimuth compression will be performed. This operation is a similar process as in range compression except it is performed in azimuth direction. Azimuth matched filtering can be conveniently performed as a frequency domain matched filter multiply at each range gate. The last operation in RDA is an azimuth IFFT in which the data is transformed back to the time domain. The final range and azimuth compressed SAR data is illustrated as a compressed complex SAR image for further processing and applications.

The RDA massively utilized FFT and IFFT algorithms in order to perform convolution with respective reference signal to achieve elevation and azimuth pulse compression. Therefore, the majority computation operations in SAR imaging formation are occupied by FFT and IFFT. It is worth to highlight that the processing performance of FFT/IFFT blocks is depending on the complex multiplication. The operation is expensive and also occupied large hardware resources such as area of chip and memories during hardware implementations. In order to reduce the hardware resources while achieving the reasonably high processing speed and throughput rate, modified complex multiplication architecture of FFT/IFFT is purposed. The conventional and the proposed complex multiplications in FFT will be compared and evaluated.

## 2. FAST FOURIER TRANSFORM ALGORITHM

Fast Fourier Transform is an effective algorithm for the Discrete Fourier Transform (DFT). The DFT is used in several applications such as frequency analysis and frequency domain signal processing in SAR. The decomposition of a sample signal in terms of sinusoidal component (complex exponential) is achieved in DFT. This is shown in (1). The symmetry and periodicity properties of the DFT significantly reduced its computational requirements. The fast implementation of DFT is known as FFT. For an N point FFT, it is also possible to implement a radix-$r$ FFT in which $N = r^M$ and $M$ is the total number of stages for the FFT. For the radix-2 algorithm, the DFT computation is partitioned into even and odd indexed outputs. This decomposition is recursively applied in order to achieve the shorter-length of DFTs and results in the full radix-2 decimation-in-frequency (DIF) FFT. The significant of speed improvement can be observed due to the radix-2 FFT requires only $N \log_2 N$ operations as compared to the DFT which requires $N^2$ operations [4]. The simple manipulation has reduced the total computational cost of the DFT by almost a factor of two. A simple radix-2 8-point FFT is shown in Figure 3. Typically a 2-point DFT will be represented with a butterfly processor.

$$X(k) = \sum_{n=0}^{N-1} x(n) W_N^{kn} \quad \text{where} \quad W_N^{kn} = e^{-j\frac{2\pi nk}{N}} \quad 0 \leq k \leq N-1 \tag{1}$$

The butterfly processor consists of the butterfly network itself, a complex adder, complex subtraction and a complex multiplier for the twiddle factors. The conventional twiddle factor multiplier is implemented with 4 real multiplications and 2 add/subtract operations as shown in (2) and Fig-
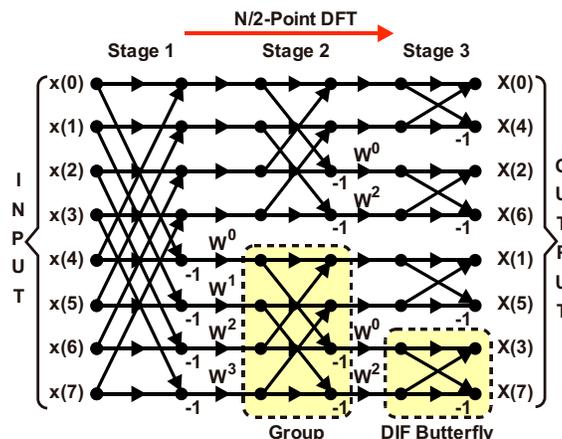


Figure 3: Decimation in frequency radix-2 8-point FFT.

ure 4.

$$R + jI = (X + jY)(C + jS)$$
$$R + jI = (C \times X - S \times Y) + j(S \times X + C \times Y) \tag{2}$$

In order to reduce the hardware resources during the implementations, one operand is pre-computed so that the complex multiplier with only 3 real multiplications and 3 add/subtract operations is built [5]. The complex twiddle factor coefficients can be simplified as $C$ and $S$. Therefore, the coefficients $C$, $C + S$ and $C - S$ will be pre-computed and stored into ROM in order to reduce the number of hardware resources by reducing the total numbers of multiplications. The final product of the complex multiplication can be simplified as real (3) and imaginary (4).

$$R = (C - S)Y + C(X - Y) \tag{3}$$
$$I = (C + S)X - C(X - Y) \tag{4}$$

This will significantly reduced the hardware resources of the complex multiplier from 4 real multiplications and 2 add/subtract operations to 3 real multiplications and 3 add/subtract operations while maintaining the reasonably throughput rate.

## 3. HARDWARE IMPLEMENTATION OF FFT IN FPGA

The proposed hardware architecture of FFT is illustrated in Figure 5. The module is designed based on the radix-2 decimation in frequency algorithm together with the in place computation in order to optimize the usage of memory. The operations of the FFT module consist of several stages which are interrupt acknowledgement, memory handling, butterfly computation and lastly data retrieval. The twiddle factor of FFT will be pre-computed and stored into ROMs. Several RAMs will be instantiated with all data of zero. The input SAR digitized raw data will be zero padded when loaded into the fixed size RAM if data is shorter than the length of the FFT else if the raw data length is longer than the length of FFT, it will be truncated. Since the butterfly processor is the core module in FFT module, therefore, the radix-2 butterfly processor of the FFT was first developed in Verilog Hardware Description Language in Quartus II CAD software tool from Altera. The conventional and modified butterfly processors are simulated and synthesis based on Altera DE2 board with Cyclone II EP2C35F672C6 device in order to verify the functionalities and also hardware resources usages.

The synthesis reports from Quartus II of both conventional and modified butterfly processors are tabulated as in Table 1.

The twiddle factor multiplier is implemented by instantiating three lpm_mult (Mega function multiplier) and three lpm_add_sub (Mega function adder) from Altera library. The proposed butterfly processor with 3 multipliers and 3 adders manage to reduce the number of limited embedded
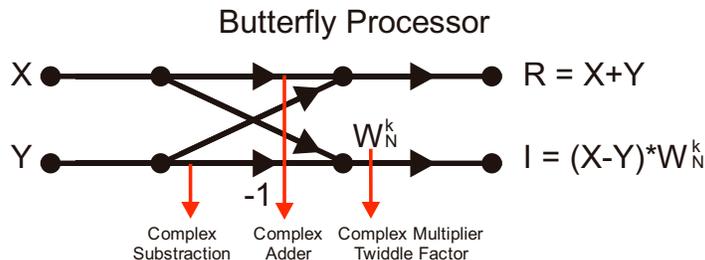


Figure 4: Radix-2 butterfly processor.

Table 1: Hardware resources for the conventional and modified butterfly processors in FPGA.

| Butterfly with 4 Multipliers and 2 Adders | Butterfly with 3 Multipliers and 3 Adders |
|---|---|
| Used 78/475 Logic Elements (LEs) | Used 87/475 Logic Elements (LEs) |
| Occupied 81 Pins | Occupied 91 Pins |
| Used 62/33216 Combinational Functions | Used 71/33216 Combinational Functions |
| Used **4/70** Embedded Multipliers | Used **3/70** Embedded Multipliers |
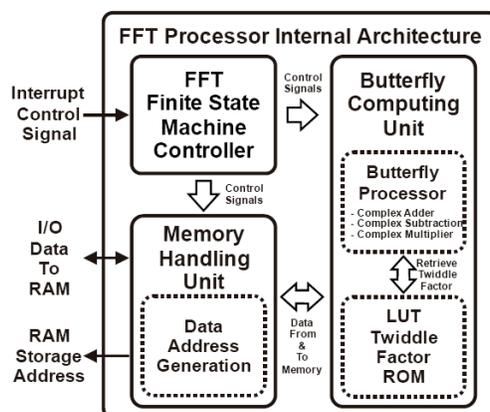
Figure 5: Radix-2 FFT module.
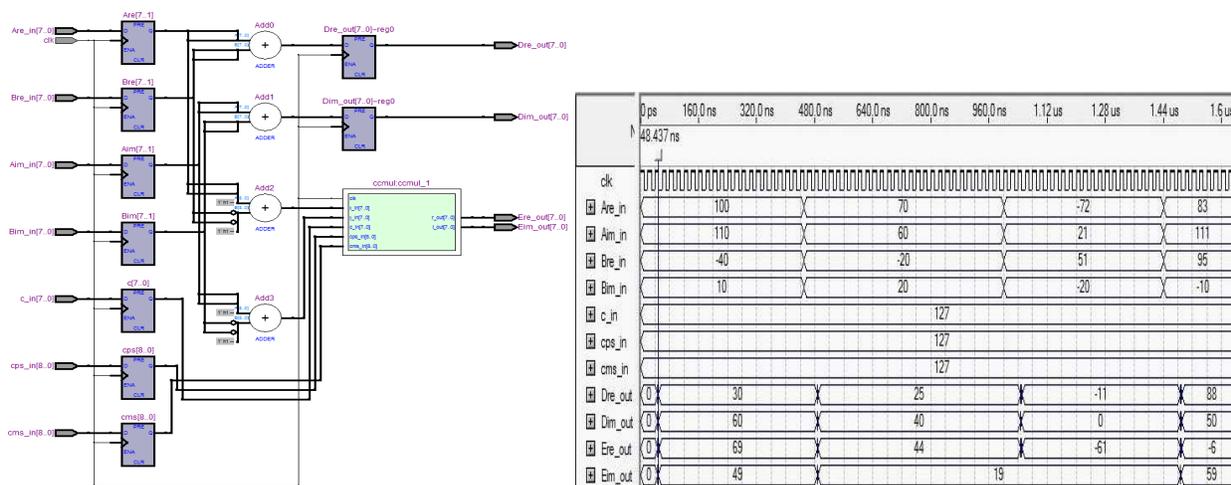


Figure 6: RTL implementation of the butterfly processor architecture and the timing simulation.

multipliers by replacing it to logic elements and also combinational functions. The clock speed of the simulation is identical with the DE2 on-board operating frequency which is 50 MHZ. From the simulated output, the propagation delay of the logic gate for the butterfly processor to complete a cycle of computation is about 50 ns which is considered reasonably short. Figure 6 shows the Register-Transfer Level (RTL) for the architecture of butterfly processor and also the timing simulation diagram.

## 4. CONCLUSION

In this paper, the modified butterfly processor for the FFT processor based on radix-2 FFT was presented and compared with conventional butterfly processor for the usages of hardware resources. The proposed architecture gives an advantage in term of hardware resources and chip area. Design works on FFT FSM Controller and Memory Handling Unit are being conducted. The designs of these two modules are challenges due to its complexity when the numbers of points for FFT are large. The future work is to test the functionality of the FFT module by providing multiple frequencies sinusoidal signal as an input signal to the FFT module and verify the outputs. The output will be examined on FPGA and compared the simulated result in MATLAB. The FFT module will be implemented in Range Doppler Algorithm in future work.

## REFERENCES

1. Cumming, I. G. and F. H. Wong, *Digital Signal Processing of Synthetic Aperture Radar Data: Algorithms and Implementation*, Artech House, 2005.

2. Wiley, C. A., "Pulse Doppler radar methods and apparatus," United States Patent, No. 3, 196, 436, Filed, August 1965.

3. Curlander, J. C. and R. N. McDounough, *Synthetic Aperture Radar, Systems and Signal Processing*, John Wiley & Sons, New York, 1991.
4. Cooley, J. W. and J. W. Tukey, "An algorithm for the machine calculation of complex fourier series," *Math Computation*, Vol. 19, 297–301, 1965.
5. Chu, E. and A. George, *Inside the FFT Black Box: Serial and Parallel Fast Fourier Transform Algorithms*, 1st Edition, CRC Press, 1999.

# Performance Evaluation of Modified MLCC Dopple Centroid Estimator

**S. B. Cheng**, **Y. K. Chan**, and **T. S. Lim**

Faculty of Engineering & Technology, Multimedia University
Jalan Ayer Keroh Lama, Bukit Beruang, Melaka 75450, Malaysia

**Abstract**— The technique to extract precise Doppler centroid parameter for the Synthetic Aperture Radar (SAR) processing is very important. It determines the final output quality and the accuracy of SAR image. The SAR raw data may contain different types of feature and scene contrasts. In order to generate a good quality image, an image quality indicator is required to measure the performance of the Doppler centroid estimator and determine the correct estimator for corresponding data. In this paper, image quality analysis using simulated point target and RADARSAT-1 raw data by various Doppler estimators. The M2LCC Doppler centroid estimator works successfully in various scene types, which is verified by the experimental results of simulated point target and RADARSAT-1 data.

## 1. INTRODUCTION

Doppler Centroid $f_{dc}$ is one of the key azimuth parameters in SAR data processing. When the platform moving along the azimuth direction, the received frequency shifted due to the Doppler effect compared to the transmitted frequency varies at each point [3]. As frequency shift is proportional to the phase information, the Doppler frequency allows researchers to discover the change of the signal phase between adjacent samples and allocates the target position. Therefore, to obtain a focus image, the correct Doppler frequency need to be applied during singal processing [4].

Since Doppler Centroid is due to the motion different between the moving platform and the target, it can easily be calculated by applying the formula of Doppler effect.

$$f_{dc} = -\frac{2v}{\lambda} \sin \theta \tag{1}$$

where $\theta$ = angle between the antenna main beam and the zero Doppler plane, $v$ = velocity of the moving platform, and $\lambda$ = wavelength of the chirp signal.

Doppler centroid estimation can be defined into two parts: baseband frequency $f_{frac}$ and Doppler ambiguity $M_{amb}$ [1].

$$f_{dc} = f_{frac} + M_{amb} * PRF \tag{2}$$

## 2. PRINCIPLE OF THE PHASE-BASED DOPPLER CENTROID ESTIMATORS

The absolute Doppler centroid is a linear function of the carrier frequency of the transmitted signal, which can be determined by the varying values of the transmitted signal frequency. The average phase increment is the average angle of the conjugated product of adjacent samples, and is referred as Average Cross Correlation (ACCC). From the ACCC, computes the slope and intercept the values can then be applied to estimate the Doppler ambiguity and fractional part of the PRF. Phase information is used to extract the absolute Doppler centroid parameter. To estimate the Doppler ambiguity, slope of the ACCC is required.

### 2.1. Multilook Cross Correlation Algorithm (MLCC)

The conventional MLCC algorithm is developed by separating the FFTed range signal into two range looks, $S_1$ and $S_2$ by a frequency difference, $\Delta f$.

$$S_1(\eta) = w_a(\eta - \eta_c) \exp\left\{\frac{-j4\pi\left(f_c - \frac{\Delta f}{2}\right)R(\eta)}{c}\right\} \tag{3}$$

$$S_2(\eta) = w_a(\eta - \eta_c) \exp\left\{\frac{-j4\pi\left(f_c + \frac{\Delta f}{2}\right)R(\eta)}{c}\right\} \tag{4}$$

where $w_a (\eta - \eta_c)$ is the azimuth envelope; $\eta$ is the azimuth time; $\eta_c$ is the time when the target is at the center of the antenna beam; $c$ is the speed of light; $f_c$ is the center frequency; $\Delta f$ is the frequency separation between two range looks; and $R(\eta)$ is the instantaneous slant range between radar and the target.

Due to the frequency separation of $\Delta f$, both looks have different phase information of ACCC. The signal difference between adjacent range cells can be determined by conjugate product $S(\eta)$ and $S(\eta + 1)$, which is in form of vector. The ACCC is denoted by summing up the resultant signal differences as

$$\overline{Look_1(\eta)} = \sum S_1(\eta) S_1^*(\eta + 1) \tag{5}$$

$$\overline{Look_2(\eta)} = \sum S_2(\eta) S_2^*(\eta + 1) \tag{6}$$

where $S_1^*$ and $S_2^*$ denote the complex conjugate of $S_1$ and $S_2$.

The ACCC angle $\emptyset_1$ and $\emptyset_2$ of $Look_1$ and $Look_2$ can be expressed as

$$\emptyset_1 = \arg\left[\overline{Look_1(\eta)}\right] = -\frac{2\pi}{PRF}K_{a1} \tag{7}$$

$$\emptyset_2 = \arg\left[\overline{Look_2(\eta)}\right] = -\frac{2\pi}{PRF}K_{a2} \tag{8}$$

The reason of dividing the FFTed range into two looks is avoid the effect of the range frequency to the Doppler Centroid estimation result.

$$K_{a1} = \frac{2v^2}{cR(\eta_c)}\left(f_0 - \frac{\Delta f_r}{2}\right) \tag{9}$$

$$K_{a2} = \frac{2v^2}{cR(\eta_c)}\left(f_0 + \frac{\Delta f_r}{2}\right) \tag{10}$$

$$K_{a2} - K_{a1} = \frac{2v^2 \Delta f_r}{cR(\eta_c)} \tag{11}$$

Obtain the difference between the two ACCC angles $\Delta\emptyset$ can be easily done by subtracting $\emptyset_1$ from $\emptyset_2$,

$$\Delta\emptyset = \emptyset_1 - \emptyset_2 \tag{12}$$

Or

$$\Delta\emptyset = \arg\left\{\overline{Look_1(\eta)}\left[\overline{Look_2(\eta)}\right]^*\right\} \tag{13}$$

The slope of the $\Delta\emptyset$ versus $\Delta f$ can be used to extract the absolute Doppler centroid frequency $f'_{dc}$

$$f'_{dc} = -\left(\frac{PRF f_0 \Delta\emptyset}{2\pi\Delta f}\right) \tag{14}$$

The baseband frequency, or fractional PRF can be determined by averaging the two ACCC angles of the looks

$$f_{rac} = -\left[\frac{PRF}{2\pi}\left(\frac{\emptyset_1 + \emptyset_2}{2}\right)\right] \tag{15}$$

The best way to estimate the Doppler ambiguity $M_{amb}$ is to subtract the fractional PRF frequency from the absolute Doppler centroid, divide the resultant value by PRF, and round the number up to the nearest integer. The equation of $M_{amb}$ can be written as

$$M_{amb} = round\left(\frac{f'_{dc} - f_{rac}}{PRF}\right) \tag{16}$$

From (14), (15) and (16), the absolute Doppler centroid $f_{dc}$ can be estimated by

$$f_{dc} = f_{rac} + (M_{amb} * PRF) \tag{17}$$

with the

$$Remainder = M_{amb}PRF - (f'_{dc} - f_{rac}) \tag{18}$$

The MLCC method is an offset dependent Doppler Ambiguity Estimator. The intercept does not pass through the (0,0) point when the graph of Doppler frequency versus range frequency is plotted. This is due to the antenna's boresight angle varies slightly with the transmission frequencies that are presented in the chirp pulse. Therefore, offset frequency $f_{os}$ is required in the MLCC algorithm and the complete formula for the MLCC absolute Doppler centroid estimation is given by

$$f_{dc} = f_{rac} + (M_{amb} * PRF) + f_{os} \tag{19}$$

MLCC method is only works best in low contrast scene [6].

## 2.2. Modified Multilook Cross Correlation Algorithm (M2LCC)

The M2LCC algorithm equally separates the azimuth range-compressed received data into four looks to estimate the absolute Doppler centroid parameter [5].

$$S_x(\eta) = w_a(\eta - \eta_c) \exp\left[\frac{-j4\pi\left(f_0 - \frac{x\Delta f}{4}\right)R(\eta)}{c}\right] \tag{20}$$

where $x = 1, 2$.

$$S_{2y}(\eta) = w_a(\eta - \eta_c) \exp\left[\frac{-j4\pi\left(f_0 + \frac{y\Delta f}{4}\right)R(\eta)}{c}\right] \tag{21}$$

where $y = 1, 2$.

Each look, indicates its respective angle: $\emptyset_1, \emptyset_2, \emptyset_3, \emptyset_4$

$$\emptyset_i = \arg\left[\overline{Look_i(\eta)}\right] \tag{22}$$

where $i = 1, 2, 3, 4$.

The fractional PRF estimation is simply applying the angles values into the formula below.

$$f_{rac} = -\left[\frac{PRF}{2\pi}\left(\frac{\emptyset_1 + \emptyset_2 + \emptyset_3 + \emptyset_4}{4}\right)\right] \tag{23}$$

Similar to the conventional MLCC algorithm, the frequency difference, $\Delta f'$ and the total phase difference of four looks, $\Delta'\emptyset$ are restructured as (28) and (31).

$$\Delta f_{ij} = f_i - f_j \tag{24}$$

$$\Delta f' = \sum \Delta f_{ij} \tag{25}$$

$$\Delta\emptyset_{ij} = \emptyset_i - \emptyset_j \tag{26}$$

or

$$\Delta\emptyset_{ij} = \arg\left\{\overline{Look_i(\eta)}\left[\overline{Look_j(\eta)}\right]^*\right\} \tag{27}$$

$$\Delta'\emptyset = \sum \Delta\emptyset_{ij} \tag{28}$$

where $i = 1, 2, 3$ and $j = 2, 3, 4$.

Finally, the absolute Doppler centroid parameter of the M2LCC can be calculated as

$$f'_{dc} = -\frac{PRF f_0 \Delta\emptyset'}{2\pi\Delta f'} \tag{29}$$

## 3. RESULTS

### 3.1. Simulated Point Target

Doppler centroid frequencies that estimated by MLCC, MLBF, M2LCC and ideal case (theoretical calculation) have been analyzed. The experimental results of the SAR image quality measurement for 3dBR, SNR and IE have been summarized in Table 1. In this ideal case, the Doppler Centroid is calculated by using (1), which is equal to $-68,200\,\text{Hz}$.

Table 1 shows that the least difference between the estimated Doppler Centroid value to the reference value ($-68,200\,\text{Hz}$) was only $184\,\text{Hz}$, which is based on M2LCC estimator, and the largest's was $378\,\text{Hz}$ by MLBF estimator. It can be proven that M2LCC managed to provide the nearest result to the reference compared to other estimators.

### 3.2. RADARSAT-1 SAR Data

Total of 3 different contrast blocks (high, medium and low contrast's scene) from the RADARSAT-1 Vancouver scene, each block has been evaluated.

As per explained in the previous section, MLBF is suitable to be used in medium to high contrast scene data. In Figure 1 and Figure 2, regardless of the parameters estimated by M2LCC, images generated from the estimated MLBF Doppler centroids' achieved better result in the quality analysis experiments. For Figure 3 which is scene of ocean of different part in the Vancouver map, has low level of signal reflectivity and contrast. The Doppler centroid parameters of these scenes can be accurately estimated by the MLCC method compared with other estimators.

Table 1: Comparison of the image qualities of simulated point target.

| Doppler Centroid (Hz) | | 3dBR (dB) | SNR (dB ) | IE (dB) |
|---|---|---|---|---|
| (MLCC) | $-68,008$ | 5.361 | 16.319 | 3.639 |
| (Ideal Case) | $-68,200$ | 5.330 | 16.410 | 3.607 |
| (M2LCC) | $-68,384$ | 5.351 | 16.321 | 3.615 |
| (MLBF) | $-68,578$ | 5.385 | 16.189 | 3.623 |

| | Reference | MLCC | MLBF | M2LCC |
|---|---|---|---|---|
| Estimated $f_{dc}$ | 6900.00 | 19274.00 | 6704.08 | 6688.10 |
| Generated Image |  |  |  |  |
| SNR | 0.28 | 0.11 | 0.27 | 0.26 |
| IE | 233.05 | 365.89 | 350.11 | 352.71 |
| 3dBR | 2.00 | 3.00 | 2.00 | 2.00 |
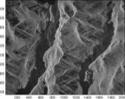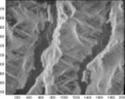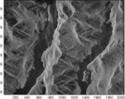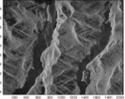
Figure 1: Quality measures for each estimator of block 1.

| | Reference | MLCC | MLBF | M2LCC |
|---|---|---|---|---|
| Estimated $f_{dc}$ | 6900.00 | 9364.60 | 6828.20 | 6876.10 |
| Generated Image |  |  |  |  |
| SNR | 0.99 | 0.44 | 1.00 | 1.00 |
| IE | 85.08 | 202.13 | 84.15 | 84.72 |
| 3dBR | 4.00 | 6.00 | 3.00 | 4.00 |
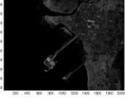
Figure 2: Quality measures for each estimator of block 3.

| | Reference | MLCC | MLBF | M²MLCC |
|---|---|---|---|---|
| Estimated $f_{dc}$ | 6900.00 | 8819.50 | 5606.50 | 23059.00 |
| Generated Image |  |  |  |  |
| SNR | 0.13 | 0.17 | 0.12 | 0.21 |
| IE | 176.42 | 69.79 | 126.74 | 121.40 |
| 3dBR | 3.00 | 2.00 | 3.00 | 2.00 |

Figure 3: Quality measures for each estimator of block 5.

## 4. CONCLUSION

The performance of the three Doppler centroid estimators have been analyzed and compared based on the generated image quality evaluation using image quality indicators. From the experimental results of the simulated point target data and the RADARSAT-1 SAR data, we can conclude that M2LCC enable to work well in both high and low contrast scene. The results shown that M2LCC generated SAR images have high SNR, and low for both 3dBR and IE indicator. Besides, a proposed implementation skim of Doppler centroid estimation to select the most precise Doppler centroid parameter among estimators has been introduced, which is recommended to be used in parallel signal processing.

**REFERENCES**

1. Cumming, I. G. and F. H. Wong, *Digital Processing of Synthetic Aperture Radar*, 1st Edition, Artech House, Norwood, MA, 2005.
2. Chan, Y. K. and V. C. Koo, "An introduction to synthetic aperture radar (SAR)," *Progress In Electromagnetics Research B*, Vol. 2, 27–60, 2008.
3. Madsen, S. N., "Estimating the doppler centroid of SAR data," *IEEE Trans. Aerospace and Electronic Systems*, Vol. 25, 134–140, Mar. 1989.
4. Li, Y., H. Fu, and P. Y. Kam, "An improved doppler parameter estimator for synthetic aperture radar," *PIERS online*, Vol. 4, No. 2, 201–206, 2008.
5. Sew, B. C., Y. K. Chan, C. S. Lim, T. S. Lim, and V. C. Koo, "Modified multilook cross correlation (MLCC) algorithm for doppler centroid estimation in synthetic aperture radar signal processing," *Progress In Electromagnetics Research C*, Vol. 20, 215–225, 2011.
6. Cumming, I. G. and S. Li, "Adding sensitivity to the MLBF doppler centroid estimator," *IEEE Trans. Geosci. Remote Sensing*, Vol. 45, No. 2, 279–292, Feb. 2007.
7. Harris, J. E., R. S. Ostler, D. M. Chabries, and R. W. Christiansen, "Quality measures for SAR images," *International Conference on Acoustics, Speech, and Signal Processing*, Vol. 2, 1064–1067, 1988.
8. Lim, T. S., C. S. Lim, V. C. Koo, H. T. Ewe, and H. T. Chuah, "Autofocus algorithms performance evaluations using an integrated SAR product simulator and processor," *Progress In Electromagnetics Research B*, Vol. 3, 315–329, 2008.

# Geometric Correction on SAR Imagery

**A. L. Choo**, **Y. K. Chan**, **and V. C. Koo**
Multimedia University, Melaka, Malaysia

**Abstract**— SAR images are generated through signal processing using the data collected by the SAR system from the target scenes on earth surface. However the SAR images generated may contain errors or distortions which cause the data in the present image to be inaccurate. These errors or distortions present in the SAR image also known as geometric distortion. Geometric distortions exist in all remote sensing images and broadly related to the target, sensor and platform. The objective of this research project is to reduce the error of SAR images through implementation of geometric correction on SAR. Geometric correction can be done by reposition of pixels form the uncorrected image location to the reference grid through geometric operations. There are few types of geometric correction methods such as registration, rectification, geocoding and orthorectification. The three main process of geometric correction are mathematical distortion model, coordinate registration and resampling. These three components also known as warping process. Mathematical distortion model such as polynomial distortion model has been generated using MATLAB for the geometric correction purpose. After coordinate registration the SAR image will be resampled. There are few types of resampling method such as nearest neighbour, bilinear interpolation and cubic convolution.

## 1. INTRODUCTION

Synthetic Aperture Radar SAR is an advanced form of side looking airborne radar which utilizes the flight path of the platform to simulate an extremely large antenna or aperture electronically. Its capability to control the source of illumination enables it to see through cloud, rain and generates high resolution images during day and night [1].

The SAR systems from the spaceborne of airborne platform points the a radar beam approximately perpendicular to the sensor's motion vector, transmitting phased-encoded pulse, and recording the radar echoes as they reflect off the Earth surface [2]. The concept of SAR system has been shown in Figure 1. Then the SAR image is generated through the image processing of the recorded radar echoes

The raw images generated through image processing usually contain errors or distortions which may cause the information of the image to be inaccurate. The correction of the errors and removal of distortion present in the data is termed pre-processing because; quite logically such operations are carried out before the data are used for particular purpose [3]. The pre-processing consists of radiometric correction and geometric correction.

## 2. GEOMETRIC DISTORTION

Each remote sensing image consist unique geometric distortion and vary considerably with different factors such as target, sensor and platform. Table 1 describes in more detail the sources of distortion for each category.

Geometric distortion may cause changes of scale over the image, irregularities in the angular relationships among the image elements, displacement of objects in an image and occlusion of one image element by another.

Table 1: Description of geometric distortion sources.

| Category | Description of Distortion Source |
| --- | --- |
| Platform (spaceborne or airborne) | Variation of movement: position changes |
| | Variation in platform attitude (low to high frequencies) |
| Sensor | Variation in sensor mechanics (scan rate, scanning velocity, etc.) |
| | Viewing Geometry: Panoramic effect with field of view |
| Earth | Earth Rotation, Curvature, topographic effect. |
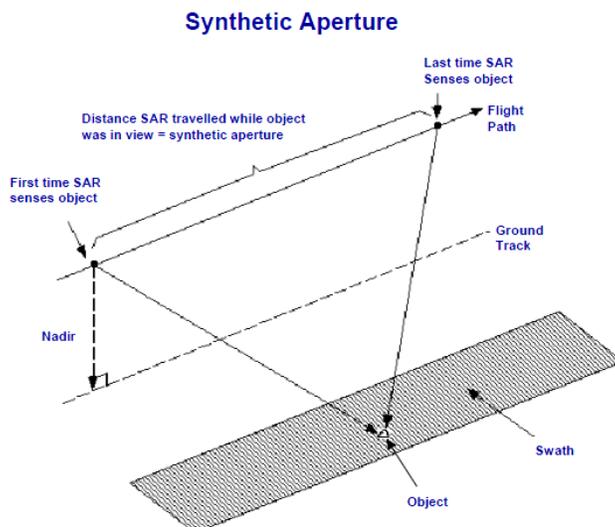
Figure 1: Concept of synthetic aperture radar.

Table 2: Various type of geometric correction.

| Type | Description |
|---|---|
| Registration | The alignment of one image to another image of the same area |
| Rectification | The alignment of an image to a map so that the image is planimetric |
| Geocoding | A special case of rectification that includes scaling to uniform, standard pixel GSI. |
| Othorectification | Require DEM(Digital elevation model), Correction of image pixel for topographic distortion |

## 3. GEOMETRIC CORRECTION

Geometric correction is the process of correction of the distortion arises from scanner characteristic and their interaction with the airborne platform and earth's figure by reposition of pixels form the uncorrected image location to the reference grid through geometric operations [4]. There are three components to the process:

- Selection of suitable mathematical distortion model(s).
- Coordinate transformation.
- Resampling( interpolation).

These three components are collectively known as warping [4]. Table 2 shows the few terms that have been used for geometric correction.

### 3.1. Mathematical Distortion Model

The mathematical distortion model such as the polynomial model relates the global coordinates in the distorted image to those in the reference image or maps,

$$x = \sum_{i=0}^{N} \sum_{j=0}^{N-i} a_{ij} x_{ref}^i y_{ref}^j, \quad y = \sum_{i=0}^{N} \sum_{j=0}^{N-i} b_{ij} x_{ref}^i y_{ref}^j \tag{1}$$

The numbers of coefficient which represent the geometric operation depend on the order of the polynomial. Usually the quadratic polynomial will sufficient for the SAR Images.

### 3.2. Ground Control Points (GCPs)

The coefficients in the polynomial model Eq. (1) can be determined by specification of GCPs to constrain the polynomial coefficients [4]. The selected GCPs must have the following characteristic:

- High contrast in all images of interest.
- Small feature size.

- Unchanging over time.
- All at same elevation (unless topographic relief is being specifically addressed.

### 3.3. Resampling

An interpolation process require to estimate a new pixel between existing pixels due to the non-integer transformed $(x, y)$ value. Table 3 describes in more detail of the types of resampling method.

Table 3: Type of resampling method.

| Type | Description |
|---|---|
| Nearest Neighbour | New pixels value get form closest pixel of old pixel |
| Bilinear Interpolation | New pixels value calculated from the weighted average of 4 ($2 \times 2$) nearest pixels |
| Cubic Convolution | New pixels are computed from weighting 16 ($4 \times 4$) surrounding DNs |

## 4. SIMULATION
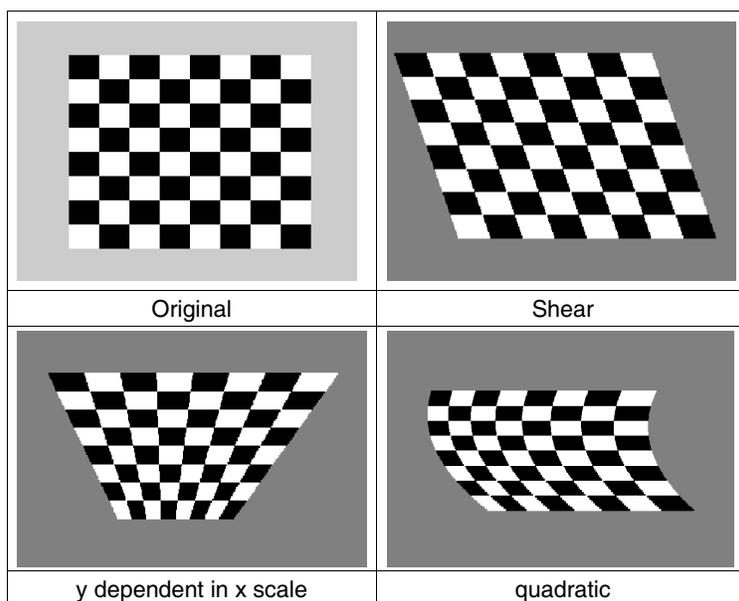


Figure 2: Polynomial geometric warps. Nearest Neighbour is used.

## 5. CONCLUSIONS

Geometric correction is an image pre-processing operation that must be implemented on the raw SAR Image to ensure the image's accuracy before any further enhancement or information extraction. In the process of geometric correction the selection of GCPs is very important as it will generated the mathematical distortion model that will relate the distorted image and the reference image. The resampling of the image will produces a better quality image.

**REFERENCES**

1. "Educational resources for radar remote sensing," Internet: http://www.ccrs.nrcan.gc.ca/ccrs /rd/programs/globsar/gsarmain_e.html, June 30, 2011.
2. Cumming, I. G. and F. H. Wong, "Introduction," *Digital Processing of Synthetic Aperture Radar Data*, Artech House, 2005.

3. Mather, P. M., "Pre-processing of remotely-sensed data," *Computer Processing of Remotely-sensed Images: An Introduction*, 3rd Edition, Wiley, 2003.

4. Schowengerdt, R. A., "Correction and calibration," *Remote Sensing: Models and Methods for Image Processing*, 3rd Edition, Elsevier, 2007.

# Design and Analysis of a High Performance Triband 20/30/44 GHz Corrugated Horn

**K. K. Chan**

Chan Technologies Inc., 15 Links Lane, Brampton, Ontario L6Y 5H1, Canada

**Abstract**— The design and analysis of a corrugated horn that operates over more than an octave bandwidth and covering three different frequency bands at 20 GHz, 30 GHz and 44 GHz is presented. This horn is used together with a dual polarized 6-port feed network to illuminate a reflector located on a spacecraft platform. Its return loss is better than 30 dB, 33 dB and 27 dB at K, Ka, and EHF bands respectively and the corresponding worst-case cross-pole levels relative to the co-pole peak are $-33$ dB, $-40$ dB and $-26$ dB. The slot and tooth widths are designed for manufacturability and the number of corrugations is minimized so that the horn can be fabricated at a low cost while still meeting the stringent electrical specifications. A limit on the level of the next higher order symmetric $TE_{31}$ mode that can be present at the horn input from the feed network without deteriorating the cross-pole performance is examined.

## 1. INTRODUCTION

For future communication satellites, multiple frequency bands may be combined together and radiated through a common aperture. This will reduce the number of antennas on board the satellite. The antenna of choice is typically an offset reflector fed by a single high performance horn. The work reported here is on the development of a single tri-band corrugated horn as feed for a reflector antenna. The requirements for the tri-band horn are listed in Table 1 for the three frequency bands, namely, Band 1: 20.2–21.2 GHz, Band 2: 30.0–31.0 GHz and Band 3: 43.5–45.5 GHz. The emphasis here is placed on the 20/30 GHz bands with a slight reduction in requirement for the 44 GHz band. The high amplitude taper at 20° off-axis is chosen to minimize spillover loss and the back lobe levels. The challenging requirements are the return loss and the peak cross-pole level, both of which are critical for a frequency reuse feed.

A literature survey of the state-of-the-art in multi-band horn design was carried out. The horn type that is frequently used to provide dual or tri-band capability is the corrugated horn with dual depth slots [1] or slots with special shapes such as ring loaded slots or stepped slots. Horns with dual depth slots typically show $-25$ to $-30$ dB peak cross-pole responses in two bands and $-20$ to $-25$ dB in the third band. This is expected since the slots can be made to exhibit approximately balanced hybrid condition in two bands. While at the third band, if present, the corrugated surface impedance should hopefully still remain capacitive. Otherwise, the dual depth slots will not give good tri-band performance. Ring loaded horns can cover a wide bandwidth with frequency ratio of not more than 1.7 : 1 for peak cross-pole level below $-30$ dB and return loss level greater than 30 dB. They do not perform well when the bands are widely separated. Granet and James [2] stated that a corrugated horn could not be easily designed to meet low cross-polarization requirement in the three bands of interest, i.e., 20/30/44 GHz regardless of the type of corrugations used. They then introduced two optimized smooth-walled horns with computed peak cross-pole levels in the

Table 1: Specifications and design values of the triband horn.

| Parameter | Specification | Design Values |
|---|---|---|
| Return Loss | Band 1: $> 30$ dB | 30.0 dB @ 20.2 GHz, 32.5 dB @ 20.7 GHz, 30.0 dB @ 21.2 GHz |
| | Band 2: $> 30$ dB | 33.6 dB @ 30.0 GHz, 44.0 dB @ 30.5 GHz, 43.1 dB @ 31.0 GHz |
| | Band 3: $> 27$ dB | 37.8 dB @ 43.5 GHz, 48.9 dB @ 44.5 GHz, 27.1 dB @ 45.5 GHz |
| Peak cross-pole Level | Band 1: $< -33$ dB | $-46.1$ dB @ 20.2 GHz, $-38.9$ dB @ 20.7 GHz, $-33.7$ dB @ 21.2 GHz |
| | Band 2: $< -30$ dB | $-42.0$ dB @ 30.0 GHz, $-40.8$ dB @ 30.5 GHz, $-41.7$ dB @ 31.0 GHz |
| | Band 3: $< -26$ dB | $-26.1$ dB @ 43.5 GHz, $-28.4$ dB @ 44.5 GHz, $-26.2$ dB @ 45.5 GHz |
| Illumination Taper @ 20° | Band 1: $< -17$ dB | $-17.5$ dB @ 20.2 GHz, $-17.6$ dB @ 20.7 GHz, $-17.7$ dB @ 21.2 GHz |
| | Band 2: $< -20$ dB | $-23.6$ dB @ 30.0 GHz, $-23.6$ dB @ 30.5 GHz, $-23.6$ dB @ 31.0 GHz |
| | Band 3: $< -22$ dB | $-26.1$ dB @ 43.5 GHz, $-28.6$ dB @ 44.5 GHz, $-33.8$ dB @ 45.5 GHz |

three bands as $-28.7/-25/-26$ dB and $-21/-27/-27.5$ dB respectively, but there is no mention of the return loss performance of the horn. The dual-depth corrugated horn design presented here, an extension to the previous work by the authors [3], not only shows much better cross-pole performance but is also about 38% shorter in axial length than that of the smooth-walled horn reported in [2]. A compact horn is an important attribute on a satellite platform.

## 2. DESIGN PROCEDURE

For ease of manufacturing, the straight slot corrugated horn is the preferred approach. One can use tri-depth corrugations, making each slot depth $\sim \lambda/4$ to conform to the balanced hybrid condition at each band, so as to obtain good performance in all frequency bands. This would make the thickness of the corrugation very thin. Simulations have shown that to maintain good cross-pole response, there must be at least 2.5 dual depth corrugations per wavelength at the highest frequency band of operation or the dual-depth pitch must be less than 0.4 wavelength. A larger pitch would lead to rapid deterioration of the cross-pole performance. Fitting three corrugations of different depths into a given pitch would lead to very small slot widths at the input matching section of the horn in order to meet the return loss requirement. Thus from a manufacturing viewpoint, the tri-depth slots approach is not be very desirable at these high frequencies.

In the dual slot depth implementation, the slot widths and tooth thicknesses would be larger to make the fabrication of the horn feasible. There are a number of possible slot depth combinations in the dual slot depth approach but to meet the present requirements, the following configuration is preferred: 1st slot depth at $\sim \lambda/4$ for band 1 and $\sim 3\lambda/8$ for band 2 with 2nd slot depth at $\sim \lambda/4$ for band 2 and $\sim 3\lambda/8$ for band 3. In this combination, cross-pole performance will be excellent at band 1 and 2 and good in band 3. It also has relatively shallower slot depths, which is an important consideration to reduce the horn wall thickness and overall weight.

The diameter of the horn aperture and the horn flare angle are then determined so that the feed pattern has the required fall-off at 20 degrees off-axis and the specified on-axis gain with minimum horn length. Through extensive simulations, a horn with 8.02 cm aperture diameter and a semi-flare angle of 14 degrees is found to meet the desired goals. A profile of the dual-depth corrugated horn is shown in Fig. 1. Besides the linear flare profile, a polynomial profile of the horn was also tried. No improvement in performance was found. Larger deviation from the linear profile led to cross-pole degradation, raised sidelobes or merged shoulders and beam broadening that are undesirable for the present application.

Next the pitch of the dual depth slots in the horn section is set. To obtain low cross-pole level, the largest pitch suitable for the horn is found to be 2.8 mm. A large pitch minimizes the number of corrugations needed to fill the horn. This pitch value was determined by a series of iterations to find the largest value possible without exceeding the cross-pole level. The corrugation configuration is shown in Fig. 1(b).

Finally, the horn input matching section is designed. To provide a very good match into the horn and to facilitate the setting up of the proper modal content for low cross-pole levels, a corrugated matching section is required. This matching section is also allowed to flare out at 14 degrees, same as that of the horn. Altogether five pairs of dual depth corrugations are needed and the pitch has to be reduced slightly to 2.5 mm from 2.8 mm for the horn section. The consequence of using less number of corrugations and larger pitches were investigated. They all lead to inferior results. The



|        (a)        |        (b)        |
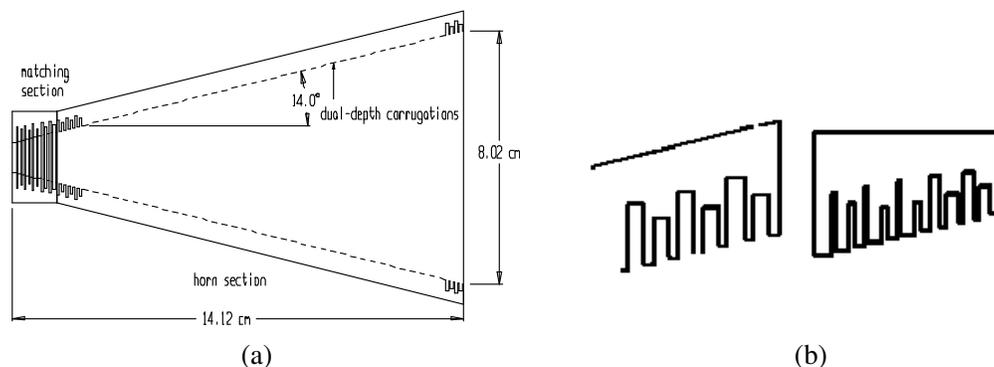
Figure 1: (a) Triband corrugated horn. (b) Corrugation details of horn and matching sections.
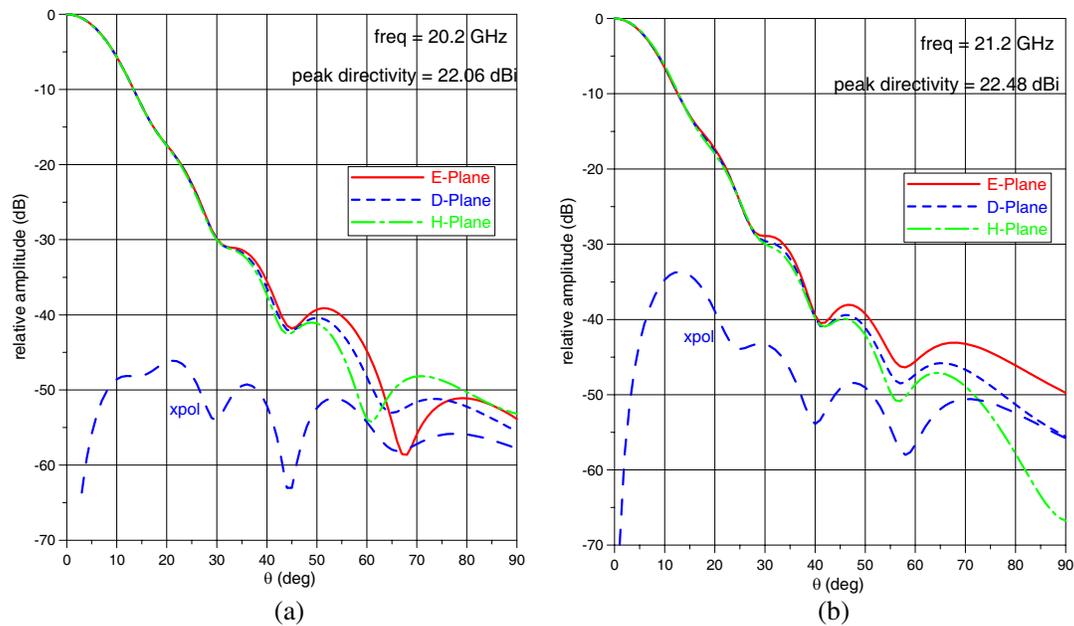
Figure 2: (a) Co- & cross-pole patterns at 20.2 GHz. (b) Co- & cross-pole patterns at 21.2 GHz.
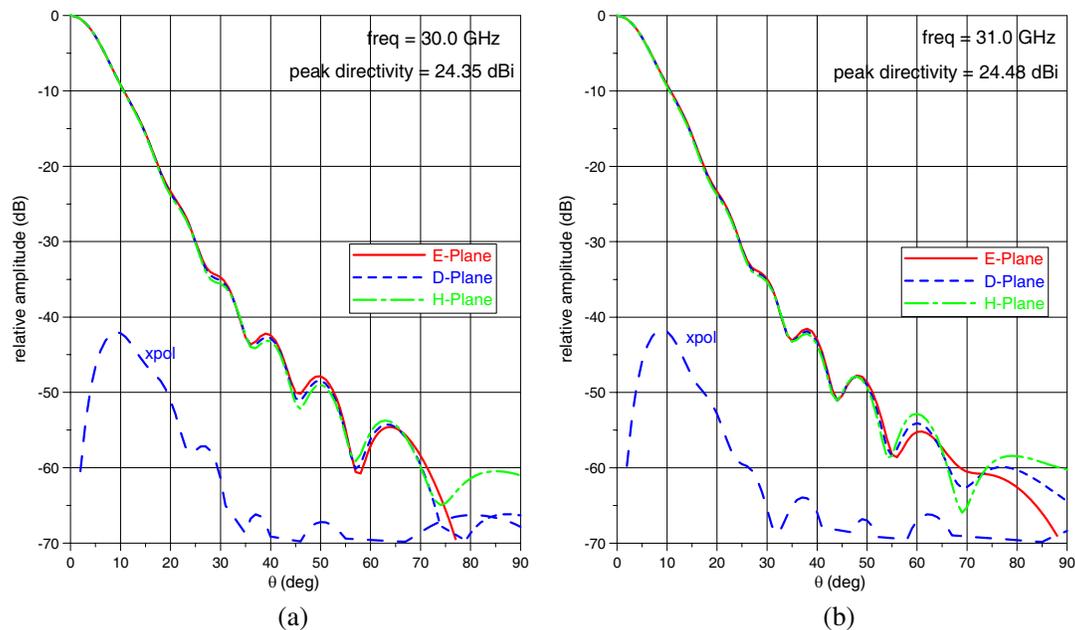


Figure 3: (a) Co- & cross-pole patterns at 30 GHz. (b) Co- & cross-pole patterns at 31 GHz.

input matching section was designed using a gradient-based optimization program. The twenty slot widths and depths available as design variables are optimized to give the required cross-pole level and return loss in all three bands. To help the optimization process converge faster, the first few slots closest to the circular waveguide input are made $\sim \lambda/2$ deep at the respective frequency band and the slot widths are kept small at $\sim 0.31$ mm. The slot width increases and the slot depth decreases towards the horn section. With this starting condition, the slot dimensions tend to converge quickly to the values that meet most of the performance specifications. After a number of runs, all of the specifications are met. The pitch is fixed throughout the optimization process. Corrugation details of the matching section are shown in Fig. 1(b).
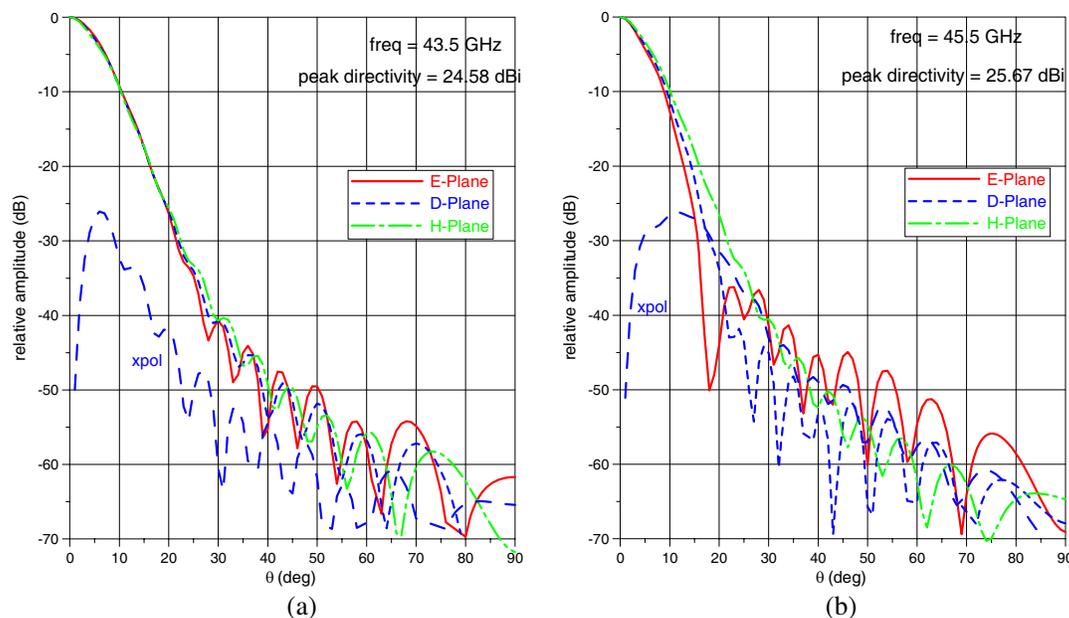
Figure 4: (a) Co- & cross-pole patterns at 43.5 GHz. (b) Co- & cross-pole patterns at 45.5 GHz.
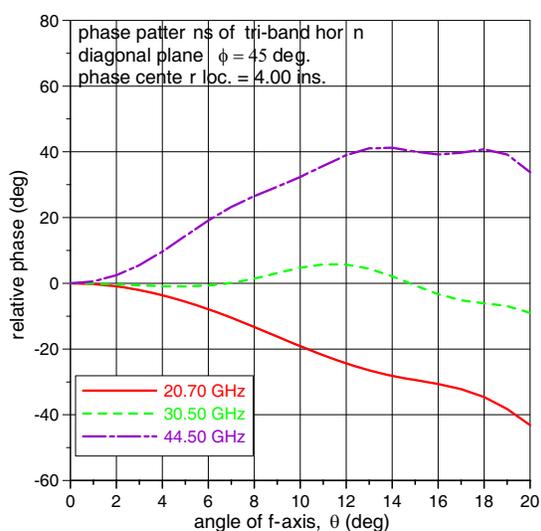


Figure 5: Phase patterns at frequency band centers.
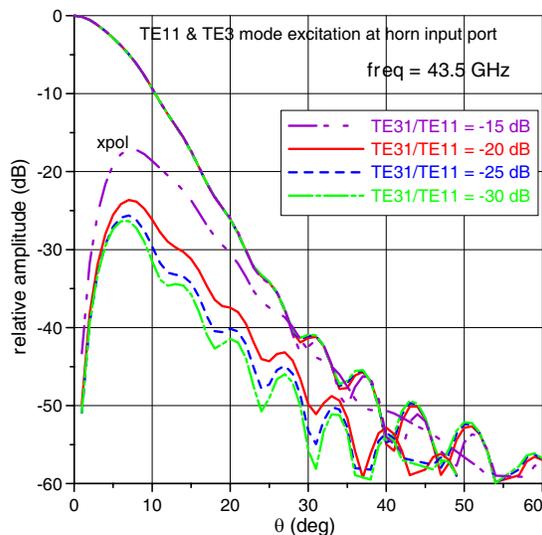
Figure 6: Influence of TE$_{31}$ mode on the radiation patterns.

## 3. PERFORMANCE PREDICTIONS

The horn assembly has three parts — input circular guide, matching section and horn section, as shown in Fig. 1(a). It has a total of 205 circular waveguide sections. Mode matching software is used to predict the horn performance. To ensure convergence at the highest frequency of operation, 26 modes are used at the input to represent the fields, which results in 215 modes at the output aperture. The co-pole and cross-pole patterns in the $E$-, $D$- and $H$-planes at the band edges are plotted in Figs. 2 to 4 to demonstrate the worst-case performances. As can be seen, the main beam is Gaussian shape with no sidelobes or merged sidelobes within the 20° reflector illumination cone. Further, the beamwidths in the $E$-, $D$- and $H$- planes are almost the same. Outside this cone, the sidelobes are below −36 dB. The cross-pole levels are also pleasingly low.

The best phase center location for the three bands is found to be approximately 4.0 inches from the aperture. A plot of the co-pole phase patterns in the diagonal plane is shown in Fig. 5 at the center band frequencies. The maximum phase error within the 3-dB beamwidth is ∼ 12° and within the 10-dB beamwidth, the error is ∼ 30°.

The horn is typically connected to a multi-band feed network. The common waveguide manifold in this network is typically overmoded with symmetric modes at the highest band but not at the two lower bands. It is also overmoded with asymmetric modes in band 2 and 3. However, by maintaining symmetry in the feed network design, excitation of the asymmetric modes is avoided. The symmetric higher order $TE_{31}$ mode at the input circular guide is typically excited at the multiplexer and usually cannot be avoided but can be controlled. Shown in Fig. 6 are the diagonal plane plots with various amplitude ratios of $TE_{31}/TE_{11}$ mode at 43.5 GHz. Field matching analysis of the horn sections must now include the $TE_{3n}$ and $TM_{3n}$ modes at the junction discontinuities. In order not to degrade the cross-pole performance at band 3, the amount of $TE_{31}$ mode generated by the feed network before launching into the horn should be less than $-25$ dB relative to the $TE_{11}$ mode.

## 4. CONCLUSIONS

The design of a corrugated horn that operates in three bands at 20/30/44 GHz has been presented. The co-pole beams are Gaussian in nature with very low cross-pole levels. Special attention is placed on the tooth and slot widths so that the horn can be manufactured without difficulty. The number of corrugations has also been minimized without sacrificing the performance of the horn. Care must be taken in the feed network design to ensure that the level of the $TE_{31}$ mode excited at the horn input does not compromise the cross-pole performance. The horn has significantly better RF performance and is more compact than comparable smooth-walled horns.

**REFERENCES**

1. Chan, K. K., S. R. Gauthier, and G. Dinham, "Multifrequency band earth station feed design," *IEEE AP-S International Symposium*, Vol. 2, 960–963, Dallas, Texas, May 1990.
2. Granet, C. and G. L. James, "Optimized spline-profile smooth-walled tri-band 20/30/44 GHz horns," *IEEE Antennas and Wireless Propagation Letters*, Vol. 6, 492–494, 2007.
3. Chan, K. K. and S. K. Rao, "Design of a triband corrugated horn," *Proceedings of the 2003 Asia-Pacific Microwave Conference*, Vol. 1, 29–32, Seoul, Korea, Nov. 4–7, 2003.

# Micro Strip Line Fed I-shaped Dielectric Resonant Antenna for Millimeter Wave Applications

**Chandra Kandula, Prasanna Kumar Sahu, Prakash Kumar Panda, and K. L. Sheeja**

Department of Electrical Engineering, NIT Rourkela, Orissa, India

**Abstract**— Here the design of a simple and a generic transmission line (T.L.) circuit approach along with a fast and generic formulation for the novel antenna model is developed. The proposed antenna is modeled as a novel shape and is placed on a material of dielectric constant of $\varepsilon$ equal to 2.2 (Rogers RT5880 material) and size of 15 mm×11 mm. The $\varepsilon$ (epsilon) value of dielectric resonator is taken to be 10.2 (material: Rogers RO3010). A simple micro strip line feeding of novel design has been used to feed the antenna. The ground plane is considered to be 10 mm×11 mm in size. Different values for width are 2.4, 2.0, 1.6 and 1.4. A good return loss is found at an optimized length of 2.0 mm. The proposed antenna is simulated and a return loss of $-10$ dB is obtained which is in the range of 30.58 GHz to 39 GHz. Here a good return loss is obtained at two peaks whose values are $-21$ dB at 31.54 GHz and a value of $-22$ dB at 35.39 GHz. In this paper a bandwidth improvement of 24.36% has been achieved. In addition to that a total efficiency of 72.88% is found at 35.39 GHz and 69% is found at 31.54 GHz. A directivity of 10.2 dBi at 35.39 GHz and a 7.61 dBi at 31.54 GHz have been claimed, besides that a significant gain of 10.59 dB at a frequency of 35.39 GHz and 8.34 dB at 31.54 GHz. The designed antenna is proposed for applications in the area of satellite communications, radio location.

## 1. INTRODUCTION

Nowadays, a lot of research work has been devoted to the development of millimeter-wave frequency band, high speed and low profile systems, at which metallic antennas, such as micro strip antennas, suffer from the high conductor and substrate losses. Dielectric resonator antennas seem to be the suitable candidates for the millimeter-wave systems due to their low profile, low conductor losses, large bandwidth (compared to the conventional microstrip antennas), and high radiation efficiency [1–5]. Dielectric resonators (DRs), made of low loss dielectric materials, are widely used in various applications. They are compact in size, low in cost and weight and could be excited using different transmission lines [2].

DRAs offer simple coupling schemes to nearly all transmission lines used at microwave and mm-wave frequencies. This makes them suitable for the continuing growth in demand for wireless communications that has pushed industry to develop new and better systems. Many of these systems are designed to operate at extremely high frequencies (EHF) to take advantage of benefits such as reduction in equipment size, wider bandwidth. These systems require new hardware solutions to overcome difficulties and limitations encountered when operating at 6 GHz, such as the high degree of oxygen absorption over distance [1]. One technology that has been proposed for EHF use is the dielectric resonator antenna (DRA). DRA offer many advantages such as low cost, ease of manufacture, wider bandwidth, smaller size [2], high radiation efficiency, and the capability to be used in many hybrid structures [7] to improve antenna's performances like directivity and bandwidth [3]. Furthermore, those improved antennas (highly directive) [4, 5] appear to have a high potential for use in many communication systems such as tunnels and underground mines.

## 2. ANTENNA GEOMETRY

The investigated antenna topology is shown in Figure 1. The radiating element of permittivity ($\varepsilon_{dr} = 10.2$), [6] novel shaped dielectric resonator of strip A having 10 mm length, 0.9 mm width and 2 mm height. The strip B of length 2 mm, width 3.5 mm and height of 2 mm. Strip C has a length of 3 mm, width 1 mm and height of 2 mm and strip D has length of 3 mm, width of 1 mm and a height of 2 mm. The dimensions are taken such that it should radiate at satellite uplink frequency. The resonator is placed on the substrate of dimensions 15 mm length, 11 mm width and a height of 1.6 mm. A partial ground of length 10 mm, width of 11 mm and a height of 0.05 mm is considered. The resonator is radiated by using micro strip line feeding technique. Micro strip line feeder of length 0.6 mm, width 5.6 mm and a height of 0.1 mm are placed on the substrate.

The proposed antenna has been optimized by changing the length of strip B along $X$ direction.
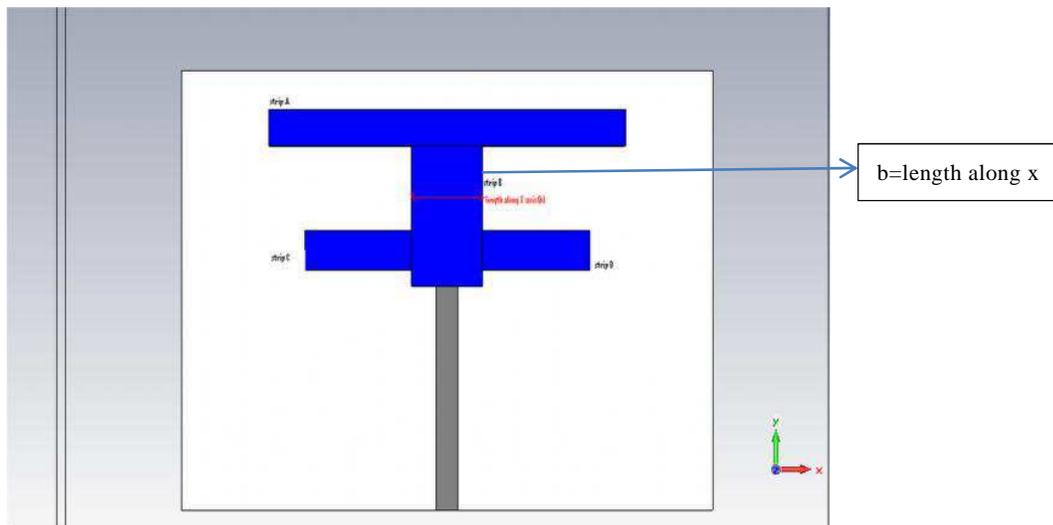
Figure 1: Geometry of proposed I shaped dra.
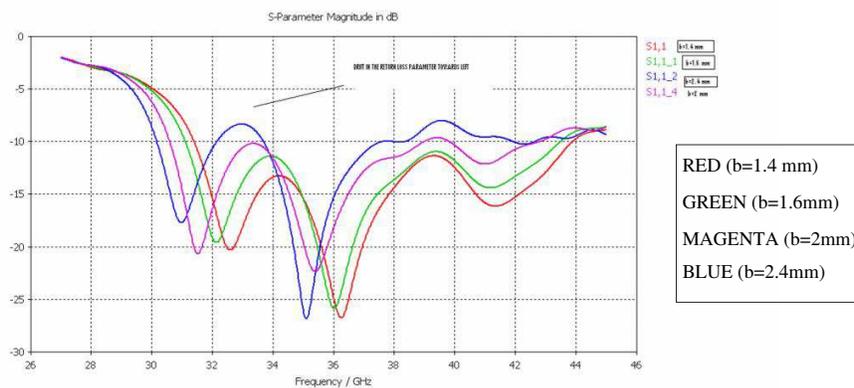


Figure 2: Simulated return loss of proposed antenna.
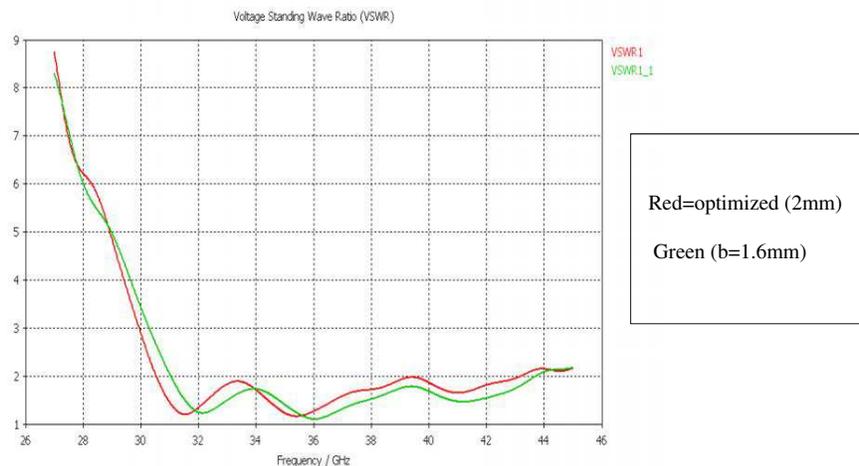


Figure 3: VSWR parameter versus frequency.

## 3. RESULTS AND DISCUSSIONS

To verify the validity of the proposed approach, the design is simulated using CST. It is reported that, in the case of DRAs on conductive silicon surfaces, high permittivity materials are more preferred as they can confine more electromagnetic field in the radiating element and hence effectively reduce the energy loss towards the substrate. In addition, their sufficiently high permittivity re-
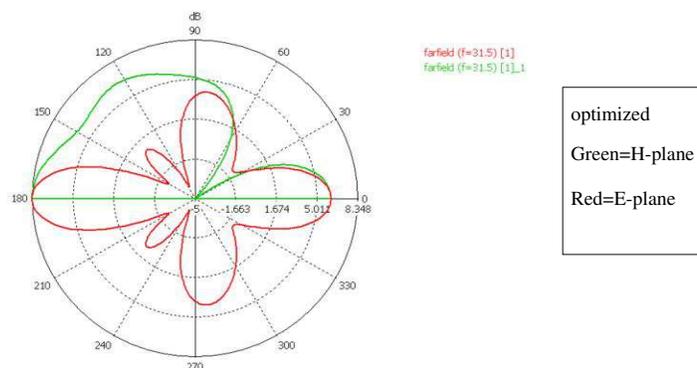
Figure 4: Gain pattern of proposed antenna at desired frequency.

duces the fringing fields from the launcher to the substrate and thereby enhancing the efficiency of the antenna. However, extremely high permittivity materials reduce the radiation efficiency of the antenna; since they could confine the fields.

The simulated return loss graph is shown in Figure 2. The proposed design has a $-10$ dB impedance bandwidth, where an increment of 24.36% is found. Here a good return loss is obtained at two peaks whose values are $-21$ dB at 31.54 GHz and a value of $-22$ dB at 35.39 GHz. An optimized length of 2 mm is taken to get desired return loss at 31 GHz. This frequency is the satellite uplink frequency. A wider bandwidth has been achieved from 30.5 GHz to 38.99 GHz for a width of $b = 2$ mm. This bandwidth is further increased for different values of $b$. A bandwidth of 31.3 GHz to 44 GHz is obtained for a length of 1.4 mm. The proposed antenna can radiate a maximum of range ka band. As we decrease the width of antenna's middle strip we will miss the 31 GHz uplink frequency. So, an optimum value of $b = 2$ mm is taken. A radiation efficiency of 69% and a considerable gain is found at desired frequency.

Therefore from Figure 2 and Figure 3, we had obtained a good return loss value which is well below the $-10$ dB and also vswr graph is confined to a maximum value of 2 only.

In addition to that the gain patterns are mentioned in the following figure.

The gain that is obtained is 8.34 dB and a directivity of 7.61 dBi is found.

## 4. CONCLUSION

In this work an I-shaped dielectric resonator antenna (IDRA) fed by micro strip line feeder for millimeter wave systems, has been proposed. The simulation results verify the proposed design strategies. The proposed design offers good performance and can be better suited for satellite applications.

## REFERENCES

1. Smulders, P. F. M., "60 GHz radio: Prospects and future directions," *IEEE 10th Symposium on Communications and Vehicular Technology*, 1–8, Benelux, Eindhoven, the Netherlands, 2003.
2. Luk, K. M. and K. W. Leung, *Dielectric Resonator Antennas*, Baldock, Herfordshire, UK, Research Studies, 2002.
3. Perron, A., T. A. Denidni, and A. R. Sebak, "High gain hybrid dielectric resonator antenna for millimeter-wave applications: Design and implementation," *IEEE Trans. Antennas Propagat.*, Vol. 57, No. 10, 2882–2892, October 2009.
4. Franson, S. J. and R. W. Ziolkowski, "Gigabit per second data transferin high-gain metamaterial structures at 60 GHz," *IEEE Trans. Antennas Propagat.*, Vol. 57, No. 10, 2913–2925, October 2009.
5. Nasimuddin and K. P. Esselle, "A low-profile compact microwaveantenna with high gain and wide bandwidth," *IEEE Trans. Antennas Propagat.*, Vol. 55, No. 6, 1880–1883, June 2007.
6. Perron, A., T. A. Denidni, and A. R. Sebak, "High gain dielectric resonator/micro strip hybrid antenna for millimeter waveapplications," *IEEE Trans. Antennas and Propagat.*, Vol. 57, No. 10, 2882–2892, Oct. 2009.
7. Liang, X.-L. and T. A. Denidni, "Cross-T-shaped dielectric resonator antennafor wideband applications," *Electronic Letters*, Vol. 40, No. 20, 1176–1177, 2008.

# Wideband Isosceles 75°-30°-75° Triangular Dielectric Resonator Antenna

**S. Maity**, **S. Dasgupta**, **and B. Gupta**

Department of Electronics and Tele-Communication Engineering
Jadavpur University, Kolkata, India

**Abstract**— A simple, wideband isosceles 75°-30°-75° triangular Dielectric Resonator Antenna (DRA) is proposed here for IEEE 802.11a/h/j/n, HiperLAN, U-NII bands. This proposed antenna configuration gives 46.5% impedance bandwidth for 2 : 1 VSWR. $E$-plane and $H$-plane radiation patterns at 5.2 GHz, 5.3 GHz and 5.8 GHz are given here.

## 1. INTRODUCTION

Nowadays, there is a deep interest in antenna systems which operate at frequencies in the millimeter and sub-millimeter wave region (100–300 GHz). Conductor loss limits the use of conventional metallic antennas in this high frequency band. Dielectric Resonator Antenna (DRA) made up of low loss dielectric material is a potential candidate for high frequency application for its high radiation efficiency. Its inherent wide band nature, light weight, compactness in size, ease of fabrication, low cost etc. make DRAs very attractive to antenna engineers. Over last decades, various bandwidth enhancement techniques have been reported in literature on DRAs. A recent updated, good survey of theoretical and experimental investigations have been reported by Petosa and Ittipiboon [1] on cylindrical, cylindrical ring, hemispherical, rectangular, equilateral triangular, hexagonal and/or trapezoidal DRAs. In this paper, an isosceles 75°-30°-75° Triangular DRA (TDRA) is reported for IEEE 802.11a/h/j/n, HiperLAN, U-NII bands.

Broadbanding techniques can be achieved in three ways mainly [2]: Stacking/Combining multiple Dielectric Resonators (DRs); lowering the total/inherent Q-factor of the resonator and by using external matching networks. Natural/artificial structural discontinuities in DRs tend to reduce their Q-factor. For example, using notch or inserting an air gap between the ground plane and the DR or the use of tunnel into DRAs is different techniques for reducing Q-factor of DRAs. Wideband characteristics can be achieved by exciting proper modes with similar electric field distributions on the DRA surface. Defected ground plane is also reported to provide wide bandwidth.

Triangular shape is the simplest geometry among polygonal (except rectangular) resonators. Literature survey shows that only very few papers ($< 10$) have been reported so far on TDRAs or more precisely equilateral TDRAs [1, 2]. Equilateral triangle shows symmetry with respect to its sides and/or angles. On the other hand, the centre of an equilateral triangle is located at the triangle's centre which gives flexibility to find the solution. For that reason, only equilateral TDRA has been reported in literature. Triangular resonator can be used efficiently in designing compact antenna array(s) with reduced mutual coupling between adjacent elements due to its smaller size. Compactness can be further improved by choosing isosceles 75°-30°-75° TDRA instead of equilateral TDRA.

## 2. ANTENNA GEOMETRY

Let us consider an isosceles 75°-30°-75° TDRA in Cartesian co-ordinate system with relative permittivity $\varepsilon_r$, base (opposite side of $\angle 30°$) $b$ median $M$ and height $h$ as depicted in Fig. 1. The antenna is aligned along the $z$-axis and the origin is located at the vertex (or tip) of triangular DRA and the $y$-axis is parallel to base.

## 3. RESONANT FREQUENCY AND EFFECTIVE DIMENSIONS

The resonance frequency is predicted using simple waveguide model. TDRA is placed on ground plane at $z = 0$ and Perfect Magnetic Walls (PMCs) are employed along its sides and at $z = h$. Enforcing the magnetic wall boundary conditions at the sides of TDRA, gives the following equation [3]:

$$\chi^2 = \frac{2}{3}\pi^2 \left[ \frac{S}{H^2} + \frac{Q}{4}\left(3J^2 + \frac{1}{G^2}\right) \right] \left(m^2 + mn + n^2\right) \tag{1}$$
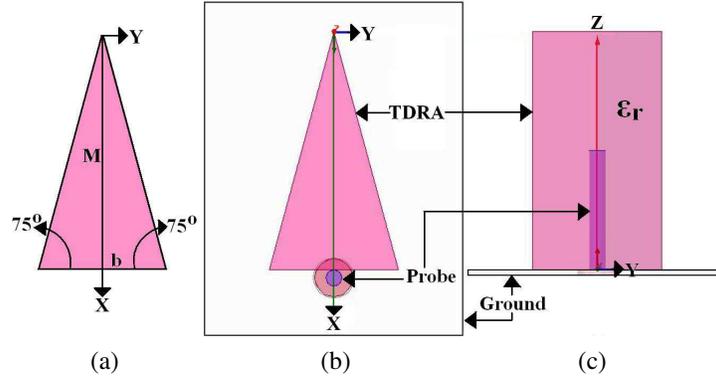
Figure 1: Geometry of isosceles $\angle 75°$ triangular DRA.

where $\chi$ is composite wave numbers along $x$ and $y$-direction togetherly and

$$
\begin{cases}
p = \sin(\theta/2), \quad q = \cos(\theta/2), \quad \theta = 5\pi/12 \\
S = 4p^2, \quad Q = 4q^2, \quad t = \sin(\varphi/2), \quad \varphi = \pi - 2\theta \\
r = (\text{b}/2)\tan(\theta/2), \quad R = r/\sin(\varphi/2) \\
G = (gr + 2tR), \quad H = (gr + R) \\
J = \frac{SG}{H^2 Q}, \quad g = \frac{1}{2p}
\end{cases}
\tag{2}
$$

The mode index satisfies the following equation:

$$
l + m + n = 0 \tag{3}
$$

Further, by applying image theory, ground plane at $z = 0$ is removed and an isolated isosceles 75°-30°-75° TDRA is formed with twice the original height. By applying continuity equation at $z = \pm h$ the following transcendental equation is obtained for the wave number $k_z$:

$$
k_z \tan(k_z h - \pi/2) = \sqrt{(\varepsilon_r - 1)\, k_o^2 - k_z^2} \tag{4}
$$

The non-separable composite wave numbers along $x$ and $y$-direction, i.e., $\chi$ and $k_z$ satisfy the separation equation:

$$
\chi^2 + k_z^2 = \varepsilon_r k_o^2 \tag{5}
$$

where $k_o$ denotes the free space wave number. On solving Equation (5), one can get the resonant frequency of an isosceles 75°-30°-75° TDRA.

Magnetic lines avoid corners which makes the effective area smaller than the actual area [4]. It is the dual of fringing of electric field which is well known for calculating effective area of microstrip patch antenna as reported in literature so far. The concept of deformed magnetic lines is used for calculating resonant frequency of TDRA [3]. Using this concept and assuming that maximum energy passes through the in-circle of isosceles 75°-30°-75° TDRA, the effective base and effective median can be expressed as [3]:

$$
b_{eff} = b - (b - 2r)/A \tag{6}
$$
$$
M_{eff} = M - (M - 2r)/A \tag{7}
$$

where $b$, $M$, $r$ are base, median and in-radius respectively and

$$
A = 2.05 \tag{8}
$$

However, we know that the Electro-Magnetic (EM) energy confined within the DRA is related to permittivity and dimensions. The effect of permittivity along the height of Rectangular DRA is given by [5]:

$$
h_{eff} = h(1 - 1/\varepsilon_r) \tag{9}
$$

Both rectangular and triangular DRA are analyzed in Cartesian co-ordinate system. Hence Equation (9) can be effectively used to calculate the effective height of TDRA.
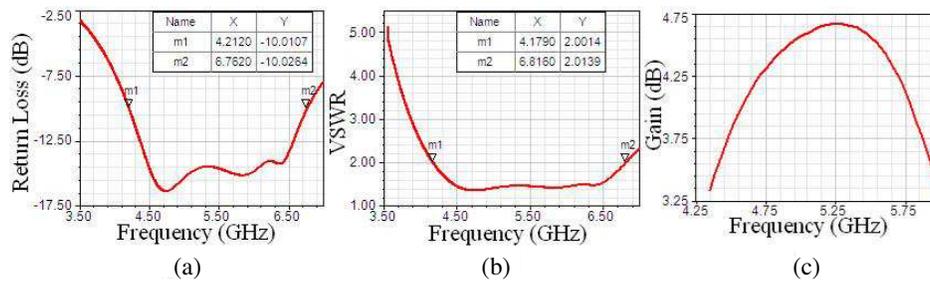
Figure 2: (a) Plot of return loss Vs frequency. (b) Plot of VSWR Vs frequency. (c) Plot of gain Vs frequency.
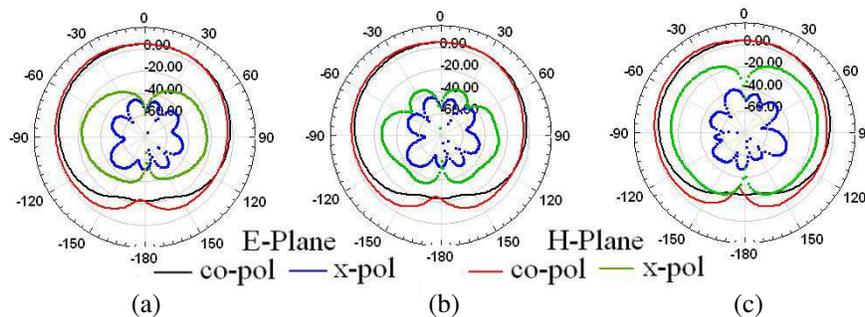


Figure 3: Radiation pattern at (a) 5.2 GHz, (b) 5.3 GHz, (c) 5.8 GHz.

## 4. RESULT AND DISCUSSION

Finite Element Method (FEM) based commercial software HFSS [6] is used to simulate the antenna structure. TDRA is excited using coaxial probe. The radius of inner conductor of probe is 0.63 mm. The probe is connected to an SMA connector. For probe inserted DRA, there might be air gap between inserted probe and DRA surface. Dielectric powder is used to fill this gap. To avoid the drilling problem, coaxial probe can be placed outside the DRA [7] as shown in Fig. 1. The length of probe is taken to 50% of the height of TDRA. If an air gap exists and is not modeled correctly, a discrepancy between computed and measured results would exist because the air gap tends to shift the resonance frequency. The size of ground plane ($5b \times 5M$) is taken two times larger from each side of TDRA.

In this work, to get a wide band isosceles 75°-30°-75° TDRA with relative permittivity $\varepsilon_r = 10$, median $M = 19$ mm and height $h = 19$ mm as depicted in Fig. 1 is simulated using HFSS. The simulated return loss and VSWR are shown in Figs. 2(a) and 2(b) respectively. It is to be noted that the 2 : 1 VSWR impedance bandwidth of the proposed antenna configuration yields a wide bandwidth covering 4.21 GHz to 6.76 GHz. This proposed antenna configuration provides a broad coverage of the 5.150 GHz–5.350 GHz band for W-LAN application, centered at 5.2 GHz. Fig. 2(c) shows the variation of gain with respect to frequency. Thus, this antenna can be used for IEEE 802.11a/h/j/n, HiperLAN and U-NII bands. $E$-plane and $H$-plane radiation patterns at 5.2 GHz, 5.3 GHz and 5.8 GHz are shown in Fig. 3.

## 5. CONCLUSION

A simple wideband probe fed isosceles 75°-30°-75° TDRA is proposed, which gives 46.5% impedance bandwidth (4.21–6.76 GHz), wide enough to cover IEEE 802.11a/h/j/n, HiperLAN and U-NII bands application. The radiation patterns are stable over this operating frequency band. Moreover, the proposed antenna has a simple structure and an easy fabrication. With these features, this antenna is very suitable for practical wideband applications.

## ACKNOWLEDGMENT

**REFERENCES**

1. Petosa, A. and A. Ittipiboon, "Dielectric resonator antennas: A historical review and the current state of the art," *IEEE Antennas and Propagation Magazine*, Vol. 52, No. 5, 91–116, October 2010.

2. Luk, K. M. and K. W. Leung, (eds.), *Dielectric Resonator Antennas*, Research Studies Press, Baldock, England, 2003.

3. Maity, S., S. Dasgupta, and B. Gupta, "More accurate resonant frequency evaluation of triangular isosceles patch antenna," *Proceedings of International Conference on Microwaves, Antenna, Propagation & Remote Sensing (ICMARS)*, Jodhpur, India, 2011.

4. Schelkunoff, S. A., *Electromagnetic Waves*, D. Van Nostrand Company, Princeton, 1943.

5. Maity, S. and B. Gupta, "Effective wave guide model (EWGM) for resonant frequency computation of rectangular dielectric resonator antennas," *Progress In Electromagnetics Research C*, Vol. 16, 1–12, August 2010.

6. Ansoft High Frequency Structure Simulator, User's Reference, 2010.

7. Maity, S., S. Dhar, and B. Gupta, "Variation of probe offset position with probe length of rectangular dielectric resonator antenna," *International Symposium on Microwaves (ISM)*, Bangalore, India, 2010.

# Resonant Frequency and Field Solution of Isosceles Triangular Dielectric Resonator Antenna

**S. Maity**, **S. Dasgupta**, and **B. Gupta**

Department of Electronics and Tele-Communication Enggineering, Jadavpur University, Kolkata, India

**Abstract**— An isoscelestriangular Dielectric Resonator Antenna (DRA) is analyzed theoretically using waveguide model and trilinear transformation. Exact internal field configurations for symmetrical/even and anti-symmetrical/odd modes are given here. A more general expression for computing resonant frequency is given here. Results are compared with published results available in open literature.

## 1. INTRODUCTION

Dielectric Resonators (DRs) as radiating elements was first carried out by Long et al. in 1980s [1]. Conductor loss limits the use of metallic antennas in millimeter and sub-millimeter region (100 GHz–300 GHz). On the other hand, Dielectric Resonator Antenna (DRA) made up of low loss dielectric material is a potential candidate for high frequency application. Its inherent wide band nature, light weight, low profile, compactness in size, ease of fabrication, low cost etc. make DRAs very attractive. Significant progress has been made in various aspects of hemispherical, circular-cylindrical and rectangular DRAs mainly, as evidenced by the more than 800 publications and over two dozen issued patents [1]. But very few papers ($< 10$) are reported so far on triangular DRA (TDRA) or more precisely equilateral TDRA [1, 2]. In this paper, isosceles Triangular DRA (TDRA) is analyzed theoretically using modified trilinear transformation, dielectric waveguide model and transverse resonance technique. Exact Internal field configurations for even and odd modes and an accurate expression for resonant frequency are given here. This analysis is based on two assumptions: (a) magnetic field lines avoid corners [3] and (b) most of the signal/energy passes through the in-circle of isosceles triangle. This theory is named as Deformed Magnetic-lines Waveguide Model (DMWM).

## 2. ANTENNA CONFIGURATION

Let us consider an isosceles ($\theta - \varphi - \theta$) TDRA in Cartesian co-ordinate system with relative permittivity $\varepsilon_r$, base (opposite side of $\varphi$) $b$ and height $h$ as depicted in Figs. 1(a)–1(c). The antenna is aligned along the $z$-axis and the origin is located at in-centre of the triangle and the $y$-axis is parallel to base.

## 3. FIELD COMPONENTS FOR SYMMETRICAL/EVEN AND ANTI-SYMMETRICAL/ODD MODE

Figure 1 shows the top view of an isosceles ($\theta - \varphi - \theta$) TDRA in standard Cartesian coordinate system $(x, y)$. One can define triangular coordinate system $(u, v, w)$ of a point P using trilinear transformation [3] such that:

$$u + v + w = 0 \tag{1}$$
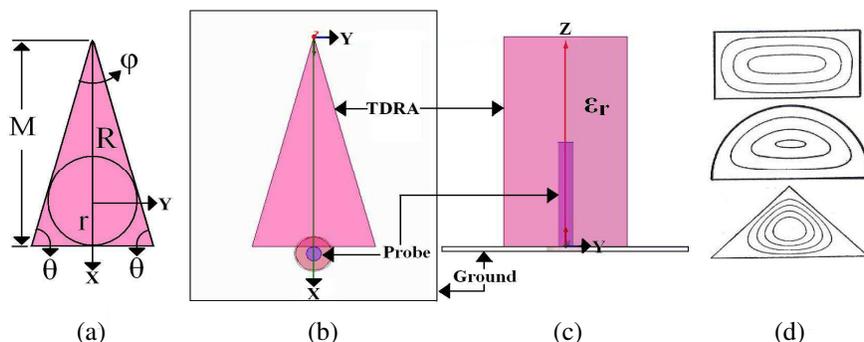


Figure 1: (a) Geometry of isosceles triangle, (b) top view of simulated TDRA, (c) side view of simulated TDRA, (d) magnetic lines in various geometry.

Now the triangle has centre at $(0,0)$ and the three sides of triangle are given by:

$$u = r, \quad v = r; \quad w = r \tag{2}$$

where $r$ is in-radius of triangle. Now the isosceles $(\theta - \varphi - \theta)$ TDRA shows either symmetry or anti-symmetry about its median $(M)$ [4]. On solving the wave equation, the $TM^z$ mode field patterns for an isosceles $(\theta - \varphi - \theta)$ TDRA $(30° \geq \theta \geq 60°)$ are given as:

A. *Field Components for $TM^z$ Even $(TM_s^z)$ Mode*

$$\begin{cases}
E_x = -jk_z / (\omega\mu\varepsilon) \times A_s \left[\sum_i (-\alpha_i)\sin\left[\alpha_i (x + R)\right] \cos\left[\beta_i (2qy)\right]\right] \times \cos(k_z z) \\
E_y = jk_z / (\omega\mu\varepsilon) \times A_s \left[\sum_i (-2q\beta_i)\cos\left[\alpha_i (x + R)\right] \sin\left[\beta_i (2qy)\right]\right] \times \cos(k_z z) \\
E_z = -j\chi^2 / (\omega\mu\varepsilon) \times A_s \left[\sum_i \cos\left[\alpha_i (x + R)\right] \cos\left[\beta_i (2qy)\right]\right] \times \sin(k_z z) \\
H_x = (1/\mu) \times A_s \left[\sum_i (-2q\beta_i)\cos\left[\alpha_i (x + R)\right]\sin\left[\beta_i (2qy)\right]\right] \times \sin(k_z z) \\
H_y = -(1/\mu) \times A_s \left[\sum_i (-\alpha_i)\sin\left[\alpha_i (x + R)\right] \cos\left[\beta_i (2qy)\right]\right] \times \sin(k_z z) \\
H_z = 0
\end{cases} \tag{3}$$

B. *Field Components for Odd Mode*

$$\begin{cases}
E_x = -jk_z / (\omega\mu\varepsilon) \times A_a \left[\sum_i (-\alpha_i) \sin\left[\alpha_i (x + R)\right] \sin\left[\beta_i (2qy)\right]\right] \times \cos(k_z z) \\
E_y = -jk_z / (\omega\mu\varepsilon) \times A_a \left[\sum_i (2q\beta_i)\cos\left[\alpha_i (x + R)\right] \cos\left[\beta_i (2qy)\right]\right] \times \cos(k_z z) \\
E_z = -j\chi^2 / (\omega\mu\varepsilon) \times A_a \left[\sum_i \cos\left[\alpha_i (x + R)\right] \sin\left[\beta_i (2qy)\right]\right] \times \sin(k_z z) \\
H_x = (1/\mu) \times A_a \left[\sum_i (2q\beta_i)\cos\left[\alpha_i (x + R)\right] \cos\left[\beta_i (2qy)\right]\right] \times \sin(k_z z) \\
H_y = -(1/\mu) \times A_a \left[\sum_i (-\alpha_i)\sin\left[\alpha_i (x + R)\right] \sin\left[\beta_i (2qy)\right]\right] \times \sin(k_z z) \\
H_z = 0
\end{cases} \tag{4}$$

where $i = 1, 2, 3$ and $A_s$, $A_a$ are constants for even and odd mode respectively and

$$\begin{cases}
\alpha_1 = \pi l/H, \quad \beta_1 = \pi\left[J(m - l) + (m + l)/G\right]/2 \\
\alpha_2 = \pi m/H, \quad \beta_2 = \pi\left[J(n - m) + (n + m)/G\right]/2 \\
\alpha_3 = \pi n/H, \quad \beta_3 = \pi\left[J(l - n) + (n + l)/G\right]/2 \\
p = \sin(\theta/2), \quad q = \cos(\theta/2), \quad S = 4p^2, \quad Q = 4q^2 \\
r = (b/2)\tan(\theta/2), \quad R = r/\sin(\varphi/2), \quad t = \sin(\varphi/2) \\
G = (gr + 2tR), \quad H = (gr + R), \quad J = SG/(H^2 Q), \quad g = 1/(2p) \\
\chi^2 = (2/3)\,\pi^2\left[S/H^2 + Q\left(3J^2 + 1/G^2\right)/4\right]\left(m^2 + mn + n^2\right) \\
l + m + n = 0
\end{cases} \tag{5}$$

The wave number in $z$-direction $(k_z)$ into DRA can be found from the following transcendental equation:

$$k_z \tan(k_z h - \pi/2) = \sqrt{(\varepsilon_r - 1)k_o^2 - k_z^2} \tag{6}$$

If $k_o$ denotes the free space wave number then, the non-separable composite wave numbers along $x$ and $y$-direction, i.e., $\chi$ and $k_z$ satisfy the separation equation:

$$\chi^2 + k_z^2 = \varepsilon_r k_o^2 \tag{7}$$

## 4. EFFECTIVE DIMENSION

The ideal contour of magnetic lines is circular. For non-circular cross sectional resonators, magnetic lines are deformed near the corner(s) [3] as shown in Fig. 1(d). The theoretical ratio of resonant frequency of semicircular and circular tube is 1.4 but in practice, it is equal to 1.6. This is because the magnetic lines avoid corners in semicircular tube which makes the effective area smaller than the actual area [3]. This can be well explained using duality. The concept of deformed magnetic lines which decreases the area is dual of fringing of electric field which increases the area. Fringing of electric field is well known for calculating effective area as reported in literature so far. But in this paper, the concept of deformed magnetic lines is used for calculating resonant frequency of TDRA.

Using this concept and assuming that maximum energy passes through the in-circle of isosceles $(\theta - \varphi - \theta)$ triangle, the effective base and effective median (perpendicular bisector of base) lengths are:

$$b_{eff} = b - (b - 2r)/A \tag{8}$$
$$M_{eff} = M - (M - 2r)/A \tag{9}$$

Table 1: Comparison of resonant frequency for $TM^z_{1,0,-1}$ mode ($\varepsilon_r = 10$).

| $\theta$ (deg) | $A$ | $M$ (mm) | $h$ (mm) | Resonant Frequency (GHz) | | | Error (%) | |
|---|---|---|---|---|---|---|---|---|
| | | | | $fr_{sim}$ | Overfelt [7] | $fr_{the}$ | Overfelt [7] | Theory |
| 30° | 1.25 | 6 | 6 | 10.75 | 12.92 | 10.68 | 20.22 | −0.6818 |
| | | 9 | 9 | 7.1 | 8.616 | 7.118 | 21.35 | 0.2508 |
| | | 18 | 18 | 3.55 | 4.308 | 3.559 | 21.35 | 0.2508 |
| 75° | 2.05 | 26 | 26 | 4.1 | —— | 4.093 | —— | −0.1733 |
| | | 29 | 29 | 3.65 | —— | 3.669 | —— | 0.534 |
| | | 30 | 30 | 3.55 | —— | 3.547 | —— | −0.0796 |

where $b$, $M$, $r$ are base, median and in-radius respectively and $A$ is a constant which differs from triangle to triangle as shown in Table 1. The effect of permittivity along the height of rectangular DRA is given by [5]:

$$h_{eff} = h(1 - 1/\varepsilon_r) \tag{10}$$

Both rectangular and triangular DRAs are analyzed in Cartesian co-ordinate system. Hence Equation (10) can be effectively used to calculate the effective height of TDRA.

## 5. RESULTS AND DISCUSSIONS

Finite Element Method (FEM) based commercial software HFSS [6] is used to simulate the antenna structures. TDRA is excited using coaxial probe as shown in Figs. 1(b)–1(c). The radius of inner conductor of probe is 0.63 mm. To reduce the complexity of our problem, we have taken $M = h$. The length of probe is taken to be 50% of the height of TDRA which is sufficient for efficient coupling of TDRA. The size of ground plane ($5b \times 5M$) is taken two times larger from each side of TDRA.

To show the accuracy and effectiveness of our proposed theory, resonant frequency is calculated using DMWM and finally are compared to published results available in open literature [7]. It is found that our results are very much accurate. Table 1 shows simulated ($fr_{sim}$) and computed resonant frequencies using above theory ($fr_{the}$) of isosceles ($\theta - \varphi - \theta$) triangle.

## 6. CONCLUSION

An isosceles ($\theta - \varphi - \theta$) triangular DRA is investigated here theoretically. Deformed Magnetic-lines Waveguide Model (DMWM) is proposed to analyze it. Internal fields for even and odd modes are given here. An accurate solution for resonant frequency is provided and verified with FEM based commercial software HFSS. Our result is compared with published results, which indicates its superiority as the most general and accurate model reported so far.

## ACKNOWLEDGMENT

## REFERENCES

1. Petosa, A. and A. Ittipiboon, "Dielectric resonator antennas: A historical review and the current state of the art," *IEEE Antennas and Propagation Magazine*, Vol. 52, No. 5, 91–116, Oct. 2010.
2. Luk, K. M. and K. W. Leung, *Dielectric Resonator Antennas*, Research Studies Press, Baldock, England, 2003.
3. Schelkunoff, S. A., *Electromagnetic Waves*, D. Van Nostrand Company, Princeton, 1943.
4. Maity, S., "Hybrid triangular dielectric resonator antenna (DRA) for WLAN/ISM application," *Proceedings of IEEE Indian Antenna Week-2011*, Kolkata, India, Dec. 2011.
5. Maity, S. and B. Gupta, "Effective wave guide model (EWGM) for resonant frequency computation of rectangular dielectric resonator antennas," *Progress In Electromagnetics Research C*, Vol. 16, 1–12, Aug. 2010.
6. Ansoft High Frequency Structure Simulator, User's Reference, 2010.
7. Overfelt, P. L. and D. J. White, "TE and TM modes of some triangular cross-section waveguides using superposition of plane waves," *IEEE Trans. Microwave Theory and Techniques*, Vol. 34, No. 1, 161–167, Jan. 1986.

# Study and Analysis of GUNN Loaded Active Microstrip Patch Antenna

**Sanghamitra Dasgupta and Bhaskar Gupta**

Department of Electronics and Tele-Communication Engineering
Jadavpur University, Kolkata-700 032, India

**Abstract**— This paper presents the design and simulated results of a compact, low-cost Gunn-diode integrated active rectangular patch antenna and compares the results with a similarly configured passive antenna. The simulation results in this paper can be used as design reference for the practical design of the active antenna.

## 1. INTRODUCTION

An antenna with some active processing elements before intercepting or producing electromagnetic wave is called an active antenna. But since the active element should have an impact on the interception of the radiation of the electromagnetic waves, an active fully integrated antenna can be defined as "an antenna whose radiation properties are intimately associated with an active element or elements behavior" [1]. Active antennas reduce size, weight and cost over conventional designs which are very useful in microwave systems [2–4]. Active antennas overcome several of the shortcomings of traditional antennas [5]. They are almost frequency independent, in the sense that their bandwidth is dependent on the active circuitry rather than the radiating element. Also a careful design of the connected amplifier can ensure a very broadband performance of the antenna. Similarly the gain of the antenna can also be controlled by the amplifier. Since the active antenna is electrically small compared to the passive one, the overall length is much less than the conventional antenna, and thus can be used in places where there is constraint on space.

In this paper, a Gunn diode has been modeled in Ansoft Designer and integrated with a rectangular microstrip patch antenna to form an active antenna which is modeled in HFSS. The simulation results are encouraging for practical application.

## 2. DESIGN SPECIFICATIONS FOR PASSIVE MICROSTRIP PATCH ANTENNA

A rectangular microstrip patch antenna has been designed and fabricated to operate at 9.5 GHz as shown in Fig. 1.

The design parameters are given below: Frequency of resonance $(f_r) = 9.5$ GHz, Free space wavelength $(\lambda_o) = 31.579$ mm, Relative permittivity of the substrate $(\varepsilon_r) = 2.2$, Height of the substrate $(h) = 0.787$ mm, Effective length of the patch $(l) = 11.021$ mm, Length extension $(\Delta_l) = 0.411$ mm, Physical length of the patch $(l_p) = 9.79$ mm, Effective width of the patch $(w_{eff}) = 14.569$ mm, Effective dielectric constant $(\varepsilon_{eff}) = 2.096$, Guided wavelength $(\lambda_g) = 21.812$ mm, Characteristic impedance $(Z_o) = 12.951$ ohm, Input impedance $(R_{in}) = 271.139$ ohm, Intrinsic conductance $(G_i) = 2.32 \times 10^{-5}$ mho, Attenuation constant $(\alpha_a) = 3.502 \times 10^{-4}$, Propagation constant $(\beta) = 0.288$.
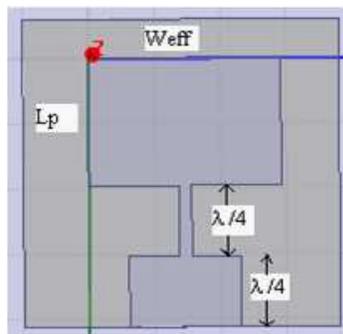


Figure 1: Rectangular Microstrip patch antenna.

## 3. DESIGN PROCEDURE

### 3.1. GUNN Diode Modeling

A Gunn diode is a two terminal device, which like a normal diode exhibits non linear I-V characteristics but have a negative resistance region. The GUNN diode must be biased within the negative resistance region to produce a RF output signal. DC voltage is applied to the diode along a path known as the radial line transformer which is a complex device that acts as the bias circuitry for the diode; the components and their magnitudes therein are crucial [6]. The advantage of Gunn diode over other active devices is that it is a relatively cheap and readily available device and so they are often used for DC to microwave conversion since no additional complex circuitry is required to create an oscillator. Also the low voltage requirements make them suitable for a wide range of applications and allow them to be used in a variety of different environments.

Gunn Diodes are two-terminal negative-impedance semi-conductors. The negative differential impedance of the Gunn diode may be modeled by a complementary pair of JFETs, as shown in Fig. 2(a) [7].

Using the GUNN diode model Gunn relaxation oscillator is designed in Ansoft Designer as shown in Fig. 2(b). This circuit will operate properly if the DC source resistance is less than the diode negative impedance and the load-line must intersect the active characteristic in the negative impedance region. Also the AC impedance of the DC source should be very high in order to ensure that the bias point becomes astable. The first and last conditions can be met by the transforming properties of a quarter-wavelength transmission line.

### 3.2. Active Antenna Design

An active antenna can be designed integrating a two-terminal device viz. GUNN diode, by positioning it at an appropriate point on the patch antenna or connected to the patch through a microstrip transformer. In both cases the purpose is to obtain maximum radiated power from the antenna. But in case of high frequency patch antenna the dimensions of the antenna become very small, therefore sometimes it is necessary to use the latter technique. Fig. 4 shows the configuration of an active microstrip patch antenna when the Gunn diode is mounted outside the patch antenna. The relations for the various impedances are as shown in the Figure where $Z_{01}$ and $Z_{02}$ are the characteristic impedances of the first and second transformer sections respectively [8].

As shown in the Fig. 3 the passive rectangular microstrip patch is designed in HFSS software and then the modeled GUNN diode as shown in Fig. 2(a) is combined in Ansoft Designer.

The total active antenna system as shown in Fig. 4 is then simulated in HFSS. Since the rectangular microstrip patch antenna integrated with GUNN diode act as a resonant structure, the $Q$-value of the whole system can be written as [9],

$$\frac{1}{Q_L} = \frac{1}{Q_e} + \frac{1}{Q} \tag{1}$$

where, $Q$ denotes the quality factor for the microstrip patch antenna, $Q_e$ is the external $Q$ which
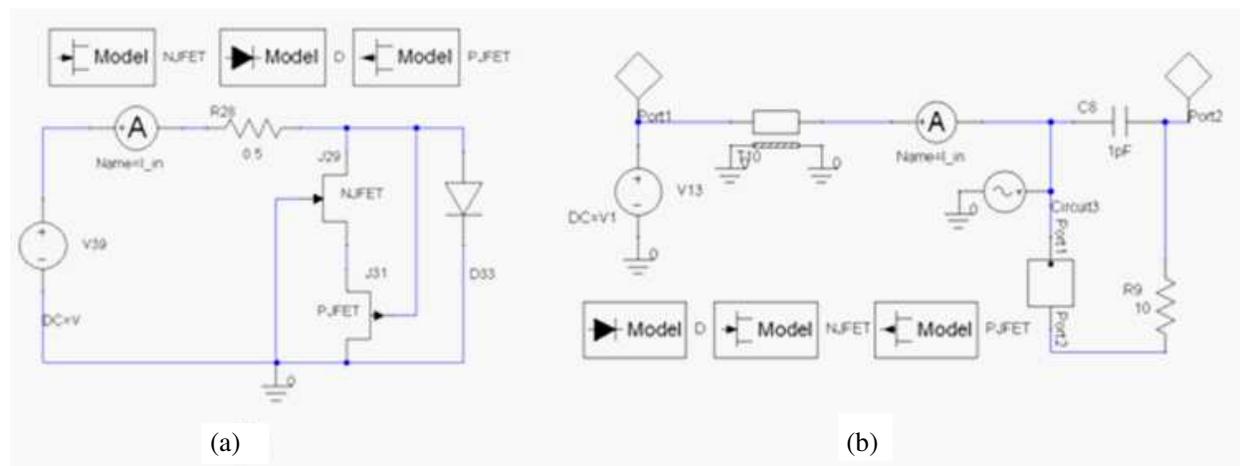


Figure 2: (a) GUNN diode. (b) GUNN diode relaxation oscillator modeled in Ansoft designer.
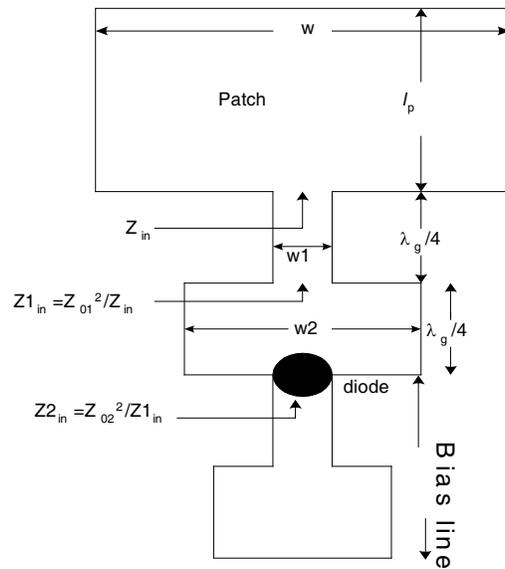
Figure 3: Rectangular active microstrip patch, Gunn diode is integrated to the patch through a microstrip transformer.
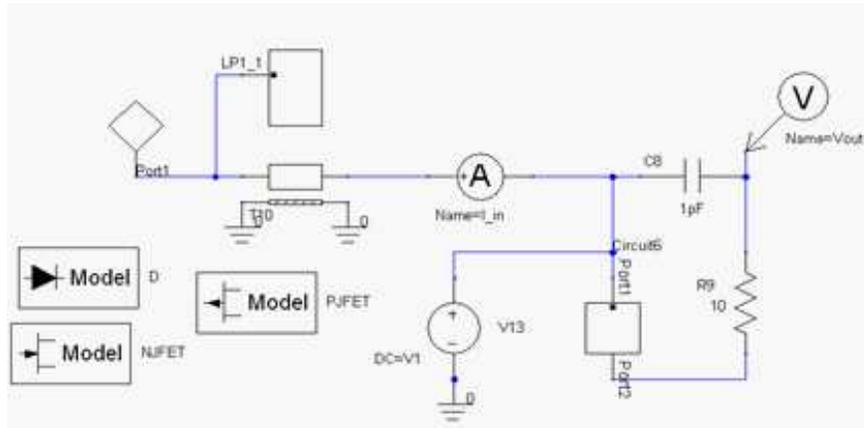


Figure 4: Active antenna modeled in Ansoft designer integrating GUNN diode.



(a)

(b)
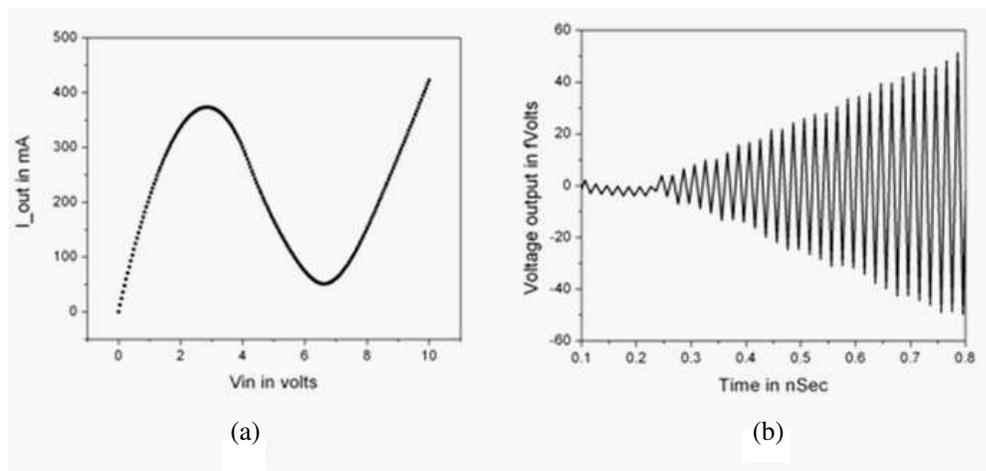
Figure 5: (a) GUNN diode I-V characteristics plot showing the negative resistance region (b) Oscillator response using GUNN diode.

would result if the resonant circuit were loss free and only the loading by the external load were present, and $Q_L$ is the loaded $Q$ when the microstrip patch antenna is integrated with Gunn diode.
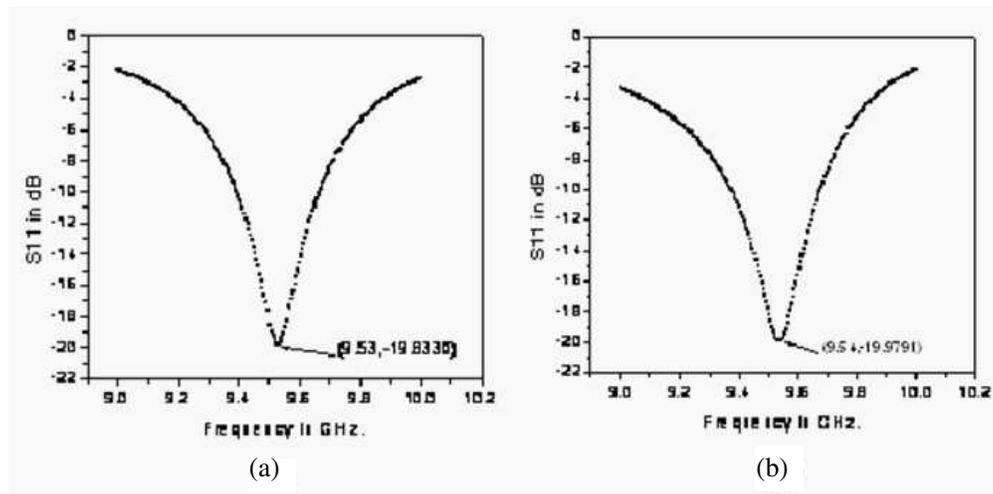
Figure 6: (a) Passive antenna $S$-parameter plot. (b) Active antenna integrated with GUNN diode $S$-parameter plot.

Since $Q$-value is inversely proportional to Band-Width (BW), active integrated Microstrip patch antenna should have a larger BW than the passive microstrip patch antenna.

### 3.3. Results and Discussion

The DC characteristics plot of the GUNN diode modeled in Ansoft Designer is shown in Fig. 2(a). For oscillation purpose the diode is to be operated in the negative resistance region as marked in the figure and the oscillation response is shown in Fig. 5(b). Fig. 6(a) shows the $S$-parameter plot of the rectangular Microstrip patch antenna modeled in HFSS as shown in Fig. 1. Fig. 6(b) shows the $S$-parameter plot of the GUNN diode integrated active Microstrip rectangular patch antenna. Comparing Figs. 6(a) & 6(b), BW has been increased by 10.9%.

### 4. CONCLUSION

In this paper, an active microstrip patch antenna design has been presented which is simulated and analyzed at 9.5 GHz. In this work the active device and the patch has been considered as a composite unit instead of taking them as independent units whereas in conventional wireless or radar systems antenna and circuit they are being considered as separate. The main disadvantage of antenna circuit integration is contradictory requirements of systems. Thick, low dielectric constant substrates are required to enhance microstrip antenna efficiency but thin, high dielectric constant substrates are needed for good circuit action. Also since efficiency of a single Gunn diode is very low proper heat sink design is very important. However this limitation can be avoided if we design large phased arrays where transmit receive function is distributed across the array. Personal communications and vehicle telematics are areas where future requirements may be fulfilled with integrated circuit-antenna modules. Also one of the applications of this technology is single chip transceiver where antenna, transmitter and receiver are made on a single semiconductor substrate.

### ACKNOWLEDGMENT

### REFERENCES

1. Behera, S. K., "Novel tuned rectangular patch antenna as a load for phase power combining," Ph.D. Thesis, 2007.
2. Montiel, C. M., F. Lu, and K. Chang, "Active-notch antennas stabilized with a slotline ring resonator for wireless applications," *IEEE Trans. on Antennas and Propagation*, Vol. 46, No. 6, 945–946, 1998.
3. Navarro, J. A. and K. Chang, *Integrated Active Antennas and Spatial Power Combining*, Wiley, New York, 1996,

4. Montiel, C. M., L. Fan, and K. Chang, "A novel active antenna with self-mixing and wide-band varactor-tuning capabilities for communications and vehicle identification applications," *IEEE Trans. Microwave Theory Tech.*, Vol. 44, 2421–2430, Dec. 1996.

5. Sodagam, S., "Active receive antennas as sensors for radars," Technical Report CReSIS TR 107, Aug. 17, 2006.

6. Michael, G., D. Headland, J. Higginbotham, R. Irwin, A. Nelms, and R. Wan, "High power gunn diode oscillators," Fourth Year Project Interim Report, Department of Electrical Engineering and Electronics, UMIST, Dec. 2003.

7. Intusoft Newsletter Issue #52, Feb. 1998, http://www.intusoft.com/nlhtm/nl52.htm.

8. Bhattacharya, A. and P. Lahiri, "New design philosophy of active microstrip patch antenna," *IEEE Trans. on Antennas and Propagation*, Vol. 3, 1284–1287, 2000.

9. Collin, R. E., *Foundations for Microwave Engineering*, 2nd Edition, 484, Wiley, 2000.

# An Explicit Fractional Step Scattered Field Formulation for Modeling General Lossy Media in the FDTD Technique

**H. H. Abdullah[1] and A. Mohsen[2]**

[1]Microwave Department, Electronics Research Institute (ERI), Dokki, Giza, Egypt
[2]Faculty of Engineering, Cairo University, Giza, Egypt

**Abstract**— During the last two decades, the finite difference time domain (FDTD) method became one of the most efficient and flexible electromagnetic numerical techniques. The accuracy of the technique is the main concern of many researchers since it is a key issue in modeling real life problems. In this paper, a formulation based on dividing the computational time step in two steps to solve the scattering from a general lossy media will be presented. In the first fractional step, each field component will be allowed to vary in only one of the two directions perpendicular to the direction of this field component. In the next fractional step, the variation in the remaining direction will be allowed. This will provide accurate computations of the fields without the need for more memory storage or additional computational time. Another important parameter in the accuracy of computations is the method of handling the incident field. In this paper, the scattered field formulation will be adopted where the incident electric field will be computed analytically at each spatial cell which results in no error in the incident field computations and thus yielding more accurate computation of the scattered fields. The proposed method is tested and the accuracy is illustrated for scattering by a lossy sphere.

## 1. INTRODUCTION

Recently, the finite difference time domain (FDTD) numerical technique has vast increase in its popularity due to its ability to treat many applications since its first proposal [1]. Many attempts to overcome the Courant-Friedrich-Levy (CFL) condition were exerted [4]. The alternating-direction implicit (ADI)-FDTD method has been developed [2, 3], which is unconditionally-stable which removes limiting the time step and has the second-order accuracy in time. A split-step FDTD which is a fractional type step method has been proposed to reduce the computational complexity [4–6]. The method is also unconditionally stable and has second-order accuracy in space. The scattered field formulations presented in [9–11] reveal good accuracies compared to the total/scattered field formulations due to the fact that the scattered field formulation takes into consideration the exact analytical calculations of the incident fields at the different FDTD cells [12]. This is in contradictory to the total/scattered field formulation which is based on the assumption of a radiating box that separates between the total field and the scattered field regions. The incident field is calculated by propagation through the FDTD lattice which allows for the numerical errors in the incident field calculations. In this paper, the split step FDTD is applied to achieve numerical unconditioned stable explicit FDTD scheme. The proposed scheme is extended to the scattered field formulation to provide accurate calculations of the scattered fields.

## 2. PROBLEM FORMULATION

Since the electromagnetic fields are the sum of incident and scattered fields. The total fields can be expressed as $E^t = E^s + E^i$ and $H^t = H^s + H^i$. The superscripts $t$, $s$, and $i$ denotes total, scattered, and incident fields, respectively.

For nonmagnetic materials, Maxwell's equations for the scattered fields can be expressed as [2]

$$\nabla X H^s = \sigma E^s + \varepsilon \frac{\partial E^s}{\partial t} + (\varepsilon - \varepsilon_0) \frac{\partial E^i}{\partial t} + \sigma E^i \tag{1}$$

$$\nabla X E^s = \mu \frac{\partial H^s}{\partial t} \tag{2}$$

The 3D Maxwell's Equations (1) and (2) for a medium with constant permittivity $\varepsilon$, constant

permeability $\mu$ and constant conductivity $\sigma$ is written in Cartesian co-ordinatesas

$$
\begin{cases}
\sigma E_x^s + \varepsilon \dfrac{\partial E_x^s}{\partial t} = \dfrac{\partial H_z^s}{\partial y} - \dfrac{\partial H_y^s}{\partial z} - \left[ (\varepsilon - \varepsilon_0) \dfrac{\partial E_x^i}{\partial t} + \sigma E_x^i \right] \\[2mm]
\sigma E_y^s + \varepsilon \dfrac{\partial E_y^s}{\partial t} = \dfrac{\partial H_x^s}{\partial z} - \dfrac{\partial H_z^s}{\partial x} - \left[ (\varepsilon - \varepsilon_0) \dfrac{\partial E_y^i}{\partial t} + \sigma E_y^i \right] \\[2mm]
\sigma E_z^s + \varepsilon \dfrac{\partial E_z^s}{\partial t} = \dfrac{\partial H_y^s}{\partial x} - \dfrac{\partial H_x^s}{\partial y} - \left[ (\varepsilon - \varepsilon_0) \dfrac{\partial E_z^i}{\partial t} + \sigma E_z^i \right]
\end{cases}
,
\quad
\begin{cases}
\mu \dfrac{\partial H_x^s}{\partial t} = \dfrac{\partial E_y^s}{\partial z} - \dfrac{\partial E_z^s}{\partial y} \\[2mm]
\mu \dfrac{\partial H_y^s}{\partial t} = \dfrac{\partial E_z^s}{\partial x} - \dfrac{\partial E_x^s}{\partial z} \\[2mm]
\mu \dfrac{\partial H_z^s}{\partial t} = \dfrac{\partial E_x^s}{\partial y} - \dfrac{\partial E_y^s}{\partial x}
\end{cases}
$$

Maxwell's equations can be splitted into two groups of 1D sub problems as follows

In the first half time step                   In the second half time step

$$
\begin{cases}
\sigma E_x^s + \varepsilon \frac{\partial E_x^s}{\partial t} = 2\frac{\partial H_z^s}{\partial y} - 2\left[ (\varepsilon - \varepsilon_0) \frac{\partial E_x^i}{\partial t} + \sigma E_x^i \right] \\[2mm]
\mu \frac{\partial H_z^s}{\partial t} = 2\frac{\partial E_x^s}{\partial y}
\end{cases}
,
\qquad
\begin{cases}
\sigma E_x^s + \varepsilon \frac{\partial E_x^s}{\partial t} = -2\frac{\partial H_y^s}{\partial z} \\[2mm]
\mu \frac{\partial H_y^s}{\partial t} = -2\frac{\partial E_x^s}{\partial z}
\end{cases}
$$

$$
\begin{cases}
\sigma E_y^s + \varepsilon \frac{\partial E_y^s}{\partial t} = 2\frac{\partial H_x^s}{\partial z} - 2\left[ (\varepsilon - \varepsilon_0) \frac{\partial E_y^i}{\partial t} + \sigma E_y^i \right] \\[2mm]
\mu \frac{\partial H_x^s}{\partial t} = 2\frac{\partial E_y^s}{\partial z}
\end{cases}
,
\qquad
\begin{cases}
\sigma E_y^s + \varepsilon \frac{\partial E_y^s}{\partial t} = -2\frac{\partial H_z^s}{\partial x} \\[2mm]
\mu \frac{\partial H_z^s}{\partial t} = -2\frac{\partial E_y^s}{\partial x}
\end{cases}
$$

$$
\begin{cases}
\sigma E_z^s + \varepsilon \frac{\partial E_z^s}{\partial t} = 2\frac{\partial H_y^s}{\partial x} - 2\left[ (\varepsilon - \varepsilon_0) \frac{\partial E_z^i}{\partial t} + \sigma E_z^i \right] \\[2mm]
\mu \frac{\partial H_y^s}{\partial t} = 2\frac{\partial E_z^s}{\partial x}
\end{cases}
,
\qquad
\begin{cases}
\sigma E_z^s + \varepsilon \frac{\partial E_z^s}{\partial t} = -2\frac{\partial H_x^s}{\partial y} \\[2mm]
\mu \frac{\partial H_x^s}{\partial t} = -2\frac{\partial E_z^s}{\partial y}
\end{cases}
$$

From the splitted equations, it is noticed that the two groups are mutually uncoupled 1D differential equations and the factor of 2 is added due to the splitting process. Note also that the incident field is computed in the first half time step while in the second time step, the incident fields are computed by propagation from the first half time step.

The update equations in the first half time step are

$$
E_{xs}^{n+1/4} = C_1 E_{xs}^{n-1/4} + Dtedy \left( H_{zs}^n (i,j,k) - H_{zs}^n (i,j-1,k) \right) - eincc * E_{xi}^n - edevcn * \frac{\partial E_{xi}^n}{\partial t} \quad (3)
$$

$$
E_{ys}^{n+1/4} = C_1 E_{ys}^{n-1/4} + Dtedz \left( H_{xs}^n (i,j,k) - H_{xs}^n (i,j,k-1) \right) - eincc * E_{yi}^n - edevcn * \frac{\partial E_{yi}^n}{\partial t} \quad (4)
$$

$$
E_{zs}^{n+1/4} = C_1 E_{zs}^{n-1/4} + Dtedx \left( H_{ys}^n (i,j,k) - H_{ys}^n (i-1,j,k) \right) - eincc * E_{zi}^n - edevcn * \frac{\partial E_{zi}^n}{\partial t} \quad (5)
$$

where

$$
C_1 = \frac{4\varepsilon - \sigma \Delta t}{4\varepsilon + \sigma \Delta t} \tag{6a}
$$

$$
Dtedx = \frac{2\Delta t}{(4\varepsilon + \sigma \Delta t)\, \Delta x} \tag{6b}
$$

$$
Dtedy = \frac{2\Delta t}{(4\varepsilon + \sigma \Delta t)\, \Delta y} \tag{6c}
$$

$$
Dtedz = \frac{2\Delta t}{(4\varepsilon + \sigma \Delta t)\, \Delta z} \tag{6d}
$$

$$
eincc = \frac{2\sigma \Delta t}{(4\varepsilon + \sigma \Delta t)} \tag{6e}
$$

$$
edevcn = \frac{2\Delta t\,(\varepsilon - \varepsilon_0)}{(4\varepsilon + \sigma \Delta t)} \tag{6f}
$$

$$
H_{xs}^{n+1/2} = H_{xs}^n + Dtmdz \left( E_{ys}^{n+1/4}(i,j,k+1) - E_{ys}^{n+1/4}(i,j,k) \right) \tag{7}
$$

$$
H_{ys}^{n+1/2} = H_{ys}^n + Dtmdx \left( E_{zs}^{n+1/4}(i+1,j,k) - E_{zs}^{n+1/4}(i,j,k) \right) \tag{8}
$$

$$H_{zs}^{n+1/2} = H_{zs}^n + Dtmdy \left( E_{xs}^{n+1/4} (i, j+1, k) - E_{xs}^{n+1/4} (i, j, k) \right) \tag{9}$$

$$Dtmdx = \frac{\Delta t}{2\mu\Delta x} \tag{10a}$$

$$Dtmdy = \frac{\Delta t}{2\mu\Delta y} \tag{10b}$$

$$Dtmdz = \frac{\Delta t}{2\mu\Delta z} \tag{10c}$$

The update equations in the second half time step are

$$E_{xs}^{n+3/4} = C_1 E_{xs}^{n+1/4} - Dtedz \left( H_{ys}^{n+1/2} (i, j, k) - H_{ys}^{n+1/2} (i, j, k-1) \right) \tag{11}$$

$$E_{ys}^{n+3/4} = C_1 E_{ys}^{n+1/4} - Dtedx \left( H_{zs}^{n+1/2} (i, j, k) - H_{zs}^{n+1/2} (i-1, j, k) \right) \tag{12}$$

$$E_{zs}^{n+3/4} = C_1 E_{zs}^{n+1/4} - Dtedy \left( H_{xs}^{n+1/2} (i, j, k) - H_{xs}^{n+1/2} (i, j-1, k) \right) \tag{13}$$

$$H_{xs}^{n+1} = H_{xs}^{n+1/2} - Dtmdy \left( E_{?-s}^{n+3/4} (i, j+1, k) - E_{zs}^{n+3/4} (i, j, k) \right) \tag{14}$$

$$H_{ys}^{n+1} = H_{ys}^{n+1/2} - Dtmdz \left( E_{xs}^{n+3/4} (i, j, k+1) - E_{xs}^{n+3/4} (i, j, k) \right) \tag{15}$$

$$H_{zs}^{n+1} = H_{zs}^{n+1/2} - Dtmdx \left( E_{ys}^{n+3/4} (i+1, j, k) - E_{ys}^{n+3/4} (i, j, k) \right) \tag{16}$$

## 3. RESULTS AND DISCUSSIONS

The validation of the scheme for the scattered field formulation and the the illustration of the unconditional stability are shown via the illumination of a lossy sphere of 8.2 unit cell radius with plane wave polarized in the $x$-direction and propagated in the $z$ direction. The permittivity of the lossy sphere is chosen to be four times that of free space while the conductivity is chosen to be $0.005\,\text{s/m}$. The computational domain has cell sizes of $\Delta x = \Delta y = \Delta z = 1/17\,\text{m}$ and a mesh size of $80 * 80 * 80$. The plane wave excitation has the form $E_x^i = 1000 \exp\left(-\propto (\tau - \beta\Delta t)^2\right)$. Where
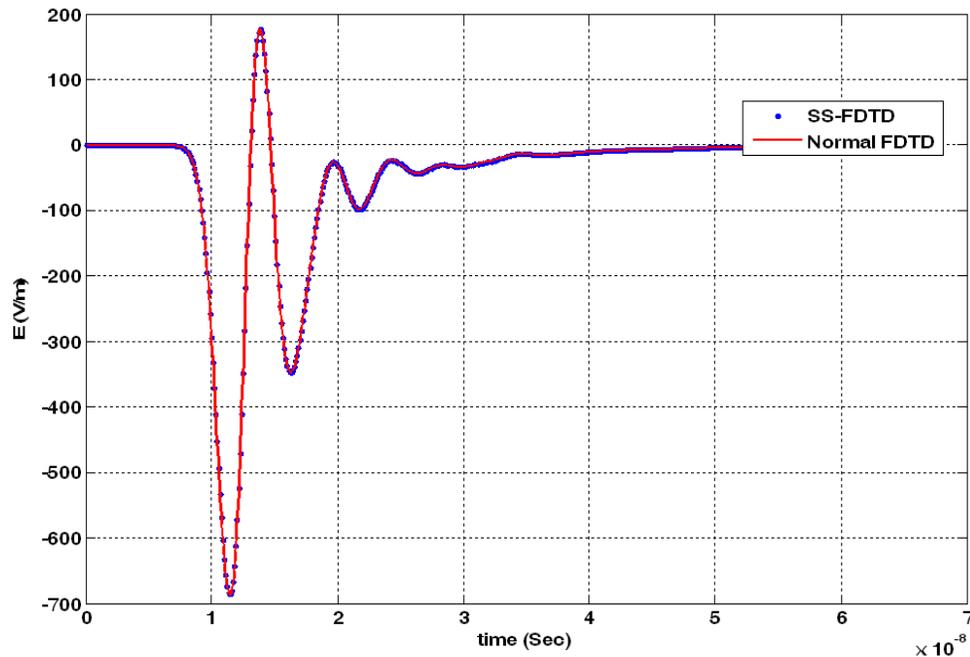


Figure 1: The scattered field at the center of lossy sphere computed using the proposed scheme and compared to the normal FDTD [4].

the time delay $\tau$ is given by $\tau = t - z/c$. $c$ is the speed of light. Let $\beta = 64$, where $\beta$ is the number of time steps in the Gaussian pulse from the peak value to the truncation value. The pulse will exist from $\tau = 0$ until $\tau = 2\beta\Delta t$; approximated as zero outside this range, with peak value at $\tau = \beta\Delta t$ and $\propto = (4/\beta\Delta t)^2$. Figure 1 shows the scattered field at the center of a lossy sphere with double the Courant limit time step. The results are compared to the normal FDTD (Yee algorithm [1]) method under the constraint of the Courant condition [4]. Excellent agreement is observed as shown in the Figure 1.

## 4. CONCLUSION

A scattered field formulation for the split stepped formulation is presented. The algorithm achieves unconditional stable FDTD method since it achieves good accuracies at time step double that of the Courant limit. The scattered field formulation provides accurate calculations for the incident electric field at each FDTD lattice cells. This formulation avoids the calculations of the fields at a radiating box in order to get the incident field by propagation through the FDTD lattice as in the conventional total/scattered field formulations. This will avoid the numerical error in the incident field calculations. The testing results reveal efficient calculation of the scattered field at the center of a lossy sphere. One of the main features of the proposed algorithm is that the update equations in each fractional step consists of uncoupled field equations which is very useful in the parallel processing algorithms. This aspect will be the subject of a future work.

**REFERENCES**

1. Yee, K. S., "Numerical solution of initial boundary value problems involving Maxwell's equations in isotropic media," *IEEE Trans. Antennas Propagat.*, Vol. 14, 302–307, 1966.
2. Zheng, F., Z. Chen, and J. Zhang, "Toward the development of a three dimensional unconditionally stable finite-difference time-domain method," *IEEE Trans. Microw. Theory Tech.*, Vol. 48, 1550–1558, 2000.
3. Zheng, F., Z. Chen, and J. Zhang, "A finite-difference time-domain method without the Courant stability Conditions," *IEEE Microw. Guide. Wave Lett.*, Vol. 11, 441–443, 1999.
4. Kunz, K. S. and R. J. Luebbers, *The Finite Difference Time Domain Method for Electromagnetics*, CRC Press, Boca Raton, FL, 1993.
5. Lee, J. and B. Fornberg, "Some unconditionally stable time stepping methods for the 3D Maxwell's equations," *J. Comput. Appl. Math.*, Vol. 166, 497–523, 2004.
6. Sun, G. and C. W. Trueman, "Efficient implementations of the Crank-Nicolson scheme for the finite-difference time-domain method," *IEEE Trans. Microw. Theory Tech.*, Vol. 54, 2196–2202, 2006.
7. Fu, W. and E. L. Tan, "Development of split-step FDTD method with higher-order spatial accuracy," *Electron. Lett.*, Vol. 40, 1252–1253, 2004.
8. Xiao, F., X. Tang, L. Guo, and T. Wu, "High-order accurate split-step FDTD method for solution of Maxwell's equations," *Electron. Lett.*, Vol. 43, 72–73, 2007.
9. Abdullah, H. H., F. M. El-Hefnawi, and A. Z. Elsherbeni, "A FDTD scattered field formulation for dispersive media," *APS-2000 Symposium*, 248–251, Salt Lake City, 2000.
10. Abdullah, H. H., F. M. EL-Hefnawi, E. A. Hashish, and A. Z. Elsherbeni, "Scattered field FDTD formulations for Debye dispersive media," *URSI, International Conference on Electromagnetic in Advanced Applications, ICEAA*, 3–6, Turin, Italy, Sep. 10–14, 2001.
11. Abdullah, H. H., F. M. El-Hefnawi, E. A. Hashish, and A. Z. Elsherbeni, "Scattered field FDTD formulation for *n*-order Debye dispersion analysis," *World Multi-Conference on Systemic, Cybernetics and Informatics, ISAS-SCI*, 122–125, Orlando, Florida, Jul. 22–25, 2001.
12. Taflove, A. and S. C. Hagness, *Computational Electrodynamics: The Finite Difference Time Domain Method*, 2nd Edition, Artech, Boston, MA, 2000.

# An Unconditionally-stable FDTD Method with Low Anisotropy in Three-dimensional Domains

**Yong-Dan Kong[1] and Qing-Xin Chu[1, 2]**

[1]School of Electronic and Information Engineering
South China University of Technology, Guangzhou, Guangdong 510640, China
[2]The State Key Laboratory of Millimeter Waves, Nanjing, Jiangsu 210096, China

**Abstract**— A novel unconditionally-stable finite-difference time-domain (FDTD) method with low anisotropy in three-dimensional (3-D) domains is presented, which is based on the split-step scheme. Symmetric operator and uniform splitting are adopted simultaneously to split the matrix derived from the classical Maxwell's equations into four sub-matrices. Accordingly, the time step is divided into four sub-steps, and a new split-step FDTD method with four sub-steps is introduced. Compared with the well-known alternating direction implicit (ADI)-FDTD method and the locally-one-dimensional (LOD)-FDTD method, the proposed method has much lower dispersion error and normalized phase velocity anisotropic error. Specifically, for the proposed method, corresponding to a certain cell per wavelength (CPW), there is a Courant-Friedrichs-Lewy number (CFLN) value making the normalized phase velocity anisotropic error to be zero.

## 1. INTRODUCTION

Recently, to remove the Courant-Friedrichs-Lewy (CFL) limitation [1] on the time step size of the FDTD method [2], an unconditionally-stable FDTD method based on the alternating direction implicit (ADI) technique was developed [3]. The ADI-FDTD method has second-order accuracy both in time and space. However, it presents large numerical dispersion error with large time steps. Subsequently, other unconditionally-stable methods such as spit-step [4, 5] and locally-one dimensional (LOD) [6, 7] FDTD methods were developed. The LOD-FDTD method can be considered as split-step approach (SS1) with first-order accuracy in time, which consumes less CPU time than that of the ADI-FDTD method. Subsequently, to improve the accuracy, unconditionally-stable split-step FDTD methods with high-order accuracy and low dispersion were proposed in [8–11]. However, these methods are proposed in 2-D domains.

To achieve high-order accuracy and low anisotropy, a novel unconditionally-stable FDTD method in 3-D domains is proposed in this paper, which is based on the split-step scheme and has four sub-steps. Specifically, the normalized numerical phase velocity error, the dispersion error and the normalized phase velocity anisotropic error of the proposed method are lower than those of the ADI-FDTD method and the LOD-FDTD method. Another important aspect of the proposed method is that for a certain CPW, there is a CFLN value making the normalized phase velocity anisotropic error to be zero.

## 2. THE SCHEME OF THE PROPOSED METHOD

In linear, isotropic, non-dispersive and lossless medium, $\varepsilon$ and $\mu$ are the electric permittivity and magnetic permeability, respectively. Then, the 3-D Maxwell's equations can be written in a matrix form as

$$\frac{\partial \vec{u}}{\partial t} = [M]\,\vec{u}. \tag{1}$$

where $\vec{u} = [E_x, E_y, E_z, H_x, H_y, H_z]^T$, and $[M]$ is the Maxwell's matrix, which is shown as follows.

$$[M] = \begin{bmatrix} 0 & 0 & 0 & 0 & -\frac{1}{\varepsilon}\frac{\partial}{\partial z} & \frac{1}{\varepsilon}\frac{\partial}{\partial y} \\ 0 & 0 & 0 & \frac{1}{\varepsilon}\frac{\partial}{\partial z} & 0 & -\frac{1}{\varepsilon}\frac{\partial}{\partial x} \\ 0 & 0 & 0 & -\frac{1}{\varepsilon}\frac{\partial}{\partial y} & \frac{1}{\varepsilon}\frac{\partial}{\partial x} & 0 \\ 0 & \frac{1}{\mu}\frac{\partial}{\partial z} & -\frac{1}{\mu}\frac{\partial}{\partial y} & 0 & 0 & 0 \\ -\frac{1}{\mu}\frac{\partial}{\partial z} & 0 & \frac{1}{\mu}\frac{\partial}{\partial x} & 0 & 0 & 0 \\ \frac{1}{\mu}\frac{\partial}{\partial y} & -\frac{1}{\mu}\frac{\partial}{\partial x} & 0 & 0 & 0 & 0 \end{bmatrix}$$

Symmetric operator and uniform splitting are exploited to decompose the matrix $[M]$ into four parts $[A]/2$, $[B]/2$, $[B]/2$, and $[A]/2$, respectively, where

$$[A] = \begin{bmatrix} 0 & 0 & 0 & 0 & 0 & \frac{1}{\varepsilon}\frac{\partial}{\partial y} \\ 0 & 0 & 0 & \frac{1}{\varepsilon}\frac{\partial}{\partial z} & 0 & 0 \\ 0 & 0 & 0 & 0 & \frac{1}{\varepsilon}\frac{\partial}{\partial x} & 0 \\ 0 & \frac{1}{\mu}\frac{\partial}{\partial z} & 0 & 0 & 0 & 0 \\ 0 & 0 & \frac{1}{\mu}\frac{\partial}{\partial x} & 0 & 0 & 0 \\ \frac{1}{\mu}\frac{\partial}{\partial y} & 0 & 0 & 0 & 0 & 0 \end{bmatrix} \quad [B] = - \begin{bmatrix} 0 & 0 & 0 & 0 & \frac{1}{\varepsilon}\frac{\partial}{\partial z} & 0 \\ 0 & 0 & 0 & 0 & 0 & \frac{1}{\varepsilon}\frac{\partial}{\partial x} \\ 0 & 0 & 0 & \frac{1}{\varepsilon}\frac{\partial}{\partial y} & 0 & 0 \\ 0 & 0 & \frac{1}{\mu}\frac{\partial}{\partial y} & 0 & 0 & 0 \\ \frac{1}{\mu}\frac{\partial}{\partial z} & 0 & 0 & 0 & 0 & 0 \\ 0 & \frac{1}{\mu}\frac{\partial}{\partial x} & 0 & 0 & 0 & 0 \end{bmatrix}$$

Then, (1) can be written as

$$\frac{\partial \vec{u}}{\partial t} = \frac{[A]}{2} \cdot \vec{u} + \frac{[B]}{2} \cdot \vec{u} + \frac{[B]}{2} \cdot \vec{u} + \frac{[A]}{2} \cdot \vec{u}. \tag{2}$$

By using the split-step scheme [4], (2) is divided into four sub-equations, from $n$ to $n+1$, one time step is divided into four sub-steps accordingly, $n \to n+1/4$, $n+1/4 \to n+2/4$, $n+2/4 \to n+3/4$, and $n+3/4 \to n+1$, by successively solving

$$\text{sub-step } 1: \frac{\partial \vec{u}}{\partial t} = 4 \cdot \frac{[A]}{2} \cdot \vec{u} \quad n \to n+1/4 \tag{3a}$$

$$\text{sub-step } 2: \frac{\partial \vec{u}}{\partial t} = 4 \cdot \frac{[B]}{2} \cdot \vec{u} \quad n+1/4 \to n+2/4 \tag{3b}$$

$$\text{sub-step } 3: \frac{\partial \vec{u}}{\partial t} = 4 \cdot \frac{[B]}{2} \cdot \vec{u} \quad n+2/4 \to n+3/4 \tag{3c}$$

$$\text{sub-step } 4: \frac{\partial \vec{u}}{\partial t} = 4 \cdot \frac{[A]}{2} \cdot \vec{u}. \quad n+3/4 \to n+1 \tag{3d}$$

Furthermore, the right side of the above equations can be approximated by using the Crank-Nicolson scheme [10]. Subsequently, four sub-procedures are generated as follows

$$\left([I] - \frac{\Delta t}{4} \cdot [A]\right) \vec{u}^{n+1/4} = \left([I] + \frac{\Delta t}{4} \cdot [A]\right) \vec{u}^n \tag{4a}$$

$$\left([I] - \frac{\Delta t}{4} \cdot [B]\right) \vec{u}^{n+2/4} = \left([I] + \frac{\Delta t}{4} \cdot [B]\right) \vec{u}^{n+1/4} \tag{4b}$$

$$\left([I] - \frac{\Delta t}{4} \cdot [B]\right) \vec{u}^{n+3/4} = \left([I] + \frac{\Delta t}{4} \cdot [B]\right) \vec{u}^{n+2/4} \tag{4c}$$

$$\left([I] - \frac{\Delta t}{4} \cdot [A]\right) \vec{u}^{n+1} = \left([I] + \frac{\Delta t}{4} \cdot [A]\right) \vec{u}^{n+3/4}. \tag{4d}$$

where $[I]$ is a $6 \times 6$ identity matrix.

## 3. NUMERICAL STABILITY AND DISPERSION ANALYSIS

By using the Fourier method, assuming $k_x$, $k_y$, and $k_z$ to be the spatial frequencies along the $x$, $y$, and $z$ directions, the field components in spectral domain at the $n$th time step can be denoted as

$$U\big|_{I,J,K}^n = U^n e^{-j(k_x I \Delta x + k_y J \Delta y + k_z K \Delta z)}. \tag{5}$$

By substituting (5) into (4a)–(4d), the following equations can be generated

$$U^{n+1} = [\Lambda]_A [\Lambda]_B [\Lambda]_B [\Lambda]_A U^n = [\Lambda] U^n. \tag{6}$$

where $[\Lambda]$ is the growth matrix, and

$$[\Lambda]_A = \begin{bmatrix} -\frac{B_y}{A_y} & 0 & 0 & 0 & 0 & \frac{4jbP_y}{A_y} \\ 0 & -\frac{B_z}{A_z} & 0 & \frac{4jbP_z}{A_z} & 0 & 0 \\ 0 & 0 & -\frac{B_x}{A_x} & 0 & \frac{4jbP_x}{A_x} & 0 \\ 0 & \frac{4jdP_z}{A_z} & 0 & -\frac{B_z}{A_z} & 0 & 0 \\ 0 & 0 & \frac{4jdP_x}{A_x} & 0 & -\frac{B_x}{A_x} & 0 \\ \frac{4jdP_y}{A_y} & 0 & 0 & 0 & 0 & -\frac{B_y}{A_y} \end{bmatrix}$$

$$[\Lambda]_B = \begin{bmatrix} \frac{B_z}{A_z} & 0 & 0 & 0 & -\frac{4jbP_z}{A_z} & 0 \\ 0 & \frac{B_x}{A_x} & 0 & 0 & 0 & -\frac{4jbP_x}{A_x} \\ 0 & 0 & \frac{B_y}{A_y} & -\frac{4jbP_y}{A_y} & 0 & 0 \\ 0 & 0 & -\frac{4jdP_y}{A_y} & \frac{B_y}{A_y} & 0 & 0 \\ -\frac{4jdP_z}{A_z} & 0 & 0 & 0 & \frac{B_z}{A_z} & 0 \\ 0 & -\frac{4jdP_x}{A_x} & 0 & 0 & 0 & \frac{B_x}{A_x} \end{bmatrix}$$

where $\partial/\partial\alpha = jP_\alpha = -2j \cdot \sin(k_\alpha\Delta\alpha/2)/\Delta\alpha$, $b = \Delta t/(2\varepsilon)$, $d = \Delta t/(2\mu)$, $A_\alpha = 4 + bdP_\alpha^2$, $B_\alpha = 4 - bdP_\alpha^2$, $(\alpha = x, y, z)$.

By using Maple 9.0, the eigenvalues of $[\Lambda]$ can be found, as

$$\lambda_1 = \lambda_2 = 1, \ \lambda_3 = \lambda_5 = \lambda_4^* = \lambda_6^* = \xi + j\sqrt{1 - \xi^2}. \tag{7}$$

where $\xi = R/S$, and

$$\begin{aligned} R =& 4096 - 6144bd(P_x^2 + P_y^2 + P_z^2) + 256b^2d^2(P_x^4 + P_y^4 + P_z^4 + 4P_x^2P_y^2 + 4P_y^2P_z^2 + 4P_x^2P_z^2) \\ &+ b^3d^3(6656 \cdot P_x^2P_y^2P_z^2 - 384(P_x^4P_y^2 + P_x^2P_y^4 + P_x^4P_z^2 + P_x^2P_z^4 + P_y^4P_z^2 + P_y^2P_z^4)) \\ &+ 16b^4d^4(4P_x^4P_y^2P_z^2 + 4P_x^2P_y^4P_z^2 + 4P_x^2P_y^2P_z^4 + P_x^4P_y^4 + P_x^4P_z^4 + P_y^4P_z^4) \\ &- 24b^5d^5(P_x^2P_y^4P_z^4 + P_x^4P_y^2P_z^4 + P_x^4P_y^4P_z^2) + b^6d^6P_x^4P_y^4P_z^4 \end{aligned} \tag{8a}$$

$$\begin{aligned} S =& 4096 + 2048bd(P_x^2 + P_y^2 + P_z^2) + 256b^2d^2(P_x^4 + P_y^4 + P_z^4 + 4P_x^2P_y^2 + 4P_y^2P_z^2 + 4P_x^2P_z^2) \\ &+ 128b^3d^3(P_x^4P_y^2 + P_x^2P_y^4 + P_x^4P_z^2 + P_x^2P_z^4 + P_y^4P_z^2 + P_y^2P_z^4 + 4P_x^2P_y^2P_z^2) \\ &+ 16b^4d^4(4P_x^4P_y^2P_z^2 + 4P_x^2P_y^4P_z^2 + 4P_x^2P_y^2P_z^4 + P_x^4P_y^4 + P_x^4P_z^4 + P_y^4P_z^4) \\ &+ 8b^5d^5(P_x^2P_y^4P_z^4 + P_x^4P_y^2P_z^4 + P_x^4P_y^4P_z^2) + b^6d^6P_x^4P_y^4P_z^4 \end{aligned} \tag{8b}$$

It is obvious that the values of $P_\alpha$ corresponding to the second-order central finite-difference scheme are all real numbers. Since $|\lambda_1| = |\lambda_2| = |\lambda_3| = |\lambda_4| = |\lambda_5| = |\lambda_6| = 1$, we can conclude that the proposed method is unconditionally stable.

Assume the field to be a monochromatic wave with angular frequency $\omega$

$$E_\alpha^n = E_\alpha e^{j\omega\Delta tn}, \quad H_\alpha^n = H_\alpha e^{j\omega\Delta tn}, \quad \alpha = x, y, z. \tag{9}$$

Then, (6) can be expressed as

$$(e^{j\omega\Delta t}[I] - [\Lambda])U^n = \mathbf{0}. \tag{10}$$

where $U^n$ is related to the initial field vector $U^0$ and defined by

$$U^n = U^0 e^{j\omega\Delta tn}. \tag{11}$$

For a nontrivial solution of (10), the determinant of the coefficient matrix should be zero as follows

$$\det(e^{j\omega\Delta t}[I] - [\Lambda]) = 0. \tag{12}$$

With reference to the eigenvalues of $[\Lambda]$ above, the dispersion relationship of the proposed method can be deduced in (13).

$$\tan^2(\omega\Delta t/2) = (1 - \xi)/(1 + \xi). \tag{13}$$

## 4. PERFORMANCES OF THE PROPOSED METHOD

In this section, the numerical dispersion and the anisotropy performances of the proposed method have been studied for different parameters such as the propagation angle, the mesh size and the time step. The results are in 3-D domains and compared with the results of previously published ADI-FDTD method and the LOD-FDTD method.

Figure 1 shows the normalized numerical phase velocities versus $\varphi$ with $\theta = 0°$, $45°$, CFLN = 2, $R = 1$, and CPW = 10 for three unconditionally-stable FDTD methods. As can be seen from Fig. 1, the normalized numerical phase velocities of the proposed method are better than those of the ADI-FDTD method and the LOD-FDTD method. Moreover, the accuracy of the ADI-FDTD method is similar to that of the LOD-FDTD method. For instance, with $\theta = 0°$, the normalized numerical phase velocities of the ADI-FDTD method, the LOD-FDTD method, and the proposed method are 0.944, 0.944, and 0.974, respectively; Corresponding the normalized numerical phase velocities errors are 5.6%, 5.6%, and 2.6%, respectively. In other word, the normalized numerical phase velocity error of the proposed method is reduced by more than 53% in comparison with the ADI-FDTD method and the LOD-FDTD method.

Figure 2 shows the dispersion errors versus CFLN with $\theta = 0°$, $45°$, $R = 1$, CPW = 50, and $\varphi = 90°$ for three unconditionally-stable FDTD methods. From Fig. 2, with CFLN = 15 and $\theta = 0°$, the dispersion errors of the ADI-FDTD method and the LOD-FDTD method are 8.5% and 8.5%. However, the dispersion error of the proposed method is 2.4%, which is lower than those of the ADI-FDTD method and the LOD-FDTD method. On the other hand, the dispersion errors of three unconditionally-stable FDTD methods increase as CFLN increases. Nevertheless, the increase of the dispersion error of the proposed method is much less pronounced than those of the ADI-FDTD method and the LOD-FDTD method. Furthermore, the value of the dispersion error of the proposed method with $\theta = 0°$ is similar to that of the value with $\theta = 45°$.

Figure 3 shows the dispersion errors versus CPW with $\theta = 0°$, $45°$, $R = 1$, CFLN = 4, and $\varphi = 90°$ for three unconditionally-stable FDTD methods. As can be seen from Fig. 3, the dispersion errors decrease as CPW increases. Moreover, the proposed method with CPW = 40 has the same dispersion error compared with the ADI-FDTD method and the LOD-FDTD method with CPW = 20. It is concluded that the proposed method with the coarsest mesh leads to the same level of accuracy as the ADI-FDTD method with the finest mesh. Such an improvement of the accuracy, which is realized by the proposed method with the coarsest mesh, lead to other advantages, such as higher computational efficiency and lower memory requirements.

Figure 4 shows the normalized phase velocity anisotropic errors versus CFLN with $\theta = 45°$, $90°$, $R = 1$, and CPW = 50 for three unconditionally-stable FDTD methods. From Fig. 4, the normalized phase velocity anisotropic errors increase as CFLN increases. However, the normalized phase velocity anisotropic error of the proposed method is lower than the other two methods. Particularly, for the proposed method, corresponding to a certain CPW, there is a CFLN value
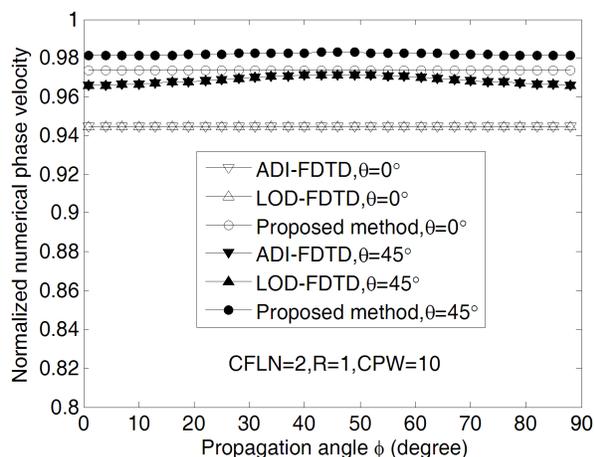


Figure 1: Normalized numerical phase velocities versus $\phi$ with $\theta = 0°$, $45°$, CFLN = 2, $R = 1$, and CPW = 10 for three unconditionally-stable FDTD methods.
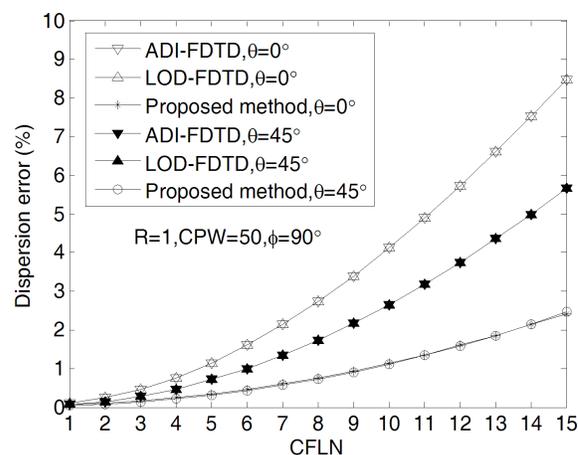
Figure 2: Dispersion errors versus CFLN with $\theta = 0°$, $45°$, $R = 1$, CPW = 50, and $\phi = 90°$ for three unconditionally-stable FDTD methods.
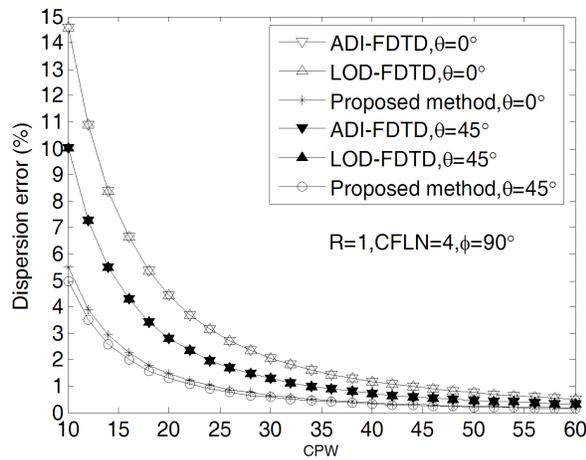
Figure 3: Dispersion errors versus CPW with $\theta = 0°$, $45°$, $R = 1$, CFLN $= 4$, and $\phi = 90°$ for three unconditionally-stable FDTD methods.
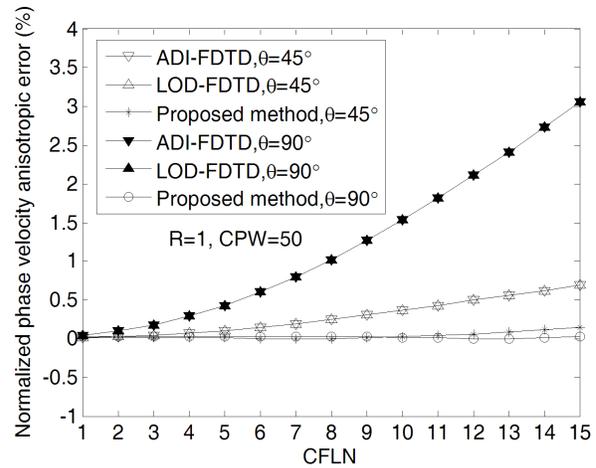


Figure 4: Normalized phase velocity anisotropic errors versus CFLN with $\theta = 45°$, $90°$, $R = 1$, and CPW $= 20$ for three unconditionally-stable FDTD methods.
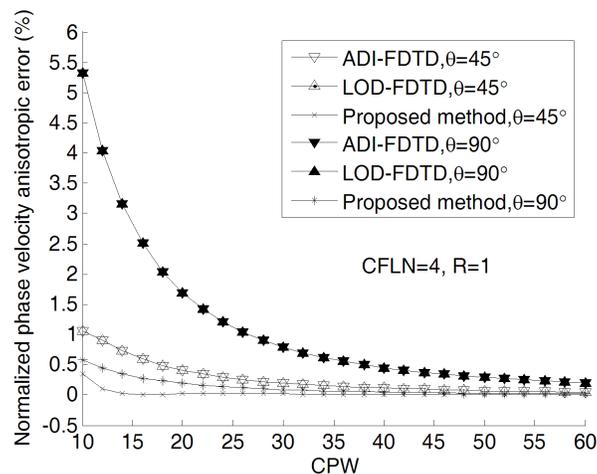


Figure 5: Normalized phase velocity anisotropic errors versus CPW with $\theta = 45°$, $90°$, CFLN $= 4$, and $R = 1$ for three unconditionally-stable FDTD methods.

causing the numerical phase velocity anisotropic error to be zero.

Figure 5 shows the normalized phase velocity anisotropic errors versus CPW with $\theta = 45°$, $90°$, CFLN $= 4$, and $R = 1$ for three unconditionally-stable FDTD methods. From Fig. 5, the normalized phase velocity anisotropic errors decrease as CPW increases, and similarly, the normalized phase velocity anisotropic error of the proposed method is lower than the other two methods. Specifically, for the proposed method, corresponding to a certain CFLN value, there is a CPW value making the normalized phase velocity anisotropic error to be zero.

## 5. CONCLUSION

A novel unconditionally-stable finite-difference time-domain (FDTD) method with low anisotropy in 3-D domains has been presented. Symmetric operator and uniform splitting are adopted simultaneously to split the Maxwell's matrix into four sub-matrices. Accordingly, the time step is divided into four sub-steps. Compared with the ADI-FDTD method and the LOD-FDTD method, the normalized numerical phase velocity of the proposed method has been improved. Furthermore, the dispersion error and normalized phase velocity anisotropic error of the proposed method have been greatly reduced. Specifically, for the proposed method, corresponding to a certain CPW value, there is a CFLN value making the normalized phase velocity anisotropic error to be zero.

**ACKNOWLEDGMENT**

**REFERENCES**

1. Taflove, A. and S. C. Hagness, *Computational Electrodynamics: The Finite-Difference Time-Domain Method*, 2nd Edition, Artech House, Boston, MA, 2000.
2. Yee, K. S., "Numerical solution of initial boundary value problems involving Maxwell's equations in isotropic media," *IEEE Trans. Antennas Propag.*, Vol. 14, No. 3, 302–307, May 1966.
3. Zheng, F., Z. Chen, and J. Zhang, "Toward the development of a three-dimensional unconditionally stable finite-difference time-domain method," *IEEE Trans. Microw. Theory Tech.*, Vol. 48, No. 9, 1550–1558, Sep. 2000.
4. Lee, J. and B. Fornberg, "A split step approach for the 3-D Maxwell's equations," *J. Comput. Appl. Math.*, No. 158, 485–505, Mar. 2003.
5. Lee, J. and B. Fornberg, "Some unconditionally stable time stepping methods for the 3D Maxwell's equations," *J. Comput. Appl. Math.*, No. 166, 497–523, Mar. 2004.
6. Shibayama, J., M. Muraki, J. Yamauchi, and H. Nakano, "Effcient implicit FDTD algorithm based on locally one-dimensional scheme," *Electron. Lett.*, Vol. 41, No. 19, 1046–1047, Sep. 2004.
7. Liu, Q. F., Z. Chen, and W. Y. Yin, "An arbitrary order LOD-FDTD method and its stability and numerical dispersion," *IEEE Trans. Antennas Propag.*, Vol. 57, No. 8, 2409–2417, Aug. 2009.
8. Fu, W. and E. L. Tan, "Development of split-step FDTD method with higher-order spatial accuracy," *Electron. Lett.*, Vol. 40, No. 20, 1252–1253, Sep. 2005.
9. Kusaf, M. and A. Y. Oztoprak, "An unconditionally stable split-step FDTD method for low anisotropy," *IEEE Microw. Wireless Compon. Lett.*, Vol. 18, No. 4, 224–226, Apr. 2008.
10. Chu, Q. X. and Y. D. Kong, "High-order accurate FDTD method based on split-step scheme for solving Maxwell's equations," *Microwave Optical Technol. Lett.*, Vol. 51, No. 2, 562–565, Feb. 2009.
11. Chu, Q. X. and Y. D. Kong, "Three new unconditionally-stable FDTD methods with high-order accuracy," *IEEE Trans. Antennas Propag.*, Vol. 57, No. 9, 2675–2682, Sep. 2009.

# SAR Computation of a Human Head Exposed to Different Mobile Headsets Using FDTD Method

**Reza Aminzadeh**[1, 2], **Mehrangiz Ashiri**[1, 2], **and Ali Abdolali**[1, 3]

[1]Bioelectromagnetics Research Group
Iran University of Science and Technology, Tehran, Iran
[2]School of Science and Engineering
Sharif University of Technology, International Campus, Kish Island, Iran
[3]Department of Electrical Engineering
Iran University of Science and Technology, Tehran, Iran

**Abstract**— Many standards are not considering Specific Absorption Rate (SAR) measurements with the use of mobile headsets. In this paper a simulation of mobile headset effects on a human head is done using FDTD-based platform, SEMCAD-X software. We designed two headset models with different case materials to observe their interaction with a Specific Anthropomorphic Mannequin (SAM) phantom as a human head model. Both headset models are installed in the left ear and the human head is rotated by 30°. As headset communicates via Bluetooth at the frequency of 2.4 GHz, we chose a suitable planar inverted F antenna (PIFA) to use with both the headset models. Spatial peak SAR values averaged over 1 g and 10 g for each model in both the environments and compared to each other. The results confirm that the value of SAR in a car is lower than free space due to the presence of dielectric materials in the car. We conclude that headset case material has a high impact on SAR changes in different environments.

## 1. INTRODUCTION

As the mobile phone technologies grow up faster, the number of people using mobile headsets is increasing. Headsets are easier to use for several people even a child or an adult. Exposure to the radiation pattern of a mobile headset seems to be safer than mobile handsets. Mobile headsets communicate to the mobile phone via Bluetooth at 2400 MHz to 2450 MHz frequency band. Bluetooth-based applications are classified in three categories. Headsets are classified in the 2nd category where the maximum radiation power is 2.5 mW (4 dBm). These days several manufacturers produce different types of headsets. Their induced SAR in a human head differs due to the antenna type, housing, operation frequency, battery type, dimensions and etc. Many standards like IEEE-1528 [1] and IEEE-1529 [2] are not considering SAR measurements with the use of mobile headsets. Several methods have been deployed for computation of SAR for mobile phones [3, 4]. Previous studies did not consider SAR measurements of a human head exposed to different mobile headsets and their interaction in different environments.

In this paper, we measured SAR values for two different headsets in free space and a car using explicit FDTD (Finite Difference Time Domain) method due to its simplicity and direct applicability to Maxwell's equations. After studying several mobile headsets, we designed two headset models based on popular models. The electromagnetic radiation was produced by a planar inverted F antenna (PIFA) provided by SEMCAD [5].

## 2. FDTD MODELING

In order to simulate the proposed scenarios and different models, FDTD-based platform simulation software, SEMCAD-X [5] is used. The simulation consists of electromagnetic modeling, working on volumetric pixels called voxels by the help of rendering a 3D object in terms of its electromagnetic characteristics and applying finite differences of Maxwell's equations in the time domain [6].

Two headset cases are designed based on popular models. Most of mobile applications as headsets are made of Acetal [7], Silicon [8] and poly carbonates. In this paper, we chose Acetal and Silicon for our headset models. In the rest of the paper the headset with Acetal case is called Model 1 and the headset with silicon case is named as Model 2. In Figure 1 two headset models mentioned above are shown.

For human head we used SAM phantom (Specific Anthropomorphic Mannequin), a homogeneous model [5] that contains two dielectric parts; SAM shell and liquid. SAM shell is a plastic shell filled with a homogeneous liquid and a loss less space as an ear. Shell parameters are different from the

model introduced by IEEE standard committee [9]. Both headset models are installed in the left ear and the human head is rotated by 30° as shown in Figure 2.

To simulate our models in a car, we used a Ferrari model provided by [5]. We also studied the role of dielectric parts like car seats, dashboard, glass, tires and etc. It is clear that other parts like trunk, chassis, wheels, hood and brakes are considered as PEC/metal parts. Figure 3 depicts the car model. In Table 1 dielectric properties of SAM phantom and headset cases are given [10].

A planar inverted F antenna whose excitation is a 50-Ohm sinusoidal voltage source at the space between the antenna and PCB is used. Figure 4 shows the antenna configuration and dimensions at 2.4 GHz. Antenna parameters are also described in Table 2. A minimum spatial resolution of $0.2 \times 0.2 \times 0.2\,\text{mm}^3$ and a maximum spatial resolution of $5 \times 5 \times 5\,\text{mm}^3$ in the $x$, $y$, and $z$ directions are chosen with a grading ratio of $1 : 2$. The amount of FDTD-grid cells are ($185 \times 135 \times 239 = 5.969$ Mcells) for both models in free space and ($590 \times 319 \times 303 = 57.0276$ Mcells) for both models in the car.

Also a bounding box setting for the antenna is made with refinement on both upper and lower boundary of 0.06 for $Z$ axis. For all solid regions a refining factor of 10 is set. The Absorbing Boundary Conditions (ABC) is set as Uniaxial Perfectly Matched Layer (U-PML) mode with a very high thickness [5]. A transient simulation time of 15 periods is set to achieve a steady state.

## 3. RESULT

There are various types of algorithms to calculate SAR when human body exposure to an electromagnetic field. We measured spatial peak SAR as defined in IEEE-1529 standard recommendation [2]. All the results are achieved with antenna source power of 0.0025 W in 2.4 GHz frequency band as it is the maximum radiation power for the 2nd class Bluetooth devices. Based on IEEE C95.1-1999 [11] and IEEE C95.1-2005 [12], the maximum value of $\text{SAR}_{1g}$ and $\text{SAR}_{10g}$ are 1.6 W/kg and 2 W/kg respectively while all of our results are lower than 0.130 W/kg. As it can be seen in Table 3, the maximum value for $\text{SAR}_{1g}$ is for model 1 in free space (0.1228 W/kg) while model 2 has the minimum value in car (0.0452 W/kg). The maximum value of $\text{SAR}_{10g}$ is for model 1 in free space (0.0455 W/kg) and the minimum value is for model 2 in car (0.0184 W/kg). Based on the results discussed above the best choice here is model 2 which has the minimum amount of SAR induced in head for both environments in car and free space. A significant decrease in SAR values



(a)                    (b)
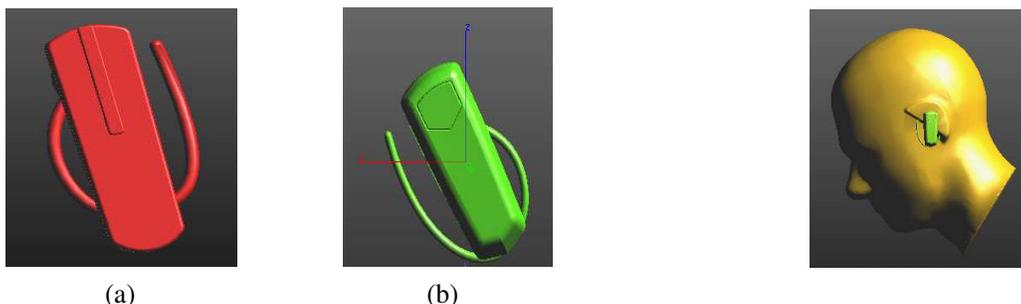
Figure 1: Designed headset CAD models ((a) model 1, (b) model 2).



Figure 2: SAM phantom and installed headset.



Figure 3: Car model.



(a)                    (b)
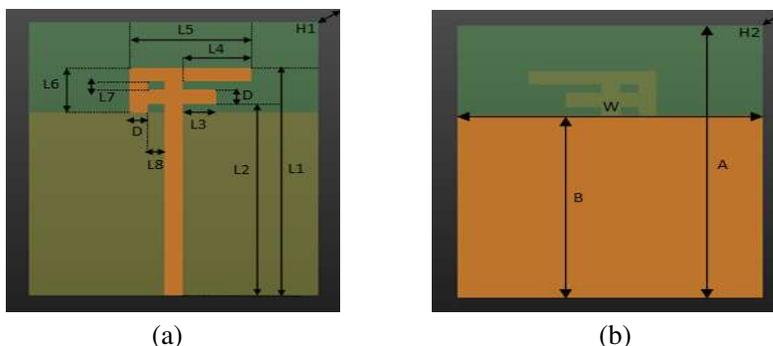
Figure 4: PIFA shape and parameters ((a) F type antenna, (b) antenna ground).

Table 1: Dielectric properties of SAM phantom and headset cases.

| Frequency | 2400 MHz–2450 MHz | |
|---|---|---|
| Material | $\delta$ (s/m) | $\varepsilon_r$ |
| SAM Shell | 0.0016 | 5 |
| SAM Liquid | 1.8 | 39.2 |
| ACETAL | 0.002 | 2.8 |
| SILICON | 0.00156 | 11.68 |

Table 2: Antenna parameters.

| P | Length (mm) | P | Length (mm) |
|---|---|---|---|
| L1 | 50 | D | 3.05 |
| L2 | 41.95 | H1 | 0.1 |
| L3 | 5.9 | A | 60 |
| L4 | 11.9 | B | 40 |
| L5 | 21 | W | 50 |
| L6 | 10 | H2 | 0.1 |
| L7 | 1.95 | H3 | 1.8 |
| L8 | 3 | | |

Table 3: Spatial SAR values averaged over 1 g and 10 g for different models.

| Models | Model 1 | | Model 2 | |
|---|---|---|---|---|
| Place of Simulation | Free Sp | Car | Free Sp | Car |
| Input Power (mW) | 2.5 | 2.5 | 2.5 | 2.5 |
| $\mathrm{SAR_{1g}}$ in Head (W/Kg) | 0.1228 | 0.0967 | 0.0984 | 0.0452 |
| $\mathrm{SAR_{10g}}$ in Head (W/Kg) | 0.0455 | 0.0358 | 0.0405 | 0.0184 |
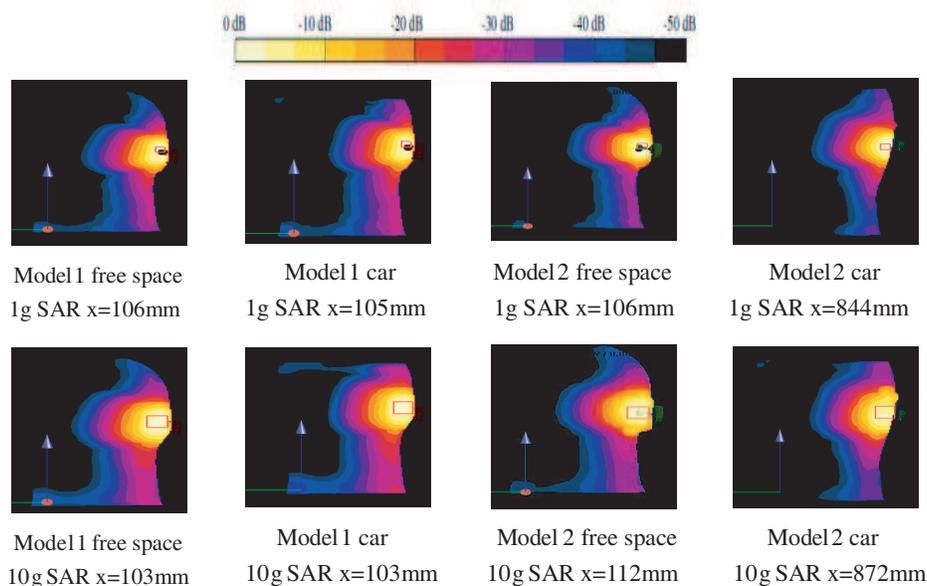


Figure 5: Slice distribution of spatial peak SAR averaged over 1 g and 10 g.

in car can be seen compared to free space. The reason is the presence of dielectric materials in the car that absorb waves radiated from the headset. Metal parts behave in the opposite way, they reflect waves radiated in the car. To study the effect of headset case material on SAR in free space and the car, we calculated SAR difference as follows:

$$\mathrm{SAR}_{dif}\,(\%) = \frac{|\mathrm{SAR}_{car} - \mathrm{SAR}_{free\,sp}|}{\mathrm{SAR}_{free\,sp}} \times 100\% \tag{1}$$

Based on the presented equation, for model 1, the difference for $\mathrm{SAR_{1g}}$ is 21.25% and for $\mathrm{SAR_{10g}}$ calculated as 21.31%. The value of $\mathrm{SAR_{1g}}$ and $\mathrm{SAR_{10g}}$ for model 2, are 54.06% and 54.56% respectively. We conclude that headset case material has a high impact on SAR changes in different environments. Figure 5 shows that the peak SAR occurs in the ear region.

## 4. CONCLUSION

In this paper, we designed two types of headset models and simulated the scenario in free space and a car model using SEMCAD FDTD-based platform. A PIFA was used at 2.4 GHz frequency

with the source input power of 2.5 mW. We calculated spatial peak SAR averaged over 1 g and 10 g for headsets in both the environments. Our results showed that the value of SAR for a headset in a car is lower than free space due to the presence of dielectric materials in the car that absorb radiated waves. We also found that the material used for the headset case can have a significant change on the amount of SAR in different environments. The obtained SAR values were lower than 0.130 W/kg. Model 2 that has a silicon case has the lowest value of SAR compared to the headset with Acetal case.

**REFERENCES**

1. IEEE Standard 1528, "IEEE recommended practice for determining the peak spatial-average specific absorption rate (SAR) in the human head from wireless communication devices: Measurement techniques," Dec. 2003.
2. "Recommended practice for determining the peak spatial-average specific absorption rate (SAR) associated with the use of wireless handsets — Computational techniques," IEEE Draft Standard-1529.
3. Al-Mously, S. I. and M. M. Abousetta, "User's hand effect on TIS of different GSM900/1800 mobile phone models using FDTD method," *Proc. of the International Conference on Computer, Electrical, and System Science, and Engineering*, Dubai, UAE, Jan. 28–30, 2009; *Proc. of the World Academy of Science, Engineering and Technology (PWASET)*, Dubai, UAE, Jan. 28–30, 2009.
4. Li, C. H., E. Ofli, N. Chavannes, and N. Kuster, "SAR and efficiency performance of mobile phone antenna with different user hand positions," *Antennas and Propagation Society International Symposium, APSURSI'09*, Jun. 2009.
5. SEMCAD X, "Reference manual for the SEMCAD simulation platform for electromagnetic compatibility, antenna design and dosimetry," SPEAG, http://www.semcad.com.
6. Smith, D., "Technical report summary electromagnetic characterization through and around human body by simulation using SEMCAD X," *NICTA*, 2008, http://www.nicta.com.au/pub?id=1504.
7. Cho, Y. J., S. H. Hwang, O. Ishida, and S. O. Park, "Dual band internal antenna of PIFA type for mobile handsets and the effect of the handset case and battery," *Proc. of IEEE*, 2005.
8. http://en.wikipedia.org/wiki/Electrical_resistivity_and_conductivity.
9. Beard, B. B., W. Kainz, T. Onishi, T. Iyama, S. Watanabe, O. Fujiwara, J. Wang, G. Bit-Babik, A. Faraone, J. Wiart, A. Christ, N. Kuster, A. Lee, H. Kroeze, M. Siegbahn, J. Keshvari, H. Abrishamkar, W. Simon, D. Manteuffel, and N. Nikoloski, "Comparisons of computed mobile phone induced SAR in the SAM phantom to that in anatomically correct models of the human head," *IEEE Trans. Electromagnetic Compatibility*, Vol. 48, No. 2, May 2006.
10. Test Report No. 105236R-RFCEP39V01, MSI Notebook (MS16G1x) Test Report, 1–38, QuieTek Co., Aug. 2010, cedocuments/notebook/ms16G1x path at www.faenl.msi.com.
11. "IEEE standard for safety levels with respect to human exposure to radio frequency electromagnetic fields, 3 kHz to 300 GHz," IEEE Standard C95.1-1999, 1999.
12. "IEEE standard for safety levels with respect to human exposure to radio frequency electromagnetic fields, 3 kHz to 300 GHz," IEEE Standard C95.1-2005, 2005.

# Transient Electromagnetic Response of a Coaxial Feeding Monopole Antenna Mounted on a Rectangular Metallic Enclosure Illuminated by Electromagnetic Pulses (EMP)

**Qingqing Zhang**[1], **Jian Wang**[1], **and Wen-Yan Yin**[1, 2]

[1]Center for Microwave and RF Technologies
Key Lab of Ministry of Education of EMC and High-Speed Electronic Systems
Shanghai Jiao Tong University, Shanghai 200240, China
[2]Center for Optical and EM Research (COER), State Key Lab of MOI
Zhejiang University, Hangzhou 310058, China

**Abstract**— As we all know, coaxial cables are often used in the feed network of various antennas. In this paper, the terminal electromagnetic interference (EMI) responses of coaxial cables as a feed network of monopole antenna are studied, which is placed in an enclosure with a window on its wall and illuminated by an external pulse. The mathematical treatment is based on the finite-difference time-domain (FDTD) method combined with equivalent feed model method, Node's thin wire method, and two-step coupling method. The results obtained by our coupling method are compared with the direct telegraph equation coupling method, with good agreement achieved. Further, the proposed method is used to perform EMI transient analysis of the practical enclosure model illuminated by external pulses with different incident and polarization directions.

## 1. INTRODUCTION

It is well known that feed networks of antennas in most information systems can be interfered by external electromagnetic pulses (EMP), and under such circumstances, source integrity problem will be caused and the system performance will be degraded [1]. Therefore, in order to protect them from the intentional interference, certain metallic enclosure or cabin will be employed as plotted in Fig. 1, with the feed network often enclosed. However, the external electromagnetic pulses in the environment will produce induced current on the antenna and it couples into the coaxial feeding cable through the interaction at the connection point between the coaxial cable and the monopole antenna [2, 3].

In the other hand, FDTD Feeding models of coaxial cables for antennas have been studied extensively in the past a few years [4, 5]. [5] proposed an equivalent feed model, which captures the equivalent connection port voltage and current of transmission lines as the source for the antenna.In this paper, a hybrid method, based on FDTD method, combined with thin wire antenna model, an equivalent feed model, and telegraph equations, is integrated for computing the EMI responses of the coaxial cable in an enclosure as shown in Fig. 1, which is illuminated by external pulses with different incident and polarization directions.

## 2. HYBRID FDTD METHOD

### 2.1. FDTD Formulas of Thin-wire Antenna

For the thin wire antenna, as shown in Fig. 1, there are several methods to model it in FDTD, such as Taflove's model [6] and Noda's model [7]. When the wire radius is very thin, the latter is more accurate. In Noda's method, applied in this paper, both adjacent electric and magnetic fields are modified by changing the relative permeability and the relative permittivity of the thin wire's adjacent cells. The modified relative permeability and the modified relative permittivity are described as

$$\mu_r' = \mu_r/m, \quad \varepsilon_r' = m\varepsilon_r \tag{1}$$

$$m = \ln\left(\frac{\delta}{a_0}\right) / \ln\left(\frac{\delta}{a}\right), \quad a_0 = 0.230\delta \tag{2}$$

where $\mu_r$ and $\varepsilon_r$ are the relative permeability and permittivity of the original medium surrounding the wire, $\delta$ is the spatial cell size of the FDTD method, $a_0$ is the equivalent radius represented by forcing the tangential components of electric field along the wire axis to be zero, and $a$ is the real
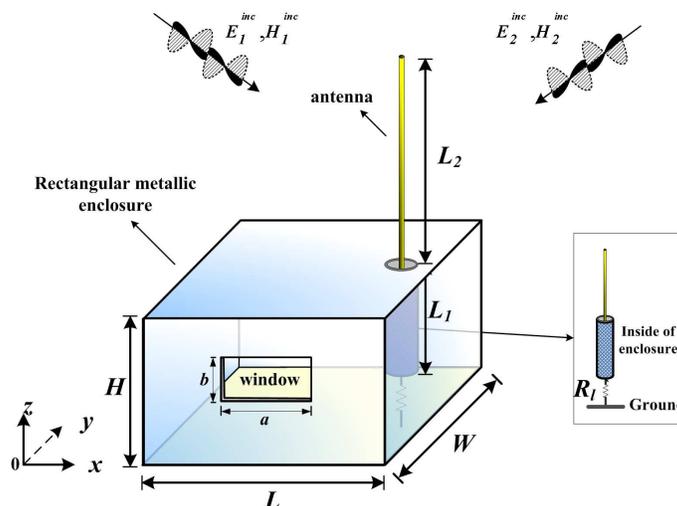
Figure 1:   Geometry of a coaxial feeding monopole antenna mounted on a rectangular enclosure with a window illuminated by external EMP.
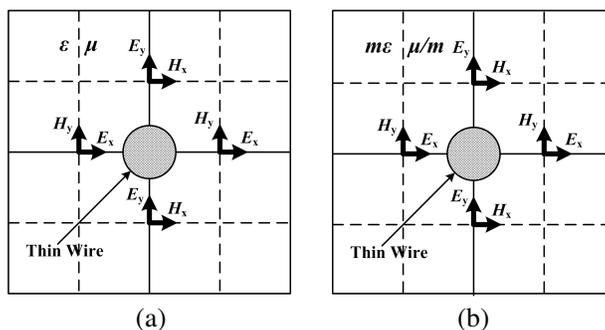


Figure 2: (a) The original adjacent field configuration; (b) the modified adjacent field configuration.

radius of thin wire. The original and modified configurations of the adjacent electric and magnetic fields of thin wire are shown in Figs. 2(a) and (b), respectively.

Then the adjacent electric and magnetic fields can be calculated by using the relative permeability $\mu'_r$ and the relative permittivity $\varepsilon'_r$ instead of the original $\mu_r$ and $\varepsilon_r$. The calculation of other field components is kept same as the original method.

### 2.2. Coaxial Cable Feed Model

An equivalent feed model for the FDTD analysis of an antenna excited by a coaxial line is proposed in [5], which is simple and accurate. In this paper, its mathematical equations are further modified for the purpose of applying it in the Cartesian coordinate system. The coaxial aperture is represented as an equivalent magnetic-frill current through the quasi-static approximation, as show in Fig. 3(a).

The equivalent magnetic-frill current, including the effect of TEM mode, is described as

$$M(x, y, z) = \frac{-2V_{inc}(t) + Z_0 \cdot I(t)}{a \ln(b/a)} \tag{3}$$

where $M$ is magnetic-frill current, $V_{inc}$ is the incident voltage, $I(t)$ is the feed current, $Z_0$ is the characteristic impedance of coaxial line, $a$ is the inner conductor radius, and $b$ is the outer conductor radius.

According to Ampere's law, the feed current $I(t)$ can be calculated by

$$I\left(t = n\Delta t\right) \equiv I^n = \Delta y \left[H_y^n \left(i_{feed} + \frac{1}{2}, j_{feed}, k_{feed}\right) - H_y^n \left(i_{feed} - \frac{1}{2}, j_{feed}, k_{feed}\right)\right]$$

$$- \Delta x \left[H_x^n \left(i_{feed}, j_{feed} + \frac{1}{2}, k_{feed}\right) - H_x^n \left(i_{feed}, j_{feed} - \frac{1}{2}, k_{feed}\right)\right] \quad (4)$$

where $i_{feed,}$ $j_{feed,}$ and $k_{feed}$ are the spatial indexes of the feed cell in $x$-, $y$-, and $z$-direction, respectively, and $\Delta t$ is the discrete time step. The update equation of the magnetic field in $y$ direction is expressed as follow:

$$H_y^{n+\frac{1}{2}} \left(i_{feed} + \frac{1}{2}, j_{feed}, k_{feed}\right) = H_y^{n-\frac{1}{2}} \left(i_{feed} + \frac{1}{2}, j_{feed}, k_{feed}\right)$$

$$- (\Delta t \cdot \mu_0 \cdot \Delta z) E_x^n \left(i_{feed} + \frac{1}{2}, j_{feed}, k_{feed}\right) + (\Delta t/(\mu_0 \cdot \Delta x)) (\ln (\Delta x/a)) E_z^n (i_{feed} + 1, j_{feed}, k_{feed})$$

$$- (\Delta t/(\mu_0 \cdot \Delta z)) (-2V_{inc} + Z_0 \cdot I^n) / (\Delta x/2) \ln (\Delta x/a) \quad (5)$$

The update equation of the magnetic field in $x$-direction can be obtained as the same way. According to transmission line theory, the total voltage at the aperture $V_{ab}$ and the reflected voltage $V_{ref}$ can be obtained by

$$V_{ab} = 2V_{inc} - Z_0 \cdot I^n \quad (6)$$
$$V_{ref} = V_{inc} - Z_0 \cdot I^n \quad (7)$$

So, when needed to calculate the terminal end response of the coaxial cable, the connection port voltage $V_{ab}$ between antenna and coaxial line when the system is illuminated by external pulse is calculated by setting the inner source zero. Then, the terminal voltage response $V_{load}$ can be obtained through transmission line model. This is our two-step coupling calculation method. In the other hand, another coaxial cable feed model is direct telegraph equation model as proposed in [4], which modify the magnetic field around the connection port using the transmission line voltage according to Faraday's Law.

## 3. NUMERICAL RESULT AND DISCUSSION

At first, the inner feed model for thin wire antenna in semi-space is considered as described in [4, 5] and the incident source is Gauss pulse described as follow:

$$U_i (t) = U_0 e^{-\frac{t^2}{2\tau_p^2}} \quad (8)$$

The outer-to-inner radius ratio $b/a$ of an air-filled coaxial line filled with $50\,\Omega$ is about 2.3 and the inner radius $a$ is $1\,\text{mm}$. The length-to-radius ratio $h/a$ of the monopole antenna is 100. The Gauss pulse wave form with unit amplitude and $\tau_p/\tau_a = 0.16$ is used as an excited voltage, where $\tau_a = h/c$ and $c$ is the velocity of light. $U_0$ is set to be $50\,\text{V/m}$. The CPML is used as a boundary condition in our simulation.

The calculated reflected voltage on the coaxial line and the input impedance of the antenna as a function of time are presented in Fig. 3(b) and Fig. 4(a), which have good agreement with the results presented in [5]. It is observed that there is certain time delay in Fig. 3(b), as different locations of the reflected voltages are selected.

Then, we further investigated the connection port voltage responses when the thin wire antenna connected with coaxial line enclosed in a enclosure is illuminated by an external pulse, without inner source. The geometry of coaxial line and antenna doesn't change here and the geometry of the cabin is set as Fig. 1, with $L = W = 30\,\text{cm}$, $H = 20\,\text{cm}$, $a = 15\,\text{cm}$, $b = 10\,\text{cm}$, $L_1 = 5\,\text{cm}$, and $L_2 = 10\,\text{cm}$. The coaxial line is loaded by $Zl = 50\,\Omega$ and the incident EMP is also Gauss pulse as described before. The voltage data obtained by our two-step coupling model and telegraph equation model is shown in Fig. 4(b) and they have good agreement.

Next, we keep the geometry of the practical model as shown in Fig. 1 not changed and consider the terminal responses of the coaxial cable in enclosure. The computational domain is discretized with the cubic cells of $\Delta x = \Delta y = \Delta z = 5\,\text{mm}$ and the time step is $\Delta t = \Delta x/(2c)$. The six-side walls of the enclosure are set as perfectly conducting planes except the windows. The CPML

(a)　　　　　　　　　　　　　　　　　　(b)
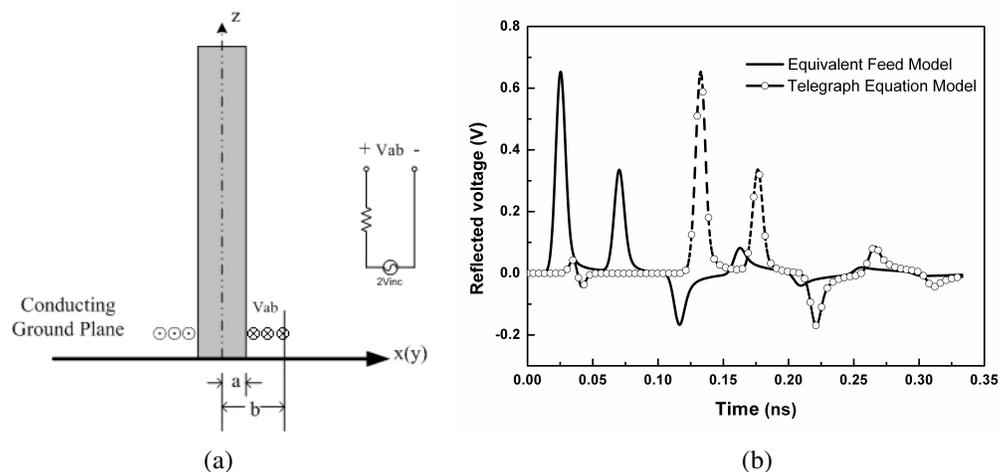
Figure 3: (a) Equivalent representation of the coaxial aperture; (b) reflected voltage on the coaxial line calculated by two feed models.



(a)　　　　　　　　　　　　　　　　　　(b)
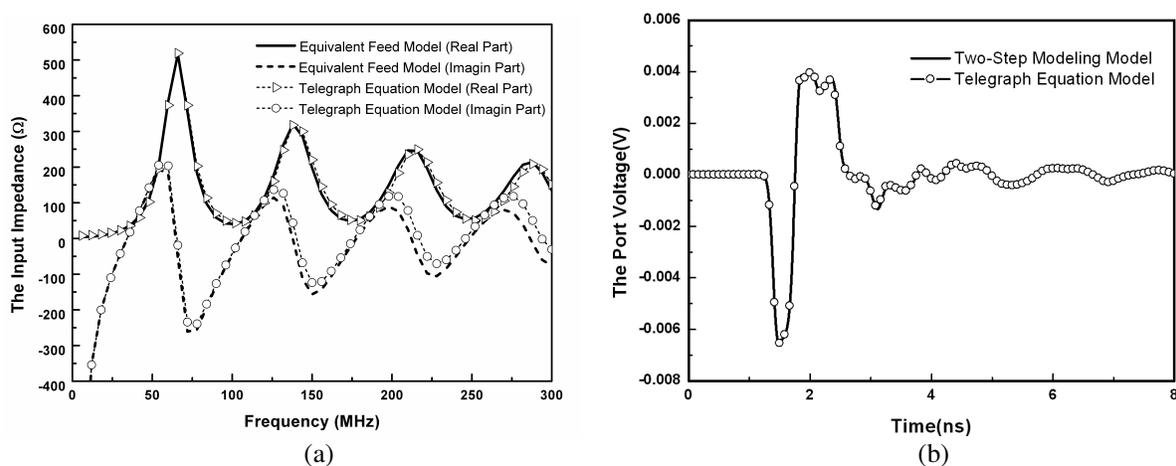
Figure 4: (a) The input impedance of monopole antenna calculated by two feed models; (b) the connection port voltage calculated by two methods when the inner source is set zero.

absorbing boundary is employed to truncate the computational domain. The incident EMP used in our simulation is described by a double-exponential function shown as follows:

$$E = E_0 k \left( e^{-\beta t} - e^{-\alpha t} \right) \tag{9}$$

where the values of the parameters are slow — with $k = 1.036$, $\alpha = 2.6 \times 108$ and $\beta = 1.5 \times 106$, medium — with $k = 1.052$, $\alpha = 4.76 \times 108$ and $\beta = 4.0 \times 106$, and fast — with $k = 1.3$, $\alpha = 6.0 \times 108$ and $\beta = 4.0 \times 107$, which includes three kind of pulses. $E_0$ is set to be $50 \, \text{V/m}$.

The terminal voltage responses when the system is illuminated by three different EMP are shown in Figs. 5(a) and (b). In these two cases, the incident wave propagates along $y$- and $z$-directions, respectively. The results presented in Fig. 5(a) show that there is only a little EM energy of the whole input energy coupling into the terminal end of the coaxial cable, so as to Fig. 5(b). We also can see that the energy of fast pulse coupling into the coaxial line is the most from Fig. 5(a). In Fig. 5(b), the terminal voltage polarity changes because of the changes of the polarization and the propagation directions of input pulses. However, the fast pulse which contains more high frequency components, couples most energy into the coaxial line. This tells us that the system may be damaged more seriously when external intentional EMI is at a high frequency and we should be careful in the high frequency design about EMC of information systems.
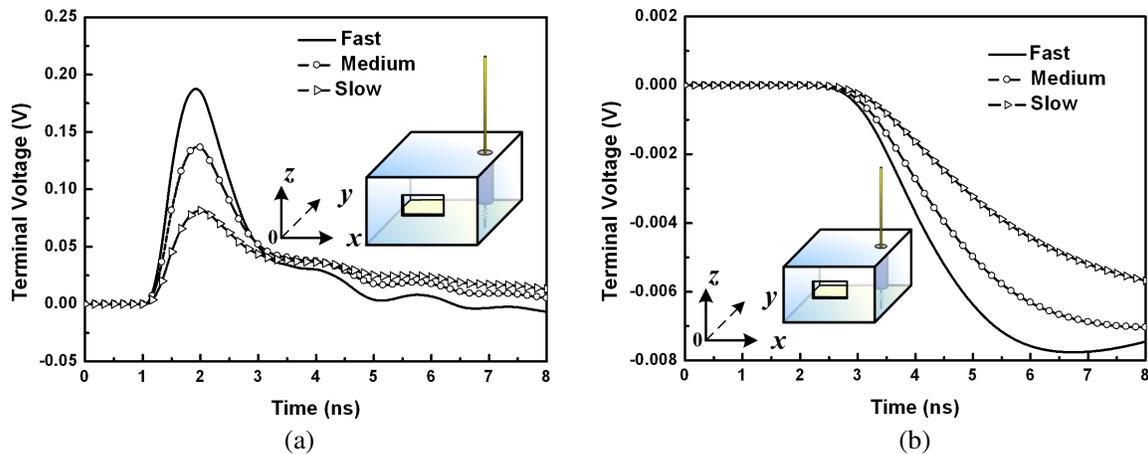
Figure 5: The terminal voltage responses of the coaxial line: (a) when the external pulse propagates in $y$ direction with $z$ direction polarization; and (b) when the external pulse propagates in $z$ direction with $x$ direction polarization.

## 4. CONCLUSIONS

In the paper, we present a hybrid methodology that combines thin wire FDTD methods, feed model, telegraph equations, and windows model together. Further, we have predicted the terminal voltage responses of the end of the transmission line when the system is illuminated by external pulses. The main advantage of our method is that external field full-wave simulation just needs to be carried out one time, and then we just need to solve the telegraph equation to obtain the terminal response of the coaxial cable. From results presented, we can conclude that different polarity direction and propagation external pulses have different interferences on the coaxial line feed network and high frequency pulses couple into it with more EM energy.

## ACKNOWLEDGMENT

## REFERENCES

1. Georgakopoulos, S. V., C. R. Birtcher, C. A. Balanis, and R. A. Renaut, "HIRF penetration and PDE coupling analysis for scaled fuselage models using a hybrid subgrid FDTD(2, 2)/FDTD(2, 4) method," *IEEE Trans. Electromagn. Compat.*, Vol. 45, No. 2, 293–305, May 2003.
2. Liu, Q. F. and W. Y. Yin, "Time-domain investigation on cable-induced transient coupling into metallic enclosures," *IEEE Trans. Electromagn. Compat.*, Vol. 51, No. 4, 953–961, Nov. 2009.
3. Wang, J., W. Y. Yin, J. P. Fang, and Q. F. Liu, "Transient analysis of transmission lines under external field coupling into an electrically large scale cabin with thin-slots," *Progress In Electromagnetics Research*, Vol. 106, 1–16, 2010.
4. Maloney, J. G., K. L. Shlager, and G. S. Smith, "A simple FDTD model for transient excitation of antennas by transmission lines," *IEEE Trans. Antennas Propagat.*, Vol. 42, No. 2, 289–292, Feb. 1994.
5. Hyun, S.-Y., S.-Y. Kim, and Y.-S. Kim, "An equivalent feed model for the FDTD analysis of antennas driven through a ground plane by coaxial lines," *IEEE Trans. Antennas Propagat.*, Vol. 57, No. 1, 161–167, Jan. 2009.
6. Taflove, A. and S. C. Hagness, *Computational Electrodynamics: The Finite-difference Time-domain Method*, 2nd Edtion, Artech House, Norwood, MA, 2000.
7. Node, T. and S. Yokoyama, "Thin wire representation in finite difference time domain surge simulation," *IEEE Trans. Power Delivery*, Vol. 17, No. 3, 840–847, Jul. 2002.

# Effect of Electromagnetic Interference (EMI) on the DC Shift, Harmonic and Intermodulation Performance of NMOSFET Current Mirror

**Muhammad Taher Abuelma'atti[1] and Ali M. T. Abuelmaatti[2]**

[1]King Fahd University of Petroleum and Minerals, Box 203, Dhahran 31261, Saudi Arabia
[2]RFMD (UK) Ltd., Millennium Way, Newton Aycliffe, County Durham DL5 6JW, UK

**Abstract**— In this paper a new approximation is presented for the nonlinear relationship between the input-current and the output-current of an NMOSFET current-mirror. Using this approximation closed-form expressions are obtained for the DC and the amplitudes of the fundamental, second- and third-harmonic and intermodulation components of the output current resulting from exciting the NMOSFET current-mirror by a DC biasing current plus a superimposed sinusoidal electromagnetic interference.

## 1. INTRODUCTION

At present there is a growing interest in designing current-mode circuits; where the input is a current and the output is a current. This is attributed to their simple structures, wider bandwidth and larger dynamic range compared to the voltage-mode circuits; where the input is a voltage and the output is a voltage. Current-mirrors using NMOSFET transistors play a crucial part in the design of current-mode circuits.

The NMOSFET current-mirror is inherently nonlinear. This nonlinearity manifests itself in generating unwanted DC components; which may alter the correct biasing and may therefore prohibit the circuit from functioning correctly. Moreover, in addition to the unwanted DC, unwanted harmonics and intermodulation products may be generated when a multisinusoidal electromagnetic interfering (EMI) signal is superimposed on the DC biasing current. These effects have been extensively studied for MOSFET and bipolar transistors and operational amplifiers [1–6]. However, only very little has been written about these effects in NMOSFET current-mirrors assuming that the amplitude of the electromagnetic interference (EMI) signal is relatively small [7]. This assumption paves the way for using a Taylor series expansion for approximating the nonlinearity of the NMOSFET current-mirror, thus, restricting the validity of the results to relatively small EMI signals only. While attempts to analyze the nonlinear performance of current mirrors due to device mismatch [8–11] and the channel length modulation [12], no attempt has been reported for studying the DC shift, the harmonic and intermodulation performance of the NMOSFET current-mirror under relatively large EMI signal. The major intention of this paper is, therefore, to present such a study.

## 2. ANALYSIS

Figure 1 shows an NMOSFET current-mirror. Assuming that the transistors are matched and working in the saturation region, with $v_{DS} > v_{GS} - V_{th}$, so that the drain current can be expressed as

$$i_D = k(v_{GS} - V_{th})^2(1 + \lambda v_{DS}) \tag{1}$$
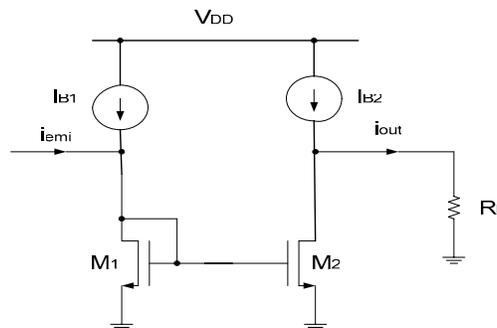


Figure 1: NMOSFET current-mirror.

In Equation (1), $i_D$ is the drain current, $v_{GS}$ is the gate-to-source voltage, $v_{DS}$ is the drain-to-source voltage, $V_{th}$ is the threshold voltage, $\lambda$ is the channel-length modulation parameter and $k = (W/L)(\mu C_{ox}/2)$, $\mu$ is the surface mobility of the channel, $C_{ox}$ is the gate oxide capacitance density, $W$ is the effective channel width, and $L$ is the effective channel length. Assuming that the input current is formed of a DC bias current, $I_{B1}$, plus a superimposed EMI multisinusoidal signal,
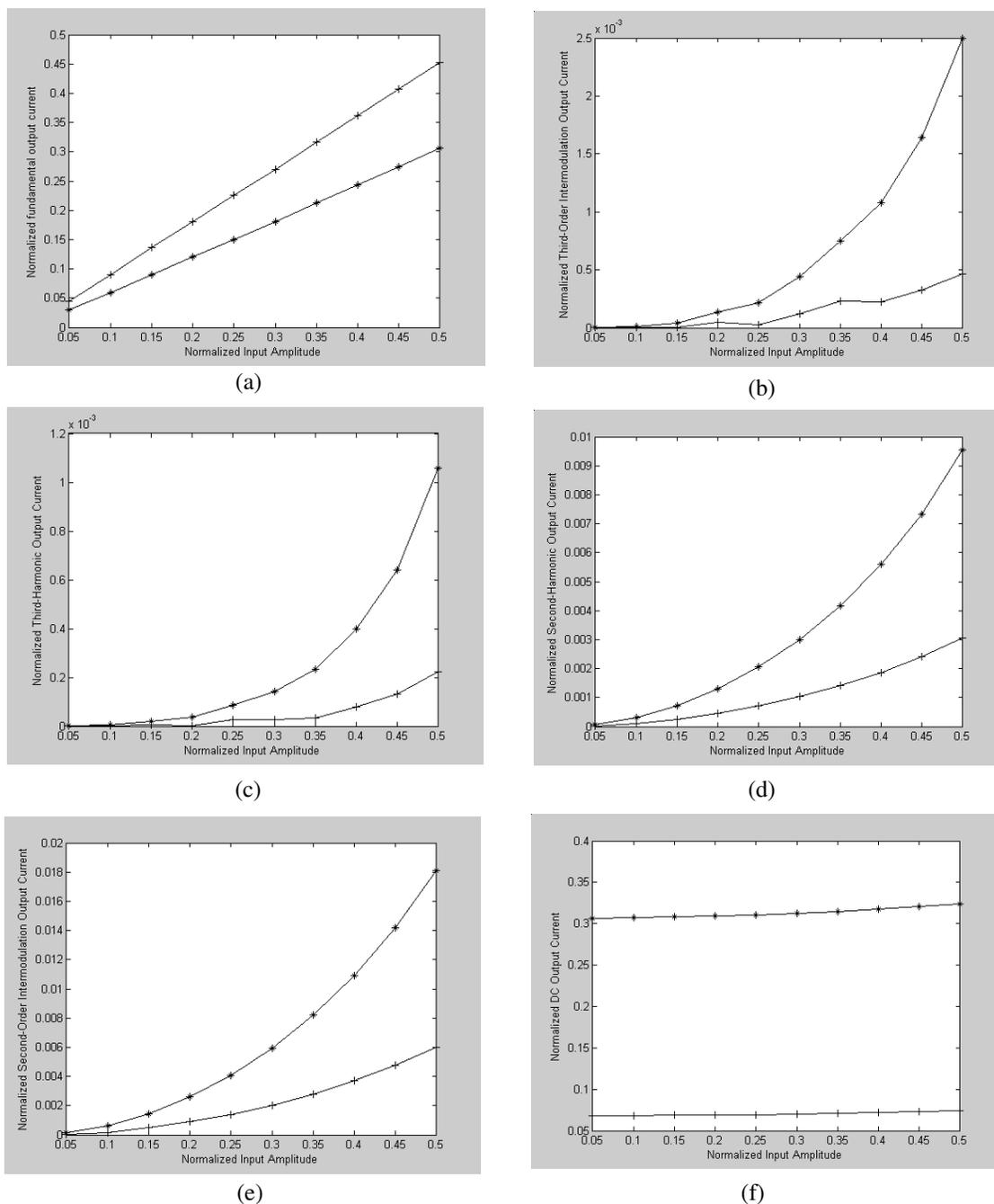


Figure 2: Normalized values of the DC, fundamental, harmonic and intermodulation components of the output current calculated using Equations (16)–(21). (a) fundamental, (b) third-order intermodulation, (c) third harmonic, (d) second-harmonic, (e) second-order intermodulatuion, and (f) DC. $+$ : $\lambda = 0.0051/V$, $V_{th} = 0.42\,\text{V}$, $k = 4.98 \times 10^{-6}\,\text{mA/V}^2$, $R_L = 1\,\text{k}\Omega$, $\beta = 0.0021$, $\gamma = 0.0707$, $\delta = 0$. $*$ : $\lambda = 0.0300/V$, $V_{th} = 0.42\,\text{V}$, $k = 4.98 \times 10^{-6}\,\text{mA/V}^2$, $R_L = 1\,\text{k}\Omega$, $\beta = 0.0126$, $\gamma = 0.424$, $\delta = 0$.

$i_{emi}$, of the form

$$i_{IN} = I_{B1} + i_{emi} \tag{2}$$

$$i_{emi} = \sum_{m=1}^{M} I_m \sin \omega_m t \tag{3}$$

then using Equations (1) and (2), the relationship between the input and output currents can be expressed as

$$\frac{i_{emi} + I_{B1}}{-i_{out} + I_{B2}} = \frac{k_1(v_{GS1} - V_{th1})(1 + \lambda_1 v_{DS1})}{k_2(v_{GS2} - V_{th2})(1 + \lambda_2 v_{DS2})} \tag{4}$$

If $\lambda_1 = \lambda_2 = \lambda$, $k_1 = k_2$, $V_{th1} = V_{th2} = V_{th}$ and $v_{DS2} = i_{out}R_L$, then Equation (4) reduces to

$$\frac{i_{emi} + I_{B1}}{-i_{out} + I_{B2}} = \frac{(1 + \lambda v_{DS1})}{(1 + \lambda i_{out} R_L)} \tag{5}$$

Using Equation (1), and ignoring the effect of the channel length modulation, the gate-to-source voltage $v_{GS1}$ can be approximated by

$$v_{GS1} = V_{th} + \sqrt{\frac{i_{emi} + I_{B1}}{k}} \tag{6}$$

Combining Equations (5) and (6), then

$$\frac{i_{emi} + I_{B1}}{-i_{out} + I_{B2}} = \frac{1 + \lambda \left( V_{th} + \sqrt{\frac{i_{emi} + I_{B1}}{k}} \right)}{1 + \lambda i_{out} R_L} \tag{7}$$

Equation (7) represents the nonlinear relationship between the EMI input current, $i_{emi}$, and the output current, $i_{out}$, of the NMOSFET current-mirror of Fig. 1. However, in its present form it cannot yield expressions for the amplitudes of the numerous frequency components of the output current resulting from a multisinusoidal EMI interference. Therefore, recourse to Taylor series approximation, assuming relatively small values of the EMI input current, $i_{emi}$, is inevitable [7]. However, by virtue of their derivation the expressions obtained for the DC shift and the amplitudes of the harmonics and intermodulation products are valid only for small values of the amplitudes of the EMI sinusoids. In order to obtain expressions that are valid over a wider range of the amplitudes of the EMI sinusoids, here we perform simple mathematical manipulations to rewrite Equation (7) in the form

$$x + \alpha xy + \alpha y + y/\delta + \beta y/\delta + \gamma\sqrt{x+1}y/\delta = \beta/\delta + \gamma\sqrt{x+1}/\delta + (1-\delta)/\delta \tag{8}$$

In Equation (8), $x = i_{emi}/I_{B1}$, $y = i_{out}/I_{B2}$, $\delta = I_{B1}/I_{B2}$, $\alpha = \lambda R_L I_{B2}$, $\beta = \lambda V_{th}$ and $\gamma = \lambda\sqrt{I_{B1}/k}$. For a typical current mirror using 0.18 μm CMOS technology with $V_{th} = 0.42$ V, $k = 4.98$ μA/V$^2$, $\lambda = 0.005 - 0.03$ and $R_L = 1$ kΩ, then $\alpha = 0.005 - 0.03$, $\beta = 0.0021 - 0.0126$ and $\gamma = 0.0707 - 0.424$. With these values of $\alpha$, $\beta$ and $\gamma$, Equation (8) can be approximated as

$$y = -\frac{x - \beta - \gamma\sqrt{x+1} - (1-\delta)/\delta}{1 + \gamma\sqrt{x+1}} \tag{9}$$

Here we propose to approximate Equation (9) using a Fourier-series expansion of the form

$$y = a_0 + \sum_{n=1}^{N} \left[ a_n \cos\left(\frac{2n\pi}{D}x\right) + b_n \sin\left(\frac{2n\pi}{D}x\right) \right] \tag{10}$$

In Equation (10), $D$, $a_0$, $a_n$, $b_n$, $n = 1, 2, \ldots, N$ are fitting parameters that can be obtained using the procedure described in [13, 14]. This procedure is simple and does not require extensive computing facilities or well-developed software. For convenience, a brief description of this procedure is given here. First, the function of Equation (9) is calculated for certain values of the parameters

$\beta$, $\gamma$ and $\delta$ for $-1 \le x \le 1$, then the offset, $y_{offset}$, at $x = 0$ is removed, and the resulting function is mirror-imaged to produce a periodic function with a complete period $= D$. Second, the resulting function is approximated by a number of straight-line segments joined end to end. Using the slopes of these segments, it is easy to obtain the parameters $a_0$, $a_n$, $b_n$, $n = 1, 2, \ldots, N$ using simple algebraic calculations. The results obtained are shown in Table 1 for different values of the parameters $\beta$, $\gamma$ and $\delta$. Using Equation (10) and the parameters in Table 1, the function of Equation (10) was calculated and compared with Equation (9). The results show that very small values of the relative root-mean-square errors (RRMSEs) $= 0.0011\%$ and $0.0013\%$ can be achieved. This confirms the validity of Equation (10) for approximating Equation (9).

## 3. DC SHIFT, HARMONIC AND INTERMODULATION PRODUCTS

Equation (10) can be used for predicting the DC shift and the amplitudes of the harmonics and intermodulation components of the output current resulting from a multisinusoidal EMI current. Thus, combining Equations (3) and (10), the normalized output current can be expressed as

$$y = a_0 + \sum_{n=1}^{N} \left[ a_n \cos \left( \frac{2n\pi}{D} \sum_{m=1}^{M} \frac{I_m}{I_{B1}} \sin \omega_m t \right) + b_n \sin \left( \frac{2n\pi}{D} \sum_{m=1}^{M} \frac{I_m}{I_{B1}} \sin \omega_m t \right) \right] \qquad (11)$$

Using the trigonometric identities of $\sin(\phi + \theta)$, $\cos(\phi + \theta)$, $\sin(\rho \sin \theta)$ and $\cos(\rho \sin \theta)$, and after simple mathematical manipulations, it is easy to show that the magnitude of the normalized DC component and the normalized amplitude of the output current component of frequency $\sum_{m=1}^{M} \alpha_m \omega_m$ and order $\sum_{m=1}^{M} |\alpha_m|$, where $\alpha_m$ is a positive or negative integer or zero, can be expressed as

$$Y_{DC} = y_{offset} + a_0 + \sum_{n=1}^{N} a_n \prod_{m=1}^{M} J_0 \left( \frac{2n\pi}{D} \frac{I_m}{I_{B1}} \right) \qquad (12)$$

$$Y_{\alpha_1, \alpha_2, \ldots, \alpha_M} = \sum_{n=1}^{N} a_n \prod_{m=1}^{M} J_{|\alpha_m|} \left( \frac{2n\pi}{D} \frac{I_m}{I_{B1}} \right), \quad \text{for } \sum_{m=1}^{M} |\alpha_m| = \text{even integer} \qquad (13)$$

$$Y_{\alpha_1, \alpha_2, \ldots, \alpha_M} = \sum_{n=1}^{N} b_n \prod_{m=1}^{M} J_{|\alpha_m|} \left( \frac{2n\pi}{D} \frac{I_m}{I_{B1}} \right), \quad \text{for } \sum_{m=1}^{M} |\alpha_m| = \text{odd integer} \qquad (14)$$

In Equations (12)–(14), $J_l(\rho)$ is the Bessel function of order $l$. Assuming that the EMI current is formed of two equal-amplitude sinusoids, Equation (3) reduces to

$$i_{emi} = I(\sin \omega_1 t + \sin \omega_2 t) \qquad (15)$$

and Equations (12)–(14) yield the following expressions for the magnitude of the normalized DC, the normalized fundamental, second- and third-harmonic and the second- and third-order intermodulations components of the output current.

$$Y_{DC} = y_{offset} + a_0 + \sum_{n=1}^{N} a_n J_0 \left( \frac{2n\pi}{D} X \right)^2 \qquad (16)$$

$$Y_1 = \sum_{n=1}^{N} b_n J_1 \left( \frac{2n\pi}{D} X \right) J_0 \left( \frac{2n\pi}{D} X \right) \qquad (17)$$

$$Y_2 = \sum_{n=1}^{N} a_n J_2 \left( \frac{2n\pi}{D} X \right) J_0 \left( \frac{2n\pi}{D} X \right) \tag{18}$$

$$Y_3 = \sum_{n=1}^{N} b_n J_3 \left( \frac{2n\pi}{D} X \right) J_0 \left( \frac{2n\pi}{D} X \right) \tag{19}$$

$$Y_{1,1} = \sum_{n=1}^{N} a_n J_1 \left( \frac{2n\pi}{D} X \right) J_1 \left( \frac{2n\pi}{D} X \right) \tag{20}$$

$$Y_{2,1} = \sum_{n=1}^{N} b_n J_2 \left( \frac{2n\pi}{D} X \right) J_1 \left( \frac{2n\pi}{D} X \right) \tag{21}$$

Using Equations (16)–(21) the normalized DC, fundamental, harmonic and intermodulation performance of the NMOSFET current mirror of Fig. 1 were calculated for different values of the normalized input amplitude $X$. The results are shown in Fig. 2. Inspection of Fig. 2 clearly shows the dependence of the output current components on the normalized input amplitude and the channel length modulation parameter. Moreover, inspection of Fig. 2 reveals that the second-order intermodulation component of the output current is dominant.

## 4. CONCLUSION

In this paper closed-form expressions are obtained for the DC shift and the amplitudes of the harmonics and intermodulation products resulting from a exciting an NMOSFET current with a DC bias current plus a multisinusoidal EMI. Using these expressions the variation of the normalized DC shift and the normalized harmonic and intermodulation performance of the NMOSFET current mirror can be investigated as a function of the variations in the normalized input amplitude of the EMI.

## REFERENCES

1. Abuelma'atti, M. T. and A. M. T. Abuelmaatti, "Effect of electromagnetic interference (EMI) on the DC shift, harmonic and intermodulation performance of diode-connected NMOSFET," *Analog Integrated Circuits and Signal Processing,* Vol. 67, 109–116, 2011.
2. Richardson, R. E., "Quiescent operating point shift in bipolar transistors with AC excitation," *IEEE Journal of Solid-State Circuits*, Vol. 14, 1087–1094, 1979.
3. Forcier, M. L. and R. E. Rishardson, "Microwave-rectification RFI response in field effect transistors," *IEEE Transctions on Electromagnetic Compatibility*, Vol. 21, 312–315, 1979.
4. Poulton, A. S., "Effect of conducted EMI on the DC performance of operational amplifiers," *Electronics Letters*, Vol. 30, 282–284, 1994.
5. Abuelma'atti, M. T., "Analysis of the effect of radio frequency interference on the DC performance of bipolar operational amplifiers," *IEEE Transactions on Electromagnetic Compatibility*, Vol. 45, 453–458, 2003.
6. Abuelma'atti, M. T., "Analysis of the effect of radio frequency interference on the DC performance of CMOS operational amplifiers," *Analog Integrated Circuits and Signal Processing*, Vol. 45, 123–130, 2005.
7. Redoute, J.-M. and M. Steyaert, *EMC of Analog Integrated Circuits*, Springer Sciences + Business Media, 2010
8. Bruun, E., "Analytical expressions for harmonic distortion at low frequencies due to device mismatch in CMOS current mirrors," *IEEE Transactions on Circuits and Systems — II: Analog and Digital Signal Processing*, Vol. 46, 937–941, 1999.
9. Bruun, E., "Worst case estimate of mismatch induced distortion in complementary CMOS current mirrors," *Electronics Letters*, Vol. 34, 1625–1627, 1998.
10. Bruun, E., "Harmonic distortion in CMOS current mirrors," *Proceedings of the IEEE International Symposium on Circuits and Systems*, 567–570, 1998.

11. Abuelma'atti, M. T., "Improved analysis for the nonlinear performance of CMOS current mirrors with device mismatch," *Frequenz*, Vol. 56, 164–169, 2002.
12. Palmisano, G., G. Plaumbo, and S. Pennisi, "High linearity CMOS current output stage," *Electronics Letters*, Vol. 31, 789–790, 1995.
13. Abuelma'atti, M. T., "Simple method for calculating Fourier coefficients of experimentally obtained waveforms," *Proceedings IEE — Science Measurement, Technology*, Vol. 141, 177–178, 1994.
14. Abuelma'atti, M. T., "A simple algorithm for fitting measured data to Fourier-series models," *International Journal of Mathematical Education in Science and Technology*, Vol. 24, 107–112, 1993.

# Near-field Characterization of a Printed Circuit Board in the Presence of a Finite-sized Metallic Ground Plane

**O. Franek**[1], **M. Sørensen**[2], **H. Ebert**[1], **and G. F. Pedersen**[1]

[1]APNet Section, Department of Electronic Systems, Faculty of Engineering and Science
Aalborg University, Niels Jernes Vej 12, Aalborg 9220, Denmark
[2]Bang & Olufsen a/s, Peter Bangs Vej 15, Struer 7600, Denmark

**Abstract**— Model of a generic printed circuit board (PCB) in a presence of a finite-sized metallic ground plane is introduced as a commonly occurring scenario of electronic module whose electromagnetic fields are disturbed by a nearby object. Finite-difference time-domain simulations are performed for this scenario and a scenario where the PCB is replaced by near field sources following Love's equivalence theorem. Both scenarios are compared and the maximum total error is evaluated as 84%. It is then demonstrated that including the bottom metallic layer of the PCB, as its characteristic feature, in the latter scenario leads to significantly lower errors — a figure of 33% is reported.

## 1. INTRODUCTION

An electronic apparatus consisting of one or several modules in an enclosure may often not fulfill requirements on electromagnetic compatibility (EMC) in terms of radiation, in spite of the fact that the particular modules may pass the requirements. There has been a growing interest in the possibility of identifying such situations early in development stage of the modules, since later changes in the design of the apparatus are costly. Electromagnetic simulations of the interaction between the modules and the apparatus have been instrumental to achieve this goal [1].

However, it is not always possible to simulate a full model of the electronic module, often because the internal structure of some parts of the module (typically integrated circuits) is unknown. Instead, designers resort to characterizing the module by the near fields it produces. These are obtained by measurement and serve as sources in the simulation [2–4].

According to Love's equivalence theorem [5], an arbitrary source of electromagnetic field (the module, in our case) can be replaced by electric and magnetic currents running over a surface entirely enclosing the source, whereas the currents are uniquely determined by electric and magnetic fields tangential to the surface (and obtained by measurement, in our case). For this theorem to hold, linearity must be ensured, and the sources have to be placed in free space. However, it is the latter condition that cannot be fulfilled in practice, since we plan to use the currents to characterize the module in the presence of other objects belonging to the apparatus enclosing the module, not in free space. In our study, we focused on this problem, and attempted to quantify the disturbance of the equivalence theorem by a finite-sized metallic ground plane placed near the equivalent sources, which we see as a common example occurring in real conditions.

## 2. NUMERICAL EXPERIMENT

We used generic printed circuit board (PCB) with dimensions $150 \times 100 \, \text{mm}$ as a simplified test PCB representing typical electronic module (Fig. 1). The test PCB is made of $2 \, \text{mm}$ thick FR4 substrate with dielectric constant $\epsilon_\text{r} = 4.35$. On the top side of the substrate there are three $3 \, \text{mm}$ wide traces with characteristic impedance $50 \, \Omega$ and matched on both ends. The bottom side of the substrate is entirely covered by a metallic layer, except a $2 \, \text{mm}$ slot across the third trace. Losses in the metallic layers as well as in the substrate have been neglected in this study.

In order to introduce disturbance from surrounding objects, the test PCB is placed at a height $h$ over a finite-sized metallic ground plane, with the bottom side of the PCB facing the ground plane. The ground plane overlaps the test PCB by a value $s$ in all directions.

For the numerical experiment we chose the well-established finite-difference time-domain method (FDTD) [6] to obtain distribution of electromagnetic fields. Three distinct scenarios were simulated (see Fig. 2):

1. The test PCB alone in free space;
2. The test PCB in the presence of the metallic ground plane;
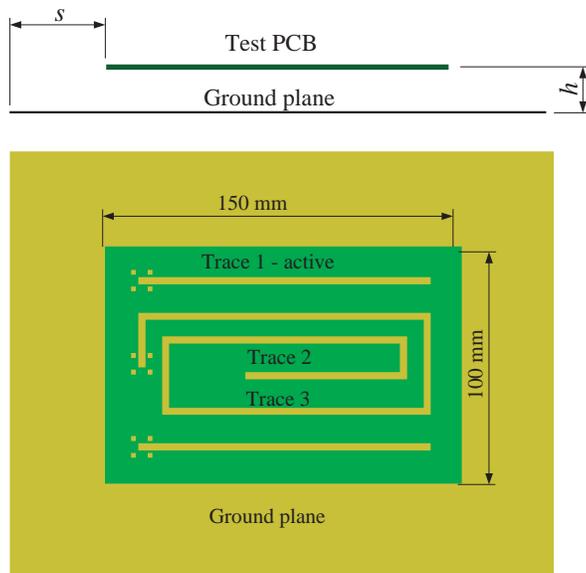
Figure 1: Schematic drawing of the test PCB on top of the finite-sized metallic ground plane.



(a) Scenario 1    (b) Scenario 2    (c) Scenario 3
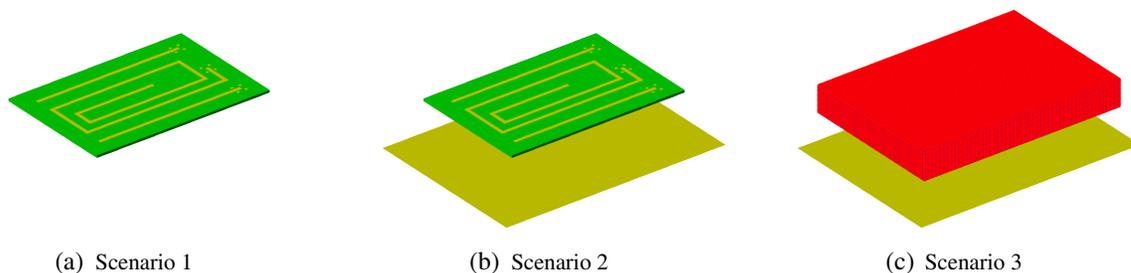
Figure 2: Simulation scenarios described in the text. Equivalent field sources (Huygens' box) are denoted by red color.

3. Equivalent field sources (obtained from 1) in the presence of the metallic ground plane.

Scenario 1 imitates the near field measurement setup where, in free space without any disturbing elements, we record the fields on a rectangular box (Huygens' box) entirely surrounding the test PCB in a 10 mm distance. Scenario 2 represents a real-world scenario when the electronic module is surrounded by other objects, in this case the ground plane. Finally, in scenario 3 we use the Huygens' box as source replacing the test PCB (inside of the Huygens' box is empty) and try to evaluate how close the electromagnetic fields calculated in this case will be to Scenario 2.

## 3. RESULTS

The simulations described in scenarios 2 and 3 were performed for all combinations of parameters $h = 15$–$40$ mm and $s = 0$–$40$ mm. Trace 1 has been excited, while the remaining two were matched on both ends. We compared the fields in scenarios 2 and 3 based on a maximum total error metric defined by

$$\text{Maximum total error} = \frac{\max |F^{(3)} - F^{(2)}|}{\max |F^{(2)}|} \times 100 \ [\%], \tag{1}$$

where $F$ stands for either electric ($E$-) or magnetic ($H$-) fields, and the superscript denotes the particular scenario in which the field has been obtained. The max function operates on all values outside of the Huygens' box.

We have observed that while at the lower end of the investigated frequency range, at 100 MHz, error of only 14% has been found, at 1 GHz the error reaches 84% ($E$-fields) due to resonant nature of the field distribution. Fig. 3 shows the error at 1 GHz for both $E$- and $H$-fields and all

(a) E-fields　　　　　　　　　　　　　　　(b) H-fields
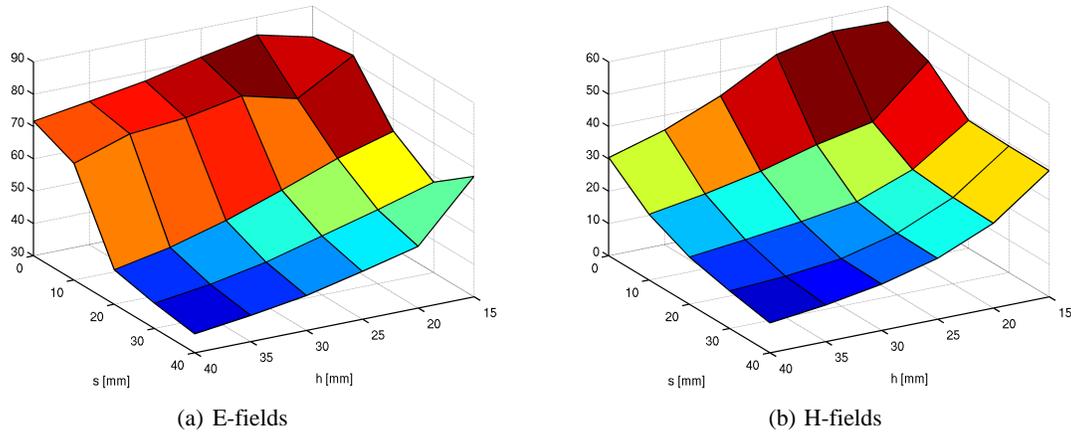
Figure 3: Maximum total error between scenarios 2 and 3 at 1 GHz when the Huygens' box is empty.



(a) E-fields　　　　　　　　　　　　　　　(b) H-fields
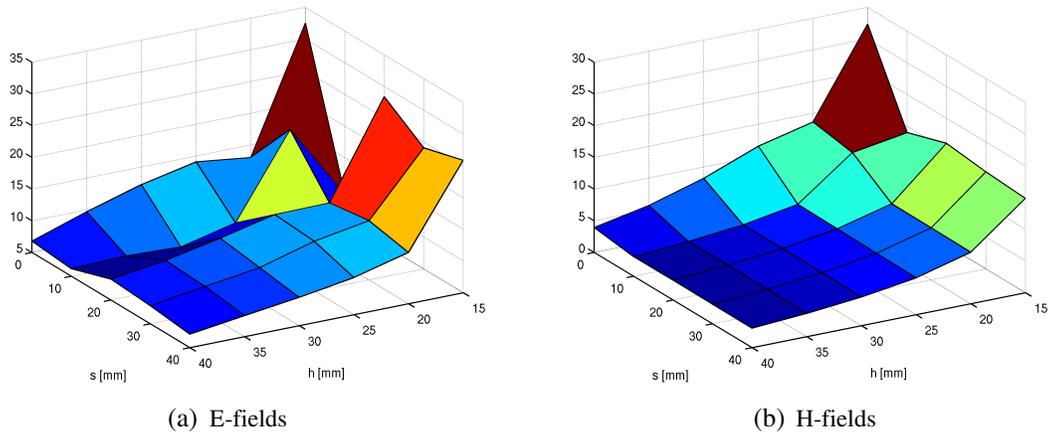
Figure 4: Maximum total error between scenarios 2 and 3 at 1 GHz when the Huygens' box contains the bottom metallic plane of the original test PCB.

combinations of parameter values. It is interesting to note that the error is generally highest when the distance and overlap is the smallest, i.e., when the bottom layer of the PCB and the ground plane form a tight parallel plate resonator.

Since the observed errors are caused by the absence of the re-scattered fields from the PCB itself, we decided to include the bottom metallic plane of the PCB as its major feature inside the equivalent surface, expecting better outcome due to re-scattering. And indeed, in this arrangement, the peak $E$-field error drops to acceptable 33% (i.e., at most $-3.5$ dB drop in magnitude). From Fig. 4, it is apparent that the error still reaches its peak for low $h$ and $s$, but for higher $h$ becomes very small, even below 15%.

## 4. CONCLUSION

The near-field characterization of a common printed circuit board using Love's equivalence theorem is a feasible technique, even though the conditions for the theorem are not entirely fulfilled. Resulting errors can be mitigated by including major features of the substituted object, without the need to use the full model. In the perspective, it appears to be possible to simulate an apparatus consisting of modules modeled only by their near-field representations, plus a few major features, and estimate unwanted radiation with a high degree of reliability.

**REFERENCES**

1. Saez de Adana, F., M. F. Cátedra, J. M. Gómez, R. Mittra, J. Berkowitsch, F. Gutiérrez, and M. Alfonsea, "A systematic approach for radiated system-level verification of unknown sources inside satellites from unit-level measurements," *IEEE Antennas and Propagation Magazine*, Vol. 52, No. 2, 71–85, 2010.

2. De Daran, F., J. Chollet-Ricard, F. Lafon, and O. Maurice, "Prediction of the field radiated at one meter from PCB's and microprocessors from near EM field cartography," *IEEE International Symposium on Electromagnetic Compatibility*, Vol. 1, 479–482, Istanbul, Turkey, May 2003.

3. Shi, J., M. A. Cracraft, J. Zhang, R. E. DuBroff, and K. Slattery, "Using near-field scanning to predict radiated fields," *IEEE International Symposium on Electromagnetic Compatibility*, Vol. 1, 14–18, Silicon Valley, CA, USA, Aug. 2004.

4. Baudry, D., A. Louis, and B. Mazari, "Overview of emission and susceptibility investigation and modeling with near-field measurements," *XXIX URSI General Assembly*, Chicago, IL, USA, Aug. 2008.

5. Balanis, C. A., *Advanced Engineering Electromagnetics*, Wiley, New York, 1989.

6. Taflove, A. and S. C. Hagness, *Computational Electrodynamics: The Finite-difference Time-domain Method*, 3rd Edition, Artech House, Boston, 2005.

# Improvement of Absorbing Frequency Bandwidth of Composite Electromagnetic Wave Absorber Made of Granular Sendust Particles Dispersed in Polystyrene Resin

**Y. Hongo[1], K. Sakai[2], Y. Sato[1], and S. Yoshikado[1]**

[1]Graduate School of Engineering, Doshisha University, Japan
[2]Graduate School of Natural Science and Technology, Okayama University, Japan

**Abstract**— Composite electromagnetic wave absorber made of sendust dispersed in resin is low-cost and contains no rare metal. In this study, granular shaped sendust particles with the average particle size of approximately 5 and 20 µm were dispersed in polystyrene resin with the volume ratio of 20–40 vol% in order to broaden the absorbing frequency bandwidth in the frequency range from above 10 GHz. Experimental results reveal that absorbing frequency bandwidth is drastically improved and the optimal volume mixture ratio of sendust is approximately 30 vol% for the average particle size of approximately 5 µm and approximately 35 vol% for approximately 20 µm.

## 1. INTRODUCTION

Electromagnetic wave absorber suitable for new electromagnetic circumstance and devices is required, especially at frequencies above 10 GHz. In order to design a metal-backed single-layer absorber of which structure is simple, the control of the frequency dependences of both the relative complex permeability $\mu_r^*$ and the relative complex permittivity $\varepsilon_r^*$ is important because the absorption of an electromagnetic wave is determined by them. In order to control both $\mu_r^*$ and $\varepsilon_r^*$, composite of two or more kinds of material is effective [1–8]. In the previous study, we have reported that the composite made of sendust, which is a soft magnetic material and an alloy of Al 5%, Si 10%, and Fe 85%, and resin, such as polystyrene resin, can be used as an absorber at frequencies between 1 to 20 GHz [9]. Composite electromagnetic wave absorber made of sendust dispersed in resin is low-cost and contains no rare metal. In addition, good absorption characteristics could be obtained in the frequency range of 10–20 GHz [2]. Moreover, the volume mixture ratio of sendust to polystyrene resin could be low because it has been reported that the frequency where the absorption of electromagnetic waves occurred increased with decreasing the amount of sendust and good absorption characteristics at frequencies between 10 and 20 GHz was expected. It has been reported that absorption characteristics depended on the particle shape of sendust and the absorption of electromagnetic waves with a wide bandwidth in the frequency range from 10 and 20 GHz could be achieved using granular sendust particle with a low volume mixture ratio [9]. However, the optimal volume mixture ratio or particle size to broad the absorbing frequency bandwidth in the frequency range from above 10 GHz has been never determined.

That the non-reflective condition is satisfied at a desired frequency range is important to design an absorber. Considering the non-reflective condition, the value of $\mu_r^*$ can be controlled by changing the volume mixture ratio of sendust in resin and the size. However, it is speculated that the frequency dependence of $\mu_r^*$ for this soft magnetic materials are determined by the natural magnetic resonance and magnetic moment due to eddy current which flows on a sendust particle [3, 10]. Therefore, flexible control of the frequency dependence of $\mu_r^*$ is difficult using the composite made of sendust and polystyrene resin. We attempt to clarify the effect of particle size and the volume mixture ratio of sendust especially at frequencies above 10 GHz. In this study, granular shaped sendust particles with the average particle size of approximately 5 and 20 µm were dispersed in polystyrene resin with the volume ratio of 20–40 vol% in order to broaden the absorbing frequency bandwidth in the frequency range from above 10 GHz.

## 2. EXPERIMENTS

Commercially available granular sendust (Nippon Atomized Metal Powders Corporation, Al 5%, Si 10%, Fe 85%) particles were used. The average particle size (diameter) of the granular sendust particles was approximately 5 and 20 µm. Chips of polystyrene resin were dissolved in acetone and the dissolved polystyrene resin and sendust particles were mixed to uniformly disperse the particles [9]. The volume mixture ratio $V$ of sendust was 20, 25, 30, 35 or 40 vol%. After mixing,

the mixture was heated to melt the polystyrene resin and was then hot-pressed at a pressure of 5 MPa into a pellet. This was allowed to cool naturally to room temperature and was processed into a toroidal-core shape for use in a coaxial line or into a rectangular shape for use in a rectangular waveguide. The sample was mounted inside the coaxial line or waveguide using silver past to ensure that no gap existed between the sample and the walls of the line/waveguide [9]. The complex scattering matrix elements $S_{11}^*$ and $S_{21}^*$ for the TEM mode (coaxial line) or $TE_{10}$ mode (waveguide) were measured using a vector network analyzer (Agilent Technology, 8722ES) by the full-two-port method in the frequency range from 0.1 to 20 GHz. The values of $\mu_r^*$ ($\mu_r^* = \mu_r' - j\mu_r''$, $j = \sqrt{-1}$) and $\varepsilon_r^*$ ($\varepsilon_r^* = \varepsilon_r' - j\varepsilon_r''$) were calculated from the data of both $S_{11}^*$ and $S_{21}^*$. The complex reflection coefficient $\Gamma^*$ for a metal backed single layer absorber of which the incident electromagnetic wave is perpendicular to the surface was then determined from the values of $\mu_r^*$ and $\varepsilon_r^*$. The return loss $R$ for each sample thickness was calculated from $\Gamma^*$ using the relation $R = 20\log_{10}|\Gamma^*|$. $R$ was calculated at 0.1 mm intervals in the sample thickness range 0.1 to 30 mm.

## 3. RESULTS AND DISCUSSION

### 3.1. Frequency Dependences of the Return Loss for Composites Made of Granular Sendust Particles

Figure 1 shows the surface microphotographs of the composites made of granular sendust particles with size of approximately 5 μm and 20 μm (here after, 5 μm particles and 20 μm particles, respectively). A bright part is a sendust particle. When granular sendust particles are dispersed in polystyrene resin, the contact of each particle becomes point contact because of its particle shape, as shown in Figure 1.

Figure 2 shows the frequency dependences of the return loss for the composite made of 5 μm and 20 μm particles for various volume mixture ratios $V$. Thickness indicated in the same figure represents the optimal one for which the absolute value of return loss becomes maximal according to the $V$ value of a particle with each diameter. The percentage indicated in the same figure represents the normalized −20 dB bandwidth (the bandwidth $\Delta f$ corresponding to a return loss of less than −20 dB divided by the absorption center frequency $f_0$). A value of −20 dB corresponds to the absorption of 99% of the incident electromagnetic wave power. Both composites had a return loss of less than −20 dB at frequencies above 10 GHz although the absorption characteristics of each were different. In particular, for the composite made of 5 μm particles, the frequencies where the
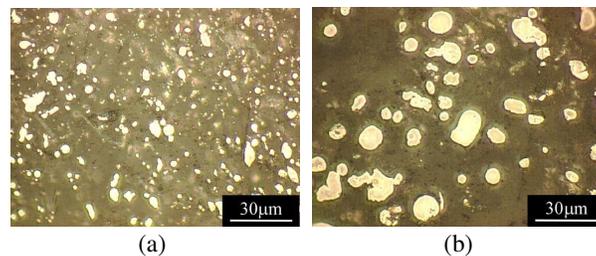


Figure 1: Surface microphotographs for composites made of (a) 5 μm particles and (b) 20 μm particles. The volume mixture ratio of sendust was 30 vol%.
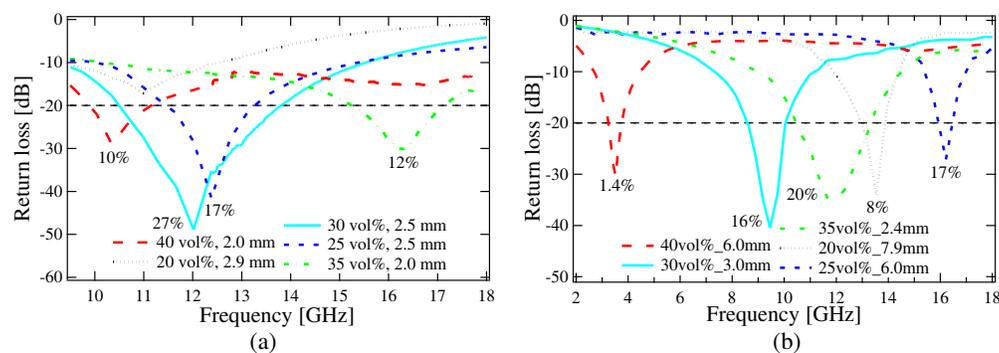


Figure 2: Frequency dependences of the return loss for composites made of (a) 5 μm particles and (b) 20 μm particles.

return loss was less than $-20$ dB existed between 10 and 20 GHz. The maximal value of normalized $-20$ dB bandwidth for the composite made of granular 5 μm particles was approximately 27% for the $V$ value of approximately 30 vol% and this value was much larger than those of a commercially available absorber (less than approximately 10%). The thickness used as a broadband absorber showed the tendency becomes thin as the $V$ value increased. On the other hand, on the whole, return loss for 20 μm particles shifted to the low frequency side, and bandwidth also decreased as seen in Figure 2. This is because the magnitude of $\varepsilon_r'$ is determined by the capacitance between adjacent particles in resin and that of $\varepsilon_r''$ is determined by the conductivity of a composite. Therefore, it is speculated that 20 μm particles are more densely to contact with each other compared with 5 μm particles. This causes the increase in conductivity of the composite made of 20 μm particles, because the composite made of particles with larger size had larger values of $\varepsilon_r'$. Experimental results reveal that the optimal volume mixture ratio of sendust is approximately 30 vol% for 5 μm particles and approximately 35 vol% for 20 μm particles in order to broaden the absorbing frequency bandwidth.

### 3.2. Measured Values of $\varepsilon_r'$, $\varepsilon_r''$ for Composites Composed of Sendust Particles with Size of 5 and 20 μm

To clarify the effects of sendust particle size on the absorption characteristics, the frequency dependences of $\mu_r^*$ and $\varepsilon_r^*$ for the composite made of 5 and 20 μm particles are discussed in the next. Figures 3 and 4 show the frequency dependences of $\varepsilon_r'$ and $\varepsilon_r''$ for the composite made of 5 and 20 μm particles, respectively. The values of both $\varepsilon_r'$ and $\varepsilon_r''$ for the composite made of 20 μm particles was larger than those for the composite made of 5 μm particles. The reason for the difference of $\varepsilon_r'$ and $\varepsilon_r''$ is considered to be as follows. The magnitude of $\varepsilon_r'$ is determined by the capacitance between particles and that of $\varepsilon_r''$ is determined by the conductivity of a composite as described before. Moreover, the apparent particle size of 20 μm particles increases owing to the particle linkage and the values of $\varepsilon_r'$ increases, because the composite made of large sendust particles had large values of $\varepsilon_r'$. From above results, the increase or decrease in $\varepsilon_r'$ and $\varepsilon_r''$ should be considered to design an absorber if the particle size is varied.
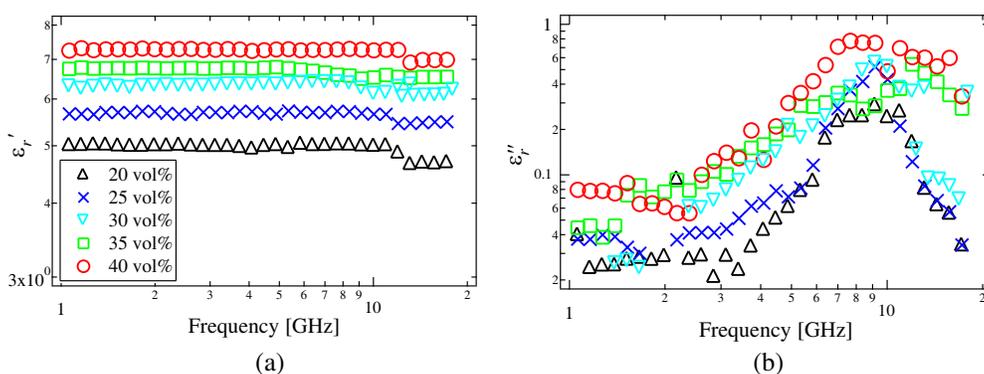


Figure 3: Frequency dependences of (a) $\varepsilon_r'$ and (b) $\varepsilon_r''$ for composites made of 5 μm particles.
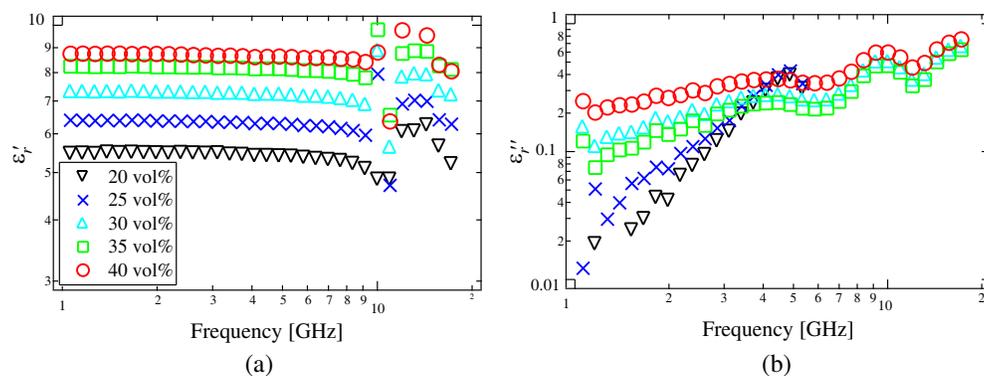


Figure 4: Frequency dependences of (a) $\varepsilon_r'$ and (b) $\varepsilon_r''$ for composites made of 20 μm particles.
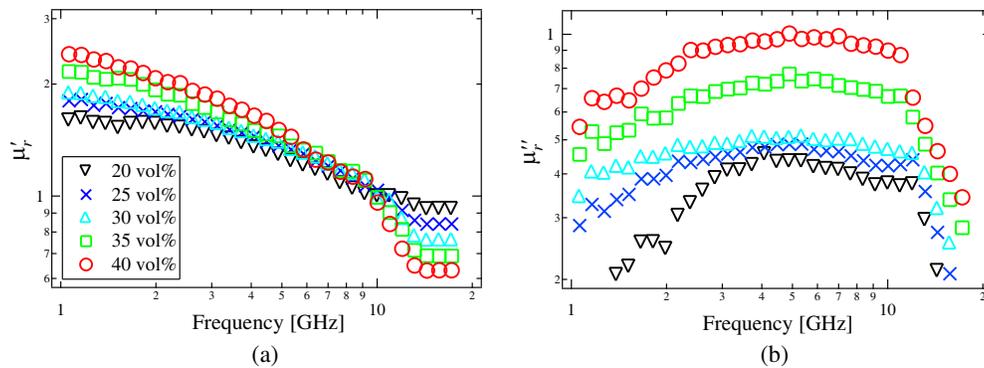
Figure 5: Frequency dependences of (a) $\mu'_r$ and (b) $\mu''_r$ for composites made of 5 μm particles.
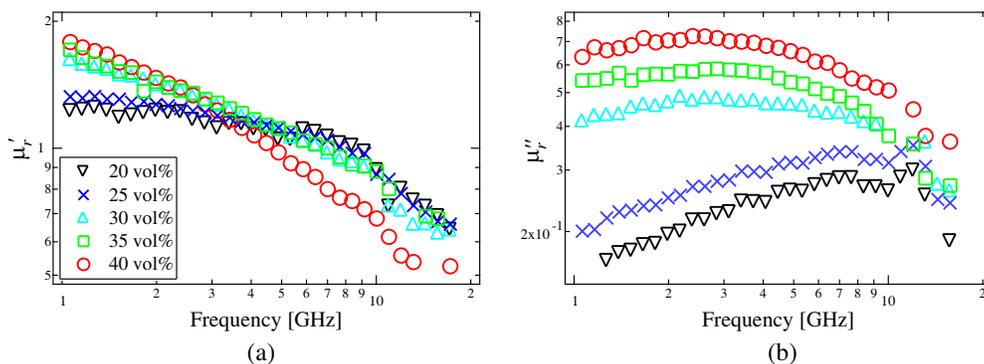


Figure 6: Frequency dependences of (a) $\mu'_r$ and (b) $\mu''_r$ for composites made of 20 μm particles.

### 3.3. Measured Values of $\mu'_r$, $\mu''_r$ for Composites Composed of Sendust Particles with Size of 5 and 20 μm

The frequency dependences of $\mu'_r$ and $\mu''_r$ for the composite made of 5 and 20 μm particles are shown in Figures 5 and 6. The values of $\mu'_r$ for both composites decreased with increasing frequency although the frequency where $\mu'_r$ begins to decrease was different. Similarly, the frequency where $\mu''_r$ begins to decrease depended on the particle size and these two composites had different frequency dependence of $\mu''_r$. However, the values of $\mu'_r$ and $\mu''_r$ for both composites were almost the same at frequencies above approximately 10 GHz. In the frequency range of several GHz, the frequency dependences of $\mu'_r$ and $\mu''_r$ for the composite made of sendust particles dispersed in polystyrene resin is explained by the natural magnetic resonance of sendust and this phenomenon depends on the particle shape of sendust [3, 10]. This is because the response of incident magnetic field is determined by the particles size. Thus, different frequency dependences of $\mu'_r$ and $\mu''_r$ were observed at frequencies of several GHz. On the contrary, in the high frequency range of tens of GHz, the effect of natural magnetic resonance is reduced with increasing frequency and the magnetic moments generated by the induced eddy current owing to the incident magnetic field affect the values of $\mu'_r$ and $\mu''_r$ because sendust is conductive [9]. It reveals that $\mu'_r$ for the composite made of 5 μm particles is independent of the frequency and is smaller than unity above approximately 10–12 GHz and decrease with increasing $V$ as seen in Figure 5(a). The phenomenon that $\mu'_r$ become less than unity has also been observed in composites made of polystyrene resin and conductive particles such as aluminum [7]. In this case, $\mu'_r$ decreases with increasing $V$ and that of $\mu''_r$ decreases in inverse proportion to the particle size of the conductive particles according to Equation (1) derived by a qualitative theoretical estimation [7].

$$1 - \mu'_e = V, \quad \mu''_e = 2V\delta/a \quad (1)$$

Here $\delta$ is the skin depth and $a$ is the diameter of the conductive particles. Result shown in Figures 5(a) was in roughly agreement with Equation (1).
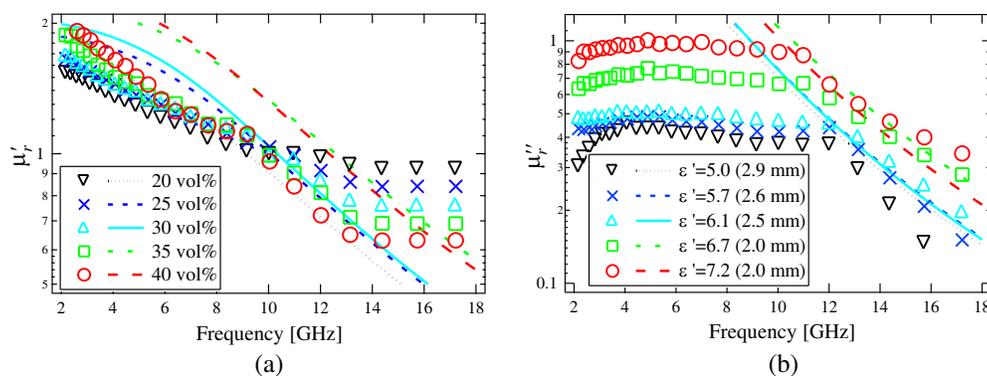
Figure 7: Measured values of (a) $\mu_r'$ and (b) $\mu_r''$ and the calculated values which satisfy the non-reflective condition for composites made of 5 μm particles.
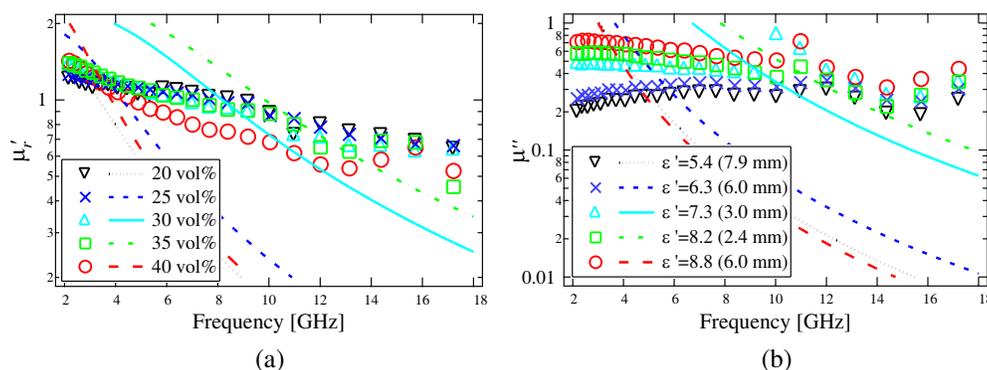


Figure 8: Measured values of (a) $\mu_r'$ and (b) $\mu_r''$ and the calculated values which satisfy the non-reflective condition for composites made of 20 μm particles.

### 3.4. Measured and Calculated Values of $\mu_r'$ and $\mu_r''$ that Satisfy the Nonreflective Condition for Composites Made of Polystyrene Resin and Sendust Particles with Size of 5 and 20 μm

To clarify the effects of sendust particle size on the absorption characteristics, the frequency dependences of $\mu_r^*$ and $\varepsilon_r^*$ for the composite made of 5 and 20 μm particles are discussed in the next. To examine the absorption characteristics caused by the difference of the frequency dependency of $\mu_r^*$ and $\varepsilon_r^*$, the values of $\mu_r'$ and $\mu_r''$ that satisfy the non-reflective condition for a metal-backed single-layer absorber were calculated [1]. It is assumed that values of $\varepsilon_r'$ used for the calculation are independent of frequency and are the same as the measured values and $\varepsilon_r''$ is zero. Figures 7 and 8 shows the measured and calculated values, which satisfy the non-reflective condition of $\mu_r'$ and $\mu_r''$. When the value of $\varepsilon_r'$ is different, it is found that the calculated values of $\mu_r'$ and $\mu_r''$ are prominently different. Therefore, it is reveals that the measured values of both $\mu_r'$ and $\mu_r''$ for the composite made of 5 μm particles could satisfy the non-reflective condition in the frequency range between 10 and 16 GHz for absorber thickness of 2–3 mm as seen in Figure 7. On the other hand, the broadband absorption feature for the composites made of 20 μm particles was not acquired for the same $V$ value. It is because for 20 μm particles, $\mu_r'$ decreased rapidly across unity with increasing frequency compared with 5 μm particles as seen in Figures 7 and 8. That $\mu_r'$ becomes smaller than unity above a few GHz are the condition with which the nonreflective conditions is satisfied.

### 4. CONCLUSIONS

Experimental results reveal that the optimal volume mixture ratio of sendust is approximately 30 vol% for the average particle size of approximately 5 μm, 35 vol% for 20 μm in order to broaden the absorbing frequency bandwidth especially at frequencies above 10 GHz. The maximal value of normalized $-20\,$dB bandwidth for the composite made of granular 5 μm particles was approximately 27% for the $V$ value of approximately 30 vol% and this value was much larger than those of a commercially available absorber. Considering the non-reflective condition, $\mu_r^*$ can be controlled by changing the volume ratio of sendust in resin and sendust particle size.

**REFERENCES**

1. Naito, Y. and K Suetake, "Application of ferrite to electromagnetic wave absorber and its characteristics," *IEEE Trans. Microwave Theory Tech.*, Vol. 19, No. 1, 65–72, 1971.
2. Nakamura, T., T. Tsutaoka, and K. Hatakeyama, "Frequency dispersion of permeability in ferrite composite materials," *J. Magn. Magn. Mater.*, Vol. 138, 319–328, 1994.
3. Tsutaoka, T., "Frequency dispersion of complex permeability in Mn-Zn and Ni-Zn spinel ferrites and their composite materials," *J. Appl. Phys.*, Vol. 93, No. 5, 2789–2796, 2003.
4. Lim, K. M., K. A. Lee, M. C. Kim, and C. G. Park, "Complex permeability and electromagnetic wave absorption properties of amorphous alloy-epoxy composites," *J. Non-Crystalline Solids*, Vol. 351, 75–83, 2005.
5. Moucka R. and A. V. Lopatin, "Enhancement of magnetic losses in hybrid polymer composites with MnZn-ferrite and conductive fillers," *J. Mater. Sci.*, Vol. 42, 9480–9490, 2007.
6. Koga, N. and T. Tsutaoka, "Preparation of substituted barium ferrite $BaFe_{12-x}(Ti_{0.5}Co_{0.5})_xO_{19}$ by citrate precursor method and compositional dependence of their magnetic properties," *J. Magn. Magn. Mater.*, Vol. 313, 168–175, 2007.
7. Sakai, K., Y. Wada, Y. Sato, and S. Yoshikado, "Design of composite electromagnetic wave absorber made of fine aluminum particles dispersed in polystyrene resin by controlling permeability," *PIERS Online*, Vol. 5, No. 7, 663–670, 2009.
8. Guan, Y., K. Sakai, Y. Sato, and S. Yoshikado, "Design of composite electromagnetic wave absorber made of fine spherical metal particles dispersed in polystyrene resin," *PIERS Online*, Vol. 7, No. 4, 301–307, 2011.
9. Sakai, K. and S. Yoshikado, "Effect of particle shape on absorption characteristics of composite electromagnetic wave absorber made of sendust particles dispersed in polystyrene resin," *ICC3 IOP Conf. Ser.: Mater. Sci. Eng.*, Vol. 18, 092019, 2011.
10. Tsutaoka, T., T. Ono, A. Tsurunaga, T. Kasagi, K. Hatakeyama, and M. Y. Koledintseva, *IEEE Int. Symp. on Electromagnetic Compatibility (EMC)*, 78–83, 2011.

# Delay Response of Gas Discharge Tubes

**Milic Pejovic**[1], **Momcilo Pejovic**[1], **Radeta Maric**[2],
**Ljubinko Timotijevic**[3], **and Koviljka Stankovic**[3]

[1]Faculty of Electronic Engineering, University of Nis
Aleksandra Medvedeva 14, Nis 18000, Serbia
[2]Electric Power Industry of Serbia
Masarikova 1-3, Belgrade 11000, Serbia
[3]Faculty of Electrical Engineering, University of Belgrade
Bulevar kralja Aleksandra 73, Belgrade 11000, Serbia

**Abstract**— Transient surge voltages, either conducted or coupled, are a rather common occurence in all electronic circuits, which makes effcient transient voltage suppression (TVS) a primary design requirement. Efficient protection against transient voltages, also called over-voltages, has two aspects: protection of integrity (no permanent damage of the protected device) and maintenance of operational functionality (operation reliability in the event of an over-voltage). Both power systems (providing energy generation, transmission and distribution) and low-voltage electronic systems are susceptible to transient voltages. The widespread use of gas discharge tubes (GDT) for over-voltage protection has been justified, since it has several advantages comparing to the other over-voltage protection components, such as the ability to conduct high currents, low intrinsic capacity, high insulating resistance, broad range of voltage protection, etc.. But, the main problem in GDT application is its relatively high response time. Electrical breakdown time delay is often refereed as delay response and it is also very important parameter of gas filled devices. The aim of this paper is to investigate dependence of the GDT delay response on the relaxation time, as well as the to determine the voltage range within which the GDT operate reliably.

## 1. INTRODUCTION

The capability of electronic components to withstand a temporary over-voltage without damage is reduced significantly as components are miniaturized. Causes, which may lead to over-voltage, are various: sometimes it is a consequence of energy redirection within a power system (switching over-voltage) or it could be an outcome of electronic discharge. In extreme conditions, a nuclear explosion may induce over-voltage. In order to protect electronic components and systems from over-voltage, suppressers diodes, metal oxide varistors and gas-discharge tubes (gas-filled surge arresters) are used. The gas discharge tubes (GDT) have several advantages comparing to other over-voltage components. These advantages are the ability to conduct high currents ($> 5\,\text{kA}$), low intrinsic capacity ($< 1\,\text{pF}$), high insulating resistance ($> \text{G}\Omega$) and the high range of voltage protection (from 70 to 1200 V) [1, 2].

GDTs are non-linear over-voltage protection components, whose operations are based on the principles of electrical breakdown in gas. The voltage for which the electrical breakdown occur in gas is called the breakdown voltage $U_d$. The $U_d$ is defined as the voltage when the discharge in the gas transits from the non-self sustaining to the self sustaining form [3] and is characterized by the rapid transition of gas from a poor electrical conductor with a resistivity of about $10^{14}\,\Omega \cdot \text{m}^{-1}$ to a relative good conductor with resistivity dependent on the particular conductions, but which is several orders of magnitude lower, typically about $10^3\,\Omega \cdot \text{m}^{-1}$ in the glow discharge, for example [4].

The electrical breakdown in gases can be static or dynamic regardless of the applied voltage type. The static (DC) breakdown occurs when the rate of change of the voltage is much lower than the rate of change of the elementary processes related to the electrical breakdown. If these rates are comparable, the breakdown is dynamic. The static breakdown voltage $U_s$ is a deterministic quantity, whereas the dynamic voltage $U_b$ has stochastic nature with a certain distribution [5].

The main problem in GDT application is its delay response [6], which is a consequence of electrical breakdown time delay. The electrical breakdown time delay $t_d$ can be defined as the time elapsed from the moment when the applied voltage reaches the breakdown voltage to the moment when it starts to decrease due the breakdown [7]. The definition of $t_d$ in this paper, for practical purposes will be the electrical breakdown time delay which is the time between the moment when the operating voltage higher then breakdown voltage is applied on GDT and the moment when GDT's considerable current starts to flow [8].

## 2. EXPERIMENTAL DETAILS

Devices used in this study were commercial GDT manufactured by companies CITEL and SIEMENS. The cross section of these components is presented in Figure 1.

Static breakdown voltage (DC spark over-voltage) of these components given by manufactures is 230 V with the $\pm 20\%$ tolerance and it was obtained for voltage increase rate of 100 V/s, while dynamic breakdown voltage (impulse spark over-voltage) is less then 750 V and this values was obtained for voltage increase rate of 1 kV/µs. SIEMENS GDTs have built in radioactive source which provides constant electron yield in interelectrode gap.

In our experiment the dynamic breakdown voltage $U_b$ for small voltage increase rate is measured using a discretized dynamic method, i.e., method of DC voltage increase in steps $U_p$ for defined duration of the step $t_p$ until breakdown. The measurements were performed using electronic system which block diagram is shown in Figure 2. Keithley 248 supplied the voltage $U_0$ on GDT which is considerably smaller than expected $U_b$ value. This voltage is increased in steps $U_p$ during time intervals $t_p$ by Keithley model 2400 until breakdown (see Ref. [8] for more details).

The electrical breakdown time delay measurements were performed with the electronic system which block diagram is presented in Figure 3. The system consists of three major parts: DC voltage supply, analogue and digital subsystem. The analogue subsystem provides two functions. It enables fast and accurate voltage switching on the GDT as well as accurate shaping of start and stop signals. The start signals is generated at the moment when the voltage is applied on the GDT. Stop signal represents the discharge through the tested devices. The role of the digital subsystem is to detect signals from the analogue subsystem and to measure time between them. Also it controls parameters relevant for electrical breakdown time delay measurement and it should provide fast data storage for a large number of measured data (see Ref. [9] for more details).

## 3. RESULTS AND DISCUSSION

In order to establish when static breakdown voltage $U_s$ can be consider as deterministic quantity, the measurement of breakdown voltage $U_b$ was performed for the small values of voltage increase rate $k = U_p/t_p$. It was shown that $U_b$ data, obtained under the same conditions, has different
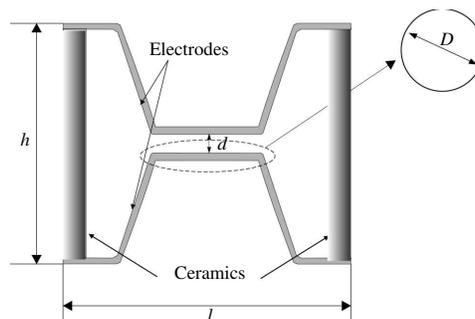


Figure 1: GDT cross-section.
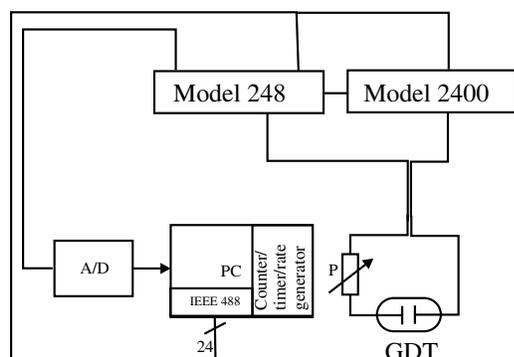


Figure 2: Block diagram of the system for breakdown voltage measurements.
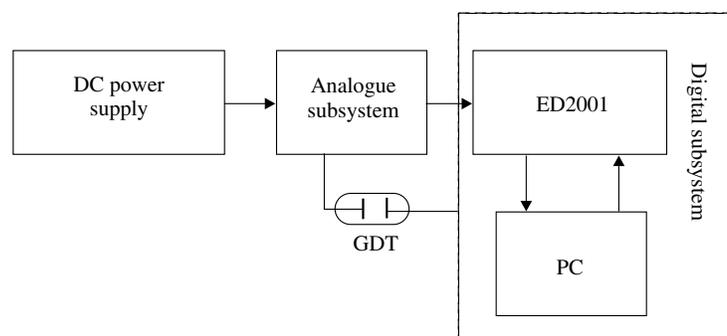
Figure 3: Block diagram of the system for electrical breakdown time delay measurements.

values. Because of that $U_s$ as deterministic quantity can be estimated from $\overline{U}_b = f(k)$ dependence, where $\overline{U}_b$ is the mean value of breakdown voltage $U_b$ [10]. The estimation of $U_s$ is performed in the following way. The $\overline{U}_b$ is determined for every value of the $k$ from certain interval and then data are fitted with linear fit ($\overline{U}_b$ was established from a series of 100 measurements of $U_b$ data for every value of $k$). The intersection of fitting curve with $\overline{U}_b$ axis (for $k = 0$) gives the $U_s$ values. In our experiment $U_s$ value for all GDT was obtained by measuring the $U_b$ for voltage increase rate $k$ interval from 1 to 10 V/s ($U_p$ was varied from 0.1 to 1 V, while $t_p = 0.1$ s).

The estimation of static breakdown voltage as a deterministic quantity from $\overline{U}_b = f(k)$ dependence was performed for ten devices from a same series manufactured by CITEL and for ten devices manufactured by SIEMENS as well. The results of such investigations for three randomly chosen devices from both companies are presented in Figures 4 and 5. It can be seen that mean value of breakdown voltage even for such small values of voltage increase rates considerably increases and that increase is following the linear tendency, i.e., experimental results can be very well fitted by a linear function (full lines in Figures 4 and 5). On these figures also present the values of $U_s$ obtained by extrapolation of linear fit until the intersection with $\overline{U}_b$ axis. $U_s$ values obtained by this method diverge for 2 to 10 V from the values given by a manufacturer (230 V). Because the tolerance given by a manufacturers is $\pm 20\%$ it can be concluded that there is a good agreement between the values of static breakdown voltage given by a manufacturers and our results.

Another important parameter of GDTs is response time also known as electrical breakdown time delay $t_d$. Figure 6 presents the dependence $\bar{t}_d = f(\tau)$ (memory curve) for GDT's manufactured by CITEL and SIEMENS, where $\bar{t}_d$ the mean value of $t_d$ and it was established from a series of 100 measurements for each value of relaxation time $\tau$ ($\tau$ is the time interval between two successive measurement when there is no voltage on the GDT).
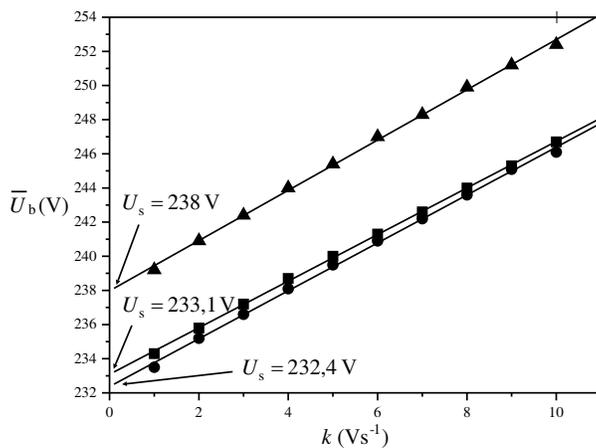


Figure 4: $\bar{U}_b = f(k)$ dependence for three GDT manufactured by CITEL.
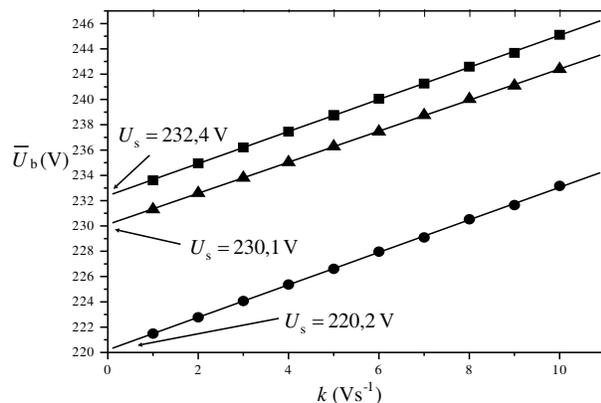


Figure 5: $\bar{U}_b = f(k)$ dependence for three GDT manufactured by SIEMENS.
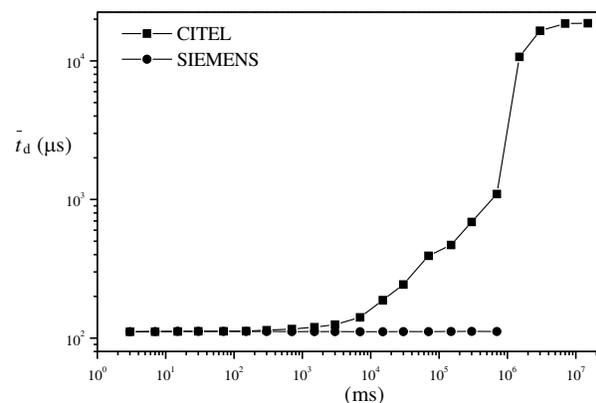
Figure 6: $\bar{t}d = f(\tau)$ dependence for GDTs manufactured by CITEL and SIEMENS.

$t_d$ values were measured for the voltage on the device $U_w = 1.5U_s$. It can be seen that the curves $\bar{t}_d = f(\tau)$ shape is very different for the devices made by CITEL and SIEMENS. Memory curve for devices made by CITEL consists from three segments: plateau, for $\tau$ up to 1 s, the area of $t_d$ rapid increase, for $\tau$ ranging from 1 s up to 2 hours and saturation region for $\tau$ grater then 2 hours. For devices manufactured by SIEMENS $\bar{t}_d$ remains constant for any value of $\tau$. Such memory curve behavior shows that the devices manufactured by SIEMENS are much more reliable for overvoltage protection then the devices manufactured by CITEL because their response time does not depend from relaxation time. The mechanisms responsible for the increase of $\bar{t}_d$ with the increase of $\tau$ (response time increase with the increase of $\tau$) for devices manufactured by CITEL are discussed in detail in the paper [11].

## 4. CONCLUSION

On the bases of dynamic breakdown voltage $U_b$ obtained for small values of voltage increase rate $k$ it was shown that it is stochastic quantity. Static breakdown voltage $U_s$ as a deterministic quantity can be estimated using $\overline{U}_b = f(k)$ dependence. Obtained $U_s$ values are in a good agreement with the values given by a manufacturer with the tolerance of $\pm 20\%$. On the bases of $\bar{t}_d = f(\tau)$ dependence it was concluded that for devices manufactured by SIEMENS delay response does not depend from relaxation time $\tau$, while for devices manufactured by CITEL delay response shows big variations with the increase of $\tau$.

## ACKNOWLEDGMENT

## REFERENCES

1. Martzolff, F. D., *IEEE Trans. Ind. Appl.*, Vol. 21, 99, 1985.
2. Osmokrovic, P., B. Loncar, and S. Stankovic, *IEEE Trans. Nucl. Sci.*, Vol. 39, 1876, 2002.
3. Raizer, Y. P., *Gas Discharge Physics,* Springer, Berlin, 1991.
4. Meek, J. M. and J. D. Craggs, *Electrical Breakdown of Gases*, Wiley, New York, 1987.
5. Pejovic, M. M., M. M. Pejovic, and K. Stankovic, *Japanese J. Appl. Phys.*, Vol. 50, 086001, 2011.
6. Loncar, B., P. Osmokrovic, and S. Stankovic, *IEEE Trans. Nucl. Sci.*, Vol. 50, 1725, 2003.
7. Strigel, R., *Electrical Breakdown of Gases*, Springer, Berlin, 1939.
8. Pejovic, M. M., *Rev. Sci. Instrum.*, Vol. 76, 015102, 2005.
9. Pejovic, M. M., D. B. Denic, M. M. Pejovic, N. T. Nesic, and N. Vasovic, *Rev. Sci. Instrum.*, Vol. 81, 105104, 2010.
10. Pejovic, M. M., C. S. Milosavljevic, and M. M. Pejovic, *IEEE Trans. Plasma Sci.*, Vol. 31, 776, 2003.
11. Pejovic, M. M. and M. M. Pejovic, *J. Phys. D: Appl. Phys.*, Vol. 39, 4417, 2006.

# Radiation Induced Noise Level in Solar Cells

**Milos Zdravkovic**[1], **Aleksandra Vasic**[2], **Bojan Cavric**[1],
**Radovan Radosavljevic**[1], **and Koviljka Stankovic**[1]

[1]Faculty of Electrical Engineering, University of Belgrade
Bulevar Kralja Aleksandra 73, Belgrade 11000, Serbia
[2]Faculty of Mechanical Engineering, University of Belgrade
Kraljice Marije 16, Belgrade 11000, Serbia

**Abstract**— One of main characteristics of all detectors is energy resolution which primarily depends on noise. Negative influence of noise on the detector functioning is in widening of the spectral line of the impulse signal and raising the detection threshold, and that is main limiting factor for detector functioning. That is the reason why lowering noise level is very important precondition for obtaining a good quality detectors, so investigation of physical basis of different types of noise is necessary for their optimization. It could be said that regardless of the detector quality, noise is present in all detectors and it depends on fundamental physical processes during fabrication and operation of these devices. The most common source of noise that is connected to the hostile working conditions is radiation. During the interaction with the material, radiation could deposit large amount of energy that could induce various effects. Due to their wide range of application, solar cells are exposed to various kinds of radiation in working environment. From the technological point of view it is very important to establish changes in output characteristics of the device (current, voltage, and efficiency) induced by the radiation that affect their operation. The aim of this paper is to investigate increased noise level in solar cells due to radiation in order to facilitate the production of more reliable devices.

## 1. INTRODUCTION

Possibilities for the application of solar systems based on photovoltaic conversion of solar energy are very wide, primarily because of their relatively low cost and very important fact that solar energy is most acceptable source of electrical energy from the environmental point of view. Regardless of very high standards in the production of electronic devices, all of them are more or less prone to the effects of aging even if they're not exposed to extreme (hostile) working conditions. One of the most limiting factors for all kinds of detectors is their noise, such as frequency dependent generation-recombination noise, burst noise and $1/f$ noise. That is why lowering noise is important for obtaining good quality detectors. It is known that low frequency noise ($1/f$ and burst noise) manifests as random fluctuation of the output current or voltage, leading to lowering of the efficiency of the device. Although not yet theoretically proven, many experimental results suggest that the origin of $1/f$ and burst noise could be fluctuation of the number free charge carriers connected to existence of the traps located in the vicinity or directly in the junction area, or fluctuation of the mobility of charge carriers [14]. In both cases these fluctuations arise from the interactions of carriers with defects, surface states and impurities, that are either introduced during manufacturing of the device, or are present as a consequence of the hostile working conditions (radiation, high temperature, humidity) [5]. This is specially emphasized when devices have large surface to volume ratio, as it is for solar cells. In this case surface effects are expected to be a major cause of low frequency noise, so good quality contacts are of great importance.

Other most common source of noise that is connected to the hostile working conditions is radiation. During the interaction with the material, radiation could deposit large amount of energy that could induce various effects [6, 7]. In semiconductors for example, defect produced by radiation are connected to the localized energy states [8, 9] which change the concentration and mobility of the charge carriers. Namely, main characteristic of semiconductors is wide range change in the concentration of charge carriers either due to existence of the impurities and defects or increased temperature. Direct recombination of the excess electrons and hole is strictly forbidden process and they usually annihilate in the localized energy states in crystal. These are so called recombination centers, and imperfections with deep or multiple energy levels significantly stimulate process of recombination. Radiation induced defects fulfill these requirements and represent such recombination centers. The main effect of the radiation is an increase of the saturation current generated within or on the surface of the depletion region. The permanent damage of the device is caused by collisions of the incident radiation with the atoms in the crystalline lattice, which could be displaced from

their positions, creating defect states [10–12]. Generation-recombination noise could be produced by fluctuations in the density of charge carriers caused by spontaneous fluctuations in the rate of generation, recombination and incidence of charge carriers. Also, the diffusion noise could increase in such conditions as a result of localized fluctuations both of the density of charge carriers, and the rate of diffusion. In both cases, these noises affect the level of the produced current [13–15].

Due to their wide range of application, solar cells are exposed to various kinds of radiation in working environment (cosmic rays, upper layers of atmosphere, military and civil nuclear facilities etc.) [5]. Moreover, spent nuclear fuels emit simultaneously, in addition to $\gamma$-rays, several neutrons also, so semiconducting device (e.g., solar cell) placed in the vicinity of these fuels sustains different kind of radiation damage both from $\gamma$-rays and from neutrons. That is the reason why very comprehensive investigations have been undertaken in order to develop semiconducting devices that could reliably operate in the conditions of the increased radiation [16]. From the technological point of view it is very important to establish changes in output characteristics of the device (current, voltage, and efficiency) induced by the radiation that affect their operation. After very high doses of radiation series resistance of the base layer could be so high that most of the power generated by the device is dissipated by its own internal resistance [17]. However, small doses of radiation carefully introduced and monitored, could have some beneficial effects on device performance due to possible relaxation of crystal lattice, leading to lowering of series resistance.

The aim of this paper is to investigate increased noise level in solar cells due to the increased temperature and radiation damage in order to facilitate the production of more reliable devices.

## 2. EXPERIMENTAL PROCEDURE

Experimental measurements concerning solar cells were carried out on the commercially available solar cells based on encapsulated monocrystalline and polycrystalline silicon from different manufacturers. Monocrystalline solar cells were irradiated with Pu-Be point neutron source. A mixture of $^{238}$Pu with beryllium is a good source of neutrons, through a nuclear reaction in which 9Be absorbs an alpha particle from $^{238}$Pu and forms $^{12}$C with the emission of a neutron. This neutron source provides a broad beam of emitted neutrons up to about 11 MeV with an intensity maximum about 5 MeV. Samples were in direct contact with the source, and maximum dose rate was dD/dt $= 0.36$ mGy/h. Polycrystalline solar cells were irradiated with Co$^{60}$ gamma source with different doses. Irradiation was performed through glass in controlled environment. Current-voltage data were used for the characterization of the properties of solar cells. Standard measurement equipment was used to measure I-V curve under different illumination levels (between 32 and 350 W/m$^2$). Reflective lamp was used as a solar simulator. From the obtained curves, all relevant parameters were obtained. Before and after every step of the irradiation, current-voltage characteristics of the diodes were measured in highly controlled conditions at room temperature with combined measurement uncertainty less than 5%.

## 3. RESULTS AND DISCUSSION

Factors that influence internal parameters of solar cells such as series and parallel resistance lead to changes in efficiency and maximum generated power in solar cell. Capability of solar cell to convert solar energy into electrical, depends on various fundamental and technological parameters. Variations from the ideal case of current transport could be represented by the ideality factor [14] that could be easily obtained from I-V characteristics of solar cells.

As could be expected, output characteristics of solar cells (current, voltage, efficiency) were strongly influenced by radiation. It is known that, depending on the energy of gamma rays, their interaction with the material is through the photoelectric and Compton effects that could produce ionization induced changes in the material.

Also, due to the inevitable presence of surface energy states (as a result of lattice defects, dislocations, impurities etc.), after silicon is irradiated with the photons, both the surface recombination velocity and the density of surface states increase. If those states correspond to deep energy levels in the silicon energy gap, they act as efficient surface recombination centers for charge carriers. Generation of electron-hole pairs due to ionization effects usually result in the generation and increase of the noise and the minimum signal that can be detected. All of these effects lead to the decrease of output current, as could be seen in Fig. 1. Regardless to the illumination level, this decrease is prominent for both doses, though the decrease was steeper for the lower dose.

Presence of the radiation induced changes in the material was confirmed by measurements of series resistance of solar cells (Fig. 2). An abrupt increase of $R_s$ was observed both doses, but
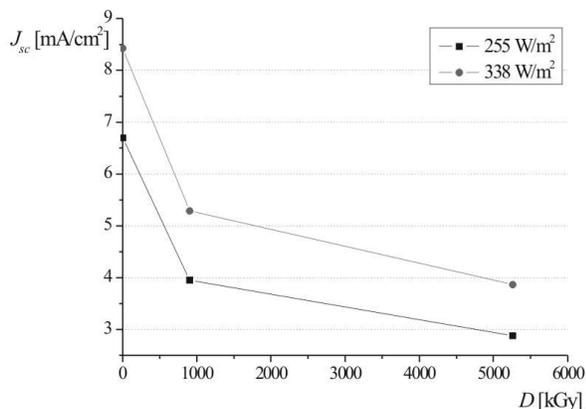
Figure 1: Dependence of $J_{sc}$ on the dose of gamma irradiation.
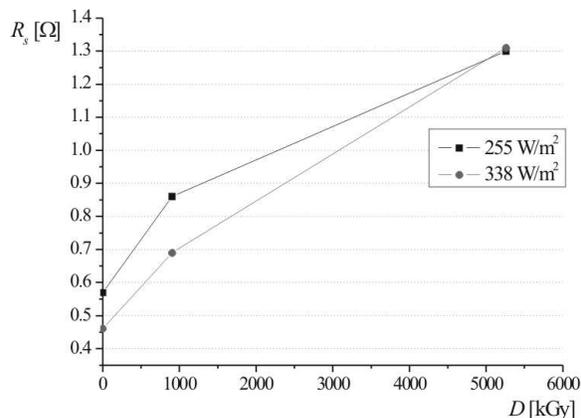


Figure 2: Dependence of $R_s$ on the dose of gamma irradiation.
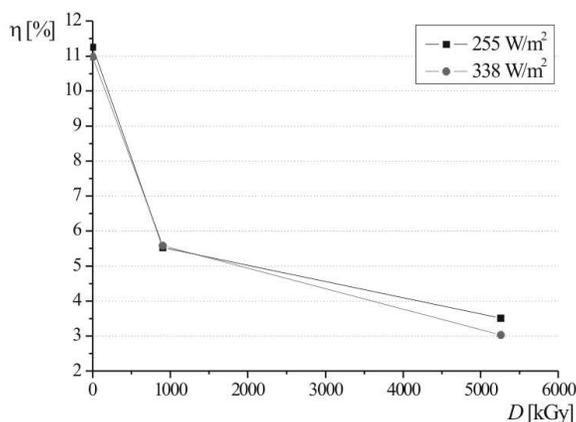


Figure 3: Dependence of efficiency on the dose of gamma irradiation for two illumination levels.

for higher dose of irradiation $R_s$ values were the same for both illumination levels, indicating that for higher doses effects of radiation are dominant over illumination effects. This increase of series resistance negatively affects other output characteristics of solar cells, primarily fill factor, and ultimately efficiency. This effect was shown in Fig. 3, where the decrease of efficiency was noticeable.

As for $J_{sc}$ dependence, decrease was steeper for the first dose of irradiation, indicating that the major disturbance of the structure, and transport mechanisms that leads to noise increase occurred at the beginning. Another interesting information that could be obtained from Fig. 3 is that efficiency decrease was independent on the illumination level. Values of the efficiency were the same (more or less) for both illumination levels, indicating that radiation has greater influence on production and transport of charge carriers than illumination. That, from the standpoint of solar cells, could be very limiting factor for their performance. It could be said that combined influence of the increased $1/f$ and burst noise due to radiation induced damage have significant negative influence on major solar cells characteristic, efficiency.

Although negative influence of radiation on electrical characteristics of the semiconducting devices is a well known and thoroughly investigated fact, especially when working in hostile conditions, in some cases irradiation could improve cell characteristics.

After initial increase of series resistance, for both illumination levels and for higher irradiation doses decrease of $R_s$ was observed (Fig. 4). This decrease is very significant from the solar cell design standpoint because it indicates possible beneficent influence of low doses of irradiation, even with neutrons. It could be explained by the fact that during fabrication process of any semiconducting device, structural defects and impurities that were unavoidably made, produce tension in the crystal lattice. Low doses of radiation could act similarly to annealing, relaxing lattice structure and
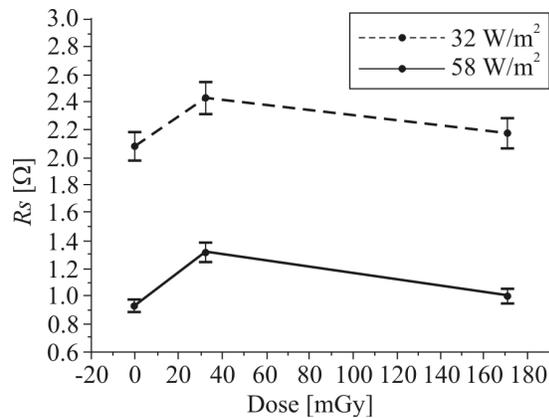
Figure 4: Dependence of the $R_s$ on doses for two illumination levels.
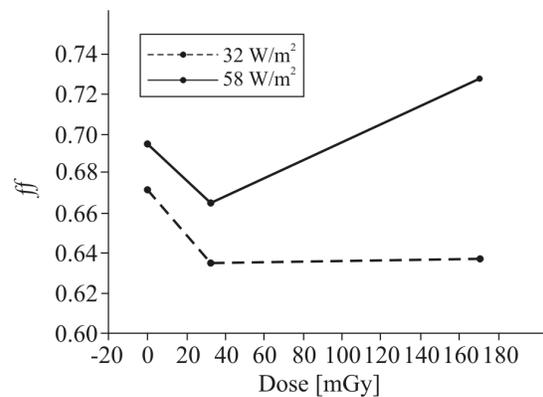


Figure 5: Dependence of the fill factor on doses for two illumination levels.

decreasing series resistance. This is especially important because other parameters of solar cells (fill factor $ff$) have shown the similar tendencies (Fig. 5). Namely, after first deterioration due to exposure to the radiation, for both parameters an increase was observed with an increase of the irradiation dose.

Although somewhat unexpected, this behavior could be explained by the fact that impurities and defects in the crystal structure which are unavoidable in the production process create certain tension of the crystal lattice. Some irradiation doses could lead, similar to the annealing, to the relaxation of crystal structure and the decease of series resistance. Considering the fact that maximum power and fill factor directly influence efficiency of the solar cells, their increase leads to an increase in efficiency.

## 4. CONCLUSION

Considered environmentally clean (non-polluting) and available in unlimited amounts, solar energy is the most promising energy source of the future (from current standpoint). As was shown in this paper, lowering noise level in solar cells based on silicon could be one way of improvement of solar cell characteristics. Increase of series resistance due to the exposure to gamma irradiation has also confirmed that damage induced by radiation increase noise level in semiconductor devices. Fluctuations of current and voltage and their decrease are the consequence of the radiation effects on the generation and transport of charge carriers. All of this inevitably lead to the decrease of the resolution of the photodetector device, lowering solar cells efficiency and for this reason monitoring of the device characteristics should be performed continuously, especially when solar cells are exposed to the severe working conditions. Although primarily negative, radiation effects could, in some cases, produce positive influence on solar cells characteristics. One way of obtaining solar cells with better output characteristics is exposure to relatively low doses of radiation (neutron, in this case). Observed improvement of the characteristics indicates that there is a possibility of using irradiation for enhancement of the solar cells quality.

## ACKNOWLEDGMENT

## REFERENCES

1. Jayaweera, P. V. V., P. K. D. D. P. Pitigala, A. G. U. Perera, and K. Tennakone, "$1/f$ noise and dye-sensitized solar cells," *Semiconductor Science Technology*, Vol. 20, 40–42, 2005.

2. Jayaweera, P. V. V., P. K. D. D. P. Pitigala, M. K. I. Senevirante, A. G. U. Perera, and K. Tennakone, "$1/f$ noise in dye-sensitized solar cells and NIR photon detectors," *Infrared Physics & Technology*, Vol. 50, 270–273, 2007.

3. Nærland, T. U., L. Arnberg, and A. Holt, "Origin of the low carrier lifetime edge zone in multicrystalline PV silicon," *Progress in Photovoltaics: Research and Apllications*, Vol. 17, 289–296, 2009.

4. Green, M. A., "Do built-in fields improve solar cell performance?," *Progress in Photovoltaics: Research and Apllications*, Vol. 17, 57–66, 2009.

5. Barth, J. L., C. S. Dyer, and E. G. Stassinopoulos, "Space, atmospheric, and terrestial radiation environments," *IEEE Transactions on Nuclear Sciences*, Vol. 50, 466–482, 2003.

6. Stanković, S., R. Ilić, P. Osmokrović, B. Lončar, and A. Vasić, "Computer simulation of gamma irradiation energy deposition in MOSFET dosimeters," *IEEE Transactions on Plasma Science*, Vol. 34, 1715–1718, 2006.

7. Vujisic, M., K. Stankovic, and A. Vasic, "Comparison of gamma ray effects on eproms and eeproms," *Nuclear Technology & Radiation Protection*, Vol. 24, 61–67, 2009.

8. Holmes-Siedle, A. G. and L. Adams, *Handbook of Radiation Effects*, Oxford University Press, New York, 2002.

9. Alexander, D. R., "Transient ionizing radiation effects in devices and circuits," *IEEE Transactions on Nuclear Sciences*, Vol. 50, 565–582, 2003.

10. Takagi, T. and J. Noda, "Gamma-ray irradiation effects in light-emitting diode and photodiodes for fiber optics," *IEEE Transactions on Nuclear Sciences*, Vol. 32, 4453–4459, 1985.

11. Barnes, C. E., "The effects of radiation on optoelectronic devices," *Proc. SPIE Fiber Optics in Adverse Enviroments*, Vol. 721, 18–25, 1986.

12. Vasic, A., P. Osmokrovic, B. Loncar, and S. Stankovic, "Extraction of parameters from I-V data for nonideal photodetectors: A comparative study," *Current Research in Advanced Materials and Processes*, Vol. 494, 83–88, 2005.

13. Vasic, A., P. Osmokrovic, M. Vujisić, Ć. Dolićanin, and K. Stanković, "Possibilities of improvement of silicon solar cell characteristics by lowering noise," *Journal of Optoelectronic and Advanced Materials*, Vol. 10, 2800–2804, 2008.

14. Vasic, A., M. Vujisic, B. Loncar, and P. Osmokrovic, "Aging of solar cells under working conditions," *Journal of Optoelectronic and Advanced Materials*, Vol. 9, 1843–1846, 2007.

15. Vasic, A., S. Stankovic, and B. Loncar, "Influence of radiation effects on the electrical characteristics of photodetectors," *Contemporary Studies in Advanced Materials and Processes*, Vol. 413, 171–174, 2003.

16. Horiushi, N., T. Nozaki, and A. Chiba, "Improvement in electrical performance of radiation-damaged silicon solar cells by annealing," *Nuclear Instruments and Methods A*, Vol. 443, 186–193, 2000.

17. Khan, M., Y. Yamaguchi, N. Ohshita, N. Dharmaraso, K. Araki, V. T. Khanh, H. Itoh, T. Ohshima, M. Imaizumi, and S. Matsuda, "Strategies for improving radiation tolerance of Si space solar cells," *Solar Energy Materials & Solar Cells*, Vol. 75, 271–276, 2003.

# Radiation Effects in Cooper Pair Insulating Thin Films

**Djordje Lazarević[1], Edin Dolićanin[2], Bratislav Iričanin[2],**
**Miloš Vujisić[2], and Koviljka Stankovic[2]**

[1]Radiation Protection Department, Institute of Nuclear Sciences Vinca
Mike Alasa 12-14, Belgrade 11000, Serbia
[2]Faculty of Electrical Engineering, University of Belgrade
Bulevar kralja Aleksandra 73, Belgrade 11000, Serbia

**Abstract**— Cooper-pair insulators are materials that exhibit superconducting behavior, but under specific conditions, regarding film thickness, bias voltage, applied magnetic field, and presence of magnetic impurities, act as insulators with thermally activated Cooper pairs as charge carriers. This paper investigates possible radiation effects in thin films of such materials. Radiation effects are predicted on the basis of Monte Carlo simulations, using 2D Josephson junction array as a model of material structure. Results of a combined theoretical and numerical analysis suggest that radiation-induced change of the Josephson junction charging energy could significantly affect the current-voltage characteristics of a Cooper-pair insulator, and that a transition to a metallic state is possible, due to radiation-induced disruption of the fine-tuned granular structure. The breaking of Cooper pairs, caused by incident and displaced ions, can also destroy the conditions for this specific insulating state to exist.

## 1. INTRODUCTION

Cooper-pair insulators (CPIs) are materials that exhibit superconducting behavior, but under specific conditions (regarding film thickness, bias voltage, applied magnetic field, and presence of magnetic impurities) act as insulators with thermally activated Cooper pairs as charge carriers [1–3]. Such behavior has been found in thin films of $\alpha$ Bi, TiN, InO$_x$, and Be [4–7]. It has been proposed, and eventually verified through simulation and experiment, that this insulating phase is characterised by a granularlike structure, consisting of superconducting droplets (i.e., islands of localized Cooper pairs) distributed throughout a matrix of normal material [8–11]. A detailed mechanism of island formation is yet to be acertained, and there are presently several competing theories about it [10–13]. Under suitable conditions, the islanding of Cooper pairs appears spontaneously in the material as a consequence of increased disorder. The phenomenon of superconducting materials turning into insulators is therefore often regarded as a disorder-driven superconductor-insulator transition.

The granular structure of a CPI can be modeled by a two-dimensional Josephson junction array (2D.JJA) [1, 14]. It is a system consisting of small superconducting islands, each coupled to its nearest neighbours by Josephson weak links. Each junction is characterized by the Josephson coupling energy, $E_J = \hbar I_c/(2e)$, where $I_c$ is the Josephson critical current, as well as by charging energies $E_c$ and $E_{c0}$, related to inter-island capacitance and capacitance to ground (substrate), respectively. The charging energy $E_c$ is the energy needed for a Cooper pair to be transferred between neighbouring islands.

Extensive studies of the conditions under which the stated materials act as either superconductors or insulators at temperatures below $1\,\text{K}$ have shown that, in terms of the JJA model, the insulating phase emerges only when the conditions determining the degree of disorder make the charging energies larger than the coupling energy ($E_c$, $E_{c0} > E_J$), with the superconducting gap still exceeding the inter-island charging energy ($\Delta > E_c$) [5, 6]. At the application of an external voltage, in addition to local phase coherence and spatial confinement of Cooper pairs, wave function phase synchronization of all Cooper pairs in the JJA occurs, giving rise to a collective current state. Dc Josephson current couples the phases of adjacent junctions, so as to provide minimal power dissipation in the array. This establishes a global phase-synchronized state, and transport occurs as a simultaneous thermal activation of Cooper pairs through the whole array [1, 2]. Resistance follows an Arrhenius-like temperature dependence:

$$R \propto \exp\left(\frac{\Delta_c}{k_B T}\right) \tag{1}$$

where $\Delta_c$ is the collective Coulomb barrier, and $k_B$ the Boltzman constant. For the 2D JJA this barrier is:

$$\Delta_c = E_c \ln \frac{L}{d} \tag{2}$$

$L$ being the characteristic linear size of the system, and $d$ the size of an elemental cell in the array [4]. The uncertainty principle applied to a Josephson junction gives $\Delta\varphi\Delta n \geq 1$, where $\varphi$ is the phase difference across the junction, and $n$ is the number of Cooper pairs transferred through the junction.

Detailed physical explanation for the insulator-superinsulator transition is based upon energy relaxation from the tunneling Cooper pairs not only to the phonons, but also to intermediate bosonic modes (electromagnetic or electron-hole excitations) [15]. Tunneling through mesoscopic junctions, such as those between superconducting islands in a 2D.JJA, requires an exchange of energy between the tunneling charge carriers and some kind of excitation modes, to compensate for the difference in energy levels at junction banks. At low temperatures characteristic of the CPI phase, charge transfer is accompanied by a two-stage energy exchange. The tunneling Cooper pairs generate electron-hole pairs that serve as an environment exchanging energy with the tunneling current and then slowly losing it to phonons. At the nano-scale typical of the granular structure in TiN films, the Coulomb interaction acquires a logarithmic dependence on the distance between charges.

This paper investigates the effects of ion beam irradiation on the properties of the described insulating state, by using numerical simulation of particle transport.

## 2. SIMULATIONS OF ION TRANSPORT

Monte Carlo simulations of ion beams traversing TiN, InO, Be, and Bi films of different thickness (10 to 20 nm) were performed in the TRIM part of the SRIM software package [16]. The fact that TRIM calculations assume target temperature to be absolute zero makes it an appropriate tool for modeling radiation effects in the Cooper pair insulating state, which exists only at very low temperatures anyway, so that thermal diffusion and annealing of displaced atoms in the film can be neglected. Another approximation inherent in TRIM is that there is no build-up of radiation damage in the target, i.e., for each new incident ion the film is assumed to contain no damage produced by previous ions. Any assessment of the degree of radiation damage in the film is therefore an underestimation of the damage that a real ion beam would have caused. Since we were primarily interested in ion beam effects in superconducting islands within the granular structure of CPIs, we used TRIM's calculation of ionization losses to estimate the scope of Cooper pair breaking in these islands, by substituting atom ionization energies with depairing energies in each of the investigated materials.

Simulations were conducted with ions chosen to represent certain well known radiation fields, such as those encountered in the space environment (hydrogen, helium, lead) [17, 18], or beams commonly used in ion implantation processes (phosphorus, boron, arsenic). Simulations were restricted to monoenergetic unidirectional beams, incident perpendicularly on the film surface. Beam energy was varied across typical energy spectra of different ion species.

## 3. DISCUSSION OF THE POSSIBLE RADIATION EFFECTS

Owing to their small thickness ($\sim 10$ nm), the investigated films are immune to ions with energies above 1 MeV. Non-ionizing energy loss of high energy ions is low, and they traverse the films without deflection, causing only slight damage [19–22].

Simulations of ion transport suggest, however, that for certain ion species there exist energy ranges in which a great number of atom displacements would occur in irradiated films. The number of atomic displacements is in direct proportion to the fluence of incident radiation, i.e., the number of particle histories followed in the Monte Carlo simulation. Space charge created by the displaced ions that finally take interstitial positions could affect the size of the Josephson junction charging energy $E_c$, which then changes the collective Coulomb barrier $\Delta_c$ according to Equation (2). The low-bias ($eV \ll \Delta_c$) current-voltage dependence in the temperature interval $E_c < k_B T < \Delta_c$ is (1):

$$I = I_c \exp\left(-\frac{(\Delta_c - eV)^2}{2\Delta_c k_B T}\right) \tag{3}$$

where $I_c$ is the Josephson junction critical current, and $e$ the elementary charge. The change in the $I$-$V$ curve, resulting from the radiation-induced change of $E_c$, is illustrated for TiN in Figure 1.
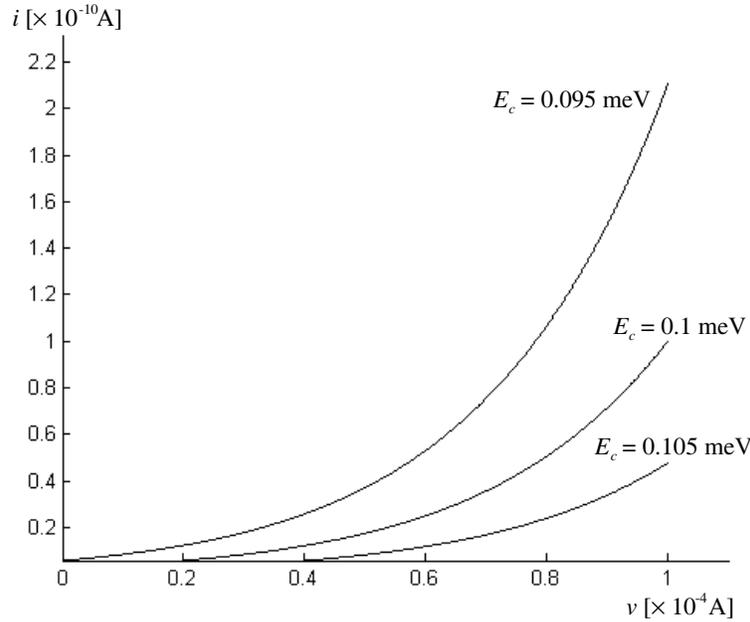
Figure 1: TiN film $I$-$V$ curves for three values of the Josephson junction charging energy $E_c$. The 5% change in $E_c$ is brought about by the space charge of the displaced ions which become interstitials in the irradiated film.

The stability of the investigated insulating state is dependent on the value of $E_c$, and only exists when $E_c > E_J$. If the radiation damage produced by ion beams is large enough to disrupt this condition, the thin film may revert to the ordinary metallic state.

Ionization energy losses by both the incident and the recoil ions observed in simulations point to a possible breaking of Cooper pairs in superconducting islands, that could destroy the insulating state during irradiation. With other conditions unchanged, this effect is expected to gradually vanish once irradiation ceases. The Cooper pairs may then reform and the insulating state restore.

## 4. CONCLUSION

Although the investigated CPI films are immune to the passage of high energy ions, simulations of ion transport reveal that significant ionization, phononic excitation, and production of displaced atoms can be expected for some energies, fluences and types of ions encountered in cosmic rays and used for implantation processes. Displacement damage, affecting primarily the value of inter-island charging energy in the 2D JJA that represents the material in the CPI phase affects the film's current-voltage charactersitics. Moreover, the conditions for the insulating state to subsist may be disrupted by ion beam irradiation, through the decrease of the charging energy or the breaking of Cooper pairs.

### ACKNOWLEDGMENT

### REFERENCES

1. Fistul, M. V., V. M. Vinokur, and T. I. Baturina, *Phys. Rev. Lett.*, Vol. 100, No. 086805, 2008.
2. Sambandamurthy, G., L. W. Engel, A. Johansson, E. Peled, and D. Shahar, *Phys. Rev. Lett.*, Vol. 94, No. 017003, 2005.
3. Nikolić, P. and Z. Tešanović, *Phys. Rev. B*, Vol. 83, No. 064501, 2011.
4. Stewart, Jr., M. D., A. Yin, J. M. Xu, and J. M. Valles, Jr., *Science*, Vol. 318, 1273–1275, 2007.
5. Baturina, T. I., A. Y. Mironov, V. M. Vinokur, M. R. Baklanov, and C. Strunk, *Phys. Rev. Lett.*, Vol. 99, No. 257003, 2007.

6. Sambandamurthy, G., L. W. Engel, A. Johansson, and D. Shahar, *Phys. Rev. Lett.*, Vol. 92, No. 107005, 2004.

7. Bielejec, E., J. Ruan, and W. Wu, *Phys. Rev. Lett.*, Vol. 87, No. 036801, 2001.

8. Sacepe, B., C. Chapelier, T. I. Baturina, V. M. Vinokur, M. R. Baklanov, and M. Sanquer, *Phys. Rev. Lett.*, Vol. 101, No. 157006, 2008.

9. Dubi, Y., Y. Meir, and Y. Avishai, *Phys. Rev. B*, Vol. 73, No. 054509, 2006.

10. Dubi, Y., Y. Meir, and Y. Avishai, *Nature*, Vol. 449, 876–880, 2007.

11. Feigel'man, M. V., L. B. Ioffe, V. E. Kravtsov, and E. A. Yuzbashyan, *Phys. Rev. Lett.*, Vol. 98, No. 027001, 2007.

12. Galitski, V. M., G. Refael, M. P. A. Fisher, and T. Senthil, *Phys. Rev. Lett.*, Vol. 95, No. 077002, 2005.

13. Pokrovsky, V. L., G. M. Falco, and T. Nattermann, *Phys. Rev. Lett.*, Vol. 105, No. 267001, 2010.

14. Imry, Y., M. Strongin, and C. C. Homes, *Physica C*, Vol. 468, 288–293, 2008.

15. Chtchelkatchev, N. M., V. M. Vinokur, and T. I. Baturina, *Phys. Rev. Lett.*, Vol. 100, No. 247003, 2009.

16. Ziegler, J. F., J. P. Biersack, and M. D. Ziegler, *SRIM, The Stopping and Range of Ions in Matter*, avaliable Online: http://www.srim.org.

17. Barth, J. L., C. S. Dyer, and E. G. Stassinopoulos, *IEEE Trans. Nucl. Sci.*, Vol. 50, 466–482, 2003.

18. Xapsos, M. A., J. L. Barth, E. G. Stassinopoulos, S. R. Messenger, R. J. Walters, G. P. Summers, and E. A. Burke, *IEEE Trans. Nucl. Sci.*, Vol. 47, 2218–2223, 2000.

19. Marjanović, N. S., M. L. Vujisić, K. D. Stanković, D. Despotović, and P. V. Osmokrović, *Nucl. Technol. Radiat. Prot.*, Vol. 25, 120–125, 2010.

20. Stanković, K. D., M. L. Vujisić, and L. D. Delić, *Nucl. Technol. Radiat. Prot.*, Vol. 25, 46–50, 2010.

21. Vujisić, M., D. Matijašević, E. Dolićanin, and P. Osmokrović, *Nucl. Technol. Radiat. Prot.*, Vol. 26, 2011, (in print).

22. Holmes-Siedle, A. G. and L. Adams, *Handbook of Radiation Effects*, 2nd Edition, 60–73, Oxford University Press, 2002.

# Expressing the Measurement Uncertainty of the Non-ionizing Radiation Survey in the Vicinity of GSM Base Stations

**Branislav Vulevic[1], Dragan Kovacevic[2], and Predrag Osmokrovic[3]**

[1]Public Company Nuclear Facilities of Serbia, Belgrade, Serbia
[2]Institute of Electrical Engineering "Nikola Tesla", Koste Glavinića 8a, Beograd 11000, Serbia
[3]Faculty of Electrical Engineering, University of Belgrade, Belgrade, Serbia

**Abstract**— The use of wireless communications devices has been increasing rapid over the past decades. Simultaneously with development of these technologies, increase public concerns about health risks of exposure to RF radiation for people residing in the vicinity of the GSM BS antennas. The public concern about the adverse effects has grown in the past ten years. The increasing number of cellular telephony subscribers has led an expansion of networks, with the installation of more base stations. This paper presents a summary values for broadband measurements of the radio frequency (RF) radiation in the vicinity of GSM base stations (GSM BS). It will be useful for determination of non-ionizing radiation exposure levels of the general public in future. The purpose of the paper is an appropriate representation of the basic information on the expressing of measurement uncertainty.

## 1. INTRODUCTION

Scientific Committee on Emerging and Newly Identified Health Risks (SCENIHR) points out that scientific studies still fail to provide support for an effect of electromagnetic fields (EMF) on self-reported symptoms, but indicate that the expectation or belief that something is harmful may play a role in symptom formation. Further epidemiological and laboratory investigations are needed [1].

In order to evaluate population exposure, knowledge of the field levels is very important. Measurements are basic both for the verification of the results obtained through the use of numerical models, and for the evaluation of the field levels when the sources are unlikely to be simulated because of their number, working condition, and complex distribution. Uncertainty in the scientific or technical context has a very specific meaning. If we make a measurement many times, we will get a range of results which are close to the "true" value. This spread in measured results can stem from differences in the exact measurement position, statistical variation in the response of the measurement instrument or differences in the way that different people read the instrument display. The uncertainty of the used measuring equipment has to be known and considered in the final assessment [2].

## 2. MEASUREMENT METHOD AND RESULTS

The European Conference of Postal and Telecommunication Administrations (CEPT) has produced ECC Recommendation (02)04 covering RF radiation [3]. This defines generally applicable measurement methods without mentioning any limit values. For such values, it refers to the EU Council Recommendation 1999/519/EC on protection of the general public [4] and to corresponding national regulations.

The ECC Recommendation envisages three cases for evaluating situations involving exposure to RF radiation:

- Case 1: Quick overview
- Case 2: Variable frequency band
- Case 3: Detailed investigation

Case 1, Quick overview, is sufficient as all the measured values remain below the Decision Level (the thresholds below the reference level on the International Commission on Non-Ionizing Radiation Protection (ICNIRP) limit values or on nationally-determined limit values). Broadbend measuring equipment is ideal for case 1. The following property are essential — measuring instrument and isotropic (non-directional) field probes must be capable of measuring the root mean square (rms) value [5].

In this case, the goal is characterization of RF electric field levels with electric field probe (Type 8.3) of EMR-300 RF radiation meter [6]. All measurements were done in points on about 1.5–1.8 m
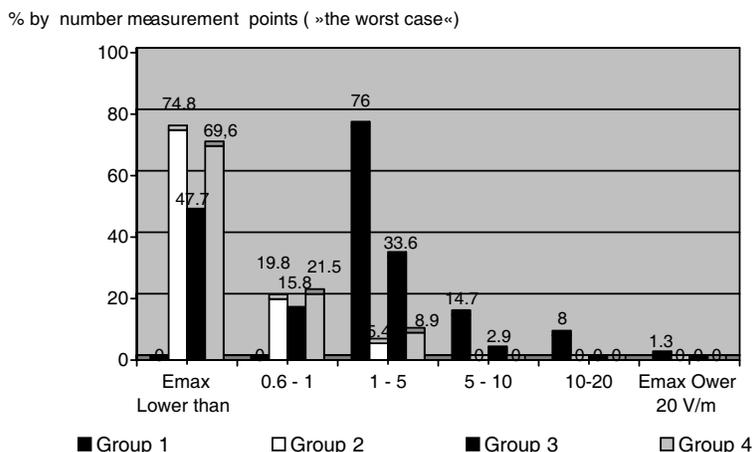
Figure 1: The percentile distribution of measurement values [5].

from ground / floor and on distance from antennas of GSM BS above 1 m ("far-field conditions") in the day-time period from 12 h to 16 h.

In order to minimize influence of other sorces of RF radiation, GSM BS were selected by means that ones are solely sorces of RF radiation in area within 150 m.

Measurements were divided into four groups:

- Group 1: Measurements on roofs where GSM BS are mounted;
- Group2: Measurements in rooms below GSM BS;
- Group 3: Measurement in rooms were situated around GSM BS;
- Group 4: Measurement around masts of GSM antennas.

The Figure 1 presents the accumulative percent of measurement values vs. RF electric field strength (100 kHz–3 GHz) for all four groups measures in the region of GSM BSfor "the worst case" (maximal value on display).

## 3. AN EXAMPLE OF EXPRESSINGTHE MEASUREMENT UNCERTAINTY

The evaluation of uncertainty should be performed following the ISO/IEC Guide [7]. The European Committee for Electrotechnical Standardization (CENELEC) issued standard EN 50413 [8] and EN 50492 [9] where useful information can be found about identification of the uncertainty components.

These are some of the uncertainty contributions [2, 10]:

a) Probe calibration, which should be carried out in an accredited laboratory;
b) Frequency interpolation, due to the fact that the probe calibration curve is determined for discrete frequencies of the reference EMF;
c) The measuring procedure followed to estimate the measured quantity and differences due to different staff carrying out the same type of measurement;
d) The effects of environmental conditions (i.e., temperature, humidity) in the measurement setup.

In this section, an example of the estimation of the uncertainty for electric field strength measurement with a calibrated PMM 8053A broadband field strength meter and isotropic probe PMM EP-300 (frequency range: 100 kHz to 3 GHz) is presented [11]. The uncertainties of the EP-300 field sensor are shown in Table 1.

Note/Conversion: $X\,[\text{dB}] = 20\log\left(\frac{x\%}{100} + 1\right)$ and $x\,[\%] = \left(10^{\frac{X\,\text{dB}}{20}} - 1\right) \cdot 100$

The measured RMS electric field strength obtained from 10 s samples for a total time of 6 min. The ambient temperature was about 25°C and the ambient relative humidity was about 57%. The high of the field sensor was 1.5 m above the ground.

In Table 2, an exampleof the uncertainty budget from CENELEC standard EN 50413 is reported for electric field strength measurements performed with a broadband measurement system (PMM 8053A -broadband field strength meter and isotropic probe PMM EP-300).

Table 1: Uncertainties associated with PMM EP-300 electric field strength sensor [11].

| Source | Quantity | Value |
|---|---|---|
| Manufacturer data sheet | Resolution | 0.01 V/m |
| | Absolute error @ 50 MHz, 20 V/m | ±0.8 dB |
| | Flatness | (3 MHz–3 GHz): ±1.5 dB |
| | Isotropy | ±0.8 dB (typycal±0.5 dB@ 930 and 1800 MHz |
| | Temperature error | 0–20°C: −0.05 dB/°C |
| | Modulation error | < ±1.25 dB |
| | Probe +8053A meter isotropy | ±0.5 dB |
| | Out of band responses | ±0.2 dB |
| Calibration certificate | Linearity (maximum error) | +1.52 dB/−0.2 dB |
| | Frequency response | +1.01 dB/−0.86 dB |
| | Probe anisotropy | +0.31 dB/−0.28 dB |
| | Calibration uncertainty | ±10%: $f \leq 300$ MHz ±15%: 300 Hz $< f \leq 3$ GHz |

Table 2: Example of an uncertainty budget for field strength measurement using a broadband measurement system [8, 10, 11].

| Influence factor | Reference | Specified uncertainty [%] | Distribution | Division factor | Standard uncertainty u(xi) [%] |
|---|---|---|---|---|---|
| Calibration | Calibration report | 15 | Normal ($k = 2$) | 2 | 7.5 |
| Isotropy (max. anisotropy of the field sensor) | Calibration report | 3.6 | Normal ($k = 2$) | 2 | 1.8 |
| Izotropy (probe and field meter) | Data sheet | 5,9 | Rectangular | 1.73 | 3.4 |
| Linearity deviation | Calibration report | 19.1 | Normal (k=2) | 2 | 9.6 |
| Frequency response | Calibration report | 12.3 | Normal ($k = 2$) | 2 | 6.2 |
| Temperature | Data sheet | 1.2 | Rectangular | 1.73 | 0.7 |
| Modulation error | Data sheet | 15.5 | Rectangular | 1.73 | 8.9 |
| Resolution | Data sheet | 0.18 | Rectangular | 1.73 | 0.1 |
| "Out of band" responses | Data sheet | 2.3 | Rectangular | 1.73 | 1.3 |
| Repeatability of indication | Measuring series | 0.8 | Normal ($k = 1$) | 1 | 0.8 |
| Combined standard uncertainty / $u_C$[%]/ | | | | | 16.84 |
| Expansion factor / k / | | | | | 1.96 |
| Expanded uncertainty / U [%]/ | | | | | 33 |

**REFERENCES**

1. European Commission, SCENIHR, Health Effects of Exposure to EMF, Available Online: http://ec.europa.eu/health/ph_risk/committees/04_scenihr/docs/scenihr_o_022.pdf.

2. Vulevic, B. and P. Osmokrovic, "Evaluation of uncertainty in the measurement of environmental electromagnetic fields," *Radiat. Prot. Dosim.*, Vol. 141, No. 2, 173–177, 2010.

3. Electronic Communications Committee (ECC), ECC Recommendation (02)04 (Revised Bratislava 2003, Helsinki 2007): Measuring Non-ionizing Electromagnetic Radiation (9 kHz–300 GHz), Edition 060207, 2007.

4. EC, "Council Recommendation of 12 July 1999 on the limitation of exposure of the general public to electromagnetic fields (0 Hz to 300 GHz)," *Official Journal of the European Community*, L199/62, 1999.

5. Vulević B., "Determination of radiofrequency radiation levels in area of gsm base stations," Master Thesis, University of Belgrade, Faculty of Electrical Engineering, 2006 (in Serbian).

6. Freeden, J. V., EMR-200/300 Radiation Meters Operating Manual, BN 2244/98.22, 2001.

7. ISO/IEC Guide 98-3:2008, "Uncertainty of measurement, Part 3: guide to the expression of uncertainty in measurement (GUM:1995)," 2008.

8. CENELEC EN 50413:2008, "Basic standard on measurement and calculation procedures for human exposure to electric, magnetic and electromagnetic fields (0 Hz–300 GHz)," 2008.

9. CENELEC EN 50492:2008, "Basic standard for the in situ measurement of electromagnetic field strength related to human exposure in the vicinity of base stations," 2008.

10. Vulević B., "An estimate of measurement uncertainty when assessing the level of electromagnetic fields in the environmental," Ph.D. Thesis, University of Belgrade, Faculty of Electrical Engineering, 2010 (in Serbian).

11. Stratakis, D., A. Miaoudakis, C. Kadsidis, V. Zacharopoulos, and T. Xenos, "On the uncertainty estimation of electromagnetic field measurements using field sensors: A general approach," *Radiat. Prot. Dosim.*, Vol. 133, No. 4, 240–247, 2009.

# Uncertainty Evaluation of Conducted Emission Measurement by the Monte Carlo Method and the Modified Least-squares Method

**Aleksandar Kovačević[1], Dragan Kovačević[2], and Predrag Osmokrović[3]**

[1]Department of Electromagnetic Compatibility and Environmental Conditions
Technical Test Centre, Vojvode Stepe 445, Belgrade 11000, Serbia
[2]Institute of Electrical Engineering Nikola Tesla
Koste Glavinića 8a, 11000 Belgrade 11000, Serbia
[3]Faculty of Electrical Engineering, University of Belgrade
Bulevar kralja Aleksandra 73, P. O. Box 3554, Belgrade 11000, Serbia

**Abstract**— This paper presents a new model which uses mixed distribution for uncertainty evaluation of conducted emission measurement. Evaluation of probability density function (PDF) for the measurand has been done using a Monte Carlo method and a modified least-squares method (combined method). For illustration, the combined method is applied in three cases for two independent input quantities. Namely, the combined method is used for the evaluation of PDF for the output quantity (mixed distribution) according to PDF from two independent input quantities, and i.e., two independent input quantities assigned by the normal distributions, two independent input quantities where the first quantity is assigned a normal distribution and the second is assigned a rectangular distribution, two independent input quantities where the first quantity is assigned a normal distribution and the second is assigned a triangular distribution. The results obtained by the Monte Carlo method and the modified least-squares method are compared to the corresponding results when applying the standard GUM (*Guide to the Expression of Uncertainty in Measurement*) procedure.

## 1. INTRODUCTION

Measurement results generally need to be accompanied by quantitative statements about their accuracy. For the sake of comparability, a standardized treatment of measurement uncertainty is essential. The *Guide to the Expression of Uncertainty in Measurement* — GUM [1] has become the standard for the evaluation of measurement uncertainty. The concept of measurement uncertainty starts from a fact that all kinds of measurement uncertainty have a random character, which means that each one of them should be associated with the corresponding probability distribution [1]. Consequently, a probability distribution can take the form of a distribution function or a probability density function [2].

For measurement uncertainty assigning of linear or linearized models, for interrelating input quantities in relation to one output quantity, the GUM suggests one standard procedure which is known as the GUM *uncertainty framework* — GUF [2]. So, for one linear model combined standard uncertainty is completely determined in the scope of the GUF. However, in order to determine coverage factor it is necessary to know the probability density function (PDF) for the output quantity which is not explicitly determined in the GUF [3]. Propagation of distributions may be applied in several ways: by analytical methods, uncertainty propagation, numerical methods [2]. In practice, propagation of distributions may be applied without approximation only to simpler cases. The GUM Supplement 1 is based on one general concept of propagating PDFs where in order to obtain PDF for the measurand of the Monte Carlo method (MCM) use was suggested. Consequently, the law of propagation of uncertainties is based on a construction of a linear approximation to the model function [4].

Some of the standardized EMC measurements include within the precisely defined ways for evaluating uncertainty in measurement [5]. EMC tests and measurements typically have large uncertainties of at least several decibels [6]. Today, electronic equipment is considered to be the critical project element of armament and military equipment means and systems. So, for example, modern telecommunication devices are characterized on one hand by the great power of ultra broadband transmitters, and on the other by sensitivity of receivers [7]. And if the fast development of information technology is added to this, it becomes clear that the correct functioning of every single device, and all of them together, is not possible without the analysis of reciprocal electromagnetic effects [8]. Many uncertainty sources in the domain of EMC measurements were not studied well

and need further studying. That is why it is important to have good knowledge about uncertainty in EMC measurement and minimize them as much as possible.

This paper presents a model for determining probability density function for the output quantity (so-called mixed distribution), according to the probability density functions for two input quantities which are independent. Point estimates parameters of a mixed distribution were done by using a combined method which consists of the Monte Carlo method and the modified least-squares method.

## 2. POINT ESTIMATES PARAMETERS OF A MIXED DISTRIBUTION BY THE MONTE CARLO METHOD AND THE MODIFIED LEAST-SQUARES METHOD

The evaluation of probability density function for the measurand (output quantity) is done using the Monte Carlo method. The procedure of estimating an output quantity using the Monte Carlo method (MCM), its standard uncertainty and the coverage interval for one output quantity for the case of uncorrelated input quantities are described in [3]. The advantage of the MCM is that it enables obtaining the results for the output quantity no matter what the shape PDFs for the input quantities are, especially with the complex model of the measurement when the analytical approach is very comprehensive.

The Monte Carlo method demands numerical calculation of approximation of probability density function, so, for these needs the pseudorandom number generator (PRNG) is developed which constitutes a key of the Monte Carlo procedure. In addition, point estimates parameters of the probability density function for the output quantity (density function of a mixed distribution) are obtained by the combined method which consists of the Monte Carlo method and the modified least-squares method. Point estimates parameters of density function of a mixed distribution can also be obtained in the analytical procedure, but is more complicated, and sometimes difficult to execute.

Point estimates parameters of density function of a mixed normal-normal distribution are determined using the following expressions:

$$\hat{m}_{1i} = 1.05x_{\min} + 0.95(x_{\max} - x_{\min})r_{m_1;i}, \quad i = 1, 2, \ldots, N \tag{1}$$

$$\hat{s}_{1i} = 0.1s + 1.25sr_{s_1;i}, \quad i = 1, 2, \ldots, N \tag{2}$$

$$m_{2j} = 1.05x_{\min} + 0.95(x_{\max} - x_{\min})r_{m_2;j}, \quad j = 1, 2, \ldots, N \tag{3}$$

$$\hat{s}_{2j} = 0.1s + 1.25sr_{s_2;j}, \quad j = 1, 2, \ldots, N \tag{4}$$

where: $x_{\min}$, $x_{\max}$ — minimum and maximum values of a mixed distribution, respectively, $s$ — empirical standard deviation of a mixed distribution, $N$ — total number of trials, $r_{m_1;i}$, $r_{s_1;i}$, $r_{m_2;j}$, $r_{s_2;j} \in (0, 1)$ — pseudorandom numbers, respectively.

Mixed coefficient is determined using the expression:

$$\varepsilon_l = r_{\varepsilon;l}, \quad l = 1, 2, \ldots, N \tag{5}$$

The procedure of determining point estimates parameters of density function of a mixed normal-normal distribution consists of several steps.

First, one determines minimum and maximum values, $x_{\min}$ and $x_{\max}$, which were taken by the random variable $x$, and then, according to the generated pseudorandom numbers ($r_{m_1;i}$, $r_{s_1;i}$, $r_{m_2;j}$, $r_{s_2;j}$ and $r_{\varepsilon;l}$, respectively), which belongs to the interval $(0, 1)$, and using the Eqs. (1)–(5), the $i$th, $j$th and $l$th are determined for these parameters. Function values are determined of a mixed normal-normal distribution for every value of random variable $x$ which belongs to midpoint of each class histogram. If histogram has $k$ classes, then there are $k$ values of this density function of a mixed distribution. Also, the empirical values of this function are determined for each one of these classes using the following formula:

$$f_j = \frac{n_j}{nh}, \quad j = 1, 2, \ldots, k \tag{6}$$

where $n_j$ — is the number of values which fall under $j$th class of histogram, $n$ is the total number of values of the mixed distribution ($n = N_1 + N_2$), which were taken by the random variable $x$, and $h$ is the class width of histogram. The function $f_j$ is the empirical density function of mixed normal-normal distribution. Class width of histogram $h$ and the number of classes of histogram $k$

are determined according to the following formulas, respectively:

$$h = \frac{x_{\max} - x_{\min}}{k} \tag{7}$$

$$k = 1 + 3.3 \log_{10} n \tag{8}$$

It is implied that $k$ is taken as an integer value. For determining the value for $k$, there exist other formulas in statistics [9].

When the midpoint of each class histogram, $x_j$, values $f_j$ and $f(x_j)$ are determined, then one determines the sum of the squared deviations of these functions according to classes, using this formula:

$$S_i = \sum_{j=1}^{k} [f(x_j) - f_j]^2, \quad i = 1, 2, \ldots, N \tag{9}$$

When the first value of the $S_1$ sum is determined, then for the second generated pseudorandom numbers ($r_{m_1; i}$, $r_{s_1; i}$, $r_{m_2; j}$, $r_{s_2; j}$ and $r_{\varepsilon; l}$, respectively), the same procedure determines the parameters of the density function of mixed normal-normal distribution and the sum $S_2$, and then, the values of the two sums are compared. The parameters of density function of a mixed normal-normal distribution, determined in this way randomly, the ones retained are those in which the minor sum of the squared deviations of these functions is obtained. The procedure continues and the new sum $S$ is determined, and the parameters with which this sum is the least, are retained. The procedure must be repeated from $10^5$ to $10^6$ times, and even more.

Point estimates parameters of density function of a mixed normal-rectangular distribution are determined using the following expressions:

$$\hat{m}_i = 1.05x_{\min} + 0.95(x_{\max} - x_{\min})r_{m; i}, \quad i = 1, 2, \ldots, N \tag{10}$$

$$\hat{s}_i = 0.1s + 1.25sr_{s; i}, \quad i = 1, 2, \ldots, N \tag{11}$$

$$\hat{a}_j = x_{\max} - 0.9(x_{\max} - x_{\min})r_{a; j}, \quad j = 1, 2, \ldots, N \tag{12}$$

$$\hat{b}_j = 1.05x_{\max} - 0.9(x_{\max} - x_{\min})r_{b; j}, \quad j = 1, 2, \ldots, N, \quad \hat{a}_j < \hat{b}_j \tag{13}$$

where: $x_{\min}$, $x_{\max}$ — minimum and maximum values of a mixed distribution, respectively, $s$ — empirical standard deviation of a mixed distribution, $N$ — total number of trials, $r_{m; i}$, $r_{s; i}$, $r_{a; j}$, $r_{b; j} \in (0, 1)$ — pseudorandom numbers, respectively. Consequently, mixed coefficient is determined using the Eq. (5).

## 3. EVALUATION OF MEASUREMENT UNCERTAINTY FOR CONDUCTED EMISSION MEASUREMENTS BY APPLICATION OF THE GUM

The basic document for evaluating and expressing uncertainty in measurement is the GUM [1]. Consequently, the GUM proposes a standard procedure which is known as GUF, which is applied to linear or linearized models. Recently, the evaluation of measurement uncertainty is based on the knowledge about the measurement process and knowledge about the input quantities which influence the results of measurement. The knowledge about the measurement process is expressed by a so-called model equation which reflects the interrelation between the measurand and the input quantities [10]. The knowledge about the input quantities is represented by the appropriate PDFs.

### 3.1. Measurement Model

This work observes conducted emissions measurements in power leads of military telecommunication devices in Faradey cage according to the method CE102 from the standard MIL-STD-461E [11]. For determining of the measurand value, the standardized measurement method is used [11].

Model equation for the evaluation of the Measurement Instrumentation Uncertainty — MIU is given in [12], in the following expression:

$$V = V_{\mathrm{r}} + L_{\mathrm{c}} + L_{\mathrm{LISN}} + \delta V_{\mathrm{sw}} + \delta V_{\mathrm{pa}} + \delta V_{\mathrm{pr}} + \delta F_{\mathrm{step}} + \delta Z + \delta M \tag{14}$$

Consequently, it is visible that the Eq. (14) represents one purely additive linear model, whose terms are independent. Information about terms of an expression in the model equation is given in the Table 1 (see the next Section).

Uncertainty budget for the case of conducted emission measurements, apart from Type B evaluation, also constitutes Type A evaluation.

This work will not consider the contribution of type A evaluation.

Table 1: The data for the input quantities $X_i$ which is used for evaluation of the Measurement Instrumentation Uncertainty, type B, according to the ISO-GUM [1], which is used for the conducted emission measurement from 10 kHz to 10 MHz.

| Input quantity | $X_i$ | Estimate $X_i$ $(x_i)$ | | Standard uncertainty $u(x_i)$ | Sensitivity coefficient $c_i$ | Contribution to the standard uncertainty $u_i(y) = c_i u(x_i)$ |
|---|---|---|---|---|---|---|
| | | Value [dB] | Probability distribution function | | | |
| Receiver reading | $V_r$ | ±0.1 | Rectangular $k_p = 1.732$ | 0.058 | 1 | 0.058 |
| LISN-receiver attenuation | $L_c$ | ±0.1 | Normal $k_p = 2.000$ | 0.050 | 1 | 0.050 |
| LISN voltage division factor | $L_{\text{LISN}}$ | ±0.2 | Normal $k_p = 2.000$ | 0.100 | 1 | 0.100 |
| Receiver sine wave voltage | $\delta V_{\text{sw}}$ | ±1.0 | Normal $k_p = 2.000$ | 0.500 | 1 | 0.500 |
| Receiver pulse amplitude response | $\delta V_{\text{pa}}$ | ±2.0 | Rectangular $k_p = 1.732$ | 1.155 | 1 | 1.155 |
| Receiver pulse repetition rate response | $\delta V_{\text{pr}}$ | ±2.0 | Rectangular $k_p = 1.732$ | 1.155 | 1 | 1.155 |
| Frequency step error | $\delta F_{\text{step}}$ | ±0.0 | Rectangular $k_p = 1.732$ | 0.000 | 1 | 0.000 |
| LISN impedance | $\delta Z$ | +2.60 −2.70 | Triangular $k_p = 2.449$ | 1.082 | 1 | 1.082 |
| LISN-receiver mismatch | $\delta M$ | +0.676 −0.734 | U-shaped $k_p = 1.414$ | −0.519 | 1 | −0.519 |

## 3.2. Values of Input Quantities

The input quantities data are given in the Table 1. The given data are obtained from the manufacturer's specifications and calibration certificates, and they are used for the evaluation of the Measurement Instrumentation Uncertainty, type B, according to the ISO-GUM [1].

## 4. EVALUATION OF THE MEASUREMENT INSTRUMENTATION UNCERTAINTY WHICH IS USED IN CONDUCTED EMISSION MEASUREMENT USING THE MONTE CARLO METHOD AND THE MODIFIED LEAST-SQUARES METHOD

The previous section presents the uncertainty budget according to the GUM for the case of conducted emission measurement according to the method CE102 from the standard MIL-STD-461E [11]. Consequently, the model equation for the evaluation of the Measurement Instrumentation Uncertainty — MIU is given with the Eq. (14). The Monte Carlo method and the modified least-squares method (combined method) are applied to two by two independent input quantities from the given expression. Namely, the combined method is used for the evaluation of probability density function for the output quantity (mixed distribution) according to probability density function from two independent input quantities, and, i.e., two independent input quantities assigned by the normal distributions, two independent input quantities where the first quantity is assigned a normal distribution and the second is assigned a rectangular distribution, two independent input quantities where the first quantity is assigned a normal distribution and the second is assigned a triangular distribution. The Monte Carlo simulations for obtaining mixed distributions are done by the procedure which was described in the Section 2 and the values are used from the Table 1. A value of $N$, the total number of trials was $10^6$. The number of data which was used for simulation is $n = 5000$. Risk conformity was $\alpha = 0.05$, that is the confidence level $(1 - \alpha)$ was 0.95. One more data that is important for our simulation was the mixed coefficient $\varepsilon$ which was 0.5. The results

obtained by the combined method are compared to the corresponding results when applying the GUM.

### 4.1. Mixed Normal-normal Distribution

The first example which was used refers to two independent input quantities $L_c$ and $L_{LISN}$ assigned by two normal PDFs. The Table 1 shows that for two given input quantities $L_c$ and $L_{LISN}$ estimates are given with $\pm 0.1$ dB and $\pm 0.2$ dB, respectively. Then the estimated values are $x_1 = x_2 = 0$, and standard uncertainties $u(x_1) = 0.05$ and $u(x_2) = 0.1$, respectively. Consequently, the associated normal PDFs are determined by expectation $m_1$ and $m_2$ equal to the given estimates $x_1$ and $x_2$, respectively, and also standard deviations $s_1$ and $s_2$ equal to the given standard uncertainties $u(x_1)$ and $u(x_2)$, respectively. After entering the given data into a computer program, generating of pseudorandom numbers is done (in our case 5000). For such generated pseudorandom numbers histogram is drawn (Fig. 1) that represents the empirical curve of a mixed normal-normal distribution.

After that, determining point estimates parameters of a mixed normal-normal distribution by the combined method is done (Section 2). With parameters that are determined like this the density function of a mixed normal-normal distribution. These values of parameters are pseudorandom and with them fitting of a mixed normal-normal distribution (estimated curve) is tried in a histogram (the empirical curve, white line). In the Fig. 1 the estimated curve is shown in a yellow line. Consequently, the theoretical curve is shown by a red line and represents the results obtained according to the GUM (Fig. 1). It is noticeable that the estimated curve fitting in histogram is very good, which indicates that the unknown parameters of this distribution are estimated well. It should be mentioned, that coming of the curve through the mid-point of each class histogram is considered to be the best fitting. Also, it is noticeable that the estimated curve differs slightly from the theoretical curve.

### 4.2. Mixed Normal-rectangular Distribution

The second example which was used refers to two independent input quantities $\delta V_{sw}$ and $\delta V_{pa}$, assigned by normal and rectangular PDFs, respectively. The Table 1 shows that for two given input quantities $\delta V_{sw}$ and $\delta V_{pa}$ estimates are given with $\pm 1$ dB and $\pm 2$ dB, respectively. Then the estimated values are $x_1 = x_2 = 0$, and standard uncertainties $u(x_1) = 0.5$ and $u(x_2) = 1.155$, respectively. As in the previous example, the given data are recorded into the computer program, and then the pseudorandom numbers ($n = 5000$) generating is done. For generated pseudorandom numbers in such way the histogram is drawn (Fig. 2), which represents the empirical curve of a mixed normal-rectangular distribution.

Determining point estimates parameters of a mixed normal-rectangular distribution is done by the combined method (Section 2). These values of parameters are pseudorandom and the fitting of a mixed normal-rectangular distribution (estimated curve) in histogram (the empirical curve) is tried with them. In the Fig. 2, the estimated curve is shown in yellow line, while the theoretical curve is shown in red line and it represents the results obtained according to the GUM. It is noticeable that fitting of the estimated curve in histogram very well does not deviate a lot from the theoretical curve.
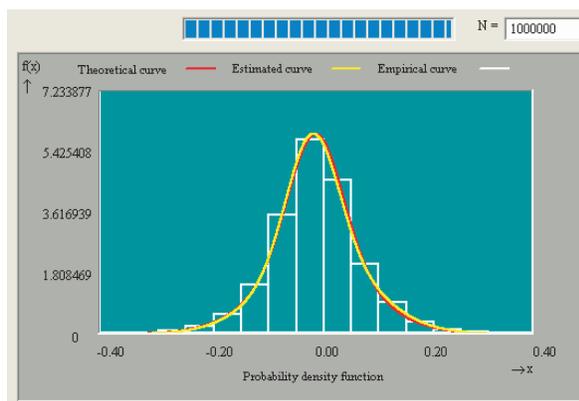


Figure 1: Mixed normal-normal distribution obtained by the combined method and GUM, respectively.
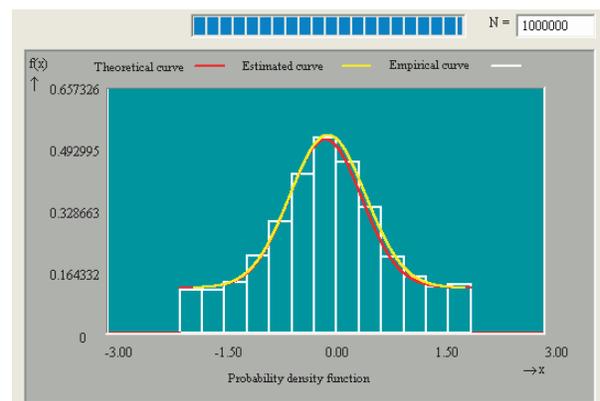
Figure 2: Mixed normal-rectangular distribution obtained by the combined method and GUM, respectively.
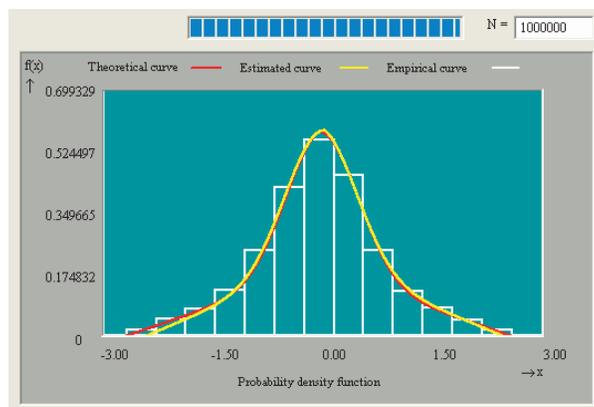
Figure 3: Mixed normal-triangular distribution obtained by the combined method and GUM, respectively.

### 4.3. Mixed Normal-triangular Distribution

The third example which was used refers to two independent input quantities $\delta V_{\mathrm{sw}}$ and $\delta Z$, assigned by normal and triangular PDFs, respectively. The Table 1 shows that for two given input quantities $\delta V_{\mathrm{sw}}$ and $\delta Z$ estimates are given with $\pm 1.0\,\mathrm{dB}$, and also $+2.60\,\mathrm{dB}$ and $-2.70\,\mathrm{dB}$, respectively. Then the estimated values are $x_1 = 0$ and $x_2 = -0.05$, and the standard uncertainties $u(x_1) = 0.5$ and $u(x_2) = 1.082$, respectively. And as in the previous example, the given data are recorded into the computer program, and then the generating of the pseudorandom numbers ($n = 5000$) is done. For such generated pseudorandom numbers the histogram is drawn (Fig. 3) that represents the empirical curve of a mixed normal-triangular distribution.

Determining point estimates parameters of a mixed normal-triangular distribution is done with the combined method (Section 2). These values of parameters are pseudorandom and with them, fitting of a mixed normal-triangular distribution (estimated curve) in a histogram (the empirical curve) is tried. In the Fig. 3 the estimated curve is presented in the yellow line. In the same figure the theoretical curve is presented in the red line and it represents the results obtained according to the GUM. It is noticeable that fitting of the estimated curve in a histogram very well and differs slightly from the theoretical curve and only at the ends.

### 5. CONCLUSIONS

In this paper the Monte Carlo method and the modified least-squares method (combined method) are described for the estimate of the output quantity, which is interrelating with two input quantities. As a representative model equation for the evaluation of the Measurement Instrumentation Uncertainty — MIU is used, and it is also used for the conducted emission measurement according to the method CE102 [11]. The Monte Carlo method (MCM) and the modified least-squares method are applied to two by two independent quantities which were associated the appropriate probability density functions (PDFs). In addition, applying MCM and the modified least-squares method produce a mixed distribution, i.e., PDF for the output quantity, which fits well (the estimated curve) in histograms and differs slightly from the produced results according to the GUM (the theoretical curve).

In this way, it is shown that applying PRNG produces valid results and have the algorithms for making representative draws. It is also shown that it can work with any PDFs for the input quantities. It is concluded that the applying combined method (MCM and the modified least-squares method) can be regarded as a reliable and easy to implement approach for evaluating the PDF for the output quantity to a satisfactory degree of approximation.

### REFERENCES

1. BIPM, IEC, IFCC, ISO, IUPAC, IUPAP, OIML, "Guide to the expression of uncertainty in measurement," International Organization for Standardization, Geneva, 1995, ISBN 92-67-10188-9.

2. JCGM, "Evaluation of measurement data — Supplement 1 to the 'Guide to the expression of uncertainty in measurement' — Propagation of distributions using a Monte Carlo method," 2008.

3. Cox, M. G. and B. R. L. Siebert, "The use of a Monte Carlo method for evaluating uncertainty and expanded uncertainty," *Metrologia*, Vol. 43, 178–188, 2006.
4. Wübbeler, G., M. Krystek, and C. Elster, "Evaluation of measurement uncertainty and its numerical calculation by a Monte Carlo method," *Meas. Sci. Technol.*, Vol. 19, 2008.
5. "Specification for radio disturbance and immunity measuring apparatus and methods — Part 4-1: Uncertainties, statistics and limit modeling — Uncertainties in standardized EMC tests," CISPR 16-4-1, 2005.
6. "The treatment of uncertainty in EMC measurements," NIS 81, NAMAS Executive: National Physical Laboratory, UK, 1994.
7. Paul, C. R., *Introduction to Electromagnetic Compatibility*, 2nd Edition, Wiley, New York, 2006.
8. Kovacevic, A. and D. Stankovic, "Testing of electromagnetic compatibility for military telecommunication equipment in screened room," *Proc. 51st Conference ETRAN 2007*, Herceg Novi, Montenegro, June 4–8, 2007.
9. Brkic, D. M., "A method for evaluation of number class intervals of histogram," *Microelectronics and Reliability*, Vol. 31, No. 2/3, 245–248, 1991.
10. Sommer, K. D. and B. R. L. Siebert, "Systematic approach to the modeling of measurements for uncertainty evaluation," *Metrologia*, Vol. 43, 200–210, 2006.
11. Standard MIL-STD-461E, "Requirements for the control of electromagnetic interference characteristics of subsystems and equipment," U.S. Department of Defense, 1999.
12. Specification for radio disturbance and immunity measuring apparatus and methods — Part 4-2: Uncertainties, statistics and limit modeling — Uncertainty in EMC measurements," CISPR 16-4-2, 2003.

# Radiation Induced Change of Serial PNP Power Transistor's Dropout Voltage in Voltage Regulators

**Vladimir Vukić[1] and Predrag Osmokrović[2]**

[1]Institute of Electrical Engineering "Nikola Tesla", University of Belgrade, Belgrade, Serbia
[2]Faculty of Electrical Engineering, University of Belgrade, Beograd, Serbia

**Abstract**— Previous examinations of voltage regulators "National Semiconductor" LM2940CT5 and "STMicroelectronics" L4940V5 in gamma radiation field pointed on similar influences of serial pnp transistor's geometry and its perimeter-to-area ratio on degradation of the transistor's forward emitter current gain. It was also perceived that even drastic fall of forward emitter current gain does not necessary lead to significant decrease of integrated circuit's radiation hardness, especially in the case of voltage regulators, devices with the negative feedback loop.

In this paper, were presented results related to the change of the serial transistor's dropout voltage and the forward emitter current gain as a function of absorbed total dose of gamma radiation. Lateral serial transistor's dropout voltage of LM2940CT5 voltage regulators decreased up to 12%, while dropout voltage of vertical serial devices in voltage regulators L4940V5 increased up to 70%. On the other hand, measured values of serial transistor's forward emitter current gain of radiation sensitive devices LM2940CT5 decreased 20–40% after the absorption of ionizing dose of $500\,Gy(SiO_2)$, while in the radiation hard voltage regulators L4940V5 was observed decrease of forward emitter current gain by 30–80 times! This was a consequence of abrupt rise of the serial transistor's base current and operation with low current of $100\,mA$ during the examination, that altogether with negative feedback loop reaction caused a significant shift of voltage regulator's serial transistor's operation point toward the left part of the characteristic $\beta(V_{BE})$, and not almost hundredfold degradation of forward emitter current gain of serial transistor in voltage regulator L4940V5.

## 1. INTRODUCTION

In the recently published papers were presented results of the examination of maximum output current and serial transistor's forward emitter current gain of low-dropout voltage regulators "National Semiconductor" LM2940CT5 and "STMicroelectronics" L4940V5 in gamma radiation fields [1, 2]. Results of change of the maximum output current and its influence on serial transistor's forward emitter current gain were analyzed.

Foregoing results pointed on the high radiation hardness of BiCMOS voltage regulators "STMicroelectronics" L4940V5 with vertical pnp transistors, also as very low radiation tolerance of conventional monolithic bipolar devices "National Semiconductor" LM2940CT5 with round lateral pnp transistors [3, 4]. Presented results related on data of maximum output current indicated on high possibility of making an error in determination of device's radiation hardness based on experiments that only analyze a change of the forward emitter current gain, particularly in electron devices with negative feedback loop [1]. On the other hand, results on the maximum output voltage gave much more reliable results on voltage regulator's radiation tolerance. During the maximum output current examination was noticed that bias conditions had the great influence on measured values of forward emitter current gain [2].

In this paper, were presented results related to the change of the serial transistor's dropout voltage and the forward emitter current gain as a function of absorbed total dose of gamma radiation.

## 2. EXPERIMENT

Integrated 5-volt positive commercial-off-the-shelf voltage regulators "ST Microelectronics" L4940V5 and "National Semiconductor" LM2940CT5 were tested in the Vinča Institute of Nuclear Sciences, Belgrade, Serbia, in Metrology — dosimetric laboratory.

$^{60}$Co was used as a source of $\gamma$ radiation and it was situated in the device for the realization of $\gamma$-field, IRPIK-B. The accepted mean energy of $\gamma$-photons was $E_\gamma = 1.25\,MeV$. The samples were irradiated in the mouth of collimator. The exposition doses measurement was exerted with the cavity ionizing chamber "Dosimentor" PTW M23361, of the volume $3 \cdot 10^{-5} m^3$. With the cavity ionizing chamber, the reader DI4 was used [2].

The current and voltage measurements were carried out with laboratory instruments "Fluke" 8050A and "Hewlett-Packard" 3466A. All measurements and the irradiation of components were performed at the room temperature of 20°C [2].

The main values used for the detection of voltage regulator's degradation due to the exposure to ionizing radiation were forward emitter current gain and serial transistor's collector-emitter dropout voltage. The measured electrical values were voltage regulator's output current, output voltage and quiescent current. The examination of the serial transistor's collector — emitter dropout voltage change was performed in the following way: input voltage was increased until output voltage dropped to 4.9 V, for the constant output current of 100 mA. Difference between the input and output voltage represents the dropout voltage of the serial transistor for a corresponding current [3].

The devices had been irradiated until the predetermined total doses were reached. To avoid the effects of recombination in semiconductor after the irradiation, all measurements were performed up to half an hour after the exposure. The devices in $\gamma$-radiation field were exposed to the total dose of $500\,Gy(SiO_2)$, with dose rate of $4\,cGy(SiO_2)/s$ [2].

More details about the experiment, sources of ionizing radiation, test procedure and technological processes implemented in the manufacturing of the examined circuits are provided in the references [2–4].

## 3. RESULTS

Data presented in Figures 1–3 were obtained by the tests of change of the serial transistor's dropout voltage on circuits "National Semiconductor" LM2940CT5 from the batch PM44AE. The data were collected during the voltage regulator's operation with the constant load current of 100 mA and constant output voltage of 4.9 V.

Although the dropout voltage rise on the serial transistor associated with the rise of absorbed total dose would be the expected effect, a noticeable decrease of dropout voltage may be observed. This phenomenon may be explained by the Early effect [5], according to the previously observed change of the maximum output current. A significant decrease of the output current caused by the reduced emitter efficiency, for approximately the same values of voltage $V_{BE}$ and the base width, must be connected with simultaneous decrease of the collector — emitter dropout voltage, $V_{CE}$. Whence the total dose of $300\,Gy(SiO_2)$ was absorbed, serial transistor dropout voltage starts to increase (Figure 1). Serial transistor's base current has the ascending trend, regardless the bias conditions, causing the steady decline of the serial transistor's forward emitter current gain, different from the most of observed trends during the examinations of maximum output current [1, 2]. Opposite to the noticed sharp decline of the base current after the absorption of very low total doses during the examinations of the maximum output current [2], whence the experiments on the change the serial transistor's dropout voltage were performed, similar effect was not perceived.

The explanation for the different responses was the much lower influence of degradation of the serial transistor's emitter injection efficiency during the operation with smaller serial tran-
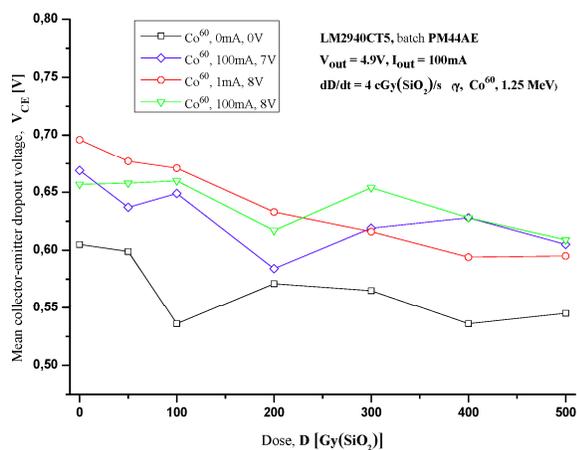


Figure 1: Change of mean collector — emitter dropout voltage in voltage regulator LM2940CT5 under the influence of $\gamma$ radiation.
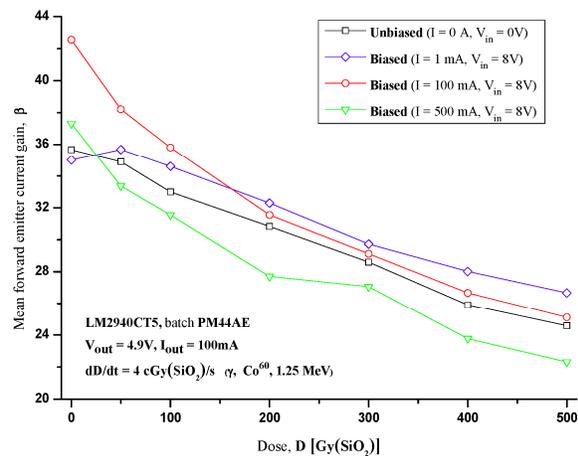
Figure 2: Change of the serial transistor's forward emitter current gain in voltage regulator LM2940CT5 under the influence of $\gamma$ radiation.
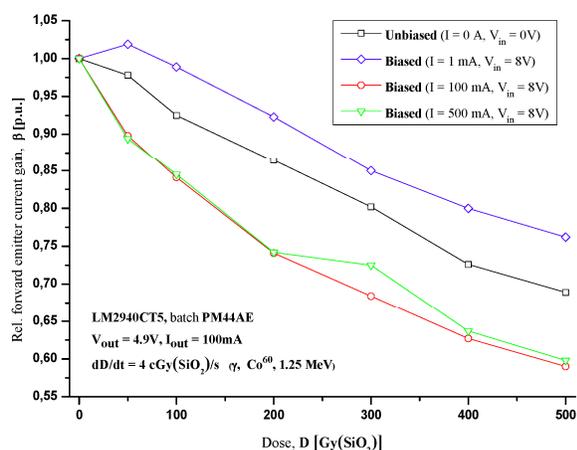
Figure 3: Relative change of the serial transistor's forward emitter current gain in voltage regulator LM2940CT5 under the influence of $\gamma$ radiation.
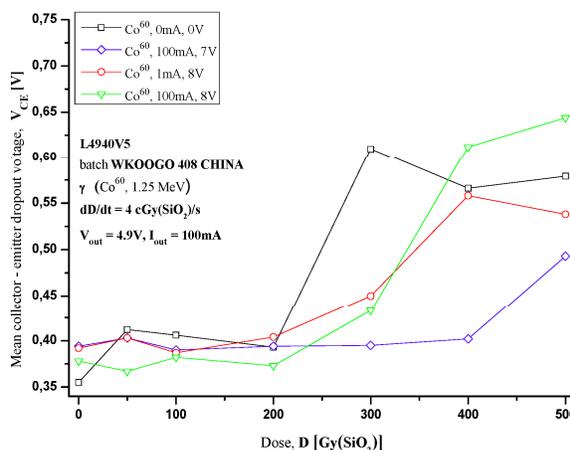
Figure 4: Change of mean collector — emitter dropout voltage in voltage regulator L4940V5 under the influence of $\gamma$ radiation.

sistor's current densities (load current of 100 mA for 1 A device, compared to the load currents of 500–800 mA in experiments related with the maximum output current [1, 2]). As previously reported [1, 2], degradation of the serial transistor's forward emitter current gain was less then expected (up to 60% for total ionizing dose of 500 Gy(SiO$_2$)), and in the case of experiment with low load current, degradation of the emitter injection efficiency of elementary round lateral pnp transistors was less expressed. Small perimeter-to-area ratio of older technological process was in this case advantage, having the small influence on spreading of the depletion region on the serial transistor's base — emitter junction [6], that is the small influence on the increase of the base current, causing the moderate degradation of the serial transistor's forward emitter current gain and preservation of its acceptable characteristics also after the absorption of total ionizing dose of 500 Gy(SiO$_2$).

In total, lateral serial transistor's dropout voltage of LM2940CT5 voltage regulators decreased up to 12%, while the measured values of serial transistor's forward emitter current gain of devices LM2940CT5 decreased 20–40% after the absorption of total ionizing dose of 500 Gy(SiO$_2$). Yet, once again have to be mentioned that the acceptable radiation tolerance of the serial transistor comprised of 350 elementary lateral pnp transistors [3] was not enough to maintain the voltage regulator's radiation tolerance, since the circuit became inoperable after the malfunction of the voltage regulator's error amplifier circuit [3].

In the Figures 4–6 were presented changes of the serial transistor's dropout voltage and the forward emitter current gain for the voltage regulators L4940V5, for the constant load current of 100 mA and output voltage of 4.9 V. Since the device L4940V5 has serial transistor with the vertical pnp power transistor, at the first glance it is quite surprising that the measured values of serial transistor's forward emitter current gain of this proven radiation hard device [4] decreased by 30–80 times! Despite of the rise of the serial transistor's collector — emitter voltage of up to 70% (for the total dose of 500 Gy (SiO$_2$)), absolute value of this voltage was not great (about 0.65 V), and the voltage regulator remained completely functional. These results led to the conclusion that fall of forward emitter current gain was the consequence of the abrupt rise of the serial transistor's base current and operation with low current of 100 mA during the examination, that altogether with the negative feedback loop reaction caused a significant shift of voltage regulator's serial transistor's operation point toward the left part of the characteristic $\beta(V_{BE})$. Almost hundredfold degradation of serial vertical pnp transistor's forward emitter current gain (for the constant values of base — emitter voltage and for comparable forward emitter current gains in the entire operating area) certainly did not occur.

The great carriers recombination in the areas of base and emitter, caused by the intensive oxide charge trapping, led to the rise of the base current up to 40 mA, for the load current of 100 mA. Analysis of characteristic $\beta = f(D)$ and $V_{CE} = f(D)$ leads to the perception of the considerable difference in response of the biased samples with the negligible load current, compared to the other samples. In the case of biased devices with the input voltage of 8 V and the output current of 1 mA, load current can be neglected, since through the serial transistor of the voltage regulator
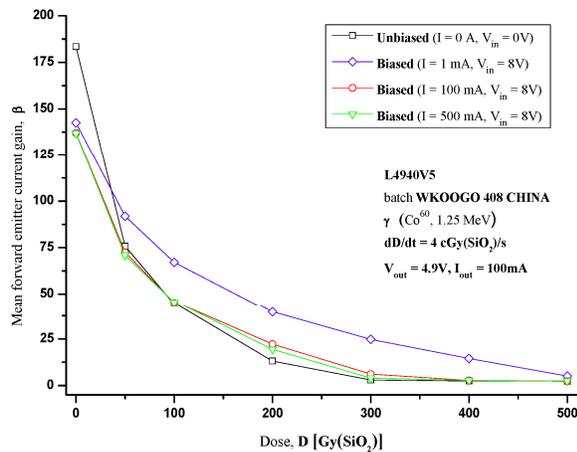
Figure 5: Change of the serial transistor's forward emitter current gain in voltage regulator L4940V5 under the influence of $\gamma$ radiation.
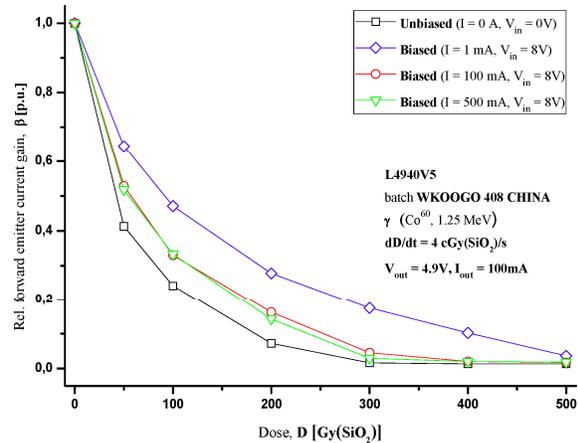
Figure 6: Change of relative value of the serial transistor's forward emitter current gain in voltage regulator L4940V5 under the influence of $\gamma$ radiation.

L4940V5 flows the current of 4 mA towards the voltage divider, even in the cases when there is no connected load on the output terminal. Positive bias voltage, that is the increased electric field in the oxide, decreases concentration of the interface states proportionally to the square root of the electric field intensity [7]. Difference is particularly noticeable in the total doses range between the 200 Gy and 400 Gy. Current flow through the n-type base cause the holes concentration to rise, so there originates increase of the base recombination. Beside the depletion of the p-type emitter surface by the positive trapped charge and the bias voltage, that spreads depletion region, increased recombination in the base area also causes rise of the base current [8].

None of the examined samples of voltage regulators L4940V5 showed output voltage fall bellow the threshold of 4.9 V, nor the excessive change of the serial transistor's dropout voltage.

## 4. CONCLUSION

In this paper, were presented results related to the change of the serial transistor's dropout voltage and the forward emitter current gain as a function of absorbed total dose of gamma radiation. Lateral serial transistor's dropout voltage of voltage regulators LM2940CT5 decreased up to 12%, while dropout voltage of vertical serial devices in voltage regulators L4940V5 increased up to 70%. On the other hand, measured values of serial transistor's forward emitter current gain of radiation sensitive devices LM2940CT5 decreased 20–40% after the absorption of ionizing dose of 500 Gy(SiO$_2$), while in the radiation hard voltage regulators L4940V5 was observed decrease of forward emitter current gain by 30–80 times. Yet, acceptable radiation tolerance of lateral pnp serial transistor was not enough for the maintenance of voltage regulator's LM2940CT5 radiation tolerance, since the circuit became inoperable after the malfunction of the voltage regulator's error amplifier circuit.

The great decrease of forward emitter current gain in voltage regulator L4940V5 was the consequence of the abrupt rise of the serial transistor's base current and operation with low current of 100 mA during the examination, that altogether with negative feedback loop reaction caused a significant shift of voltage regulator's serial transistor's operation point toward the left part of the characteristic $\beta(V_{BE})$, and not almost hundredfold degradation of forward emitter current gain. Biased operation of voltage regulators L4940V5 with input voltage 8 V and negligible load current led to noticeable improvement of radiation hardness, primarily due to the increased accumulation of the n-type base and reduced space charge area, with reduced recombination in the base. Also, positive bias voltage had influence on the suppression of formation of the interface traps.

Presented results are sharp illustration of possible deceptive conclusion about the electron device's radiation hardness that may originate from analysis of only few parameters (even if among them is such an important parameter as the forward emitter current gain), without consideration of complete collection of data for the entire circuit's operation area.

**ACKNOWLEDGMENT**

**REFERENCES**

1. Vukić, V. and P. Osmokrović, "Radiation induced forward emitter current gain degradation of lateral and vertical PNP power transistors in voltage regulators," *PIERS Proceedings*, 1188–1192, Xi'an, China, Mar. 22–26, 2010.

2. Vukić, V. and P. Osmokrović, "Impact of forward emitter current gain and geometry of pnp power transistors on radiation tolerance of voltage regulators," *Nuclear Technology & Radiation Protection*, Vol. 24, No. 3, 179–185, 2010.

3. Vukić, V. and P. Osmokrović, "Total ionizing dose degradation of power bipolar integrated circuit," *Journal of Optoelectronics and Advanced Materials*, Vol. 10, No. 1, 219–228, 2008.

4. Vukić, V. and P. Osmokrović, "Total ionizing dose response of commercial process for synthesis of linear bipolar integrated circuits," *Journal of Optoelectronics and Advanced Materials*, Vol. 8, No. 4, 1538–1544, 2006.

5. Gray, P., P. Hurst, S. Lewis, and R. Mayer, *Analysis and Design of Analog Integrated Circuits*, J. Wiley & Sons, New York, 2001.

6. Wu, A., R. D. Schrimpf, H. J. Barnaby, D. M. Fleetwood, R. L. Pease, and S. L. Kosier, "Radiation-induced gain degradation in lateral PNP BJTs with lightly and heavily doped emitters," *IEEE Transactions on Nuclear Science*, Vol. 44, No. 6, 1914–1921, 1997.

7. Shaneyfelt, M. R., J. R. Schwank, D. M. Fleetwood, P. S. Winokur, K. L. Hughes, and F. W. Sexton, "Field dependence of interface-trap buildup in polysilicon and metal gate MOS devices," *IEEE Transactions on Nuclear Science*, Vol. 37, No. 6, 1632–1640, 1990.

8. Schmidt, D. M., D. M. Fleetwood, R. D. Schrimpf, R. L. Pease, R. J. Graves, G. H. Johnson, K. E. Galloway, and W. E. Combs, "Comparison of ionizing-radiation-induced gain degradation in lateral, substrate and vertical PNP BJTs," *IEEE Transactions on Nuclear Science*, Vol. 42, No. 6, 1541–1549, 1995.

# Microwave Absorption in Nonuniform Plasma with Different Magnetic Field Configurations Using the Magneto-ionic Appleton-Hartree Theory

**M. S. Bawa'aneh**[1,2], **Ahmed M. Al-Khateeb**[3], **Sayeed Makkiyil**[1], **Saud Al Awfi**[4], **Ibrahim Abualhaol**[1], **and Ghada Assayed**[2],

[1]Khalifa University of Science, Technology and Research, P. O. Box 573, Sharjah, United Arab Emirates
[2]Department of Physics, The Hashemite University, P. O. Box 150459, Zarqa, Jordan
[3]Department of Physics, College of Science, King Faisal University, P. O. Box 400, Al-Hufof, Saudi Arabia
[4]Department of Physics, Faculty of Science, Taibah University, P. O. Box 30002, Madina, Saudi Arabia

**Abstract**— Microwave propagation in a nonuniform, collisional, and magnetized plasma slab with different magnetic field configurations is investigated using the magneto-ionic Appleton-Hartree theory. For the zero B-field case, a narrow stealth band is obtained, while for parallel and perpendicular propagation with respect to the B-field, results show a wider stealth band in the vicinity of $\omega_{ce}$. An electron cyclotron frequency of about $4\,\mathrm{GHz}$ could result in almost total absorption of the C-band.

## 1. INTRODUCTION

As radio waves travel in the ionosphere, electrons of the ionosphere oscillate coherently with the electric field of the radio wave, while the motion of the positive ions may be neglected due their high inertia. Electron collisions with neutral particles of the ionosphere provides a mechanism of energy transfer from the radio wave into thermal heating of the ionosphere. Electromagnetic wave reflection, absorption and scttering in plasma has attracted much attention lately because of the special opprotunities that plasma stealth technology offers, where by changing different plasma parameters one can control the absorption rates of microwaves in plasma [1, 2].

In this work, microwave propagation in a nonuniform, collisional, and magnetized plasma slab with different magnetic field configurations is investigated, and nonuniformity in plasma is simplified by dividing the plasma slab into uniform subslabs [3, 4]. The dielectric constant withina subslab is obtained using the magneto-ionic Appleton-Hartree theory [5, 6]. This theory was developed to describe electromagnetic wave propagation in ionized media in the presence of static magnetic fields. Magneto-ionic and optical-ray theories lead to useful and satisfactory description of wave propagation and reflection. Within the magneto-ionic theory, waves are assumed to be of a plane wave nature with a complex propagation constant, namely, vary as $e^{i\omega t - Kx}$, where $\omega$ is the EM wave frequency and $K$ the propagation constant. Also, electron motion only is assumed to be responsible for electromagnetic response due to high mobility.

## 2. FORMULATION AND NUMERICAL RESULTS

To simplify the study of the EM wave interaction with the nununiform plasma, the plasma slab (with a certain density profile) is divided into uniform layers, where the propagation constant for the $m$th layer is given by $ck^{(m)} = \omega\sqrt{\epsilon_r^{(m)}}$, where $c$ is the speed of light in vacuum, $\omega$ is the EM wave frequency and $\epsilon_r^{(m)}$ the dielectric function for the $m$th layer. Two different methods are widely used in literature; one method depends on the summation of successive reflected and transmitted powers at the interface between each two layers (neglecting multiple reflections between them) to obtain the total reflected and transmitted powers [2], while the second method uses the scattering matrix method (SMM) where global reflection and transmission rates are calculated [4].

Considering Maxwell's equations and ignoring thermal effects, one can obtain the magneto-ionic Appleton-Hartree equation [5, 6], namely

$$-n^2 = -\frac{K^2}{\mu\epsilon\omega^2} = 1 + \frac{1}{A + iB - \dfrac{D_T^2}{2(1 + A + iB)} \pm \sqrt{\dfrac{D_T^4}{4(1 + A + iB)^2} + D_L^2}}, \qquad (1)$$
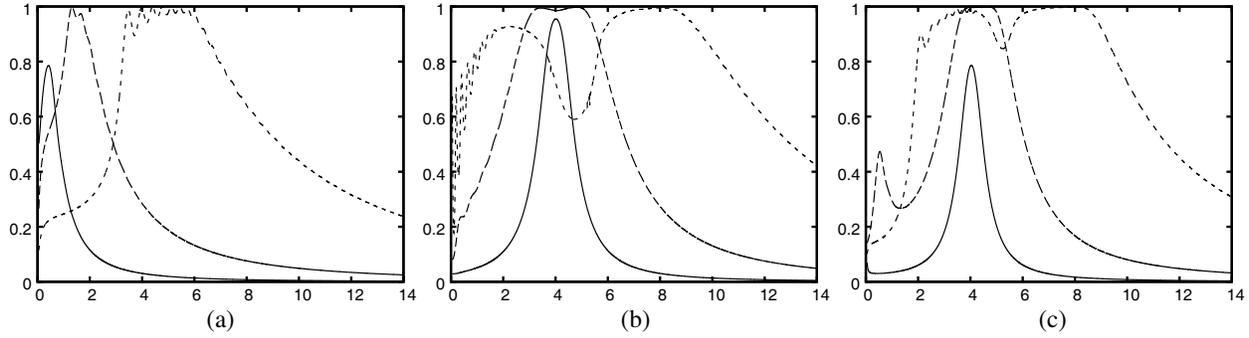
Figure 1: Normalized absorption versus wave frequency (GHz) for (a) zero B-field, (b) parallel propagation and (c) perpendicular propagation. Narrow to wide peaks in each figure correspond to initial density values $N_0 = 10^{15}$, $10^{16}$, $10^{17}\,\mathrm{m}^{-3}$, respectively. Other arameters are $\nu = 400\,\mathrm{MHz}$, $a = 30\,\mathrm{cm}$. For (b) and (c), $f_{ce} = 4\,\mathrm{GHz}$.
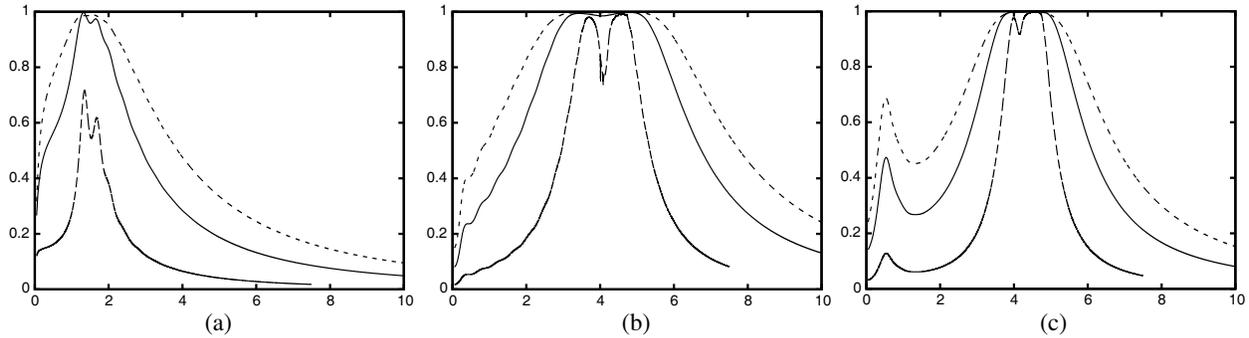


Figure 2: Normalized absorption versus wave frequency (GHz) for (a) zero B-field, (b) parallel propagation and (c) perpendicular propagation. Narrow to wide peaks in each figure correspond to collision frequency values $\nu = 100$, $400$, $800\,\mathrm{MHz}$. Other parameters are $N_0 = 10^{16}\,\mathrm{m}^{-3}$, $a = 30\,\mathrm{cm}$. For (b) and (c), $f_{ce} = 4\,\mathrm{GHz}$.

where $n = \frac{K}{\sqrt{\mu\epsilon}\,\omega}$ is the index of refraction, $A = -\frac{\omega^2}{\omega_{\mathrm{pe}}^2}$, $B = \frac{\omega\nu}{\omega_{\mathrm{pe}}^2}$, $D_T = \frac{\omega\mu\epsilon H_T}{n_e e}$ and $D_L = \frac{\omega\mu\epsilon H_L}{n_e e}$, and $H_L$ and $H_T$ are the longitudinal and transverse components of the external $dc$ magnetic field components, respectively. This equation governs the propagation of high frequency radio waves through a magneto-ionic medium.

In the rest of this section, we will be obtaining the absorption coefficients of an electromagnetic wave incident on a nonuniform plasma with a $dc$ magnetic field with different orientations; we will consider the three cases of magnetic fields perpendicular to the propagation direction, parallel to the propagation direction and the zero magnetic field case. All figures represent the normalized absorption rate versus the EM wave frequency (GHz). Figure 1 shows the normalized absorption versus wave frequency (GHz) for (a) zero B-field, (b) parallel propagation and (c) perpendicular propagation. Narrow to wide peaks in each figure correspond to initial density values $N_0 = 10^{15}$, $10^{16}$, $10^{17}\,\mathrm{m}^{-3}$, respectively. Other arameters are collision frequency $\nu = 400\,\mathrm{MHz}$ and plasma width $a = 30\,\mathrm{cm}$. For Figures 1(b) and 1(c), the electron cyclotron frequency $f_{ce} = 4\,\mathrm{GHz}$. Figure 2 shows the normalized absorption versus wave frequency (GHz) for (a) zero B-field, (b) parallel propagation and (c) perpendicular propagation. Narrow to wide peaks in each figure correspond to collision frequency values $\nu = 100$, $400$, $800\,\mathrm{MHz}$. Other parameters are $N_0 = 10^{16}\,\mathrm{m}^{-3}$ and $a = 30\,\mathrm{cm}$. For Figures 2(b) and 2(c), $f_{ce} = 4\,\mathrm{GHz}$.

The figures show higher maximum absorption and wider peak for parallel propagation compared to perpendicular propagation and zero field case.

## 3. CONCLUSION

Microwave propagation in a nonuniform, collisional, and magnetized plasma slab with different magnetic field configurations is investigated. For the zero B-field case, a narrow stealth band is obtained, while for parallel and perpendicular propagation with respect to the B-field, results show a wider stealth band in the vicinity of $\omega_{ce}$. An electron cyclotron frequency of about $4\,\mathrm{GHz}$ could

result in almost total absorption of the C-band. The results also show higher maximum absorption and wider peak for parallel propagation compared to perpendicular propagation.

**REFERENCES**

1. Ginsburg, V. L., *The Propagation of Electromagnetic Waves in Plasma*, Pergammon, New York, 1970.
2. Laroussi, M., "Interaction of microwave with atmospheric pressure plasmas," *Int. J. Infrared Millim. Waves*, Vol. 16, 2069–2083, 1995.
3. Laroussi, M. and J. Reece Roth, "Numerical calculation of the refletion, absorption and transmission of microwaves by a nonuniform plasma slab," *IEEE Transactions on Plasma Science*, Vol. 21, 366–372 1993.
4. Hu, B. J., G. Wei, and S. L. Lai, "SMM analysis of reflection, absorption and transmission from nonuniform magnetized plasma slab," *IEEE Transactions on Plasma Science*, Vol. 27, 1131–1136, 1999.
5. Appleton, E. V., "Wireless Studies of the Ionosphere," *Journal of the Institution of Electrical Engineers*, Vol. 71, 642–650, 1932.
6. Hartree, D. R., "The propagation of electromagnetic waves in stratified medium," *Proc. Camb. phil. Soc.*, Vol. 25, 97–120, January 1929.

# The Statistical Character of Atmospheric Noise Temperature Induced by Rain at Millimeter Wave Band in Xi'an, China

**Shuhong Gong**, **Meng Wei**, **Tiancheng Zheng**, **and Xiangdong Li**

School of Science, Xidian University, Xi'an 710071, China

**Abstract**— The mechanism of troposphere producing noise to communication systems is investigated, and the importance of the effects is analyzed. The contribution of rain and other precipitate particles to antenna noise temperature is discussed. The annual CDFs (Cumulative Distribution Functions) of noise temperature and the reduction of G/T induced by rain at millimeter wave band in Xi'an, China are discussed under the orbital parameters of the satellites of Xinnuo-No. 1 etc. The possible effects induced by atmospheric noise on MIMO system at millimeter wave band are analyzed. The results show that the rain-induced noise temperature can not be neglected. It is necessary to investigate the effects of weather phenomena on antenna noise temperature in detail, for instance rain, snow, dust-storm and so on.

## 1. INTRODUCTION

The Millimeter wave communication system has many advantages, such as high capacity, narrow beam, small size of terminal device, high anti-interference ability, and good electromagnetism compatibility. It has become a research focus on exploiting and applying new communication technique at millimeter wave band in the future communication field. The research on radio waves propagation properties plays an important role in communication system design. The propagation and scattering effects induced by atmospheric on electromagnetic wave, such as refraction, reflection, scattering, phase shifting, depolarization, scintillation and so on, will cause direct influence on channel capacity, transmission rate, signal quality and system stability, which are more serious and negligible at high frequencies [1–4].

In fact, the absorbing mediums not only lead to attenuation, scattering effect but also become the source of radiation noise. The noise will decrease the signal-to-noise ratio and affect the transmission quantity of communication system, for example, they can decrease the transmission rate and increase the bit error rate. So, antenna noise must be considered in designing wireless communication systems [1–9].

The research on other propagation properties is really more than on the noise properties. So, the noise temperature statistic properties are analyzed using the rain data measured in Xi'an, China. The rain-induced noise temperature in a frequency range of 30 GHz–50 GHz and the statistical distribution of G/T reduction are calculated, based on the orbital parameters of the satellites of Xinnuo-I, Yatai-II etc. And, the results are analyzed. The results of this paper provide the foundation for us to study the properties of MIMO channel at millimeter-wave bands.

## 2. NOISE TEMPERATURE AND ATMOSPHERE NOISE

The absorption and scattering of atmospheric and precipitate particles are the important reasons for influencing the wireless communication system performance. In fact, the absorbing mediums not only cause attenuation but also become the source of radiation noise, when electromagnetic wave propagates through them. Radio noise emitted by a distant star can be a source of information in radio astronomy, while that emitted from earth's surface can be used for remote sensing. However, these noises, so called background noise or sky noise, may be a limiting factor for communication systems, which is unpredictable and has interference with signal. There are many kinds of noise sources, such as cosmic background (2.7 K), galactic noise, emission from atmospheric gases (oxygen and water vapor), emissions from clouds and rain, the earth surface and the sun, etc. The noise power received at a given frequency usually is expressed by the so-called brightness temperature, or noise temperature, which is a measure of the power being radiated in a given band by this source in the direction of the receiving antenna. Brightness temperature, or noise temperature, is equal to the physical temperature of a blackbody (perfect absorber) emitting the same power in the same band. The relation between noise temperature $T_n$ and received noise power $P_n$ can be expressed as [7–11]

$$P_n = k_B T_n B_n \tag{1}$$

where $k_B$ is Boltzmann constant, $B_n$ is the bandwidth of receiver.

The clear atmospheric and precipitate particulates will also radiation noise when radio waves interact with them, so called atmospheric noise. At frequencies below 1 GHz, radio noise caused by atmospheric radiation is less than a few Kelvins, which can be ignored. However, at higher frequencies, Ku and Ka band for example, the radio noise caused by atmospheric emission can not be ignored. The atmospheric and precipitate particulates will not only cause attenuation but also generated noise, both of them will reduce the system signal-to-noise ratio. So the atmospheric noise can not be neglected and needs to be considered in designing wireless system. The atmosphere consists of gaseous, liquid, and solid constituents. The hydrometeors (clouds, rain, snow, ice) are the dominant noise source in the microwave region. However, other particles, such as dust, smoke and sand, are minor noise source, which impact on antenna noise by covering on the antenna.

According to radiation theory, brightness temperature $T_B$ of atmospheric is expressed as [11]

$$T_B = \int_0^\infty T(l)\kappa(l)e^{-\tau(l)}\mathrm{d}l + T_\infty e^{-\tau_\infty} \tag{2}$$

In (2), $T(l)$ is the atmosphere temperature; $\kappa(l)$ is the absorption coefficient; $T_\infty$ is the cosmic background noise temperature, $\tau_\infty$ is optical depth along the path between cosmic background and receiving antenna; $\tau(l)$ is optical depth along the path $l$, can be written as

$$\tau(l) = \int_0^l \kappa(l')\mathrm{d}l' \tag{3}$$

Let, $\kappa(l) = \kappa$, $T(l) = T_m$, the optical depth through the total path is $\tau(l) = \kappa l$. The Equation (2) becomes

$$T_B = T_m \int_0^{L_0} e^{-\kappa l}\kappa\mathrm{d}l + T_\infty e^{-\tau_\infty} \tag{4}$$

where, $\kappa$ is the mean absorption coefficient, $T_m$ is the mean ambient temperature. In (4), the integration covers all radiation sources of atmospheric from the ground to the atmosphere top $L_0$.

When radio waves pass through atmosphere, the waves suffer molecular absorption and scattering at centimeter and millimeter bands. In the troposphere, the gaseous absorption is primarily due to water vapor and oxygen [8]. There are 29 absorption lines for $H_2O$ up to 1097 GHz, and 44 lines for $O_2$ up to 834 GHz. Relatively narrow and weaker ozone ($O_3$) lines are above 100 GHz [8]. Based on the radiation theory, (4) can be simplified as [10]:

$$T_{atm} = T_B = T_m(1 - e^{-\tau_0}) = T_m\left(1 - e^{-\kappa L_0}\right) = T_m\left(1 - 10^{-\frac{A(\mathrm{dB})}{10}}\right) \tag{5}$$

The attenuation and radiation caused by gases and precipitate particulates make $G/T$ decrease, which will affect the transmission rate, error rate etc [13, 14]. $G$ and $T$ are separately the antenna gain and the noise temperature, which can be expressed as [8, 10]

$$G = G_{vac}(\mathrm{dB}) - A(\mathrm{dB}) \tag{6}$$
$$T = T_{vac}(\mathrm{K}) + T_{atm}(\mathrm{K}) \tag{7}$$

where, $G_{vac}$ is antenna gain in vacuum, $A$ is atmospheric loss, $T_{vac}$ is the vacuum noise temperature, $T_{atm}$ is the atmospheric noise temperature. Thus, the reduction of $G/T$ is given by (8) [8, 10]

$$\Delta(G/T) = -A_{atm}(\mathrm{dB}) - 10\log[(T_{vac} + T_{atm})/T_{vac}] \tag{8}$$

## 3. SIMULATION AND DISCUSSION

Atmosphere and precipitate particulates can cause attenuation and radiation noise, which reduce SNR. SNR plays a significant role in estimating the channel capacity and error-rate of communication system. Literatures [12–15] have analyzed the capacity and error-rate in a fade channel. It can be concluded from these literatures that the research on the statistical properties of $S/N$ is

important for estimating the performance of communication system. So, it is important to estimate the G/T reduction induced by atmosphere and precipitate particulates.

The rain-induce noise temperature and G/T reduction are simulated for the frequencies from 30 GHz to 50 GHz, based on the rain rate data measured in Xi'an, China, and the orbital parameters for the satellites of Xinnuo-No. 1 etc. The rain data are listed in Table 1, and the orbital parameters are listed in Table 2. The link elevation-angles are listed in Table 3, which are calculated based

Table 1: The statistical result of rain rate measured in Xi'an, China.

| Percent (%) | 0.0025 | 0.0038 | 0.0048 | 0.0053 | 0.0061 | 0.0076 | 0.0086 |
|---|---|---|---|---|---|---|---|
| $R$ (mm/h) | 55.0000 | 50.0000 | 45.0000 | 40.0000 | 35.0000 | 30.0000 | 25.0000 |
| Percent (%) | 0.0283 | 0.1311 | 0.3729 | 1.5862 | 2.4157 | 3.7483 | |
| $R$ (mm/h) | 10.0000 | 5.0000 | 3.0000 | 1.0000 | 0.5000 | 0.0500 | |
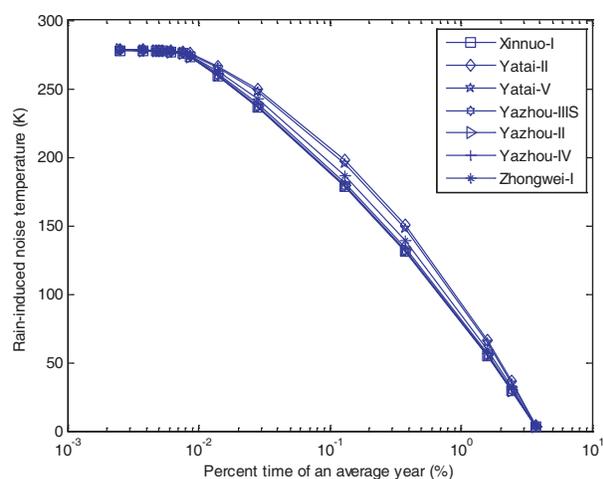


Figure 1: Rain-induced noise temperature at 30 GHz.
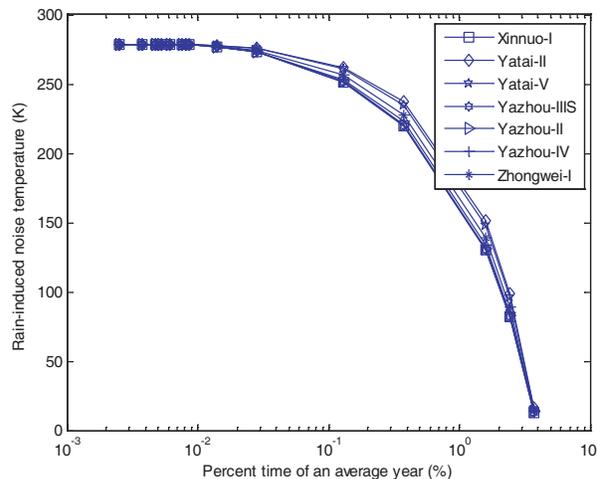


Figure 2: Rain-induced noise temperature at 50 GHz.
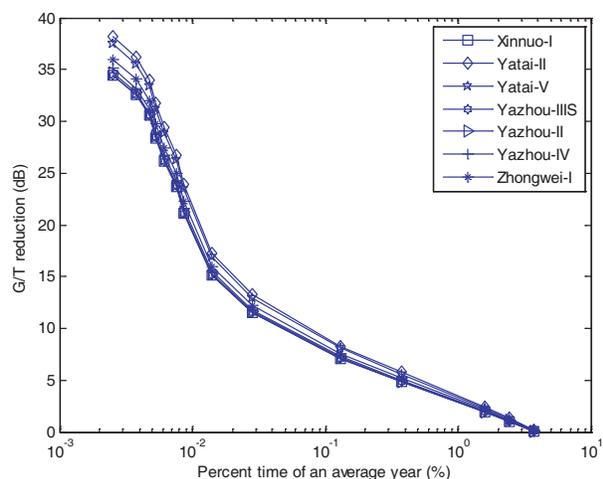


Figure 3: The G/T reduction at 30 GHz.
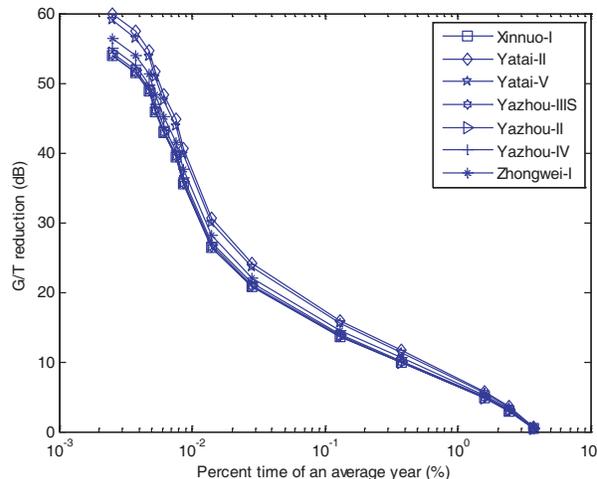


Figure 4: The G/T reduction at 50 GHz.

Table 2: The orbital parameters for the satellites of Xinnuo-I etc.

| Satellite | Xinnuo-I | Yatai-II | Yatai-V | Yazhou-IIIS | Yazhou-II | Yazhou-I | Zhongwei-I |
|---|---|---|---|---|---|---|---|
| Orbital position (E°) | 110.5 | 76.5 | 138 | 105.5 | 100.5 | 122.2 | 87.5 |

Table 3: The elevation angle of different links.

| Satellite | Xinnuo-I | Yatai-II | Yatai-V | Yazhou-IIIS | Yazhou-II | Yazhou-IV | Zhongwei-I |
|---|---|---|---|---|---|---|---|
| Elevation angel (°) | 50.2400 | 37.6501 | 39.4042 | 50.1572 | 49.3586 | 47.6865 | 44.3390 |

on the parameters in Table 2. Fig. 1 and Fig. 2 show the annual probability distribution of rain-induced noise temperature. The annual probability distribution of G/T reduction is shown in Fig. 3 and Fig. 4. In this paper, the average temperature $T_m$ is supposed as 278.15 K centigrade, and $T_{vac}$ is 210 K.

## 4. CONCLUSION

Any absorbing mediums not only lead to attenuation, scattering effect, but also become the source of radiation noise. The noise reduces G/T, and affects the performance of communication system. From the results in this paper, the following conclusions can be obtained: the reduction of G/T can not be ignored; and it is significant to take the influences of rain-induced noise temperature into account; with the increase of frequency, both rain-induced noise temperature and G/T reduction tended to increase. Taking 0.01% as an example, the rain-induced noise temperature is about 280 K from 30 GHz to 50 GHz, and the reduction of G/T is approximately 25 dB–35 dB. The research of this paper is the fundamental of investigating the characteristics of MIMO channel at millimeter-wave bands.

## REFERENCES

1. Hao, X., *Radio Wave Propagation*, 487–531, Electronic Industy Press, Beijing, China, 2000.
2. Gong, S., "Study on some problems for radio wave propagating and scattering through troposphere," Chinese Thesis, Xi'dian University, Xi'an, China, Aug. 2008.
3. Verma, A. K., K. K. Jha, and R. K. Tewari, "Effect of the atmosphere on radio and radar performance," *TENCON'89. Fourth IEEE Region 10 International Conference*, 844–847, 1989.
4. Ishimaru, A. A, "Theory and application of wave propagation and scattering in random media," *Proceedings of the IEEE*, Vol. 65, No. 7, 1030–1061, 1977.
5. Sizun, H., *Radio Wave Propagation for Telecommunication Applications*, 13–254, Springer Berlin Heidelberg, New York, 2003.
6. Gimonet, M. E., et al., "Chapter 2.3: Scintillation/dynamics of the signal," 2.3–2-9, COST Project 255, Final Report, Office for Official Publications of the European Community, Luxembourg, 2002.
7. Lv, H., J. Cai, and Z. Gan, *Satellite Communication System*, 2nd Edition, 45–73, Posts and Telecom Press, Beijing, 2001.
8. Ho, C., S. Slobin, and K. Gritton, "Atmospheric noise temperature induced by clouds and other weather phenomenaat SHF band (1–45 GHz)," 5–119, Prepared for the United States Air Force Spectrum, Efficient Technologies for Test and Evaluation and Advanced Range Telemetry for Edwards Air Force Base, California, JET Propulsion Laboratory Calisornia Institute of Technology, 2005.
9. Chakraborty, D., "Technical considerations of T-1 carrier transmission via ku-band domestic satellites," *IEEE Communications Magazine*, Vol. 26, No. 3, 46–55, 1988.
10. Marzano, F. S., "Modeling antenna noise temperature due to rain clouds at microwave and millimeter-wave frequencies," *IEEE Transactions on Antennas and Propagation*, Vol. 54, No. 4, 1305–1317, 2006.
11. Kraus, J. D., *Radio Astronomy*, 2nd Edition, 1–200, Cygnus-Quasar Books, 1986.
12. Raina. M. K., "Atmospheric emission measurements of attenuation by microwave radiometer at 19.4 GHz," *IEEE Transactions on Antenas and Propagation*, Vol. 44, No. 2, 188–191, 1996.

13. Yeh, L. P., "Multiple-acess tradeoff study for intra-south American satellite communication system," *IEEE Transactions on Communication Technology*, Vol. 16, No. 5, 721–730, 1968.

14. Filip, M. and E. Vilar, "Optimum utilization of the channel capacity of a satellite link in the presence of amplitude scintillation and rain attenuation," *IEEE Transactions on Communications*, Vol. 38, No. 11, 1958–1965, 1990.

15. Chang, D. D. and O. L. de Weck, "Basic capacity calculation methods and benchmarking for MF-TDMA and MF-CDMA communication satellites, *International Journal of Satellite Communications and Networking*, Vol. 23, 153–171, 2005.

# On the Influence of Spatial-temporal Fluctuations of Electron Density and Magnetic Field Fluctuations on the Angular Power Spectrum of Scattered Electromagnetic Wave by Magnetized Plasma Slab

**G. V. Jandieri[1], A. Ishimaru[2], and K. Yasumoto[3]**

[1]Department of Physics, Georgian Technical University, Georgia
[2]Department of Electrical Engineering, University of Washington, USA
[3]Department of Computer Science and Communication Engineering, Kyushu University, Japan

**Abstract**— Influence of temporal fluctuations of both electron density and external magnetic field fluctuations on scattered ordinary and extraordinary waves by magnetized plasma slab is investigated using the ray-optics method. Transport equation for frequency fluctuations of scattered radiation has been derived. Amplification of frequency fluctuations in the collisional magnetized plasma slab is possible due to temporal fluctuations of plasma parameters and depends on the anisotropy factor and the direction of wave propagation with respect to the imposed magnetic field. Correlation functions of the phase and frequency fluctuation are obtained for arbitrary correlation functions of fluctuating plasma parameters. Broadening of the angular power spectrum is analyzed analytically and numerically for the anisotropic Gaussian correlation function using the remote sensing data.

## 1. INTRODUCTION

Statistical characteristics of scattered radiation in the ionosphere have been well studied [1]. The geomagnetic field plays a key role in the dynamics of plasma in the ionosphere. Investigation of statistical moments in randomly inhomogeneous magnetized plasma is of a great practical importance. Scintillation effects and the angle-of-arrival of scattered electromagnetic waves by anisotropic collision magnetized ionospheric plasma slab for both power-law and anisotropic Gaussian correlation functions of electron density fluctuations were investigated in the complex geometrical optics approximation on the basis of stochastic eikonal equation [2, 3]. Second order statistical moments of scattered electromagnetic waves in the ionospheric plasma at directional fluctuations of an external magnetic field were considered by perturbation method in [4, 5]. In these papers fluctuating plasma parameters were random functions only of spatial coordinates. The influence of temporal fluctuations of both electron density and external magnetic field on scattered ordinary and extraordinary waves has not been considered till now. These fluctuations in absorptive medium (collision magnetized plasma) can lead to the amplification of frequency of scattered radiation. Conditions of amplification caused due to electron density and external magnetic field fluctuations are obtained in geometrical optics approximation.

In Section 2 the dispersion equation of the complex phase and stochastic differential equation for phase fluctuations are derived at spatial-temporal fluctuations of electron density and external magnetic field fluctuations in collisionless magnetized plasma. The solution satisfies the boundary condition. Second order statistical moment such as the broadening of the angular spectrum of scattered electromagnetic waves by turbulent magnetized plasma slab is obtained for arbitrary correlation functions of randomly varying plasma parameters. In Section 3 transfer equation for the frequency fluctuations in collisional magnetized plasma slab is derived taking into account temporal fluctuations of both turbulent magnetized plasma parameters and external magnetic field, and anisotropy factors of ionospheric irregularities. Numerical examples are demonstrated in Section 4 for anisotropic Gaussian correlation function including anisotropy factor of electron density inhomogeneities and the angle of inclination of prolate irregularities with respect to the geomagnetic field using the remote sensing data. Conclusion is given in Section 5.

## 2. FORMULATION OF THE PROBLEM

Electric field $E$ in non-conducting, non-stationary magnetized plasma satisfies the wave equation:

$$\left[ \frac{\partial^2}{\partial x_i \partial x_j} - \Delta \delta_{ij} + \frac{1}{c^2} \frac{\partial^2}{\partial t^2} \varepsilon_{ij}(\mathbf{r}, t) \right] E_j(\mathbf{r}, t) = 0. \tag{1}$$

where $\varepsilon_{ij}$ is the second rank tensor [6]: $\varepsilon_{xx} = \varepsilon_{yy} \equiv \eta = 1 - v/(1 - u)$, $\varepsilon_{zz} \equiv \varepsilon = 1 - v$, $\varepsilon_{xz} = \varepsilon_{zx} = \varepsilon_{yz} = \varepsilon_{zy} = 0$, $\varepsilon_{xy} = -\varepsilon_{yx} \equiv \mu = -iv\sqrt{u}/(1 - u)$; $v = \omega_{pe}^2/\omega^2$ and $u = \Omega_e^2/\omega^2$ nondimensional plasma parameters, $\omega$ is the angular frequency of an incident wave, $\omega_{pe} = (4\pi Ne^2/m)^{1/2}$ is the angular plasma frequency, $N$ is electron density, $e$ and $m$ are the charge and the mass of an electron, $\Omega_e = |e|H_0/mc$ is the angular gyrofrequency for the magnetic field, $H_0$ is the strength of an external magnetic field directing along the $z$ axis, $c$ is the speed of light in the vacuum. In ray-(optics) approximation [7] substituting $E_i(\mathbf{r}, t) = A_i(\mathbf{r}, t) \exp[iS(\mathbf{r}, t)]$ in the Equation (1) and taking into account that phase fluctuations substantially exceed amplitude fluctuations, we obtain the dispersion equation for the complex phase:

$$
i\frac{\partial^2 S}{\partial x_i \partial x_j} - \frac{\partial S}{\partial x_i}\frac{\partial S}{\partial x_j} - i\frac{\partial^2 S}{\partial x_j^2}\delta_{ij} + \left(\frac{\partial S}{\partial x_j}\right)^2 \delta_{ij}
$$
$$
+ \frac{1}{c^2}\left[\frac{\partial^2 \varepsilon_{ij}}{dt^2} + i\varepsilon_{ij}\frac{\partial^2 S}{dt^2} + 2i\frac{\partial \varepsilon_{ij}}{dt}\frac{\partial S}{\partial t} - \varepsilon_{ij}\left(\frac{\partial S}{\partial t}\right)^2\right] = 0. \tag{2}
$$

Using the perturbation method electron density and external magnetic field we present as the sum of constant mean and fluctuating terms, which are random functions of the spatial coordinates and time $N = \langle N_0 \rangle + N_1(\mathbf{r}, t)$ and $H_0 = \langle H_0 \rangle + h_1(\mathbf{r}, t)$ (angular brackets denote statistical average). The fluctuating term of the complex phase satisfies the stochastic differential equation:

$$
\frac{R_1}{c}\frac{\partial S_1}{\partial t} + R_2\frac{\partial S_1}{\partial y} + R_3\frac{\partial S_1}{\partial z} = k_0 F_{1n}(\mathbf{r}, t) + k_0 F_{1h}(\mathbf{r}, t), \tag{3}
$$

where

$$
\begin{aligned}
R_1 &= 2\left[(N_*^2 - \eta_0)(N_*^2\varepsilon_0\cos^2\theta - 2\eta_0\varepsilon_0 + N_*^2\eta_0\sin^2\theta) + \eta_0(-N_*^2\varepsilon_0\cos^2\theta - N_*^2\eta_0\sin^2\theta\right.\\
&\quad \left. +\eta_0\varepsilon_0) - 2\mu_0^2(N_*^2\sin^2\theta - \varepsilon_0) + \varepsilon_0\mu_0^2\right],\\
R_2 &= 2N_*\sin\theta\left[-N_*^2\varepsilon_0\cos^2\theta - \eta_0(N_*^2 + N_*^2\sin^2\theta - \eta_0 - \varepsilon_0) + \mu_0^2\right],\\
R_3 &= 2N_*\cos\theta\left[2\varepsilon_0\eta_0 - N_*^2\varepsilon_0(1 + \cos^2\theta) - N_*^2\eta_0\sin^2\theta\right],\\
F_{1n}(\mathbf{r}, t) &= B_1\left[-k_0^2\varepsilon_{1n}(\mathbf{r}, t) + \varepsilon_{1n}''(\mathbf{r}, t)/c^2\right] + B_2\left[k_0^2\mu_{1n}(\mathbf{r}, t) - \mu_{1n}''(\mathbf{r}, t)/c^2\right]\\
&\quad +B_3\left[-k_0^2\eta_{1n}(\mathbf{r}, t) + \eta_{1n}''(\mathbf{r}, t)/c^2\right],\\
B_1 &= (N_*^2 - \eta_0)(N_*^2\cos^2\theta - \eta_0) + \mu_0^2,\\
B_2 &= 2\mu_0(N_*^2\sin^2\theta - \varepsilon_0),\\
B_3 &= (N_*^2\sin^2\theta - \varepsilon_0)(N_*^2 + N_*^2\cos^2\theta - 2\eta_0) - N_*^4\sin^2\theta\cos^2\theta;
\end{aligned}
$$

indices $n$ and $h$ determine electron density and magnetic field fluctuations, respectively; index "0" indicate regular components of the tensor $\langle\varepsilon_{ij}^{(0)}\rangle$; functions $F_{1n}(\mathbf{r}, t)$ and $F_{1h}(\mathbf{r}, t)$ contain temporal derivatives of fluctuating terms $\varepsilon_{ij}^{(1)}(\mathbf{r}, t)$. Vector $\tau$ of an incident wave lying in the $yoz$ plane (principle plane) has the regular phase $S_0(\mathbf{r}) = k_0 N_*(\tau\mathbf{r}) = k_0 N_*(y\sin\theta + z\cos\theta) - i\omega_0 t, k_0 = \omega_0/c$, $\theta$ is the angle between the imposed magnetic field and the direction of a wavevector of the incident wave. For collisionless magnetized plasma the refractive index is given [6] as:

$$
N_*^2 = 1 - \frac{2, v(1 - v)}{2(1 - v) - u\sin^2\theta \pm \sqrt{u^2\sin^4\theta + 4u(1 - v)^2\cos^2\theta}},
$$

sign " +" corresponds to the ordinary wave, sign "–" devoted to the extraordinary wave.

The solution of Equation (3) satisfying the boundary condition $\varphi_1(\kappa, z = 0, \omega) = 0$ has been obtained using the two-dimensional Fourier transformation. Correlation function of the phase of scattered radiation taking into account that the observation points spaced apart at distances $\rho_x$

and $\rho_y$ has the following form:

$$
\langle S_1(x + \rho_x, y + \rho_y, L, t) S_1^*(x, y, L, t) \rangle_n
$$

$$
= 2\pi \frac{v_0^2 k_0^2 L}{R_3^2} \int\limits_{-\infty}^{\infty} d\omega dk_x dk_y \left(1 + \frac{\omega^2}{\omega_0^2}\right)^2 \left\{ \left[\left(B_1 + \frac{B_3}{1 - u_0}\right)^2 + \frac{B_2^2 u_0}{(1 - u_0)^2}\right] \right.
$$

$$
\cdot W_n \left[k_x, k_y, \frac{1}{R_3}\left(R_1 \frac{\omega}{c} - R_2 k_y\right), \omega\right] + \frac{u_0}{(1 - u_0)^4} \left(B_2^2 + 4 u_0 B_3^2\right)
$$

$$
\left. W_h \left[k_x, k_y, \frac{1}{R_3}(R_1 \frac{\omega}{c} - R_2 k_y), \omega\right] \right\} \cdot \exp(ik_x \rho_x + ik_y \rho_y), \tag{4}
$$

where $W_{n,h}(\kappa, k_z, \omega)$ are arbitrary correlation functions of electron density and magnetic field fluctuations. In particular, for non-magnetized plasma if its parameters do not fluctuate in time, at $\theta = 0^0$ (quasilongitudinal propagation), $\rho_x = \rho_y = 0$ (one receiving antenna), for isotropic Gaussian correlation function of electron density fluctuations we obtain the well-known expression for the variance of phase fluctuation $\langle S_1^2 \rangle = \sigma_n^2 \sqrt{\pi} v_0^2 k_0^2 L l$ [8], $\sigma_n^2$ is the variance of electron density fluctuations, $L$ is a thickness of inhomogeneous plasma slab. Geometrical optics approximation imposed the restriction on the path length of wave propagation $l_{path}/\omega_0 l_{n,h}^2 \ll 1$ ($l_{n,h}$ are characteristic spatial scales of electron density and magnetic fields fluctuation, respectively).

Knowledge of the phase correlation function allows us to calculate second order statistical moments of scattered electromagnetic waves. In particular, spatial (angular) power spectrum which is equivalent to the ray intensity (brightness) in radiation transfer equation [9]. It can be obtained by Fourier transformation from the correlation function of scattered field and has a Gaussian form for strong fluctuations of the phase [10]:

$$
G(k_x, k_y, z) = G_0 \exp\left[-\frac{k_x^2}{2\langle k_x^2 \rangle} - \frac{(k_y - \Delta k_y)^2}{2\langle k_y^2 \rangle}\right], \tag{5}
$$

where $G_0$ is the amplitude of spectral curve, $\Delta k_y$ determines the displacement of the spatial power spectrum of the received radiation caused by random inhomogeneities, while $\langle k_y^2 \rangle$ and $\langle k_x^2 \rangle$ determine the width of this spectrum in the $yoz$ and $xoz$ planes, respectively:

$$
\Delta k_y = \frac{1}{i} \frac{\partial W_\varphi}{\partial \rho_y}\bigg|_{\rho_x = \rho_y = 0}, \quad \langle k_y^2 \rangle = -\frac{\partial^2 W_\varphi}{\partial \rho_y^2}\bigg|_{\rho_x = \rho_y = 0}, \quad \langle k_x^2 \rangle = -\frac{\partial^2 W_\varphi}{\partial \rho_x^2}\bigg|_{\rho_x = \rho_y = 0}. \tag{6}
$$

The derivatives of the correlation function of the phase are taken at the point $\rho_x = \rho_y = 0$.

## 3. TRANSFER EQUATION FOR FREQUENCY FLUCTUATION

Solving (3), two-dimensional spectral function of the frequency fluctuations $\omega_1(\mathbf{r}, t) = \partial S_1/\partial t$ of scattered electromagnetic waves by collisional magnetized plasma slab with both electron density and external magnetic field fluctuations satisfies the stochastic differential equation:

$$
\frac{\partial \Omega}{\partial z} + i\left(\frac{R_2}{R_3} k_y - \frac{R_2}{R_3} \frac{\omega}{c}\right) \Omega(\kappa, z, \omega) = i \frac{v_0 k_0}{R_3} \omega \left(1 + \frac{\omega^2}{\omega_0^2}\right) \left[\left(\tilde{B}_1 - i\tilde{B}_2 \frac{\sqrt{u_0}}{1 - u_0} + \tilde{B}_3 \frac{1}{1 - u_0}\right)\right.
$$

$$
\left. n_1(\kappa, z, \omega) - \frac{\sqrt{u_0}}{(1 - u_0)^2}(i\tilde{B}_2 - 2\sqrt{u_0}\tilde{B}_3)h_1(\kappa, z, \omega)\right], \tag{7}
$$

where $\tilde{B}_i$ are complicated random functions of the spatial coordinates and time containing regular and collisional terms of the second rank permittivity tensor. Correlation function of the frequency fluctuations has the following form:

$$
\langle \omega_1(x + \rho_x, y + \rho_y, L, t + \tau) \omega_1^*(x, y, L, t) \rangle_n
$$

$$
= \pi \frac{v_0^2 k_0^2 c}{\Phi_1''} \int\limits_{-\infty}^{\infty} d\omega \omega \left(1 + \frac{\omega^2}{\omega_0^2}\right)^2 \left[\exp\left(2\Phi_1'' \frac{L\omega}{c}\right) - 1\right] \left[(\Psi_1^2 + \Psi_2^2) \cdot W_n\left(\rho_x, \rho_y, -\Phi_1' \frac{\omega}{c}, \omega\right)\right.
$$

$$
\left. + (\Psi_3^2 + \Psi_4^2) W_h\left(\rho_x, \rho_y, -\Phi_l' \frac{\omega}{c}, \omega\right)\right] \exp(-i\omega\tau) \tag{8}
$$
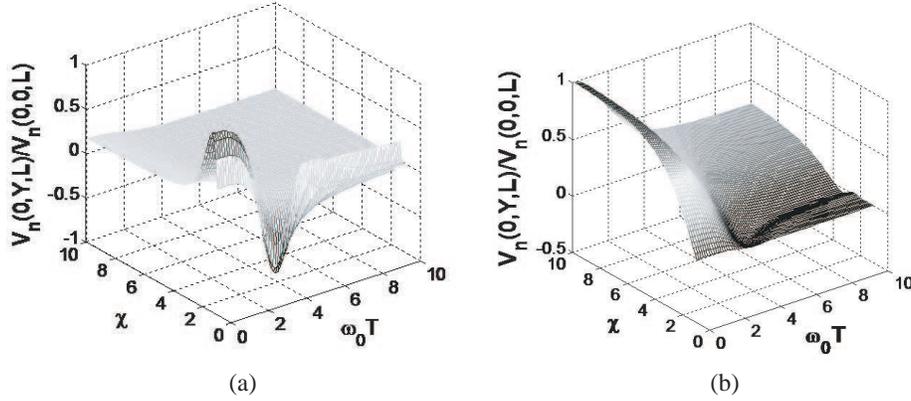
Figure 1: 3-D pattern of the normalized correlation function of the phase fluctuations of scattered radiation by magnetized plasma slab versus anisotropy factor $\chi$ and temporal parameter $\omega_0 T$ for: (a) ordinary wave, (b) extraordinary wave.
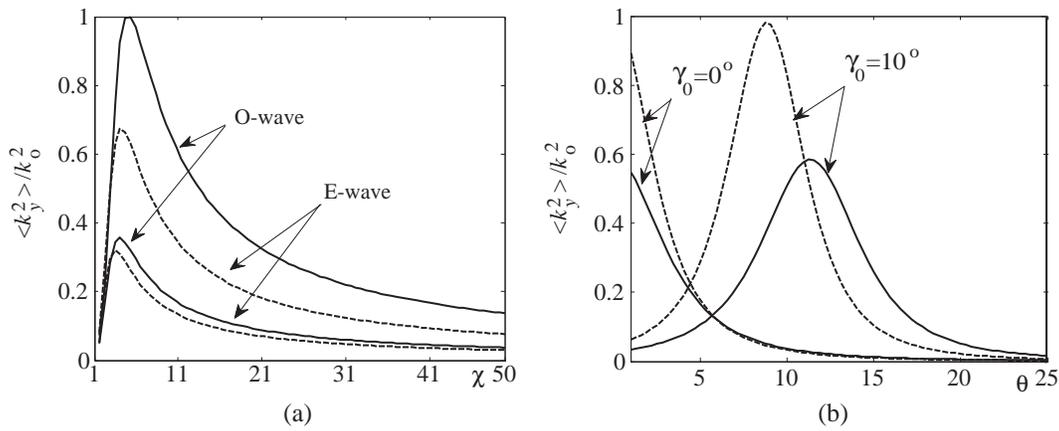


Figure 2: Dependence of the broadening of the angular power spectrum in the principle plane versus: (a) anisotropy factor $\chi$ at $\theta = 100°$, $\gamma_0 = 0°$ (solid line), $\gamma_0 = 5°$ (dash line), (b) angle of an incident wave $\theta$ with respect to the external magnetic field for the ordinary wave (solid line) and extraordinary wave (dash line) at $\chi = 5$.

where integrands are complicated functions of collisional magnetized plasma parameters. Variance of the frequency fluctuations $\langle \omega_1^2 \rangle = [\text{Re}\langle \omega_1 \omega_1 \rangle + \langle \omega_1 \omega_1^* \rangle]/2$ depends on the geometry of the task and parameters of a turbulent plasma slab. Analysis show that temporal fluctuations of collisional magnetized plasma parameters lead to the amplification of the frequency fluctuations even for isotropic Gaussian correlation function. Numerical calculations show that the amplification of frequency fluctuations depends on the direction of wavevector of an incident wave, characteristic temporal scales of fluctuating parameters (electron density and external magnetic field fluctuations have different scales), the anisotropy factor and the angle of inclination of prolate irregularities with respect to the imposed magnetic field, absorption coefficient (collision frequency of electrons with other plasma particles).

## 4. NUMERICAL RESULTS AND DISCUSSIONS

Experiments registering the phase difference of coherent signals radiating by the Earth satellite show that irregular phase variations are caused by the electron density irregularities. In the analytical calculations we use anisotropic Gaussian correlation function of electron density fluctuation [2]:

$$W_D(k_x, k_y, \rho_z) = \frac{\sigma_N^2}{4\pi} \frac{l_\parallel^2}{\chi \Gamma_0} \exp\left(-\frac{m^2}{l_\parallel^2}\rho_z^2 + ink_x\rho_z\right) \exp\left(-\frac{k_x^2 l_\parallel^2}{4\Gamma_0^2} - \frac{k_y^2 l_\parallel^2}{4\chi^2}\right), \qquad (9)$$

where $m^2 = \chi^2/\Gamma_0^2$, $\Gamma_0^2 = \sin^2\gamma_0 + \chi^2\cos^2\gamma_0$, $n = (\chi^2 - 1)\,\sin\gamma_0\cos\gamma_0/\Gamma_0^2$, $\sigma_N^2$ is the variance of the electron density fluctuations; $\chi = l_\parallel/l_\perp$ (ratio of longitudinal and transverse linear scales of plasma irregularities with respect to the external magnetic field) is the anisotropy factor, $\gamma_0$ is the inclination angle of prolate irregularities with respect to the imposed magnetic field. Numerical calculations were carried out for the ionospheric $F$-layer; frequency of an incident wave $0.1\,\mathrm{MHz}$, $v_0 = 0.28$, $u_0 = 0.22$, $l_\parallel = 10\,\mathrm{km}$.

## 5. CONCLUSION

The features of the angular power spectrum of scattered ordinary and extraordinary waves are considered in the magnetized plasma slab. Temporal fluctuations of plasma permittivity fluctuations and anisotropy factor of prolate irregularities have a substantial influence on these waves. Frequency fluctuations are amplified at temporal fluctuations of collisional magnetized plasma parameters. The direction of wave propagation and anisotropy of turbulent plasma parameters can lead to the variation of the amplification value.

**REFERENCES**

1. Xu, Z.-W., J. Wu, and Z.-S. Wu, "A survey of ionospheric effects on space-based radar," *Waves in Random Media*, Vol. 14, S189–S273, 2004.
2. Jandieri, G. V., A. Ishimaru, V. G. Jandieri, A. G. Khantadze, and Z. M. Diasamidze, "Model computations of angular power spectra for anisotropic absorptive turbulent magnetized plasma," *Progress In Electromagnetics Research*, Vol. 70, 307–328, 2007
3. Jandieri, G. V., A. Ishimaru, K. Yasumoto, A. G. Khantadze, and V. G. Jandieri, "Angle-of-arrival of radio waves scattered by turbulent collisional magnetized plasma layer," *International Journal of Microwave and Optical Technology*, Vol. 4, No. 3, 160–169, 2009.
4. Jandieri, G. V., A. Ishimaru, N. N. Zhukova, T. N. Bzhalava, and M. R. Diasamidze, "On the influence of fluctuations of the direction of an external magnetic field on phase and amplitude correation functions of scattered radiation by magnetized plasma slab," *Progress In Electromagnetics Research B*, Vol. 22, 121–143, 2010.
5. Jandieri, G. V., A. Ishimaru, K. Yasumoto, V. G. Jandieri, and N. N. Zhukova, "To the problem of electromagnetic waves propagation in turbulent magnetized plasma slab," *Proceedings of the XXX URSI General Assembly and Scientific Symposium*, F02.10, Istanbul, Turkey, Aug. 2011.
6. Ginzburg, V. L., *Propagation of Electromagnetic Waves in Plasma,* Gordon and Beach, New York, 1961.
7. Ishimaru, A., *Wave Propagation and Scattering in Random Media, Multiple Scattering, Turbulence, Rough Surfaces and Remote Sensing,* Vol. 2, IEEE Press, Piscataway, New Jersey, USA, 1997.
8. Gershman, B. N., L. M. Erukhimov, and Y. Yashin, *Wave Phenomena in the Ionosphere and Space Plasma,* Moscow, Nauka, 1984 (in Russian).
9. Rytov, S. M., Y. A. Kravtsov, and V. I. Tatarskii, *Principles of Statistical Radiophysics, Waves Propagation Through Random Media,* Vol. 4, Berlin, New York, Springer, 1989.
10. Gavrilenko, V. G., A. A. Semerikov, and G. V. Jandieri, "On the effect of absorption on multiple wave-scattering in magnetized turbulent plasma," *Waves in Random Media*, Vol. 9, 427–440, 1999.

# An Ultra-wideband CMOS LNA for 3–10 GHz with Low Power Consumption

**Chien-Hua Lai and Jeng-Rern Yang**

Microwave Laboratory, Department of Communication Engineering
Yuan Ze University, Jhongli City, Taoyuan Country 320, Taiwan

**Abstract**— The Low-Noise Amplifier (LNA) was used for an Ultra-Wide-Band (UWB) application with low power consumption. The low power consumption UWB LNA was designed with standard 0.18 μm CMOS technology. Low power consumption was achieved through the use of the inter stage technique, and current reused topology, with a peaking inductor. The input matching stage used an improved Chebyshev filter to achieve the input return loss, and inductive shunt-peaking was applied to the output matching. The LNA exhibited the maximum $S_{21}$ of 14.6 dB. The power consumption was 5.95 mW at $V_{dd} = 1.2$ V.

## 1. INTRODUCTION

The requirement of high-speed and high data-rate wireless communications has increased in recent years. Traditionally, the transmission of the digital flow was achieved by the use of wired transmission, such as USB, connected lines, and the Internet, or slow speed wireless connections for WiFi, Bluetooth, WLAN, or infrared ray. For IEEE 802.11b and 802.11g standards, the operation frequency is 2.4 GHz with data-rates of 11 and 54 Mbps, respectively. The operation frequency of the 802.11a standard is 5.2/5.7 GHz, which avoids the crowded 2.4 GHz band for less interference and higher data rate. Unlike narrow-band systems, the ultra-wide-band (UWB) systems are an emerging wireless technology that can transmit data over a wide frequency band for short ranges with low power consumption and higher data rates. In 2002, the Federal Communication Commission (FCC) allowed the frequency between 3.1 GHz to 10.6 GHz for UWB. The amplifier must meet several stringent requirements, such as broadband input matching to minimize the return loss, sufficient gain to suppress the noise of a mixer, low noise figure (NF) to enhance receiver sensitivity, low power consumption to increase battery life, and small die area to reduce the cost. This paper presents a low power amplifier with a simple Chebyshev filter. The input matching network used the inductive peaking technique and output matching used inductive shunt-peaking and increased the inductive series-peaking to enhance the bandwidth. The UWBLNA circuit design details are illustrated in Section 2. Spectra simulation results and comparison with other recently reported UWB LNAs are presented in Section 3. Conclusions are offered in Section 4.

## 2. CIRCUIT TOPOLOGY AND ANALYSIS

### 2.1. The Main Schematic of the LNA

The complete schematic of the UWB LNA is shown in Fig. 1. The First stage improved the traditional Chebyshev band pass filter [1], the middle stage used current reused technique to reduce power consumption, and the final stage used the inductive shunt-peaking technique [2].

At the circuit, $C_1$, $C_3$, $C_2$, $L_1$, $L_2$ and $M_1$ are the input matching stage. $C_4$ is a bypass capacitance and $L_5$ is RF chock. $L_4$ is used to enhance bandwidth and $C_5$ is the coupling capacitance. $M_2$ is used to improve isolation and $R_1$ and $L_6$ are output matching.

### 2.2. Input Impedance Matching

Input impedance matching is a critical design challenge in an ultra-wideband system. Fig. 2 shows a traditional band pass filter matching network. Fig. 3 is an improved band pass filter matching network. One inductor can be reduced to obtain a smaller area to reduce cost.

We calculated the input impedance in Fig. 3. The input impedance was calculated as follows:

$$Z_{in} = \frac{1}{SC_1} + \left\{ \left[ \frac{1}{SC_3} \| SL_1 \right] \| \left[ \frac{1}{SC_2} + SL_2 \right] \right\}$$

Figure 4 shows the circuit design. The following equation is the total equivalent input impedance:

$$Z_{in} = \frac{1}{SC_1} + \left\{ \left[ \frac{1}{SC_3} \| SL_1 \right] \| \left[ \frac{1}{SC_2} + SL_2 + SC_{gs} \right] + \frac{gm}{SC_{gs}} \right\}$$
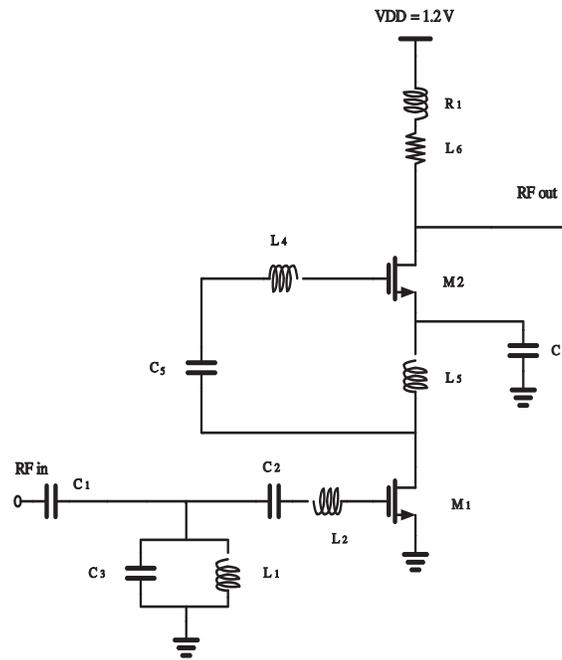
Figure 1: The main schematic of the LNA.
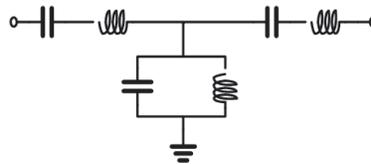


Figure 2: The traditional band pass filter.
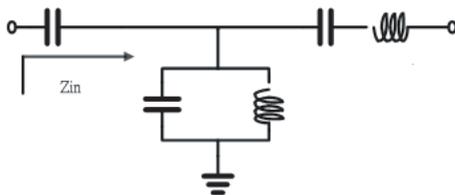


Figure 3: The improved band pass filter.
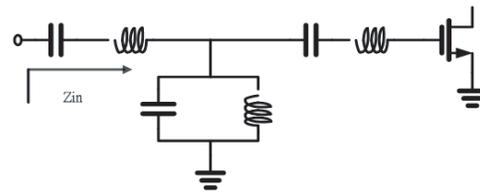


Figure 4: The circuit design.

## 2.3. Inter Stage Technique

The current-reused topology is proposed in this circuit design for a high gain performance. Fig. 5 shows the DC operation mode of this topology, in which $M_1$ and $M_2$ is a cascode amplifier. The AC operation mode is shown in Fig. 6, in which $L$ and $C$ separate $M_1$ and $M_2$ to form a two-stage common-source cascade amplifier. Conversely, this topology achieved low power consumption and high gain because the RF signal was amplified by two times with the same current and did not require the use of the second stage amplifier.

## 2.4. Wideband Output Impedance Matching

Figure 7 shows the configuration of output impedance matching and inductive shunt-peaking, which offers the advantage of enhanced bandwidth. The equivalent output impedance is calculated as follows:

$$R_{out} \approx \left( r_{o1} + \frac{1}{SC_4} \right) \| (SL_6 + R_1)$$

The impedance is approximated to 50 ohm to enable the output matching to achieve the wide band matching.
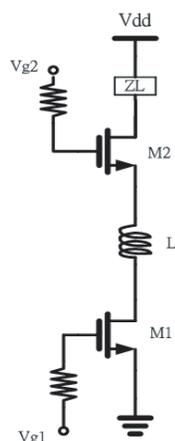
Figure 5: DC mode.
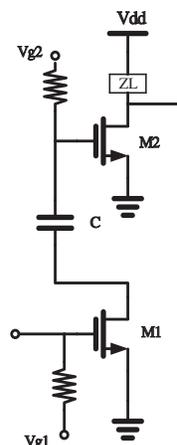


Figure 6: AC mode.
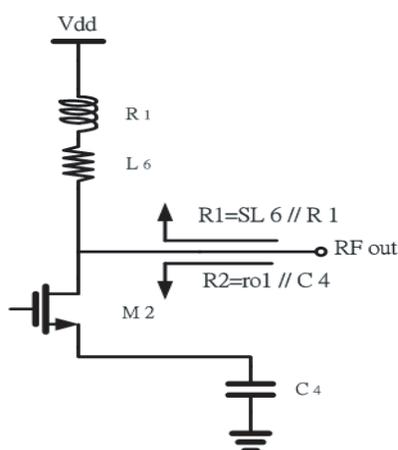


Figure 7: Schematic of wideband matching.

Table 1: Performance summary and comparison to other wideband 0.18 mm CMOS LNAs.

|           | BW (GHz)   | $S_{11}$ (dB) | $S_{21}$ (dB) (max) | NF (dB)  | PDC (mW) | Chip size              |
|-----------|------------|---------------|---------------------|----------|----------|------------------------|
| [4]       | 3.1–10.6   | $< -10$       | 20                  | 4–6      | 21.6     | $1.2\,\mathrm{mm^2}$   |
| [5]       | 3.1–10.6   | $< -9.4$      | 10.4                | 4–7      | 9        | $0.59\,\mathrm{mm^2}$  |
| [6]       | 3.1–10.6   | $< -11$       | 9.7                 | 4.5–5.1  | 20       | $0.5\,\mathrm{mm^2}$   |
| [7]       | 3.1–10.6   | $< -19$       | 17.5                | 3.1–5.7  | 33.2     | $1.1\,\mathrm{mm^2}$   |
| [8]       | 3–10       | $< -10$       | 21                  | 2.5–4.2  | 30       | $1.8\,\mathrm{mm^2}$   |
| This work | 3–10       | $< -10$       | 14.6                | 4.8–2.9  | 5.95     | $0.72\,\mathrm{mm^2}$  |

## 3. SIMULATED RESULTS

The proposed UWB LNA was simulated by Advanced Design System (ADS) by using 0.18-µm CMOS process TSMC model parameters. The LNA operated with a 1.2 V power supply and consumed 5.95 mW. The characteristic of band pass filter input matching network LNA are shown below. As shown in Fig. 8, the simulated input reflection coefficients ($S_{11}$) are lower than −10 dB. Fig. 9 shows the Noise Figure of the LNA, the minimal value of which is 2.97. Fig. 11 shows the $S_{21}$ of the LNA. The LNA achieved 14.6 to 13.6 dB power gain within the bandwidth. The output reflection coefficients ($S_{22}$) are shown in Fig. 10. Fig. 12 is the layout of the UWB LNA.

Table 1 is a summary of implemented 3–10 GHz CMOS LNAs. As shown in Table 1, the CMOS LNA exhibits the lowest power consumption; and the simulation results indicate that the proposed LNA design methodology was suitable for 3–10 GHz UWB or higher frequencies, such as wideband communication applications.
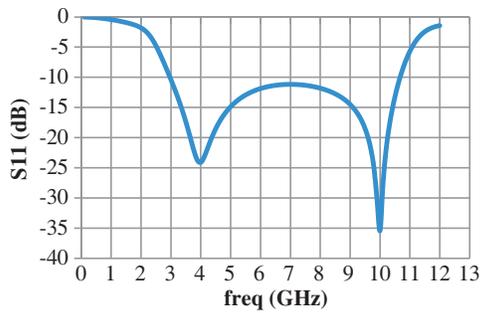
Figure 8: Simulated input reflection coefficients ($S_{11}$).
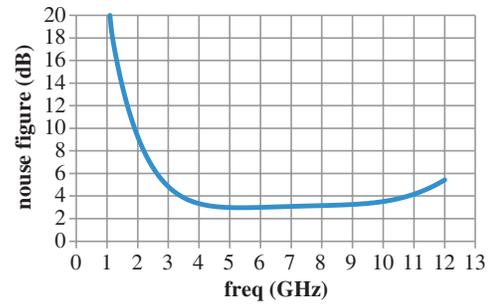


Figure 9: Simulated noise figure (NF).
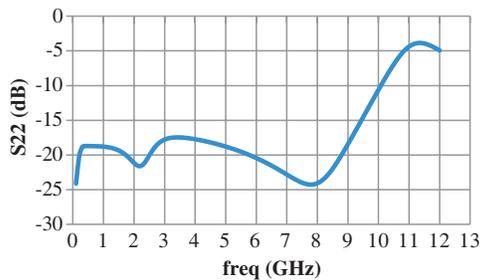


Figure 10: Simulated output reflection coefficient ($S_{22}$).
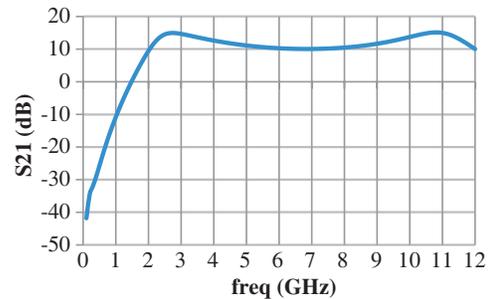


Figure 11: Simulated power gain ($S_{21}$).
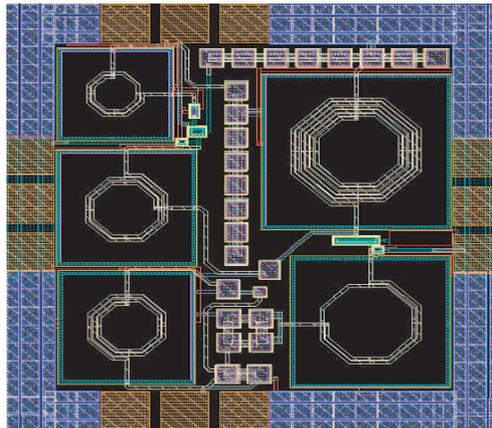


Figure 12: Layout.

## 4. CONCLUSION

The feasibility of the proposed wideband matching topology for achieving optimal input matching and high power gain is demonstrated in this paper. The implemented LNA exhibited maximal power gain of 14.6 dB, input return of less than $-10$ dB, and a minimal noise figure (NF) of 2.97 dB was obtained in the frequency range of 3.0–10.0 GHz with a power dissipation of 5.95 mW under a 1.2 V power supply. The LNA was designed in standard 0.18 μm CMOS technology. The simulation results verify the concept of the LNA.

## ACKNOWLEDGMENT

## REFERENCES

1. Wang, Y.-L., M.-L. Her, and H.-H. Lin, "Design and implementation of LNA with high gain and low power consumption for UWB system," *Proceedings of the 15th Asia-Pacific Conference on Communications*, 2009.

2. Yang, H.-Y., Y.-S. Lin, and C.-C. Chen, "2.5 dB NF 3.1–10.6 GHz CMOS UWB LNA with small group-delay variation," *Electronics Letters*, No. 20083425, The Institution of Engineering and Techology, November 29, 2008.

3. Bevilacqua, A. and A. M. Niknejad, "An ultra-wideband CMOS LNA for 3.1 to 10.6 GHz wireless receivers," *IEEE Journal of Solid-State Circuits*, 2004.

4. Gao, Y., Y. Zheng, and B. Ooi, "A 0.18-μm CMOS UWB LNA with 5 GHz interference rejection," *IEEE RFIC Symp. Dig.*, 47–50, Kobe, Japan, June 2007.

5. Liao, C. and S. Liu, "A broadband noise-canceling CMOS LNA for 3.1–10.6 GHz UWB receivers," *IEEE J. Solid-State Circuits*, Vol. 42, No. 2, 329–339, 2007.

6. Lu, Y., K. Yeo, A. Cabuk, J. Ma, M. Do, and Z. Lu, "A novel CMOS low-noise amplifier design for 3.1- to 10.6-GHz ultra-wide-band wireless receivers," *IEEE Trans. Circuits Syst. I*, Vol. 53, No. 8, 1683–1692, 2006.

7. Ismail, A. and A. Abidi, "A 3–10-GHz low-noise amplifier with wideband LC-ladder matching netwoerk," *IEEE J. Solid-State Circuits*, Vol. 39, No. 12, 2269–2277, 2004.

8. Bevilacqua, A. and A. M. Niknejad, "An ultrawideband CMOS low noise amplifier for 3.1–10.6 GHz wireless receivers," *IEEE Journal of Solid State Circuits*, Vol. 39, No. 12, 2259–2268, December 2004.

# Design Investigation of a Novel Bandpass Filter Using Trisection Open Loop Resonator

**Hossein Saghlatoon and Mohammad H. Neshati**

Department of Electrical Engineering, Ferdowsi University of Mashhad, Iran

**Abstract**— In this paper, a novel band pass microwave filter is designed and numerically investigated. A trisection open loop resonator is implemented to provide a narrow band pass filter at 2.4 GHz. The proposed filter is numerically investigated using ADS software package. Reflection coefficient and transmission coefficient of the filter are reported. Results show that at the centre frequency of 2.4 GHz for the proposed filter, 3 dB bandwidth of transmission coefficient is only 30 MHz, which exhibits measured loaded quality factor of 80. The proposed trisection open loop resonator band pass filter is successfully designed and implemented and the measured results are in a very good agreement with those obtained by numerical investigation.

## 1. INTRODUCTION

With the rapid development of wireless communication systems, there is an increasingly demand for high quality components at microwave frequencies. Filters are one of the most important components in these systems. High performance filters with small size, low cost, high selectivity and low pass band loss are the main requirements for the microwave circuits using microstrip components. The system sensitivity of a communication system is increased by decreasing pass band loss of a filter. Also, the bandwidth guard between adjacent channels of a multiplexed communication system is decreased by increasing the selectivity of the filter. As a result, better spectrum efficiency is obtained. High filter selectivity requires high filter order and more resonators. Due to the low unloaded $Q$ factor of the microstrip resonators, pass band loss of these filters is increased. Moreover, for cascaded microstrip filters, these requirements become contradictory. Filters satisfying both requirements are cross-coupled filters. They offer no coupling between adjacent resonators. The simplest type of these filters is the trisection filters, proposed in [2, 3]. They present asymmetric characteristics and one transmission zero out of the pass band, leading to a very sharp decreasing frequency response at the stop band of the filter.

In this paper, a novel band pass filter consist of three square open loop resonator with the centre frequency of 2.4 GHz is introduced. The proposed filter is numerically investigated using Advanced Design System (ADS) software package and also is experimentally investigated. Results show that, pass band loss of less than 3 dB is achieved. Also 3 dB measured bandwidth of transmission coefficient is 30 MHz.

## 2. BANDPASS FILTER STRUCTURE

The lowpass prototype of the proposed filter is shown in Fig. 1. Each resonator represents a frequency invariant immittance inverter and $J_{ij}$ are the characteristic admittance of the inverter. In our case $J_{12} = J_{23} = 1$ for the inverters along the main path of the filter. The bypass inverter
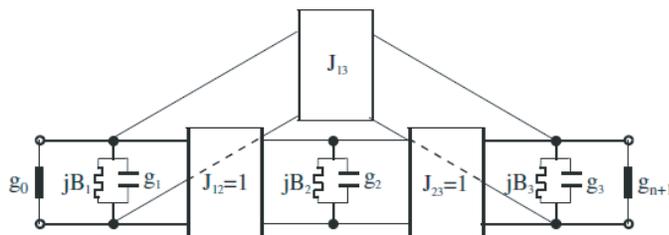


Figure 1: Low pass protptypr of the proposed filter.
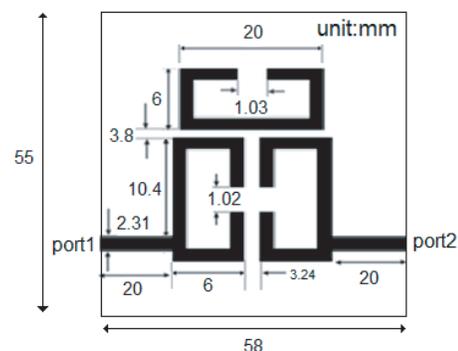


Figure 2: Layout of the proposed filter.

with a characteristic admittance $J_{13}$ accounts for cross coupling between adjacent resonators. $g_i$ and $Bi$ $(i = 1, 2, 3)$ denote the capacitance and the frequency invariant susceptance of the low pass prototype filter, respectively. $g_0$ and $g_4$ are the resistive terminations.

Based on the centre frequency and required fractional bandwidth, the element values of the low pass prototype filter are founded $g_1 = g_3 = 0.695$, $B_1 = B_3 = 0.185$, $g_2 = 1.245$, $B_2 = -0.615$, $J_{12} = J_{23} = 1.0$, $J_{13} = -0.457$ [1]. Also, the centre frequency of individual resonator, their external quality factor and mutual coupling between adjacent resonators using Equations (1) and (2) are summarized in Table 1. The generalized coupling matrix is derived in Equation (4) [1, 6]. In these equations $f_{BW}$ is the fraction bandwidth, which is the bandwidth of the filter divided by centre frequency. The proposed filter is shown in Fig. 2, which is designed and implemented using TLY5A031 substrate with dielectric constant of 2.2 and 31 mil heights.

$$Q_{e1} = \frac{\omega_o}{\omega_o g_o} \left( \frac{g_1}{f_{BW}} + \frac{B_1}{2} \right), \quad Q_{e3} = \frac{\omega_{o3}}{\omega_o g_o} \left( \frac{g_3}{f_{BW}} + \frac{B_3}{2} \right) \tag{1}$$

$$M_{ij} = \frac{\omega_o}{\sqrt{\omega_{oi}\omega_{oj}}} \frac{f_{BW} J_{ij}}{\sqrt{\left( g_i + \frac{f_{BW}}{2} B_i \right) \left( g_j + \frac{f_{BW}}{2} B_j \right)}} \tag{2}$$

$$M_{ii} = \frac{\omega_{oi}^2 - \omega_o^2}{\omega_o \omega_{oi}} \tag{3}$$

$$M = \begin{bmatrix} -0.124 & 1.0769 & -0.563 \\ 1.0769 & 0.194 & 1.0769 \\ -0.563 & 1.0769 & -0.124 \end{bmatrix} \tag{4}$$

## 3. SIMULATION RESULTS

Proposed filter is numerically investigated using ADS. Scattering coefficients of the filter is shown in Fig. 3(a) and Fig. 3(b). $S_{11}$ is shown in Fig. 3(a). It can be seen that a good matching condition is obtained at the resonance frequency of 2.4 GHz. Also the transmission coefficient, $s_{12}$ is shown in Fig. 3(b). It can be seen that a very low passband loss is obtained at the centre frequency of the proposed bandpass filter.



Figure 3: Numeical results of scaterring coefficients. (a) $S_{11}$. (b) $S_{12}$.

Table 1: Parameters of different resonators.

| | |
|---|---|
| $f_{o1}$ | 2.3947 GHz |
| $f_{o2}$ | 2.4098 GHz |
| $f_{o3}$ | 2.3947 GHz |
| $M_{12}$ | 0.0448 |
| $M_{13}$ | −0.0272 |
| $M_{23}$ | 0.0448 |
| $Q_{e_1}$ | 14.848 |
| $Q_{e_3}$ | 14.848 |
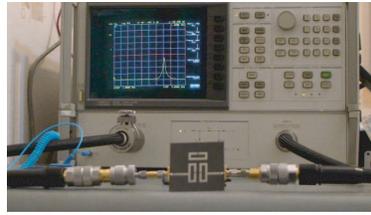
Figure 4: Experimental setup for the proposed bandpass filter.



(a)                                      (b)

Figure 5: Numeical results of scaterring coefficients. (a) $S_{11}$. (b) $S_{12}$.



Figure 6: Measured and simulated transmission coefficient, $S_{12}$ versus frequency.

Table 2: Measured and experimental results.

| Parameters | Measured | Simulation |
|---|---|---|
| centre frequency | 2.417 GHz | 2.4 GHz |
| 3 dB bandwidth of $S_{12}$ | 30 MHz | 25 MHz |
| passband loss | −3.5 dB | −0.3 dB |
| 3 dB Impedance Bandwidth | 25 MHz | 10 MHz |

## 4. MEASURED RESULTS

Setup for measuring the filter characteristics is shown in Fig. 4. Measured reflection coefficient, from 1.8 GHz to 3 GHz, is shown in Fig. 5(a). It can be seen that a good matching condition is obtained at 2.4 GHz. Experimental results for transmission coefficient, in same frequency span is also shown in Fig. 5(b). It can be seen that passband of better than −3.5 dB is obtained at the resonance frequency of 2.4 GHz. To verify the measured and experimental results, variation of $S_{12}$ versus frequency is shown in Fig. 6., for both measured and simulation results. It can be seen that experimental results agree well with those obtained by numerical Investigation. The precise results of the proposed filter are summarized in Table 2.

## 5. CONCLUSIONS

This paper describes design and analysis of a trisection open loop resonator bandpass filter with resonance frequency of 2.4 GHz. Designed filter is numerically investigated by ADS software package. Proposed filter was implemented and experimental set up was carried out for measuring reflection

and transmission coefficient. Measured results show that resonance frequency of 2.417 GHz with low loss passband of $-3.5$ dB is obtained. Also, 3 dB bandwidth of measured transmission coefficient is 30 MHz, which exhibits a loaded quality factor of 80. Apart from, error in passband loss between measurement and simulation, due to considering ideal case with no loss in simulation, there is a good agreement between measured and numerical results.

**REFERENCES**

1. Hong, J.-S. and M. J. Lancaster, *Microstrip Filters for RF/Microwave Applications*, John Wiley & Sons, Inc., Copyright © 2001, 2001.
2. Hong, J.-S. and M. J. Lancaster, "Microstrip, cross-coupled trisection bandpass filters with asymmetric frequency characteristics," *IEE Proc. — Microwave, Antennas Propagation*, Vol. 146, 84–90, Feb. 1999.
3. Tsai, C.-M., et al., "Microstrip trisection cross-coupled bandpass filter with I-shaped resonator," *Proceeding of International Symposium on Communications*, Nov. 2001.
4. Iliev, I. and M. Nedelchev, "CAD of cross-coupled miniaturized hairpin bandpass filters," *ICEST*, Nis, Yugoslavia, 2002.
5. Hong, J. S. and M. J. Lancaster, "Theory and experiment of novel microstripslow-wave open-loop resonator filters," *IEEE Transaction on Microwave Theory & Tech.*, Vol. 45, No. 12, Dec. 1997.
6. Miraftab, V. and Y. Ming, "Generalized lossy microwave filter coupling matrix synthesis and design using mixed technologies," *IEEE Transaction on Microwave Theory & Tech.*, Vol. 56, No. 12, Dec. 2008.

# Remotely Controllable Robotic System to Detect Shallow Buried Objects with High Efficiency by Using an Holographic 4 GHz Radar

**I. Arezzini[1], M. Calzolai[1], L. Lombardi[1], L. Capineri[1], and Y. Kansal[2]**

[1]Dipartimento Elettronica e Telecomunicazioni, Università di Firenze, Firenze 50139, Italy
[2]Birla Institute of Technology and Science, Pilani, India

**Abstract**— The ambit of non-destructive testing has several diagnostic methods, each with its own characteristics. The microwave high resolution imaging methods allows the detection of shallow buried objects with high plane resolution. The diagnostic method that uses the holographic subsurface radar up to 4 GHz (RASCAN 4/4000) allows obtaining images of the dielectric contrast at a high spatial resolution (about 1 cm). The scanning of large areas of several square meters with a subsurface radar requires an automatic scanning tool that must also associate the obtained dielectric contrast data with the relative position of measurement. The necessity of an automated scanning system has led to the creation of a robotic platform, equipped with a wireless remote connection, with a high degree of expandability and flexibility, also for use with other types of sensors (acoustic, ultrasonic, . . . ).

The mechanical part of the robotic system consists of a motorized platform, which is entrusted with the advancement; and of a system for the scanning motion of radar head, transverse to the direction of advancement. The electronic part consists of several modules connected together by a bus 485 and connected remotely to a computer by a Bluetooth wireless connection. The developed computer software sends control instructions to the robot and plots the obtained dielectric contrast data along with the relative position of measurement to obtain a picture of the scan.

The holographic radar, Rascan type 4/4000 can be programmed to scan the surface with up to 10 discrete frequencies in order to get high phase contrast for objects buried at different depths.

The developed robotic system successfully scans large areas of land to detect shallow buried objects, while being remotely controlled through a computer.

The trajectory control was carried out on Flex board, with *dsPIC®* processor onboard and programmed with *Scicoslab*, an integrated development environment equipped with visual programming tools.

The position of robotic platform is measured with optical position sensors and used also in the trajectory control system.

## 1. INTRODUCTION

Non-destructive testing methods for the detection of shallow buried objects or cavities include ultrasound, infrared and ground penetrating radar techniques. The advantage of the ground penetrating radar is the fast acquisition and possibility to operate without any contact with the surface. These characteristics ascertain that the probing antenna can be mounted on a robotic vehicle that can scan large surfaces in lesser time than the standard method of manual scanning.

The sub-superficial radar through a holographic technique allows obtaining images of the microwave dielectric constant with a high spatial resolution (1 cm). The microwave holographic radar used is RASCAN 4/4000 with working frequency up to 4 GHz [1].

The produced system is a robotic platform designed to be used with the holographic radar RASCAN 4/4000 while maintaining certain flexibility for use with other types of sensors (acoustic, optical, infrared). In Fig. 1 is shown the architecture of the robot.

The robot is a differential drive rover, with the direction and movement being determined by the speed of the two front wheels.

The movement of the robot is performed by two frontal motors (model *615 30Q 1/64* from *Bernio Elettromeccanica s.n.c.*), on the rear part are two pivoting wheels.

The robot is also provided with speed and position control in which the individual velocity and position of each of the two engines is monitored via optical encoders (model *SE22-300-2-CPU-S* from *VEMtech s.c.r.l.*) mounted on each of the two motors.

The realization of the control system is based on a model of the robot in which there are three distinct elements:
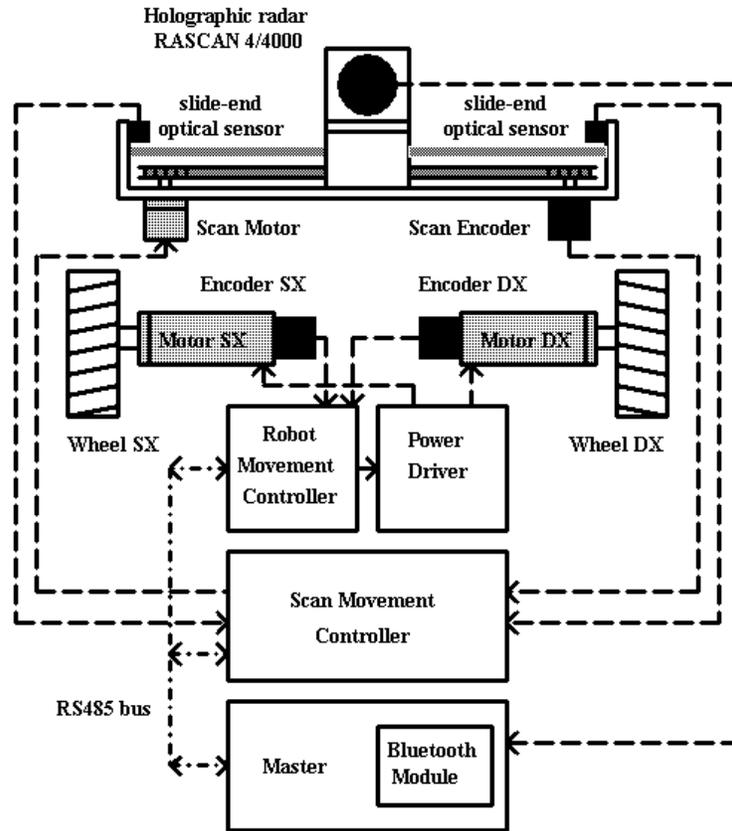
Figure 1: Block Scheme of the robotic radar object scanner.
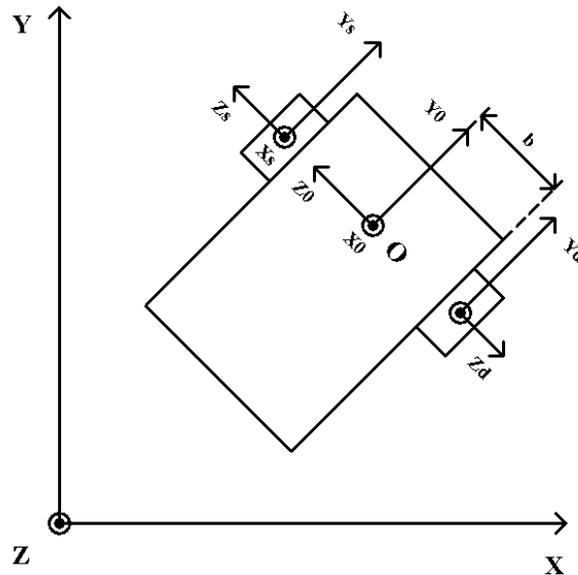


Figure 2: Configuration space robot.

- The body of robot.
- The left wheel of the robot.
- The right wheel of the robot.

Figure 2 shows the configuration space of the robot with respect to the absolute axes. The wheels and the body of the robot make an angle $\theta$ with the Cartesian abscissa, and determine the pose of the robot relative to the point O.

The movement controller of the robot consists of a high-level and two low-level controllers, one for each wheel. The high-level control system for tracking the trajectory was designed using a Lyapunov controller.

In Fig. 3 is shown the expression of low-level controller in the Laplace domain.

In Table 1 are mentioned the quantities used in the low-level controller and their explanation. It also specifies the following values and makes the following assumptions:

- $T_v \approx T_m$.
- $K_p = 7$ obtained from experimental testing.
- $K_v = 34$.

The controller described has been implemented on *Flex* board and developed in *Scicoslab* [2] integrated environment, using a visual programming language appropriately customized with new graphical blocks.

The control board is flanked by the power board that mounts two *TB6549 Toshiba* drivers.

The electronics on board of the robot is composed of a control card, the power of the control board for the lateral movement of the radar and the holographic master card, both of which are connected to the control board through RS485 Flex. The master board communicates with a remote PC via Bluetooth.

Both the RS485 bus communications, between the circuit boards mounted on the robot and the between the master card and the remote PC via Bluetooth use the same type of communication protocol, the structure and description of the frame of which are shown in Table 2.

The holographic radar has two receiving antennas, for parallel and perpendicular polarization, with each antenna is associated an output analog channel.

The frequency of the radar is selected by an external voltage that controls an internal VCO.

$$L(s) = \frac{Kv\ Km}{s^2} \frac{Tv\ s + 1}{Tm\ s + 1}\ (s + Kp)$$

$$Km = \frac{1}{Ke} \qquad Tm = \frac{Ra\ J}{Ke\ Kt}$$

Figure 3: Expression of low-level controller.

Table 1: Quantities used in low-level controller and their explanation.

| | |
|---|---|
| $R_a$ | amour resistance ($1.45\,\Omega$) |
| $K_e$ | motors dielectric constant ($1\,\text{Vs/rad}$) |
| $K_t$ | motor torque constant ($1\,\text{Nm/A}$) |
| $J$ | moment of inertia respect to the axis of the motor ($0.0193\,\text{kgm}^2$) |



Figure 4: Measurement setup with indicate TIN and PMA-2 position.

The Master Communication Card manages communications, measures the two output analog channels from the holographic radar and also generates the necessary VCO voltage to select the desired operating frequency.

A test is performed with setup shown in Fig. 4 with metallic a TIN buried at 2 cm of depth and PMA-2 plastic simulant mine buried at 3 cm of depth.

The blue disk indicates the position of the TIN and yellow disk indicates the position of PMA-2. The disks are obviously removed during robot scanning.

In Fig. 5 are shown the viewgrams of output signals from holographic radar RASCAN 4/4000 obtained during an experiment done on the field (see Fig. 4). The samples are acquired along one scan line with length of about 1m and passing thro the center of the tin and PMA-2 targets. The scan has been repeated three times to check the repeatability of the measurements. Two metal

Table 2: Frame Structure of the communication protocol.

| Name of field | Length [byte] | Description |
|:---:|:---:|:---:|
| Header | 2 | *Header* identifies the beginning of the frame. The values of the 2 bytes are fixed and their values are: DLE = 16 STX = 2 |
| Packet type | 1 | *Packet type* is the value that identifies the packet type. The following table shows packet types and their identifiers. <table><tr><td>PACKET TYPE</td><td>IDENTIFIER</td></tr><tr><td>Data</td><td>17</td></tr><tr><td>Command</td><td>18</td></tr><tr><td>Flux</td><td>19</td></tr><tr><td>Signals</td><td>20</td></tr></table> |
| Paralen | 1 | *Paralen* indicates the length in bytes of the packet. |
| Message | variable | *Message* represents the information content. |
| CRC | 1 | *CRC* allows error checking, is calculated by initially putting CRC = 0 and then make the XOR with the previous bytes excluding the 2-byte header. |
| Trailer | 2 | *Trailer* Identifies the end of the frame. The values of the 2 bytes are fixed and their values are: DLE = 16, STX = 3 |
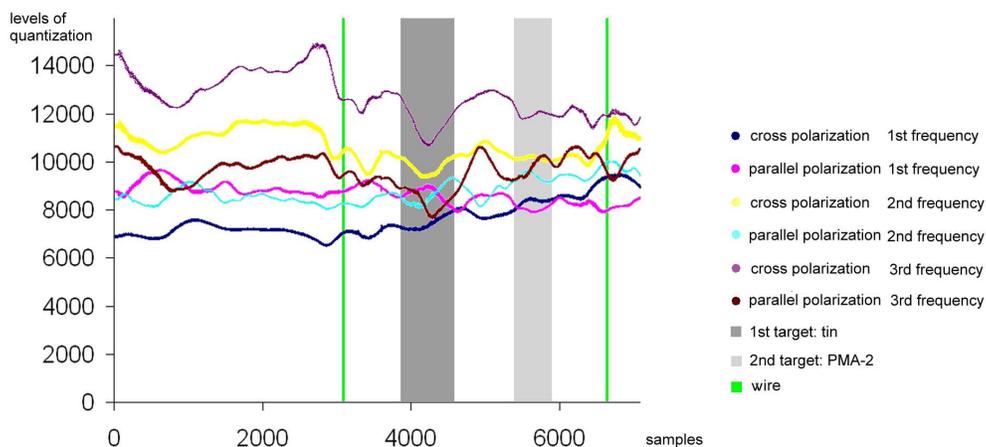


Figure 5: Signals from two output channels for 3 programmed frequencies: Grey color band indicate TIN and PMA-2 positions and green color lines two metal wires.

wires perpendicular to scanning line are placed on the ground surface to have a reference target to align multiple measurements. These two targets are shown with green lines in Fig. 5, while the tin and the small plastic PMA-2 are shown with grey bands with dimensions corresponding to their diameter. There is a good correlation between the tin position and the variation of the phase contrast signal while it is less evident the PMA-2 target. The full acquisition of the surface will be implemented and the corresponding phase contrast images will be further processed with feature extraction and classification algorithms that have been already developed for interpretation of holographic images [3].

## ACKNOWLEDGMENT

**REFERENCES**

1. Ivashov, S., V. V. Razevig, I. A. Vasiliev, A. V. Zhuravlev, T. D. Bechtel, and L. Capineri, "Holographic subsurface radar of RASCAN type: Development and applications," *IEEE Journal of Selected Topics in Earth Observations and Remote Sensing*, accepted on June 5, 2011, in Print Digital Object Identifier JSTARS-2010-00097.
2. http://erika.tuxfamily.org/scilabscicos.html.
3. Windsor, C. G. and L. Capineri, "Distinguishing buried mines from battlefield clutter using holographic radar," *Progress In Electromagnetics Research Symposium Abstracts*, March 20–23, 2011, Marrakesh, Morocco.

# Design of ARC Filters by Leap-Frog Method

**L. Fröhlich, J. Sedláček, and M. Friedl**

Brno, FEEC BUT, UTEE, Kolejni 2906/4, Brno 612 00, Czech Republic

**Abstract**— The sphere concerning frequency filters is constantly developing and there are many principles of non-cascade realizations which can be used for the design of *ARC* filters. Unfortunately, due to a very difficult design of the certain types of filter synthesis methods these filter realizations are not properly described and there is no detailed description of their usage in practice. One of these realizations is the *Leap-Frog* filter synthesis method.

The article describes the method of the filter design of *ARC* filters growing from the connection of the *RLC* filters. This method of the design is not used very often due to fact of a very difficult design and bigger amount of active elements (*OAs*). But on the other hand, this method exhibits considerable advantages as very small filter sensitivity and excellent dynamic qualities. Thus, it is ideal by filter realizations with area of switching capacitors and their following usage in integrated circuits. The aim of contribution will be following — from the created complete analysis of filters realizing *LP*, *HP*, *BP*, *BR*, *LPN* and *HPN* filters with either configurations *T* or *Π* prescribe their filter design and create a suitable description for their optimal using. Some circuits will be realized physically for the evaluation of the filter design method as well as frequency usage of designed filters by using of modern active elements (*OAs*).

## 1. INTRODUCTION

The *Leap-Frog* method of filter synthesis is leading to non-cascade filter block connections. Circuit structure of *ARC* filters created with the help of *Leap-Frog* combines the method of cascade block realization and realization growing from ladder *RLC* filters.

The principle of realization is based on the transfer of qualities of impedance coupled elements of ladder *RLC* filters to equivalently reacting connection with impedance distinguished *ARC* blocks of 1st order or 2nd order. The transformation on the resulting *ARC* circuit is realized according voltage and current ratio of the ladder *RLC* filter. These ratios are simulated by dyad of voltage relations. Integral or differential relations between current and voltage on inductors or capacitors are simulated by integrators which can be made by *OA* with capacitor in feedback [1].

If we want to design a circuit with the help of this method, there are several possibilities. The easiest one may be the use of description of original *RLC* circuit with the help of signal flow graph and their following transfer to the block structure with integrators. The easiest structures with integrators are defined crosswise connected capacitor or lengthwise connected inductor. Conversely, the most difficult structures are defined with crosswise connected of parallel combination or crosswise series of combination of inductor or capacitor.

## 2. THE SYNTHESIS OF LEAP-FROG FILTERS

For defining of complete design and detecting individual qualities and parameters it is enough to design *ARC* circuits for the lowest possible order of filter. Thus for *LP* and *HP* it is suitable to realize 2nd and 3rd order and for *BP* and *BR* of 4th and 6th order for the filter configuration in form Π and *T*. With the help of these designs it is obvious in which situations it is necessary to add other summation of current to the circuit, with what number of *OA* we have to count, detection of dynamic qualities or spread of building elements, sensitivity.

As an example for this article can be presented filter design of 3rd order *LP* filter in *T* configuration for input parameters $F_M = 10\,\text{kHz}$, $F_P = 15\,\text{kHz}$, $K_{ZVL} = -3\,\text{dB}$ a $K_{POT} = -15\,\text{dB}$ with Tchebyshev approximation. In the Fig. 1, there is a connection of *RLC* filter with the division of elements for creating of formulas.

For creation of signal flow graph we have to set circuit formulas for individual elements, see (1), (2), (3), (4) and (5):

$$I_{R1} = \frac{U_{R1}}{R_1} = \frac{U_1 - U_{C2} - U_{L1}}{R_1}, \tag{1}$$

$$I_{L1} = \frac{U_{L1}}{pL_1} = \frac{U_1 - U_{R1} - U_{C2}}{pL_1}, \tag{2}$$

$$U_{C2} = \frac{I_{C2}}{pC_2} = \frac{I_{L1} - I_{L3}}{pC_2}, \tag{3}$$

$$I_{L3} = \frac{U_{L3}}{pL_3} = \frac{U_{C2} - U_2}{pL_3}, \tag{4}$$

$$I_{R2} = \frac{U_{R2}}{R_2} = \frac{U_2}{R_2}. \tag{5}$$

According to set of formulas it is not a problem to realize formulation of individual elements of $RLC$ circuit with the help of signal flow graph, see Fig. 2. It is obvious that in signal flow graph some changes are realized with the red color. It was necessary to add other two summations of current between $I_{R1}$ and $-I_{L1}$, $I_{L3}$ and $-I_{R2}$ which leads to increase of number of $OA$ in the circuit for two. And also to adjust the formula (2), (3) and (5) due to the polarity of currents and voltage and their connection, multiplying whole formula by the value $-1$.

To reach realization of $ARC$ filters with the help of available integrator it is necessary to transfer current node $-I_{L1}$ a $I_{L3}$ to voltage with the help of multiplying of current and voltage chosen by regulating rezistor $R_N$. After this modification we get $-U_{IL1} = (R_N^2/pL_1)I_{UL1}$. The same modification can be applied also for node $I_{L3}$. Final connection of signal flow graph from which we will deduce setting of $ARC$ circuit can be seen in the Fig. 3.
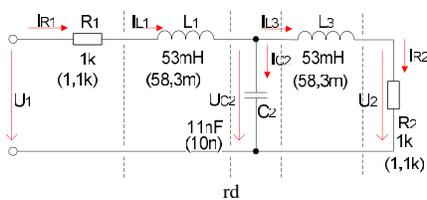


Figure 1: $RLC$ filter of $LP$ of the 3rd order in $T$ configuration.
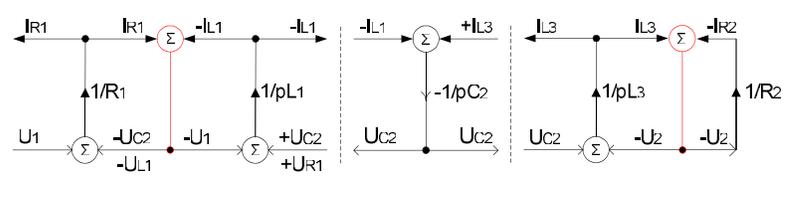
Figure 2: Scheme of $RLC$ elements with help of signal flow graph.
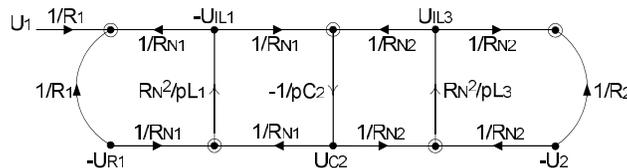


Figure 3: Final scheme of signal flow graph.
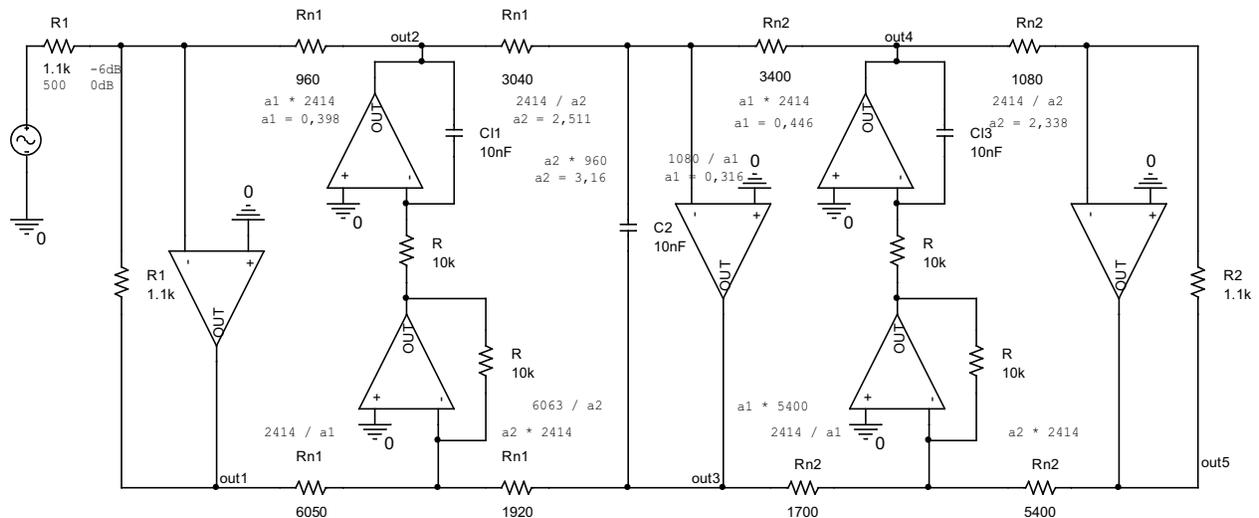


Figure 4: $ARC$ filters with integrators and description of possible design of dynamical ratios in the circuit.

With the help of final signal flow graph it is not problematic to set resulting $ARC$ circuit. In the resulting circuit of $ARC$ filters the realization of the coil is obvious with the help of two $OA$ (amplifier + inverting integrating transfer I-U) and capacitors with the help of one $OA$ (inverting integrating transfer I-U). Thus it is obvious that $LP$ with $\Pi$ configuration must be much easier. On the one hand, due to realization only on coil of the circuit. But on the other hand also due to unadding additional current summation. As it is in our case, due to series connection of the certain element with loading resistors. Complete scheme of filter is depicted in Fig. 4.

The biggest advantage of these connections is the possibility of compensation of scatter of building elements mainly capacitors due to re-counting of original $RLC$ circuit, see Fig. 1. Due to this re-counting so that the value of capacitors $C_2 = 10\,\text{nF}$ and option of the value of capacitors $C_{l1}$ a $C_{l3}$ to the same value, there is a spread of element value $k_C = 1$ and $k_R = 10.4$. The option of the value $k_C = 1$ is problematic mainly for $BP$ and $BR$ by the $T$ filter configuration by choice the option of approximation with the zero transfer.

In $ARC$ connection there are certain modifications of regulation rezistor $R_N$. These modifications are cause by dynamical modifications in the circuit so that maximum transfer on the individual outputs was the most consistent. The principle is realized so that the direct way from input to output is multiplying by constant $a_1$ — decay and after that divided by constant $a_2$ — gain. In the second part we will divide by constant $a_1$ and after that multiple by constant $a_2$. Thus all maxims will be in acceptable extent and the circuit gains the excellent dynamics. Simulations with the help of the programme $PSpice$ for verification of dynamical ratios in the circuit after a modification, are seen in the Fig. 5. The last modification is defining the whole filter transfer. It is possible to keep whole transfer outgoing from $RLC$ circuit, it means $-6\,\text{dB}$ or lengthwise resistor $R_1$ or multiple constant $K$ according to the required whole transfer.
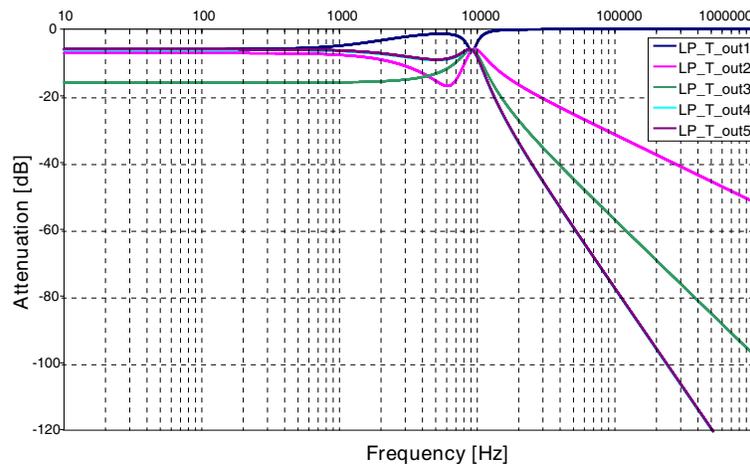


Figure 5: Simulation of dynamical ratios after the modification of transfers on individual outputs of the circuits.
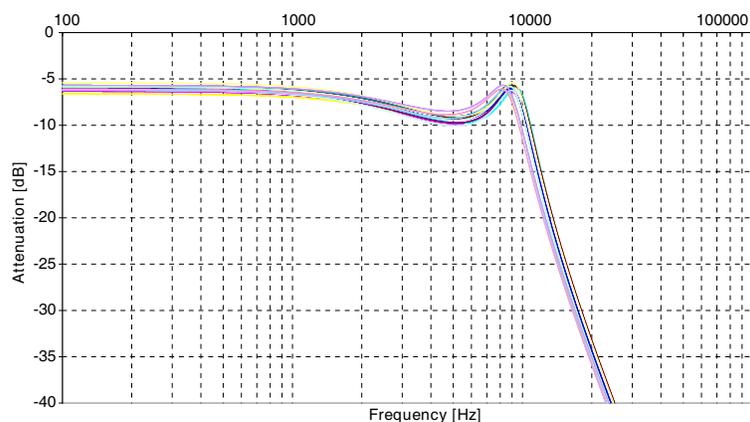


Figure 6: Sensitivity simulation of $ARC$ filter with real elements.

Table 1: Overview of the number of $OA$ for filters $LP$, $HP$, $BP$ and $BR$ designed by the Leap-Frog method.

| Order of filter $LP$ | | 2 | 3 | 4 | 5 | 6 | 7 | 8 | 9 | 10 |
|---|---|---|---|---|---|---|---|---|---|---|
| Number of $OA$ | $\Pi$ | 4 | 4 | 7 | 7 | 10 | 10 | 13 | 13 | 16 |
| | $T$ | 4 | 7 | 7 | 10 | 10 | 13 | 13 | 16 | 16 |
| Order of filter $HP$ | | 2 | 3 | 4 | 5 | 6 | 7 | 8 | 9 | 10 |
| Number of $OA$ | $\Pi$ | 6 | 8 | 11 | 13 | 16 | 18 | 21 | 23 | 26 |
| | $T$ | 6 | 9 | 11 | 14 | 16 | 19 | 21 | 24 | 26 |

| Order of filter $BP$ | | 4 | 6 | 8 | 10 | 12 | 14 |
|---|---|---|---|---|---|---|---|
| Number of $OA$ | $\Pi$ | 7 | 9 | 13 | 15 | 19 | 21 |
| | $T$ | 7 | 11 | 13 | 17 | 19 | 23 |
| Order of filter $BP$ | | 4 | 6 | 8 | 10 | 12 | 14 |
| Number of $OA$ | $\Pi$ | 9 | 12 | 17 | 20 | 25 | 28 |
| | $T$ | 9 | 14 | 17 | 22 | 25 | 30 |

The fact that $ARC$ circuits designed with the help of the methods outgoing from the characteristic of $RLC$ circuit exhibit practically the lowest sensitivity is demonstrated in the Fig. 6.

For the comparison of this method with other design methods, it can be also important to consider the number of $OA$ in the circuit, as it is shown in the Table 1. This design method is specific by the highest number of $OA$. It is necessary to think in advance with which kind of filter configuration we will realize the circuit due to the overall number of $OA$. For $LP$ and $HP$ it is much suitable to use $\Pi$ filter configuration or to use $T$ filter configuration in case of even orders of the filter. For $BP$ and $BR$ is much more suitable to use $\Pi$ filter configuration.

## 3. CONCLUSION

To sum up, it can be said that even despite the difficulty with the design it is possible to design certain circuits with the help of this method. Mainly, this will include $LP$ and $BP$ filters which contain acceptable number of $OA$, on the contrary with $BR$ or $HP$ filters which have a big number of $OAs$ in the circuit. For the use of $LP$ or $BP$ filters it is supported by the small spread of the building elements and the possibility of design of the capacity values in tolerance orders $E6$ or $E12$. Except for this, these circuits represent the smallest sensitivities and excellent dynamical ratios. Due to the overall problematic of these circuits, the circuit program is created for the complete synthesis of these circuits. The program will enable to display of the dynamical ratios in the circuit and the option of the capacitor values for capacitors orders. The program is the advantage for the designer so that they needn't work out the synthesis for particular input parameters and at the same time they could compare these resulting circuits with filters designed using other methods.

**REFERENCES**

1. Sedláek, J. and K. Hájek, "Kmitočtové filtry," 1. vydání, 535, BEN, Technická Literatura, Praha, 2002, ISBN 80-7300-023-7.
2. Dimopoulos, H. G. and A. G. Constantinidis, "Linear transformation active filters," *IEEE Trans. CAS*, Vol. 25, No. 10, 845–852, 1978.
3. Ghausi, M. S. and K. R. Laker, *Modern Filter Design*, Practice Hall, New Persey, 1981.
4. Kapustin, V. I., *Aktivnye RC-filtry Vyskovo Porjadka*, Radio i svjaz, Moskva, 1985.
5. Sedra, A. and K. Martin, "Design of signal-flow graph (SFG) aktive filters," *IEEE Trans. CAS*, Vol. 25, No. 4, 185–195, 1978.

# Programme for Synthesis of ARC Leap-frog Filters

**L. Fröhlich**, **J. Sedláček**, and **M. Friedl**

FEEC, BUT, UTEE, Kolejní 2906/4, Brno 612 00, Czech Republic

**Abstract**— Concerning the difficulty of the design method of *ARC* filters with the non-cascade *Leap-Frog* realization, which combines qualities of block realizations and realization growing from ladder *RLC* filters, the programme for a complete synthesis of these *ARC* filters was created.

The article deals with the complete design and the description of the programme, outgoing from a suitably set of developing diagram. The process enables filter design from the choice of the input values, the selection of approximation types with or without zero transfer, the choice of transfer functions *LP*, *HP*, *BP*, *BR* to the possibility to choose required kind of the filter configurations in *T* or Π form.

The resulting output of the programme is the circuit diagram of filter including all numeric values of the circuit element. Then program offers also output of complete analysis of designed filter according to the input required parameters with displaying of all important transfer characteristics, with the possibility to control and change of dynamical ratios in each block of filter. The presented programme should be used mainly for the wider usage of these filter types, which exhibit in comparison to other filter realizations many advantages in practice.

## 1. INTRODUCTION

The article describes and shows the realization of the programme for the design of *ARC* filters with the help of the *Leap-Frog* method. Concerning the realization of the programme, which is outgoing from the set input parameters of the user, the realized programme *NAF* perfectly fits [9]. This complex programme contains the complete synthesis of *RLC* filters. Due to the fact that the *Leap-Frog* method is based on the *RLC* ladder filters, *NAF* programme is ideal for the implementation of this method.

To create the many parts of the programme, firstly it was necessary to analyze complete designs of the basic connections of *ARC* filters realized with the help of *Leap-Frog* method. Thus, for both configurations of the filter connection Π and *T*, and also for approximations with or without zero transfer and the applying of the modified method of node voltage (method of stamp) for proper modification of active element connection for optimization of transfer of each filter blocks of *ARC* circuits have been necessary to investigate.

## 2. IMPLEMENTATION OF LEAP-FROG PART TO FOLLOWING PROGRAMME

In the Fig. 1, there is a developing diagram which defines the implementation of the part of *ARC_LF* programme to the current *NAF* programme. As it has been mentioned above, the *NAF* programme contains the complete synthesis of *RLC* filters outgoing from the defined required input values. Here belongs the choice of the type of the filter, type of approximation and required input parameters for the target type of the filter is possible. After the realization of these steps, the user gains the filter order and after applying the choice of the loading resistors, the programme make automatically the complete syntheses of *RLC* filter. Main display of this programme part can be seen in the Fig. 2, where the original part of *NAF* programme is shown.

After the realization of these steps, the implemented part of the programme gets the complete input values in several spheres, which are not problematic for creation of the set image of *RLC* circuit by completing individual *R*, *L* and *C* elements. As the complete analysis of *Leap-Frog* filters for *LP* and *HP* of 2nd and 3rd order and *BP* and *BR* of 4th and 6th order was created before the start of the programming, it was found out where and under which circumstances we can add other summation of the current into the circuit, and how to approach to the solution of the problems concerning dynamical ratios for the individual parts of the circuit and which *RLC* elements of the filters belong to the set integrator type. Then, there was no problem to define the complete *ARC* circuit with the help of the conditions in the source code, see the Fig. 3.

In the Fig. 3, we can see the complete illustration of the circuit diagram of *ARC* filters realized with the help of *Leap-Frog* method. For the illustrated circuit, there is a table in the left part, where are given the values re-counted from *RLC* filter. Apart from these values, there is also an element value ratio of building elements $k_R$ and $k_C$ shown. Other possibilities how to modify this

*ARC* circuit is the scheme of the dynamical ratios in the circuit. Currently, the programme enables only to display the diagram of the output module characteristics outgoing from *RLC* circuit, see Fig. 1. With the help of method of stamp, the circuit will enable to display output module transfer characteristics of the *ARC* circuit for the various *OA* models. The programme also offers the possibility to choose value of filter elements from *E*12 tolerance order. This change can be seen in the Fig. 4, where the values of the *ARC* circuit are modified according the capacitor value of *RLC* filter $C_1 = 10\,\text{nF}$. (Than the element value ratio of the building elements of the circuit $k_C$ was optimized).
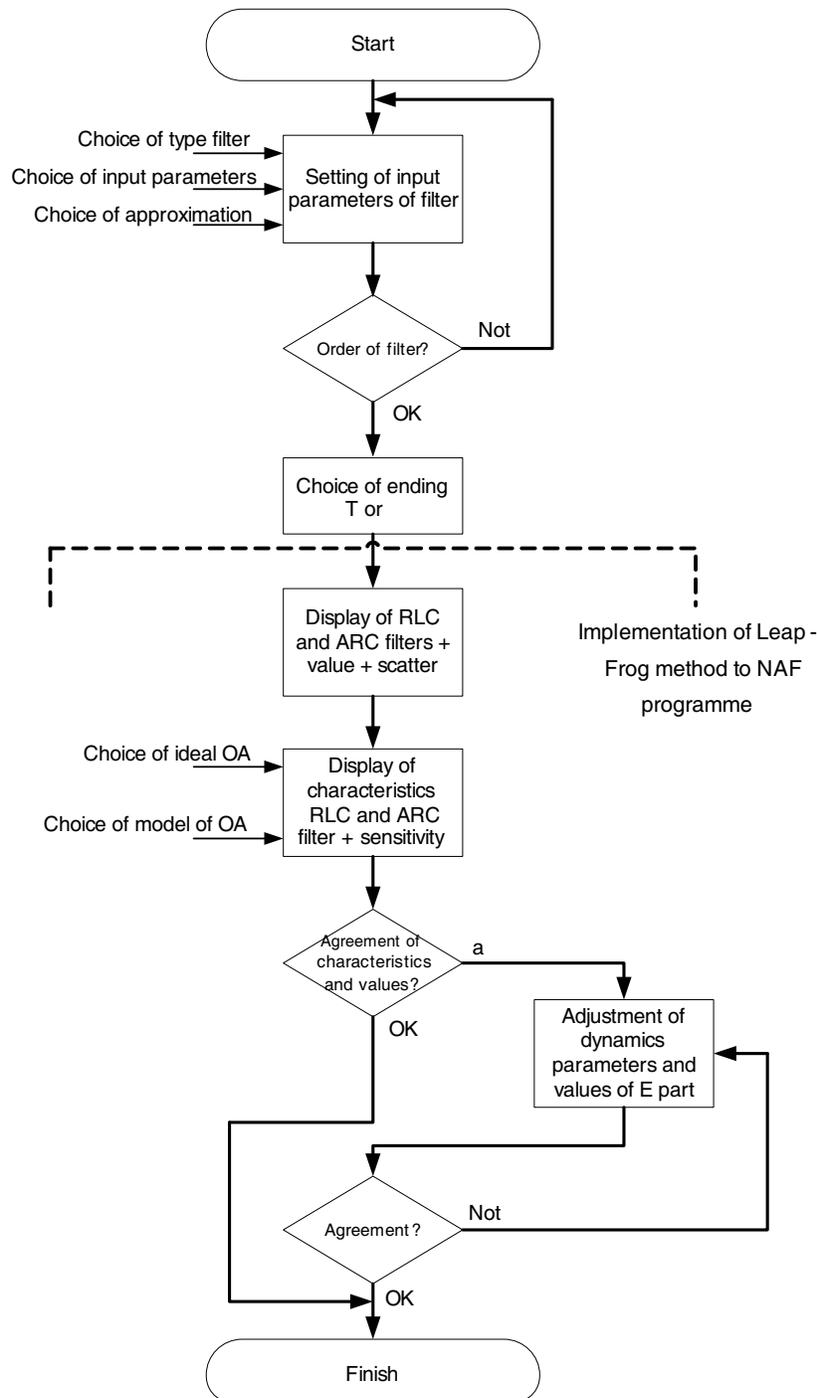


Figure 1: Developing diagram for implementation of the part of *ARC_LF* to programme *NAF*.
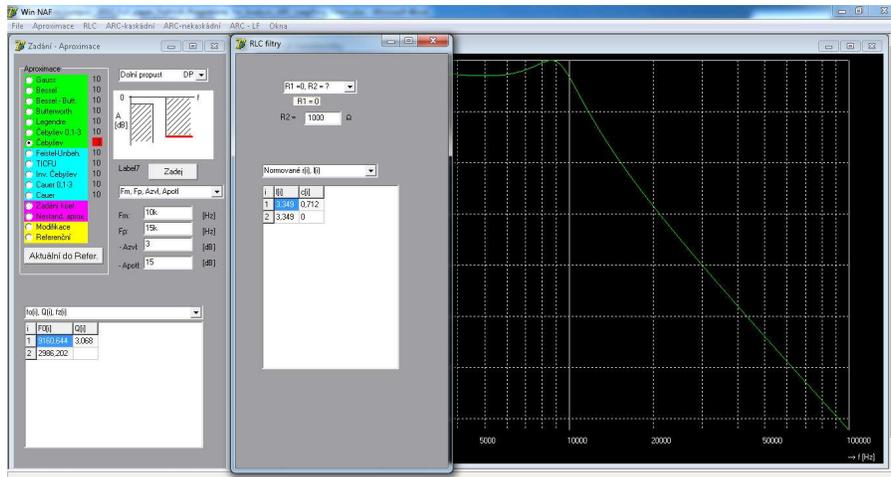
Figure 2: Main display of the initial original part of *NAF* programme.
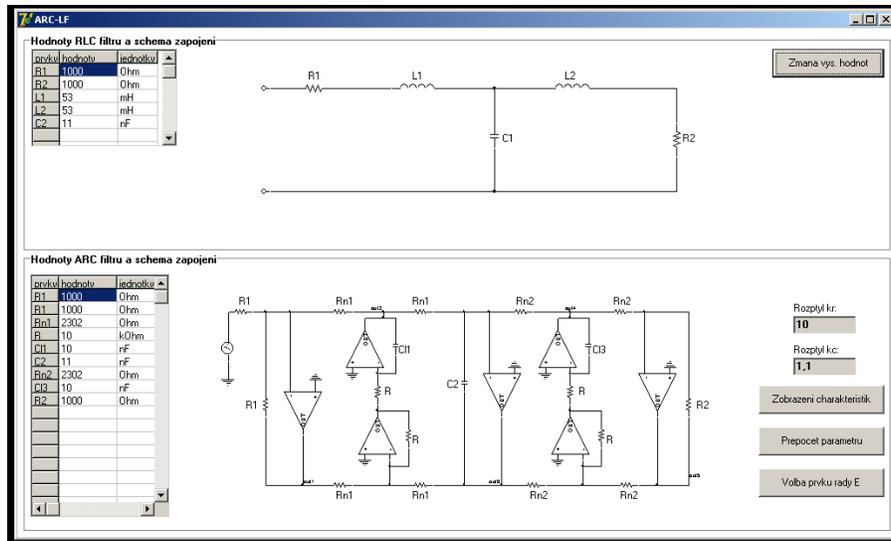


Figure 3: Illustration of the part of the programme *ARC_LF-LP* of 3rd order with the element *T*-unmodified values of the *RLC* circuit.
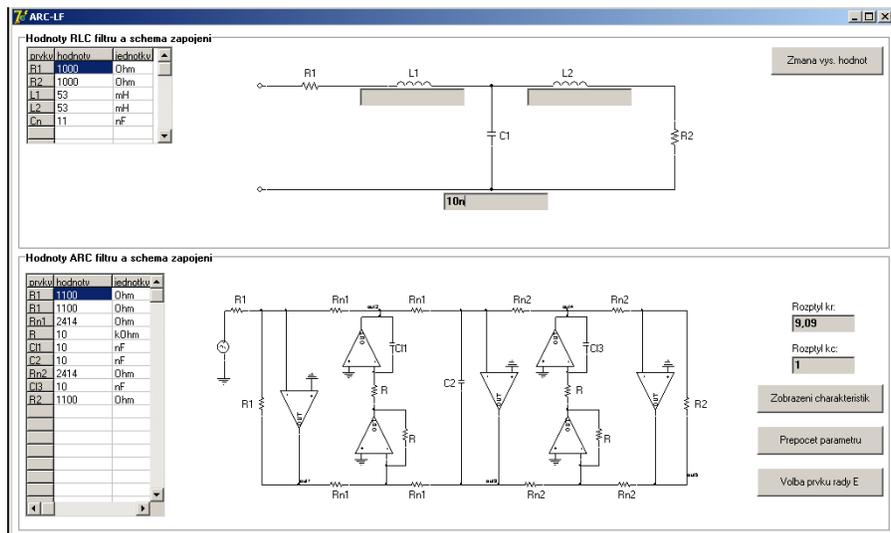


Figure 4: Illustration of output display of the programme *ARC_LF*.

## 3. CONCLUSIONS

In the article here is explained main idea, prescribed some parts and illustrated main parts from derived programme for the complete *ARC* filter synthesis using *Leap-Frog* method realization. The main goal for the creation of this programme was to contribute in area filter optimization and help to wider using of this method, which is difficult by manual design, but exhibit many advantages mainly for *LP* and *BP* filter types — as excellent dynamical ratios, practically the lowest sensitivities, small spread of filter element values and the possibility to design filter with required values of capacitors in practice.

## ACKNOWLEDGMENT

## REFERENCES

1. Sedláček, J. and K. HáJek, *Kmitočové Filtry*, 1. Vydání, 535, Technická Literatura, BEN, Praha, 2002, ISBN 80-7300-023-7.
2. Dimopoulos, H. G. and A. G. Constantinidis, "Linear transformation active filters," *IEEE Trans. CAS*, Vol. 25, No. 10, 845–852, 1978.
3. Ghausi, M. S. and K. R. Laker, *Modern Filter Design*, Practice Hall, New Persey, 1981.
4. Kapustin, V. I., *Aktivnye RC-filtry Vyskovo Porjadka*, Radio i Svjaz, Moskva, 1985.
5. Sedra, A. and K. Martin, "Design of signal-flow graph (SFG) aktive filters," *IEEE Trans. CAS*, Vol. 25, No. 4, 185–195, 1978.
6. Sedláček, J., *Optimalizace v Syntéze Filtrů RLC*, Habilitační Práce, VA Brno, 1994.
7. HÁJek, K., *Optimalizovaný Návrh Filtrů ARC s Vyuzitím Počítače*, Habilitační Práce, VA Brno, 1994.
8. Biolek, D., *Resíme Elektronické Obvody*, 1. Vydání, 520, Technická Literature, BEN, Praha, 2004, ISBN 80-7300-125-X.
9. Sedláček, J. and K. HáJek, "Nafid program as powerful tool in filter education area," *Proc. of International Conference, CBLIS'97*, PK 1–10, Leicester, 1997.

# Novel Compact Triple-bandpass Filter Using $\lambda/4$ Resonator Pairs with Common via Ground

**Fei Liang**[1], **Hongwen Gan**[2], **Zhiyong Wang**[2], **and Wenzhong Lu**[1]

[1]Department of Electronic Science and Technology
Huazhong University of Science and Technology, 1037 Luoyu Road, Wuhan 430074, China
[2]Base Station Supporting Products Division
Wuhan Hongxin Telecommunication Technologies Co., LTD, China

**Abstract**— A novel asymmetric dual quarter-wavelength ($\lambda/4$) microstrip resonator is proposed, which is composed of two different $\lambda/4$ resonators that share the same grounding via. One of the resonators takes the form of stepped-impedance resonator (SIR) which is designed to operate at 2.4 GHz and 5.2 GHz, the other resonator takes the form of uniform-impedance resonator (UIR) which operats at 3.6 GHz. In this study, the structure of asymmetric dual $\lambda/4$ resonator is utilized to design triple-bandpass filter (BPF). Compared with the triple-bandpass filter using $\lambda/2$ SIR microstrip resonator, the size of filter with this structure can be miniaturized obviously and the design procedure can also be simplified. To verify the presented concept, example of filter with a triple-band chebyshev response operating at 2.4 GHz, 3.6 GHz, and 5.2 GHz was designed and fabricated. The measured results are in good agreement with the full-wave simulation results.

## 1. INTRODUCTION

Wireless standards produce new consumer systems, such as Bluetooth, wireless local area networks (WLANs), and worldwide interoperability for microwave access (WiMAX). Multiband communication systems which operate at different communication standards simultaneously have the advantages of high stability, high reliability, and high integrity. The rapid developing of multiband communication systems enables a single filter to support dual- or tri-band operations [1].

Many design methodologies have been studied to realize filters with multi-passband responses. In [2, 3], dual and triple bandpass filters are designed by using SIRs. In [4–6], triple-bandpass filters are realized by using tri-section SIRs which can provide more design parameters in controlling the resonant frequencies. In [7], transmission zeros produced by cross-coupling are used to split one of the single band into two by adjusting the coupling matrix, the spurious modes of SIRs are used to realize the third passband. Recently most reported papers about triple-passband filters with microstrip structure mainly base on the half-wavelength ($\lambda/2$) resonator while there are very few papers utilizing quarter-wavelength ($\lambda/4$) resonator which possesses two principal advantages including shorter resonator length and higher spurious frequency that make it feasible in designing the high-performance BPFs.

In this letter, we propose a new tri-band BPF which can operate at 3.6 GHz WiMAX channel and 2.4/5.2 GHz WLAN bands with size miniaturization using asymmetric dual quarter wavelength resonator. An experimental example of filter with triple-band Chevbyshev response was designed and implemented with microstrip structure to verify the proposed concept.

## 2. THE BASE PROPERTY OF ASYMMETRIC DUAL QUARTER-WAVELENGTH RESONATOR

Figure 1 shows the physical structure of the proposed asymmetric dual $\lambda/4$ resonator. This resonator is basically composed of two different $\lambda/4$ resonators (A and B).

As is shown in Fig. 1, The $W$ represents the width of resonator A and B. $L_1$ and $L_2$ represent the length of resonator A and B respectively. The D is the diameter of via. When $L_1$ is not equal to $L_2$, the interference between the resonator A and B will not occur. Fig. 2 shows the fundament
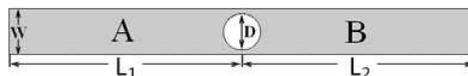


Figure 1: Layout of proposed asymmetric dual $\lambda/4$ microstrip resonator.

frequencies of resonator A and B varying with the value of $L_2$ while other variables keeping stable. In Fig. 2, $f_{A1}$, $f_B$, and $f_{A2}$ represent the fundamental frequencies of resonator A, resonator B and the first spurious frequency of resonator A respectively. It is obvious from Fig. 2 that with the increase of $L_2$, $f_{A1}$ and $f_{A2}$ almost keep unchangeable while $f_B$ gradually decreases. It is the property of this structure that makes it realize multi-passband filter feasible and easily.

In order to explain the most advantage of asymmetric dual $\lambda/4$ resonator, we define $f_0$, $f_1$, and $f_2$ as the fundament frequency, first spurious frequency, and second spurious frequency of the resonator respectively. As we know, the traditional $\lambda/2$ SIRs not only can control the spurious frequency but also reduce the size of resonator. However, this advantage of $\lambda/2$ SIRs is only on the condition that $f_1 > 2f_0$. If we make the $\lambda/2$ SIRs operating at the frequencies while $f_1 < 2f_0$, it will enlarge the size instead of reducing it. For the traditional $\lambda/4$ SIRs, it also have the same limitation while operating at frequencies that $f_1 < 3f_0$. So the two type resonators mentioned above are not suitable to operate the frequencies that $f_1 < 2f_0$, especially $f_1 \leqslant 1.5f_0$. However, to the asymmetric dual $\lambda/4$ resonator, it can overcome the disadvantages mentioned above while keeping compact size, lower impedance ratio and higher freedom of design. The frequencies $f_0$ and $f_1$ can be realized at random which are controlled by the length of $L_1$ and $L_2$ that shown in the Fig. 1. Take an example to illustrate the advantages of asymmetric dual $\lambda/4$ resonator. The frequencies of $f_1$ and $f_2$ are 2.4 GHz and 4.5 GHz respectively. All three structures of resonator mentioned above are utilized to operate at the proposed frequencies. Fig. 3 is shown the comparison of these different resonators where $\lambda_g$ is the guided wavelength at 2.4 GHz on the substrate. It is obvious that the asymmetric dual $\lambda/4$ resonator can overcome the disadvantages of other two resonators while keep compact size and higher design freedom.

For the purpose of operating at three frequencies simultaneously, there are two typical methods aiming to resolve it. One is adjusting the impedance ratio and the electronic length ratio of the two sections of traditional $\lambda/2$ SIRs properly [8]. However, the resonance frequencies of the SIRs
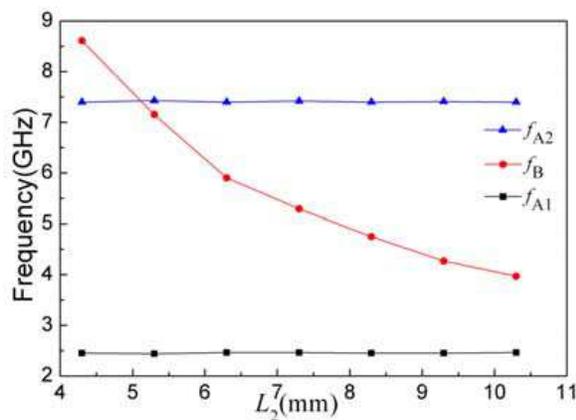


Figure 2: The frequencies of resonators A and B varying with $L_2$.
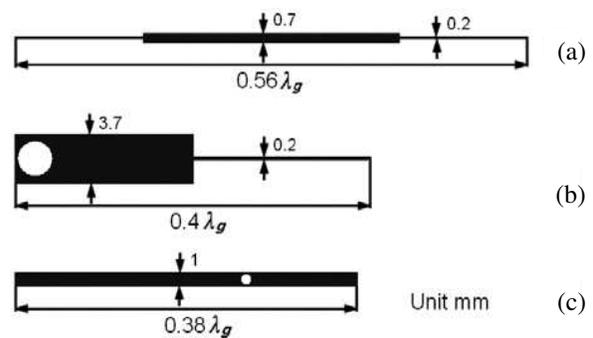
Figure 3: Comparison of three different resonators: (a) half-wavelength, (b) quarter-wavelength and (c) asymmetric $\lambda/4$ resonator.
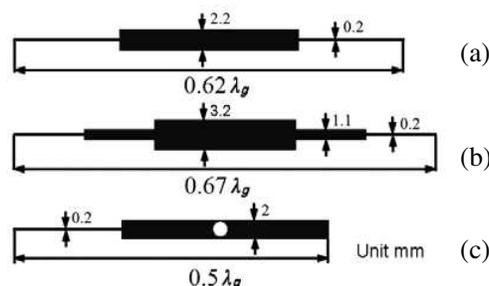


Figure 4: Comparison of the three different methods (a) method 1 [8], (b) method 2 [6] and (c) asymmetric dual $\lambda/4$ resonator.

are dependant, complicating the filter design. The other is using tri-section SIRs by properly determining the impedance ratio, but it is difficult to acquire different external quality factors and coupling coefficients to simultaneously satisfy the specifications of all passbands [6]. To asymmetric dual $\lambda/4$ SIRs, if only one of the dual resonators takes the form of SIR which is shown in Fig. 3(c), it can very easy obtain desired three frequencies. Take an example to illustrate the advantages of asymmetric dual $\lambda/4$ resonator in triple-band application. The desired frequencies of $f_0$, $f_1$, and $f_2$ are 2.4 GHz, 3.6 GHz, and 5.2 GHz respectively. All three structures of resonators mentioned above are utilized to operate at the proposed frequencies. Fig. 4 is shown the comparison of these different resonators. It is obvious that the asymmetric dual $\lambda/4$ resonator has the compact size and higher design freedom.

## 3. DESIGN OF A TRIPLE-PASSBAND CHEBYSHEV FILTER

To verify the feasibility of asymmetric dual $\lambda/4$ resonator realizing multi-band filter, a triple-bandpass filter with Chebyshev frequency response operating at 2.4 GHz, 3.6 GHz, and 5.2 GHz was designed and fabricated. The filter was fabricated on Rogers 3035 substrate with a relative dielectric constant of 3.5, a thickness of 0.762 mm, and a loss tangent of 0.002. Fig. 5 shows the circuit configuration of the filter.

As is shown in Fig. 5, the asymmetric dual $\lambda/4$ resonator is composed of the section $A_n$ and $B_n$ ($n = 1, 2$). The section $A_n$ take the form of SIR which operate at the center frequencies of the first passband ($f_1$) and the third passband ($f_3$) while the section $B_n$ operating at the center frequency of the second passband ($f_2$). Sections C, D and E operate at the center frequencies of the first ($f_1$), second ($f_2$) and third ($f_3$) passband respectively. The section C is composed of dual identical $\lambda/4$ resonators which operate at the same center frequency of the first passband aiming to avoid the interference of the first spurious frequency of $f_1$ to the third passband ($f_3$). The lumped circuit element values of the low-pass prototype filer for the first passband is found to be $g_0 = 1$, $g_1 = 1.1088$, $g_2 = 1.3061$, $g_3 = 1.7703$, $g_4 = 0.818$, $g_5 = 1.3354$, and for the second and the third passband are found to be $g_0 = 1$, $g_1 = 1.2275$, $g_2 = 1.1525$. The external quality factors $Q_e$ can then be found as $Q_{e1} = 17.9$ for the first passband, $Q_{e2} = 17.5$ for the second passband, and $Q_{e3} = 12.3$ for the third passband. Fig. 6 shows the external quality factors versus the length of $L_{11}$. After full wave simulation being carried out by HFSS, the main dimensions of the propose filter mentioned in Fig. 5 are as follow: $W_1 = 1.6$ mm, $W_2 = 1$ mm, $W_3 = 0.5$ mm, $d_1 = 0.4$ mm, $d_2 = 0.2$ mm, $d_3 = 1.4$ mm, $L_1 = 18.5$ mm, $L_2 = 4.3$ mm, $L_3 = 4$ mm, $L_4 = 12.3$ mm, $L_5 = 8$ mm, $L_6 = 22.8$ mm, $L_7 = 9$ mm, $L_8 = 3.3$ mm, $L_9 = 8.8$ mm, $L_{10} = L_{11} = 9$ mm. The diameter of via$_1$ and via$_2$ are 1.2 mm and 0.6 mm respectively.

Measurement was carried out using an Agilent E8362 analyzer. The measured and simulated results of the filter are illustrated in Fig. 7. The measured center frequencies of the three passband are 2.4, 3.6 and 5.2 GHz. The measured fractional bandwidths of triple-bands are $\text{FBW}_1 = 6.2\%$, $\text{FBW}_2 = 7\%$, and $\text{FBW}_3 = 10\%$ respectively, while the passband insertion losses are approximately
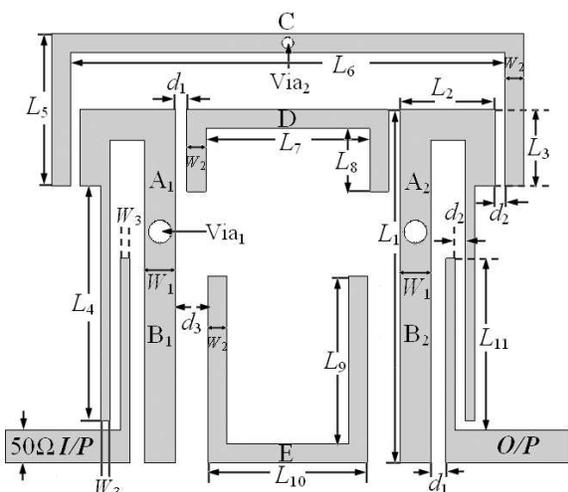


Figure 5: Schematic layout of the triple-band Chebyshev filter.
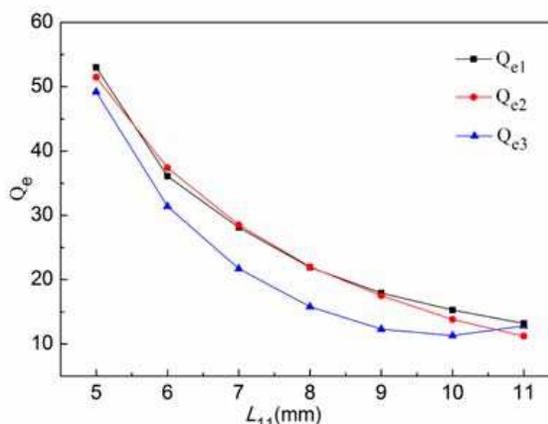
Figure 6: External quality factors versus the length of $L_{11}$.
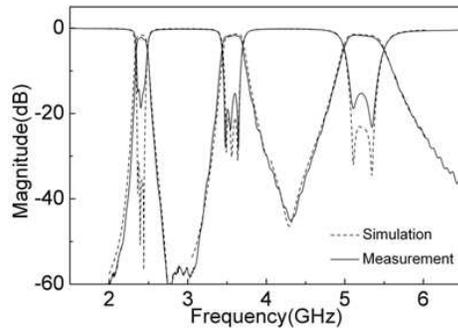
Figure 7: Simulated and measured results of triple-passband filter.
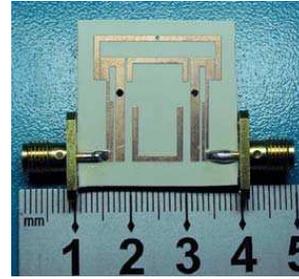


Figure 8: Photography of Fabricated filter.

Table 1: Comparison with other reported dual-band BPFs.

|  | Ref. Freq. of Band 1/2/3 | Order | Insertion Loss (dB) Band 1/2/3 | Equiv. Size mm$^2$ |
|---|---|---|---|---|
| [3] | 2.4/3.5/5.25 | 2 | 2.0/2.4/1.7 | 410 |
| [6] | 1.57/2.45/3.5 | 2 | 0.77/1.5/1.8 | 1450 |
| [7] | 3/4.2/4.55 | 4 | 2.9/2.4/3.0 | 880 |
| [8] | 2.3/3.7/5.3 | 3 | 2.5/1.9/2.9 | 1200 |
| This work | 2.4/3.6/5.2 | 3 | 2/1.4/1.5 | 650 |

2.4, 1.4 and 1.5 dB at the first, second and third passband. The insertion losses would be attributed mainly to the conductor and dielectric losses. The measured results are in good agreement with simulated predictions.

A comparison of the various published triple-band filters is shown in Table 1. The equivalent size of the filters is calculated after multiplying size by a factor $= \varepsilon_r/3.38$ in order to compare area miniaturization of the filters irrespective of dielectric constant of the substrate.

## 4. CONCLUSION

A novel filter structures using asymmetric dual $\lambda/4$ resonators have been proposed in this work. It not only achieve size miniaturization and via reduction but also realize the multi-passband characteristic at the same time by making use of the proposed resonators. Base on the basic Chebyshev filter, a triple-passband filter with asymmetric dual $\lambda/4$ resonators have been carefully designed and fabricated. Thanks for the use of this novel structure, the proposed filter features good multi-band characteristic and compact size. With these advantages, this type of filter will find plenty of applications in RF circuits.

## ACKNOWLEDGMENT

## REFERENCES

1. Chang, S. F. R., W. L. Chen, S. C. Chang, C. K. Tu, C. L. Wei, and C. H. Chien, "A dual-band RF transceiver for multi-standard WLAN applications," *IEEE Trans. Microw. Theory Tech.*, Vol. 53, No. 3, 1048–1055, Mar. 2005.

2. Zhang, Y. P. and M. Sun, "Dual-band microstrip bandpass filter using stepped-impedance resonators with new coupling schemes," *IEEE Trans. Microw. Theory Tech.*, Vol. 54, No. 10, 3779–3785, Oct. 2006.

3. Chen, F.-C. and Q.-X. Chu, "Design of compact tri-band bandpass filters using assembled resonators," *IEEE Trans. Microw. Theory Tech.*, Vol. 57, No. 1, 165–171, Jan. 2009.

4. Chen, Y. C., Y. H. Hsieh, C. H. Lee, and C. I. G. Hsu, "Tri-band microstrip BPF design using tri-section SIRs," *IEEE AP-S Symp.*, 3113–3116, Honolulu, HI, Jun. 2007.

5. Lin, X. M. and Q. X. Chu, "Design of triple-band bandpass filter using tri-section stepped-impedance resonators," *Proc. Int. Microw. Millimeter Wave Tech. Conf.*, 1–3, Guilin, China, Apr. 2007.

6. Hsu, C. I. G., C. H. Lee, and Y. H. Hsieh, "Tri-band bandpass filter with sharp passband skirts designed using tri-section SIRs," *IEEE Microw. Wireless Compon. Lett.*, Vol. 18, No. 1, 19–21, Jan. 2008.

7. Chen, B.-J., T.-M. Shen, and R.-B. Wu, "Design of tri-band filters with improved band allocation," *IEEE Trans. Microw. Theory Tech.*, Vol. 57, No. 7, 1790–1796, Jul. 2009.

8. Chen, C. F., T. Y. Huang, and R. B. Wu, "Design of dual- and triple-passband filters using alternately cascaded multiband resonators," *IEEE Trans. Microw. Theory Tech.*, Vol. 54, No. 9, 3550–3558, Sep. 2006.

# A New Tunable Dual-mode Bandpass Filter Design Based on Fractally Slotted Microstrip Patch Resonator

**Jawad K. Ali[1], Nasr N. Hussain[2], Ali J. Salim[1], and Hussam Alsaedi[1]**

[1]Department of Electrical and Electronic Engineering, University of Technology, Baghdad, Iraq
[2]Communication Engineering Department, Technical College of Najaf, Najaf, Iraq

**Abstract**— A dual-mode slotted microstrip patch resonator is introduced in this paper for use in wireless communication applications. The slot structure, etched inside the patch resonator, is in the form of the 2nd iteration Koch fractal curve; using the conventional square microstrip patch resonator as the initiator. Modeling and performance evaluation of the proposed filter design have been carried out using a method of moment based EM simulator, IE3D. Simulation results show that the resulting resonator filter has good transmission and return loss responses. The modeled resonator has been found to possess a side length of about 0.22 the guided wavelength, which represents a size reduction of about 81% as compared with that based on the conventional square microstrip patch without slot. In addition, slits have been symmetrically etched in the external edges of the patch structure, in an attempt to provide the resonator with tuning facility. Besides the tuning possibility, these slits have been found to offer further size reduction without worsening the resulting filter performance; providing the designer with more degrees of freedom.

## 1. INTRODUCTION

Among the earliest predictions of the use of fractals in the design and fabrication of filters is that of Yordanov et al. [1]. Their predictions are based on their investigation of Cantor fractal geometry. Since then, dramatic developments in wireless communication systems have presented new challenges to design and produce high-quality miniaturized components. These challenges stimulate microwave circuits and antennas designers to seek out for solutions by investigating different fractal geometries [2–6]. Hilbert fractal curve has been used as a defected ground structure in the design of a microstrip lowpass filter operating at the L-band microwave frequency [2]. Sierpinski fractal geometry has been used in the implementation of a complementary split ring resonator [3]. Split ring geometry using square Sierpinski fractal curves has been proposed to reduce the resonant frequency of the structure and achieve improved frequency selectivity in the resonator performance. Koch fractal shape is applied to mm-wave microstrip bandpass filters integrated on a high-resistivity Si substrate. Results showed that the 2nd harmonic of fractal shape filters can be suppressed as the fractal factor increases, while maintaining the physical size of the resulting filter design [4]. Based on Peano fractal geometry, a miniaturized multi-resonator bandpass filter with 2nd harmonic reduction has been reported in [7]. Minkowski type fractal geometry has been successfully used in producing high performance miniaturized dual-mode microstrip bandpass filters [8, 9].

In this paper, a new dual mode slot microstrip square patch resonator bandpass filter is presented. The slot has a square structure with its four edges have been modified by applying Koch pre-fractal curve to each of them. This produces successive miniaturized design structures for the dual-mode microstrip bandpass filters as compared with those based on the conventional square patch microstrip resonator. The resulting bandpass filters are supposed to have noticeably miniaturized sizes with adequate reflection and transmission responses. In addition, the proposed bandpass filter can be further miniaturized by inserting slits in the resonator outer structure. These slits have the role of tuning besides miniaturization.

## 2. THE PROPOSED FILTER CONFIGURAION

The proposed microstrip dual mode bandpass filer configuration consists of a square microstrip patch resonator. A square slot structure has been etched in the patch such that the patch and the slot are co-centered. The edges of the slot have been modified to be in the shape of Koch fractal geometry with different iteration levels. To demonstrate the fractal generation process of the slot structure, the first two iterations are shown in Figure 1. The starting pattern, Figure 1(a), is Euclidean since the slot has the initial square shape. The process of replacing the slot edges with the first and second iteration Koch pre-fractal geometries are shown in Figures 1(b) and 1(c) respectively. The resulting pre-fractal structure has the characteristic that the perimeter increases to infinity while maintaining the volume occupied.
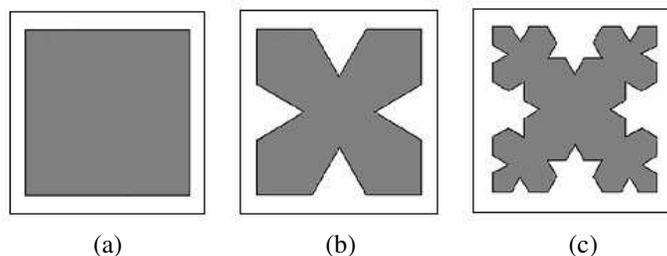
Figure 1: The proposed microstrip resonator structure with the inner slot has (a) a square shape, (b) and (c) Koch fractal shaped edges of the first and second iterations respectively.
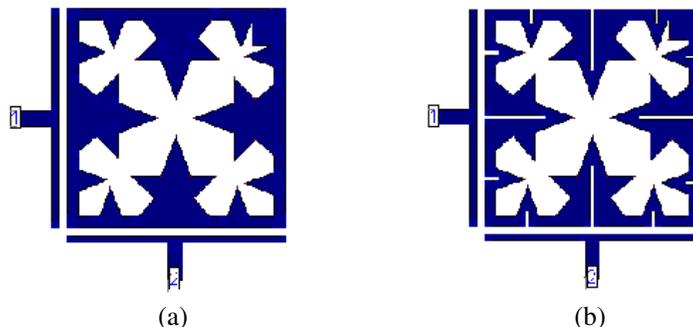


Figure 2: The modeled microstrip patch resonator bandpass filer structure with the inner slot has Koch fractal shaped edges (a) without tuning slits, and (b) with tuning slits.

This increase in length decreases the required volume occupied for the pre-fractal bandpass filter at resonance. It has been found that:

$$P_n = \left(\frac{4}{3}\right)^n P_{n-1} \tag{1}$$

where $P_n$ is the perimeter of the $n$th iteration pre-fractal structure. Theoretically, as $n$ goes to infinity the perimeter goes to infinity. The ability of the resulting structure to increase its perimeter in the successive iterations was found very triggering for examining its size reduction capability as a microstrip bandpass filter.

In practice, shape modification of the resulting structures in Figures 1(b) and 1(c) is a way to increase the surface current path length compared with that of the conventional square patch resonator; resulting in a reduced resonant frequency or a reduced resonator size, if the design frequency is to be maintained. It is expected then, that higher iterations will exhibit further miniaturization ability owing to its extra space filling property. Theoretically the size reduction process goes on further as the iteration steps increase. An additional property that the presented scheme possesses is the symmetry of the whole structure in each of the iteration levels about its diagonal. This property is of special importance in the design of dual-mode resonators [10, 11]. The length of the conventional microstrip dual-mode square microstrip patch resonator has been determined using the classical design equations reported in the literature [10] for a specified operating frequency and given substrate properties. This length is slightly less than half the quarter guided wavelength at its fundamental resonant frequency in the resonator.

## 3. THE PROPOSED FILER DESIGN

A dual-mode microstrip patch bandpass filter with the patch has the slot structure corresponding to the 2nd iteration Koch pre-fractal geometry, Figure 1(c), has been designed for the ISM band applications at 2.4 GHz. The modeled filer is shown in Figure 2(a). The filter structure has been supposed to be etched using a substrate with a relative dielectric constant of 10.8 and thickness of 1.27 mm. The input/output ports have a 50 Ω characteristic impedance.

A small perturbation has been applied to each dual-mode resonator at a location that is assumed at a 45° offset from its two orthogonal modes. The dimensions of the perturbation of the modeled
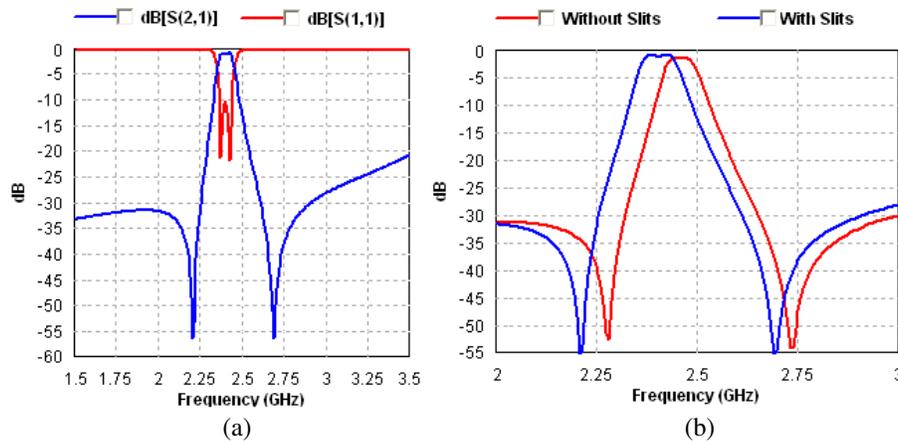
Figure 3: The return loss and transmission responses of; (a) the filter depicted in Figures 1(a) and (b) both filters depicted in Figure 1, with and without tuning slits.

filter must be tuned for the required filter performance, since the nature and the strength of the coupling between the two degenerate modes of the dual-mode resonator are mainly determined by the perturbation's size and shape. However, extensive details about this subject can be found in [12, 13]. A second filter, similar to that depicted in Figure 1(a), has been also modeled with slits inserted in the outer edges of the resonator as shown in Figure 2(b).

## 4. PERFORMANCE EVALUATION

Filter structures, depicted in Figures 2(a) and 2(b), have been modeled and analyzed at the design frequency, using the commercially available EM simulator, IE3D [14]. This simulator performs electromagnetic analysis using the method of moments (MoM). The resonator side length is equal to 10.18 mm, which represents about 0.22 the guided wavelength. On another word, this represents a size reduction of about 81% as compared with the conventional square patch resonator. The corresponding simulation results of return loss and transmission responses of these filters are shown in Figure 3. It is implied that the resulting pre-fractal based resonator bandpass filters offer adequate performance curves. As can be seen, the filter responses show two transmission zeros symmetrically located around the deign frequency. However, these responses and their consequent poles and zeros could be, to a certain extent, controlled through the variation of the perturbation dimensions and/or the input/output coupling used. As shown in Figure 3(b), the inserted slits can be used to gain further miniaturization or to provide provides the designer with a practically useful means to tune the resulting filter response to the specified design frequency.

## 5. CONCLUSION

A Koch fractal based slotted patch resonator filter design has been presented in this paper, as a new technique for miniaturization of microstrip bandpass filter based on the dual-mode square patch resonator. The presented filter patch resonator has a square slot, with its edges in the form of 2nd iteration Koch pre-fractal geometry, is designed and its performance has been analyzed using the method of moments (MoM) at the ISM band. Simulation results show that this filter possesses reasonable return loss and transmission performance responses and offers size reduction of about 81% as compared with the conventional microstrip square patch bandpass filter. The filter with slits provides a tuning feature or can be used for further miniaturization. As the practical fabrication tolerances may permit, it is expected that the higher iterations based filter structures will offer further size reductions. The proposed technique can be generalized, as a flexible design tool, for compact microstrip bandpass filters for a wide variety of wireless communication systems.

## REFERENCES

1. Yordanov, O. I., I. Angelov, V. V. Konotop, and I. V. Yurkevich, "Prospects of fractal filters and reflectors," *Proceedings of IEE Seventh International Conference on Antenna and Propagation, ISCAP91*, York, UK, 1991.
2. Chen, J., Z. B. Weng, Y. C. Jiao, and F. S. Zhang, "Lowpass filter design of hilbert curve ring defected ground structure," *Progress In Electromagnetics Research*, Vol. 70, 269–280, 2007.

3. Crnojevic-Bengin, V., V. Radonic, and B. Jokanovic, "Complementary split ring resonators using square sierpinski fractal curves," *Proceedings of the 36th European Microwave Conference*, Manchester, UK, 2006.

4. Kim, I. K., N. Kingsley, M. A. Morton, S. Pinel, J. Papapolymerou, M. M. Tentzeris, J. Laskar, and J. G. Yook, "Koch fractal shape microstrip bandpass filters on high resistivity silicon for the suppression of the 2nd harmonic," *Jour. Kor. Electromag. Engin. Soc.*, Vol. 6, No. 4, 1–10, 2006.

5. Xiao, J. K., Q. X. Chu, and S. Zhang, "Novel microstrip triangular resonator bandpass filter with transmission zeros and wide bands using fractal-shaped defection," *Progress In Electromagnetics Research*, Vol. 77, 343–356, 2007.

6. Wu, G. L., W. Mu, X. W. Dai, and Y. C. Jiao, "Design of novel dual-band bandpass filter with microstrip meander-loop resonator and CSRR DGS," *Progress In Electromagnetics Research*, Vol. 78, 17–24, 2008.

7. Ali, J. K. and Y. S. Miz'el, "A new miniature fractal-based bandpass filter design with 2ne harmonic suppression," *Proceedings 3rd IEEE International Symposium on Microwave, Antenna, Propagation and EMC Technologies for Wireless Communication*, Beijing, China, Oct. 2009.

8. Ali, J. K., "A new miniaturized fractal bandpass filter based on dual-mode microstrip square ring resonator," *Proceedings of the 5th International Multi-conference on Signals, Systems and Devices, IEEE SSD'08,* Amman, Jordan, Jul. 2008.

9. Ali, J. K. and N. N. Hussain, "An extra reduced size dual-mode bandpass filter for wireless communication systems," *PIERS Proceedings*, 1467–1470, Suzhou, China, Sep. 12–16, 2011.

10. Hong, J. S. and M. J. Lancaster, *Microstrip Filters for RF/Microwave Applications*, John Wiley and Sons Inc., New York, 2001.

11. Chang, K. and L. H. Hsieh, *Microwave Ring Circuits and Related Structures*, 2nd Edition, John Wiley and Sons Ltd., New Jersey, 2004.

12. Görür, A., "Description of coupling between degenerate modes of a dual-mode microstrip loop resonator using a novel perturbation arrangement and its dual-mode bandpass filter applications," *IEEE Trans. Microwave Theory Tech.*, Vol. 52, No. 2, 671–677, 2004.

13. Amari, S., "Comments on description of coupling between degenerate modes of a dual-mode microstrip loop resonator using a novel perturbation arrangement and its dual-mode bandpass filter applications," *IEEE Trans. Microwave Theory Tech.,* Vol. 52, No. 9, 2190–2192, 2004.

14. IE3D User's Manual, Release 12.3, Zeland Software, Inc., Fremont, CA, 2007.

# The Design of Wideband DC-35 GHz IF Modules for 78–113 GHz Receiver Array

**Hsiao-Feng Teng[1], Jing-Cheng Wu[1], Tzi-Hong Chiueh[1], and Robert Hu[2]**

[1]National Taiwan University, Taipei 100, Taiwan, R.O.C.
[2]National Chiao Tung University, Hsinchu 300, Taiwan, R.O.C.

**Abstract**— To facilitate simultaneous detection of the 78–113 GHz millimeter-wave electromagnetic spectra, compact DC-35 GHz IF modules have been designed where the down-converted signals will be divided and further transformed into four 8.7 GHz bands, thus suitable for fiber-optics signal transfer and digital-signal processing. This paper will detail the design methodology and related microwave circuits that constitute the wideband modules; measured results will also be presented. In additional to the intended radio-astronomical instrumentation, this work can be used in applications such as geographical remote sensing and human biological sensors.

## 1. INTRODUCTION

For the efficient exploration and exploitation of the anisotropy of cosmic microwave background radiation in the millimeter-wave frequency range, the radio-astronomical receiver's intermediate frequency (IF) is preferred to be very wideband [1]. In the proposed receiver, as shown in Fig. 1, the incoming signal will be sent to the cryogenic W-band InP low noise amplifier and, through the waveguide, to the room-temperature mixer [2]. The resulting DC-34.8 GHz IF is then fed into the room-temperature wideband modules. Four separate bands can now be extracted by the use of amplifiers, filters, and another three mixers whose local oscillator (LO) frequencies are fixed at 17.4 GHz, 17.4 GHz and 26.1 GHz, respectively. The reason for not choosing 8.7 GHz for down-converting the second band is because this LO frequency is bordering the final DC-8.7 GHz band, thus any residual 8.7 GHz LO at the output of the mixer will be hard to remove; by contrast, the 17.4 GHz LO is far from the DC-8.7 GHz band and can be easily suppressed if necessary. In the following session, detailed description will be provided for the complete DC-34.8 GHz system, which also includes the LO module and the optical-transfer circuits.

## 2. DC-34 GHz WIDEBAND MODULE DESIGN

To retain compact and flexible, the core IF circuits are split into three modules. As shown in Fig. 2, the first module begins with a traveling-wave amplifier Agilent-AMMC5024, and then a multi-section 3 dB Wilkinson power divider, which has its output ports connected to the same type of amplifiers. The second module starts with a 3 dB power divider, followed by the amplifiers Hittite-HMC462. The DC-8.7 GHz band signals can now be extracted by a low-pass filter; the 8.7–17.4 GHz band is obtained using a band-pass filter, a mixer Marki-M1R0920, and then a low-pass filter. The reason why there are two identical amplifiers at the output of the power divider in IF module 2, rather than the more straightforward arrangement of one amplifier followed by the power divider, is to eliminate the rippled response due to the finite output-port isolation of the passive power divider itself. In the one-amplifier arrangement, for example, the reflected DC-8.7 GHz signal by the band-pass filter on the second band will re-emerge on the other branch and cause a rippled response there. Likewise, the 8.7–17.4 GHz signal reflected by the low-pass filter on the first band can re-appear on the second band. The IF module 3 has its power divider followed by two identical amplifiers Eudyna-FMM5709X. The mixers used in the third and fourth bands are Hittite HMC292 and HMC329. Fig. 3 shows the measured results.

Now the four DC-8.7 GHz IF bands can be further amplified by Sirenza-SNA176 and then sent to the optical transmitter Oepic-LF1030-LCF11 for long-distance signal transfer, as shown in Fig. 4. In our design, the antenna array has 6 dishes; with dual polarization for each dish, there will be a total of 6 (dish) times 2 (polarization) times 4 (bands), i.e., 48 optical fibers needed at least. Obviously, the use of either waveguides or coaxial cables for data transfer is not economical. Since the accumulated gain versus frequency up to this point reveals a discernible negative slope, a gain equalizer is added where the series LC is resonating at 8.7 GHz and the quarter-wavelength transmission lines corresponds to that of 8.7 GHz. At low frequency, this equalizer resembles a Π-shape resistive attenuator made of R1 and R2 only; at 8.7 GHz, the two ports of the equalizer
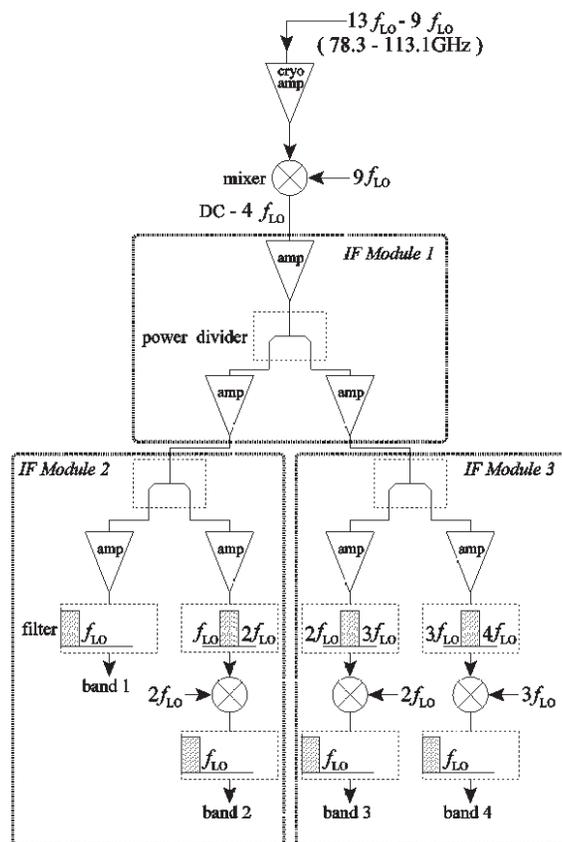
Figure 1: Schematic of the front-end circuits used in the wideband radio-astronomical receiver. With $f_{LO} = 8.7$ GHz, the incoming 78.3–113.1 GHz signals will be amplified and down-converted into DC-34.8 GHz, which will be further divided into four bands.
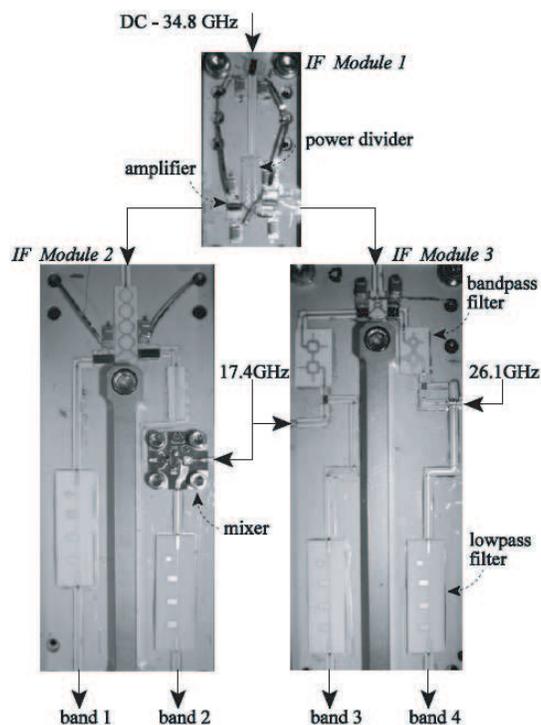


Figure 2: Photograph of IF modules 1, 2, and 3 used in the wideband system. Bands 1–4 are of each DC-8.7 GHz. The LO signals come from the LO module.
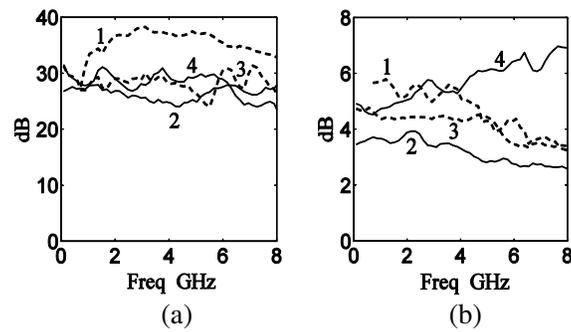
Figure 3: Measured results of the four IF bands. (a) Curves 1–4 are the gain for bands 1–4. (b) The corresponding noise figures.
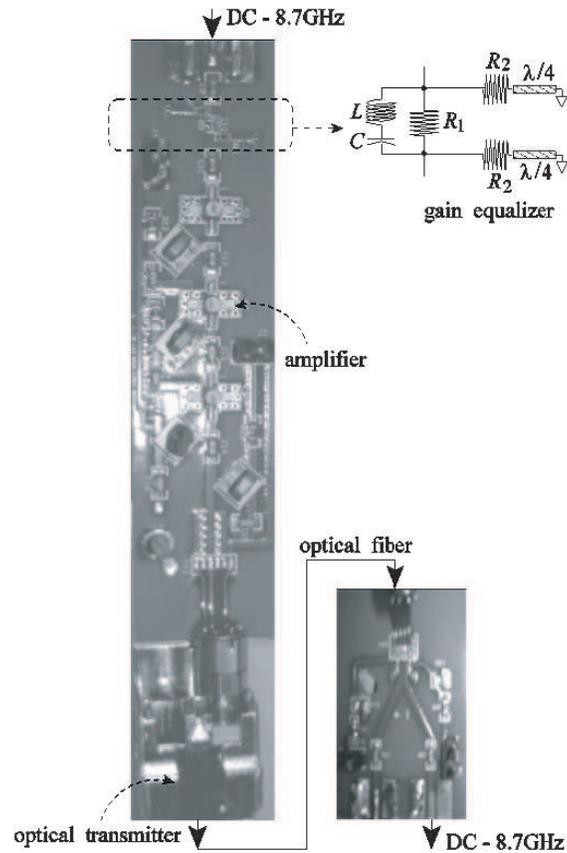


Figure 4: Photograph of the optical circuits for IF signal transfer. The quarter wavelength corresponds to that of 8.7 GHz.

are joining together and thus low-loss is expected. Proper choice of the constituting components ensures simultaneous low input reflection coefficient and positive gain slope [3]. The measured results of the optical modules are shown in Fig. 5.

Figures 6 and 7 show the schematic and photograph of the LO circuit where the 8.7 GHz LO comes from a YIG oscillator. The input power divider is followed by variable attenuators TriQuint-TGL4203 and amplifiers Hittite-HMC441. To obtain multiple 17.4 GHz output signals, the frequency doubler TriQuint-TGC1430F, medium power amplifier TriQuint-TGA9088A, and Lange couplers TriQuint-TGB2001 are employed. On the second branch of the LO module, the 26.1 GHz LO signal coming out of the frequency tripler TriQuint-TGC1430G will be sent into a medium-power amplifier TriQuint-TGA1073G and then a narrow-band coupled-line filter to ensure a clear spectral line. Multiple 26.1 GHz LO signals are made possible by the use of Lange couplers TriQuint-TGB4001. The Walsh function modulated 26.1 GHz by Hittite-HMC524 mixer will be sent to an external tripler to generate the intended 78.3 GHz LO for the front-end W-band mixer [4]. The LO signals provided by this module will now be able to support two receivers, as one for parallel polarization and one for perpendicular polarization.

(a)          (b)
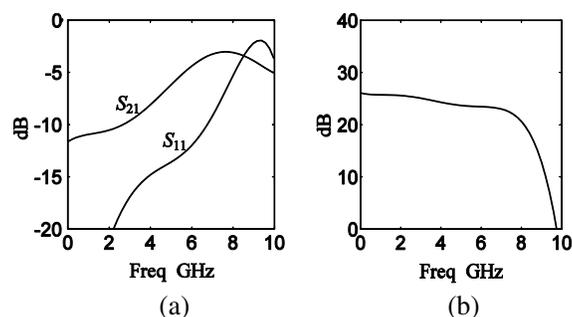
Figure 5: Measured results of the optical modules. (a) Gain and input reflection coefficient of the gain equalizer. (b) Overall gain.
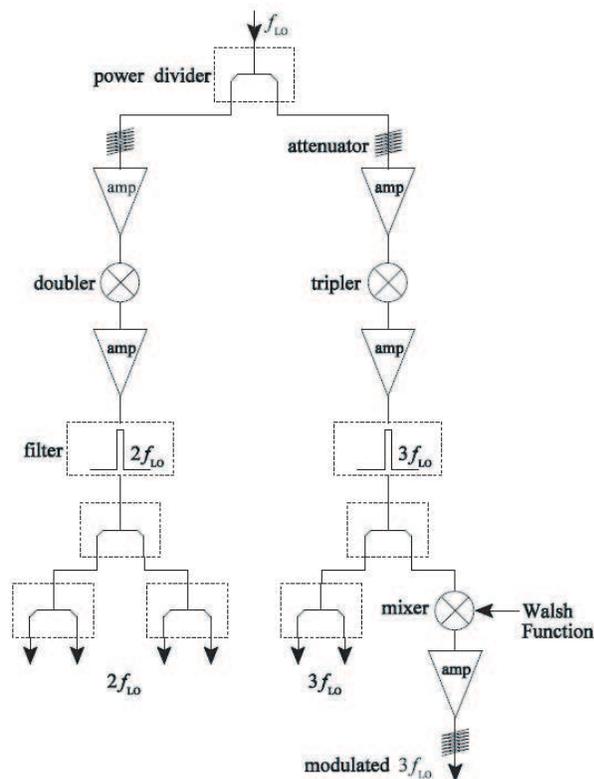


Figure 6: Schematic of the LO module with $f_{LO} = 8.7$ GHz. The modulated $3f_{LO}$ will be multiplied again by another tripler for driving the front-end W-band mixer.
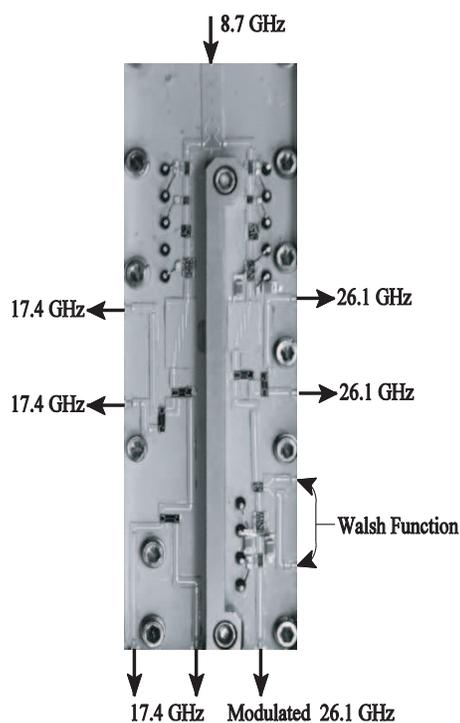


Figure 7: Photograph of the LO module. Both in-phase and quadrature Walsh functions are needed for modulating one 26.1 GHz LO signal.

## 3. CONCLUSION

Compact DC-35 GHz wideband modules for the 78–113 GHz radio-astronomical receiver have been successfully designed and built, therefore allows simultaneous detection of wideband microwave signals in a receiver array.

**REFERENCES**

1. Thompson, A. R., J. M. Moran, and G. W. Swenson, *Interferometry and Synthesis in Radio Astronomy*, 2nd Edition, Wiley, 2001.
2. Erickson, N. R., R. M. Grosslein, R. B. Erickson, and S. Weinreb, "A cryogenic focal plane array for 85.115 GHz using MMIC preamplifiers," *IEEE Trans. Microwave Theory Techniques*, Vol. 47, No. 12, 2212–2219. Dec. 1999.
3. Mellor, D. J., "On the design of matched equalizers of prescribed gain versus frequency pro-files," *MTT-S International Microwave Symposium Digest*, Vol. 77, 308–311, Jun. 1977.
4. Granlund, J., A. R. Thompson, and B. G. Clark, "An application of Walsh functions in radio astronomy instrumentation," *IEEE Trans. Electromagnetic Compatibility*, Vol. EMC-20, No. 3, 451–453, Aug. 1978.

# A New High-Q Resonator Using Combination of D-SR and S-SRR with $\mu$-near Zero Metamaterial

**H. Lee[1], K. C. Yoon[2], D. K. Lee[1], T. S. Jung[1], and J.-C. Lee[1]**

[1]Department of Wireless Communications Engineering, Kwangwoon University, South Korea
[2]Energy-Display R&D Center, Korea Electronics Technology Institute, South Korea

**Abstract**— In this paper, a new high-$Q_L$ resonator using a combination of double spiral resonator (D-SR) and single split ring resonator (S-SRR) with $\mu$-near zero metamaterial is suggested. S-SRR is applied to a resonator to get high-$Q_L$ performance and D-SR is used to obtain $\mu$-near zero characteristic for size reduction. The resonator is designed to operate at 9.2 GHz and the experimental result shows the $Q$-factor value of 140.

## 1. INTRODUCTION

The metamaterials have opened the door to novel design methods for miniaturization and compatibility with planar circuit technology [1]. For example, metamaterials such as ENZ (Epsilon-Near-Zero), MNZ (Mu-Near-Zero), and CRLH (Composite Right/Left Handed) metamaterials have been proposed [2–4]. One interesting application of these structures is the superior frequency selection characteristic in the microwave circuits. Traditional methods for these resonators using half-wavelength short-circuit stubs have some drawbacks which are large size and degrading device performance [5]. The SRR (Split Ring Resonator) and SR (Spiral Resonator) with MNZ method in metamaterials technique have been used in designing sundry devices requiring the compact-size or adjustable size and high quality performance [5–7]. Because of the sharp band-rejection characteristic, the SR and SRR are appropriate for the narrow BPF or band-stop filter (BSF) and other circuits necessitating a high-$Q_L$. The single-SRR and SR which has its theoretical basis in Veselago's work about metamaterial in late 1960's, has engendered great research interests in recent years [1]. After Pendry's pioneering experimental work on the SRR or SR of MNZ metamaterial in 1992 [8], a great deal of research have been reported in the literature, taking advantage of the compact size and high-$Q_L$ of the proposed SRR and SR.

The resonator suggested in this paper has combination of D-SRR and S-SRR where high-$Q_L$ characteristic can be obtained due to strong coupling effect between multiple rings (spiral and split) structures. In addition, because of the geometric characteristics, the size of resonator can be adjusted without variation of the resonant frequency.

## 2. A NEW HIGH-$Q_L$ RESONATOR WITH MNZ METAMATERIAL

The proposed resonator is composed of a dense array of two SRs (D-SR) and the single-SRR surrounding a D-SR as shown in Fig. 1(a). The symbol (mm) of $a(0.39)$, $b(0.91)$, $d(0.58)$, $e(1.1)$, $i(0.65)$, and $h(1.41)$ is a length of the SRs and the $c(1.53)$, $f(1.72)$, $l(3.6)$, and $m(1.15)$ is a length
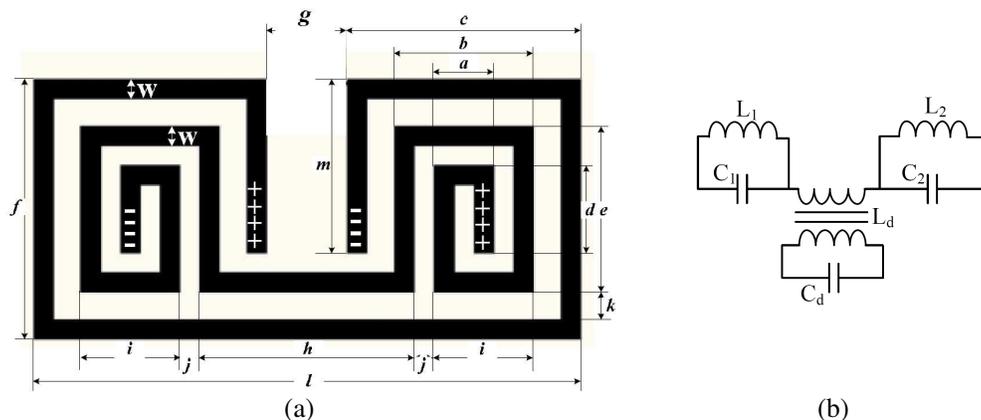


Figure 1: The proposed resonator with MNZ metamaterial (a) structure, (b) equivalent circuit.
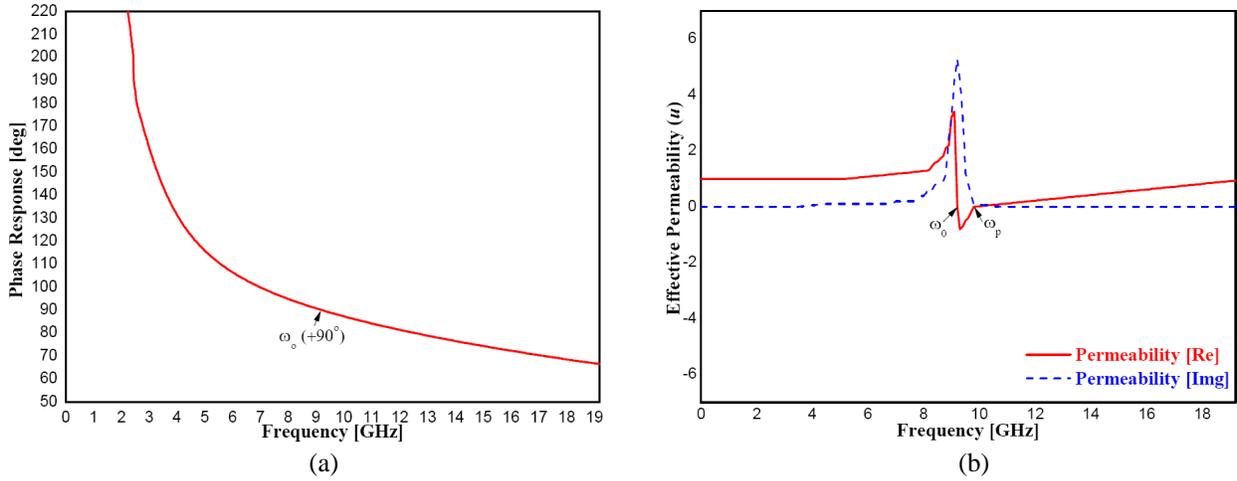
Figure 2: Simulation results for zero-value of permeability in the resonator (a) phase response, (b) zero-value permeability.
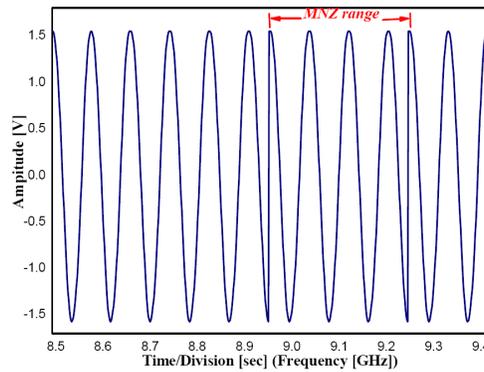


Figure 3: Simulation of signal-wave form with negative refraction index for the proposed resonator using MNZ metamaterials.

of the single-SRR. Also, the $k(0.18)$ is a coupling gap between SRs and SRR. Fig. 1(b) shows the equivalent circuit of the proposed resonator. $L_1$ and $L_2$ are total inductances corresponding to the length of each resonator, respectively and $C_1$ and $C_2$ are capacitances corresponding to the left and right coupling gaps $j(0.13)$ between two lines which belong to SR's line, respectively. Also, the $L_d$ is inductance corresponding to the magnetic coupling between SRR and SR, and the $C_d$ is capacitance corresponding to the $g$ of SRR. Total inductance $L_i(L_1//L_2)$ and capacitance $C_i(C_1//C_2)$ determine the resonant frequency $(\omega_0)$ at the equivalent circuit of the proposed resonator. The resonant frequency $(\omega_0)$ of the resonator is given by (1) [9],

$$\omega_0 = \sqrt{\frac{2}{\pi r_0 L_t C_t}} \tag{1}$$

where $r_0$ is the average radius of a SRR. When a wave propagates through a resonator in artificial media, its magnetic field induces current in the spiral-rings, creating the magnetic response [1]. The effective permeability, $\mu_{eff}$ is calculated by the following expression [1] given by (2),

$$\mu_{eff}(\omega) = 1 - \frac{F\omega_0^2}{\omega_0^2 - \omega_p^2 + j\omega\zeta} = 1 - \frac{F\omega_0^2(\omega_0^2 - \omega_p^2)}{(\omega_0^2 - \omega_p^2) + (\omega_0\zeta)^2} + j\frac{F\omega_0^2\zeta}{(\omega_0^2 - \omega_p^2) + (\omega_0\zeta)^2}$$

$$\omega_p = c\sqrt{\frac{3p}{\pi \ln(2wa^3/\delta)}} \tag{2}$$

where $\omega_p$ is called as the magnetic plasma frequency [1]. In the Equation (2), $F = \pi(a/p)^2$, $a$ is the inner radius of the smaller ring, $w$ is the width of the rings, $\delta$ is the radial spacing between
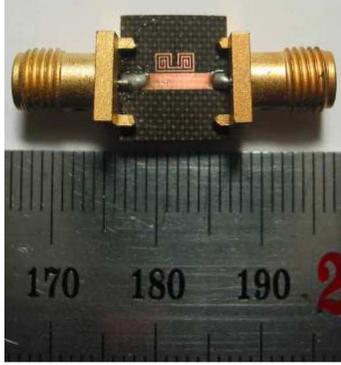
Figure 4: A photograph of the new resonator with MNZ metamaterial.
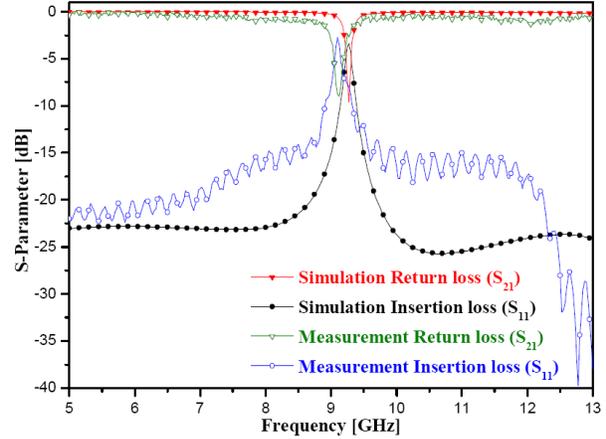
Figure 5: Simulation and measurement results for the new resonator with MNZ metamaterial.

Table 1: Change of the resonant frequency by variation of $g$.

| $g$ [mm] | $\omega_0$ [MHz] | $\Delta\omega$ [MHz] |
|---|---|---|
| 0.03 | 8546 | – |
| 0.13 | 9032 | +486 |
| 0.23 | 9203 | +171 |
| 0.33 | 9267 | +64 |
| 0.43 | 9284 | +17 |

the rings, $p$ is the average cell size of rings, $c$ is the speed of light, and $\zeta = 2pR'/a\mu_o$. Here, $R'$ is metal resistance per unit length [1]. Therefore, the negative value of the effective permeability in the vicinity of resonance inhibits signal propagation. Also, the proposed resonator of the MNZ metamaterial exhibits positive phase response of $+90°$ while the general resonator with double positive (DPS) material has negative phase response of $-90°$ [8].

## 3. EXPERIMENTAL RESULTS OF THE NOVEL HIGH-$Q_L$ RESONATOR

The experimental results for the positive phase response $(+90°)$ of the resonant frequency in the proposed resonator is shown in Fig. 2(a) and Fig. 2(b) shows the simulation results for the real and imaginary parts of the negative permeability at the proposed resonator in MNZ metamaterial. From the figure, the $\omega_p$ is called the magnetic plasma frequency. Here, the magnetic plasma frequency indicates the point of the permeability from negative value to zero. Thus, the frequency range of $(\omega_p - \omega_0)$ is zero-value of permeability region [8]. This means that it has the negative refraction phenomenon because the permeability of frequency domain becomes zero. Then, the frequency range is called zero-order-resonant (ZOR) or MNZ [3]. Since the distance between $\omega_0$ and $\omega_p$ can be decided with the size of the inner spiral rings and outer split ring, the size of the spiral rings and split ring can be used to control the effective permeability to be zero-value. It is important because zero-value permeability can adjust the direction of wave-propagation. Fig. 3 shows the simulation results for the signal-wave form of the proposed resonator in MNZ metamaterial.

The photograph of the proposed resonator which is fabricated on the Teflon substrate ($\varepsilon_r = 2.54$) with copper thickness of $0.18\,\mu m$, and the dielectric height of $0.54\,mm$ is shown in Fig. 4. The size of the resonator is $3.59 \times 1.72\,mm^2$.

Figure 5 shows the simulation and measurement results for the proposed resonator. From the figure, the simulated $Q_L$ of 193 and the measured $Q_L$ of 140 is obtained at the center frequency. In this work, the simulation has been carried out by ADS 2009A and IE3D. The measurement has been carried out by HP-8510 C vector network analyzer (VNA).

The $Q_L$ corresponds to the $3\,dB$ bandwidth of $S_{21}$ [5]. In this work, we confirmed that the optimized coupling gap between rings (spiral and split) has very strong magnetic coupling which leads to high-$Q_L$. The simulation was performed for the optimization of a coupling gap, $g$ in

Fig. 1(a). In general, according to transmission-line theory a resonant frequency down shifts as the size of a resonator increases. However, in case of the proposed resonator with MNZ metamaterial it shows opposite phenomenon compared to transmission-line theory. The resonant frequency moves to higher value as the size of the resonator increases at least in the short variation range of $g$ which is from $0.03\,mm$ to $0.43\,mm$. Table 1 shows the simulation results for variation of the resonant frequency as a function of $g$. It is presented that the resonant frequency is changed by variation of $g$ every increase in value of $0.1\,mm$.

## 4. CONCLUSION

In this paper, a new high-$Q_L$ resonator using combination of double spiral and single split ring resonator with $\mu$-near zero (MNZ) metamaterial has been designed. The proposed resonator provides sharp band-rejection characteristic because of strong coupling effect which leads to high quality factor between spiral and split structure. Also, the proposed resonator has positive phase response due to zero-value permeability, which means that it has MNZ metamaterial structure. The experimental result shows the $Q_L$ value of 140 at the resonant frequency of $9.17\,GHz$. It can be fabricated with MEMS (Micro-electro mechanical systems), NEMS (Nano-electro mechanical systems) and HMIC (Hybrid Microwave Integrated Circuits) or MMIC technique due to its entirely planar structure.

## ACKNOWLEDGMENT

**REFERENCES**

1. Solymar, L. and E. Shamonina, *Waves in Metamaterials*, Oxford University, 2009.
2. Smith, D. R., W. J. Padilla, D. C. Vier, S. C. Nemat-Nasser, and S. Schultz, "Composite medium with simultaneously negative permeability and permittivity," *Phys. Rev. Lett.*, Vol. 84, 4184–4187, May 2000.
3. Radisic, V., Y. Qian, R. Coccioli, and T. Itoh, "Novel 2-D photonic bandgap structure for microstrip lines," *IEEE Microwave Guided Wave Lett.*, Vol. 8, 69–71, Feb. 1998.
4. Radisic, V., Y. Qian, and T. Itoh, "Broad-band power amplifier using dielectric photonic bandgap structures," *IEEE Microwave Guided Wave Lett.*, Vol. 8, No. 1, 13–15, Jan. 1998.
5. Yoon, K. C., B. K. Jeon, D. K. Lee, and J. C Lee, "I-band high quality factor new split-ring resonator with broad-side coupling using the left-handed meta-material technique," *Proc. Asia-Pacific Microwave Conf.*, 1126–1129, Dec. 2010.
6. Pendry, J. B., A. J. Holden, D. J. Robbins, and W. J. Stewart, "Magnetism from conductors and enhanced nonlinear phenomena," *IEEE Trans. Microwave Theory Tech.*, Vol. 47, No. 11, 2075–2084, Nov. 1999.
7. Lee, H. J., H. S. Lee, K. H. Yoo, and J. G. Yook, "On the possibility of biosensors based on split ring resonators," *Proc. 38th European Microwave Conf.*, 1222–1225, Oct. 2008.
8. Cui, T. J., D. R. Smith, and R. Liu, *Metamaterials Theory, Design, and Applications*, Springer, 2009.
9. Marqués, R., F. Mesa, J. Martel, and F. Medina, "Comparative analysis of edge and broadside coupled split ring resonators for metamaterial design theory and experiments," *IEEE Trans. Antennas Propag.*, Vol. 51, No. 10, 2572–2581, Oct. 2003.

# A Differential-mode Wideband Band-pass Filter for UWB Application

**M. Li**, **F. Zhang**, **Kyosoon Choi**, **Jaeyeong Lee**, and **J. C. Lee**

Department of Wireless Communications Engineering, Kwangwoon University
447-1 Wolgye-Dong, Nowon-Ku, Seoul 139-701, Korea

**Abstract**— A differential-mode wideband bandpass filter with good common-mode suppression is designed in this paper. The structure is divided to behave like a bandpass or bandstop filer under differential- or common-mode operation. The open stubs in bandstop filter are used to control the 3 dB bandwidth of bandpass filter with reducing the 3 dB cutoff bandwidth of bandstop filter slightly. To validate the design idea, a differential-mode bandpass filter centered at 4 GHz with a 3-dB BW of 55% and near 30 dB common-mode suppression is designed and fabricated.

## 1. INTRODUCTION

Ultra-Wideband (UWB) technology is different from the conventional narrow band system design. For the transmission of information, the former works at short duration pulses while the latter uses continuous waves. The advantages of UWB are low cost, low power and high date rate transmission in short-distance applications. In 2002, the Federal Communications Commission (FCC) authorized the unlicensed use of UWB in the range of 3.1 to 10.6 GHz. Since then, more UWB devices have been presented and focused including filers.

On the other hand, balanced circuits play an important role in modern communication systems for their higher immunity to the environmental noise when compared with that of the single-ended signaling. Until now, many amplifiers, mixers and oscillators have been developed as balanced components. Also, to meet the requirement, several narrow band or dual mode balanced filters have also been reported for a narrow balanced system [1–4]. Among them, just a few papers worked for the wideband differential-mode BPF. In [5], a four coupled-line UWB differential mode BPF is proposed while it is difficult to integrate with other differential-mode circuits since there is no common ground plane. In [6, 7], the wideband differential-mode BPFs are constructed with a fractional BW of 65% and 110%, respectively, but both of them suffer from poor frequency selectivity and large size. In [8], the filter has a fractional bandwidth of 80% and a small size with poor common-mode suppression. In [9], a highly selective differential-mode BPF with a common-mode suppression of about 20 dB has been introduced.

In this study, we propose a wideband differential-mode bandpass filter on microstrip line. The equivalent half circuits are used to analyze and compare the bandwidths under the differential- and common-mode excitations. Then, a differential-mode BPF with the center frequency of 4 GHz and a fractional bandwidth of about 55% is designed and measured.

## 2. DESIGN OF THE DIFFRENTIAL-MODE BPF

The proposed differential–mode wideband BPF is shown in Fig. 1(a). Since it is a symmetrical structure, it can be divided into two parts with a perfect electric or magnetic wall at the symmetrical plane, under differential-mode or common-mode excitation. Fig. 1(b) and Fig. 1(c) show the equivalent half circuits under those two operations respectively. Therefore, we can start the design from those two structures.

The structure shown in Fig. 1(b) is a bandpass filter, which is composed with four shunt short stubs of $\lambda/4$ and one connecting line of $\lambda/2$ between them. The simpler equivalent schematic is described in Fig. 2, where $Zp = Z2||Z3$. There are three reflection zeros in the passband. The middle zero is generated by two $\lambda/4$ short stubs. The location of the rest zeros is dependent on the characteristics impedances of stubs and connecting line.

The structure shown in Fig. 1(c) is a bandstop filter. It consists of two parallel microstrip lines and two $\lambda/4$ open stubs. The two parallel lines, one is $\lambda/2$ length and another is $\lambda$ length, lead to the basic frequency response of the bandstop filter. There are three transmission zeros in the stopband region. Also, the symmetrical transmission zeros can be obtained from the impedances of two transmission lines, too. The function of two open stubs is to increase the insertion loss with sharper rejection skirt and without changing the transmission zero frequencies, while the 3-dB

(a)



(b)                                                    (c)
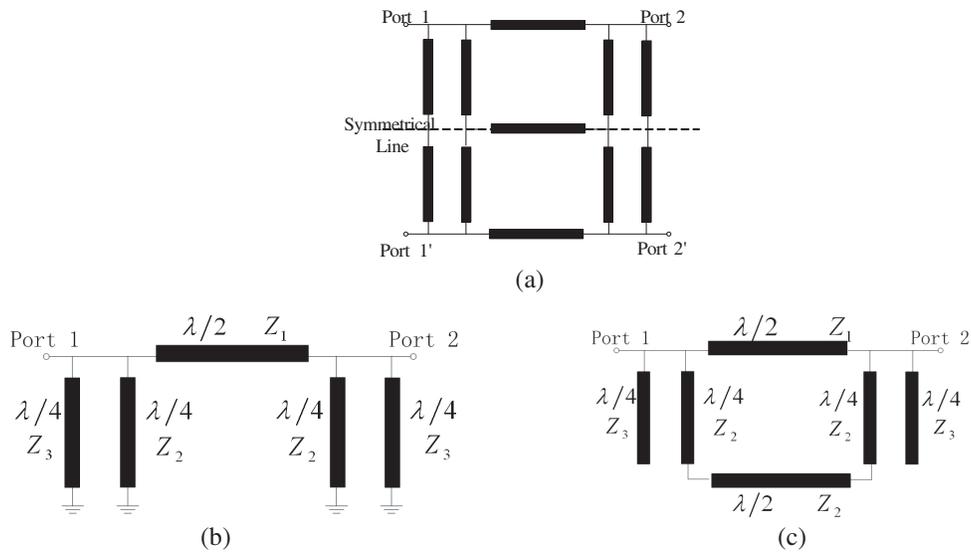
Figure 1: (a) Schematic diagram of the proposed differential-mode wideband BPF, (b) differential-mode and (c) common-mode equivalent half circuit.
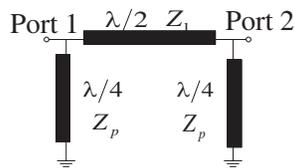


Figure 2: Simpler equivalent circuit for the differential-mode half circuit.



(a)                                                    (b)
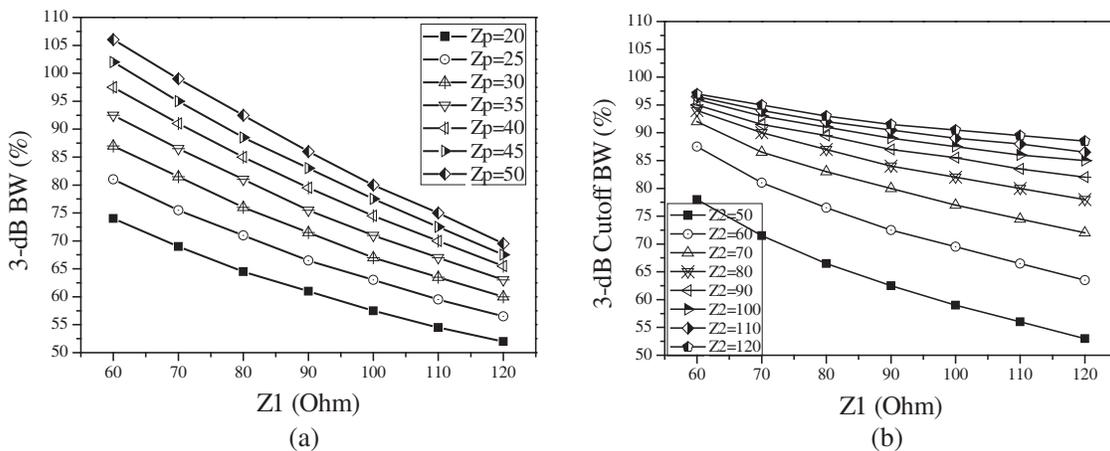
Figure 3: (a) Relationship between 3-dB BW with $Z_1$ and $Z_p$. (b) Relationship between 3-dB cutoff BW with $Z_1$ and $Z_2$.

cutoff bandwidth with the open stubs will be decreased slightly [10]. In addition, the two open stubs are used to realize the controllability of $Z_p$ under the differential-mode operation.

To let the common-mode stopband cover the entire differential-mode passband, the 3-dB cutoff frequency of the bandstop filter should be larger than the 3-dB BW of the bandpass filter as much as possible if the 3-dB BW of bandpass filter meets the design requirements under the differential-mode excitation. This maximum optimized difference value between them can be obtained from the function of and with considering return loss and common-mode suppression.

For simplicity, Figs. 3(a) and (b) give the bandwidth versus impedances at the center frequency, $f_0 = 4.0\,\text{GHz}$. For the same value of $Z_1$, the maximum margin of bandwidth between the BPF and BSF can be obtained from the biggest $Z_2$ and the smallest $Z_p$ in the given value range. Since
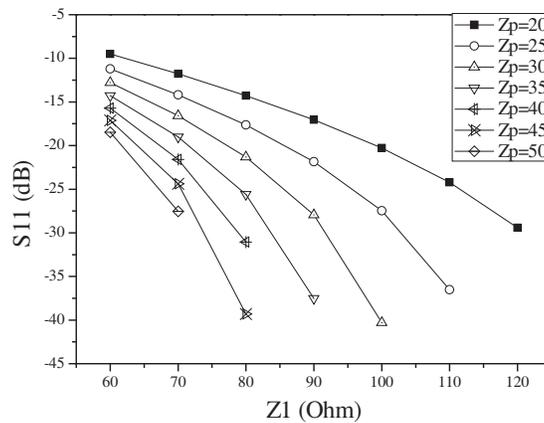
Figure 4: Relationship between return loss with $Z_1$ and $Z_p$.
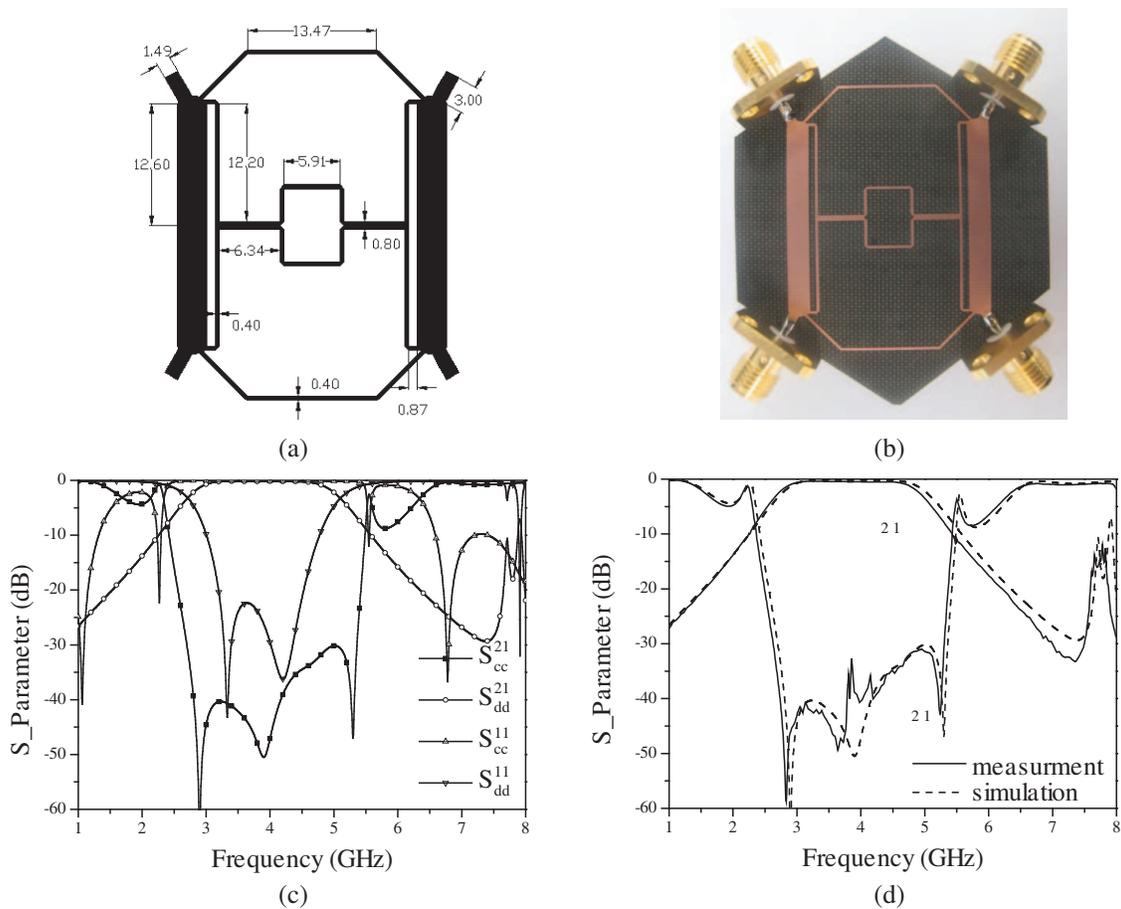


Figure 5: (a) Layout of the filter with dimensions in mm. (b) Photograph of the filter. (c) Full-wave EM simulation. (d) Comparison of simulated and measured response.

$Z_p = Z_2||Z_3$, the impedance of $Z_3$ can be determined. The return loss of the bandpass filter limits the choice of $Z_p$ as shown in Fig. 4. Even so, the better difference value between the bandwidths of BPF and BSF also can be obtained by choosing the impedances $Z_2$ and $Z_3$ appropriately.

## 3. SIMULATED AND MEASURED RESULTS

Following the above procedures, the impedance values of the differential-mode wideband bandpass filter are chosen as $Z_1 = 100$ ohm, $Z_2 = 100$ ohm, $Z_3 = 100$ ohm for center frequency of 4 GHz. This filter was fabricated on a 0.54 mm thick Teflon substrate with dielectric constant of 2.54. Figs. 5(a) and (b) show its physical layout and fabricated photograph. As a four-port balanced

device, the two-port differential- and common-mode $S$-parameters $S^{dd}$ and $S^{cc}$ can be deduced from the standard four-port $S$-parameters $S^{std}$ [11]. The simulation is accomplished by using IE3D, ADS, and the simulated response has been shown in Fig. 5(c). The full-wave measurement is finished by using Agilent E5071B. Fig. 5(d) shows the measured and simulated different- and common-mode results of the fabricated balanced filter. This differential-mode passband filter has a 3 dB BW of about 55% in the frequency range of 2.67–4.89 GHz. Over this frequency range, the common-mode suppression is smaller than 30 dB.

## 4. CONCLUSIONS

In this paper, a wideband differential-mode BPF with good common-mode suppression is designed. The open stubs in the bandstop filter are used to decrease the BW of bandpass filter to separate the two BWs. Finally, a demonstration filter with a 3 dB BW of about 55% at the central frequency of 4 GHz and good common-mode suppression has been implemented.

## ACKNOWLEDGMENT

**REFERENCES**

1. Wu, C. H., C. H. Wang, and C. H. Chen, "Novel balanced coupled-line bandpass filters with common-mode noise suppression," *IEEE Trans. Microwave Theory Tech.*, Vol. 55, No. 2, 287–295, Feb. 2007.
2. Wu, C. H., C. H. Wang, and C. H. Chen, "Balanced coupled-resonator bandpass filters using multisection resonators for common-mode suppression and stopband extension," *IEEE Trans. Microwave Theory Tech.*, Vol. 55, No. 8, 1756–1763, Aug. 2007.
3. Shi, J. and Q. Xue, "Balanced bandpass filters using center-loaded half-wavelength resonators," *IEEE Trans. Microwave Theory Tech.*, Vol. 58, No. 4, 970–977 Apr. 2010.
4. Chen, X. W., "Design of balanced dual-band bandpass filter with self-feedback structure," *EERI Journal*, Vol. 31, No. 4, 475–477, Aug. 2009.
5. Saitou, A., K. P. Ahn, H. Aoki, K. Honjo, and K. Waanabe, "Differential mode bandpass filters with four coupled lines embedded in self complementary antennas," *IEICE Trans. Electron,* Vol. E90-C, No. 7, 1524–1532, Jul. 2007.
6. Lim, T. B. and L. Zhu, "A differential-mode wideband bandpass filter on microstrip line for UWB application," *IEEE Microwave Wireless Compon. Lett.*, Vol. 19, No. 10, 632–634, Oct. 2009.
7. Lim, T. B. and L. Zhu, "Differential-mode ultra-wideband bandpass filter on microstrip line," *Electron. Lett.*, Vol. 45, No. 22, 1124–1125, Oct. 2009.
8. Lim, T. B. and L. Zhu, "Differential-mode wideband bandpass filter with three transmission zeros under common-mode operation," *Proc. Asia-Pacific Microwave Conf.*, 159–162, Dec. 2009.
9. Lim, T. B. and L. Zhu, "Highly selective differential-mode wideband bandpass filter for UWB application," *IEEE Microwave Wireless Compon. Lett.*, Vol. 19, No. 10, 632–634, Oct. 2009.
10. Tang, C. W. and M. G. Chen, "A microstrip ultra wideband bandpass filter with cascaded broadband bandpass and bandstop filter," *IEEE Trans. Microwave Theory Tech.*, Vol. 55, No. 11, 2412–2418, Nov. 2007.
11. Bockelman, D. E. and W. R. Eisenstant, "Combined differential and common-mode scattering parameters: Theory and simulation," *IEEE Trans. Microwave Theory Tech.*, Vol. 43, No. 7, 1530–1539, Jul. 1995.

# Design of Double-Pole-Double-Throw Bandpass Filter-Integrated Switches

**S. F. Chao and M. W. Shih**

National Kaohsiung Marine University, Taiwan

**Abstract**— In this paper, a double-pole-double-throw (DPDT) filter-integrated switch is proposed. The circuit integrates a DPDT switch and a microwave bandpass filter into a single circuit component. The circuit consists of four switchable feed lines and four hairpin resonators. The feed lines are connected via p-i-n diodes to the two symmetric taped points of each I/O half-wavelength resonator. Therefore, the I/O signal paths can be selected by applying different bias voltages to the p-i-n diodes. Moreover, the defected-ground-structure (DGS) is also adopted to improve the stopband rejection. At the thru port, the measured insertion loss is about 3.1 dB at the center frequency of 1.5 GHz with a 3 dB fractional bandwidth of 7%. The isolations are 42 dB and 43 dB at the center frequency and are higher than 26 dB from dc to 8.5 GHz at the two isolated ports. The proposed circuit successfully increases the level of integration of the RF front end, and the circuit size is also reduced.

## 1. INTRODUCTION

A microwave switch is a essential component to control RF signal flow in the modern communication systems. Several literatures using passive FETs or pin diodes have been reported [1–3]. However, these switches are wideband designs, implying that they can not provide adequate band selectivity for a system application. Therefore, a bandpass filter will be needed to cascade with a switch to reject out-of-band signals.

Recently, several methods were proposed to integrated the building blocks of the RF front into a multi-function circuit [4–8]. In [4], an SPDT bandpass filter-integrated switch that integrate an SPDT switch and a bandpass filter was proposed. In [5], a 40 GHz multiple-port MMIC filter-integrated switch was realized to show a high level integration. Switchable dual-band bandpass filters that achieve independent switching control of band selection was proposed in [6, 7]. In [8], a balun-integrated bandpass switchplexer that integrates an SPDT switch, a diplexer, and a balun was demonstrated.

Multiple-input-multiple-output (MIMO) techniques are widely used in microwave communication systems. To meet the increasing demands of MIMO applications, in this paper, a DPDT filter-integrated switches is presented. The proposed circuit integrates an MMIC DPDT switch and a microwave bandpass filter into a single circuit. The circuit is implemented by connecting the feed lines via p-i-n diodes to the two symmetric taped points of each I/O half-wavelength resonator. Thus, the signal flow can be controlled by applying different bias voltages to the p-i-n diodes.

## 2. DPDT FILTER-INTEGRATED SWITCH $A$

Figure 1 shows the circuit schematic of the proposed DPDT filter-integrated switch. The circuit is composed by four hairpin resonator to form a 4th-order bandpass response. Moreover, four feed lines are connected via p-i-n diodes to the two symmetric taped points of each I/O half-wavelength resonator. When forward biased, the equivalent circuit of the p-i-n diode is a small resistor $R_{on} = 1\,\Omega$ series with a parasitic inductor $L_p = 0.8\,\text{nH}$. Under reverse biased, the equivalent circuit is a small capacitor $C_{off} = 0.18\,\text{pF}$ series with a parasitic inductor $L_p = 0.8\,\text{nH}$. By applying different bias voltage to the p-i-n diodes, the feed lines could be connected to or disconnected from the resonators. In this circuit, port 1–2 are the two input ports, and port 3–4 are the two output ports. It is noted that the capacitors $C_b$ are dc blocking capacitors, and the resistors $R_g = 1\,\text{k}\Omega$ provide dc ground path for diodes $D_{1A}$, $D_{2A}$, $D_{3A}$, and $D_{3A}$. All the diodes in the circuit are biased via resistors $R_b = 1\,\text{k}\Omega$. If one wants the RF signal to go from port 1 to port 3, the diodes $D_{1A}$ and $D_{3A}$ are forward biased and the shunt diodes $D_{1B}$ and $D_{3B}$ are reverse biased. The RF signal will pass through diodes $D_{1A}$ and $D_{3A}$, and diodes $D_{1B}$ and $D_{3B}$ prevent the RF signal leaking to the ground. At the same time, port 2 and port 4 are isolated, diodes $D_{2A}$ and $D_{4A}$ are reversed biased and the shunt diodes $D_{2B}$ and $D_{4B}$ are forward biased. Diodes $D_{2A}$ and $D_{4A}$ are small capacitors that can block the RF signal from entering port 2 and port 4, and diodes $D_{2B}$ and $D_{4B}$ are small resistors that could bypass the RF signal to ground for further improving the isolations. Similarly,
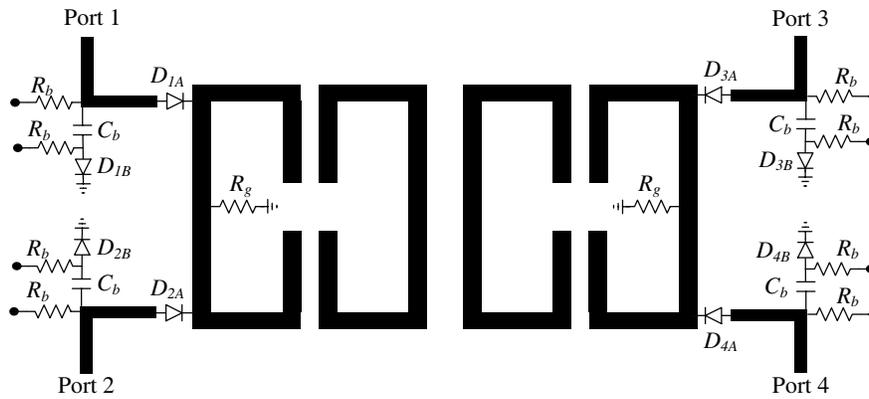
Figure 1: Circuit schematic of the DPDT filter-integrated switch $A$.



Figure 2: Photograph of the DPDT filter-integrated switch $A$.

the RF signal could be selected from one of the two input/output ports by applying corresponding voltages to the diodes on the feed lines.

The circuit was designed to have a 4th-order Butterworth bandpass response at 1.5 GHz, and 3-dB fractional bandwidth $\Delta_{3\,\mathrm{dB}}$ of 7% in the on state. The coupling coefficients and the external quality factor $Q_{ext}$ can be obtained as

$$M_{12} = \frac{\Delta_{3\,\mathrm{dB}}}{\sqrt{g_1 g_2}} = M_{34} = 0.059$$

$$M_{23} = \frac{\Delta_{3\,\mathrm{dB}}}{\sqrt{g_2 g_3}} = 0.038$$

$$Q_{ei} = \frac{g_0 g_1}{\Delta_{3\,\mathrm{dB}}} = Q_{eo} = 10.9$$

where $M_{ij}$ represents the coupling coefficient between resonators $i$ and $j$, $g_n$ is the low-pass prototype parameter, and $Q_{ei}$ and $Q_{eo}$ are the external quality factors associated with the input and output couplings, respectively [9].

The circuit is fabricated on the RO4003C substrate with $\epsilon_r = 3.58$, $h = 0.8\,\mathrm{mm}$, and $\tan\delta = 0.001$. Fig. 2 is the photograph of the DPDT filter-integrated switch $A$. Fig. 3(a) shows the results when port 1-port 3 are at thru states, and it is observed that a bandpass response with a passband insertion loss of 3.0 dB at center frequency of 1.49 GHz was measured. At the same time, the measured isolations of the two isolated ports are 42 dB and 40 dB at the center frequency, and are better than 20 dB from dc to 2.7 GHz as shown in Fig. 3(b).

## 3. DPDT FILTER-INTEGRATED SWITCH $B$

In DPDT filter filter-integrated switch $A$, the bandpass response at the thru port suffers from unwanted spurious response and the isolation at the isolated ports are not good at higher frequencies. Thus, defected-ground-structure (DGS) lowpass filters are adopted to suppress the spurious response at the thru port and also improve the isolations at the isolated ports [10]. Fig. 4 shows the
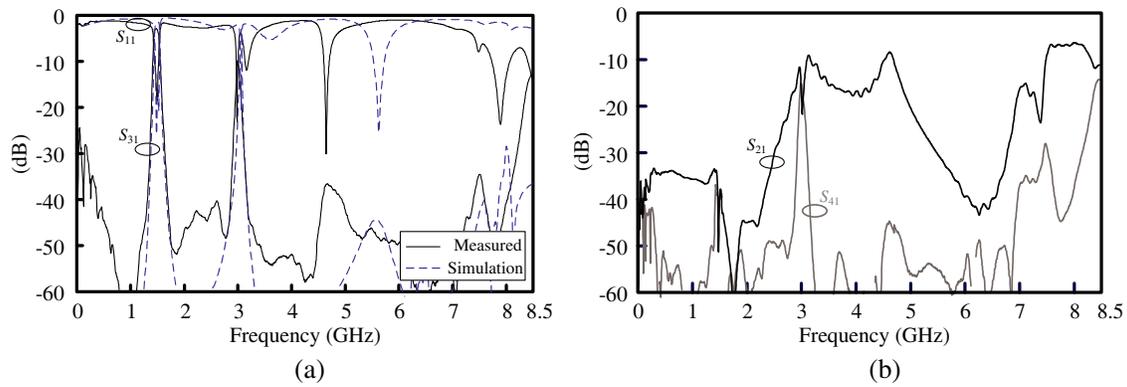
Figure 3: Measurement results of the DPDT filter-integrated switch $A$.
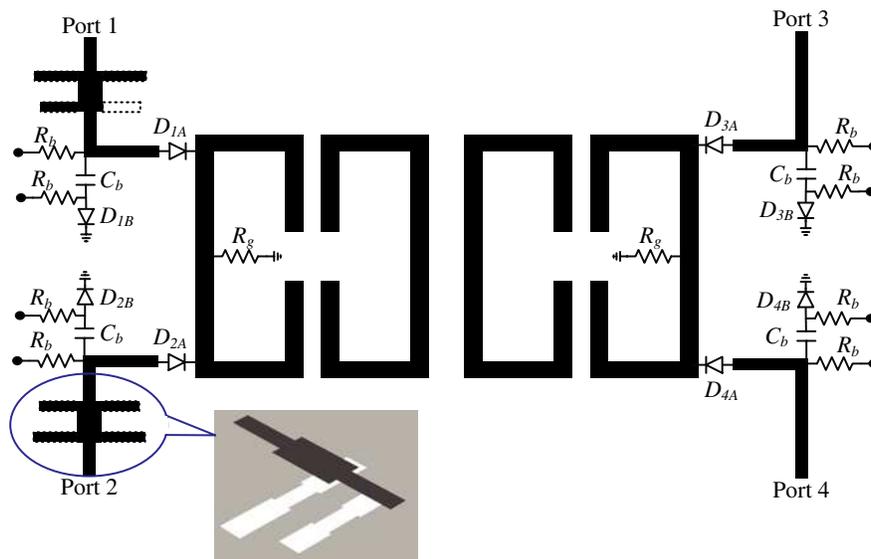


Figure 4: Circuit schematic of the DPDT filter-integrated switch $B$.
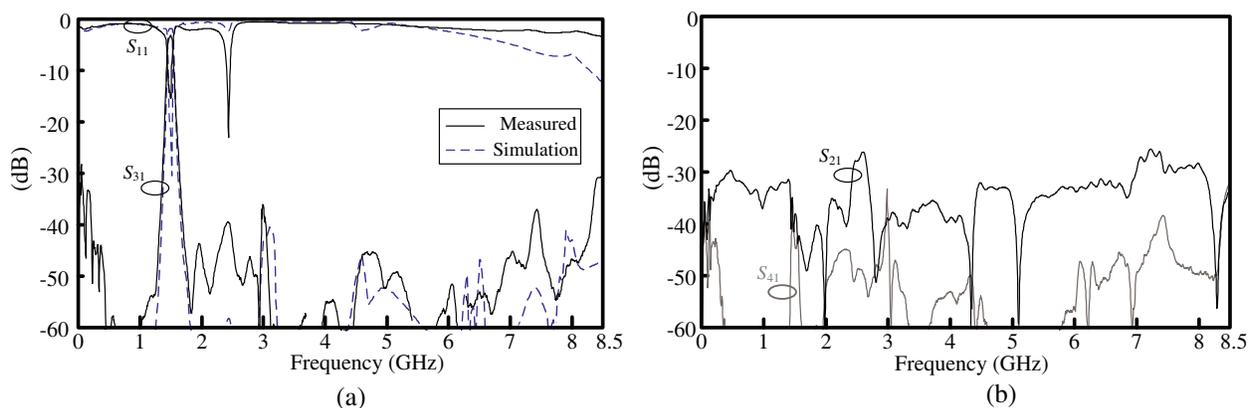


Figure 5: Measurement results of the DPDT filter-integrated switch $B$.

circuit schematic of the DPDT filter filter-integrated switch $B$. It is noted that the DGS lowpass filters are cascaded at the two input feed lines of this circuit, and the 3-dB cutoff frequency of the lowpass filter is designed at 2 GHz to suppress the spurious of the bandpass response while adding minimum insertion loss to the passband. Fig. 5 shows the measurement results of the DPDT filter-integrated switch $B$. Compared with example $A$, the measured passband insertion loss is 3.1 dB at the center frequency with a stopband rejection better than 30 dB up to 8.5 GHz, as seen in Fig. 5(a).

In Fig. 5(b), the isolations at the high frequencies are improved, which are better than 26 dB from dc to 8.5 GHz.

## 4. CONCLUSION

In this paper, double-pole-double-throw (DPDT) filter-integrated switches are designed and implemented. The proposed circuit integrates a DPDT switch and a microwave bandpass filter into a single circuit component. The circuit is formed by connecting feed lines via p-i-n diodes to the two symmetric taped points of each I/O half-wavelength resonator. Therefore, the I/O signal paths can be selected by applying different bias voltages to the p-i-n diodes. In this way, the circuit can be used to select RF signal from two different antennas and also reject out-of-band interference in a MIMO system. It is believed that the circuit successfully increases the level of integration of the RF front end, and the overall circuit size is also reduced.

## ACKNOWLEDGMENT

### REFERENCES

1. Chao, S.-F., H. Wang, C.-Y. Su, and J. G. J. Chern, "A 50 to 94-GHz CMOS SPDT switch using traveling-wave concept," *IEEE Microw. Wireless Compon. Lett.*, Vol. 17, No. 2, 130–132, 2007.
2. Park, P., D. H. Shin, and C. P. Yue, "High-linearity cmos T/R switch design above 20 GHz using asymmetrical topology and ac-floating bias," *IEEE Trans. Microw. Theory Tech.*, Vol. 57, No. 4, 948–956, 2009.
3. Lai, R.-B., J.-J. Kuo, and H. Wang, "A 60–110 GHz transmission-line integrated spdt switch in 90 nm cmos technology," *IEEE Microw. Wireless Compon. Lett.*, Vol. 20, No. 2, 85–87, 2010.
4. Chao, S.-F., C.-H. Wu, Z.-M. Tsai, H. Wang, and C. H. Chen, "Electronically switchable bandpass filters using loaded stepped-impedance resonators," *IEEE Trans. Microw. Theory Tech.*, Vol. 54, No. 12, 4193–4201, 2006.
5. Chao, S.-F., C.-C. Kuo, Z.-M. Tsai, K.-Y. Lin, and H. Wang, "40-GHz MMIC SPDT and multiple-port bandpass filter-integrated switches," *IEEE Trans. Microw. Theory Tech.*, Vol. 55, No. 12, 2691–2699, 2007.
6. Dai, G. L. and M. Y. Xia, "Design of compact dual-band switchable bandpass filter," *Electronics Letters*, Vol. 45, No. 10, 506–507, 2009.
7. Deng, P.-H. and J.-H. Jheng, "A switched reconfigurable high-isolation dual-band bandpass filter," *IEEE Microw. Wireless Compon. Lett.*, Vol. 21, No. 2, 71–73, 2011.
8. Lin, Y.-S., P.-C. Wang, C.-W. You, and P.-Y. Chang, "New designs of bandpass diplexer and switchplexer based on parallel-coupled bandpass filters," *IEEE Trans. Microw. Theory Tech.*, Vol. 58, No. 12, 3417–3426, 2010.
9. Hong, J.-S. and M. J. Lancaster, *Microstrip Filter for RF/Microwave Applications*, K. Chang, Ed., Wiley, New York, 2001.
10. Ahn, D., J.-S. Park, C.-S. Kim, J. Kim, Y. Qian, and T. Itoh, "A design of the low-pass filter using the novel microstrip defected ground structure," *IEEE Trans. Microw. Theory Tech.*, Vol. 49, No. 1, 86–93, 2001.

# E-band Transmitter Module Using a LCP Substrate

**Young Chul Lee[1], Salizul Jaafar[2], Mohd. Fadzil Amiruddin[2],
Suhandi Bujang[2], and Azzemi Ariffin[2]**

[1]Division of Marine Electronics and Communication Engineering
Mokpo National Maritime University (MMU), Korea
[2]System Technology, Telecom Malaysia Research & Development (TMR&D), Korea

**Abstract**— We present a 70 GHz Amplitude-Shift-Keying (ASK) transmitter module based on a system-on-package (SoP) technology using a liquid-crystal polymer (LCP) substrate for point-to-point wireless communication applications. Four monolithic microwave integrated circuits (MMICs), which are two frequency multipliers (MTLs), a driver amplifier (DA), and a ASK modulator, are used in the metal-backed LCP SoP module. Its size is $15.8 \times 13.0 \times 2.2 \, \text{mm}^3$ and its output power is $-8.2 \, \text{dBm}$ at the local oscillation (LO) frequency of 12.48 GHz with 5.0 dBm, intermediate frequency (IF) of 20 MHz with $\pm 25 \, \text{mV}$ and $-0.7 \, \text{V}$ for off-set.

## 1. INTRODUCTION

Recently, because various high-speed data services such as 3.5G, 4G mobile communications, WiMax, etc. have progressed, the demands for high-capacity and -speed Ethernet networks have rapidly increased. High-capacity and speed networks can be implemented by using a millimeter wave (mm-wave) [1, 2], free space optical (FOS) [3], and fiber-optic network. In the case of FOS and fiber-optic communications, there are some limitations related to natural environment such as fog and rain and install expense. The high-capacity and speed wireless communications using mm-waves are a competitive alternative in respects of install time, cost, and natural environments, compared to the FOS and fiber-optic communications, short-range wireless communication applications. Commercial wireless point-to-point (PtP) links using a 60, 70, and 80 GHz band have developed for high-capacity and -speed Ethernet applications. However, because of additional propagation loss due to oxygen absorption at 60 GHz [4], 60 GHz PtP links are limited. Contrarily, in the case of E-band such as 70 and 80 GHz bands, longer link range and higher speed because of no oxygen absorption and more available bandwidth, respectively, can be offered [5].

To commercially realize these E-band link applications, a cost effective radio module is indispensable. The system-on-package (SoP) approach [6–9] using a low-temperature co-fired ceramic (LTCC) and liquid-crystal polymer (LCP) technology has been demonstrated to be suitable technology integrating active and passive circuits into a compact single substrate. Although the LTCC technology has provided very dense multilayer integration and excellent electrical performance, the design at mm-wave bands has become challenging due to limitation of design rules [10]. The LCP's low loss ($\tan \delta = 0.002 \sim 0.004$), low cost, low water absorption (0.04%) and low permittivity ($\varepsilon_r = 2.9 \sim 3.0$) make very attractive for RF and mm-wave SoP applications.

In this paper, a 70 GHz ASK Tx LCP SoP module has been presented for wireless gigabit PtP applications. Four GaAs MMIC chips and DC bias components has been fully integrated into the metal backed LCP substrate. The implemented Tx LCP SoP module is as small as $15.8 \times 13.0 \times 2.2 \, \text{mm}^3$. The measured Tx performance is presented.

## 2. DESIGN AND FABRICATION OF AN ASK TRANSMITTER LCP MODULE

The radio systems with an ASK modulation technique [11] have been widely used for mm-wave applications because of its simplicity and power efficiency. And also, in the case of an ASK non-coherent de-modulation technique by using a simple envelope detector, there are no needs of a coherent LO signal. Especially, the ASK modulation has been investigated and utilized for gigabit transmitting systems using millimeter-wave bands whose analog-digital converter (ADC) is hard to be implemented.

A block diagram of a 70 GHz ASK transmitter (Tx) is shown in Fig. 1. Its carrier center frequency is 72.1 GHz, and also its bandwidth is 2.2 GHz. The Tx part consists of a up-converting mixer, and three commercially available GaAs MMICs: two frequency multipliers (MTLs, 2X and 3X) and a driving amplifier (DA). The external local oscillation (LO) signal of 12.017 GHz for the Tx is multiplied by 6 times and amplified in order to drive the up-converting mixer.

In order to integrate the designed 70 GHz ASK Tx into the LCP SoP single module, the metal-backed LCP substrate incorporating a WR12 waveguide is used. The probe-type WR12-to-microstrip transition is designed on the LCP substrate. The cavities to mount MMICs were formed in the LCP substrate. The metal lines on the LCP were gold-plated. In order to compensate parasitics due to wire-bonding between the MMIC and LCP board, microstrip-type matching circuits were designed on the LCP substrate. Fig. 2 shows the vertical structure of the 70 GHz Tx LCP SoP module and the fabricated one. This module was designed for testing using GSG probe tips. A GSG-type IF, LO, and RF port were designed. For effective analysis of the ASK Tx module, the two blocks, MTL (2x and 3x) and DA, were also designed. The designed 70 GHz ASK Tx module was fabricated in the commercial foundry. The whole size of the LCP module is $15.8 \times 13.0 \times 2.2 \, \text{mm}^3$ as shown in Fig. 2(b).
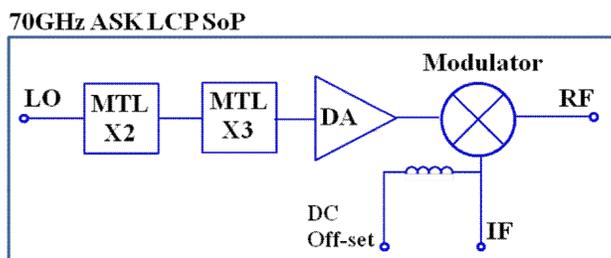


Figure 1: Block diagram of a 70 GHz ASK transmitter for point-to-point wireless communication systems.



(a) Vertical structure

(b) Fabricated module (15.8x13.0x2.2 mm$^3$)
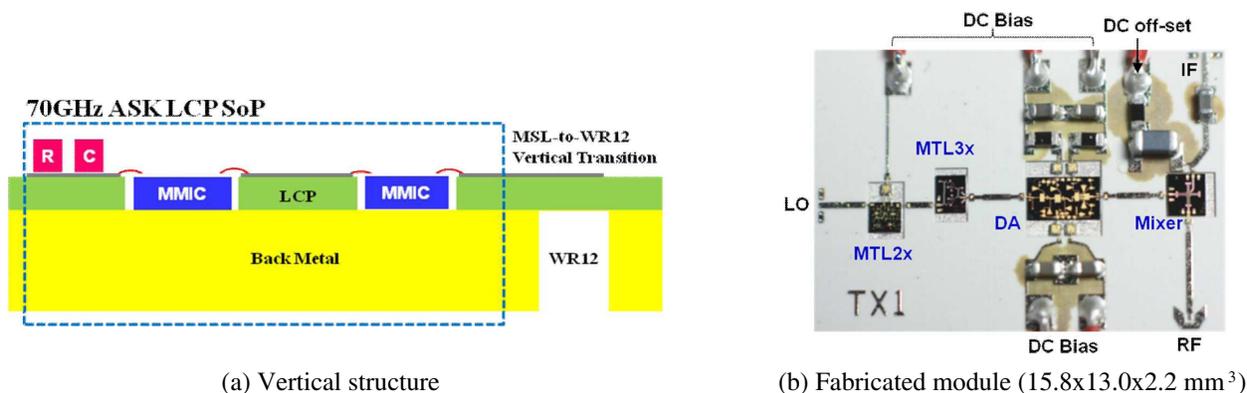
Figure 2: Block diagram of a 70 GHz ASK transmitter for point-to-point wireless communication systems.
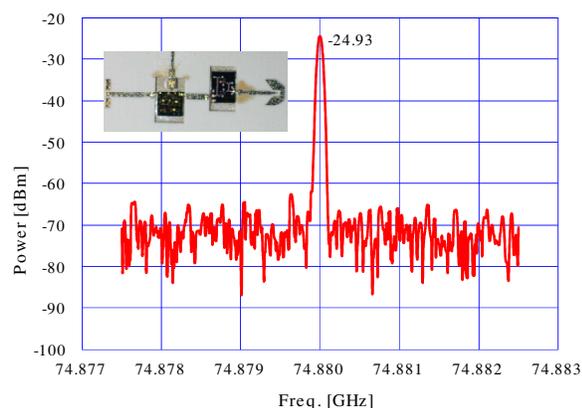


Figure 3: Measured spectrum results of the fabricated MTL block [Inset: the fabricated MTL block consisting of the 2X and 3X MTL].
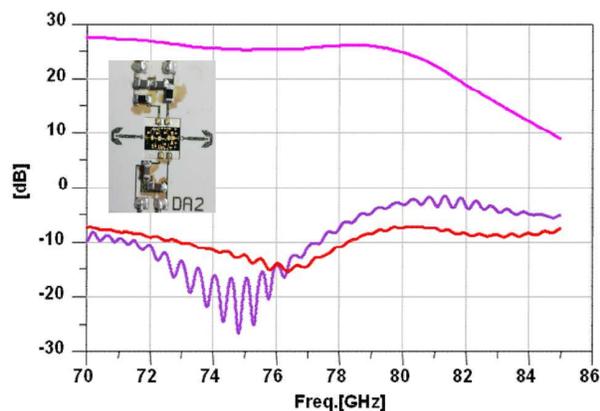
Figure 4: Measured s-parameters characteristics of the fabricated DA module [Inset: the fabricated DA block].
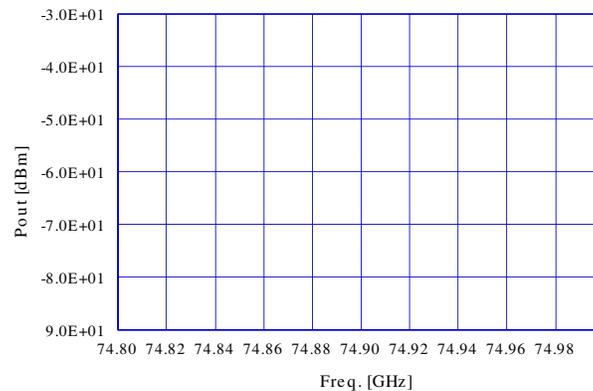
Figure 5: Measured spectrum characteristics of the fabricated ASK Tx LCP SoP module (The attenuator with the loss of 24.8 dB was connected to the RF port).

## 3. MEASURED RESULTS

The frequency spectrum characteristics of the fabricated MTL block consisting of the 2X and 3X MTL MMIC were characterized in Fig. 3. This figure shows clearly that an input frequency of 12.48 GHz with a power of 5.22 dBm was normally multiplied to 74.88 GHz (by 6 times). The measured output power was $-10.93$ dBm considering an attenuator with -14dB loss. The 2X MTL dissipated 83 mA at 2.5 V.

In order to drive the double-balanced mixer MMIC integrated in the Tx, the LO signal from the MTL block should be amplified up to 14 dBm by using the DA. Fig. 4 shows the characteristics of the fabricated DA block. At 74 GHz, a $S_{11}$ and $S_{22}$ are lower than $-10$ dB and an insertion loss of 25 dB is achieved. Total current of 87 mA at $V_g = 0$ V and $V_d = 4$ V was dissipated.

Figure 5 shows the measured RF spectrum of the fabricated ASK Tx LCP SoP module. For ASK modulation, the IF signal generated by a pulse pattern generator (Agilent Tech. 81110A) was used to the IF port of the ASK Tx module and also an off-set voltage of $-0.7$ V was forced to it. At the LO frequency of 74.9 GHz with the power of 5 dBm and IF of 20 MHz with $\pm 50$ mV, the output power ($P_{out}$) of $-8.2$ dBm is achieved.

## 4. CONCLUSION

In this paper, the 70 GHz ASK transmitter SoP module using the metal backed LCP substrate has been presented for point-to-point wireless communication applications. The whole Tx circuitry including a ASK modulator, two frequency multipliers, a driving amplifier, and all DC bias components are fully integrated into the single LCP substrate. Its size is $15.8 \times 13.0 \times 2.2$ mm$^3$ and its output power is $-8.2$ dBm at the LO frequency of 12.483 GHz with 5.0 dBm, intermediate frequency (IF) of 20 MHz with $\pm 25$ mV and $-0.7$ V for off-set.

## REFERENCES

1. Smulders, P., "Exploiting the 60 GHz band for local wireless multimedia access: Prospects and future directions," *IEEE Commun. Magzine*, 140–147, 2002.
2. Ohata, K., K. Maruhashi, M. Ito, S. Kishimoto, K. Ikuina, T. Hashiguchi, K. Ikeda, and N. Takahashi, "1.25 Gbps wireless Gigabit Ethernet link at 60 GHz-band," *IEEE MTT-S International Microwave Symposium*, 373–376, 2003.
3. Kamalakis, T., et al., "Hybrid free space optical/millimeter wave outdoor links for broad-band wireless access networks," *18th Annual IEEE Symposium on PIMRC*, 2007.
4. Marcus, M. and B. Pattan, "Millimeter-wave propagation: Spectrum management implications," *IEEE Microwave Magazine*, 54–62, 2005.
5. Sevimli, O., V. Dyadyuk, D. Abbott, J. Bunton, R. Kendall, L. Stokes, M. Shen, and S. Smith, "Multi-gigabit wireless link development," *Auswireless Conference*, 2006.
6. Lee, Y. C., T.-W. Kim, A. B. Ariffin, and N.-G. Myoung, "60-GHz amplitude shift- keying receiver ltcc system-on-package module," *Microwave and Optical Technology Letters*, Vol. 53, No. 4, 758–761, 2011.

7. Jung, D. Y., W.-I. Chang, K. C. Eun, and C. S. Park, "60-GHz system-on-package transmitter integrating sub-harmonic frequency amplitude shift-keying modulator," *IEEE Transactions on Microwave Theory and Techniques*, Vol. 55, No. 8, 1786–1793, 2007.

8. Aihara, K., M. J. Chen, and A.-V. Pham, "Development of thin-film liquid-crystal-polymer surface-mount packages for Ka-band applications," *IEEE Transaction on Microwave Theory and Techniques*, Vol. 56, No. 9, 2111–2117, 2008.

9. Aihara, K., A. Pham, D. Zeeb, T. Flack, and E. Stoneham, "Development of multi-layer liquid crystal polymer Ka-band receiver modules," *Asia-Pacific Microwave Conference (APMC)*, 2007.

10. Pinel, S., S. Sarkar, R. Bairavasubramanian, J.-H. Lee, M. Tentzeris, J. Papapolymerou, and J. Laskar, "Highly integrated LTCC and LCP millimeter wave functions for 3D-SOP high data rate wireless systems," *Electronic Components and Technology Conference*, 764–768, 2005.

11. Tarusawa, Y., H. Ogawa, and T. Hirota, "A new constant resistance ASK modulator using double-sided MIC," *IEEE Transaction on Microwave Theory and Techniques*, Vol. 35, No. 9, 819–822, 1987.

# Effect of Finger-patterned Electrodes on Tunability of Tunable Capacitors

**Young Chul Lee[1], Baek Ju Lee[2], and Kyung Hyun Ko[2]**

[1]Division of Marine Electronics and Communication Engineering
Mokpo National Maritime, University (MMU), Korea
[2]Department of Materials Science and Engineering, Ajou University, Korea

**Abstract**— In this paper, the effect of the finger-patterned electrodes on a tunability of tunable capacitors has been investigated. Two tunable capacitors with finger-pattern electrodes, a metal-insulator-metal (MIM) capacitor with the finger-pattern metal on the top electrode and a sandwich inter-digital capacitor (IDC) embedding a dielectric layer between finger-pattern metal layers, are fabricated using a low-loss and high-tunability para/ferroelectric multi-layer thin film dielectrics and analyzed in terms of $S_{11}$, effective capacitance and tunability compared to the conventional MIM capacitor. At 25 V and 2 GHz, the maximum tunability of the finger-patterned capacitor is 38% that is 5.8% higher value than that of the convention one. At the same DC voltage of 8 V, the novel sandwich IDC shows the tunability of 18% which over 12% higher than that of the convention MIM one. These results demonstrate that high-fringe electric fields induced due to the finger-pattern electrodes improve their tunability.

## 1. INTRODUCTION

Recently, several types of the communication technologies such as reconfigurable RF [1] and software defined radio (SDR) [2] have been developed in order to achieve seamless roaming, intelligent operation, and effective use of frequency bands. Therefore, various tunable components have been developed constantly for several years using tunable dielectrics [3–7] as well as microelectromechanical systems (MEMS). Ferro- or para-electrics technologies based on barium-strontium titanate (BST) [3, 4] bismuth zinc niobate (BZN) [5–7] or lead zinc niobate (PZN) [8] has pursued for low loss, low voltage and high operation frequency. Recently, in order to increase the tunability and reduce the DC bias voltage, an inter-digital capacitor (IDC) [5, 8] embedding its electrodes into the tunable dielectrics. However, in the case of metal-insulator-metal (MIM) tunable capacitors, it is difficult to improve their tunability using other methods other than thin-film materials. Ferroelectric thin-films based on BST have shown high-tunability characteristics in spite of relatively lossy feature, compared to the low-loss para-electric ones. In order to compensate or optimize opposite features between ferr- and para-electric dielectrics, a para/ferro/para-electric thin-film multilayer (BZN/BST/BZN) has been proposed for low-loss and high-tunability applications [9].

In this paper, MIM tunable capacitors with finger patterns on the top electrode (finger-type capacitor) are fabricated in order to improve their tunability by enhancing fringe electric ($E$)-fields and they are characterized in terms of effective capacitance and tunability as a function of line width and area of the top electrode, in comparison with the conventional capacitors with a rectangle-type electrode.

## 2. FABRICATION OF MIM TUNABLE CAPACITORS

A vertical structure of the MIM tunable capacitor using a multi-layer thin-film dielectric is shown in Fig. 1(a). The multi-layer (BZN/BST/BZN) dielectric is utilized for low-loss and high-tunability purpose. The tunable capacitors were fabricated on a quartz substrate in coplanar waveguide (CPW) configuration. The first metal (Ti/Pt = $100/1,000$Å) was deposited and defined as a bottom electrode of the MIM capacitor by using lift-off process. For the multi-layer thin-film dielectric, the first BZN pyrochlore thin-film of 700Å was deposited by RF-magnetron sputtering. The deposition was carried out from stoichiometric $Bi_2(Zn_{1/3}Nb_{2/3})_2O_7$ ceramic target in an high purity $O_2/Ar$ mixture atmosphere. The detailed process conditions were described in detail at the previous work [7]. Using the Inductive Coupled Plasma (ICP) dry etcher the BZN film was patterned and then the second thin-film (BST) of 1,500Å was deposited using a $B_6S_4T$ target and then etched. The final thin-film BZN dielectric of 700Å was deposited and patterned. The photolithography and etching process were carried out by using the same photo mask and dry etcher, respectively, for the multi-layer dielectric. After patterning of each layer, post-annealing processes were carried
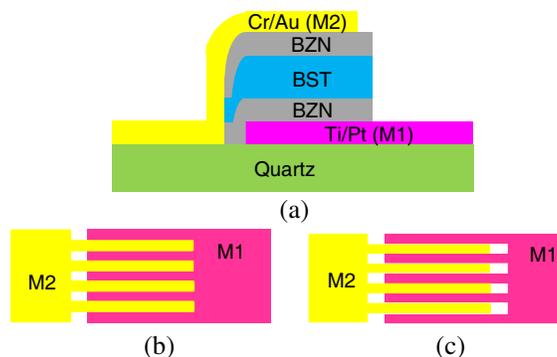
Figure 1: (a) Vertical structure of a conventional MIM tunable capacitor using a multi-layer (BZN/BST/BZN: 700Å/1,500Å/700Å) dielectric. The thickness of a bottom (Ti/Pt) and top (Cr/Au) electrode is 100/1,000Å thick [Inset: the fabricated conventional tunable MIM capacitor], (b) metal layout of the MIM capacitor with the finger-pattern on the top metal (M1) and (c) novel IDC embedding the multi dielectrics between the finger-pattern on the top (M1) and bottom (M2) electrode).

Table 1: Characteristics of the thin-film dielectric analyzed by using dot capacitors.

| Dielectric Thin Films | $\varepsilon_r$ | tan$\delta$ | Tunability |
|---|---|---|---|
| BST (4,000Å) | 250 | 0.028 | 48% |
| BZN (4,000Å) | 165 | 0.003 | 18% |
| BZN/BST/BZN ((1,000Å/2,000Å/1,000Å) | 225 | 0.005 | 47% |

out at 550°C for 5 minutes in air to crystallize the film. The lift-off pattern as the second metal (Cr/Au = 100Å/1,000Å) was defined on the top of the multi-layer dielectric as the top electrode. Figs. 1(b) and (c) show a MIM tunable capacitor with the finger-pattern metal on the top electrode and a sandwich inter-digital capacitor (IDC) embedding a dielectric layer between finger-pattern metal layers (the top and bottom electrode). The IDC is designed without spacing between two electrodes.

Table 1 presents characteristics of each thin-film and multi-layer dielectric used for fabrication of the MIM tunable capacitors for this work. Their characteristics were measured at 10 MHz and 20 V by using a metal-insulator-metal (MIM) (Pt/dielectric/Ag) dot (250 µm diameter) capacitor on a Si/SiO$_2$(3,000Å)/TiO$_2$(200Å)/Pt wafer. The multi-layer (BZN/BST/BZN) [9] thin-film dielectric shows a low-loss and high-tunability feature, compared with the lossy BST and low tunable BZN thin-film, respectively.

## 3. MEASURED RESULTS

The effective capacitance ($C_{eff}$) and percentage tunability ($T$) of the fabricated capacitors were analyzed by measuring complex reflection coefficients ($S_{11}$) with a vector network analyzer (HP 8510C) and a probe station. Using the measured $S_{11}$ data, the $C_{eff}$, and tunability are analyzed by using following equations.

$$C_{eff} = -\frac{1}{2\pi \cdot freq. \cdot \text{Im}(Z_{11})} \ [\text{F}] \tag{1}$$

$$T = \frac{C_{\max} - C_{\min}}{C_{\max}} \ [\%] \tag{2}$$

$Z_{11}$ is the total impedance of the device under test calculated from the measured $S_{11}$. $C_{\min}$ and $C_{\max}$ are the measured minimum and maximum capacitance, respectively, within the applied bias voltage range.

Figure 2(a) shows measured $S_{11}$ data on the Smith Chart of the fabricated MIM tunable capacitors with the rectangle- and finger-type capacitor. The test frequency and DC bias voltage are from 100 MHz to 3 GHz and 0 V, respectively. The self-resonant frequency (SRF) of all capacitors is over
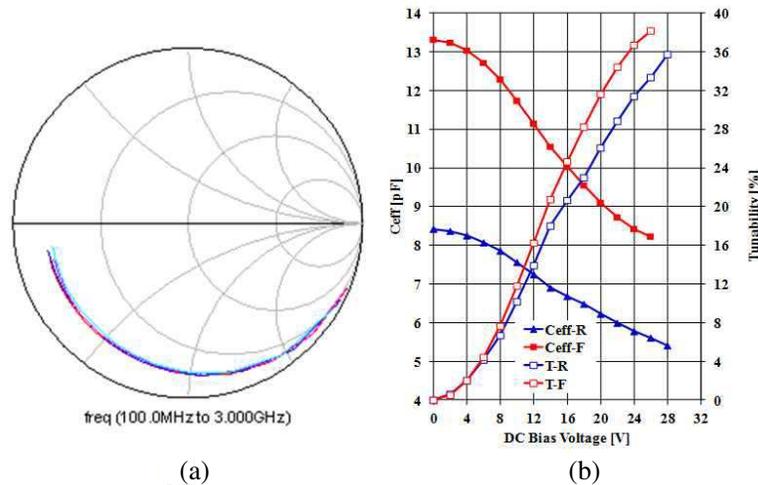
Figure 2: Measured $S_{11}$ characteristics on the Smith Chart (a) and effective capacitance ($C_{eff}$) and tunability ($T$) results of the fabricated MIM capacitors with the rectangle- and finger-type electrode.
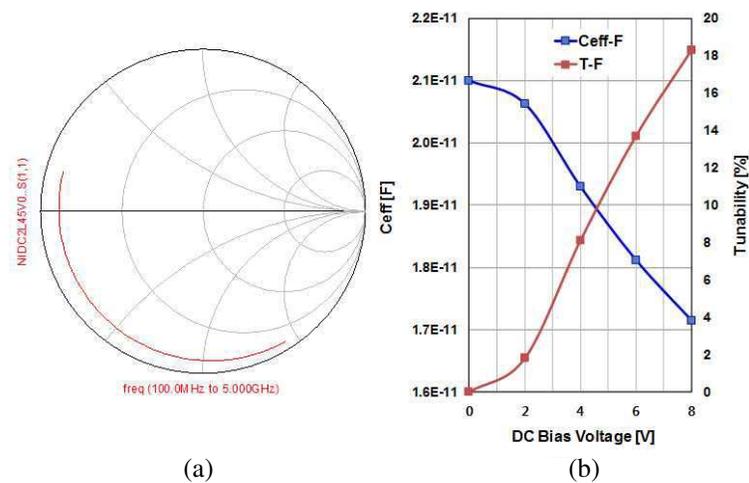


Figure 3: Measured $S_{11}$ characteristics on the Smith Chart (a) and effective capacitance ($C_{eff}$) results of the fabricated sandwich IDC.

3 GHz. The $S_{11}$ traces on the Smith Chart reveal poor Q-factor characteristics that result from plasma damage of thin-film dielectrics due to the dry etcher [10] and thin-thickness of the metal layer. Fig. 2(b) shows $C_{eff}$ and tunability of the finger-patterned capacitor with the line width (LW) of 2 μm as a function of applied DC bias voltage at 2 GHz, compared to the conventional one with the same electrode area. Due to the fringe $E$-fields, $C_{eff}$ of the finger-patterned capacitor decreases sharply, compared to the conventional one, as the DC bias voltage increases. Especially, at 25 V and 2 GHz, the maximum tunability of the finger-patterned capacitor is 38% that is 5.8% higher value than that of the convention one.

Figure 3 shows measured $S_{11}$ results (a) on the Smith Chart and $C_{eff}$ (b) of the sandwich IDC with the LW of 2 μm as a function of applied DC bias voltage at 1 GHz. The SRF of 2.25 GHz is observed because of high resistance of the electrode. Its breakdown voltage was as low as 10 V. That results from high fringe $E$-fields due to the finger-pattern electrodes of the IDC. At 8 V and 1 GHz, its tunability is 18% which is higher than that of the previous two MIM capacitors in spite of different frequency.

## 4. CONCLUSIONS

In this paper, the effect of the finger-patterned electrodes on a tunability of tunable capacitors using a MIM capacitor with the finger-pattern metal on the top electrode and a sandwich IDC embedding a dielectric layer between finger-pattern metal layers has been presented. Using a low-

loss and high-tunability para/ferroelectric multi-layer thin film dielectrics, tunable capacitors were fabricated and analyzed in terms of their $S_{11}$, $C_{eff}$ and tunability. At 25 V and 2 GHz, the maximum tunability of the finger-patterned MIM capacitor is 38% that is 5.8% higher value than that of the convention one. At the same DC voltage of 8V, the novel sandwich IDC shows the tunability of 18% which over 12% higher than that of the conventional MIM one. From this work, the finger-pattern electrodes induce high-fringe electric fields and also improve tunability.

## ACKNOWLEDGMENT

## REFERENCES

1. Boeck, G., D. Pienkowski, R. Circa, Ma. Otte, B. Heyne, P. Rykaczewski, R. Wittmann, and R. Kakerow, "RF front-end technology for reconfigurable mobile systems," *IEEE Microwave and Optoelectronics Conference 2003*, Vol. 2, 863–868, 2003.

2. Tuttlebee, W. H. W., "Software-defined radio: Facets of a developing technology," *IEEE Personal Communications Magazine*, Vol. 6, No. 2, 38–44, April 1999.

3. Tombak, A., F. T. Ayguavives, J.-P. Maria, G. T. Stauf, A. I. Kingon, and A. Mortazawi, "Low voltage tunable barium strontium titanate thin film capacitors for RF and microwave applications," *IEEE MTT-S International Microwave Symposium*, Vol. 3, 1345–1348, 2000.

4. Fardin, E. A., A. S. Holland, K. Ghorbani, E. K. Akdogan, W. K. Simon, A. Safari, and J. Y. Wang, "Polycrystalline $Ba_{0.6}Sr_{0.4}TiO_3$ thin films on r-plane sapphire: Effect of film thickness on strain and dielectric properties," *Appl. Phys. Lett.*, Vol. 89, 182907-182907-3, 2006.

5. Lee, Y. C., Y. P. Hong, D. M. Kim, and K. H. Ko, "Very high tunable inter-digital capacitor using bismuth zinc niobate thin-film dielectrics for microwave applications," *IEE Electronics Letters*, Vol. 42, 851–853, 2006.

6. Lu, J., S. Schmidt, D. S. Boesch, N. Pervez, R. A. York, and S. Stemmer, "Low-loss tunable capacitors fabricated directly on gold bottom electrodes," *Appl. Phys. Lett.*, Vol. 88, 112905-112905-3, 2006.

7. Hong, Y. P., S. Ha, H. Y. Lee, Y. C. Lee, K. H. Ko, D. W. Kim, H. B. Hong, and K. S. Hong, "Voltage tunable dielectric properties of rf sputtered $Bi_2O_3$-$ZnO$-$Nb_2O_5$ pyrochlore thin films," *Thin Solid Films*, Vol. 419, 183–188, 2002.

8. Lee, Y. C., Y. P. Hong, and K. H. Ko, "Low-voltage and high-tunability interdigital capacitors employing lead zinc niobate thin films," *Appl. Phys. Lett.*, Vol. 90, 182908-182908-3, 2007.

9. Lee, B. J. and K. H. Ko, "Enhancement of BST Tunability using Para-Ferro electric multi-layer thin film," *Journal of the European Ceramic Society*, submitted, 2010.

10. York, R., A. Nagra, E. Erker, T. Taylor, P. Periaswamy, J. Speck, S. Streiffer, and O. Auciello, "Microwave integrated circuits using thin-film BST," *Proceedings of the 12th IEEE International Symposium on Applications of Ferroelectrics*, Vol. 1, 195–200, 2000.

11. Hegg, M. C. and A. V. Mamishev, "Influence of variable plate separation on fringing electric fields in parallel-plate capacitors," *2004 International Symposium on Electrical Insulation*, 384–387, 2004.

12. Lee, Y. C. and K. H. Ko, "A tunable capacitor using a finger patterned electrode," *Microwave and Optical Technology Letters*, Vol. 51, 418–421, 2009.

# Dumbbell Resonators to Reduce Crosstalk on Slotted Ground Plane

**Ding-Bing Lin**[1], **Chen-Kuang Wang**[1], **Chi-Hao Lu**[1], **and Jui-Hung Chou**[2]

[1]Graduate Institute of Computer and Communication Engineering
National Taipei University of Technology, Taiwan
[2]Graduate Institute of Communication Engineering, National Taiwan University, Taiwan

**Abstract**— By placing dumbbell resonators with different length on the slotted ground plane, the crosstalk noise can be decreased. The dumbbell resonators can be implemented on printed circuit board without additional cost by just designing length of dumbbell resonators to improve crosstalk. Theories of designing concept are half-wavelength resonances and parallel capacitance from dumbbell resonators. The experimental results indicate that proposed method of dumbbell resonators has better performance than original board.

## 1. INTRODUCTION

Nowadays, the fabrication technology for integrated circuit (IC) is improved, million transistors are integrated into one chip and the number of transistors are increased rapidly [1]. As to suppress power/ground coupling noise between different parts on the PCBs, using the etched slot on the power or ground planes is effective method since lower manufacture costs [2–5]. In modern circuits design, signal traces usually cross the slotted ground plane due to dense circuit layout. Therefore, split reference plane is used between different power planes with different dc levels. When a signal trace cross the slotted or split reference plane that the return path can't flow directly across the slot [6]. Although using differential pair has better immunity to slotted reference plane, in DDR memory module, we can't use it to solve slotted ground plane issue. A longer return path increases inductance values that it causes impedance discontinuity and radiated emission. The impedance discontinuities would degrade the signal quality and cause the signal integrity (SI) problem. On the other hand, crosstalk is one noise source in PCBs and is of particular concern in high-density and high-speed circuits, is one major source of noise to interfere with SI [7]. A very high coupling coefficient caused by a coupled microstrip lines crossing slotted ground plane is, therefore, to form serious crosstalk coupled to the other victim lines [8]. In which, crosstalk can be aggravated because return path coupling is increased. Figure 1 shows coupled microstrip lines crossing the slotted reference plane.

Using a short bridge connecting between two split reference planes is an effective method. Although the bridge can provide a shortened return current path, these two split planes have different power levels and should be isolated at dc can be destroyed [5]. Using decoupling capacitors to connect split reference plane to replace shorting bridges is now mostly effective techniques in the industry [9]. This method can provide the shortened return path at high frequencies and maintain partition of different power levels. However, effectiveness of this method can be limited due to equivalent series inductance significantly dominates the impedance behavior of a decoupling capacitor at higher frequencies [5].

In this paper, the coupled microstrip lines over the slotted ground plane are investigated. We proposed placing dumbbell resonators to reduce the crosstalk and enhance the signal integrity. The dumbbell resonators can provide an efficient shorting return path between slotted ground plane at high frequencies. This method has no need additional components and it only etch in PCBs easily.

## 2. DUMBBELL RESONATORS

Figure 2 shows the concept of the dumbbell resonators structure on slotted ground plane. A coupled microstrip lines can perpendicularly cross the slotted ground plane ($36 \times 2$ mm). Dumbbell resonators are placed on PCB which consists of four symmetrically located at two sides of the coupled microstrip lines and one located between coupled microstrip lines.

As shown in Figure 2, these dumbbell resonators also cross the slots with two terminals being kept open. Distances between center of the dumbbell resonators and the center of coupled microstirp lines are $S_{dr1}$ to $S_{dr5}$, respectively. The length of the dumbbell resonators are $L_{dr1}$ to $L_{dr5}$, respectively. In which, five dumbbell resonators have same width of two ends and width of center area called $W_{\text{dumbbell}}$ and $W_{drc}$.

In two ends of dumbbell resonators, be formed the parallel capacitances between dumbbell resonators and ground plane without slot area. All of dumbbell resonators reveal the phenomenon of half-wavelength resonances between two terminals with open circuit. These can provide an efficient shorting path between the slotted ground planes at resonant frequency due to return current can through parallel capacitances to form the another return path. The shortened return path has lower inductance effect. In order to expend improved bandwidth, we use different length of dumbbell resonators to cause different resonant frequencies to form the wideband improvement of coupling effects. By adjusting the length, width of dumbbell resonators at both ends, and center width of dumbbell resonators, the resonant frequency could be shifted. Through adjusting parameter, we can shift resonant frequency to interested frequency in different applications.

## 3. EXPERIMENTAL RESULTS

To verify the proposed methodology for NEXT and FEXT improvement, the waveforms of the NEXT and FEXT on victim line are measured. We chose the parameter values as follows: the thickness of the FR4 with dielectric constant 4.4 was 1.6 mm, copper thickness was 0.035 mm, width of microstrip lines were 3 mm, board width was 40 mm, and trace length 80 mm. The dumbbell resonators structure is used to improve NEXT and FEXT, where physical dimension of the dumbbell resonators is shown in Table 1. The operating frequency of most modern electronic products is less than 6 GHz [4]. To validate the theoretical results, we made measurement in the
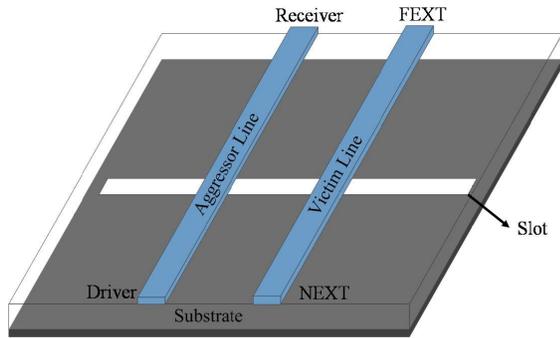


Figure 1: Geometry of the coupled microstrip lines over slotted reference plane.
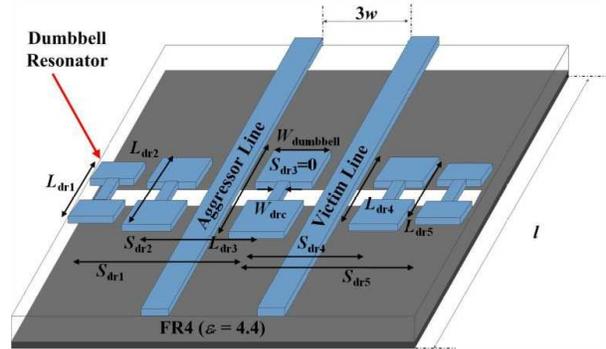


Figure 2: Physical structure of the slotted ground plane with dumbbell resonators.
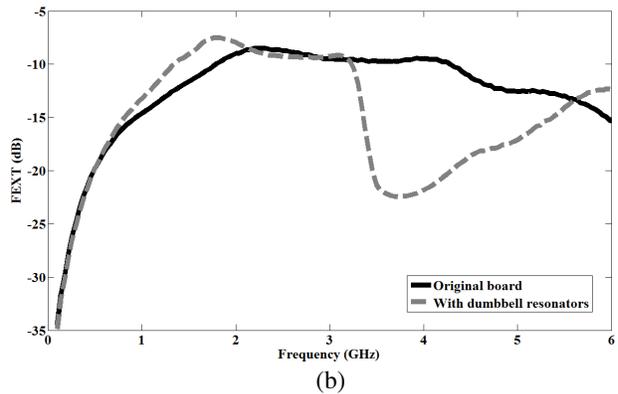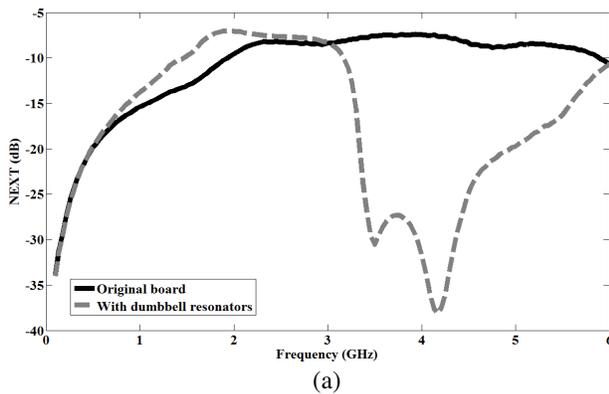


Figure 3: Comparison of crosstalk experimental results in the frequency domain. (a) NEXT. (b) FEXT.

Table 1: Physical dimension of dumbbell resonators.

| Variable | (mm) | Variable | (mm) | Variable | (mm) |
|---|---|---|---|---|---|
| $W_{\text{dumbbell}}$ | 5 | $S_{dr1}$ | 16.5 | $S_{dr2}$ | 11 |
| $S_{dr3}$ | 0 | $S_{dr4}$ | 11 | $S_{dr5}$ | 16.5 |
| $L_{dr1}$ | 10 | $L_{dr2}$ | 14 | $L_{dr3}$ | 18 |
| $L_{dr4}$ | 14 | $L_{dr5}$ | 10 | $W_{drc}$ | 1 |

frequency range from 100 MHz to 6 GHz. Figures 3(a) and 3(b) show the experimental results of NEXT and FEXT in the frequency domains for the original board and with dumbbells resonators structure, respectively. In dumbbell resonators structure, the improved bandwidth of the proposed method from 3 GHz to 6 GHz for NEXT and 3.2 to 5.7 GHz for FEXT, which the coupling noise can be improved in high frequency compared to original board.

## 4. CONCLUSION

A simple generic dumbbell resonators structure is presented to allow effective decreasing crosstalk and improving impedance discontinuities of coupled microstrip lines on slotted ground plane. These experimental results confirmed that our proposed dumbbell resonators structure not only shows better performance, but also no requires extra components to reduce noise significantly. Nonetheless, the proposed approach can get the reduction of magnitude than original board. With the help of new method, we can attain excellent signal integrity.

**REFERENCES**

1. Kim, J., Y. Jeong, J. Kim, J. Lee, C. Ryu, J. Shim, M. Shin, and J. Kim, "Modeling and measurement of interlevel electromagnetic coupling and fringing effect in a hierarchical power distribution network using segmentation method with resonant cavity model," *IEEE Trans. Adv. Packag.*, Vol. 31, No. 3, 544–557, Aug. 2008.
2. Wei, C., F. Jun, R. Yong, S. Hao, J. L. Drewniak, and R. E. DuBroff, "DC power bus noise isolation with power-plane segmentation," *IEEE Trans. Electromagn. Compat.*, Vol. 45, No. 2, 436–443, May 2003.
3. Wu, T. L., H. H. Chuang, and T. K. Wang, "Overview of power integrity solutions on package and PCB: Decoupling and EBG isolation," *IEEE Trans. Electromagn. Compat.*, Vol. 52, No. 2, 346–356, May 2010.
4. Wu, T. L., Y. H. Lin, T. K. Wang, C. C. Wang, and S. T. Chen, "Electromagnetic bandgap power/ground planes for wideband suppression of ground bounce noise and radiated emission in high-speed circuits," *IEEE Trans. Microw. Theory Tech.*, Vol. 53, No. 9, 2935–2942, Sep. 2005.
5. Chuang, H. H. and T. L. Wu, "Suppression of common-mode radiation and mode conversion for slot-crossing GHz differential signals using novel grounded resonators," *IEEE Trans. Electromagn. Compat.*, IEEE Early Access, 2010.
6. Bogatin, E., *Signal Integrity-simplified*, Prentice-Hall, 2003.
7. Kayama, S., M. Sonehara, T. Sato, K. Yamasawa, and Y. Miura, "Cross-talk suppression in high-density printed circuit boards using magnetic composite filled in spacing between signal lines," *IEEE Trans. Magn.*, Vol. 45, No. 10, 4801–4803, Oct. 2009.
8. Ding, T. H., U. S. Li, W. Zhang, X. Yan, and Y. Z. Qu, "Analysis of the crosstalk in electromagnetic band-gap structure," *Proc. Asia Pacific Microw. Conf.*, 657–660, Dec. 2009.
9. Kim, J., H. Lee, and J. Kim, "Effect on signal integrity and radiated emission by split reference plane on high-speed multilayer printed circuit boards," *IEEE Trans. Adv. Packag.*, Vol. 28, No. 4, 724–735, Nov. 2005.

# An Ultra-low-voltage CMOS VCO Using Parallel Capacitor for Phase Noise Reduction

**Chun-Yi Lin**, **Pei-Zong Rao**, **Hsen-Hung Chiu**, **and Shyh-Jong Chung**

Institute of Communication Engineering, National Chiao Tung University, Hsinchu, Taiwan

**Abstract**— In this work, a 7.92 GHz ultra-low-voltage LC-tank voltage controlled oscillator (VCO) is introduced. The proposed LC-tank VCO adopts a NMOS cross-coupled topology and additional parallel capacitors for low voltage operation and phase noise reduction. The measured phase noise at 600 KHz frequency offset is $-98$ dBc/Hz and at 1 MHz offset is $-108$ dBc/Hz, respectively. The proposed VCO achieves a figure-of-merit (FOM) value of $-187$ dBc/Hz, drawing 0.87 mW from a 0.62 V supply. The proposed circuit topology is designed for ultra wide-band (UWB) applications and implemented in TSMC 0.18 μm 1P6M CMOS technology.

## 1. INTRODUCTION

The Federal Communications Commission (FCC) of the United States approved the UWB technology in commercial usage in 2002. Fig. 1 shows the proposed multi-band OFDM (MB-OFDM) UWB frequency synthesizer architecture for Group A, it includes a PLL that generates a 7920 MHz output to a divide-by-15 divider; therefore, 528 MHz quadrature signal mixes with 3960 MHz by single-side-band (SSB) mixer, so that the synthesizer can produce 3 bands for Group A in a MB-OFDM alliance (MBOA) UWB system. The fast frequency synthesizer switches over major of UWB frequency band for the transceiver, in which VCO is the indispensable component [1]. Low power consumption due to battery life and accurate LO frequencies are required.

Several fully integrated CMOS LC-tank VCOs in various CMOS technologies have been demonstrated [2–5]; however, it has to be a trade-off between voltage supply, power consumption, and phase noise when we design the oscillator. In addition, the figure of merit (FOM) calculation is used to score all what we are concerned about, and this work shows the better FOM value than other oscillators in comparison.

## 2. ANALYSIS OF LC VCO

For VCO design, LC tank is a preferred choice in the radio frequency (RF) circuit design because of its good phase noise and low power consumption; however it involves large chip area and narrow frequency tuning range. This LC-VCO oscillator can be simply modeled by $R$, $L$, $C$ components
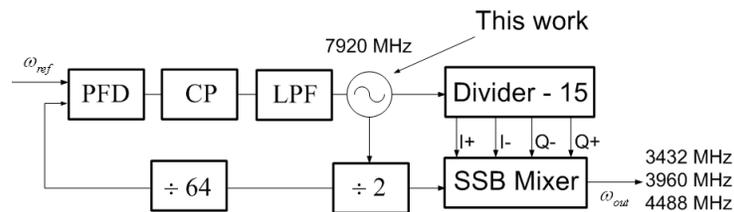


Figure 1: Architecture of proposed UWB frequency synthesizer.



$$R_p = Q_L^2 R_L // Q_C^2 R_C$$
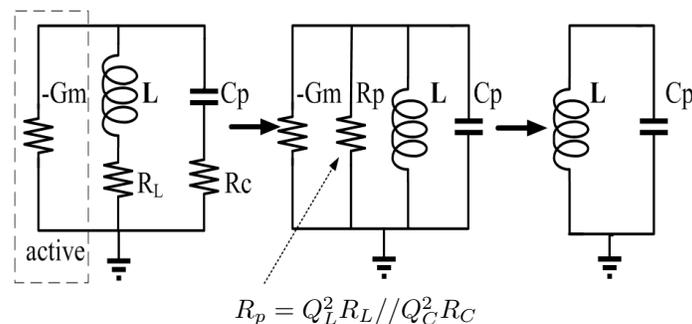
Figure 2: Basic LC-VCO with LC tank and negative conductance.

in Fig. 2. The loss of the LC tank is mainly contributed by the on-chip inductor. The admittance of the LC tank can be described as [6]:

$$Y(j\omega) = \frac{1}{j\omega L} + j\omega C_p + \frac{1}{R_p} - G_m \tag{1}$$

where $R_p$ is the equivalent parallel resistance of the LC tank. At resonance frequency, the real and imaginary part of admittance are both zero, thus $\text{Image}[Y(j\omega_0)] = 0$. The frequency of oscillation ($\omega_0$) is given by

$$\omega_0 \approx \frac{1}{\sqrt{LC_p}} \tag{2}$$

To guarantee the circuit on the oscillation, follows the condition $\text{real}\{Y(j\omega_0)\} \leqq 0$. The negative conductance $-G_m$ should be designed so that

$$G_m \geq \frac{1}{R_p} \approx \frac{1}{R_L Q_L^2} = \frac{1}{(\omega_0 L)Q_L} = \frac{\omega_0 C}{Q_L} \tag{3}$$

For the cross-coupled differential pair which the single ended impedance $-G_m$ is equal to $-g_m$ The power consumption of the VCO core circuit can be given by

$$P_{Loss} = V_{DD} \times (I_{M1} + I_{M2}) = 2V_{DD}I_{M1} \tag{4}$$

where $I_{M1}$ and $I_{M2}$ are the current cross transistors $M1$ and $M2$,

$$I_{M1} = \frac{1}{2}\mu_n C_{ox}\frac{W}{L}(V_{GS} - V_T)^2 = \frac{1}{2}\frac{g_m^2}{\mu_n C_{ox}\frac{W}{L}} \tag{5}$$

where $\mu_n$ is the NMOS mobility of charge carriers and $C_{ox}$ is the oxide capacitance per unit area. The VCO is a symmetric circuit so that $I_{M1}$ is equal to $I_{M2}$. Therefore $P_{Loss}$ can be derived as

$$P_{Loss} = V_{DD}\frac{g_m^2}{\mu_n C_{ox}\frac{W}{L}} = \frac{V_{DD}}{\mu_n C_{ox}\frac{W}{L}}\frac{C}{LQ_L^2} \tag{6}$$

from which the higher inductor quality value $Q_L$ and larger inductor to capacitor ratio will lead to lower power loss of the VCO. The standard inductor has higher $Q_L$ but larger size than symmetrical one, it is trade-off between chip area and power consumption.

Phase noise is defined as the ratio between the carrier power and the noise power at a frequency offset from the carrier, $\Delta\omega$, and it also can be seen as the inverse of Signal-to-Noise Ratio (SNR). So an RF system needs higher SNR means that the oscillator needs better phase noise performance. And the phase noise can is modified in [7]:

$$L(\Delta\omega) = 10\log\left[KTR_{eff}(1+F)\left(\frac{\omega_0}{\Delta\omega}\right)^2\frac{1}{V_{rms}^2}\right] \tag{7}$$

where the effective resistance $R_{eff}$ is given by

$$R_{eff} = R_c + R_l + \frac{1}{R_p \cdot (\omega_0 C)^2} \tag{8}$$

The effective model of capacitor that used in the circuit is an ideal capacitor series with a small resistance. This work parallels capacitors $C_8$ and $C_9$ to VCO core circuit additionally in order to decrease the capacitor resistance $R_c$. From (7) illustrates that reduce $R_{eff}$ can lower the phase noise.

## 3. THE CIRCUIT DESIGN OF THE PROPOSED VCO

The circuit topology and die microphotograph of the proposed LC-tank VCO fabricated by 0.18 μm TSMC CMOS process are shown in Fig. 3 and Fig. 4. The die size of VCO is 680 μm × 530 μm. This circuit is composed of two parts: active circuits and passive circuits. The VCO core is composed of NMOS cross-coupled pair supplying negative resistance. The oscillation frequency can be decided
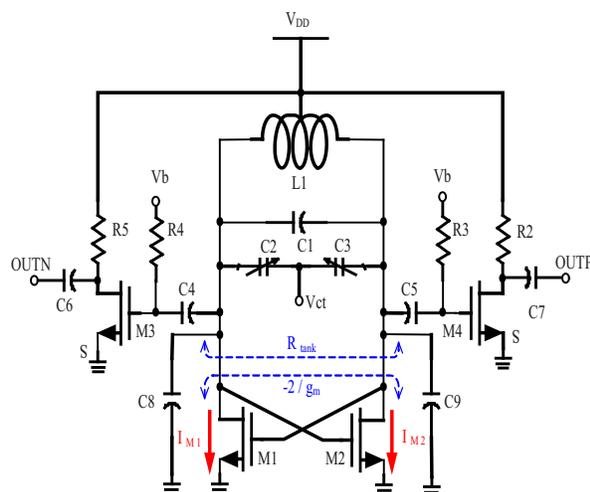
Figure 3: Schematic of the ultra-low-voltage VCO.
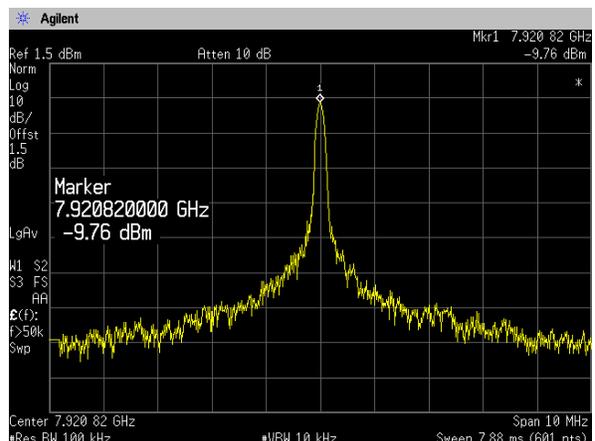


Figure 4: The spectrum output of the 7.92 GHz VCO.

by (2). Considering resonance circuit, the tank inductors utilizes a thick top metal. The resistivity of inductor substrate has been increased in order to reduce substrate loss and improve quality factor [8]. Compared with the traditional spiral circuit, under the same inductance value condition, the symmetric inductor has higher Q value and smaller size. Deciding the width and inductance value firstly in design flow will lead to better performance.

Adopting accumulation mode varactor, as it is a MOS transistor in accumulate region. No electronic hole will be injected into MOS channel; therefore, it has higher quality and wider adjustable range as compared to the MOS in inversion region [9]. Active Port framework can be categorized into three types: complementary cross-coupled pair, PMOS cross-coupled pair, and NMOS cross-coupled pair [10]. In order to operate at low supply voltage, we have comparison among the different cross-coupled pairs. First, PMOS cross-coupled pair provides input negative impedance in low frequency range, but in high frequency range circuit behavior deviates to power sinking load resulting in output loss. Second, PMOS cross-coupled pair has lower transconductance than NMOS cross-coupled pair in the same frequency range. This will result in more parasitic capacitance, lowering varactor capacitance value, and restraining adjustable range. Third, PMOS cross-coupled pair has the limit to larger head room, which will lead to output signal amplitude decrease. Finally, Complementary cross-coupled pair has two sets of bias voltage respectively, thus it cannot be applied to low-voltage mode. Based on the reasons above, this research adopts NMOS cross-coupled pair for active port framework of the low voltage VCO. The buffer transistor $M_3$ ($M_4$) with a resistor $R_5$ ($R_6$) is employed to achieve output matching for testing purposes.

In order to improve the phase noise characteristic and avoid increasing power consumption for larger amplitude, we aim to the enhancement of LC-tank quality. Adding capacitors $C_8$ and $C_9$ in transistor $M_N$ between source and drain, the Q value of LC-tank can be enhanced and get better performance on phase noise [11]. If we do not add the additional capacitors ($C_8$, $C_9$) but use the source and drain transistor parasitic capacitor ($C_{gs}$) instead, we can not lower the equivalent conductance of LC-tank owing to the limited negative conductance and the capacitor value. It restrains the Q value from increasing. Therefore, we may obtain the enhanced Q value of LC-tank by adding larger additional capacitor to compensate for shortage of utilizing transistor parasitic capacitor.

## 4. MEASUREMENT RESULTS

A common drain NMOS buffer is adopted for the VCO measurement. A 13.5 GHz Agilent E4445A PSA series spectrum analyzer is employed for free-running mode VCO output spectrum and phase noise measurements. The measured oscillation frequency with 7.92 GHz is shown in Fig. 5 and the measured phase noise is $-108$ dBc/Hz at 0.34 V tuning voltage. The power consumption of the VCO core circuit is 0.87 mW with 0.62 V supplied. The carrier frequency can be tuned from 7.71 GHz to 8.01 GHz, achieving 300 MHz tuning range with carrier frequency at 7.92 GHz under
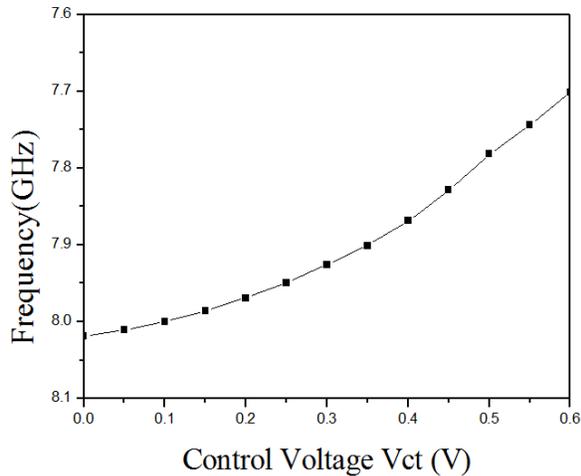
Figure 5: The frequency tuning range of the 7.92 GHz VCO.
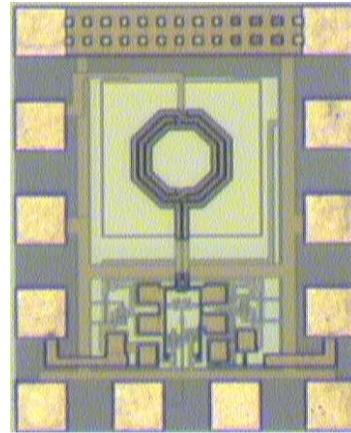


Figure 6: Die photograph of VCO.

varied control voltage from 0 V to 0.62 V, which is depicted in Fig. 6. The FOM is defined as:

$$FOM = L(\Delta\omega) - 20\log\left(\frac{\omega_0}{\Delta\omega}\right) + 10\log\left(\frac{p}{1mW}\right) \tag{9}$$

where $L(\Delta\omega)$ is the phase noise at $\Delta\omega$ offset frequency from $\omega_0$ the carrier frequency, and $P$ is the power dissipation of the VCO core. The measured value of FOM is 187 at 0.62 V supply voltage.

## 5. CONCLUSIONS

The ultra-low-power LC-tank VCO with NMOS cross-coupled pair and cross-paralleled capacitor structure has been presented. By usage of 0.62 V to produce 7.92 GHz oscillation signal output, the phase noise is −108 dBc/Hz at 1 MHz frequency offset. The power consumption of VCO core circuit draws only 0.87 mW and FOM value is −187 dBc/Hz. The proposed LC-tank VCO could be employed in MB-OFDM UWB frequency synthesizer architecture for Group A.

## ACKNOWLEDGMENT

**REFERENCES**

1. Lee, J. and D. W. Chiu, "A 7-band 3–8 GHz frequency synthesizer with ins band-switching time in 0.18 μm CMOS technology," *IEEE Int. Solid-State Circuits Conf. Dig. Tech. Papers*, 204–205, San Francisco, CA, USA, Feb. 2005.
2. Hsieh, H. H., K. S. Chung, and L. H. Lu, "Ultra-low-voltage mixer and VCO in 0.18 μm CMOS," *IEEE RFIC Symp. Dig.*, 167–170, Long Beach, CA, USA, Jun. 2005.
3. Hsu, M. T., C. Y. Chiang, and T. Y. Chih, "Design of low power with low phase noise of VCO by CMOS process," *Proc. IEEE Asia Pacific Microwave Conf.*, Suzhou, China, Dec. 2005.
4. Linten, D., L. Aspemyr, W. Jeamsaksiri, J. Ramos, A. Mercha, S. Jenei, S. Thijs, R. Garcia, H. Jacobsson, P. Wambacq, S. Donnay, and S. Decoutere, "Low-power 5 GHz LNA and VCO in 90 nm RF CMOS," *Symp. VLSI Circuits Dig. Tech. Papers*, 372–375, Honolulu, Hawaii, USA, Jun. 2004.
5. Berny, A. D., A. M. Niknejad, and R. G. Meyer, "A wideband low-phase-noise CMOS VCO," *Proc. IEEE Custom Integrated Circuits Conf.*, 555–558, San Jose, CA, USA, Sep. 2003.
6. Luong, H. C. and Gerry C. T. Leung, "*Low-Voltage CMOS RF Frequency Synthesizers*, Cambridge, 2004.
7. Craninckx, J. and M. Steyaert, "Low-noise voltage-controlled oscillators using enhanced LC-tanks," *IEEE Trans. on Circuits and Systems II*, Vol. 42, No. 12, 794–804, 1995.
8. Burghartz, J. N. and B. Rejaei, "On the design of RF spiral inductors on silicon," *IEEE Trans. Electron Devices*, Vol. 50, No. 3, 718–729, Mar. 2003.

9. Andreani, P. and S. Mattison, "On the use of MOS varactors in RF VCOs," *IEEE J. Solid-Satate Circuits*, Vol. 35, No. 6, 905–910, Jun. 2000.
10. Zhan, J. H. C., J. S. Duster, and K. T. Kornegay, "A comparative study of MOS VCOs for low voltage high performance operation," *IEEE Int. Symposium on Low Power Electronics and Design*, 244–247, Newport, CA, USA, 2004.
11. Do, M. A., R. Zhao, K. S. Yeo, and J. G. Ma, "1.5 V 1.8 GHz band pass amplifier," *Proc. IET Circuits, Devices and System*, 331–333, Dec. 2000.

# Research for RFID Tag Implementation in Vehicle Environments

**Shih-Chung Tuan**[1], **Hsi-Tseng Chou**[2], **and Shih-Peng Liang**[2]

[1]Department of Communication Engineering, Oriental Institute of Technology, Pan-Chiao, Taiwan
[2]Department of Communication Engineering, Yuan Ze University, Chung-Li 320, Taiwan

**Abstract**— In this paper we study UHF RFID for applications under the vehicle environment and faced problems characteristic. RFID applications for the vehicle identified and electronic charging system in the expressway, pass in and out administrative system, number plate management and parts of car such as burglar-proof system have extensive using and develop prospectively. In above described to consider on the basis of convenience and cost down, the passive tag in vehicle environment are adopted. For example: number plate on the vehicle body's location that is in large-scale metal environment. Inside windshield of the car that is semi-closed metal environment. These environments for propagation characteristic of RFID system are damaging and interfere with and then will influence the range employed. The solution proposed simulation and measurement analyzing and according with the industry technical application of current RFID then developed the applicable products (Tag). To reach static and dynamic behavior detected for vehicle environment that the application category of RFID increased.

## 1. INTRODUCTION

This paper is to study the application of the radio frequency identification (RFID) system with UHF to automotive environments, and also to study the problems in the application. In the future, RFID in the car-mounted system can be applied to the highway electronic identification charges, car park entrance management system, car plate management and vehicle body (parts) identification and theft. These applications can prospectively be further developed in the future and create economies of scale. In these applications mentioned above, due to convenience and cost factors, passive tags are mostly used in an automotive environment (for example: if passive tags are placed on vehicle bodies or on car plates, they are in a large metal environmental condition [1–4]; however, if passive tags are placed inside windshields, they are in a semi-enclosed metal environmental condition). Nevertheless, these environments are destructive and interfering in the RFID's transmission characteristics, and thus will affect the scope of application. The methods and the results of this study are not only academic but also practical, with enhancement in the application to the RFID industry. This paper explores and identifies problems and proposes solutions, using simulation and quantitative analysis combined with the existing RFID technology. This study furthermore develops suitable products (Tag) and technology integration to achieve the purpose of the application of the RFID in automotive environments to dynamic (high/medium/low speed) reading identification.

## 2. DESIGN OF THE WINDSHIELD RFID TAG AND PERFORMANCE VERIFICATION

With the application of the UHF radio frequency identification automotive systems, we have conducted the Windshield RFID Tag design and performance testing Passive Windshield RFID Tag Design Indicator as Table 1. The design of the Windshield RFID Tag must take both the physical and chemical properties of the marker into account to successfully produce the functions of identification and communication in close proximity to markers. A complete design can therefore be applied to practical areas. The Windshield RFID Tag is designed for the purpose of being attached to windshields. The RFID Tag is a variable impedance device in which IC impedance changes with frequency. Thus, a Loop structure is adopted to connect IC, combining with Coupling Dipole to design dipole antenna. The length of $\lambda/4$ of Dipole with Meander Line can help match Chip impedance. Windshield RFID Tag Structure As shown in Figure 1 the RFID Tag is not like usual antenna design in which $-10\,\mathrm{dB}$ reflection loss is used. The industry standard is generally $-3\,\mathrm{dB}$ to $-5\,\mathrm{dB}$. For broadband or the short-distance reading RFID tag, the standard is $-3\,\mathrm{dB}$; and for narrowband or the remote reading RFID tag, the standard is $-5\,\mathrm{dB}$. In the simulation of the RFID Tag, the $S_{11}$ is $-3\,\mathrm{dB}$ at $915\,\mathrm{MHz}$. However. In physical testing, the Tag needs to be enclosed with paper material to become Label where the frequency will be shifted to low frequency by $20$–$40\,\mathrm{MHz}$. Therefore, the RFID simulation pre-design needs to be shifted at higher frequency. After actual performance testing and verification, the maximum effective reading distance and the radiation pattern of this model of Windshield RFID Label meet the requirements of our experiments.

| Item | Design Indicator | Explanation |
|------|------------------|-------------|
| 1 | Frequency | 902MHz~928MHz |
| 2 | Impedance match | Monza 3 Chip Set impedance match equivalent model |
| 3 | Tag making procedure | Aluminium etches making procedure |
| 4 | Antenna size and Type | Inlay Size:88.6×17.25mm Meander Line/Dipole/Folded/loop Coupling |
| 5 | Parameters | glass/Inlay $\varepsilon_r$ fine tune |
| 6 | Antenna gain | >1dBi @center frequency |
| 7 | Effective distance | >4M |

Table 1: Passive windshield RFID tag design indicator.
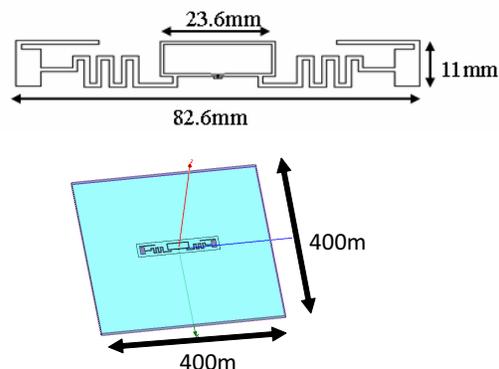


Figure 1: Windshield RFID tag structure.
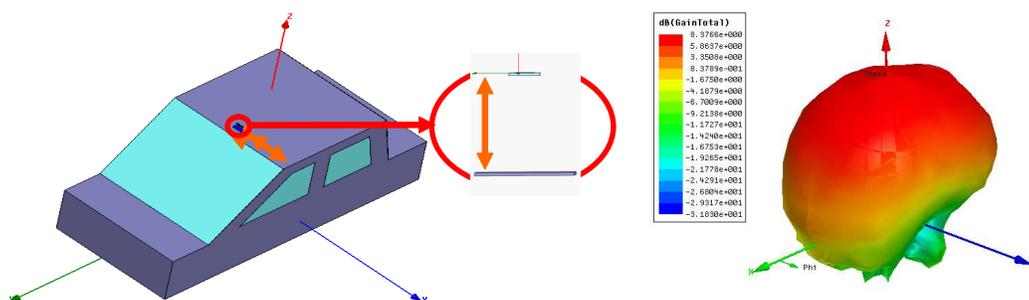


Figure 2: Top position of a car in which the tags are attached to car body and tag antenna 8.37 dBi at 920 MHz radiation pattern.

## 3. SIMULATION OF THE APPLICATION OF RFID IN THE AUTOMOTIVE ENVIRONMENT

First, we construct the model of the car-body environment and simulated of the RFID tag, which is specifically designed for the present study and attached to car body, to observe how the radiation pattern of the RFID tag. Second, to verify whether the simulated RFID tag's radiation pattern is accurate, we scale the car body structure down by one sixth and scale the operating frequency up by a sixfold up to 5.5 GHz, to simulate each of the parameters and implement 5.5-GHz antenna. In addition, we take measurement with the spherical measuring system of the anechoic chamber, and compare and verify the numerical results. The purpose of the present experiment is to study how the RFID Tag attached to car body changes, and observe how Tag's radiation pattern and reading distance change with different car body environments. The positions in which the Tags are attached to car body are: (1) the windshield position (inside car body), (2) the car plate position (outside car body), (3) the top position of a car (outside car body), and (4) the car door position (outside car body). Because the primary structure of car body is composed of large metals, the metal car body certainly affects the RFID Tag's characteristics and its performance [1–4]. Therefore, we construct the model of car-body structure, simulations with different positions of the Tag mentioned above and observe how the Tag's radiation pattern changes (as shows in Figure 2). A miniaturized model of car body structure is about 651 mm in length, about 284 mm in width, and about 250 in height. We use Styrofoam to make up the frame of car body and attach copper foil to the outer surface of the car body structure to simulate the metal properties of car body. In order to consist with the simulation of large real car discussed in the last paragraph: (1) we implement the simplified 5.5-GHz omni-directional dipole antenna design to correspond to the omni-directional Windshield RFID Tag (the use of the windshield position); (2) we implement the simplified 5.5 GHz directional patch antenna design to correspond to directional tag antenna (the use of the car plate position/the top position of a car/the car door position) (as shown in Figures 3 and 4). After simulation and verification, the change of the radiation pattern and the radiation directions of the tag antenna on the model of the real car body are consistent with that of the 5.5-GHz antenna on the model of the miniaturized car body as Table 2.

Table 2: Directional patch antenna simulation and measurement.

| Radiation Gain Pattern @5500MHz (dBi) | | |
|---|---|---|
| Antenna Type | Simulation | Measurement |
| 5.5G omni-directional antenna | 3.43 | 2.28 |
| 5.5G directional antenna | 8.27 | 7.122 |

| Radiation Gain Pattern @5500MHz (dBi) | | |
|---|---|---|
| Tag attached position | Simulation | Measurement |
| Windshield position(1) | 9.24 | 7.46 |

| Radiation Gain Pattern @5500MHz (dBi) | | |
|---|---|---|
| Tag attached position | Simulation | Measurement |
| car plate position(2) | 8.38 | 6.61 |

| Radiation Gain Pattern @5500MHz (dBi) | | |
|---|---|---|
| Tag attached position | Simulation | Measurement |
| top position of a car(3) | 8.86 | 6.71 |
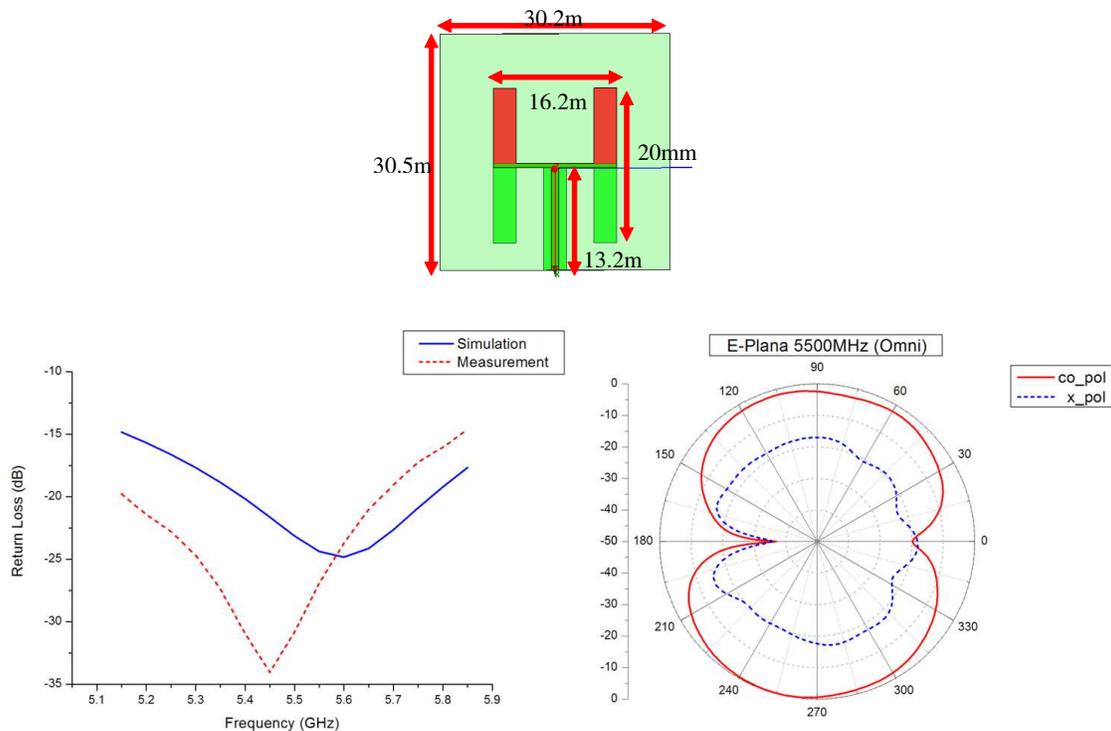


Figure 3: 5.5 GHz omni-directional dipole antenna design.

## 4. DYNAMIC TEST OF THE APPLICATION OF RFID IN THE AUTOMOTIVE ENVIRONMENT

We conduct an automotive dynamic reading test with the UHF radio frequency identification system, including constructing the framework of the gate system, measuring the tag antenna used, measuring and analyzing the field intensity of the gate system. Furthermore, we conduct tests with vehicles at a speed of 20 km, 40 km, and 60 km per hour [5]. In the tests, we demonstrate that the windshield RFID tag and the gate reading system can be applied to real vehicle dynamic reading. The test analyses show that the test label (1) (the Windshield RFID Label) has the maximum reading distance of 4.85–5.15 M in the windshield background environment; the test label (2) (the metal label) has the maximum reading distance of 4.85–5.53 M in the automotive metal environment; and the test label (3) (the common label) has the maximum reading distance of 4.48–5.61 M in the context of automotive plastic parts. All of the reading distances are within 4 and 5 M, and the reading radiation pattern also meet the required goals. We thus attach these tags to car body to conduct a dynamic test with real vehicles. We conduct dynamic testing with the

RFID tag attached to car body. When tags are located at different positions, in order to improve the tags' reading levels, constructing a gate system is needed to produce a reading zone as shown in the Figure 5. We expect the tags in different positions passing through the reading zone can detect all tags. Therefore, the design of testing the gate system and sufficient radiation power of its reading zone are very import. As shown in the Figure 6, the field intensity of 0.5 m–1.5 m away from the gate is relatively high. Regardless of the left, right, high or low position, the field intensity is above −8 dBm. Most of the tags can be read in this zone. We conduct a test with a dynamic running vehicle. The vehicle passes through the gate reading system respectively at a speed of 20 km, 40 km, and 60 km per hour. We record the tag reading status from nine positions on the vehicle. With each speed, we conduct the dynamic reading tests ten times to observe the stability of the dynamic reading of the gate system. The test results are shown in a histogram. As shown in the results of the field intensity test and analysis, the dynamic reading gate system designed and constructed for the present experiment has stable radiation energy at about 0.5–1.5 m. Besides, for the included tests of the metal tag and our Windshield Tag, the metal tag on the car plate and the windshield tag can be stably read in repeated tests of running vehicles at a speed of 60 km per hour.
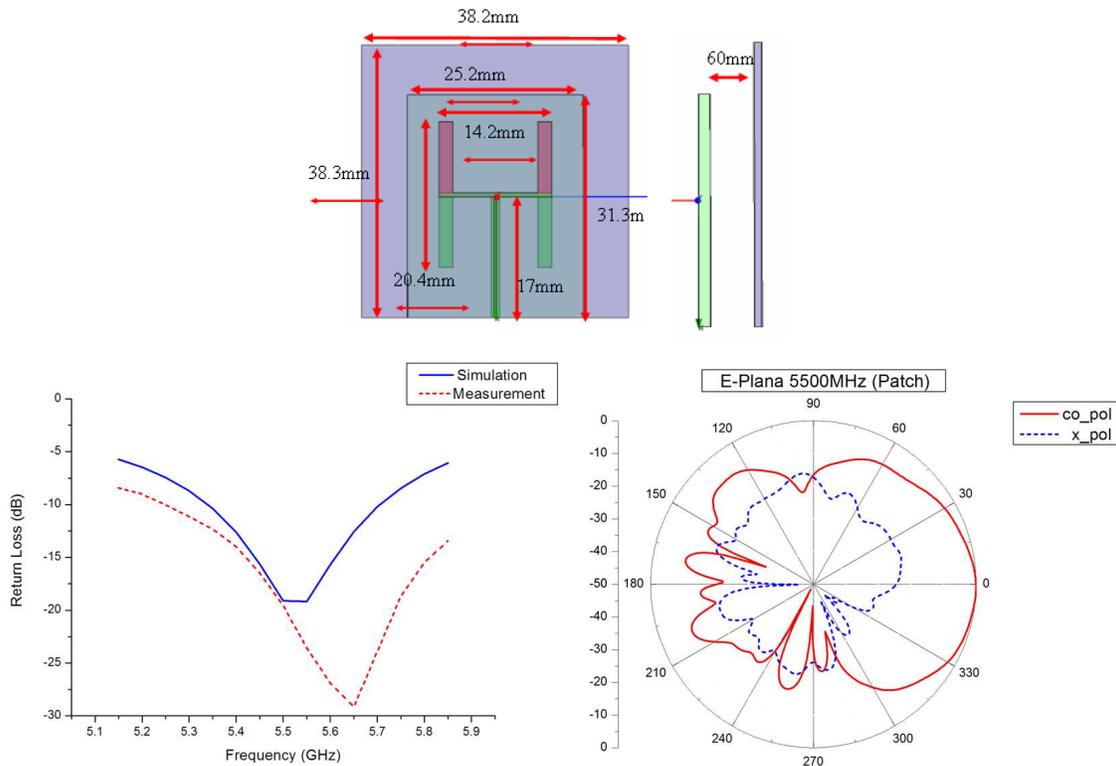


Figure 4: 5.5 GHz directional patch antenna design.
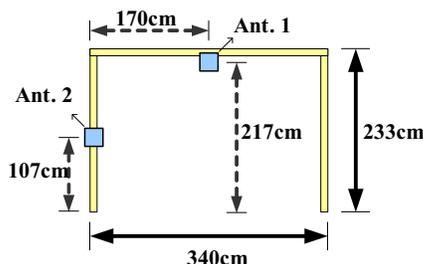


Figure 5: RFID dynamic test gate system.
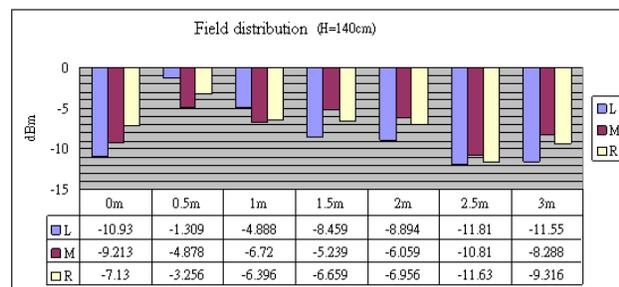


Figure 6: Field intensity distribution ($H = 140$ cm).

| | 0m | 0.5m | 1m | 1.5m | 2m | 2.5m | 3m |
|---|---|---|---|---|---|---|---|
| L | -10.93 | -1.309 | -4.888 | -8.459 | -8.894 | -11.81 | -11.55 |
| M | -9.213 | -4.878 | -6.72 | -5.239 | -6.059 | -10.81 | -8.288 |
| R | -7.13 | -3.256 | -6.396 | -6.659 | -6.956 | -11.63 | -9.316 |

## 5. CONCLUSIONS

The two major cores are the Windshield RFID Tag designed for the present experiment and the RFID dynamic gate reading system. For the Windshield RFID Tag attached to the upper center position of a windshield, we test its performance of the tag dynamic reading. We also test and analyze the field intensity of the dynamic gate reading system, and find that it has stable radiation energy at about 0.5–1.5 m. For a running vehicle, the Windshield tag can be stably read in repeated tests at a speed of 60 km per hour.

**REFERENCES**

1. "UHF Gen2 STRAP," DataSheet RI-UHF-STRAP-08, Texas Instruments Incorporation.
2. Seshagiri Rao, K. V., P. V. Nikitin, and F. L. Sander, "Antenna design for UHF RFID tags: A review and a practical application," *IEEE Transactions on Antennas and Propagation*, Vol. 53, No. 12, 3870–3876, December 2005.
3. Nikitin, P. V. and K. V. Seshagiri Rao, "Theory and measurement of backscattering from RFID tags," *IEEE Antennas and Propagation Magazine*, Vol. 48, No. 6, 212–218, December 2006.
4. Lu, C.-S., "Characteristic investigation on the UHF passive RFID tag design when it is pasted on a large metal body," Master Thesis, Department of Communications Engineering, YZU, June 2009.
5. Impinj Incorporation. "SPEEDWAY RFID REDER (IPJ-R1000) User Guide," RFID Reader (IPJ-R1000) User Guide, http://www.impinj.com/support/downloadable_documents.aspx# Speedway Reader.

# Second Harmonic Reduction of Miniaturized Dual-mode Microstrip Bandpass Filters Using Fractal Shaped Open Stub Resonators

**Jawad K. Ali and Hussam Alsaedi**

Department of Electrical and Electronic Engineering, University of Technology, Baghdad, Iraq

**Abstract**— Higher harmonics normally accompany the performance of bandpass filers; and the miniaturized microstrip dual mode bandpass filters are not an exception. The use of the conventional open stub resonator to reduce such harmonics is not a practical solution since it has a length of a quarter the guided wavelength at the harmonic frequency. This will make the miniaturized filter larger. In this paper, the use of a fractal based open stub, with high space filling property, has been investigated as a more practical solution of the 2nd harmonic reduction of the miniaturized dual mode bandpass filters. The proposed stub has the Peano fractal shape geometry which is characterized by its high space-filling property. The Peano based stub has been applied to many miniaturized filter reported in the literature. Modeling and performance evaluation of the presented filters have been carried out using a full-wave electromagnetic EM simulator, from Sonnet Software Inc. Simulation results show that the introduction of the proposed stub maintains the physical size of the filter under test and improves the filter performance by reducing the harmonics to satisfactory levels. This might presents a solution for second harmonic reduction of a wide variety of miniaturized dual mode bandpass filters with different miniaturization levels.

## 1. INTRODUCTION

Dual-mode microstrip bandpass filters based on square ring resonators have been widely used in microwave applications because of their attractive features such as compact size, high selectivity, and simple design. An additional challenge has been added; this filter has to meet the ever increasing need to produce miniaturized circuits. Consequently, many techniques have been proposed to design compact dual-mode filters. However, the conventional square ring resonator filters and their miniaturized variants suffer from the spurious harmonics which need to be suppressed. Numerous techniques have been proposed for harmonic suppression of the dual mode resonator microstrip bandpass filters [1–10].

Spur lines [1–3] and open stubs [4–6] have been adopted as frequency notched structures at the input and/or the output of the dual mode bandpass filter as widely used technique to suppress or reduce the second harmonic. Other techniques, such as the use of corrugated couplers [7, 8], periodic loading inside the ring resonator [9], the defected ground plane [10], have also been proposed to meet this task. The open stub method has been proved to be a good solution for second harmonic suppression of the conventional square ring resonator filters. This method is opposed by the compactness requirements, when the square resonator is being reduced in size by applying the shape modification techniques, as in the case of applying the different fractal geometries [11–13] to produce compact filter design.

In this paper, the application of a fractal shaped open stub has been proposed for the suppression of the second harmonic of the miniaturized dual-mode ring resonator based bandpass filters. It is hopeful that the proposed fractal open stub, due to the space-filling property the fractal shape possesses, will solve the conflict between the size reduction gained from shape modification of the square ring resonator based filters and the harmonics normally accompanying their performances.

## 2. THE PEANO FRACTAL GEOMETRY

The Peano curve was, in fact, the first set of space-filling curves [14]. One interesting feature of the Peano-curve algorithm is that it has a relatively higher compression rate than other fractal curves in filling a 2-D region, which, consequently, suggests that the Peano resonator may resonate at a lower fundamental resonant frequency than the others. The steps of growth of the Peano fractal curve, up to the 3rd iteration, have been outlined in Figure 1.

For a Peano resonator, made of a thin conducting strip in the form of the Peano curve with side dimension $S$ and order $n$, the length of all the line segments $L(n)$ is given by [14]

$$L(n) = (3^n + 1)S \tag{1}$$

The open stub has been thought of as a series bandstop filter or frequency-notched structure in the input/output microstrip lines of the dual-mode bandpass filter. However, adding a conventional
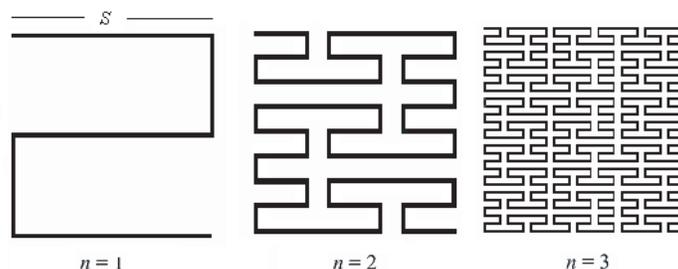
Figure 1: The first three iteration levels of the Peano fractal curve generation process.
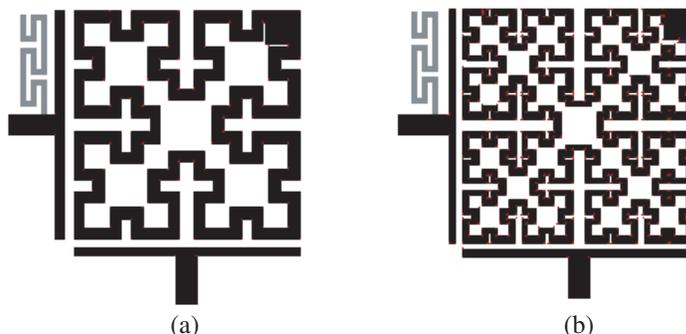


Figure 2: The modeled dual-mode microstrip bandpass filter structures with the Peano shaped open stubs connected at their inputs.

open stub will act against compact filter design. Instead, we think that replacing this with a fractal shaped open stub of high space-filling property, such as Peano fractal curve, will maintain both filter miniaturization and harmonic suppression.

## 3. THE PROPOSED HARMONIC SUPPRESSION METHOD

The proposed Peano shaped open stub has been applied on two dual-mode fractal based microstrip ring resonator filter structures reported in one of the author's work [11], as two case studies, to demonstrate the validity of the proposed method as depicted in Figure 2. These resonators are fractally generated based on the second and third iteration Minkowski-like pre-fractal curves, and have been designed for the ISM band applications at 2.4 GHz. The filter structures have been supposed to be etched using a substrate with a relative dielectric constant of 10.8 and thickness of 1.27 mm. The input/output ports are with 50 Ω characteristic impedance. The resulting dimensions of these filters are of about 8.05 and 6.05 mm respectively.

Filter structures, depicted in Figures 2(a) and 2(b), have been modeled and analyzed at the design frequency, using a full-wave electromagnetic EM simulator, from Sonnet Software Inc. [15]. Open stub resonators, based on sections of Peano second iteration structures as shown in Figure 1, have to be added at the inputs of the two filters. The required harmonic reduction has been reached after suitable dimension scaling of the stub lengths and observing the resulting filter responses. Figures 3 and 4 show the transmission responses of the two filters with and without the proposed stub resonators. The resulting transmission performance, shown in Figure 3, for the filter structure depicted in Figure 2(a) without the open stub, exhibits a second harmonic at 4.4 GHz. Adding the Peano shaped open stub at the input of this filter, results in a reduction of the related second harmonic to a level of more than −10 dB.

It is clear that the addition of the stub affects only the second harmonic and maintains the required filter fundamental frequency performance unchanged. In addition, the resulting filter size with the stub added has only been slightly changed. On the other hand, the resulting performance of the filter structure depicted in Figure 2(b), without the open stub, shows a second harmonic at 4.1 GHz, as shown in Figure 4. Adding the Peano shaped open stub at the input of this filter, results in a second harmonic reduction to a level of more than −10 dB.

For the dual-mode filter depicted in Figure 2(a), it has been found the Peano resonator side
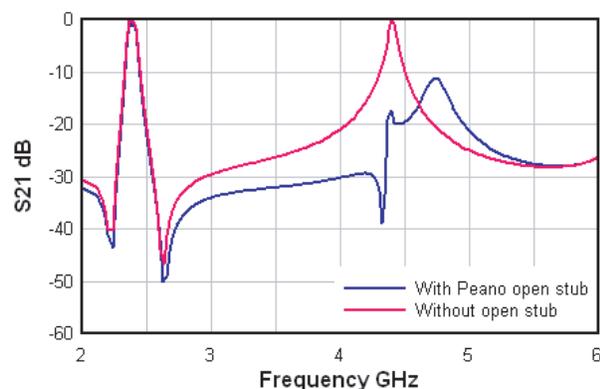
Figure 3: The transmission responses of the filter depicted in Figure 2(a) with and without the Peano shaped open stub resonator.
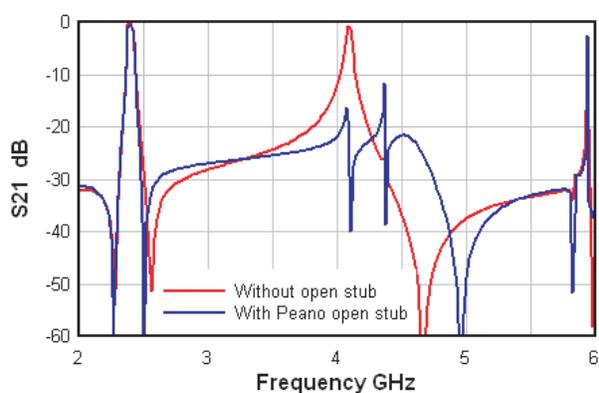


Figure 4: The transmission responses of the filter depicted in Figure 2(b) with and without the Peano shaped open stub resonator.

length is equal to 3.9 mm, which represents 0.083 the guided wavelength, $\lambda_g$ which is calculated as

$$\lambda_g = \frac{\lambda_\circ}{\sqrt{\varepsilon_{\text{eff}}}} \qquad (2)$$

While the corresponding stub length for the filter depicted in Figure 2(b), is of about 2.78 mm which represents $0.59\lambda_g$.

## 4. CONCLUSION

A Peano fractal shaped open stub has been proposed in this paper in an attempt to reduce the second harmonic of the miniaturized dual-mode ring based microstrip bandpass filters. The Peano based stub has been applied to two miniaturized filters reported in the literature. Modeling and performance evaluation of the presented filters have been carried out using a full-wave electromagnetic EM simulator, from Sonnet Software Inc. Simulation results show that the introduction of the proposed stub almost maintains the physical size of the filters under test and improves the filter performance by reducing the harmonics to satisfactory levels. It is hopeful that the proposed method is useful in the miniaturized UWB antenna design as a simple means to create the required notch in the antenna response.

## REFERENCES

1. Karacaoglu, U., D. Sanchez-Hernandez, I. D. Robertson, and M. Guglielmi, "Harmonic suppression in microstrip dual-mode ring-resonator bandpass filters," *Proceedings of IEEE MTT-S International Microwave Symposium Digest*, San Francisco, USA, Jun. 1996.
2. Griol, A., J. Marti, and L. Sempere, "Microstrip multistage coupled ring bandpass filters using spur-line filters for harmonic suppression," *Electron. Lett.*, Vol. 37, No. 9, 572–573, Sep. 2001.
3. Hu, W., T. Yoshimasu, and H. Liu, "A novel dual-mode square loop passband filter with second spurious passband suppression," *Proceedings of 2006 International Conference on Communications, Circuits and Systems*, Guilin, Jun. 2006.
4. Huang, X. D. and C. H. Cheng, "A novel microstrip dual-mode bandpass filter with harmonic suppression," *IEEE Microwave and Wireless Components Lett.*, Vol. 16, No. 7, 404–406, 2006.
5. Noori, A. A., "A novel microstrip dual-mode band-pass filter for harmonic suppression," *Engineering and Technology*, Vol. 28, No. 11, 2207–2211, 2010.
6. Jeon, B.-K., H. Nam, K.-C. Yoon, B.-W. Jeon, Y.-W. Kim, and J.-C. Lee, "Design of a patch dual-mode bandpass filter with second harmonic suppression using open stubs," *Proceedings of Asia-Pacific Microwave Conference*, Yokohama, Dec. 2010.
7. Sewter, J. and C. E. Saavedra, "Microstrip ring resonator using slow wave structure exhibiting harmonic suppression," *Proceedings of International Symposium on Antenna Technology and Applied Electromagnetics, ANTEM*, Montréal, Canada, Jul. 2002.
8. Fraresso, J. and C. E. Saavedra, "Narrowband bandpass filter exhibiting harmonic suppression," *Electron. Lett.*, Vol. 39, No. 16, 1189–1190, Aug. 2003.

9. Wang, Y.-Z., C.-A. Wang, and K.-Y. Lin, "Miniaturized dual-mode quasi-elliptic function bandpass filter with wide rejection bandwidth," *Proceedings of Asia-Pacific Microwave Conference*, Yokohama, Dec. 2006.

10. Leong, C. C., S. W. Ting, and K. W. Tam, "Multi-spurious suppression for microstrip dual-mode bandpass filter using triple $U$-shaped defected ground structure," *Proceedings of IEEE Asia Pacific Conference on Circuits and Systems*, Macao, Nov. 2008.

11. Ali, J. K., "A new miniaturized fractal bandpass filter based on dual-mode microstrip square ring resonator," *Proceedings of the 5th International Multi-conference on Signals, Systems and Devices, IEEE SSD'08,* Amman, Jordan, Jul. 2008.

12. Ali, J. K., "A new fractal microstrip bandpass filter design based on dual-mode square ring resonator for wireless communication systems," *Iraqi Journal of Applied Physics, IJAP*, Vol. 5, No. 1, 7–12, 2009.

13. Hettstedt, F., T. Lehmann, and R. Knoechel, "Novel dual-mode microstrip bandpass filter," *IEEE Microwave Mag.*, Vol. 10, No. 1, 155–157, 2009.

14. Zhu, J., A. Hoorfar, and N. Engheta, "Peano antennas," *IEEE Antenna and Wireless Propagation Lett.*, Vol. 3, 71–74, 2004.

15. *EM User's Manual*, Version 11.0, Sonnet Software, Inc., Mar. 2007.

# Coupled-line Bandpass Filters Using Mixed Half-wave and Quarter-wave Resonators with Improved Out-of-band Response

**Shih-Cheng Lin and Chi-Wen Hsieh**

Department of Electrical Engineering, National Chiayi University, Chiayi City 60004, Taiwan, R.O.C.

**Abstract**— This study presents a thorough design methodology, including the concept discussion and detailed design formulas to design coupled-line filters utilizing both half-wave and quarter-wave resonators. With careful derivations of the design equations, open-ended parallel and short-ended anti-parallel coupled-line sections may be used with arbitrary coupled lengths. The wide rejection band is principally contributed by the simultaneous utilization of mixed half-wave and quarter-wave resonators in the implemented circuit. Specifically, a 3rd-order bandpass filter centering at $1\,\mathrm{GHz}$ with fractional bandwidth $9.48\%$ is implemented for validating the described concept. The stopband with satisfactory rejection level of $33\,\mathrm{dB}$ up to $8.69f_0$ has been accomplished in the sample filter. This is a good achievement in improving out-of-band response with such simple structure. The experimental results are well-predicted by full-wave simulations.

## 1. INTRODUCTION

Parallel-coupled bandpass filters (BPFs) constructed with half-wavelength ($\lambda/2$) parallel-coupled-line (PCL) sections are pretty attractive due to the features of easy realization in planar circuits, simple design procedure and moderate realizable bandwidth [1]. In addition, those filters based on $\lambda/4$ PCL sections [2–4] have become more and more popular due to the size reduction and superior out-of-band performance. As well known, $\lambda/2$ PCL filters fabricated by inhomogeneous transmission line (TL) technology possess their first spurious passband around two times of center frequency ($f_0$) due to the inherent resonant nature of $\lambda/2$ resonators. However, those filters composed of $\lambda/4$ uniform stepped-impedance resonators (UIRs) possess higher-order harmonics occurring around $(2n+1)f_0$ ($n = 1, 2, \ldots$). Thus, by making good use of $\lambda/4$ resonators, one may make less effort of implementing a filter with better out-of-band rejection. In the past years, various attempts have been made to design microwave filters with good out-of-band response by either simply suppressing the unwanted passbands [5] or pushing the spurious response higher [6]. For the later method, the 1st spurious passband may be pushed up to roughly at most $5f_0$ by a deformation of the line width using the SIRs [7] to avoid transverse resonance. Therefore, it is of great importance to find alternative approaches in order to efficiently tackling the spurious issues. Special techniques have been discovered and proposed to improve the out-of-band performance, such as taking advantage of uniplanar compact photonic-bandgap (UC-PBG) structure in a microstrip BPF to extend the stopband [8], modified version of coupled-line filter introducing microstrip gaps to create a transmission zero (TZs) was reported to suppress the spurious harmonic at $2f_0$ [9], by means of proper tappings at both input and output resonators to introduce TZs exactly at the spurious frequencies, By using various dissimilar $\lambda/4$ stepped-impedance resonators [10], and etc..

In comparison with the spurious-suppression method discussed so far, in this research, a novel coupled-line BPF based on mixed utilization of $\lambda/2$ and $\lambda/4$ SIRs is proposed and investigated in detail. Without losing the simple design procedure of classical PCL filters, the complete design formulas are derived to facilitate the procedure. The schematic layout of 3rd-order filter is shown in Fig. 1 in advance. As can be seen, this specific filter is composed of $\lambda/2$ and $\lambda/4$ SIRs with parallel and anti-parallel coupled lines as coupling stages. Since the harmonic resonances of $\lambda/2$ and $\lambda/4$ SIRs except for the fundamental one are well misaligned, the stopband is extended up to $8.69f_0$ without demanding SIRs possessing large impedance difference.

## 2. SIRS AND COUPLED-LINES

### 2.1. Stepped-impedance Resonators (SIRs)

The basic resonating components of the proposed filter are two different SIRs exhibited in Fig. 2. The both types of SIR are all composed of two TL sections of different line widths for different characteristic impedances. The resonant condition can be obtained by manipulating the input impedance of the SIRs:

$$R_z = \tan\theta_1 \cdot \tan\theta_1, \text{ where } R_z = Z_2/Z_1 \text{ is the impedance ratio of SIR.} \tag{1}$$
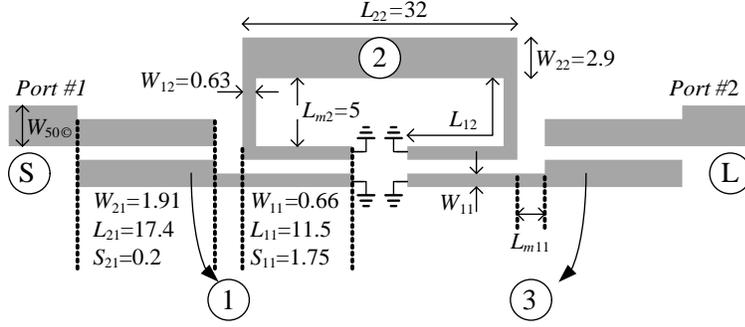
Figure 1: The schematic layout of the proposed 3rd-order microstrip coupled-line filter using mixed $\lambda/2$ and $\lambda/4$ SIRs.
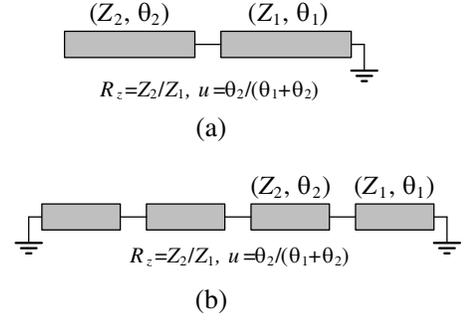
Figure 2: The utilized stepped-impedance resonators: (a) $\lambda/4$ open-ended SIR. (b) $\lambda/2$ short-ended SIR.
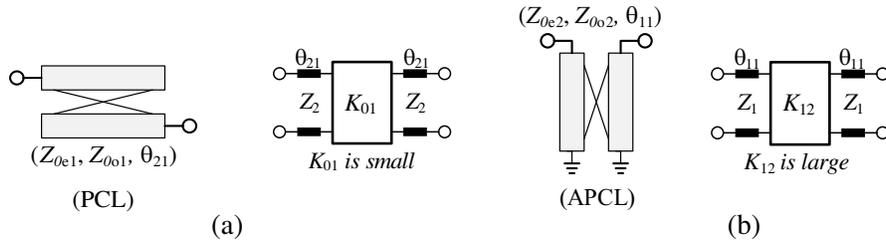


Figure 3: The main building blocks of the filter: (a) Open-ended PCL. (b) Short-ended APCL.

Due to the boundary condition, only odd-mode resonances exist in $\lambda/4$ SIRs. However, both odd- and even-mode resonances can be found in $\lambda/2$ SIRs. For design convenience, both types of the adopted SIRs have been chosen with $R_z = 2\,(\Omega/\Omega)$, $Z_1 = 50\,\Omega$, $Z_2 = 100\,\Omega$, $u = 0.5$ as design parameters. If both SIRs have their fundamental resonances at $f_0 = 1\,\text{GHz}$, the $\lambda/4$ SIRs will resonate under odd-mode condition while the $\lambda/2$ ones will resonate at both even- and odd-mode conditions. As a result, the calculated electrical lengths $\theta_1$ and $\theta_2$ under resonance will be $35.26°$ and the frequency ratio of the first higher order resonant frequency to the fundamental frequency $(f_{sp1}/f_0)$ is 4.1 times.

### 2.2. Parallel and Anti-parallel Coupled Lines

After determining the resonating components in the filter, one may need to design the coupling stages which are parallel and anti-parallel coupled lines here. Displayed in Figs. 3(a) and 3(b) are the interested PCL and APCL sections for interstage coupling, respectively. For the open-ended PCL section in Fig. 3(a), it may be modeled as an impedance inverter with two TL sections of image impedance $Z_2$ attached on opposite sides. With $K_{01}$ as the required impedance-inverter value, one may calculate the corresponding even- and odd-mode impedances by

$$Z_{0e1} = -\frac{2Z_2 \sin(\theta_{21})\left[K_{01} \cdot Z_2 + \left(K_{01}^2 + Z_2^2\right)\sin(\theta_{21})\right]}{-K_{01}^2 + Z_2^2 + \left(K_{01}^2 + Z_2^2\right)\cos(2\theta_{21})} \tag{2a}$$

$$Z_{0o1} = -\frac{2Z_2 \sin(\theta_{21})\left[-K_{01} \cdot Z_2 + \left(K_{01}^2 + Z_2^2\right)\sin(\theta_{21})\right]}{-K_{01}^2 + Z_2^2 + \left(K_{01}^2 + Z_2^2\right)\cos(2\theta_{21})}. \tag{2b}$$

As for the short-ended APCL section shown in Fig. 3(b), with $K_{12}$ as the required impedance-inverter value and $Z_1$ as the image impedance, the corresponding even- and odd-mode impedances are given by

$$Z_{0e2} = Z_1 + K_{12}\csc(\theta_{11})\sec(\theta_{11}) \text{ and } Z_{0o2} = Z_1 - K_{12}\csc(\theta_{11})\sec(\theta_{11}) \tag{3}$$

With the converion equations from inverter value to corresponding even- and odd-mode impdeances of coupled-line sections, the two coupling strctures can now be employed as parts of filter design.
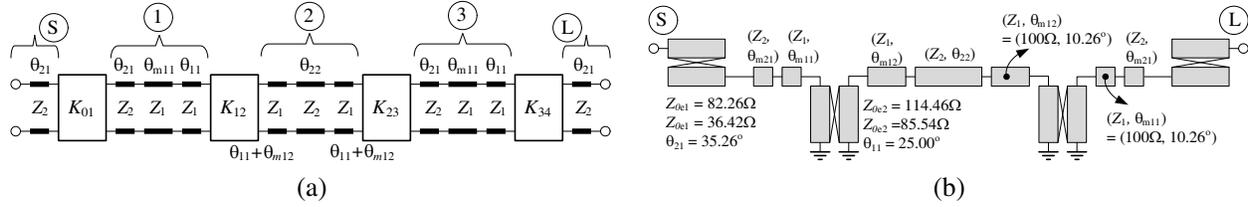
Figure 4: The equivalent circuit model of the proposed BPF using mixed half-wave and quarter-wave resonators. ($\theta_{m21}$ is about zero while $\theta_{m11}$ and $\theta_{m12}$ are about 10.26° for layout convenience).

## 3. FILTER DESIGN AND IMPLEMENTATION

### 3.1. BPF Design

The schematic layout of the proposed filter has been shown in Fig. 1 in advance. After understanding all the aforementioned design parameters which will be incorporated in our filter design, the proposed BPF design may be launched. The equivalent-circuit model of the proposed filter may be concluded as Figs. 4(a) and (b). Resonators 1 and 3 are two identical $\lambda/4$ SIRs due to structure symmetry while resonator 2 is $\lambda/4$ SIR. Both types of coupled-line sections are modeled as impedance ($K$) inverters accordingly.

In designing a parallel-coupled BPF, one needs to determine the filter specification first. Without losing generality, a 3rd-order BPF with center frequency of $f_0$ and fractional bandwidth of $\Delta$ will be designed for 0.1 dB ripple Chebyshev response. The related inverter values for the given filter specification may be obtained by

$$(K_{01})^{-1} = (K_{34})^{-1} = \sqrt{\frac{Y_0 \cdot \Delta \cdot b_{SC,\lambda/4}}{g_0 g_1}} \quad \text{and} \quad K_{12} = K_{23} = \sqrt{\frac{\Delta^2 \cdot x_{OC,\lambda/4} \cdot x_{SC,\lambda/2}}{g_1 g_2}}, \quad (4)$$

where $Y_0$ is the system port characteristic admittance and $\{g_0, g_1, g_2, g_3, g_4\}$ are the corresponding lowpass prototype parameters. Notably, several slope parameters in (4) have to be carefully defined in order to acquire the proper design parameters. In Equation 4(a), $b_{SC,\lambda/4}$ indicates the susceptance slope calculated by the input admittance of the adopted $\lambda/4$ resonator seen from the open end. In Equation 4(b), $x_{OC,\lambda/4}$ indicates the reactance slope calculated by the input impedance of the adopted $\lambda/4$ resonator seen from the short-circuited end with the other end kept open-circuited while $x_{SC,\lambda/2}$ represents the reactance slope calculated by the input impedance of the $\lambda/2$ resonator seen from the short-circuited end with the other end kept short-circuited. Because the simultaneous use of $\lambda/4$ and $\lambda/2$ SIRs, the resonances of resonators 1, 3 and those of resonator 3 are successfully misaligned at even-mode resonance. Besides, the inherent TZs contributed by the PCL and ACPL sections are properly designed at odd-mode resonances. Thus, at those unwanted spurious resonances (spurious even- and odd-mode resonances), weak electromagnetic coupling may travel through the coupling path. One may expect the proposed filter has good stopband performance.

### 3.2. BPF Implementation

For demonstration and validate the discussion, a 3-pole sample filter based on the abovementioned procedure is fabricated on the low-cost FR4 board ($\varepsilon_r = 4.4$, $h = 1.58$ mm, $\tan \delta = 0.02$). The grounding via hole is drilled by the 0.6 mm-diameter bit and filled with the conductive liquid silver to provide good connecting capability. The related element values for the three-pole lowpass prototype filter with 0.1 dB ripple Chebyshev response are $\{g_0, g_1, g_2, g_3, g_4\} = \{1, 1, 2, 1, 1\}$. The BPF with center frequency $f_0$ of 1 GHz and fractional bandwidth $\Delta$ of 9% is going to be designed. The utilized two $\lambda/4$ SIRs 1 & 3 and one $\lambda/2$ SIR 2 are all designed with the same impedance ratio $R_z = 2$ (characteristic impedances $Z_1$ of 100 Ω and $Z_2$ of 50 Ω) and length ratio $u = 0.5$. Therefore, the calculated SIR electrical lengths $\theta_1$ and $\theta_2$ are both identically equal to 35.26°. The calculated design parameters corresponding for the prescribed 3rd-order filter response are thus $K_{01} = K_{34} = 212.44$ Ω, $K_{12} = K_{23} = 5.54$ Ω, respectively. Applying the inverter values and the desired coupled-line lengths into Equations (2) and (3), the required even- and odd-mode impedances can be obtained and are all annotated in Fig. 4(b). The geometric dimensions of final fabricated circuit are accordingly provided in Fig. 1. Note that the dimensional sizes have been fine-tuned by full-wave simulator for optimized filter response. As a result, the measured/simulated transmission and reflection coefficients are illustrated in Fig. 5. The measured center frequency is at
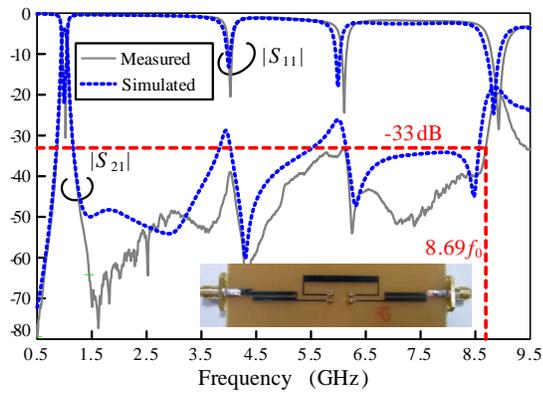
Figure 5: Measured/simulated results of the proposed coupled-line filter using mixed $\lambda/2$ and $\lambda/4$ resonators.
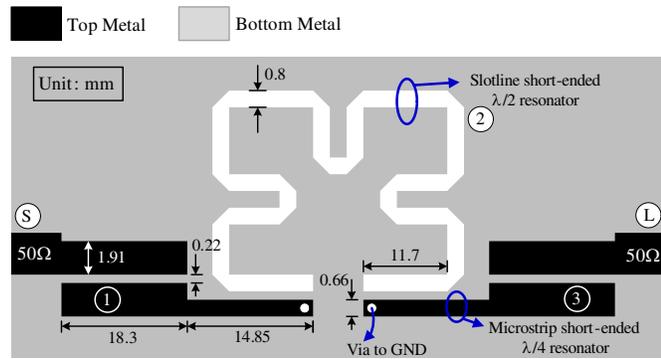


Figure 6: Alternative coupled-line filter with microstrip coupled-line sections and composite microstrip-slotline CPL sections using $\lambda/2$ and $\lambda/4$ resonators.

1.005 GHz, the measured fractional bandwidth is about 9.48%, and the in-band minimum insertion loss is 4.48 dB. Remarkably, the stopband extends up to $8.69 f_0$ with rejection level of 33 dB.

Alternatively, the filter may be implemented by composite microstrip-slotline structure as shown in Fig. 6. The simultaneous usage of microstrip and slotline resonators facilitates the filter design and further extends the CPL to composite structure. The main design issue lies on finding the equivalent CPL parameters (even- and odd-mode impedances). Due to the limited space for this article, the design idea and implementation results of the novel filter will be included in the future research paper.

## 4. CONCLUSION

Theoretical design approach for the parallel-coupled BPF using mixed $\lambda/4$ and $\lambda/2$ SIRs is carefully investigated. The complete design equations are derived in detail. The alternative utilization of open-ended PCL and short-ended APCL provides the design flexibility when using different types of resonators as resonating components. Benefiting from the simultaneous use of $\lambda/4$ and $\lambda/2$ SIRs, the electromagnetic coupling at those spurious harmonics are significantly reduced. The proposed approach can be extended to higher-order filter design since the given design concept are general. The presented filter may find application in modern microwave communication systems which demand wide out-of-band rejection for suppressing the unwanted interferences.

## ACKNOWLEDGMENT

## REFERENCES

1. Cohn, S. B., "Parallel-coupled transmission-line-resonator filters," *IEEE Trans. Microwave Theory Tech.*, Vol. 6, 223–231, Apr. 1958.
2. Chang, K. F. and K. W. Tam, "Miniaturized cross-coupled filter with second and third spurious responses suppression," *IEEE Microwave Wireless Compon. Lett.*, Vol. 15, 122–124, Feb. 2005.
3. Sagawa, M., M. Makimoto, and S. Yamashita, "Geometrical structures and fundamental characteristics of microwave stepped-impedance resonators," *IEEE Trans. Microwave Theory Tech.*, Vol. 45, 1078–1085, Jul. 1997.
4. Lee, S.-Y. and C.-M. Tsai, "New cross-coupled filter design using improved hairpin resonators," *IEEE Trans. Microwave Theory Tech.*, Vol. 48, 2482–2490, Dec. 2000.
5. Chang, K. F. and K. W. Tam, "Miniaturized cross-coupled filter with second and third spurious responses suppression," *IEEE Microwave Wireless Compon. Lett.*, Vol. 15, 122–124, Feb. 2005.
6. Kuo, J.-T., "Parallel coupled microstrip filters with suppression of harmonic response," *IEEE Microwave Wireless Compon. Lett.*, Vol. 15, 383–385, Oct. 2002.
7. Sagawa, M., M. Makimoto, and S. Yamashita, "Geometrical structures and fundamental characteristics of microwave stepped-impedance resonators," *IEEE Trans. Microwave Theory Tech.*, Vol. 45, 1078–1085, Jul. 1997.

8. Yang, F.-R., K.-P. Ma, Y. Qian, and T. Itoh, "A uniplanar compact photonic-bandgap (UC-PBG) structure and its applications for microwave circuits," *IEEE Trans. Microwave Theory Tech.*, Vol. 47, 1509–1514, Aug. 1999.

9. Chang, C.-Y. and T. Itoh, "A modified parallel-coupled filter structure that improves the upper stopband rejection and response symmetry," *IEEE Trans. Microwave Theory Tech.*, Vol. 39, 310–314, Feb. 1991.

10. Lin, S.-C., P.-H. Den, Y.-S. Lin, C.-H. Wang, and C. H. Cheng, "Wide-stopband microstrip bandpass filters using dissimilar quarter-wavelength stepped impedance resonators," *IEEE Trans. Microwave Theory Tech.*, Vol. 54, No. 3, 1011–1018, Mar. 2006.

# Design of K-band CMOS Frequency Divider Integrating a Marchand-type Transformer

**Sen Wang and Chen-Chin Lin**

Department of Electronic Engineering, National Taipei University of Technology, Taipei, Taiwan

**Abstract**— In this paper, a design of K-band frequency divider integrating a Marchand-type transformer based on 0.18-µm RF CMOS process is presented. The edge-coupled transformer is used to characterize and to provide differential signals for the CML frequency divider. The amplitude imbalance between $S_{21}$ and $S_{31}$ of the transformer is negligible below 35 GHz, and the phase imbalances are within 2° from 5 GHz to 33 GHz. Moreover, the insertion losses of the transformer are less than 6 dB from 21 GHz to 34 GHz. The 16 : 1 frequency divider formed by four 2 : 1 CML stages works correctly at entire K band with a total power consumption of 25 mW.

## 1. INTRODUCTION

Frequency dividers are used commonly in phase-locked loops (PLLs) and high-speed synthesizers [1]. Typically, flip-flop-based or current-mode logic (CML) frequency dividers operating beyond 20 GHz consume high power consumption even based on the low-cost and low-power CMOS processes [2, 3]. Moreover, large voltage swings, or input sensitivity are required to drive the frequency dividers correctly. Theses frequency dividers are implemented on advanced 0.12-µm bulk or silicon on insulator (SOI) CMOS processes for high-speed logic operations. A CML frequency divider features wide bandwidth and differential input characteristics. Therefore, in order to characterize the CML frequency divider, a broadband and single-to-differential balun or transformer must be included in the measurement set-up. However, the balun is not accessible easily, especially at high frequencies. Moreover, planar CMOS transformers suffer high loss due to the low-resistivity silicon substrate [4]. Therefore, most on-chip transformers are realized on high-resistivity GaAs substrate [5].

In this paper, we propose the block diagram of the frequency divider integrating a Marchand-type transformer as shown in Figure 1. The transformer and four 2 : 1 CML stages are designed based on TSMC 0.18-µm one-poly six-metal (1P6M) RF CMOS process. The broadband transformer consisting two coupled lines is achieved by a high coupling coefficient in an edge-coupled layout. Therefore, the electrical performance of the frequency divider is characterized and calibrated by the transformer with a compact chip size, wide bandwidth, and acceptable loss at K band. Moreover, the operating frequency of the divider covers the entire K band with low power consumption, and the output signals are close to square waveforms which are applicable to low-frequency logic circuits. The design will be detailed in the following sections. In Section 2, the circuit design and the Marchand-type transformer of the circuits will be discussed. And the simulated results are also reported in Section 3. Finally, Section 4 concludes this work.

## 2. CIRCUIT DESIGN

Figure 2 shows the 2 : 1 static frequency divider based on the master-slave D-type flip-flop (DFF) connecting the slave outputs and the master inputs. The differential property reduces the switching
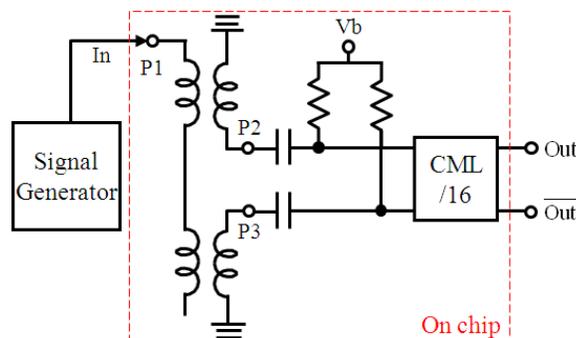


Figure 1: Block diagram of the frequency divider measurement set-up.

noise and power line noise. The CML can operate at low power supply and high voltage swing due to the omission of the tail current of $M_1$ and $M_2$, though it requires a large input sensitivity to drive itself. Moreover, $M_7$ and $M_8$ work in the linear region lowering the RC time constant, hence the operating frequency of the CML is increased at the same power consumption. Four 2 : 1 CML stages are cascaded to form the proposed 16 : 1 frequency divider as shown in Figure 1. Transistors in the 1st stage are sized to work properly at high frequencies with decent input sensitivity, and transistors in other stages are sized to drive the subsequent stage correctly with appropriate dc level and small-signal swing. The aspect ratio of $M_{1-2}$, $M_{3-4}$, $M_{5-6}$ and $M_{7-8}$ in the 1st stage is (64/0.2), (30/0.2), (3/0.2), and (12/0.2), respectively. By increasing the aspect ratio of $M_{1-2}$ and $M_{7-8}$ in the 1st stage, the maximum operating frequency can be increased.

Figure 3(a) shows the coupled-line model with characteristic impedance $Z$ and electrical length $\theta$ of the three-port Marchand-type transformer. The $S_{21}$ and $S_{31}$ in the $3 \times 3$ $S$-parameter matrix of the transformer can be expressed as

$$S_{21} = \frac{(x^3 y - xyz^2 - xy^3)}{z^2(z^2 + y^2)} \tag{1}$$

$$S_{31} = \frac{(xyz^2 + xy^3 - x^3 y)}{z^2(z^2 + y^2)} \tag{2}$$

where $x = \sqrt{1 - k^2}$, $y = jk \sin \theta$, $z = \sqrt{1 - k^2} \cos \theta + j \sin \theta$, and $k$ is the coupling coefficient [6]. Therefore, desired amplitude and phase responses of the transformer can be obtained by designing proper $k$ and $\theta$ from (1) and (2). The symmetrical layout of the Marchand-type transformer using two edge-coupled lines is shown in Figure 3(b). The first coupled line is open-circuited in one end with P1 in the other end. Moreover, the second coupled line is short-circuited at the center with P2 and P3 in the ends. The width and gap of the coupled lines are $4 \, \mu m$ and $2 \, \mu m$, respectively, for low loss and compact chip area considerations. The small line gap of the interleaved layout contributes a high coupling coefficient $k$ ($\sim 0.81$). Moreover, the coupled lines are realized on top
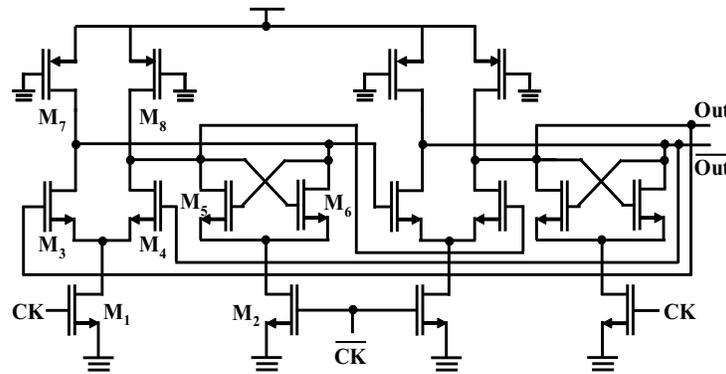


Figure 2: Schematic of the CML.



(a)             (b)
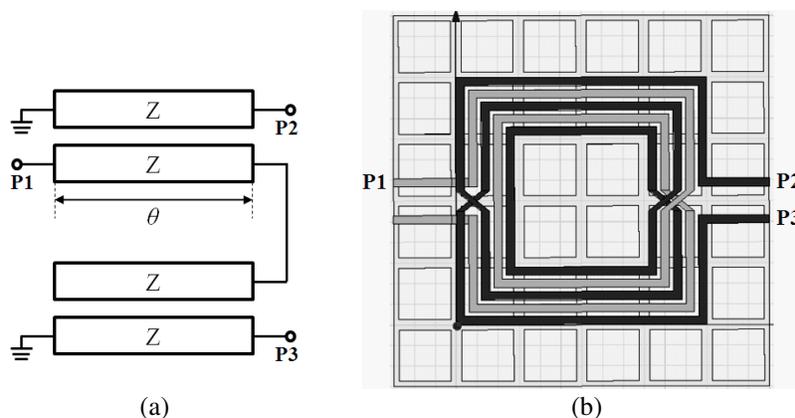
Figure 3: (a) Simplified coupled-line model and (b) symmetrical layout of the Marchand-type transformer.
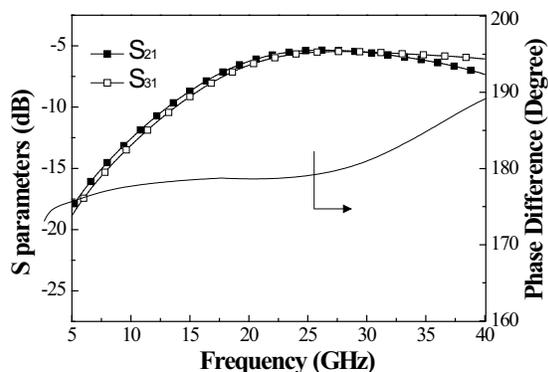
Figure 4: Simulated results of $S_{21}$, $S_{31}$, and phase difference between $\angle S_{21}$ and $\angle S_{31}$.
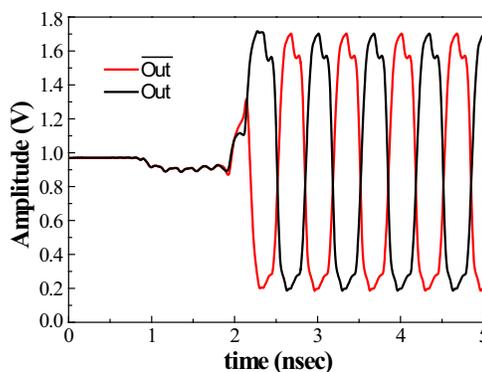


Figure 5: Output waveforms with a 24-GHz, 0-dBm input signal.
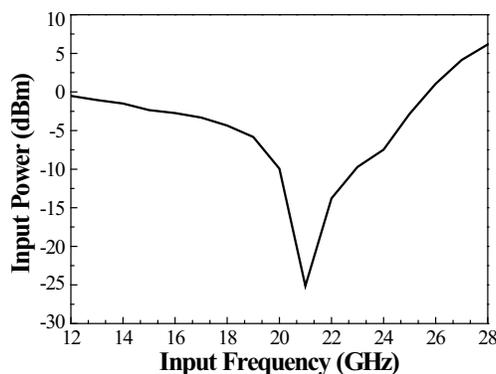


Figure 6: Input sensitivity of the frequency divider.

metal layer ($M_6$) to achieve high $Q$ lines, and a meshed ground plane with a periodicity of 30 μm are realized on bottom metal layer ($M_1$) to cut off induced loop currents. Therefore the low-loss CMOS transformer can be obtained with a compact chip size of 120 μm × 180 μm.

## 3. SIMULATION RESULTS

Post-simulation results of the K-band frequency divider integrating a Marchand-type transformer are based on TSMC 0.18-μm RF CMOS process. The simulated insertion losses and phase difference between $S_{21}$ and $S_{31}$ of the Marchand-type transformer are shown Figure 4. The amplitude imbalance between $S_{21}$ and $S_{31}$ is negligible below 35 GHz due to the symmetrical layout. The insertion losses are less than 6 dB from 21 GHz to 34 GHz. Moreover, the minimum insertion losses are about 5.3 dB at 26 GHz. The phase imbalances are within 2° from 5 GHz to 33 GHz. The strong coupling coefficient leads the compact transformer with a minimal amplitude imbalance and an almost 180° phase difference to work correctly at entire K band.

The overall power consumption of the frequency divider is about 25 mW with a 1.8 V power supply and Vb of 0.7 V which is biased through two 5-kΩ resistors, as shown in Figure 1. Figure 5 shows the output waveforms of the proposed architecture as shown in Figure 1, with a 24-GHz, 0-dBm input signal. There is about 2n seconds propagation time delay from the input port to the output port due to the transformer and the 4-stage CMLs. Moreover, the 1.5 GHz output signal is close to square waveforms between 0.2 V to 1.7 V which is applicable to low-frequency circuits. Finally, the input sensitivity of the frequency divider regardless of the loss of the transformer is shown in Figure 6. The operating frequency of the frequency divider is from 12 GHz to 28 GHz covering the entire K band.

## 4. CONCLUSION

A design of K-band frequency divider integrating a Marchand-type transfomer is presented in this paper. The transformer and the CML frequency divider are design based on 0.18-μm 1P6M RF CMOS process. The edge-coupled transformer with a compact chip size, wide bandwidth and

acceptable loss at K band is used to characterize and to provide differential signals for the CML frequency divider. The 16 : 1 frequency divider is formed by four 2 : 1 CML stages. The first stage is designed mainly for the highest operating frequency and input sensitivity, and the others are designed mainly for driving the subsequent stage correctly with appropriate dc level and small-signal swing. Moreover, the frequency dividers can operates at entire K band with appropriate input sensitivity. The divided output waveforms, or voltage swings are convinced that the frequency divider is suitable for low-frequency circuit applications such as PLLs and synthesizers.

## ACKNOWLEDGMENT

## REFERENCES

1. Craninckx, J. and M. Steyaert, "A 1.8-GHz low-phase-noise voltage-controlled oscillator with prescaler," *IEEE J. Solid-State Circuits*, Vol. 30, 1474–1482, Dec. 1995.
2. Knapp, H., H.-D. Wohlmuth, M. Wurzer, and M. Rest, "25 GHz static frequency divider and 25 Gb/s multiplexer in 0.12-µm CMOS," *ISSCC Dig. Tech. Papers*, 302–303, Feb. 2002.
3. Plouchart, J.-O., J. Kim, H. Recoulers, N. Zamdmer, Y. Tan, M. Sherony, A. Ray, and L. Wagner, "A power-efficient 33 GHz 2 : 1 static frequency divider in 0.12-mm SOI CMOS," *Proc. IEEE RFIC*, 329–323, 2003.
4. Long, J. R., "Monolithic transformers for silicon RFIC design," *IEEE J. Solid-State Circuits*, Vol. 35, No. 9, 1368–1382, Sept. 2000.
5. Lin, C.-S., P.-S. Wu, M.-C. Yeh, J.-S. Fu, H.-H. Chang, K.-Y. Lin, and H. Wang, "Analysis of multiconductor coupled-line Marchand baluns for miniature MMIC design," *IEEE Trans. Microwave Theory and Tech.*, Vol. 55, No. 6, 1190–1199, Jun. 2007.
6. Sachse, K., "The scattering parameters and directional coupler analysis of characteristically terminated asymmetric coupled transmission lines in an inhomogeneous medium," *IEEE Trans. Microwave Theory and Tech.*, Vol. 38, No. 4, 417–425, Apr. 1990.

# Broadband Resistive Active Power Combiner

**B. Ravelo and E. R. Rajkumar**

IRSEEM, EA 4353 at the Graduate School of Engineering ESIGELEC
Av. Galilée, BP 10024, 76801 Saint-Etienne-du-Rouvray Cedex, France

**Abstract**— Till now, most of the power combiners used in microwave engineering is designed with passive circuits. Due to the losses, the application of these passive power combiners is limited. For this reason, our attention is attracted by the development of active power combiner based on the use microwave transistors. This letter addresses an investigation of an active power combiner susceptible to operate in very wide frequency band. Analytical approach illustrating the functioning principle of the active power combiner understudy is established and practical results from a proof of concept were proposed. The theory is mainly focused on the $S$-parameter analysis and followed by synthesis process enabling to determine the power combiner parameters. This latter is based-on the use of simple active cell comprising field effect transistor (FET) in cascade with shunt resistor similarly to resistive amplifier topology. Detailed $S$-parameter theoretic analysis of innovative two-way power combiner is provided. Moreover, according to basic characteristics of used FET, mathematical formulas illustrating how to synthesize each element of power combiner are established. Then, design of broadband active in-phase power combiner capable to operate with unequal gain is performed. For the validation of theoretical prediction, two-way power combiner containing three FETs was designed and simulated by using Advanced Design System (ADS) microwave circuit simulator from Agilent$^{\mathrm{TM}}$. According to the employed PHEMT FET-EC-2612 bias regime, for 3-V DC supply voltage, the simulated power combiner consumes 90 mA. Therefore, interesting results showing insertion gains $|S_{31}|_{\mathrm{dB}}$ and $|S_{32}|_{\mathrm{dB}}$ above 6 dB with very good flatness accompanied by excellent return- and isolation-losses respectively, better than $-10$ dB and below $-20$ dB at all three accesses are obtained from 1 GHz to 9 GHz. Furthermore, by tuning an element of simulated active power combiner, gain control according to proposed analytic formulas is evidenced. In addition, in the indicated frequency range, a good flatness constant ratio, $\lambda = |S_{32}|/|S_{31}| = 1.050 \pm 0.002$ was also found between the two input accesses. Finally, potential applications of the active power combiner proposed are discussed.

## 1. INTRODUCTION

The power combiner (PC) is one of key elements constituting the RF/microwave wired/wireless front-end telecommunication architectures [1–3]. It is particularly useful for adding signals from phased-array receiver for example in satellite communication and radio stations. This microwave device is generally employed for adding two or several high frequency signals from the separated propagation channels [4–6]. This combining function is also frequently found in the high frequency test bench as in radio spectrum area [7, 8]. One quotes the application example of radio testing process and the design of receiver and transmitter spurious emission equipments. The PC can be incorporated also in near-electromagnetic (EM) field measurement RF test benches to associate the signals captivated by the EM-probes [9]. Since some decades earlier, research and development of more performing design techniques of power splitter and combiner have been one of intensive effort subjects of numerous microwave engineers. Recently, by using travellingwave waveguide, microwave structure exhibiting a 15-dB return-loss bandwidth of 15% with a power combining efficiency of approximately 80% was fabricated and published in [10]. More recently, novel topologies of power divider/combiner with variable power dividing ratio [11] and capable to operate simultaneously in dual-band and unequal power dividing were proposed [12]. Nevertheless, these devices were simply implemented with passive structures. So, limitations either in terms of losses or in operating frequency bandwidth were naturally met. So, these losses can distorte considerably the operating signal. This signal degradation is mainly due to the amplitude differences and somehow the phase shifts between the arms of the PCs. Moreover, frequency limitation of about some GHz appears when working with certain topologies like the well-known Wilkinson PC [13, 14] and the classical 6-dB resistive splitter/combiner [15]. Moreover, the most distributed electronic structures are intended to work at frequencies above 4 GHz. In this case, analytical study and control of operating signal amplitude and phase remain difficult to perform because of the undesired and unavoidable spurious effects related to technological fabrication tolerances. In order to deal with this technical limitation, broadband active power-splitter and power-combiner capable to operate up to tens of

GHz and implemented in MMIC technology are introduced in [16, 17]. For compensating loss and control delay of multi-antenna UWB beamforming systems, CMOS distributed active PC providing variable gain and delay is presented in [18]. Moreover, the topology proposed in this document is rather expensive to implement and analytically more complicated.

For this reason, we intend to investigate on the active topology mainly based on the use of active cell composed of FET in cascade with a shunt resistor, $R$. This topology consists of field effect transistor (FET) in cascade with a shunt resistor at the output. In fact, this topology presents a flexibility to operate easily with unequal gain as expected. The main benefits of such topology are the ease of unbalanced effect compensation when considering multi-channel wave propagation medium and also the guarantee of $0°$-outphase between the input- and output-branches. Thanks to the nonreciprocity of FETs, isolation between different branches of PC should be substantially ensured.

This article is structured in three different sections. Section 2 will be consecrated to the analytical study based on the $S$-parameter approach. For that, a three-port active PC is examined. Afterwards, validation results upholding the relevance of theoretic prediction are presented in Section 3. Finally, the conclusion and prospects of this work will be drawn in last Section 4.

## 2. ANALYSIS AND SYNTHESIS OF THE PC TOPOLOGY

Proposed First of all, one points out that for the sake of analytical simplification, the FETs are assumed as its model composed of voltage-controlled current source with transconductance, $g_m$ and associated with a shunt drain-source resistance, $R_{ds}$. Let us consider the three-port PC with two input ports, denoted, 1 and 2, and an output port, 3 schematized in Fig. 1. One can see that this combiner is constituted by three Y-active cells, containing three FETs, formed by the basic cell formed by an FET and a parallel resistance. The two input accesses act also as the gate pins of two upstream transistors whilst the output access corresponds to drain pin of the downstream transistor. To ensure the input matching, shunt resistances, $R_1$ and $R_2$ are connected at the transistor inputs. then, a shunt output resistance, $R_i$ and $R_3$ are also connected to the other transistor for inter-stage and output matchings.

In order to alleviate analytical calculations, one supposes that the FETs of the under study circuit are ideal and unilateral (perfectly isolated, $S_{21} = 0$), identical and having same electrical characteristics, $g_m$ and $R_{ds}$. Meanwhile, the PC of Fig. 2 must present following $S$-parameters. Because of the non-reciprocity hypothesis, certain elements of the equivalent $[S]$-matrix can be calculated independently to others by cutting the circuit with different elementary parts of cells. For example, $S_{11}$-, $S_{22}$- and $S_{33}$-return-loss parameters depend only on the resistances, $R_1$, $R_2$ and $R_3$, respectively. So, analytical calculations allow to demonstrate that they are equal to those of the active basic cells separately written as:

$$S_{11,22} = (R_{1,2} - Z_0)/(R_{1,2} + Z_0), \tag{1}$$

and

$$S_{33} = [R_3(R_{ds} - Z_0) - Z_0 R_{ds}]/[R_3(R_{ds} + Z_0) + Z_0 R_{ds}], \tag{2}$$

with $Z_0$ is the reference impedance (here, equal to $50\,\Omega$). Therefore, one establishes the following detailed expressions of $S_{31}$- and $S_{32}$-transmission parameters:

$$S_{31,32} = \alpha R_{1,2}/(Z_0 + R_{1,2}), \tag{3}$$
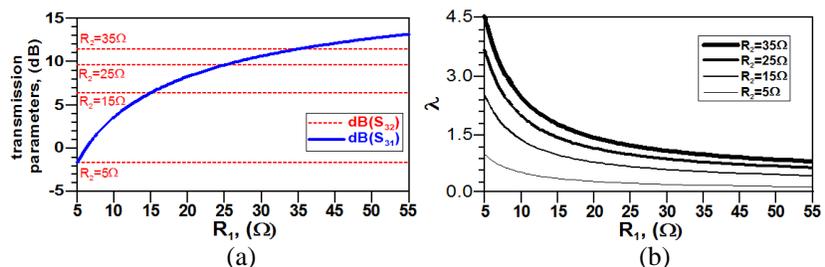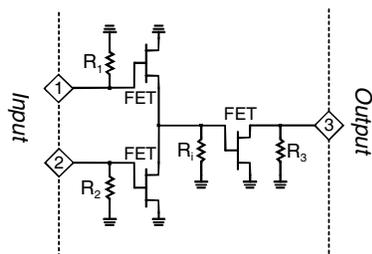


Figure 1: Active PC with three Y-active cells.

Figure 2: (a) $|S_{31}|_{dB}$ and $|S_{32}|_{dB}$, and (b) $\lambda$ versus $R_1$ and $R_2$ for $g_m = 100\,\text{mS}$, $R_{ds} = 100\,\Omega$ and $R_i = 36\,\Omega$.

where

$$\alpha = 2g_m^2 R_{ds}^2 Z_0 R_i R_3 / \left\{ (2R_i + R_{ds})[Z_0(R_3 + R_{ds}) + R_3 R_{ds}] \right\}. \tag{4}$$

Fig. 3 materialize an example of graphical interpretation of above expressions of transmission parameters, $S_{31}$ and $S_{32}$. Fig. 4(a) illustrates the evolutions of insertion gains, $S_{31}$ and $S_{32}$ according to $R_1$ or $R_2$. In order to quantify the unequal gain functionality, letting denote $\lambda$, the ratio between two transmission parameters, $S_{31}$ and $S_{32}$. The literal expression of $\lambda$ can be deduced from (3):

$$\lambda = S_{32}/S_{31} = R_2(Z_0 + R_1)/[R_1(Z_0 + R_2)]. \tag{5}$$

As depicted in graphs of Fig. 4, simultaneous control of the output transmission parameters and $\lambda$ in function of these two resistances can be made by fixing $R_i$. It is interesting to note that tuning of the output transmission parameters without change of $\lambda$ can be realized easily by acting on $R_i$.

Similar to all electronic functions, the design process of the proposed PC requires explicit and pragmatic methodology with clear synthesis methods. Knowing the characteristics of the FET, $g_m$ and $R_{ds}$ and regarding the given matching level, $S_{11}$ and the unequal gain, $\lambda$, one can establishes the synthesis relations for the determination of $R_1$, $R_i$, $R_2$ and $R_3$ by inverting (1)–(3). During the synthesis process, it is crucial to verify the following conditions involved from the analysis equations of the previous subsection. One demonstrates that the input and output return losses; $S_{11}$ and $S_{22}$ are linked by equation:

$$S_{22} = \lambda(1 + S_{11}) - 1. \tag{6}$$

Due to the non-reciprocity of the FET considered ideal ($S_{12} = 0$), all isolation losses of the proposed PC are automatically equal to zero ($S_{12} = S_{13} = S_{21} = S_{23} = 0$). Then, it is interesting to underline that according to the matching condition $|S_{11}| < 1$, the following conditions must be satisfied during the synthesis process:

$$\lambda < 2/(1 + S_{11}), \tag{7}$$

and

$$S_{31} < g_m^2 R_{ds} Z_0(1 + S_{11})(1 - S_{33})/4. \tag{8}$$
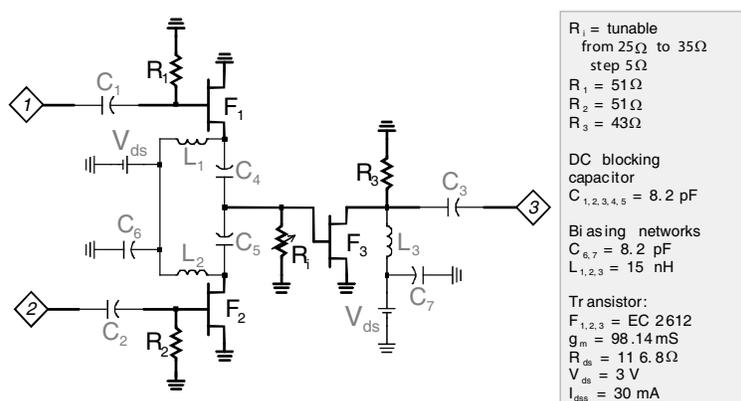


Figure 3: Active PC simulated including the bias networks (RF-part in thick lines and bias networks in thin lines).
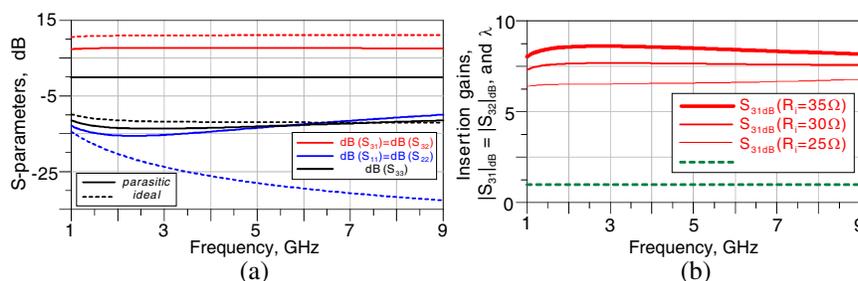


Figure 4: (a) $S$-parameters of equal active PC for $R_i = 30\,\Omega$, (dashed curves: low frequency ideal model and full curves: complete model). (b) Simulation results: insertion gains, $S_{21}$, $S_{31}$ and the corresponding ratio $\lambda$.
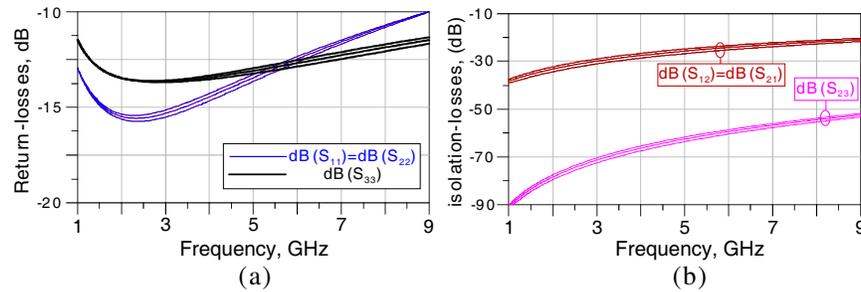
Figure 5: Simulation results: (a) return losses $S_{11}$, $S_{22}$ and $S_{33}$ and, (b) isolation losses $|S_{12}| = |S_{21}| = |S_{23}|$.
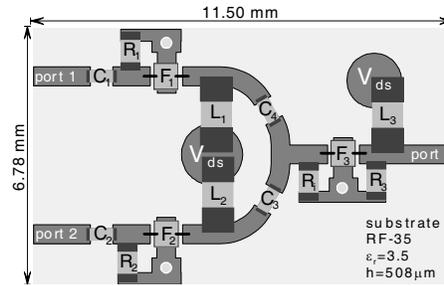


Figure 6: Layout of the active PC designed in Momentum environment.

Till now, all established theory is given for the simplified FET model without parasitic capacitance and inductance ($C_{gs}$, $C_{gd}$, $C_{ds}$, $L_s$, $L_g$, $L_d$, ...). To evidence the FET parasitic influences which is particularly important in the radio frequency applications, simulations with linear FET complete model will be explored in the next section.

## 3. VALIDATION RESULTS

As aforementioned, the simulation results introduced in this section were carried out with the commercial microwave circuit simulator, ADS from Agilent$^{\text{TM}}$. Noting that during the design of this active device, a 40 GHz super low noise PHEMT FETs referenced EC-2612 (manufactured by Mimix Broadband$^{\text{TM}}$) were employed. According to the manufacturer datasheet, this FET presents an equivalent circuit model including the drain and gate bond wires. It presents the intrinsic characteristics, $g_m = 98.14\,\text{mS}$ and $R_{ds} = 116.8\,\Omega$. Fig. 4 shows the detailed circuit schematic of the three-access active PC under studied. This diagram includes the DC-blocking capacitors and the biasing networks (traced in thin line) which are composed of 8.2-pF capacitors and 15-nH inductors. Similar to the topology invoked in Fig. 2 of the previous section, each input-output branch of this PC comprises two-stage of basic cell shown in Fig. 1. The parameters or resistive elements of the PC simulated were synthesized and voluntarily optimized for the achievement of the value $\lambda = 1$. In order to design an ordinary equal active PC, one should connect same resistor values at the two-input accesses $R_1 = R_2 = 51\,\Omega$. By considering the insertion gains, $|S_{31}|_{\text{dB}}$ and $|S_{32}|_{\text{dB}}$, equal to 6.5 dB, with the eventual optimization for the adjustment and the correction of realistic parasitic effects, one fixes $R_i = 30\,\Omega$ and $R_3 = 43\,\Omega$. As indicated in Fig. 7, during the simulation, the FET is assumed to work in saturated drain current, gate bias was set at floating ground, $V_{gs} = 0$ and $I_{dss} = 30\,\text{mA}$. Furthermore, it is interesting to emphasize that the active PC under consideration consumes 90 mA when feeding at DC voltage $V_{ds} = 3\,\text{V}$. After $S$-parameter simulations, as shown in Fig. 5, by considering the FET complete model taking into account the parasitic inductive and capacitive parasitic elements, one gets $S_{31} = S_{32}$ above 7 dB with flatness widely below 1 dB, and return losses better than $-10$ dB from 1 GHz to 9 GHz. Moreover, this figure sketches out also the comparison of insertion gains and return losses of the active PC with the ideal FET model (see dotted curves) and with the complete model proposed by the manufacturer. As depicted in Fig. 4, $|S_{31}|_{\text{dB}} = |S_{32}|_{\text{dB}}$, is linearly controlled and increases progressively from mean values of 6.5 dB to 8.5 dB and averagely, step about 1 dB from 1 GHz to 9 GHz.

By comparing these two-models, one evaluates a gain difference of about 3 dB. By tuning the intermediary resistance, $R_i$ from $R_{i,\text{min}} = 25\,\Omega$ to $R_{i,\text{max}} = 35\,\Omega$ step $R_{i,step} = 5\,\Omega$, one gets the $S$-parameters plotted in Figs. 4 and 5.
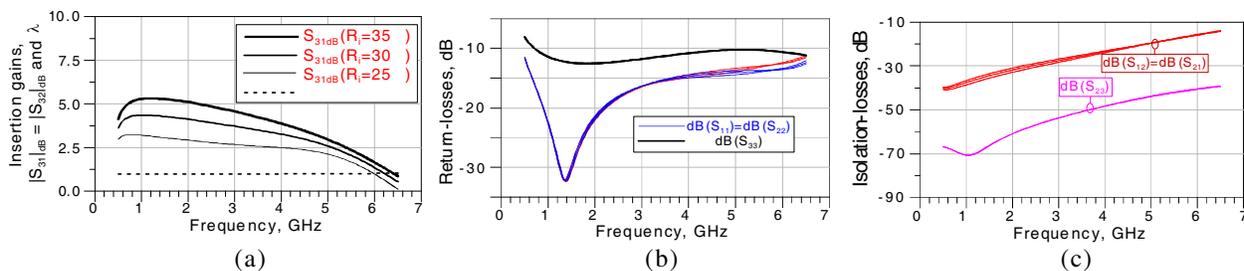
Figure 7: EM-circuit co-simulation results. (a) insertion gains, (b) return and isolation, (c) losses.

According to the simulations, the gain ratio, $\lambda = |S_{32}|/|S_{31}|$ of this PC in this frequency band is maintained equal to $1.050 \pm 0.002$. As seen in Figs. 5(a) and 5(b), the return- and isolation-losses at all accesses are not sensitive to the variation of $R_i$ and here, they are respectively, better than $-10$ dB and $-20$ dB. It is worth noting also that these excellent isolation loss levels are due to the non-reciprocity of utilized transistor FET EC-2612. Fig. 6 represents the layout of the PC designed in Momentum environment of ADS. This layout was printed on the RF-35 substrate having $\varepsilon_r = 3.5$-relative permittivity and thickness $h = 508\,\mu$m. The conductor used is Copper metal having thickness $t = 35$-μm.

It is noteworthy that the localized components used here correspond to realistic models available in ADS library with tolerances $+/-5\%$. By using these manufacturer realistic models deduced from the measured $S$-parameters of the passive components $R$, $L$ and $C$ and those of the PHEMTs FET EC-2612, one gets the transmission parameters of Fig. 7. As the practical model of the inductances proposed by the manufacturer are limited to 6.5 GHz. The EM-circuit simulations were performed from 0.5 GHz to 6.5 GHz. At noted that one employs here the measured $S$-parameters of the FET EC-2612 corresponding to the bias points $V_{ds} = 2$ V and $I_{ds} = 10$ mA. The non-linearity of the circuit tested is analyzed using the real specs of the FET used. So, a raw idea obtained by using datasheet of the device, where the individual device has $P_{1\,dB}$ of 16-dBm (referenced to the output), by using the real model of the capacitors and inductors, as expected one gets the same $P_{1\,dB}$ as the transistor.

Moreover, harmonic balance (HB) simulations with two tone RF frequencies, $f_0 = 2.5$ GHz with frequency spacing $\Delta f = 50$ MHz and with fixed input power $P_{in} = -30$ dBm was carried out. Therefore, one gets the output power spectrum shown in Fig. 12. Compared to the results presented in [18], one top of the design facility, the insertion gains plotted in Fig. 9 are better in terms of flatness and controllability. As reviewed in [19, 20], the interference and overpowered phenomena can be generated in wireless-communication systems because of nonlinear active devices. In general, such a wreaking effect can create undesired RF signal distortions.

## 4. CONCLUSION

A design methodology of wide-band active $0°$-PC is investigated. The topology of the presented active PC is simply based-on the use of active cell composed of FET cascaded with a shunt resistor. To alleviate the mathematical equations, the considered FET was assumed by its model equivalent circuit comprising voltage-controlled current source associated shunt drain-source resistance. Further conditions required during the design process of the proposed PC were discussed. The originality of the present work lies on the simplicity of $S$-parameter analysis by considering the Y-architecture based on the resistive active cell. Compared with the classical passive PC devices (Wilkinson- and resistive-PCs) existing in the literature, the one investigated in this paper offers good tradeoffs in terms of compactness, operating frequency bandwidth and capable to provide loss compensations or amplification. In planar hybrid technology, the size of the proposed active PC depends on the lumped elements especially on the performance of transistors employed. Additionally, it allows also to control the signal amplitude differences in several ways subsystems, like phased-array. The functioning and performances of the under study PC were highlighted by EM/circuit cosimulations. With the considered prototype, the feasibility of gain control and the transmission parameter ratio of twoway active $0°$-PC with the achievement of good return- and isolation-loss levels were evidenced in broadband width. One of the potential applications of the presented PC structure could be improvement of MIMO system terminals [21] through design of compact and very low-loss microwave digital receiver and transmitter by integrating into mixer,

adder, digital/RF-modulator and -demodulator circuitry. As ongoing research, using further enhanced presented design technique, N-way reconfigurable devices with reciprocal function dedicated for RF/microwave systems is in foremost concern of my future work. Thanks to the outstanding benefit in terms of isolation levels, we would implement also new concept of multiplex microwave devices with M-input and N-output ways with amplification function.

**REFERENCES**

1. Chen, L., X.-H. Wang, X.-W. Shi, T.-L. Zhang, and J.-Z. Tong, "Design of a broadband frequency offset van atta array," *Progress In Electromagnetics Research Letters*, Vol. 13, 161–171, 2010.
2. Joardar, S., M. Jaint, V. Bandewar, and A. B. Bhattacharya, "An innovative portable ultra wide band stereophonic radio direction finder," *Progress In Electromagnetics Research*, Vol. 78, 255–264, 2008.
3. NASA's Jet Propulsion Laboratory, "Four-way Ka-band power combiner. A prior X-band design has been adapted to Ka band," *NASA Tech Briefs*, 13, Pasadena, CA, USA, Dec. 2007.
4. Chen, H. and Y. X. Zhang, "A novel compact planar six-way power divider using folded and hybrid-expanded coupled lines," *Progress In Electromagnetics Research*, Vol. 76, 243–252, 2007.
5. Wu, Y., Y. Liu, S. Li, C. Yu, and X. Liu, "Closed-form design method of an N-way dual-band Wilkinson hybrid power divider," *Progress In Electromagnetics Research*, Vol. 101, 97–114, 2010.
6. Catoiu, M., "A novel 3-way hybrid combiner/divider for high power C-class microwave amplifiers," *Proc. of IEEE MTT-Symposium IMS*, Vol. 1, 31–34, Phoenix, AZ, USA, 2001.
7. ETSI EN 301 489-1, "Electromagnetic compatibility and Radio Spectrum Matters (ERM); ElectroMagnetic Compatibility (EMC) standard for radio equipment and services; Part 1: Common technical requirements," 1.3.1 Edition, 36, European Telecommunications Standards Institute, Sep. 2001.
8. http://www.ce-mag.com/archive/02/Spring/em_stand1.html.
9. Baudry, D., A. Louis, and B. Mazari, "Characterization of the open ended coaxial probe used for near field measurements in EMC applications," *Progress In Electromagnetics Research*, Vol. 60, 311–333, 2006.
10. Li, L. A., B. J. Hilliard, J. R. Shafer, J. Daggett, E. J. Dickman, and J. P. Becker, "A planar compatible traveling-wave waveguide-based power divider/combiner," *IEEE MTT*, Vol. 56, No. 8, 1889–1898, Aug. 2008.
11. Lin, Z. and Q.-X. Chu, "A novel approach to the design of dual-band power divider with variable power dividing ratio based on coupled-lines," *Progress In Electromagnetics Research*, Vol. 103, 271–284, 2010.
12. Li, X., Y.-J. Yang, L. Yang, S.-X. Gong, X. Tao, Y. Gao, K. Ma, and X.-L. Liu, "A novel design of dual-band unequal Wilkinson power divider," *Progress In Electromagnetics Research C*, Vol. 12, 93–100, 2010.
13. Wilkinson, E. J., "An n-way power divider," *IRE Trans. on MTT*, Vol. 8, 116–118, Jan. 1960.
14. Pozar, D. M., *Microwave Engineering*, 3rd Edition, John Wiley & Sons, New York, 2005.
15. http://www.microwaves101.com/encyclopedia/Resistive_splitters.cfm.
16. Barta, G. S., K. E. Jones, G. C. Herrick, and E. W. Strid, "Surface-mounted GaAs active splitter and attenuator MMICs used in a 1–10 GHz leveling loop," *IEEE MTT*, Vol. 34, No. 12, 1569–1575, Dec. 1986.
17. Majidi-Ahy, R., C. Nishimoto, J. Russel, W. Ou, S. Bandy, G. Zdasiuk, C. Shih, Y. C. Pao, and C. Yuen, "4–40 GHz MMIC distributed active combiner with 3 dB gain," *Electronics Letters*, Vol. 28, No. 8, 739–741, 1992.
18. Safarian, A., L. Zhou, and P. Heydari, "CMOS distributed active cower combiners and splitters for multi-antenna UWB beamforming transceivers," *IEEE JSSC*, Vol. 42, No. 7, 1481–1491, Jul. 2007.
19. Cripps, S. C., "The intercept point deception," *IEEE Microwave Magazine*, 44–50, Feb. 2007.
20. Johnson, M. R., "Reviewing the basics of intermodulation distortion," *Microwave & RF, Design Feature*, 74–82, Sep. 2007.
21. Ranvier, S., "Radiowave propagation and antennas for high data rate mobile communications in the 60 GHz band," Ph.D. Thesis Report, Department of Radio Science and Engineering (Former Radio Laboratory), Helsinki University of Technology (TKK), Mar. 2009.

# Triple Band Fractal Koch Antenna for Wearable Application

**M. E. Jalil**, **M. K. A. Rahim**, **N. A. Samsuri**, and **N. A. Murad**

Radio Communication Engineering Department, Faculty of Electrical Engineering
University Technology Malaysia, Skudai 81310, Johor, Malaysia

**Abstract**— This report presents Triple-band Fractal Koch Textile antenna using first iteration of Koch geometry of a dipole antenna structure for wearable applications. In order to reduce the overall length of the dipole antenna structure, the flare angle of the antenna design is varied to three different values which are 30, 45 and 60 degree respectively. The radiating elements of the antenna are made of adhesive copper fabric, whilst the substrate is given a property of denim textile material. The proposed antennas are simulated in CST Studio and have been optimized to operate within the ISM frequency bands (0.902–0.928 GHz, 2.4–2.5 GHz and 5.725–5.875 GHz). The simulation results are then compared with valid measurements and the results are further discussed in this paper.

## 1. INTRODUCTION

Development of wearable application systems have been rapidly increased within the area of wireless communications technology. The integration between mobile electronic devices and sensors with wireless technology enable good growth for wearable applications. The wearable applications are widely used in the paramedic, monitoring, fire fighter and military sector for tracking, navigation, mobile computing and data collection activities. Nowadays, the performances of wearable devices are optimized by compact size, movable and robust. For example, body centric wireless communications are developed in medical applications. There are three types of communication systems, these are in-body, on-body and off-body [1, 2]. The properties of the antenna such as compact size, simple fabrications, mechanical flexibility, comfort to the user and low cost are the main requirements for all modern wearable application system [3]. Many new designs of wearable antennas are developed by other researchers such as patches, button, wired and conductive textiles [4]. Textile antennas are proposed for wearable antenna because they can be easily integrated with clothing. A number of researches have working on designing various type of textile antenna for wearable applications such as planar, dipole, monopole and microstrip patch antenna. The size of the antenna became the main issue on the wearable antenna. The antenna must have a compact size while maintaining the antenna's performance. In order to produce a compact size antenna, fractal Koch antenna is introduced for size reduction [5].

## 2. MATERIAL AND METHOD

The wearable, durable and flexible conductive materials are the most important aspect for textile antenna. A good material has the ability to overcome the impact of bending and can operate properly in close proximity to the human body. Permittivity and loss tangent are critical parameters to be considered when selecting material. Normally, textile materials have low dielectric constant which can reduce the surface wave loss and improving the impedance bandwidth of antenna. Denim textile, which has thickness of 0.78 mm is proposed as the substrate for this wearable antenna. The permittivity of denim textile is 1.7 and the loss tangent is 0.025. The proposed textile antenna consists of conductive textile which is an adhesive conductive fabric as the radiating element and a non-conductive textile while denim fabric as the substrate. Technically, the conductive fabric is attached on the denim textile using iron with controlled temperature.

## 3. ANTENNA CONSIDERATION

Some modifications of dipole antenna structure based on previous published paper have been done in order to obtain the specification of the designed antenna. To achieve the design, the parameters of dipole straight arm are calculated using Equation (1)

$$l = 0.5 \times \frac{c}{f\sqrt{\varepsilon_r}} \tag{1}$$

where $l$ is length of two straight dipole arm, $c$ is velocity of speed in ms$^{-1}$, $f$ is determined resonant frequency in Hz and $\varepsilon_r$ is dielectric constant of used material. In this paper, the proposed antennas

Figure 1: Multiband wearable antenna design.



(a)



(b)



(c)
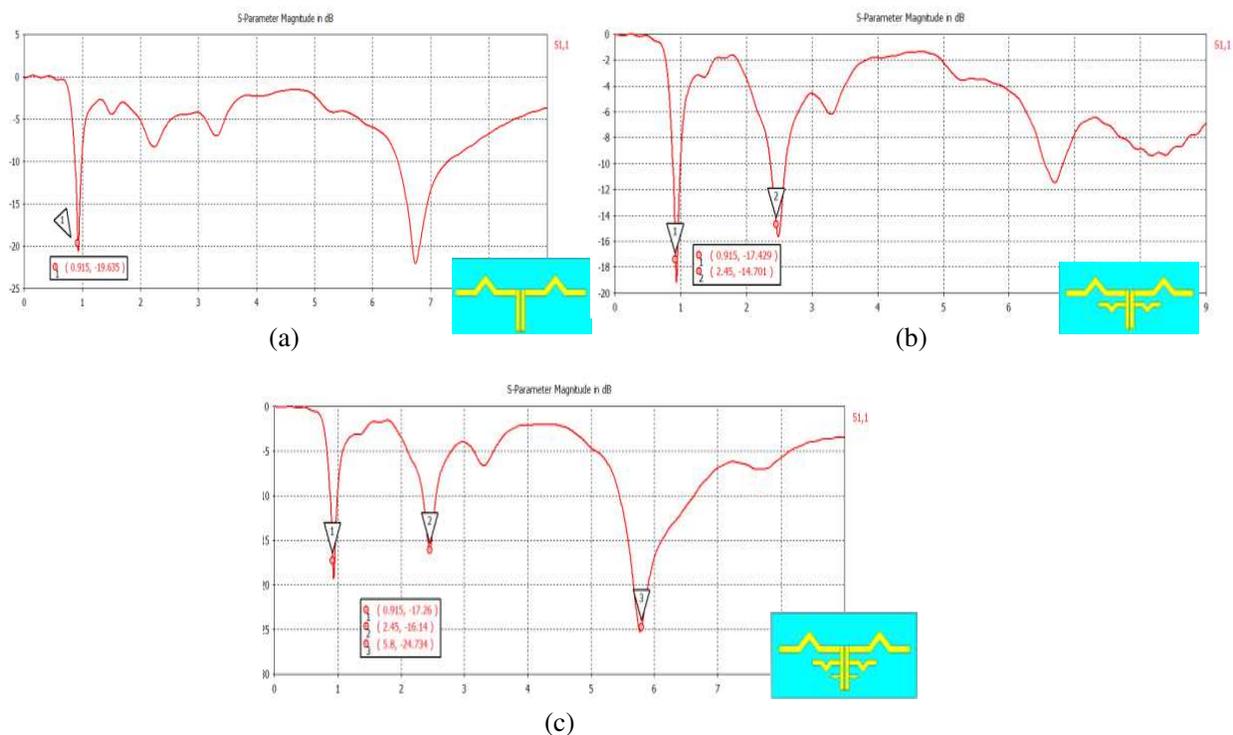
Figure 2: Design procedure and parametric. (a) First (driven) dipole arm. (b) Additional second dipole arm. (c) Additional third dipole arm.

are designed without ground plane. The 50 ohm SMA connector is used for antenna feeding at the determined position of the antenna. To match the 50 ohm impedance, the width of main feed element is determined based on the substrate used. The dimension of length and width of the overall antenna is 140 mm × 60 mm which is also the size of denim substrate. In this report, a triple arm dipole antenna for triple-band operating frequencies are explained in Figure 2. The driven first arm dipole structure is added to other two arm dipole structures to resonate at three frequency bands. The combination of three arm length is carried out to perform at three different resonant frequencies (0.915 GHz, 2.45 GHz and 5.8 GHz) are shown in Figure 2. The second and the third arm structures are inverted to avoid overlapping between the arm structures as well as to reduce the total size of the antenna. The height of feed line is 32 mm after optimization on the antenna size and performance. The width of first arm (5 mm), second arm (4 mm) and third arm structure (2 mm) is determined based on the desired bandwidth. The flare angle is varied to three different flare angles which are 30 degree, 45 degree and 60 degree. The antenna are designed and optimized at three ISM band with different flare angle.

The specification of three designed antenna after optimization process are shown in Table 1. Three fractal Koch antennas are designed and simulated using Computer Simulation Technology (CST) software to analyze antenna performance in term of return loss, gain, efficiency and radiation pattern. Comparison between simulated and measurement results are discussed in term of antenna return loss.

Table 1: Specifications for the three designed antenna with different flare angle.

| Types of antenna | Types of arm | Arm length |
|---|---|---|
| Antenna with 30 degree of flare angle | 1st | 63.00 mm |
| | 2nd | 27.30 mm |
| | 3rd | 8.55 mm |
| Antenna with 45 degree of flare angle | 1st | 59.40 mm |
| | 2nd | 26.70 mm |
| | 3rd | 8.40 mm |
| Antenna with 60 degree of flare angle | 1st | 56.70 mm |
| | 2nd | 25.20 mm |
| | 3rd | 7.65 mm |



(a) 30 degree



(b) 45 degree
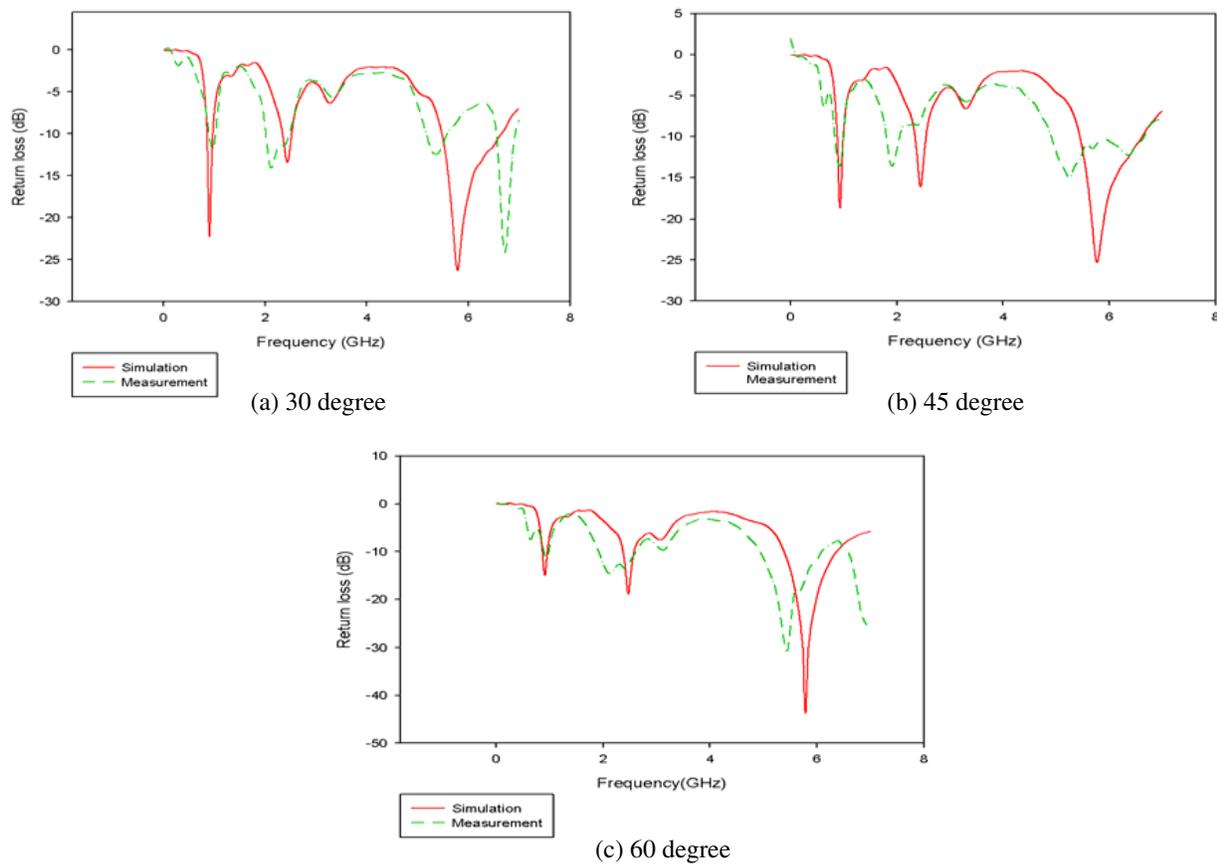


(c) 60 degree

Figure 3: Simulated and measured results of return loss for three designed antenna which consist of 30 degree, 45 degree and 60 degree flare angle.

## 4. RESULT AND DISCUSSION

Figure 3 shows the comparison between simulated and measured return loss for 30, 45, 60 degree of flare angles for the multiband antenna. Similar trend between simulated and measured results can be seen in the graphs as shown in Figure 3. From the results, it can be seen that the resonance frequencies are slightly shifted to the left; that is predicted contributed by fabrication errors. Comparing the three flare angles' measurements results, only 60 degree flare angle results satisfy the ISM bands requirements with good agreement between simulation and measurement.

The polar simulation radiation pattern on $E$-plane and $H$-plane at three resonant ISM band (0.915 GHz and 2.45 GHz and 5.8 GHz) with three different flare angles (i.e., 30, 45, 60) are shown in Figure 4. The antennas with different flare angle have similar polar radiation pattern at the three ISM band. Omni directional radiation pattern is suitable for wearable antenna since it radiates

(a) 0.915 GHz          (b) 2.45 GHz          (c) 5.8 GHz
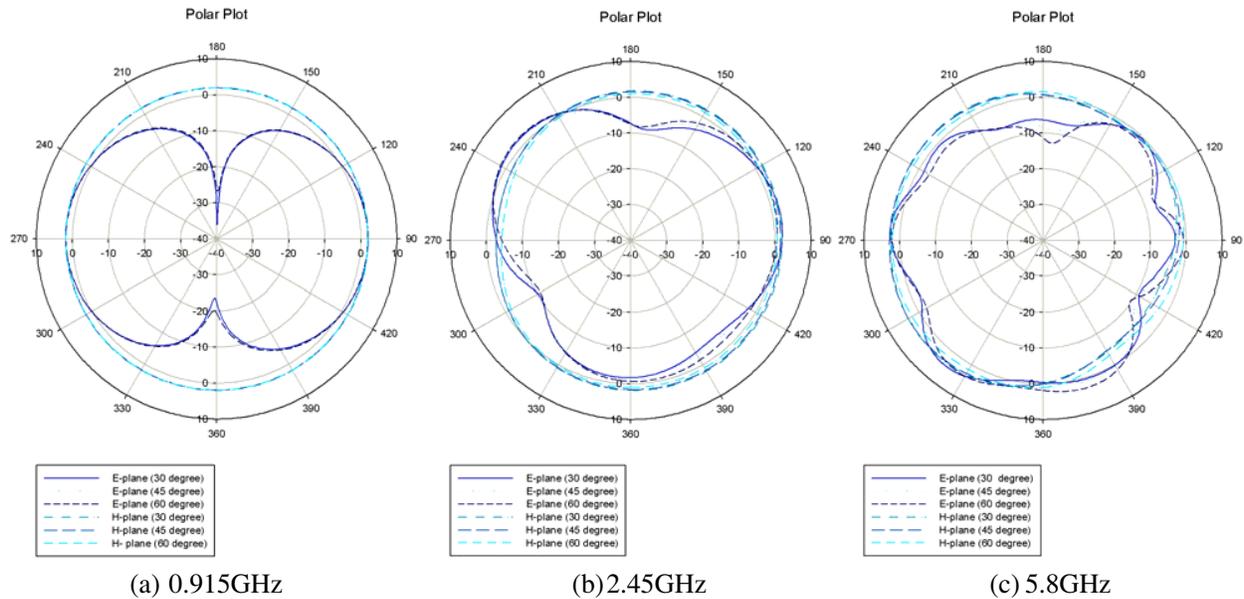
Figure 4: Simulated $E$-plane and $H$-plane radiation pattern results of three designed triple band antenna at frequency 0.915 GHz, 2.45 GHz and 5.8 GHz.

Table 2: The resonant frequency, frequency range simulated, gain efficiency simulation result for gain and efficiency for three designed fractal antenna.

| Types antenna | Resonant ISM band | Frequency range | Gain (dB) | Efficiency (%) |
|---|---|---|---|---|
| Antenna with 30 degree flare angle | 0.915GHz | 0.85–0.98 | 2.03 | 98 |
| | 2.45GHz | 2.34–2.52 | 2.45 | 92 |
| | 5.8GHz | 5.48–6.63 | 4.31 | 94 |
| Antenna with 45 degree flare angle | 0.915GHz | 0.88–0.99 | 1.95 | 96 |
| | 2.45GHz | 2.33–2.52 | 2.19 | 92 |
| | 5.8GHz | 5.43–6.61 | 4.30 | 93 |
| Antenna with 60 degree flare angle | 0.915GHz | 0.86–0.96 | 1.97 | 96 |
| | 2.45GHz | 2.38–2.58 | 2.19 | 91 |
| | 5.8GHz | 5.43–6.37 | 3.77 | 94 |

energy in the horizontal and vertical planes, which ensure the wearable antenna to receive signals from any direction. Table 2 shows the simulated result of gain and efficiency for three designed antennas with different flare angles at resonant ISM band. The antenna give higher gain at the higher frequency.

## 5. CONCLUSIONS

The 60 degree flare angle multiband fractal antenna can reduced the size for all the arm antenna which consist of first arm length (56.7 mm), second arm (25.2 mm) and third arm (7.65 mm) compared with other dipole antenna. Simulation results of the antenna frequency range, gain, and efficiency are also presented in this report. The simulated and measured result of the 60 degree flare angle shows that the proposed antennas has $S_{11} < -10$ dB at three ISM bands. The compact size antenna are produced with reduce the size of antenna

## ACKNOWLEDGMENT

**REFERENCES**

1. Rais, N. H. M., P. J. Soh, F. Malek, N. B. M Hashim, and P. S. Hall, "A review of wearable antenna," *Loughborough Antenna Propogation Coference*, 2009.
2. Ma, L., R. M. Edwards, S. Bashir, and M. I. Khattak, "A wearable flexible multiband antenna based on a square slotted printed monopole," *Loughborough Antennas & Propagation Conference*, 2008.
3. Osman, M. A. R., M. K. A. Rahim, M. Azfar, N. A. Samsuri, F. Zubir, and K. Kamardin, "Design, implementation and performance of ultra wideband textile antenna," *Progress In Electromagnetics Research B*, Vol. 27, 307–325, 2011.
4. Thalmann, T., Z. Popovic, B. M. Notaros, and J. R. Mosig, "Investigation and design of a multi-band wearable antenna," *3rd European Conference on Antennas and Propagation*, Berlin, Germany, Mar. 23–27, 2009.
5. Karim, M. N. A., M. K. A. Rahim, T. Masri, and O. Ayop, "Analysis of fractal koch dipole antenna For UHF band," *IEEE International RF and Microwave Conference Proceeding*, 2008.

# Determination of Moisture Content of Hevea Rubber Latex Using a Microstrip Patch Antenna

**N. Z. Yahaya**[1], **Z. Abbas**[1], **M. A. Ismail**[1], **and B. Mohd Ali**[2]

[1]Department of Physic, Faculty of Science, Universiti Putra Malaysia
43400 UPM Serdang, Selangor Darul Ehsan, Malaysia
[2]Faculty of Engineering, Universiti Putra Malaysia
43400 UPM Serdang, Selangor Darul Ehsan, Malaysia

**Abstract**— A microstrip patch sensor for determination of moisture content in Hevea Rubber Latex is presented in this paper. The microstrip patch sensor was designed to operate at microwave frequency range from 0.1 to 5 GHz on a RT/Duroid substrate with $6.15 \pm 0.015$ permittivity and 1.27 mm thickness. The width and length of the rectangular patch antenna was 18 mm and 38 mm, respectively. The reflection coefficient of the sensor loaded with Hevea latex at various percentages of moisture content from approximately 42.47% (fresh latex) to 77.57%. Calibration equations have been established between moisture content and magnitude of reflection coefficient at several selected frequencies. These equations were used to predict the amount of moisture content on Hevea latex based on the measured reflection coefficient values. The actual values of moisture content were obtained using standard oven drying method. The lowest mean relative error between actual and predicted moisture contents was 0.06 at 3 GHz.

## 1. INTRODUCTION

The superiority of Hevea rubber latex brings on a high demand in the industrial production which leads to high price. The price itself depends on the percentage of dry rubber content or moisture content.

Various techniques have been proposed to determine the dry rubber content (DRC) of hevea latex. Some of these include an experimental study based on titration method [1] and microwave measurement techniques [2, 3]. An annular photoelectric sensor was also used to determine moisture content of Hevea latex by applying the Lambert's law [4]. Unfortunately, all the techniques are too time consuming and laborious.

Recently, microstrip antennas have been widely used in many applications such as communications, medical and agriculture [5–9]. This paper presents the application of microstrip sensor in the determination of moisture content in hevea latex in the frequency range between 100 MHz and 5 GHz. The objective is to establish the relationship between reflection coefficient of the sensor and moisture content in Hevea latex.

## 2. MATERIAL AND METHODS

### 2.1. Microstrip Antenna

The proposed patch antenna sensor was designed using Microwave Office version 7.03. The resonant frequency was at 3.18 GHz. The sensor was fabricated using a RT/Duroid substrate with 6.15 permittivity and 1.27 mm thickness. The width and length of rectangular patch were 18 mm and 38 mm, respectively. A 50 ohm SMA female connector was used as the feeding port of the microstrip.

### 2.2. Sample Preparation

The samples were obtained from Universiti Putra Malaysia's Research Park. Fresh hevea latex samples typically have moisture contents approximately 42.47% wet basis. The actual moisture content was determined using standard an oven drying method [10].

$$\text{Moisture content (\%)} = (m_{wet} - m_{dry})/m_{wet} \times 100\% \tag{1}$$

where $m_{wet}$ and $m_{dry}$ are the initial and final mass before and after drying.

### 2.3. Reflection Measurements

The experimental setup consists of a microstrip patch sensor, Hevea latex samples with various percentages of moisture contents. The Professional Network Analyzer (PNA) was used to measure the reflection coefficient of the sensor with and without the samples in frequency range between 0.1–5 GHz. The calibration procedure was performed using Agilent's open, short and load standards from 0.1 GHz to 5 GHz to establish a 50 ohm calibration plane between the sensor and the coaxial cable.
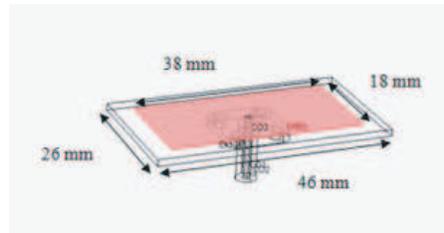
Figure 1: The design schematic of the microstrip patch antenna.
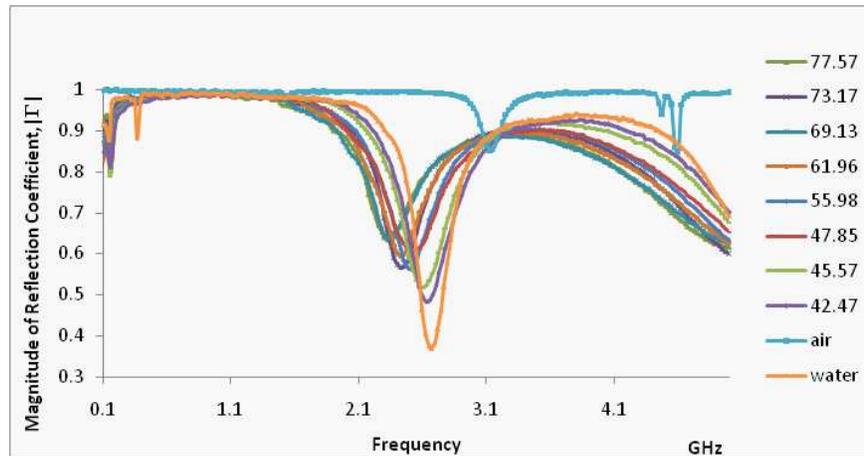


Figure 2: Variation in the magnitude of reflection coefficient, $|\Gamma|$ with frequency for Hevea rubber latex various percentages of moisture content.

Table 1: Calibration equation and regression coefficient for 1 GHz, 2 GHz, 3 GHz, 4 GHz and 5 GHz.

| Frequency | calibration equation | regression coefficient |
|---|---|---|
| 1 GHz | $y = -659125x^2 + 1E + 06x - 637536$ | $R^2 = 0.1058$ |
| 2 GHz | $y = -201.52x^2 - 130.94x + 361.79$ | $R^2 = 0.8385$ |
| 3 GHz | $y = 1177.2x^2 - 1554.9x + 539.55$ | $R^2 = 0.9554$ |
| 4 GHz | $y = -186.83x + 230.24$ | $R^2 = 0.3385$ |
| 5 GHz | $y = 1116.3x^2 - 1826x + 786.93$ | $R^2 = 0.8692$ |

## 3. RESULTS AND DISCUSSIONS

The variation in the magnitude of reflection coefficient $|\Gamma|$ with frequency is shown in Figure 1. It can be clearly seen that the reflection coefficient of all the samples follow closely the reflection coefficient profile of air. The measured resonance frequency of the unloaded sensor (air) was similar to the calculated frequency using Microwave Office. A series of shift in resonant frequency can be clearly seen with increase moisture content in the samples. These were almost coincidental with the material relaxation frequency of the hevea latex samples of different percentages of moisture content. For moist materials, the maximum absorption of microwave energy occurs at relaxation frequency approximately from 2.3 GHz to 3.2 GHz [11]. The resonance peaks of the loaded sensor were shifted to the left from 3.2 GHz to 2.3 GHz corresponding to 42.47% to 77.57% moisture content.

The reduced of magnitude reflection coefficient, $|\Gamma|$ samples at frequencies higher than 3.2 GHz were probably due to sudden increase in the values of the dielectric loss factor of the material. Calibration equations were established relating the magnitude of reflection coefficient to moisture content at some selected frequencies as listed in Table 1.

The accuracy of the calibration equations were determined by comparing the actual and predicted moisture contents as shown listed Table 2. The relationship between predicted and actual values of moisture content is best represented by calibration equation at 3 GHz with the highest regression coefficient value, $R^2 = 0.9554$ and lowest mean relative error 0.06.

Table 2: Comparison between actual values and predicted moisture content for 1 GHz, 2 GHz, 3 GHz, 4 GHz and 5 GHz.

| MAGNITUDE | | | | | |
|---|---|---|---|---|---|
| **Actual moisture content** | predicted moisture content | | | | |
| | 1 GHz | 2 GHz | 3 GHz | 4 GHz | 5 GHz |
| **42.47** | −293306 | 43.74 | 42.06 | 1.07254 | 41.31 |
| **45.57** | −292787 | 47.25 | 42.53 | 1.07262 | 43.30 |
| **47.85** | −292669 | 49.66 | 49.22 | 1.07267 | 50.18 |
| **55.98** | −292179 | 57.75 | 63.02 | 1.07271 | 62.28 |
| **61.96** | −291134 | 80.02 | 67.99 | 1.07285 | 70.29 |
| **69.13** | −291805 | 71.41 | 74.07 | 1.07287 | 79.16 |
| **73.17** | −291842 | 81.34 | 76.25 | 1.07297 | 81.39 |
| **77.57** | −291651 | 100.83 | 78.52 | 1.07307 | 82.25 |
| **mean relative error** | 5168 | 0.11 | 0.06 | 0.98 | 0.09 |

## 4. CONCLUSION

A microstrip patch antenna for rapid and accurate measurement of moisture content in Hevea latex has been successfully used to determine moisture content in latex based on reflection measurement. The accuracy of sensor was determined by comparing the predicted moisture content with the actual moisture content using oven drying.

## ACKNOWLEDGMENT

## REFERENCES

1. Alex, R., C. K. Premalatha, R. B. Nair, and B. Kuriakose, "Measurement of dry rubber content of fresh natural rubber latex by a titration method," *J. Rubber Res.*, Vol. 6, No. 4, 221–230, 2003.
2. Hamza, Z. P., K. F. Anna Dilfi, M. N. Muralidharan, and K. Thomas, "Microwave oven for the rapid determination of total solids content of natural rubber latex," *International Journal of Polymeric Materials*, Vol. 57, No. 9, 918–923, 2008.
3. Jayanthy, T., "Measurement of dry rubber content in Latex using microwave technique," *Measurement Science Review*, Vol. 5, No. 3, 2005.
4. Zhao, Z. M., X. D. Jin, L. Zhang, and X. L. Yu, "A novel measurement system for dry rubber content in concentrated natural latex based on annular photoelectric sensor," *International Journal of Physical Sciences*, Vol. 5, No. 3, 251–260, Mar. 2010.
5. Gagnadre, I., C. Gagnadre, and J. P. Fenelon, "Circular patch antenna sensor for moisture content measurement on dielectric material," *Electronics Letters*, Vol. 31, No. 14, 1167–1168, May 1995.
6. Abbas, Z., *A Microstrip Sensor for Determination of Harvesting Time for Oil Palm Fruits*, Master's Dissertation, Universiti Putra Malaysia, 1993.
7. El Sabbagh, M. A., O. M. Ramahi, S. Trabelsi, S. O. Nelson, and L. Khan, "Use of microstrip patch antennas in grain and pulverized materials permittivity measurement," *Antennas and Propagation Society International Symposium*, Vol. 4, 42–45, Jun. 2003.
8. Miyai, Y., "A new microwave moisture meter for grain," *Journal of Microwave Power*, Vol. 13, No. 2, 1978.
9. Abegaonkar, M. P., R. N. Karekar, and R. C. Aiyer, "A microwave microstrip ring resonator as a moisture sensor for biomaterials: Application to wheat grains," *Meas. Sci. Technol.*, Vol. 10, 195–200, 1999.
10. Chin, H. C., "Method of measuring the dry rubber content of field latex," *RRIM Training Manual on Analytical Chemistry, Latex and Rubber Analysis*, Vol. 63, Rubber Research Institute Malaysia, Kuala Lumpur,

11. Funebo, T. and T. Ohlsson, "Dielectric properties of fruits and vegetables as a function of temperature and moisture content," *Journal of Microwave Power and Electromagnetic Energy*, Vol. 34, No. 1, 1999.

# Generation and Propagation of a Stochastic Electromagnetic Gaussian Schell-model Beam

**Yahong Chen, Fei Wang, and Yangjian Cai**

School of Physical Science and Technology, Soochow University, Suzhou 215006, China

**Abstract**— In this paper, we give a review of our recent research on the propagation and generation of a stochastic electromagnetic Gaussian Schell-model (EGSM) beam. A tensor method was introduced to treat the propagation of an EGSM beam. The EGSM beam was generated experimentally and its beam parameters were measured based on the technique for measuring the fourth-order correlation function.

## 1. INTRODUCTION

Gaussian Schell-model (GSM) beam is a typical model for a scalar partially coherent beam, whose intensity distribution and spectral degree of coherence satisfy Gaussian distribution, and it has been explored widely in the past decades [1]. Recently, more and more attention is being paid to stochastic electromagnetic beam (i.e., vector partially coherent beam) due to its important applications in free-space optical communication, radar systems, optical imaging, and particle trapping [2–9]. Stochastic EGSM beam was introduced as a natural extension of scalar GSM beam [2–5]. In the past several years, the propagation and generation of an EGSM beam have been studied extensively. In this paper, we present a brief review of our recent research on the propagation and generation of an EGSM beam.

## 2. PROPAGATION OF AN EGSM BEAM

The second-order statistical properties of an EGSM beam can be characterized by the $2 \times 2$ cross-spectral density (CSD) matrix $\overleftrightarrow{W}(\mathbf{r}_1, \mathbf{r}_2)$ specified at any two points with position vectors $\mathbf{r}_1$ and $\mathbf{r}_2$ in the source plane with elements [10]

$$W_{\alpha\beta}(\tilde{\mathbf{r}}) = A_\alpha A_\beta B_{\alpha\beta} \exp\left[-\frac{ik}{2}\tilde{\mathbf{r}}^T \mathbf{M}_{0\alpha\beta}^{-1} \tilde{\mathbf{r}}\right], \quad (\alpha = x, y; \beta = x, y), \tag{1}$$

where $\tilde{\mathbf{r}}^T = (\mathbf{r}_1^T \ \mathbf{r}_2^T)$, $A_\alpha$ is the square root of the spectral density of electric field component $E_\alpha$, $B_{\alpha\beta} = |B_{\alpha\beta}|\exp(i\phi)$ is the correlation coefficient between the $E_x$ and $E_y$ field components, satisfying the relation $B_{\alpha\beta} = B_{\beta\alpha}^*$, $\mathbf{M}_{0\alpha\beta}^{-1}$ is a $4 \times 4$ matrix of the form [10]

$$\mathbf{M}_{0\alpha\beta}^{-1} = \begin{pmatrix} \frac{1}{ik}\left(\frac{1}{2\sigma_{\alpha\beta}^2} + \frac{1}{\delta_{\alpha\beta}^2}\right)\mathbf{I} & \frac{i}{k\delta_{\alpha\beta}^2}\mathbf{I} + \mu_{\alpha\beta}\mathbf{J} \\ \frac{i}{k\delta_{\alpha\beta}^2}\mathbf{I} + \mu_{\alpha\beta}\mathbf{J}^T & \frac{1}{ik}\left(\frac{1}{2\sigma_{\alpha\beta}^2} + \frac{1}{\delta_{\alpha\beta}^2}\right)\mathbf{I} \end{pmatrix}, \tag{2}$$

where $\sigma_{\alpha\beta}$ and $\delta_{\alpha\beta}$ denote the widths of the spectral density and correlation coefficient, respectively. $A_\alpha$, $B_{\alpha\beta}$, $\sigma_{\alpha\beta}$, $\delta_{\alpha\beta}$ and $\mu_{\alpha\beta}$ are independent of position but, in general, depend on the frequency.

After propagation through a paraxial ABCD optical system in free space, the elements of the CSD matrix can be expressed in the following form [10]

$$W_{\alpha\beta}(\tilde{\rho}) = A_\alpha A_\beta B_{\alpha\beta} \left[\text{Det}\left(\bar{\mathbf{A}} + \bar{\mathbf{B}}\mathbf{M}_{0\alpha\beta}^{-1}\right)\right] \exp\left[-\frac{ik}{2}\tilde{\rho}^T\left(\bar{\mathbf{C}} + \bar{\mathbf{D}}\mathbf{M}_{0\alpha\beta}^{-1}\right)\left(\bar{\mathbf{A}} + \bar{\mathbf{B}}\mathbf{M}_{0\alpha\beta}^{-1}\right)^{-1}\tilde{\rho}\right], \tag{3}$$
$$(\alpha = x, y; \beta = x, y)$$

where Det stands for the determinant of a matrix, $\tilde{\rho}^T = (\rho_1^T \ \rho_2^T)$ with $\rho_1$ and $\rho_2$ being the transverse position vectors in the output plane, Here $\bar{\mathbf{A}}$, $\bar{\mathbf{B}}$, $\bar{\mathbf{C}}$ and $\bar{\mathbf{D}}$ are $4 \times 4$ matrices of the form:

$$\bar{\mathbf{A}} = \begin{pmatrix} \mathbf{A} & 0\mathbf{I} \\ 0\mathbf{I} & \mathbf{A}^* \end{pmatrix}, \quad \bar{\mathbf{B}} = \begin{pmatrix} \mathbf{B} & 0\mathbf{I} \\ 0\mathbf{I} & -\mathbf{B}^* \end{pmatrix}, \quad \bar{\mathbf{C}} = \begin{pmatrix} \mathbf{C} & 0\mathbf{I} \\ 0\mathbf{I} & -\mathbf{C}^* \end{pmatrix}, \quad \bar{\mathbf{D}} = \begin{pmatrix} \mathbf{D} & 0\mathbf{I} \\ 0\mathbf{I} & \mathbf{D}^* \end{pmatrix}, \tag{4}$$

where $\mathbf{A}$, $\mathbf{B}$, $\mathbf{C}$ and $\mathbf{D}$ are the $2 \times 2$ sub-matrices of the general astigmatic ABCD optical system, and "*" denotes the complex conjugate. $\mathbf{I}$ is a $2 \times 2$ identity matrix.

After propagation through a paraxial ABCD optical system in turbulent atmosphere, the elements of the CSD matrix can be expressed in the following form [7]

$$W_{\alpha\beta}(\tilde{\rho}) = \frac{A_\alpha A_\beta B_{\alpha\beta}}{\left[\det\left(\tilde{\mathbf{A}} + \tilde{\mathbf{B}}\mathbf{M}_{0\alpha\beta}^{-1} + \tilde{\mathbf{B}}\tilde{\mathbf{P}}\right)\right]^{1/2}} \exp\left[-\frac{ik}{2}\tilde{\rho}^T\left(\tilde{\mathbf{C}} + \tilde{\mathbf{D}}\mathbf{M}_{0\alpha\beta}^{-1} + \tilde{\mathbf{D}}\tilde{\mathbf{P}}\right)\left(\tilde{\mathbf{A}} + \tilde{\mathbf{B}}\mathbf{M}_{0\alpha\beta}^{-1} + \tilde{\mathbf{B}}\tilde{\mathbf{P}}\right)^{-1}\tilde{\rho}\right]$$

$$\times \exp\left[-\frac{ik}{2}\tilde{\rho}^T\tilde{\mathbf{P}}\tilde{\rho} - \frac{ik}{2}\tilde{\rho}^T\left(\tilde{\mathbf{B}}^{-1T} - \frac{1}{4}\tilde{\mathbf{P}}^T\right)\left(\mathbf{M}_{0\alpha\beta}^{-1} + \tilde{\mathbf{B}}^{-1}\tilde{\mathbf{A}} + \tilde{\mathbf{P}}\right)^{-1}\tilde{\mathbf{P}}\tilde{\rho}\right], \tag{5}$$

where

$$\tilde{\mathbf{P}} = \frac{2}{ik\rho_0^2}\begin{pmatrix} \mathbf{I} & -\mathbf{I} \\ -\mathbf{I} & \mathbf{I} \end{pmatrix}, \quad \rho_0 = \text{Det}[\mathbf{B}]^{1/2}\left(1.46k^2C_n^2\int_0^l \text{Det}[\mathbf{B}(z)]^{5/6}dz\right)^{-3/5}, \tag{6}$$

$\rho_0$ is the coherence length of a spherical wave propagating in the turbulent medium, $\mathbf{B}(z)$ is the sub-matrix for back-propagation from the output plane to the propagation distance $z$, and $C_n^2$ is the structure constant of turbulent atmosphere.

With the help of Eq. (3) and Eq. (5), we can study the propagation properties of an EGSM beam through paraxial ABCD optical system in free space or turbulent atmosphere conveniently, and they can be applied to study the propagation of an EGSM beam with twist phase [11]. As an application example, we study the propagation properties of an EGSM beam in a bare Gaussian cavity of length $L$ which consists of two spherical mirrors each with radius of curvature $R$ and Gaussian reflectivity profile with radius $\varepsilon$, and is equivalent to a sequence of identical thin spherical lenses with focal length $f = R/2$, followed by the amplitude filters with a Gaussian transmission function for the equivalent (unfolded) optical system. The distance between each lens-filter pair is equal to $L$. After the EGSM beam travels between two mirrors for $N$ times, $\mathbf{A}$, $\mathbf{B}$, $\mathbf{C}$ and $\mathbf{D}$ for the equivalent optical system become

$$\begin{pmatrix} \mathbf{A} & \mathbf{B} \\ \mathbf{C} & \mathbf{D} \end{pmatrix} = \begin{pmatrix} \mathbf{I} & L\cdot\mathbf{I} \\ \left(-\frac{2}{R} - i\frac{\lambda}{\pi\varepsilon^2}\right)\mathbf{I} & \left(1 - \frac{2L}{R} - i\frac{\lambda L}{\pi\varepsilon^2}\right)\mathbf{I} \end{pmatrix}^N. \tag{7}$$

We calculate in Fig. 1 the on-axis degree of polarization versus $N$ for different values of cavity parameter $g$ and the initial correlation coefficients with. From Figs. 1(a) and (b), one sees that the on-axis degree of polarization of an EGSM beam can be modulated by choosing suitable parameters
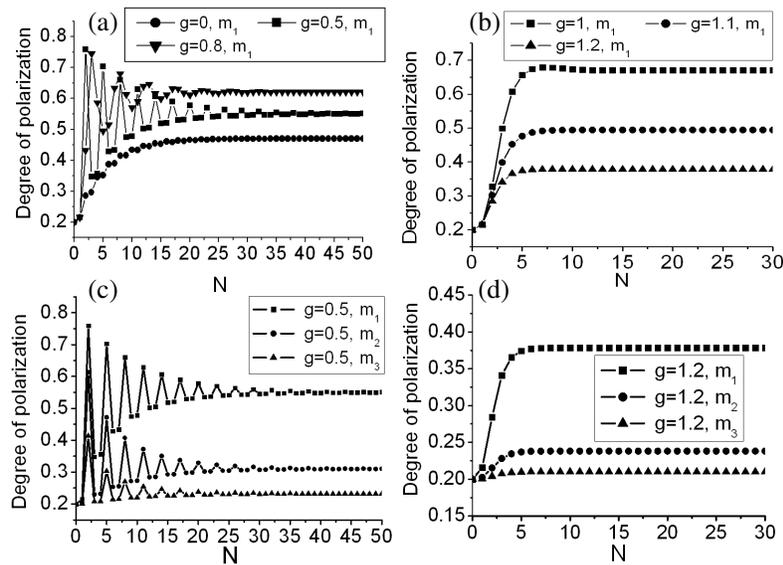


Figure 1: On-axis degree of polarization versus $N$ for different values of cavity parameter g and the source correlation coefficients. $m_1$: $\delta_{xx} = \delta_{yy} = 0.1\,\text{mm}$, $\delta_{xy} = \delta_{yx} = 0.2\,\text{mm}$. $m_2$: $\delta_{xx} = \delta_{yy} = 0.25\,\text{mm}$, $\delta_{xy} = \delta_{yx} = 0.5\,\text{mm}$. $m_3$: $\delta_{xx} = \delta_{yy} = 0.5\,\text{mm}$, $\delta_{xy} = \delta_{yx} = 1\,\text{mm}$. $\varepsilon = 0.8\,\text{mm}$, $\lambda = 590\,\text{nm}$, $A_x = A_y = 0.707$, $B_{xy} = B_{yx} = 0.2$, $\sigma_x = \sigma_y = 1\,\text{mm}$, $L = 30\,\text{cm}$.

of the cavity. Our numerical results (not present here to save space) also show that we can modulate the propagation factor, spectral shift and spectral degree of coherence of an EGSM beam by a Gaussian cavity [10, 14–16].

The tensor method also can be applied to study the propagation of an EGSM beam through a phase aperture [17]. After propagation through a circular phase aperture whose phase delay is $\phi$ and radius is $a$ in free space, the elements of the CSD matrix can be expressed in the following form [17]

$$
\begin{aligned}
W_{\alpha\beta}\left(\tilde{\rho}\right) \;=\; & A_{\alpha}A_{\beta}B_{\alpha\beta}\left\{\det\left[\tilde{\mathbf{I}}+\tilde{\mathbf{B}}\mathbf{M}_{0\alpha\beta}^{-1}\right]^{-1/2}\exp\left[-\frac{ik}{2}\tilde{\rho}^{T}\mathbf{M}_{1\alpha\beta}^{-1}\tilde{\rho}\right]\right. \\
& +\left[\exp\left(-i\phi\right)-1\right]\sum_{m=1}^{M}A_{m}\det\left[\tilde{\mathbf{I}}+\tilde{\mathbf{B}}\mathbf{M}_{0\alpha\beta}^{-1}+\tilde{\mathbf{B}}\tilde{\mathbf{B}}_{m}\right]^{-1/2}\times\exp\left[-\frac{ik}{2}\tilde{\rho}^{T}\mathbf{M}_{2\alpha\beta}^{-1}\tilde{\rho}\right] \\
& +\left[\exp\left(i\phi\right)-1\right]\sum_{p=1}^{M}A_{p}^{*}\det\left[\tilde{\mathbf{I}}+\tilde{\mathbf{B}}\mathbf{M}_{0\alpha\beta}^{-1}+\tilde{\mathbf{B}}\tilde{\mathbf{B}}_{p}\right]^{-1/2}\exp\left[-\frac{ik}{2}\tilde{\rho}^{T}\mathbf{M}_{3\alpha\beta}^{-1}\tilde{\rho}\right] \\
& +\left[\exp\left(-i\phi\right)-1\right]\left[\exp\left(i\phi\right)-1\right]\sum_{m=1}^{M}\sum_{p=1}^{M}A_{m}A_{p}^{*}\det\left[\tilde{\mathbf{I}}+\tilde{\mathbf{B}}\mathbf{M}_{0\alpha\beta}^{-1}+\tilde{\mathbf{B}}\tilde{\mathbf{B}}_{mp}\right]^{-1/2} \\
& \left.\exp\left[-\frac{ik}{2}\tilde{\rho}^{T}\mathbf{M}_{4\alpha\beta}^{-1}\tilde{\rho}\right]\right\},
\end{aligned}
\tag{8}
$$

where $\tilde{\mathbf{I}}$ is a $4\times4$ identity matrix

$$
\begin{aligned}
\mathbf{M}_{1\alpha\beta}^{-1} &= \left(\mathbf{M}_{0\alpha\beta}+\tilde{\mathbf{B}}\right)^{-1}, \quad \mathbf{M}_{2\alpha\beta}^{-1} = \left[\left(\mathbf{M}_{0\alpha\beta}^{-1}+\tilde{\mathbf{B}}_{m}\right)^{-1}+\tilde{\mathbf{B}}\right]^{-1}, \\
\mathbf{M}_{3\alpha\beta}^{-1} &= \left[\left(\mathbf{M}_{0\varepsilon\beta}^{-1}+\tilde{\mathbf{B}}_{p}\right)^{-1}+\tilde{\mathbf{B}}\right]^{-1}, \quad \mathbf{M}_{4\alpha\beta}^{-1} = \left[\left(\mathbf{M}_{0\alpha\beta}^{-1}+\tilde{\mathbf{B}}_{mp}\right)^{-1}+\tilde{\mathbf{B}}\right]^{-1}.
\end{aligned}
\tag{9}
$$

with

$$
\begin{aligned}
\tilde{\mathbf{B}} &= \left(\begin{array}{cc} z\mathbf{I} & 0\mathbf{I} \\ 0\mathbf{I} & -z\mathbf{I} \end{array}\right), \quad \tilde{\mathbf{B}}_{m} = \left(\begin{array}{cc} -\frac{2iB_{m}}{ka^{2}}\mathbf{I} & 0\mathbf{I} \\ 0\mathbf{I} & 0\mathbf{I} \end{array}\right), \\
\tilde{\mathbf{B}}_{p} &= \left(\begin{array}{cc} 0\mathbf{I} & 0\mathbf{I} \\ 0\mathbf{I} & -\frac{2iB_{p}^{*}}{ka^{2}}\mathbf{I} \end{array}\right), \quad \tilde{\mathbf{B}}_{mp} = \left(\begin{array}{cc} -\frac{2iB_{m}}{ka^{2}}\mathbf{I} & 0\mathbf{I} \\ 0\mathbf{I} & -\frac{2iB_{p}^{*}}{ka^{2}}\mathbf{I} \end{array}\right).
\end{aligned}
\tag{10}
$$

In the derivation of Eq. (8), we have expanded the aperture function into a finite sum of complex Gaussian functions, and $A_{m}$ and $B_{m}$ are the expansion and Gaussian coefficients. Our numerical results show that we can shape the beam profile and modulate the polarization and spectral degree of coherence of the EGSM beam by a circular phase aperture [17].

## 3. GENERATION OF AN EGSM BEAM

Now we introduce briefly our recent research on experimental generation of an EGSM beam [18]. Part 1 of Fig. 2 shows our experimental setup for generating an EGSM source. After passing through $P_{1}$, the initial linearly polarized He-Ne laser beam passes through a Mach-Zehnder interferometer (MZI). Two orthogonally polarized beams are superimposed together at the output of the MZI, then the combined beam illuminates a RGGP producing a stochastic electromagnetic beam. After passing through a collimating thin lens $L_{3}$ and a GAF, an EGSM source is generated. $P_{1}$ whose transmission axis forms an angle $\theta$ with the $x$-axis is used to adjust the ratio $A_{x}/A_{y}$ of the field by varying $\theta$. $L_{1}$ and $L_{2}$ in Fig. 1 are used to control the focused beam spot sizes of the $x$- and $y$-linearly polarized beams on the RGGP through adjusting the distance from $L_{1}$ to RGGP and the distance from $L_{2}$ to RGGP. $\sigma_{x}$ and $\sigma_{y}$ of the generated EGSM beam are determined by the transmission function of the GAF. The coherence parameters $\delta_{xx}$, $\delta_{yy}$ and $\delta_{xy}(\delta_{yx}=\delta_{xy})$ are determined by the focused beam spot sizes on the RGGP. $L_{1}$ and $L_{2}$ have the same focal length ($f=10\,\mathrm{cm}$), and the eikonals along two arms of the MZI are the same. Then the transmitted light

just behind the GAF is set as an EGSM source. $\phi_{xy} = 0$ due to the same eikonals along two arms of the MZI. Part 2 of Fig. 2 shows our experimental setup for measuring the parameters of the generated EGSM source. The EGSM beam emitted from the source first passes through a linear polarizer $P_2$ and a thin lens $L_4$ with focal length $f = 15$ cm, then is split into two beams by a beam splitter. The transmitted and reflected beams going through two separated optical paths will arrive at single photon detectors $D_1$ and $D_2$, which scan the transverse planes of $u$ and $v$, respectively. Both the distances from the Gaussian amplitude filter to $L_4$ and from $L_4$ to $D_1$ and $D_2$ are $2f$ (i.e., $2f$-imaging system). The output signals from $D_1$ and $D_2$ are sent to an electronic coincidence circuit to measure the fourth-order correlation function between the two detectors (i.e., intensity correlation function) [18].

First, we adjust $P_2$ to set its transmission axis along $x$-axis. In this case, only the element $W_{xx}$ exists behind $P_2$. By measuring the intensity distribution and its maximum intensity $I_{x\,\text{max}}$ at plane $u$ or $v$ with the help of the single photon detector $D_1$ or $D_2$, we can obtain the values of the parameters $\sigma_x$ and $A_x$. To measure $\delta_{xx}$, we fix $D_2$ at $v = 0$, and $D_1$ scans along the plane $u$. The coincidence circuit records the fourth-order correlation between $D_1$ and $D_2$. Through the relation between the second-order correlation and fourth-order correlation, we can obtain the value of $\delta_{xx}$. If we adjust $P_2$ to set its transmission axis along $y$-axis, only the element $J_{yy}$ exists behind $P_2$. Then through a similar operation for obtaining $\sigma_x$, $A_x$ and $\delta_{xx}$, we can measure the values of the parameters $\sigma_y$, $A_y$ and $\delta_{yy}$. Fig. 3 shows the experimental scheme for measuring the parameters $|B_{xy}|$ and $\delta_{xy}$. Different from the part 2 of Fig. 2, in this case, $P_2$ is removed, and the BS is replaced with a PBS. After passing through the PBS, the $x$ component and $y$ component of the field will arrive at $D_1$ and $D_2$, respectively. Following the same procedure for obtaining $\delta_{xx}$, $D_2$ is fixed at $v = 0$, and $D_1$ scans along the plane $u$, and the coincidence circuit record the distribution of the normalized fourth-order correlation function. Through the relation between the
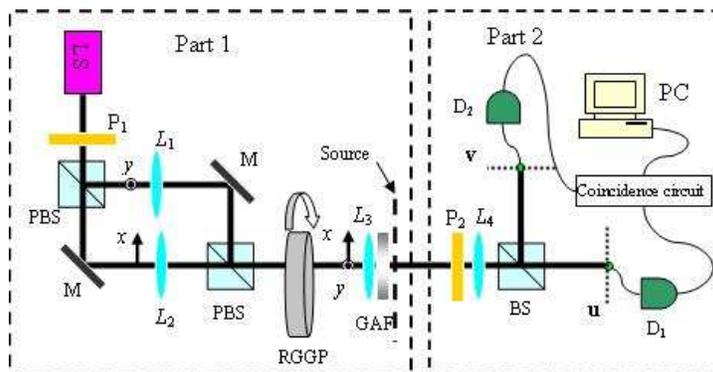


Figure 2: Experimental setup for generating an EGSM source and measuring its beam parameters. LS, He-Ne laser; $P_1$, $P_2$, linear polarizer; BS, $50:50$ beam splitter; PBS, polarization beam splitter; $L_1$, $L_2$, $L_3$, $L_4$, thin lens; $M$, reflecting mirror; RGGP, rotating ground-glass plate; GAF, Gaussian amplitude filter; $D_1$, $D_2$, single photon detector.
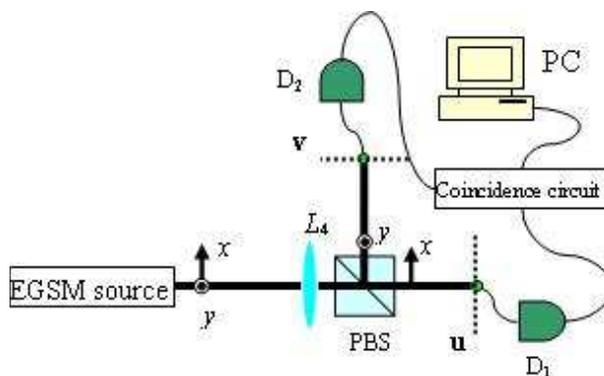


Figure 3: Experimental scheme for measuring the parameters $|B_{xy}|$ and $\delta_{xy}$.

second-order correlation and fourth-order correlation, we can obtain the values of $|B_{xy}|$ and $\delta_{xy}$. Our experimental results reported in [18] agree well with the theoretical results.

## 4. CONCLUSIONS

In conclusion, we have presented a brief review of our recent search on the propagation and generation of an EGSM beam. Our theoretical formulae provide a convenient way for studying the propagation of an EGSM beam through complex optical system in free space or turbulent atmosphere. Our experimental method for measuring the parameters of the EGSM beam provides a convenient way for study the propagation of an EGSM beam experimentally, and can be applied to study the interaction of an EGSM beam with matter.

## REFERENCES

1. Mandel, L. and E. Wolf, *Optical Coherence and Quantum Optics*, Cambridge U. Press, 1995.
2. Wolf, E., *Introduction to the Theory of Coherence and Polarization of Light*, Cambridge U. Press, 2007.
3. Wolf, E., "Unified theory of coherence and polarization of random electromagnetic beams," *Phys. Lett. A*, Vol. 312, 263–267, 2003.
4. Gori, F., M. Santarsiero, G. Piquero, R. Borghi, A. Mondello, and R. Simon, "Partially polarized Gaussian schell-model beams," *J. Opt. A: Pure Appl. Opt.*, Vol. 3, 1–9, 2001.
5. Korotkova, O., M. Salem, and E. Wolf, "Beam conditions for radiation generated by an electromagnetic Gaussian Schell-model source," *Opt. Lett.*, Vol. 29, 1173–1175, 2004.
6. Korotkova, O., "Scintillation index of a stochastic electromagnetic beam propagating in random media," *Opt. Commun.*, Vol. 281, 2342–2348, 2008.
7. Cai, Y., O. Korotkova, H. T. Eyyuboğlu, and Y. Baykal, "Active laser radar systems with stochastic electromagnetic beams in turbulent atmosphere," *Opt. Express*, Vol. 16, 15835–15846, 2008.
8. Tong, Z., Y. Cai, and O. Korotkova, "Ghost imaging with electromagnetic stochastic beams," *Opt. Commun.*, Vol. 283, 3838–3845, 2010.
9. Zhao, C., Y. Cai, and O. Korotkova, "Radiation force of scalar and electromagnetic twisted Gaussian Schell-model beams," *Opt. Express*, Vol. 17, 21472–21487, 2009.
10. Yao, M., Y. Cai, H. T. Eyyuboğlu, Y. Baykal, and O. Korotkova, "The evolution of the degree of polarization of an electromagnetic Gaussian Schell-model beam in a Gaussian cavity," *Opt. Lett.*, Vol. 33, 2266–2268, 2008.
11. Lin, Q. and Y. Cai, "Tensor ABCD law for partially coherent twisted anisotropic Gaussian-Schell model beams," *Opt. Lett.*, Vol. 27, 216–218, 2002.
12. Cai, Y. and O. Korotkova, "Twist phase-induced polarization changes in electromagnetic Gaussian Schell-model beams," *Appl. Phys. B*, Vol. 96, 499–507, 2009.
13. Zhu, S. and Y. Cai, "Spectral shift of a twisted electromagnetic Gaussian Schell-model beam focused by a thin lens," *Appl. Phys. B*, Vol. 99, 317–323, 2010.
14. Zhu, S. and Y. Cai, "$M^2$-factor of a stochastic electromagnetic beam in a Gaussian cavity," *Opt. Express*, Vol. 18, 27567–27581, 2010.
15. Korotkova, O., M. Yao, Y. Cai, H. T. Eyyuboğlu, and Y. Baykal, "State of polarization of a stochastic electromagnetic beam in an optical resonator," *J. Opt. Soc. Am. A*, Vol. 25, 2710–2720, 2008.
16. Yao, M., Y. Cai, and O. Korotkova, "Spectral shift of a stochastic electromagnetic Gaussian Schell-model beam in a Gaussian cavity," *Opt. Commun.*, Vol. 283, 4505–4511, 2010.
17. Wu, G. and Y. Cai, "Modulation of spectral intensity, polarization and coherence of a stochastic electromagnetic beam," *Opt. Express*, Vol. 19, 8700–8714, 2011.
18. Wang, F., G. Wu, X. Liu, S. Zhu, and Y. Cai, "Experimental measurement of the beam parameters of an electromagnetic Gaussian Schell-model source," *Opt. Lett.*, Vol. 36, 2722–2724, 2011.

# A Software Based Framework for Estimating Patient Displacement in Magnetic Induction Tomography

**Mamatjan Yasin**[1], **Ali Roula**[2], **Doga Gürsoy**[3], **and Andy Adler**[1]

[1]Carleton University, Ottawa, K2E7E8, Canada
[2]University of Glamorgan, Pontypridd, CF371DL, UK
[3]Graz University of Technology, Graz, A-8010, Austria

**Abstract**— Magnetic induction tomography (MIT) is a contactless, inexpensive and non-invasive technique for imaging the conductivity distribution inside volume conductors. Time-difference imaging can be used for the monitoring of patients in critical care. This includes monitoring of cerebral strokes and breathing, as well as continuous screening of edema. However, MIT signals are much more sensitive to body movements than to the conductivity changes inside of the body. This is because small movements during data acquisition can spoil the signals of interest and cause significant image artifacts. Thus, it is crucial to accurately estimate and factor body movements into image reconstruction.

**Methods:** We proposed quantitative methods for identifying and estimating object movements from simulated MIT data prior to the image reconstruction step. A simulation was performed based on a 16 channel MIT system where a finite-difference based MIT software package was used to generate reference data from a homogenous tank without a target, and subsequent measurement of moved phantom with a target placed close to edge of the tank. The movement was estimated using frequency domain analysis (FFT).

**Results:** Results show that movements of 1% of the radius of the tank cause image blurring but the artifacts can be minimized by appropriate regularization. Higher amounts of movements totally distorted the images which require artifact compensation or acquisition of new measurements. The percentage errors for FFT based movement estimation were 23% (1 mm), 0.3% (6.7 mm) and 6% (14.4 mm) for a displacement of 1% (1.3 mm), 5% (6.7 mm) and 10% (13.5 mm), respectively, where the displacements were chosen relative to the radius of the tank. It was found that the accuracy of movement estimation is related to the size of the background in real measurements.

## 1. INTRODUCTION

Magnetic Induction Tomography (MIT) is a relatively new, non-invasive technique for imaging the distribution of the electrical properties (conductivity, permittivity and permeability) of objects. MIT was proposed for numerous medical applications such as monitoring of cerebral stroke, breathing (aeration and ventilation of the lung) and continuous screening of edema [1].

Time-difference imaging can be used for monitoring the progression of the stroke, breathing or oedema to be used for continuous screening and monitoring of patients in critical care. However, it is a challenging task to do accurate measurements and to post-process the data properly in the emergency care unit since it is a highly dynamic scenario [2]. Small movements can spoil the measured data and cause significant image artifacts, which prevent the detection of the conductivity changes inside of the body. Static imaging may not reflect the dynamics of objects in monitoring applications. Especially, artifacts associated with motion of head and functional imaging of lung require keeping track the motions and compensating the artifacts.

In other tomographic fields such as CT or EIT, various software and hardware based movement detection approaches and management strategies can be grouped into two categories. First category can be named as the software based (signal/image processing) approach that may include pattern recognition, eigenvalue analysis (ICA, PCA), neural networks, edge detection and level set methods. Second one is the hardware approach and includes pressure sensitive mattresses, recording of patient movement via magnetic or optical sensors. The choice of the techniques is generally dependent on the application. For instance, considering a smart-bed application, pressure sensitive mattresses are more suitable, but a system based on a video recording or stereo tracking of patient movement is an alternative if other techniques are not appropriate. Gürsoy and Scharfetter proposed strategies for compensating patient movement in MIT based on a priori information [3].

MIT is a low resolution imaging technique that estimation and compensation of motion artifacts in MIT are a challenging task as this requires new approaches and measurements needs to

be fast processed to detect movements [4]. The goal of this paper is to estimate the movements and compensate to improve image stability and improve image quality, particularly for the continuous monitoring of patients. Based on a preliminary study, a quantitative method were proposed for identifying and estimating object movements from simulated MIT data prior to the image reconstruction step. The software based movement estimation includes frequency domain analysis (FFT). The management strategies include reconstructing images by (i) minimizing movement artifacts for small movements; (ii) compensating for the movements if these are accurately estimated, or (iii) taking a new MIT measurement if movements are too severe.

## 2. METHODOLOGY

### 2.1. Overview

In this paper, algorithmic methods were proposed for identifying and estimating object movements from simulated MIT data prior to the image reconstruction step. In time or frequency domain, the measured raw data from each individual sensor is preprocessed or post-processed using those concepts in digital signal processing, which include FFT, advanced statistical approaches (ICA) or wavelet based approaches.

### 2.2. Phantom

The homogenous tank (radius of $13.5\,\text{cm}$ and height of $20\,\text{cm}$) has the conductivity of $1\,\text{Sm}^{-1}$, and the small cubic target has the conductivity of $3\,\text{Sm}^{-1}$. A simulation was performed based on a 16 channel MIT system. A finite-difference based MIT software package was used to generate (i) reference data without a target and movement, and (ii) simulate whole tank movement with a target placed close to edge of the tank.

### 2.3. MIT Image Reconstruction

A Newton-type algorithm with Tikhonov regularization is applied to solve the inverse problem which is written as,

$$\Delta\sigma = (\mathbf{S}^T\mathbf{S} + \lambda\mathbf{I})^{-1}\mathbf{S}^T\left[\frac{(\mathbf{V}_i - \mathbf{V}_r)}{\mathbf{V}_r}\right] = \mathbf{S}^T[(\mathbf{S}^T\mathbf{S} + \lambda\mathbf{I})^{-1}\Delta\mathbf{V}] \tag{1}$$

where $\Delta\sigma$ is the change of the conductivity, $\lambda$ is the regularization parameter, $\mathbf{I}$ is the identity matrix, $S$ sensitivity matrix (Jacobian), and $\Delta\mathbf{V}$ is the difference between a reference signal $\mathbf{V}_r$ and subsequent measured signal $\mathbf{V}_i$. The size of $\Delta\mathbf{V}$ is equal to the number of measurements (precisely the excitation and detection coil combinations).

An appropriate selection of $\lambda$ is important in image reconstruction and it can be seen as a low-pass filter from a signal processing perspective. There is a trade-off between improving resolution and avoidance of noise amplification. More commonly used methods for estimating $\lambda$ are L-curve method, generalized cross validation (GCV) and Morozov's discrepancy principle.

### 2.4. Signal Analysis

Movements cause the changes/distortion in MIT signals, which means both the phase and magnitude in frequency domain are correspondingly distorted as well. The strength of the distortion due to the movement is proportional to the size of dislocation. Following algorithm is implemented to estimate the dislocation of a body:

   i. Find the phase change after the movement ($\Delta\mathbf{V}_m$).
  ii. Find the FFT for both $\mathbf{V}_r$ and $\Delta\mathbf{V}_m$.
 iii. Find the peaks (main index) from $\Delta\mathbf{V}_m$ and use it as an index value due to the movement.
 iv. correlate them using the index value in both $\mathbf{V}_r$ and $\Delta\mathbf{V}_m$ in frequency domain (magnitude of movement/magnitude of normal signal).
  v. Multiply with a certain factor (i.e., *10) which is related to the size of a tank in real measurement.

## 3. RESULTS

The proposed method equally works well on both measured raw signals through preprocessing and reconstructed images through post-processing, so only post-possessing results are presented. The results in Figure 1 show that there are certain correlation between the distortion magnitude and the size of movement with larger distortion with increasing movement size.

Figure 2 shows the effect of regularization (filtering) value and the non-negativity constraint. The row one is for the reconstructed images with 1% movement and row two is for 5% movement, and columns is for increased regularization. It can be seen that the increased regularization (filtering) reduced certain movement noise (row 2) and a smooth object appeared, but it also get rid of useful information in row 1 which leads to losing of spatial resolution.

Figure 3 shows the reconstructed images after eliminating the movement artifact based on a priori information. For known amounts of movement, the image artifacts can be suppressed.

Table 1 presents the estimated movement and percentage error for 3 types of movements.
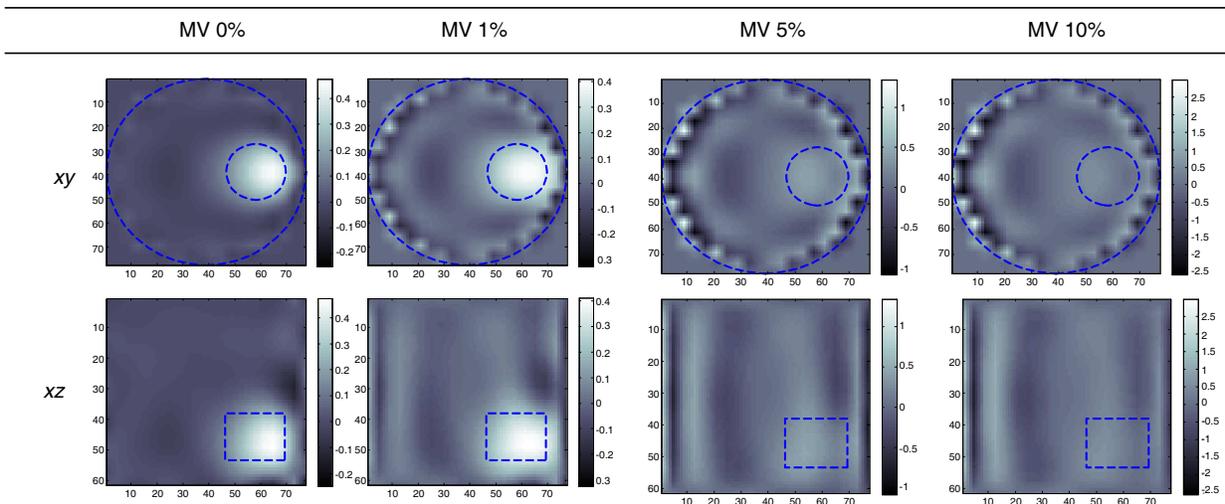


Figure 1: Reconstructed images with movements of 1% (1.3 mm), 5% (6.7 mm) and 10% (13.5 mm) relative to the radius of the tank. Note: MV stands for movement, row 1 is for $xy$ plane and row 2 is for $xz$ plane.
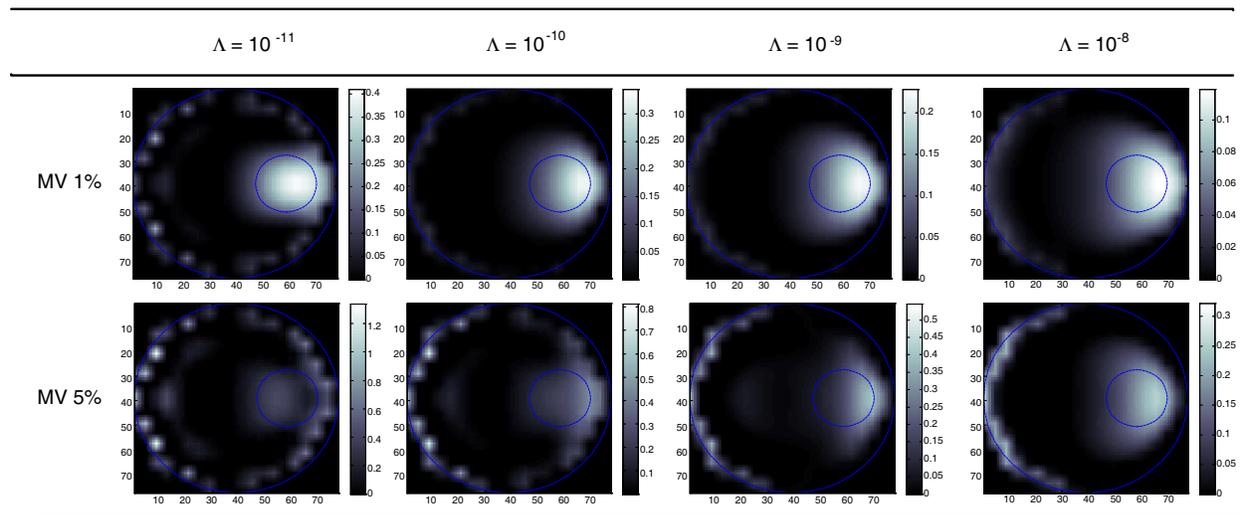


Figure 2: Reconstructed images with varying the regularization (filtering) value and the non-negativity constraint.

Table 1: Estimated movement and percentage error (movement in mm).

| Original movement | Estimated movement | Percentage error (%) |
|---|---|---|
| 1.3 (1%) | 1 | 23 |
| 6.75 (5%) | 6.73 | 0.3 |
| 13.5 (10%) | 14.4 | 6 |
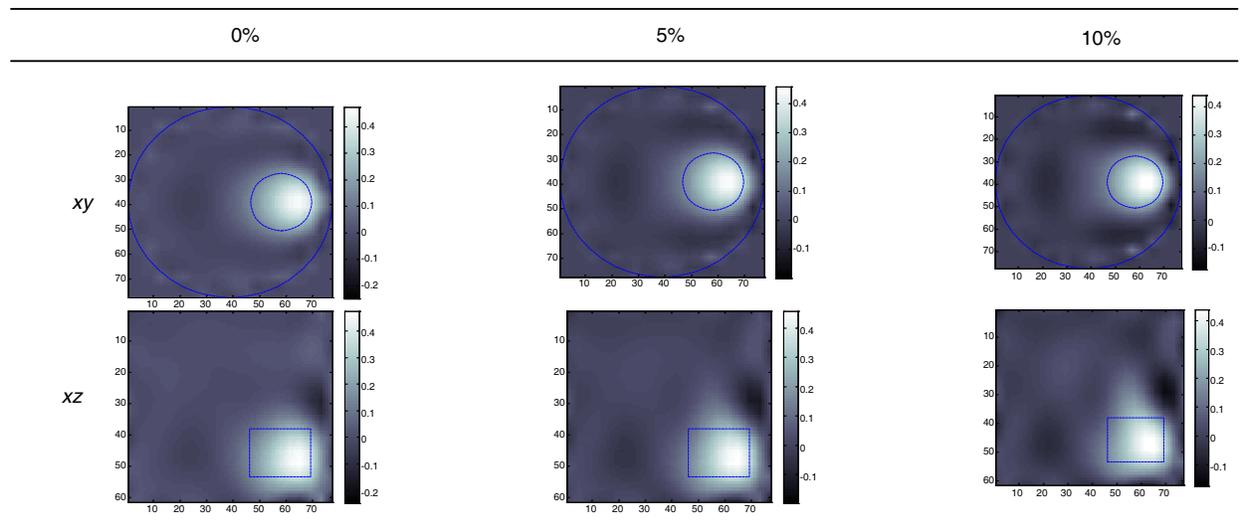
Figure 3: Reconstructed images after movement artefact compensation using a priori information.

## 4. DISCUSSIONS AND CONCLUSIONS

In this paper, the effect of body displacement for signal and image quality was investigated, and quantitative methods and algorithms were proposed to estimate the displacement to identify and compensate imaging artifacts caused by the displacement. An FFT based approach was evaluated for the movement estimation due to its simplicity in discriminating signals from noise. Frequency analysis provides hints about the motions, since the upper and lower frequency sideband components appear as ghosts either side of the primary image. The percentage errors for FFT based movement estimation were 23%, 0.3% and 6% for movement of 1% (1.3 mm), 5% (6.7 mm) and 10% (13.5 mm) of the radius of the tank. Studies also showed that movement less than 2% blur the image but the artifacts can be minimized by regularization approach without artifact compensation or taking new measurements.

The accuracy of the movement estimation was found to be related with the size of the background in the real measurement study. Following management strategies are proposed once movements are identified, images are reconstructed by (i) minimizing movement artefacts for small movements; (ii) compensating for the movements if these are accurately estimated, or (iii) taking a new MIT measurement if movements are too severe.

For certain applications, multi-frequency measurement and absolute imaging can be used since they are not affected by the movement under a criterion that the movement is taken place in two separate measurements not during the measurement. Although multi-frequency MIT may offer advantages in terms of reducing movement artefacts and provide more useful diagnostic information for medical applications, the frequency dependencies of MIT received signal is a major limitation.

Measurement noise and image artifacts caused by the body displacement are a major problem in patient monitoring that makes it challenging to acquire accurate measurement and perform post-processing properly. The framework could help improve the stability of MIT measurements for a long period and produce better reconstructed image quality. The advantages of the software approach compared to hardware approach are faster processing and cost-effectiveness as it does not require any extra hardware. A further study will be conducted using statistical and wavelet approaches under this framework, and further movement will be tested in both simulation and reality to provide dynamic compensation.

**REFERENCES**

1. Griffiths, H., "Magnetic induction tomography," *Measurement Science & Technology*, Vol. 12, 1126–1131, 2001.
2. Maimaitijiang, Y., M. A. Roula, and J. Kahlert, "Approaches for improving image quality in magnetic induction tomography," *Physiol. Meas.*, Vol. 31, S147–S156, 2010.
3. Gürsoy, D. and H. Scharfetter, "Reconstruction artefacts in magnetic induction tomography due to patient's movement during data acquisition," *Physiol. Meas.*, Vol. 30, No. 6, S165–S174, 2009.

4. Maimaitijiang, Y., H. C. Wee, S. Watson, M. A. Roula, R. Patz, and R. J. Williams, "Evaluations of parallel FFT implementations on GPU and multi-core pcs for magnetic induction tomography," *World Congress on Medical Physics and Biomedical Engineering (WC2009)*, Munich, Germany, 2009.

# Effects of Loop Shape, Size and Filling Factor on RF Transmit Performance for a 7 T Multi-channel Loop Array

**M. Kozlov and R. Turner**

Planck Institute for Human Cognitive and Brain Sciences, Leipzig, Germany

**Abstract**— We present numerical investigations of transmit only loop-based RF arrays, with different loop shapes, sizes and geometrical filling factors. Using RF circuit and frequency domain 3-D EM co-simulation, we analyzed arrays with inductor-based decoupling networks, and compared the results with arrays tuned by minimization of the power reflected by the entire array, with no dedicated decoupling network. After tuning by reflected power minimization, the transmit performance of a shielded loop array with no dedicated decoupling network was only weakly dependent on filling factor, provided that its diameter was less than 280 mm. Performance was strongly affected by geometrical filling factor only if the diameter was more than 280 mm and the array was unshielded.

## 1. INTRODUCTION

For a single loop coil the excitation profile is strongly influenced by the distance between array and load [1]. However, there are no reliable transmit performance data for a loop-based array, loaded by a realistic head model, as a function of array to load distance (geometrical filling factor), or array shape. Furthermore, it is hard to compare literature values for transmit performance, because data for B1+ field versus array input power ($\mathbf{P}_{transmit}$) and power budget are rarely reported. While parallel transmission and RF shimming are hot topics, for many practical applications so far the workhorse for driving a multi-channel transmit RF coil has been a single power amplifier followed by a power splitter and phase shifter to excite circular polarization (CP) mode. The two types of 8-channel loop based 7 T array investigated were accordingly excited, applying 1 W power to each port ($\mathbf{P}_{transmit} = 8$ W), with a sequential 45 degree phase increment. Data obtained after performing simulated RF shimming will be reported separately.

## 2. METHOD

In the simulation, for array type #1, eight rectangular planar resonance coil elements were mounted on rectangular acrylic supports, assembled to give an octagonal cross section with extreme dimensions of 230 mm by 255 mm, as in our previous research [2]. The planar single loop elements were simulated with width 85 and length 120 mm. RF array type #2 comprised 8 channels with identical rectangular loops (length 120 mm, angular size 40 degree), mounted on a cylindrical acrylic former with diameter ranging from 220 mm to 300 mm. 8 capacitors (represented as green patches on the copper strip in Fig. 1) were placed in each loop to provide tune, shunt, and distributed capacitor functionality. **Q** factor of all capacitors is equal 1000, and the inductor was simulated as lossless. The realistic 3-D EM model included all coil construction details for the resonance elements, simulated with precise dimensions and material electrical properties. The loads utilized were the
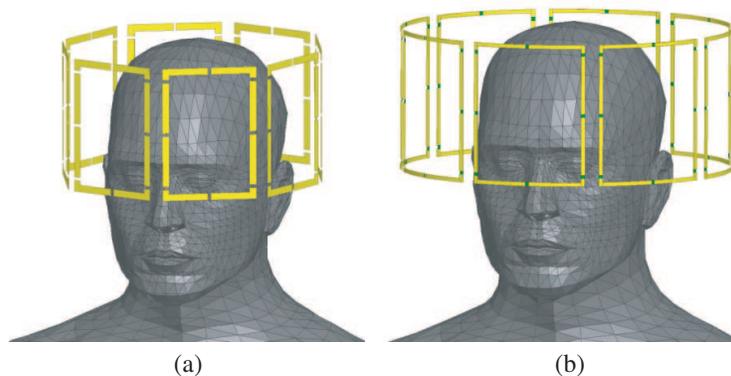


Figure 1: Array geometry: (a) type #1, (b) type #2.

Ansoft human body (head, shoulders, torso) with scaling factor: $X = 0.9$, $Y = 0.9$, $Z = 0.9$. The scanner gradient shield (with diameter of 683 mm and length 1200 mm) was always included in the numerical domain for the simulation of unshielded and shielded arrays. The distance between the shielded array and a 300 mm long local shield was varied to maintain approximately the same ratio of the distances of coil to load center and shield to load center.

Our investigation was performed using RF circuit and 3-D EM co-simulation [3]. For all geometries the array was either tuned, matched and decoupled using inductive decoupling network, or alternatively tuned by minimization of the power reflected by the entire array ($\mathbf{P}_{array\_refl}$) with no dedicated decoupling network.

The results reported were obtained under the following array design conditions: a) the values of the fixed capacitors were not limited to the commercially available range, b) zero tolerance in component values was assumed, c) all tuning, matching and decoupling optimizations reached global minima for the criterion parameter vector selected. The optimization criteria were a) for decoupled arrays: the impedance matching ($\mathbf{S}_{xx}$) for each element was required to be less than $-30$ dB, and the inter-element coupling ($\mathbf{S}_{xy}$) for each adjacent element pair to be decoupled was required to be less than $-18$ dB, at the Larmor frequency ($\mathbf{F}_{MRI}$) (thus there were 16 criteria for 8-element arrays); b) for arrays with no dedicated decoupling network, the reflected power $\mathbf{P}_{array\_refl}$ was required to be zero (a single criterion). This latter approach is not concerned with minimization of $\mathbf{S}_{xx}$ and $\mathbf{S}_{xy.}$. Instead, in most cases this optimization yielded highly coupled array elements and pure $\mathbf{S}_{xx}$ matching [4].

The array was excited in circular polarization mode, applying 1 W power to each port (array transmit power, $\mathbf{P}_{transmit} = 8$ W), with a sequential 45 degree phase increment. We analyzed the quantities related to the power budget, obtained by direct calculation from volume and surface loss densities or wave quantities: a) $\mathbf{P}_{array\_refl}$, the power reflected by the entire array; b) $\mathbf{P}_{radiated}$ the radiated power; c) $\mathbf{P}_{array\_internal}$, the inherent coil losses produced by lossy capacitors, dielectrics, and conductors; and d) $\mathbf{P}_{load}$ the power absorbed by the load. One volume of interest ($\mathbf{VOI}$) was defined as the entire human brain. The array transmit properties were evaluated by considering the values of a) $\mathbf{B}_1+_V$, the value of $\mathbf{B}_1+$ averaged over $\mathbf{VOI}$, and its root-mean-square inhomogeneity (evaluated as a percentage "%"); b) $\mathbf{B}_1+_s$, the mean $\mathbf{B}_1+$ averaged over the transverse central slice through the $\mathbf{VOI}$, and its root-mean-square inhomogeneity (evaluated as a percentage "%"); c) $\mathbf{P}_V$, the power deposited in the $\mathbf{VOI}$; d) $\mathbf{E}_V = \mathbf{B}_1 +_V /\sqrt{\mathbf{P}_V}$, the $\mathbf{VOI}$ excitation efficiency; e) $\mathbf{SAR}_{10g}$, the peak SAR averaged over 10 gram; and f) $\mathbf{B}_1+_V/\sqrt{\mathbf{SAR}_{10g}}$, the safety excitation efficiency. Parameters also evaluated were the $\mathbf{S}$ parameter matrix; $\mathbf{Q}_{loaded}$, the quality factor for the first array element; $\mathbf{maxS}_{21}$, the maximum value of coupling between adjacent elements; and $\mathbf{maxS}_{31}$, the maximum value between the second adjacent elements.

Although widely used for indirect evaluation of $\mathbf{P}_{array\_internal}$ and $\mathbf{P}_{load}$ [5], the $\mathbf{Q}_{load}/\mathbf{Q}_{unload}$ ratios are not tabulated here, since $\mathbf{P}_{array\_internal}$ and $\mathbf{P}_{load}$ were directly evaluated and also because the use of $\mathbf{Q}_{load}/\mathbf{Q}_{unload}$ can mislead the array power budget analysis at 300 MHz. The reasons for this are as follows: a) both for unloaded and loaded coils, radiation losses and the coupling between array elements differ significantly; b) the coupling between power supply and coil is altered by coil loading, which can invalidate the general requirement of critical coupling that enables calculation of the $\mathbf{Q}$-factor; and c) the reflected power $\mathbf{P}_{array\_refl}$ is not taken into account.
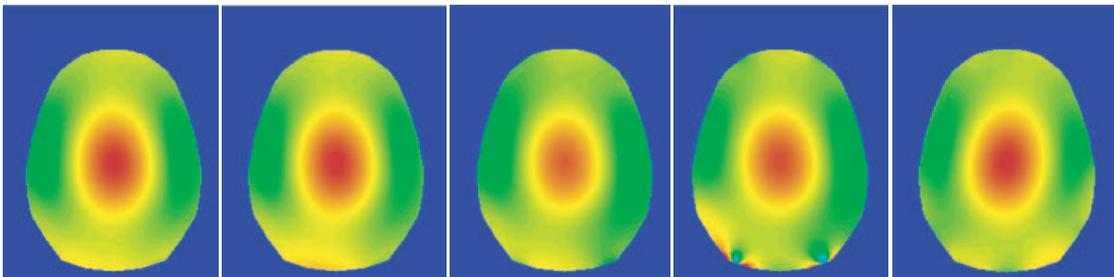


Figure 2: $\mathbf{B}_1+$ central transverse slices rescaled to individual maxima. From left to right arrays: Ø300 mm, Ø280 mm, Ø250 mm, Ø220 mm, 230 mm by 255 mm.

## 3. RESULTS AND DISCUSSION

For excitation in CP mode of the entire brain, for all arrays, the ratio of $\mathbf{B}_1+_V/\sqrt{\mathbf{P}_V}$ was equal to $1.0\,\mu\text{T}/\sqrt{\text{W}}$ with only $+/-3\%$ variation. The best transmit performance, which was estimated as $\mathbf{B}_1+_{brain}/\sqrt{\mathbf{P}_{transmit}}$, was ensured by the dominance of non-conservative fields, and delivery of the maximal $\mathbf{P}_V$ power to the brain. Taking into account the knowledge that $\mathbf{P}_V$, $\mathbf{P}_{load}$, $\mathbf{P}_{radiated}$ and $\mathbf{P}_{array\_internal}$ are all closely interrelated, the larger values of $\mathbf{P}_{array\_refl}$, and fraction of both $\mathbf{P}_{array\_internal}$ and $\mathbf{P}_{radiated}$ in array absorbed power ($\mathbf{P}_{transmit}-\mathbf{P}_{array\_refl}$), the smaller $\mathbf{P}_V$ and poorer the array coil performance.

Relative to the decoupled array, there was significantly increased coupling between elements for arrays tuned by minimization of $\mathbf{P}_{array\_refl}$ with no dedicated decoupling network. However, because this strategy minimized $\mathbf{P}_{array\_refl}$ to zero, slightly reduced the contribution of $\mathbf{P}_{array\_internal}$ in the array power budget, and maintained a constant level of $\mathbf{P}_{radiated}$ (consequently maximizing $\mathbf{P}_V$), it gave the best possible CP mode excitation performance for a given distance to the load and the shape of the array.

The effects of loop shape, size and filling factor on RF transmit performance depended on whether the array was decoupled. Shielded arrays with no dedicated decoupling network showed the least influence of array diameter on transmit performance. Increasing the array diameter from 220 to 300 mm resulted in a decrease of both $\mathbf{B}_1+_V$ and $\mathbf{B}_1+_s$, by as much as 6 and 8% correspondingly. Strikingly, in order to excite the same brain with the same $\mathbf{B}_1+_V$, the 300 mm diameter array thus utilized only 12% more power.

For array type #1, with rectangular elements, the values of $\mathbf{B}_1+_V$ and $\mathbf{B}_1+_s$, are lower, by as much as 5% and 1% correspondingly, as compared with the 250mm diameter array type #2.

Table 1: Unshielded array performance for different shapes and diameters.

| Coil shape | Ø300mm | | Ø280mm | | Ø250mm | | Ø220mm | | 230 mm by 255 mm | |
|---|---|---|---|---|---|---|---|---|---|---|
| Tuning | R | I | R | I | R | I | R | I | R | I |
| $\mathbf{P}_{reflected}$, W | 0 | 1.19 | 0 | 1.00 | 0 | 0.70 | 0 | 0.5 | 0 | 0.51 |
| $\mathbf{P}_{radiated}$, W | 1.41 | 1.12 | 1.00 | 0.86 | 0.53 | 0.50 | 0.24 | 0.25 | 0.42 | 0.53 |
| $\mathbf{P}_{array\_internal}$, W | 0.47 | 0.49 | 0.39 | 0.43 | 0.31 | 0.35 | 0.23 | 0.26 | 0.28 | 0.29 |
| $\mathbf{P}_{body}$, W | 6.12 | 5.20 | 6.61 | 5.71 | 7.16 | 6.45 | 7.53 | 6.99 | 7.30 | 6.67 |
| $\mathbf{P}_{brain}$, W | 2.21 | 1.84 | 2.41 | 2.05 | 2.64 | 2.34 | 2.76 | 2.52 | 2.58 | 2.39 |
| $\mathbf{B}_1+_{brain}$, μT | 1.48 | 1.36 | 1.56 | 1.44 | 1.65 | 1.56 | 1.71 | 1.63 | 1.57 | 1.51 |
| Inhomogeneity brain, % | 23 | 23 | 23 | 23 | 23 | 23 | 23 | 24 | 24 | 24 |
| $\mathbf{B}_1+_{slice}$, μT | 1.64 | 1.51 | 1.75 | 1.62 | 1.87 | 1.76 | 1.95 | 1.86 | 1.83 | 1.75 |
| Inhomogeneity slice, % | 18 | 18 | 18 | 18 | 18 | 18 | 18 | 18 | 21 | 22 |
| $\mathbf{SAR}_{10g}$, W/kg | 3.95 | 3.38 | 4.38 | 3.82 | 4.90 | 4.44 | 5.19 | 4.89 | 4.61 | 4.26 |
| $\mathbf{B}_1+_V/\sqrt{\mathbf{SAR}_{10g}}$, μT/$\sqrt{\text{(W/kg)}}$ | 0.74 | 0.74 | 0.75 | 0.74 | 0.74 | 0.74 | 0.75 | 0.74 | 0.74 | 0.73 |
| $\mathbf{Q}_{loaded}$ for 1st element | 18 | 36 | 16 | 33 | 12 | 27 | 7 | 19 | 9 | 15 |
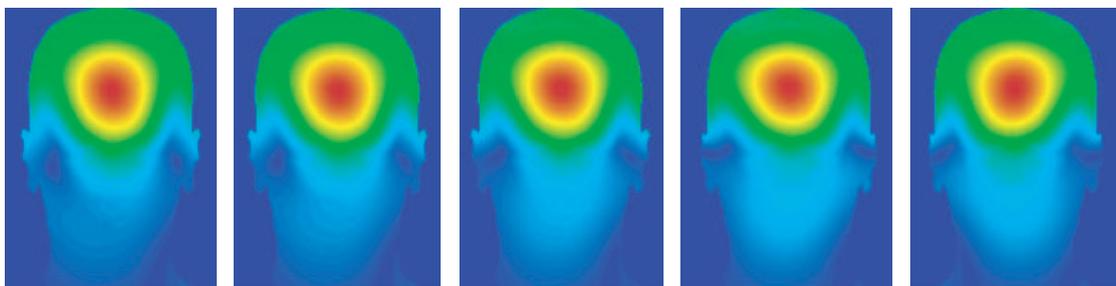


Figure 3: $\mathbf{B}_1+$ coronal slices. From left to right arrays: Ø300 mm, Ø280 mm, Ø250 mm, Ø220 mm, 230 mm by 255 mm.

Table 2: Shielded array performance for different shapes and diameters.

| Coil shape | Ø300mm | | Ø280mm | | Ø250mm | | Ø220mm | | 230 mm by 255 mm | |
|---|---|---|---|---|---|---|---|---|---|---|
| Tuning | R | I | R | I | R | I | R | I | R | I |
| $\mathbf{P}_{reflected}$, W | 0 | 0.45 | 0 | 0.40 | 0 | 0.33 | 0 | 0.31 | 0 | 0.46 |
| $\mathbf{P}_{radiated}$, W | 0.18 | 0.17 | 0.11 | 0.11 | 0.05 | 0.05 | 0.02 | 0.02 | 0.22 | 0.19 |
| $\mathbf{P}_{array\_internal}$, W | 1.04 | 1.19 | 0.82 | 0.97 | 0.54 | 0.67 | 0.33 | 0.42 | 0.66 | 0.69 |
| $\mathbf{P}_{body}$, W | 6.78 | 6.19 | 7.07 | 6.52 | 7.41 | 6.95 | 7.65 | 7.25 | 7.12 | 6.66 |
| $\mathbf{P}_{brain}$, W | 2.47 | 2.24 | 2.59 | 2.38 | 2.70 | 2.53 | 2.76 | 2.60 | 2.60 | 2.40 |
| $\mathbf{B}_1+_{brain}$, μT | 1.60 | 1.53 | 1.65 | 1.58 | 1.69 | 1.64 | 1.73 | 1.67 | 1.67 | 1.61 |
| Inhomogeneity brain, % | 24 | 24 | 23 | 23 | 24 | 24 | 24 | 25 | 24 | 24 |
| $\mathbf{B}_1+_{slice}$, μT | 1.81 | 1.73 | 1.88 | 1.80 | 1.95 | 1.88 | 1.99 | 1.93 | 1.92 | 1.85 |
| Inhomogeneity slice, % | 19 | 19 | 18 | 18 | 18 | 18 | 18 | 19 | 18 | 18 |
| $\mathbf{SAR}_{10g}$, W/kg | 4.35 | 4.04 | 4.61 | 4.36 | 4.87 | 4.74 | 5.08 | 4.95 | 4.70 | 4.42 |
| $\mathbf{B}_1+_V/\sqrt{\mathbf{SAR}_{10g}}$, μT/$\sqrt{(}$ W/kg) | 0.77 | 0.76 | 0.77 | 0.76 | 0.76 | 0.75 | 0.77 | 0.76 | 0.77 | 0.77 |
| $\mathbf{Q}_{loaded}$ for 1st element | 41 | 77 | 32 | 67 | 19 | 48 | 11 | 30 | 12 | 22 |
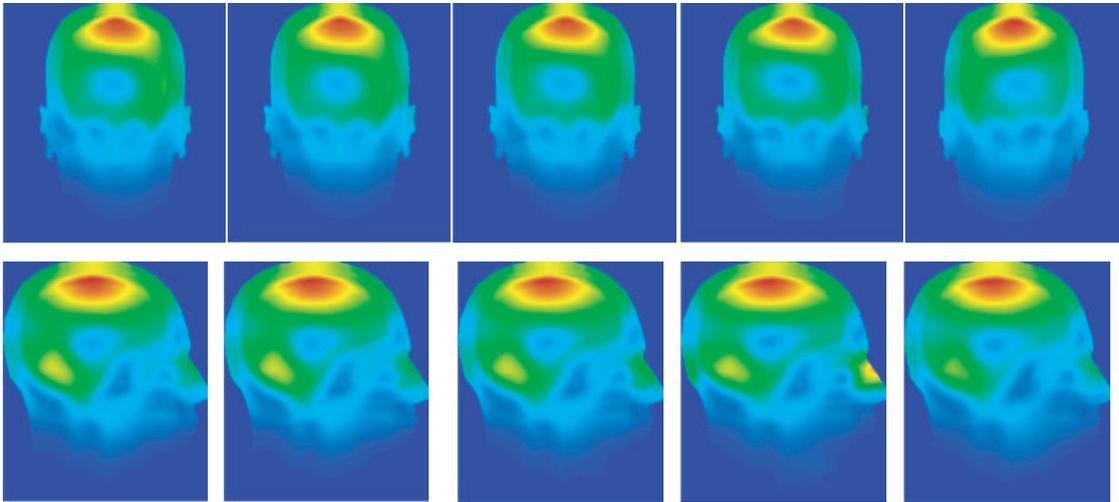


Figure 4: SAR profiles. Top coronal, bottom sagittal. From left to right arrays: Ø300 mm, Ø280 mm, Ø250 mm, Ø220 mm, 230 mm by 255 mm.

Predictably, the radiated power ($\mathbf{P}_{radiated}$) is larger (up to 16% of $\mathbf{P}_{transmit}$) when the 300 mm diameter array is unshielded.

For all arrays investigated, there was no striking difference in $\mathbf{B}_1+$ distribution within the central transverse slice, when the data are rescaled to the maximum value calculated in the brain (Fig. 1). The simulated slice and whole brain inhomogeneity also varied only slightly (Table 1).

For inductively decoupled arrays, $\mathbf{P}_{array\_refl}$ can be unexpectedly high. For example, for an array diameter of 300 mm, $\mathbf{S}_{21}$ and $\mathbf{S}_{31}$ are equal to $-15.3/-10.7$ dB and $-14.0/-9.8$ dB for the shielded and unshielded array respectively. This relatively small increase of coupling for the unshielded array results in a 100% rise of $\mathbf{P}_{array\_refl}$, which increases to 14% of $\mathbf{P}_{transmit}$. Taking into account the much smaller $\mathbf{P}_{radiated}$ and $\mathbf{P}_{array\_refl}$ (despite the same relative increase of $\mathbf{P}_{array\_refl}$) the transmit performance of the array type#1 dropped relatively less when unshielded than the 300 mm diameter array.

The difference is negligible between SAR profiles for array type #1 and RF arrays of type #2 with diameters in the range 250–300 mm. Only for an array with diameter of 220 mm is there an additional SAR hot spot, in the noise area (Fig. 3).

## 4. CONCLUSION

For an transmit only array excited by a single power source, followed by a power splitter and phase shifters operating in the CP mode, there was no advantage to use an array with shape adapted to the human head. After tuning by reflected power minimization, the transmit performance of a shielded loop array with no dedicated decoupling network was only weakly dependent on geometrical filling factor, provided that its diameter was less than 280 mm. Performance was strongly affected by geometrical filling factor only if the diameter was more than 280 mm and the array was unshielded. As an important result, analysis of the power balance is clearly to be regarded as key for understanding the relative improvement or degradation of array performance.

## REFERENCES

1. Prince, J. L. and J. M. Links, *Medical Imaging Signals and Systems*, Pearson Prentice Hall, New Jersey, 2006.
2. Kozlov, M. and R. Turner, "Comprehensive analysis of transmit performance for an 8-element loop MRI RF coil at 300 MHz," *Proceedings of the 40th European Microwave Conference*, 328–331, Paris, France, Sep. 2010.
3. Kozlov, M. and R. Turner, "Fast MRI coil analysis based on 3-D electromagnetic and RF circuit co-simulation," *Journal of Magnetic Resonance*, No. 200, 147–152, 2009.
4. Kozlov, M. and R. Turner, "Analysis of transmit performance optimization strategies for multi channel MRI array," *PIERS Proceedings*, 1622–1626, Marrakesh, Morocco, Mar. 20–23, 2011.
5. Lemdiasov, R., A. Obi, and R. Ludwig, "A numerical postprocessing procedure for analyzing radio frequency MRI coils," *Concepts in Magnetic Resonance Part A*, Vol. 38A, No. 4, 133–147, 2011.

# Radiation Pattern Decoupling for Compact Transmitting Antenna Arrays

**C. H. Niow and H. T. Hui**

Department of Electrical and Computer Engineering, National University of Singapore, Singapore

**Abstract**— An effective method is proposed to compensate for the coupled array patterns of the compact antenna arrays due to mutual coupling. By using the mutual impedances of the antenna elements and the principle of pattern multiplication, it is possible to design compensation networks remove the distortion in the coupled array patterns. Equations to realize the compensation networks are derived. Numerical examples on the dipole and monopole arrays are discussed to demonstrate the validity and accuracy of the compensation method.

## 1. INTRODUCTION

The development of small-size electronic devices led to the recent interest in the design of compact antenna arrays [1]. However, such compact antenna arrays suffer from the effects of mutual coupling [2] as it limits the array size that the array elements can be placed close together. The antenna mutual coupling has a significant effect on the compact antenna arrays performance such as gain, bandwidth and beamforming capabilities.

Various decoupling methods [2–9] were proposed to overcome the mutual coupling effects in the compact antenna arrays. However, these decoupling methods could only be applied for receiving arrays [2–6] or for input ports of the feeding networks [7–9]. For array signal processing algorithms, it is crucial to have isolated element radiation patterns from the compact antenna arrays even if there is strong mutual coupling between the antenna elements. Isolated element radiation patterns cannot be achieved in conventional port-decoupling methods although they can remove the mutual coupling between the input ports and guarantee maximum power transfer between the source and the antenna array.

In this paper, we propose a simple but effective compensation method to decouple the coupled radiation patterns in the transmitting compact antenna arrays due to mutual coupling so that the radiation patterns of the individual antenna element effectively appear as isolated element patterns. We will demonstrate the design of a compensation network based on the mutual impedances [10] to restore the isolated element patterns from the coupled radiation patterns so that the total array radiation pattern can be predicted using the principle of pattern multiplication [11]. We will also demonstrate the compensation method with some typical numerical examples on array pattern calculations and beamforming performance of antenna arrays.

## 2. THE COMPENSATION METHOD

Consider a two-element transmitting antenna array where Antenna #1 is excited by a voltage source $V_{s1}$ and antenna #2 is excited by $V_{s2}$. The internal impedances of the two voltage sources are $Z_{g1}$ and $Z_{g2}$, respectively. To account for the mutual coupling effect, the two antennas are represented by their equivalent circuits shown in Figure 1.
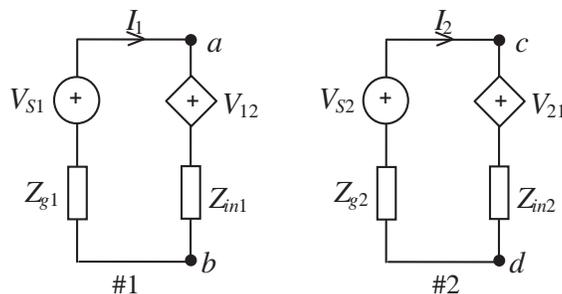


Figure 1: The equivalent circuits of the two-element transmitting antenna array.

$V_{12}$ and $V_{21}$ are the coupled voltages at antenna #1 and antenna #2, respectively. $Z_{in1}$ and $Z_{in2}$ are the input impedances looking from the antenna terminals into antenna #1 and antenna

#2 respectively. The distortion of the radiation pattern of the array caused by the coupled voltage sources $V_{12}$ and $V_{21}$ can be expressed using the mutual impedances $Z_{12}$ and $Z_{21}$ [11] of the array as

$$V_{12} = Z_{12}I_2 \tag{1a}$$
$$V_{21} = Z_{21}I_1 \tag{1b}$$

where $I_1$ and $I_2$ are the currents on antennas. In order to restore the isolated radiation patterns of the array, the coupled voltages $V_{12}$ and $V_{21}$ have to be compensated from the feeding voltages to the antennas. That means the feeding circuits of the antennas have to be modified with two controlled voltage sources added to the excitation voltages $V_{S1}$ and $V_{S2}$ in order to compensate the coupled voltages $V_{12}$ and $V_{21}$. Let these compensated voltages be $V'_{S1}$ and $V'_{S2}$, which can be expressed as

$$\begin{bmatrix} V'_{S1} \\ V'_{S2} \end{bmatrix} = \begin{bmatrix} 1 & \frac{Z_{12}}{Z_{A2}} \\ \frac{Z_{21}}{Z_{A1}} & 1 \end{bmatrix} \begin{bmatrix} V_{S1} \\ V_{S2} \end{bmatrix} \tag{2}$$

where $Z_{A1} = Z_{g1} + Z_{in1}$ and $Z_{A2} = Z_{g2} + Z_{in2}$. Equation (2) means that if the antennas are excited with the compensated voltages $V'_{S1}$ and $V'_{S2}$ instead of the excitation voltages $V_{S1}$ and $V_{S2}$, the two antenna elements will produce the isolated radiation patterns as if they were produced by the two excitation voltages $V_{S1}$ and $V_{S2}$ without the effect of mutual coupling. The results obtained are desirable because the radiation pattern of the array can now be predicted accurately using the principle of pattern multiplication [11].

The two-element antenna array in (2) can be easily generalized to that of an $n$-element antenna array which can be expressed as

$$\begin{bmatrix} V'_{S1} \\ V'_{S2} \\ \vdots \\ V'_{Sn} \end{bmatrix} = \begin{bmatrix} 1 & \frac{Z_{12}}{Z_{A2}} & \cdots & \frac{Z_{1n}}{Z_{An}} \\ \frac{Z_{21}}{Z_{A1}} & 1 & \cdots & \vdots \\ \vdots & \vdots & \ddots & \vdots \\ \frac{Z_{n1}}{Z_{A1}} & \cdots & \cdots & 1 \end{bmatrix} \begin{bmatrix} V_{S1} \\ V_{S2} \\ \vdots \\ V_{Sn} \end{bmatrix}. \tag{3}$$

Equation (3) is important in the analysis of mutual coupling in transmitting antenna arrays and the design of array feeding networks although it is not explicitly derived before. The proposed compensation method can also accommodate another matching circuit in the feeding network such as a conventional port-decoupling network. This can be accomplished by changing the impedances of $Z_{g1}, Z_{g2}, \ldots$, and $Z_{gn}$ so as to match the antenna impedances $Z_{in1}, Z_{in2}, \ldots$, and $Z_{in(n)}$.

## 3. NUMERICAL RESULTS AND DISCUSSIONS

Consider a seven-element compact monopole ULA used for beamforming. The length of each monopole is $\lambda/4$ and the radius is $1/100$ of its length. The separation $d$ between adjacent monopoles is $0.15\lambda$. The monopoles are parallel to the $z$ axis and an infinite ground plane is at the $xy$-plane. In Table 1, we calculate the compensation voltages of the monopole elements when a single beam

Table 1: The compensation voltages of the seven-element monopole array for forming different main-beam directions.

| | $\varphi = 0°$ | $\varphi = 30°$ | $\varphi = 60°$ | $\varphi = 90°$ |
|---|---|---|---|---|
| $V'_{S1}$ | $1.088\angle -10.35°$ | $1.101\angle -11.29°$ | $1.169\angle -11.9°$ | $1.28\angle -6.99°$ |
| $V'_{S2}$ | $1.332\angle -49.44°$ | $1.361\angle -45.48°$ | $1.53\angle -28.83°$ | $1.618\angle -4.9°$ |
| $V'_{S3}$ | $1.421\angle -104.27°$ | $1.495\angle -90.87°$ | $1.626\angle -56.45°$ | $1.656\angle -11.2°$ |
| $V'_{S4}$ | $1.551\angle -151.62°$ | $1.583\angle -133.99°$ | $1.638\angle -85.57°$ | $1.647\angle -12.74°$ |
| $V'_{S5}$ | $1.487\angle 154.06°$ | $1.587\angle 176.55°$ | $1.702\angle -117.4°$ | $1.656\angle -11.2°$ |
| $V'_{S6}$ | $1.676\angle 95.42°$ | $1.751\angle 127.84°$ | $1.767\angle -141.76°$ | $1.618\angle -4.9°$ |
| $V'_{S7}$ | $1.606\angle 48.53°$ | $1.654\angle 85.43°$ | $1.419\angle -167.34°$ | $1.28\angle -6.99°$ |

Table 2: The excitation voltages of the seven-element monopole array for forming different main-beam directions.

| | $\varphi = 0°$ | $\varphi = 30°$ | $\varphi = 60°$ | $\varphi = 90°$ |
|---|---|---|---|---|
| $V_{S1}$ | $1\angle 0°$ | $1\angle 0°$ | $1\angle 0°$ | $1\angle 0°$ |
| $V_{S2}$ | $1\angle -54°$ | $1\angle -46.8°$ | $1\angle -27°$ | $1\angle 0°$ |
| $V_{S3}$ | $1\angle -108°$ | $1\angle -93.5°$ | $1\angle -54°$ | $1\angle 0°$ |
| $V_{S4}$ | $1\angle -162°$ | $1\angle -140.3°$ | $1\angle -81°$ | $1\angle 0°$ |
| $V_{S5}$ | $1\angle -216°$ | $1\angle -187.1°$ | $1\angle -108°$ | $1\angle 0°$ |
| $V_{S6}$ | $1\angle -270°$ | $1\angle -233.8°$ | $1\angle -135°$ | $1\angle 0°$ |
| $V_{S7}$ | $1\angle -324°$ | $1\angle -280.6°$ | $1\angle -162°$ | $1\angle 0°$ |

—— Compensation voltages, $V'_{S1}$ and $V'_{S2}$
– – Direct excitation voltages, $V_{S1}$ and $V_{S2}$
–o– Pattern multiplication method

—— Compensation voltages, $V'_{S1}$ and $V'_{S2}$
– – Direct excitation voltages, $V_{S1}$ and $V_{S2}$
–o– Pattern multiplication method
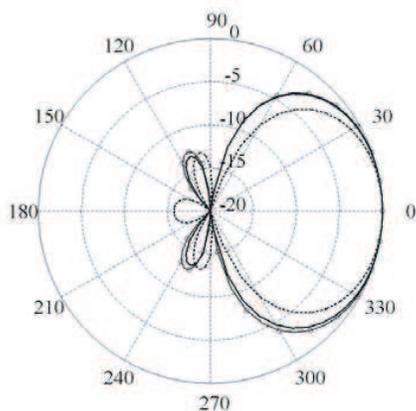


Figure 2: The normalized array radiation patterns for the seven-element monopole array at $d = 0.15\lambda$ when the main beam direction is excited at $\varphi = 0°$.
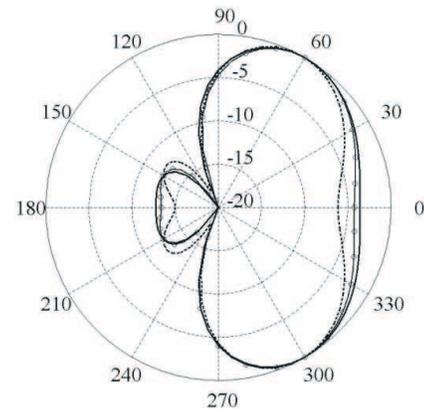
Figure 3: The normalized array radiation patterns for the seven-element monopole array at $d = 0.15\lambda$ when the main beam direction is excited at $\varphi = 60°$.

is formed towards four different directions using (3). The compensation voltages in Table 1 are compared with the direct excitation voltages in Table 2.

A comparison of Tables 1 and 2 shows that the mutual coupling effect is very strong as the compensation and the direct excitation voltages are very different. We calculated the compensated array patterns for two of the cases as shown in Figures 2 and 3. They are also compared with the array patterns obtained using the direct excitation voltages and the principle of pattern multiplication method.

From Figures 2 and 3, we observed that mutual coupling has a significant effect on the radiation patterns. Nevertheless, the array patterns obtained using the compensation voltages are almost exactly the same as the array patterns obtained using the principle of pattern multiplication. Hence, it is clear that the compensation method can also be applied to $n$-element antenna arrays.

## 4. CONCLUSIONS

We have investigated the problem of mutual coupling in transmitting compact antenna arrays and proposed an effective method to compensate for the mutual coupling in the coupled array patterns. By using the mutual impedances of the antenna elements, we showed that it is possible to design compensation networks that can remove the distortion on array patterns due to the mutual coupling effect. The compensated array patterns enable us to predict the radiation characteristics of compact antenna arrays using the principle of pattern multiplication based on their ideal and isolated element patterns. We have laid down the equations for the construction of such compensation networks. With these compensation networks, further conventional port-decoupling and matching circuits

can be designed and connected to their inputs to achieve maximum power transfer from the source to the antennas. Numerical examples on the dipole and monopole arrays have demonstrated the validity and accuracy of the method.

**ACKNOWLEDGMENT**

**REFERENCES**

1. Volmer, C., J. Weber, R. Stephan, K. Blau, and M. A. Hein, "An eigen-analysis of compact antenna arrays and its application to port decoupling," *IEEE Trans. Antennas Propagat.*, Vol. 56, No. 2, 360–370, 2008.
2. Gupta, I. and A. Ksienski, "Effect of mutual coupling on the performance of adaptive arrays," *IEEE Trans. Antennas Propagat.*, Vol. 31, No. 5, 785–791, 1983.
3. Steyskal, H. and J. S. Herd, "Mutual coupling compensation in small array antennas," *IEEE Trans. Antennas Propagat.*, Vol. 38, No. 12, 1971–1975, 1990.
4. Hui, H. T., "Improved compensation for the mutual coupling effect in a dipole array for direction finding," *IEEE Trans. Antennas Propagat.*, Vol. 51, No. 9, 2498–2503, 2003.
5. Li, X. and Z. P. Nie, "Mutual coupling effects on the performance of MIMO wireless channels," *IEEE Antennas Wireless Propagat. Lett.*, Vol. 3, 344–347, 2004.
6. Goossens, R. and H. Rogier, "A hybrid UCA-RARE/Root-MUSIC approach for 2-D direction of arrival estimation in uniform circular arrays in the presence of mutual coupling," *IEEE Trans. Antennas Propagat.*, Vol. 55, No. 3, 841–849, 2007.
7. Andersen, J. B. and H. H. Rasmussen, "Decoupling and descattering networks for antennas," *IEEE Trans. Antennas Propagat.*, Vol. 24, No. 6, 841–846, 1976.
8. Lau, B. K., J. B. Andersen, G. Kristensson, and A. F. Molisch, "Impact of matching network on bandwidth of compact antenna arrays," *IEEE Trans. Antennas Propagat.*, Vol. 54, No. 11, 3225–3238, 2006.
9. Coetzee, J. C. and Y. Yu, "Port decoupling for small arrays by means of an eigenmode feed network," *IEEE Trans. Antennas Propagat.*, Vol. 56, No. 6, 1587–1593, 2008.
10. Jordan, E. C., *Electromagnetic Waves and Radiating Systems*, Prentice-Hall, Englewood Cliffs, N.J., 1968.
11. Balanis, C. A., *Antenna Theory: Analysis and Design.* 3rd Ed., Wiley, New York, 2005.

# Wideband Beamforming for Compact Receiving Antenna Arrays

**C. H. Niow**, **H. T. Hui**, **and T. S. Yeo**

Department of Electrical and Computer Engineering
National University of Singapore, Singapore 117576, Singapore

**Abstract**— An effective compensation method is proposed to eliminate the beamforming distortions in compact antenna arrays due to the effects of mutual coupling. By using the receiving mutual impedances with the optimal Riblet-Chebyshev weights, it is possible to restore the distorted antenna array patterns for effective beamforming. Equations are derived to determine the compensated Riblet-Chebyshev weights used to restore the distorted antenna array patterns. Numerical examples using a compact antenna array are discussed to demonstrate the effectiveness of the proposed compensation method.

## 1. INTRODUCTION

Wideband beamforming has gained popularity in several applications such as radar and mobile communication due to the ability for the beam to steer to the desired direction over a wide frequency bandwidth. For the wideband beamformer to function accurately in the receiving antenna arrays, it requires accurate knowledge of the voltages or currents excited at the antenna ports by the incoming signals. However, the presence of mutual coupling cause the beamforming patterns to be distorted. The mutual coupling effects tend to increase as the antenna separation reduces [1]. Hence, the antenna arrays are often limited by their array size.

Several wideband beamforming techniques have been proposed recently. Sekiguchi and Karasawa proposed a wideband beamspace adaptive array that uses FIR fan filters to construct a multibeam forming network which can suppress interference signals having a wide fractional bandwidth [2]. Ward et al. introduced a beamspace preprocessing structure based on frequency-invariant beamforming [3]. It uses the Direction-of-Arrival (DOA) estimator in time-domain processing instead of frequency decomposition. Olen and Compton proposed a numerical technique for pattern synthesis in arrays that allows a set of array coefficients to be found to steer the main beam in a given direction while meeting the sidelobe specification [4]. Bialkowski and Uthansakul proposed deriving the beamforming weights using an inverse discrete Fourier transform technique while neglecting the mutual coupling between the array elements [5]. Wang and Hui proposed an optimal wideband beamforming based on frequency domain multiple-input and single-output system identification [6].

In this paper, we propose a compensation method which restores the beamforming patterns in compact receiving antenna arrays due to mutual coupling effects over a wide frequency bandwidth. To achieve a small beamwidth, we use the Riblet-Chebyshev weighting function [7] as it has a smaller beamwidth as compared to Dolph-Chebyshev weighting function [8] for antenna separation less than half a wavelength.

## 2. THE COMPENSATION METHOD

Consider an $N$-element uniform linear array (ULA) where $N$ is an odd interger. The element spacing is $d$. The optimal Riblet-Chebyshev weights [6] over a wide frequency bandwidth are

$$\mathbf{W}(f) = [w_1(f), w_2(f), \ldots, w_N(f)]^T \tag{1}$$

where $f$ is the frequency, $w_i(f)$ $(i = 1, 2, \ldots, N)$ are the Riblet-Chebyshev weights and $T$ is the transpose. These weights are derived obtained based on isolated radiation pattern for each antenna element. In reality, the isolated radiation pattern is distorted by mutual coupling effects even when the antenna elements are sufficiently far apart. Moreover, the Riblet-Chebyshev weights are sensitive to mutual coupling effects, especially for compact antenna arrays. Hence, the distorted radiation pattern must be compensated first before the Riblet-Chebyshev weights can be applied. The distorted radiation pattern can be compensated using the receiving mutual impedance

matrix [9] over a wide frequency bandwidth as

$$
\begin{bmatrix}
1 & -\frac{Z_t^{12}(f)}{Z_L} & \cdots & -\frac{Z_t^{1N}(f)}{Z_L} \\
-\frac{Z_t^{21}(f)}{Z_L} & 1 & \cdots & -\frac{Z_t^{2N}(f)}{Z_L} \\
\vdots & \vdots & \ddots & \vdots \\
-\frac{Z_t^{N1}(f)}{Z_L} & -\frac{Z_t^{N2}(f)}{Z_L} & \cdots & 1
\end{bmatrix}
\begin{bmatrix}
V_1(f) \\
V_2(f) \\
\vdots \\
V_N(f)
\end{bmatrix}
=
\begin{bmatrix}
U_1(f) \\
U_2(f) \\
\vdots \\
U_N(f)
\end{bmatrix}
\tag{2}
$$

$$
Z(f)V(f) = U(f) \tag{3}
$$

where $V_i(f)$ $(i = 1, 2, \ldots, N)$ are the coupled terminal voltages, $U_i(f)$ $(i = 1, 2, \ldots, N)$ are the uncouple terminal voltages, $Z_t^{ij}(f)$ $(i, j = 1, 2, \ldots, N$ and $i \neq j)$ are the receiving mutual impedance [9] and $Z_L$ is the terminal load impedance. To restore the distorted radiation patterns, we compensate the coupled terminal voltages $\mathbf{V}(f)$ using the receiving mutual impedance $\mathbf{Z}(f)$ to obtain the uncoupled terminal voltages $\mathbf{U}(f)$ in the following manner:

$$
\mathbf{U}(f) = \mathbf{Z}^{-1}(f)\mathbf{V}(f). \tag{4}
$$

From here, we can apply the Riblet-Chebyshev weights $\mathbf{W}(f)$ to the uncoupled terminal voltages $\mathbf{U}(f)$ to obtain the undistorted beam pattern $P(f)$ as:

$$
P(f) = \mathbf{U}(f)^T \mathbf{W}(f). \tag{5}
$$

The transfer functions for $\mathbf{W}(f)$ and $\mathbf{Z}(f)$ can be derived by applying the system identification method. For example, to find the transfer function of $\mathbf{Z}(f)$, we use the following rational function with real coefficients [11]

$$
Z_i(z) = \frac{B_i(z)}{A_i(z)} = \frac{b_{i0} + b_{i1}z^{-1} + \ldots + b_{im}z^{-m}}{a_{i0} + a_{i1}z^{-1} + \ldots + a_{in}z^{-n}} \qquad i = 1, 2, \ldots, N \tag{6}
$$

to the values of the frequency domain data in the identification set. The estimates of the polynomial parameters $\boldsymbol{\theta}_i = [b_{i0}, b_{i1}, \ldots, b_{im}, a_{i0}, a_{i1}, \ldots, a_{in}]$ for the transfer function $\mathbf{Z}(f)$ can be determined by solving the following optimization problem [12]

$$
\hat{\boldsymbol{\theta}} = \arg\min_{\theta} \mathbf{D}(\boldsymbol{\theta}) \tag{7}
$$

$$
\mathbf{D}_i(\boldsymbol{\theta}) = \sum_{k=1}^{N} \left| Z_i(f_k) - Z_t^{1i}(f_k) \right|^2 \tag{8}
$$

$$
Z_i(f) = Z_i(z)|_{z = e^{j2\pi f}} \tag{9}
$$

## 3. NUMERICAL RESULTS AND DISCUSSIONS

To demonstrate the effectiveness of the compensation method, we consider the same ULA using a half-wavelength dipole elements with $N = 9$ at $d = 0 \cdot 2\lambda_0$ over a normalized frequency band from $0 \cdot 5f_0$ to $1 \cdot 5f_0$ where $f_0 = c/\lambda_0$. We consider the beam direction for incident signal at $\theta = 0°$. Figures 1, 2 and 3 shows the compensated beam patterns over the normalized frequency band at $0 \cdot 5f_0$, $1f_0$ and $1 \cdot 5f_0$. Table 1 shows the Riblet-Chebyshev weights at $0 \cdot 5f_0$, $1f_0$ and $1 \cdot 5f_0$ [6].

From the figures, we can see that the compensated beam patterns remain stable over a wide frequency bandwidth. The uncompensated beam patterns are distorted due to the mutual coupling effects. The compensated beam patterns are almost exactly the same as the theoretical beam patterns. This shows the validity of the proposed compensation method.

Table 1: Riblet-Chebshev weights at $0 \cdot 5f_0$, $1f_0$ and $1 \cdot 5f_0$ for 9-element ULA at $d = 0 \cdot 2\lambda_0$.

| $f(f)_0$ | $w_1 = w_9$ | $w_2 = w_8$ | $w_3 = w_7$ | $w_4 = w_6$ |
|----------|-------------|-------------|-------------|-------------|
| 0.50 | 0.0189 | −0.1332 | 0.4278 | −0.8135 |
| 1.00 | 0.0439 | −0.2025 | 0.5133 | −0.8476 |
| 1.50 | 0.1721 | −0.2712 | 0.6724 | −0.7169 |
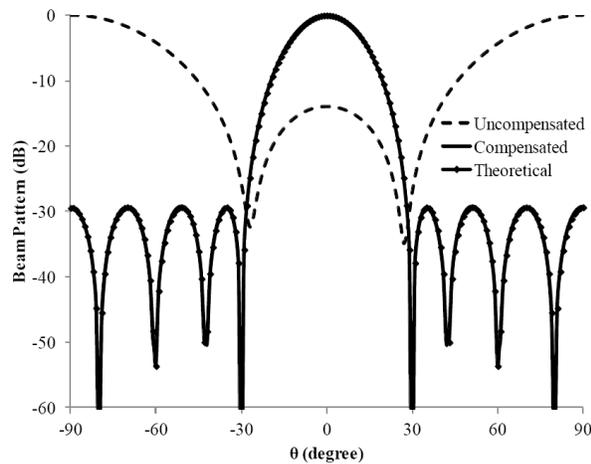
Figure 1: Normalized array antenna radiation patterns for $\theta = 0°$ at $0.5f_0$.
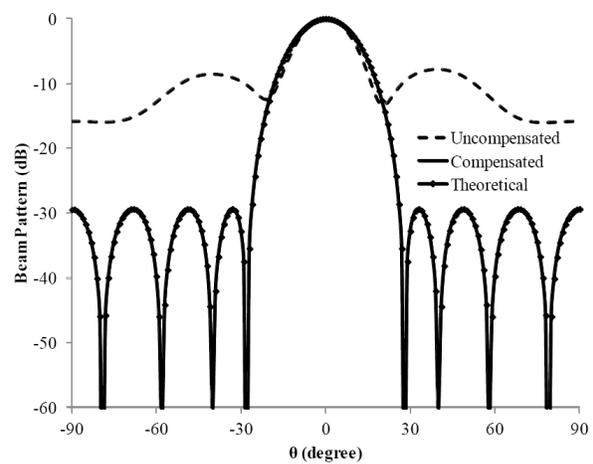


Figure 2: Normalized array antenna radiation patterns for $\theta = 0°$ at $1f_0$.
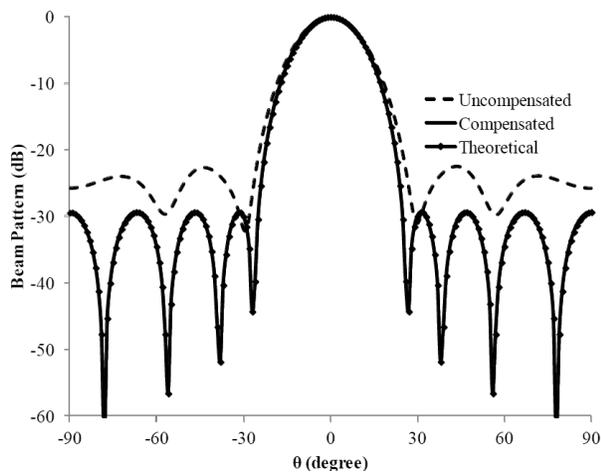


Figure 3: Normalized array antenna radiation patterns at $\theta = 0°$ at $1.5f_0$.
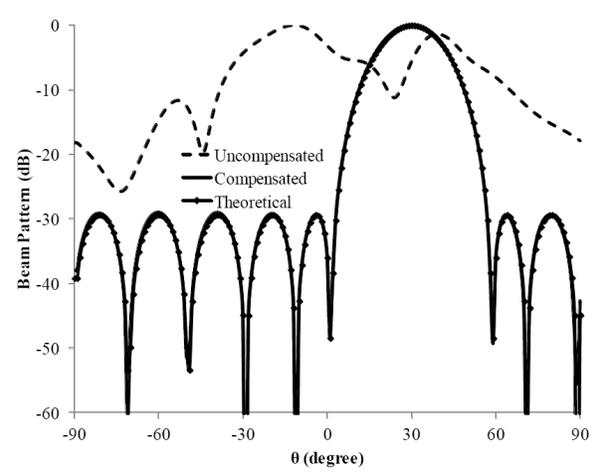


Figure 4: Normalized array antenna radiation patterns for $\theta = 30°$ at $1f_0$.

Next, we consider the beam direction for incident signal at $\theta = 30°$ as shown in Figure 4. From the figure, we can see that the beam pattern is compensated even at a different beam angle. The compensation method is effective in beamforming over a wide frequency bandwidth for compact receiving antenna arrays where the element spacings are less than half a wavelength.

## 4. CONCLUSIONS

A method to compensate the beam patterns due to mutual coupling is proposed. Using the technique of system identification, we derived the transfer functions for the receiving mutual impedance and the Riblet-Chebyshev weights over a wide frequency bandwidth. The simulation results show the validity of the compensation method.

## ACKNOWLEDGMENT

## REFERENCES

1. Gupta, I. and A. Ksienski, "Effect of mutual coupling on the performance of adaptive arrays," *IEEE Trans. Antennas Propagat.*, Vol. 31, No. 5, 785–791, 1983.
2. Sekiguchi, T. and Y. Karasawa, "Wideband beamspace adaptive array utilizing FIR fan filters for multibeam forming," *IEEE Trans. Signal Process.*, Vol. 48, No. 1, 277–284, 2000.

3. Ward, D. B., Z. Ding, and R. A. Kennedy, "Broadband DOA estimation using frequency invariant beamforming," *IEEE Trans. Signal Process.*, Vol. 46, No. 5, 1463–1469, 1998.

4. Olen, C. A. and R. T. Compton, "Numerical pattern synthesis algorithm for arrays," *IEEE Trans. Antennas Propagat.*, Vol. 38, No. 10, 1666–1676, 1990.

5. Bialkowski, M. E. and M. Uthansakul, "A wideband array antenna with beam-steering capability using real valued weights," *Microw. Opt. Technol. Lett.*, Vol. 48, No. 2, 287–291, 2006.

6. Wang, B. H., H. T. Hui, and M. S. Leong, "Optimal wideband beamforming for uniform linear arrays based on frequency-domain MISO system identification," *IEEE Trans. Antennas Propagat.*, Vol. 58, No. 8, 2580–2587, 2010.

7. Riblet, H. J., "Discussion on 'A current distribution for broadside arrays which optimizes the relationship between width and sidelobe level'," *Proc. IRE*, Vol. 35, No. 5, 489–492, 1947.

8. Dolph, C. L., "A current distribution for broadside arrays which optimizes the relationship between width and sidelobe level," *Proc. IRE*, Vol. 34, No. 6, 335–348, 1946.

9. Hui, H. T., "A new definition of mutual impedance for application in dipole receiving antenna arrays," *IEEE Antennas Wireless Propag. Lett.*, Vol. 3, No. 1, 364–367, 2004.

10. Wang, B. H. and H. T. Hui, "Wideband mutual coupling compensation for receiving antenna arrays using the system identification method," *IET Microw. Antennas Propag.*, Vol. 5, No. 2, 184–191, 2011.

11. Levy, E., "Complex curve fitting," *IRE Trans. Autom. Control*, Vol. 4, No. 5, 2245–2260, 1994.

12. Pintelon, R., P. Guillaume, Y. Rolain, J. Schoukens, and H. van Hamme, "Parametric identification of transfer functions in the frequency domain — A survey," *IEEE Trans. Autom. Control*, Vol. 39, No. 11, 2245–2260, 1994.

# A Simple Channel Simulator for Multiuser MIMO Broadcast Channel Systems

**Chong Pei Ho**, **Hieu Duy Nguyen**, **Xuan Wang**, **and Hon Tat Hui**

Department of Electrical and Computer Engineering, National University of Singapore, Singapore

**Abstract**— This paper presents an effort to construct a multiuser (MU) multiple-input multiple-output (MIMO) broadcast channel (BC) model. Our method is able to adequately build in the correlation and mutual coupling, which are important factors affecting the multi-antenna arrays. This helps to decrease the need for complex mathematical analysis and allows an easy simulation of the MU MIMO BC performance. The charac-terizations of MU MIMO systems are done and the impact of varying the number of transmitting and receiving antennas is explored. These insights are useful in physical realization of the systems.

## 1. INTRODUCTION

In recent years, as demands for increasing capacity networks rises, researches in antenna array communication are of much greater interest. Multiple-input-multiple-output (MIMO) systems are hence a natural extension of developments [1] since MIMO systems are able to turn multipath propagation, which is usually a pitfall in wireless transmission, into a benefit. By doing so, the performance and capacity of the MIMO systems are increased tremendously.

The capacity of single-user MIMO Gaussian channels was first studied by Foschini and Gans [2], and Telatar [3]. The researches on MIMO systems are also extended to the multiuser cases which can be classified as MIMO multiple access channel (MAC) and MIMO broadcast channels (BC). The sum rate of MIMO MAC system is easy to be obtained due to its convex property [4–7]. The sum rate of the MU MIMO BC achieved with Dirty Paper Coding (DPC) [8], however, is not of the convex form. Based on the duality between MIMO MAC and BC systems, sum rate of MU MIMO BC can be obtained [6, 7]. Also, in [9], Weingarten showed that the capacity region achieved by using the DPC is exactly the same as that of the MU MIMO BC, given that the transmit powers are equal. Here, the method to calculate the (DPC) sum-rate capacity of the BC is the sum power iterative water filling method proposed in [7].

In this paper, our effort will be focused on modelling the MU MIMO BC system. Efficient and accurate channel modeling is important to help predict the performance of MIMO communication systems. However, due to the large number of parameters that are involved in channel modeling, an analytical approach is usually too difficult. This leads to the use of computer simulations. The challenge is to employ a method that is able to take all the parameters into account, and is also able to apply to most applications. Various methods are available for the simulation of the capacity of single user MIMO systems [10]. Such simulation is lacking in MU MIMO system where extensive researches on its performance are still very much ongoing. In this paper, an efficient simulation algorithm to simulate the MU MIMO system is presented.

The method of modelling a single user MIMO system was proposed by Hui and Wang [11] which involves having scatterers around both the transmitting and receiving antennas to introduce random scattering events. This work is extended in this paper to include the MU MIMO system, where instead of only one single user in the receiving end, two users were implemented. Various MU MIMO systems will be built and characterizations can be done. From there, the impact of varying the number of transmitting antennas and receiving antennas will be examined.

In this paper, we consider a two user BC system, where each user $j$ and $k$ has $R_j = R_k > 1$ receiving antennas and the broadcast transmitter has $T \geq 1$ transmitting antennas. The transmitting antennas are surrounded by $P$ scatterers where $P$ is fixed at 50 in the far field, and this provides the scattering events. On the receiving side, both users are surrounded by $Q$ scatterers which is varied when appreciate to investigate the effects of scattering on the capacity.

Between the two antennas, the paths of the signals are assumed to be completely random and that each propagation paths are associated with a loss factor which follows a Gaussian distributed random number which has a mean of 0 and a variance of 1. The model of the MU BC MIMO system is summarised in Fig. 1. As shown in Fig. 1, the signals follow a propagation path when travelling from the transmitter to the receivers. The loss factor associate with the path will cause the $E$-field that is received in the scatterers at the receiving end, which in turns affects the current

induced in the receiving antennas. Each antenna is designed with the intrinsic impedance of $50\,\Omega$ and by multiplying that with the induced currents, the induced voltages across each antenna can be found. This allows us to obtain the channel matrices, $\mathbf{H}_1$ for user 1 and $\mathbf{H}_2$ for user 2. With the channel matrices, the sum-rate capacity of the system can be calculated.

## 2. SYSTEM MODEL

We consider a narrowband MU BC MIMO system with $T$ transmitting antennas and $R_j = R_k > 1$ receiving antennas. For simplicity, the receiving antennas are named as $r$-th antenna, $r = 1, 2, \ldots, R$, as shown in Fig. 1. We denote the signal voltages at the input ports of the $t$-th transmit antennas as $V_{in,1}, V_{in,2}, \ldots, V_{in,T}$, and the signal voltages received at the output ports of the $r$-th receive antennas as $V_{out,1}, V_{out,2}, \ldots, V_{out,R}$. The antenna terminal loads for the transmitting and receiving antennas are denoted by $Z_L$. The MIMO channel response can then be defined as

$$h_{ij} = \frac{V_{out,i}}{V_{in,j}}, \begin{cases} i = 1, 2, \ldots, R \\ j = 1, 2, \ldots, T \end{cases}. \tag{1}$$

From (1), the channel matrix can then be defined as

$$\mathbf{H} = \begin{bmatrix} h_{11} & \ldots & h_{1T} \\ \vdots & \ddots & \vdots \\ h_{R1} & \ldots & h_{RT} \end{bmatrix}. \tag{2}$$

The channel matrix of each user can be found, and in the case of two users, two channel matrices $\mathbf{H}_1$ and $\mathbf{H}_2$ are obtained. With the channel matrices, the sum power iterative water filling method can then be used to calculate the sum-rate capacity [7]. Before moving on to discuss the steps that that are taken for the simulations, several assumptions have to be made as follows:

1) The transmitter and receiver are assumed to be separated by a large distance $D$ [11].
2) The systems are narrow-band and stationed in flat-fading environments [11].
3) The transmit power that the transmitter used is assumed to be $10\,\mathrm{dB}$.
4) The two users do not communicate with each other, i.e., non-cooperative.
5) There are no scatterers present in the region that is between the users.

A clearer definition of the antenna spacing and user distance is shown in Fig. 2.

Assume a $2 \times 2 \times 2$ systems which has two transmitting antennas and two receiving users with two antennas each, the exact steps taken for the simulation are listed below

1) Using a unit voltage source $V_{in,j}$ excite the $j$-th transmitting antenna.
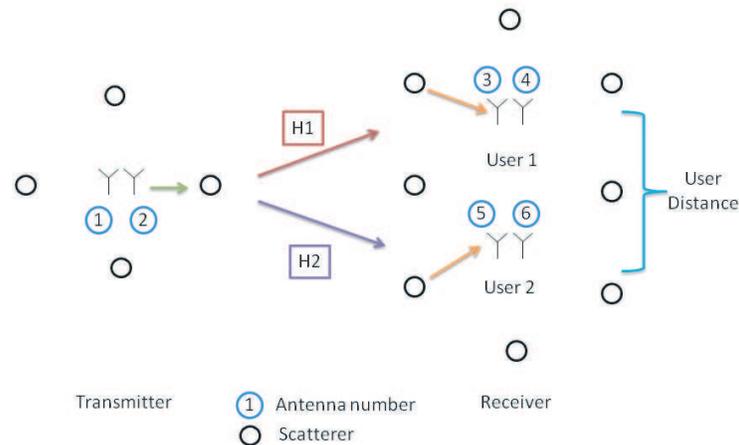


Figure 1: The system model used in this paper. It has the transmitters on the left and two users of two antennas each on the right. The users are separated by a parameter known as user distance. The scatterers exist in the far field and provide the scattering events. In between the transmitter and receivers, the signals go through propagation paths that are associated with a loss factor.
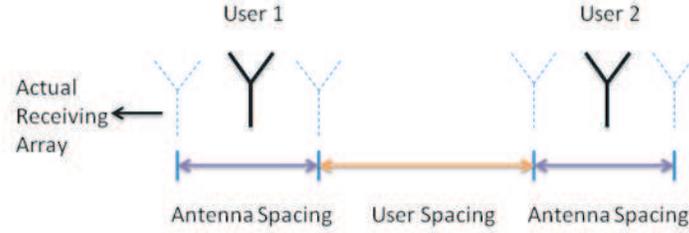
Figure 2: This picture showing the definitions of antenna spacing and user spacing that are used in this paper.

2) The electric far field of this antenna $E_{j,p}$ is numerically determined in all the directions of the scatterers around the transmitter.

3) Each value of the far field is multiply by an independent complex Gaussian random variable which has a zero mean and a unit variance. The resultant far fields from all the scatterers are then added together. This total sum is denoted as $S$.

4) The $i$-th receiving antenna is excited with a large number of plane wave sources. The number of plane wave sources is similar to the number of scatterers around the receiver. Each of these plane waves will be multiply with $S$ that was obtained in Step 3.

5) Obtain the load current induced when excited by all the plane waves obtained in Step 4. With the load current, the voltage $V_{out,i}$ that is developed across the terminal load $Z_L$ can be determined numerically.

6) As discussed above, the channel response $h_{ij}$ which is given by $V_{out,i}/V_{in,j}$ can be obtained. This corresponds to a single channel realisation.

7) Repeat Step 1, expect that the unit voltage source is now applied across the $(j+1)$-th transmitting antenna. This will continue until the $T$-th transmitting antenna is being simulated.

8) With all the channel responses of the system, the channel matrices $\mathbf{H}_1$ and $\mathbf{H}_2$ can thus be calculated and obtained. $\mathbf{H}_1$ is obtained by considering the channel responses of Antenna 1 and 2 at the transmitter and Antenna 3 and 4 at the receiver. Similarly, $\mathbf{H}_2$ is obtained by considering 1 and 2 at the transmitter and Antenna 5 and 6 at the receiver.

9) $\mathbf{H}_1$ and $\mathbf{H}_2$ are then used to calculate the sum capacity using the sum power iterative water filling algorithm

## 3. CAPACITY SIMULATION

### 3.1. Normalization

Normalization is needed to remove the actual distances of the scatterers from the transmitting antennas and from the receiving antennas and the path loss for wave propagation from the transmitter to the receiver. The normalization method that will be used is to [11] calculate the average power received by a single isolated antenna when all the transmitting antennas are transmitting in the same rich multipath environment. All the channel matrix elements are then divided by this average power.

In subsequent simulations, the antennas are designed with the following parameters. Each monopole is designed to be of length 29.8 mm and the operating frequency is 2.4 GHz. The antenna load impedance is fixed at 50 Ω.

### 3.2. Simulation Results — $4 \times 2 \times 2$ System

The first simulation is a $4 \times 2 \times 2$ system, which has four transmitting antennas transmitting and on the receiving side, there are two users which two antennas each. In order to characterize the MU MIMO system, we vary two parameters which are the antenna spacing and the user spacing. The number of scatterers at both sides is kept at 50. Table 1 summarizes the cases that we are considering. Case 1 allows the investigation of antenna spacing on the sum-rate capacity. In case 2, by keeping the antenna spacing constant, the effect of user spacing can be examined.

In case 1, the user spacing is kept at $1\lambda$ to remove correlation due to user spacing. This retains the impact of antenna spacing on sum-rate capacity. In addition, by keeping the user spacing to a $1\lambda$, it prevents the error arising from the lack of considerations for scatterers that are present

in between the two users. For case 2, the antenna spacing is kept at $0.4\lambda$ in order to minimize the correlation effect due to the proximity of surrounding antennas. When the antenna spacing is varied from $0.05\lambda$ to $0.4\lambda$, the following sum-rate capacity is obtained. When the user spacing is varied from $0.05\lambda$ to $0.7\lambda$, the following sum-rate capacity is obtained.

In both cases, it can be seen that as the antenna spacing and user spacing increases, the sum-rate capacity increases. This is similar to the case of the Single User MIMO Systems. The main reason for the increase in capacity is that when the antenna or user spacing increases, the amount of correlation between the antennas decreases. This reduces the mutual coupling effect and brings about a higher capacity. When the mutual coupling effect is insignificant, the simulated sum-rate capacity approaches the i.i.d case. In both cases, the distance between the antenna and the user spacing is found to be $0.4\lambda$ in order for the sum-rate capacity to converge.

### 3.3. Simulation Results — $6 \times 3 \times 2$ System

In this section, the number of antenna elements is increased. This will allow a deeper insight to the changes of the sum-rate capacity when the number of antenna elements increases. The system simulated is $6 \times 3 \times 2$ which has six transmitting antennas and the receiving side has two users of

Table 1: Simulation parameters for two cases.

| Simulation Cases | Antenna Spacing | User spacing |
|---|---|---|
| 1 | Varied from $0.05\lambda$ to $0.5\lambda$ | Kept at $1\lambda$ |
| 2 | Kept at $0.4\lambda$ | Varied from $0.05\lambda$ to about $0.7\lambda$ |
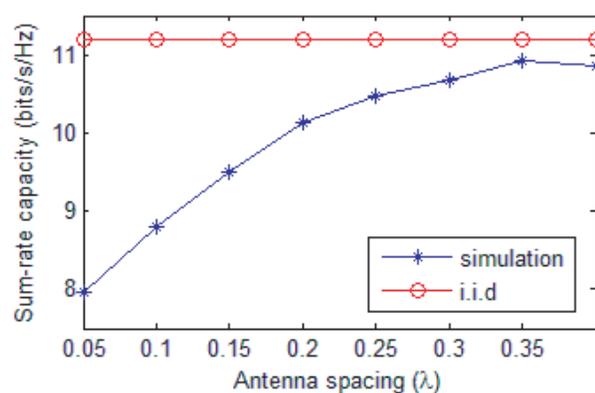


Figure 3: This graph shows the effect of different antenna spacing on the sum-rate capacity. The user spacing is kept constant at $1\lambda$.
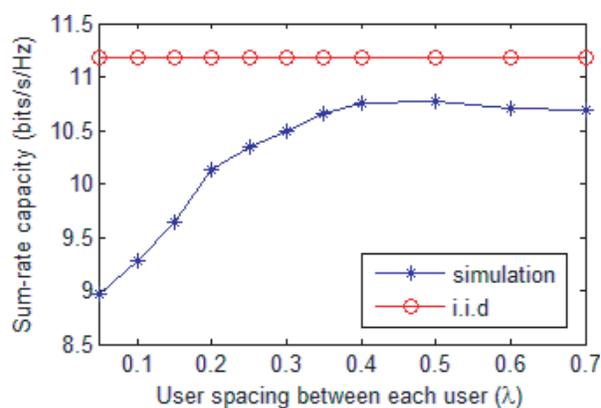


Figure 4: This graph shows the effects of varying user spacing on the sum-rate capacity. The antenna spacing is fixed at $0.4\lambda$.
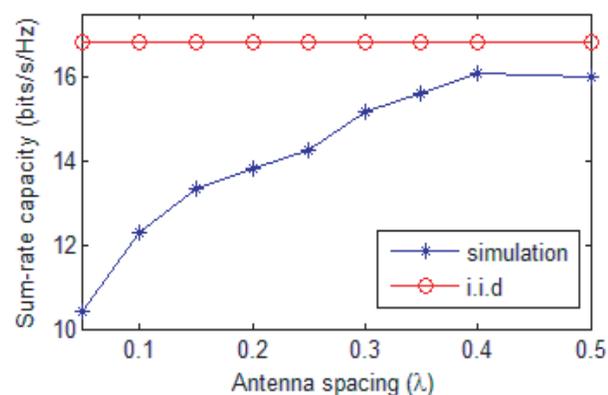


Figure 5: The graph shows the effect of different antenna spacing of the MIMO array have on the sum-rate capacity when the number of antennas increases. The user spacing is kept at $1\lambda$.
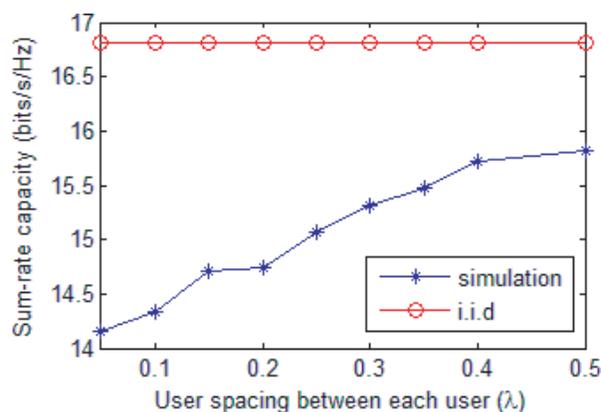


Figure 6: This graph shows the effect of different user spacing of the MIMO array have on the sum-rate capacity when there are more antenna elements. The antenna spacing is kept constant at $0.4\lambda$.

Table 2: Sum-rate capacities of various systems.

| MU MIMO System | Sum-rate Capacity (bits/s/Hz) |
| --- | --- |
| $4 \times 2 \times 2$ | 5.9828 |
| $6 \times 2 \times 2$ | 6.2975 |
| $4 \times 2 \times 2$ | 5.9828 |
| $6 \times 3 \times 2$ | 7.307 |

three receiving antennas each. When the antenna spacing is varied from $0.05\lambda$ to $0.5\lambda$, the sum-rate capacity in Fig. 5 is obtained. When the user spacing is varied from $0.05\lambda$ to $0.7\lambda$, the sum-rate capacity in Fig. 6 is obtained.

From the results, it can be seen that as the number of antenna at both the transmitting side and receiving side increases, the systems' sum-rate capacities increase as well. Despite an increase in overall capacity, the capacity per antenna actually decreases. This is due to the increase in mutual coupling effect when the number of antenna elements increases.

### 3.4. Simulation Results — Comparison

In this section, simulations will be done to examine the effect of varying the number of transmitting antennas and receiving antennas separately. To do so, the following systems will be compared. They are namely, $4 \times 2 \times 2$ and $6 \times 3 \times 2$ for the investigation of the effect of the number of receiving antennas, and $4 \times 2 \times 2$ and $6 \times 2 \times 2$ for the investigation of the effect of varying the transmitting antennas. This section is useful in practical applications as sum-rate capacity is obtained quickly by using the simulation process derived in this paper. In the simulations of the various systems, the antenna spacing is kept at $0.4\lambda$ and the user spacing is $1\lambda$. The power received per receiving antenna is 1W after the normalization process. The results are summarized in Table 2. It shows the effects on the sum-rate capacity when the number of transmitting antennas and receiving antennas are changed.

As seen in the table, when the number of transmitting and receiving antennas increases, the sum-rate capacity increases as well. However, it can be seen that when the number of receiving antennas increases, the increase in capacity is greater. This is because in the $6 \times 2 \times 2$ system, the system is not maximizing its capabilities as not all its transmitting beams are utilized at the same time.

### 4. CONCLUSION

In this paper, a simulation procedure for MU MIMO BC systems has been presented. It provides a much simpler method to model MU MIMO channels which are difficult and impractical to be analyzed using a theoretical approach. This paper also presented several results through the simulations. The simulations of the $4 \times 2 \times 2$ and $6 \times 3 \times 2$ systems show that the sum-rate capacities changes according to the effect of correlation and mutual coupling, the effects which are not yet extensively covered in MU MIMO research. The final comparison across various systems helped to examine the effects of the number of transmitting antennas and receiving antennas. This will give good insights to practical implementations.

**REFERENCES**

1. Bliss, D. W., K. W. Forsythe, and A. M. Chan, "MIMO wireless communication," *Lincoln Laboratory Journal*, Vol. 15, 2005.
2. Foschini, G. J. and M. J. Gans, "On limits of wireless communications in a fading environment when using multiple antennas," *Wireless Personal Commun.*, Vol. 6, 311–335, 1998.
3. Telatar, E., "Capacity of multi-antenna gaussian channels," *European Trans. on Telecomm.*, Vol. 10, No. 6, 585–596, Nov. 1999.
4. Verdu, S., "Multiple-access channels with memory with and without frame synchronism," *IEEE Trans. Inf. Theory*, Vol. 35, No. 3, 605–619, May 1989.
5. Yu, W., W. Rhee, S. Boyd, and J. Cioffi, "Iterative water-filling for vector multiple access channels," *Proc. IEEE Int. Symp. Inf. Theory*, 322, Washington D.C., Jun. 24–29, 2001.
6. Vishwanath, S., N. Jindal, and A. Goldsmith, "Duality, achievable rates and sum-rate capacity of gaussian MIMO broadcast channels," *IEEE Trans. Inf. Theory*, Vol. 49, No. 10, 2658–2668, Oct. 2003.

7. Jindal, N., W. Rhee, S. Vishwanath, S. A. Jafar, and A. Goldsmith, "Sum power iterative water-filling for multi-antenna gaussian broadcast channels," *IEEE Trans. Inf. Theory*, Vol. 51, No. 4, 1570–1580, Apr. 2005

8. Costa, M. H., "Writing on dirty paper," *IEEE Trans. Inf. Theory*, Vol. 29, No. 3, 439–441, May 1983.

9. Weingarten, H., Y. Steinberg, and S. Shamai (Shitz), "The capacity region of the gaussian multiple-input multiple-output broadcast channel," *IEEE Trans. Inf. Theory*, Vol. 52, No. 9, 3936–3964, Sep. 2006.

10. Viberg, M., T. Boman, U. Carlberg, L. Pettersson, S. Ali, and E. Arabi, "Simulation of MIMO antenna systems in simulink and embedded matlab," *Nordic MATLAB User Conference*, Stockholm, 2008.

11. Hui, H. T. and X. Wang, "Building antenna characteristics into multiple-input and multiple-output channel simulation," *International Journal of Electronics*, Vol. 97, No. 6, 703–714, Jun. 2010.

12. Vucetic, N. and J. Yuan, *Space Time Coding*, John Wiley & Sons, 2003.

# Influence of the Position of Decoupling Capacitors on RF Transmit Performance for a 7 T MRI Loop Array

**M. Kozlov and R. Turner**

Planck Institute for Human Cognitive and Brain Sciences, Leipzig, Germany

**Abstract**— We present numerical investigations of capacitively decoupled loop-based arrays with three typical capacitor placements. In idealized array design conditions, and using the CP excitation mode, the transmit performance and safety excitation efficiency of the unshielded 85 mm length arrays investigated are similar for three typical decoupling capacitor positions. However, different capacitor positions entail different sensitivities to distributed capacitor values, changes of load, etc., and these sensitivities also depend nonlinearly on the distance to the local shield and the length of the array.

## 1. INTRODUCTION

Use of capacitive decoupling is often proposed for minimization of coupling in MRI RF loop-based arrays. There are three typical capacitor placements (Figure 1): the middle ("**M**" position) of the long leg [1]; just above the first capacitor and just below the third capacitor of the long leg ("**E**" position) [2], or between each end of the long leg ("**S**" position). How the decoupling capacitor position influences the array's transmit performance has not yet been explored systematically. For an 8-channel loop-based 7 T RF coil array, we investigated the effect of decoupling capacitor position on array transmit performance and safety excitation efficiency of an array excited in CP mode. While performance characteristics might be improved using RF shimming on a per-subject basis, this strategy is laborious and can cause significant delay in routine MRI examination.

## 2. METHOD

In the simulation, eight resonance coil elements were mounted on rectangular acrylic supports, assembled to give an octagonal cross section with extreme dimensions of 230 mm by 255 mm, as in our previous research [1]. The planar single loop elements were simulated for a range of sizes: width 85 mm; length 85, 150 mm. The realistic 3-D EM model included all coil construction details for the resonance elements, simulated with precise dimensions and material electrical properties. The loads utilized were the Ansoft human body models with different scaling factors: head #1 with scaling $X = 0.9$, $Y = 0.9$, $Z = 0.9$ simulating a small head, and head #2 with scaling $X = 0.95$, $Y = 0.975$, $Z = 0.9$ simulating a large head, which practically fully occupied the coil volume.

The scanner gradient shield (with diameter of 683 mm and length 1200 mm) was always included in the numerical domain for the simulation of unshielded and shielded arrays. The distance between the shielded array and a 300 mm long local shield was varied between 10 mm and 80 mm.

Our investigation was performed using RF circuit and 3-D EM co-simulation [2]. The RF circuit simulator was Agilent ADS software, and Ansoft HFSS was chosen as the 3-D EM tool for its robustness in handling complex coil geometry. For all geometries the array was tuned, matched



(a)                (b)                (c)
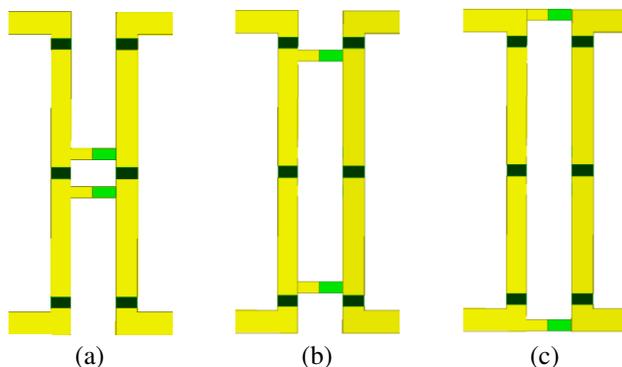
Figure 1: Position of decoupling capacitors: (a) the middle — "**M**"; (b) just above the first capacitor and just below the third capacitor of the long leg — "**E**"; (c) between each end of the long leg — "**S**".
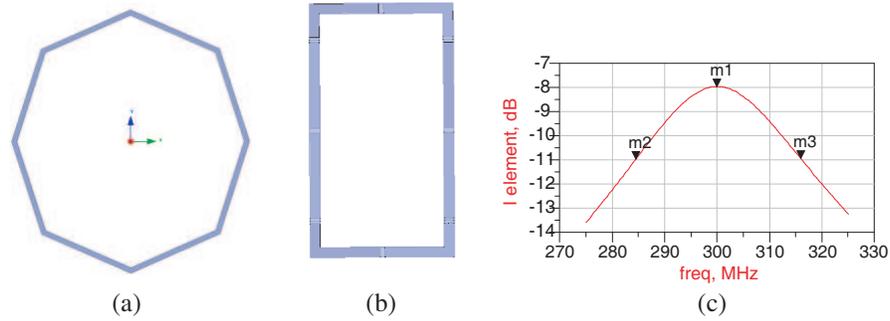
Figure 2: (a) Array transverse cross section; (b) shape of one planar single loop element; setup for $\mathbf{Q}_{load}$ calculation.

and decoupled using capacitive decoupling networks [3]. The results reported were obtained under the following array design conditions: a) the values of the fixed capacitors were the same and not limited to the commercially available range, b) zero tolerance in component values was assumed, c) all tuning, matching and decoupling optimizations reached their global minima. The optimization criteria were: the impedance matching ($\mathbf{S}_{xx}$) for each element was required to be less than $-30\,\mathrm{dB}$, and the inter-element coupling ($\mathbf{S}_{xy}$) for each adjacent element pair to be decoupled was required to be less than $-18\,\mathrm{dB}$, at the Larmor frequency ($\mathbf{F}_{MRI}$) (thus there were 16 criteria).

The array was excited in circular polarization mode, applying $1\,\mathrm{W}$ power to each port (array transmit power, $\mathbf{P}_{transmit} = 8\,\mathrm{W}$), with a sequential 45 degree phase increment. We analyzed the quantities related to the power budget, obtained by direct calculation from volume and surface loss densities or wave quantities: a) $\mathbf{P}_{array\_refl}$, the power reflected by the entire array; b) $\mathbf{P}_{radiated}$ the radiated power; c) $\mathbf{P}_{array\_internal}$, the inherent coil losses produced by lossy capacitors, dielectrics, and conductors; and d) $\mathbf{P}_{load}$, the power absorbed by the load. The entire human brain was defined as one volume of interest ($\mathbf{VOI}$). The array transmit properties were evaluated by considering the values of a) $\mathbf{B}_1+_V$, the value of $\mathbf{B}_1+$ averaged over $\mathbf{VOI}$, and its root-mean-square inhomogeneity (evaluated as a percentage "%"); b) $\mathbf{B}_1+_s$, the mean $\mathbf{B}_1+$ averaged over the transverse central slice through the $\mathbf{VOI}$, and its root-mean-square inhomogeneity (evaluated as a percentage "%"); c) $\mathbf{P}_V$, the power deposited in the $\mathbf{VOI}$; d) $\mathbf{E}_V = \mathbf{B}_1+_V/\sqrt{\mathbf{P}_V}$, the $\mathbf{VOI}$ excitation efficiency; e) $\mathbf{SAR}_{10g}$, the peak SAR averaged over $10\,\mathrm{gram}$; and f) $\mathbf{B}_1+_V/\sqrt{\mathbf{SAR}_{10g}}$, the safety excitation efficiency. Parameters also evaluated were the $\mathbf{S}$ parameter matrix; $\mathbf{Q}_{loaded}$, the quality factor for the first array element; $\mathbf{maxS}_{21}$, the maximum value of coupling between adjacent elements; and $\mathbf{maxS}_{31}$, the maximum value between the second adjacent elements.

## 3. RESULTS AND DISCUSSION

For given array length, the safe excitation efficiency $\mathbf{B}_1+_V/\sqrt{\mathbf{SAR}_{10g}}$, which defines MRI scanner performance, and the brain excitation efficiency $\mathbf{B}_1+_V/\sqrt{\mathbf{P}_V}$ are nearly equal for a given head model, in all arrays investigated. Increasing array length from 85mm to 150 mm resulted in about 7% drop of the brain excitation efficiency and in about 7% increased of $\mathbf{P}_V/\mathbf{P}_{load}$ ratio. These oppositely directed effects resulted in very similar $\mathbf{B}_1+_V$ for the same $\mathbf{P}_{load}$ for all arrays investigated. Thus differences in absolute array transmit excitation efficiency ($\mathbf{B}_1+_V/\sqrt{\mathbf{P}_{transmit}}$) are determined only by variations of $\mathbf{P}_{array\_refl}$, radiated power ($\mathbf{P}_{radiated}$) and the array internal losses ($\mathbf{P}_{array\_internal}$). The larger the sum of these losses, the poorer the array transmit performance.

For a given array closely coupled to a load, the position of the decoupling capacitor had relatively little influence on $\mathbf{P}_{radiated}$ at all distances between array and shield. For the arrays with the capacitor in positions "$\mathbf{M}$" and "$\mathbf{S}$", the fraction of $\mathbf{P}_{array\_internal}$ actually delivered to the array ($\mathbf{P}_{transmit} - \mathbf{P}_{array\_refl}$) is similar for a given shield distance. For a locally shielded array with the capacitor in "$\mathbf{E}$" position, the current through the long leg significantly increased, compared to the unshielded case, and to arrays with the same shield distance but with the capacitor in position "$\mathbf{M}$" and "$\mathbf{S}$". This resulted in significantly increased copper and distributed capacitor losses, and hence an increase in $\mathbf{P}_{array\_internal}$.

For an array of length $150\,\mathrm{mm}$, a relatively small adjustment of the distributed capacitor values ($\mathbf{C}_d$) results in significant variation of the power reflected by the entire coil ($\mathbf{P}_{array\_refl}$) (e.g., for an array with distance to shield $= 60\,\mathrm{mm}$, $\mathbf{C}_d = 5.5\,\mathrm{pF}$ -> $\mathbf{P}_{array\_refl} = 2/1.4\,\mathrm{W}$, $\mathbf{C}_d = 5.15\,\mathrm{pF}$

Table 1: Data for coil length 85 mm.

| Distance to local shield, mm | No | | | | | | 60 | | | | | |
|---|---|---|---|---|---|---|---|---|---|---|---|---|
| head | 1 | 1 | 1 | 2 | 2 | 2 | 1 | 1 | 1 | 2 | 2 | 2 |
| capacitor position | **M** | **E** | **S** | **M** | **E** | **S** | **M** | **E** | **S** | **M** | **E** | **S** |
| $\mathbf{P}_{array\_refl}$, W | 0.22 | 0.46 | 0.34 | 0.17 | 0.4 | 0.34 | 0.29 | 0.60 | 0.43 | 0.28 | 0.51 | 0.23 |
| $\mathbf{P}_{radiated}$, W | 0.79 | 0.66 | 0.58 | 0.59 | 0.49 | 0.40 | 0.05 | 0.04 | 0.04 | 0.03 | 0.03 | 0.03 |
| $\mathbf{P}_{array\_internal}$, W | 0.32 | 0.28 | 0.47 | 0.26 | 0.27 | 0.2 | 0.36 | 0.44 | 0.33 | 0.38 | 0.39 | 0.29 |
| $\mathbf{P}_{load}$, W | 6.67 | 6.60 | 6.61 | 6.98 | 6.84 | 7.06 | 7.30 | 6.92 | 7.20 | 7.31 | 7.07 | 7.45 |
| $\mathbf{P}_V$, W | 2.47 | 2.46 | 2.39 | 2.62 | 2.58 | 2.52 | 2.72 | 2.54 | 2.56 | 2.67 | 2.55 | 2.57 |
| $\mathbf{B}_1+_V$, µT | 1.53 | 1.52 | 1.53 | 1.44 | 1.43 | 1.44 | 1.61 | 1.57 | 1.60 | 1.47 | 1.45 | 1.48 |
| Inhomogeneity brain, % | 25 | 25 | 25 | 25 | 25 | 25 | 26 | 26 | 26 | 26 | 26 | 26 |
| $\mathbf{B}_1+_{slice}$, µT | 1.82 | 1.82 | 1.82 | 1.73 | 1.78 | 1.72 | 1.96 | 1.91 | 1.94 | 1.80 | 1.78 | 1.82 |
| Inhomogeneity slice, % | 18 | 18 | 18 | 18 | 18 | 17 | 18 | 17 | 18 | 17 | 17 | 17 |
| $\mathbf{SAR}_{10g}$, W/kg | 4.52 | 4.55 | 4.36 | 4.56 | 4.37 | 4.18 | 4.91 | 4.62 | 4.56 | 4.62 | 4.46 | 4.41 |
| $\mathbf{B}_1+_V/\sqrt{\mathbf{SAR}_{10g}}$, µT/$\sqrt{}$ (W/kg) | 0.72 | 0.71 | 0.73 | 0.67 | 0.67 | 0.68 | 0.73 | 0.73 | 0.73 | 0.68 | 0.68 | 0.70 |
| $\mathbf{Q}_{loaded}$ for 1st element | 14.1 | - | 15.2 | 12.2 | - | 13 | 23.2 | - | 21.3 | 18.3 | - | 17.3 |
| $\mathbf{maxS}_{21}$ | −11.3 | −11.7 | −15 | −12.7 | −13.1 | −16.3 | −11.4 | −13.2 | −16.1 | −13.0 | −15.4 | −17.6 |
| $\mathbf{maxS}_{31}$ | −14.5 | −14.3 | −11.9 | −17.7 | −15.5 | −13.2 | −20.3 | −16.5 | −13.3 | −25 | −16.1 | −14.5 |

Table 2: Data for coil length 150 mm.

| Distance to local shield, mm | no | | | | | | 60 | | | | | |
|---|---|---|---|---|---|---|---|---|---|---|---|---|
| head | 1 | 1 | 1 | 2 | 2 | 2 | 1 | 1 | 1 | 2 | 2 | 2 |
| capacitor position | **M** | **E** | **S** | **M** | **E** | **S** | **M** | **E** | **S** | **M** | **E** | **S** |
| $\mathbf{P}_{array\_refl}$, W | 1.58 | 1.00 | 0.76 | 1.16 | 1.1 | 0.43 | 2.02 | 0.83 | 0.68 | 1.41 | 1.11 | 0.44 |
| $\mathbf{P}_{radiated}$, W | 1.27 | 1.04 | 1.02 | 1.13 | 0.81 | 0.83 | 0.11 | 0.07 | 0.14 | 0.09 | 0.05 | 0.08 |
| $\mathbf{P}_{array\_internal}$, W | 0.5 | 0.29 | 0.10 | 0.14 | 0.29 | 0.10 | 0.27 | 0.86 | 0.14 | 0.26 | 0.69 | 0.17 |
| $\mathbf{P}_{load}$, W | 4.65 | 5.67 | 6.12 | 5.57 | 5.80 | 6.64 | 5.60 | 6.24 | 7.04 | 6.24 | 6.15 | 7.31 |
| $\mathbf{P}_V$, W | 1.83 | 2.26 | 2.37 | 2.29 | 2.39 | 2.64 | 2.24 | 2.39 | 2.74 | 2.49 | 2.37 | 2.82 |
| $\mathbf{B}_1+_V$, µT | 1.25 | 1.40 | 1.45 | 1.28 | 1.33 | 1.42 | 1.42 | 1.50 | 1.60 | 1.39 | 1.38 | 1.51 |
| Inhomogeneity brain, % | 23 | 24 | 24 | 24 | 23 | 23 | 25 | 25 | 25 | 24 | 24 | 24 |
| $\mathbf{B}_1+_{slice}$, µT | 1.38 | 1.55 | 1.62 | 1.42 | 1.48 | 1.58 | 1.60 | 1.73 | 1.80 | 1.72 | 1.59 | 1.70 |
| Inhomogeneity slice, % | 25 | 25 | 24 | 24 | 24 | 23 | 25 | 22 | 25 | 23 | 22 | 24 |
| $\mathbf{SAR}_{10g}$, W/kg | 3.08 | 4.00 | 4.03 | 3.44 | 3.72 | 4.24 | 3.68 | 4.09 | 4.58 | 4.21 | 3.83 | 4.45 |
| $\mathbf{B}_1+_V/\sqrt{\mathbf{SAR}_{10g}}$, µT/$\sqrt{}$( W/kg) | 0.71 | 0.70 | 0.72 | 0.69 | 0.69 | 0.69 | 0.74 | 0.74 | 0.75 | 0.70 | 0.70 | 0.71 |
| $\mathbf{Q}_{loaded}$ for 1st element | 9.5 | - | 7.6 | 7 | - | 7 | 14 | - | 11 | 11 | - | 8.4 |
| $\mathbf{maxS}_{21}$ | −12 | −18 | −17 | −15 | −16 | −20 | −17 | −20 | −20 | −20 | −15 | −24 |
| $\mathbf{maxS}_{31}$ | −16 | −10 | −10.4 | −16 | −10 | −11 | −13 | −9.5 | −11.5 | −14 | −10 | −12.7 |

-> $\mathbf{P}_{array\_refl} = 1/0.7$ W, $\mathbf{C}_d = 5$ pF -> $\mathbf{P}_{array\_refl} = 0.4/0.3$ W for middle and large head sizes respectively), and thus improvement of the array performance can be obtained. This effect is most pronounced for the "**M**" position, about half as much for the "**E**" position, and relatively small for the "**S**" position.

For an array of length 85 mm, adjustment of $\mathbf{C}_d$ results in a relatively smaller variation of $\mathbf{P}_{array\_refl}$ (e.g., for an array with distance to shield = 60 mm, $\mathbf{C}_d = 10$ pF -> $\mathbf{P}_{array\_refl} = 0.85$ W, $\mathbf{C}_d = 9$ pF -> $\mathbf{P}_{array\_refl} = 0.37$ W for middle size head), for all capacitor position.

Neither the strongest coupling between adjacent array elements, nor the mean value of coupling between adjacent (or all) array elements in conjunction with its standard deviation can be used as a reliable figure-of-merit for the coil element isolation required for the optimal transmit performance. For example, for a 150 mm long array with shield distance of 60 mm and distributed capacitors 5.5 pF, the strongest coupling between any array elements is $-14$ dB, but $\mathbf{P}_{array\_refl} = 2$ W (25% of $\mathbf{P}_{transmit}$). For the same array with distributed capacitors 5.0 pF, the strongest coupling between any array elements is $-13$ dB, but $\mathbf{P}_{array\_refl} = 0.42$ W (5.25% of transmit power). For an 85 mm long array the strongest coupling between any array elements is $-10$ dB, however $\mathbf{P}_{array\_refl} = 0.16$ W (2% of $\mathbf{P}_{transmit}$). Because $\mathbf{P}_{array\_refl}$ depends on the product of the entire $S$-parameter matrix and the excitation vector, the rarely reported phases of coupling coefficients play a significant role in defining the constructive and destructive interference of power from each array element input.

For the same head, $\mathbf{B}_1+$ inhomogeneity calculated over the entire brain varies little with coil length, distance to shield, or position of decoupling capacitor, when the shield distance is more than 20 mm. For smaller shield distances, $\mathbf{B}_1+_{brain}$ decreases, with a simultaneous decrease in homogeneity.

It should be noted that the spectrum of $\mathbf{I}_{elem}$ significantly differed for the array with a capacitor at the "$\mathbf{M}$" or "$\mathbf{S}$" positions relative to the position "$\mathbf{E}$". For the latter position, the $\mathbf{I}_{elem}$ spectrum is not a single resonance and its shape is significantly asymmetrical (Figure 6). $\mathbf{Q}_{load}$ for these arrays cannot be calculated and therefore it is not reported.

Figures 3 and 4 show an array with length of 150 mm and capacitor at the "$\mathbf{M}$" position. Here, neither distributed capacitors of 3.25 pF nor distributed capacitors of 5.5 pF provide stable performance for both the first and the second circular polarization modes, despite good performance
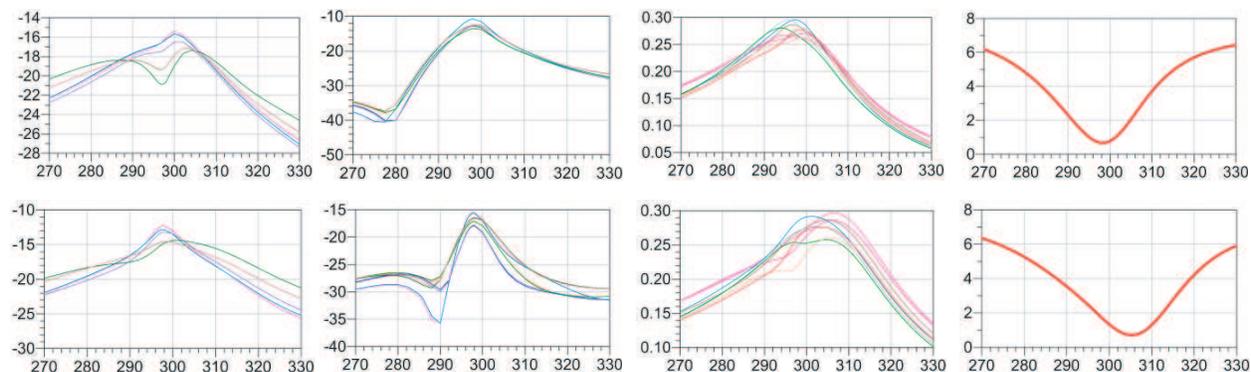


Figure 3: Properties of an array with length of 150 mm and position of decoupling capacitors "$\mathbf{M}$" in CP mode. Value of distributed capacitors: 3.25 pF for top row and 5.5 pF for bottom. From left to right $\mathbf{S}_{21}$, $\mathbf{S}_{31}$, $\mathbf{I}_{elem}$, $\mathbf{P}_{refl}$.
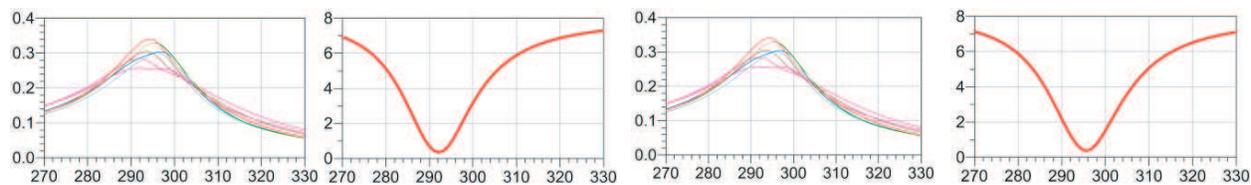


Figure 4: The same arrays as in Figure 3 in CP2 mode. Left $\mathbf{I}_{elem}$ and $\mathbf{P}_{refl}$ for distributed capacitors of 3.25 pF; right $\mathbf{I}_{elem}$ and $\mathbf{P}_{refl}$ for distributed capacitors of 5.5 pF.
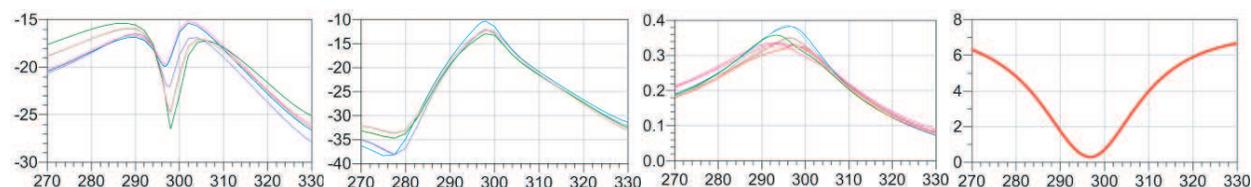


Figure 5: Properties of an array with length of 150 mm and position of decoupling capacitors "$\mathbf{S}$" in CP mode. From left to right $\mathbf{S}_{21}$, $\mathbf{S}_{31}$, $\mathbf{I}_{elem}$, $\mathbf{P}_{refl}$.
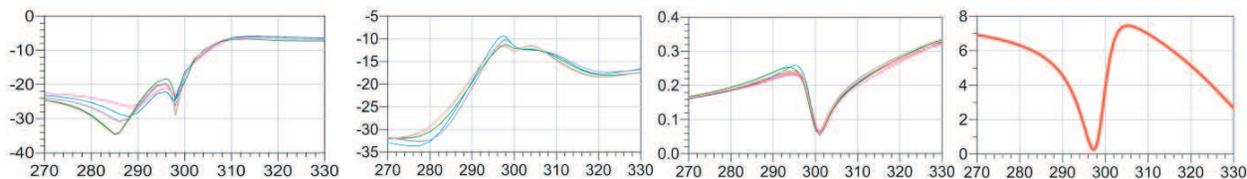
Figure 6: Properties of an array with length of 150 mm and position of decoupling capacitors "**E**" in CP mode. From left to right $\mathbf{S}_{21}$, $\mathbf{S}_{31}$, $\mathbf{I}_{elem}$, $\mathbf{P}_{refl}$.

in one of modes given and relative good decoupling. Thus, if an array is designed for wide range of static RF shimming and/or multi-mode operations, optimization of transmit performance for CP only mode could result in sub-optimal performance in other modes.

## 4. CONCLUSION

Given the assumptions of ideal common-mode current suppression and idealized array design conditions (specifically: fixed capacitors not restricted to commercially available values, zero component value tolerance, all tuning/matching/decoupling optimizations reaching their global minima), the transmit performance and safety excitation efficiency of the unshielded arrays of length 85 mm closely coupled to a load were similar for three typical decoupling capacitor positions, in the CP excitation mode. However, different capacitor positions entail different sensitivities to distributed capacitor values, changes of load, etc., and these sensitivities also depend nonlinearly on the distance to the local shield and the length of the array. In a given configuration, the reflected power provides an excellent figure-of-merit for array decoupling and transmit performance. Multi-parameter complex sensitivity analysis for the desired excitation modes should be performed before final coil design decisions are made.

## REFERENCES

1. Gilbert, K. M., A. T. Curtis, J. S. Gati, L. M. Klassen, and R. S. Menon, "A radiofrequency coil to facilitate B1+ shimming and parallel imaging acceleration in three dimensions at 7 T," *NMR Biomed*, Dec. 8, 2010, [Epub Ahead of Print].
2. Kim, K., N. Darji, T. Herrmann, J. Mallow, Z.-H. Cho, O. Speck, and J. Bernarding, "Improved B1+ field using a 16-channel transmit head array and an 8-channel pTx system at 7 T," *Proceedings 19th ISMRM*, 3829, Montreal, Canada, May 2011.
3. Kozlov, M. and R. Turner, "Fast MRI coil analysis based on 3-D electromagnetic and RF circuit co-simulation," *Journal of Magnetic Resonance*, No. 200, 147–152, 2009.

# Side Lobe Level Reduction of Linear Antenna Arrays Using a Hybrid Approach Based on MoM/GA Algorithms

**Amr H. Hussein**[1], **Haythem H. Abdullah**[2], **Salah Khamis**[1],
**Ahmed M. Attiya**[2], **and Mohammed Nasr**[1]

[1]Faculty of Engineering, Tanta University, Tanta, Egypt
[2]Electronics Research Institute, Cairo, Giza, Dokki, Egypt

**Abstract**— Side lobe level (SLL) reduction has a great importance in recent communication systems. It is considered as one of the most important applications of digital beamforming since it reduces the effect of interference arriving outside the main lobe. This interference reduction increases the capacity of the communication systems. In this paper, our home made synthesis scheme that is based on the Method of Moments and the Genetic Algorithm to synthesize linear antenna arrays is utilized. The algorithm accepts a desired radiation pattern and provides the excitation coefficients that realize the required pattern. If this pattern is applied to the synthesis scheme, it results in the optimum element spacing and the excitation coefficients that lead to maximum SLL reduction with a minimum number of array elements. The MoM/GA scheme provides SLL reduction with exactly the same half power beamwidth (HPBW) as the original array pattern.

## 1. INTRODUCTION

Many research efforts attempted to reduce the SLL of the linear antenna arrays by introducing non-uniform spacing between the antenna array elements and position perturbation with the aid of the GA algorithms [1–8]. An iterative method for SLL reduction by introducing non-uniform spacing between the antenna elements was introduced in [1]. The amplitude of the excitation is assumed to be constant. This iterative method suffers some drawbacks such as; the small reduction in the SLL and the half power beamwidth broadening which corresponds to the reduction in the SLL. More attempts in SLL reduction of linear antenna arrays by changing the spaces among array elements in terms of GA was introduced in [6]. Unfortunately, this algorithm is limited for antenna arrays of little number of antenna elements and the more the number of elements, the less the benefit from non-uniform allocation.

Position perturbation of the array elements is used for reducing the SLL of phased antenna arrays [7]. It results in a reduction in the SLL at the central part of the visible region but with higher side lobes at both sides of the pattern, which requires special treatment by using directional elements in the array structure. Other attempts for SLL reduction are presented in [8] using the real coded genetic algorithm (RGA) optimization technique. The RGA results in a uniformly spaced array structure with much larger array size than the original array structure.

In this paper, the MoM/GA algorithm [9] is utilized to synthesis the low SLL radiation pattern. The input to the algorithm is the desired radiation pattern and the output is the excitation coefficients and the element spacing. The key issue in the SLL reduction is the synthesis of a desired pattern having smooth behavior that permits the array synthesis with minimum number of array elements.

## 2. PROBLEM FORMULATION

The array factor of a linear antenna array consisting of $M$ isotropic antenna elements positioned symmetrically along the $z$-axis with uniform element spacing $d$ is given by:

$$AF(\theta) = \sum_{n=1}^{M} a_n \exp\left(j\left(n - \frac{M+1}{2}\right)kd\cos\theta\right) \qquad (1)$$

where $a_n$ is the excitation coefficient of the $n$th element, $d$ is the element spacing, and $k = 2\pi/\lambda$ is the free space wave number [1]. Recently, we presented a synthesis technique based on a combination between the method of moments and the genetic algorithm (MoM/GA) [9]. The MoM/GA is utilized to reconstruct new element locations and excitations that fulfill the required characteristics in the desired pattern. This synthesis method has shown its ability of reducing the number of

elements for linear arrays with pencil-beam patterns and shaped-beam patterns as mentioned in [9]. In this paper, the capabilities of this method are extended to synthesize the linear antenna arrays with maximum SLL reduction with minimum number of antenna elements. The algorithm is based on solving a system of linear equations which is written in a matrix form as

$$[Z]_{M \times M}[I]_{M \times 1} = [V]_{M \times 1} \tag{2}$$

where $[I]_{M \times 1} = [a_1, a_2, a_3, \ldots, a_M]^T$ is the excitation coefficients vector to be determined. The elements of the $[Z]_{M \times M}$ matrix take the form

$$z_{mn} = \int_0^\pi e^{j(n-m)kd\cos(\Theta)} d\Theta \tag{3}$$

The aim of this paper is to introduce a scheme for filling the matrix $[V]_{M \times 1}$ in order to achieve the minimum side lobe level that corresponds to a specific number of array elements. The matrix $[V]_{M \times 1}$ has the complete information about the desired radiation pattern.

The procedure starts by generating a pattern $AF(\Theta)$, *original pattern*, of a known linear antenna array that achieves the required beamwidth. This pattern is multiplied by a rectangular function *shaping function* of the same beamwidth in order to remove the side lobes. The shaping function is designed as follows

$$f_{shaping}(\Theta) = \text{rect}\left(\frac{\Theta - \phi_o}{w}\right) \tag{4}$$

where $\phi_o$ is the main beam direction with respect to the array line and $w$ is the width of the rectangular pulse which equals the main lobe widest beamwidth. Multiplying the original pattern by the appropriate shaping function, we get the shaped pattern as follows

$$AF_{shaped}(\Theta) = AF(\Theta) \times f_{shaping}(\Theta) \tag{5}$$

The resulting shaped pattern $AF_{shaped}(\Theta)$ will be raised by a certain level $h$ allowing the smooth extension of the pattern slightly above the zero level. The raised $AF_{sh\_raised}(\Theta)$ pattern is given by

$$AF_{sh\_raised}(\Theta) = AF_{shaped}(\Theta) + h \times \text{rect}\left(\frac{\Theta - \phi_o}{w}\right) \tag{6}$$

where $h$ is the amplitude of the rectangular function that represents the raising level of the shaped pattern. The raised pattern $AF_{sh\_raised}(\Theta)$ values will be raised to an exponent $n$ in order to keep the desired beamwidth that is changed slightly by raising the pattern by the level $h$. This process contributes greatly in smoothing the desired pattern in such a way that it prevents the appearance of the undesired harmonics that affect the SLL. The resultant pattern is applied as the desired pattern within the synthesis scheme presented in [9] such that $AF_d(\Theta) = [AF_{sh\_raised}(\Theta)]^n$. In this case, the elements of the vector $[V]_{M \times 1}$ are given by

$$V_m = \int_0^\pi [AF_{sh\_raised}(\Theta)]^n e^{-j\left(m - \frac{M+1}{2}\right)kd\cos(\Theta)} d\Theta \tag{7}$$

In addition to the use of GA to optimize the spacing between elements, it is also utilized to get the optimum $n$ and $h$ that achieves the minimum SLL. The Cost Function (CF) to be minimized is given by

$$\text{CF} = 1 - \frac{|\text{SLL}_o - \text{SLL}_s|}{|\text{SLL}_o|} \tag{8}$$

where $\text{SLL}_o$ and $\text{SLL}_s$ are the side lobe levels of the original and synthesized patterns respectively. The GA optimization tool in Matlab is used to estimate the optimum values of $d$, $n$, and $h$ while the corresponding excitation coefficients are determined using Eq. (2) applying the MoMFor $\lambda/2$ arrays the initial value of $d$ is set to $d = 0.5\lambda$ and theGA optimization process for $d$, $n$, and $h$ is performed within the ranges $0.5\lambda \leq d \leq 0.95\lambda$ ,$1 \leq n \leq 2$ and $L_- \leq h \leq L_- + 5$ where $L_-$ is the height of the negative portion of the shaped pattern. The optimization process is done under the constraint that the HPBW does not change its value.

# 3. RESULTS AND DISCUSSIONS

## 3.1. SLL Reduction of Broadside $\lambda/2$ Uniform Antenna Array Pattern Using the Same Number of Elements

Consider the twenty four elements $\lambda/2$ Uniform array reported in [8]. It's SLL $= -13.21$ dB, HPBW=4.14°, and the main lobe bottom beamwidth $w=13°$. Using the same number of antenna elements, SLL reduction is performed by adjusting the shaping function parameters of Eq. (4) such that $\phi_o = 90°$, and $w = 13°$. Fig. 1(a) shows the shaping function, and the original array pattern. Multiplying the original pattern by the shaping function the shaped pattern is obtained as shown in Fig. 1(b). Applying the GA algorithm, the optimized values of $d$, $n$, and $h$ are obtained after 51 GA iteration cycles such that $d = 0.886\lambda$, $n= 1.35$, and $h= 7$. Raising the shaped pattern by $h= 7$ gives the final shaped pattern shown in Fig. 1(c). The final shaped pattern is used as the desired pattern in the proposed scheme. The synthesized pattern has a very low side lobe level of SLL $= -65.7557$ dB with the same HPBW $= 4.14°$ as the original pattern as shown in Fig. 2 compared to the analytical Uniform array pattern and the synthesized pattern using the RGA method of Fig. 4 presented in [8].

In comparison with the RGA method, the proposed scheme provides much lower side lobe level than the RGA algorithm which has a value of SLL $= -54.94$ dB with a difference of about 10.8175 dB. Also the proposed scheme provides smaller element spacing of $d = 0.886\lambda$, while the RGA algorithm provides element spacing of $d = 0.8999\lambda$. In this case the synthesized array size is $0.3336\lambda$ less than the RGA algorithm.In point of view of the computation time, the proposed MoM/GA scheme takes only 51 iterations while the RGA takes 400 iterations. The excitation coefficients, the element spacing and the HPBW of the synthesized pattern are listed in Table 1 compared to the analytical Uniform array.

## 3.2. SLL Reduction of Broadside $\lambda/2$ Uniform Antenna Array Pattern with Reduced Number of Elements

The previous example is repeated with reduced number of antenna elements. The final shaped pattern of Fig. 1(c) is used as the desired pattern without any changes in the values of $n$ and $h$. For a specific number of antenna elements $M$, the GA is used to determine only the optimum element spacing $d$. The corresponding excitation coefficients are determined analytically using the MoM procedure. As test examples, SLL reduction is performed at $M = 20$, 18, and 16 antenna elements. The synthesized patterns have much lower SLL than the original pattern with exactly the

Table 1: Element spacing, SLL, and HPBW of the synthesized arrays with 24, 20, 18, and 16 antenna elements, compared to the analytical 24-elements $\lambda/2$ uniform array.

| Uniform array | | Synthesized arrays using the MoM/GA algorithm | | | |
|---|---|---|---|---|---|
| **M = 24** | | **M = 24** | **M = 20** | **M = 18** | **M = 16** |
| **d** $= 0.5\lambda$ | | **d** $= 0.886\lambda$ | **d** $= 0.896\lambda$ | **d** $= 0.912\lambda$ | **d** $= 0.922\lambda$ |
| $a_1$ | 1 | $a_1$ | 0.0928 | 0.5546 | 1.1415 | 2.4465 |
| $a_2$ | 1 | $a_2$ | 0.2826 | 1.0983 | 2.0003 | 3.412 |
| $a_3$ | 1 | $a_3$ | 0.6364 | 1.9232 | 3.133 | 4.6158 |
| $a_4$ | 1 | $a_4$ | 1.2057 | 3.0133 | 4.4535 | 5.8881 |
| $a_5$ | 1 | $a_5$ | 2.0227 | 4.3159 | 5.8571 | 7.1039 |
| $a_6$ | 1 | $a_6$ | 3.0862 | 5.7337 | 7.2156 | 8.1447 |
| $a_7$ | 1 | $a_7$ | 4.3516 | 7.1337 | 8.392 | 8.9054 |
| $a_8$ | 1 | $a_8$ | 5.7293 | 8.3648 | 9.2591 | 9.3071 |
| $a_9$ | 1 | $a_9$ | 7.0924 | 9.2824 | 9.7192 | |
| $a_{10}$ | 1 | $a_{10}$ | 8.294 | 9.7725 | | |
| $a_{11}$ | 1 | $a_{11}$ | 9.1915 | | | |
| $a_{12}$ | 1 | $a_{12}$ | 9.6716 | | | |
| **HPBW** $= 4.14°$ | | **HPBW** $= 4.14°$ | **HPBW** $= 4.14°$ | **HPBW** $= 4.14°$ | **HPBW** $= 4.14°$ |
| **SLL** $= -13.21$ dB | | **SLL** $= -65.7557$ dB | **SLL** $= -46$ dB | **SLL** $= -30$ dB | **SLL** $= -21.6$ dB |
| | | | **Reduction of elements = 16.66%** | **Reduction of elements = 25%** | **Reduction of elements = 33.33%** |
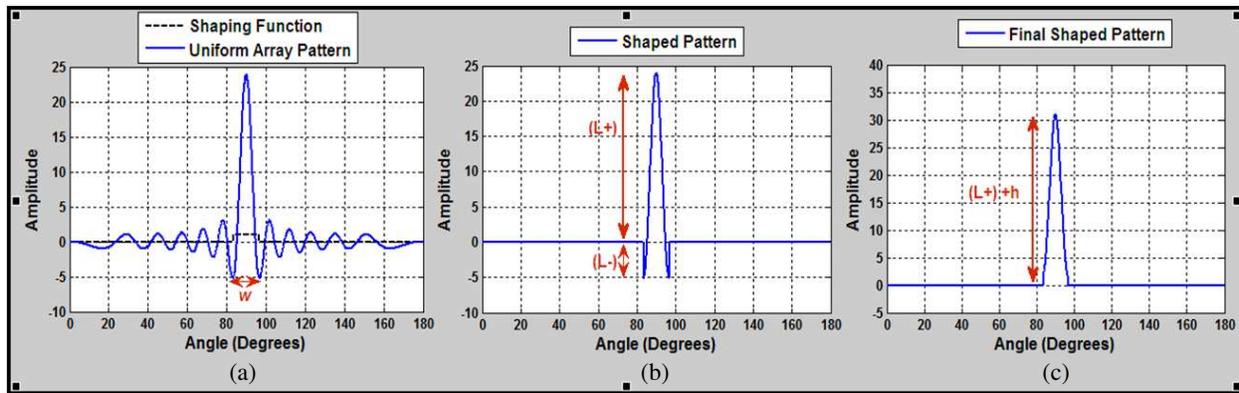
Figure 1: (a) Shaping function. (b) Shaped pattern. (c) Shaped pattern with positive offset.
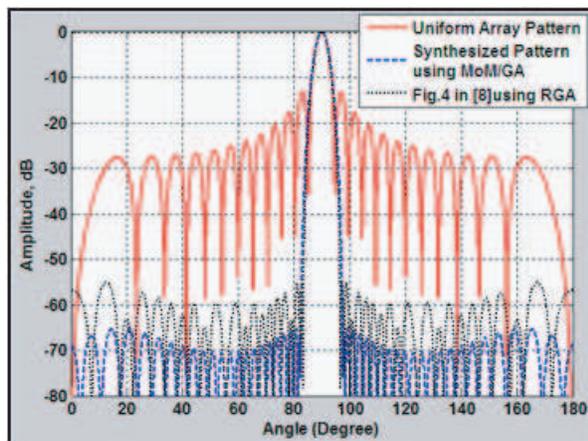


Figure 2: The synthesized radiation pattern with 24 elements.
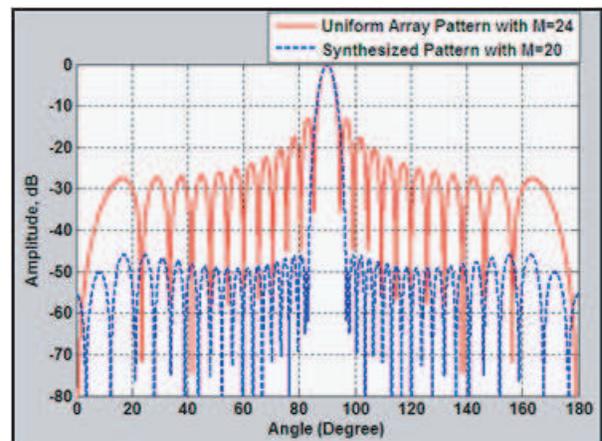
Figure 3: Synthesized radiation pattern with 20 elements, and $d = 0.896\lambda$ element spacing.

same HPBW. The excitation coefficients, the element spacing, and the HPBW of the synthesized patterns are listed in Table 1 compared to the analytical Uniform array. For clarity, the synthesized pattern at $M = 20$ is shown in Fig. 3.

## 4. CONCLUSION

In this paper, a new scheme based on a combination between the MoM, and the GA is presented for linear antenna arrays synthesis with maximum side lobe level reduction. The MoM/GA scheme aims to determine the optimum uniform element spacing and the excitation coefficients that guarantee maximum SLL reduction without affecting the main lobe beamwidth. In addition, SLL reduction is performed with a reduced number of antenna elements. The MoM/GA algorithm results in extremely low SLLs using only a few tens of GA iterations. It is characterized by a fast convergence, and a less computational complexity compared to other methods such as the RGA algorithm and the position perturbation algorithm.

## REFERENCES

1. Hodjat, F. and S. Hovanessian, "Nonuniformly spaced linear and planar array antennas for sidelobe reduction," *IEEE Transactions on Antennas and Propagation*, Vol. 26, No. 2, 198–204, Mar. 1978.
2. Yan, K.-K. and Y. L. Lu, "Sidelobe reduction in array-pattern synthesis using genetic algorithm," *IEEE Transactions on Antennas and Propagation*, Vol. 45, No. 7, Jul. 1997.
3. Ares-Pena, F. J., J. A. Rodriguez-Gonzalez, E. Villanueva-Lopez, and S. R. Rengarajan, "Genetic algorithms in the design and optimization of antenna array patterns," *IEEE Transactions on Antennas and Propagation*, Vol. 47, No. 3, Mar. 1999.
4. Kumar, B. P. and G. R. Branner, "Design of unequally spaced arrays for performance improvement," *IEEE Transactions on Antennas and Propagation*, Vol. 47, No. 3, Mar. 1999.

5. Marcano, D. and F. Duran, "Synthesis of antenna arrays using genetic algorithms," *IEEE Antennas Propagat. Magazine*, Vol. 42, No. 3, Jun. 2000.

6. Tian, Y. and J. Qian, "Improve the performance of a linear array by changing the spaces among array elements in terms of genetic algorithm," *IEEE Transactions on Antennas and Propagation*, Vol. 53, No. 7, 2226–2230, Jul. 2005.

7. Sayidmarie, K. H. and A. H. Aboud, "Improvement of array radiation pattern by element position perturbation," *5th International Multi-Conference on Systems, Signals and Devices, IEEE SSD*, 1–6, Jul. 20–22, 2008.

8. Das, S., S. Bhattacherjee, D. Mandal, and A. K. Bhattacharjee , "Optimal sidelobe reduction of symmetric linear antenna array using genetic algorithm," *Annual IEEE India Conference (INDICON)*, 1–4, Dec. 17–19, 2010.

9. Hussein, A. H., H. H. Abdullah, A. M. Salem, S. Khamis, and M. Nasr, "Optimum design of linear antenna arrays using a hybrid MoM/GA algorithms," *IEEE Antennas Wireless Propag. Lett.*, in press.

10. Balanis, C. A., *Antenna Theory: Analysis and Design*, 3rd Edition, Wiley, New York, 2005.

# Fixed Beamwidth Electronic Scanning Antenna Array Synthesis and Its Application to Multibeam Pattern Synthesis

**Amr H. Hussein[1], Haythem H. Abdullah[2], Mohammed Nasr[1],**
**Salah Khamis[1], and Ahmed M. Attiya[1]**

[1]Faculty of Engineering, Tanta University, Tanta, Egypt
[2]Electronics Research Institute, Dokki, Giza, Egypt

**Abstract**— In some applications, where, the scanning rate is not a critical factor, mechanically rotating system is sufficient to do fixed beamwidth scanning. The electronic scanning is an optimum solution to the high scanning rate applications, but it suffers from the beamwidth broadeningand gain variations with steering angles. In this paper, a fixed beamwidth electronic scanning algorithm is proposed. The proposed algorithm is based on synthesizing sets of excitation coefficients to direct the main beam at some scanning angles. The synthesis takes into consideration the fixation of the beamwidth at these angles. The synthesis of the excitation coefficients will be done using a scheme based on the moment method due to its accuracy in solving such problems. The optimum spacing between elements will be determined using the genetic algorithm. One of the main advantages of the proposed algorithm is the applicability of synthesizing multibeam antenna array of fixed beamwidths using the superposition principle.

## 1. INTRODUCTION

The synthesis of fixed beamwidth scanned antenna arrays with minimum number of antenna elements is of main concern in many applications such as Radar systemsand Tracking systems. Some of applications have mechanical steering systems, where a directive antenna array of a specific beam is mounted on a mechanical rotating system that directs the array to any direction keeping its beam unchanged such as rolling radar [1]. But the rate of direction change of the mechanical system is slow. The electronic scanning is used when it is necessary to vary the direction, or rate of change of direction of the array beam faster than is possible by mechanical movement of the aperture [2]. But electronic scanned radars suffer from the beamwidth variations with steering the main beam direction. The variations in the antenna array beamwidth as a function of the steering angle results in corresponding gain variations, and broadening of the main beam beamwidth which may cause signals from different transmitters to interfere with the desired transmitter signal. In this paper, it is introduced a new algorithmbased on a combination between the method of moments (MoM) [3] and the genetic algorithm(GA) [4–7]. The proposed algorithm is used for the synthesis of scannedlinear antenna arrays, and multi-beam antenna arrays with fixed minimum beamwidth at any direction with minimum number of equispaced antenna elements.

## 2. PROBLEM FORMULATION

### 2.1. Synthesisof Fixed MinimumBeamwidth Scanned Antenna Arrays

One of the most commonly used scanned antenna arrays is the phase scanned antenna array that is a linear array of uniformly spaced elements, where the direction of the main beam can be steered to any direction by adding progressive phase shift to the array excitation coefficients. But in addition to changing the main beam direction, beam steering changes the beamwidth. The main lobe becomes broader as the beam is steered away from broadside direction. Consequently, for a linear antenna array the end-fire beam is wider than the broadside beam [8]. The array factor of a linear antenna array consisting of isotropic antenna elements positioned symmetrically along the $z$-axis with uniform element spacing $d$ is given by:

$$AF(\theta) = \sum_{n=1}^{N} a_n \exp\left(j\left(n - \frac{N+1}{2}\right)kd\cos\theta\right) \quad (1)$$

where $a_n$ is the excitation coefficient of the $n$th element, $d$ is the element spacing, and $k = 2\pi/\lambda$ is the free space wave number [9]. Recently, we presented a synthesis technique based ona combination between the method of moments and the genetic algorithm (MoM/GA) [9]. The MoM/GA is utilized to reconstruct new element locationsand excitations that fulfill the required characteristics

in the desired pattern. This synthesis method has shown its ability of reducingthe number of elements for linear antenna arrays with pencil-beampatterns and shaped-beam patterns as mentioned in [9]. The MoM/GA algorithm is based on solving a system of linear equations which is written in a matrix form as

$$[Z]_{M \times M}[I]_{M \times 1} = [V]_{M \times 1} \tag{2}$$

$[I]_{M \times 1}$ is the excitation coefficients vector to be determined, such that $[I]_{M \times 1} = [a_1, a_2, a_3, \ldots, a_M]^T$. The elements of the $[Z]_{M \times M}$ matrix take the form

$$z_{mn} = \int_0^\pi e^{j(n-m)kd\cos(\Theta)} d\Theta \tag{3}$$

To get a radiation pattern with approximately the same minimum beamwidth as the broadside pattern at any steering direction $\phi_o$ the following procedure is followed:

    A. The excitation coefficients $a_n|_{\phi_o=90°}$ of the broadside pattern $AF(\Theta)|_{\phi_o=90°}$ are calculated.

    B. Adding phase shift $\beta = +(90 - \phi_o)$ to the angle $\Theta$ and replacing $a_n$ by $a_n|_{\phi_o=90°}$ in Eq. (1).

    C. As a result, a replica of the broadside pattern is generated and rotated by $\phi_o$ from the array line $AF(\Theta + 90 - \phi_o)$ whose equation is given by

$$AF(\Theta+90 - \phi_o) = \int_{n=1}^N (\mathbf{a_n}|_{\phi_o=90°}) e^{j(n - \frac{N+1}{2})kd\cos\phi(\Theta+90-\phi_o)} \tag{4}$$

The resultant pattern is applied as the desired pattern within the synthesis scheme presented in [9] such that $AF_d(\Theta) = AF(\Theta+90 - \phi_o)$. In this case, the elements of the vector $[V]_{M \times 1}$ are given by

$$V_m = \int_0^\pi AF_d(\Theta) e^{-j(m - \frac{M+1}{2})kd\cos(\Theta)} d\Theta \tag{5}$$

The excitation coefficients $a_n$ are determined by solving the linear system of Eq. (2).

    For multibeam synthesis, the directions of the multibeam need to be assigned first, then by applying the MoM/GA to synthesis each individual beam, the excitation coefficients for each direction will be available. By summing the excitation coefficients at all the desired directions and applying this summation to excite the array, the multibeam pattern will be achieved.

## 2.2. Estimation of the Optimum Element Spacing

In order to get the optimum element spacing, GA is utilized. The required cost function is written as follows

$$CF = \{|SLL_d| - |SLL_s|\}_{HPBW_s=HPBW_B} \tag{6}$$

$SLL_d$ and $SLL_s$ are the desired and the synthesized patterns side lobe levels, respectively. $HPBW_B$ is the desired pattern half power beamwidth at the broadside direction $\phi_o = 90°$, and $HPBW_s$ is the synthesized pattern half power beamwidth at the desired direction $\phi_o$. In this sequence, it is assumed no error in the $HPBW$. For a specific number of elements $M$, the GA searches for the optimum $d$ that provides a zero error in the $HPBW$ and at the same time introduces a minimum errorin the $SLL$.

## 2.3. Implementation of Fast and Continuous Range Fixed Beamwidth Scanning

Ordinary digital beam scanning techniques are based on generating a set of excitation coefficients that corresponds to the desired directions, and store them in lock up table (LUT). But these techniques suffer from; the huge memory storage especially for antenna arrays consisting of large number of elements, small scanning angle resolution, and the discrete scanning.

    For $N$ elements array, $N$ excitation coefficients for each direction are necessary. The proposed scheme solved these problems by generating two polynomial sets, $P_{nr}(\phi)$, and $P_{ni}(\phi)$, each of order $Q$ that are used to determine the real and imaginary parts of the excitation coefficients, respectively. The required memory size in this technique is $[2 \times N \times (Q + 1)]$ to store the $2N$ polynomials coefficients where $(Q+1)$ is the number of coefficients per polynomial. The polynomials generation follows these steps: ***Step (1)***: By solving Eq. (2) for the set of main beam directions

$\phi_0 = 0, 1, 2, 3, \ldots, 90$, we get 91 different excitation coefficients sets. These excitation coefficients are arranged in a matrix form $[C]_{NX91}$ that could be expressed as follows

$$[C]_{N \times 91} = \begin{bmatrix} a_1(0) & a_1(1) & a_1(2) & a_1(3) & \ldots & a_1(90) \\ a_2(0) & a_2(1) & a_2(2) & a_2(3) & \ddots & a_2(90) \\ a_3(0) & a_3(1) & a_3(2) & a_3(3) & \ldots & a_3(90) \\ \vdots & \vdots & \vdots & \vdots & \ldots & \vdots \\ \vdots & \ddots & \vdots & \vdots & \ddots & \vdots \\ a_N(0) & a_N(1) & a_N(2) & a_N(3) & \ldots & a_N(90) \end{bmatrix} \tag{7}$$

Each column of the coefficient matrix $[C]_{N \times 91}$ represents the excitation coefficients for a specific tilting angle $\phi_0$. The excitation coefficients are of complex values such that

$$a_n(\phi_0) = r_n(\phi_0) + jb_n(\phi_0) \quad n = 1, 2, 3, \ldots, N \tag{8}$$

The excitation coefficients $a_n(90° + \phi)$ equal the conjugate of the excitation coefficients at $(90° - \phi)$.

$$a_n(90° + \phi) = a_n(90° - \phi)^* \tag{9}$$

**Step (2)**: Substitute each coefficient of Eq. (7) by its real and imaginary parts. By using curve fitting techniques in Matlab $(2N)$ polynomials of order $(Q)$ are generated. The first set ofpolynomials, $P_{nr}(\phi)$, are used to fit the real parts of the excitation coefficients within each row of the coefficient matrix $[r_n(0)\, r_n(1)\, r_n(2)\, r_n(3) \ldots r_n(90)]$ where

$$P_{nr}(\phi) = p_{n1}\phi^Q + p_{n2}\phi^{Q-1} + \ldots + p_{n(Q+1)}, \quad n = 1, 2, 3, \ldots, N \tag{10}$$

where $\{p_{n1}, p_{n2}, p_{n3}, p_{n4}, \ldots, p_{nQ}, p_{n(Q+1)}\}$ are the coefficients of the $n$th polynomial.

The second set of polynomials, $P_{ni}(\phi)$, are used to fit the imaginary parts of the excitation coefficients within each row of the coefficient matrix $[b_n(0)\, b_n(1)\, b_n(2)\, b_n(3) \ldots b_n(90)]$ where

$$P_{ni}(\phi) = c_{n1}\phi^Q + c_{n2}\phi^{Q-1} + \ldots + c_{n(Q+1)}, \quad n = 1, 2, 3, \ldots, N \tag{11}$$

$\{c_{n1}, c_{n2}, c_{n3}, c_{n4}, \ldots, c_{nQ}, c_{n(Q+1)}\}$ are the coefficients of the $n$th polynomial.

The excitation coefficients at $90° < \phi_0 \leq 180°$ are obtained from Eq. (9).

## 3. RESULTS AND DISCUSSIONS

### 3.1. Synthesis of Multibeam Pattern with Fixed Beamwidths within The Sector ($0° \leq \phi_o \leq 180°$)

Consider a twenty elements $\lambda/2$ Tschebyscheff array with $SLL = -30\,\text{dB}$ [11] where the broadside beam pattern is chosen as the desired pattern at all directions. The radiation pattern at the broadside direction has the minimum half power beamwidth ($HPBW_{\min} = 6.1879°$), while the end-fire direction has the maximum half power beamwidth ($HPBW_{\max} = 38.674°$) in case of normal phase scanning. The change in the $HPBW$ from end-fire to broadside direction equals $\Delta_{HPBW} = HPBW_{\max} - HPBW_{\min} = 38.674° - 6.1879° = 32.4861°$. For the fixed beamwidth synthesis within the sector ($0° \leq \phi_o \leq 180°$), the end-fire main beam at $\phi_o = 0°$ is required to be close to that of the broadside main beam. This can be achieved using numbr of antenna elements $M = M_{\min} = 2N = 40$ elements with optimum element spacing $d = 0.33\lambda$. There is a slight change in the synthesized end-fire pattern beamwidth compared to the broadside beamwidth of $\Delta_{HPBW} = 6.961° - 6.1879° = 0.7731°$. An acceptable side lobe level $SLL = -25.7368\,\text{dB}$ is noticed.To get the same $HPBW = 6.961°$, and $SLL = -25.7368\,\text{dB}$ as the synthesized array using the ordinary $\lambda/2$ Tschebyscheff array it requires at least $N = 480$ antenna elements. Using this array structure,one can synthesize multibeam patterns with relatively fixed beamwidths at all directions. The synthesized multibeam pattern at angles of $0°$, $40°$, and $120°$ is shown in Fig. 1.

### 3.2. Implementation of Fixed Beamwidth Scanning Using The Coefficient Fitting Procedure

Consider a 20 elements $\lambda/2$ Tschebyscheff pattern. Applying the proposed coefficient fitting procedureand by using the fitting polynomials with $M_{\min} = 2N = 40$, it is found that the optimum element spacing using the GA is $d = 0.33\lambda$ and the best fitting ploynomials are of order $Q = 24$.
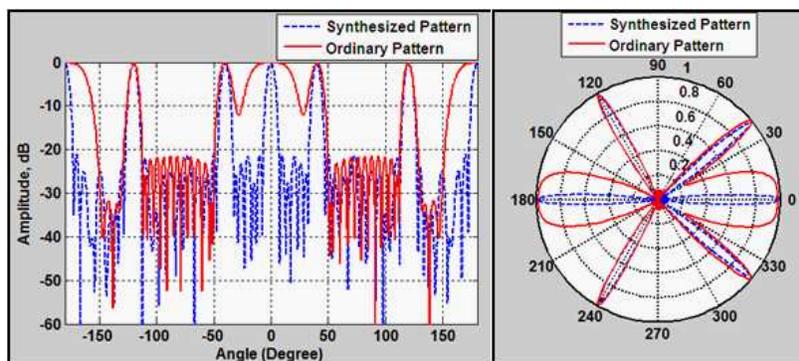
Figure 1: Synthesized multibeam pattern of fixed beamwidth beams directed at $\phi_1 = 0°$, $\phi_2 = 40°$ and $\phi_3 = 120°$ compared to the ordinary multibeam $\lambda/2$ Tschebyscheff pattern.
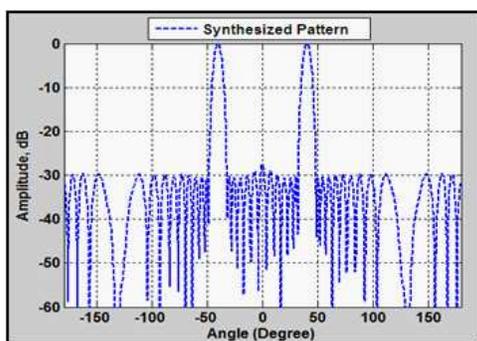


Figure 2: Synthesized pattern of the minimum beamwidth $HPBW_{\min} = 6.1879°$ directed at $\phi_o = 40.345°$.
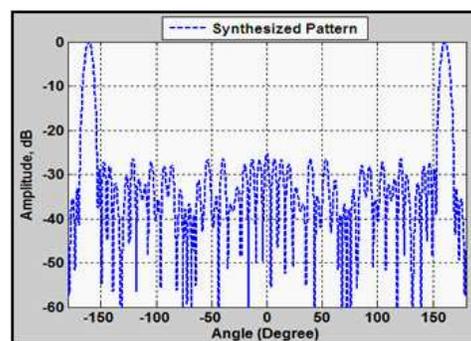


Figure 3: Synthesized pattern of the minimum beamwidth $HPBW_{\min} = 6.1879°$ directed at $\phi_o = 161.077°$.

So the memory locations required to store the polynomial coefficients is $2 \times 40 \times (24 + 1) = 2000$. Fixed beamwidth patterns at $\phi_o = 40.345°$ and $\phi_o = 161.077°$ are synthesized using the polynomials fitting functionsthat gives the same $HPBW = 6.1879°$ at the broadside direction as shown in Fig. 2 and Fig. 3.

## 4. CONCLUSION

An efficient use of the MoM/GA algorithm to synthesis fixed beam width radiation pattern at different angles is presented. The MoM is used to estimate the excitation coefficients of the antenna array while the GA is used to estimate the optimum element spacing. The array synthesis with fixed beamwidth is performed with the minimum number of antenna elements which is much lower than the required number of elements in case of the ordinary phased scanningarrays. The proposed algorithm has efficiently overcome the beamwidth broadeningand gain variations with steering angles in the phase scanned arrays. In addition, a high rate and continuous fixed beamwidth scanning technique is presented. The proposed technique requires much lower memory storage than the traditional digital beam scanning techniques which are based on the look-up tables. Also the proposed technique can be used when it is necessary to vary the direction, or rate of change of direction of the array beam faster than that is possible by the mechanical movement of the stationary beam arrays.

## REFERENCES

1. Tietjen, B. W., "The rolling radar," *2005 IEEE International Radar Conference*, 16–21, May 9–12, 2005.
2. Radford, M. F., "Electronically scanned antenna systems," *Proceedings of the Institution of Electrical Engineers*, Vol. 125, No. 11, 1100–1112, Nov. 1978.
3. Harrington, R. F., *Field Computation by Moment Methods*, IEEE Press, 1993.
4. Rahmat-Samii, Y. and E. Michielssen, *Electromagnetic Optimization by Genetic Algorithms*, John Wiley & Sons, Inc., 1999.

5. Houck, C. R., J. A. Joines, and M. G. Kay, "A genetic algorithm for function optimization: A matlab implementation," http://www.ie.ncsu.edu:80/mirage/GAToolBox/gaot/.

6. Ting, C.-K., "On the mean convergence time of multi-parent genetic algorithms without selection," *Advances in Artificial Life*, 403–412, 2005, ISBN 978-3-540-28848-0.

7. Haupt, R. L. and D. H. Werner, *Genetic Algorithms in Electromagnetics,* IEEE Press Wiley-Interscience, 2007.

8. Hansen, R. C., *Phased Array Antennas*, Wiley & Sons, 1998.

9. Hussein, A. H., H. H. Abdullah, A. M. Salem, S. Khamis, and M. Nasr, "Optimum design of linear antenna arrays using a hybrid MoM/GA algorithms," *IEEE Antennas Wireless Propag. Lett.*, Vol. 10, 2011.

10. Balanis, C. A., *Antenna Theory: Analysis and Design*, 3rd Edition, Wiley, New York, 2005.

11. Orfanidis, S. J., *Electromagnetic Waves and Antenna*, 2004, Available: http://www.ece.rutgers.edu/~orfanidi/ewa/.

# Mutual Coupling Compensation for a Compact Array in Direction Finding

**Yantao Yu[1], Choon Hock Niow[2], and Hon Tat Hui[2]**

[1]College of Communication Engineering, Chongqing University, Chongqing, China
[2]Department of Electrical & Computer Engineering
National University of Singapore, Singapore

**Abstract**— Multiport antenna arrays are more and more widely used in wireless communication systems. The strong mutual coupling effect between the elements of compact arrays may cause significant system performance degradation. Recently, a method using receiving mutual impedances has been proposed for mutual coupling compensation. In this paper, a compact monopole array is constructed and used in direction finding. For comparison, experiments are conducted with mutual coupling compensated by using the conventional mutual impedances and the receiving mutual impedances, respectively. The measured results show that the mutual coupling effect can be effectively removed using the receiving mutual impedances and the performance of direction finding can be greatly improved.

## 1. INTRODUCTION

Multiport antenna arrays are more and more widely used in wireless communication systems. The strong mutual coupling effect between the elements of compact arrays may cause significant system performance degradation. For application of direction-of-arrival (DOA) estimation, for example, MUSIC [1], the estimation errors are mainly contributed by the mutual coupling effect between array elements. When there is mutual coupling, compensation methods are usually required in order to obtain the correct array manifold. There have been many compensation methods [2, 3] proposed in the past. A typical method is the one using the conventional mutual impedances (CMI) [4] to characterize the mutual coupling effect. This method has been frequently used in both transmitting and receiving arrays. Recently, a modified method using receiving mutual impedance (RMI) [5] has been suggested for use in receiving antenna arrays. Many theoretical results [5, 6] have indicated that this new method is much more accurate in characterizing the mutual coupling effect in receiving arrays. In this paper, we report a group of experimental results by using the RMI to compensate for the mutual coupling effect in DOA estimation. A simple monopole array was constructed and its receiving mutual impedances and conventional mutual impedances were measured. DOA experiments were then performed inside the anechoic chamber.

## 2. THE DIFFERENT MUTUAL IMPEDANCES

The receiving mutual impedance was suggested in [7] for use in receiving antenna arrays. It has been noted before [8] that the mutual coupling problems are different in transmitting and receiving arrays. The difference between the receiving mutual impedance and the conventional mutual impedance is caused by the different current distributions when antennas are in different operational modes. The theoretical calculation of the receiving mutual impedance can be found from [7], while the measurement procedure is as in [9].

With the receiving mutual impedances $Z_t^{ki}$, the relationship between the uncoupled voltages $U_k$ and the received voltages $V_k$ can be written as:

$$\begin{bmatrix} U_1 \\ U_2 \\ \vdots \\ U_N \end{bmatrix} = \begin{bmatrix} 1 & -\frac{Z_t^{12}}{Z_L} & \cdots & -\frac{Z_t^{1N}}{Z_L} \\ -\frac{Z_t^{21}}{Z_L} & 1 & \cdots & -\frac{Z_t^{2N}}{Z_L} \\ \vdots & \vdots & \ddots & \vdots \\ -\frac{Z_t^{N1}}{Z_L} & -\frac{Z_t^{N2}}{Z_L} & \cdots & 1 \end{bmatrix} \begin{bmatrix} V_1 \\ V_2 \\ \vdots \\ V_N \end{bmatrix}. \tag{1}$$

While with the conventional mutual impedances $Z_{ij}$ [10], a different equation relating the open-

circuit voltages $V_{ok}$ to the received voltages $V_k$ is achieved.

$$
\begin{bmatrix} V_{o1} \\ V_{o2} \\ \vdots \\ V_{oN} \end{bmatrix} = \begin{bmatrix} 1 + \frac{Z_{11}}{Z_L} & \frac{Z_{12}}{Z_L} & \cdots & \frac{Z_{1N}}{Z_L} \\ \frac{Z_{21}}{Z_L} & 1 + \frac{Z_{22}}{Z_L} & \cdots & \frac{Z_{2N}}{Z_L} \\ \vdots & \vdots & \ddots & \vdots \\ \frac{Z_{N1}}{Z_L} & \frac{Z_{N2}}{Z_L} & \cdots & 1 + \frac{Z_{NN}}{Z_L} \end{bmatrix} \begin{bmatrix} V_1 \\ V_2 \\ \vdots \\ V_N \end{bmatrix}.
\tag{2}
$$

## 3. THE EXPERIMENTS OF DIRECTION OF ARRIVAL

In this study, DOA estimation experiments were carried out with a seven-monopole array. The monopole has a length of 30 mm and a diameter of 1 mm. The distance between elements is 25 mm, which is about $0.2\lambda$ at 2.4 GHz. The measured receiving mutual impedances were used to compensate for the mutual coupling effect in the received antenna terminal voltages and the measurement results were compared with the corresponding results obtained by using the conventional mutual impedances.

When there was only one incoming signal, a transmitting horn antenna serving as the signal source and the monopole array were mounted at the two ends of an anechoic chamber. The position of the horn antenna was set at an angle of $\phi = 105°$ with reference to the center of the monopole array. The $S_{21}$ parameter which indicates the relative power received by the monopoles were measured and converted into a relative voltage quantity. In this way, all the received voltages on the antenna elements were measured, which were then compensated using the measured receiving mutual impedances. The signal direction was then estimated using the MUSIC algorithm based on the compensated received voltages. Fig. 1 shows the results of the MUSIC spectra which were obtained with the mutual coupling in the received voltages being compensated by different methods: (i) by using the receiving mutual impedance (RMI), (ii) by using the conventional mutual impedance (CMI), and (iii) no compensation at all (NC). It can be seen from Fig. 1 that mutual coupling did not have a significant effect on the DOA estimation when there was only one source. For the case with no compensation (NC), the estimated arrival angle was 104.3°, which was 0.7° away from the actual source direction. The estimated arrival angles using CMI and RMI are 107.5° (with error of 2.5°) and 104.1° (with error of 0.9°), respectively. In the following experiment, it will be shown that when there were two signal sources, the RMI and CMI could make a much bigger difference.

In the case of two incoming signals, two horn antennas were fed from the output port of the vector network analyzer through a power divider. The MUSIC estimation results of the two sources coming from angles 68.6° and 111.7° are shown in Fig. 2. It can be seen that both the NC case and the CMI case failed to correctly indicate the directions of the two sources. While with the RMI used, the MUSIC spectrum correctly indicated the source directions with relatively small errors. It can be seen that the DOA estimations using RMI are much more accurate than that using CMI.
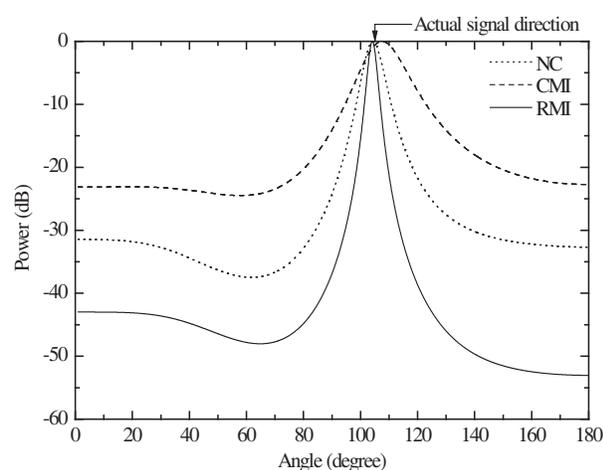


Figure 1: The MUSIC spectra for the DOA estimation of a single source at $\phi = 105°$.
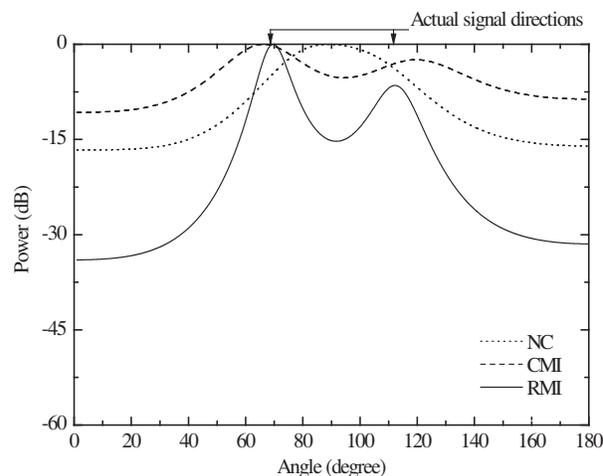


Figure 2: The MUSIC spectra for the estimation of two sources at $\phi = 68.6°$ and $\phi = 111.7°$.

## 4. CONCLUSIONS

The performance of DOA estimation using the receiving mutual impedances for mutual coupling compensation has been experimentally studied in this paper. A seven-monopole antenna array was used in DOA estimation employing the MUSIC algorithm. The measured results show the significant improvements in DOA estimation when the mutual coupling effect is compensated by using the receiving mutual impedances.

## ACKNOWLEDGMENT

## REFERENCES

1. Schmidt, R. O., "Multiple emitter location and signal parameter estimation," *IEEE Trans. Antennas Propag.*, Vol. 34, No. 3, 276–280, 1986.
2. Dandekar, K. R., H. Ling, and G. Xu, "Experimental study of mutual coupling compensation in smart antenna application," *IEEE Trans. Wireless Commun.*, Vol. 1, No. 3, 480–487, 2002.
3. Ye, Z. and C. Liu, "2-D DOA estimation in the presence of mutual coupling," *IEEE Trans. Antennas Propag.*, Vol. 56, No. 10, 3150–3158, 2008.
4. Gupta, I. J. and A. A. Ksienski, "Effect of mutual coupling on the performance of adaptive arrays," *IEEE Trans. Antennas Propag.*, Vol. 31, No. 5, 785–791, 1983.
5. Hui, H. T., "Improved compensation for the mutual coupling effect in a dipole array for direction finding," *IEEE Trans. Antennas Propag.*, Vol. 51, No. 9, 2498–2503, 2003.
6. Hui, H. T., "An effective compensation method for the mutual coupling effect in phased arrays for magnetic resonance imaging," *IEEE Trans. Antennas Propag.*, Vol. 53, No. 10, 3576–3583, 2005.
7. Hui, H. T., "A practical approach to compensate for the mutual coupling effect in an adaptive dipole array," *IEEE Trans. Antennas Propag.*, Vol. 52, No. 5, 1262–1269, May 2004.
8. Daniel, J., "Mutual coupling between antennas for emission or reception — Application to passive and active dipole," *IEEE Trans. Antennas Propag.*, Vol. 22, 347–349, Mar. 1974.
9. Hui, H. T., "A new definition of mutual impedance for application in dipole receiving antenna arrays," *IEEE Antennas and Wireless Propagation Letters*, Vol. 3, 364–367, 2004.
10. Jordan, E. C., *Electromagnetic Waves and Radiating Systems*, Chapter 11, Prentice-Hall Inc., Englewood Cliffs, N. J., 1968.

# Effects of Microstrip Feed Line Width on $1 \times 4$ Rectangular Microstrip Antenna Array Electrical Parameters and Estimation with Artificial Neural Networks

**O. Dundar[1], D. Uzer[2], S. S. Gultekin[2], and M. Bayrak[3]**

[1]Electronic Communication Program
Eregli Kemal Akman Technical Vocational School of Higher Education
Selcuk University, Konya, Turkey
[2]Department of Electrical and Electronics Engineering
Faculty of Engineering-Architecture, Selcuk University, Konya, Turkey
[3]Department of Electrical and Electronics Engineering
Faculty of Engineering, Mevlana University, Konya, Turkey

**Abstract**— In this study, $1 \times 4$ rectangular microstrip array antennas are designed at $16\,\text{GHz}$ resonant frequency for KU Band usage on Duroid 5880 substrate that has a thickness of $0.254\,\text{mm}$ and a dielectric constant of 2.2. Designs are simulated using HFSS v12. At these designs, by changing the feed line widths systematically, for each antenna, electrical parameters like $S_{11}$ response, directivity, gain, radiation efficiency etc. are investigated for 26 array antennas in simulation media. Also, directivity and gain values are predicted with an Artificial Neural Network model. The network has four inputs as dielectric substrate thickness, resonant frequency and dielectric constant of the substrate and three outputs as directivity, gain and radiation efficiency. Multilayer perceptron structure for Artificial Neural Network model and Levenberg-Marquart learning algorithm for training the network are used. The network model is trained with 20 of 26 design data and is tested with the rest 6 ones. It is seen that the results from simulations and the neural network model are compatible with similar studies in the literature.

## 1. INTRODUCTION

Microstrip antenna is simply a conductive radiating patch whose bottom surface covered with ground plane and between two conductive surfaces there is a dielectric substrate layer [1]. Although these types of antennas have lots of advantage and application areas, their electrical parameters are depend on antennas' physical parameters.

Thanks to microstrip antenna arrays' lightness, low profile and cost, they generally use in Ku Band application like VSAT, Radiometric place based fire sensation and microelectromecanic systems between a large space [2]. In this study, a single antenna was design by using formulas in literature used for classic rectangular microstrip antenna design then a $1 \times 4$ element patch array antenna was designed that between a $0.428\lambda$ wavelength space with antenna elements [2].

## 2. ANTENNA DESIGN

A single antenna, seen in Figure 1, was designed on Duroid 5880 dielectric substrate that has a thickness of $0.254\,\text{mm}$ and a dielectric constant of 2.2 with a length of $7.41\,\text{mm}$ and a width of $6.2\,\text{mm}$ using classic rectangular microstrip antenna design formulas in the literature [3–5]. From this single patch design, a $1 \times 4$ patch antenna array contained 4 same size elements was obtained like seen in Figure 2 and between these antenna elements there were $0.428\lambda$ spaces.

## 3. EFFECTS OF FEEDLINE WIDTH ON ELECTRICAL PARAMETERS OF A $1 \times 4$ RECTANGULAR MICROSTRIP PATCH ARRAY

The feed line was connected to connector with a $50\,\Omega$ coaxial cable. The patch side of the feed line had a $100\,\Omega$ impedance. In literature a traditional quarter wavelength converter was applied between $100\,\Omega$ patches and the feed line [1]. From different the literature, in this study the line width between $100\,\Omega$ patch and $50\,\Omega$ feed input was changed 0.2 to $0.7\,\text{mm}$. At total 26 antenna arrays were designed and these antennas were simulated by HFSS software. The simulation results are given in Table 1. From Table 1, it is seen that $S_{11}$ response, directivity, gain and radiation efficiency increase with the increased feed line widths. The largest $S_{11}$ value is for values between $0.50$–$0.60\,\text{mm}$. It can be said that the most efficient values of $S_{11}$ response, directivity, gain and radiation efficiency are for No. 18 array with a $0.54\,\text{mm}$ width. A comparison of $S_{11}$ response,
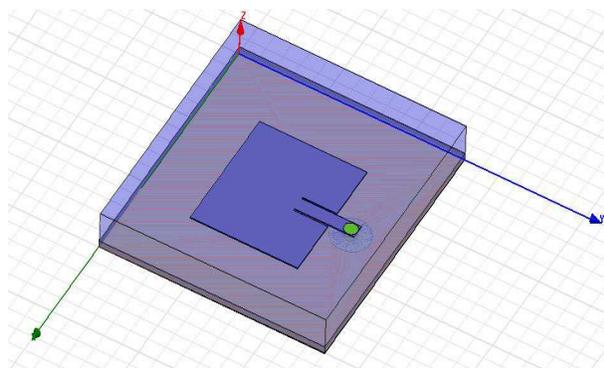
Figure 1: Single patch antenna.
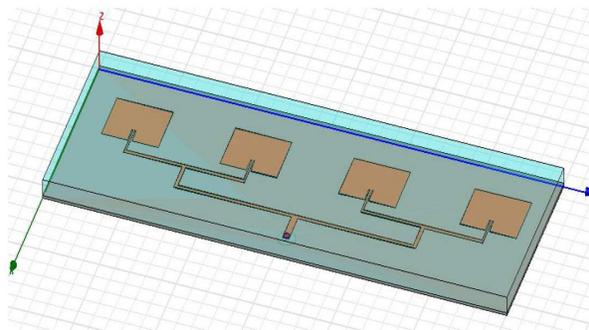


Figure 2: $1 \times 4$ array antenna.

Table 1: Electrical parameters variation against feed line lengths.

| No | Thickness $(t)$ (mm) | $f_r$ (GHz) | $f_{rHFSS}$ (GHz) | $S_{11}$ (dB) | Directivity $(D)$ (dB) | Gain $(G)$ (dB) | Radiation Efficiency $(Re)$ (dB) | BW (%) |
|---|---|---|---|---|---|---|---|---|
| 1 | 0.20 | 16 | 16.34 | −13.07 | 11.52 | 10.95 | 0.88 | 3.31 |
| 2 | 0.22 | 16 | 16.31 | −13.34 | 11.41 | 10.85 | 0.88 | 3.56 |
| 3 | 0.24 | 16 | 16.35 | −14.30 | 11.47 | 10.94 | 0.88 | 3.62 |
| 4 | 0.26 | 16 | 16.32 | −13.55 | 11.49 | 10.93 | 0.88 | 3.94 |
| 5 | 0.28 | 16 | 16.29 | −13.68 | 11.45 | 10.92 | 0.88 | 4.06 |
| 6 | 0.30 | 16 | 16.28 | −14.17 | 11.47 | 10.93 | 0.88 | 4.31 |
| 7 | 0.32 | 16 | 16.09 | −14.95 | 11.45 | 10.88 | 0.88 | 4.27 |
| 8 | 0.34 | 16 | 16.14 | −14.04 | 11.50 | 10.96 | 0.88 | 4.44 |
| 9 | 0.36 | 16 | 16.10 | −14.84 | 11.49 | 10.94 | 0.88 | 4.44 |
| 10 | 0.38 | 16 | 16.07 | −15.53 | 11.49 | 10.96 | 0.88 | 6.75 |
| 11 | 0.40 | 16 | 16.05 | −16.80 | 11.50 | 10.97 | 0.89 | 4.19 |
| 12 | 0.42 | 16 | 16.06 | −16.96 | 11.50 | 10.99 | 0.89 | 4.37 |
| 13 | 0.44 | 16 | 16.00 | −17.30 | 11.46 | 10.91 | 0.88 | 4.30 |
| 14 | 0.46 | 16 | 16.05 | −18.68 | 11.53 | 10.98 | 0.88 | 4.19 |
| 15 | 0.48 | 16 | 16.03 | −19.44 | 11.50 | 10.97 | 0.89 | 4.19 |
| 16 | 0.50 | 16 | 16.03 | −19.91 | 11.51 | 10.97 | 0.88 | 4.36 |
| 17 | 0.52 | 16 | 16.00 | −20.95 | 11.57 | 11.00 | 0.88 | 3.94 |
| **18** | **0.54** | **16** | **16.00** | **−22.61** | **11.54** | **11.02** | **0.89** | **3.88** |
| 19 | 0.56 | 16 | 16.02 | −22.97 | 11.47 | 10.93 | 0.88 | 4.26 |
| 20 | 0.58 | 16 | 15.97 | −25.63 | 11.52 | 11.01 | 0.89 | 3.81 |
| 21 | 0.60 | 16 | 15.99 | −26.97 | 11.48 | 10.94 | 0.89 | 3.87 |
| 22 | 0.62 | 16 | 15.80 | −23.30 | 11.42 | 10.90 | 0.89 | 1.88 |
| 23 | 0.64 | 16 | 15.80 | −31.34 | 11.38 | 10.88 | 0.89 | 2.13 |
| 24 | 0.66 | 16 | 15.82 | −22.97 | 11.46 | 10.92 | 0.88 | 1.94 |
| 25 | 0.68 | 16 | 15.84 | −17.09 | 11.43 | 10.90 | 0.89 | 1.56 |
| 26 | 0.70 | 16 | 15.81 | −19.43 | 11.45 | 10.92 | 0.89 | 1.75 |

directivity, gain and radiation efficiency values between No. 18 design and the design in literature with quarter wavelength converter is given in Table 2 [2].

Table 2: Comparison of No. 18 design with [2].

| Antenna Parameters | $S_{11}$ Response | | $-3.70\,\text{dB}$ | | $-22.61\,\text{dB}$ |
|---|---|---|---|---|---|
| | Simulation Frequency | | 16.10 GHz | | 16.00 GHz |
| | Directivity | $1 \times 4$ **Patch** | 11.52 dB | $1 \times 4$ **Patch** | 11.54 dB |
| | Gain | | 10.837 dB | | 11.02 dB |
| | Radiation Efficiency | | 0.85 | | 0,89 |

Table 3: Train and test data set for ANN model and iteration results.

| | No | **Inputs** | | | | **Simulation Outputs** | | | **ANN Outputs** | | |
|---|---|---|---|---|---|---|---|---|---|---|---|
| | | $f_r$ (GHz) | $t$ (mm) | $\varepsilon_r$ | $h$ (mm) | $D$ (dB) | $G$ (dB) | Re | $D_{ANN}$ (dB) | $G_{ANN}$ (dB) | Re |
| **Train Set** | 1 | 16 | 0.20 | 2.2 | 0.254 | 11.5200 | 10.9500 | 0.8800 | 11.5200 | 10.9500 | 0.8800 |
| | 2 | 16 | 0.22 | 2.2 | 0.254 | 11.4100 | 10.8500 | 0.8800 | 11.4100 | 10.8500 | 0.8800 |
| | 3 | 16 | 0.24 | 2.2 | 0.254 | 11.4700 | 10.9400 | 0.8800 | 11.4700 | 10.9400 | 0.8800 |
| | 4 | 16 | 0.26 | 2.2 | 0.254 | 11.4900 | 10.9300 | 0.8800 | 11.4900 | 10.9300 | 0.8800 |
| | 5 | 16 | 0.28 | 2.2 | 0.254 | 11.4500 | 10.9200 | 0.8800 | 11.4500 | 10.9200 | 0.8800 |
| | 6 | 16 | 0.30 | 2.2 | 0.254 | 11.4700 | 10.9300 | 0.8800 | 11.4700 | 10.9300 | 0.8800 |
| | 7 | 16 | 0.32 | 2.2 | 0.254 | 11.4500 | 10.8800 | 0.8800 | 11.4500 | 10.8800 | 0.8800 |
| | 8 | 16 | 0.34 | 2.2 | 0.254 | 11.5000 | 10.9600 | 0.8800 | 11.5000 | 10.9600 | 0.8800 |
| | 9 | 16 | 0.36 | 2.2 | 0.254 | 11.4900 | 10.9400 | 0.8800 | 11.4900 | 10.9400 | 0.8800 |
| | 10 | 16 | 0.38 | 2.2 | 0.254 | 11.4900 | 10.9600 | 0.8800 | 11.4900 | 10.9600 | 0.8800 |
| | 11 | 16 | 0.40 | 2.2 | 0.254 | 11.5000 | 10.9700 | 0.8900 | 11.5000 | 10.9700 | 0.8900 |
| | 12 | 16 | 0.42 | 2.2 | 0.254 | 11.5000 | 10.9900 | 0.8900 | 11.5000 | 10.9900 | 0.8900 |
| | 13 | 16 | 0.44 | 2.2 | 0.254 | 11.4600 | 10.9100 | 0.8800 | 11.4600 | 10.9100 | 0.8800 |
| | 14 | 16 | 0.46 | 2.2 | 0.254 | 11.5300 | 10.9800 | 0.8800 | 11.5300 | 10.9800 | 0.8800 |
| | 15 | 16 | 0.48 | 2.2 | 0.254 | 11.5000 | 10.9700 | 0.8900 | 11.5000 | 10.9700 | 0.8900 |
| | 16 | 16 | 0.50 | 2.2 | 0.254 | 11.5100 | 10.9700 | 0.8800 | 11.5100 | 10.9700 | 0.8800 |
| | 17 | 16 | 0.52 | 2.2 | 0.254 | 11.5700 | 11.0000 | 0.8800 | 11.5700 | 11.0000 | 0.8800 |
| | 18 | 16 | 0.54 | 2.2 | 0.254 | 11.5400 | 11.0200 | 0.8900 | 11.5400 | 11.0200 | 0.8900 |
| | 19 | 16 | 0.56 | 2.2 | 0.254 | 11.4700 | 10.9300 | 0.8800 | 11.4700 | 10.9300 | 0.8800 |
| | 20 | 16 | 0.58 | 2.2 | 0.254 | 11.5100 | 11.0100 | 0.8900 | 11.5100 | 11.0100 | 0.8900 |
| **Test Set** | 21 | 16 | 0.60 | 2.2 | 0.254 | 11.4800 | 10.9400 | 0.8800 | 11.5133 | 11.0048 | 0.8795 |
| | 22 | 16 | 0.62 | 2.2 | 0.254 | 11.4200 | 10.9000 | 0.8900 | 11.4479 | 10.8504 | 0.8592 |
| | 23 | 16 | 0.64 | 2.2 | 0.254 | 11.3800 | 10.8800 | 0.8900 | 11.3387 | 10.6007 | 0.8969 |
| | 24 | 16 | 0.66 | 2.2 | 0.254 | 11.4600 | 10.9200 | 0.8800 | 11.2747 | 10.5991 | 0.9949 |
| | 25 | 16 | 0.68 | 2.2 | 0.254 | 11.4300 | 10.9000 | 0.8900 | 11.2661 | 10.5997 | 1.0066 |
| | 26 | 16 | 0.70 | 2.2 | 0.254 | 11.4500 | 10.9200 | 0.8900 | 11.2655 | 10.5997 | 1.0074 |

## 4. ESTIMATION OF DIRECTIVITY, GAIN AND RADIATION EFFICIENCY WITH AN ARTIFICIAL NEURAL NETWORK MODEL

Directivity, gain and radiation efficiency of the designed a $1 \times 4$ array patch antenna was estimated with a four input-three output ANN model for constant width, frequency thickness and dielectric value [7, 8]. The ANN model had a Multi-Layer Perceptron (MLP) structure and for training the structure, Levenberg-Marquardt (LM) algorithm was used [7–10]. MLP structure and ANN model are given in Figure 3. Train and test data set for ANN model and iteration results are given in Table 3.

In Table 3, given ANN inputs are resonant frequency ($f_r$), feed line width ($t$), dielectric constant of the substrate ($\varepsilon_r$) and dielectric substrate thickness ($h$), while outputs are directivity ($D$), gain ($G$) and radiation efficiency ($R_e$). ANN-LM network has a $4 \times 9 \times 10 \times 3$ structure and epoch number is 205. Train performance of the network is 2,34.10–31. Train and test graphics obtained from train results are given in Figure 4.

(a)                          (b)
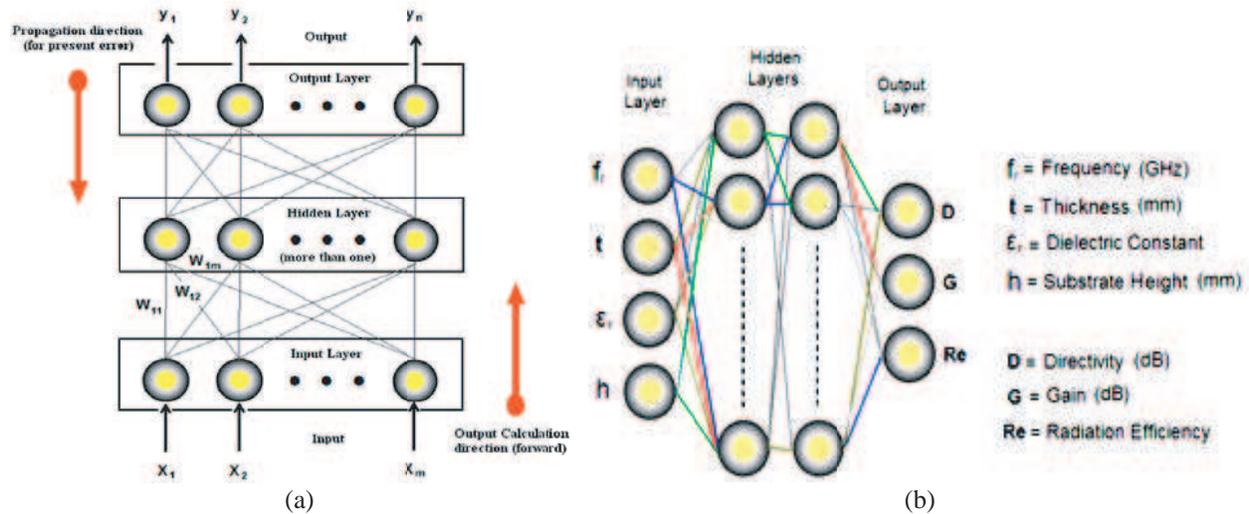
Figure 3: Multilayer perceptron structure and ANN model structure.
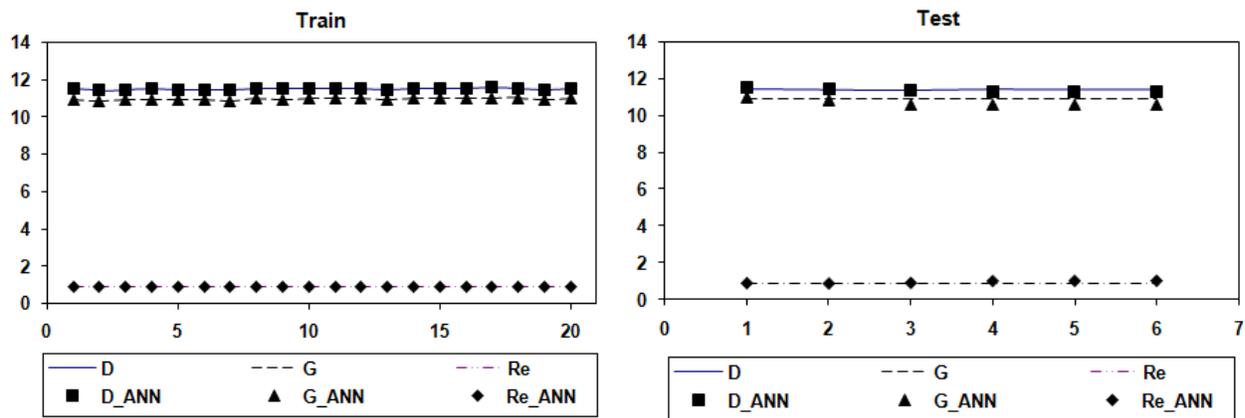


Figure 4: Train and test graphics obtained from iterations.

## 5. CONCLUSION

In this study, 26 $1 \times 4$ patch antenna arrays were designed. When the electrical parameters of these antennas were investigated, it was shown in Table 1 that No. 18 design had the best performance compared to the literature from Table 2. This study was presented as an alternative of traditional quarter wavelength converters in the literature.

Also, the obtained antenna parameters were used for an ANN model testing and it was seen from the graphics, directivity, gain and radiation efficiency values were estimated. It is observed from the results that this estimation is enough successful.

## REFERENCES

1. Garg, R., P. Bhartia, I. Bahl, and A. Ittipiboon, *Microstrip Antenna Design Handbook*, 293–296, Artech House, 1995.
2. Khan, O. M., Z. Ahmad, and Q. Islam, "Ku band microstrip patch antenna array," *IEEE*, 1-4244-1494-6/07, 2007.
3. Balanis, C. A., *Antenna Theory Analysis and Design*, 2nd Edition, Chapter 14, Wiley, 1997.
4. James, I. J. and P. S. Hall, *Handbook of Microstrip Antennas*, Vol. 1, Peter Peregrinus Ltd., 1989.
5. Green, D. W., "Broadbanding of microstrip antenna," www.cwnp.com/learning_center/search_details. php?doc_id=jbM80iLL-12k, 2002.

6. HFSS v 12, http://www.ansoft.com/products/hf/hfss.
7. Rumelhart, D. E. and J. L. McClelland, *Parallel Distributed Processing, Explorations in the Microstructure of Cognition*, The MIT Press, Cambridge, 1986.
8. Haykin, S., *Neural Networks: A Comprehensive Foundation*, Macmillan College Publishing Company, 1994.
9. Levenberg, K., "A method for the solution of certain non-linear problems in least squares," *The Quart. Appl. Math.*, Vol. 2, 164–168, 1944.
10. Marquardt, D., "An algorithm for least-squares estimation of nonlinear parameters," *SIAM J. Appl. Math.*, Vol. 11, 431–441, 1963.

# Fractal Inspired Patch Antenna on Metamaterial

**S. Suganthi[1], S. Raghavan[2], and D. Kumar[3]**

[1]Shri Angalamman College of Engineering and Technology, Trichy, India
[2]National Institute of Technology, Trichy, India
[3]Periyar Maniammai University, Thanjavur, India

**Abstract**— This paper proposes a novel design of a compact microstrip antenna on a metamaterial (MTM) substrate. This antenna is composed of a fractal outlined square patch as the main radiating element. The MTM used is a combination of multiple slip ring resonators (MSSR) along with a Wire Strip on a FR4 substrate. Another novelty in this design is that the structure utilizes co-planar waveguide (CPW) system and a microstrip feed. Hence, the ground plane lies along the antenna plane which makes fabrication easier. The design and simulation have been carried out using HFSS 3D electromagnetic simulation software. Initially an investigation has been made to confirm that the preferred MSRR and Wire structure exhibit metamaterial property. With a separate coding written in MATLAB for Nicolson-Ross-Wier method, the negative permeability and negative permittivity have been verified to be present. The magnetic permeability is found to be more predominant in large frequency ranges. Then square fractal antenna has been designed and simulated separately and it resonates at multiple frequencies. Finally with MTM loading, this antenna was found to resonate at multiple frequencies with a comparatively reduced return loss, improved gain and focused radiation.

## 1. INTRODUCTION

Microstrip antennas are largely used in many wireless communication systems because of their low profile and light weight. However these antennas inherently suffer from narrow bandwidth. Multiple resonances with single patch are not readily easier without the help of array of patches [4]. Hence, the large physical size of the array is considered to be a limitation for such requirements [1]. For improving this, several investigations have been performed [2]. With the introduction of fractal shapes in antenna engineering, the multi-band resonance with single antenna has become attractive [3]. The term fractal was originally introduced by B. B. Mandalbrot and latter followed by many investigators in the field of miniaturized antenna design [5]. The co-planar wave guide feed system has been widely used for miniaturized antenna design since this transmission line can be easily integrated along with the antenna on the same substrate [6–7]. Left handed metamaterials(LHM) are the engineered structures which exhibit electromagnetic properties not found in naturally existing materials. V. G. Veselago in 1968, provided a theoretical report [8] on the concept of metamaterial(MTM). Followed by him there have been several contributions [9–14] on the existence of several metamaterial structures, use and applications of MTMs. The MTMs are artificial man-made structures which possess negative permittivity, negative permeability and negative refractive index in some frequencies of interest. There are several methods existing to verify the MTM properties of materials as found in [16]. It has been reported that the use of a LHM in near environment of patch antenna enhances antenna performances [15]. This paper presents a report on the use of a LHM as the substrate material for a fractal inspired patch antenna which uses CPW feed system. A possibility of multi-resonant property is found retained in this structure along with the existence of MTM property.

## 2. METHODS AND MATERIALS

In this section, the design methodologies are described. The general steps involved in the design are as follows: Firstly, the basic radiating (antenna) structure is chosen. As it is desired to have fractal concept, the outer contour of the patch is modified to possess fractal shape as shown in Figure 1(a). This is obtained from the basic square patch as a second iteration. The iteration method has been explained in [6] and hence not presented here. Secondly, the desired MTM structure is chosen. In this work, it is a combination of split ring resonator (SRR) and a thin conducting rod as depicted in Figure 1(b). Thirdly, as seen in Figure 1(c), the proposed antenna is loaded with the preferred MTM structure.

For the design of fractal antenna copper is used as the conducting material. A dielectric substrate of size $36 \, \text{mm} \times 36 \, \text{mm}$ made up of FR4 with relative permittivity of 4.4 and thickness of 1.6 mm is
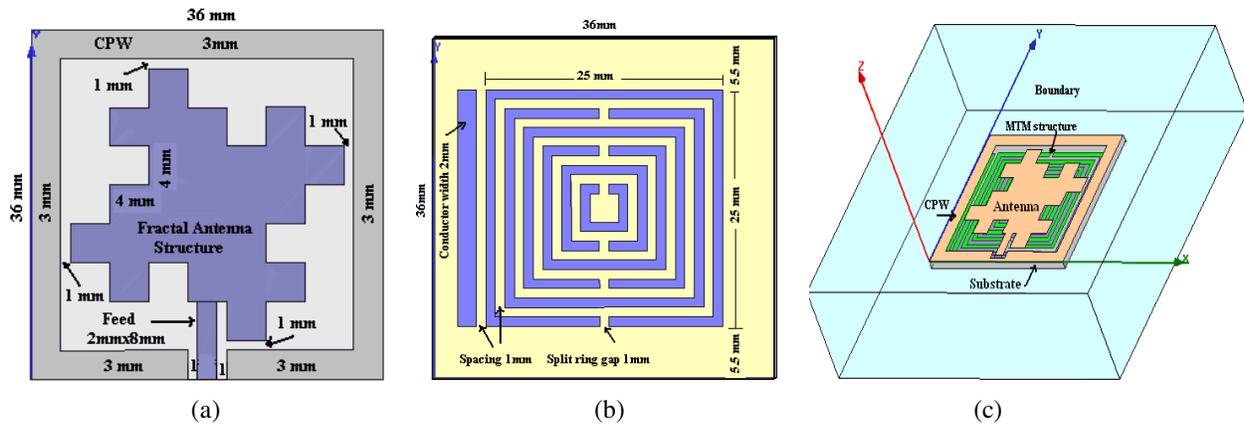
Figure 1: (a) Geometry of the proposed fractal antenna (top view). (b) MSRR with thin conductor (bottom view). (c) MTM loaded antenna with boundary enclosure.
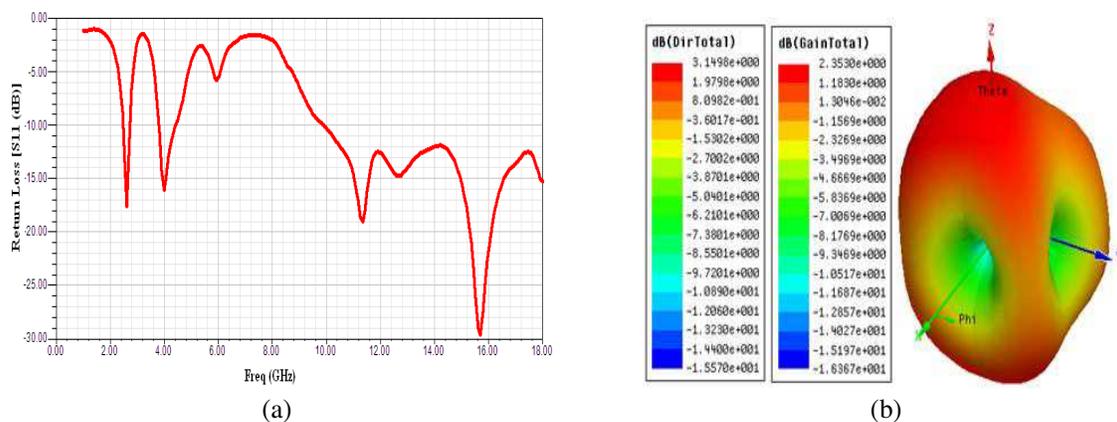


Figure 2: Performance characteristics of proposed antenna. (a) Return loss. (b) 3D radiation pattern, directivity and gain.

chosen. The preferred antenna structure is printed on this board. The dimensions are as indicated in the Figure 1. The MTM antenna consisting of a thin conductor of $2\,\text{mm} \times 25\,\text{mm}$ size and MSRR (six in this work) has been separately designed on the FR4 of the same size and property as mentioned above. The MTM property of SRR structure can be verified by any one of the four popular methods such as Nicolson-Ross-Wier (NRW), NIST iteration technique, new non-iterative technique and short circuit technique as reported in [16]. In all these methods, the $S$-parameters obtained from simulated or measurement results are required for verification. In this paper, the effective medium theory [16, 17] is used to extract the permittivity and permeability from the $S$-parameters using NRW approach as it is straight forward involving simplest equations and fewer steps. A separate MATLAB code has been developed for this and the $S_{11}$ and $S_{21}$ parameters are exported to MATLAB for determining the medium properties. The permittivity and permeability of the medium are related to $S$-parameters by the Equations (1) and (2) as given below.

$$\varepsilon_r = \frac{2}{jk_0d}\frac{1-V_1}{1+V_1} \tag{1}$$

$$\mu_r = \frac{2}{jk_0d}\frac{1-V_2}{1+V_2} \tag{2}$$

where $k_0$ is a wave number equivalent to $2\pi/\lambda_0$, $d$ is the thickness of the substrate and $V_1$ and $V_2$ are terms representing the composite of $S_{11}$ and $S_{21}$ as given in Equations (3) and (4). The term $k_0d$ is expected to be very much less than unity for meeting the condition that the antenna must be smaller in size [16, 17].

$$V_1 = S_{21} + S_{11} \tag{3}$$
$$V_2 = S_{21} - S_{11} \tag{4}$$

(a)                                                                  (b)
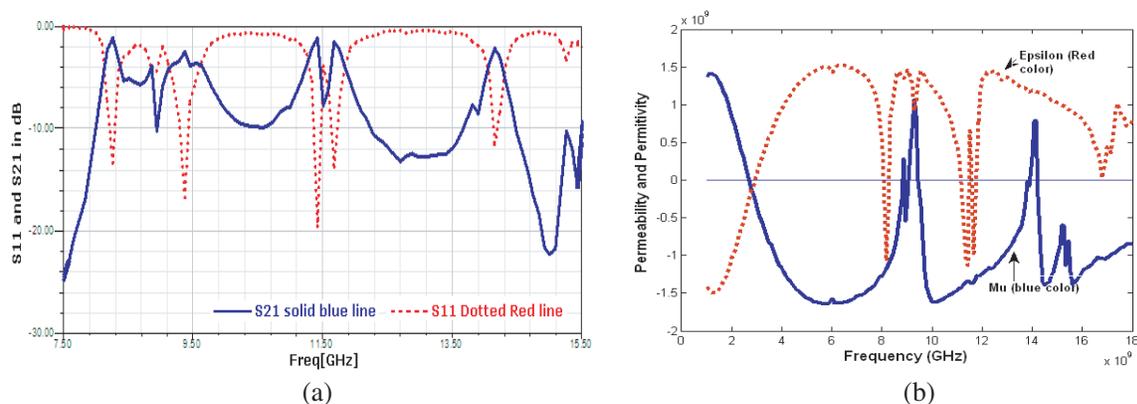
Figure 3: MSRR Performance (a) The reflection ($S_{11}$) and transmission ($S_{21}$) parameters. (b) The retrieved relative permeability and permittivity.



(a)                                                                  (b)
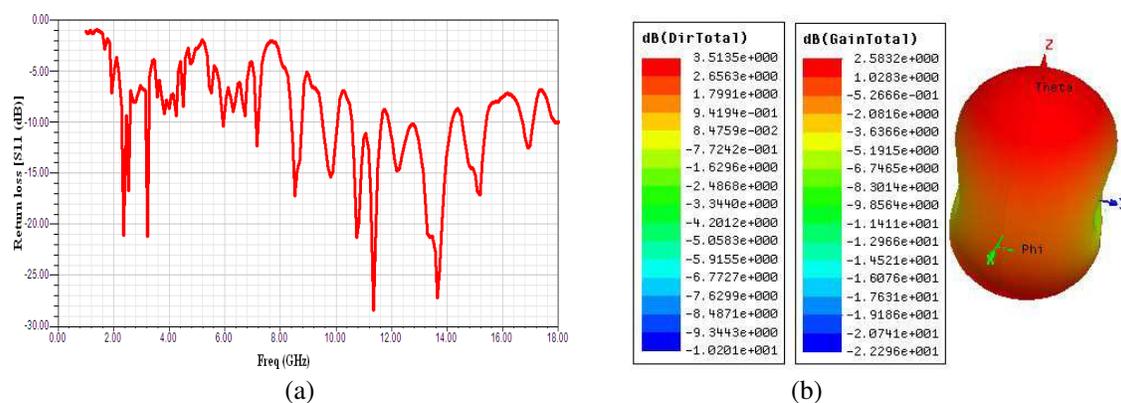
Figure 4: Performance characteristics of MTM loaded antenna. (a) Return loss. (b) 3D radiation pattern, directivity and gain.

## 3. SIMULATION

For the design and simulation of the proposed antenna, the MTM structure (for obtaining required $S$-parameters) and the MTM loaded proposed antenna, the 3D electromagnetic simulation software HFSS has been used. The simulation in all the three cases has been swept over a frequency range from 1 to 18 GHz. In the MTM simulation, the PEC has been assumed on the left and right side of $y$-axis, PMC has been assumed on the top and bottom sides of $z$-axis and port 1 and 2 are assumed on each face of the enclosed boundary in the $x$-axis.

## 4. RESULTS AND DISCUSSION

Figure 2 shows the performance of the proposed antenna. As found in Figure 2(a), the return loss characteristics of proposed antenna are $-14.74$ dB, $-12.86$ dB, $13.27$ dB, $-20.99$ dB and $-19.35$ dB for resonant frequencies of 2.62 GHz, 3.99 GHz, 11.34 GHz, 12.62 GHz and 15.69 GHz respectively. The gain is 2.35 dB and the directivity is 3.15 dB. The MSRR structure is simulated and found possessing MTM property with dominating MNG. Figure 3 indicates the reflection ($S_{11}$) and transmission ($S_{21}$) properties of the MSRR structure along with the relative permittivity and permeability characteristics as obtained from the Equations (1) and (2).

The performance characteristics of MTM loaded antenna is depicted in Figure 4. There are multi-resonant frequencies such as 2.37 GHz, 2.54 GHz, 3.22 GHz, 5.95 GHz, 7.15 GHz, 8.52 GHz, 9.8 GHz, 10.74 GHz, 11.34 GHz, 12.28 GHz, 13.64 GHz, and 15.18 GHz where the MTM structure exhibits either negative permittivity and/or permeability, thus behaving as SNG (that is, MNG or ENG or DNG) at various frequencies with reduced return loss values such as $-21.12$ dB, $-16.73$ dB, $-21.21$ dB, $-10.44$ dB, $-12.35$ dB, $-17.23$ dB, $-15.45$ dB, $-21.35$ dB, $-28.4$ dB, $-14.61$ dB, $-27.15$ dB and $-17.4$ dB respectively and improved gain (2.58 dB) and directivity (3.51 dB) with much shaped radiation pattern.

## 5. CONCLUSION

The design and simulation of fractal inspired metamaterial antenna were carried out to verify the possibility of multi-resonant behavior. The outcomes of the results are satisfactorily encouraging. The MTM loaded antenna structure also resonates at multiple frequencies with a shift in frequencies towards lower end and much reduced return loss values. The performances of the antenna in the presence of the MTM, are superior in terms of reduced return loss, improved gain and focused radiation. This is because of the presence of negative permittivity and negative permeability in the prepared metamaterial. The future work would be to experimentally verify the same properties. This type of antenna can be of use in multi-frequency wireless applications.

## ACKNOWLEDGMENT

## REFERENCES

1. Tsachtsiris, G., C. Soras, M. K. Araboikis, and V. Makios, "A reduced size fractal rectangular curve patch antenna," *IEEE*, 912–915, 2003.
2. Douglas, H. W. and S. Ganguly, "An overview of fractal antenna engineering research," *IEEE Antennas and Propagation Magazine*, Vol. 45, No. 1, 38–57, 2003.
3. Liu, Y., S.-X. Gong, and D.-M. Fu, "Microstrip fractal antenna for multi-band communication," *IEEE*, 600–602, 2002.
4. Douglas, H. W., R. L. Haupt, and P. L. Werner, "Fractal antenna engineering: The theory and design of fractal antenna arrays," *IEEE Antennas and Propagation Magazine*, Vol. 41, No. 5, 37–59, 1999.
5. Suganthi, S., S. Raghavan, and D. Kumar, "Miniature fractal antenna design and simulation for wireless applications," *IEEE RAICS*, 57–61, 2011.
6. Suganthi, S., S. Raghavan, and D. Kumar, "A novel planar square fractal antenna for wireless devices," *IEEE MRRS*, 82–85, 2011.
7. Zhu, J. and G. V. Eleftheriades, "Dual band metamaterial inspired small monopole antenna for WiFi applications," *IEEE Electronic Letters*, Vol. 45, No. 22, 2009.
8. Veselago, V. G., "The electrodynamics of substances with simultaneously negative values of $\varepsilon$ and $\mu$," *Soviet Physics Uspekhi*, Vol. 10, No. 4, 509–514, 1968.
9. Smith David, R. and N. Kroll, "Negative refractive index in left-handed materials," *Physics Review Letters*, Vol. 85, No. 14, 2933–2936, 2000.
10. Pendry, J. B., "Negative refraction," *Contemporary Physics*, Vol. 45, No. 3, 191–202, 2004.
11. Christophe, C., A. Lai, and T. Itoh, "The challenge of homogenization in metamaterials," *New Journal of Physics*, Vol. 7, No. 167, 1–15, 2005.
12. Christophe, C. and T. Itoh, "Metamaterials for high-frequency electronics," *Proceedings of the IEEE*, Vol. 93, No. 10, 1744–1752, 2005.
13. Ahmad, A. S., M. Z. M. Zani, M. H. Jusoh, N. H. Baba, R. A. Awang, and M. F. Ain, "Circular patch antenna on metamaterial," *European Journal of Scientific Research*, Vol. 45, No. 3, 391–399, 2010.
14. Cheng, Z., J.-J. Ma, L. Li, and C.-H. Liang, "Multiresonant metamaterial based on asymmetric triangular electromagnetic resonators," *IEEE Antennas and Wireless Propagation Letters*, Vol. 9, 99–102, 2010.
15. Akram, B. and J. B. H. Tahar, "Optimization of a patch antenna performances using left-handed metamaterial," *PIERS Proceedings*, 419–421, Marrakesh, Morocco, Mar. 20–23, 2011.
16. Smith, D. R., D. C. Vier, T. H. Koschny, and C. M. Soukoulis, "Electromagnetic parameter retrieval from inhomogeneous metamaterials," *Physics Review*, E71, 036617-1–11, 2005.
17. Pattnaik Shayam, S., J. G. Joshi, S. Devi, and M. R. Lohokare, "Electrically small rectangular microstrip patch antenna loaded with metamaterial," *IEEE*, 247–250, 2010.

# CPW-fed Slot Patch Antenna for 5.2/5.8 GHz WLAN Application

**Vepuri Niranjan**, **Alok Kumar Saxena**, and **Kumar Vaibhav Srivastava**

Department of Electrical Engineering, Indian Institute of Technology, Kanpur, India

**Abstract**— In microwave and millimeter wave applications, slot antennas fed by coplanar waveguide (CPW) are receiving increasing attention. In this paper, a CPW-fed patch antenna with slots is presented. The antenna consists of patch structure with two rectangular slots on it. The physical size of the proposed antenna is 30 mm × 24 mm. Antenna was designed on a polyflon polyguide substrate with dielectric constant = 2.32 and thickness of 1.59 mm. The impedance bandwidth of the proposed antenna is 4.1 GHz ranging from 4.8 GHz to 8.9 GHz and has a fractional bandwidth of 60%. The proposed CPW-fed slot patch antenna produces a 30% higher bandwidth compared to the conventional CPW-fed patch antenna. The antenna is resonating at 5.5 GHz and gives monopolar radiation pattern at this frequency. This antenna can be used in 5.2 GHz/5.8 GHz WLAN application.

## 1. INTRODUCTION

Recently, with the wireless communications, such as the wireless local area network (WLAN), having evolved at astonishing rate, it has been well known that the future communication technology pressingly demands integration of more than one communication system into a limited equipment space. This has stimulated the interest in investigation of various WLAN antennas that are low-profile, lightweight, flush mounted and single-feed, to fit in the limited equipment space of WLAN devices, and have dual or multi-frequency capabilities to satisfy the WLAN standards in the 2.4 GHz (2.4–2.484 GHz)/5.2(5.15–5.35 GHz)/5.8(5.75–5.825 GHz)-GHz operating bands. So far many antenna designs with dual band or wideband operation capabilities to satisfy the IEEE 802.11 standards have been developed and presented [1–4]. Among these antennas, coplanar waveguide (CPW)-fed antennas has become very popular owing to its many attractive features such as wider bandwidth, low radiation loss, a simple structure of a single metallic layer and easy integration with WLAN integrated circuits [5–7].

In this paper, we propose a CPW-fed slot patch antenna with wideband operation suitable for the use in the 5.2/5.8 GHz wireless local network (WLAN) applications. The geometry parameters of the antenna including the patch dimensions, the size of the coplanar ground planes, and the space between the ground planes and the patch, the slots width are all optimized using Ansoft HFSS to achieve good wideband operation. Details of the antenna design are described, and simulation results and radiation characteristics of the proposed antenna are presented.

## 2. ANTENNA DESIGN

Figure 1 shows the geometrical configuration of the proposed CPW-fed slot patch antenna for wideband operation. The antenna designed here has a single layer metallic structure and is etched on a side of an inexpensive polyflon polyguide substrate with a dielectric constant of 2.32 and thickness of 1.59 mm, whereas the other side is without any metallization. A 50 Ω CPW transmission line is used for feeding the antenna which consists of a signal strip thickness of $W_c$ and a gap distance of s between the signal strip and the coplanar ground plane. The basis of the antenna is a rectangular patch with dimensions $L_p$ and $W_p$ which is centered and connected at the end of the CPW feed line. To achieve the wideband operation, the patch is embedded with a two rectangular slots with the width 'c' as shown in the figure. By using the slot inside the patch, a new resonator will be excited whose resonant frequency is higher than the patch resonant frequency. Since we have included two slots, three resonators will be excited when combined gives a wideband response.

To investigate the performance of the proposed antenna configuration in terms of achieving wideband operation, a commercially available Ansoft HFSS was used for the required analysis and to obtain the proper geometrical parameters as shown in the figure below.

## 3. RESULTS AND DISCUSSION

The simulated return loss against frequency for the proposed CPW-fed slot patch antenna was shown in Fig. 2. The antenna achieves a −10 dB impedance bandwidth of 60.3% ranging from 4.8 GHz to 8.9 GHz, with respect to the central frequency at 6.8 GHz. So, the antenna can operate

over the bands which cover the required bandwidths of the IEEE 802.11 WLAN standards in the bands at 5.2 GHz and 5.8 GHz. By comparing the proposed antenna return loss with that of CPW-fed patch antenna without slots [8], this antenna produces 30% higher bandwidth and the resonant frequency is decreased from 6.5 GHz to 5.5 GHz.
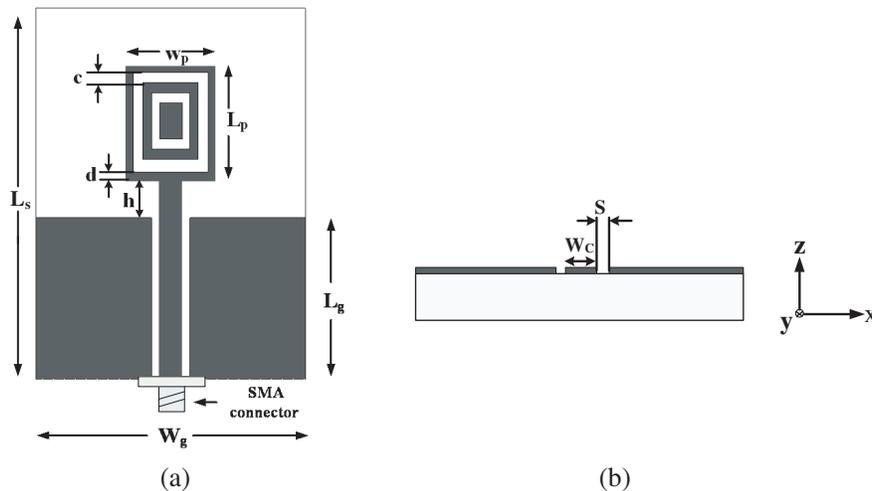


Figure 1: Geometrical configuration of proposed CPW-fed slot patch antenna. (a) Top view. (b) Side view. $L_s = 24$ mm, ($W_g = 30$ mm, $L_g = 15$ mm, $W_c = 1.55$ mm, $W_p = 6$ mm, $L_p = 7$ mm, $s = 0.2$ mm, $c = 0.6$ mm, $d = 0.3$ mm, $h = 0.7$ mm).
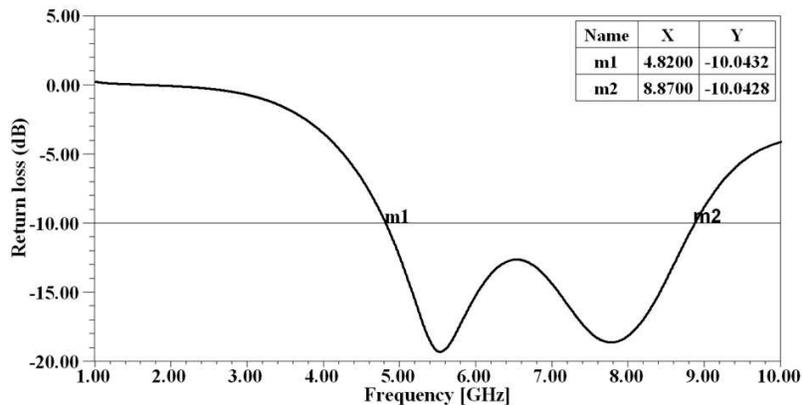


Figure 2: Simulated return-loss characteristics of the CPW-fed slot patch antenna.
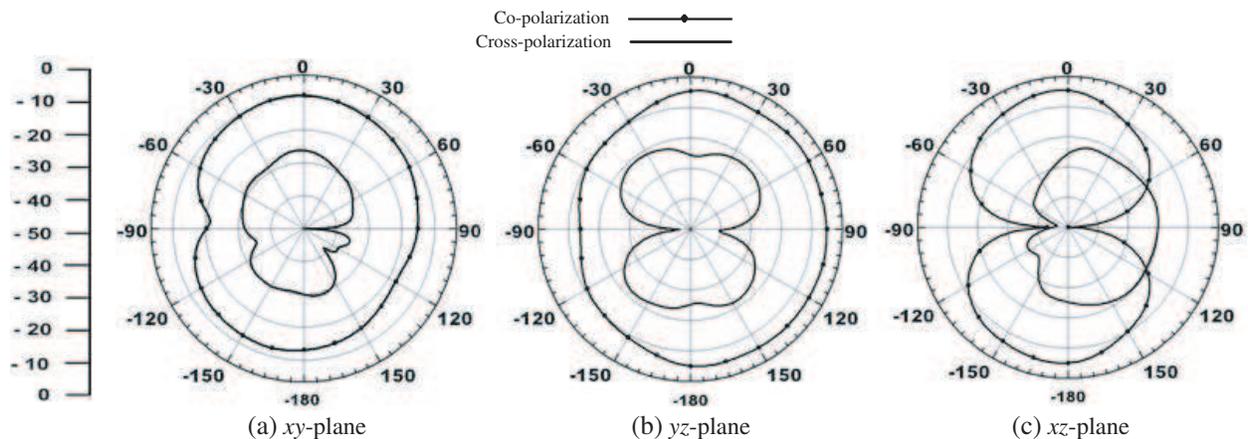


Figure 3: Simulated radiation patterns of CPW-fed slot patch antenna at 5.5 GHz. (a) $xy$-plane, (b) $yz$-plane, (c) $xz$-plane.
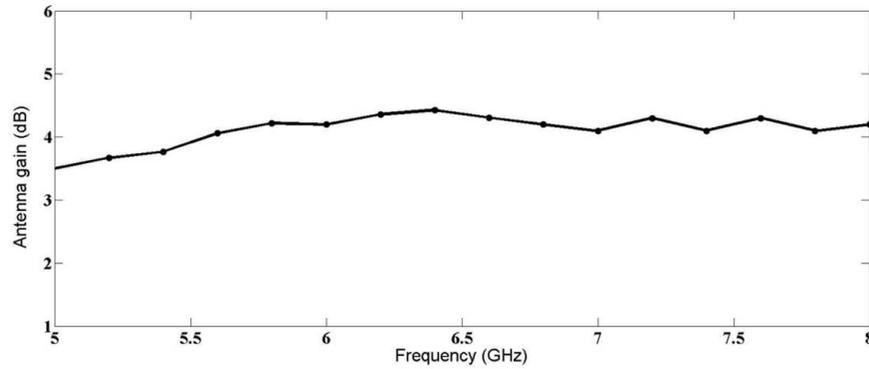
Figure 4: Simulated peak antenna gain for frequencies across the band (5 GHz–8 GHz) for the proposed antenna.

Radiation characteristics of the proposed antenna are also examined. Fig. 3 plots the radiation patterns in the elevation direction ($x$-$z$ and $y$-$z$ planes) and azimuthal direction($x$-$y$ plane) at 5.5 GHz of the proposed antenna. From the figure we can observe the general radiation like patterns in $x$-$z$ and $y$-$z$ planes and nearly omnidirectional pattern in the $x$-$y$ plane are observed. The peak gain of the antenna is 3.8 dBi at the resonant frequency and the radiation efficiency is found to be 91%.

Finally, the antenna gain against frequency for the proposed antenna across the band is shown in Fig. 4. For the whole band, the antenna gain is within the range of 3.4–4.4 dBi.

## 4. CONCLUSION

A CPW-fed patch antenna with two rectangular slots for wideband operation has been successfully designed and simulated. With the insertion of the slots into the patch, the proposed antenna can provide a large bandwidth with the same dimensions and suitable radiation characteristics to be applied in 5.2/5.8 GHz WLAN systems.

## ACKNOWLEDGMENT

## REFERENCES

1. Teng, P.-L., H.-T. Chen, and K.-L. Wong, "Compact wideband planar monopole antenna," *Microw. Opt. Technol. Lett.*, Vol. 36, No. 5, March 2003.
2. Kuo, Y.-L. and K.-L. Wong, "Printed double-T monopole antenna for 2.4/5.2 GHz dual-band WLAN operations," *IEEE Trans. Antennas Propagation*, Vol. 51, No. 9, September 2003.
3. Chen, H.-D., J.-S. Chen, and Y.-T. Cheng, "Modified inverted-L monopole antenna for 2.4/5.2 GHz dual-band operations," *Electronic Letters*, Vol. 39, No. 22, October 2003.
4. Chung, K., T. Yun, and J. Choi, "Wideband CPW-fed monopole antenna with parasitic elements and slots," *Electronic Letters*, Vol. 40, No. 27, August 2004.
5. Deng, S.-M., M.-D. Wu, and P. Hsu, "Analysis of coplanar waveguide-fed microstrip antennas," *IEEE Trans. Antennas Propagation*, Vol. 43, 734–737, July 1995.
6. Giauffret, L. and J.-M. Laheurte, "Theoretical and expiremental characterisation of CPW-fed microstrip antennas," *IEEE Proc. — Microw. Antennas Propag.*, Vol. 143, No. 1, February 1996.
7. Liu, W.-C. and C.-M. Wu, "Broadband dual-frequency CPW-fed planar monopole antenna with rectangular notch," *Electronic Letters*, Vol. 40, No. 11, May 27, 2004.
8. Antoniades, M. A. and G. V. Eleftheriades, "A broadband dual-mode monopole antenna using NRI-TL metamaterialLoading," *IEEE Antennas and Wireless Propagation Letters*, Vol. 8, 2009.

# Method of Moments Analysis for Antenna Arrays with Optimum Memory and Time Consumption

**Kamel S. Sultan**, **Haythem H. Abdullah**, and **Esmat A. Abdallah**

Electronics Research Institute, Dokki, Giza, Egypt

**Abstract**— For some applications, single element antennas are unable to meet the gain or radiation pattern requirements. Combining several antenna elements in an array is a possible solution. In order to get accurate analysis of the antenna arrays, full wave analysis techniques such as the method of moments (MoM), the finite difference time domain (FDTD), etc are required. Unfortunately, these methods are heavy computational methods that consume long time and large computational resources. Even with the appearance of the high performance parallel processing resources, the computational time and memory usage still large due to the nature of the problem. So, in this paper, the MoM is chosen to analyze large problems such as antenna arrays taking into consideration the reduction of its needed computational resources and time consuming. The MoM is a well-established and an accurate full wave analysis method. The MoM is applied to solve the electric field integral equation (EFIE) on conducting objects with the use of RWG basis function that is used with triangular segmentation of the scatterer surface. The proposed procedure is to decompose the computational domain into subdomains taking interaction between domains iterativly until steady state is noticed. The proposed procedure minimizes the time and memory consumption greatly.

## 1. INTRODUCTION

The MoM for discretizing integral equations in electromagnetics is an extremely powerful and versatile general numerical methodology for electromagnetic field simulation in antenna and scattering applications [1]. However, traditional MoM analysis is inherently limited to electrically small and moderately large electromagnetic structures, because its computation costs (in terms of memory and CPU time) increase rapidly with an increase in electrical size of the problem. Since that time computer technology has grown at a staggering pace, and computational electromagnetics and the moment method have followed closely behind [2]. The domain decomposition method (DDM) [3–11] is one of the most successful approaches to the Method of Moments (MoM) analysis of large scattering and antenna problems. The idea behind the DDM is to decompose the whole computational domain into small sub-domains with some prescribed partition boundary conditions. Such a procedure divides large electromagnetic problems to small sub-domain problems, transform complex boundary conditions to simple ones, and presents an effective means to break through the bottleneck of memory storage. At the same time, a highly parallelizable computation structure is achieved. The key point of the DDM is the enforcement of boundary conditions on subdomain interfaces. There are usually two DDM approaches: one is the approach of [4–8] based on the Schwarz alternating method, which ensures coupling between the adjacent elements by the transmission condition (TC) [9] and proceeds with iterative solution until convergence is achieved by changing data interfaces between subdomains. Another one is the direct method using Steklov technique [12–14], which imposes the continuity of the fields on the partition interfaces and generates a global coupling matrix. The solution of this matrix produces the unknown tangential fields on the partition interfaces. In this paper, the problem of antenna array is treated since the array elements is already separated and does not need boundary conditions between domains. The separation between array elements are exploited by dividing the array into separate elements each analazyed separately. The mutual coupling between elements are taken into consideration by taking the scattered field from the adjacent elements as incident wave on the current analyzed element. By repeating the analysis several times until steady state is observed, the coupling between elements is considered to be taken into consideration accurately. So, the problem of time and memory consumption will be solved for large extent.

## 2. FORMULATION

Let $S$ denote the surface of an open or closed perfectly conducting scatterer. An electric field, defined to be the field due to an impressed source in the absence of the scatterer, is incident on and induces surface currents $J$ on $S$. If $S$ is open, $J$ is regarded as the vector sum of the surface
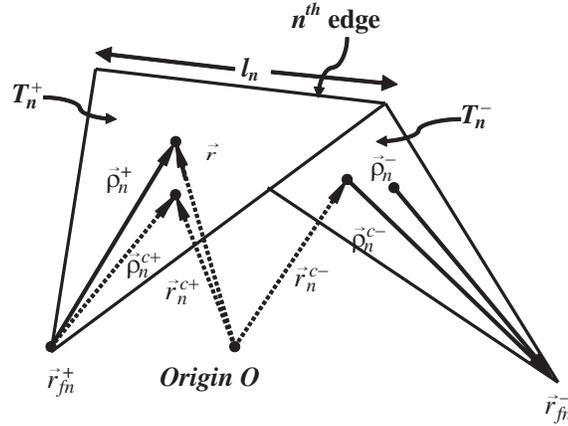
Figure 1: Triangular pair and geometrical parameters associated with interior edges.

currents on opposite sides of $S$; hence the normal component of $J$ must vanish on boundaries of $S$ [15]. To solve for the current distribution on the scatterer surface, one needs to discretize the current on the conductor surface. The best method to do that is by using the triangular patches to model the surface of the scatterer. The choice of the triangular patches is due to the fact that it is capable of accurately conforming to any geometric surface or boundary. Figure 1 shows two triangular patches $T_n^+$ and $T_n^-$ sharing one edge. Points in $T_n^+$ may be designated either by the position vector $\vec{r}$ defined with respect to the origin 0, or by the position vector $\rho_n^+$ defined with respect to the free vertex of $T_n^+$. The points in $T_n^-$ can be defined by the position vector $\rho_n^-$ which is directed toward the free vertex of $T_n^-$. The plus or minus designation of the triangles is determined by the choice of a positive current reference direction for the $n$th edge, the reference for which is assumed to be from $T_n^-$ to $T_n^+$. The position vector from the origin to the centroid of the patch $T_n^\pm$ is designated by $\vec{r}_m^{c\pm}$. $\vec{r}_{fn}^+$, and $\vec{r}_{fn}^-$ are the positive and the negative triangle vertices opposite to the shared edge.

After detailed study of the literature, one can recast the problem into a problem of solving linear system of equations in the form

$$[Z_{mn}][I_n] = [V_m] \tag{1}$$

where

$$Z_{mn} = l_m l_n \left( \frac{j\omega\mu}{4\pi} \alpha_{mn} + \frac{1}{j\omega\pi\varepsilon} \beta_{mn} \right) \tag{2}$$

$$\alpha_{mn} = \alpha_{m^+n^+} + \alpha_{m^+n^-} + \alpha_{m^-n^+} + \alpha_{m^-n^-} \tag{3}$$

$$\beta_{mn} = \beta_{m^+n^+} + \beta_{m^+n^-} + \beta_{m^-n^+} + \beta_{m^-n^-} \tag{4}$$

$$\alpha_{m^\pm n^\pm} = \frac{1}{4A_{n^\pm}} \left( \int_{P_{n^\pm}} G_m^{c\pm}\left(\vec{r}\right) \vec{\rho}_n^\pm d\acute{S} \right) \cdot \vec{\rho}_m^\pm \tag{5}$$

$$\beta_{m^\pm n^\pm} = \frac{(s_{m^\pm})(s_{n^\pm})}{4A_{n^\pm}} \left( \int_{P_{n^\pm}} G_m^{c\pm}\left(\vec{r}\right) d\acute{S} \right) \tag{6}$$

where

$$s_m = \begin{cases} +1, & m = m^+ \\ -1, & m = m^- \end{cases}, \quad s_n = \begin{cases} +1, & n = n^+ \\ -1, & n = n^- \end{cases}, \quad \text{and} \quad G_m^{c\pm}(\acute{r}) = \frac{e^{-jk\left|\vec{r}_m^{c\pm} - \vec{r}\right|}}{\left|\vec{r}_m^{c\pm} - \vec{r}\right|} \tag{7}$$

$$V_m = \frac{l_m}{2} \left( \vec{E}^i\left(\vec{r}_m^{c+}\right) \cdot \vec{\rho}_m^{c+} + \vec{E}^i\left(\vec{r}_m^{c-}\right) \cdot \vec{\rho}_m^{c-} \right)$$

Note that, the plus or minus signs over $m$ refers to the positive or negative observation patches respectively, while that over $n$ refers to the source positive or negative patches, respectively. After solving the linear system of equations the scattered field is straight forward calculated.

Consider $N$ element array synthesis using the MoM and assume that $M$ discretization segments per array element are used. By applying the DDM in order to take the mutual coupling between the array elements into consideration [10]; it is required to have a $[Z]$ matrix with $(M \times N) \times (M \times N)$ elements. But in fact, the mutual coupling between array elements decreases with the increase of the distance between elements, e.g., the base station antenna arrays. In this paper, the solution domain is decomposed into $N$ domains, one for each array element. Since the incident wave is the field that exists in the absence of the scatterer, each element will be analyzed using its own excitation in conjunction with the scattered waves from the preceding analyzed element.

The analysis of all elements will be repeated for each element from two to three times according to the distance between elements until steady state solution is reached. In this way the memory requirement will be $M \times (N \times N) \times 3$ at maximum which is efficient when the number of elements $M$ exceeds three. By reducing the $[Z]$ matrix, not only its computational time will be reduced but also the computational time of the inverse matrix will also be reduced.

## 3. RESULTS AND DISCUSSIONS

In this section numerical results are presented for surface current distributions induced on an array of 5 flat plates $0.15\lambda$ distance apart illuminated by plane wave normally incident on the plates surfaces. Figure 2 shows two of the 5 elements of the array as a sample of the most critical elements which affected greatly with coupling. Each square plate has the dimension of $(0.15\lambda \times 0.15\lambda)$. Figure 3 shows the current induced on each plate at $BB'$. It is noted that the current distribution reaches the steady state after the third iteration only.
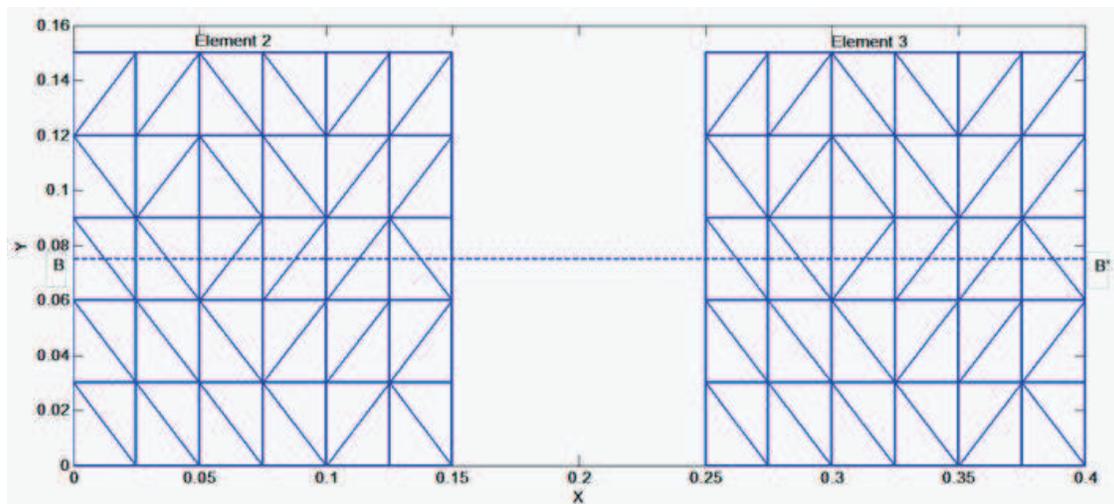


Figure 2: Two squares of $0.15\lambda \times 05\lambda$ each separated by a distance of $\lambda/10$.
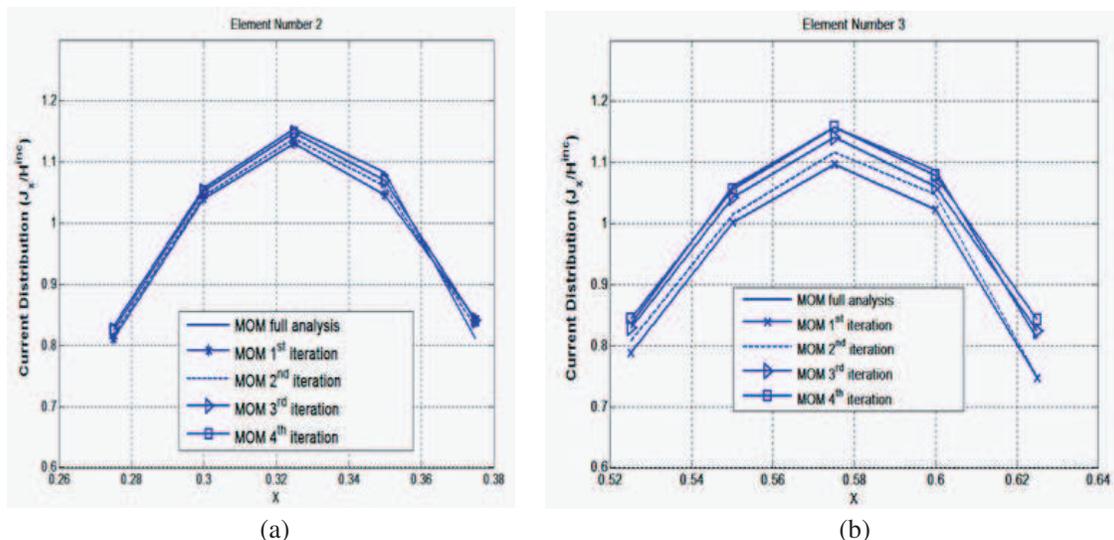


Figure 3: (a) Current distribution on element number 2. (b) Current distribution on element number 3.

## 4. CONCLUSIONS

The domain decomposition of the method of moments for arbitrarily shaped conducting object was introduced. The application of the proposed procedure was applied to a 5 element array of flat plates illuminated by a normally incident plane wave. the convergence was reached after only three iterations which needs only $5 \times M \times M \times 3$ instead of $(5 \times M) \times (5 \times M)$ or 71114 memory locations instead of 119025 memory locations. It is worth to mention that the saving in memory will be more evedent with the large number of array elements.

## ACKNOWLEDGMENT

## REFERENCES

1. Harrington, R. F., "Field computation by moment methods," *IEEE Series on Electromagnetic Waves*, New York, 1993.
2. Djordjevic, M. and B. M. Notaros, "Higher order hybrid method of moments-physical optics modeling technique for radiation and scattering from large perfectly conducting surfaces," *IEEE Trans. Antennas Propag.*, Vol. 53, No. 2, 800–813, Feb. 2005.
3. Martini, E., G. Carli, and S. Maci, "A domain decomposition method based on a generalized scattering matrix formalism and a complex source expansion," *Progress In Electromagnetics Research B*, Vol. 19, 445–473, 2010.
4. Despres, B., "Domain decomposition method and the Helmholtz problem," *Proc. Int. Symp. Mathemat. Numerical Aspects Wave Propagat. Phenomena*, 44–52, Strasbourg, France, 1992.
5. Stupfel, B, "A fast-domain decomposition method for the solution of electromagnetic scattering by large objects," *IEEE Trans. Antennas Propag.*, Vol. 44, No. 10, 1375–1385, Oct. 1996.
6. Gander, M. J., "Optimized Schwarz method for Helmholtz problems," *Proce. 13th Int. Conf.*, 245–252, Domain Decomposition, 2001.
7. Stupfel, B. and M. Mognot, "A domain decomposition method for the vector wave equation," *IEEE Trans. Antennas Propag.*, Vol. 48, No. 5, 653–660, May 2000.
8. Thiele, G. A., "Overview of selected hybrid methods in radiating system analysis," *Proc. IEEE*, Vol. 80, No. 1, 66–78, Jan. 1992.
9. Duan, Y., S.-J. Lai, and T. Huang, "Coupling projection domain decomposition method and meshless collocation method using radial basis functions in electromagnetics," *Progress In Electromagnetics Research Letters*, Vol. 5, 1–12, 2008.
10. Barka, A. and P. Caudrillier, "Domain decomposition method based on generalized scattering matrix for installed performance of antennas on aircraft," *IEEE Trans. Antennas and Proagp.*, Vol. 55, No. 6, 1833–1842, Jun. 2007.
11. Hodges, R. E. and Y. Rahmat-Samii, "An iterative current-based hybrid method for complex structures," *IEEE Trans. Antennas Propag.*, Vol. 45, No. 2, 265–276, Feb. 1997.
12. Choi-Grogan, Y. S., K. Eswar, P. Sadayappan, and R. Lee, "Sequential and parallel implementations of the partitioning finite-element method," *IEEE Trans. Antennas Propag.*, Vol. 44, No. 12, 1609–1616, Dec. 1996.
13. Wolfe, C. T., U. Navsariwala, and S. D. Gedney, "A parallel finite-element tearing and interconnecting algorithm for solution of the vector wave equation with PML absorbing medium," *IEEE Trans. Antennas Propag.*, Vol. 48, No. 2, 278–283, Feb. 2000.
14. Cangellaris, A. C. and R. Lee, "The bymoment methods for two-dimensional electromagnetic scattering," *IEEE Trans. Antennas Propag.*, Vol. 38, No. 9, 1429–1437, Sep. 1990.
15. Rao, S. M. and D. R. Wilton, "Electromagnetic scattering by surfaces of arbitrary shape," *IEEE Trans. Antennas Propag.*, Vol. 30, No. 3, 409–418, May 1982.

# Frequency Sensitivity of Lossless Planar Devices by FEM

**A. Kiaee**, **R. Sarraf Shirazi**, and **S. R. Hosseini**

Department of Electrical Engineering, Amirkabir University of technology, Tehran, Iran

**Abstract**— In this paper numerical calculation of frequency sensitivity of a planar device using finite element is presented. The finite element method has been shown to be an efficient and flexible way of computing the equivalent circuit parameters of N-port planar devices (microstrip, stripline, rectangular waveguide, etc.). In addition it can provide at little extra cost the sensitivity of admittance parameters to change in operating frequency. This way, frequency sensitivity of the equivalent circuit parameters can be found by two dimensional finite element method. This approach has been implemented by triangular finite elements and the sensitivity was computed for microstrip bend: the agreement with previously published result was excellent.

## 1. INTRODUCTION

In this paper we describe how Foster reaction theorem and finite element can be used to calculate $Y$ parameter frequency sensitivity of a planar device using data of a single simulation and at a little extra computational cost

A planar device can be defined as one in which electromagnetic fields do not vary significantly in one dimension [1, 2] so that the simulation can be carried out in a plane. Rectangular waveguide at dominant mode is an example of perfect planar device. After introduction of magnetic wave guide model for analysis of microstrip structures [3] these classes of microwave structures were added in planar devices by using equivalent relative permittivity, width and magnetic walls at two side ends [3, 4].

Determining frequency sensitivity can be help full in determining broadband calculation of circuit parameters since in each simulation beside the circuit parameters their sensitivity relative to frequency gets calculated. In resonant structures calculating frequency sensitivity due to change in structure parameter can be very useful for tuning bandwidth.

## 2. THEORY

Because our goal is to calculate the frequency sensitivity of planar device we first begin by defining equivalent circuit parameters and planar device.

We assume $e_i$ and $h_i$ are tangential electric and magnetic field at port $i$ due to the dominant mode wave incident on port $i$, when this wave carries unit real power to the port.

In general tangential electric and magnetic field on ports are

$$E_t = V_i e_i \tag{1}$$
$$H_t = I_i h_i \tag{2}$$

which gives voltage and current definitions.

It can be shown that the admittances we compute are normalized to wave impedance of the guide [2].

We assume fields do not vary significantly in $y$ dimension so the electric field can be represented as

$$E = E(x, z) a_y \tag{3}$$

where $a_y$ is a unit vector in $y$ dimension.

Substituting Equations (1)–(3) in electric field the vector wave equation

$$\nabla \times \nabla \times E - k^2 E = 0 \tag{4}$$

it simplifies to simple 2-D scalar wave equation

$$\begin{aligned}
\nabla_t^2 E + k^2 E &= 0 \quad \text{on} \quad \Omega \\
E &= E_0 \quad \text{on} \quad \partial\Omega_{D1} \\
E &= 0 \quad \text{on} \quad \partial\Omega_{D2} \\
\frac{\partial E}{\partial n} &= 0 \quad \text{on} \quad \partial\Omega
\end{aligned} \tag{5}$$

where $\Omega$ is area of the device, $\partial\Omega_{D1}$ is Dirichlet excitation interface, $\partial\Omega_{D2}$ is electric wall, $\partial\Omega_N$ is magnetic wall and $E_0$ equals prescribed value of electric field due to unit power.

It has been shown that solving the Equation (5) is equivalent to solving the following variation problem [5].

$$
\begin{cases}
\partial F(E) = 0 \\
E = 0 \quad\quad \text{on} \quad \partial D2 \\
E = E_0 \quad\quad \text{on} \quad \partial D1
\end{cases}
\tag{6}
$$

where

$$
F(E) = \frac{1}{2}\int_{\Omega} \{(\nabla_t E)^2 - k_0^2\varepsilon_r E^2\}d\Omega
\tag{7}
$$

Using triangular elements it reduces to the following equation

$$
F = \frac{1}{2}[E]^T([S] - k_0^2[T])[E]
\tag{8}
$$

where $[S]$ and $[T]$ are well-known finite element global matrices [5, 6]. After applying Dirichlet boundary condition it reduces to the form of $[A] \cdot [E] = [B]$. Solving the preceding equation yields electric field on device.

It has been shown that $Y$ parameters of the device can be calculated by [2]

$$
[Y_{mn}] = \frac{-jb}{k_0\eta_0}\int_{\Omega} \left\{\nabla_t E^{(m)} \cdot \nabla_t E^{(n)} - k_0^2\varepsilon_r E^{(m)} E^{(n)}\right\} d\Omega
\tag{9}
$$

where

　　$m$, $n$ port numbers,
　　$b$ dimension of structure in $y$ direction,
　　$\eta_0$ intrinsic impedance of free space,
　　$[Y_{mn}]$ Normalized admittance matrix,
　　$E^{(k)}$ Electric field when there is normalized voltage on port $k$ and all other ports are short-circuited.

In this paper we show how the same data can be used to also calculate frequency sensitivity of $Y$ parameters

In [7] it has been shown by the means of foster theory of reaction that susceptance sensitivity of a lossless device with respect to angular frequency can be calculated as

$$
\frac{\partial B}{\partial \omega} = \frac{4(W_m + W_e)}{VV*}
\tag{10}
$$

where $W_e$ and $W_m$ are average electric and magnetic energy respectively.

If we substitute the planar electric field from Equations (1)–(3) it reduces to

$$
[S_{mn}] = \frac{-jb}{k_0\eta_0\omega_0}\int_{\Omega} \left\{\nabla_t E^{(m)} \cdot \nabla_t E^{(n)} + k_0^2\varepsilon_r E^{(m)} E^{(n)}\right\} d\Omega
\tag{11}
$$

where

　　$m$, $n$ port numbers,
　　$b$ dimension of structure in $y$ direction,
　　$\eta_0$ intrinsic impedance of free space,
　　$[S_{mn}]$ Normalized admittance sensitivity matrix,
　　$E^{(k)}$ Electric field when there is normalized voltage on port $k$ and all other ports are short-circuited.

Using triangular elements it reduces to

$$
[S_{mn}] = \frac{-jb}{k_0\eta_0\omega_0}[E]^T([S] + k_0^2[T])[E]
\tag{12}
$$

where $[S]$ and $[T]$ are well-known global matrices [5, 6].

By means of Equation (12) using the same data from simulation sensitivity of network parameters get calculated in addition to network parameters themselves.

### 3. RESULTS

A computer program has been written to implement above numerical method single examples has been selected to verify the method in each case numerical results are compared to theoretical or experimental results.

### 3.1. Uniform Air-filled Parallel Microstrip Ring

It has been shown that dynamic properties of microstrip transmission lines can be approximated by planar waveguide model [3, 4] by considering an effective dielectric constant [8] and width.
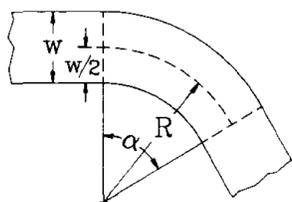
Figure 1: Microstrip ring.
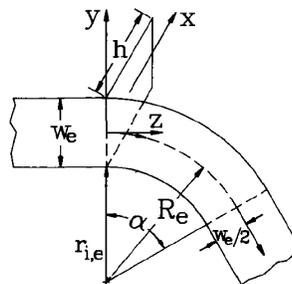
Figure 2: Microstrip ring equivalent planar waveguide model.
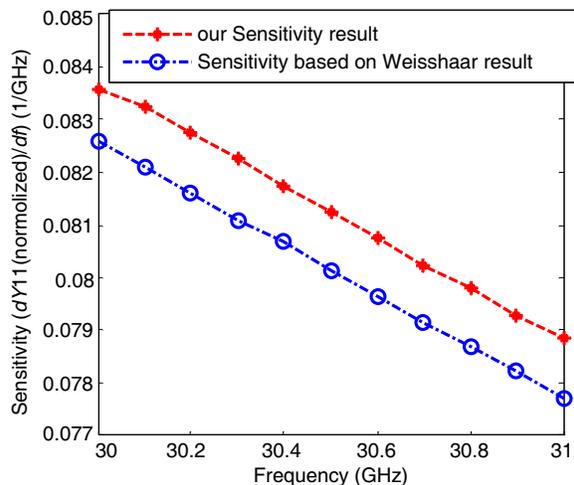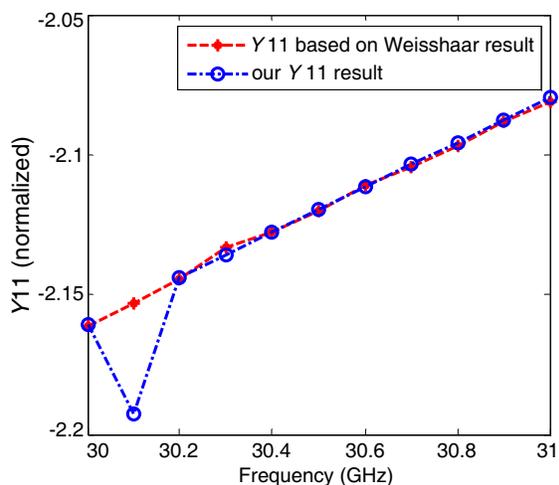
Figure 3: $Y_{11}$ and its frequency sensitivity of microstrip bend using our method and the same data obtained from weeshar paper.
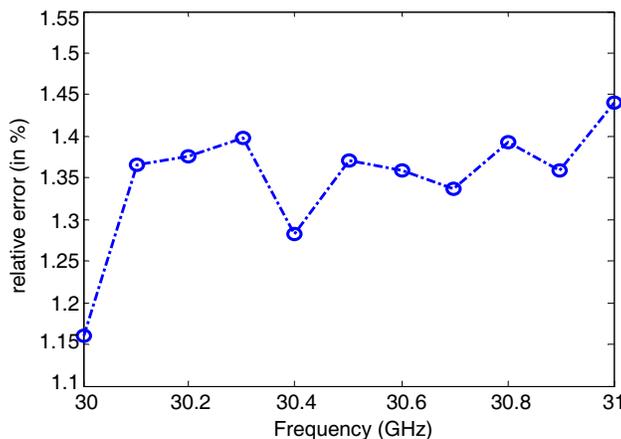
Figure 4: Relative error between Sensitivity based on Weisshaar result and our sensitivity result.

Weisshaar et al. using this method and considering effective radius have modeled microstrip ring and calculated scattering parameters of it [9].

In this paper using waveguide model, circuit parameters have calculated and compared to results which are obtained using data reported in [9].

In Figs. 1–2, $\alpha = 90°$, $W$, $W_e$, $R$ and $R_e$ are line width, effective line width, line curvature radius and effective line curvature radius, respectively.

## 4. CONCLUSIONS

It has been shown simulation data not only can be used for circuit parameters extraction, but also can be used in achieving frequency sensitivity. Frequency sensitivity can be lead to structure shape optimization.

## ACKNOWLEDGMENT

## REFERENCES

1. Garcia, P. and J. P. Webb, "Optimization of planar devices by the finite element method," *IEEE Transactions on Microwave Theory and Techniques*, Vol. 38, No. 1, Jan. 1990.
2. Webb, J. P. and S. Parihar, "Finite element analysis of $H$-plane rectangular waveguide problems," *Proc. Inst. Elec. Eng.*, Vol. 133, Pt. H, 103–109, Jan. 1986.
3. Kompa, G. and R. Mehran, "Planar waveguide model for calculating microstrip componenets," *Electron. Lett.*, Vol. 11, 459–460, 1975.
4. Gupta, K. C., R. Grag, and I. J. Bahl, *Microstrip Lines and Slotlines*, Artech House, Norwood, MA, 1979.
5. Jin, J.-M., *The Finite Element Method in Electromagnetics*, Wiley, 2002.
6. Sadiku, M. N. O., *Numerical Techniques in Electromagnetics*, CRC Press, 2000.
7. Collin, R. E., *Foundations for Microwuve Engineering*, 147, McGraw-Hill, New York, 1966.
8. Kirschning, M., R. H. Jansen, and N. H. L. Koster, "Measurement and computer-aided modeling of microstrip discontinuities by an improved resonator method," *IEEE MTT-S Int. Microwave Symp. Dig.*, 495–497, 1983.
9. Weisshaar, A. and V. K. Tripathi, "Perturbation analysis and modeling of curved microstrip bends," *IEEE Transactions on Microwave Theory and Techniques*, Vol. 38, No. 10, Oct. 1990.

# Classification of Multi-rate CDMA Signals Using Compressed Cyclostationary Features

**Said E. El Khamy**[1], **Amr El Helw**[2], **and Azza Mahdy**[2]

[1]Department of Electrical Engineering, Faculty of Engineering
Alexandria University, Alexandria, Egypt
[2]Department of Communication & Electronics Engineering
Arab Academy for Science and Technology and Maritime Transport, Cairo, Egypt

**Abstract**— The cyclostationarity property of wideband spread spectrum signals is of a great importance in signals identification and classification. This paper is aimed to the classification of 3G CDMA signals with multiple values of processing gain to serve multimedia signals of different data rates. Our studies show that the cyclostationary features of the CDMA signals become completely different as the processing gain is changed. In particular it is found that the number of the generated peaks in the cyclic spectra increases as the processing gain increases. This increase affects the classification performance. A neural network classifier is used to distinguish between CDMA signals with Phase Shift Keying modulation that are spread using different processing gains. The cyclostationary features are compressed using the wavelet transform. Percentage of successful classification was calculated using 10-folds cross validation.

## 1. INTRODUCTION

The Cognitive Radio technology aims to use the available radio resources efficiently in order to face the transmission challenges introduced by the increasing quality of service requirements of users [1]. There are three major tasks of cognitive radio which includes spectrum sensing analysis, channel identification, and transmit and power control. Channel identification predicts the channel status and acquires the information needed by the receiver for detection. Transmission power control chooses the appropriate transmission power levels to allow secondary user occupation based on channel state information. Many spectrum sensing techniques were introduced such as matched filter detection, energy detection, and cyclostationary feature detection. A matched filter signal detector requires the knowledge of data for coherent detection which is so difficult to achieve. Energy detection determines a spectrum hole or an occupied band without the knowledge of the occupying signal type [2]. It is only appropriate for high signal-to-noise ratio scenarios, whereas cyclostaionary features detection is used to solve weak signal detection problems by exploiting the cyclic properties presented in modulated or coded signals. This makes classification of signals became clear and adequate. Previous work in this area has been covered in many researches. The theoretical foundation of cyclostationary random processes had been covered by William A. Gardner in [3]. Detection of unknown signal in AWGN channel using spectral correlation had been discussed in [4]. Classification of digital signals in fading channel using cyclostationary properties of digital modulated signals had been studied in [5–7] using second order and higher order statistics. In this paper, we studied the effect of increasing the processing gain in a wide band spread spectrum signal on the number of peaks present in the cyclic spectra. Classification of two spread BPSK signals with different processing gain has been performed by neural network after compressing the cyclic features using wavelet transform. This paper is organized as follows. Section 2 covers an overview on some theoretical backgrounds on cyclostationarity and spread spectrum. The proposed technique is introduced in Section 3. Simulation results and conclusions are drawn in Sections 4 and 5 respectively.

## 2. OVERVIEW ON THEORITICAL BACKGROUND

### 2.1. Cyclostationarity

Cyclostaionary properties characterize special types of random processes for which the signal characteristics are periodically time-variant [3]. It means that the statistical mean and autocorrelation vary with time periodically. The autocorrelation function of a cyclostationary signal is defined as:

$$R_x \left( t + T + \frac{\tau}{2}, t + T - \frac{\tau}{2} \right) = R_x \left( t + \frac{\tau}{2}, t - \frac{\tau}{2} \right) \tag{1}$$

where $t$ and $\tau$ are two independent random variables. Equation (1) shows that the autocorrelation is periodic with a period $T$ for each value of $\tau$ [3]. Accordingly, we can use Fourier Series Expansion to represent (1):

$$R_x\left(t + \frac{\tau}{2}, t - \frac{\tau}{2}\right) = \sum_\alpha R_x^\alpha(\tau) e^{j2\pi\alpha t} \tag{2}$$

where $\{R_x^\alpha\}$ are the Fourier coefficients. The Fourier Transform of the periodic auto-correlation results in the instantaneous spectral density function which is defined as:

$$S_x(t, f) = \int_{-\infty}^{\infty} R_x\left(t + \frac{\tau}{2}, t - \frac{\tau}{2}\right) e^{-j2\pi f\tau} d\tau \tag{3}$$

this is expressed using Fourier series:

$$S_x(t, f) = \sum_\alpha S_x^\alpha(f) e^{j2\pi\alpha t} \tag{4}$$

### 2.2. Direct Sequence-spread Spectrum

Spread spectrum techniques assure secure transmission and interference resistance. In direct sequence-spread spectrum (DS-SS), a signal is said to be spread in frequency domain by a pseudo random code [6]. This spreading code has low cross-correlation properties, and each chip duration is much shorter than an information bit. The signal power decreases by a factor equals to the processing gain such that the resulting power is similar to the noise power. That is why a DS-SS signal is said to be hidden in the noise or, in other words, has a low probability of intercept.

### 3. THE PROPOSED TECHNIQUE

In this technique, we use a pseudo random sequence generated by maximal length shift register to modulate a Binary Phase Shift Keying signal with certain processing gain. This results in a direct sequence spread spectrum signal. Our target is to study the effect of varying the processing gain of a DS-SS signal on peaks distribution of the cyclic spectrum. The overall system structure is shown in Figure 1. We use frequency smoothing method to calculate the cyclic spectrum. First we get the Fast Fourier transform of the DS-SS signal and then divide the spectrum into segments with equal lengths by a frequency smoothing window [8]. This is indicated in Equation (5) in time-domain:

$$z(n) = \sum_{m=-M}^{M} X_{j+m}(n) X_{k+m}^*(n) W(m) \tag{5}$$

where $j$ and $k$ are integers that determine the values of $\alpha$ and $f$ such that:

$$\alpha = \frac{j - k}{N}, \quad \text{and} \quad f = \frac{j + k + M2 - M1}{2N} \tag{6}$$
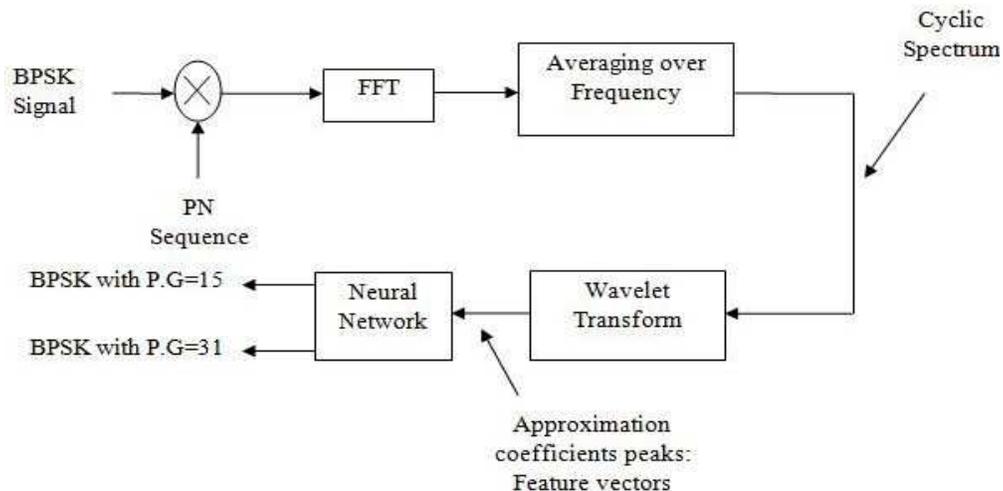


Figure 1: The overall system structure.
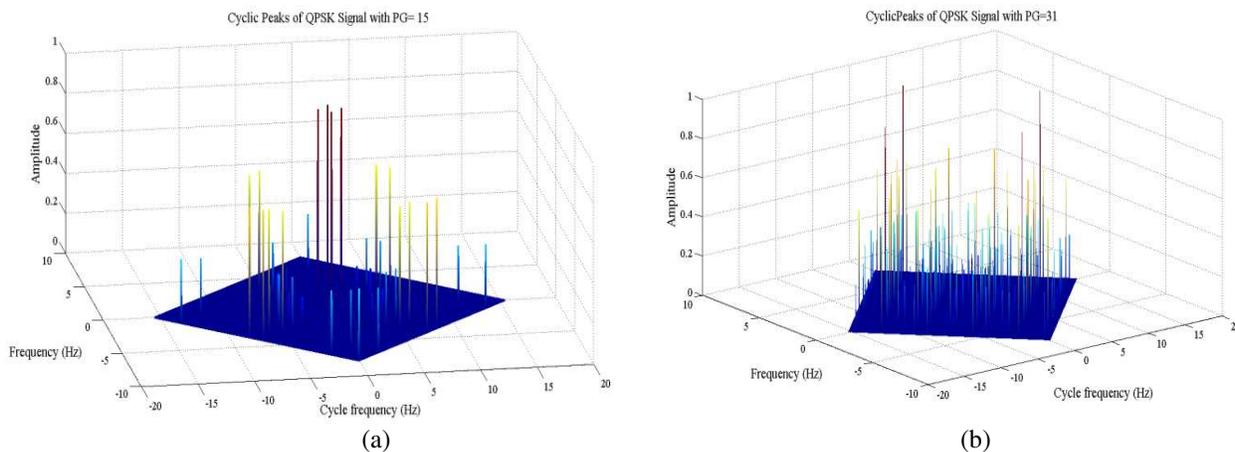
Figure 2: Cyclic peaks of QPSK signals: (a) PG = 15, (b) PG = 31.
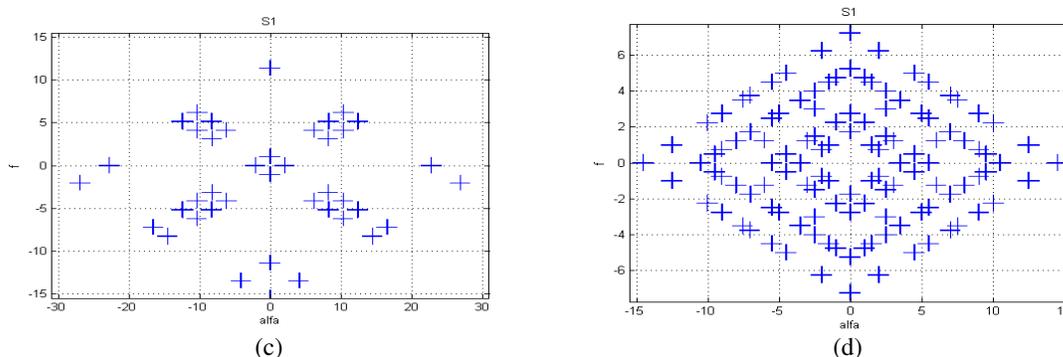


Figure 3: Peaks locations for QPSK Signals: (a) PG = 15, (b) PG = 31.

$X(n)$ is the segmented sequence and $W(m)$ is a frequency smoothing window that is centered at zero and of width $M = M2 + M1 + 1$. We set a threshold value to consider only significant peaks present in the cyclic spectrum. This is shown in Figure 2 as well as the peaks locations in Figure 3 for QPSK signals.

These peaks are distinguished features for each DS-SS signal with different processing gain. Since cyclostationary detectors require long observation times, it is important to reduce features length. Therefore, wavelet decomposition is used to compress the cyclic features length. The detailed wavelet coefficients showed insignificant features, so we considered only the peak values of the approximation coefficients to be the feature vectors required for classifying two BPSK-DS-SS signals. These two signals are spread by two PN sequences with different processing gain. Finally, these feature vectors are to be fed into a neural network classifier input.

## 4. SIMULATION RESULTS

It is required to classify QPSK signals spread with PN sequences with lengths: $N = 15$ and 31 and study the effect of varying the code rate on the cyclic spectrum of DS-SS signals such that the total rate is constant. Before classification, the cyclic spectrum of DSSS signals with PN sequences of $N = 15, 31, 63, 127, 255$ shows an increase in the number of peaks (features) as the code rate increases. This gives distinguished cyclic spectra. This effect has been tested for BPSK as well. Table 1 shows that by increasing the PN sequence length while maintaining the total data rate constant the number of peaks increases as well in the cyclic spectra of QPSK and BPSK signals. A fitting curve is drawn in Figure 4 to relate the number of cyclic peaks and the increased code length. This curve shows that the increase is slightly linear proportional values of data sequence length and code length, and increases in a quadratic manner when the PN sequence length is much greater than the information length.

In order to test the effect of this increase on the classification of cyclostationary signals, we chose two BPSK signal spread with PN sequences of lengths 15 and 31 such that the total sequence length is 930. We used the proposed technique to generate the required feature vectors and then apply them to a neural network classifier. The classifier performance has been studied in a channel
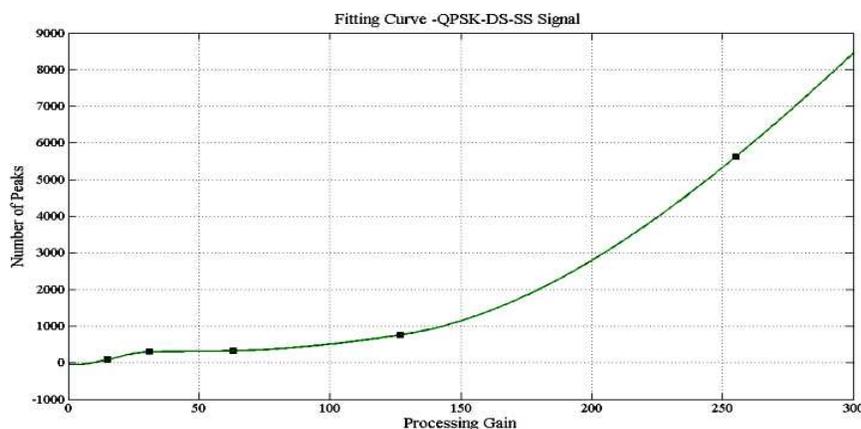
Figure 4: Fitting curve relating the increased code length with the number of cyclic peaks.

Table 1: The number of cyclic spectra peaks versus the increase in the processing gain.

| Processing Gain ($N$) | Data length | QPSK Peaks | BPSK Peaks |
|---|---|---|---|
| 15 | 62 | 93 | 469 |
| 31 | 30 | 304 | 690 |
| 63 | 14 | 335 | 738 |
| 127 | 7 | 769 | 786 |
| 255 | 3 | 5632 | 4852 |

Table 2: Results for AWGN channel.

| AWGN Channel | | | |
|---|---|---|---|
| Compressed Features | 8 | 15 | 30 |
| % Error | %20.5 | %18.5 | %13.5 |
| % Successful Classification | %79.5 | %81.5 | %86.5 |

Table 3: Results for a noise-free channel.

| Noise Free Channel | | | |
|---|---|---|---|
| Compressed Features | 8 | 15 | 30 |
| % Error | %6.5 | %3 | %0 |
| % Successful Classification | %93.5 | %97 | %100 |

that is free of noise, and AWGN channel with signal-to-noise ratio of $-3$ dB. We used 10-folds cross validation to calculate the percentage of successful classification. The results are summarized in Tables 2 and 3. The results show 100% and 86.5% of successful classification for a reduction percentage of 96.77% of features length in a noise-free channel and AWGN respectively.

## 5. CONCLUSION

This paper presented a method to study the effect of increasing the processing gain of DS-SS signals on the number of peaks present in the cyclic spectrum. This method is tested on BPSK and QPSK signals. The results showed an almost linear increase in the number of cyclic peaks for a proportional code and data lengths, as well as a quadratic increase when the code length is much greater than the data length. Further, this effect also has been tested by classifying two BPSK signals spread with code lengths of 15 and 31 using neural network classifier. Classification has been performed in two different channel environments, giving a classification percentage of %100 in noise free channel and %86.5 in AWGN for a reduction percentage of %96.77 in the sequence length. As a future work, we can apply this technique to OFDM signals in multipath environment and study its efficiency.

**REFERENCES**

1. Haykin, S., D. J. Thomson, and J. H. Reed, "Spectrum sensing for cognitive radio," *Proceedings of the IEEE*, Vol. 97, No. 5, 849–877, 2009.
2. Cabric, D., A. Tkachenko, and R. W. Brodersen, "Experimental study of spectrum sensing based on energy detection and network cooperation," *The 2nd Annual International Wireless Internet Conference (WICON)*, TAPAS Workshop, Aug. 2006.
3. Gardner, W. A., *Introduction to Random Process with Applications to Signals and Systems*, 301–354, MacMillan, 1986.
4. Gardner, W. A., "Exploitation of spectral redundancy in cyclostationary signals," *IEEE Signal Processing Magazine*, Vol. 8, 14–36, Apr. 1991, ISSN 1053-5888.
5. Like, E., V. D. Chakravarthy, P. Ratazzi, and Z. Wu, "Signal classification in fading channels using cyclic spectral analysis," *EURASIP Journal on Wireless Communications and Networking*, Vol. 97, 849–877, May 2009.
6. Sklar, D., *Digital Communications: Fundamentals and Applications*, 720–735, Prentice Hall, 2004.
7. Sutton, P. D., J. Lotze, K. E. Nolan, and L. E. Doyle, "Cyclostationary signature detection in multipath rayleigh fading environments," *2nd International Conference on Cognitive Radio Oriented Wireless Networks and Communications*, Orlando, Florida, 2007.
8. Brown, W. A. and H. Loomis, "Digital implementations of spectral correlation analyzer," *IEEE Transactions on Signal Processing*, Vol. 41, No. 2, Feb. 1993.

# New Numerical Method for Solving Maxwell Equations with Strong Singularity

**V. A. Rukavishnikov and A. O. Mosolapov**

Computing Center of Far-Eastern Branch, Russian Academy of Sciences
Kim-Yu-Chen Str. 65, Khabarovsk 680000, Russia

**Abstract**— In this note we introduce a notion of $R_\nu$-generalized solution to Maxwell equations with strong singularity in a 2D nonconvex polygonal domain. We develop a new weighted edge FEM. Results of numerical experiments prove the efficiency of this method.

## 1. INTRODUCTION

Maxwell equations are used in mathematical models of electromagnetic fields, for example, in plasma physics, electrodynamics and engineering of high-frequency devices. As a rule, in practical problems the computational domain is nonconvex with reentrant corners or edges on its boundary. Such geometry singularities leads to strong electromagnetic fields in their neighborhood, and a solution of Maxwell equations is strongly singular, i.e., it does not belong to the Sobolev space $H^1$ ($W_2^1$).

For numerical solution of such problems P. Ciarlet, Jr., F. Assous and others developed the singular complement method (SCM). This method consists in splitting of the space of solutions into a two-term direct sum, where the first term contains the regular part of solution and the second contains the singular part (see [1–4]).

Another approach to solving Maxwell equations with strongly singular solution was developed by M. Costabel and M. Daug. This method is based on regularization of the initial equation with a weighted divergence term. The resulting elliptic problem considered in a special weighted space is equivalent to the original one (see [5, 6].

For boundary value problems with strongly singular solutions we developed the theory of numerical methods based on the conception of $R_\nu$-generalized solution (see, for example, [7–11]). This conception allows us, depending on the singularity of input data (coefficients and right hand sides of equations and boundary conditions) and geometry of the boundary, to define a weighted space or a set containing the solution. It is also possible to build a regularizator which bounds the influence of singularity to the accuracy of numerical solution.

In the present paper we develop the weighted edge finite element method (FEM) based on the conception of $R_\nu$-generalized solution of the Maxwell equations with strong singularity due to a reentrant corner on the boundary. Numerical experiments of model problems showed that the rate of convergence of the numerical solution to the exact one is more than one and a half times better in comparison with the results established in [3, 6] and [12]. Another advantage of this method is simplicity of the solution determination which is an additional benefit for numerical experiments.

## 2. NOTATIONS AND PRELIMINARIES

We denote two- and three-dimensional Euclidian spaces by $R^2$ and $R^3$, respectively, with the Cartesian coordinates $x = (x_1, x_2)$, $x = (x_1, x_2, x_3)$. Let $\Omega$ be a bounded simply connected domain in these spaces with the boundary $\partial\Omega$. Let $\mathbf{n}$ be the unit outward normal to $\partial\Omega$. In the case $\Omega \subset R^2$ $\boldsymbol{\tau}$ means a unite tangent vector to $\partial\Omega$. For vector-functions $f : R^3 \to R^3$ or $f : R^3 \times [0, T] \to R^3$ we use the notation $\bar{E}(x) = (E_1(x), E_2(x), E_3(x))$. Vector-functions $f : R^2 \to R^2$ are denoted by boldface latin letters: $\mathbf{E}(x) = (E_1(x), E_2(x))$.

In the 2D case the notations curl and **curl** distinguish between scalar and vector curl operators:

$$\text{curl}\mathbf{E} = \frac{\partial E_2}{\partial x_1} - \frac{\partial E_1}{\partial x_2}, \quad \mathbf{curl}f = \left( \frac{\partial f}{\partial x_2}, -\frac{\partial f}{\partial x_1} \right).$$

Let us recall the definitions of some functional spaces associated with Maxwell equations:

$$H_0(\text{curl}, \Omega) = \{\mathbf{E} \in H(\text{curl}, \Omega) | \mathbf{E} \cdot \boldsymbol{\tau} = 0, \, x \in \partial\Omega\}, \quad H(\text{div}, \Omega) = \{\mathbf{E} \in \mathbf{L}_2(\Omega) | \text{div}\mathbf{E} \in L_2(\Omega)\},$$
$$H(\text{div}0, \Omega) = \{\mathbf{E} \in H(\text{div}, \Omega) | \text{div}\mathbf{E} = 0\}, \quad V = H_0(\text{curl}, \Omega) \cap H(\text{div}0, \Omega).$$

Let the domain $\Omega \subset R^2$ have one special point $O(0,0)$ on its boundary. Let $B_\delta(O)$ be an open ball centered at point $O(0,0)$ with radius $\delta$. We introduce a weight function $\rho(x)$ which coincides with the distance to the point $O(0,0)$ in $B_\delta(O)$ and it is equal to $\delta$ outside $B_\delta(O)$.

We introduce a weighted Sobolev space $H_{2,\nu}^k(\Omega)$ with the norm

$$\|f\|_{H_{2,\nu}^k(\Omega)} = \left( \sum_{|\lambda| \le k} \int_\Omega \rho^{2(\nu+|\lambda|-k)}(x) \left| D^\lambda f \right|^2 dx \right)^{1/2},$$

where $D^\lambda = \frac{\partial^{|\lambda|}}{\partial x_1^{\lambda_1} \partial x_2^{\lambda_2}}$, $\nu$ is nonnegative real, $\lambda = (\lambda_1, \lambda_2)$, $\lambda_1$, $\lambda_2$ are nonnegative integers and $|\lambda| = \lambda_1 + \lambda_2$. When $k = 0$ $H_{2,\nu}^0(\Omega) = L_{2,\nu}(\Omega)$. For the corresponding spaces of vector-functions we use notations $\mathbf{H}_{2,\nu}^k(\Omega)$, $\mathbf{L}_{2,\nu}(\Omega)$.

A subspace of $\mathbf{H}_{2,\nu}^k(\Omega)$ composed of the vector-functions with zero tangential component on $\partial\Omega$ is denoted by $\overset{\circ}{\mathbf{H}}_{2,\nu}^k(\Omega)$: $\overset{\circ}{\mathbf{H}}_{2,\nu}^k(\Omega) = \{\mathbf{E} \in \mathbf{H}_{2,\nu}^k(\Omega) \mid \mathbf{E} \cdot \boldsymbol{\tau} = 0 \text{ a. e. on } \partial\Omega\}$.

## 3. PROBLEM STATEMENT

Let $\Omega \subset R^3$. We suppose (see [1,6]) that following conditions are satisfied: $\partial\Omega$ is a perfect conductor; the physical environment is vacuum; free charges are absent; electromagnetic field and current density are monochromatic with circular frequency $\omega$: $\bar{E}(x,t) = \bar{E}(x)\exp(-i\omega t)$, $\bar{B}(x,t) = \bar{B}(x)\exp(-i\omega t)$, $\bar{J}(x,t) = \bar{J}(x)\exp(-i\omega t)$. Then the Maxwell equations with appropriate boundary conditions read:

$$i\omega\bar{E} + c^2\mathbf{curl}\bar{B} = \frac{1}{\varepsilon_0}\bar{J}, \quad -i\omega\bar{B} + \mathbf{curl}\bar{E} = 0, \quad \mathrm{div}\bar{E} = 0, \quad x \in \Omega,$$
$$\bar{E} \times \mathbf{n} = 0, \quad \bar{B} \cdot \mathbf{n} = 0, \quad x \in \partial\Omega, \tag{1}$$

where $\bar{E}$ and $\bar{B}$ are, respectively, the electric and magnetic fields, $\bar{J}$ is the current density, and $c$ and $\varepsilon_0$ are the speed of light and dielectric permittivity.

In what follows we assume that the data does not depend on variable $x_3$. As noted in [1], we can decouple initial system (1) in two systems of unknowns $\bar{E} = (E_1, E_2, 0) = \mathbf{E}$, $\bar{B} = (0, 0, B_3) = B$ (so called TE mode) and $\bar{E} = (0, 0, E_3) = E$, $\bar{B} = (B_1, B_2, 0) = \mathbf{B}$ (TM mode).

Let $\Omega$ be a L-shaped domain with one reentrant corner on its boundary. Later in this paper we assume that $\Omega = (-1, 1) \times (-1, 1) \backslash [0, 1] \times [-1, 0]$.

Using standard technique (see [1]), we reduce the original problem for the TE mode to the first boundary value problem of the second order:

$$\mathbf{curl}\,\mathrm{curl}\mathbf{E} - k^2\mathbf{E} = \mathbf{f}, \tag{2}$$
$$\mathrm{div}\mathbf{E} = 0, \quad x \in \Omega, \tag{3}$$
$$\mathbf{E} \cdot \boldsymbol{\tau} = 0, \quad x \in \partial\Omega. \tag{4}$$

It is well known that for a non-convex domain the solution of (2)–(4) belongs to $V$ and does not belong to $\mathbf{H}^1(\Omega)$ ([1, 5, 6]). In other words, problem (2)–(4) has a strongly singular solution.

Let us introduce the notion of $R_\nu$-generalized solution for problem (2)–(4). Denote by

$$a(\mathbf{E}, \mathbf{F}) = (\mathrm{curl}\mathbf{E}, \mathrm{curl}(\rho^{2\nu}\mathbf{F})) - k^2(\mathbf{E}, \rho^{2\nu}\mathbf{F}), \quad b(\mathbf{F}) = (\mathbf{f}, \rho^{2\nu}\mathbf{F})$$

the bilinear and linear forms, respectively.

**Definition 1.** *A vector-function $\mathbf{E} \in \overset{\circ}{\mathbf{H}}_{2,\nu}^1(\Omega)$ is called $R_\nu$-generalized solution of problem (2)–(4) if it satisfies the condition (3) and for any $\mathbf{F} \in \overset{\circ}{\mathbf{H}}_{2,\nu}^1(\Omega)$ the identity $a(\mathbf{E}, \mathbf{F}) = b(\mathbf{F})$ holds.*

## 4. CONSTRUCTION OF A SCHEME OF THE FINITE ELEMENT METHOD

We construct a scheme of the weighted edge FEM for the determination of an approximate $R_\nu$-generalized solution of the problem (2)–(4). This method is based on the $H(\mathrm{curl})$-conforming edge FEM proposed by J.-C. Nédélec in 1980-s. Moreover, the finite element subspace is formed by solenoidal basis functions so that condition (3) holds automatically.
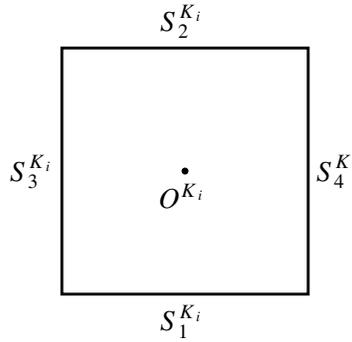
Figure 1: The rule of the local numeration.

We divide $\bar{\Omega}$ into the set $\{K\} = \{K_i\}_{i=1}^{N_h}$ of the closed squares $K_i$ by means of vertical and horizontal straights $x_1 = -1 + jh$, $x_2 = -1 + lh$, $j, l = \overline{0, N}$, where $N$ is a positive even integer, $h = \frac{2}{N}$ and $N_h = \frac{3N^2}{4}$. Square $K_i$ we name as element.

Let $S_1, \ldots, S_{S_h}$ be the set of sides of the squares $K$ which does not belong to $\partial\Omega$, $S = \{S_i, i = 1, \ldots, S_h, S_i \notin \partial\Omega, S_h = \frac{3N^2}{2} - 2N\}$. We denote by $M_i$ the center of the side $S_i$, $i = \overline{1, S_h}$.

For every element $K_i$ we denote by $O^{K_i} = (o_1^{K_i}, o_2^{K_i})$ its center, $S_j^{K_i}$ are its sides and $M_j^{K_i} = (m_{1j}^{K_i}, m_{2j}^{K_i})$ are the centers of $S_j^{K_i}$, $j = \overline{1, 4}$. The rule of the local numeration of the $S_j^{K_i}$, $j = \overline{1, 4}$ is depicted on Figure 1.

We introduce form functions of the element $K_i$ associated with its sides:

$$\psi_1^{K_i} = \frac{1}{h}\rho^{-\nu}(m_{11}^{K_i}, x_2)\left(\frac{h}{2} + o_2^K - x_2\right)\mathbf{i}, \quad \psi_2^{K_i} = \frac{1}{h}\rho^{-\nu}(m_{12}^{K_i}, x_2)\left(\frac{h}{2} + x_2 - o_2^{K_i}\right)\mathbf{i},$$

$$\psi_3^{K_i} = \frac{1}{h}\rho^{-\nu}(x_1, m_{23}^{K_i})\left(\frac{h}{2} + o_1^{K_i} - x_1\right)\mathbf{j}, \quad \psi_4^{K_i} = \frac{1}{h}\rho^{-\nu}(x_1, m_{24}^{K_i})\left(\frac{h}{2} + x_1 - o_1^{K_i}\right)\mathbf{j},$$

where $\mathbf{i}$ and $\mathbf{j}$ are the standard basis vectors of $R^2$.

For the every side $S_i \in S$ we introduce weighted basis function $\psi_i$ in the following way. Let $K_m$ and $K_n$ be two finite elements with common side $S_i$, and let $\psi_j^{K_m}$, $\boldsymbol{\psi}_l^{K_n}$ are the form functions associated with side $S_i$. Then the corresponding basis function

$$\psi_i = \begin{cases} \psi_j^{K_m}, & x \in K_m, \\ \psi_l^{K_n}, & x \in K_n, \\ 0, & x \in \bar{\Omega} \setminus (K_m \cup K_n). \end{cases}$$

Denote by $\mathbf{V}_h$ the linear span of $\{\psi_i\}_{i=1}^{S_h}$. It is obvious that $\mathbf{V}_h \subset \overset{\circ}{\mathbf{H}}_{2,\nu}^1(\Omega)$. We shall approximate $R_\nu$-generalized solution of problem (2)–(4) in this subspace.

**Definition 2.** *A function $\mathbf{E}_\nu^h \in \mathbf{V}_h$ satisfying the identity $a(\mathbf{E}_\nu^h, \mathbf{v}_h) = b(\mathbf{v}_h)\forall\mathbf{v}_h \in \mathbf{V}_h$ is called the approximate $R_\nu$-generalized solution of problem (2)–(4).*

An approximate solution $\mathbf{E}_\nu^h$ will be found in the form $\mathbf{E}_\nu^h = \sum_{i=1}^{S_h} d_i\psi_i$, where $d_i = \rho^\nu(M_i)g_i$, $g_i = $ const. The unknowns $d_i$ are defined from the system of equations

$$A\mathbf{d} = \mathbf{b}, \tag{5}$$

where $\mathbf{d} = (d_1, \ldots, d_{S_h})^T$, $A = (A_{ij})$, $i, j = \overline{1, S_h}$, $A_{ij} = a(\psi_i, \psi_j)$, $\mathbf{b} = (b_1, \ldots, b_{S_h})^T$, $b_i = b(\psi_i)$.

## 5. RESULTS OF NUMERICAL EXPERIMENTS

We developed a program "Proba-III" for carrying out a set of numerical tests using our FEM described in Section 4 and GMRES-method for solving system (5). The errors of numerical approximations to the $R_\nu$-generalized solution was computed as module between approximate and exact solutions in the points $M_i$ and in the norm of space $\mathbf{L}_{2,\nu}(\Omega)$. We present here the results

Table 1: Dependence of error $\|\mathbf{E} - \mathbf{E}_\nu^h\|_{\mathbf{L}_{2,\nu}(\Omega)}$ on the number of segments of fragmentation $N$, $\beta = -6.5$, $\delta = 0.06$, $\nu = 3.5$.

| $N$ | 32 | 64 | 128 |
|---|---|---|---|
| $\|\mathbf{E} - \mathbf{E}_\nu^h\|_{\mathbf{L}_{2,\nu}(\Omega)}$, $k = k_1$ | 0.0001249 | 0.0000650 | 0.0000333 |
| $\|\mathbf{E} - \mathbf{E}_\nu^h\|_{\mathbf{L}_{2,\nu}(\Omega)}$, $k = k_2$ | 0.0001249 | 0.0000646 | 0.0000274 |

Table 2: The numbers of points (in percentage of their total number) where the errors are less than the given limit value $\bar{\Delta} = 0.001$, $\beta = -6.5$, $\delta = 0.06$, $\nu = 3.5$.

| $N$ | 32 | 64 | 128 |
|---|---|---|---|
| $n_1$, $k = k_1$ | 42.93% | 63.30% | 83.57% |
| $n_2$, $k = k_2$ | 42.93% | 69.28% | 83.40% |



(a)



(b)
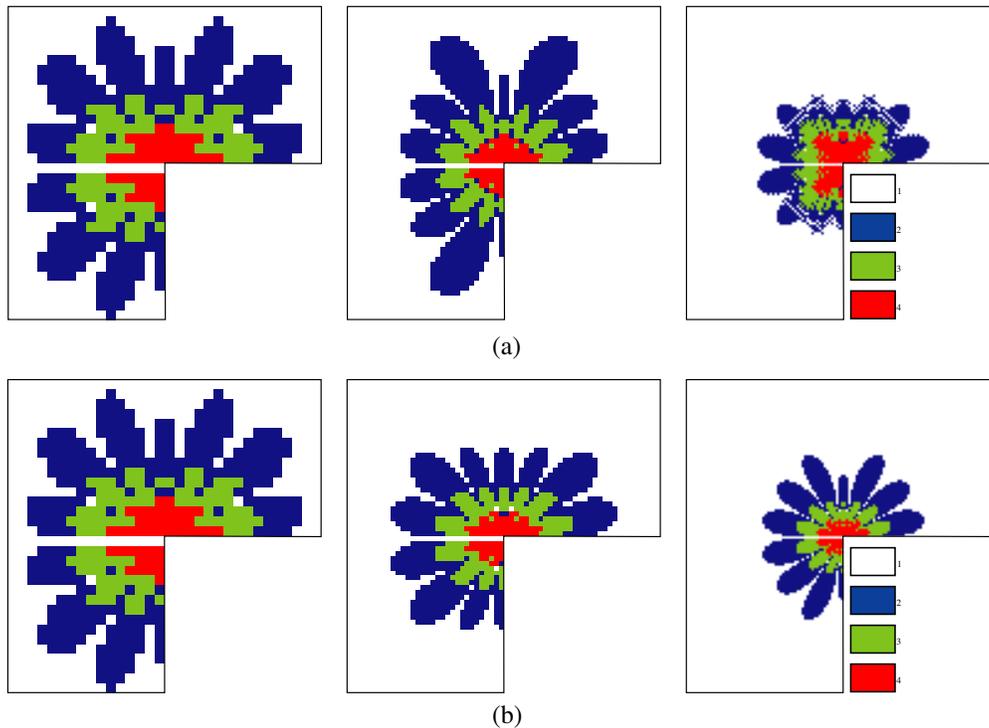
Figure 2: Distribution of the points $M_i$ with error $\delta_{1i}$ for the component $E_{1\nu}^h$ of the approximate $R_\nu$-generalized solution, (a) $k = 220$, (b) $k = 300$.

of numerical experiments for one model problem. To do this, introduce an auxiliary function $\varphi = (x_1 x_2(x_1^2 - 1)(x_2^2 - 1))^2 (\sqrt{x_1^2 + x_2^2})^{\beta+2}$. Define $\mathbf{E} = \mathbf{curl}\varphi$. Substituting $\mathbf{E}$ in Equation (2), we get the right hand side $\mathbf{f}$ for the different coefficients (wave numbers) $k_1 = 220$ and $k_2 = 300$ (frequencies are 10.497 GHz and 14.314 GHz respectively). Numerical experiments were realized on meshes with different step $h$.

In Table 2 for the determined approximate $R_\nu$-generalized solutions we present the numbers of points $n_1$ and $n_2$ (in percentage of their total number) where the errors $\delta_{1i} = |E_1(M_i) - E_{1\nu}^h(M_i)|$, $\delta_{2i} = |E_2(M_i) - E_{2\nu}^h(M_i)|$, $i = \overline{1, S_h}$, are less than the given limit value $\bar{\Delta} = 0.001$.

On Figure 2 we depict the distribution of the points $M_i$ with error $\delta_{1i}$ for the component $E_{1\nu}^h$ of the approximate $R_\nu$-generalized solution on different meshes. The figures for the component $E_{2\nu}^h$ are analogous.

The series of numerical experiments showed that:

1. approximate solution by a proposed FEM converges to an exact $R_\nu$-generalized solution in the weight space $\mathbf{L}_{2,\nu}(\Omega)$ with the first rate;

2. the numbers of points where the errors are greater than the given limit value $\bar{\Delta}$ decreases with mesh refinement; the radius of the neighborhood containing these points decreases when $h$ decreases.

**ACKNOWLEDGMENT**

**REFERENCES**

1. Assous, F., P. Ciarlet, and J. Segré, "Numerical solution to the time-dependent Maxwell equations in two-dimensional singular domain: The singular complement method," *J. Comput. Phys.*, Vol. 161, 218–249, 2000.
2. Assous, F., P. Ciarlet, and E. Garcia, "Singular electromagnetic fields: Inductive approach," *C. R. Acad. Sci. Paris, Ser. I.*, Vol. 341, 605–610, 2005.
3. Assous, F., P. Ciarlet, E. Garcia, and J. Segré, "Time-dependent Maxwell's equations with charges in singular geometries," *Comput. Methods in Appl. Mech. Engrg.*, Vol. 196, 665–681, 2006.
4. Buffa, A., P. Ciarlet, and E. Jamelot, "Solving electromagnetic eigenvalue problems in polyhedral domains," *Numer. Math.*, Vol. 113, 497–518, 2009.
5. Costabel, M., M. Daug, and C. Schwab, "Exponential convergence of hp-FEM for Maxwell's equations with weighted regularization in polygonal domains," *Math. Model. Meth. Appl. Sci.*, Vol. 15, 575–622, 2005.
6. Costabel, M. and M. Daug, "Weighted regularization of Maxwell equations in polyhedral domains," *Numer. Math.*, Vol. 93, 239–277, 2002.
7. Rukavishnikov, V. A., "On differentiability properties of an $R_\nu$-generalized solution of the Dirichlet problem," *Sov. Math., Dokl.*, Vol. 40, 653–655, 1990.
8. Rukavishnikov, V. A. and H. I. Rukavishnikova, "The finite element method for the first boundary value problem with compatible degeneracy of the initial data," *Russ. Acad. Sci., Dokl., Math.*, Vol. 50, No. 2, 335–339, 1995.
9. Rukavishnikov, V. A. and A. Y. Bespalov, "Exponential convergency rate in a finite element method for a Dirichlet problem with singularity of solution," *Dokl. Math.*, Vol. 62, No. 2, 266–270, 2000.
10. Rukavishnikov, V. A., "Methods of numerical analysis for boundary value problems with strong singularity," *Russ. J. Numer. Anal. Math. Model.*, Vol. 24, 565–590, 2009.
11. Rukavishnikov, V. A. and H. I. Rukavishnikova, "The finite element method for a boundary value problem with strong singularity," *J. Comput. Appl. Math.*, Vol. 234, 2870–2882, 2010.
12. Jamelot, E., "A nodal finite element method for Maxwell's equations," *C. R. Acad. Sci. Paris, Ser. I.*, Vol. 339, 809–814, 2004.
13. Jin, J. M., *The Finite Element Method in Electromagnetics*, 2nd Edition, John Wiley & Sons, Inc., New York, 2002.

# Efficiency Enhancement by Harmonic Phase Tuning in Class-F Amplifiers

**Ken Hiraga and Toshio Nojima**

Hokkaido University, Sapporo 060-0814, Japan

**Abstract**— Load impedance at harmonic frequencies has been considered one of the most important factors in decreasing the power dissipation of power amplifiers for radio transmitters. This paper shows an analysis of the negative effects on efficiency produced by harmonic phase errors. As a means of addressing this issue, we introduce a harmonic reflection filter for Class-F amplifiers. The filter can provide tunable phases for the second and third harmonics independently and promises to be a useful means of achieving precise harmonic phases.

## 1. INTRODUCTION

Power efficiency in power amplifiers has long been a major issue in the field of radio transmitters. Accordingly, many techniques that reduce the power dissipation in active devices have been proposed [1, 2]. The use of class-F amplifiers has been considered one of the most effective approaches to improving the power efficiency of microwave power amplifiers for radio transmitters. In ideal class-F operation, the drain current waveform is half-sinusoidal, the drain voltage waveform is rectangular, and voltage and current do not coexist simultaneously in active devices (e.g., transistors), hence there is no power dissipation in the devices. Microwave power amplifiers achieve these operating conditions with a load circuit that has short-circuited impedance in even-harmonic frequency bands, open-circuited impedance in odd-harmonic frequency bands, and matched impedance in fundamental frequency bands [3]. To realize these types of load impedance, load circuits have been made using discrete components in low frequency bands [4]. In microwave bands, microstrip line circuits have been utilized [5] and load circuits in which up to seventh harmonic impedance is considered have been proposed [6].

However, some packaged high-frequency power devices have electric length and parasitic components on the input- or output-pins. Moreover, there are individual differences among each of these devices. These factors limit harmonic phase precision, which deteriorates efficiency in class-F operation. Therefore, to realize precise harmonic phases, load circuits should have a fine tuning mechanism. To address this issue, Harmonic Matching and Reflection Amplifiers (HMRAs) [7] include a mechanism to optimize the second harmonic phase condition. However, no consideration has been given to third harmonic phase tuning in HMRAs.

In this paper, we use numerical analysis to clarify the negative effects on efficiency produced by harmonic phase errors in class-F amplifiers with the second and third harmonics. As a solution for dealing with harmonic phase errors, we introduce a harmonic reflection filter circuit for Class-F amplifiers that can provide tunable phases for the second and third harmonics independently.

## 2. ANALYSIS OF EFFICIENCY DETERIORATION DUE TO HARMONIC PHASE ERRORS IN CLASS-F OPERATION

The drain efficiency is 100% for ideal class-F operation with an infinite number of harmonics in operating waveforms [8]. However, in practical circuits, there are some undesirable factors such as operating frequency limits, on-resistance, and fabrication errors, class-F operation is based on a finite number of harmonics. Efficiency levels achieved with a finite number of harmonics are shown in Table 1, which was previously provided in [8]. Here, $n$ represents the maximum order of harmonics in the drain voltage and $m$ represents that in the drain current. In this table, the "$n = 1$, $m = 1$" column is class-A operation, which has the waveforms of pure sinusoidal voltage and current. The "$n = \infty$, $m = \infty$" condition represents the ideal class-F operation, which has the waveforms of complete half sinusoidal current and complete rectangular voltage. For example, "$n = 3$, $m = 2$" represents the class-F operation in which drain voltage contains up to the third harmonic and drain current contains up to the second harmonic. This operation has a maximum drain efficiency of 81.6%. On the other hand, the "$n = 1$, $m = 2$" condition has a maximum drain efficiency of 70.7%. Thus, optimization up to the third harmonic can increase the drain efficiency obtained in operations without the third harmonic by 10 percent. This demonstrates the importance of maintaining the third harmonic.

Table 1: Maximum efficiency of class-F amplifiers.

| n/m | 1 | 2 | 4 | . . . | $\infty$ |
|-----|------|------|------|-----|-------|
| 1 | 50.0 | 70.7 | 75.0 | | 78.6 |
| 3 | 57.7 | 81.6 | 86.6 | | 90.7 |
| 5 | 60.4 | 85.4 | 90.5 | | 94.8 |
| . . . | | | | | |
| $\infty$ | 63.7 | 90.0 | 95.5 | | 100.0 |

The equations below represent drain waveforms of class-F operation with harmonic phase errors for the case where $n = 3$ and $m = 2$. Equations (1) and (2) represent the waveforms of drain voltage $v_d(t)$ and drain current $i_d(t)$ respectively. Here, $f$ is fundamental frequency, $t$ is time, $\phi_3$ is a third harmonic phase error, and $\phi_2$ is a second harmonic phase error. $V_{DC}$ and $I_{DC}$ are DC components in the voltage and current respectively. $V_1$ and $I_1$ are the amplitudes of the fundamental components in the voltage and current respectively. $V_3$ is the amplitude of the third harmonic component in voltage and $I_2$ is that of the second harmonic component in current.

$$v_d(t) = V_{DC} + V_1 \sin 2\pi ft + V_3 \sin 3(2\pi ft - \phi_3) \tag{1}$$
$$i_d(t) = I_{DC} - I_1 \sin 2\pi ft - I_2 \cos 2(2\pi ft - \phi_2) \tag{2}$$

Obtainable maximum drain efficiency with harmonic error $\eta$ is calculated as the following equation, in which $\eta$ is a function of phase errors. Here, $I_1$, $V_1$, and $I_{DC}$ are the functions of the phase errors $\phi_2$ and $\phi_3$. On the other hand, $V_{DC}$ is a constant value because the voltage of the DC power supply is fixed.

$$\eta = \frac{I_1 V_1}{V_{DC} I_{DC}} \tag{3}$$

The optimum values of $V_1$ and $V_3$ to obtain maximum efficiency when the third harmonic phase error is $\phi_3$ are calculated as the function of $\phi_3$ using numerical analysis following the procedure given below. A similar procedure can be used to obtain the values of $I_1$ and $I_2$.

**Step1:** $\phi_3$ is set to a certain value. Here, the range of $\phi_3$ is $0 < \phi_3 < 60$ degrees because $v_d(t)$ takes the same value at every 120 degrees of $\phi_3$ and is symmetric about $\phi_3 = 0$.

**Step2:** When $\phi_3$ is given, $V_3$ with minimum $v_d(t)$ peak value is searched and determined as the optimum value.

**Step3:** When $v_d(t)$ peak value is minimized, $V_1$ can be maximized under the condition that $v_d(t)$ cannot take a minus value. $v_d(t)$ with maximum $V_1$ is the optimum waveform.

Figure 1 shows class-F operation drain waveforms. The broken lines show the optimum waveforms with the second harmonic in the current and the third-harmonic in the voltage. The solid lines show the waveforms with harmonic phase errors. Harmonic phases in the drain waveforms may contain errors due to the load impedance condition. When drain waveforms contain errors, a transistor's power dissipation is magnified and consequently its efficiency is deteriorated. For example, when the third harmonic phase error in the voltage waveform is $\phi_3 = 10$ degrees, the drain voltage waveform is the solid-line curve shown in Fig. 1(a). When the second harmonic phase error in the current waveform is $\phi_2 = 20$ degrees, the drain current waveform is the solid-line curve shown in Fig. 1(b). Under these conditions, drain efficiency is as low as 58.2%.

Figure 2 shows the relationship of the drain efficiency to $\phi_3$ and $\phi_2$. When $\phi_3$ is more than 20 degrees, drain efficiency does not depend on $\phi_3$. This means that the third harmonic cannot contribute to efficiency improvement if its phase error takes such a value. The same can be said when $\phi_2$ more than 40 degrees. Second and third harmonic phase errors significantly deteriorate efficiency.

Hence, precise harmonic phase conditions in both second and third harmonic are very important in class-F amplifiers. To realize them, it is preferable that the phase conditions are tunable independently without influencing the phase at the fundamental frequency. Conventional circuits did not have such tuning functions.
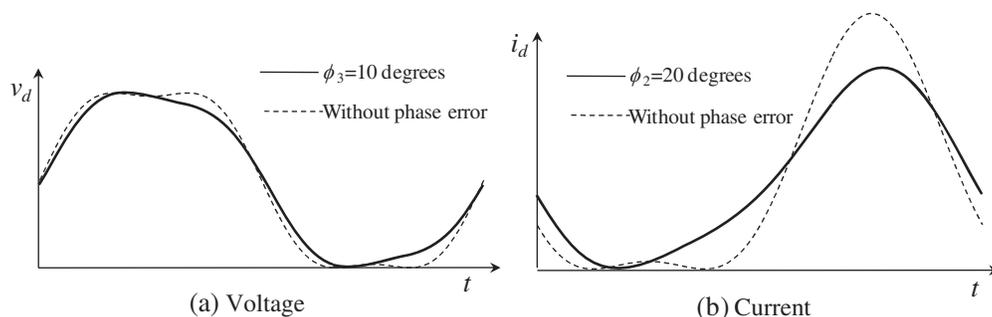
Figure 1: Class-F operation drain waveforms.
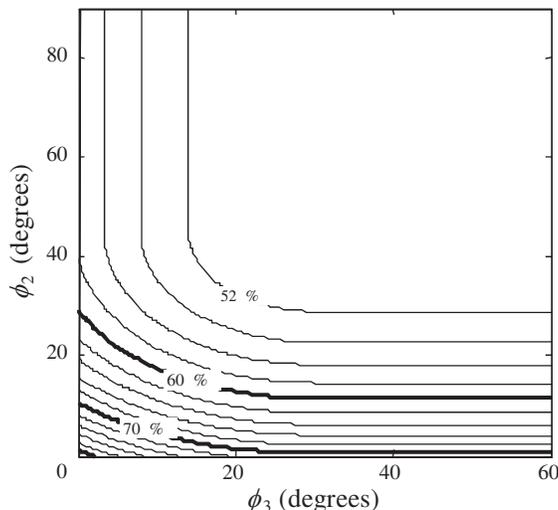


Figure 2: Drain efficiency with harmonic phase errors.

### 2.1. Basic Construction

To realize the precise phase condition in harmonic frequencies, we introduce a harmonic filter that enables fine tuning of second and third harmonic phases independently without influencing the phase at the fundamental frequency. This can be applied to HMRAs. Fig. 3 shows the block diagram of an HMRA with second and third harmonic control mechanisms. The HMRA itself, which was proposed in [7], was able to control only the second harmonic phase. This amplifier configuration is considered to be an extension of [4]. The output matching circuit has the function of matching the transistor's output impedance and load impedance at the fundamental, second harmonic, and third harmonic frequencies.

The harmonic filter reflects the second and third harmonics to the output-matching circuit in appropriate phase and has no effect on the fundamental frequency. It can tune the reflection phases of the second and third harmonics independently without changing the load impedance for the fundamental frequency. The reflection phases can be tuned by using a harmonic tuning control mechanism. This makes it possible to realize optimum load impedance at harmonic frequencies thus overcoming the problem of optimum load impedance not being realizable due to individual differences among transistors. We believe the use of this filter is a promising way to reduce the difficulties involved in designing and fabricating high-efficiency amplifier circuits, as well as to improve the yield ratio.

Here, we describe the basic structure of our harmonic filter that enables second and third harmonic tuning As shown in Fig. 4, it is composed of a number of open or short stubs, an LC series resonator whose resonant frequency is the fundamental frequency, a second harmonic tuner, a third harmonic tuner, and transmission lines. The second and third harmonic tuners are components whose reflection coefficients are variable pure imaginary numbers. For example, they are line stretchers that are short- or open-circuited at the far end. The input impedance is seen from the "input" point in the figure and the operation mechanism is as described below.
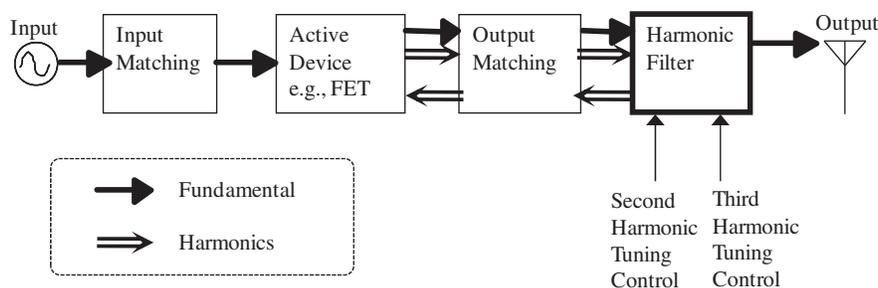
Figure 3: HMRA using our harmonic filter.
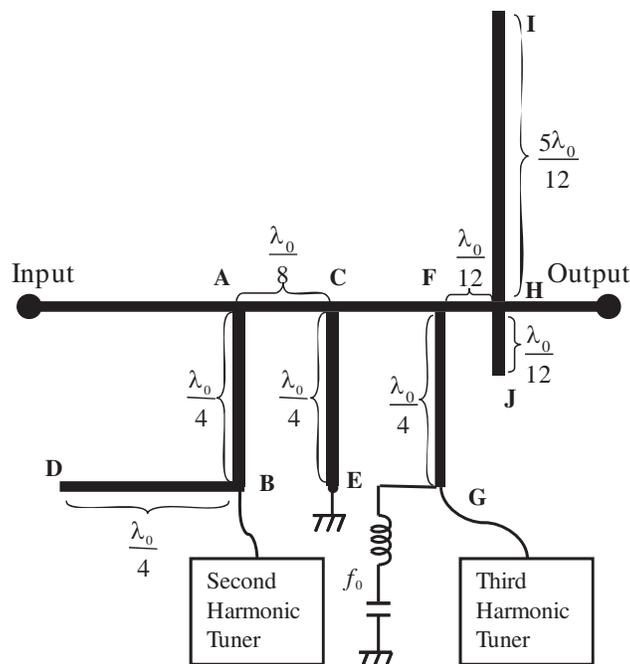


Figure 4: Proposed harmonic filter.

## 2.2. Characteristics at the Fundamental Frequency

Point B is short-circuited because the open stub BD whose length is quarter-wavelength is connected at this point. Thus the input impedance of ABD seen at A is open-circuited. The input impedance of the short stub CE is open-circuited because the length of this stub is quarterwave length.

Point G is short-circuited because the series resonator is connected to it. Since the length of the transmission line FG is quarterwavelength, the input impedance of FG seen at F is open-circuited. The two open stubs HJ and HI connected at H have no effect on the fundamental frequency because the sum of the lengths of these stubs is halfwavelength. Consequently, the harmonic filter has no effect on the fundamental frequency.

## 2.3. Characteristics at Second-harmonic Frequency

The wavelength in second-harmonic frequency is half of that in fundamental frequency.

The input impedance of BD seen at B is open-circuited because the length of open stub BD is half-wavelength. Since the length of transmission line AB is half-wavelength, the input impedance of ABD seen at A is the same as the input impedance of the second-harmonic tuner that is connected at B. This tuner has pure imaginary reflection coefficients as described above. Point C is short-circuited because E is also short-circuited and the length of the transmission line CE is half-wavelength. Hence, the input impedance of AC seen at point A is open-circuited because the length of the transmission line AC is quarter-wavelength, and the circuit components connected at the right side of point A have no effect on the second harmonic frequency. Consequently, the reflection coefficient of this filter is a pure imaginary number. This imaginary number can be tuned by the second-harmonic tuner.

## 2.4. Characteristics at Third-harmonic Frequency

The wavelength in third-harmonic frequency is one-third of that in fundamental frequency. Point B is short-circuited because the length of open stub BD is 3/4-wavelength. Since the length of transmission line AB is 3/4-wavelength, the input impedance of ABD seen at A is open-circuited The input impedance of CE seen at C is open-circuited because E is short-circuited and the length of the transmission line CE is 3/4-wavelength. Hence, ABD and CE connected to the transmission line AC have no effect on the third harmonic frequency The open stub HJ whose length is quarter-wavelength makes point H short-circuited. Since the length of transmission line FH is quarter-wavelength and the input impedance of FH seen at point F is open circuited, the components connected at the right side of point F have no effect on the third harmonic frequency The series resonator has open-circuited impedance at all frequencies other than the fundamental frequency. Transmission line FG whose length is 3/4-wavelength has the same effect as that of quarter-wavelength at the third harmonic. Hence, the input impedance seen at F is the inverse of that of the thirdharmonic tuner connected at G. In other words, the reflection coefficient of FG seen at F is a pure imaginary number. Consequently, the reflection coefficient of this filter is a pure imaginary number at the third harmonic.

## 2.5. Input Impedance Transition During Harmonic Tunings

As described above, the harmonic filter can tune the reflection phases of the second and third harmonics independently without affecting impedance at the fundamental frequency. The input impedance of the second harmonic is not changed when the input impedance of the third harmonic is changed and vice-versa.

Figures 5(a), (b), and (c) show the harmonic filter's input impedance transition when the harmonic tuners' reactance is changed. Here, $L_2$ and $L_3$ respectively denote the length of the second and third harmonic tuner's transmission lines. The filter output is terminated under a 50 ohm load, when the fundamental frequency is 2 GHz. Fig. 5(a) shows the input impedance when $L_2 = 2\,\text{mm}$ and $L_3 = 0\,\text{mm}$, (b) shows the same when $L_2 = 0\,\text{mm}$ and $L_3 = 0\,\text{mm}$, and (c) shows the same when
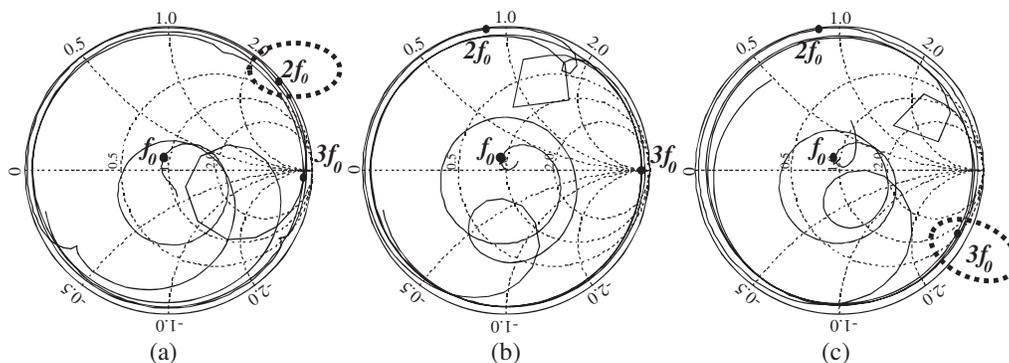


Figure 5: Simulated input impedance transition of the harmonic filter. (a) $L_2 = 2\,\text{mm}$, $L_3 = 0\,\text{mm}$, (b) $L_2 = 0\,\text{mm}$, $L_3 = 0\,\text{mm}$, (c) $L_2 = 0\,\text{mm}$, $L_3 = 1.33\,\text{mm}$.
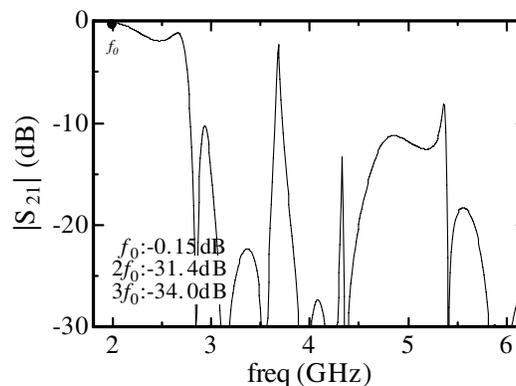


Figure 6: Simulated Transmission characteristics of the harmonic filter.

$L_2 = 0$ mm and $L_3 = 1.33$ mm. The change in $L_2$ causes a change only in the second-harmonic reflection phase without changing the impedance at the fundamental and third harmonic frequencies. The change in $L_3$ causes a change only in the third harmonic reflection phase without changing the impedance at the fundamental and second harmonic frequencies.

By making use of these characteristics, we can easily tune the harmonic load condition by tuning the second and third harmonic tuners in sequence. This circuit simplifies the precise phase tuning for the second and third harmonics for the achievement of highly efficient class-F operations.

Figure 6 shows the transmission characteristics of the harmonic filter. Insertion loss is $-0.15$ dB at the fundamental frequency, $-31$ dB at the second harmonic, and $-34$ dB at the third harmonic. The fundamental frequency passes through the filter, while the second and third harmonics are reflected by the filter.

## 3. CONCLUSION

In this paper, we used calculation to clarify the negative effects on class-F operation efficiency produced by second and third harmonic phase errors. When the third harmonic error is more than 20 degrees, the third harmonic cannot contribute to efficiency improvement if the phase error of the third harmonic takes such a value. As a solution to handle this issue, we introduced a harmonic reflection filter circuit for Class-F amplifiers that can provide tunable phases for the second and third harmonics independently. The harmonic filter reflects the second and third harmonics at the appropriate phase and has no effect on the fundamental frequency. The filter simplifies the precise phase tuning for the second and third harmonics and promises to enable the achievement of highly efficient class-F operations.

## REFERENCES

1. Cripps, S. C., *RF Power Amplifiers for Wireless Communications*, Artech House, 1999.
2. Raab, F. H., P. Asbeck, S. Cripps, P. B. Kenington, Z. B. Popovic, N. Pothecary, J. F. Sevic, and N. O. Sokal, "Power amplifiers and transmitters for RF and microwave," *IEEE Transactions on Microwave Theory and Techniques*, Vol. 50, No. 3, 814–826, Mar. 2002.
3. Snider, D. M., "A theoretical analysis and experimental confirmation of the optimally loaded and overdriven RF power amplifier," *IEEE Transactions on Electron Devices*, Vol. 14, No. 12, 851–857, Dec. 1967.
4. Tyler, V. J., "A new high-efficiency high-power amplifier," *Marconi Review*, Vol. 21, No. 130, 96–109, 3rd Quarter, 1958.
5. Sechi, F. N., "High efficiency microwave FET power amplifiers," *Microwave Journal*, 59–63, Nov. 1981.
6. Honjo, K. and Y. Kabayashi, "Ultra-high effciency power amplifier circuits using high fmax microwave transistors," *IEICE Transactions on Electronics,* Vol. J85-11, 953–960, Nov. 2002.
7. Nishiki, S. and T. Nojima, "High efficiency harmonic matching and reflection amplifier (HMRA)," *Proc. 1990 IEICE (Japan) Autumn Conf.*, B-31 1, 1990 (in Japanese).
8. Raab, F. H., "Maximum efficiency and output of Class-F power amplifiers," *IEEE Transactions on Microwave Theory and Techniques*, Vol. 49, No. 6, 1162–1166, Jun. 2001.

# Compact Microstrip Bandstop Filter with Controllable Triple Stopband Response

**Shry-Sann Liao**[1], **Shih-Yi Yuan**[1], **Yu-Lun Wu**[2], **and Ting-Yao Huang**[1]

[1]Department of Communication Engineering, Feng-Chia University
100, Wen-Hua Rd., Taichung 407, Taiwan, R.O.C.
[2]Ph.D. Program in Electrical and Communications Engineering, Feng-Chia University
100, Wen-Hua Rd., Taichung 407, Taiwan, R.O.C.

**Abstract**— The purpose of this study is to design a triple-band bandstop filter and miniaturize the circuit by bending stubs In this study, a general design methodology of a triple-band bandstop filter with compact and controllable triple stopband response is proposed. A compact-size triple-band bandstop filter with center frequencies 0.9, 1.57 and 2.1 GHz was implemented and verified. Simulated and measured results are in good agreement.

## 1. INTRODUCTION

Recently, microwave passive components and devices with multi-band operation become more and more important in modem communication systems and have been focused much attention for the miniaturization and multifunction requirement of the portable equipments [1–3]. Multiple band microwave components with compact size and low cost are required and studied. On the other hand, multi-bandstop filters are desired for their effective suppression of spurious signals in wireless communication systems. Other advantage is its low passband insertion loss and group delay due to its resonators resonates in the stopband rather than in the passband.

There are few papers about multiband bandstop filter. The paper [4] proposed one equilateral triangle to get the triple stopband performance. Y. Wang proposed single ring resonator structure [5] to get three bandstop responses by changing the gap of ring resonator. The problems in the conventional design of dual-band bandstop filter are large size and the construction limited in dual-band In this study, a general design methodology of triple-band bandstop filter with compact and controllable triple stopband response is proposed.

## 2. DESIGN DESCRIPTIONS

The structure of the conventional n-order bandstop filter, using series LC resonators and admittance inverters, is shown in Fig. 1. The parameters' including inductors $L_i$, capacitors $C_i$ and admittance inverter $J_{i,i+1}$ are described by the following formulas [6]:

$$L_i = \frac{1}{\omega_a^2 C_i} = \frac{\Delta g_i}{\omega_a Z_0} \quad (i = 1 \text{ to } n) \tag{1}$$

$$J_{0,1} = \sqrt{\frac{\omega_a G_0 C_1}{\Delta g_0 g_1}} \tag{2}$$

$$J_{i,i+1} = \frac{\omega_a}{\Delta} \sqrt{\frac{C_i C_{i+1}}{g_i g_{i+1}}} \quad (i = 1 \text{ to } n-1) \tag{3}$$

$$J_{n,n+1} = \sqrt{\frac{\omega_a C_n C_{n+1}}{\Delta g_n g_{n+1}}} \tag{4}$$

where $\omega_a$ is the center angular frequency of the bandstop filter, $\Delta$ is the ratio of bandwidth, and $g_i$ $(i = 0, 1, 2,\dots n+1)$ is the element values of Chebyshev prototype lowpass filter. The series LC resonator is replaced by the open stub of a quarter-wavelength microstrip line. The length of the open stub is quarter-wavelength depends on its resonant frequency $\omega_a$.

The tripleband bandstop filter is considered by adding the other two different stopband circuits to the original single stopband circuit by shunt their LC series resonance circuits, is shown in Fig. 2. Where $L_{x,n}$ and $C_{x,n}$ is equivalent inductance and capacitance which corresponding to the center

frequency $\omega_0$ and $\omega_1 < \omega_2 < \omega_3$. Each formula of the J-inverter is similar to (2)–(4) expect $\omega_a$ has to modify by $\omega_0$,

$$\omega_0 = \frac{\omega_1 + \omega_2 + \omega_3}{3} \tag{5}$$

The shunt circuit of Fig. 2 can be replaced by $L_{eq,n}$ and $C_{eq,n}$, which is shown in Fig. 3.

$$L_{eq,i} = \frac{1}{\omega_0^2 C_{eq,i}} = \frac{\Delta g_i}{\omega_0 Z_0} \quad (i = 1 \text{ to } n) \tag{6}$$

The problems of triple-band bandstop filter are the bands are too close and bandwidths are too wide so that stopbands affect among them, and the position of the third stub which corresponding the third stopband. The first problem is solved by changing the impedance of the J-inverter. The Fig. 4(a) shows a conventional dual-band bandstop filter [6], which connects open stubs in two sides of main line (J-inverter). Consider to rearrange the position of the open stub from two sides to one side of J-inverter. Then the other side leaves the space to insert the third stub. However, the stopband shifts and performance decreases due to the coupling of two adjacent open stubs. Therefore, adjusting the distance of two open stubs and bending stubs not only decrease the coupling of two adjacent open stubs, but also miniaturizing the circuited dimension, as show in Fig. 4(b).
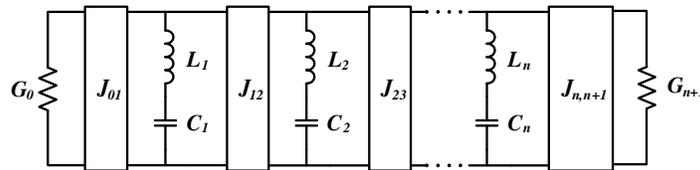


Figure 1: A conventional $n$-order bandstop filter by LC series resonant and the J-inverter.
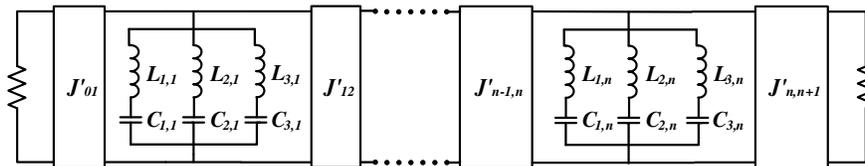


Figure 2: The $n$-order triple-band bandstop filter.
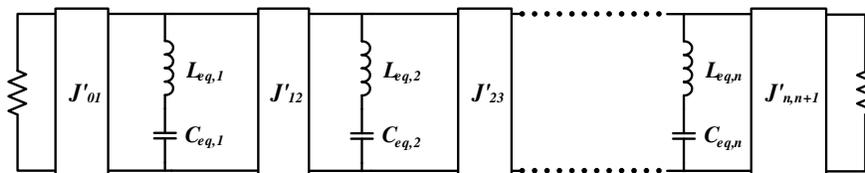


Figure 3: The equivalent circuit of $n$-order triple-band bandstop filter.
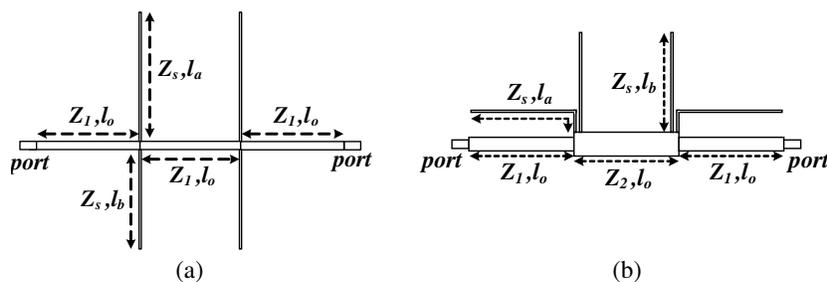


Figure 4: (a) A conventional dual-band bandstop filter. (b) The compact circuit of (a) with bending stubs.
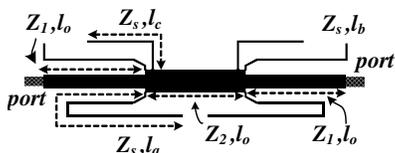
Figure 5: A compact triple-band bandstop filter.
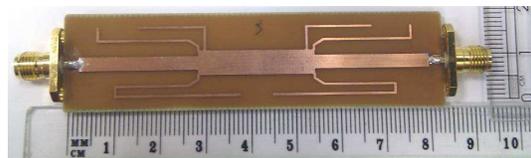


Figure 6: The photograph of the fabricated triple-band bandstop filter.
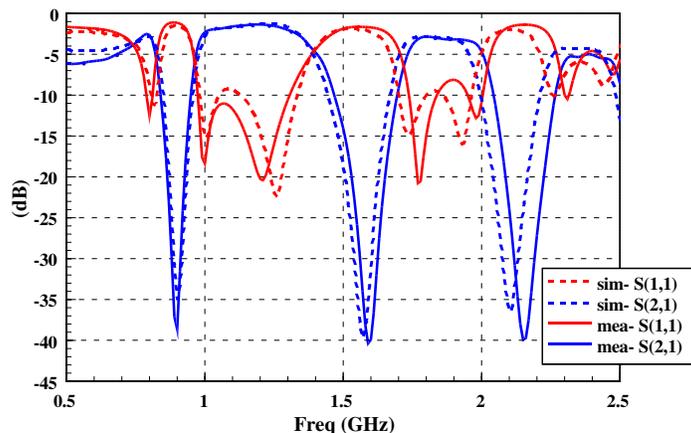


Figure 7: The simulated and measured results of the triple-band bandstop filter.

## 3. IMPLEMENTATION AND MEASUREMENTS

For verification, a compact-size microstrip triple-band bandstop filter was designed, simulated, and fabricated. The center frequencies of the triple-band bandstop filter are 0.9, 1.57 and 2.1 GHz, respectively. The parameters were calculated following the designed description discussed in Section 2. A full-wave IE3D simulator was used for all simulations, and the filter was constructed using an FR4 substrate with $\varepsilon_r = 4.6$, $\tan\delta = 0.022$, thickness $= 0.8$ mm, and metal thickness $= 0.02$ mm. The length of J-inverter $l_0$ (25.5 mm), is shown in Fig. 5, is quarter-wavelength of $\omega_0$, and is determined by using (5).

Therefore, the impedance $Z_1$, $Z_2$ and $Z_s$ are 32.19 Ω, 20.75 Ω. and 91.5 Ω, respectively. The length of open stub $l_a$ (46.0 mm), $l_b$ (25.8 mm) and $l_c$ (19.1 mm) are quarter-wavelength of 0.9, 1.57 and 2.1 GHz, respectively. The circuited dimension is reduced more by using the branch of bending. A 2-order triple-band bandstop filter circuit is shown in Fig. 6.

The size of this circuit is about $15.2 \times 82.4$ mm$^2$. The microstrip filter is fabricated and then measured using a network analyzer E5071B. The comparison of measurement and simulation frequency response is shown in Fig. 7.

The three transmission zeros are $-38.66$ dB at 0.9 GHz, $-40.36$ dB at 1.59 GHz, and $-39.92$ dB at 2.15 GHz. The stopbands for less than $-20$ dB are 0.86 to 0.93 GHz, 1.53 to 1.66 GHz and 2.04 to 2.23 GHz, respectively. Simulated and measured results are in good agreement.

## 4. CONCLUSIONS

The design and implementation of a compact-size triple-band bandstop filter has been described and verified. The center frequencies of the triple-band bandstop filter are 0.9, 1.57 and 2.1 GHz, respectively. The three transmission zeros are $-38.66$ dB at 0.9 GHz, $-40.36$ dB at 1.59 GHz, and $-39.92$ dB at 2.15 GHz. The size of this compact circuit is about $15.2 \times 82.4$ mm$^2$ which has been reduced to 20% in the circuit area compared to the conventional design ($77 \times 82.4$ mm$^2$). The problem of the coupling of two adjacent open stubs can be solved by adjusting the distance of two open stubs and bending stubs.

## REFERENCES

1. Chen, J., C.-H. Liang, J.-Z. Chen, and B. Wu, "Analytical design of triple passband of microwave filters using frequency transformations method," *Microwave and Optical Technology Letters*, Vol. 53, No. 10, 2199–2201, Oct. 2011.

2. Wang, C., P. Xu, B. Li, and Z.-H. Yan, "A compact and multiband antenna for WLAN and WiMAX applications," *Microwave and Optical Technology Letters and EMC Technologies for Wireless Communications*, Vol. 53, No. 9, 2016–2018, Sep. 2011.

3. Lung, C.-K., K.-S. Chin, and J. S. Fu, "Tri-section Stepp ed-imp edance resonators for design of dual-band bandstop filter," *Proceedings of 39th European Microwave Conference*, 771–774, Sep. 2009.

4. Xiao, J.-K., X.-P. Lu, H.-F. Huang, and W.-L. Dai, "Muti-mode band stop filter using defected equilateral triangular patch resonator," *International Symposium on Antennas Propagation and EM Theory (ISAPE)*, 1252–1255, Nov. 2010.

5. Wang, Y., J. Zhou, and W. Hong, "A multiband bandstop filter using a single ring resonator for a wireless access communication system," *Microwave Journal*, Vol. 54, No. 3, 102, Mar. 2011.

6. Matthaei, G., L. Young, and E. M. T. Jones, *Microwave Filter, Impedance-Matching Networks, and Coupling Structures*, Artech House, Norwood, MA, 1980.

# The Design of 40 GHz Active Power Splitter

**Ching-Ying Huang**[1], **Dow-Chih Niu**[2], **Robert Hu**[1], **and Christina F. Jou**[1]

[1]School of Electrical Engineering, National Chiao Tung University, Hsinchu, Taiwan
[2]Chun Shan Institute of Science and Technology, Taoyuan, Taiwan

**Abstract**— Based on the idea of distributed amplifier, a wideband active power divider is designed using 90 nm CMOS process to provide positive gain and superb isolation between its two output ports from quasi-DC up to 40 GHz. Compared with our previously demonstrated 20 GHz one, the requirement of good input matching over the whole bandwidth poses an even severe constraint in the development of this 40 GHz active power splitter, as the tradeoff between gain and bandwidth becomes more intricate now. Mutual-coupling inductors are therefore adopted in the circuit's artificial transmission line to improve both the input return loss and allow the use of larger transistors in the gain stage. The fabricated circuit exhibits good input and output matching and has better than 10 dB output-port isolation across the whole band, with the bias of 1.8 V and 190 mA. Related circuit theories and mathematics will also be presented in this paper.

## 1. INTRODUCTION

Power splitter is one of the critical components used in beam-forming or array system, and it can be constructed by combining multi-section transmission lines so as to extend its bandwidth; however, this passive wideband power splitter fails to provide good isolation between its two output ports across the whole bandwidth, especially when quasi-DC frequency is considered [1]. Previously, with this in mind, a DC-20 GHz active power splitter design has been designed using commercial 0.18 μm CMOS process, which has 7 dB gain and output-port isolation better than 30 dB from quasi-DC to 20 GHz. In this manuscript, we want to further extend the bandwidth to 40 GHz using 90 nm CMOS process so that it is eligible for use in fiber-optic communication system and other broadband scientific instrumentations. In the following, we will detail how the use of mutual-coupling inductance can effectively remove the constraints imposed on bandwidth and the underlying mathematics. Simulated results and the circuit layout will then be presented, followed by measurement and discussions.

## 2. DC-40 GHz ACTIVE POWER SPLITTER DESIGN

In order to retain both wideband and symmetry for the two output branches, the design of active power splitter borrows the concept of distributed amplifier circuit. As shown in Figure 1, the schematic can be divided into three parts. The first is the input artificial transmission line where $L_{in}$ is the lumped spiral inductor and $C_{in}$ is the equivalent input capacitance of the gain cell; the second part is the gain cell itself, which contains two cascode transistor stages; the third is the output artificial $L_{out}C_{out}$ transmission line. For simplicity, the small but still non-zero series resistance and shunt admittance of all these lines are not included in the following analysis. Theoretically, the system impedance $Z_0$ of an infinite LC line can be calculated as [2]

$$Z_0 = \sqrt{\frac{L}{C}\left(1 - \frac{\omega^2}{\omega_0^2}\right)}, \tag{1}$$

where $\omega_0 = 2/\sqrt{LC}$. So for the distributed amplifier we can see that in order to maintain a 50 Ω input impedance and large transconductance (the latter in fact implies a large transistor and therefore a large input capacitance $C$), the conductance $L$ needs to be large too. This in turn poses a limit to the available bandwidth. By treating the active power splitter as a dual-output distributed amplifier, with twice the equivalent input capacitance now, the bandwidth will be halved if we want to maintain the same gain. If smaller transistors (roughly half the original size) are employed to sustain the bandwidth, then the overall voltage gain will be reduced by half, i.e., 6 dB, at least in theory. In our previously designed power splitter using 0.18 μm CMOS process, smaller transistors are indeed been adopted to ensure the 20 GHz bandwidth, while the gain boosting are made through the use of source and gate inductors inside the cascode gain stages [3].

In this 40 GHz circuit design, in addition to the aforementioned techniques and the advanced 90 nm CMOS process, something more robust has to be resorted to and it is the mutual-coupling
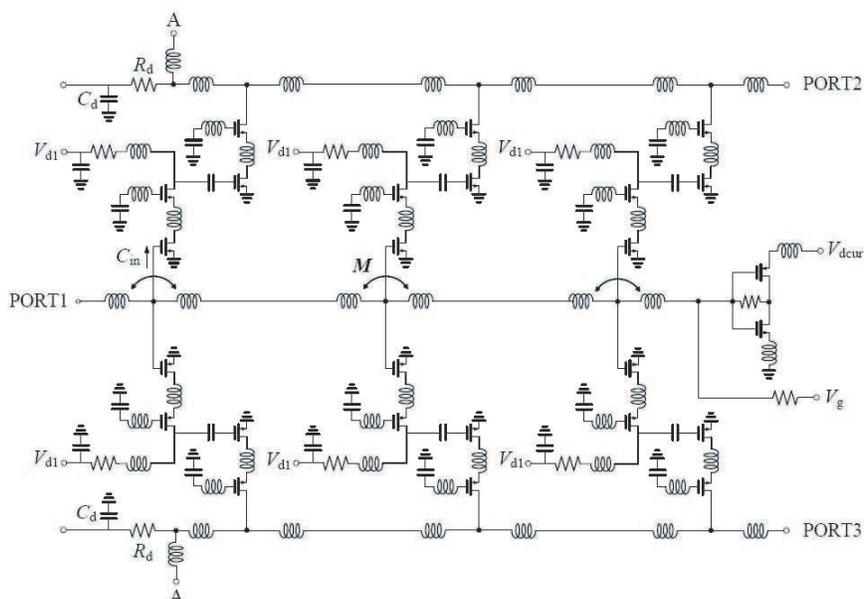
Figure 1: Schematic of the DC-40 GHz active power divider where port 1 on the left is for input while ports 2 and 3 on the right are for output. Each gain cell is made of two cascade transistor circuits. Not all the gate biases for the transistors are indicated here.



(a)                                          (b)
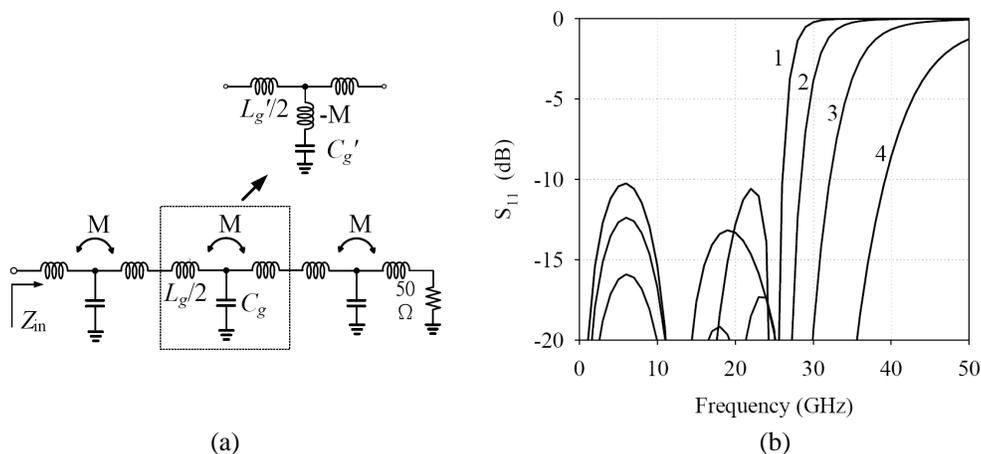
Figure 2: Artificial mutual-coupling transmission line and the simulated input reflection coefficient. (a) By allowing mutual-coupling $M$, a negative inductor does exist and is in series with the capacitor, as indicated by the arrow. (b) Curves 1, 2, 3, and 4 correspond to $M$ of 0, 0.2, 0.4, and 0.6, respectively. Apparently, with increasing $M$, the bandwidth becomes wider.

inductance [4]. In Figure 2(a), by allowing positive mutual coupling $M$ between conductors, a more complicated LC T-type circuit can be derived from the original LC network, as

$$L'_g = 0.5L_g + M; \quad C'_g = \frac{C_g}{[1 + \omega^2 M * C_g]} \tag{2}$$

And the cutoff frequency can therefore be extended as

$$f'_g = \frac{1}{\pi\sqrt{L'_g C'_g}} = \frac{1}{\pi\sqrt{L_g C_g * \left(1 - \frac{2M}{L_g}\right)}} \tag{3}$$

Figure 2(b) shows the simulated input return loss for a finite LC transmission line where $C_g$ is 0.2 pF and $L_g$ is 0.3 nH. With $M$ set at 0, 0.2, 0.4, and 0.6, the bandwidth (as defined by input reflection smaller than $-10$ dB) is increasing accordingly. With the bandwidth constraint greatly

(a)　　　　　　　　　　　　　　　　(b)
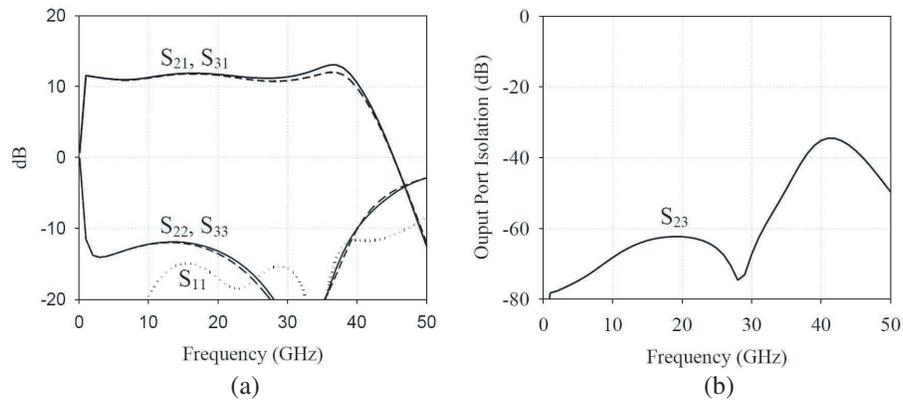
Figure 3: Simulated $S$-parameters of the DC-40 GHz active power splitter.
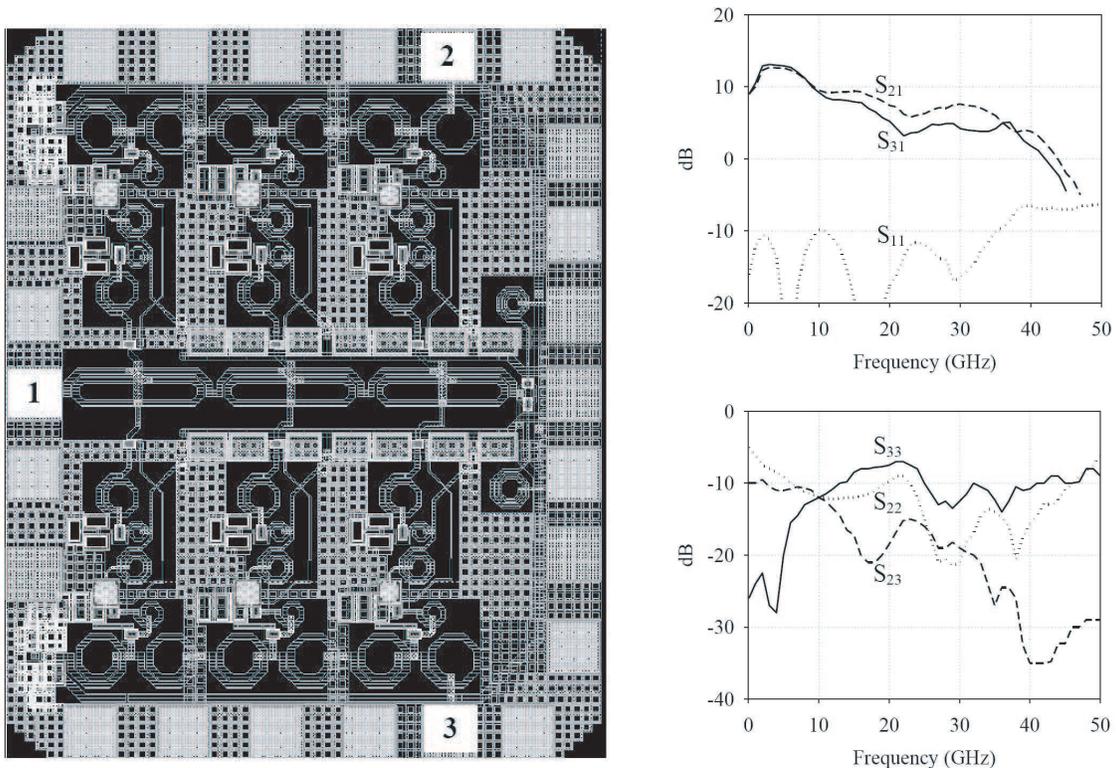


Figure 4: Layout of the 40 GHz power splitter and its measured results. Port 1 is the input, and ports 2 and 3 are the output.

released, large transistors can now be used more freely for achieving larger gain, especially at high frequency. Figure 3 shows the simulated results of this active power splitter design, which has its gain higher than 10 dB and both its input and output return loss better than 10 dB; the output-port isolation is larger than 40 dB across the whole bandwidth.

## 3. MEASURED RESULTS

Figure 4 shows the photograph of the splitter circuit and its measured results. This circuit is fabricated using commercial 90 nm CMOS process and the chip size is $0.82 \times 0.98 \, \text{mm}^2$. The layout is arranged to be as symmetric as possible to ensure near-identical performance of the two outputs. With supply voltage $V_d = 1.8$ Volt and current $I_d = 105$ Amp, the total power consumption is 190 mWatt; the gate bias voltage $V_g$ is 0.8 Volt, with negligible current in this case. In the on-wafer measurement, both input and output reflection coefficients are close to the simulated results; however, their gain responses fail to meet the expectation, especially at high frequency. One speculation for the poor gain performance is the lack of well-defined ground sheet, since so many

components have to be crammed into this small chip; rather, we use wide metal grids to emulate the ground but, apparently, this ground substitution is insufficient. In our next design iteration, we plan to designate the whole metal 1 and 2 layers as ground in expectation of better results. As for the limited output-port isolation, it is due to the signal leakage through the commonly-shared DC bias bus. This can be resolved by applying two separate bias buses on chip: one for port 2 and the other for port 3.

## 4. CONCLUSIONS

We have successfully demonstrated the design of 40 GHz active power splitter using 90 nm CMOS process in the simulation. In addition to the gate and source inductors in the cascode gain stages for gain boosting, the technique of mutually-coupled inductor is also employed at the input artificial transmission line to effectively extend the bandwidth even in the presence of large transistors. Though still run short of the expectation, a few more design iterations in the near future will surely improve the measured results.

## ACKNOWLEDGMENT

## REFERENCES

1. Huang, J. Y., H. I. Wu, R. Hu, C. F. Jou, and D. C. Niu, "A DC-20 GHz CMOS active power divider design," *Asia-Pacific Microwave Conference*, 524–526, Yokohama, Japan, Dec. 2010.
2. Aitchison, C. S., "The intrinsic noise figure of the MESFET distributed amplifier," *IEEE Trans. Microwave Theory Tech.*, Vol. 33, No. 6, 460–466, Jun. 1985.
3. Kimura, S. and Y. Imai, "0–40 GHz GaAs MESFET distributed baseband amplifier IC's for high-speed optical transmission," *IEEE Trans. Microwave Theory Tech.*, Vol. 44, No. 11, 2076–2082, Nov. 1985.
4. Entesari, K., A. R. Tavakoli, and A. Helmy, "CMOS distributed amplifiers with extend flat bandwidth and improved input matching using gate line with coupled inductors," *IEEE Trans. Microwave Theory Tech.*, Vol. 57, No. 12, 2862–2871, Dec. 2009.

# Dielectric Measurement Using a Planar Ring Sensor for Low-loss Powder Form Materials

**K. Y. You and H. K. Mun**

Radio Communication Engineering Department, Universiti Teknologi Malaysia
UTM Skudai 81310, Malaysia

**Abstract**— This paper uses planar ring sensor for dielectric measurements of low-loss powder materials by applying conversion of measured reflection coefficient to relative dielectric constant via a lumped-element model. The ring sensor has been fabricated using 1.58 mm thickness of FR4 substrate and designed to operate at a frequency range between 1 GHz to 3 GHz at room temperature. This sensor was tested on free space and various types of powder. In this study, the predicted dielectric constant is in general agreement with the results obtained using a commercial dielectric probe.

## 1. INTRODUCTION

The first planar ring technique was used to measure the dielectric properties of materials based on resonant methods [1]. The planar ring resonator methods have since become popular due to the dielectric response of material under test quite sensitive to the radiation fields from the planar ring. Furthermore, the resonant equation that is used to predict the value of the dielectric materials is simple and easy. However, a single small resonator ring can-not be applied in the broadband dielectric measurements due to the fact that the resonant phenomenon only exists at a certain frequency [1–3].

In this study, we have attempted to produce an empirical equation to describe the input impedance properties of the planar ring from 1 GHz to 3 GHz. This empirical equation is modeled as a function of the dielectric constants and loss tangents for the materials under test. Finally, the dielectric constant of the material can be predicted from the reflection/transmission measurement via the formulation. The procedures of this study are described in Sections 2, 3 and 4.

## 2. METHODOLOGY

In this work, the microstrip ring sensor has been designed using Microwave Office software (AWR) for operation frequency range between 1 and 3 GHz, where its resonance frequency is located at 2.4 GHz. The ring sensor has been constructed using low cost FR4 substrate with thickness $h = 1.58$ mm, relative permittivity $\varepsilon_r = 4.2$ and loss tangent $\tan \delta = 0.02$. All the dimensions of sensor have been sketched by using AutoCAD software and printed on transparent paper, then delineated on the substrate by standard photolithography and etching. The sensor was then held on an aluminum ground with two SMA connectors, which allowed it to be connected to the ports of E5071C Network Analyzer. Finally, the sensor was covered with an acrylic holder as shown in Figure 1.

The dimensions for the ring sensor were tabulated in Table 1.

The powder samples were placed into the sample holder up to a height of 27 mm. The reflection coefficient $\Gamma$ of powder samples have been measured using the E5071C Network Analyzer at a frequency range between 1 GHz to 3 GHz. Before measurements, calibration kits (open, short and

Table 1: Dimensions of ring sensor.

| **Dimension** (mm) | |
|---|---|
| Width of the feed line $W$ | 3.09 |
| Width of the ring $W_r$ | 13.05 |
| Inner ring radius $R_i$ | 4.30 |
| Outer ring radius $R_o$ | 17.35 |
| length of 50 Ω feed line $l$ | 8.15 |
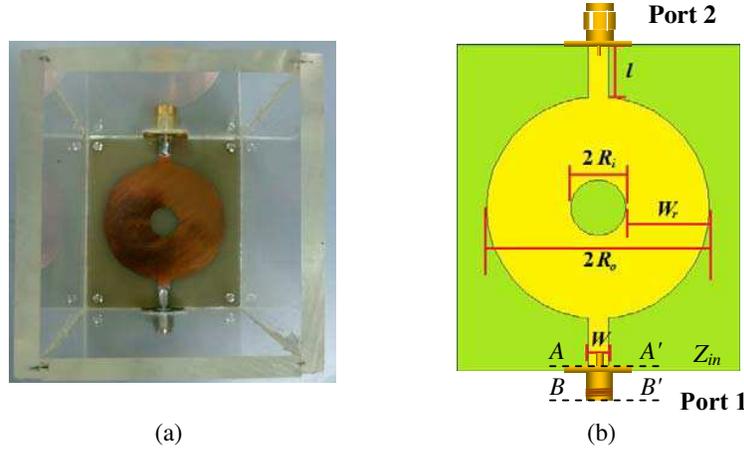
Figure 1: (a) Actual configuration and (b) dimensions of the ring sensor.
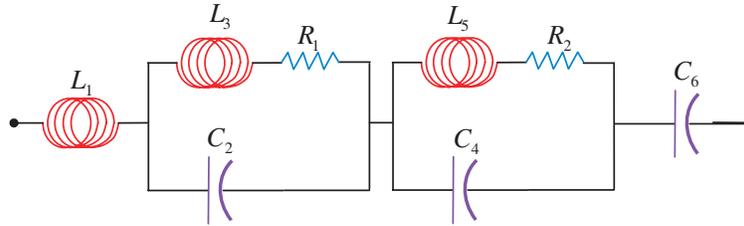


Figure 2: Corresponding circuit for the input impedance, $Z_{in}$ of microstrip ring sensor.

load) have been used for full two-port SOLT calibration at the both ends of $50\,\Omega$ coaxial cable. The reflection port 1 was connected to one end of the coaxial cable (plane $BB'$), while the transmission port 2 was connected to the other end of the cable. The reflection coefficient $\Gamma_{AA'}$ at transition junction between the SMA connector coaxial line and the $50\,\Omega$ microstrip line (plane $AA'$) is calculated from [4]:

$$\Gamma_{AA'} = \Gamma_{BB'} \exp(2jk_c z) \tag{1}$$

where $\Gamma_{BB'}$ is the reflection coefficient at the SMA connector, $k_c$ is the propagation constant and the symbol $z$ is the length in meters (including fringing effect length) for the coaxial line. The calculated reflection coefficient $\Gamma_{cal}$ is determined by Equation (2) below.

$$\Gamma_{cal} = \frac{Z_{in} - 50}{Z_{in} + 50} \tag{2}$$

Two port measurements have been performed but only one port impedance is investigated in this study. The input impedance $Z_{in}$ at port 1 of the ring sensor is modeled by lumped element [5] as expressed in Equation (3) with corresponding circuit shown in Figure 2. The input impedance $Z_{in}$ is only applicable for the values of relative permittivity $\varepsilon_r$ from 1 to 4. Capacitance $C$ and inductance $L$ in Equation (3) are corresponding to the propagation of electric and magnetic field within the sensor respectively; while resistance $R$ represents the conductance loss due to losses within the transmission line and imperfect soldering.

$$Z_{in} = j\omega L_1 + \frac{1}{j\omega C_2 + \left[\frac{1}{j\omega L_3 + R_1}\right]} + \frac{1}{j\omega C_4 + \left[\frac{1}{j\omega L_5 + R_2}\right]} + \frac{1}{j\omega C_6} \tag{3}$$

For powder with a broad range of permittivity values, optimizing $RLC$ values to simulation is easier than measuring them. The $RLC$ values in Equation (3) are obtained by optimizing Equation (3) to the AWR simulation results. The $RLC$ values obtained are fitted with the relative permittivity $\varepsilon_r$ and loss tangent $\tan\delta$ by using the regression polynomial method. The polynomial functions of relative permittivity $\varepsilon_r$ and loss tangent $\tan\delta$ for the $RLC$ values are shown in Table 2. The predicted dielectric constant $\varepsilon_r$ of powder samples are calculated indirectly from the measured reflection coefficient $\Gamma_{AA'}$ which was shifted by using Equation (1). The value of predicted dielectric

Table 2: Parametric $RLC$ in (3) as a polynomial functions of relative permittivity and loss tangent.

| Parametric element, $RLC$ | Polynomial Expression |
|---|---|
| Capacitance $C$ (F) | $C_2 = (-4.7335 \times 10^{-13} \tan^2 \delta + 4.8538 \times 10^{-13} \tan \delta + 1.9522 \times 10^{-13})\varepsilon_r$ $+1.4129 \times 10^{-13} \tan^2 \delta + 1.1587 \times 10^{-13} \tan \delta + 5.5086 \times 10^{-12}$ $C_4 = (3.4611 \times 10^{-14} \tan^2 \delta - 1.0978 \times 10^{-13} \tan \delta + 1.2797 \times 10^{-13})\varepsilon_r$ $+1.4402 \times 10^{-14} \tan^2 \delta + 3.0488 \times 10^{-16} \tan \delta + 2.2011 \times 10^{-12}$ $C_6 = 15.0 \times 10^{-12}$ |
| Inductance $L$ (H) | $L_1 = (-1.0252 \times 10^{-10} \tan^2 \delta + 1.7778 \times 10^{-10} \tan \delta + 5.8553 \times 10^{-11})\varepsilon_r$ $+1.8259 \times 10^{-10} \tan^2 \delta - 2.1333 \times 10^{-10} \tan \delta + 2.5189 \times 10^{-9}$ $L_3 = (5.8098 \times 10^{-11} \tan^2 \delta - 8.0309 \times 10^{-11} \tan \delta + 8.0213 \times 10^{-12})\varepsilon_r$ $-5.8997 \times 10^{-12} \tan^2 \delta - 2.6381 \times 10^{-11} \tan \delta + 8.5077 \times 10^{-10}$ $L_5 = 0.89 \times 10^{-9}$ |
| Resistance $R$ (Ω) | $R_1 = (6.1004 \times 10^{-1} \tan^2 \delta - 4.4682 \times 10^{-1} \tan \delta + 2.4278 \times 10^{-1})\varepsilon_r$ $-7.1606 \times 10^{-1} \tan^2 \delta + 1.0992 \tan \delta + 1.3222$ $R_2 = 2.50$ |
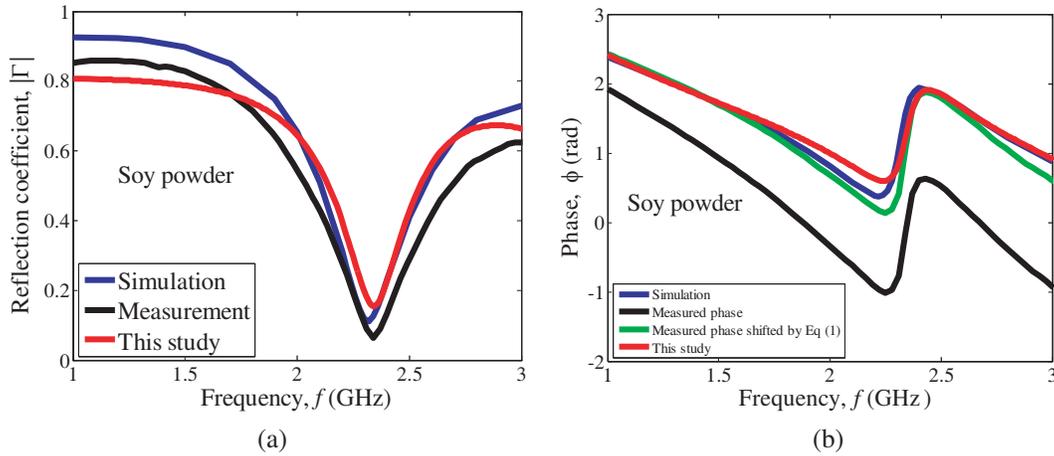


Figure 3: Variation in (a) magnitude reflection coefficient $|\Gamma|$ and (b) phase ⌀ with frequency for ring sensor tested with soy powder.

constant $\varepsilon_r$ was obtained by minimizing the difference between the measured reflection coefficient $\Gamma_{AA'}$ and the calculated reflection coefficient $\Gamma_{cal}$ through an error function given as follows.

$$\xi = \text{Re}\,(\Gamma_{cal}) - w\text{Re}\,(\Gamma_{AA'}) \qquad (4)$$

where $w = 0.98$ denotes the weight parameter.

## 3. RESULTS AND DISCUSSIONS

Figures 3(a) and (b) show the comparison of the simulated, measured and calculated reflection coefficient $\Gamma$ ring sensor tested with soy powder. There are small deviations between the measurement and simulation for the magnitude of reflection coefficient $|\Gamma|$ for soy powder. The deviations are due to the slight change of permittivity $\varepsilon_r$ with frequency for low cost FR4 substrate in actual case, which however the $\varepsilon_r$ is assumed constant as $\varepsilon_r = 4.2$ in the simulation design. Also, the quality of SMA connectors and soldering parts also contribute to the error. In addition, the calculated magnitude of reflection coefficient $|\Gamma|$ for soy powder in this study is considerable close to the measurement and simulation results.

In Figure 3(b), the measured phase ⌀ is shifted to match the simulation result by applying Equation (1) with $z = 0.0244\,\text{m}$. The simulations, measured with a shifted and calculated phase

Table 3: Comparison between the predicted dielectric constant and measured dielectric constant.

| Samples | Dielectric constant $\varepsilon_r$ at 2.64 GHz | | Dielectric constant $\varepsilon_r$ at 2.70 GHz | |
|---|---|---|---|---|
| | Commercial dielectric probe | This study | Commercial dielectric probe | This study |
| Air | 0.9822 | 1.2761 | 0.9988 | 1.1767 |
| Soy powder | 2.3882 | 2.9377 | 2.3917 | 3.0244 |
| Barley powder | 3.3748 | 3.1002 | 3.3734 | 3.1808 |
| Wheat powder | 3.4835 | 3.4018 | 3.4792 | 3.2727 |
| Rice powder | 3.2161 | 3.7735 | 3.2094 | 3.8512 |

shift ø in this study have almost the same result. In this study, the designed ring sensor has been tested with air, soy, barley, wheat, and rice powder for dielectric constant $\varepsilon_r$ prediction. The compared results between the predicted dielectric constant and measured dielectric constant by using 85070E Agilent dielectric probe at 2.64 GHz and 2.70 GHz are illustrated in Table 3.

## 4. CONCLUSIONS

This study is a preliminary study for developing lumped-element impedance model of planar ring sensor for dielectric measurements of low-loss powder. The model has been verified through comparison of predicted dielectric constants with those measured by commercial dielectric probe for air and various types of powder.

## ACKNOWLEDGMENT

## REFERENCES

1. Troughton, P., "Measurement technique in microstrip," *Electronics Letters*, Vol. 5, No. 2, 25–26, 1969.
2. Somporn, S., W. Thanakit, S. Tanee, and A. Prayoot, "A microstip folded resonator sensor for measurement of dielectric constant," *Proceedings of ECTI*, 245–248, Krabi, Thailand, May 14–17, 2008.
3. Heinola, J. M., K. P. Utti, J. P. Strom, M. Kettunen, and P. Silventoinen, "A strip line ring resonator method for determination of dielectric properties of printed circuit board material in function of frequency," *Annual Report Conference on Electrical Insulation and Dielectric Phenomena, CEIDP'04*, 692–695, Boulder, Colorado, USA, Oct. 2004.
4. You, K. Y., J. Salleh, Z. Abbas, and L. L. You, "A rectangular patch antenna technique for the determination of moisture content in soil," *PIERS Proceedings*, 850–854, Cambridge, USA, Jul. 5–8, 2010.
5. Yarman, B. S., *Design of Ultra Wideband Antenna Matching Networks*, Springer Science, Germany, 2008.

# Linearized 2.4 GHz Power Amplifier

**Bilge Türkel and Mehmet Fatih Çağlar**

Department of Electronics and Communication Engineering, Faculty of Engineering & Architecture
Süleyman Demirel University, Isparta, Turkey

**Abstract**— This study proposes a 2.4 GHz class-A single stage power amplifier, whose linearity performance is enhanced by using ATF501P8 pHEMT transistor. For improving linearity performance of power amplifier a nonlinear diode-based power amplifier linearization technique has been applied which component values of linearizer circuit is optimized. Optimum linearized power amplifier can transmit 26.45 dBm output power for 15 dBm input power with 11.45 dB transducer power gain and 31.089% power added efficiency.

## 1. INTRODUCTION

The power amplifier (PA) is one of the key components in mobile communication handsets determining the power consumption and, thus, the battery life of the handsets, and has seen a reduction in module size, supply voltage, and quiescent current. Moreover, in order to accommodate higher data rate and global roaming around the multistandard communication environments, linearity and multimode/multiband capability are being highlighted as the most significant issues of PAs for recent mobile handsets [1]. One of the largest current sinks in a radio is the transmit PA; thus, this is an obvious target for improvement. The basic idea is to take an already efficient PA, which is inherently nonlinear, and introduce additional circuitry to make it more linear [2]. However many trade-off situations have strengthen design complexity in linear and nonlinear simulation steps. Optimization techniques for ambitious final layout have needed before circuit has been printed.

RF PAs are large signal devices that exhibit nonlinear effects with increasing input power. The important parameters that define the performance of an RF PA are gain, phase deviation, 1-dB compression point, amplitude-to-amplitude (AM-AM) distortion and amplitude-to-phase (AM-to-PM) distortion [3].

Nonlinear distortion produced in a given circuit can be reduced by pre- or post-distorting the signal applied to or from the circuit. Such complementary distortion cannot reduce the original distortion to zero in practice because of distortion of distortion, but it can result in greatly reduced output distortion over a limited amplitude range [4]. By far the most popular approach in handheld mobiles is the well-known RF pre-distortion. The approach tends to be stable and provides modest efficiency enhancement. It has advantages historically in terms of miniaturized size and low complexity, making it attractive for monolithic implementations [5].

In this study, to design a highly linearized 2.4 GHz PA, a diode-based linearizer circuit which elements optimized has been used, which also involves input single-stub matching networks that provides suitable gain. Firstly a highly linear RF power transistor has been selected. After setting DC conditions for A-class working and needed output power, input and output matching networks and linearizer circuit have been simulated with whole circuit. Agilent's ADS software has been used for simulation and optimization. The results of performance and design variables which are fundamental output power ($P_{out}$), transducer power gain ($G_T$), power added efficiency (PAE), total harmonic distortion (THD), gain reduction, AM-AM distortion and AM-PM distortion have been presented in comparison manner as with linearizer circuit or not.

## 2. POWER AMPLIFIER DESIGN

Preferred ADS software has unique advantages in use of simulation of RF/microwave circuit and system design. Such as the friendly interface, model base of integrity and RF performance simulation and optimization of convenience [6]. For designing any kind of amplifier, e.g., low noise amplifier (LNA), driver amplifier or PA etc. the first thing to do is choosing proper transistor. In this work we have been willing to design a highly linear and high efficiency PA so ATF501P8 PHEMT discrete transistor has been chosen Nonlinear package model of transistor has been used especially for practical expectations.

Secondly a suitable biasing point of the transistor has been investigated. Thereafter selecting proper biasing point of the transistor biasing circuit has been designed. To obtain DC characteristics a common source voltage divider circuit has been preferred and biasing circuit has been completed

by combining block of capacitors and inductors. These blocks will behave as a DC feed-RF block in the DC trajectory [7]. Afterward designing biasing circuit it has been needed to verify given $s$-parameters of the transistor. At chosen biasing point, the $s$-parameter simulation of nonlinear model of the transistor has been compared with $s$-parameters of the transistor given at datasheet. The results have enough approximation each other and this has proved that linear simulation $s$-parameter file values in datasheet or obtained $s$-parameters could have been used. To gain more realistic simulation results we have preferred to apply $s$-parameters of simulation including nonlinear model of the transistor. The stability analysis of the transistor has been the next step. It is highly recommended that the amplifier circuit is made unconditionally stable at all frequencies to ensure that it does not produce unwanted oscillations [8]. Simulation results have shown that transistor was not unconditional stable in the frequency range of 0.1–18 GHz so it has been needed to set transistor unconditional stable. An ADS Amplifier Design Guide that stabilizes an unstable circuit is used to stabilize the transistor circuit. A negative feedback has been applied between drain and gate including a capacitor and a resistor.

After achieving the transistor unconditional stable in the operating frequency range, the output matching network has been designed with load-pull technique and the input matching has been designed with maximum available gain method. Both of them have single-stub matching networks.

## 3. LINEARIZER CIRCUIT OPTIMIZATION

Haskins et al. has proposed the initial results in a study on a diode-based PA linearization technique [2]. To linearize PA they have optimized the diode parameters. In this study, to improve linearity performance of PA the diode parameters haven't optimized like C. Haskins et al.'s work. All component values of linearizer circuit have been optimized to investigate the best biasing point for realistic diode biasing. HMPP-3860 single Minipak surface mount RF PIN diode has been handled As shown in Figure 1, the linearizer circuit with nonlinear equivalent model of diode and optimized circuit element values has been used. The block diagram of the whole PA circuit is shown in Figure 2.
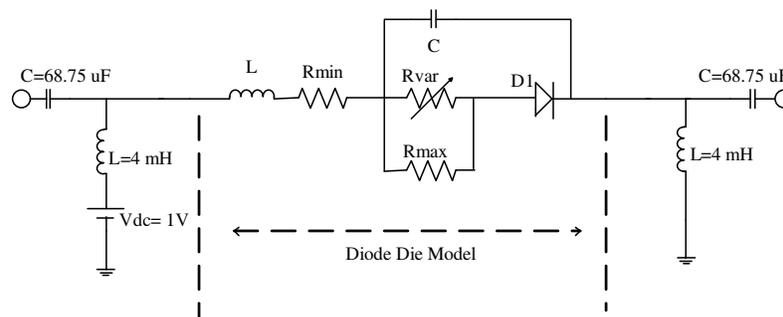


Figure 1: Optimized linearizer circuit.
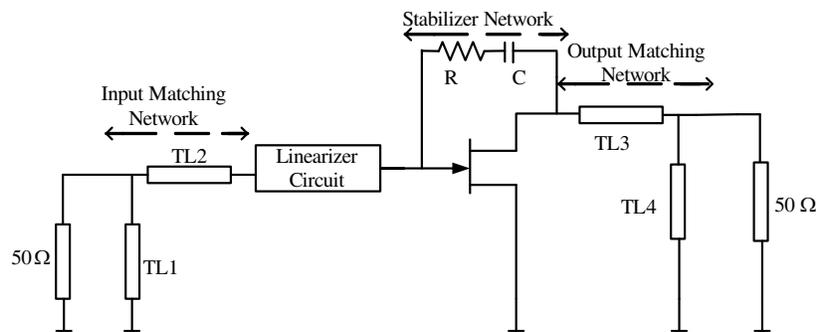


Figure 2: Block diagram of linearized, stabled and matched power amplifier.

## 4. SIMULATION RESULTS

In this section, simulation results of PA with and without linearizer have been introduced. According to the simulation results, PA without linearizer has 27.443 dBm $P_{out}$, 12.443 $G_T$ and 41.131% PAE at 1 dB gain compression point. In addition to, results of THD analysis are: the magnitude of second harmonic is $-0.418$ dBm while third harmonic's is $-5.544$ dBm and THD ratio is 0.043. Linear analysis has been demonstrated that PA without linearizer has 13.566 dB linear power gain, $-38.273$ dB input return loss (RL) and $-17.910$ dB output RL. Power amplifier with linearizer has 26.405 dBm $P_{out}$, 11.405 dB $G_T$ and 31.089% PAE for the same input power of 15 dBm like as without linearizer power amplifier. The magnitude of the second harmonic and third harmonic is $-9.221$ dBm and $-18.106$ dBm respectively, with 0.018 THD. The output spectrum of power amplifier with and without linearizer is shown in Figure 3. Linear analysis has been demonstrated that PA with linearizer has 11.776 dB linear power gain, $-12.811$ dB input RL and $-13.940$ dB output RL. The basic aim of the study is to improve linearity performance of power amplifier designed for by applying a linearization method. Therefore, simulation results of the optimized and linearized PA should have been compared without and with linearizer. A comparison in terms of $P_{out}$, $G_T$, PAE, THD and gain reduction has been given in Table 1.

AM-AM, AM-PM distortions and $G_T$ of the PA with and without linearizer have shown in Figure 4, Figure 5 and Figure 6, respectively.
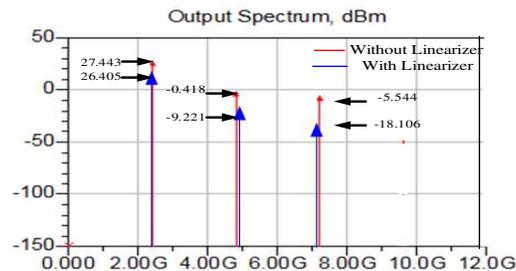


Figure 3: Output spectrum of power amplifier with and without linearizer.
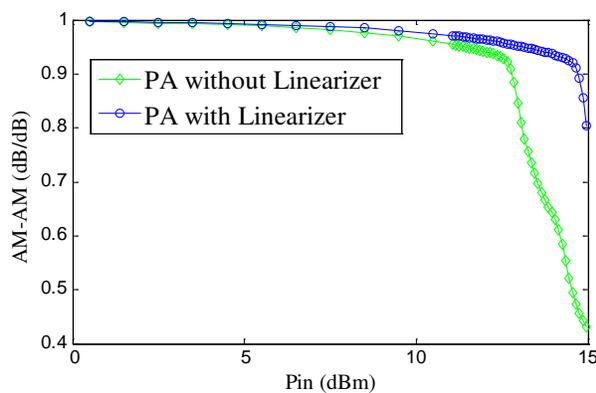


Figure 4: AM-AM of power amplifier with and without linearizer.
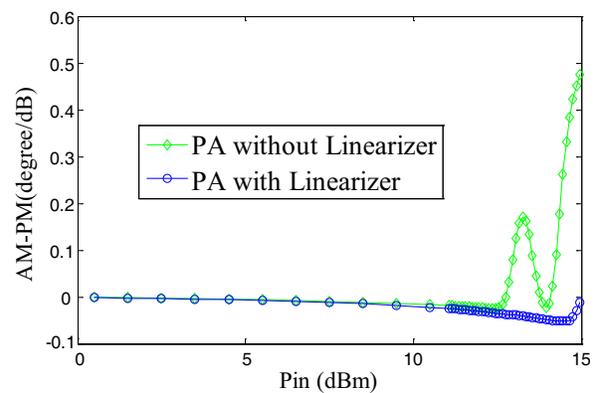


Figure 5: AM-PM of power amplifier with and without linearizer.

Table 1: Comparison of PA performance parameters with and without linearizer circuit.

| Power Amplifier | Without Linearizer | With Linearizer |
|:---:|:---:|:---:|
| $P_{out}$ [dBm] | 27.443 | 26.405 |
| $G_T$ [dB] | 12.443 | 11.405 |
| PAE [%] | 41.131 | 31.089 |
| THD | 0.043 | 0.018 |
| Gain reduction | 1.074 | 0.3359 |
| $NF$ [dB] | 1.448 | 2.589 |
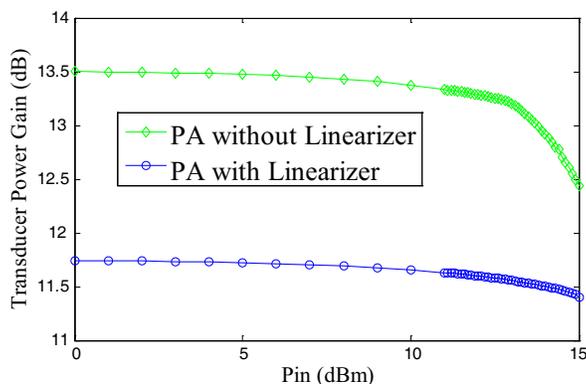
Figure 6: Transducer power gain of power amplifier with and without linearizer.

According to whole simulation results of the PA with linearizer and without linearizer, it could have been said that linearizer circuit compensates AM-AM and AM-PM behavior satisfactorily. AM-AM and AM-PM behavior of an ideal linearized PA should be as flatness as possible and should not change suddenly and dramatically whole entire of input power. If Figures 3 and 4 are reviewed, AM-AM changes about 0.5 dB without linearizer while it changes 0.09 dB, as well as AM-PM changes 0.30° without linearizer while it changes 0.035° PA with linearizer also suppresses second and third harmonics, second harmonic improved 8.803 dB while third harmonic improved 12.562 dB which compared to without linearizer.Suppressing second and third harmonics also reduces THD as specified that THD of the PA with linearizer is 0.018 while it is 0.043 without linearizer.

## 5. CONCLUSION

A 2.4 GHz power amplifier has been linearized with series diode linearizer which has been located input port of the power transistor. Linearizer circuit component values have been optimized for best performance. AM-AM, AM-PM behaviors have been improved as well as THD is reduced, therefore linearity performance of 2.4 GHz power amplifier is enhanced. However,while linearity performance of the PA has been being upgraded some of other parameters have degraded like $G_T$, PAE, input RL, and output RL It is known that there is a tradeoff between efficiency and linearity for power amplifiers. After linearizing PA, if design criteria have been still introduced, some losses have might be accepted. Still providing design criteria, the linearized PA has 26.405 dBm $P_{out}$, 11.405 dB $G_T$, 31.089% PAE 11.776 dB linear power gain, 12.811 dB input RL and −13.94 dB output RL.

**REFERENCES**

1. Noh, Y. S. and C. S. Park, "PCS/W-CDMA dual-band MMIC power amplifier with a newly proposed linearizing bias circuit," *IEEE J. Solid-State Circuits*, Vol. 37, No. 9, 1096–1099, Sep. 2002.
2. Haskins, C., T. Winslow, and S. Raman, "FET diode linearizer optimization for amplifierpre-distortion in digital radios," *IEEE Microwave and Guided Wave Letters*, Vol. 10, No. 1, 21–23, Jan. 2000.
3. Sen, S., S. Devarakond, and A. Chatterjee, "Low cost AM/AM and AM/PM distortion measurement using distortion-to-amplitude transformations," *IEEE International Test Conference ITC 2009*, Philadelphia, USA, Nov. 2009.
4. Macdonald, J. R., "Nonlinear distortion reduction by complementary distortion," *IRE Trans. Audio*, Vol. 7, 128–133, Sep.–Oct. 1959.
5. Yum, T. Y., L. Chiu, C. H. Chan, and Q. Xue, "High-efficiency linear RF amplifier — A unified circuit approach to achieving compactness and low distortion," *IEEE Transactions on Microwave Theory and Techniques*, Vol. 54, No. 8, 3255–3266, Aug. 2006.
6. Dong, J., Q. Wang, and F. Xie, "Design of 2.4 GHz power amplifier used in WLAN 802.11b by pHEMT," *2nd International Conference on Future Computer and Communication*, Vol. 1, 722–724, Wuhan, China, May 2010.
7. Rakluea, P. anf J. Nakasuwan, "A 3.5 GHz WiMAX power amplifier using Si-LDMOS," *International Conference on Control, Automation and Systems*, 1544–1547, Seoul, Korea, Oct. 2008.
8. Payne, K., "Practical RF amplifier design using the available gain procedure and the advanced design system EM/Circuit Co-Simulation capability," http://cp.literature.agilent.com/litweb/pdf/5990-3356EN.pdf.

# Sequential Tuning of Waveguide PIN Diode Limiters

**T. Kacmajor, J. J. Michalski, and M. Mazur**

TeleMobile Electronics Ltd., Poland

**Abstract**— A new method of tuning waveguide PIN diode limiters is presented here. It is based on the use of Artificial Neural Network (ANN), which models the relationship between physically measured scattering characteristics in the frequency domain and the positions of limiter tuning elements. The limiter is treated as a device consisting of $R$ subsections. Each subsection is associated with one tuning screw and is obtained by successive removal of tuning elements. The ANN builds $R$ inverse models of these subsections which are used for calculating proper positions of tuning element. The tuning experiment was conducted on limiter built as a cascade of 3 PIN diode sections (6 tuning elements).

## 1. INTRODUCTION

Many microwave devices like filters, antennas or amplifiers require, due to their imperfections, the postproduction process of tuning. There has been a lot of effort put in order to improve this process, especially in large-scale production of microwave filters. Recently, methods using Artificial Intelligence have been proposed [1], where, parallel[1] filter tuning is performed with the use of Artificial Neural Networks. The ANN training is based on patterns consisting of physical reflection characteristics (input vectors) and corresponding positions of the tuning elements (output vectors). Neuro-Fuzzy concept was described in [2], which employed fuzzy logic and was another multidimensional approximator of the relation between scattering characteristics and tuning screws. In contrast to the parallel tuning approach, novel sequential tuning of microwave filters with use of ANN was proposed in [3]. It is the procedure that we mostly benefit from in the process of tuning a waveguide PIN diode limiters presented here. Limiters are normally tuned by experienced operators by means of observing their characteristics and adjusting them to the required levels. To enhance the quality and speed of this process a sequential tuning method has been developed which also allows us to automate the procedure. In the method described in [3], the cavities, couplings and cross-coupling of filters are sequentially tuned with use of ANN created for each sub-filter. The above-mentioned concepts with some modifications turned out to be successful in tuning waveguide limiters.

At the beginning of this elaboration, we introduce the basics of the waveguide limiter. Next, the method of sequential tuning is presented. Then, the conducted experiment is described and discussed, followed by conclusion.

## 2. WAVEGUIDE LIMITER

Limiters are protecting devices which allow for limiting the power level and prevent the damage of receivers. There are many factors which may result in high level of power in receiver ports: another outer high power RF source, interactions (couplings) between neighboring microwave guides or reflection of transmitting signal in TRx (Transmitter and Receiver) unit. When a dangerous power level appears, the limiter is going into high-loss state, limiting the transmitted power. When such destructive power level is no longer present, the limiter is going into low-loss state, allowing for standard functioning of the receiver. The limiter must consist of detecting and limiting parts. Diode limiters may be divided to passive and active ones. In passive limiters the limiting diode also functions as a detector or is directly connected, in one current loop, to a detector diode [4, 5] In the second group of limiters, a detector is a separate device which controls polarization of PIN diodes [6].

The limiter has two working stages which must be taken into consideration in design and tuning process. The PIN diodes resistance characteristics may vary from element to element and, even more so, from one production batch to another. Parasitic reactance related to a package may not be the same for every diode. As a result, theoretical efforts made to obtain a device proof to changes of active element parameters are not effective. Experimental tuning of limiter structure is performed by changing the position of screws. This results in a change of dimensions of coaxial posts and also of diode position. Tuning screws affect the parameters $l_1$ and $l_2$ presented in schematic diagram of waveguide section of PIN diode limiter in Fig. 1.

---

[1]In parallel tuning, the algorithm generates corrections for all tuning elements simultaneously.
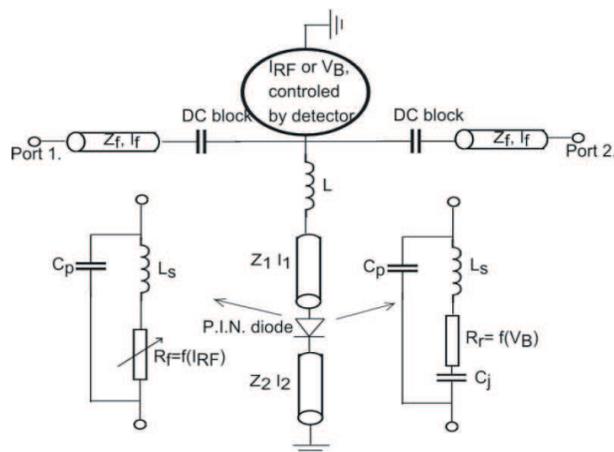
Figure 1: Schematic diagram of waveguide section of PIN diode limiter. Equivalent circuits for PIN diode biased forward and backwards are also presented (on the left and on the right from PIN diode respectively).

The waveguide limiter investigated in this paper contains a set of high power PIN diodes, either biased forward by current or backwards by blocking voltage, controlled by a separate circuit containing a detecting diode. The described limiter consists of three parts, each one with an implemented PIN diode. In high-loss state (low resistance of PIN diode) the diodes shorten the waveguide and cause reflection of RF signal, so that the basic $TE_{10}$ is not transmitted. This is the main effect. In low-loss state (high resistance of PIN diode caused by blocking voltage) the diodes do not shorten the waveguide, but they are not ideally transparent due to their shape, fixings, packaging and polarizing circuits. To reduce these effects, the diodes may be placed in cavities or at coaxial posts, reducing their fixing parasitic reactance. Besides, the cavity system may work as a filter allowing us to limit the pass band of the system.

In Fig. 1 a schematic diagram of one section of a waveguide PIN diode limiter is presented [6]. The waveguide section has $Z_f$ impedance and $l_f$ length, in front of the active element and behind it. The PIN diode is fixed between two coaxial posts (described with characteristic impedances $Z_1$, $Z_2$ respectively), whose positions, directly related to lengths $(l_1, l_2)$, are tuned with two screws. As the diodes are mounted in waveguide structure, the DC control signals for forward and backward biasing $(I_{RF}$ and $V_B)$ must be separated from waveguide with DC blocking structure. The equivalent circuit of the PIN diode biased forward and backwards is also presented in this figure. Low and high resistances $R_f$ and $R_r$ are obtained respectively. $C_p$ and $L_s$ are the parasitic parameters of the diode package. $C_j$ is the reverse biased junction capacitance.

By cascading a number of diode sections an increased level of attenuation and low leakage can be obtained.

## 3. TUNING METHODOLOGY

In this work we use the concept introduced in elaboration [3]. The basics of this method are as follows.

Scattering parameters of the limiter with $R$ tuning elements can be generally expressed as a function of all tuning element deviations.

$$S(\omega) = H(\omega, \Delta Z_1, \Delta Z_2, \ldots, \Delta Z_R) \tag{1}$$

The scattering parameters are defined in such a way that, for all tuning element deviations equal zero $\Delta Z_n = 0$, they represent the characteristics $S^0$ of a properly tuned limiter

$$S^0(\omega) = H(\omega, 0, 0, \ldots, 0) \tag{2}$$

In customization procedure we use a properly tuned limiter as a template to build $R$ subsection inverse models. For a limiter having $R$ tuning elements as the $r$th subsection, we define the limiter having $1, 2, \ldots, r-1$, tuning elements properly tuned and the elements $r+1, \ldots, R$ removed. So, only the $r$th tuning element can be changed in order to adjust characteristics (Fig. 2).

The inverse models, for all $R$ subsections, are built based on physically measured reflection characteristics. In the process of building inverse models, we start from the $R$th tuning element

(the last tuning element at the limiter output). Following the procedure [3], for every $r$th subsection we create $(2K + 1)$ training vectors as a set of the following pairs $P_n = \{S_n^k, \Delta Z_n^k\}$ where $\Delta Z_n^k = \{-K, -K + u, -K + 2u, \ldots, 0, \ldots, K - 2u, K - u, K\}$. The value of $u$ defines the minimal angle change in (deg) of each of the tuning elements. The maximum tuning element increment in both directions is defined by $K$ being the multiple value of $u$. For each $r$th subsection, with $\Delta Z_r = 0$, $S_r^0$ represents proper (tuned) scattering characteristics. After creating the $P_r$ set, the next $P_{r-1}$ set for $(r\text{-}1)$ subsection model can be created. After creating the last subsection set $P_1$, all of the tuning elements are removed. For every set $P_r$, we create the operator $A_r \; : \; S(Z_r) \to \Delta Z_r$ which maps detuned $S(Z_r)$ characteristic to the tuning element deviation $\Delta Z_r$. The operator $A_r$ is modeled by artificial neural network $\text{ANN}_r$. The characteristics $S_r^k$ and $\Delta Z_r^k$ are used as input and output vectors respectively. For each subsection model the following definition of error (3) is applied to check the ANN learning ability during the ANN training process

$$L_r = \frac{\sum_{k=1}^{2K+1} \left| \Delta Z_r^{k_0} - \Delta Z_r^{k_x} \right|}{2K + 1} \, [u] \tag{3}$$

where $r$ — subsection model number, $k$ — tuning element increment index, $\Delta Z_r^{k_0}$ — the correct value of the tuning element increment, $\Delta Z_r^{k_x}$ — the tuning element increment value generated by ANN, both for the corresponding $S_r^k$. After $\text{ANN}_r$ is trained, it works for the $r$th subsection as a mapper of measured detuned reflection characteristic $S_r^*$ to the tuning element deviation $\Delta Z_r$, which is the source of the detuning (Fig. 3).

Creating inverse models and tuning are both performed in low-loss state of the limiter. The tuning process consists of positioning the screws in proper location one by one using $A_r$ operator for $r$th subsection. We start with the $A_1$ operator which, for the measured detuned subsection characteristic $S_1$, generates the tuning element increment $A_1 \; : \; S_1(Z_1) \to \Delta Z_1$. The increment $\Delta Z_1$, after the application on the tuning element $Z_1$, sets the tuning element in the proper position $Z_1 + \Delta Z_1$, thus obtaining a proper scattering characteristic $S_1^0 = f(Z_1 + \Delta Z_1)$ for the first subsection. If we finally obtain $\Delta Z_1 = 0$, the first element is set into proper position and the subsection is tuned. The same procedure is repeated for $r = 2$ until $r = R$.

## 4. TUNING EXPERIMENT

The tuning experiment was conducted on the waveguide limiter shown in Fig. 4. It is composed of 3 PIN diode sections, so 6 screws act as tuning elements.

The goal of the tuning process is to obtain required parameters of three-section limiter. These parameters are presented in Table 1.
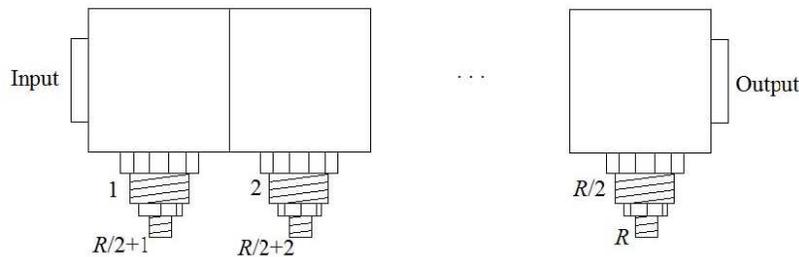


Figure 2: Waveguide limiter as a cascade connection of $R$ subsections.
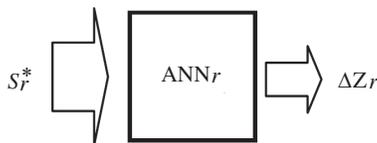


Figure 3: ANNr as a mapper of detuned scattering characteristics to tuning element deviations that caused detuning.
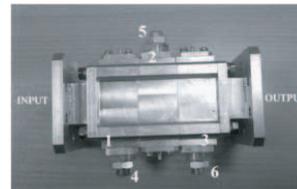


Figure 4: Waveguide limiter with numbered screws.

The ANN training sets $P_r$ were prepared by manual change of tuning elements. The reflection characteristics were sampled at 256 complex points. The inverse models were built by ANN based on previously tuned limiter called Inverse Model Template (IMT). The screw extraction path of IMT was as follows: 6, 5, 4, 3, 2, 1. It means that the tuning was performed in the opposite direction 1, 2, 3, 4, 5, 6. The new device to be tuned by our method is called Tuned Limiter (TL). In all figures, the properly tuned characteristics of the IMT, which serve as individual subsection templates, are represented by solid lines. The characteristics of the TL are represented by dotted lines.

Figures 5 and 6 present characteristics measured before tuning with PIN diode biased backwards.

After the whole tuning process, characteristics of limiter in low-loss state were as presented in Fig. 7. Although the model of IMT relied on reflection characteristics, it can be seen after tuning, that transmission is fully tuned and fulfills the specified requirements. To check the tuning results against the transmission attenuation requirement in high-loss state, PIN diodes were set in forward biased mode.

It can be seen that the limiter is very well tuned in high-loss state as well. The curves belonging to IMT and TL are very similar to each other.

Table 1: Specification of the waveguide limiter.

| PARAMETER | Value |
|-----------|-------|
| Frequency range | 5.4–5.8 GHz |
| $|S_{21}|$ for high losses | $< -50$ dB |
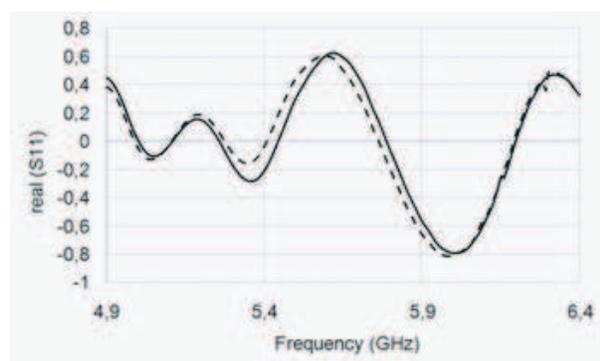


Figure 5: Real part of reflection. All tuning elements 1–6 are removed. Solid line — IMT characteristic, dotted line — TL characteristic. Low-loss state of the limiter.
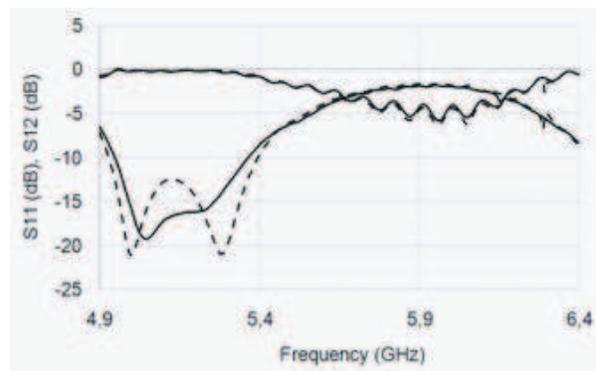


Figure 6: Transmission and reflection in (dB). All tuning elements 1–6 are removed. Solid line — IMT characteristic, dotted line — TL characteristic. Low-loss state of the limiter.
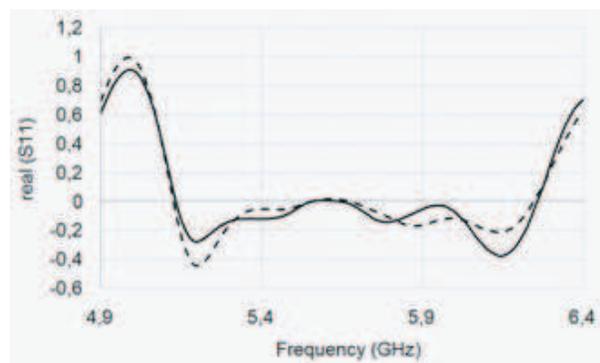


Figure 7: Real part of reflection. All tuning elements 1–6 are tuned. Solid line — IMT characteristic, dotted line — TL characteristic. Low-loss state of the limiter.
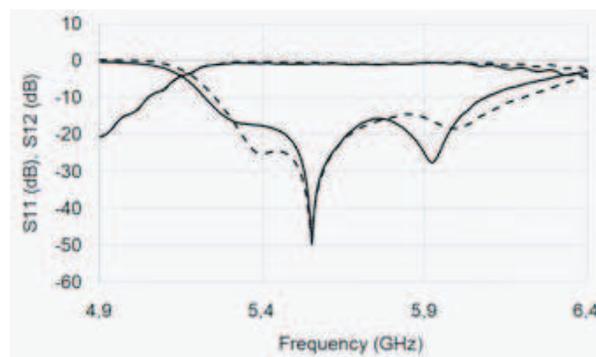


Figure 8: Transmission and reflection in (dB). All tuning elements 1–6 are tuned. Solid line — IMT characteristic, dotted line — TL characteristic. Low-loss state of the limiter.
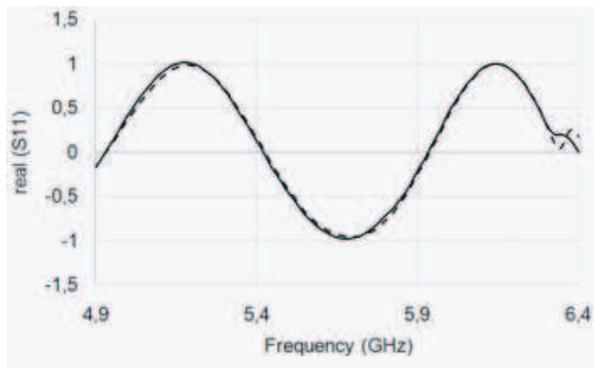
Figure 9: Real part of reflection. All tuning elements 1–6 are tuned. Solid line — IMT characteristic, dotted line — TL characteristic. High-loss state of the limiter.
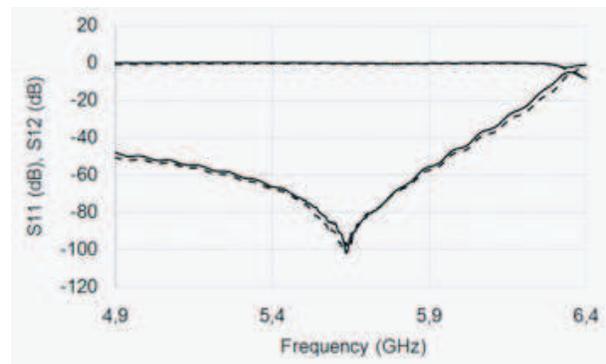
Figure 10: Transmission and reflection in (dB). All tuning elements 1–6 are tuned. Solid line — IMT characteristic, dotted line — TL characteristic. High-loss state of the limiter. Low-loss state of the limiter.

## 5. CONCLUSIONS

Among microwave devices which require tuning, a new one, i.e., the waveguide PIN diode limiter has proved to be fully tunable by the methods of Artificial Intelligence introduced in [3]. These methods relieve humans of the challenging task and the necessity of having knowledge about certain devices. The conducted experiments have indicated that a 3-diode limiter can be easily tuned using this method.

## ACKNOWLEDGMENT

## REFERENCES

1. Michalski, J. J., "Artificial neural networks approach in microwave filter tuning," *Progress In Electromagnetics Research M*, Vol. 13, 173–188, 2010.
2. Kacmajor, T. and J. J. Michalski, "Neuro-fuzzy approach in microwave filter tuning," *IEEE International Microwave Symposium*, Baltimore, 2011.
3. Michalski, J. J., "Inverse modeling in application for sequential filter tuning," *Progress In Electromagnetics Research*, Vol. 115, 113–129, 2011.
4. Drozdovski, N. V. and L. M. Drozdovskaia, "Microstrip and waveguide passive power limiters with simplified construction," *Journal of Microwaves and Optoelectronics*, Vol. 1, No. 5, 14–29, December 1999.
5. Drozdovski, N. V., "Microwave passive power limiters based on MESFETs," *Microwaves and Optoelectronics J.*, Vol. 1, No. 2, 26–36, April 1998.
6. Mao, R., G. Yang, and X. Tang, "Genetic algorithm optimization of waveguide limiter," *Asia-Pacific Microwave Conference Proceedings*, 2005.

# Dynamics of a System of Bilaterally Coupled Chaotic Gunn Oscillators

**B. C. Sarkar**[1], **D. Ghosh**[1], **C. Koley**[1], **A. Guin**[1], **and S. Sarkar**[2]

[1]Department of Physics, Burdwan University, India
[2]Electronics Department, Burdwan Raj College, India

**Abstract**— Experimental studies on a system of two bilaterally coupled chaotic Gunn oscillators (BC-CGO) indicate the effect of coupling coefficient ($K_{ij}$) on the dynamical state of the system. For some values of $K_{ij}$, spectrally similar chaotic outputs are obtained from the GOs, while the transition of chaos to signals with discrete components is noted for other values of $K_{ij}$.

## 1. INTRODUCTION

The problem of coupled oscillations of a system of oscillators, be it mechanical, electronic or biological, is being studied in recent years [1]. In the field of RF and microwave engineering, studies on the coupled oscillations of GOs have application related as well as academic importance [2, 3]. Recently the authors have reported a detailed study on the dynamics of two sinusoidally oscillating bilaterally coupled Gunn oscillators (BCGOs) [4]. The study revealed that depending on the relative free running frequencies of the oscillators and the values of coupling factors, the states of synchronous, quasi-periodic and chaotic oscillations would occur. The interest of the present work is to experimentally examine the phenomenon of coupled oscillations of two chaotically oscillating GOs. The arrangement of BC-CGO may produce synchronized chaotic oscillations in two CGOs or can modify the nature chaoticity of a CGO depending on the coefficient of coupling between the two ($K_{12}$ or $K_{21}$) and the spectral characteristics of an individual CGO. In Section 2 a simple yet robust technique of chaos generation in a GO and the arrangement for implementing a BC-CGO system are described. The spectral nature of a single CGO output and the effects of bilateral coupling are also given in this section. Experimental results on the correlation between the outputs of CGOs in coupled condition are given in Section 3 and some critical comments are included in Section 4.

## 2. FREQUENCY DOMAIN RESPONSE OF CGOS IN ISOLATED AND COUPLED STATE

Figure 1 shows the block diagram of the experimental setup used to study the dynamics of the BC-CGO by measuring the oscillator output spectra. However, omitting the coupling paths, the same system can be used to examine the properties of the CGOs separately.

A waveguide type GO is designed by placing a Gunn diode (biased in the negative differential resistance (NDR) region) in a dimension adjustable waveguide. The GO frequency is tuned both electrically and/or mechanically by varying the dc bias voltage in the NDR region or by changing the dimension of the cavity respectively. To generate chaotic oscillation in a GO, we start by choosing a dc bias voltage in the non-oscillatory region of the GO with a weak RF signal injected into the GO cavity. The frequency ($f_{RF}$) of the injected signal is nearly equal to the resonant frequency of the cavity and its power ($P_{RF}$) is taken a factor of magnitude less than that of the normal GO output power. A circulator (CR) is used to inject the external RF signal into the GO cavity and to apply
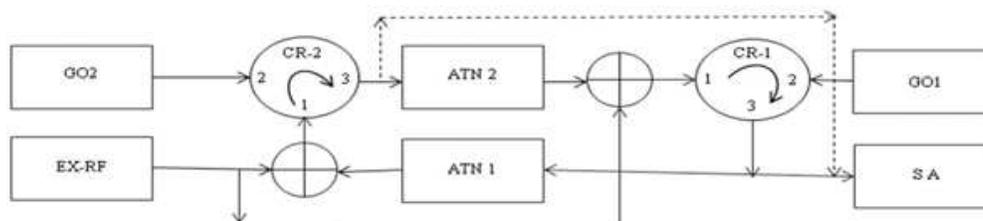


Figure 1: Simplified functional structure of BCGO.

the GO signal to a spectrum analyser (SA) as shown in Figure 1. With the gradual increase of the dc bias ($V_B$), a signal with broad band continuous spectra (BBCS) is observed at the GO output beyond a certain value of $V_B$. This value depends on $f_{RF}$ and $P_{RF}$ of the injected RF signal. In Figures 2(a)–2(c), the output spectra of GO1 in the isolated mode of operation are shown indicating the states of no-oscillation, chaotic oscillation and periodic oscillation for $V_B$ values 3.30 volt, 5.0 volt and 6.0 volt respectively. The BBCS signal, so obtained can be identified as a chaotic signal (CS) both qualitatively and quantitatively. The relative power of the component signals in the generated chaos can be changed by the variation of $f_{RF}$ or $V_B$.

Two CGOs are designed adopting the method described above. $V_B$ values of the two GOs are adjusted separately but an identical RF signal is injected in the two separate cavities Figure 1. Two attenuators (ATN1 and ATN 2) are used to independently control the coefficient of coupling between the CGOs ($K_{12}$ and $K_{21}$). The observations are summarized as follows: (i) The output spectra of two CGOs (as observed in the SA) change with the variation of the coupling factors $K_{12}$ and $K_{21}$. For a range values of $K_{12}$ and $K_{21}$ the output spectra of the CGOs are found to be identical. Figure 3(a) depicts the obtained spectra for a set of $f_{RF}$, $K_{12}$ and $K_{21}$. (ii) The variation of $f_{RF}$ has a very little effect on the obtained output spectra of the CGO in the chaotic mode. (iii) For a fixed $f_{RF}$ and $K_{12}$, the variation of $K_{21}$ results in the change of BBCS output into a spectra with discrete components Figure 3(b).

## 3. TIME DOMAIN RESPONSE OF CGOS IN COUPLED STATE

The product of two CGO outputs ($E_1(t)$ and $E_2(t)$) is obtained using a circuit comprising of a magic tee, two waveguide mounted tunable square-law detectors, a difference amplifier (DA) and a low pass filter (LPF) [5]. The time averaged product $\langle E_1(t) * E_2(t) \rangle$ thus obtained gives a quantitative measure of the time domain correlation between $E_1(t)$ and $E_2(t)$ in the coupled state.
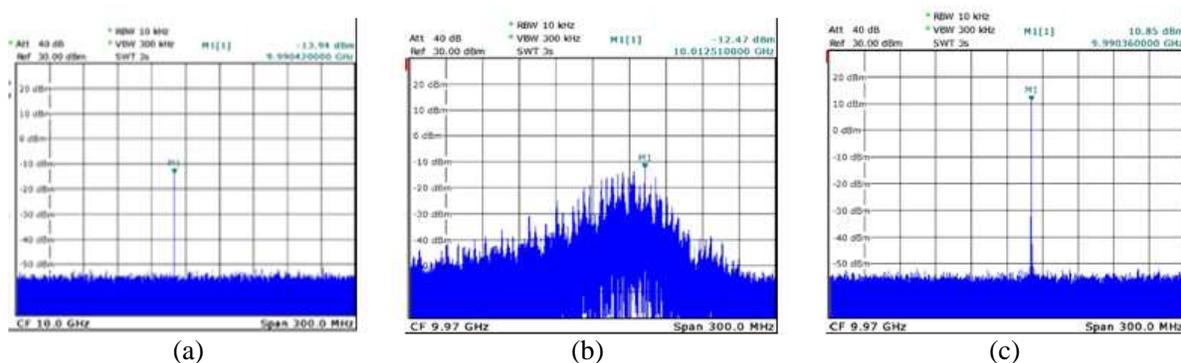


Figure 2: The output spectrum of GO1 in isolated mode when $P_{RF} = 10\,\text{dBm}$ and $f_{RF} = 9.997\,\text{GHz}$: (a) No oscillation for $V_B = 3.30\,\text{Volts}$. (b) Chaotic oscillation for $V_B = 5\,\text{Volts}$. (c) Periodic oscillation for $V_B = 6\,\text{Volts}$.
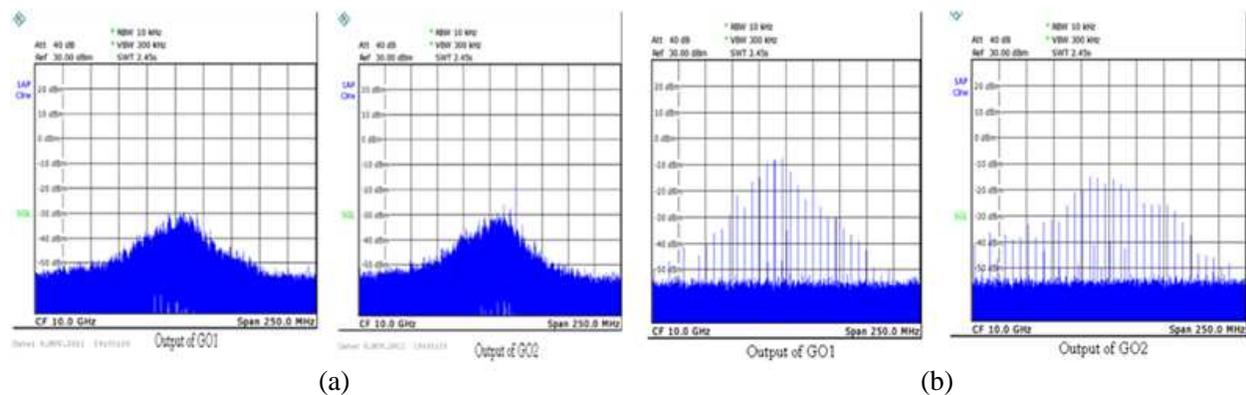


Figure 3: The output Spectra of two CGOs in a bilaterally coupled condition. $P_{RF} = 0\,\text{dBm}$, $f_{RF} = 10.025\,\text{GHz}$, $V_{B1} = 5.82\,\text{Volts}$, $V_{B2} = 5.82\,\text{Volts}$: (a) $K_{12} = 0.92$, $K_{21} = 1$. (b) $K_{12} = 0.92$, $K_{21} = 0.425$.

Table 1: $V_{B1} = 5.82$ Volts, $V_{B2} = 5.82$ Volts, $K_{12} = 0.92$, $K_{21} = 1$ and $P_{RF} = 0$ dBm.

| $f_{RF}$ (GHz) | 9.925 | 9.935 | 9.945 | 9.955 | 9.965 |
|---|---|---|---|---|---|
| Obtained d.c output (mv) | 120 | 100 | 100 | 80 | 80 |

As $E_1(t)$ and $E_2(t)$ are chaotic in nature they contain a large number of component signals having all possible frequencies (at least theoretically) within the bandwidth of the signal. If $E_1(t)$ and $E_2(t)$ be synchronized, a component signal of frequency $f_1$ in $E_1(t)$ and $E_2(t)$ would have a time constant phase difference ($\phi_1$). Thus in $\langle E_1(t) * E_2(t) \rangle$, the component signal $f_1$ would contribute a dc term proportional to $\phi_1$. However, the ac components present in $\langle E_1(t) * E_2(t) \rangle$ due to cross multiplication of component signals would be filtered out by the LPF. Thus $\langle E_1(t) * E_2(t) \rangle$ would be significantly a dc voltage in nature. We have obtained dc voltages at the LPF output when two CGO output spectra are chaotic and similar in nature. This can be a case of phase synchronization between two CGOs. The variation of the obtain dc voltage with the variation of the $f_{RF}$ for a fixed set of $K_{ij}$ values in the chaotic region of operation of the system is given in the Table 1.

## 4. CONCLUSION

Describing the generation of microwave chaotic oscillations with the help of an under-biased GO having injected RF signal in the GO cavity, the effects of bilateral coupling between two such GOs are reported. It is observed that for some optimum values of coupling factors, two CGOs produce spectrally similar broad band signals (possibly synchronized in nature). For some other conditions of coupling, the chaos changes to signals having discrete components. Further studies in this direction would have important practical implications.

## ACKNOWLEDGMENT

## REFERENCES

1. Guckenheimer, J. and P. Holmes, *Nonlinear Oscillations, Dynamical Systems and Bifurcation of Vector Fields*, Springer, New York, 1983.
2. Ram, R. J., R. Sporer, H. R. Blank, and R. A. York, "Chaotic dynamics in coupled microwave oscillators," *IEEE Trans. Microwave Theory and Technique*, Vol. 48, 1909–1916, 2000.
3. Anishchenko, V., S. Astakhov, and T. Vadivasova, "Phase dynamics of two coupled oscillators under external periodic force," *Europhysics Letters*, Vol. 86, 2009.
4. Sarkar. B. C., D. Sarkar, S. Sarkar, and J. Chakraborty, "Studies on the dynamics of bilaterally coupled X-band gunn oscillators," *Progress In Electromagnetics Research B*, Vol. 32, 149–167, 2011.
5. Sarkar, S., T. Banerjee, D. Mondal, and B. C. Sarkar, "Theory and performance of an electrically controlled microwave phase shifter," *Indian Journal of Pure and Applied Physics*, Vol. 43, 215–220, 2005.

# Application of PSO Algorithm for Optimizing the Dimensions of Tunable Interdigitated Capacitor

**G. Lakshmi Narayana Rao**, **Sravan Kumar**, **Samrat L. Sabat**, and **K. C. James Raju**

School of Physics, University of Hyderabad
Central University PO, Hyderabad, Andhra Pradesh 500046, India

**Abstract**— In this paper, we describe an approach to optimize the dimensions of a tunable interdigitated capacitor using particle swarm optimization (PSO) algorithm. Analytical model of an interdigitated capacitor (IDC) is developed using conformal mapping method (CMM) and partial capacitance technique (PCT). The dimensions of IDC operating at 1 GHz frequency with capacitance values of 1 pF to 5 pF are extracted using PSO algorithm. The structural dimensions of tunable IDCs are simulated using finite difference time domain (FDTD) based software (IMST's Empire). The designed IDC shows approximately 20% tunability with 30% variation in dielectric constant of the tunable BST (Barium Strontium Titanate ($Ba_{0.5}Sr_{0.5}TiO_3$)) thin film on which the modeled IDC structure is patterned. The obtained results from numerical simulation shows that PSO algorithm is able to calculate the dimensions of tunable IDCs accurately and successfully and this technique can be applied to extract the dimensions of any planar microwave device.

## 1. INTRODUCTION

The emerging technology of ferroelectric thin film based tunable devices offer significant advantages over devices based on conventional approaches involving varactors, MESFETs or ferrite based devices [3]. These thin film devices make use of the voltage dependent dielectric constant of a ferroelectric material in its paraelectric state for obtaining the tunability [2]. $Ba_{0.5}Sr_{0.5}TiO_3$ (BST) is one of the popular ferroelectric materials used for this application, which can give up to 50% tunability under the application of less than 2 kV/cm of bias [3]. Tunable filters and phase shifters are important components for reconfigurable antennas and software defined radios [3, 4] and the key control element in them is the variable capacitor. The IDCs are also used for different applications like artificial transmission line using left/ right handed behavior [5]. Using ferroelectric thin films, tunable devices can be fabricated either as a parallel plate capacitor or as a planar IDC. Since there is no buried electrode for an IDC, the chances of breakdown or shorting through pin holes can be avoided at the cost of miniaturization. Also IDC got the important advantage that it requires only a single mask processing. Tunable IDCs are smaller in size compared to other competing conventional technologies, highly tunable and have ease of fabrication got great potential as tunable elements in microwave devices. Due to its multi layer structure, designing an IDC at high frequencies for desired values of capacitance is a tedious and time consuming work.

In this paper, we have formulated this as an optimization problem and solved it using PSO technique. This problem can be solved using classical optimization technique, such as gradient method and Levenberg-Marquand technique. But the disadvantage with these approaches is that it may lead to suboptimal solution [1]. To avoid this in recent years a heuristic optimization technique such as genetic algorithm (GA) and PSO has been reported in literature [11, 12]. Due to its low algorithmic complexity, many real world problems are solved using this technique [12].

## 2. TUNABLE INTERDIGITATED CAPACITOR

Interdigitated capacitors employ coupled "fingers" to form a horizontal, rather than vertical capacitor structure. One can easily make a tunable capacitor using the BST thin film material deposited on a dielectric substrate, because the dielectric constant of BST is a function of applied electric field. The IDC structure is patterned on BST ferroelectric thin film having a dielectric constant of 250 and thickness 1 micron, which is deposited on MgO (Magnesium Oxide) dielectric substrate having a dielectric constant of 9.6 and thickness 500 microns. The IDC layout and its cross sectional view is given in Figures 1(a) and (b).

The capacitance of an IDC on a multilayer substrate is equal to the sum of capacitance of each finger with the substrate that between the fingers and the effective capacitance of finger ends. It should be noted that since the metal IDC pattern is over a multilayer, comprising substrate and thin film BST, each of these capacitances are an effective capacitance influenced by the field coupled to these layers. Each of these effective capacitances can be modeled using partial capacitance
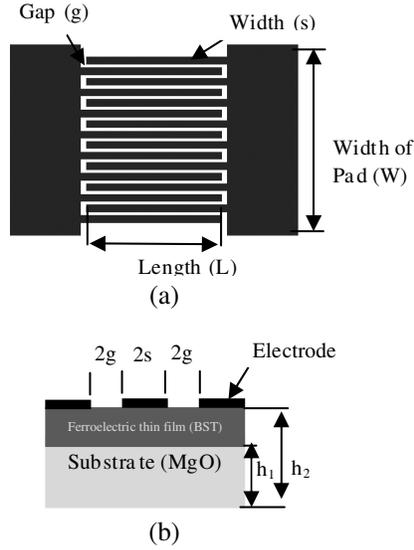
Figure 1: (a) Tunable interdigitated capacitor layout and its (b) cross sectional view.
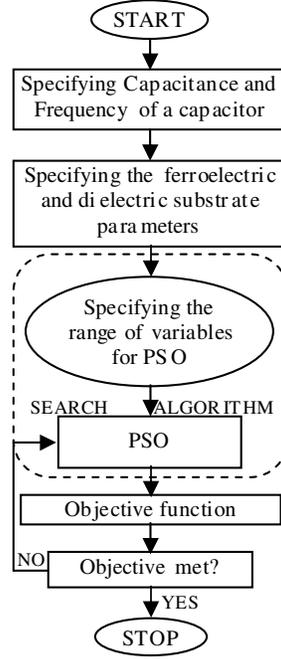
Figure 2: Optimization algorithm for IDC physical dimensions.
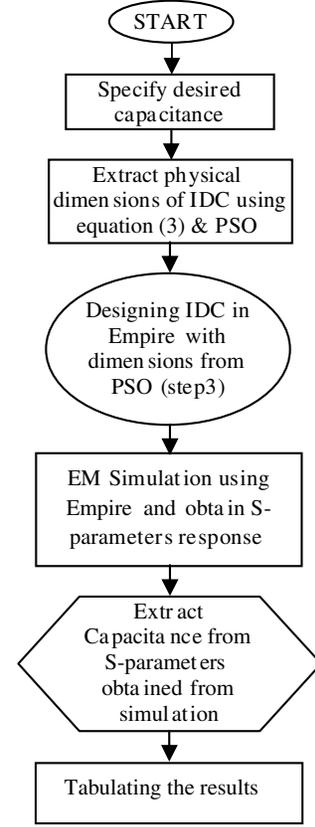
Figure 3: Design procedure of a tunable IDC.

technique (PCT) to separate the multi-layered substrate to multiple single layers. Further, using conformal mapping method (CMM), it is possible to transform an IDC on a single layer into a parallel plate capacitor [7, 8]. Following this method, the total capacitance of an IDC consists of three parts:

$$C = C_t + C_p + C_e \tag{1}$$

$C_t$ — Effective capacitance of a three finger capacitor on multilayers; $C_p$ — Effective capacitance of remaining pair finger structures on multilayers, and $C_e$ — Effective capacitance corresponding to finger ends on multilayers.

The total capacitance of a tunable IDC can be expressed in terms of effective dielectric constant of three finger capacitance ($\varepsilon_{teff}$), pair finger capacitance ($\varepsilon_{peff}$) and end capacitance of fingers ($\varepsilon_{eeff}$) which can be expressed as functions of physical dimensions using the complete elliptical integral of first kind [9].

$$C = C_t + C_p + C_e = 4\varepsilon_0 \varepsilon_{teff} \frac{K(k'_{t0})}{K(k_{t0})} + (n-3)\,\varepsilon_0 \varepsilon_{peff} \frac{K(k_{p0})}{K(k'_{p0})} + 4ns(2+\pi)\varepsilon_0 \varepsilon_{eeff} \frac{K(k_{e0})}{K(k'_{e0})} \tag{2}$$

Here $n$ is the number of fingers, $\varepsilon_0$ is dielectric constant of air, $K(k_{(t,p,e)0})$ are complete elliptical integrals of first kind and $K(k'_{(t,p,e)0}) = K\left(\sqrt{1 - K(k_{(t,p,e)0})^2}\right)$. The variables $k_{t0}$, $k_{p0}$, $k_{e0}$ are dependent on physical dimensions of IDC and they are explained in detail by Zheyao Wang, et al. [7]. The subscripts $t$, $p$ and $e$ in the equation represents the three finger capacitance part, pair finger capacitance part and the finger end capacitance part respectively of an IDC. The effective dielectric constants $\varepsilon_{peff}$, $\varepsilon_{teff}$ and $\varepsilon_{eeff}$ are dependent on physical dimensions of IDC, dielectric substrate and ferroelectric thin film as well as on the dielectric properties of the dielectric layers [7]. Since we know the capacitance dependence on physical dimensions through Equation (2), it is possible to optimize the dimensions for desired capacitance values with known ferroelectric layer characteristics and substrate parameters.

### 3. PROBLEM FORMULATION

Designing a tunable IDC involves

1. Formulating the analytical model for a tunable multilayer IDC.
2. Specifying the capacitance, operating frequency, substrate and BST material properties.
3. Optimizing the physical dimensions of tunable IDC for desired capacitance.
4. Generating a layout for EM simulation.

Main focus of this paper is to optimize the physical dimensions of a tunable IDC for desired capacitance operating at specified frequency. Selection of suitable combination of IDC dimensions yields an optimum solution for required capacitance. The functional relationship between capacitance and physical dimensions of tunable IDC is presented in Equation (2).

This problem is formulated as a minmax optimization problem. The objective is to find optimum values of structural parameters $\mathbf{x}* = [2g, 2s, l, N]$ that minimizes the difference between desired and simulated capacitance value.

### 4. PARTICLE SWARM OPTIMIZER

This section provides a brief introduction of the PSO technique and its application to a tunable IDC design. PSO algorithm is inspired by the social behavior of bird flocking or fish schooling developed by Kennedy in 1995 [12]. In PSO, a set of particles ($N_P$) in the swarm is defined. Each particle represents a potential solution in the solution space and is characterized by its position and velocity. The number of parameters to be optimized determines the dimension of the problem. The position and velocity of $i$th particle ($i = 1, 2, \ldots, N_P$) in the $D$th dimension are represented as $X_i = (x_{i1}, x_{i2}, x_{i3}, \ldots x_{iD})$ and $V_i = (v_{i1}, v_{i2}, v_{i3}, \ldots v_{iD})$, respectively. Each particle updates its position and velocity based on its own best position, ($p_{best}$) as well as the best position of the entire swarm ($g_{best}$).

The practical implementation of classical PSO involves the following steps.

1) Parameter initialization: The dimensions, range and number of particles are defined and each particle's initial position and velocity in the swarm is initialized to independent random values. For a $D$-dimensional problem with $N$ particles, the position vector is represented as $X(t) = (X_1(t), X_2(t), X_3(t), \ldots X_N(t))$ where $X_i = (x_{i1}, x_{i2}, x_{i3}, \ldots, x_{iD})$ and the velocity vector is represented as $V(t) = (V_1(t), V_2(t), V_3(t), \ldots V_N(t))$, $V_i = (v_{i1}, v_{i2}, v_{i3}, \ldots, v_{iD})$.

2) Set iteration = 1.

3) Evaluate the desired objective function of each particle based on their positions.

4) Each particle's current fitness value is compared with previous $p_{best}$ value. If the current value is better than the previous value, then set the $p_{best}$ value to the current value.

5) Determine $g_{best}$ of the swarm as best of all particles $p_{best}$.

6) Update the velocity and position of each particle as follows.

$$
\begin{aligned}
V_{i,d}^{t+1} &= V_{i,d}^t + C_1^t * rand_1 * \left(pbest_{i,d}^t - X_{i,d}^t\right) + C_2^t * rand_2 * \left(gbest_d^t - X_{i,d}^t\right) \\
X_{i,d}^{t+1} &= X_{i,d}^t + V_{i,d}^{t+1}
\end{aligned}
\tag{3}
$$

where $C_1$ and $C_2$ are the learning factors that determines the relative influence of cognitive and social component respectively in search space. In this paper, the values of $C_1$ and $C_2$ are decreased with each iteration [7]. $rand_1$ and $rand_2$ are independent random numbers uniformly distributed in the range [0, 1]. $V_{i,d}^t$, $X_{i,d}^t$ and $pbest_{i,d}^t$ are the velocity, position and the personal best of $i$th particle in $d$th dimension for the $t$th iteration respectively. The $pbest_{i,d}^t$ is the $d$th dimension of best particle in the swarm for the $t$th iteration.

7) Update the generation number using $t = t + 1$. Proceed to Step 3 if $t < t_{\max}$ or all the design specifications are not satisfied.

8) Output the best solution $g_{best}$ and its fitness value.

The above design approach is used to optimize the IDC dimensions. IDC dimension required to realize capacitance values from $1\,\mathrm{pF}$–$5\,\mathrm{pF}$ at $1\,\mathrm{GHz}$ were thus calculated using this procedure. The experiments are performed in a DELL Work Station (Dell Precision T5400) and the code is written in MATLAB 7. The results obtained are tabulated in Table 1.

## 5. NUMERICAL SIMULATION OF MODELED IDC

The modeled tunable IDCs are simulated in IMST's Empire 3D electromagnetic simulator. Empire 3D simulator follows FDTD method for calculating the electromagnetic field distribution for 3D structures. The obtained tunable IDC dimensions from PSO algorithm are used to generate a layout and the IDC layout is imported to Empire software for full wave EM simulation. In the Empire layout, the substrate and BST tunable thin film material parameters are defined from the specifications chosen for the IDC design procedure. A coplanar waveguide (CPW) probe is used to extract the $S$-parameters of IDC in the frequency range of 0.5 GHz to 1.5 GHz. The simulated $S$-parameter values obtained from Empire simulation of the IDC layouts are used to extract the capacitance of IDCs using the Equation (5) [7].

$$C = \text{Im}\left[\frac{(1 - S_{11})}{2\pi f Z_L (1 + S_{11})}\right] = \frac{-\text{Im}[S_{11}]}{\pi f Z_L (1 + \text{Re}[S_{11}])^2 + \text{Im}[S_{11}]^2} \tag{4}$$

The tunable IDC capacitances obtained from the numerical simulation (Empire) in the frequency range of 0.5 GHz–1 GHz are shown in Figure 4 and tabulated in Table 1. The capacitance in Figure 4 shows that the capacitance is linear in the frequency range of 1 GHz, which is most desirable for all microwave monolithic integrated circuit (MMIC) applications. The capacitance of a tunable IDC is dependent on the dielectric constant of substrate (MgO) and BST layer. The dielectric constant of BST is voltage dependent and hence the IDC capacitance is tunable by external bias.

The dimensions of an interdigitated capacitor for 1 pF–5 pF are optimized using PSO and the
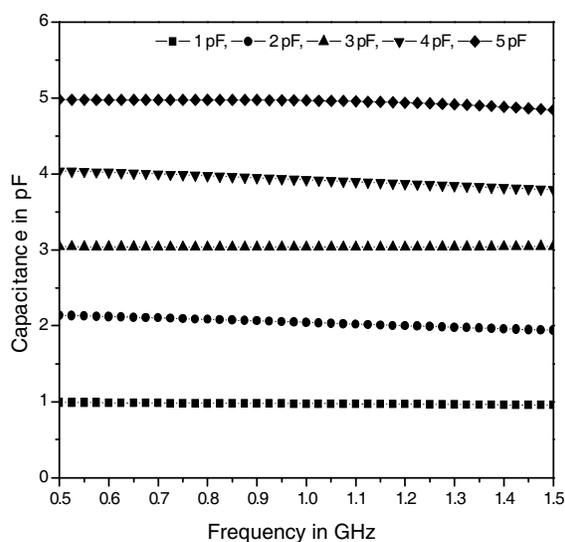


Figure 4: Numerical simulation results of a modeled tunable interdigitated capacitor.
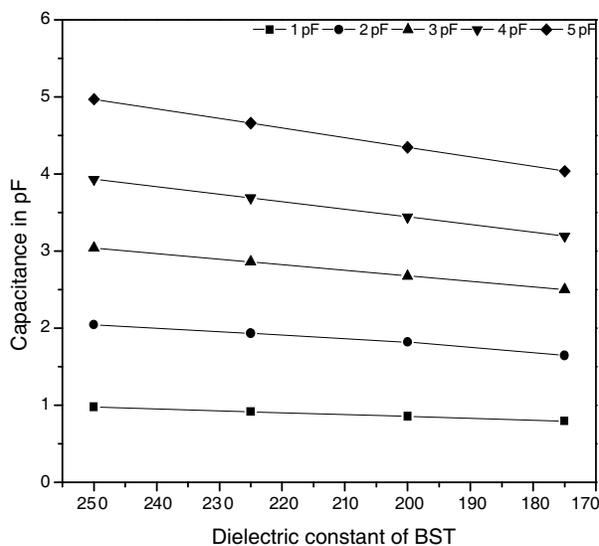
Figure 5: Capacitance tunability of a tunable interdigitated capacitor.

Table 1: Obtained dimensions of an IDC using PSO technique.

| S. No | Desired Capacitance values (pF) | Dimensions of an IDC for desired capacitance | | | | Capacitance extracted from Numerical Simulation (Empire) for the obtained dimensions of an IDC (pF) | Relative deviation % |
| --- | --- | --- | --- | --- | --- | --- | --- |
| | | Width (2s) (μm) | Gap (2g) (μm) | Length (l) (μm) | No of Fingers (n) | | |
| 1 | 1 | 14 | 10 | 228 | 8 | 0.97 | 2.44 |
| 2 | 2 | 14 | 10 | 176 | 20 | 2.04 | 2.13 |
| 3 | 3 | 11 | 8 | 681 | 8 | 3.03 | 1.14 |
| 4 | 4 | 12 | 10 | 389 | 11 | 3.93 | 1.75 |
| 5 | 5 | 13 | 9 | 892 | 12 | 4.97 | 0.63 |

Table 2: Tunable results of IDC.

| S. No | Modeled Capacitance (pF) | Capacitance in pF for different $\varepsilon$ values of BST | | | | Tunability % |
|---|---|---|---|---|---|---|
| | | $\varepsilon = 175$ | $\varepsilon = 200$ | $\varepsilon = 225$ | $\varepsilon = 250$ | |
| 1 | 1 | 0.79 | 0.85 | 0.91 | 0.98 | 18.8 |
| 2 | 2 | 1.64 | 1.81 | 1.93 | 2.04 | 19.5 |
| 3 | 3 | 2.50 | 2.68 | 2.86 | 3.03 | 17.6 |
| 4 | 4 | 3.19 | 3.44 | 3.69 | 3.93 | 18.7 |
| 5 | 5 | 4.03 | 4.34 | 4.67 | 4.97 | 18.8 |

obtained gap ($2g$), width ($2w$), length ($l$) and number of fingers ($n$) of an IDC for desired capacitances are show in Table 1. These IDCs are simulated using 3D electromagnetic simulation, IMST's Empire software for validating the PSO method in optimizing the IDC dimensions for a desired capacitance. The extracted capacitances of IDCs from numerical simulations are tabulated in Table 1 and they are close to desired values. The relative deviation from the desired and simulated capacitance is less than 2.5% and it shows the PSO method is working in for designing the IDC. It is also observed that the relative deviation is lower for higher desired capacitance values; hence this optimization procedure is recommended for IDCs of moderately high capacitance values. The frequency dependent of capacitance is also studied and the capacitance is linear from 0.5 GHz to 1.5 GHz and they are shown in Figure 4. The same IDC designs are simulated with 30% variation in the dielectric constant of BST layer for tunability analysis and are shown in Figure 5.

The optimized dimensions of IDCs for desired capacitances are simulated by varying the dielectric constant of BST for tunability analysis. The dielectric constant of BST is from 250 to 175 in steps of 25 and the capacitance of an IDC is extracted for each dielectric constant variation and they are given in Table 2. The average tunability with 30% variation, i.e., varying dielectric constant from 250 to 175 is 18% for desired capacitances and they are show in Table 2. The Figure 5 shows the IDC capacitance tunability with decrease in dielectric constant.

## 6. CONCLUSION

In this paper, we used PSO algorithm to design tunable IDCs using CMM and PCT. The PSO algorithm is used to optimize the dimensions of IDCs at 1 GHz. The layouts of the designed IDCs are simulated using the 3D EM simulator (Empire) and the relative deviation between simulated and designed is less than 2.5%. Average tunability of designed IDCs is 18% with 30% variation in the dielectric constant of the BST layer.

**REFERENCES**

1. Nocedal, J. and S. J. Wright, *Numerical Optimization*, Springer, Verlag, 1999.
2. Gevorgian, S. S. and E. L. Kollberg, "Do we really need ferroelectrics in paraelectric phase only in electrically controlled microwave devices?," *IEEE Trans. Microwave Theory Tech.*, Vol. 49, No. 11, 2117–2124, Nov. 2001.
3. York, R., et al., "Microwave integrated circuits using thin-film BST," *Proc. 12th IEEE Int. Symp. Applications Ferroelectrics*, Vol. 1, 195–200, 2000.
4. Ezhilvalavan, S. and T.-Y. Tseng, "Progress in the developments of (Ba; Sr)TiO (BST) thin films for gigabit era DRAMs," *Mater. Chem Phys.*, Vol. 65, No. 3, 227–248, 2000.
5. Sánchez-Martínez, J. J., E. Marquez-Segura, P. Otero, and C. Camacho-Peñalosa, "Artificial transmission line with left/right-handed behavior based on wire bonded interdigital capacitors," *Progress In Electromagnetics Research B*, Vol. 11, 245–264, 2009.
6. Stauf, G. T., S. Dilodeau, R. K. Watts, and K. Roderick, "BaSrTiO thin films for integrated high frequency capacitors," *IEEE Int. Symp. Appl. Ferroelect.*, Vol. 1, 103–106, Aug. 1996.
7. Wang, Z., J. Liu, and L. Liu, "Permittivity measurement of $Ba_{0.5}Sr_{0.5}TiO_3$ ferroelectric thin films on multilayered silicon substrates," *IEEE Transactions on Instrumentation and Measurement*, Vol. 55, No. 1, Feb. 2006.
8. Gevorgian, S. S., T. Martinsson, P. L. J. Linn, Senior, and E. L. Kollberg, "CAD models for multilayered substrate interdigital capacitors," *IEEE Transactions on Microwave Theory and Techniques*, Vol. 44. No. 6, Jun. 1996.

9. Sabat, S. L., L. D. S. Coelho, and A. Abraham, "MESFET DC model parameter extraction using quantum particle swarm optimization," *Microelectronics Reliability*, Vol. 49, No. 6, 660–666, Poland, Jun. 2009.

10. Ouaddari, M., S. Delprat, F. Vidal, M. Chaker, and K. Wu, "Microwave characterization of ferroelectric thin-film materials," *IEEE Transactions on Microwave Theory and Techniques*, Vol. 53, No. 4, Apr. 2005.

11. Gao, Y., "Genetic algorithm based parameter extraction for power GaAs MESFET," *Microw. Rev.*, Vol. 12, 47–48, 2001.

12. Eberhart, R. and J. Kenedy, "Particle swarm optimization," *Proceedings of IEEE Int. Conference on Neural Networks*, 1114–1121, Piscataway, NJ, Nov. 1995.

# A Novel Passive Dual-band Bandpass Microwave Filter Using Microstrip Loop Resonators

**Sholeh Jahani Maleki**[1], **Samaneh Sadi**[2], **Kambiz Sadat Najafi**[3], **and Massoud Dousti**[1]

[1]Department of Electronic Engineering, Islamic Azad University (IAU)
Science and Research Branch, Tehran, Iran
[2]Department of Electrical Engineering
Islamic Azad University (IAU), South Tehran Branch, Tehran, Iran
[3]Departement of Electrical Engineering
Islamic Azad University (IAU), Islamshahr Branch, Tehran, Iran

**Abstract**— In this paper, a novel passive dual-band bandpass filter using microstrip loop resonators is proposed, which allows two transmission paths to microwave signals. Each of them using dual-mode resonators results in respective passband. This can provide convenience to easily change one passband frequency, while another keeps almost the same. Several attenuation poles in the stopband are realized to improve the selectivity of the proposed bandpass filter. It is designed and simulated on RT/Duroid6010 substrate with permittivity of 10.8 and thickness of 1.27 mm. Compact size, low loss, dual band and high selectivity characteristics are realized by this type of filter structure. The filter of this type has 0.9% and 1.4% bandwidth at 1.8 GHz and 2.4 GHz, respectively.

## 1. INTRODUCTION

Modern wireless communication systems demand microwave devices operating in multiple separated frequency bands. For example, for Some mobile phone networks, like global systems for mobile communications (GSM) and Wireless LAN protocols (WLAN), such as Bluetooth and the IEEE 802.11b specifications, the RF transceiver must be able to receive and transmit 1.8 GHz and 2.4 GHz signals. Therefore, the bandpass filter, as a key component filtering unwanted frequency in RF systems [1], is necessitated to generate two or more frequency bands. A number of publications have provided a variety of solutions to the realization of dual-band bandpass filter [2–4]. A dual-band bandpass filter has been proposed using stepped impedance resonators (SIRs) [1, 4–6] and equal-length coupled-serial-shunted lines [7, 8]. However, it is difficult to generate two adjacent passbands using SIR. Recently, The dual-mode resonator using patch [9] or square loop [10, 11] has attracted much attention in design of single frequency filter, which meets the demands for compact size, low radiation and high-performance filters. The microstrip dual-mode bandpass filter permits the compact filter development with narrowband and high-$Q$ for modern telecommunication systems.

In this paper, a dual-band bandpass filter using loop resonators with square patches is presented, which needs only single input and output. The filter provides two transmission paths to an RF signal, and each of them is realized using a dual-mode square loop and meander loop resonators. The patches used in resonators are called perturbation element. Each path generates its own passband, and there is good isolation between them. Compared with the conventional dual band filter, the filter is smaller in size and better in performance.

## 2. MICROSTRIP MEANDER LOOP RESONATOR

Based on a variety of symmetric dual-mode resonating structures, dual-mode microstrip bandpass filters have been investigated by many researchers for applications in both wired and wireless communication. The schematic layout of the dual-mode meander loop resonator are shown in Figure 1, which shows that the meander loop resonator has the advantage of compact size. This resonator is designed at 1.8 GHz. For dual-mode operation, a perturbation is introduced in the resonator in order to couple its two degenerate modes. The response of the dual-mode filter can be changed from elliptic to Chebyshev by simply adjusting the size of the perturbation. The appearance of the two transmission zeros in the response, is due to the presence of a parasitic coupling between the input and output. Frequency response is shown in Figure 2. It is clearly observed that two poles in stopband are realized, which can improve the selectivity of the filter.
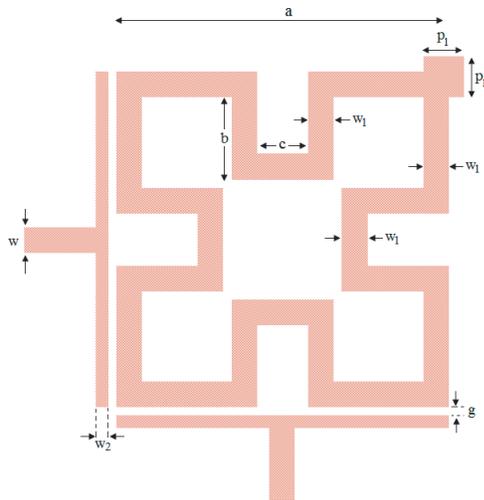
Figure 1: Layout of meander loop resonator with outer corner patch perturbation.
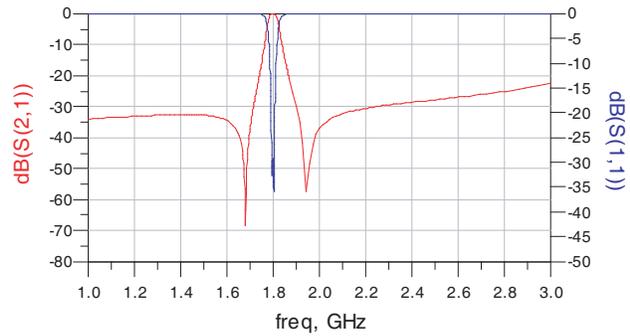


Figure 2: Simulated frequency response of meander loop resonator.
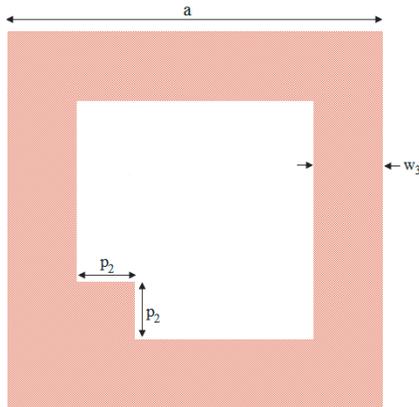


Figure 3: Layout of square loop resonator with inner corner patch perturbation.
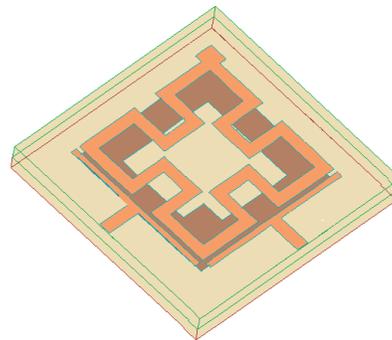


Figure 4: 3-D view of proposed dual-band bandpass filter.

## 3. MICROSTRIP SQUARE LOOP RESONATOR

Figure 3 shows layout of a dual-mode microstrip square loop resonators with an inner perturbation patch. For dual-mode operation, a perturbation is introduced in the resonator in order to couple its two degenerate modes. The square loop consists of four identical arms in length. Different filter responses can be obtained with different positions and size of the perturbation, which is analyzed in detail in [10]. The fundamental resonance occurs when $a \approx \frac{\lambda_g}{4}$, where $\lambda_g$ is guided wavelengh

$$\lambda_g = \frac{c}{f\sqrt{\varepsilon_{eff}}} \tag{1}$$

where $c$ is the velocity of light in free space, and $\varepsilon_{eff}$ is the effective dielectric constant of the substrate. According to (1), for a fixed resonant frequency, $a = \lambda_g/4$ is decreased to realize size reduction as $\varepsilon_{eff}$ increased. Similarly, for a fixed $\varepsilon_{eff}$, the resonant frequency $f$ is decreased as $a$ increased. So the fundamental resonant frequency is shifted down. Therefore, to obtain $2.4\,\text{GHz}$, this square resonator is designed at $2.66\,\text{GHz}$. It is designed and simulated on a substrate with permittivity of 10.8 and thickness of $1.27\,\text{mm}$.

## 4. PROPOSED BANDPASS FILTER DESIGN

The 3-D view of proposed dual-band bandpass filter is shown in Figure 4. The substrate 2 without ground plane at its bottom side is stacked on the mid-layer loop, which increases the $\varepsilon_{eff}$ effectively.
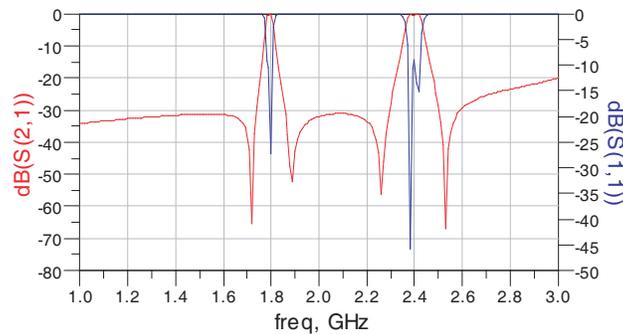
Figure 5: Simulated frequency response of dual-band bandpass filter.

So the fundamental resonant frequency is shifted down from 2.66 GHz to 2.4 GHz. The bottom side of substrate 1 is ground plane. The substrate with dielectric constant $\varepsilon_r = 10.8$ and thickness $h = 1.27$ mm are used for our proposed bandpass filter design. The size of substrate 2 on the mid-layer loop is $22 \times 22$ mm$^2$. The dimensions of the proposed filter are as follows: $a = 13$ mm, $w_1 = 1$ mm, $b = 3.17$ mm, $c = 2$ mm, $p_1 = 1.6$ mm, $w_2 = 0.5$ mm, $w_3 = 2.3$ mm, $p_2 = 2$ mm and $w = 1$ mm, which is the width of $50\,\Omega$ microstrip line

The feed-line using microstrip line type gives the convenience to connect with other circuits in systems. The two loops located on mid-layer and top-layer provide two transmission paths to RF signal. The proposed filter generates two separated passbands by using two loops resonating different frequency, mid-layer loop for higher passband, and top-layer loop for lower passband. In addition, each dual-mode loop generates own passband and two attenuation poles at respective stopbands, which keeps good selectivity of the proposed filter. In order to reduce the coupling between the two perturbation patches and the mutual effects of the two passbands, the two patches are located at different corners of top-layer loop and mid-layer loop.

## 5. SIMULATED RESULTS

The simulation is accomplished by using EM simulator tool (ADS). Figure 5 shows the simulated results of the proposed dual-mode dual-band bandpass filter centered at 1.8 GHz and 2.4 GHz, the minimum insertion losses of the two passbands are $-0.01$ dB and $-0.0001$ dB, respectively. Four attenuation poles at 1.72, 1.89, 2.26, and 2.53 GHz are realized. Quality factor for first and second bands are 56 and 35, respectively. Which can greatly improve the selectivity of the proposed dual-mode dual-band bandpass filter. The return losses of the two bands are better than $-25$ dB and $-15$ dB, respectively.

## 6. CONCLUSION

In this paper, a dual-band bandpass filter using loop structure is presented with the advantages of low loss, narrow bandwidth. The two dual-mode loop resonators on different layers generate respective passband, and changing the operating frequency of each of them does not vary that of the other. Four attenuation poles in the stopbands are realized to improve the selectivity of the filter and isolation between the two passbands. Morever, this new structure has size reduction of about 30% against the loop filter at the same center frequency. By this new design, the traditional dual band bandpass filter's performance is improved.

## REFERENCES

1. Xiao, J. K. and Y. Li, "Novel compact microstrip square ring bandpass filters," *Journal of Electromagnetic Waves and Applications*, Vol. 20, No. 13, 1817–1826, 2006.
2. Miyake, et al., "A miniaturized monolithic dual band filter using ceramic lamination technique for dual-mode portable telephones," *IEEE MTT-S Int. Dig.*, 789–792, 1997.
3. Dai, X.-W., C.-H. Liang, B. Wu, and J.-W. Fan, "Novel dual-band bandpass filter design using microstrip open-loop resonators," *Journal of Electromagnetic Waves and Applications*, Vol. 22, No. 2–3, 219–225, 2008.
4. Wang, J., Y.-X. Guo, B.-Z. Wang, L.-C. Ong, and S. Xiao, "High-selectivity dual-band stepped-impedance bandpass filter," *Electronics Letters*, Vol. 42, No. 9, 538–540, 2006.

5. Sun, S. and L. Zhu, "Novel design of dual-band microstrip bandpass filters with good in-between isolation," *IEEE APMC*, Suozhou, 2005.

6. Xiao, J.-K., S.-W. Ma, S. Zhang, and Y. Li, "Novel compact split ring stepped-impedance resonator (SIR) bandpass filters with transmission zeros," *Journal of Electromagnetic Waves and Applications*, Vol. 21, No. 3, 329–339, 2007.

7. Tsai, L.-C. and C.-W. Hsue, "Dual-band bandpass filters using equallength coupled-serial-shunted lines and z-transform techniques," *IEEE Trans. Microw. Theory Tech.*, Vol. 52, No. 4, 1111–1117, 2004.

8. Tsai, L.-C. and C.-W. Hsue, "Dual-band bandpass filters using equallength coupled-serial-shunted lines and z-transform techniques," *IEEE Trans. Microw. Theory Tech.*, Vol. 52, No. 4, 1111–1117, 2004.

9. Hong, J.-S. and M. J. Lancaster, "Microstrip triangular patch resonator filters," *IEEE MTT-S International Microwave Symposium Digest*, Vol. 1, 331–334, Jun. 2000.

10. Görür, A., "Description of coupling between degenerate modes of a dual-mode microstrip loop resonator using a novel perturbation arrangement and its dual-mode bandpass filter applications," *IEEE Trans. Microw. Theory Tech.*, Vol. 52, No. 2, 671–677, 2004.

11. Hseih, L.-H. and K. Chang, "Compact dual-mode elliptic-function bandpass filter using a single ring resonator with one coupling gap," *Electron. Lett.*, Vol. 36, 1626–1627, 2000.

# A Miniaturized Dual-narrowband Bandpass Filter Using Microstrip Open-loop and Complementary Split Ring Resonators (CSRRs) for Personal Communication Systems (PCS's)

**S. Sadi[1], M. Dousti[2], and A. Moradikordalivand[3]**

[1]Department of Electrical Engineering
Islamic Azad University (IAU), South Tehran Branch, Tehran, Iran
[2]Department of Electrical Engineering
Islamic Azad University (IAU), Science and Research Branch, Tehran, Iran
[3]Faculty of Electrical Engineering, University Technology Malaysia, Malaysia

**Abstract**— In this paper, a compact dual-narrowband bandpass filter is designed and proposed using microstrip open-loop and complementary split ring resonators. The proposed dual-band BPF consists of four open-loop resonators in combination with three complementary split ring resonators which realizes a dual-band BPF with a size reduction about 64% in comparison with the conventional one. Additionally, transmission zeroes of the proposed structure guarantee the sharpness the skirts of scattering parameters of dual-band BPF. The frequency response of the filter is simulated using an EM simulation tool.

## 1. INTRODUCTION

Current advancements in modern wireless communication systems demonstrate the needs for smaller and low-cost microwave components. In this connection, several communication systems such as personal ones operate in dual bands are necessary for narrow-band kinds of such components. Dual-narrowband bandpass filters (BPF) are one of the most popular components increasingly investigated in the most recent studies. Many dual-band BPFs have been introduced by different topologies in several investigations; however, they still have complicated structures and occupy a relatively large area on their substrates [1–3]. For instance, a dual-band BPF has been proposed in [3] where it has been designed to use for multi-layered technology with a size about $30 \times 28 \, \text{mm}^2$ on its substrate.

Moreover, a dual-band bandpass filter has recently been developed using stepped-impedance resonators (SIRs) which provide a dual-band band pass. Though its size is about $433 \, \text{mm}^2$, it is still relatively large on circuit boards [4].

Furthermore, another dual-band BPF has been analyzed and introduced in [5] designed using short-circuited stubs which is difficult to implement accompanied by an active size around $24 \times 19.5 \, \text{mm}^2$.

Besides, several techniques based on microstrip open and closed loop resonators have been discussed on different studies [6, 7]. Although they have simple design procedure, they occupy large area on their substrate. For example a dual-band bandpass filter size that has been introduced using this technique has been reported around $26 \times 28 \, \text{mm}^2$.

It is well known that these open-loop resonators usually have compact size; however, they are not capable of providing dual-band behavior by themselves. On the other hand, another kind of resonators named as complementary split ring resonators have been introduced in the recent years to realize dual-band behavior. These resonators have been widely utilized in several studies; however, their combination of them with the open-loop resonators has not been observed yet.

Here is a novel compact dual-band BPF designed and simulated using the combination of these two well-known resonators. The proposed BPF realizes a compact dual-band that its size is reported to be about $16 \times 16 \, \text{mm}^2$. It is designed and simulated on a 50-mil-thickness substrate with a constant dielectric of 10.8.

## 2. DESIGN PROCEDURE

As stated, this paper introduces a new kind of dual-band BPF developed using a combination of microstrip open-loop and complementary split ring resonators. To get an analytical view of this proposed filter, the structure of the conventional BPF is presented in [8] initially followed. Fig. 1 shows the schematic diagram and the equivalent circuits of the electrical and magnetic coupling of the conventional BPF.
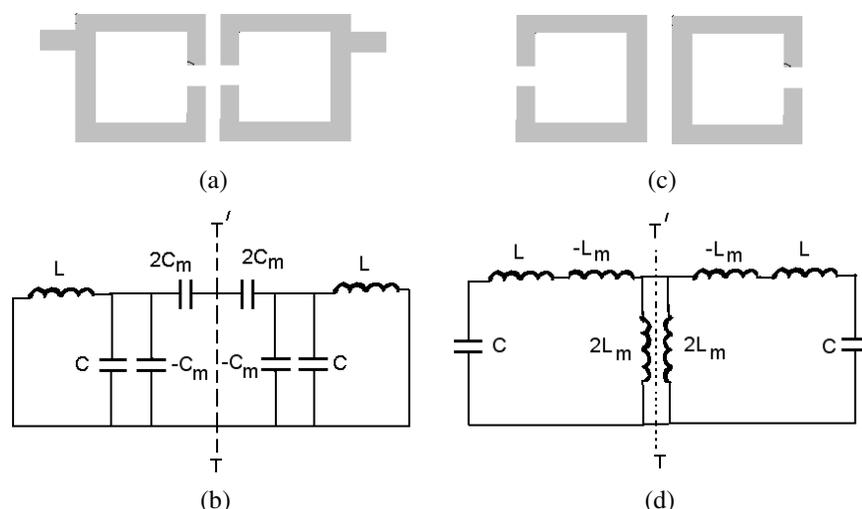
Figure 1: (a) The structure and (b) equivalent circuit of the electrical coupling and (c) structure and (d) equivalent circuit of the magnetic coupling of the conventional $\mu$-Strip open-loop resonators.
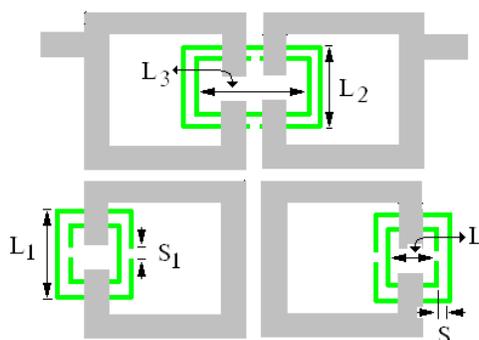


Figure 2: The proposed topology for the design of dual-narrowband BPF with: $L = 2.3\,\text{mm}$, $L_1 = 3.5\,\text{mm}$, $L_2 = 3.5\,\text{mm}$, $L_3 = 9\,\text{mm}$, $S = S_1 = 0.2\,\text{mm}$, $W = 0.2\,\text{mm}$ for all CSRRs and the dimensions of the microstrip open-loop are the same as their original values presented in [8].

As observed, this structure consists of four microstrip open-loop resonators which have been somehow arranged to provide electrical, magnetic and mixed couplings among these resonators.

To develop this compact filter for providing dual-band behavior, the gaps in its structure can be provided by a complementary split ring resonators (CSRRs). To design a compact dual-narrowband BPF, the proposed structure shown in Fig. 2 is considered.

Observing the proposed structure, the two coupled gaps for the electrical coupling are supported with a CSRR together and each of the other two ones is provided with a CSRR. Following, the equivalent circuit model of each part of the proposed dual-band BPF is derived. The equivalent circuit of each gap with this resonator is quite well-known as presented in Fig. 3(a); however, the one for the coupled gaps is more complicated.

To synthesize the equivalent circuit of the first part of the proposed structure including the coupled gaps and the complementary split ring resonator the equivalent circuit model of two coupled gaps is initially followed. As indicated in Fig. 4(a), the two coupled gaps can be represented by two coupled capacitor with the coupling coefficient M. According to the transmission line theories, it is well known that a pair of two coupled capacitors is exactly equal to an admittance inverter including coupling capacitor as a multiple of the resonant frequency as shown in Fig. 3(b). On the other hand, the admittance inverter can be expressed as a capacitive circuit as presented in Fig. 3(c) where the parallel ones have the positive capacitance and the series one has the negative one.

Afterwards, the obtained equivalent circuit in Fig. 4(c) can be replaced by that in the final network provided in Fig. 3(b) based on the circuit theories. Needless to say, the parallel LC circuit and the series one including $Cc'$, $Lc'$ and $C'$ is the equivalent circuit of the complementary split ring resonator.

(a)  (b)
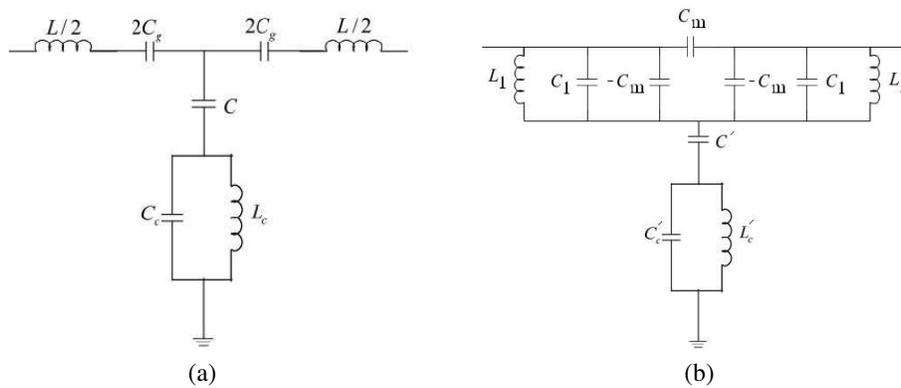
Figure 3: Equivalent circuit model of (a) a single gap with CSRR (b) the coupled Gaps with CSRR.



(a)  (b)  (c)
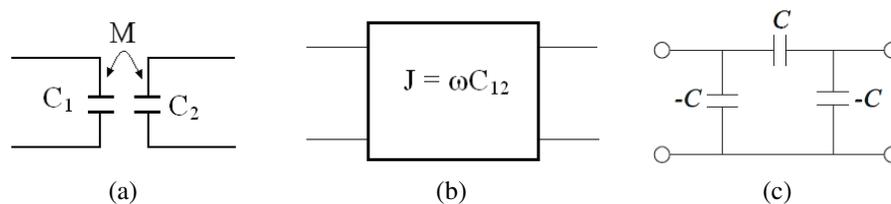
Figure 4: The equivalent circuit of (a) two coupled capacitors (b) admittance inverter (c) capacitance circuit of admittance inverter.



(a)  (b)
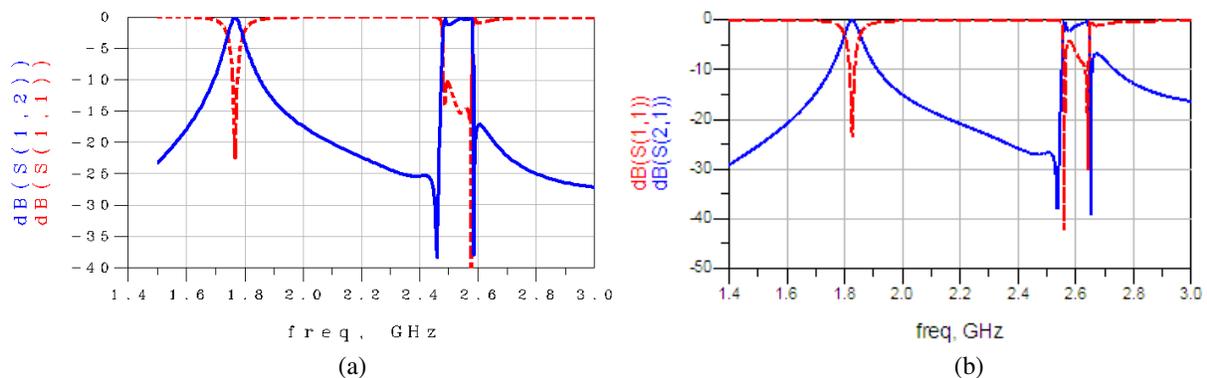
Figure 5: The simulated performance of the preposed dual-narrowband BPF.

As indicated in [8, 9], the structure without CSRR, provides a resonant frequency, and as shown in [10], the CSRR provides another one which a dual-band BPF can be designed using a combination of these two resonators.

## 3. SIMULATION RESULTS

According to the given specifications in the previous sections, a compact dual-band bandpass filter can be designed and simulated using a novel combination of microstrip open-loop and complementary split ring resonators. The proposed topology shown in Fig. 1 is thus implemented and simulated using an EM simulator tool (ADS). A fine tuning process is carried out to optimize the dimensions in order to have a dual-band bandpass filter.

Figure 5(a) shows the simulated frequency response of the proposed dual-band bandpass filter where the dashed lines and the solid lines represent the return and insertion losses of the component, respectively, also Fig. 5(b) shows the simulated frequency response of the equivalent circuit proposed dual-band bandpass filter,and they are compeletly coordinate.

Simulated central frequencies are 1765 MHz and 2530 MHz with 3-dB bandwidths of 2.8% (from 1740 MHz to 1790 MHz) and 3.9% (from 2480 MHz to 2580 GHz), respectively, making this compact

dual-band BPF very attractive and suitable for applications in the mobile and personal communication systems (PCS's). Besides, the maximum insertion losses are reported to be 0.05 dB and 1 dB in the first and second bands, respectively. The return losses for these two bands are better than $-20$ dB and $-10$ dB, respectively. The active area occupied on the substrate is about $16 \times 16 \, \text{mm}^2$ for this filter in comparison with that of the conventional one presented in [6] which has been reported about $26 \times 28 \, \text{mm}^2$ where a size reduction about 64% is obtained with this proposed filter.

## 4. CONCLUSION

A miniaturized dual-narrowband bandpass filter has been designed and proposed using microstrip open-loop and complementary split ring resonators (CSRRs) for applying in mobile and personal communication systems (PCS's). The proposed dual-band BPF has been reported that it is consisted of four open-loop resonators in combination with three complementary split ring resonators which realized a dual-band BPF with a size reduction about 60% in comparison with the conventional one. Moreover, transmission zeroes of the proposed structure guarantee the sharpness of the dual-band BPF's scattering parameters of the skirts. The frequency response of the filter has been simulated using an EM simulation tool.

## REFERENCES

1. Uchida, H., H. Kamino, K. Totani, N. Yoneda, M. Miyazaki, Y. Konishi, S. Makino, J. Hirokawa, and M. Ando, "Dual-band-rejection filter for distortion reduction in RF transmitters," *IEEE Trans. Microw. Theory and Tech.*, Vol. 52, No. 11, Nov. 2004.

2. Lai, M.-I. and S.-K. Jeng, "Compact microstrip dual-band bandpass filters design using genetic-algorithm techniques," *IEEE Trans. Microw. Theory and Tech.*, Vol. 54, No. 1, Jan. 2006.

3. Kapitanova, P., D. Kholodnyak, S. Humbla, R. Perrone, J. Mueller, M. A. Hein, and I. Vendik, "Right- and left-handed transmission line resonators and filters for dual-band applications," *Microw. Opt. Tech. Lett.*, Vol. 51, No. 3, Mar. 2009.

4. Mondal, P. and M. K. Mandal, "Design of dual-band bandpass filters using stub-loaded open-loop resonators," *IEEE Trans. Microw. Theory Tech.*, Vol. 56, 2010–2013, 2008.

5. Chen, F.-C., Q.-X. Chu, and Z.-H. Tu, "Design of compact dual-band tri-band bandpass filters using $\lambda 4$ and $\lambda/2$ resonators," *Microw. Opt. Tech. Lett.*, Vol. 51, No. 3, Mar. 2009.

6. Hsieh, L.-H., G. L. Stolarczyk, and K. Chang, "Microstrip dual-band bandpass filters using parallel-connected open-loop ring resonators," *International Journal of RF and Microwave Computer-Aided Engineering*, Mar. 2008.

7. Nosrati, M. and Z. Atlasbaf, "A novel model of small sized dual-band rectangular ring bandpass filter," *7th International Symposium on Antennas, Propagation, and EM Theory (IS-APE2006)*, Sep. 2006.

8. Hong, J. S. and M. Lancaster, "Couplings of microstrip square open-loop resonators for cross-coupled planar microwave filters," *IEEE Trans. Microw. Theory Tech.*, Vol. 44, 2099–2109, Nov. 1996.

9. Nosrati, M. and Z. Atlasbaf, "A compressed planar band-pass filter using microstrip square resonators with interdigital capacitor," *7th International Symposium on Antennas, Propagation, and EM Theory (ISAPE2006)*, Sep. 2006.

10. Baena, J. D., J. Bonache, F. Martín, R. Marqués Sillero, F. Falcone, T. Lopetegi, M. A. G. Laso, G.-G. Joan, I. Gil, M. F. Portillo, and M. Sorolla, "Equivalent-circuit models for split-ring resonators and complementary split-ring resonators coupled to planar transmission lines," *IEEE Trans. Microwave Theory Tech.*, Vol. 53, No. 4, 1451–1461, Apr. 2005.

# A Novel Miniaturized Narrow Band Bandpass Filter Utilizing Microstrip Open-loop Ring Resonators for Narrow-band Applications

**Massoud Dousti[1], Parisa Taheri[2], Samaneh Sadi[2], and Majid Zamani[1]**

[1]Department of Electronic Engineering
Science and Research Branch, Islamic Azad University (IAU), Tehran, Iran
[2]Department of Electronic Engineering
South Tehran Branch, Islamic Azad University, Tehran, Iran

**Abstract**— In this paper, a novel compact topology of microstrip open-loop ring resonator is introduced to design narrowband bandpass filters with better performance in making trade-off between insertion loss and bandwidth. The proposed structure comprises of two microstrip open-loop ring resonators only with magnetic coupling instead of electrical, magnetic and mixed ones in the conventional ones.

The performance of this novel bandpass filter is simulated using an EM simulation tool and simultaneously compared with the conventional one which confirms the priority of this filter to them. The proposed NB BPF provides a narrowband bandpass filter with a bandwidth of 0.91% and better insertion and return losses in comparison with the conventional ones. Additionally, a size reduction about 36% is also reported by this novel layout.

## 1. INTRODUCTION

Wireless personal communication services (PCS), global system for mobile communications (GSM) and satellite receiver links are some of the important applications which increasingly demand ultra narrowband (NB) filters with a FBW of 1%–3% and sometimes less than 0.5%. These filters should have lighter weight, less compact size, lower insertion loss and sharper selectivity in the passbands. many different models have been introduced to design a NB BPF with different topologies; however, there has always been a fundamental challenge to achieve a sort of trade-off between insertion loss (IL) and bandwidth (BW) in the design of such filters so that to realize a narrower BW, insertion loss must be scarified or vice versa. For example, dual-mode ring resonators BPF are one of the simplest kind such components by which a narrowband BPF can be designed, though their bandwidth is around 4% [1–4].

In these studies, several topologies such as end-coupled as well as tapped line ones are used to enhance coupling strength between input/output and resonators have been used; however, they have not realized a narrow-band bandpass filter with desirable narrowband and low insertion loss yet.

Additionally, several compact bandpass filters have been recently reported using microstrip open loop resonators with and without interdigital. These filters are highly compact in size with low insertion loss; though, they have also realized a 3-dB bandwidth of around 4% [5, 6].

Another technique has been proposed in [7] to design narrowband BPFs using microstrip open-loop resonators with coupled and crossing Lines. This one has demonstrated a NB BPF with a bandwidth of 2% with the insertion loss of 3.1 dB where dielectric overlays have been used to compensate this relatively high insertion loss at the expense of the increase of BW and implementation cost.

This problem, a good trade-off between IL and BW, has reported such a critical result that the designers have utilized high-temperature superconducting thin-film technology to remedy conductor and dielectric losses [8–10].

In this paper, a novel coupling scheme is introduced for open-loop $\mu$-strip resonators by which a narrower-band BPF is designed and developed. Initially, a sample NB BPF is designed and simulated utilizing two $\mu$-strip open-loop resonators realizing a 3-dB bandwidth of 0.91%. As presented, this NB BPF has a high level of insertion loss in practice. To compensate this extra loss, the topology of the proposed BPF is developed by double layout of this proposed filter in parallel. In the wake of this modification, the 3-dB BW of the filter is sacrificed and increased up to 2.4%.

The proposed NB BPF is subsequently designed and fabricated on a 50-mil-thickness RT/Duroid with dielectric constant 10.5. Furthermore, the measured and simulated results are simultaneously presented.

## 2. THE CONVENTIONAL MICROSTRIP OPEN-LOOP RING RESONATORS

By consulting the design procedure of the conventional microstrip open-loop ring resonators which have been established [5, 6], it is revealed that in fact, their structures have utilized three types of couplings including electrical, magnetic and mixed ones. Ignoring the mixed coupling which is created among loops; the other ones have an inevitable role in realizing this kind of NB BPF. In this structure, a lot of magnetic current is conducted via mixed couplings among loops and then coupled to another loop via magnetic couplings and at the same time, the other part is transferred via electrical coupling in another path. Fig. 1 shows the distribution of electromagnetic current on the structure of the conventional microstrip open-loop bandpass filter at its central resonant frequency (2.52 GHz).

Observing the simulated structure shows that most of this current is distributed in the input ports as well as the crossed above loop. In fact, a lot of these currents are perished as a conductor loss in the transmission lines especially around capacitive gaps. In another study, a different topology has been introduced to these resonators; however, the insertion loss has not been reduced completely yet [11]. In the next section, a novel compact structure is proposed by which a much narrower bandpass filter can be designed with better insertion and return loss in pass band.

## 3. THE PROPOSED NB BPF USING NOVEL TOPOLOGY OF THE MICROSTRIP OPEN-LOOP RING RESONATORS

As indicated in Fig. 2, a novel topology of the microstrip open-loop ring resonator is proposed in this paper. Contrary to the conventional one, in this structure, the electrical and magnetic coupling structures are only utilized.

To verify the magnetic current distribution on the proposed structure, the performance of this filter is simulated at its central resonant frequency (2.51 GHz) using an EM simulation tool (ADS) as provided in Fig. 3.

Observing the magnetic current distribution on the novel structure in which most of this current exists on the open-loop resonator instead of being around the input terminal is contrary to the conventional one. This is because of the increase of matching between resonators and input/output terminals.

To justify this phenomenon mathematically, the internal loss of the structure can be expressed
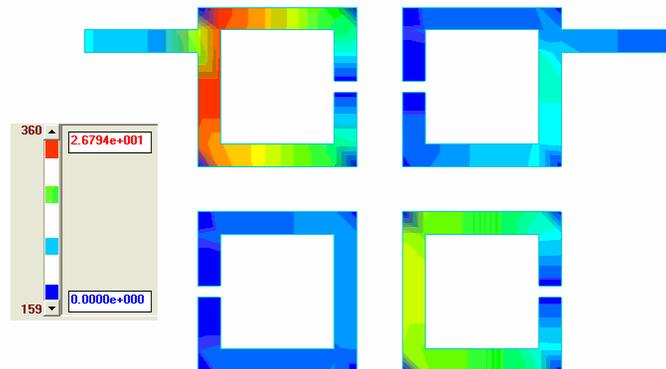


Figure 1: The current distribution on the structure of the conventional filter at its resonant frequency.
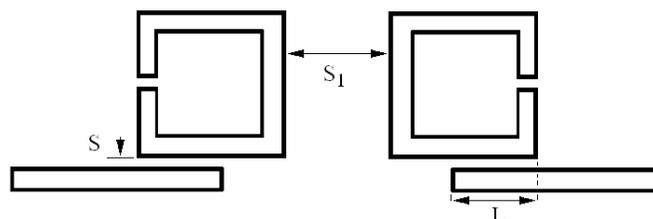


Figure 2: The proposed structure to design NB BPF using microstrip open-loop ring resonators with $L = 4$ mm, $S = 0.6$ mm, $S_1 = 5$ mm, and other parameters of the layout are exactly the same as those of the conventional one.
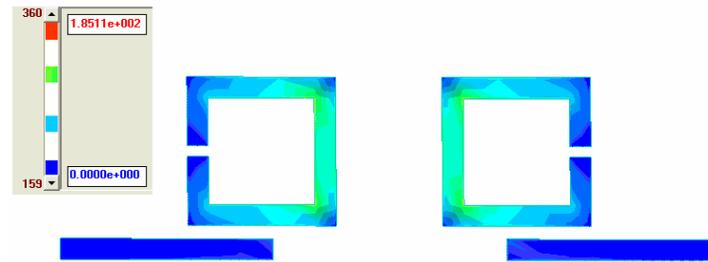
Figure 3: The current distribution on the structure of the proposed filter at its resonant frequency.
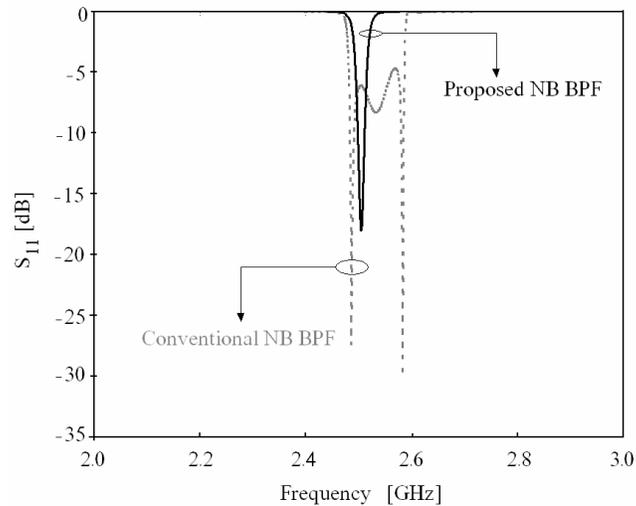


Figure 4: A comparison between the return losses of the conventional and the proposed NB BPFs.

in terms of quality factor of the network regardless of dielectric and conductor loss as follows [12]:

$$L_I = L_T = 10 \log \left[ 1 + (Q_L \, \varepsilon_f)^2 \right] \tag{1}$$

where the quality factor of QL is directly proportional to the mismatching of the structure, the more the matching is realized the more this factor is increased in the resonant frequency as indicated in Equation (2).

$$Q_L = \frac{f_r}{3\text{-dB Bandwidth}} \tag{2}$$

According to current distribution on the conventional and proposed models, it can be concluded that the maximum value of matching can be demonstrated by using the novel topology of the microstrip open-loop ring resonator and subsequently, the minimum value of bandwidth can be obtained by this technique. To examine the performance of the proposed layout and compare to the conventional ones, the frequency responses of these two filters are simultaneously simulated using an EM simulator tool.

Initially, the realization of the further matching in the proposed layout is verified where Fig. 4 provides the return loss of the two narrowband bandpass filters.

Observing the performance of these two filters in terms of their return loss in their passbands, the maximum level of this parameter is reported to be around $-7$ dB and $-17$ dB for the conventional and proposed NB BPFs, respectively. This fact simply reveals that one of the disadvantages of the conventional topology is suffering from high level of mismatching in their structures which is improved by the proposed layout to some extents.

Similarly, the performance of these two filters is examined in terms of their insertion loss where is shown in Fig. 5.

As indicated in Fig. 5, the proposed NB BPF provides a bandwidth of 0.91% from 2491.9 MHz to 2517.8 MHz at the central resonant frequency of 2510 MHz in comparison of that of 4% for the
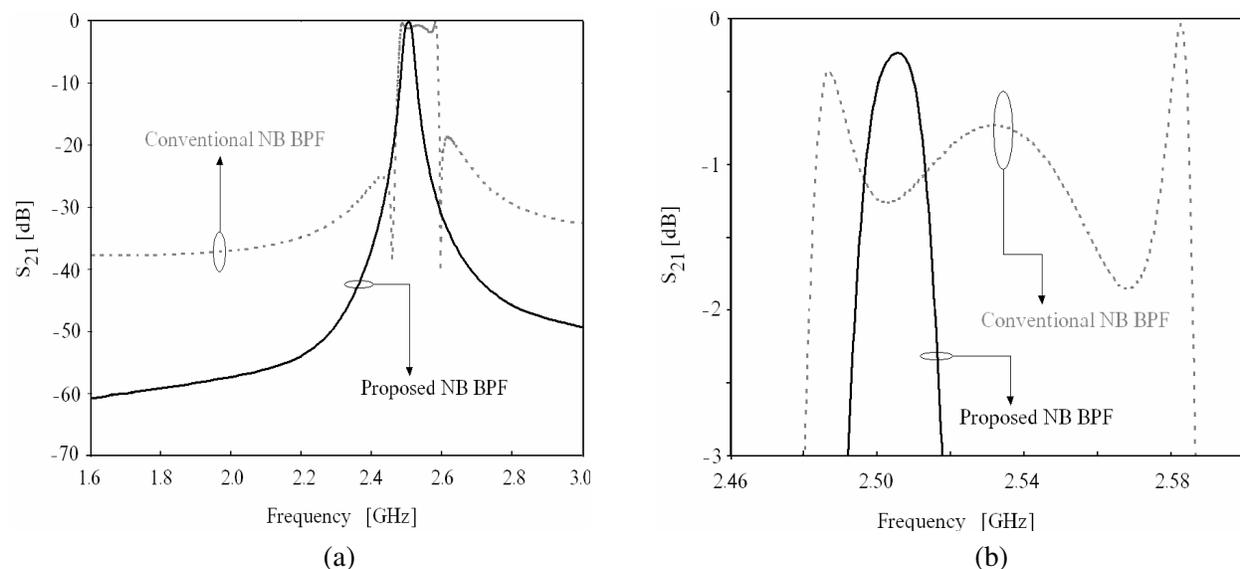
Figure 5: (a) A comparison between the insertion losses of the conventional and the proposed NB BPFs, (b) within 3 dB bandwidth.

conventional one which makes the proposed filter a better candidate for personal communication systems (PCSs). Additionally, the proposed NB BPF occupies an area about $31 \times 8.6\,\text{mm}^2$ on its substrate in comparison with that of the conventional one around $26 \times 16\,\text{mm}^2$ which results in a size reduction about 36%.

According to the performance of these filters within 3-dB, the maximum insertion loss of the proposed filter is reported to be about 0.25 dB in comparison with that of the conventional one which is around 1.9 dB. According to the given specifications, the results of this study prove this fact that the proposed NB BPF can be used to wireless personal communication services. As indicated in Fig. 5, the proposed NB BPF provides a bandwidth of 0.91% from 2491.9 MHz to 2517.8 MHz at the central resonant frequency of 2510 MHz in comparison of that of 4% for the conventional one which makes the proposed filter a better candidate for personal communication systems (PCSs). Additionally, the proposed NB BPF occupies an area about $31 \times 8.6\,\text{mm}^2$ on its substrate in comparison with that of the conventional one around $26 \times 16\,\text{mm}^2$ which results in a size reduction about 36%.

According to the performance of these filters within 3-dB, the maximum insertion loss of the proposed filter is reported to be about 0.25 dB in comparison with that of the conventional one which is around 1.9 dB. According to the given specifications, the results of this study prove this fact that the proposed NB BPF can be used to wireless personal communication services (PCS), global system for mobile communications (GSM) and satellite receiver links are which demand ultra narrowband (NB) filters with a FBW of 1%–3%.

## 4. CONCLUSION

In this paper, a novel solution has been introduced to design narrowband bandpass filters with better performance in making trade-off between insertion loss and bandwidth. The proposed topology has reported that it consists of two microstrip open-loop ring resonators only with magnetic coupling instead of electrical, magnetic and mixed ones in the conventional ones.

The performance of this novel pandpass filter has been simulated using an EM simulation tool which confirms the priority of this filter to the conventional ones. The proposed NB BPF has realized a narrowband bandpass filter with a bandwidth of 0.91% and better insertion and return loss in comparison with the conventional one. Additionally, a size reduction about 36% has been obtained by this novel layout.

## REFERENCES

1. Guglielmi, M. and G. Gatti, "Experimental investigation of dual-mode microstrip ring resonator," *Proc. 20th European Microwave Conf.*, 901–909, Budapest, Hungary, Sep. 10–13, 1990.

2. Curtis, J. A. and S. J. Fiedziuszko, "Multi-layered planar filters based on aperture coupled, dual mode microstrip or stripline resonators," *IEEE MTT-S Int. Microwave Symp. Dig.*, 1203–1206, Albuquerque, NM, Jun. 1–5, 1992.

3. Hong, J. S. and M. J. Lancaster, "Bandpass characteristics of new dual mode microstrip square loop resonators," *Electron. Lett.*, Vol. 31, No. 11, 891–892, May 1995.

4. Hong, J. S. and M. J. Lancaster, "Microstrip bandpass filter using degenerate modes of a novel meander loop resonator," *IEEE Microwave Guided Wave Lett.*, Vol. 5, 371–372, Nov. 1995.

5. Hong, J. S. and M. J. Lancaster, "Realization of quasielliptic function filter using dual-mode microstrip square loop resonators," *Electron. Lett.*, Vol. 31, No. 24, 2085–2086, Nov. 1995.

6. Nosrati, M. and Z. Atlasbaf, "A compressed planar band-pass filter using microstrip square resonators with interdigital capacitor," *7th International Symposium on Antennas, Propagation, and EM Theory (ISAPE2006)*, Sep. 2006.

7. Yu, C.-C. and K. Chang, "Novel compact elliptic-function narrow-band bandpass filters using microstrip open-loop resonators with coupled and crossing lines," *IEEE Trans. Microwave Theory Tech.*, Vol. 46, No. 7, 952–958, Jul. 1998.

8. Hong, J.-S., M. J. Lancaster, D. Jedamzik, and R. B. Greed, "On the development of superconducting microstrip filters for mobile communications applications," *IEEE Trans. Microw. Theory and Tech.*, Vol. 47, No. 9, 1656–1663, 1999.

9. Matthaei, G. L., "Narrow-band, fixed-tuned, and tunable bandpass filters with zig-zag hairpin-comb resonators," *IEEE Trans. Microw. Theory and Tech.*, Vol. 51, No. 4, 1214–1219, 2003.

10. Hejazi, Z. M., M. C. Scardelletti, F. W. van Keuls, A. A. Omar, and A. Al-Zayed, "EM full-wave analysis and testing of novel quasi-elliptic microstrip filters for ultra narrowband filter design," *Progress In Electromagnetics Research*, Vol. 85, 261–288, 2008.

11. Yeo, K. S. K., M. J. Lancaster, and J.-S. Hong, "The design of microstrip six-pole quasi-elliptic filter with linear phase response using extracted-pole technique," *IEEE Trans. Microwave Theory Tech.*, Vol. 49, No. 2, 321–327, Feb. 2001.

12. Rizzi, P. A., *Microwave Engineering: Passive Circuit*, Prentice-Hall, Englewood Cliffs, NJ, 1988.

# A New Wavelet Space Time Coding Technique Designed for UWB MISO Systems

**Said E. El-Khamy**[1], **Ehab Farouk Badran**[2], **and Amira Ibrahim Zaki**[2]

[1]Department of Electrical Engineering, Faculty of Engineering
Alexandria University, Alexandria, Egypt
[2]Department of Electronics and Communication Engineering
Arab Academy for Science and Technology, Alexandria, Egypt

**Abstract**— A new MISO-STC scheme designed specifically for Ultra-Wideband (UWB) systems is introduced in this paper. The proposed scheme is based on multiplexing multiple symbols in the wavelet domain of the UWB pulses in addition to the spatial multiplexing offered by using multiple transmitting antennas. Rake receivers are used to collect the energy in the dense multipath channel components. The suggested technique is referred to as the wavelet space time coding scheme (WSTC). In WSTC four symbols are transmitted on the same UWB transmission pulse with the same bandwidth, symbol duration, and number of transmitting antennas of the conventional MISO-STC scheme. The used mother wavelet (MW) is selected to be highly correlated with transmitted pulse shape and such that the multiplexed signal has almost the same spectral characteristics as those of the original UWB pulse. The simulation results show that the proposed WSTC scheme has better performance than the conventional scheme in addition to increasing the data rate to four times that of the conventional STC scheme.

## 1. INTRODUCTION

UWB is a developing short range technique that provides a high data rate. The UWB transmission allows it to be used with systems and fields like in WLAN (Wireless Local Area Network), biomedical and military fields [1–3].

UWB transmission consists of a train of very short pulses. The UWB transmitted pulse is of $-10$ dB bandwidth $\geq 500$ MHz or of fractional bandwidth $> 20\%$. According to the Federal Communication Committee (FCC) regulations, the UWB systems are allowed to transmit over the frequency band between 3.1 and 10.6 GHz with very low power. These strict regulations on UWB systems in addition to the channel effect which is extremely frequency selective, limit the achievable data rates, and transmission range [1, 2]. The UWB channel is characterized by its dense multipath channel. The UWB channel is enriched with resolvable multipath components due to transmission using ultra-short pulses in nanosecond. The Rake receiver can be used to enhance the performance of the UWB system by capturing most of the energy of the multipath components using number of fingers (i.e., performing multipath diversity) [1–5].

To overcome the FCC power limitations, the UWB systems are implemented and studied with MIMO systems. UWB MIMO systems are presented in [6, 7] to obtain multi data stream (MS) transmission. It is also presented with space–time coding (STC) based on Alamouti's scheme [8, 9] using MRC (maximum ratio combiner) Rake receiver in [10] and [11], to make use of multipath diversity in addition to spatial diversity and thus increase channel performance and/or capacity [12] and [13].

The wavelet transform has been extensively used in the wireless communication field especially in UWB communications [14]. Wavelet transform (WT) was introduced in [15] as a new modulation scheme WSK (Wavelet Shift Keying) which is considered as a generalization of "Wavelet based OFDM (Orthogonal Frequency Division Multiplexing)". Also the OFDM scheme characteristics are enhanced by using OWDM (Orthogonal Wavelet Division Multiplexing) in a Rayleigh fading channel as illustrated in [16]. On the other hand the OFDM system is studied with DWT (Discrete Wavelet Transform) and DMWT (Discrete Multi-Wavelet Transform) to reduce the level of interference and increase spectral efficiency in [17]. It is shown in [17] that DMWT-OFDM proposes much lower bit error rate (BER), increases the signal to noise ratio (SNR), and thus can be used as an alternative to the conventional OFDM.

The WT is also used recently in the UWB communication field. The WT is used in analysing the UWB signal to detect it in the presence of background noise in [18]. The WT is used in [19] and [20] as an UWB pulse shaper to satisfy the FCC limits in addition to enhancing the spectral efficiency, and to cancel narrowband and wideband interferences in [21] and [22].

In this paper WSTC scheme (WSTC) is proposed to increases the data rate and enhance the performance of conventional STC in [10, 11] without increasing the bandwidth. The paper is organized as follows: In Section 2, the channel model used in simulation is introduced. Section 3 discusses the system model for a single transmitting and receiving antenna (SISO), and the conventional STC UWB systems in [10, 11]. Section 4 presents the proposed WSTC scheme. Section 5 introduces the simulations and results. Finally, the conclusions are shown in Section 6.

## 2. CHANNEL MODEL

The channel models used is the modified Saleh-Valenzuela (SV) model [23]. It has an impulse response mathematical model given by:

$$h(t) = \sum_{m=0}^{M-1} \alpha(m)\delta(t - \tau(m)) \tag{1}$$

where, $M$ is the number of multipath components, while, $\alpha(m)$ and $\tau(m)$ are the gain and the delay of the $m$th path respectively. The gain of the channel due to measurements as states in [23] follows the log-normal distribution, while the arrival times of the clusters and the rays included follow the Poisson one.

## 3. SYSTEM MODEL

This section, presents the system model used in this paper for an UWB SISO and MISO systems for pear-to-pear communication. In the UWB communications binary symbols $s = \pm 1$ are transmitted over a train of ultra-short pulses. The system has $N_t$ transmit and $N_r$ receive antennas. The binary symbol is pulse shaped by monocycle pulse. Then the symbols are modulated by PAM (Pulse amplitude modulation) modulation and transmitted repeatedly over $N_f$ frames each of time duration $T_f$ ($T_s = N_f T_f$, where $T_s$ is the symbol duration). The pulse waveform $w(t)$ has typical duration $T_w$ between 0.2–2 ns, resulting in transmission over an ultra-wide bandwidth. Assuming that the CIR is known at the receiver and the channel is constant for a block of symbols

### 3.1. SISO Scheme

If a single transmit and receive antennas are assumed (SISO), and PAM modulation, the transmitted waveform for the binary symbol $s$ is given by:

$$S(t) = s\sqrt{\frac{E}{N_f}} \sum_{n_f=0}^{N_f-1} w(t - n_f T_f) \tag{2}$$

where, $E$ is the symbol energy, and pulse shape $w(t)$ is of unit energy. The multipath channel can be expressed in terms of multipath delays and gains as in (1). Note that, $\tau(m) > \tau(m-1)$, and $T_m = \tau(M-1)$ is the maximum delay spread of the dense multipath channel. To avoid the ISI simply choose $T_f \geq T_m + T_w$. The modelled multipath fading channel is assumed to be quasi-static (i.e., constant during a block of symbols).

A Rake receiver is used at the receiver to collect multipath diversity. It uses $L$ finger (matched filters), where $L \leq M$, and uses $w(t)$ as the correlator reference template with an autocorrelation function $R_w(\tau)$ [10].

### 3.2. Analog STC MIMO Scheme

For a MISO the output of the first transmit antenna during each symbol $T_s = N_f T_f$ is given by [11]:

$$S_0(t) = s\sqrt{\frac{E}{2N_f}} \sum_{n_f=0}^{N_f-1} (-1)^{n_f} w(t - n_f T_f) \tag{3}$$

and of the second transmit antenna is:

$$S_1(t) = s\sqrt{\frac{E}{2N_f}} \sum_{n_f=0}^{N_f-1} w(t - n_f T_f) \tag{4}$$

## 4. PROPOSED WAVELET SPACE TIME CODING TECHNIQUE

This section illustrates the proposed wavelet space timecoding (WSTC). The WSTC combines four symbols using the IDWT and multiple transmitting antennas (multiplexing in frequency and space) and send them on the same bandwidth and same symbol duration of the conventional STC presented in Section 3. It is like sending half of the symbols on half of the bandwidth of the transmitted pulse on different transmitting antennas. The WSTC code word is shown in Figure 1 while the transmitter and receiver are shown in Figure 2 and Figure 3 respectively. For a MISO WSTC ($N_t = 2$ and $N_r = 1$), the output of the first transmit antenna during each symbol $T_s = N_f T_f$ is given by

$$S_0(t) = \sqrt{\frac{2E}{N_f}} \sum_{n_f=0}^{N_f-1} w_0(t - n_f T_f) \tag{5}$$

and for the second antenna is given by

$$S_1(t) = \sqrt{\frac{2E}{N_f}} \sum_{n_f=0}^{N_f-1} (-1)^{n_f} w_1(t - n_f T_f) \tag{6}$$

where $w_0(t)$ and $w_1(t)$ are the transmitted pulse $w(t)$ embedded with $s_1$, $s_2$ and $s_3$, $s_4$ respectively. $w_0(t)$ is the IDWT of the approximation waveform $x_1(t) = s_1 \sqrt{\frac{E}{N_f}} w_a(t)$ and the detail waveform $x_2(t) = s_2 \sqrt{\frac{E}{N_f}} w_d(t)$ while $w_1(t)$ is that of $x_3(t) = s_3 \sqrt{\frac{E}{N_f}} w_a(t)$ and $x_4(t) = s_4 \sqrt{\frac{E}{N_f}} w_d(t)$ respectively. The $\sqrt{2}$ factor in Equation (7) and Equation (8) is eliminated as the symbol energy is not
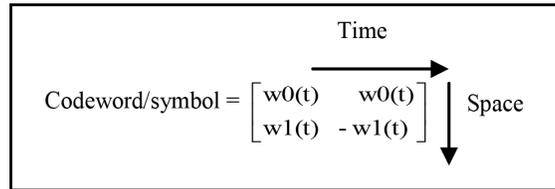


Figure 1: WSTC codeword per symbol for $N_f = 2$.
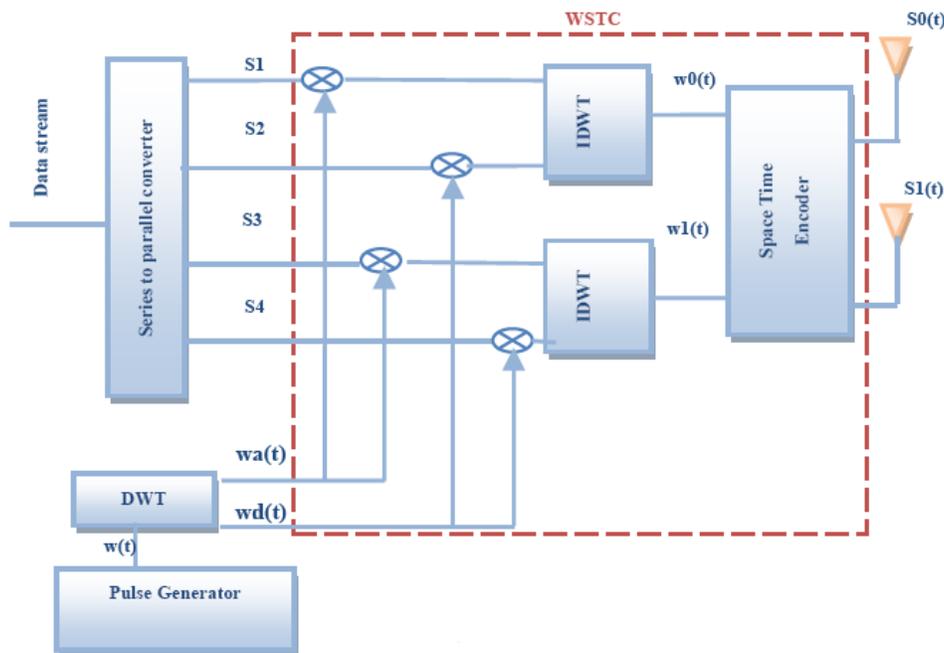


Figure 2: WSTC transmitter.
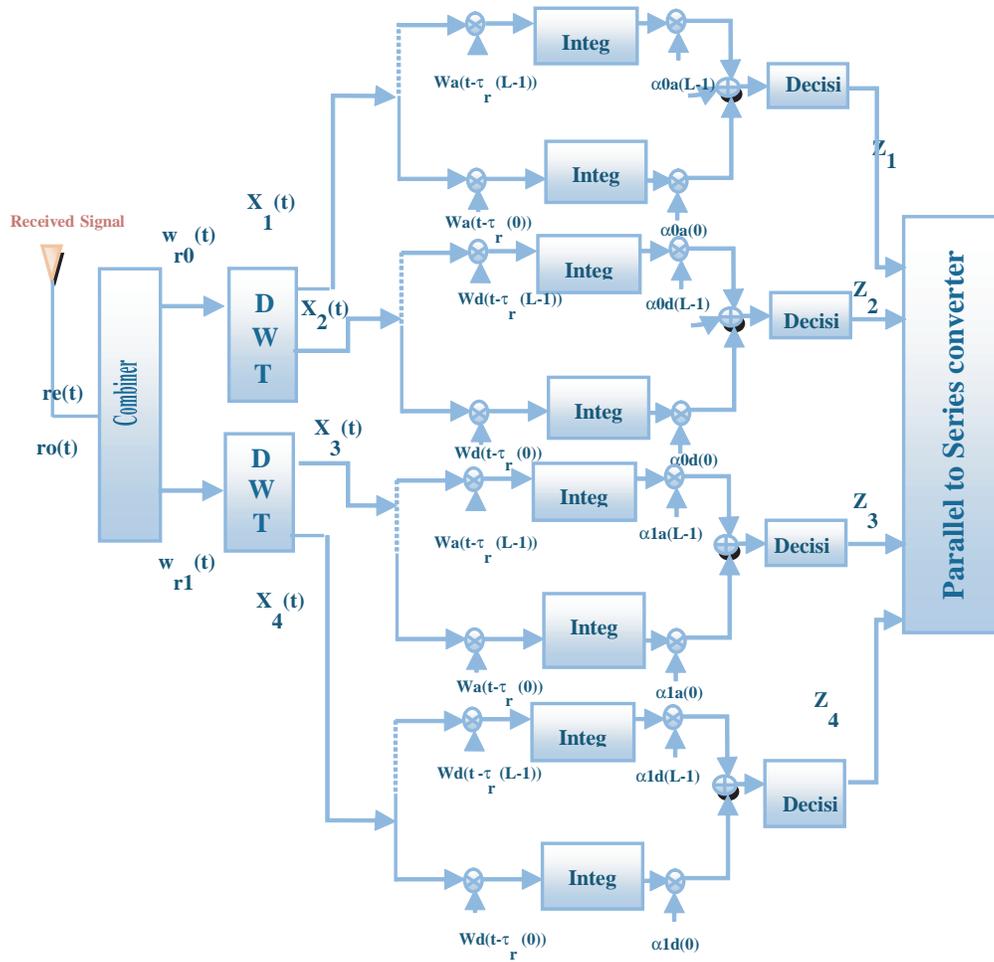
Figure 3: WSTC receiver.

divided amongst the two transmitting antennas. The received noisy signal per even frame for $M$ multipath components is as follows

$$r_e(t) = S_0(t) * h_{00}(t) + S_1(t) * h_{10}(t) + +\eta_e(t)$$
$$= \sqrt{\frac{2E}{N_f}} \sum_{m=0}^{M-1} (\alpha_{00}(m)w_0(t - \tau_{00}(m))) + \alpha_{10}(m)w_1(t - \tau_{10}(m))) + \eta_e(t) \tag{7}$$

And for odd frames

$$r_o(t) = S_0(t) * h_{00}(t) - S_1(t) * h_{10}(t) + \eta_o(t)$$
$$= \sqrt{\frac{2E}{N_f}} \sum_{m=0}^{M-1} (\alpha_{00}(m)w_0(t - \tau_{00}(m)) - \alpha_{10}(m)w_1(t - \tau_{10}(m))) + \eta_o(t) \tag{8}$$

where $\eta_e(t)$ and $\eta_o(t)$ are the additive white Gaussian noise (AWGN) with zero mean and $\sigma^2$ variance of the even and off frames respectively.

The even and odd frames are combined using a combiner to generate wave forms $w_{r0}(t)$ and $w_{r1}(t)$, which are the estimated waveforms of the transmitted ones $w_0(t)$ and $w_1(t)$ respectively. The estimated waveforms are

$$w_{r0}(t) = r_e(t) + r_o(t) = 2\sqrt{\frac{2E}{N_f}} \sum_{m=0}^{M-1} \alpha_{00}(m)w_0(t - \tau_{00}(m)) + \eta_e(t) + \eta_o(t) \tag{9}$$

$$w_{r1}(t) = r_e(t) - r_o(t) = 2\sqrt{\frac{2E}{N_f}} \sum_{m=0}^{M-1} \alpha_{01}(m)w_1(t - \tau_{01}(m)) + \eta_e(t) - \eta_o(t) \tag{10}$$

By applying the DWT to the estimated waveform, their approximation and detail components (carrying the symbols) $X_1(t)$ and $X_2(t)$ respectively for $w_{ro}(t)$ and $X_3(t)$ and $X_4(t)$ for $w_{r1}(t)$ are obtained as

$$X_1(t) = 2s_1 \sqrt{\frac{E}{N_f}} \sum_{m=0}^{M-1} \alpha_{00}(m)w_a(t - \tau_{00}(m)) + \varepsilon_1(t) \tag{11}$$

$$X_2(t) = 2s_2 \sqrt{\frac{E}{N_f}} \sum_{m=0}^{M-1} \alpha_{00}(m)w_d(t - \tau_{00}(m)) + \varepsilon_2(t) \tag{12}$$

$$X_3(t) = 2s_3 \sqrt{\frac{E}{N_f}} \sum_{m=0}^{M-1} \alpha_{10}(m)w_a(t - \tau_{10}(m)) + \varepsilon_3(t) \tag{13}$$

$$X_4(t) = 2s_4 \sqrt{\frac{E}{N_f}} \sum_{m=0}^{M-1} \alpha_{10}(m)w_d(t - \tau_{10}(m)) + \varepsilon_4(t) \tag{14}$$

where $\varepsilon_1(t)$ and $\varepsilon_3(t)$ are the approximation components of $\eta_e(t)+\eta_o(t)$ and $\eta_e(t)-\eta_o(t)$ successively while $\varepsilon_2(t)$ and $\varepsilon_4(t)$ are their detail components. The approximation and detail components are passed by a Rake receiver. The output per Rake finger for each component is

$$x_1(l) = 2s_1 \sqrt{\frac{E}{N_f}} \alpha_{r0a}^2(l) + \left( \int_0^{T_f} \varepsilon_1(t)w_a(t - \tau_r(l))dt \right) \alpha_{r0a}(l) \tag{15}$$

$$x_2(l) = 2s_2 \sqrt{\frac{E}{N_f}} \alpha_{r0d}^2(l) + \left( \int_0^{T_f} \varepsilon_2(t)w_d(t - \tau_r(l))dt \right) \alpha_{r0d}(l) \tag{16}$$

$$x_3(l) = 2s_3 \sqrt{\frac{E}{N_f}} \alpha_{r1a}^2(l) + \left( \int_0^{T_f} \varepsilon_3(t)w_a(t - \tau_r(l))dt \right) \alpha_{r1a}(l) \tag{17}$$

$$x_4(l) = 2s_4 \sqrt{\frac{E}{N_f}} \alpha_{r1d}^2(l) + \left( \int_0^{T_f} \varepsilon_3(t)w_d(t - \tau_r(l))dt \right) \alpha_{r1d}(l) \tag{18}$$

where $Rw_a(t)$ and $Rw_d(t)$ are the autocorrelation of $w_a(t)$ and $w_d(t)$ respectively, and for $p = 0, 1$.

$$\alpha_{rpa}(l) = \sum_{m=0}^{M-1} \alpha_{p0}(m)Rw_a(\tau_r(l) - \tau_{p0}(m)) \quad \text{and} \quad \alpha_{rpd}(l) = \sum_{m=0}^{M-1} \alpha_{p0}(m)Rw_d(\tau_r(l) - \tau_{p0}(m))$$

By summing up the Rake finger outputs and the $N_f$ frames, the resulting decision statistics equivalent to symbol $s_1$, $s_2$, $s_3$ and $s_4$ are given by

$$Z_1 = s_1 \sqrt{N_f E} \sum_{l=0}^{L-1} \alpha_{r0a}^2(l) + \sum_{nf=0}^{\frac{N_f}{2}-1} \sum_{l=0}^{L-1} \left( \int_0^{T_f} \varepsilon_1(t)w_a(t - \tau_r(l))dt \right) \alpha_{r0a}(l) = s_1 \sqrt{N_f E} E_{m0a} + \psi_1 \tag{19}$$

$$Z_2 = s_2 \sqrt{N_f E} \sum_{l=0}^{L-1} \alpha_{r0d}^2(l) + \sum_{nf=0}^{\frac{N_f}{2}-1} \sum_{l=0}^{L-1} \left( \int_0^{T_f} \varepsilon_2(t)w_d(t - \tau_r(l))dt \right) \alpha_{r0d}(l) = s_2 \sqrt{N_f E} E_{m0d} + \psi_2 \tag{20}$$

$$Z_3 = s_3 \sqrt{N_f E} \sum_{l=0}^{L-1} \alpha_{r1a}^2(l) + \sum_{nf=0}^{\frac{N_f}{2}-1} \sum_{l=0}^{L-1} \left( \int_0^{T_f} \varepsilon_3(t)w_a(t - \tau_r(l))dt \right) \alpha_{r1a}(l) = s_3 \sqrt{N_f E} E_{m1a} + \psi_3 \tag{21}$$

$$Z_4 = s_4\sqrt{N_f E}\sum_{l=0}^{L-1}\alpha_{r1d}^2(l) + \sum_{nf=0}^{\frac{N_f}{2}-1}\sum_{l=0}^{L-1}\left(\int_0^{T_f}\varepsilon_4(t)w_d(t-\tau_r(l))dt\right)\alpha_{r1d}(l) = s_4\sqrt{N_f E}E_{m1d}+\psi_4 \quad (22)$$

where $E_{mpa}$ and $E_{mpd}$ are the energy captured by the Rake receiver, and $\psi_b$ is the noise component and $b = 1,\ldots,4$.

Note that Rake receiver is composed of number of correlator fingers, where the reference waveform are delayed versions of the approximation and detail waveforms of $w(t)$, where, the delays are equivalent to the delays of the multipath components. The mother wavelet (MW) transform function used is chosen to be with high similarity with the transmitted pulse and poor with the noise.

## 5. SIMULATION AND RESULTS

In this section the simulation, results and comparison between different systems, conventional STC and WSTC UWB systems are illustrated. In order to compare systems with different bit rates, a figure of merit $F$ [1/(bit/sec/Hz)] for comparison is used, which is given by

$$F = \frac{BER}{Bandwidth\ efficiency} = \frac{BER \cdot Bandwidth}{Bit\ rate} \quad (23)$$

As stated in section II the channel used is the modified SV-model. The main parameters of the channel are presented in the IEEE802.15.3a proposal for the line-of-sight (LOS) channel CM1 [23]. The used frame duration $T_f = 100$ nsec, with $N_f = 2$. The transmission monocycle pulse $w(t)$ used is with pulse width 0.5 ns and unit energy. The transmission monocycle pulse $w(t)$ used was first chosen to be the second derivative of the Gaussian function [1]. It showed a very bad performance
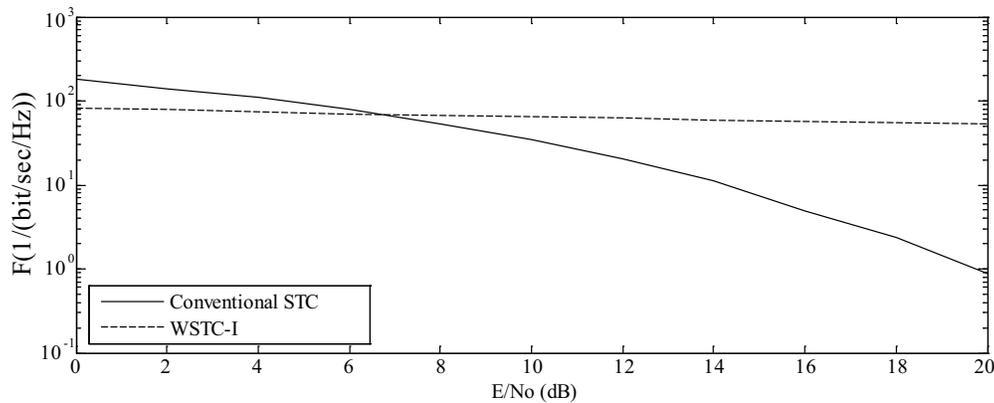


Figure 4: The conventional STC and WSTC using 2nd derivative Gaussian.
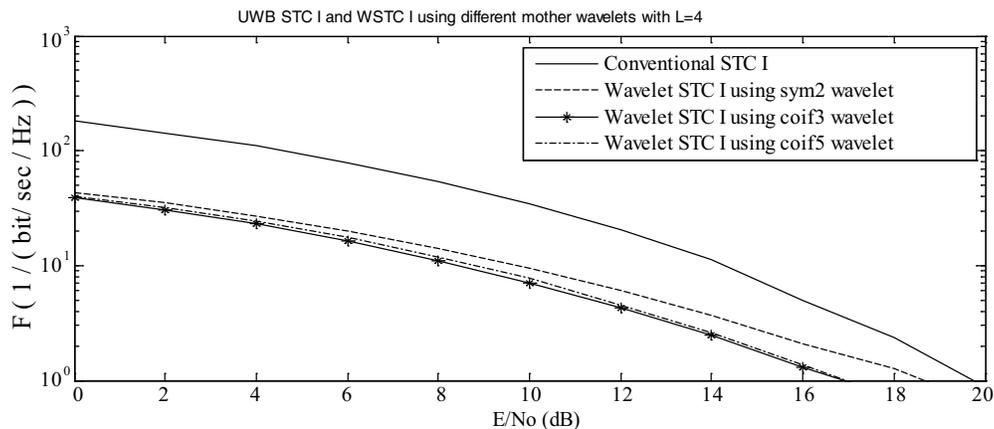


Figure 5: The conventional STC and WSTC using the detail component of the 2nd derivative Gaussian pulse as the transmission pulse with different MW'.

when embedded by the symbols using different MW. Figure 5 shows the performance of WSTC verses conventional STC using second derivative Gaussian pulse and Coiflet 3 MW for embedding the symbols with $L = 4$. The transmitted pulse is re-shaped to enhance the performance and to keep the spectrum limitations of the FCC. The $w(t)$ is then taken to be the wavelet detail component of the 2nd derivative Gaussian pulse using MW's with high similarity with the 2nd derivative Gaussian pulse. The examined MW's are the Symlets, and Coiflets [14, 24–26]. Figure 6 shows a comparison of WSTC using different MW's. It is concluded from Figure 6 that Coiflet 3 presents nearly the same performance as Coiflet 5. But if the MW Coiflet 5 is used, the transmitted pulse will not be able to keep the same bandwidth and spectrum shape after multiplexing the symbols in the wavelet domain (i.e., after the IDWT process in the transmitter) as shown in Figure 7. Thus, the MW Coiflet 3 is preferred due to its good performance, keeping the spectrum characteristics approximately the same when embedded with different symbols and restrict to the FCC spectrum regulations. This can be concluded from Figure 8, which illustrates the spectrum of the transmitted pulse ($w_0(t)$ or $w_1(t)$) after being embedded with different symbols ($s_1$, $s_2$ or $s_3$, $s_4$). Notice that the spectrum of the pulse $w(t)$ (i.e., before embedding the symbols) is the same as the case $s_1 = s_2$ in Figure 8.

The performance of the proposed WSTC using Coiflet 3 MW is compared to the conventional one using $L = 1$, 4 and 8 in Figure 9. Figure 9 shows that WSTC outperforms the conventional one for $L = 1$ by about 8 dB, for $L = 4$ by 3 dB and for $L = 8$ by about 4 dB for low symbol energy to noise power spectral density ratio $E/N_o$ (required by the FCC regulations). Figure 9 shows also that as $L$ increase, the performance is enhanced (increasing the multipath gain. Figure 9 shows that one of the benefits of the WSTC is that it introduces a better performance with $L = 1$ than the conventional STC with $L = 8$ for low $E/N_o$. Thus WSTC also decreases the receiver complexity. The performance is examined too with different non-line-of-sight (NLOS) channels CM2, CM3, and CM4 presented in the IEEE802.15.3a proposal [2, 23]. The WSTC also succeeded to enhance
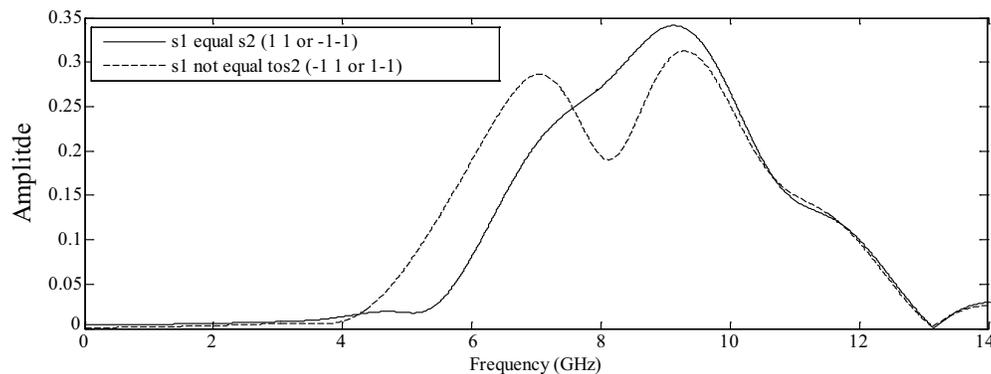


Figure 6: The spectrum of the transmitted pulse $w_o(t)$ symbols are multiplexed in the wavelet domain (same for $w_1(t)$) using MW Coiflet 5.
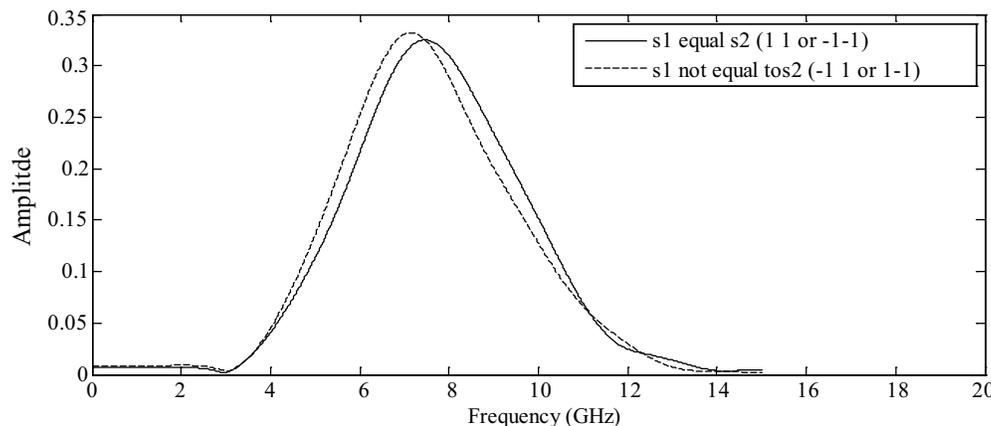


Figure 7: The spectrum of the transmitted pulse $w_o(t)$ after symbols are multiplexed in the wavelet domain (same for $w_1(t)$) using MW Coiflet 3.
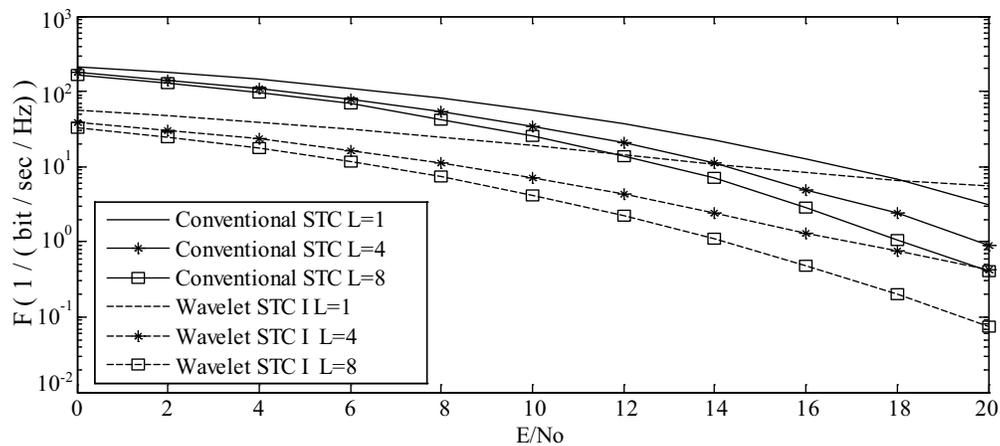
Figure 8: The performance of conventional STC and WSTC UWB system using Coiflet 3 MW and different $L$ Rake fingers.
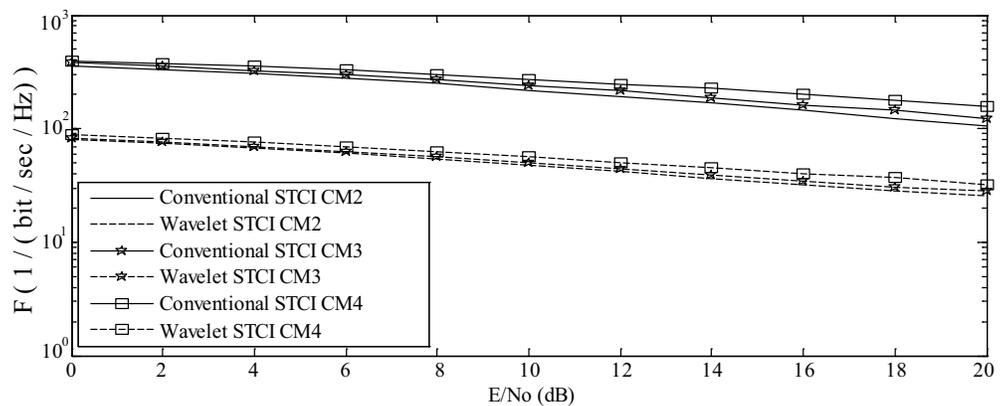


Figure 9: The performance of conventional STC and WSTC UWB system using Coiflet 3 MW and $L = 4$ Rake receiver for different channel models.

the performance for the non-line of sight (NLOS) channel models CM2, CM3, and CM4. This is estimated from Figure 10 that illustrates the performance of WSTC for different channel models and $L = 4$.

## 6. CONCLUSION

The WSTC scheme is proposed to increase the transmission rate to four times that of the conventional STC in addition to enhancing the performance. The WSTC scheme multiplexes different symbols in the wavelet domain of the UWB pulses and transmits different multiplexed symbols on multiple transmitting antennas to offer spatial multiplexing. The simulation results showed that WSTC leads the conventional STC in performance for different channel models CM1, CM2, CM3, and CM4. The WSTC for CM1 also outperforms the conventional STC with less number of fingers, thus reduces the receiver complexity. The enhancement in performance takes place due to the high correlation of the MW used with the transmitted signal.

**REFERENCES**

1. Choi, J. D. and W. E. Stark, "Performance of ultra-wideband communications with suboptimal receivers in multipath channels," *IEEE Journal on Selected Areas in Communications*, Vol. 20, No. 9, December 2002.
2. Oppermann, I., M. Hämäläinen, and J. Iinatti, *UWB Theory and Applications*, John Wiley & Sons, Ltd., England, 2004.
3. Ghavami, M., L. B. Michael, and R. Kohno, *Ultra Wideband Signals and Systems in Communication Engineering*, John Wiley & Sons, Ltd., England, 2004.
4. Mielczarek, B., M. Wessman, and A. Svensson, "Performance of coherent UWB rake receivers with channel estimators," *IEEE 58th, Vehicular Technology Conference*, Vol. 3, October 2003.

5. Win, M. Z., G. Chrisikos, and N. R. Sollenberger, "Performance of rake reception in dense multipath channels: Implications of spreading bandwidth and selection diversity order," *IEEE Journal on Selected Areas in Communications*, Vol. 18, No. 8, August 2000.

6. Nguyen, H., F. Zheng, and T. Kaiser, "Antenna selection for time reversal MIMO UWB systems," *Vehicular Technology Conference — VTC*, Spring, 2009.

7. Liu, H., R. C. Qiu, and Z. Tian, "Error performance of pulse-basedultra-wideband MIMO systems over indoor wireless channels," *IEEE Transactions on Wireless Communications*, Vol. 4, No. 6, November 2005.

8. Alamouti, S. M., "A simple transmit diversity technique for wireless communications," *IEEE Journal on Select Areas in Communications*, Vol. 16, No. 8, October 1998.

9. Gershman, A. B. and N. D. Sidiropoulos, *Space-Time Processing for MIMO Communications*, John Wiley & Sons, Ltd., England, 2005.

10. Yang, L. and G. B. Giannakis, "Analog space-time coding for multi-antenna ultra-wideband transmissions," *IEEE Transactions on Communications*, Vol. 52, No. 3, March 2004.

11. Kaiser, T., F. Zheng, and E. Dimitrov, "An overview of ultra-wide-band systems with MIMO," *IEEE Proceedings*, Vol. 97, No. 2, February 2009.

12. Zhang, Y. and H. Dai, "A real orthogonal space-time coded UWB scheme for wireless secure communications," *EURASIP J. Wireless Comm. and Networking*, 2009.

13. Mucchi, L. and F. Puggelli, "Two new space-time codes for UWB range extension," *International Journal of Ultra Wideband Communications and Systems (IJUWBCS)*, Vol. 1, No. 1, 49–57, Inderscience Publisher, 2009.

14. Lakshmanan, M. K. and H. Nikookar, "A review of wavelets for digital wireless communication," *Wireless Personal Communications*, Vol. 37, No. 3, May 2006.

15. Oliveira, H. M., H. A. Silva, and E. A. Bouton, "Wavelet shift-keying: A new digital modulation," *XX Simpósio Bras. de Telecomunicações*, Rio de Janeiro, October 2003.

16. Hassen, F. S., "The performance of orthogonal wavelet division multiplexing (OWDM) in flat rayleigh fading channel," *Journal of Engineering and Development*, Vol. 12, No. 1, March 2008.

17. Kattoush, A. H., W. A. Mahmoud, and S. Nihad, "The performance of multiwavelets based OFDM system under different channel conditions," *Digital Signal Processing*, Vol. 20, No. 2, March 2010.

18. Chernogo, L. F. and O. V. Lasorenko, "Application of the wavelet analysis for detecting ultra-wideband signals in noise," *VIIIth International Conference on Mathematical Methods in Electromagnetic Theory*, 2000.

19. Yu, L. and L. B. White, "Design of complex wavelet pulses enabling PSK modulation for UWB impulse radio communications," *Auswireless Conference*, 2006.

20. Kim, Y., B. Jang, C. Shin, and B. F. Womack, "Orthonormal pulses for high data rate communications in indoor UWB systems," *IEEE Communications Letters*, Vol. 9, No. 5, May 2005.

21. Das, B. and S. Das, "Interference cancellation schemes in UWB systems used in wireless personal area network based on wavelet based pulse spectral shaping and transmitted reference UWB using AWGN channel model," *International Journal of Computer Applications*, Vol. 2, No. 2, May 2010.

22. Emmanuel, L. and X. N. Fernando, "Wavelet-based spectral shaping of UWB radio signal for multisystem coexistence," *Computers and Electrical Engineering Journal*, Vol. 36, No. 2, March 2010.

23. Foerster, J., M. Pendergrass, and A. F. Molisch, "A channel model for ultra-wideband indoor communications," *Proceedings of the 6th International Symposium on Wireless Personal Multimedia Communications*, 116–120, Yokosuka, Japan, 2003.

24. Hosseini, H., N. B. Fisal, and S. K. Syed-Yusof, "Wavelet packet based multicarrier modulation for cognitive UWB systems," *Signal Processing: An International Journal (SPIJ)*, Vol. 4, No. 2, 75–84, June 10, 2010.

25. Akansu, A. N., W. A. Serdijn, and I. W. Selesnick, "Emerging applications of wavelets: A review," *Physical Communication*, Vol. 3, No. 1, 2010.

26. El-Khamy, S. E. and M. Al-Ghoniemy, "The wavelet transform a review and application to enhanced data storage reduction in mismatched filter receivers," *Proceedings of the National Radio Science Conference, NRSC*, Cairo, Egypt, March 1996.

# Linear Regression Route Roughness Parameter to Correct Hata Path Loss Prediction Formula for 1800 MHz

**Mahdi A. Nisirat**[1], **Mahamod Ismail**[1], **Liyth Nissirat**[1], **and Salim Alkhawaldeh**[2]

[1]Department of Electrical, Electronics and System Engineering
Universiti Kebangsaan Malaysia, 43600 UKM Bangi, Selangor Darul Ehsan, Malaysia
[2]Department of EE, Faculty of Engineering Tech., Al-Balqa' Applied University, Jordan

**Abstract**— Propagation path loss models are going under intensive improvement to allow for more accurate predictions. Such improvements should include terrain areas that are not been exposed extensively in most of the earlier models. In this paper the main equation of Hata urban model is modified by a relation that includes the standard deviation of the measuring campaign route elevations ($\sigma$). This relation is consisting of two regression formulas, as a function of $\log(\sigma)$, modifying both the intercept point (DC value) and the slope of Hata urban model. Root Mean Square Error (RMSE) difference between this model and the measured filtered raw data path loss has overcome RMSE calculated for Hata suburban model, by up to 13 dB. Areas where data are collected would be assumed suburban by Hata model. Data were obtained from mobile service providers in Amman city and Madaba city, Jordan for the frequency band of 1800 MHz.

## 1. INTRODUCTION

Empirical path loss models are usually statistical models proposed to calculate average path loss relation. Many of these models are currently going under precise investigation to correct any shortcomings due to different situations such as urban and rough terrain landscape. In addition to that current and future mobile systems are aiming more toward small-cell system layout. Such small area coverage, distance $(d) < 1$ km, relies heavily on the accuracy of the used path loss model. Hata path loss model was originally proposed for macro-cell coverage, $d > 1$ km, and lack the adaptation of rough topography [1]. Different studies have shown that Hata model could be used with high accuracy given that transmit antenna height is above average roof top [1, 2]. Single Terrain roughness parameter has been used to correct Hata path loss model for the 900 MHz band for small area coverage in [1]. In that study the standard deviation of the measuring route $\log(\sigma)$ is used to correct the intercept point of Hata suburban relation. In this paper the standard deviation parameter $\log(\sigma)$ is used to correct for both the intercept point and the slope of Hata path loss relation for the 1800 MHz band, where Hata path loss relation is assumed of the general form $P_L = A + B \log 10(d)$. Here $A$ is inferred to be the intercept point and $B$ is the slope.

This paper introduces, in the first section, data collection and authentication process used to assure that data obtained from mobile service providers are valid and can be used for propagation analysis. Secondly, a thorough analysis of standard deviation correlation to path loss phenomena is presented. In the last section, an example of one location route is shown in addition to RMSE analysis.

## 2. DATA COLLECTION AND AUTHENTICATION

Data are obtained by Umniah mobile company, working as a mobile service provider in Jordan in the frequency band of 1800 MHz. Data are analyzed and collected by Ericsson Test Mobile System (TEMS) software with an antenna mounted on a moving vehicle, with an average speed of 20 km/h, 1.5 meter above ground level. The sample rate was about 4 samples per second. Data were collected from two cities mainly Amman city and Madaba city and it was originally obtained in a form of excel sheets containing different received power levels from different antennas with multi sectors. To make sure that path taken were regular or quasi regular and to assure that latitudes given are correct, a KML code file was generated by MATLAB to show the measurement path on Google Earth.

## 3. SYSTEM PARAMETERS MODELING AND DERIVATION

In this paper, the effect of the standard deviation of the elevations along the measuring route $\log(\sigma)$ on path loss general relation is analyzed. The analysis covers the effect of route standard deviation, representing path terrain roughness factor, on both parameters of the path loss relation, mainly the

intercept point, A, and the slope, B. twenty different areas, categorized by Hata as suburban areas, with building elevations less than 9 meter and transmit antenna above roof top are specified. The average of the filtered path loss relation obtained is then subtracted from Hata path loss relation, of the given route, to get an intercept point DC shift difference called $\delta_{DC}(d)$. This procedure is used again with the slope difference between the average filtered data and Hata path loss relation but after normalizing data over the distance $d$ to get a factor called $\delta_s(d)$. The summary of this procedure is given in Fig. 1 below.

Linear regression relation between the standard deviation $\log(\sigma)$ and both of the values $\delta_{DC}(d)$, and $\delta_s(d)$ are then obtained such that they would be of the form

$$\delta_{DC}(\sigma) = K_1 + K_2 \log(\sigma) \quad \text{and} \quad \delta_S(\sigma) = F_1 + F_2 \log(\sigma) \tag{1}$$

where $K_1$, $K_2$, $F_1$, $F_2$ are the regression parameters and has been found to be 23.36, $-16.66$, 8.95, and $-6.46$ respectively. A high correlation factor between the $\delta_{DC}(\sigma)$ and $\log(\sigma)$ of 0.995, and between $\delta_s(\sigma)$ and $\log(\sigma)$ of 0.99 is obtained.

This relation is used as a correction factor over Hata urban formula. The new proposed model would be of the form

$$L_{(proposed)}(\text{dB}) = L_{(Hata,urban,smallarea)}(\text{dB}) + \delta_{DC}(\sigma) + \delta_S(\sigma)\log(d) \tag{2}$$

Or

$$L_{(proposed)}(\text{dB}) = 69.55 + 26.16\log f_c - 13.82\log h_r - a(h_r) + \delta_{DC}(\sigma) + [(44.9 - \log h_c) + \delta_s(\sigma)]\log d \tag{3}$$

where $L_{(Hata,urban,smallarea)}(\text{dB})$ is Hata path loss relation for urban areas given in [3], $f_c$ is the operating frequency in MHz, $h_r$ is the receiving antenna height in meter, $h_t$ is the transmit antenna height in meter, $d$ is the distance between transmit and receive antennas in meter, and $a(h_r)$ is Hata correction factor for small areas given as [3]

$$a(h_r) = (1.1\log(f_c) - 0.7)h_r - (1.56\log f_c - 0.8)\,\text{dB} \tag{4}$$

## 4. RESULTS AND DISCUSSION

One route is chosen as a clarifying example. This route is located in Abdoun area, west of Amman and has a standard deviation parameter of $\sigma = 3.90$. The path taken and location is shown in Fig. 2.

Over all more than 75 percent of the routes under study are corrected and less RMSE, compared to Hata suburban model, is obtained. Such a result supports the efficiency of this proposed model, where corrections used by Hata for suburban areas are replaced by a correction factor depending on the terrain roughness of the route used to collect the data. Fig. 3 shows the path loss comparison between the proposed model and Hata suburban model. In this example the achieved proposed model RMSE is 2.75 dB, compared to RMSE for Hata suburban model of 13.90 dB.
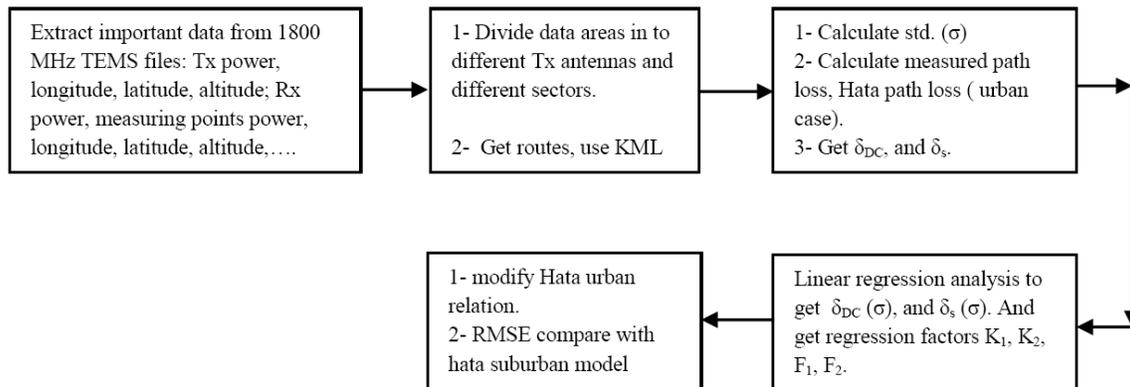


Figure 1: Procedure followed to implement the proposed model.
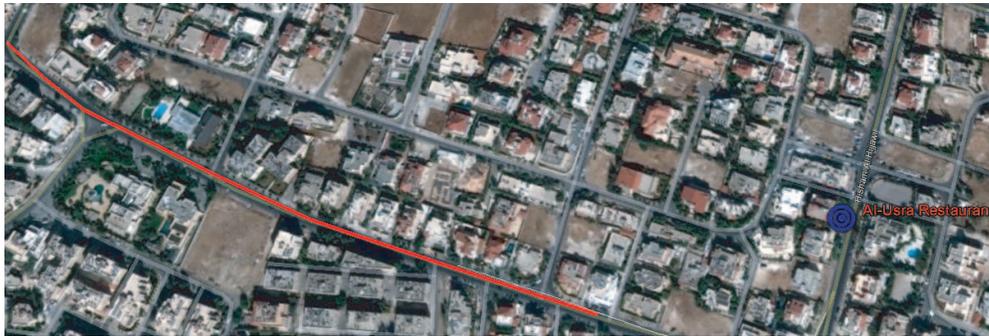
Figure 2: Al — Usra Restaurant Tx at Abdoun area with terrain Standard deviation $\sigma = 3.90$, west of Amman. Dimensions are $300\,\text{m} \times 600\,\text{m}$ [Google Earth].
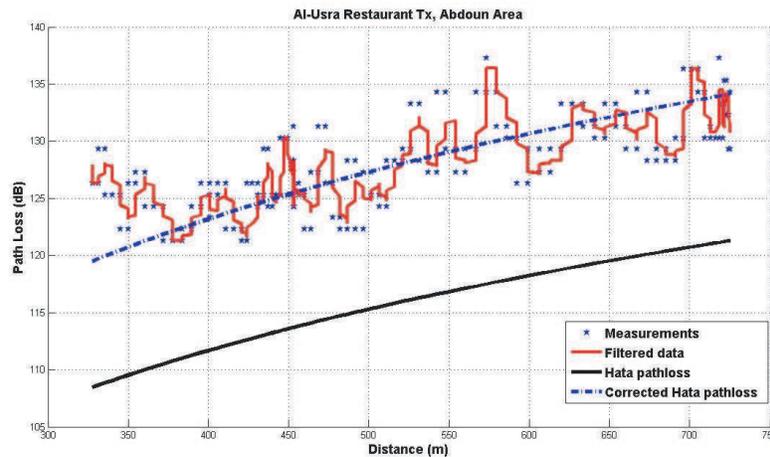


Figure 3: Abdoun area proposed path loss compared to Hata suburban path loss.

## 5. CONCLUSION

In this proposed model, the correction factor used in Hata model for urban areas is modified by a roughness correction factor depending on the standard deviation of the elevations of the measuring route. Better RMSE results are achieved using such correction factor, which highlights the need to include terrain roughness correction factors in any future path loss correction formula. More than 75 percent of the areas under study are corrected with less RMSE of up to $13\,\text{dB}$.

## REFERENCES

1. Nisirat, M. A., M. Ismail, L. Nissirat, and S. Al-Khawaldeh, "A terrain roughness correction factor for hata path loss model at $900\,\text{MHz}$," *Progress In Electromagnetics Research C*, Vol. 22, 11–22, 2011.
2. Fujitani, T., S. Tomisato, and M. Hata, "Experimental study of mobile propagation loss correction formula for a slope terrain area," *IEEE Vehicular Technology Conference*, 1–5, 2010.
3. Hata, M., "Empirical formula for propagation loss in land mobile radio services," *IEEE Transaction Vehicular Technology*, 317–325, 1980.

# Impact of Wireless Channel Modeling on SAR Estimation in Indoor Environment

**O. Jawad[1], D. Lautru[2], J. M. Dricot[1], F. Horlin[1], and P. De Doncker[1]**

[1]OPERA Departement, Université Libre de Bruxelles (ULB)
avenue F.D. Roosevelt 50 1050 Bruxelles, Belgium
[2]UPMC Univ Paris 06, UR 2, L2E F-75005, Paris, France

**Abstract**— The development of wireless technologies led to the birth of numerical dosimetry for non-ionizing radiation. In another hand, the studies of communication channel improve the knowledge of the electromagnetic environment. This paper studies the impact of wireless channel modeling spatial parameters on the exposure of a simple body model. The whole body Specific Absorption Rate (SAR) is evaluated with different conditions of exposure in order to do a statistical study of SAR. The point is to identify the parameters of Wireless Channel which led to significant SAR's variation.

## 1. INTRODUCTION

The study of whole-body exposure to electromagnetic fields emitted by mobile terminals and base stations led to the development of standards and guidelines proposed by the International Commission on Non-Ionizing Radiation Protection (ICNIRP) [1]. Nowadays, numerical dosimetry took an important place into assessing compliance with these guidelines. The decrease of exposure levels lay down by governments lead to the necessity to evaluate precisely the level of exposure.

SAR calculation is a target of numerical dosimetry. The improvement of human body models and the development of hybrid methods which take into account propagation modeling show the importance of this domain of research. A deeper understanding of the electromagnetic environment emerged in the last decade. This knowledge enables to finely simulate the wireless channel parameters which define the exposure conditions.

In a first part, the wireless channel model will be presented, in a second part, the body numerical model and the electric field will be explained. A third part will discuss about the results on SAR will be discussed.

## 2. THE WIRELESS CHANNEL IN INDOOR ENVIRONMENT

The wireless channel models are based on experimental data and identification algorithms. In [2], a Multi-Input Multi-Output (MIMO) channel is completely described in order to simulate a real electromagnetic environment in indoor situation. The algorithm of identification detects one by one the channel MultiPath Components (MPCs); the measurements are analyzed statistically in order to define a stochastic channel model. Currently, channel modeling is based on clusters: it has been proven that waves propagate as bundles named clusters. Inside each cluster, the MPCs are grouped together in the angular and delay domains. The Figure 1 shows a 2D cylindrical model of a human body exposed to such clusters.
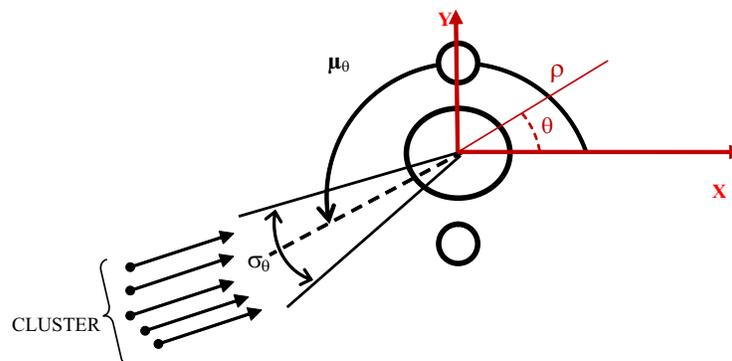


Figure 1: Human Body model exposed to clusters.

The number of cluster depends on the environment. In this paper we will focus on exposure to a single cluster. The number of MPCs will be considered as constant, and equal to twenty ($N_{MPCs} = 20$). $N_{MPCs}$ must be significant otherwise the cluster has no sense. The incident electric field is a TMz uniform plane wave and assumed to be plane:

$$E_i(\alpha_i, \vec{\beta}(\theta_i), \vec{\rho}) = \alpha_i e^{j\vec{\beta}(\theta_i)\cdot\vec{\rho}} \text{ [V/m]} \tag{1}$$

with

$$\vec{\beta}(\theta_i) = \beta\left(\cos\theta_i \vec{1}_x + \sin\theta_i \vec{1}_y\right) \tag{2}$$

where $\alpha_i$ is the amplitude of the plane wave, $\theta_i$ is the angle of incidence and $\beta_1$ is the wave number. This parameters are the most important in order to assess the transmitted electric field. The cluster groups the MPCs together in the angular domain. The angles of incidence of the waves are chosen according to a normal distribution with mean $\mu_\theta$ and angular spread $\sigma_\theta$:

$$\theta_i = N(\mu_\theta, \sigma_\theta) \tag{3}$$

The amplitudes will follow a complex normal distribution:

$$\alpha_i = \sqrt{\frac{P_{Cl}}{2N_{MPCs}}}\left(N(0,1) + j \cdot N(0,1)\right) \tag{4}$$

with $P_{Cl}$ the power of the cluster which will be constant for all the simulations in this paper. The power of the cluster is equal to one Watt. In our study, the impact of four parameters on SAR estimation will be investigated: the angular spread, the angle of incidence of the cluster, the angles of incidence and the amplitudes of MPCs.

## 3. 2D HUMAN BODY MODEL

The 2D cylindrical body model is composed of three uniform cylinders, a trunk and two arms. The physical and electromagnetic parameters of our models are presented in Table 1. The frequency of interest is 2 GHz. The complex relative permittivity is defined as

$$\hat{\varepsilon}_r = \varepsilon_r - j\frac{\sigma}{\omega\varepsilon_0} \tag{5}$$

with $\sigma$ the conductivity in Siemens per meter and $\omega$ the pulsation in radian per second. In order to compute the electric field inside the body, an iterative method is used to assess the incident, scattered and transmitted field [3].

For the $k$-th realization of the amplitude and angle of incidence, the electric field inside the body is given by

$$E_{tot}^k = \sum_{i=1}^{N_{MPCs}} E_i^k(\alpha_i, \vec{\beta}(\theta_i), \vec{\rho}) \tag{6}$$

Table 1: Body model parameters.

|  | Trunk and Arms |
|---|---|
| Trunk length (m) | 1.80 |
| Trunk radius (m) | 0.15 |
| Density (kg/m$^3$) | 523.4 |
| Relative permittivity | 38.5678 |
| Conductivity (S/m) | 1.2667 |
| Relative Permeability | 1 |
| Arms length (m) | 0.80 |
| Arms radius (cm) | 3.6 |
| Distance arm-trunk (cm) | 6.0 |

In order to study the impact of cluster's parameters variation on SAR we will make $N_r = 1500$ realizations in order to achieve convergence. The different scenarios are presented in the fourth part.

The whole body SAR for $k$-th realization is defined as, with $M$ the total mass of the body:

$$\text{SAR}_{WB}^k = \frac{1}{M} \int_V \frac{\sigma \left| E_{tot}^k \right|^2}{2} dV. \ [\text{W} \cdot \text{kg}^{-1}] \tag{7}$$

The averaged whole body $\text{SAR}_{WB}$ and the standard deviation are calculated with the classic definitions:

$$\langle \text{SAR}_{WB} \rangle = \frac{1}{N_R} \sum_{k=1}^{N_R} \text{SAR}_{WB}^k \tag{8}$$

$$std\,(\text{SAR}_{WB}) = \sqrt{\langle \text{SAR}_{WB}^2 \rangle - \langle \text{SAR}_{WB} \rangle^2} \tag{9}$$

## 4. RESULTS

In order to study the impact of the four parameters we decided to define two different configurations (Table 2). In each configuration, one parameter follows its probability density function, the other parameters being fixed. The random parameter takes $N_{MPCs} * N_r = 20 * 1500$ different values.

### 4.1. Case No. 1

Figure 2 represents the mean of $\text{SAR}_{WB}$ and his standard deviation as a function of the angular spread. Figure 2 shows that for all angular spreads, the standard deviation has the same order of magnitude as the means. It shows that the stochastic approach is important and necessary. By increasing the angular spread, the mean $\text{SAR}_{WB}$ values are reduced. This can be explain by the fact that the angles of incidence of different MPCs are more concentrated when the angular spread is tight yielding constructive interferences.

### 4.2. Case No. 2

Figure 3 represents the mean $\text{SAR}_{WB}$ and its standard deviation as a function of the angle of incidence of the cluster. We can notice that mean values and standard deviations have again the same order of magnitude. For angles of incidence between $0°$ and $70°$, the values of $\text{SAR}_{WB}$ increases until $70°$ with a minimum value at $30°$. Between $70°$ and $90°$, the level of averaged $\text{SAR}_{WB}$ reaches a maximum value between $80\,\mu\text{W/kg}$ and $85\,\mu\text{W/kg}$ for $P_{Cl} = 1\,\text{W}$.

Table 2: Different configurations for studying parameter impact.

|              | Case No. 1                  | Case No. 2                    |
| ------------ | --------------------------- | ----------------------------- |
| $\alpha_i$   | random                      | random                        |
| $\mu_\theta$ | fixed to $0°$               | fixed from $0°$ to $90°$      |
| $\sigma_\theta$ | fixed from $5°$ to $45°$  | fixed to $8°$                 |
| $\theta_i$   | fixed                       | fixed                         |
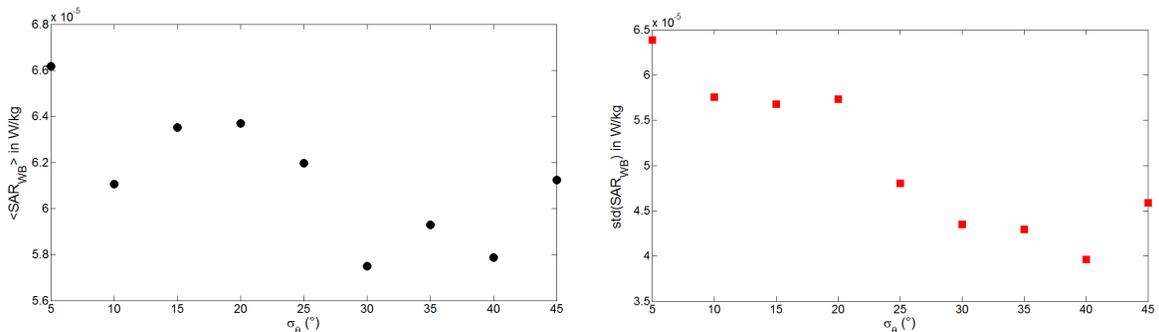


Figure 2: Results of mean of $\text{SAR}_{WB}$ and his standard deviation in function of angular spread.
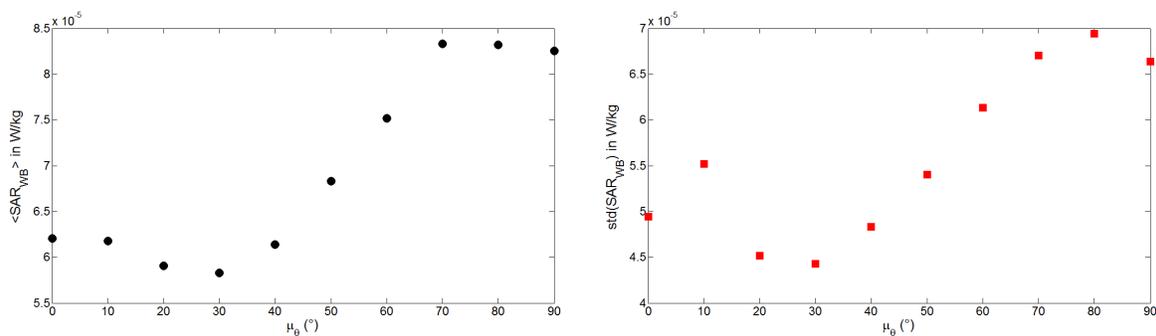
Figure 3: Results of mean of $\text{SAR}_{WB}$ and his standard deviation in function of cluster's angle.

## 5. CONCLUSION

The statistical study of the SAR in clustered wireless channels shows the importance of studying the dependence of averaged SAR with exposure conditions. The analysis of SAR values with respect to channel variable like angular spread or cluster's angle allows us to identify the worst cases of exposure.

## REFERENCES

1. ICNIRP, "Guidelines for limiting exposure to time-varying electric, magnetic, and electromagnetic fields (up to 300 GHz)," *Health Physics*, 1998.

2. Quitin, F., C. Oestges, F. Horlin, and P. De Doncker, "A polarized clustered channel model for indoor MIMO systems at 3.6 GHz," *IEEE Trans. Vehic. Tech.*, 3685–3693, Oct. 2010

3. Jawad, O., D. Lautru, S. Van Roy, J.-M. Dricot, F. Horlin, and P. De Doncker, "Statistical study of SAR in clustered wireless channels," *Antennas and Propoagation (Eucap)*, 2580–2584, 2011.

# Analytical and Experimental Study of Spatial Focusing by UWB Time-Reversal in Indoor Environment

**T. Mavridis**[1, 2], **F. Bellens**[1, 2], **F. Quitin**[1], **A. Benlarbi-Delaï**[2], and **P. De Doncker**[1]

[1]OPERA Wireless Comm. Group, Université Libre de Bruxelles, Belgium
[2]Université Pierre et Marie Curie, L2E, France

**Abstract**— The Time Reversal (TR) technique enables to concentrate the transmitted power on a certain area, where the receiver is located. In this paper, a closed-form analytical solution for the spatial distribution of the energy of a time-reversed system is proposed. This model is based on a plane wave expansion in a local area. Theoretical results are compared with experimental measurements to assess the validity of the Ultra-wideband TR method.

## 1. INTRODUCTION

The popularity of wireless communication technologies has increased the need for reliable, high-speed communications. To cope with the need for high-data rate transmissions, technologies have been proposed that use large bands of the RF spectrum, such as ultra-wideband (UWB).

Focusing techniques enable to spatially concentrate the emitted signals. It implies communications with multiple users with a higher reliability by lowering the interferences. Time Reversal (TR) appears to be an efficient technique to assess time and spatial focusing of the signal. Interesting properties of TR focusing are the high performances in a multipath environment and that the line-of-sight is not required.

The properties and the quality of the TR focusing has been widely investigated in [1, 2]. Time Reversal has already been proved in indoor [3] and intra-vehicular environments [4]. The performances have been studied in those papers but no analytical expression of the spatial distribution of the received signal has been proposed.

In this paper, a new analytic formalism based on physical properties of electromagnetic waves is developed. This formalism allows to characterize the performances of the spatial focusing of the TR method. Furthermore a study of the optimization and the tradeoffs between different wave parameters has been done. Finally, experiments are presented to assess the validity of the theoretical results.

The paper is organized as follows. In Section 2, the TR model of the spatial distribution of the energy is proposed. The analysis of the different parameters introduced in Section 2 is presented in Section 3. The measurement results and the comparison with the theory are presented in Section 4. Finally, Section 5 concludes the paper.

## 2. TIME REVERSAL MODELLING

### 2.1. Energy Calculation

The TR technique is a two-step transmission method. First, the receiver sends a pilot broadcast signal to the transmitter. The transmitter learns the channel impulse response $h(\tau)$ by sampling a received (known) signal. The second step consists of the transmission itself: the transmitter filters the signal with the time reversed version of the impulse response $h^*(-\tau)$ (where $^*$ is the complex conjugate operation). Considering that the channel remains static, the receiver will obtain the transmitted signal through the equivalent channel $h(\tau) \otimes h^*(-\tau)$ as described in [4] where $\otimes$ represents the convolution operation. In this paper, the total energy $\mathcal{E}$ over the bandwidth is considered by integrating the equivalent channel. If the transmitted signal has unit energy, the energy of the received signal will be the following:

$$\mathcal{E}(\vec{r}) = \int_0^\infty |h_{\vec{r}}(\tau) \otimes h_{\vec{r_0}}^*(-\tau)|^2 d\tau \tag{1}$$

where $\vec{r}$ is the position of the evaluated energy, and $\vec{r_0}$ is the position where the energy is being focused (the receiver position). The Parseval equality is then used in (1) to introduce the frequency response $H(f)$ which is the Fourier transform of the impulse response $h(\tau)$:

$$\mathcal{E}(\vec{r}) = \int_{\Delta f} |H_{\vec{r}}(f) H_{\vec{r_0}}^*(f)|^2 df \tag{2}$$

where $\Delta f$ is the bandwidth.

## 2.2. Plane Wave Expansion

To resolve Equation (2), a mathematical expression of the frequency response depending on the environment parameters has to be introduced. The following plane wave expansion has been chosen:

$$H_{\vec{r}}(f) = \sum_{i=0}^{N} a_i e^{j\phi_i} e^{-j\omega\tau_i} e^{-j\vec{\beta}_i \cdot \vec{r}} \tag{3}$$

where $a_i$, $\phi_i$ and $\tau_i$ are, respectively, the amplitude, the phase and delay of the $i$th wave, $N$ is the number of waves and $\omega$ is the pulsation of the signal. In this equation, $\vec{\beta}_i = \omega/c \cdot \vec{1}_i$ is the wave vector where $c$ is the speed of light and $\vec{1}_i$ is the propagation direction of the $i$th wave. Those parameters are evaluated at $\vec{r}_0$ position. To develop an analytical solution of the time reversed energy, a local spatial area where those parameters can be assumed as constant is introduced.

The size of this local area is defined by studying the bandwidth availability and the phase shift $\beta\Delta R$ of a wave calculated in two extremal positions ($\Delta R$ is the distance between those positions and by consequence, it is the size of the local area). It can be shown [6] that $\beta\Delta R$ has to be smaller than $\frac{2\pi f_c}{\Delta f}$ where $f_c$ is the carrier frequency. Finally, it infers that $\Delta R_\lambda < \frac{f_c}{\Delta f}$ where the size of the local area has been defined in wavelength unit. This condition defines the spatial size of the area where the energy distribution will be assessed in this paper.

## 2.3. Spatial Time Reversed Energy

To simplify (3), a change of coordinate system is done by choosing $\vec{r}_0$ as the center of the local area by defining $\vec{r}_0 = \vec{0}$, $\vec{r} = \vec{\Delta r}$,

$$H_{\vec{r}}(f) = \sum_{i=0}^{N} a_i e^{j\phi_i} e^{-j\omega\tau_i} e^{-j\vec{\beta}_i \cdot \Delta\vec{r}} \quad \text{and} \quad H_{\vec{r}_0}(f) = \sum_{i=0}^{N} a_i e^{j\phi_i} e^{-j\omega\tau_i} \tag{4}$$

The vector $\Delta\vec{r}$ is introduced as the difference between the position where the energy is calculated $\vec{r}$ and the focus position $\vec{r}_0$. By introducing (4) in (2) and by integrating over the band $[f_c - \Delta f/2,\ f_c + \Delta f/2]$, a closed-form expression is obtained for the spatial distribution of the energy:

$$
\begin{aligned}
\mathcal{E}(\vec{r}) = \sum_{i=1}^{N}\sum_{h=1}^{N}\sum_{l=1}^{N}\sum_{m=1}^{N} \alpha_{ihlm} \Bigg( & \cos\left(\Phi_1^{ihlm} + 2\Psi_1^{ihlm} f_c\right) \operatorname{sinc}\left(\Psi_1^{ihlm}\Delta f\right) \\
& + \cos\left(\Phi_2^{ihlm} + 2\Psi_2^{ihlm} f_c\right) \operatorname{sinc}\left(\Psi_2^{ihlm}\Delta f\right) \Bigg)
\end{aligned}
\tag{5}
$$

where the following simplifications of notations have been done:

$$
\begin{aligned}
\alpha_{ihlm} &= a_i a_h a_l a_m \\
\Phi_1^{ihlm} &= \phi_i - \phi_h - \phi_l + \phi_m \\
\Phi_2^{ihlm} &= \phi_i - \phi_h + \phi_l - \phi_m \\
\Psi_1^{ihlm} &= \pi\left(\tau_i - \tau_h - \tau_l + \tau_m + \Delta\vec{1}_{lm}\frac{\Delta\vec{r}}{c}\right) \\
\Psi_2^{ihlm} &= \pi\left(\tau_i - \tau_h + \tau_l - \tau_m - \Delta\vec{1}_{lm}\frac{\Delta\vec{r}}{c}\right).
\end{aligned}
\tag{6}
$$

In (6), $\Delta\vec{1}_{lm}$ has been defined as the difference of propagation direction between the $l$th and $m$th wave and is equal to $\vec{1}_l - \vec{1}_m$. It can be observed in (5) that the spatial distribution of the energy depends on the number of waves $N$, the angle of incidence, magnitude, phase and delay of the waves but also on the carrier frequency and the bandwidth. This closed-form solution allows to define the best combination of parameters in order to improve the focusing properties of the TR technique.

## 3. SIMULATIONS

### 3.1. Conditions

A system defined by its bandwidth $\Delta f$ can sample the signal each $1/\Delta f$. To be considered as different, two waves must have a difference of arrival time higher than this sampling time. If this condition is not met, the waves will be sampled in the same tap and be considered as the same one. In the following sections, it will be assumed that the difference between the delays in the simulations is always higher than $1/\Delta f$. To allow 2D focusing, it can be seen in (5) that at least three waves are needed. In the next sections, an assumption will be made that at least three waves are available. Those conditions are easily verified in indoor environments.

### 3.2. Delay Spread, Phases and Number of Waves

The phases and delays can not be fixed in a deterministic way because of their high dependence on the environment parameters. In this case, they will be kept random. In Figure 1, the phases are varying uniformly in $[0, 2\pi]$ and the delays are chosen uniformly in $[0, 10/c]$ to study their influence in the spatial energy distribution.

It can be seen in Figure 1, that the delay and phase have no influence on the spatial distribution of the energy. The focus radius at $-1.5\,\mathrm{dB}$ is about $0.2\lambda_c$. An increasing number of waves does not change the focus radius but decreases the side lobes.

### 3.3. Angular Spread

In Figure 2(b), the focus area at a relative energy of $-1.5\,\mathrm{dB}$ is studied. The simulation was based on the system presented in Figure 2(a). This system is made up of three plane waves incident on the focus point. The propagation direction of the plane wave 1 has been taken for reference. The angle $\theta_1$ ($\theta_2$) is defined by the angle between the first wave and the second (third) one. On Figure 2(b), the normalized area has been presented. It is the area where the energy is above $-1.5\,\mathrm{dB}$ divided by the optimal case (the minimum area is obtained when $\theta_1 = \theta_2 = 120°$). This figure allows to study by how much times the focus size is growing when the angular spread is modified.
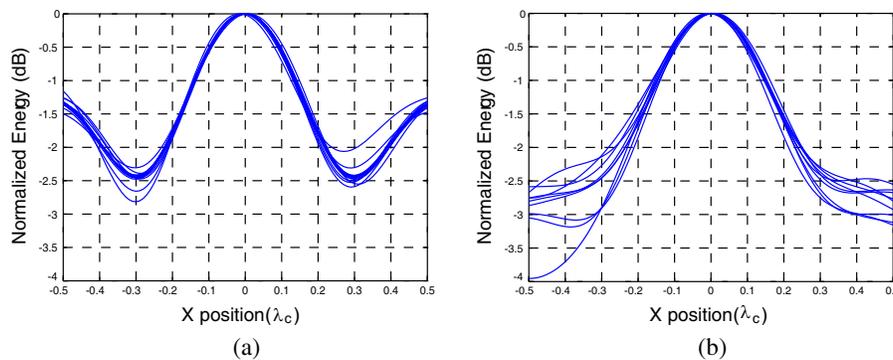


Figure 1: Spatial distribution of the energy for random phases and delays. (a) $N = 3$, (b) $N = 10$.
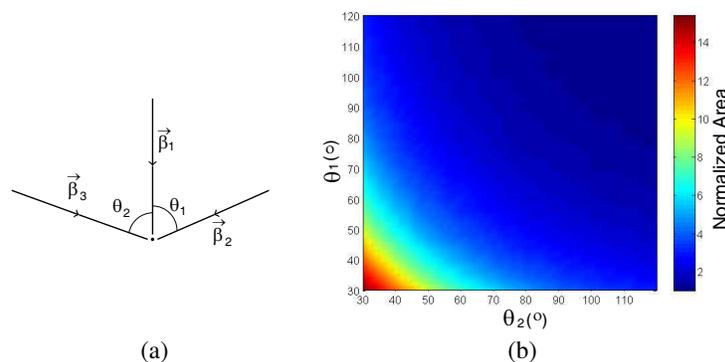


Figure 2: Focus spot normalized (by the optimal case) area. Study of the variation of the angular incidence of the secondary waves. (a) Analyzed system mad up three incident waves. (b) Normalized area of the focus point when the angular spread varies.

By taking the worst case represented in Figure 2 ($\theta_1 = \theta_2 = 30°$), it can be seen that the focus area can be fourteen times higher than the optimal case (in that case the signal can not be considered as spatially focused). It can be inferred that an optimal focus quality is obtained when the angular spread is maximized. Others simulations have been calculated for systems made up of different numbers of wave $N$ and the best focus spot size is always obtained for an uniform angular arrival.

### 3.4. Carrier Frequency and Bandwidth

If a maximal angular spread is considered, the last parameters that can affect the distribution of energy are the carrier frequency and the bandwidth. In this case, it can be observed that the bandwidth has almost no effect on the focus spot size but can decrease the height of the side lobes. In fact, the increase of the bandwidth has the same effect on the energy distribution as the number of waves (see Section 3.1).

As presented in Figure 1, the focus radius is about $0.2\lambda_c$ and it can be observed that this value does not change with the carrier frequency. When this value is converted in spatial metrics (not in terms of wavelength), it can be inferred that the focus spot width is decreasing as the carrier frequency is going up. It can be shown that this relation vary according to $1/f_c$.

### 3.5. Conclusion about the Parameters Optimization

Each parameter has a different influence on the spatial energy distribution. The system resources (frequency parameters) can be modified and optimized but the physical parameters exclusively depend on the environment and are generally fixed. In order to design the focus spot size, the carrier frequency and the angular spread have to be increased. The last one can be modified by using a multiple antennas system. In order to increase the discrimination between the focus point energy and side lobes, the bandwidth and the number of waves have to be as high as possible. One way to increase the multipath is to obstruct the line-of-sight between the transmitter and receiver (see Section 4).

## 4. EXPERIMENTAL RESULTS

### 4.1. Measurement Setup

Experimental measurements were performed in order to assess the performances of the theoretical results of Sections 2 and 3. Three transmit antennas $(\text{Tx})_i$ were used to increase the angular spread. The line-of-sight has been obstructed to increase the multipath. The channel frequency responses $H_i(f)$ were collected with a four-port VNA in an indoor environment with $f_c = 6.85\,\text{GHz}$ and $\Delta f = 7.5\,\text{GHz}$ by a step of $7.5\,\text{MHz}$. The receiver (Rx) was moved on a $10\,\text{cm}$ square grid by a $2\,\text{mm}$ step. The Rx has been moved with an automatic positioning device. The TR is applied as a posteriori treatment thanks to Equation (2).

In order to simulate a SISO (single input single output) with a high angular spread, the transfer function of the system will be defined as $H_{\text{system}}(f) = H_1(f) + H_2(f) + H_3(f)$ where the $H_i(f)$'s are the transfer functions of the channel between the receiver (Rx) and $i$th transmitter (Txi).

### 4.2. Measurement Results

An example of the spatial distribution of the energy by applying TR is given in Figure 3. It can be seen that the focal radius is about $0.2\lambda_c$. The location of the focal spot can be moved, and similar results are observed when the receiver position is changing.

As can be seen in Figure 3, the decrease of the bandwidth does not change the size of the focus area but the side lobes are higher in the (b) case than the (a) one as predicted in Section 3.4. These results can be compared with the theoretical conclusions and can assess the validity of our TR model.

### 4.3. Comparison with Theory

To examine the measurement results, the theoretical Equation (5) requires the determination of the parameters of the plane waves. The use of a ray identification algorithm (SAGE [5]) is required. It models the spatial distribution of the impulse response and can work out the plane waves parameters: $a_i$, $\phi_i$, $\tau_i$ and $\theta_i$. By using the model developed in the previous part, the experiment results can be compared with the theory.

As can been seen, the energy level and the area around the focal point fits with the theoretical simulation. Others comparisons have been done by varying the different parameters to assess the validity of this model. The results were successful.
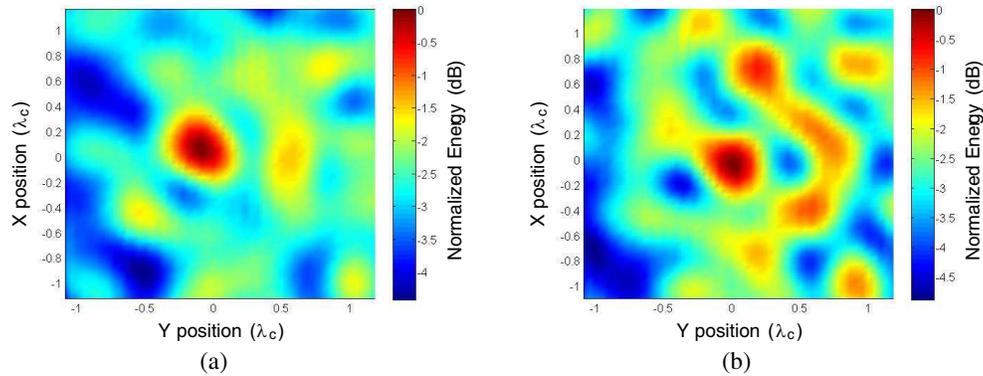
Figure 3: Relative energy received for $f_c = 6.85\,\text{GHz}$. (a) $\Delta f = 7.5\,\text{GHz}$, (b) $\Delta f = 1.5\,\text{GHz}$.
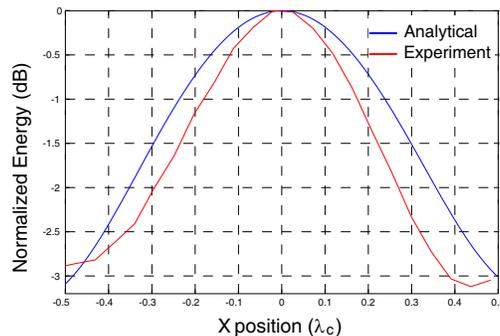


Figure 4: Relative energy received for three base stations simulating a SISO system. Comparison between the experiment result and the analytical calculations.

## 5. CONCLUSION

In this paper, a new analytical formalism of the Time Reversed spatial energy distribution based on a local plane wave expansion has been developed. UWB Experiments has been done to prove the validity of the energy distribution in a local area around the receiver position described by the model presented in this paper. Those analytical results show the parameters influence on the focusing quality and allow to make an optimisation of the system design. The Time Reversed focusing method has also been applied in different (indoor and intra-vehicular) environments to test this modelling and the results were successful. We have also shown that the evolution of the energy distribution follows the equations presented here when the parameters described in Section 3, are modified.

The analytical equations described here can be used to make the design of the environment and predict the focusing quality in a static channel when a UWB Time Reversal system is used.

## REFERENCES

1. Oestges, C., A. Kim, G. Papanicolaou, and P. Paulraj, "Characterization of space-time focusing in time-reversed random fields," *IEEE Trans. Antennas Prop.*, Vol. 53, 283–293, Jan. 2005.

2. Emami, E., J. Hansen, A. D. Kim, G. Papanicolaou, A. Paulraj, D. Cheung, and C. Prettie, "Predicted time reversal performance in wireless communications using channel measurements," *Proc. IEEE Comlet*, 2002.

3. Zhou, C. and R. C. Qiu, "Spatial focusing of time-reversed UWB electromagnetic waves in a hallway environment," *Proc. IEEE 38th Southeastern Symp. on Syst. Theo.*, Cookeville, TN, USA, 2006.

4. Bellens, F., F. Quitin, J.-M. Dricot, F. Horlin, A. Benlarbi-Delai, and P. De Doncker, "Performance evaluation of time reversal in intra-vehicular environment," *Proc. Eur. Antennas and Propagation Conf. (EUCAP)*, 2011.

5. Quitin, F., C. Oestges, F. Bellens, S. Van Roy, F. Horlin, and P. De Doncker, "Extracting specular-diffuse clusters from MIMO channel measurements," submitted to *22nd Symposium on Personal, Indoor and Mobile Radio Communications (PIRMC)*, 2011.

6. Oestges, C. and B. Clerckx, "MIMO wireless communications," *Elsevier Academic Press*, 42–45, 2007.

# Characterization of the Polarization of Received Electromagnetic Waves in Indoor Communication Channels

**Ali Panahandeh[1, 2], François Quitin[3], Jean-Michel Dricot[1], François Horlin[1], Claude Oestges[2], and Philippe De Doncker[1]**

[1]OPERA Department, Université Libre de Bruxelles (ULB), Belgium
[2]ICTEAM Electrical Engineering Department, Université Catholique de Louvain (UCL), Belgium
[3]Electrical and Computer Engineering Department, University of California, Santa Barbara, USA

**Abstract**— Compared to classical spatial MIMO wireless systems, cross-polarized MIMO systems are an interesting way to reduce equipment size while still maintaining low inter-antenna correlation. In this paper, the time-variation of the polarization of the received waves is investigated. In this scenario, a theoretical formulation is proposed in order to obtain the parameters of the elliptical polarization, based on the signals received on three perpendicularly polarized antennas. A measurement campaign has been performed in an indoor-to-indoor scenario and at a frequency of 3.6 GHz. Based on these measurements and the proposed theoretical formulation, the time-variation of the parameters describing the polarization ellipse is analyzed and a time-variant statistical model is proposed.

## 1. INTRODUCTION

Polarized MIMO systems have been proposed as a space- and cost-effective alternative to classical co-polar MIMO systems. By using perpendicularly polarized co-located antennas, the inter-antenna correlation remains low, while maintaining a compact antenna system [1].

Let's consider a MIMO system where the receive antenna is a tri-polarized antenna system made of three co-located perpendicular omnidirectionnal antennas. In an idealistic case where there are no Interacting Objects (IOs) in the environment surrounding the transmitter and the receiver, the polarization of the wave transmitted from the transmitter antenna stays the same at the receiver side. However in a realistic scenario where the environment is made of many IOs, the polarization of the transmitted wave will change. The multi-path components at the receiver will in this case, each have different polarization properties. A fraction of a linearly polarized wave will for instance be depolarized, into its perpendicular components leading to an elliptical polarization [2] (the linearly and the circularly polarization could each be defined as a special case of an elliptical polarization).

The superposition of the different multi-path components having each a different elliptical polarization scheme will lead to another elliptical polarization scheme. In a dynamic scenario, the IOs could change their position and/or shape over time, leading to a more dynamic receive scheme where the global receive polarization ellipse also changes over time.

Previous works have been done in order to model the multi-polarized MIMO channel for different sources (spatial/temporal) and scales of variation [3–5]. While these works tend at characterizing the signals received at one vertical and two horizontal perpendicular antennas, no work has been done in order to model the polarization of the received waves from an electromagnetic point of view. The aim of this paper is to dynamically characterize the receive polarization ellipse for a particular scenario. This new approach has the advantage to be transposable to any orientation of a receiver with multi-polarized co-located antennas. Based on the theoretical analysis and the measurement campaign described later in this article, a statistical model of the receive polarization ellipse is developed.

The paper is organized as follow: Section 2 gives the theoretical formulation in order to obtain a 3D representation of the polarization wave. Section 3 shows the experimental measurement campaign. Section 4 presents the results derived from the measurement. Section 5 concludes this paper.

## 2. THEORETICAL FORMULATION OF THE ELLIPTICAL POLARIZATION

An elliptically polarized wave may be resolved in two linearly polarized waves having different phase and amplitude and being perpendicular to each-other. Different set of parameters may be used in order to define an elliptical polarization in the three dimensional (3D) space. Based on the signals received on one vertical and two horizontal perpendicular antennas, a particular set of parameters

defining the elliptical polarization in the 3D space is obtained. In the two dimensional (2D) case, the passage from the received signals on two perpendicular antennas to the elliptical polarization parameters is immediate [6]. In a more realistic 3D scenario, this passage is less intuitive and requires the knowledge of the orientation of the polarization plane (characterized by the vector normal to its surface (Figure 1(a)).

Let's consider three received signals $(s_V(\vec{r}, t),\ s_{H1}(\vec{r}, t),\ s_{H2}(\vec{r}, t))$ on three perpendicular antennas. The phasor associated with these signals is given by:

$$\vec{s} = \begin{pmatrix} s_x \\ s_y \\ s_z \end{pmatrix} = \begin{pmatrix} s_{H1} e^{j\phi_{H1}} \\ s_{H2} e^{j\phi_{H2}} \\ s_V e^{j\phi_V} \end{pmatrix} \tag{1}$$

where $s_V$, $s_{H1}$ and $s_{H2}$ are the amplitudes and $\phi_V$, $\phi_{H1}$ and $\phi_{H2}$ are the phases of the received signals on the vertical and the two perpendicular horizontal antennas.

In [7], the normal to the polarization plane is obtained for an arbitrary electric or magnetic field. This analysis is based on the spectral density tensor which is a second rank tensor formed from the wave fields.

The normal to the polarization plane is given by the vector **V** [7]:

$$\mathbf{V} \equiv (\mathbf{V}_x, \mathbf{V}_y, \mathbf{V}_z) \tag{2}$$

where

$$\mathbf{V}_x = -\frac{1}{2} \operatorname{Im}\{s_y s_z^*\} \quad \mathbf{V}_y = -\frac{1}{2} \operatorname{Im}\{s_x s_z^*\} \quad \mathbf{V}_z = -\frac{1}{2} \operatorname{Im}\{s_x s_y^*\} \tag{3}$$

The normal to the polarization plane is characterized by its azimuthal and elevation angles $\phi$ and $\theta$ (where $0 < \phi < \pi$ and $0 < \theta < \pi$). These angles are defined in the coordinate system formed by the three receive antennas.

The signal components in the Cartesian basis $(\vec{1_x},\ \vec{1_y},\ \vec{1_z})$ are transformed into the spherical basis $(\vec{1_{e_\theta}},\ \vec{1_{e_\phi}},\ \vec{1_{e_r}})$ by the following transformation [8]:

$$\begin{pmatrix} s_r \\ s_\theta \\ s_\phi \end{pmatrix} = \begin{pmatrix} \sin\theta\cos\phi & \sin\theta\sin\phi & \cos\theta \\ \cos\theta\cos\phi & \cos\theta\sin\phi & -\sin\theta \\ -\sin\phi & \cos\phi & 0 \end{pmatrix} \cdot \begin{pmatrix} s_x \\ s_y \\ s_z \end{pmatrix} \tag{4}$$

where the radial component $s_r$ will be zero.

Having the two transverse components $s_\theta$ and $s_\phi$, the elliptical polarization parameters in the polarization plane are obtained by the classical 2D relations (Figure 1(b)).



<p style="text-align:center">(a)　　　　　　　　　　　　　　　　　　　　(b)</p>
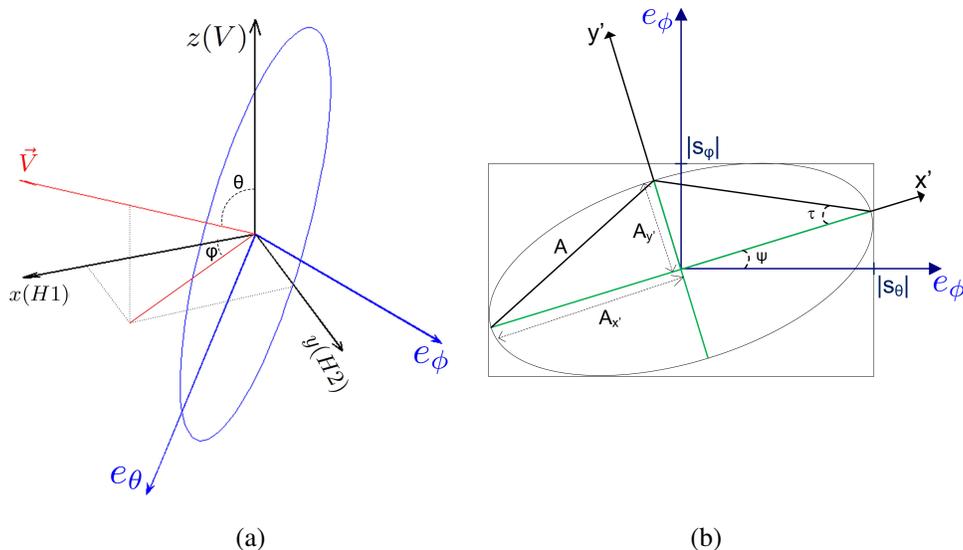
Figure 1: (a) The 3D representation of the received polarization ellipse. (b) The representation of the polarization ellipse in the polarization plane.

The phase angle between the two transverse components is given by:

$$\delta = phase(s_\phi) - phase(s_\theta) \tag{5}$$

The orientation of the polarization ellipse in the polarization plane is determined by the tilt angle of the ellipse in the transverse basis. The tilt angle is defined as the angle between the major axis of the polarization ellipse and the $e_\theta$ axis and is given by:

$$\psi = \frac{1}{2}\arctan\frac{2|s_\theta||s_\phi|\cos(\delta)}{|s_\theta|^2 - |s_\phi|^2} \tag{6}$$

The ellipticity angle $\tau$ is given by:

$$\tau = \frac{1}{2}\arcsin\frac{2|s_\theta||s_\phi|\sin(\delta)}{|s_\theta|^2 + |s_\phi|^2} \tag{7}$$

The ellipticity rate $e$ is given by:

$$e = \tan(\tau) \tag{8}$$

The amplitude of the wave $A$ is given by :

$$A = \sqrt{|s_\theta|^2 + |s_\phi|^2} \tag{9}$$

Finally, the length of the semi-minor and the semi-major axis are given by:

$$\begin{aligned} A_{y'} &= |A\sin(\tau)| \\ A_{x'} &= |A\cos(\tau)| \end{aligned} \tag{10}$$

Having the orientation of the normal to the polarization plane ($\theta$ and $\phi$), the orientation of the polarization ellipse in the polarization plane ($\psi$) and the length of the semi-major and the semi-minor axis, the received polarization ellipse could be obtained in 3D space.

In the following, the temporal variations of the polarization ellipse are characterized based on an indoor-to-indoor measurement campaign.

## 3. EXPERIMENTAL SETUP

A measurement campaign has been performed using the ULB/UCL Elektrobit MIMO channel sounder. The working frequency was 3.6 GHz with a 100 MHz bandwidth. The transmitter and receiver unit of the sounder were connected using a 32-meter N-cable, to run the sounder on a unique clock to avoid phase drift. Both the transmitter and the receiver were tri-pole antennas, composed of three perpendicular co-located short linear antennas. Each cycle recorded the complete $3 \times 3$ channel matrix. The channel sample rate was 291.212 Hz and a total of 30000 cycles were recorded (over 100 s recording time). The floor plan of the measurements is given in Figure 2.

The measurements were performed in a Corridor-to-Office (C2O) scenario and at a total of three different positions. The transmitter and the receiver were staying static during the measurements while people were moving in between. To allow the reproduction of the model and to have the same orientation of the basis, in all the three measurement positions, the same orientation was imposed for the transmitter and the receiver tri-pole antennas.

The measured impulse responses were averaged over 3 successive impulse responses to increase the measurement SNR, yielding a final channel sampling rate of 97.07 Hz. Finally, the narrowband MIMO matrices were obtained by summing the wideband impulse responses in the delay domain. In order to characterize the receive polarization ellipse in the different positions, the transpose of these narrowband MIMO matrices will be used in the further data treatment. While only the vertically polarized antenna is considered at the transmitter side, all the three antennas are considered at the receiver side.

## 4. RESULTS

In the following analysis, the results taken from the location 3 are considered. The conclusions hold for the location 1 and 2. Based on the measurements and the theoretical expressions presented earlier in this paper, the temporal variations of the 5 parameters describing the receive polarization ellipse in the 3D space are analyzed and a statistical model is deduced.
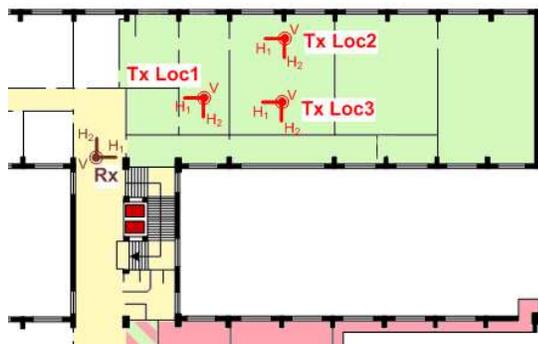
Figure 2: Floor plan of the measurements.
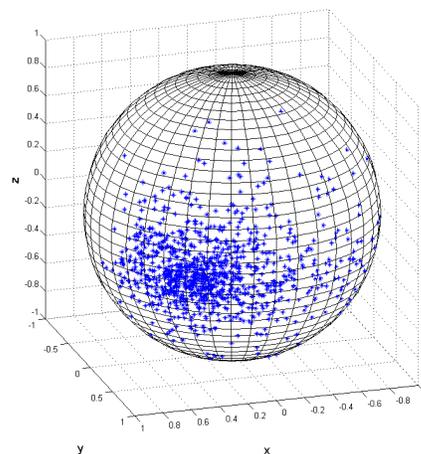


Figure 3: The directions of the normal to the polarization plane in 3D space.

Table 1: Statistical distributions of the parameters describing the polarization ellipse.

| Parameters of ellipse | Type of distribution | Parameters of the distribution | |
|---|---|---|---|
| $\theta$ | Normal | $\mu$ (radian) | $\sigma$ (radian) |
| | | 1.61 | 0.42 |
| $\phi$ | Log-normal | $\mu$ (dB) | $\sigma$ (dB) |
| | | 0.07 | 0.59 |
| $\psi$ | Normal | $\mu$ (radian) | $\sigma$ (radian) |
| | | 0.27 | 0.22 |
| $A_{x'}$ | Log-normal | $\mu$ (dB) | $\sigma$ (dB) |
| | | -8.55 | 0.27 |
| $A_{y'}$ | Log-normal | $\mu$ (dB) | $\sigma$ (dB) |
| | | -9.47 | 0.43 |

In order to obtain the statistical distribution of each parameter, the temporal samples of each parameter are first averaged over ten successive samples yielding a total number of 984 samples. Based on these temporal samples, the statistical distribution that follows each parameter is obtained using the Maximum Likelihood Estimator. These distributions and their respective parameters are given in Table 1. In Figure 3, the directions of the normal to the polarization plane are presented in 3D space for different temporal samples. We notice the concentration of these vectors in a privileged direction which corresponds to the direction of incidence of the main beam.

In order to study the time-variant dynamics of the channel, the autocorrelation functions of all the parameters have been analyzed. In the time-resolution used in these measurements ($1/97\,\text{Hz} \approx 10\,\text{ms}$), no significant temporal correlations was found for the tilt-angle $\psi$. However for the other parameters, the autocorrelation function has a lower decaying slope at the beginning which was best fitted with a decaying exponential function. The parameters of these exponential models are given in Table 2. In previous works treating multi-polarized MIMO channels, no attention has been paid to fix a particular orientation for the receive antenna system. While this approach has the advantage to model the channel in a situation where the orientation of the receive antenna system does not stay the same all the time, it does not let the model to be transposable to a particular orientation of the receive antenna system. In fact the receive antenna system is made of three perpendicular co-located antennas and as the orientation of this antenna system changes, the channel changes as well. The approach used in this paper for modeling the multi-polarized channel could be applied to any orientation of the receive antenna system, by projecting the receive elliptical

Table 2: Exponential models of the autocorrelation functions.

| $y = \exp(-bt)$ | $b\ (s^{-1})$ |
|:---:|:---:|
| $A_{x'}$ | 1.24 |
| $A_{y'}$ | 4.42 |
| $\theta$ | 2.66 |
| $\phi$ | 3.82 |

polarization to the receive antenna system. Moreover, with this new approach, the performance of wireless communications could be improved, by adapting the receive antenna system based on the informations on the receive elliptical polarization.

## 5. CONCLUSION

In this paper, a time varying statistical model of the elliptical polarization of the received waves was presented for a particular indoor-to-indoor scenario. The proposed model was based on a theoretical formulation which was applied to the results obtained from an indoor-to-indoor measurement campaign. The statistical distributions of the parameters describing the polarization ellipse in the 3D space were obtained. In order to study the time-variant dynamics of the channel, the autocorrelation functions of all the parameters have been analyzed. Except for one of the parameters (the tilt-angle) which has no temporal correlation in the time-resolution used for the measurement, exponential models were proposed for the autocorrelation functions of the four other parameters. Although a linearly polarized transmitted wave is received in many different polarization schemes, the orientation of the normal to the polarization plane was found to have a privileged direction. Future work will consist in: i) further enhancement of the model by considering a higher number of measurement positions, ii) considering other measurement scenarios, iii) analyzing other types of environment.

## REFERENCES

1. Lukama, L. C., K. Konstantinou, and D. J. Edwards, "Performance of a three-branch orthogonal polarization diversity scheme," *VTC 2001 Fall. IEEE VTS 54th*, 2033–2037, 2001.
2. Oestges, C. and B. Clerckx, *MIMO Wireless Communications: From Real-world Propagation to Space-time Code Design*, Academic Press, 2007.
3. Quitin, F., F. Bellens, A. Panahandeh, J.-M. Dricot, F. Dossin, F. Horlin, C. Oestges, and P. de Doncker, "A time-variant statistical channel model for tri-polarized antenna systems," *PIMRC*, 64–69, 2010.
4. Panahandeh, A., F. Quitin, J. M. Dricot, F. Horlin, C. Oestges, and P. de Doncker, "Multi-polarized channel statistics for outdoor-to-indoor and indoor-to-indoor channels," *VTC2010*, 1550–2252, May 2010.
5. Mansoor S., M. Zhang, A. F. Molisch, F. Tufvesson, and S. H. Simon, "Polarized MIMO channels in 3D: Models, measurements and mutual information," *IEEE J. Select. Areas Commun.*, Vol. 24, 514–527, 2006.
6. Smith, G. S., *An Introduction to Classical Electromagnetic Radiation*, Cambridge University Press, 1997.
7. Carozzi, T., R. Karlsson, and J. Bergman, "Parameters characterizing electromagnetic wave polarization," *Physical Review*, Vol. 61, 2024–2028, 2000.
8. Moon, P. H. and D. E. Spencer, *Field Theory Handbook: Including Coordinate Systems, Differential Equations, and Their Solutions*, Verlag, Springer, 1961.

# Genetic Algorithm Optimization Tool for Multi-user Detection of SDMA-OFDM Systems

**M. A. Alansi**, **I. M. Elshafiey**, and **A. M. Al-Sanie**

Electrical Engineering Department, King Saud University, Riyadh 11421, P. O. Box 800, Saudi Arabia

**Abstract**— A tool is presented for achieving a near-optimum multi-user detector (MUD) based on the Genetic Algorithm (GA) techniques for Space Division Multiple Access (SDMA) Orthogonal Frequency Division Multiplexing (OFDM) communication systems. The tool involves methods for substantially reducing the GA search space to minimize the convergence time. GA parameters are investigated and the tool is investigated for the challenging overloaded scenario problem. Results reveal that the proposed tool provides a useful compromise means between performance and computational complexity. Simulation outcomes indicate that the tool surpasses the conventional low complexity methods, such as the minimum mean-square error (MMSE), and approaches the optimal performance of the Maximum Likelihood (ML) detector, while maintaining reduced complexity.

## 1. INTRODUCTION

Genetic Algorithms (GAs) are a powerful optimization tool and are well suited for optimization problems involving large search space, including mechanisms to escape from local optima. GA is an evolutionary computation methodology in which progression is performed through the application of dedicated operators-Selection, Crossover and Mutation, which introduce various control parameters for the evolution from one population to the next. Originally, the method was developed by John Holland and popularized by one of his students, David Goldberg [1]. GAs has been applied for solving different optimization problems in various fields and they are very efficient in attaining a near-optimal solution in a much shorter time as compared to the conventional point-by-point exhaustive search, especially in large solution spaces [2]. One application is the optimization of the cost functions for the detection of user signals in wireless communication as in the Code Division Multiple Access (CDMA) [3].

Orthogonal Frequency Division Multiplexing (OFDM) and Multiple Input Multiple Output (MIMO) are the most competitive technologies to satisfy future requirements of wireless access systems. MIMO systems can be used for multiple users in Space Division Multiple Access (SDMA) [4] and the SDMA have been combined with OFDM in order to mitigate the technical challenges of channel impairments and enhance the spectral efficiency [5]. SDMA enables support of multiple users within the same time and frequency slots, implementing user-specific channel impulse responses (CIRs). However, the non-orthogonality nature of the CIRs raises a challenge to the process of multi-user detection (MUD), and different schemes have been proposed at the Base Station (BS) receiver to identify the user signals based on their CIRs.

Maximum likelihood (ML) methods are known as an optimum tool for MUD, but they are associated with high computational complexity that grows exponentially with the increase of the number of simultaneous supported users. Additionally, in the overloaded scenario problem which means that number of users are higher than number of receive antennas, the classic MUD can't detect and separate the users signal, large search space and the number of solutions is increasing. Moreover, the convergence time to get the required solution among all users will increase and consequently high computation complexities will be achieved.

This paper presents the MUD from a combinatorial optimization viewpoint, where the GA is used to optimize the performance of the SDMA-OFDM system in overloaded scenario problem using initial population from the output of simple Minimum Mean Square Error (MMSE) MUD. The major advantage of the proposed GAs-MUD is that it provides a good compromise between the performance and computational complexity. This capability casts the developed GA tool more flexible than limited low-complexity conventional techniques, or highly demanding ML optimal detector approach. The rest of this paper is arranged as follows: Section 2 describes the SDMA-OFDM model and the classic detectors, whereas in Section 3 the Genetic Algorithms are illustrated. The simulation results are introduced in Section 4 and conclusions are drawn in Section 5.

## 2. UPLINK SDMA-OFDM MODEL AND MUD TECHNIQUES

In SDMA-OFDM systems, the transmitted signals of $L$ simultaneous uplink mobile users — each equipped with a single transmit antenna are received by the $P$ different receiver antennas of the BS as shown in Fig. 1. At the BS, the received signal was corrupted by the Gaussian noise at the antenna array elements yielding

$$y = Hx + n \tag{1}$$

where $y = [y_1, y_2, \ldots, y_p]$ is the received signals vector, $x = [x^{(1)}, x^{(2)}, \ldots, x^{(L)}]$ is the transmitted signals vector and $n$ is the dimensional noise vector. The Frequency Domain Channel Transfer Function matrix (FD-CHTF) $H$ is constituted by the set of channel transfer function vectors $H^l$ where $l = 1, \ldots, L$ users:

$$H = [H^1 H^2, \ldots, H^L] \tag{2}$$

As shown in Fig. 1, MUD techniques are applied at the BS for detecting the different user's transmitted signals with the aid of their unique CIRs.

Among the various MUDs, MMSE exhibit the lowest complexity, but they suffer from performance loss. ML optimum detector considered as a reference to other detection methods [6] and the ML method minimizes the Euclidean distance between the received signal vectors and the product of all possible transmitted signal vectors with the given channel. The ML detection methods determines the estimate of the transmitted signal vector $x$ as

$$\tilde{x}_{ML} = \arg \min ||y - Hx||^2 \tag{3}$$
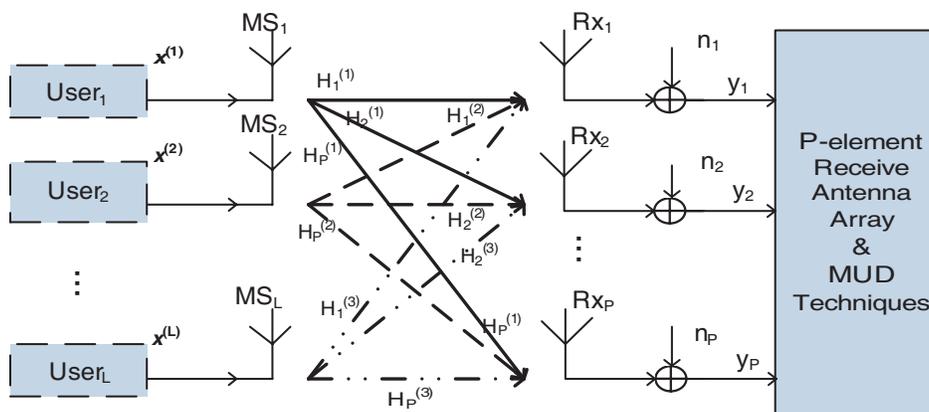


Figure 1: Schematic model of SDMA-OFDM uplink channel system.
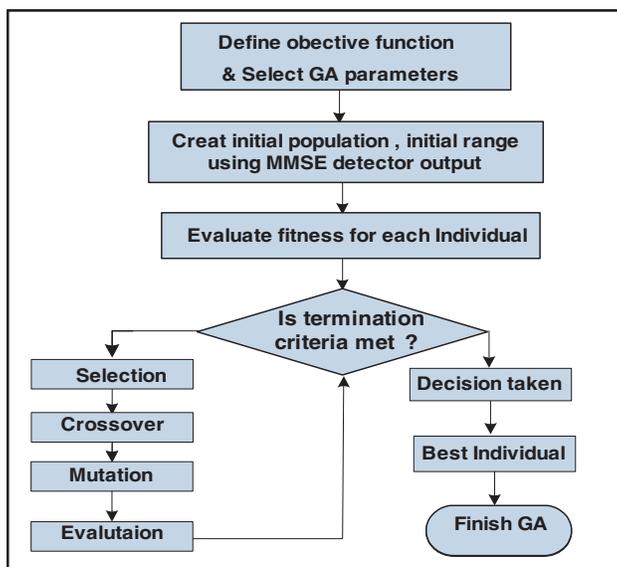


Figure 2: Flowchart of GA optimized MUD techniques.

where $||y - Hx||^2$ corresponds to the ML metric. Optimum ML detector attempts to find the best vector of data bits in a set with all possibilities. However, the numbers of evaluations or attempts depend on the number of users in the system and the set of constellation symbol point. The ML detector has a complexity on the order of $O^{(2L \cdot \log 2 M)}$, where $M$ represent the constellation size [7]. Thus when the number of users increases, ML detector quickly becomes infeasible.

## 3. GENETIC ALGORITHM BASED MULTI-USER DETECTION

GA assisted MUD techniques is basically an optimization and search technique that mimics elements seen in natural evolution and it could be used in computing to find exact or approximate solutions to optimization and search problems. In order to restrict the search space, GA implement search mechanisms aims to find a solution based on an objective function (or fitness value).

An important step to apply the GA is to define the objective function that is unique for each optimization problem; this is the link between the algorithm and the real-world problem. The ML decision metric of (3) can be used in the GA-MUD, where the decision metric required for the receive antenna, namely the antenna specific objective function is defined by:

$$\Omega_p(x) = |y_p - H_p x|^2 \tag{4}$$

where $y_p$ is the received symbol at the input of the $p$th receiver, while $H_p$ is the $p$th row of the channel transfer function $H$. Thus, the estimated transmitted symbol vector based on the knowledge of the received signal at the $p$th receiver antenna is given by:

$$\tilde{x}_{GA} = \arg\min |\Omega_p(x)| \tag{5}$$

The main steps of GA implemented in SDMA-OFDM system as shown in Fig. 2 are described below:

Step 1: Define the objective function as in (4), and then set the parameters of GA including the probability and type of mutation and crossover operations, maximum number of generations, population size, and the termination criteria.

Step 2: Evaluate the fitness for each individual in the population, where the fit individual in our MUD minimization problem will have the lowest numerical value. The first/initial generation is produced.

Step 3: Test the termination criteria like reaching the maximum number of generations or getting the minimum tolerance error between the received signal $y$ and the multiplication between channel matrix $H$ and transmitted signal $x$ as in (4).

If the termination criteria are not met with the previous population generated, GA operators will be applied as the following:

A- Individuals are selected according to their fitness for the production of offspring.
B- Binary representation is used in this work with double point crossover.
C- All offsprings will be mutated with a certain probability. By mutation individuals are randomly altered.
D- The fitness of the offspring is then computed using (4) and evaluated as in Step 2. This cycle is performed until the optimization criteria are reached.

Step 4: If the new individual generated will met the termination criteria, the decision will be taken; this individual or gene is chosen as the best gene and finish the algorithm.

## 4. SIMULATION RESULTS

SDMA-OFDM system is implemented under *Matlab* environment. Different CIR's applied for the SDMA users, where these channels are Rayleigh fading channel based on the standard ITU channel model for high delay spread vehicular test environment is applied [8]. Perfect channel estimation is assumed to be done at the BS. FFT size is set to 512 along with 5-MHz bandwidth in the OFDM system with QPSK modulation. The MUD methods used are MMSE, optimal ML, and near optimal performance using the GA tool. The output of the MMSE method is applied as an initial population for GA optimization.

The Bit Error Rate (BER) of the system in the overloaded system is showing in Fig. 3. Six users ($Nu = 6$) are transmitting data and two receive antennas ($Nr = 2$) at the BS receiver. This figure reveals that the presented MUD problem cannot be solved using the MMSE detector,
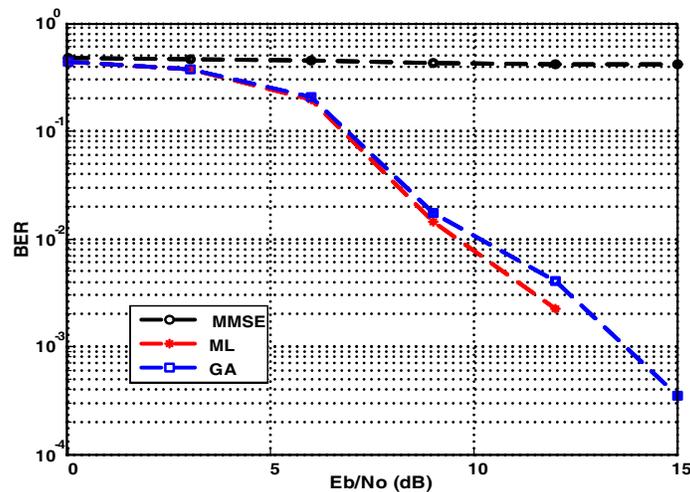
Figure 3: Performance optimization for MUD schemes using GA in overloaded scenario.
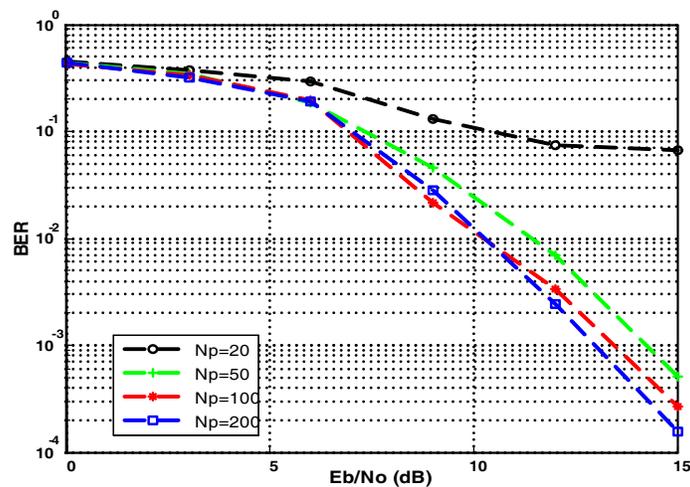


Figure 4: GA performance for different population sizes $(Np)$.

whereas the GA tool provides near optimal performance at lower complexity than the ML. The complexity comparison between ML and GA can be illustrated, where the search space for ML scheme includes 4096 possible solutions corresponding to the number of users included and value of modulation order, while GA tool reduced the search space to 1000 achievable solutions equivalent to the population size $(Np)$ multiplied by the maximum number of generations $(Ng)$.

Figure 4 shows the performance of GA for various numbers of individuals, where the continuing rising of population size will develop the performance to approach ML detector output. The system include six users $(Nu = 6)$ and four receive antennas $(Nr = 4)$ at the BS. Maximum number of generation is fixed to $Ng = 20$, where the population sizes used are $Np = 20$, $Np = 50$, $Np = 100$, $Np = 200$.

## 5. CONCLUSIONS

In this paper, we have introduced a GA tool that is applicable in the context of an SDMA OFDM system for determining the optimized solution among large number of solutions in the search space including overloaded scenario. Unlike conventional techniques such as the MMSE-MUD, the tool is capable of supporting an overloaded scenario, in which the number of users surpasses the number of receiver antennas. Controlling the operational parameters, the tool provides a means of adaptively obtaining the necessary performance under complexity limitations. Increasing the population size, for example, allows the gradual enhancement of the results to approach the ML detector output. One interesting feature of the GA tool is that the operational time can be kept fixed while enhancing the performance making use of the parallelizability of the algorithm. This

allows the implementation of real time operating systems using the developed tool.

## ACKNOWLEDGMENT

## REFERENCES

1. Haupt, R. L. and S. E. Haupt, *Practical Genetic Algorithms*, 2nd Ed., John Wiley & Sons, USA, 2004.
2. Chen, S., T. R. Newman, J. B. Evans, and A. M. Wyglinski, "Genetic algorithm-based optimization for cognitive radio networks," *Sarnoff '10 Proceedings of the 33rd IEEE Conference*, Sarnoff, 2010.
3. Lin, D., Y. Xu, W. Song, H. Luo, and X. Liu, "Genetic algorithm based multiuser detection for CDMA systems," *IEEE 6th CAS Symp. on Emerging Technologies*, China, May 31–June 2, 2004.
4. Münster, M., B. Choi, T. Keller, and L. Hanzo, *OFDM and MC-CDMA for Broadband Multiuser Communications WLANs and Broadcasting*, John Wiley and IEEE Press, 2003.
5. Vandenameele, P., L. Van Der, and M. G. E. Engels, "A combined OFDM/SDMA approach," *IEEE Journal on Selected Areas in Communications*, 2312–2321, November 2000.
6. Proakis, J., *Digital Communications*, McGraw-Hill, 2008.
7. Alansi, M., I. Elshafiey, and A. Al-Sanie, "Multi user detection for SDMA OFDM communication systems," *IEEE SIECPC*, Riyadh, Saudi Arabia, April 23–26, 2011.
8. Vaiapury, K., M. Nagarajan, and S. Kumaran, "Performance evaluation of preamble detection under ITU and SUI channel models in mobile WiMAX," *First COMSNETS*, Bangalore, January 2009.

# Methods for the Assessment of the Performance of Short-range Multi-hop Wireless Network Communications

**M. A. Collett and T. H. Loh**

National Physical Laboratory, Teddington, Middlesex, UK

**Abstract**— Wireless Sensor Networks (WSNs) are envisaged to perform critical monitoring for applications such as healthcare, security and industrial monitoring, resulting in ever increasing demands for understanding and quantification of the reliability and stability of WSN-based systems when deployed in real environments. This can be challenging as real environments are rapidly changing with a range of scattering and interference effects which can have a significant influence upon the communications performance. The complexity and autonomy of such systems makes defining repeatable and reliable performance measurement techniques challenging, but without such tests users will be unable to make informed decisions about their procurement and design choices. In this paper, we demonstrate the sensitivity of WSN communications to a scattering environment and propose one method for assessing the performance of a WSN in establishing and maintaining communications in such a highly multi-path environment. A metric of network coverage is defined to be the proportion of nodes in a network visible to the base station at any given time. This allows the rapid, repeatable and reproducible characterization of a WSN system. It is found that the network coverage within a loaded reverberation chamber is highly sensitive to stirrer position and for the SunSPOT system investigated, only a 52% average network coverage is achievable.

## 1. INTRODUCTION

Wireless sensor networks (WSNs) constitute complex, autonomous, distributed systems employing multiple technologies. They are suited to deployment across a wide range of application areas within a wide range of environments. One challenge for those planning to commission a WSN for their particular application is that there is a large range of products and product types to choose from. It is challenging for users to determine which type of system would be most suited to their application and environment, and indeed, how best to configure their chosen system. Communications in particular is a critical factor in the viability of a WSN in a given environment, yet there are few methods for quantifying, evaluating and comparing the performance of the complex, multi-hop networking of a whole WSN system. Currently evaluation is commonly carried out by simulation [1], within idealized anechoic environments [2] or within uncontrolled non-repeatable environments such as offices [3]. Each of these approaches has their own benefits, but none of them can achieve all of the following: repeatability and reproducibility of measurements; reproduction of realistic environmental effects and assignment and consistent choice of performance metrics. All of these points must be satisfied if WSNs are to be reliably tested in a way to give results which aid users and developers. Crucially a set of tests resulting in reliable performance indicators is necessary if WSNs are ever going to be adopted for critical applications. Without such information users cannot perform a cost-benefit analysis to understand the benefits and risks of a given WSN deployment.

This paper highlights the need for repeatable and reproducible testing methods for WSN performance in realistic environments. Firstly, the behaviour of a single link is investigated in a multipath environment, highlighting the challenges introduced by multiple reflections. Secondly, a simple method for assessing one aspect of WSN communications performance is proposed and presented. A network is configured in such a way to ensure that multi-hop communications is required for all the nodes to communicate with the base station in an anechoic environment. The network is then moved to a loaded reverberation chamber and the environment is changed through the actuation of a rotating reflector, and the statistics of network coverage measured. This approach allows an assessment of the sensitivity of the network to a reflective environment, whilst remaining reproducible and repeatable as results are viewed over a large range of configurations.

## 2. MEASUREMENTS

The measurements described within this paper were carried out using a Sun Microsystems SunSPO-T [4]. This WSN research platform includes an IEEE 802.15.4 compliant radio, integrated inverted 'F' antenna, microprocessor, battery power supply and sensor suite (including thermistors and

accelerometers). This is intended to be a flexible easy to program research platform with similar functionality and characteristics to many commercially available WSNs.

## 2.1. Single Link Performance

Firstly, a simple set of measurements were carried out on a single wireless link between two SunSPOTs. One of the nodes was programmed to continually transmit packets at a rate of 10 Hz, and the other node was configured to measure the RSSI (received signal strength indication) of each packet, as well as other link quality metrics of CORR [5] and packet loss rate (both of these metrics are close to binary in that they indicate a perfect link up until the point the link is completely lost, hence the results are not shown). This process was carried out over a range of node separations, and in three environmental configurations: in an anechoic chamber; in a reverberation chamber at floor level and in a reverberation chamber 60 cm above floor level. The purpose of these measurements was to assess the ability of the nodes to measure the quality of their own links, and also to investigate and highlight the effect of a reflective environment. A Log-Log plot of the received signal strength against separation for the three configurations is shown in Figure 1. It can be seen from the linear fit that for the anechoic case (which is equivalent to free space) the received signal strength follows an inverse-square law, consistent with the Friis transmission equation. This not only shows that the environment is un-perturbing, but also that the nodes are capable of reasonable measurement of the relative received signal strength. For the reverberation chamber cases, it can be seen that the maximum transmit range is far reduced (to 12 cm when 60 cm above the floor, and 27 cm when on the floor). In the anechoic environment, the nodes could communicate at the extremes of available separation, 6 m apart. Within the reverberation chamber the received signal strength also becomes far less predictable with position.

## 2.2. Whole Network Performance

For this test, a small network of five nodes was deployed in a simple grid-like pattern (Figure 2(a)). The transmit power was adjusted such that free space communications between the base station and the row furthest from it (Row B) could only be achieved by intermediate nodes (Row A) relaying the messages. This was to ensure that multi-hop communications was implemented for the short distances available within our chambers. The spacing was also intended to ensure there were two equal length paths for each of the nodes in the far row to choose between.

It was decided to test the effects of a highly reflective, multi-path environment upon this system. This was chosen to represent one of the many challenges facing those considering deploying WSNs in industrial settings. In order to establish such an environment, whilst keeping the measurements isolated from uncontrollable external influences and repeatable, they were carried out in the NPL reverberation chamber [6]. In these measurements, it was desirable to recreate the levels of reflection typical within industrial environments, by adding some absorbing material into the chamber. This allowed a realistic, yet controlled and repeatable environment to be constructed. The chamber loaded with some absorber, and the location of the network under test is shown in Figure 2(b). Two
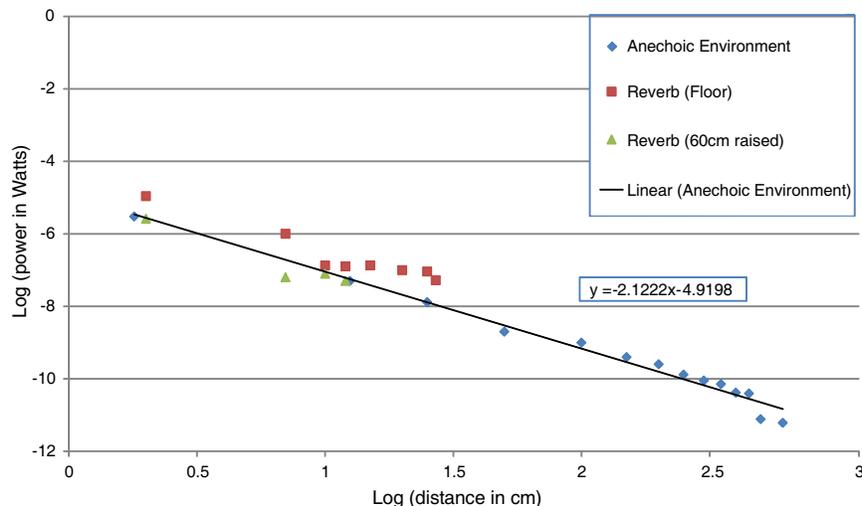


Figure 1: Log-Log plot of received signal strength for a range of distances in an anechoic (blue diamond, and linear fit) and multipath reverberant (red square and green triangle) environments.
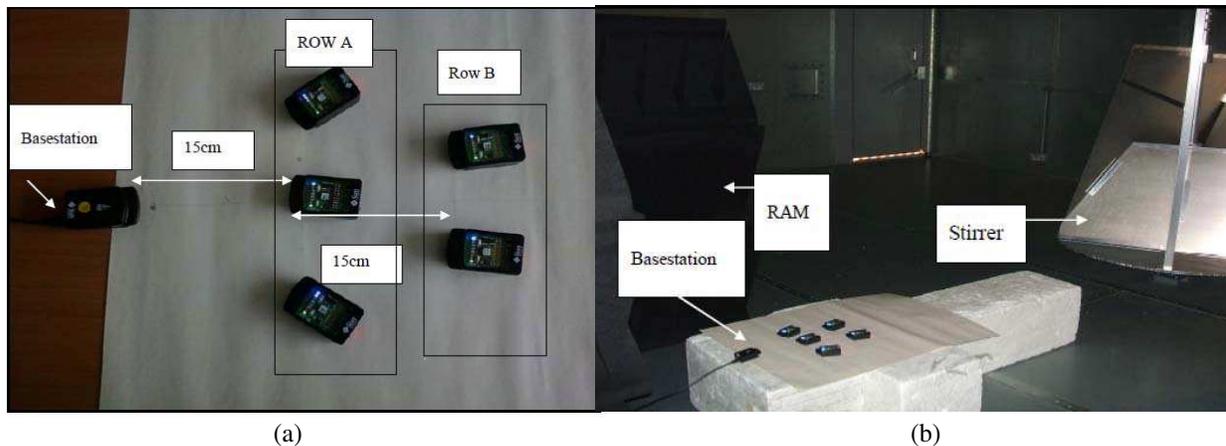
Figure 2: (a) Network arrangement and (b) reverberation chamber setup.

additional nodes were also mounted on the wall behind the stirrer removing the line of sight component and exceeding the free space range (in order to investigate potential benefits of a multipath environment). The next stage was to determine what metrics of performance would be meaningful, useful and comparable between systems. There are many performance metrics which could potentially be of interest to those deploying WSNs. These include for individual links: received signal strength; symbol error rate; packet error rate and Latency. For a whole network potential metrics include: packet error rate; time for data to get from one location to another; coverage (fraction of nodes which can communicate with the base station at any instant in time); agility (how long to react to changes in environment or network) and Redundancy of links. All of these parameters could provide valuable insight into the performance of a WSN, and the importance and weight given to these are dependent upon the user requirements and interests. A challenge for many industrial systems is that they are intentionally very closed systems (as the manufacturers want to protect their IP, and ensure security for the users). This means that for many systems it is not possible to access information such as the routing tables, signal strength or packet error rate. For this study, a single metric was chosen, namely the Coverage, defined as the fraction of the total number of nodes which could be observed by the base station either directly or via messages relayed from other nodes. The coverage was observed for a large number of stirrer positions within the chamber. Moving the stirrer acts to randomise the location of nulls and hot spots in the wireless signals caused by the multipath effects. Averaging over several stirrer positions allows for highly repeatable and reproducible measurement results.

## 3. RESULTS

The reverberation stirrer was moved through a range of 21 positions (equally spaced totaling one whole rotation), with the coverage measured at each position. The results are shown in Figure 3. As can be seen, the coverage factor is highly dependent upon the stirrer position, and can range from 100% (all nodes visible) to 0% (no nodes visible). This is consistent with the prediction of the spatial sensitivity to communications within a reflective environment indicated by Figure 1, and acts to highlight how important this effect is for making deployment decisions. From the information gathered during these measurements it was found that the mesh networking algorithm was able to respond to the challenging environment, with several occasions where more than three hops were required for one node to see the base station in spite of the challenging multipath. It can also be seen that the multipath environment gives some situations where links are present which would be absent were it a free space environment. For example, the fact that the nodes on the wall can be seen at all, and also that for position 21, nodes in row B can be seen with none visible in row A. For this set of measurements, the average coverage factor for the small network investigated was found to be 52%. This was aided by the ability of the network to employ multi-hop communications, and without this feature, the average coverage factor would have been approximately 30% (this is the coverage factor if we only include nodes that can be directly seen by the base station). Both of these results highlight how useful multi-hop communications can be, but also how important its behaviour is in maintaining a robust network. Similar measurements

| stirrer position | ROW A Nodes | | | Nodes on Walls | | ROW B Nodes | | no: of nodes visible | % of node visibility |
|---|---|---|---|---|---|---|---|---|---|
| | 47D2 | 54FE | 2CDB | 4C5B | 2FAD | 62C6 | 2FAA | | |
| 1 | | | | | | | | 5 | 71.43 |
| 2 | | | | | | | | 6 | 85.71 |
| 3 | | | | | | | | 2 | 28.57 |
| 4 | | | | | | | | 7 | 100.00 |
| 5 | | | | | | | | 0 | 0.00 |
| 6 | | | | | | | | 1 | 14.29 |
| 7 | | | | | | | | 1 | 14.29 |
| 8 | | | | | | | | 0 | 0.00 |
| 9 | | | | | | | | 6 | 85.71 |
| 10 | | | | | | | | 5 | 71.43 |
| 11 | | | | | | | | 4 | 57.14 |
| 12 | | | | | | | | 3 | 42.86 |
| 13 | | | | | | | | 7 | 100.00 |
| 14 | | | | | | | | 0 | 0.00 |
| 15 | | | | | | | | 4 | 57.14 |
| 16 | | | | | | | | 5 | 71.43 |
| 17 | | | | | | | | 0 | 0.00 |
| 18 | | | | | | | | 5 | 71.43 |
| 19 | | | | | | | | 7 | 100.00 |
| 20 | | | | | | | | 4 | 57.14 |
| 21 | | | | | | | | 4 | 57.14 |
| count | 12 | 11 | 8 | 9 | 10 | 13 | 13 | | |
| % Visible | 49.2 | | | 45.2 | | 61.9 | | Average Visibility | 51.7 |

Figure 3: Table showing network coverage within the reverberation chamber for a range of stirrer positions. Red areas indicate that a node is visible.

were repeated four times, with the network at a range of positions within the chamber, and with a range of stirrer step sizes. The average Coverage factor for each of these measurements sets was in the range 50–55%, showing good repeatability when averaging over sufficient stirrer configurations. Such studies will be valuable in informing system users of the likely level of redundancy required, as well as the most appropriate system and configuration choices for their application.

## 4. CONCLUSION

A significant challenge in measuring performance of a WSN is in specifying test conditions in the following areas:

1. Environment: What type of environmental features do we wish to recreate and test for?
2. Network Configuration: What size, layout, transmit power and type of platform do we wish to investigate?
3. Performance Metric: What parameters of performance are we interested in and have access to?

This set of measurements has shown some potential choices for the above parameters, and applied those to a single testbed system. It has been found that wireless communications is highly unpredictable within a reflective environment (as expected). It was also found that WSN communications is significantly aided by the ability to perform multi-hop communications. The fact that for this level of reflective environment allowed an average coverage factor of only 52% highlights how important it is to carefully select and deploy a WSN appropriately, with respect to environment, location, protocol and level of redundancy. In the future such measurements will be applied to a wide range of WSN platforms, to allow direct comparisons to be made. This will also allow WSN developers to understand the implications of their design choices, and users to be able to specify a system suited to their needs. Defining the level of necessary redundancy is one benefit of carrying out such measurements prior to deployment.

## ACKNOWLEDGMENT

**REFERENCES**

1. Notani, S. A., "Performance simulation of multihop routing algorithms for Ad-Hoc wireless sensor networks using TOSSIM," *10th International Conference on Advanced Communication Technology, ICACT*, Vol. 1, 508–513, Feb. 17–20, 2008.

2. Takizawa, K., K. Watanabe, M. Kumazawa, Y. Hamada, T. Ikegami, and K. Hamaguchi, "Performance evaluation of wearable wireless body area networks during walking motions in 444.5 MHz and 2450 MHz," *Engineering in Medicine and Biology Society (EMBC), Annual International Conference of the IEEE*, 2010.

3. Graham, B., C. Tachtatzis, F. Di Franco, M. Bykowski, D. C. Tracey, N. F. Timmons, and J. Morrison, "Analysis of the effect of human presence on a wireless sensor network," *International Journal of Ambient Computing and Intelligence*, Vol. 3, No. 1, 1–13, Jan.–Mar. 2011.

4. Sun Microsystems SunSPOT, http://www.sunspotworld.com/.

5. CORR definition, http://www.sunspotworld.com/javadoc/com/sun/spot/peripheral/radio/RadioPacket.html.

6. Arnaut, L. R. and P. D. West, "Evaluation of the NPL unturned stadium reverberation chamber using mechanical and electronic stirring techniques," NPL Rep. CEM, 11, 1998.

# A Rigorous Measurement Technique for Radiation Pattern Characterisation of Embedded Wireless Communication Systems

**T. H. Loh and M. A. Collett**

The National Physical Laboratory, Teddington, Middlesex, United Kingdom

**Abstract**— A rigorous measurement technique using native signals to characterise the radiation patterns of single receiving antenna wireless communication systems is presented. A scalar pattern measuring process, robust to modulated and bursty signals, has been validated against the traditional vector network analyzer pattern measuring method. The receiver comprised a single receiving antenna and a calibrated RF spectrum analyzer. Initial evaluation used a Bluetooth signal emulator test device comprising a monopole antenna, extracted from a MICAz wireless sensor network platform, and fed by a RF signal generator. Following a rigorous assessment of the technique, it was applied to investigate the radiation pattern from a MICAz sensor mote. The results show good repeatability and demonstrate that the technique is robust and would be valuable for assessing the performance of embedded radio system designs.

## 1. INTRODUCTION

There has been a proliferation of wireless communication systems, using mobile phone handsets and wireless sensor devices, to meet the existing and future demands for increased communication capacity using higher data rates. Electronic components, antennas and devices embedded within wireless systems are continually decreasing in size, resulting in highly complex structures. However, the operating environment of these devices can have a significant effect on the antenna performance and coverage, leading to unforeseen detrimental behavior of the device with a corresponding loss of communication capacity. Traditional prototype antenna testing using a vector network analyser often employs a coaxial feed cable to the antenna. Such a cable, which would not be present in practice, can support common mode currents that radiate and distort the true radiation pattern of the antenna under test [1].

Investigations [2–4], have been carried out to determine the radiation pattern of wireless sensor motes without describing the methodology used. It is important to have a good understanding of the radiation characteristics of the WSN nodes, and how to obtain them, as these characteristics ultimately affect the WSNs operating characteristics and deployment feasibility.

WSNs are often employed for critical monitoring applications such as structural health [5], healthcare [6], or security. This makes it a critical factor in the sensor network system design and deployment. Testing of whole systems and configurations is necessary despite the measurement challenge that the embedded radio devices within these systems are often only capable of emitting a modulated, bursty and intermittent signal. To address these issues, we present a rigorous spectrum analyser (SA)-based method for the measurement of the radiation pattern of embedded radio devices emitting intermittent modulated signals and assess it with a vector network analyser (VNA)-based method. The results for the MICAz sensor mote are presented as representing a typical device emitting an intermittent IEEE 802.15.4 [7] compliant modulated signal.

## 2. MEASUREMENT DETAILS

All measurements were conducted using the small-antenna test range at the U.K. National Physical Laboratory (NPL). The following provides the relevant details:

### 2.1. Reflectionless Chamber

This test range is housed in a screened anechoic room 7.15 m long × 6.25 m high × 6.25 m wide, covered with pyramidal absorber with normal incidence reflectivity of better than −40 dB above 400 MHz [1]. The wall and ceiling absorber is covered by RF transparent white polystyrene end caps, for improved room illumination, and the floor is covered with polystyrene walkover caps for improved range access. The chamber contains an azimuth positioner system, shown in Figure 1(a).

### 2.2. Devices under Test

Figures 1(b) to 1(e) show the two devices tested. Figures 1(b) and 1(c) shows a monopole antenna element extracted from a MICAz sensor mote and Figures 1(d) and 1(e) shows a complete MICAz sensor mote. The MICAz sensor mote was programmed to continuously send messages over a
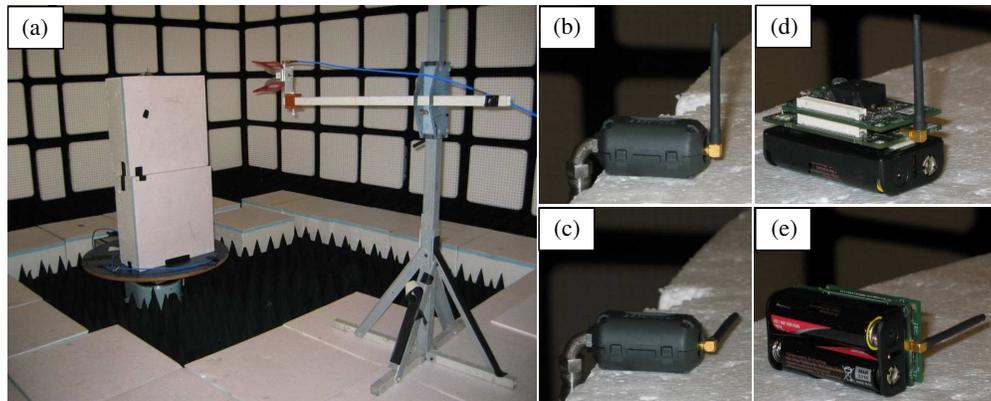
Figure 1: Photographs of both the experimental setup in the NPL small-antenna test range and the test items.
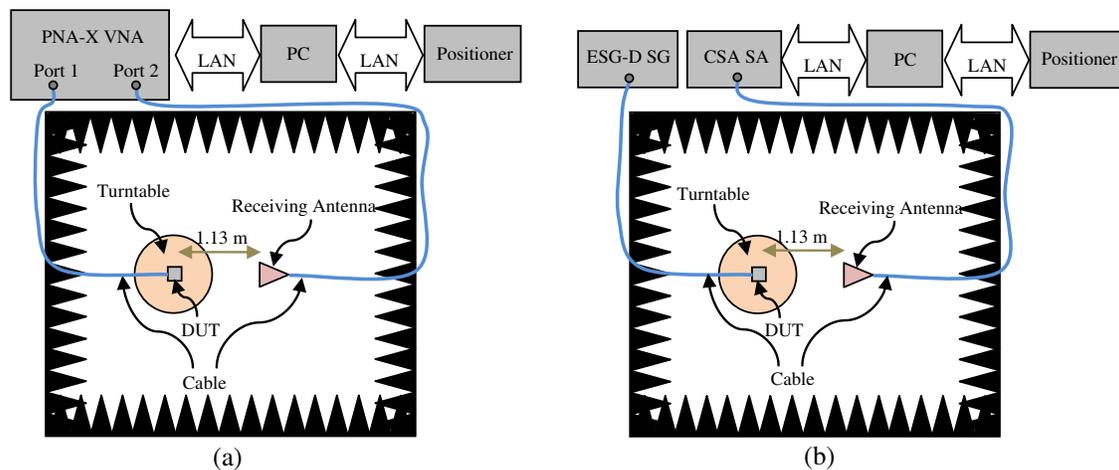


Figure 2: Layout of the measurement system used for: (a) VNA-based method; (b) SA-based method. For the SA-based method, the ESG-D SG and cable are not needed for MICAz sensor mote measurement.

channel conforming to IEEE 802.15.4. All measurements were made at a centre frequency of 2.405 GHz. The radiation pattern measurements were made for the MICAz monopole antenna element using both the VNA-based and SA-based method, whereas for the MICAz sensor mote only the SA-based method was used.

As depicted in Figures 1(b)–1(e) the MICAz monopole antenna element is terminated in a coax pigtail and has an MMCX connector. To measure its radiation pattern, a MMCX-to-SMA adaptor was employed between the monopole antenna and the cable. A ferrite ZCAT Series 2035-0930 clamp filter was used to reduce common mode currents on the cable. The gain of the monopole antenna depends on how its ground plane is embedded within the circuit board of the MICAz sensor mote. Extracting it from the MICAz sensor mote might influence its measured radiation characteristics.

### 2.3. Measurement Systems

Figure 2 shows the layout of the measurement system used for both the VNA-based and SA-based method. As depicted Figure 2, the devices under test (DUTs) were used as the source and an ETS-Lindgren 3117 double-ridged waveguide horn antenna was used to receive the transmitted signal. The 3117 horn was mounted on a low permittivity polystyrene walkover block. The distance between the source antenna and the DUT was 1.13 m and the height of the antennas above the top of the walkover foam was 1.225 m. For each set of measurements, the DUT was continuously rotating on an Orbit azimuth automated positioner with the pattern acquired at 1° steps. The DUT was placed over the centre of the rotation of the azimuth positioner.

A two-port Agilent Technology PNA-X VNA was used for the CW measurement of the radiation pattern of the MICAz monopole at a power level of 10 dBm. For the SA-based measurement, the receiving antenna was connected via a coaxial cable to an Agilent CSA N1996A Spectrum Analyser,

which was configured for a frequency span of 6 MHz about the centre frequency of 2.405 GHz. The spectrum analyser was programmed to operate in maximum-hold mode to automatically capture the spectrum of the transmitted signal. The peak value of each maximum-hold spectra was recorded and plotted against the measurement angle. The frequency range, maximum-hold duration, and bandwidth of the spectrum analyser were chosen to suit the characteristics of the DUT. This method assumes that the DUT is radiating continually with a stable transmitted long-term peak power.

A Hewlett Packard E4433B ESG-D Series Signal Generator (SG) was used for the SA-based radiation pattern measurement of the MICAz monopole antenna element. It fed the antenna with an emulated burst-mode Bluetooth (BT) modulated signal with a peak power of 10 dBm at a centre frequency of 2.405 GHz. This recreated the conditions of an intermittent and modulated emitter. The AA batteries of the MICAz sensor mote were replaced before each measurement to ensure stability of the transmitted power.
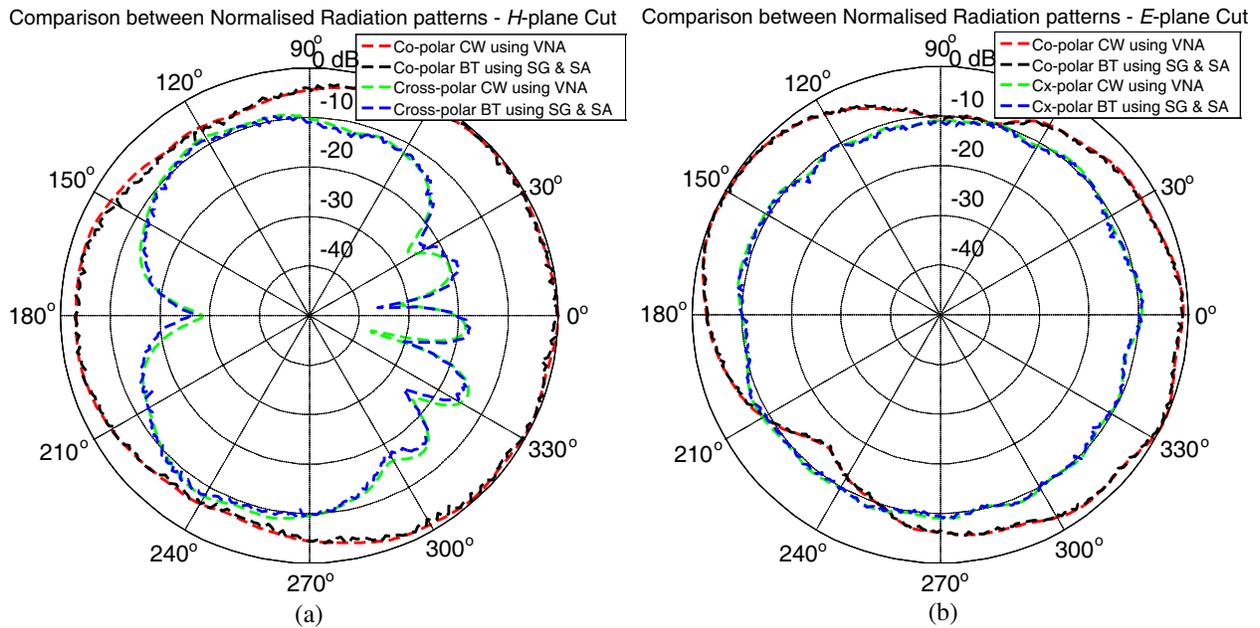


Figure 3: Radiation pattern measurement of MICAz monopole antenna element: (a) $H$-plane cut; (b) $E$-plane cut.
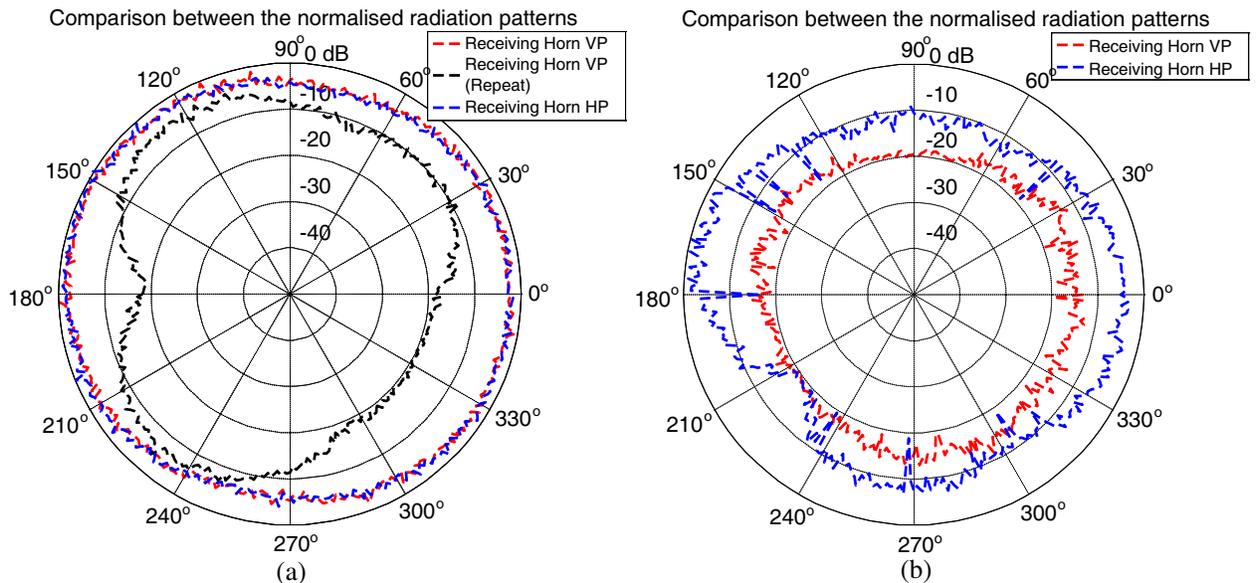


Figure 4: Radiation pattern measurement of MICAz sensor mote: (a) $H$-plane cut; (b) $E$-plane cut.

## 3. RADIATION PATTERN OF MICAz MONOPOLE ANTENNA ELEMENT

The MICAz monopole antenna element was measured at 2.405 GHz for both the SA-based method and its validating the VNA-based method. The SA-based method was chosen to be robust to burst mode signals that have some short-term variation relative to the maximum-hold duration. Figure 3 shows the co-polar and cross-polar radiation pattern measurement in the $H$-plane and $E$-plane for the MICAz monopole antenna, using both the SA and VNA measurement systems. Figure 3 shows that the SA-based method using the Bluetooth signal agrees very closely with the VNA-based method using a CW signal.

## 4. RADIATION PATTERN OF MICAz SENSOR MOTE

The radiation pattern measurements were performed at 2.405 GHz for the MICAz sensor mote using only the SA-based method. As depicted in Figure 4, the measurement of the signal strength around the $E$- and $H$-plane show that the radiation pattern from the MICAz sensor mote is largely isotropic, with around 10 dB maximum variation. This variation is likely to be caused by the presence of the battery pack, which will block part of the signal for some orientations. This is consistent with the known communications performance of this system. From Figure 4(a), the good repeatability results have clearly demonstrated that the proposed technique is robust to modulated and bursty signals.

## 5. CONCLUSIONS

There is an increasing need to understand the radiation performance of wireless communication systems, and its influence on the overall performance of the wireless communication network. To this end, a pattern measuring method has been presented that is robust to modulated and bursty signals. The method was used to measure the radiation pattern of a MICAz monopole antenna element fed with an emulated Bluetooth signal. It was validated against a conventional CW VNA measurement showing excellent agreement.

The radiation pattern from a MICAz sensor mote has also been characterised using the new method. Such systems are commonly used and share characteristics with most WSN platforms. This showed that the method was robust to modulated and bursty signals as demonstrated by the good repeatability of the results.

## REFERENCES

1. Loh. T. H., M. Alexander, P. Miller, and A. L. Betancort, "Interference minimisation of antenna-to-range interface for pattern testing of electrically small antennas," *4th European Conference on Antennas and Propagation (EuCAP 2010)*, Barcelona, Spain, Apr. 11–16, 2010.
2. Holland, M. M., R. G. Aures, and W. B. Heinzelman, "Experimental investigation of radio performance in wireless sensor networks," *2nd IEEE Workshop on Wireless Mesh Networks (WiMesh 2006)*, 140–150, Reston, Virginia, USA, Sep. 2006.
3. Jin, K. S., J. C. McEachen, and G. Singh, "RF characteristics of Mica-Z wireless sensor network motes," *The 49th IEEE International Midwest Symposium on Circuits and Systems (MWSCAS'06)*, 100–104, San Juan, Puerto Rico, Aug. 2006.
4. Su, W. and M. Alzagha, "Channel propagation measurement and simulation of MICAz mote," *WSEAS Trans. on Computers*, Vol. 7, No. 4, 259–264, Apr. 2008.
5. Harms, T., S. Sedigh, and F. Bastianini, "Structural health monitoring of bridges using wireless sensor networks," *IEEE Instrumentation & Measurement Magazine*, Vol. 13, No. 6, 14–18, Dec. 2010.
6. Harvard University. CodeBlue project: Wireless Sensor Networks for Medical Care. Available: http://www.eecs.harvard.edu/~mdw/proj/codeblue/ (Last accessed Nov. 2011).
7. IEEE Standard 802, Part 15.4: Wireless Medium Access Control (MAC) and Physical Layer (PHY) Specifications for Low Rate Wireless Personal Area Networks (WPANs), 2003.

# Characterization of Indoor 30 GHz Bandwidth Multipath Channel Propagation

**W. N. W. Ibrahim**, **M. El-Hadidy**, and **T. Kaiser**

The University of Duisburg-Essen, Germany

**Abstract**— This paper presents and analyzes the results of 30 GHz multipath channel simulations of a real-world indoor environment. Based on simulation of Line of Sight (LoS) and Non Line of Sight (NLoS) scenario, the statistical parameters of the propagation channel such as the path loss, the shadowing, the root mean square (RMS) delay spread and mean excess delay are inspected. A linear relationship between the antenna separation and received power of each path is found. The results will be offered for the 30 GHz bandwidth communication system designers.

## 1. INTRODUCTION

Nowadays, the demand of wireless communication especially in indoor environment has increased rapidly in order to provide high speed digital transmission between two terminals for multimedia applications. Furthermore, if the wireless medium needs to be shared among many users in the same network system, the aggregate network capacity of hundreds of megabits per second or even up to gigabits per second may be needed. One solution in order to achieve such considerably high capacity is to use an extremely large bandwidth which is basically related to small wavelength concept. Thus, it leads to the invention of small size antennas and other device which could be used as portable device such as hand phone, tablet pc, laptop and others.

The use of 30 GHz bandwidth communication system from 10 GHz to 40 GHz is a very promising candidate for high-data-rate and short-range indoor wireless communications. Thus, many important aspects of the 30 GHz bandwidth wireless system have not yet been thoroughly investigated. To our knowledge, no literature review on characterizing 30 GHz bandwidth propagation channel is available at the moment. Some research work on both deterministic [1] for 40–60 GHz and statistical modeling [2] at 20 GHz and 40 GHz have been reported. Previous studies on propagation related to the Extremely High Frequency (EHF) range such as at 27 GHz to 40 GHz in outdoor environment [3], the 40 GHz range in indoor environment [4] where else [5] is about statistical parameters for frequency at 30 GHz. Main objective of this work is to obtain a better assessment of the potential of 30 GHz bandwidth indoor communication system by characterizing the propagating channel from 10 GHz to 40 GHz.

The remainder of the paper has been organized as follows. Section 2 presents the channel simulations in indoor environment. Section 3 present and analyze the characterization of the propagation including the path loss and time dispersion parameters. Finally, section 4 gives the conclusion.

## 2. CHANNEL SIMULATIONS IN REAL-WORLD INDOOR ENVIRONMENT

Channel characterization refers to extracting the channel parameters from a deterministic channel modeling for an indoor real-world environment. Simulation of 30 GHz bandwidth communication has been performed based on a ray-tracing tool "Wireless Insite" from Remcom [6]. A typical real-world indoor environment considering Line of Sight (LoS) and Non Line of Sight (NLoS) scenarios have been explored. For LoS scenario, a grid of $(6 \times 5)$ points of receives antenna with sub-distance of 1 m and a grid of $(5 \times 3)$ points with the same sub-distance for NLoS scenario had been considered as shown in Figures 1 and 2 respectively.

## 3. ANALYSIS OF MULTIPATH PROPAGATION CHANNEL

An important aspect in propagation research is the performance of communication systems. Thus, channel fading will degrades the performance of communication systems. There are two types of fading which are small scale fading and large scale fading. Small scale fading is caused by multipath propagation where else path loss and shadowing will describe the large scale fading.

The received power, $P_r$ at any distance, $d$ for multipath propagation signals behave differently from a single path propagation channel. The reason of that is the interference and diffraction effects that have a direct dramatic influence on the total received power at the receiving antenna. This
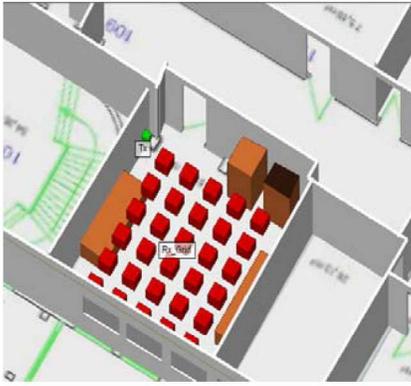
Figure 1: LoS scenario in the ray-tracer.



Figure 2: NLoS scenario in the ray-tracer.
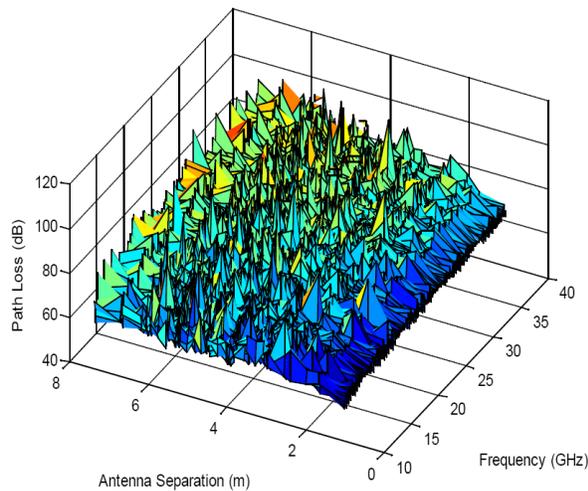


Figure 3: Path loss of LoS 30 GHz bandwidth considering multipath propagation.
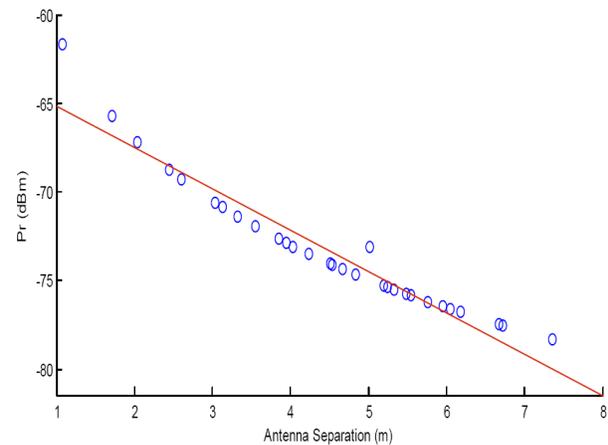


Figure 4: Received power of first path at 40 GHz.

could be clearly illustrated in Figure 3, where the total received power is decreased with increasing the frequency and the separation distance as well but not with the same linear performance shown is Figure 4 of the single path propagation.

Figure 4 shows the received power of the first path at frequency of 40 GHz where the receive power decreases linearly with the distance of transmitter and receiver.

### 3.1. Path Loss and Shadowing

Path loss (PL) of the propagation channels in dB is the mean signal power loss in the propagation channel. It's normally follows the power distance law. Path Loss is frequency dependent and it do not depends on the antenna gain or transmitted power level. Shadowing is a phenomenon when the signal power observed ant any distance or point will deviate from its mean. Large scale fading or path loss is defined as

$$PL(d) = PL_0(d_0) + 10 * n \log(d/d_0) - S_\sigma \qquad (1)$$

where $d$ is the separation distance between transmitter and receiver antenna, $n$ is the path loss exponent and $PL_0$ is the path loss at reference separation distance $d_0$ which is 1 meter. $S$ is the shadowing parameter with $\sigma$ is the standard deviation of variation of the shadowing in dB. Parameter $n$ and $\sigma$ can be determined from the simulation data through the least mean squares error fitting method. Figure 5 shows that the path loss is increase with the increasing of the frequency. Figure 6 compares the path loss models for LoS and NLoS scenario. At 40 GHz, it shows that in line of sight scenario the path loss exponent $n$ is 3.7 and shadowing is 4.75 dB where else in non line of sight scenario the path loss exponent $n$ is 6.8 and the shadowing is 3.61 dB. The path loss exponent in NLoS is higher than LoS case. The path loss exponent for line of sight scenario at 30 GHz, however is similar to the one found in the literature [5].
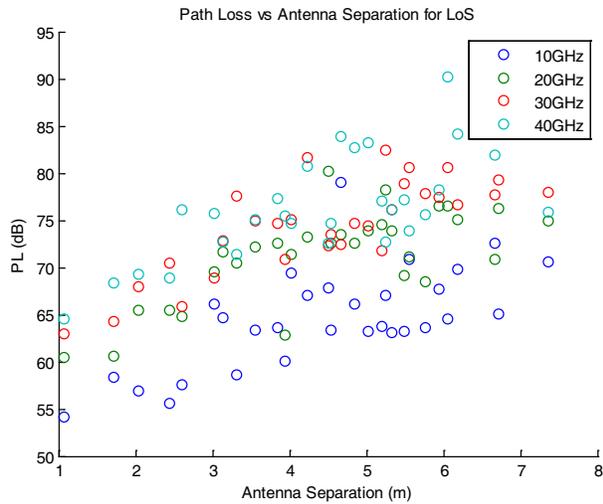
Figure 5: Path loss for LoS.
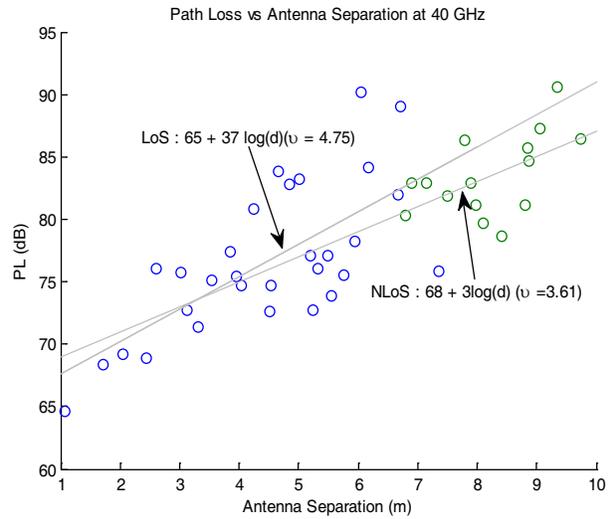


Figure 6: Path loss vs antenna separation at 40 GHz.
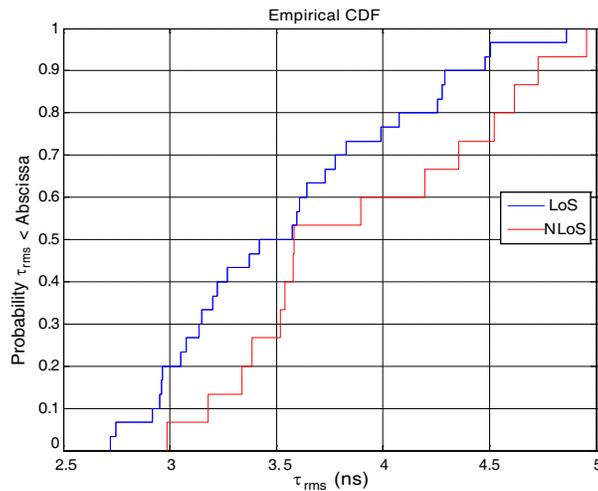


Figure 7: CDF of RMS delay spread for LoS and NLoS.

### 3.2. Time Dispersion

Time dispersion phenomenon mainly caused by the multipath propagation in the channel. It can highly affect the transmitted data rate and reduce the capacity in any communication system. The time dispersive properties of multipath channels are most commonly quantified by its mean excess delay, $\tau_m$ and rms delay, $\tau_r ms$.

The mean excess delay is the mean delay value in the power delay profile and is defined by

$$\tau_m = \frac{\sum_k h_k \tau_k}{\sum_k h_k^2} \tag{2}$$

where $\tau_k$ is the delay and $h_k$ is the signal amplitude. The RMS delay spread is the square root of the second central moment of a power delay profile [2]. It is the standard deviation of the mean excess delay. It is a good measure of the multipath spread. It gives an indication of the nature of the inter-symbol interference (ISI). It is defined as

$$\tau_{rms} = \sqrt{\frac{\sum_k h_k^2 \tau_k^2}{\sum_k h_k^2} - (\tau_m)^2} \tag{3}$$

Figure 7 shows the combined cumulative distribution functions of the RMS delay spread values for both line of sight and non line of sight. It appears that $\tau_{rms}$ is higher in non line of sight

environment compared to the line of sight environment. For line of sight, the mean of $\tau_{rms}$ is 3.55 ns, however it is 3.9 ns for non line of sight scenario. Besides that, the value is lower compared to the typical value available in literature [4, 5].

## 4. CONCLUSION

In this paper, we investigated channel characteristics of 30 GHz multipath channel simulations of a real-world indoor environment in both LoS and NLoS scenarios. The large scale characterization considering the path loss has been presented through the linear regression path loss. We found that the rms delay spread in NLoS is higher than in LoS.

**REFERENCES**

1. Smulders, P. F. M., "Deterministic modelling of indoor radio propagation at 40–60 GHz," *Wireless Personal Communications*, Vol. 1, No. 3, 127–135, 1995.
2. Zhang, J., Z. Muhi-Eldeen, J. Richter, M. Al-Nuaimi, and L. Ivrissimtzis, "Statistical modelling of building scatter in metropolitan cells at 20 and 40 GHz for fixed wireless access links," *Proc. International Conference on ITS Telecommunications*, 358–361, Chengdu, June 2006.
3. Roche, J. F., H. Lake, D. T. Worthington, C. K. H. Tsao, and J. T. Bettencourt, "Radio propagation at 27–40 GHz," *IEEE Trans. Antennas Propag.*, Vol. 18, No. 4, 452–462, 1970.
4. Talbi, L. and G. Y. Delisle, "Experimental characterization of EHF multipath indoor radio channels," *IEEE J. Sel. Areas Commun.*, Vol. 14, No. 3, 431–440, 1996.
5. Beauvarle, D. and K. L. Virga, "Indoor propagation characteristics for wireless communications in the 30 GHz range," *Proc. Antennas and Propagations Society International Symposium*, 288–291, Aug. 2002.
6. El-Hadidy, M., "Realistic UWB MIMO channel model considering analogue aspects and antennas effects," Druck und Verlag, DruckTeam, Hanover, Germany, 2009, ISBN 978-3-925658-10-5.

# RFID and Bluetooth Technology for Tagging and Transmission of Data to POS (Point of Sale)

**R. Mardeni and T. W. Lee**

Faculty of Engineering, Multimedia University
Jalan Multimedia, Cyberjaya, Selangor 63100, Malaysia

**Abstract**— This work describes a study on wireless technology which involve on RFID and Bluetooth technology for tagging and transmission of data to point of sale in Malaysia. The objective of this study is to using RFID and Bluetooth technology for item tagging and data transmission. The expectation of this project study is to allow certain item to be tag that easily to be identified and localized by using RFID technology which will communicate with personal computer. Besides, data encryption for Bluetooth was pairing with personal computer need to perform to achieve secure and simple pairing feature when customer transaction is done. It did involve hardware and software. Moreover, from the simulation result, there will be using double side band modulation to design on RFID reader for better item tagging.

## 1. INTRODUCTION

As our country business is grow that lead to a lot of transaction is required at the checkout point. As we observed from the shopping mall, the point of sale terminal becomes crowded easily. The only solution to overcome this problem is using RFID technology and Bluetooth technology for item tagging and data transmission. Unlike the barcode system, the RFID technology does not required any line of sight. The RFID technology will involve reader, antenna and tag [1]. The reader will act like a transmitter and receiver which will communicate with the tag and personal computer. Each of the tag will carry with a unique tracking identifier coding. Thus, with the item being tag with RFID tag and pass through the RFID reader, the specific item will be easily to recognize and identify of their location [4]. Besides this, Bluetooth technology becomes very common on our mobile phone. Many mobile phones will acquire with Bluetooth communication link. With this kind of technology, we can use it to perform the authorization of transaction on point of sale system. The RFID reader and tag are obtained from Impinj for analysis purpose. Besides, PC connected for Bluetooth mobile phone also performed studied and analysis. The entire system will show on Figure 1.

## 2. WIRELESS COMMUNICATION FOR POINT OF SALE SYSTEM

### 2.1. Experimental Result and Discussion

In Figure 2, it showing the RFID reader transmits signal and ASK signal when reader is communicated with tag [2]. The amplitude shift keying (ASK) can be defined as below equation:

$$s(t) = Am(t)\cos 2\pi fct, \quad 0 < t < T \tag{1}$$
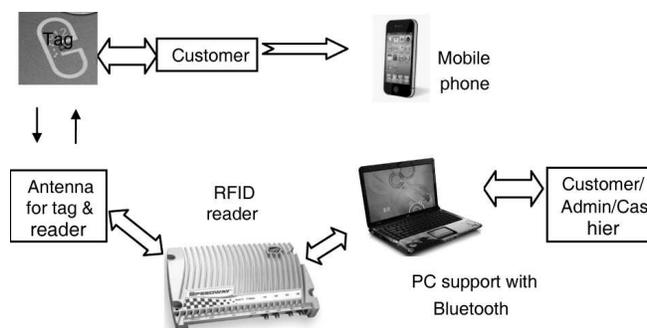


Figure 1: POS system using RFID and Bluetooth technology.
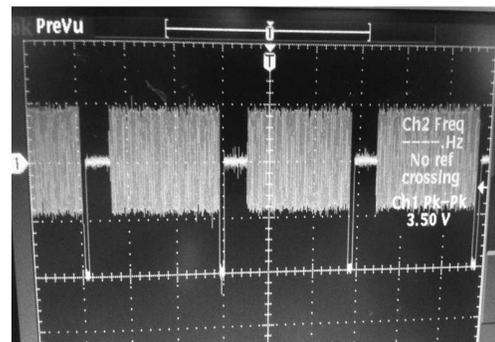


Figure 2: Reader and tag communicate result of the ASK signal.

where $A$ is a constant, $m(t) = 1$ or 0, $fc$ is the carrier frequency, and $T$ is the bit duration. It has a power $P = A2/2$, so that $A = 2P$. Thus Equation (1) can be written as

$$
\begin{aligned}
s(t) &= \text{sqrt}(2P)\cos 2\pi fct, \quad 0 < t < T \\
&= \text{sqrt}(PT)\text{sqrt}(2/T)\cos 2\pi fct, \quad 0 < t < T \\
&= \text{sqrt}(E)\text{sqrt}(2/T)\cos 2\pi fct, \quad 0 < t < T
\end{aligned}
\tag{2}
$$

Thus, the single side band (SSB) modulation can be defined as below equation:

$$
s(t) = u(t)\cos\left((f_c t + \theta)\right) \mp \hat{u}(t)\sin\left((f_c t + \theta)\right)
\tag{3}
$$

where $f_c$ is the carrier frequency, $\theta$ is the Initial phase parameter $\hat{u}(t)$ is the Hilbert transform of the input $u(t)$.

Modulated power for SSB is

$$
P_{SSB} = \frac{V_{DC}^2}{2} + \left(\frac{V_m}{2\sqrt{2}}\right)^2 = \frac{V_{DC}^2}{2} + \frac{V_m^2}{8}
\tag{4}
$$

However for up-conversion part, after signal already modulated into SSB, the signal for I & Q will combine and amplifier before pass through the bandpass filter. The bandwidth of the signal will be determined by analog bandpass filtering design. The type of bandpass filter select is using the Bessel function as shown on below equation:

For integer value of $n$,

$$
J_n(x) = \frac{1}{\pi} \int_0^\pi \cos(n\tau - x\sin\tau)d\tau
\tag{5}
$$

This type of filter is select because it given a best band selected.

As tags provided by Impinj will encode the backscattered data as FM0 (bi-phase space) baseband at the data rate. FM0 inverts the baseband phase at every symbol boundary; a data-0 has an additional mid-symbol phase inversion [5]. As tag and reader communicated, this will result of the ASK signal as shown on Figure 2.

Figure 3 show the developed of the prototype software which will communicate with the RFID reader through the Ethernet connection to detect for the tag existing. Each of the tag programmed for specific of EPC (Electronic Product Code) number in order to track and identify the items [3] once the tag already stick onto the product. If read rate was high, it indicated that the distance between the tag and reader is near.

### 2.2. Bluetooth Transceiver

To avoid frequency interference in the ISM band, the sender divides the transmission time into 625-microsecond slots, and uses a new hop frequency for each slot [8]. Although the data rate is only 1 Mbps, a much larger bandwidth of 79 MHz is required to simulate the frequency hopping.
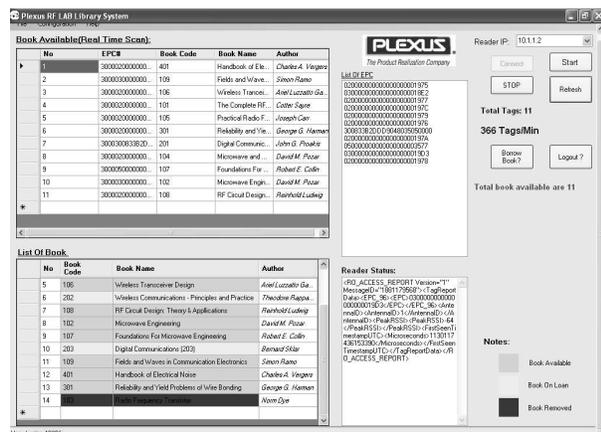


Figure 3: Prototype software design for RFID tagging system.
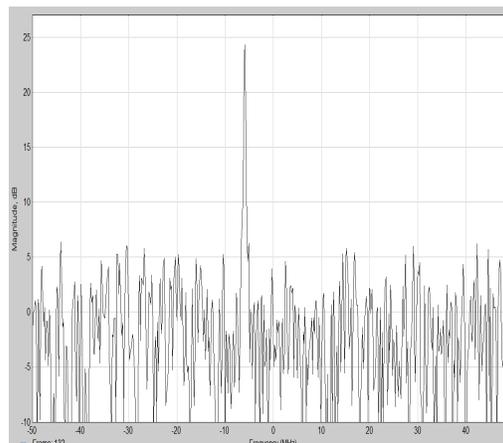


Figure 4: Received signal spectrum.

This received spectrum as shown on Figure 4. In Bluetooth communication, it uses GFSK/GMSK for modulation and M-FSK for demodulation [7]. The modulation equation for GMSK as shown below [6]:

$$h_{GAUSS}(t) = K\sqrt{\frac{2\pi}{\ln(2)}}Be^{-2\frac{(B\pi)^2}{\ln(2)}r^2} \tag{6}$$

Gaussian shaped bit stream $gGMSK(t)$, which is equal to convolution of $gRECT(t)$ and thus $hGAUSS(t)$ becomes:

$$g_{GMSK}(t) = -\frac{K}{2\sqrt{\ln(2)}}\left[Erf\left(2B\pi\frac{t-\frac{T_b}{2}}{\sqrt{\ln(4)}}\right) - Erf\left(2B\pi\frac{t+\frac{T_b}{2}}{\sqrt{\ln(4)}}\right)\right] \tag{7}$$

where $Erf(t)$ is error function given by

$$Erf(x) = \frac{2}{\sqrt{\pi}}\int_0^x e^{-t^2}dt. \tag{8}$$

## 3. CONCLUSION

As a conclusion, in this paper, wireless communication such as RFID system and Bluetooth system is used to study for the POS system improvement. RFID tagging enables for the item tracking and identified easily compare for the barcode system used. Meanwhile, Bluetooth system enables for the fast transaction to make a purchase and securely with using asymmetric algorithm suggested. Finally, the design for such this wireless communication system is useful for our POS system improvement at Malaysia.

## ACKNOWLEDGMENT

**REFERENCES**
1. Impinj, "RFID and semiconductor intellectual property technologies," http://www.impinj.com.
2. "How does RFID tag technology works," *ScienceProg*, http://www.scienceprog.com/how-does-rfid-tagtechnology-works/.
3. The EPCglobal Network, "Standards," http://www.epcglobalna.org/Standards/TheEPCglobal Network/tabid/184/Default.aspx.
4. Rekik, Y., E. Sahin, and Y. Dallery, "Inventory inaccuracy in retail stores due to theft: An analysis of the benefits of RFID," *International Journal of Production Economics*, Vol. 118, No. 1, 189–198, 2009.
5. Hsu, Y.-C., A.-P. Chen, and C.-H. Wang, "A rfid-enabled traceability system for the supply chain of live fish," *IEEE International Conference on Automation and Logistics*, 81–86, Sep. 1–3, 2008.
6. Vilovic, I. and B. Zovko-Cihlar, "Performance analysis of wireless network using Bluetooth and IEEE 802.11 devices," *Proceedings of the 46th International Symposium in Electronics in Marine*, 235–240, 2004.
7. Bluetooth SIG, *Profiles Specification of the Bluetooth System*, Version 1.1, 2001.
8. Mathew, A., N. Chandrababu, K. Elleithy, and S. Rizvi, "IEEE 802.11 & Bluetooth interference: Simulation and coexistence," *7th Annual Conference on Communication Networks and Services Research*, 217–223, 2009.

# LTE-FDD and LTE-TDD for Cellular Communications

**A. Z. Yonis**[1], **M. F. L. Abdullah**[1], **and M. F. Ghanim**[2]

[1]Faculty of Electrical and Electronic Engineering, Department of Communication Engineering
University of Tun Hussein Onn Malaysia, Johor, Malaysia
[2]Computer Engineering Department, College of Engineering, University of Mosul, Mosul, Iraq

**Abstract**— LTE-Advanced (Long Term Evolution-Advanced) is used on fourth generation (4G) in mobile phone technology as many providers are beginning to augment their networks with LTE. As known, mobile phone traffic is divided into two parts: an uplink and a downlink. This paper presents the LTE two duplexing modes: LTE-TDD (Time Division Duplexing) and LTE-FDD (Frequency Division Duplexing). Where LTE-TDD favored by a majority of implementations because of flexibility in choosing uplink to downlink data rate ratios, ability to exploit channel reciprocity, ability to implement in non-paired spectrum and less complex transceiver design. In the case of FDD operation there are two carrier frequencies, one for uplink transmission ($f_{UL}$) and one for downlink transmission ($f_{DL}$). During each frame, there are thus ten uplink subframes and ten downlink subframes, so uplink and downlink transmission can occur simultaneously within a cell. LTE-FDD implies that downlink and uplink transmission take place in different, sufficiently separated, frequency bands, while TDD implies that downlink and uplink transmission take place in different, non overlapping time slots. Thus, TDD can operate in unpaired spectrum, whereas FDD requires paired spectrum. Also the required flexibility and resulting requirements to support LTE operation in different paired and unpaired frequency arrangements are discussed in this Paper. This paper focuses on the main difference between LTE-FDD and LTE-TDD in how they divide the single channel to provide paths for both uploading (mobile transmit) and downloading (base-station transmit). FDD does this by dividing the frequency band allotted into two discrete smaller channels. TDD uses the entire channel but alternates between uploading and downloading and in the case of TDD uplink and downlink communication taking place in the same frequency band but in separate non-overlapping time slots; there is typically a high fading correlation between the downlink and uplink.

## 1. INTRODUCTION

With full coverage in the 3 GPP Release 8 specifications of both TDD and FDD modes of operation, LTE can effectively be deployed in both the paired and unpaired spectrum. LTE TDD and FDD modes have been greatly harmonized in the sense that both modes share the same underlying framework, including radio access schemes OFDMA in downlink and SC-FDMA in uplink, basic subframe formats, configuration protocols, etc.. As clear indication of the harmonization, the TDD mode is included together with the FDD mode in the same set of specifications, including the physical layer where there are just a few differences due to the uplink/downlink switching operation. In terms of architecture there are no differences between FDD and TDD and the very few differences in the MAC and higher layer protocols relate to TDD specific physical layer parameters. Procedures are kept the same. Thus there will be high implementation synergies between the two modes allowing for efficient support of both TDD and FDD in the same network or user device. Coexistence would of course still require careful analysis. Another key feature of the LTE-TDD mode (known also as TD-LTE) is the commonality with TD-SCDMA. In this paper, the detailed aspects of LTE-TDD that differ from the LTE-FDD mode are introduced. Further, information related to both the link and system performance of the LTE TDD mode of operation is given [1].

## 2. SPECTRUM FLEXIBILITY

A high degree of spectrum flexibility is the main characteristic of the LTE radio-access technology. The aim of this spectrum flexibility is to allow for the deployment of LTE radio access in difference frequency bands with different characteristics, including different duplex arrangements and different sizes of the available spectrum [2].

### 2.1. Flexibility in Duplex Arrangement

One important part of the LTE requirements in terms of spectrum flexibility is the possibility to deploy LTE-based radio access in both paired and unpaired spectrum. Therefore, LTE supports

both frequency- and time-division-based duplex arrangements. FDD as illustrated on the left in Figure 1, implies that downlink and uplink transmission take place in different, sufficiently separated, frequency bands. TDD as illustrated on the right in Figure 1 implies that downlink and uplink transmission take place in different, non-overlapping time slots. Thus, TDD can operate in unpaired spectrum, whereas FDD requires paired spectrum [1].

Operation in both paired and unpaired spectrum has been supported by 3GPP radio-access technologies even before the introduction of LTE by means of FDD-based WCDMA/HSPA in combination with TDD-based TD-SCDMA radio. However, this was then achieved by means of, at least in the details, relatively different radio-access technologies leading to additional effort and complexity when developing and implementing dual-mode terminals capable of both FDD and TDD operation. LTE, on the other hand, supports both FDD and TDD within a single radio-access technology, leading to a minimum of deviation between FDD and TDD for LTE-based radio access.

In the case of differences between FDD and TDD, these differences will be explicitly indicated. Furthermore, the TDD mode, also known as TD-LTE, is designed with coexistence between TD-LTE and TD-SCDMA in mind to simplify a gradual migration from TD-SCDMA to TD-LTE.

LTE also supports half-duplex FDD at the terminal (illustrated in the middle of Figure 1). In half-duplex FDD, transmission and reception at a specific terminal are separated in both frequency and time. The base station still uses full-duplex FDD as it simultaneously may schedule different terminals in uplink and downlink; this is similar to, for example, GSM operation. The main benefit with half-duplex FDD is the reduced terminal complexity as no duplex filter is needed in the terminal. This is especially beneficial in the case of multi-band terminals which otherwise would need multiple sets of duplex filters.

## 3. DUPLEX SCHEMES

Spectrum flexibility is one of the key features of LTE. In addition to the flexibility in transmission bandwidth, LTE also supports operation in both paired and unpaired spectrum by supporting both FDD- and TDD-based duplex operation with the time–frequency structures illustrated in Figure 2.

Although the time-domain structure is, in most respects, the same for FDD and TDD, there are some differences, most notably the presence of a special subframe in the case of TDD. The special subframe is used to provide the necessary guard time for downlink–uplink switching.

### 3.1. Frequency-division Duplex (FDD)

In the case of FDD operation (upper part of Figure 2), there are two carrier frequencies, one for uplink transmission ($f_{UL}$) and one for downlink transmission ($f_{DL}$). During each frame, there
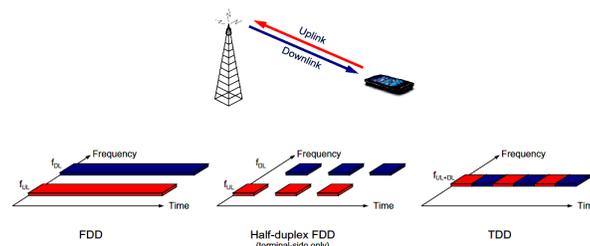


Figure 1: Frequency and time-division duplex [1].
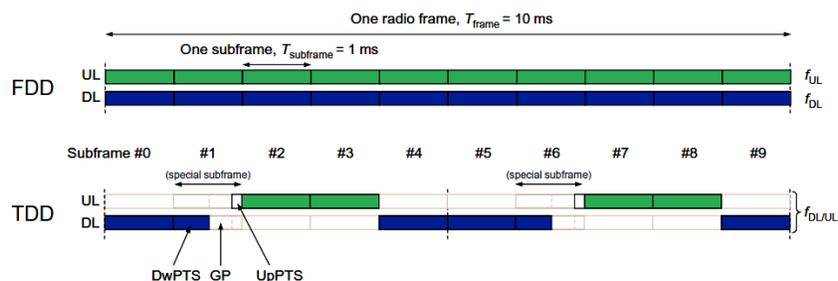


Figure 2: Uplink/downlink time-frequency structure for FDD and TDD [2].
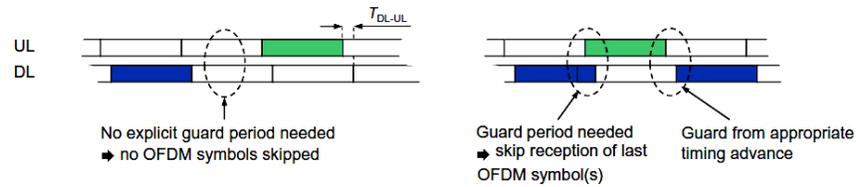
Figure 3: Guard time at the terminal for half duplex FDD [2].

are thus ten uplink subframes and ten downlink subframes, and uplink and downlink transmission can occur simultaneously within a cell [3]. Isolation between downlink and uplink transmissions is achieved by transmission/reception filters, known as duplex filters, and a sufficiently large duplex separation in the frequency domain. Even if uplink and downlink transmission can occur simultaneously within a cell in the case of FDD operation, a terminal may be capable of full-duplex operation or only half-duplex operation for a certain frequency band, depending on whether or not it is capable of simultaneous transmission/reception. In the case of full-duplex capability, transmission and reception may also occur simultaneously at a terminal, whereas a terminal capable of only half-duplex operation cannot transmit and receive simultaneously. Supporting only half-duplex operation allows for simplified terminal implementation due to relaxed duplex-filter requirements. This applies especially for certain frequency bands with a narrow duplex gap.

Hence, full duplex support is frequency-band dependent such that a terminal may support only half-duplex operation in certain frequency bands while being capable of full-duplex operation in the remaining supported bands. It should be noted that full/half-duplex capability is a property of the terminal; the base station is operating in full duplex irrespective of the terminal capabilities. Hence, as the relevant transmission structures and timing relations are identical between full-duplex and half-duplex FDD, a single cell may simultaneously support a mixture of full-duplex and half-duplex FDD terminals. Half-duplex operation has an impact on the sustained data rates that can be provided to/from a single mobile terminal as it cannot transmit in all uplink subframes, but the cell capacity is hardly affected as typically it is possible to schedule different terminals in uplink and downlink in a given subframe. Since a half-duplex terminal is not capable of simultaneous transmission and reception, the scheduling decisions must take this into account and half-duplex operation can be seen as a scheduling restriction. If a terminal is scheduled such that downlink reception in one subframe immediately precedes a subframe of uplink transmission, a guard time is necessary for the terminal to switch from reception to transmission. This is created in such cases by allowing the terminal to skip receiving the last OFDM symbol(s) in the downlink subframe, as illustrated in Figure 3.

**3.2. Time-division Duplex (TDD)**

In the case of TDD operation (Upper part of Figure 2), there is a single carrier frequency only and uplink and downlink transmissions are separated in the time domain on a cell basis [4]. As seen in the figure, some subframes are allocated for uplink transmissions and some subframes for downlink transmission, with the switch between downlink and uplink occurring in the special subframe (subframe 1 and, in some cases, subframe 6).

Like FDD, LTE TDD supports bandwidths from 1.4 MHz up to 20 MHz but depending on the frequency band, the number of supported bandwidths may be less than the full range. For example, for the 2.5 GHz band, it is not likely that the smallest bandwidths will be supported. Since the bandwidth is shared between uplink and downlink and the maximum bandwidth is specified to be 20 MHz in Release 8, the maximum achievable data rates are lower than in LTE FDD. This way the same receiver and transmitter processing capability can be used with both TDD and FDD modes enabling faster deployment of LTE.

The TDD system can be implemented on an unpaired band (or in two paired bands separately) while the FDD system always requires a pair of bands with a reasonable separation between uplink and downlink directions, known as the duplex separation. In a FDD UE implementation this normally requires a duplex filter when simultaneous transmission and reception is facilitated. In a TDD system the UE does not need such a duplex filter. The complexity of the duplex filter increases when the uplink and downlink frequency bands are placed in closer proximity. In some of the future spectrum allocations it is foreseen that it will be easier to find new unpaired allocations than paired allocations with sensible duplex separation thereby increasing further the scope of applicability for TDD.

However, since uplink and downlink share the same frequency band, the signals in these two transmission directions can interfere with each other. This is illustrated in Figure 4, with the use of TDD on the same frequency without coordination and synchronization between sites in the same coverage area.

For uncoordinated deployment (unsynchronized) on the same frequency band, the devices connected to the cells with different timing and/or different uplink/downlink allocation may cause blocking for other users. In LTE TDD the base stations need to be synchronized to each other at

Table 1: Comparison between FDD-LTE and TDD-LTE.

| FDD-LTE | TDD-LTE |
|---|---|
| Uses Frequency-Division Duplex | Uses Time-Division Duplex |
| Generally better suited for applications like voice calls that have symmetric traffic, because traffic in both directions is always constant. | Is better at reallocating traffic than FDD-LTE such as Internet or other data centric services. |
| It requires paired spectrum with different frequencies with guard band. | Does not require paired spectrum since transmit and receive occurs in the same channel |
| Is appears when planning sites for base stations. Because FDD base stations use different frequencies for receiving and transmitting, they effectively do not hear each other and no special planning is needed. | With TDD, special considerations need to be taken in order to prevent neighboring base stations from interfering with each other. |
| Allows for easier planning than TDD LTE. | It is cheaper than FD LTE since in TDD-LTE no need of duplexer to isolate transmission and receptions. |
| FDD LTE is full duplex this means that both the upload and download are always available. | TDD LTE is half duplex as either upload or download can use the channel but not at the same time. |
| With FDD, the bandwidth cannot be dynamically reallocated and the unused bandwidth is wasted. | TDD can allocate more time for the part that requires more bandwidth, thereby balancing the load |
| FDD-LTE every downlink subframe can be associated with an uplink subframe | TD-LTE the number of downlink and uplink subframes is different and such association is not possible. |
| An FDD system uses a duplexer and/or two antennas that require spatial separation and, therefore, cannot reuse the resources. The result is more costly hardware [5]. | In TDD, both the transmitter and receiver operate on the same frequency but at different times. Therefore, TDD systems reuse the filters, mixers, frequency sources and synthesizers, thereby eliminating the complexity and costs associated with isolating the transmit antenna and the receive antenna. |
| FDD cannot be used in environments where the service provider does not have enough bandwidth to provide the required guard-band between transmit and receive channels. | TDD utilizes the spectrum more efficiently than FDD. |
| It is requires two interference-free channels. | It is requires only one interference-free channel. |
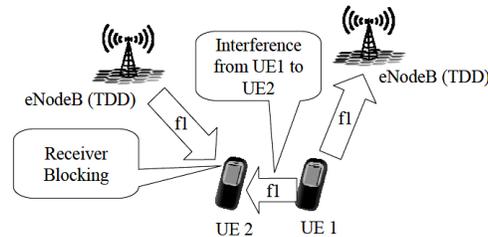
Figure 4: Interference from uplink to downlink in uncoordinated TDD operation.

frame level in the same coverage area to avoid this interference. This can be typically done by using, for example, satellite based solutions like GPS or Galileo or by having another external timing reference shared by the LTE TDD base stations within the same coverage area. LTE FDD does not need the base station synchronization. There is no interference between uplink and downlink in FDD due to the duplex separation of the carriers.

## 4. SUMMARY AND COMPARISON

The two versions of LTE are very similar. In fact, they differ only in the physical layer and, as a result, the version implemented is transparent to the higher layers. This means that UEs will be able to support both TDD-LTE and FDD-LTE with one chipset with only minor modifications required. The Table 1 shows the main comparison between FDD-LTE and TDD-LTE.

## 5. CONCLUSION

The uplink coverage with respect to a specific data rate in TDD-LTE is generally worse than FDD-LTE due to the fact that the uplink transmission is not continuous. The percentage of coverage for control and data channels is, however, very similar to that of FDD-LTE. In terms of spectrum efficiency, the performances of TDD-LTE and FDD-LTE are similar for non-delay sensitive traffic. The lower performance of TDD-LTE is due to the guard periods mentioned above. Overall, TDD-LTE offers operators a great alternative to FDD. Its natural suitability for asymmetric applications, low latency, high throughput, and security make it a flexible and cost-effective solution for the next generation wireless networks. TDD is more flexible than FDD in meeting the need to dynamically reconfigure the allocated upstream and downstream bandwidth in response to customer needs. In summary, TDD is a more desirable duplexing technology that allows system operators to receive the most from their investment in spectrum and telecom equipment, while meeting the needs of each individual customer

## ACKNOWLEDGMENT

## REFERENCES

1. Holma, H. and A. Toskala, *LTE for UMTS: OFDMA and SC-FDMA Based Radio Access*, 267, John Wiley & Sons Ltd., United Kingdom, 2009.
2. Dahlman, E., S. Parkvall, and J. Sköld, *4G LTE/LTE-Advanced for Mobile Broadband*, 100–137, Elsevier Ltd., UK, 2011.
3. Dahlman, E., S. Parkvall, J. Sköld, and P. Beming, *3G Evolution: HSPA and LTE for Mobile Broadband*, 2nd Edition, 318, Elsevier, Department in Oxford, UK, 2008.
4. Parkvall, S. and D. Astely, "The evolution of LTE towards IMT-advanced," *Journal Of Communications*, Vol. 4, No. 3, 146–153, Apr. 2009.
5. Progri, I., *Geolocation of RF Signals: Principles and Simulations*, 115, Springer, USA, 2011.

# A RFID Reader Suppressive Interferences Due to Multipath

**S. Duangsuwan and S. Promwong**

Faculty of Engineering, King Mongkut's Institute of Technology Ladkrabang
Chalongkrung Road, Ladkrabang, Bangkok 10520, Thailand

**Abstract**— The radio-frequency identification (RFID) are growing rapidly, especially at 2.45 GHz that is very high speed transmission for toll collection. In addition, there are many problems from the effects of interference due to multipath fading, which leading to bandwidth limitation and channel distortion. Consequently, the rapidly signal processing of RFID reader could be still lacks the demands on improvement. The interference cancelation is proposed by using the blind filtering equalization on previously. In this paper, we proposed the suppressive interfering due to multipath rician fading chanenl based on the successive interference cancellation (SIC) technique for improve the convergence of the constant modulus (CM) algorithm. Also as the result, the quantitative evaluation of mitigate interferences are shown.

## 1. INTRODUCTION

The RFID technology originating from the rader uses two-way communications. Its practicable operation frequency is established in the criteria of industry, science and medical (ISM), especially backscatter case become the hot point of research [1]. Although RFID system had been put into use, the problem of multipath interference [2] and the inter-symbol interference (ISI) has been disturbing in application of industrial field continuously. There is many demand specific signal processing algorithm of RFID system [3]. Due to the limited processing capabilities with the limited available energy of state-of-the-art reader, RFID system features a highly imbalanced share of signal processing capability. There are variously to studies the complex signal processing, whether as the multiple input multiple output (MIMO) [4], beamforming [5] have been considered to improve the fading and interferences. In [6] the interference reduction is purposed by blind filtering equalization. Anyway, blind equalization with CM algorithm has been slowly of convergence to iterative reduction. Consequently, this paper we focused on a compensation of convergence by using the SIC technique for decrement of interference, which leading to the signal to interference plus noise (SINR) is degraded due to multipath fading channel.

## 2. RELATED WORK

In a multipath propagation environment, signal components with various delays result in the delay spread. The bandwidth, within the correlation between fading at the included frequencies is assumed to change less than 3 dB is coherent bandwidth $B_c \approx 1/\tau_{RMS}$. With a maximum increase distance of 10 meters at 2.45 GHz operated with multiple antenna receiver side in the Fig. 1(a) of **x** received signal, MIMO can reduced fading problem, the coherent bandwidth is $B_c > 30$ MHz as the Fig. 1(b). The required signal bandwidth for the maximum data rate of 640 kbps is approximately 2.56 MHz, and thus much smaller than $B_c$. Hence, the channel can be assumed to be flat frequency. On the other hand, the frequency selective in RFID signals of multipath propagation need to considered and identified. Furthermore, the effect of multipath fading is reported in [4] reference; the ricean fading channel propagation is characteristic implementation as expressed,

$$\mathbf{H} = \sqrt{\frac{K}{1+K}} * h_{i,j}^{LOS}(t) + \sqrt{\frac{1}{1+K}} * h_{i,j}^{NLOS}(t) \tag{1}$$

where $K$(dB) is ricean factor can calculated as $10\log_{10}\left(\frac{A^2}{2\sigma^2}\right)$, $A^2$ is average received signal and multipath direction of $l$. Also, the channel impulse responds $h_{l,M_r}(t) = \alpha(\phi)e^{j\alpha(-\phi)}$ is time varying depending on amplitude and phase respectively.

The interference channel model of frequency selective channel can wroth by matrix **H** of MIMO dimension. The received signal model is

$$y(k) = \sqrt{\frac{E_s}{M_r}} \begin{bmatrix} h_{11} & \cdots & h_{1M_r} \\ \vdots & \vdots & \vdots \\ h_{M_t 1} & \cdots & h_{M_t M_r} \end{bmatrix} \begin{bmatrix} x_1(t) \\ \vdots \\ x_{M_r}(t) \end{bmatrix} + \sqrt{\frac{E_i}{M_r}} h_i + \begin{bmatrix} n_1(t) \\ \vdots \\ n_{M_r}(t) \end{bmatrix} \tag{2}$$

(a)                                                    (b)
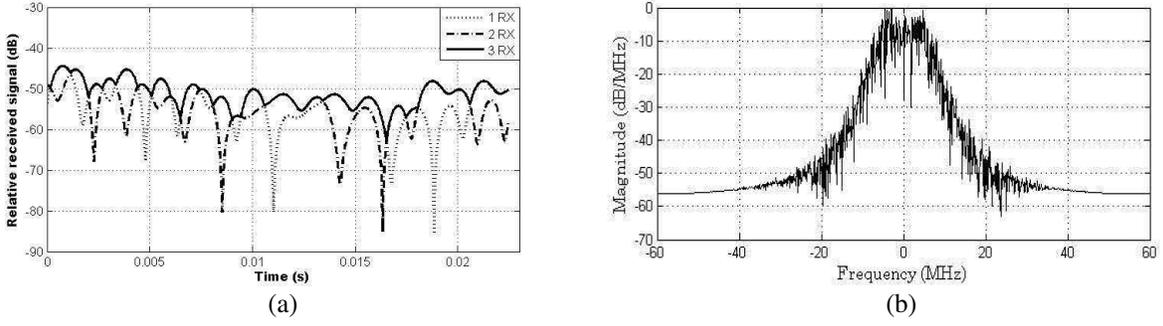
Figure 1: (a) Multipath fading of time-varying system. (b) Channel bandwidth of ISO 18000-4 2.45 GHz.



(a)                                                    (b)
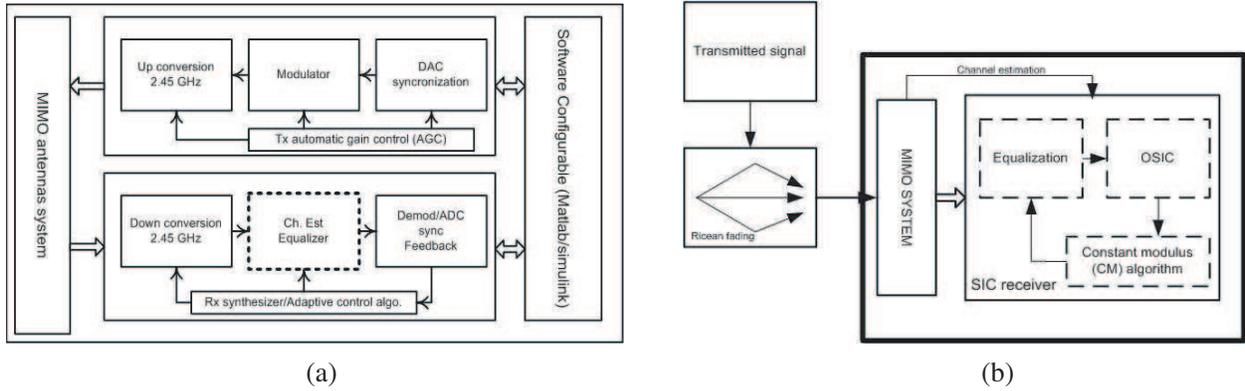
Figure 2: The proposed of RFID system (a) block diagram of RFID reader, (b) RFID suppressive interferences.

Hence, $\sqrt{E_i/M_r} * h_{l,M_r}(t)$ is interference signal in multipath propagation and $n(t)$ is additive white gaussian noise (AWGN) relative with noise density $\sigma^2$. We assume that the backscatter $x(t)$ signal from $M_t$ transmit antennas and arrival at $M_r$ receive antennas and allows modeling the channel matrix $\mathbf{H}$, that is, the $M_r \times M_t$ channel gain matrix whose entries $h_{M_t M_r}(t)$ are line-of-sight (LOS) direction. Therefore, the carrier-interference ratio (CIR) is expressed $CIR = \sqrt{E_s}/h_{l,M_r}^2 + \sigma^2$ of channel non line-of-sight (NLOS).

$$y = \sum_{i=1}^{M_r} \sqrt{\frac{E_s}{i}} \mathbf{w}[\mathbf{H}_e \mathbf{x} + \mathbf{n}] \tag{3}$$

In Eq. (3) is output signal after beamforming and depend on weight coefficient $\mathbf{w}$ of update, also maximum ratio combining (MRC) are evaluated.

## 3. SYSTEM ANALYSIS

We consider the imperfect MIMO channel model given where the r M taps processing is mixed by the channel matrix.

The proposed ZF and MMSE channel estimator are applied to decouple of $M_r$ linear elements, as the system by using

$$\mathbf{H}_{e,zf} = (\mathbf{H}^*\mathbf{H})^{-1}\mathbf{H}^* \text{ and } \mathbf{H}_{e,mmse} = \left(\mathbf{H}^*\mathbf{H} + \frac{1}{\text{snr}}\mathbf{I}\right)^{-1}\mathbf{H}^* \tag{4}$$

where $\mathbf{H}^*$ is matrix transposed (conjugate), $\text{snr} = \sqrt{E_s/\sigma_{M_r}^2}$ is average signal to noise ratio of desired signal at spatial element, and $\mathbf{I}$ is identical matrix covariant of $E[\sigma^*\sigma]^2$, we obtain receiver antenna with output SNR

$$SNR_{zf} = \frac{\text{snr}}{[(\mathbf{H}^*\mathbf{H})^{-1}]} \text{ and } SNR_{mmse} = \frac{\text{snr}}{\left[\left(\mathbf{H}^*\mathbf{H} + \frac{1}{\text{snr}}\mathbf{I}\right)^{-1}\right]} \tag{5}$$

The RFID reader rapid processing can be show as the Fig. 3, blind algorithm is proposed, no training sequence are used, constant modulus (CM) algorithm is signal property a beamformer weight vector that minimizes a cost function of the from $\nabla = \frac{1}{2}[|y|^2 - 1]^2$, according to the steepest descent algorithm, the weight iterative formula of CMA algorithm can be obtained as

$$\mathbf{w}(k + 1) = \mathbf{w}(k) - \mu\nabla \tag{6}$$

where $\mu$ is step size of optimizes weighting and $k$ is number of tab processing, this method is also more robust if the signals undergoes severe fading during training and mitigate interference and we propose order SIC suppressive multipath interference, because of this technique capable SINR improvement for RFID reader.

## 4. PERFORMANCE AND SIMULATION RESULTS

This paper, we confirmed by computer simulation, as [5] was presented covers smart antenna. The addition, according to previous work is compared. The simulation of rapid signal processing RFID reader based on standard ISO18000-4 mode 1 microwave band and sampling of intermediate frequency (IF) at 100 MHz. In the Fig. 2, covers implementation specific consideration of digital architecture, the transmitter covers the digital to analog conversion (DAC) and synchronization continuous carrier frequency, the ASK modulation, upconversion and MIMO antenna processing. This process can be controlled according with software defined configuration running on the DSP. The receiver is considered, as a Fig. 2(b), the optimized step size $\mu = 0.05$ and $k = 3$. In the Eq. (5), the frequency selective fading of time varying can be improvement SNR of channel equalizes. Therefore, the instantaneous SINR can be review as expressed

$$SINR(\text{dB}) = 20\log_{10}\left[\frac{1}{\frac{1}{CIR} + \frac{1}{SNR}}\right] \tag{7}$$

Consequently, we discussed the performance evaluation of channel equalization by using modifies algorithm. In the Fig. 4, that our proposed (a) shown as capable to reduce the interferences of iterative number, which optimized by OSIC fast processing than ZF-CMA and MMSE-CMA as well as (b) shown algorithm efficiency.



(a)　　　　　　　　　　　　　　　　　　(b)
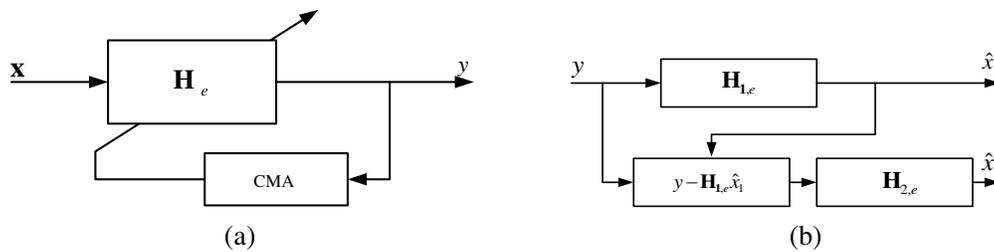
Figure 3: (a) Model of adaptive equalization by CMA algorithm. (b) Model of SIC receiver.



(a)　　　　　　　　　　　　　　　　　　(b)
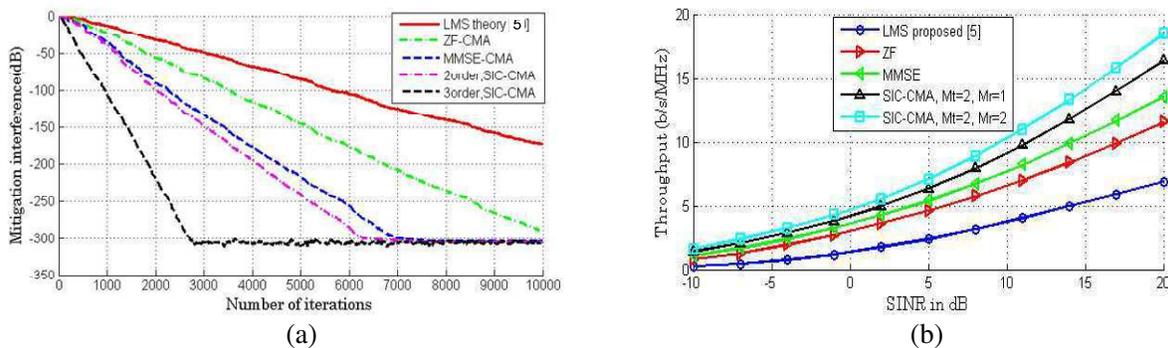
Figure 4: Simulation results $K = 6$ dB [6], $M_t \times M_r$ channel matrix and snr snr $= 8$ dB (a) quantitative evaluation of mitigate interferences, (b) performance evaluation of suppressive cancellation algorithm.

**5. CONCLUSIONS**

This paper, proposed the novel equalization algorithm of RFID reader to suppressive interference due to multipath fading based on successive interference cancellation (SIC) structure. We considered the linear equalizer likely zero forcing (ZF) and minimum mean square error (MMSE) are estimated error and including the equalization by using CMA algorithm. However, the ZF-CMA and MMSE-CMA [6] algorithms have been conducted to inadequate of convergence. Therefore, the order SIC can solve convergence more than the linear equalization and also improvement the throughput of system as well as the signal to interference plus noise (SINR) have been increased. However, this technique can be realized based on software-defined RFID reader.

**REFERENCES**

1. Fan, Z., S. Qiao, J. T. Huang-Fu, and L.-X. Ran, "Signal descriptions and formulations for long range UHF RFID readers," *Progress In Electromagnetic Research*, Vol. 71, 109–127, 2007.
2. Kim, D.-Y, H.-G. Yoon, B.-J. Jang, and J.-G. Yook, "Interference analysis of UHF RFID systems," *Progress In Electromagnetic Research B*, Vol. 4, 115–126, 2008.
3. Angerer, C., R. Langwieser, and M. Rupp, "RFID reader receiver for physical layer collision recovery," *IEEE Transaction on Communications*, Vol. 58, No. 12, 3526–3537, 2010.
4. Kim, D. Y., H. S Jo, H. Yoon, C. Mun, B. J. Jang, and J. G. Yook, "Reverse-link interrogator range of a UHF MIMO-RFID system in nakagami $m$ fading channel," *IEEE Transaction on Industrial Electronic*, Vol. 54, No. 4, 1468–1477, 2010.
5. Sakil, M. and Y. Soo Kim, "A simple LMS algorithm based smart antenna to solve the reader collision problems in RFID system," *Proceedings of ICIMT*, 426–430, Jeju Island, Korea, Dec. 2009.
6. Duangsuwan, S. and S. Promwong, "Performance evaluation of RFID reader with blind filtering equalization for SDR platform," *Proceedings of ITC-CSCC*, 1064–1076, Gyeongju, Korea, Jun. 2011.

# Measurement and Parameter Description of Time-varying Ultra-wideband Infostation Channel

**U. A. K. Chude-Okonkwo, R. Ngah,**
**Yasser K. Zahedi, S. M. Zaid, and T. A. Rahman**
Wireless Communication Center, Universiti Teknologi Malaysia, Malaysia

**Abstract**— In this article, we present the measurement and description of channel parameters for the time-varying Infostation UWB channel. We also consider how such parameters can be used to improve system performance in terms of optimally combating inter-symbol interference (ISI) and inter-channel interference (ICI) in the case of multiband OFDM.

## 1. INTRODUCTION

The concept of infostation [1–3] presents a new way to look at the problem of providing high data rate wireless access. It is an isolated pocket area with small coverage (hundreds of meters) of high bandwidth connectivity that collects information requests from mobile users and delivers data while users are going through the coverage area. Infostations can be located in heavily populated areas such as airports, shops, pubs, hotels, and along highways. One of the technologies that have the potential to deliver the envisaged high-data rate infostation services is the UWB signaling [3]. The UWB has the basic attributes of extremely low transmission power, operating at unlicensed frequency, high data rate, multipath immunity and low cost. Existing channel characterization and measurement for the UWB channel have been limited to the case where the channel is assumed to be stationary over the transmission duration. However, for many infostation scenarios, time variation is expected due to the mobility of one of the communication terminals/scatterers. Hence, the existing channel models cannot be used to describe this new target scenario where terminal mobility is expected.

Time-varying channels are often modeled as stationary random processes using the concept of the wide-sense stationary uncorrelated scattering (WSSUS) assumption [4]. Unfortunately, in time-varying UWB channel, the WSSUS assumption is invalid. The nature of the time-varying channel is such that the spatial structures of the multipath components, i.e., their number, time-of-arrivals (TOA), angle-of-arrivals (AOA) and magnitudes, change with time and location, leading to nonstationary statistics. Hence, non-WSSUS characterization [5, 6] of the channel is required. For the UWB channel, the fine time resolution implies narrow delay bins which enable paths to move fast from one tap to another [7]. Hence, the time evolution of the UWB channel cannot be decomposed into the time evolution of the individual taps, but of the individual paths.

In this article, we present the measurement and the descriptions of channel parameters for the time-varying Infostation UWB channel. We also consider how such parameters can be used to improve system performance in terms of combating ICI in the case of multiband OFDM and mismatch in channel estimation.

The rest of this paper is organized as follows. In Section 2, the basic system model is specified. The Infostation UWB channel measurement setup is presented in Section 3. Section 4 is devoted to describing the post processing of the measurement data and the description of the how the channel parameters can be used to improve system performance in terms of optimally combating ISI and ICI in the case of multiband OFDM.

## 2. SYSTEM MODEL

Channels can be characterized by their response function in time and/or frequency domain say $\mathcal{P}(t, f)$. The variation among the statistics of the measured channel responses taken over a given appreciable interval is assumed to be insignificant (stationary) in the WSSUS case. Unfortunately, in time-varying UWB channel this is not the case as the channel is non-WSSUS. In essence, non-WSSUS scattering function can be viewed as a set of evolutionary functions that are more or less the instantaneous responses $\mathcal{P}(t, f)_i$, $i = 1, 2, 3, \ldots, I$ of the channel to an input. Although the coherence parameters of these instantaneous channel realizations vary from one to another, for practical rationality we consider channel coherency only with respect to the reference channels response regard as being WSSUS say $\mathcal{P}(t, f)_1$. The coherency of $\mathcal{P}(t, f)_1$ is ensured by restricting

(a)                                                (b)
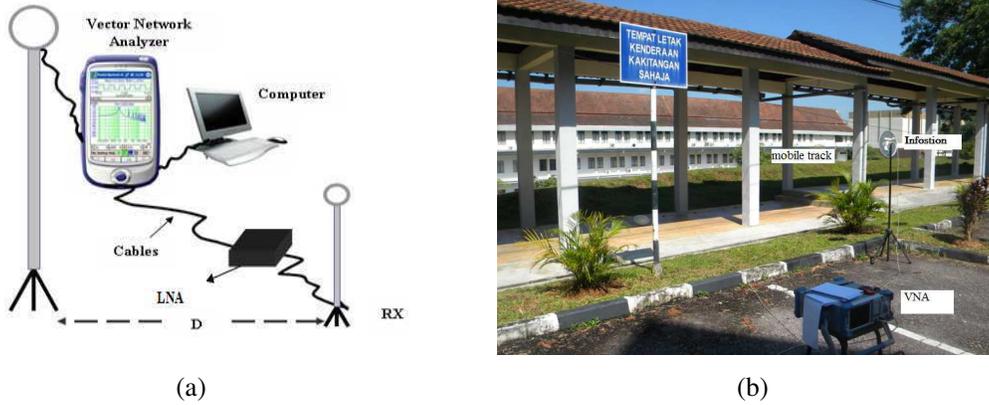
Figure 1: (a) Illustration of measurement setup. (b) Real measurement setup.

the measurement sampling time $J_v$ at $J_v = \lambda/2$. All other sets of $\Psi = \{\mathcal{P}(\tau, s)_i : \{i \neq 1\} \in Z\}$ are defined only by stationarity the parameters. Hence, the non-WSSUS channel is completely characterized by the coherence time $T_c$ and bandwidth $B_c$ [8], and the stationarity time $T_s$ and bandwidth $B_s$ [5].

## 3. INFOSTATION UWB CHANNEL MEASUREMENT

The complex channel response is measured with a vector analyzer (VNA) R&S®ZVL13. Measurements were carried out at various locations along a path way within the vicinity of Wireless Communication Centre (WCC) complex Universiti Teknologi Malaysia, as shown in Fig. 1 for the frequency range 3.1–3.628 GHz. The speed of the mobile is about 2 m/s, and measurements were taken at each location marked $A_1 - A_8$. At each location, the measurement is repeated 50 times. The VNA records the variation of 1001 complex tones within the band. This recording is done by sweeping the spectrum in about $20 \times J_v$ time interval. Apart from the mobile antenna, all the objects (potential scatterers) are kept stationary throughout the duration of the measurement. The antennas (monopoles) are of the same height, 1.5 m and the transmit power is $-42$ dB for all measurements. The signal from the receiving antenna is passed through a low noise amplifier (LNA) with a gain of 24 dB. The distances between the locations are, $A_1 - A_2 = 40$ cm, $A_2 - A_3 = 40$ cm, $A_3 - A_4 = 40$ cm, $A_4 - A_5 = 40$ cm, $A_5 - A_6 = 40$ cm, $A_6 - A_7 = 40$ cm and $A_7 - A_8 = 40$ cm.

## 4. MEASUREMENT DATA PROCESSING AND PARAMETER DESCRIPTION

The description of the post processing and parameter description for the channel measurement data is given in this section. Since the velocity of the mobile is constant throughout the measurement run, and LOS propagation exists for all measurements, the coherence time for all measurement is approximately constant. Hence, the values of $T_s/T_c$ at $A_1$, $A_2$, $A_3$, $A_4$, $A_5$, $A_6$, $A_7$ and $A_8$ are infinity as long as constant velocity is maintained and LOS propagation exists.

The VNA effectively receives a channel output $Y(t)$. In order to obtain the statistical model of the time-variant response from the measured complex channel responses, we apply the autoregressive (AR) model proposed in [9]. Let $Y(f_p, t; A)$ be the time-varying complex received sign measured at a location $A$ and time $t$. Then the first and second order statistics of the measured channel are captured by the model: $Y(f_p, t; A) = \sum_{n=1}^{N} a_n Y(f_{p-n}, t; A) + V(f_p)$, where $V(f_p)$ is a complex white noise process and $a_n$ is the function representing the $n$th time-varying AR coefficient. We take the inverse fast Fourier transform (IFFT) of $Y(t)$ to arrive at the passband time domain response of the system. We choose $2^{15}$ — point IFFT which ensures an oversampled period $T$ of 6.1035 ps, which is many times oversampled compared to the Nyquist rate. This oversampling is critical to our analyses as it allows us to accurately approximate the delay version of the received signal as a delay of indices in its sampled version. At a threshold of $-10$ dB, the measured responses are sampled at the interval of $1/(2BT)$, where $B = 528$ MHz is the bandwidth of the system. The normalized PDP for the positions $A_1$, $A_2$, $A_3$, $A_4$, $A_5$, $A_6$, $A_7$ and $A_8$ are shown in Fig. 2.

From Fig. 2, the coherence bandwidth value of 7.56 MHz is computed by assuming that the response at the reference position $A_1$ upholds the WSSUS assumption. The computed $B_s$ for the
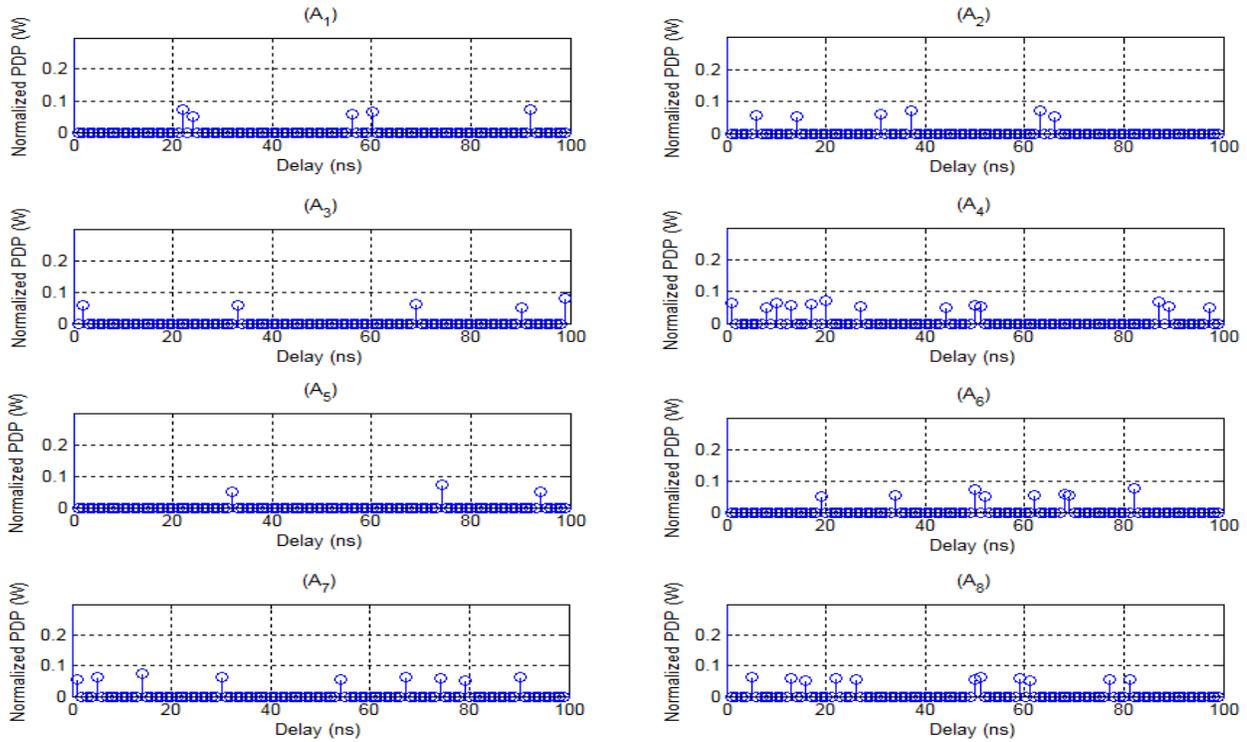
Figure 2: Normalized PDP (in watts) for positions $A_1$, $A_2$, $A_3$, $A_4$, $A_5$, $A_6$, $A_7$ and $A_8$.

positions $A_2$, $A_3$, $A_4$, $A_5$, $A_6$, $A_7$ and $A_8$ (non-WSSUS) are approximately 33.47 MHz, 36.6 MHz, 91.7 MHz, 1711.33 MHz, 114.6 MHz, 76.88 MHz and 306.22 MHz, respectively. These $B_s$ values are computed at $-10$ dB threshold. The implication of the ratio $B_s/B_c$ can be observed in the case of multiband orthogonal frequency division multiplex (MB-OFDM) UWB. Let us consider the MB-OFDM system designed with $Ns$ number of subcarriers and subcarrier spacing of $Fs$ MHz. In order to combat fading in MB-OFDM, the bandwidths of the subcarriers should be equal or less than the $B_c$ to avoid ISI. However, the choice of small value for $Fs$ implies that the system will be more susceptible to ICI. Hence, the choice of the value of $Fs$ should be optimal between combating frequency selective fading and ICI. If we consider a total bandwidth of 528 MHz, the value of $Fs$ for 128, 64 32 and 16 subcarriers are 4.125 MHz, 8.25 MHz, 16.5 MHz and 33 MHz, respectively. Hence, the choice of 128 subcarrier ensures good ISI performance but with increased error due to ICI, and the choice of 16 subcarriers ensures good ICI performance but with increased susceptibility to ICI. The optimal choice will be to choose the number of subcarriers such that $kFs = B_c$, where the value of $k$ should be chosen to take care of the time-varying nature of $B_c$. Conventionally, $k$ is chosen to be fixed and of low value, which implies a fixed number of subcarriers. The SNR degradation caused by ICI is given by [10]:

$$D \cong \frac{10}{\ln 10} \frac{1}{3} \left( \frac{\pi f_e}{Fs} \right)^2 \left( 1 + \frac{E_s}{N_0} \right) \tag{1}$$

where $f_e$ is the frequency offset. If we consider the above channel measurement, then the SNR degradations for 128, 64, 32 and 22 subcarriers are shown in Fig. 3.

Figure 3 shows that the SNR degradation for 22 subcarriers ($k = 1$) is better than the performance at $k < 1$ (128, 64 and 32 subcarriers). However, when $k$ is greater than unity, ISI degradation sets in. This implies that instead of a fixed value for $k$, some form of adaptive subcarrier bandwidth can be employed. The value of stationarity bandwidth can provide information that can be used to adjust $k$ for optimal performance. The values of $B_s/B_c$ at $A_1$, $A_2$, $A_3$, $A_4$, $A_5$, $A_6$, $A_7$ and $A_8$ are approximately, $\infty$, 4.4, 4.8, 12.13, 226.5, 15.2, 10.2, 40.5, respectively. We can define the bandwidth utilization parameter $U$ by: $U \cong -B_{co}^{-1} (((\Im B_{co})/\Im - 1) - B_{co})$, where, $\Im = B_s/B_c$ and $B_{co}$ is the reference coherence bandwidth. Hence, the values of $U$ at $A_1$, $A_2$, $A_3$, $A_4$, $A_5$, $A_6$, $A_7$ and $A_8$ are approximately, $-18.42\%$, 26.02%, 8.98%, 0.44%, 7.06%, 10.90% and 2.41%, respectively. The negative sign in $U$ indicates that $k$ is greater than 1 by the given percentage and the positive
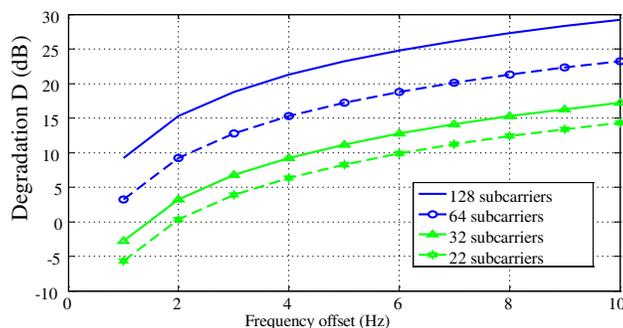
Figure 3: SNR degradation as a function of subcarrier spacing.

sign in $U$ indicates that $k$ is less than 1 by the given percentage. Therefore, this nonstationarity information can be employed to adjust the values of $k$ in order to optimize the system performance at any time instant.

## 5. CONCLUSION

The measurement and parameter description for the time-varying UWB Infostation channel is presented. The analysis emphasized on the nonstationary properties of the UWB due to the movement of the mobile terminal. Coherence and stationarity parameters were obtained and used to analyze the performance of the measured channel with respect to ICI and ISI in MB-OFDM. From results it implies that some form of adaptive technique using the joint knowledge of the coherence and stationarity parameters will greatly improve the performance of the Infostation channel in terms of combating ICI and ISI.

## ACKNOWLEDGMENT

## REFERENCES

1. Goodman, D. J., J. Borras, N. B. Mandayam, and R. D. Yates, "Infostation: A new system model for data and messaging services," *Proc. IEEE 47th Vehicular Technology Conf.*, May 969–973, 1997.
2. Rajappan, G., et al., "Mobile infostation network technology," *Proc. SPIE on Wireless Sensing and Processing*, Orlando, 2006.
3. Chowdhury, H., J. P. Mekela, and K. Pahlavan, "Statistical information transfer in random crossing of infostation coverage," *Proc. 2005 Finnish Signal Processing Symposium*, Kuopio, Finland, August 2005.
4. Bello, P., "Characterization of randomly time-variant linear channel," *IEEE Trans. Commun.*, Vol. 11, No. 4, 360–393, 1963.
5. Matz, G., "On non-WSSUS wireless fading channels," *IEEE Trans. Wirel. Commun*, Vol. 4, No. 5, 2465–2478, 2005.
6. Chude Okonkwo, U. A. K., et al., "Time-scale domain characterization of nonstationary wideband vehicle-to-vehicle propagation channel," *Proc. IEEE APACE 2010*, 1–6, Malaysia, November 9–10, 2010.
7. Tse, D. and P. Viswanath, *Fundamentals of Wireless Communications*, Cambridge University Press, New York, 2005.
8. Molisch, A. F., *Wireless Communications*, 2nd Edition, John Wiley, New Jersey, 2005.
9. Howard, S. J. and K. Pahlavan, "Autoregressive modelling of wideband indoor radio propagation," *IEEE Trans. Commun.*, Vol. 40, No. 9, 1540–1552, 1992.
10. Pollet, T., M. Blade, and M. Moeneclaey, "BER sensitivity of OFDM systems to carrier frequency offset and wiener phase noise," *IEEE Trans. Commun.*, Vol. 43, No. 2/3/4, 191–193, 1995.

# Small Loop-type Mobile Antenna with Less Interference of Nearby Conductors for Wi-Fi Application

**Hyunmin Jang**, **Yang Liu, Jongin Ryu**, **and Hyeongdong Kim**

Hanyang University, Seoul, Korea

**Abstract**— A small loop-type mobile antenna with less interference of nearby conductors for Wi-Fi application is proposed. The proposed antenna has a small volume of $8 \times 4 \times 3 \, \text{mm}^3$ to be easily implemented within mobile devices and a simple structure using chip capacitors without any extra matching network. In this paper, we place a LCD under the proposed antenna to discuss the effects of conductors. The proposed antenna has less effect to the LCD and radiates efficiently over Wi-Fi band. The $-6 \, \text{dB}$ bandwidth was measured as $120 \, \text{MHz}$ from 2.38 to 2.5 GHz, and the measured antenna efficiency is 50.2%.

## 1. INTRODUCTION

Recently, the smart phone is widely used in our life to do many things such as social network services (SNS), a media player, a camera and web browser. For customer satisfaction, mobile device manufacturers tend to design a smart phone which has a large and high-resolution display, a sensitive touch panel and compact design. Because of these demands, an antenna which is applied in mobile devices is strongly required to reduce its size on the printed circuit board (PCB). To reduce the size of an antenna, various methods have been reported in several reports [1–4] such as suitably designing shorting structures of planar inverted-F antenna (PIFA) and using high permittivity. However, those methods were needed to test proposed antennas under the practical condition to guarantee its performances because the performance of an antenna can be affected by changes in circumstances around the antenna, especially nearby conductors.

In this paper, we proposed a small loop-type mobile antenna with less interference of nearby conductors for Wi-Fi application. To describe effects of nearby conductors, we arranged a $45 \times 78 \times 1.75 \, \text{mm}^3$ liquid crystal display (LCD) under the ground plane as a nearby conductor. The resonant frequency and input impedance of an antenna are controlled by changing the values of chip capacitors without extra matching circuits around a clearance. The result shows a quite good affordable bandwidth with suitable realized efficiency over Wi-Fi band even though the proposed antenna is fully covered with the LCD.

## 2. ANTENNA DESIGN

As shown in Fig. 1, the proposed antenna structure was very simple with three chip capacitors. The proposed antenna had $4 \times 8 \, \text{mm}^2$ clearance on a 1 mm thick FR4 substrate of size $40 \times 80 \, \text{mm}^2$. Top and bottom side of the FR4 substrate was covered with a copper plane and connected through via. The clearance existed on both sides. The LCD was arranged in parallel with the ground plane. A gap was 2 mm between the ground plane and the LCD. The proposed antenna was composed of a feeding loop and a radiating loop with chip capacitors. The feeding loop controlled the input impedance by changing the feeding loop size or the chip capacitor $C_1$ value and produced magnetic coupling to excite the radiating loop ($C_1 = 0.5 \, \text{pF}$ used here). The radiating loop consisted of chip capacitors which controlled the resonant frequency and a $1.5(W) \times 5(L) \times 3(H) \, \text{mm}^3$ conductor element which reduced the interference of nearby conductor as the LCD ($C_2 = 0.7 \, \text{pF}$ and $C_3 = 0.7 \, \text{pF}$ used here) [5]. The proposed antenna was fed through a coplanar waveguide with ground (CPWG) whose width and length are 0.8 mm and 5 mm, respectively. Through the radiating loop, loop-type current distribution appears on the ground plane. It means the ground plane works as a main radiator. Therefore, the proposed antenna can be regarded a ground antenna [6]. The size of the chip capacitor was $1 \times 0.5 \times 0.5 \, \text{mm}^3$ for length, width, and height, respectively.

## 3. SIMULATED AND MEASURED RESULTS

Figure 2 shows the simulated and measured return loss for the proposed antenna. The simulated result was obtained by using Ansoft HFSS and good agreement with the measured result. The simulated and measured return losses were $-30.0 \, \text{dB}$ and $-35.1 \, \text{dB}$ at the resonant frequency (2.44 GHz), respectively. The measured bandwidth with $-6 \, \text{dB}$ return loss was from 2.38 to 2.5 GHz, which
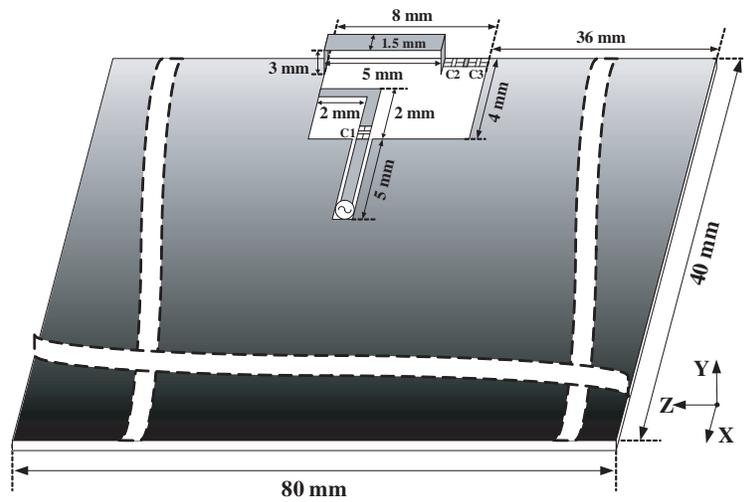
Figure 1: Configuration of the proposed antenna.
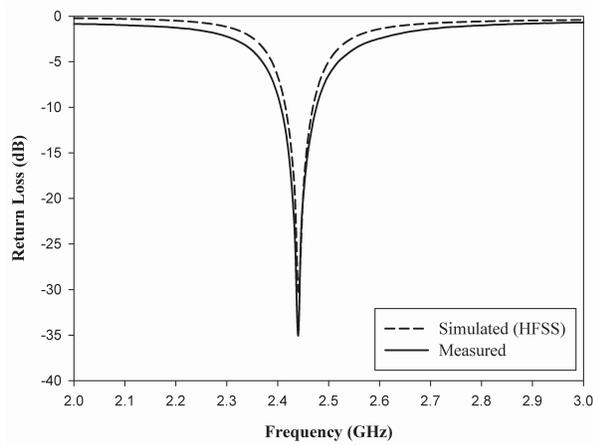


Figure 2: Simulated and measured return loss.
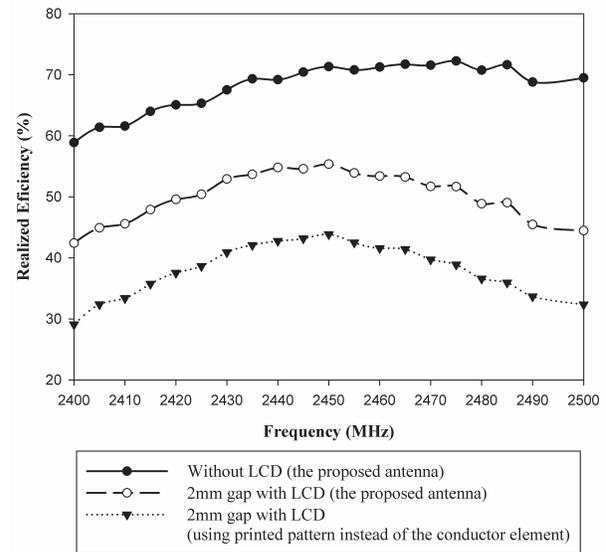


Figure 3: Measured realized efficiency.
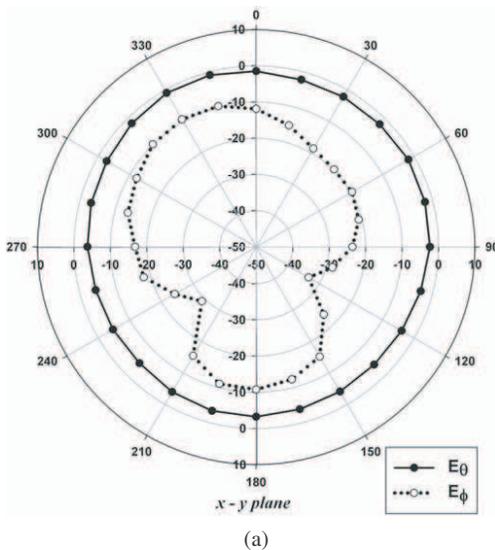


(a)
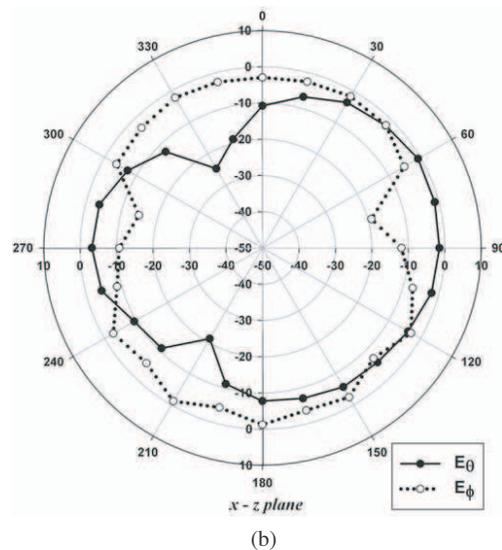
(b)
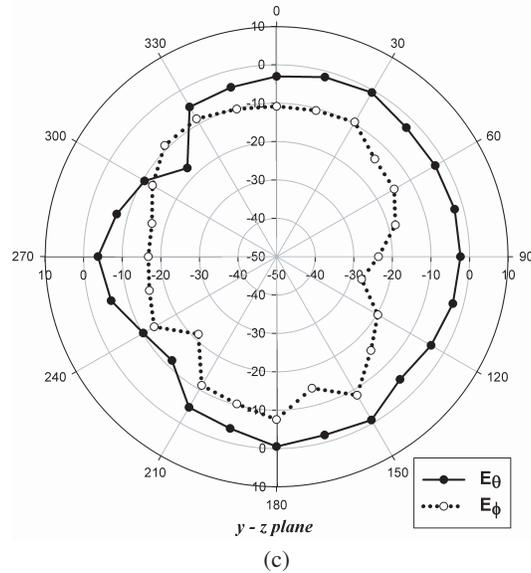
Figure 4: Measured radiation patterns.

properly covers Wi-Fi band. As shown in Fig. 3, the measured realized efficiency decreased about 18% over Wi-Fi band when the LCD was arranged in parallel with the proposed antenna and ground plane. However, the proposed antenna was still suitable for Wi-Fi application because of its adequate realized efficiency. In addition, the measured radiation efficiency from 2.4 to 2.5 GHz was about 12% higher than using printed pattern instead of the conductor element in the radiating loop. This result demonstrated that the proposed antenna had less interference of nearby conductors as the LCD. Fig. 4 shows the measured radiation patterns in $xy$-, $xz$-, $yz$-planes for the frequency at 2.44 GHz. The omnidirectional radiation pattern was measured in $E\phi$ of the $xy$-plnae.

## 4. CONCLUSION

The small loop-type mobile antenna with less interference of nearby conductors for Wi-Fi application is presented. The proposed antenna has simpler structure and more compact size than conventional antennas for mobile devices. The Resonant frequency and input impedance controls can be easily accomplished using chip capacitors, so additional matching network is not necessary. To reduce the effects of the nearby conductors, the $1.5 \times 5 \times 3\,\mathrm{mm}^3$ conductor element is used in the radiating loop. The simulated and measured results show the performances of the proposed antenna are not only enough to meet requirements to obtain a public institution's approval but also able to apply the 2.4 GHz ISM band application such as Wi-Fi, Bluetooth and Zigbee. From these advantages, the proposed antenna can be efficiently applied in the mobile devices market.

## ACKNOWLEDGMENT

## REFERENCES

1. Cho, Y.-J., Y.-S. Shin, and S.-O. Park, "Internal PIFA for 2.4/5 GHz WLAN applications," *Electron. Lett.*, Vol. 42, 8–10, 2006.
2. Yu, Y.-C. and J.-H. Tarng, "A novel modified multiband planar inverted-F antenna," *IEEE Antennas Wirel. Propag. Lett.*, Vol. 8, 189–192, 2009.
3. Chiu, C.-Y., K.-M. Shum, and C.-H. Chan, "Tunable via-patch loaded PIFA with size reduction," *IEEE Trans. Antennas Propag.*, Vol. 55, 65–71, 2007.
4. Ryu, H. K., E. Kim, and J. M. Woo, "Miniaturisation of printed inverted-F antenna using chip coupler for bluetooth applications," *Electron. Lett.*, Vol. 46, 883–885, April 2010.
5. Jang, H., H. Choi, and D. Lee, "Ground radiator using capacitor (Priority number: 10-2010-0133923)," Patent Application KR, 2011-0031913.
6. Choi, H., O. Cho, H. Lee, and B. Park, "Ground radiation antenna (Priority number: 10-2010-0056207)," Patent Application KR 2010-0133919.